

AD-A226 177

MATERIALS  
RESEARCH  
SOCIETY  
SYMPOSIUM PROCEEDINGS



VOLUME 173

# Advanced Organic Solid State Materials

EDITORS

Long Y. Chiang  
Paul M. Chaikin  
Dwayne O. Cowan

DTIC FILE COPY

DTIC  
ELECTE  
AUG 31 1990  
S D

DISTRIBUTION STATEMENT A  
Approved for public release  
Distribution Unlimited

MRS

# REPORT DOCUMENTATION PAGE

Form Approved  
OMB No. 0704-0188

Public reporting burden for this collection of information is estimated to average 1 hour per response, including the time for reviewing instructions, searching existing data sources, gathering and maintaining the data needed, and completing and reviewing the collection of information. Send comments regarding this burden estimate or any other aspect of the collection of information, including suggestions for reducing the burden, to Washington Headquarters Service, Directorate for Information Operations and Reports, 1215 Jefferson Davis Highway, Suite 1204, Arlington, VA 22202-4302, and to the Office of Management and Budget, Paperwork Reduction Project (0704-0188), Washington, DC 20503.

<b>1. AGENCY USE ONLY (Leave blank)</b>		<b>2. REPORT DATE</b> 8 August 1990	<b>3. REPORT TYPE AND DATES COVERED</b> Final 26 Nov 89 - 25 Nov 90	
<b>4. TITLE AND SUBTITLE</b> Symposium on Polymer-Based Molecular Composites and Symposium on Electrical, Optical, and Magnetic Properties of Organic Solid State Materials			<b>5. FUNDING NUMBERS</b> 61102F 2303 A3	
<b>6. AUTHOR(S)</b> J. E. Mark, Long Y. Chiang, Paul M. Chaikin, and Dwaine O. Cowan				
<b>7. PERFORMING ORGANIZATION NAME(S) AND ADDRESS(ES)</b> Materials Research Society 9800 McKnight Road, Suite 327 Pittsburgh, PA 15237-6005			<b>8. PERFORMING ORGANIZATION REPORT NUMBER</b> AFOSR-TR-90 0884	
<b>9. SPONSORING/MONITORING AGENCY NAME(S) AND ADDRESS(ES)</b> AFOSR/NC Building 410, Bolling AFB DC 20332-6448			<b>10. SPONSORING/MONITORING AGENCY REPORT NUMBER</b> AFOSR-90-0089	
<b>11. SUPPLEMENTARY NOTES</b>				
<b>12a. DISTRIBUTION/AVAILABILITY STATEMENT</b> APPROVED FOR PUBLIC RELEASE; DISTRIBUTION IS UNLIMITED.			<b>12b. DISTRIBUTION CODE</b>	
<b>13. ABSTRACT (Maximum 200 words)</b> See Back				
<b>14. SUBJECT TERMS</b>			<b>15. NUMBER OF PAGES</b> 710	
			<b>16. PRICE CODE</b>	
<b>17. SECURITY CLASSIFICATION OF REPORT</b> UNCLASSIFIED	<b>18. SECURITY CLASSIFICATION OF THIS PAGE</b> UNCLASSIFIED	<b>19. SECURITY CLASSIFICATION OF ABSTRACT</b> UNCLASSIFIED	<b>20. LIMITATION OF ABSTRACT</b> SAR	

## Advanced Organic Solid State Materials

AFOSR-TR- 90 0884

MATERIALS RESEARCH SOCIETY SYMPOSIUM PROCEEDINGS VOLUME 173

## Advanced Organic Solid State Materials

Symposium held November 27-December 2, 1989, Boston,  
Massachusetts, U.S.A.

EDITORS:

**Long Y. Chiang**

Exxon Research and Engineering Company, Annandale, New Jersey, U.S.A.

**Paul M. Chaikin**

Princeton University, Princeton, New Jersey, U.S.A.

**Dwaine O. Cowan**

The Johns Hopkins University, Baltimore, Maryland, U.S.A.

AVAILABLE FOR \$47.00 from Materials  
Research Society, 9800 McKnight Rd.  
Suite 327, Pittsburgh, PA 15237  
TELECON 8/28/90

VG

Accession For	
NTIS CRA&I	<input checked="" type="checkbox"/>
DTIC TAB	<input type="checkbox"/>
Unannounced	<input type="checkbox"/>
Justification	
By	47.00
Distribution	per call
Availability Codes	
Dist	Avail and/or Special
A-1	21



MATERIALS RESEARCH SOCIETY  
Pittsburgh, Pennsylvania





This work was supported in part by the U.S. Army Research Office under Grant Number DAAL03-89-G-0121. The views, opinions, and/or findings contained in this report are those of the authors and should not be construed as an official Department of the Army position, policy, or decision unless so designated by other documentation.

This work was supported by the Air Force Office of Scientific Research, Air Force Systems Command, USAF, under Grant Number AFOSR 90-0089.

Single article reprints from this publication are available through University Microfilms Inc., 300 North Zeeb Road, Ann Arbor, Michigan 48106

CODEN: MRSPDH

Copyright 1990 by Materials Research Society.  
All rights reserved.

This book has been registered with Copyright Clearance Center, Inc. For further information, please contact the Copyright Clearance Center, Salem, Massachusetts.

Published by:

Materials Research Society  
9800 McKnight Road  
Pittsburgh, Pennsylvania 15237  
Telephone (412) 367-3003  
Fax (412) 367-4373

Library of Congress Cataloging in Publication Data

Advanced organic solid state materials : symposium held November 27-December 2, 1989, Boston, Massachusetts, U.S.A. / editors, Long Y. Chiang, Paul M. Chaikin, Dwaine O. Cowan.

p. cm. — (Materials Research Society symposium proceedings : ISSN 0272-9172 ; v. 173)

"Proceedings of the Symposium on the Electrical, Optical, and Magnet Properties of Organic Solid State Materials held at the Fall Meeting of the Materials Research Society"—Pref.

Includes bibliographical references.

ISBN 1-55899-061-5

1. Organic conductors—Congresses. 2. Organic compounds—Optical properties. I. Chiang, Long Y. II. Chaikin, Paul M. III. Cowan, Dwaine O. IV. Materials Research Society. Fall Meeting (1989 : Boston, Mass.) V. Symposium on the Electrical, Optical, and Magnet Properties of Organic Solid State Materials (1989 : Boston, Mass.) VI. Series: Materials Research Society symposium proceedings : v. 173.

QD382.C66A35 1990  
620.1'1297—dc20

90-5598  
CIP

Manufactured in the United States of America

## Contents

PREFACE	xv
MATERIALS RESEARCH SOCIETY SYMPOSIUM PROCEEDINGS	xvii
PART I: ORGANIC FERROMAGNETICS	
*ELECTRON-DONATING RADIALENES. POTENTIAL DONORS FOR MOLECULAR ORGANIC (SUPER)CONDUCTORS AND FERROMAGNETS Z. Yoshida, T. Sugimoto, and Y. Misaki	3
SYNTHESIS OF BULK HIGH SPIN DENSITY CHARGE TRANSFER COMPLEXES FOR ORGANIC MAGNETS Long Y. Chiang, Ravindra B. Upasani, D.P. Goshorn, and P. Tindall	15
CHARGE TRANSFER COMPLEX OF HEXAKIS (ALKYLTHIO) BENZENE WITH TETRAFLUOROTETRACYANOQUINODIMETHANE (tEDTB) <sub>2</sub> TCNQF <sub>4</sub> D. Chasseau, M. Alleaume, G. Bravic, R. Lapouyade, J.P. Morand, J. Amiell, and P. Delhaes	27
FERROMAGNETIC INTERMOLECULAR INTERACTION AND CRYSTAL STRUCTURE OF -NITRONYL NITROXIDE Kunio Awaga, Tamotsu Inabe, and Yusei Maruyama	33
*MAGNETIC PROPERTIES OF MICROCRYSTALLINE "POLY(PHENYL-DIACETYLENES)" CARRYING RADICAL OR CARBENE CENTERS ON THE SIDE CHAINS Noboru Koga, Katsuya Inoue, Noriko Sasagawa, and Hiizu Iwamura	39
*ROLE OF TOPOLOGY IN SPIN ALIGNMENT OF ORGANIC MATERIALS Koichi Itoh, Takeji Takui, Yoshio Teki, and Takamasa Kinoshita	51
ROLE OF HIGH-SPIN MOLECULES AS MODELS FOR ORGANIC FERRO- AND FERRI-MAGNETS, AND PI-TOPOREGULATED MAGNETIC POLYMERS Takeji Takui, Makoto Endoh, Masayuki Okamoto, Kazunobu Satoh, Toyohiro Shichiri, Yoshio Teki, Takamasa Kinoshita, and Koichi Itoh	63
THERMAL STABILITY OF MAGNETIC PROPERTIES IN DEHYDROGENATED TRIARYLMETHANE RESINS Michiya Ota and Sugio Otani	71
POLYPHENOXY RADICALS: SYNTHESIS AND HOMO-POLYMERIZATION OF 2-(3,5-DI-t-BUTYL-4-HYDROXYPHENYL)ISOBUTYL METHACRYLATE Ravindra B. Upasani, Long Y. Chiang, and D.P. Goshorn	77
*Invited Paper	

ORGANIC POLYRADICAL MODELS FOR ORGANIC MAGNETIC MATERIALS	83
David A. Modarelli, Frank C. Rossitto, Masaki Minato, and Paul M. Lahti	
FERROMAGNETIC INTERACTIONS IN A SERIES OF SCHIFF-BASE METAL-ORGANIC POLYMERS	89
F. Palacio, F.J. Lazaro, J. Garin, J. Reyes, and M.C. Moron	
PART II: ORGANIC METALS AND SUPERCONDUCTORS	
*PREPARATION AND PROPERTIES OF ORGANIC SUPERCONDUCTOR $\kappa$ -(BEDT-TTF) <sub>2</sub> Cu(NCS) <sub>2</sub> AND ITS RELATED MATERIALS	95
Gunzi Saito	
*SUPERCONDUCTING AND NORMAL STATE PROPERTIES OF ORGANIC METALS $\beta$ -(BEDT-TTF) <sub>2</sub> X	107
M. Tokumoto, N. Kinoshita, K. Murata, H. Bando, and H. Anzai	
TRANSFER INTEGRALS AND BAND STRUCTURES IN (ET) <sub>2</sub> X SALTS	119
Oliver H. LeBlanc, Jr., Margaret L. Blohm, and Richard P. Messmer	
SPECIFIC HEAT MEASUREMENTS ON $\kappa$ -(BEDT-TTF) <sub>2</sub> Cu(NCS) <sub>2</sub>	125
R.G. Goodrich and Jing-Chun Xu	
PRESSURE DEPENDENCE OF THE STRUCTURAL AND ELECTRONIC PROPERTIES OF ORGANIC SUPERCONDUCTORS	131
D. Chasseau, J. Gaultier, H. Houbib, M. Rahal, L. Ducasse, M. Kurmoo, and P. Day	
THIN FILM FORMATIONS OF CHARGE TRANSFER COMPLEXES WITH METALLIC PROPERTIES BY VACUUM DEPOSITION METHOD	137
M. Yudasaka, K. Hironaga, H. Yamochi, K. Nakanishi, and G. Saito	
SYNTHESIS, CRYSTAL STRUCTURE AND SPECTROSCOPIC STUDIES OF NEW CHARGE TRANSFER COMPOUNDS OBTAINED BY REACTION OF TTF AND THE POLYOXOANION [Mo <sub>6</sub> O <sub>19</sub> ] <sup>2-</sup>	143
C. Bellitto, D. Attanasio, M. Bonamico, V. Fares, P. Imperatori, and S. Patrizio	
A NEW SYNTHETIC METAL PRECURSOR: DIMETHYL-TETRATHIO-TETRACENE AND RELATED COMPOUNDS	149
Toshio Maruo, Megh Singh, M. Thomas Jones, Nigam P. Rath, and Dong Min	
TETRANITROQUINODIMETHANE (TNQ)--ELECTRON-DEFICIENT PROTOTYPE FOR A NEW SERIES OF ORGANIC SOLID STATE MATERIALS	155
David J. Vanderah, A.T. Nielsen, R.A. Hollins, and Chris Baum	

\*Invited Paper

ELECTRON PARAMAGNETIC RESONANCE STUDIES OF DONOR-ACCEPTOR SALTS IN POLYMER MEDIA Yang-Cheng Fann and Susan Ann Jansen	161
STUDIES ON THE FORMATION OF SWITCHING AND MEMORY STORAGE MATERIALS CONSTRUCTED FROM METALLO-ORGANIC CHARGE-TRANSFER COMPLEXES Hailing Duan, Dwaine O. Cowan, and Jerome Kruger	165
PHYSICAL CHARACTERIZATION OF ORGANIC RADICALS BY LOW-FIELD EPR SPECTROMETRY Mehdi Moussavi, Marc Beranger, Denis Luret, Nelly Kernevez, and Liliane Secourgeon	171
*NEW ELECTRICALLY CONDUCTING SOLIDS BASED ON NICKEL(II) - BIS(1,3-DITHIOLE-2-THIONE-4,5-DISELENOLATE) A.M. Kini, M.A. Beno, S. Budz, H.H. Wang, and J.M. Williams	177
BRIDGED MACROCYCLIC TRANSITION METAL COMPLEXES, A NEW TYPE OF SEMICONDUCTING MATERIALS Michael Hanack, A. Hirsch, A. Lange, M. Rein, G. Renz, and P. Vermehren	189
DISCOTIC LIQUID CRYSTALLINE PORPHYRINS: PHOTO-PHYSICAL AND PHOTOELECTRICAL PROPERTIES OF LARGE-AREA CRYSTALLINE FILMS Brian A. Gregg, Marye Anne Fox, and Allen J. Bard	199
*LOW-DIMENSIONAL CRITICAL BEHAVIORS AND COMPETITION BETWEEN ORDER PARAMETERS IN THE ORGANIC METAL $(TMTSF)_2ClO_4$ F. Pesty, P. Garoche, and M. Heritier	205
HIGH MAGNETIC FIELD PHASES OF THE $(TMTSF)_2X$ ( $X = ClO_4, PF_6$ ) CHARGE TRANSFER COMPLEXES J.S. Brooks, N.A. Fortune, P.M. Chaikin, L.Y. Chiang, G. Montambaux, and Jos. A.A.J. Perenboom	217
MAGNETIC EVIDENCE FOR REENTRANT FIELD-INDUCED SPIN DENSITY WAVES M.J. Naughton, R.V. Chamberlin, X. Yan, P.M. Chaikin, and L.Y. Chiang	227
SOUND PROPAGATION IN CDW AND SDW Attila Virosztek and Kazumi Maki	233
SOUND VELOCITY STUDY OF BECHGAARD SALTS $(TMTSF)_2PF_6$ AND $(TMTSF)_2ClO_4$ X.D. Shi, L. Chiang, R. Upasani, and P.M. Chaikin	239
SOUND VELOCITY MEASUREMENTS IN $(TMTTF)_2X$ SALTS, $X = ReO_4, AsF_6, SbF_6$ S.E. Brown, H.H.S. Javadi, and R. Laversanne	245

\*Invited Paper

QUANTUM HALL EFFECT AND RAPID OSCILLATIONS IN (TMTSF) <sub>2</sub> PF <sub>6</sub> UNDER PRESSURE	251
S.T. Hannahs, J.S. Brooks, W. Kang, P.M. Chaikin, L.Y. Chiang, and R. Upasani	
ANGULAR DEPENDENCE OF THE MAGNETORESISTANCE IN (TMTSF) <sub>2</sub> ClO <sub>4</sub>	257
M.J. Naughton, O.H. Chung, L.Y. Chiang, S.T. Hannahs, and J.S. Brooks	
ELECTRON TUNNELING IN CHARGE-DENSITY AND SPIN-DENSITY WAVES	263
X.Z. Huang and K. Maki	
PART III: ORGANIC CONDUCTING POLYMERS	
FIBERS OF CONDUCTING POLYMERS: HIGH ELECTRICAL CONDUCTIVITY COMBINED WITH ATTRACTIVE MECHANICAL PROPERTIES	269
Alejandro Andreatta, S. Tokito, P. Smith, and A.J. Heeger	
*THE POLYANILINES: A NOVEL CLASS OF CONDUCTING POLYMERS	283
Alan G. MacDiarmid and Arthur J. Epstein	
*POLYANILINE: AN OLD POLYMER WITH NEW PHYSICS	293
A.J. Epstein and A.G. MacDiarmid	
THE 0.9eV ABSORPTION BAND OF POLYANILINE: A MORPHO- LOGICALLY SENSITIVE ELECTRONIC ABSORPTION	305
D. Zhang, J.-H. Hwang, and S.C. Yang	
AQUEOUS COLLOIDAL DISPERSIONS OF POLYANILINE PARTICLES	311
Steven P. Armes and Mahmoud Aldissi	
V <sub>2</sub> O <sub>5</sub> XEROGELS AS HOSTS FOR CONDUCTIVE POLYMERS. INTER- CALATIVE POLYMERIZATION OF ANILINE, PYRROLE AND 2,2'- BITHIOPHENE	317
Chun-Guey Wu, Henry O. Marcy, Donald C. DeGroot, Carl R. Kannewurf, and Mercouri G. Kanatzidis	
CHEMICAL AND PHYSICAL PROPERTIES OF SOLUBLE PART OF EMERALDINE: COMPARISON WITH INSOLUBLE EMERALDINE	323
R. Laversanne and P. Vaca	
POLYANILINE AS A REVERSIBLY SWITCHABLE ELECTROCHROMIC MATERIAL	329
Woan-Ru Shieh, Sze C. Yang, Charles Marzocco, and Jyun-Huei Hwang	
MOISTURE EFFECTS IN THE CONDUCTING POLYMER, POLYANILINE	335
J.P. Travers, C. Menardo, M. Nechtschein, S.K. Manohar, and A.G. MacDiarmid	

\*Invited Paper

SPECTROSCOPIC AND MOLECULAR WEIGHT STUDIES OF POLY-TOLUIDINES	341
Y. Wei, K.F. Hsueh, S. Nagy, A. Ray, A.G. MacDiarmid, J. Dykins, A.J. Epstein, and G.E. Wnek	
ELECTRICALLY CONDUCTIVE COMPOSITE OF POLYANILINE AND POLY(p-PHENYLENE-TEREPHTHALAMIDE)	347
Xian-Tong Bi, C. Wang, and J.S. Bao	
OPTICAL STUDIES OF POLYANILINES: EFFECTS OF ALKYL RING-SUBSTITUTION AND SOLVENT ENVIRONMENT	353
Anjan Ray, Alan G. MacDiarmid, John M. Ginder, and Arthur J. Epstein	
INFRARED REFLECTION-ABSORPTION STUDY OF THE ANILINE ELECTROPOLYMERIZATION ON STAINLESS STEEL	359
F. Gaillard, G. Bouyssoux, and S.N. Kumar	
EVALUATION OF THIN FILM CAPACITORS FABRICATED FROM HETEROGENEOUS POLYPYRROLE BASED LANGMUIR-BLODGETT FILMS	363
R.B. Rosner and M.F. Rubner	
HETEROCYCLIC POLYMERS AND COPOLYMERS WITH CONTROLLED OPTOELECTRONIC PROPERTIES	369
Jose P. Ruiz, Kasinath Nayak, Andrew D. Child, Dennis S. Marynick, and John R. Reynolds	
SYNTHESIS, STRUCTURE, INFRARED SPECTRA, AND IODINE DOPING OF UNSUBSTITUTED POLYAZINES	375
William B. Euler and Benjamin C. Gill	
GENERATION OF STABLE RADICAL CATIONS (POLARONS) AND DICATIONS (BIPOLARONS) ON MODEL THIOPHENE OLIGOMERS	379
Denis Fichou and Gilles Horowitz	
PHOTOLUMINESCENCE AND ODMR STUDIES OF PRISTINE AND PHOTODEGRADED POLY(3-HEXYLTHIOPHENE) FILMS AND SOLUTIONS	385
L.S. Swanson, J. Shinar, L.R. Lichty, and K. Yoshino	
HELICAL CONFORMATIONS OF CONDUCTING POLYMERS	391
Miklos Kertesz and Changxing Cui	
RESONANT RAMAN SCATTERING OF POLY-3-ALKYLTHIOPHENES	397
C. Botta, S. Luzzati, A. Bolognesi, M. Catellani, S. Destri, and R. Tubino	
HALL EFFECT AND MAGNETORESISTANCE IN UNDOPED POLY(3-HEXYLTHIOPHENE)	403
Azar Assadi, Christer Svensson, and Magnus Willander	
*INSULATOR-METAL TRANSITION AND CONDUCTION PROCESSES IN TRANS-POLYACETYLENE	409
Esther M. Corwell, Howard A. Mizes, and Surendar Jeyadev	

\*Invited Paper

DETERMINATION OF CORRELATION PARAMETERS IN $\pi$ -CONJUGATED POLYMERS	419
J. Tinka Gammel, D.K. Campbell, E.Y. Loh, Jr., S. Mazumdar, and S.N. Dixit	
OPTICAL SPECTROSCOPY OF THE CHARGE ACCUMULATION LAYER IN MIS STRUCTURES WITH POLYMERIC INSULATOR AND SEMI-CONDUCTOR LAYERS	425
J.H. Burroughes and R.H. Friend	
REVERSIBLE PHOTOPRODUCTION OF STABLE CHARGED DEFECTS IN <u>TRANS-POLYACETYLENE</u>	431
Carolyn F. Hoener	
TEMPERATURE DEPENDENCE OF THE PICOSECOND PHOTOCURRENT IN STRETCHED TRANS-POLYACETYLENE FILMS WITH BELOW GAP EXCITATION	437
A.D. Walser, R. Dorsinville, R. Tubino, and R.R. Alfano	
THE EFFECTS OF CONJUGATION LENGTH AND SUBSTITUENTS ON THE CONDUCTIVITY OF OXIDATIVELY DOPED p,p'-DISUBSTITUTED DIPHENYLPOLYENES	443
Linda S. Sapochak, David W. Polis, Art N. Bain, Paul Bryson, Larry R. Dalton, and C.W. Spangler	
THERMALLY ACTIVATED CHARGE HOPPING TRANSPORT STUDIES IN A $\pi$ -CONJUGATED POLYMER	447
L. Samuel, P.N. Sanda, R.D. Miller, and D. Thompson	
BAND-TO-BAND TRANSITIONS IN POLY (PHENYL METHYL SILANE)	453
R.G. Kepler and J.M. Zeigler	
THE DOPING OF POLY-p-PHENYLENE SULFIDE AND ITS OLIGOMERS: A SPECTROSCOPICAL STUDY	459
P. Piaggio, D. Giribone, C. Cuniberti, and G. Dellepiane	

PART IV: NON-LINEAR OPTICAL PROPERTIES  
OF ORGANIC MOLECULES AND POLYMERS

*NONLINEAR OPTICAL POLYMERS: CHALLENGES AND OPPORTUNITIES IN PHOTONICS	467
A.F. Garito, J.W. Wu, G.F. Lipscomb, and R. Lytel	
*NEW SECOND-ORDER NONLINEAR OPTICAL ORGANIC CRYSTALS	487
D.S. Donald, L.-T. Cheng, G. Desiraju, G.R. Meredith, and F.C. Zumsteg	
SYNTHESIS, THERMAL BEHAVIOR, AND SECOND-ORDER NONLINEAR OPTICAL PROPERTIES OF CONJUGATED, ACCEPTOR/DONOR COMPOUNDS	499
James F. Wolfe, Susan P. Ermer, Steven M. Lovejoy, Doris S. Leung, Kenneth P. Aron, Glenn A. Hansen, and Steven P. Bitler	

\*Invited Paper

NOVEL PHOTOCROMIC ZWITTERIONS FOR MULTIFREQUENCY DATA STORAGE	507
G.J. Ashwell, E.J.C. Dawnay, A.P. Kuczynski, and M. Szablewski	
ELECTRO-OPTIC AND NONLINEAR OPTICAL PROPERTIES OF 2,6-DIBROMO-N-METHYL-4-NITROANILINE (DBNMNA) CRYSTALS	513
Ajay Nahata, Keith A. Horn, and James T. Yardley	
QUADRATIC NONLINEAR OPTICAL PROPERTIES OF DIVA CRYSTAL	519
T. Wada, C.H. Grossman, S. Yamada, A. Yamada, A.F. Garito, and H. Sasabe	
FERROELECTRICITY OF CHIRAL COMPOUNDS IN HIGHLY ORDERED SMECTIC PHASES	525
Stanislaw Wróbel, Matthias Pfeiffer, Ashók M. Biradar, and Wolfgang Haase	
LANGMUIR-BLODGETT FILMS OF POTENTIAL UNIDIMENSIONAL ORGANIC RECTIFIERS	531
Robert M. Metzger and Charles A. Panetta	
L.B. FILMS EXHIBITING COOPERATIVE SPIN TRANSITION, FOR 2D MOLECULAR MEMORY DEVICES	537
P. Coronel, A. Ruaudel-Teixier, A. Barraud, and O. Kahn	
EFFECTS OF MOLECULAR RIGIDITY ON ELECTRIC FIELD INDUCED ALIGNMENT AND ORIENTATIONAL STABILITY OF DIPOLAR CHROMOPHORE COMPOSITES	543
H.E. Katz, M.L. Schilling, G. Washington, C.W. Dirk, W.R. Holland, T. Fang, and K.D. Singer	
THE EFFECT OF MATRIX ATTACHMENT ON THE THIRD ORDER NONLINEAR OPTICAL PROPERTIES OF DYES	551
David W. Polis, Mamoun M. Bader, and Larry R. Dalton	
SEMIORGANICS: A NEW CLASS OF NLO MATERIALS	557
P.R. Newman, L.F. Warren, P. Cunningham, T.Y. Chang, D.E. Cooper, G.L. Burdge, P. Polak-Dingels, and C.K. Lowe-Ma	
FUSED, THREE-RING DONOR-ACCEPTOR MOLECULES AS POTENTIAL MATERIALS FOR EFFICIENT SECOND HARMONIC GENERATION	563
Malcolm R. McLean, Mamoun Badr, Larry R. Dalton, Robert L.S. Devine, and William H. Steier	
OPTICAL AND MAGNETIC PROCESSES AND THE SIDE CHAINS OF DIACETYLENIC MATERIALS	567
Daniel J. Sandman, Gregory P. Hamill, Mark Levinson, Philip G. Rossoni, Elizabeth A. Yost, and Georgia C. Papaefthymiou	
INVESTIGATIONS OF A NEW REVERSIBLE STRAIN INDUCED CHROMIC TRANSITION IN POLYDIACETYLENE ELASTOMERS	577
R.A. Nallicheri and M.F. Rubner	



SYNTHESIS AND PROPERTIES OF A FULLY CONJUGATED POLY-DIACETYLENE: POLY(1,4-BIS (3-QUINOLYL)-1,3-BUTADIYNE) Satya S. Talwar, Manjunath B. Kamath, and K.N. Babu	583
ORGANIC POLYMER SEMICONDUCTOR SUPERLATTICES Samson A. Jenekhe and Wen-Chang Chen	589
LARGE CUBIC NONLINEAR OPTICAL PROPERTIES OF ORGANIC SEMICONDUCTOR SUPERLATTICES Samson A. Jenekhe, Wen-Chang Chen, Saukwan Lo, and Steven R. Flom	595
SYNTHESIS AND SECOND-ORDER NONLINEAR OPTICAL PROPERTIES OF NEW COUMAROMETHACRYLATE-METHYLMETHACRYLATE COPOLYMERS R.A. Henry, J.M. Hoover, A. Knoesen, S.T. Kowel, G.A. Lindsay, and M.A. Mortazavi	601
SYNTHESIS AND CHARACTERIZATION OF THIRD ORDER NONLINEAR OPTICAL MATERIALS L.P. Yu, M. Chen, L.R. Dalton, X.F. Cao, J.P. Jiang, and R.W. Hellwarth	607
NONLINEAR OPTICAL PROPERTIES OF TWO THIOPHENE-BASED POLYCONJUGATED SYSTEMS: PHOTOINDUCED ABSORPTION AND THIRD HARMONIC GENERATION SPECTROSCOPY R. Zamboni, C. Taliani, G. Ruani, A.J. Pal, and F. Kajzar	613
ROTATIONAL DIFFUSION OF CHROMOPHORES INSIDE A GLASSY POLYMERIC FILM STUDIED BY ELECTROOPTICAL INTERFEROMETRY R. Meyrueix and G. Mignani	619
SECOND ORDER NONLINEAR OPTICS AND POLYMER PHYSICS OF CORONA POLED, DOPED POLYMER MATERIALS Hilary L. Hampsch, Jian Yang, George K. Wong, and John M. Torkelson	625
ENHANCED THIRD ORDER OPTICAL NONLINEAR RESPONSE IN POLYTHIOPHENE FILMS--POLARON CONTRIBUTIONS Lina Yang, R. Dorsinville, R. Zamboni, C. Taliani, R. Tubino, and R.R. Alfano	631
PHOTOEXCITATIONS IN POLY(2,5-THIENYLENE VINYLENE) I.D.W. Samuel, A.J. Brassett, N.F. Colaneri, R.A. Lawrence, D.D.C. Bradley, K.E. Meyer, R.H. Friend, H. Murata, S. Tokito, T. Tsutsui, and S. Saito	637
OPTICAL CHARACTERIZATION OF POLYDIACETYLENE LANGMUIR-BLODGETT FILM ON SILICON SUBSTRATES P. Miller, A.K.M. Rahman, S.V. Broude, and S. Tripathy	643
ELECTRONIC STRUCTURE OF LONG POLYENES: STATES AND TRANSITION DIPOLES Bryan E. Kohler	649

THEORETICAL CALCULATIONS ON NONLINEAR SUSCEPTIBILITIES OF ORGANIC CRYSTALS Yuzo Itoh, Tomoyuki Hamada, Atsushi Kakuta, and Akio Mukoh	659
ELECTRONIC STRUCTURES AND NONLINEAR OPTICAL PROPERTIES FOR CROSS-CONJUGATED POLYENE Yuhei Mori and Yoshimichi Okano	665
QUANTUM LATTICE FLUCTUATIONS AND NONLINEAR OPTICS OF CONDUCTING POLYMERS J. Yu, B. Friedman, and W.P. Su	671
THEORETICAL STUDIES OF THE NONLINEAR OPTICAL PROPERTIES OF L-ARGININE PHOSPHATE C.A. Langhoff	677
EFFECTS OF IN-PLANE $\pi$ ' BONDING ON ELECTRONIC TRANSITION ENERGIES FOR INORGANIC POLYMERS Kim F. Ferris, Steven M. Risser, and Angela K. Hanson	683
THEORETICAL CALCULATIONS OF THE NONLINEAR DIELECTRIC FUNCTION OF INHOMOGENEOUS THIN FILMS Steven M. Risser and Kim F. Ferris	687
NONLINEAR OPTICAL STUDIES OF MIXED $\pi$ -CONJUGATED POLYMER MULTILAYERS BY SECOND HARMONIC GENERATION H. Koezuka, T. Kurata, A. Tsumura, and H. Fuchigami	691
EFFICIENT SECOND HARMONIC GENERATION IN HYDRAZONE, DERIVATIVES OF SUBSTITUTED AROMATIC ALDEHYDES Richard S. Potember, Robert C. Hoffman, and Karen A. Stetyick	697
AUTHOR INDEX	703
SUBJECT INDEX	707
MATERIALS RESEARCH SOCIETY SYMPOSIUM PROCEEDINGS	711

Society for assistance in preparing the symposium and this volume. We acknowledge with gratitude financial assistance from:

Air Force Office of Scientific Research  
Allied-Signal, Inc.  
Army Research Office  
E.I. du Pont de Nemours and Co., Inc.  
Exxon Research and Engineering Co.  
GTE  
IBM, Almaden Research Center  
Matsushita Electric Industrial Co.  
Xerox Corporation

January 1990

Long Y. Chiang  
Paul M. Chaikin  
Dwayne O. Cowan

## Preface

This volume contains the proceedings of the Symposium on The Electrical, Optical and Magnetic Properties of Organic Solid State Materials held at the Fall Meeting of the Materials Research Society, November 27 - December 2, 1989. This was the first MRS symposium to address the new and rapidly emerging area of organic solids designed for a broad spectrum of electrical, magnetic and optical properties. Most organic compounds in the past have been prepared for either their biological properties or, in the case of polymers, for their structural properties. This could be the dawn of a new era in organic materials. The symposium consisted of 20 invited presentations and 110 contributed papers. These were organized into the following areas:

1. Organic Ferromagnets
2. Synthetic Organic Metals and Organic Superconductors
3. Spin Density Waves in Organic Charge-Transfer Complexes
4. Organic Conducting Polymers
5. Nonlinear Optical Properties of Organic Materials

The purpose of this symposium was to provide a forum for discussion of the fundamental science and emerging technology in which speakers from different disciplines could share their knowledge and give direction to a key area of materials science that is critical not only to an energy conscious society but also to the further application of new organic materials. The symposium was interdisciplinary in scope, with participants from materials science, chemistry, physics and engineering, as well as international in character with scientists from the United States, Japan, France, Italy, West Germany, United Kingdom, India and Spain.

The selection of invited speakers was made so that there was representation from academia, industry and government laboratories; and so that each of the five general research areas were considered. The invited domestic scientists who were able to participate were Professors Brooks (Boston University), Epstein (Ohio State University), Garito (University of Pennsylvania), Heeger (UCSB), MacDiarmid (University of Pennsylvania), Wudl (UCSB), and Drs. Cornwell (Xerox), Donald (E.I. du Pont de Nemours), Elsenbaumer (Allied-Signal), Kini (Argonne Lab.), Sandman (GTE), Torrance (IBM), and Townsend (Bellcore). The invited foreign scientists who participated were Professors Garoche (France), Itoh (Japan), Iwamura (Japan), Saito (Japan), Tokumoto (Japan), Yoshida (Japan), and Zyss (France).

The symposium co-chairmen thank all of the participants for making the meeting an exciting and stimulating one. We thank the officers and staff of the Materials Research

---

**MATERIALS RESEARCH SOCIETY SYMPOSIUM PROCEEDINGS**

---

*Recent Materials Research Society Symposium Proceedings*

- Volume 145—III-V Heterostructures for Electronic/Photonic Devices, C.W. Tu, V.D. Mittera, A.C. Gossard, 1989, ISBN: 1-55899-018-6
- Volume 146—Rapid Thermal Annealing/Chemical Vapor Deposition and Integrated Processing, D. Hodul, J. Gelpey, M.L. Green, T.E. Seidel, 1989, ISBN: 1-55899-019-4
- Volume 147—Ion Beam Processing of Advanced Electronic Materials, N.W. Cheung, A.D. Marwick, J.B. Roberto, 1989, ISBN: 1-55899-020-8
- Volume 148—Chemistry and Defects in Semiconductor Heterostructures, M. Kawabe, T.D. Sands, E.R. Weber, R.S. Williams, 1989, ISBN: 1-55899-021-6
- Volume 149—Amorphous Silicon Technology-1989, A. Madan, M.J. Thompson, P.C. Taylor, Y. Hamakawa, P.G. LeComber, 1989, ISBN: 1-55899-022-4
- Volume 150—Materials for Magneto-Optic Data Storage, C.J. Robinson, T. Suzuki, C.M. Falco, 1989, ISBN: 1-55899-023-2
- Volume 151—Growth, Characterization and Properties of Ultrathin Magnetic Films and Multilayers, B.T. Jonker, J.P. Heremans, E.E. Marinero, 1989, ISBN: 1-55899-024-0
- Volume 152—Optical Materials: Processing and Science, D.B. Poker, C. Ortiz, 1989, ISBN: 1-55899-025-9
- Volume 153—Interfaces Between Polymers, Metals, and Ceramics, B.M. DeKoven, A.J. Gellman, R. Rosenberg, 1989, ISBN: 1-55899-026-7
- Volume 154—Electronic Packaging Materials Science IV, R. Jaccodine, K.A. Jackson, E.D. Lillie, R.C. Sundahl, 1989, ISBN: 1-55899-027-5
- Volume 155—Processing Science of Advanced Ceramics, I.A. Aksay, G.L. McVay, D.R. Ulrich, 1989, ISBN: 1-55899-028-3
- Volume 156—High Temperature Superconductors: Relationships Between Properties, Structure, and Solid-State Chemistry, J.R. Jorgensen, K. Kitazawa, J.M. Tarascon, M.S. Thompson, J.B. Torrance, 1989, ISBN: 1-55899-029
- Volume 157—Beam-Solid Interactions: Physical Phenomena, J.A. Knapp, P. Borgesen, R.A. Zuhr, 1989, ISBN 1-55899-045-3
- Volume 158—In-Situ Patterning: Selective Area Deposition and Etching, R. Rosenberg, A.F. Bernhardt, J.G. Black, 1989, ISBN 1-55899-046-1
- Volume 159—Atomic Scale Structure of Interfaces, R.D. Bringans, R.M. Feenstra, J.M. Gibson, 1989, ISBN 1-55899-047-X
- Volume 160—Layered Structures: Heteroepitaxy, Superlattices, Strain, and Metastability, B.W. Dodson, L.J. Schowalter, J.E. Cunningham, F.H. Pollak, 1989, ISBN 1-55899-048-8
- Volume 161—Properties of II-VI Semiconductors: Bulk Crystals, Epitaxial Films, Quantum Well Structures and Dilute Magnetic Systems, J.F. Schetzina, F.J. Bartoli, Jr., H.F. Schaake, 1989, ISBN 1-55899-049-6
- Volume 162—Diamond, Boron Nitride, Silicon Carbide and Related Wide Bandgap Semiconductors, J.T. Glass, R.F. Messier, N. Fujimori, 1989, ISBN 1-55899-050-X
- Volume 163—Impurities, Defects and Diffusion in Semiconductors: Bulk and Layered Structures, J. Bernholc, E.E. Haller, D.J. Wolford, 1989, ISBN 1-55899-051-8
- Volume 164—Materials Issues in Microcrystalline Semiconductors, P.M. Fauchet, C.C. Tsai, K. Tanaka, 1989, ISBN 1-55899-052-6
- Volume 165—Characterization of Plasma-Enhanced CVD Processes, G. Lucovsky, D.E. Ibbotson, D.W. Hess, 1989, ISBN 1-55899-053-4
- Volume 166—Neutron Scattering for Materials Science, S.M. Shapiro, S.C. Moss, J.D. Jorgensen, 1989, ISBN 1-55899-054-2

---

MATERIALS RESEARCH SOCIETY SYMPOSIUM PROCEEDINGS

---

- Volume 167—Advanced Electronic Packaging Materials, A. Barfknecht, J. Partridge, C.-Y. Li, C.J. Chen, 1989, ISBN 1-55899-055-0
- Volume 168—Chemical Vapor Deposition of Refractory Metals and Ceramics, T.M. Besmann, B.M. Gallois, 1989, ISBN 1-55899-056-9
- Volume 169—High Temperature Superconductors: Fundamental Properties and Novel Materials Processing, J. Narayan, C.W. Chu, L.F. Schneemeyer, D.K. Christen, 1989, ISBN 1-55899-057-7
- Volume 170—Tailored Interfaces in Composite Materials, C.G. Pantano, E.J.H. Chen, 1989, ISBN 1-55899-058-5
- Volume 171—Polymer Based Molecular Composites, D.W. Schaefer, J.E. Mark, 1989, ISBN 1-55899-059-3
- Volume 172—Optical Fiber Materials and Processing, J.W. Fleming, G.H. Sigel, S. Takahashi, P.W. France, 1989, ISBN 1-55899-060-7
- Volume 173—Electrical, Optical and Magnetic Properties of Organic Solid-State Materials, L.Y. Chiang, D.O. Cowan, P. Chaikin, 1989, ISBN 1-55899-061-5
- Volume 174—Materials Synthesis Utilizing Biological Processes, M. Alper, P.D. Calvert, P.C. Rieke, 1989, ISBN 1-55899-062-3
- Volume 175—Multi-Functional Materials, D.R. Ulrich, F.E. Karasz, A.J. Buckley, G. Gallagher-Daggitt, 1989, ISBN 1-55899-063-1
- Volume 176—Scientific Basis for Nuclear Waste Management XIII, V.M. Oversby, P.W. Brown, 1989, ISBN 1-55899-064-X
- Volume 177—Macromolecular Liquids, C.R. Safinya, S.A. Safran, P.A. Pincus, 1989, ISBN 1-55899-065-8
- Volume 178—Fly Ash and Coal Conversion By-Products: Characterization, Utilization and Disposal VI, F.P. Glasser, R.L. Day, 1989, ISBN 1-55899-066-6
- Volume 179—Specialty Cements with Advanced Properties, H. Jennings, A.G. Landers, B.E. Scheetz, I. Odler, 1989, ISBN 1-55899-067-4

---

MATERIALS RESEARCH SOCIETY MONOGRAPH

---

Atom Probe Microanalysis: Principles and Applications to Materials Problems, M.K. Miller, G.D.W. Smith, 1989; ISBN 0-931837-99-5

*Earlier Materials Research Society Symposium Proceedings listed in the back.*

---

PART I

---

## Organic Ferromagnetics

ELECTRON-DONATING RADIALENES. POTENTIAL DONORS FOR  
MOLECULAR ORGANIC (SUPER)CONDUCTORS AND FERROMAGNETS

YOSHIDA Z. SUGIMOTO T. AND MISAKI Y.

Department of Synthetic Chemistry, Kyoto University, Yoshida, Kyoto 606,  
Japan

ABSTRACT

The electron-donating [n]radialenes (n=3,4,5) were prepared with the aim of developing both new type of organic (super)conductors and unprecedented organic/molecular ferromagnets. The charge-transfer (CT) complexes of 1,3-dithiole[4]radialene with TCNQ and of 1,3-benzodithiole-[4]radialene with TCNQF<sub>4</sub> and DDQ showed comparatively high electrical conductivities in compressed pellets. The single crystals of PF<sub>6</sub> and ClO<sub>4</sub> salts of 1,3-benzodithiole[4]radialene radical cation revealed temperature change of electrical conductivity characteristic of a semiconductor. The magnetic properties of the bis(trifluoroacetate)salt of thioxanthene[3]-radialene dication and of the CT complexes of 1,3-benzodithiole[5]-radialene with DDQ, TCNQF<sub>4</sub>, and hexacyanohexamethylenecyclopropane, were also investigated from the ESR and/or magnetic susceptibility measurements.

INTRODUCTION

It seems likely that the creation of novel electron donors having skeletal structures different from those of the hitherto known systems will be required for ultimate accomplishment of high T<sub>c</sub> organic superconductors and organic ferromagnetic materials. [n]Radialene is a unique cyclic  $\pi$  system composed of an n-membered ring and n of exocyclic double bonds [1]. Electron donating [n]radialene, that is [n]radialene substituted with n of electron donating groups is considered to be a multi-step redox system exhibiting characteristic electrochemical properties.

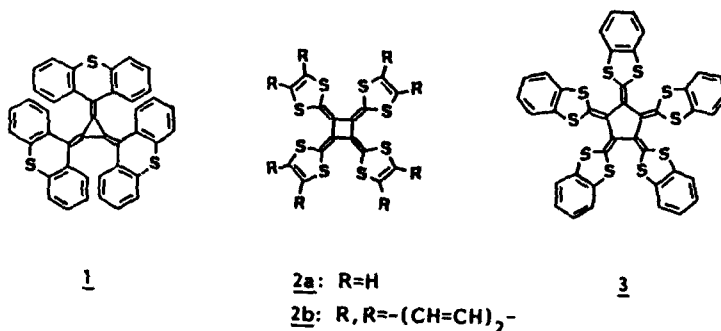
Of those, electron-donating [4]radialene will be a donor component for preparing organic (super) conductors. On the other hand, on HMO consideration assuming that the molecular symmetry of [n]radialene is of C<sub>n</sub> or higher, odd-numbered radialene can possess a pair of degenerate



HOMO. Thus electron-donating [3]- and [5] radialenes have a potential as donor components for preparing organic ferromagnetic materials.

SYNTHESES AND ELECTROCHEMICAL PROPERTIES OF ELECTRON-DONATING  
[n]RADIALENES

No electron-donating [n]radialene has been reported so far except for tetrakis(N-carboethoxy-4H-pyridin-4-ylidene)cyclobutane (N-carboethoxy-4H-pyridenyl[4]radialene) [2]. We tried to synthesize electron-donating [n]radialenes (n=3,4,5) which have stronger electron-donating 1,3-dithiol or thiopyranyl groups than N-carboethoxy-4H-pyridenyl groups. As a result of our efforts for several years the following radialenes were synthesized: tris(thioxanthen-9-ylidene)cyclopropane (1) [3], tetrakis(1,3-dithiol-2-ylidene)cyclobutane (2a) [4], tetrakis(1,3-benzodithiol-2-ylidene)cyclobutane (2b) [4], and pentakis(1,3-benzodithiol-2-ylidene)cyclopentane (3) [5]. We continue our synthetic study of 1,3-dithiole[3]radialene (4). These electron-donating radialenes are air-stable, orange crystalline solids that are soluble in most organic solvents. To estimate their electron-donating properties their redox potentials were measured by using cyclic voltammetry and compared with that of a most familiar electron-donor, tetrathiafulvalene (TTF). Figure 1 shows the cyclic voltammograms of 1, 2a, 2b and 3 in benzonitrile. The redox processes are apparently due to one-step two-electron transfer for 1, two-step two-electron transfer for 2a and 2b, and one-step four-electron transfer for 3, respectively. The detailed analysis using digital simulation suggests that these redox processes are actually due to overlapping two-step one- or two-electron transfer. The redox potentials are summarized in Table I.



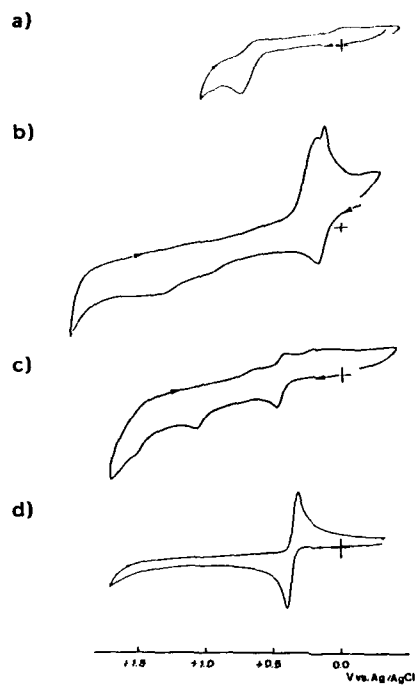


Figure 1. Cyclic voltammograms of (a) 1, (b) 2a, (c) 2b, and (d) 3 in benzonitrile containing  $(n\text{-Bu})_4\text{NClO}_4$  at room temperature.

Table I. The redox potentials<sup>a</sup> of 1, 2a, 2b and 3 measured in benzonitrile at room temperature.

Radialene	$E_1$	$E_2$	$E_3$	$E_4$
<u>1</u>	+0.70 <sup>b</sup>			
<u>2a</u>	+0.19 <sup>b,c</sup>		+0.98 <sup>c</sup>	+1.30 <sup>c</sup>
<u>2b</u>	+0.46 <sup>b</sup>		+1.09 <sup>c</sup>	+1.59 <sup>c</sup>
<u>3</u>		+0.36 <sup>d</sup>		
TTF	+0.34	+0.71		

<sup>a</sup> V vs. Ag/AgCl. <sup>b</sup>  $(E_1 + E_2)/2$ . <sup>c</sup> Irreversible step.  
 Anodic peak potentials. <sup>d</sup>  $(E_1 + E_2 + E_3 + E_4)/4$ .

The redox potential of 1 is much larger than those of 2a, 2b, and 3, suggesting a poor electron-donating property of 1 besides the large steric bulkiness.

ELECTRON-CONDUCTING AND MAGNETIC PROPERTIES OF CHARGE-TRANSFER COMPLEXES, AND RADICAL CATION AND DICATION SALTS OF ELECTRON-DONATING [n]RADIALENES

The charge-transfer (CT) complex formation of the four electron-donating radialenes with familiar electron acceptors, TCNQ, tetrafluoro-TCNQ (TCNQF<sub>4</sub>), DDQ, and hexacyanohexamethylenecyclopropane (HCTMC), was investigated [6]. As expected, 1 formed no CT complex even with strong electron acceptors. On the other hand, there was CT complex formation of 2a with all the electron acceptors above and of 2b and 3 with the others except TCNQ. The other complexes 2a-TCNQ (1:2) [7], 2b-TCNQF<sub>4</sub> (1:1) [7] and 2b-DDQ (3:5) were actually insulators, in which the electrical conductivity ( $\sigma$ ) was  $<10^{-8}$  S/cm at room temperature. The 2a·(TCNQ)<sub>2</sub>, 2b·TCNQF<sub>4</sub>, and (2b)<sub>3</sub>·(DDQ)<sub>5</sub> complexes showed  $\sigma_{r.t.}$  values of  $3.2 \times 10^{-2}$ ,  $7.5 \times 10^{-2}$ , and  $2.4 \times 10^{-6}$  S/cm, respectively, in compressed pellets. The activation energies of higher electrical conducting 2a·(TCNQ)<sub>2</sub> and 2b·TCNQF<sub>4</sub> complexes were 0.057 and 0.04-0.06 eV, respectively. Attempts to get single crystals of the two complexes were unsuccessful. On the other hand, we tried to prepare the radical cation salts by electrolytic oxidation of the radialenes in the presence of various tetra-n-butyl-ammonium salts [6]. Only, the PF<sub>6</sub> and ClO<sub>4</sub> salts of radical cation of 2b ((2b)<sub>3</sub>·(PF<sub>6</sub>)<sub>4</sub> and 2b·(ClO<sub>4</sub>)<sub>2</sub>) could be obtained as single crystals albeit in very small size. The  $\sigma_{r.t.}$  of the PF<sub>6</sub> salt was ca. 1 S/cm while for the ClO<sub>4</sub> salt it was impossible to measure the  $\sigma_{r.t.}$  because of its small size. Figures 2 and 3 show the temperature change of electrical resistance (R) for the PF<sub>6</sub> and ClO<sub>4</sub> salts, respectively. In both cases the R values increase with lowering temperature, indicating a behavior characteristic of semiconductors. The E<sub>a</sub> values were 0.05 and 0.02 eV for the PF<sub>6</sub> and ClO<sub>4</sub> salts, respectively. At present we could not get radialene-based organic metals in both the CT complex and radical cation salts.

According to the second McConnell model ferromagnetic interaction in a chain of alternating radical cation donors and radical anion acceptors could be achieved by configurational mixing of a virtual triplet excited state with the ground state [8]. In order to reveal such a ferromagnetic

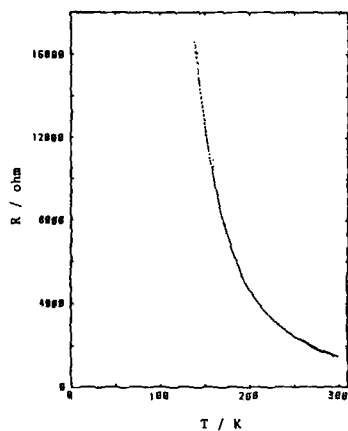


Figure 2. The plot of resistance (R, ohm) vs. temperature (T, K) for single crystals of  $(2b)_3 \cdot (PF_6)_4$ .

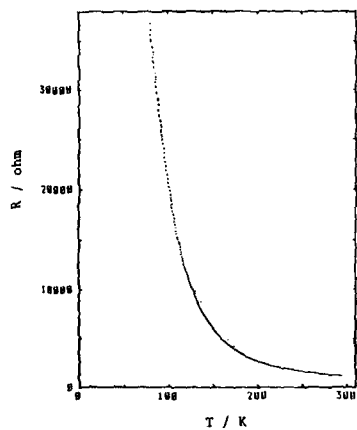


Figure 3. The plot of resistance (R, ohm) vs. temperature (T, K) for single crystals of  $2b \cdot (ClO_4)_2$ .

behavior the donor or acceptor component needs to occupy at least one pair of degenerate highest occupied (HO) or lowest unoccupied (LU) molecular orbitals (MO's). Electron-donating odd-numbered [n]radialenes (n=3 and 5) are of much interest as a donor component for preparing the CT complex and radical cation solids in bulk ferromagnetism, because these radialenes can have a pair of degenerate HOMO's in comparatively high energy, assuming that the molecular symmetry is  $C_3$  or  $C_5$ , or higher. Now, the magnetic properties of radical cation salts of  $\underline{1}$  [6] and of CT complexes of  $\underline{3}$  as well as the spin states of the dicationic  $\underline{1}$  and  $\underline{3}$ , were investigated by ESR and magnetic susceptibility measurements. The tribromide salt of radical cation of  $\underline{1}$  ( $\underline{1}^+ \cdot Br_3^-$ ) was obtained by the reaction of  $\underline{1}$  with  $Br_2$  in  $CCl_4$ . Unfortunately, this salt was too unstable and decomposed gradually in air. Furthermore, the exchange of  $Br_3^-$  with some other anion,

$\text{BF}_4^-$ ,  $\text{ClO}_4^-$ ,  $\text{BPh}_4^-$ ,  $\text{PF}_6^-$  etc., was also unsuccessful, because a gradual decomposition occurred when  $\text{I}^+\cdot\text{Br}_3^-$  was dissolved in  $\text{CH}_3\text{CN}$  as the reaction solvent. In contrast to the radical cation salt, the dication salt was comparatively stable even in air [3]. The bis(trifluoroacetate) salt of dication ( $\text{I}^{2+}\cdot 2\text{CF}_3\text{CO}_2^-$ ) was used to investigate the spin state of  $\text{I}^{2+}$  in the solid by use of ESR spectroscopy. The ESR spectrum at 298K showed one sharp signal with a linewidth of 0.55mT at  $g=2.00509$ . By cooling to 77K a fine structure appeared together with a half-field resonance signal at 164.8 mT (Figure 4).

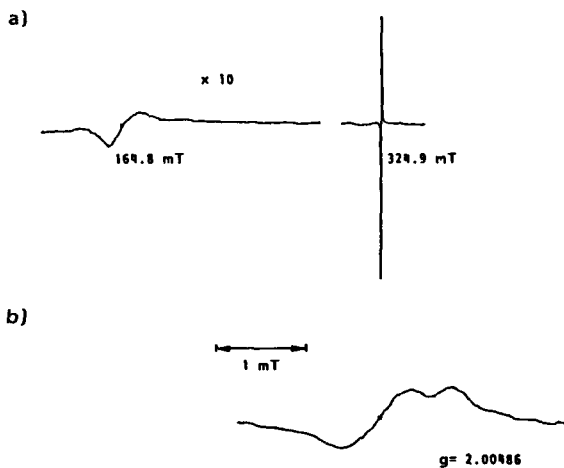
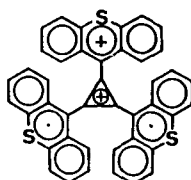


Figure 4. ESR spectrum of  $\text{I}^{2+}\cdot 2\text{CF}_3\text{CO}_2^-$  at  $-196\text{ }^\circ\text{C}$ : (a) the whole spectrum (the half-field resonance ( $\Delta m_S = \pm 2$ ) signal was measured with the 10-fold amplitude; (b) the expanded central signal at 324.9 mT.

From analysis of the spectrum only one of the zero-field splitting parameters,  $D$  was determined to be ca. 0.7 mT. The very small value strongly suggests that the radical pair distantly resides at the thioxanthanyl groups. Furthermore, the intensity of the central signal



gradually decreased with lowering temperature. From the quantitative analysis on the temperature change of the signal intensity in the range of 298-77 K, it is concluded that the triplet state lies 0.07 eV higher in energy. As discussed in pentaarylcyclopentadienyl cations, whose ground state is a singlet with a triplet lying 0.002-0.04 eV higher, it is likely also for  $\underline{1}^{2+}$  that the singlet is favored because the large  $\pi$  electron system decreases electron correlation and the complex structure allows easy Jahn-Teller distortion. Nevertheless, we suppose that  $\underline{1}^{2+}$  might become a ground state triplet in solution and in the solid with different counter anions, other than  $\text{CF}_3\text{CO}_2^-$ , where there is no preference toward a Jahn-Teller distortion. On the other hand, for  $\underline{3}$  the magnetic properties of CT complexes with DDQ ( $\underline{3}\cdot(\text{DDQ})_2$ ), TCNQF<sub>4</sub> ( $\underline{3}\cdot(\text{TCNQF}_4)_4$ ), and HCTMC ( $\underline{3}\cdot(\text{HCTMC})_2$ ) were investigated [5]. The  $\underline{3}\cdot(\text{DDQ})_2$  and  $\underline{3}\cdot(\text{TCNQF}_4)_4$  salts were prepared by mixing of  $\underline{3}$  and DDQ or TCNQF<sub>4</sub> in an equimolar amount. The  $\underline{3}\cdot(\text{HCTMC})_2$  salt was obtained by the reaction of  $\underline{3}^{4+}\cdot 4\text{BF}_4^-$  with  $[(n\text{-Bu})_4\text{N}^+]_2(\text{HCTMC})^{2-}$  in  $\text{CH}_3\text{CN}$  because a neutral HCTMC is too troublesome to handle. The IR spectra in a KBr pellet showed the CN stretching bands at 2221  $\text{cm}^{-1}$  for  $\underline{3}\cdot(\text{DDQ})_2$ , 2215 and 2166  $\text{cm}^{-1}$  for  $\underline{3}\cdot(\text{HCTMC})_2$ , and 2201  $\text{cm}^{-1}$  for  $\underline{3}\cdot(\text{TCNQF}_4)_4$ ; respectively, which are almost the same as those of the anion radical of DDQ ( $\text{DDQ}^{\cdot-}$ ), the dianion of HCTMC ( $\text{HCTMC}^{2-}$ ), and the anion radical of TCNQF<sub>4</sub> ( $\text{TCNQF}_4^{\cdot-}$ ). In considering the IR results together with the redox potentials of  $\underline{3}$  (+0.36 V vs. Ag/AgCl) and the acceptors (DDQ: +0.46 and -0.42 V; HCTMC +1.14 and +0.29 V; TCNQF<sub>4</sub>: +0.54 and -0.09 V), the CT complex salts  $\underline{3}\cdot(\text{DDQ})_2$ ,  $\underline{3}\cdot(\text{HCTMC})_2$ , and  $\underline{3}\cdot(\text{TCNQF}_4)_4$ , are actually in the form  $\underline{3}^{2+}\cdot(\text{DDQ}^{\cdot-})_2$ ,  $\underline{3}^{4+}\cdot(\text{HCTMC}^{2-})_2$ , and  $\underline{3}^{4+}\cdot(\text{TCNQF}_4^{\cdot-})_4$ , respectively. This result is important on understanding the magnetic properties of the salts. The magnetic susceptibility of each salt was measured and subjected to temperature change in the range of 298-4.5 K. Figures 5-7 show the plots of the observed ( $\chi_{\text{obs}}$ ) or the inverse paramagnetic susceptibility ( $\chi_{\text{para}} = \chi_{\text{obs}} - \chi_{\text{dia}}$ , where  $\chi_{\text{dia}}$  is the diamagnetic susceptibility) vs. temperature for  $\underline{3}\cdot(\text{HCTMC})_2$ ,  $\underline{3}\cdot(\text{DDQ})_2$ , and  $\underline{3}\cdot(\text{TCNQF}_4)_4$ , respectively. For  $\underline{3}\cdot(\text{HCTMC})_2$  there was almost no change

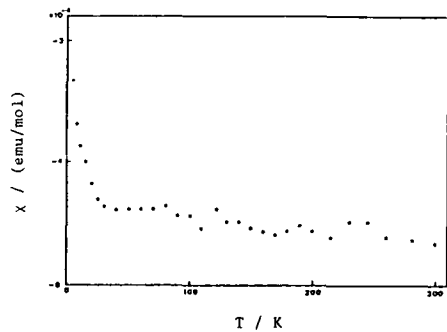


Figure 5. The temperature change of the  $\chi_{\text{obs}}$  for  $\underline{3}\cdot(\text{HCTMC})_2$ .

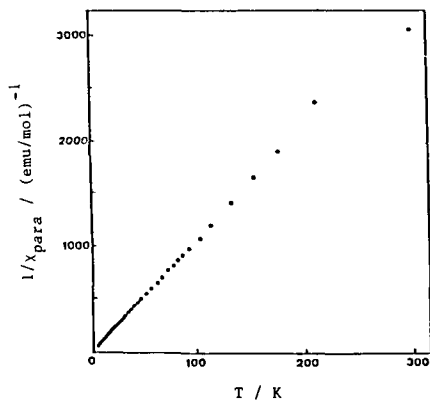


Figure 6. The temperature change of the reverse  $\chi_{\text{para}}$  for  $\underline{3}\cdot(\text{DDQ})_2$ .

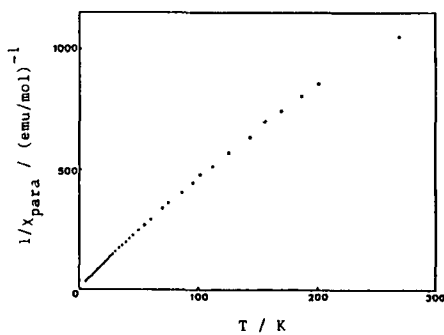


Figure 7. The temperature change of the reverse  $\chi_{\text{para}}$  for  $\underline{3}\cdot(\text{TCNQF}_4)_4$ .

of  $\chi_{\text{obs}}$ , but at very low temperature region a slight increase was observed. This salt is undoubtedly diamagnetic even if it is an contaminated impurity of triplet (and also doublet) species. In correspondence with this, the ESR spectrum at 298 K showed one very weak signal with a fine structure ( $D'=0.00096 \text{ cm}^{-1}$ ,  $E'=0.00011 \text{ cm}^{-1}$ ) characteristic of a triplet, which is very likely due to contaminant ion by  $\underline{3}^{2+}$  (Figure 8). On the other hand, for the other two salts a

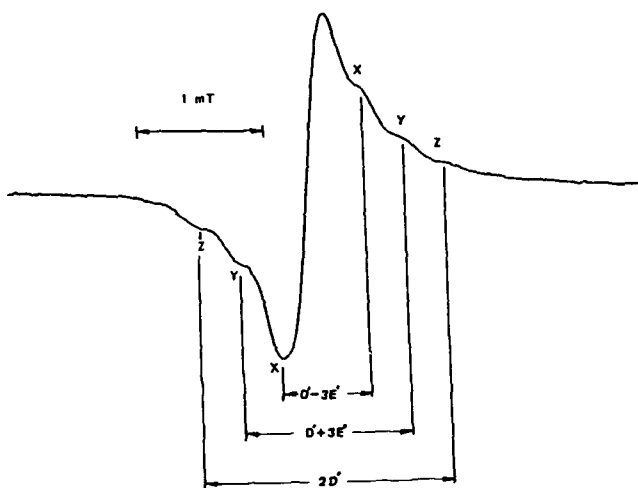


Figure 8. ESR spectrum of  $\underline{3} \cdot (\text{HCTMC})_2$  at room temperature.

temperature dependence on the  $\chi_{\text{para}}$  obeyed a Curie-Weiss law in the whole measured temperature range. The Weiss constant ( $\Theta$ ) was ca. -2 K for  $\underline{3} \cdot (\text{DDQ})_2$ . While for  $\underline{3} \cdot (\text{TCNQF}_4)_4$  the dependence of the inverse  $\chi_{\text{para}}$  on temperature exhibited a slightly complicated behavior, and  $\Theta$  was also found to be -2 K from a Curie-Weiss plot in the low temperature region of 170-5 K. Accordingly, for these salts it is concluded that the radical species of  $\underline{3}$  and DDQ, and of  $\underline{3}$  and TCNQF<sub>4</sub> are weak-antiferromagnetically coupled. In addition, the experimental  $\chi_{\text{para}}$ 's at 298 K are  $3.3 \times 10^{-4}$  and  $9.5 \times 10^{-4}$  emu/mol, for  $\underline{3} \cdot (\text{DDQ})_2$  and  $\underline{3} \cdot (\text{TCNQF}_4)_4$ , respectively, and their values are equal to only a few percent of those



calculated with use of mutually non-interacting spin systems of  $\underline{3}^{2+}$  ( $S=1$  if it is a ground state triplet) and two  $\text{DDQ}^{\cdot-}$  ( $S=1/2$ ) species, and of four  $\text{TCNQF}_4^{\cdot-}$  ( $S=1/2$ ) species. These results indicate the presence of small amounts of doublet and triplet species surviving in the salts presumably as a result of a Jahn-Teller distortion of  $\underline{3}^{2+}$  and a strong-antiferromagnetic interaction between a pair of  $\text{DDQ}^{\cdot-}$ 's or  $\text{TCNQF}_4^{\cdot-}$ 's. Nevertheless, the ESR measurement of  $\underline{3} \cdot (\text{DDQ})_2$  demonstrated involvement of a ground state triplet, which is most conceivably due to a non Jahn-Teller distorted  $\underline{3}^{2+}$ , albeit in a very small amount. Thus, a weak half-field resonance signal due to  $\Delta m_s = \pm 2$  transition appeared at 163.9 mT together with a strong signal at 327.6 mT ( $g=2.00523$ ) in the ESR spectrum at 298 K, as shown in Figure 9. The signal intensity measured at each temperature

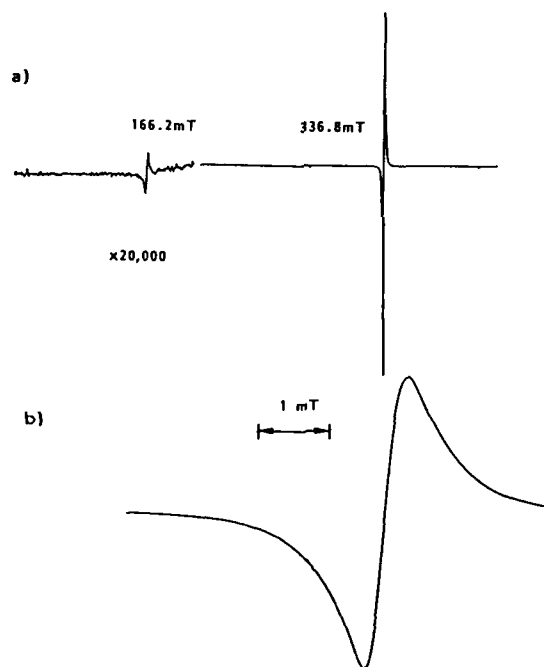


Figure 9. ESR spectra of  $\underline{3} \cdot (\text{DDQ})_2$  at room temperature: (a) the whole spectrum (the half-field resonance ( $\Delta m_s = \pm 2$ ) (163.9 mT) was measured in a 20,000 times larger amplitude than the central signal (327.6 mT); (b) the expanded central signal.

in the range of 298-4.5 K, obeyed a Curie law (Figure 10). The fine

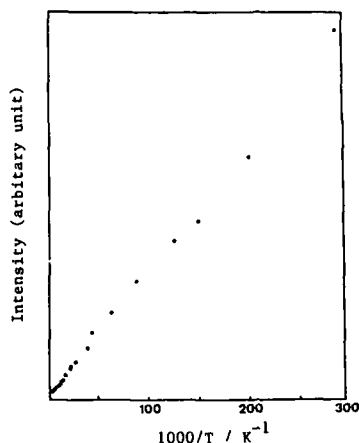


Figure 10. Temperature change of  $\Delta m_s = +2$  signal intensity for  $3 \cdot (\text{DDQ})_2$ .

structure was not observed at any temperature. In consideration of very small zero-field splitting parameters of  $3^{2+}$  observed in  $3 \cdot (\text{HCTMC})_2$ , it is probable that the parameters are very small also in  $3 \cdot (\text{DDQ})_2$  and the fine structure is hidden by the strong central signal.

#### CONCLUSION

Although research on organic super conductors seems to be decreasing since the discovery of high- $T_c$  ceramic superconductors, it should be important to prepare organic superconductors with higher  $T_c$  and to elucidate the detailed mechanisms of superconductivity. Research on organic ferromagnetic materials is still in the cradle.

To the best of our belief, further development of both fields should depend ultimately on the creation of promising new organic donors such as [n]radialenes with electron donating chalcogen groups (n: 3-5), despite the fact that electron donating [n]radialenes investigated have not yet led to either organic superconductors or ferromagnetic materials.

With regards to organic ferromagnets, the 1:1 CT complexes of  $\underline{4}$  with appropriate acceptors might exhibit favorable magnetic properties, if  $\underline{4}^{2+}$  retains its ground state triplet in the complexes. In this sense, such sort of electron-donating [3]radialenes should be the prospective donors for organic ferromagnets.

#### ACKNOWLEDGEMENT

We thank Dr. H. Awaji, H. Nakagawa, T. Kajita, Y. Arai, Y. Yamamoto, H. Oka, Y. Matsumura, H. Hatakeyama and Y. Hosotani for their collaboration in synthetic study. We also thank Prof. N. Kasai and Dr. Y. Kai for their collaboration in X-ray crystallographic study. We deeply appreciate to Prof. H. Inokuchi, Dr. T. Enoki, and Dr. H. Anzai for electric conductivity measurement, to Dr. J. Yamauchi, Prof. Y. Maruyama, and Dr. T. Inabe for ESR measurement, and to Prof. T. Shinjo and Dr. N. Hosoito for magnetic susceptibility measurement.

The financial support from the Ministry of Education, Science and Culture is greatly acknowledged.

#### REFERENCES

1. This name was first proposed by J. R. Platt: see footnote 3 in E. Weiltin, F. Gerson, J. N. Murrell, E. Heilbronner, *Helv. Chim. Acta*, 44, 1400 (1961).
2. M. Horner, S. Hünig, *Angew. Chem. Int. Ed. Engl.*, 16, 410 (1977).
3. T. Sugimoto, Y. Misaki, T. Kajita, T. Nagatomi, Z. Yoshida, J. Yamauchi, *Angew. Chem. Int. Ed. Engl.* 27, 1078 (1988).
4. T. Sugimoto, H. Awaji, Y. Misaki, Z. Yoshida, Y. Kai, H. Nakagawa, N. Kasai, *J. Am. Chem. Soc.*, 107, 5792 (1985).
5. T. Sugimoto, Y. Misaki, Z. Yoshida, J. Yamauchi, *Molecular Crystals, Liquid Crystals*, in press.
6. Y. Misaki, Ph.D. Thesis, Kyoto University (1989).
7. T. Sugimoto, H. Awaji, T. Sugimoto, Y. Misaki, Z. Yoshida, *Synth. Metal*, 19, 569 (1987).
8. H. M. McConnell, *Proc. R. A. Welch Found. Chem. Res.*, 11, 144 (1967).

## SYNTHESIS OF BULK HIGH SPIN DENSITY CHARGE TRANSFER COMPLEXES FOR ORGANIC MAGNETS

LONG Y. CHIANG,<sup>a,\*</sup> RAVINDRA B. UPASANI,<sup>a,b</sup> D. P. GOSHORN,<sup>a</sup> AND P. TINDALL<sup>c</sup>

<sup>a</sup> Corporate Research Laboratories, Exxon Research and Engineering Company, Annandale, New Jersey 08801

<sup>b</sup> Department of Physics, Princeton University, Princeton, New Jersey 08544

<sup>c</sup> Department of Chemistry, State University of New York, Stony Brook, New York 11794

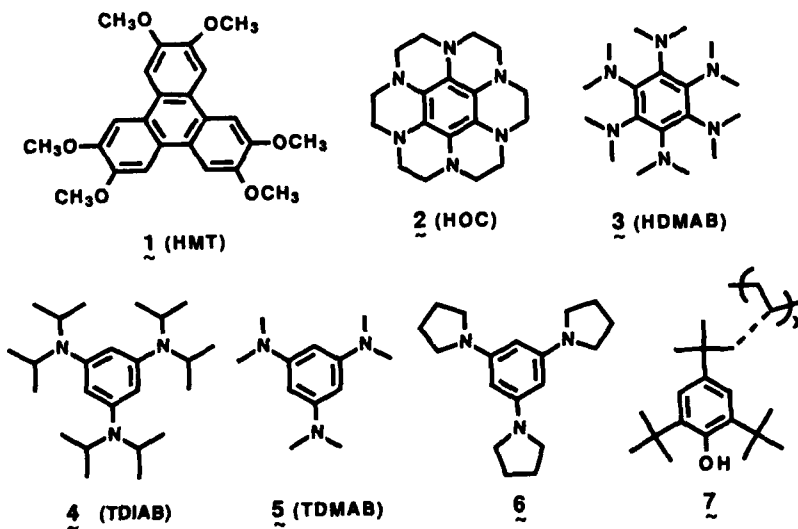
### ABSTRACT

We describe a synthetic approach to the preparation of high spin density organic solid as a probe to organic ferromagnetism utilizing an external doping process to achieve a molecular sequence of alternate donors and acceptors in different spin states for, in principle, the ground state ferrimagnets. In contrast to the irreversibility of electron oxidations of many triaminobenzene derivatives, we found that, by substituting three hindered diisopropylamino groups on benzene, stable monocationic TDIAB radicals can be obtained. In the case of HDMAB its cationic radicals can be stabilized in a strong acid medium. The observed bulk spin densities of 0.18 - 0.23 spins 1/2 per donor molecule in TDIAB-PF<sub>6</sub> and HDMAB-PF<sub>6</sub> solids are significant comparing to the diamagnetic properties normally obtained in solids of simple cationic salts of planar organic donor molecules. The results imply that a small degree of molecular spin separation due to the steric effect can readily increase sharply the paramagnetic spin density of solids. We also found that the introduction of arsenic pentafluoride into molecular crystals disintegrates the long range order of crystal without rearranging the molecular stacking sequence in HMT complexes. Arsenic pentafluoride serves as not only the oxidant, but also the physical molecular separator. That results in a molecular spin separation of triplet dicationic HMT spins from each other at high doping level. This concept of molecular spin separation explains the observation of static magnetic data with an observed high spin density of many doped HMT charge transfer complexes. Without the molecular spin separation, the segregated-stack complexes, such as HMT-(AsF<sub>5</sub>)<sub>3,4</sub> and HMT-DDQ-(AsF<sub>5</sub>)<sub>4,1</sub>, should instead give a low net bulk spin density with no triplet resonance after the intermolecular spin exchanges resemble to those observed in the case of HMT<sup>2+</sup>(ClO<sub>4</sub>)<sub>2</sub> crystals.

### INTRODUCTION

Three dimensional bulk ferromagnetism requires a high density of stable spins and a constructive intermolecular coupling between spins. Several theoretical considerations toward the design of organic ferromagnetism have been reviewed.<sup>1,2,3</sup> The spin containing organics have been used in various approaches to organic magnets are charge transfer complexes,<sup>4,5,6</sup> molecular radicals,<sup>7</sup>

polycarbenes,<sup>8</sup> and polyradicals.<sup>9</sup> Recently, we proposed a synthetic approach, which is derived from the McConnell's model,<sup>1</sup> for ground state bulk ferromagnetism or ferrimagnetism at solid state.<sup>5</sup> Experimentally, our approach involves an external doping process to oxidize the organic donors, such as 2,3,6,7,10,11-hexamethoxytriphenylene (HMT, **1**) possessing a  $D_{3d}$  symmetry, to their dicationic state with triplet spin characters<sup>10</sup> in a pre-arranged solid state structure. A systematic study of this approach has substantiated that the process of vapour phase chemical doping at the solid state of organics can be utilized as a general method for the preparation of high spin density organic solid state materials exhibiting an anomalously weak antiferromagnetic or, in some cases, ferrimagnetic coupling between spins.



Based on some experimental results from the chemical doping on HMT molecules, it seems to be plausible that a mechanism of molecular spin separation induced by dopants at solid state may play a major role in the generation of bulk high density of spins. This observation prompts us to synthesize highly hindered benzene analog organic donors, with a at least  $C_3$  symmetry, such as hexakis-(dimethylamino)benzene<sup>11</sup> (HDMAB, **3**) and 1,3,5-tris(diisopropylamino)benzene<sup>12</sup> (TDIAB, **4**) and hindered polyphenols (**7**) to examine the effect of sterically induced molecular spin separation on their magnetic properties in solid state. If the spins (either doublet or triplet) in aromatic organics can be sterically separated from each other far enough in solid state to prevent the intermolecular antiferromagnetic spin coupling while maintaining a certain degree of spin interaction through space, a

material with bulk constructive magnetic properties may be made at low temperatures.

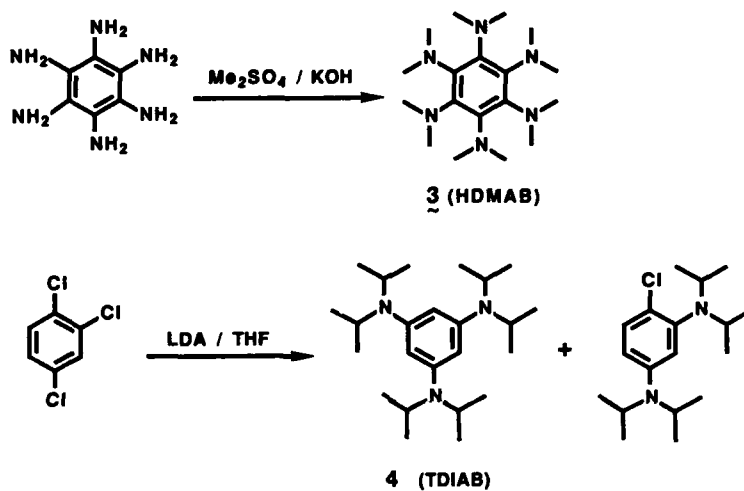
Here we also report the experimental results based on our synthetic approach using triplet molecules of 2,3,6,7,10,11-hexamethoxytriphenylene (HMT, 1) as a donor to complex with various organic acceptors, followed by a chemical doping with arsenic pentafluoride at the solid state of the complex. A similar study on the charge transfer complexes of octadecahydrohexaazacoronene<sup>13</sup> (HOC, 2) will be reported later.

## RESULTS AND DISCUSSION

The synthesis of high spin molecules and polymers including polycarbenes is the main focus of chemist to search for organic magnets. However, many of high spin organics, except some hindered nitroxyls and phenoxyls, are found to be thermally and chemically unstable. Even the simple cationic salts of hexakis(dimethylamino)benzene (HDMAB, 3) and many triaminobenzene derivatives, such as 1,3,5-tris(dimethylamino)benzene (TDMAB, 5) and 1,3,5-tris(pyrrolidinamino)benzene (6) were found<sup>4</sup> to be unstable showing irreversible electron oxidations in their cyclic voltammetry. The low stability of cationic HDMAB is mainly due to the high steric hindrance of six dimethylamino groups surrounding benzene that results in a minimum conjugation of  $\pi$ -electrons with the unpaired electrons of nitrogen. To stabilize the cation radical of this type of molecular system, a proper combination of a suitable degree of steric hindrance around the benzene ring and a maximum conjugation between  $\pi$ -electrons and unpaired nitrogen electrons is desirable. Indeed, we found that, by substituting all the methyl groups of 1,3,5-tris(dimethylamino)benzene (5) by isopropyl groups to a compound of 1,3,5-tris(diisopropylamino)benzene (4, TDIAB) synthesized by a route as shown in Scheme 1, a pronounced improvement over the cationic radical stability was observed.

The cyclic voltammetry of TDIAB shows a reversible one-electron oxidation with a half-wave potential of  $E_{1/2} = 0.47$  V vs. SCE using tetra-*n*-butylammonium hexafluorophosphate as an electrolyte in methylene chloride. The chemical oxidation of TDIAB was carried out by a doping reaction with one equivalent of nitrosonium hexafluorophosphate in acetonitrile under an inert atmosphere to give dark brown solids of TDIAB-PF<sub>6</sub> (14), which is soluble in many common organic solvents. Interestingly, in the case of HDMAB we found that its monocationic salt can be made by the chemical oxidation of HDMAB in trifluoroacetic acid with one equivalent of nitrosonium hexafluorophosphate in a minimum amount of acetonitrile under an inert atmosphere, followed by the evaporation of solvents to give dark

purple solids of HDMAB-PF<sub>6</sub> (15). During the reaction the trifluoroacetic acid solution of HDMAB turned immediately to purple upon the addition of NOPF<sub>6</sub>. Without trifluoroacetic acid the same solution turned to purple and then slowly to brown with a decomposition of HDMAB+<sup>1</sup>. The UV-visible spectrum of TDIAB-PF<sub>6</sub> and HDMAB-PF<sub>6</sub> complexes indicate a strong absorption with a peak maximum at 390 nm and a weak absorption at 582 nm for TDIAB-PF<sub>6</sub> and a absorption with a peak maximum at 450 nm for HDMAB-PF<sub>6</sub>.



**Scheme 1**

The formation of monocationic HDMAB radicals was substantiated by the solid state ESR spectroscopic study as shown in the spectrum of Figure 1a, which was taken at 130K. A similar spectrum can also be obtained at 300K. The full breadth of the spectrum is approximately 95 G. A hyperfine splitting of 7.3 G was measured from the peak maxima. If this uniformly-spaced splitting persists throughout the breadth, the spectrum would consist of 13 lines, which is consistent with the hyperfine coupling of the unpaired HDMAB radical with six nitrogen atoms ( $S = 1$ ). In the case of the monocationic TDIAB radical, the solid state ESR spectrum (Figure 1b) shows a breadth of approximately 80 G with five broad lines corresponding to the hyperfine coupling of the TDIAB unpaired radical with three nitrogen atoms, where the relative intensities of the sixth and seventh lines being too weak to detect. The hyperfine splitting of these lines was found to be 13.6 G. The nature of this large magnitude of splitting is currently under investigation.

The static magnetic susceptibility ( $\chi_g$ ) data were obtained with a Faraday magnetometer (4K-300K) and a vibrating sample magnetometer (1.3K-4.2K), where the significant contribution of ferromagnetic impurities and the temperature-independent diamagnetic susceptibilities ( $\chi_o$ ) to the measured magnetizations were corrected for via magnetization vs magnetic field isotherms at several temperatures for each sample. The spin densities ( $n$ ) were computed from the molar Curie constant  $C_M$  using the relation  $C_M = N_A g^2 S(S+1) m_B^2 / 3K_B$ , where  $N_A$  is a Avogadro's number,  $m_B$  is the Bohr magneton,  $K_B$  is Boltzmann's constant, and where we have assumed the Lande factor  $g = 2$  and spin  $S = 1/2$ . The temperature dependence of reciprocal magnetic susceptibilities  $(\chi_g - \chi_o)^{-1}$  of TDIAB-PF<sub>6</sub> (14) and HDMAB-PF<sub>6</sub> (15) solids are studied. Both complexes 14 and 15 were found to be paramagnetic with a curie constant  $C_M = 0.086$  and  $0.068$  cm<sup>3</sup>-K/mole, corresponding to a spin density of 0.23 spins 1/2 per TDIAB molecule and 0.18 spins 1/2 per HDMAB molecule, respectively. The observed large negative Weiss temperature of both complexes reveals that the magnetic interactions between the spins are strongly antiferromagnetic.

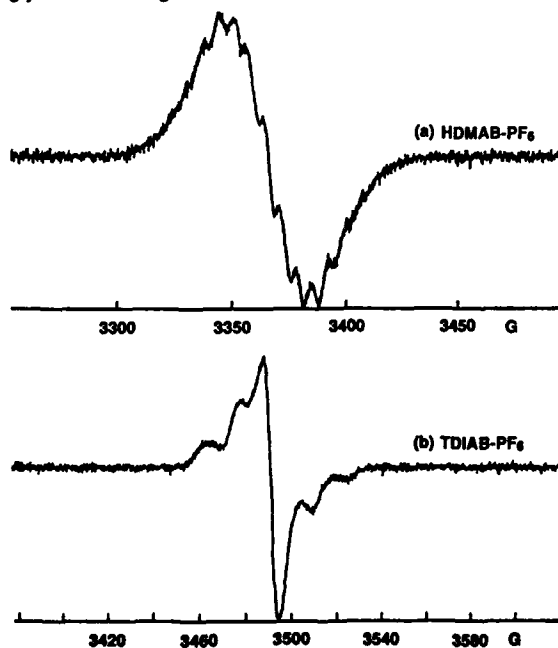
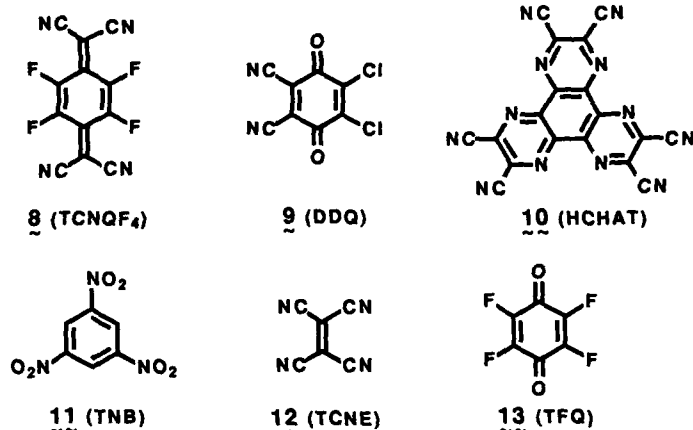


Figure 1: The ESR spectrum of (a) monocationic HDMAB (15) solids at 130K showing a hyperfine coupling (13 lines) of radical with six nitrogen atoms and (b) monocationic TDIAB (14) solids at 300K. Both (a) and (b) gives  $g = 2.003$  at the center of spectrum.



In the case of 2,3,6,7,10,11-hexamethoxytriphenylene (HMT), the stability of triplet state can be followed by the disappearance of its characteristic ESR peaks. For example, the dicationic HMT is not stable in neutral solution at ambient temperature as indicated by its irreversible cyclic voltammogram. It can be stabilized under a strong acidic condition such as in trifluoroacetic acid (TFA) to give a reversible two electrons oxidation. The third electron oxidation is not reversible even in trifluoroacetic acid. However, tricationic HMT can be stable in strong acid (TFA-HF<sub>3</sub>SO<sub>3</sub>) below -70°C.<sup>14</sup> The triplet resonance of dicationic HMT can be observed by the ESR study only below -80°C in dilution solution of dichloromethane. Recently, we have demonstrated that HMT dication can be actually stabilized in solid state by the electrochemical oxidation of HMT giving a crystalline perchlorate salt.<sup>15</sup> The same technique can also be used to prepare crystals of HMT<sup>+1</sup>-HMT<sup>+2</sup> with a mixed spin state. Unfortunately, all the monocationic HMT, dicationic HMT, and monocationic HMT-dicationic HMT mixed crystals showed very weakly paramagnetic properties with Curie constants corresponding to only 4.0 to 4.4 mole% of spins 1/2. The results revealed that an oxidation of triplet molecules such as HMT to a homogeneous or heterogeneous doublet and triplet spin states in crystal does not lead to a spin donor pair model mechanism for ferromagnetism as proposed by Torrance.<sup>6</sup> Instead, a long range antiferromagnetic spin ordering dominates this type of molecular system.

Here we demonstrate that the introduction of molecular spin separation phenomena to modify the molecular packing of HMT<sup>+2</sup> solids does diminish the diamagnetism in solids. The molecular spin separation can be induced by an external doping process at the solid state of donors or complexes. In our synthetic approach for the preparation of ground state ferro or ferrimagnetism,<sup>5,16</sup> we carried out the complexation of triplet donor molecule HMT (1) with various organic acceptors, such as tetrafluorotetracyanoquinodimethane (8, TCNQF<sub>4</sub>), 2,3-dichloro-5,6-dicyano-1,4-benzoquinone (9, DDQ), 2,3,6,7,10,11-hexacyanohexaazatriphenylene (10, HCHAT), 1,3,5-trinitrobenzene (11, TNB), tetracyanoethylene (12, TCNE), and tetrafluoro-1,4-quinone (13, TFQ), followed by a chemical doping of the resulting complex at solid state by arsenic pentafluoride. For example, when acceptors 8, 9, 10, 11, 12, and 13 were allowed to react with HMT, it formed crystals with a molecular composition of (HMT)<sub>2</sub>-TCNQF<sub>4</sub> (16), HMT-DDQ (17), HMT-HCHAT (18), HMT-TNB (19), HMT-(TCNE)<sub>1.5</sub> (20), and HMT-TFQ (21). Among them, (HMT)<sub>2</sub>-TCNQF<sub>4</sub> and HMT-DDQ were proved to possess a mixed-stack structure of ..ADDADD.. and ..ADAD.., respectively required in the McConnell's model.



The oxidation process was carried under various conditions and dopants, such as  $\text{AsF}_5$ ,  $\text{Cl}_2$ ,  $\text{SbF}_5$ ,  $\text{NOBF}_4$ , or  $\text{NOPPF}_6$ . The best was to perform the doping of complexes 16 - 21 at its solid state with an arsenic pentafluoride gas under an inert atmosphere. Under this condition, the original molecular stacking sequence in the complex can be sustained even though the disorder of the molecular packing in the complex was found to increase substantially with the increasing amount of doping as monitored by the powder x-ray diffraction. After doping the sample was kept for at least one day before measurements to allow the equilibration of absorbed  $\text{AsF}_5$  penetration into the core of crystal. It became a powder-like material. The degree of oxidation ( $n$ ) can be manipulated by the length of doping period and determined by the amount increase of arsenic contain in the product.

As a result, we were able to generate species in average close to a half cationically charged HMT, monocationically charged HMT, nearly dicationically charged HMT, or dicationically charged HMT in  $\text{AsF}_5$  doped  $(\text{HMT})_2\text{-TCNQF}_4$  (16) complex with a doping length of three minutes, one hour, three hours, or nine hours, respectively. In general, this type of complex with an oxidation state of HMT less than dication was found to be stable at ambient temperature under an inert atmospheric pressure. Interestingly, the triplet resonances of dicationic HMT in the solid state of doped complex 16 stable from 5K to 298K was observed by the ESR study.<sup>10</sup> The spectrum shows the zero field splitting parameters  $D = 0.038 \text{ cm}^{-1}$  and  $E \sim 0$ , consistent with the trigonal symmetry of the parent molecule and with previous measurements of the triplet state of HMT in solution.<sup>14</sup> The triplet intensity increases with the amount of doping. This triplet resonance persists even after six months or longer storage at ambient temperature. The measured magnetic susceptibilities of these complexes were described in previous reports,<sup>5</sup> showing linear relationships

between the inverse susceptibilities vs. temperature and following the Curie-Weiss law from room temperature to near 1K. These results reflect that the observed triplet state of dicationic HMT in the solid is a ground state. This along with axial symmetry of spins indicates a stabilization of triplet HMT<sup>+2</sup> in a TCNQF<sub>4</sub> (a non-trigonal symmetry molecule) sandwich of the mixed-stack matrix without a distortion of the orbital degeneracy of HMT. It possibly attributes to the sufficient free spacing surrounding TCNQF<sub>4</sub> molecules in solid arising from the incomparable size between HMT and TCNQF<sub>4</sub>. That allows free motions of TCNQF<sub>4</sub> to average the environmental difference around HMT molecules. The study of spin multiplicity of doped (HMT)<sub>2</sub>-TCNQF<sub>4</sub> complex was also carried out by the measurement of magnetization as a function of the magnetic field. The data are shown in Figure 2.17 A complete saturation on magnetization was observed in the magnetic field higher than 60kG with a saturated magnetization of  $8.7 \times 10^3$  G-cm<sup>3</sup>/mol. It shows a good agreement between the experimental and the theoretical curves calculated from the Brillouin functions for magnetization with a spin state of a 50% - 50% mixture of magnetization at  $S = 1$  and  $S = 1/2$ . These data suggest that up to 50% of the magnetization at low temperatures may arise from  $S = 1$  spin triplets, the remainder coming from  $S = 1/2$  doublets.

Similar doping experiments with AsF<sub>5</sub> were carried out on neutral HMT and complexes HMT-DDQ (17), HMT-HCHAT (18), HMT-TNB (19), and HMT-(TCNE)<sub>1.5</sub> (20) for 2-3h to give an average charge of HMT close to +2.0. The temperature dependent reciprocal magnetic susceptibility of these doped complexes are summarized in Figure 3. They all show linear relationships to the Curie-Weiss equation from 250 - 4K. The bulk spin density ( $n$ ) and the Weiss temperature ( $\theta$ , in parenthesis), calculated from the Curie constant and their inverse magnetic susceptibility data, of these doped complexes 17, 18, 19, and 20 was found to be 0.73 (-2.0K), 0.53 (0K), 0.41 (-0.3K), and 0.46 (+0.6K) spins 1/2 per molar complex, respectively. Interestingly, the AsF<sub>5</sub> doping on neutral HMT molecules also afforded a high spin density solid ( $n = 0.59$  spins 1/2 per molar complex) of HMT-(AsF<sub>5.5</sub>)<sub>3.4</sub> with a Weiss temperature of -1.9K. The results reveal that the vapor phase chemical doping process can be utilized as a general method for the preparation of high spin density organic charge transfer complexes regardless the mixed or segregated molecular stacking sequence in the structure of complex.

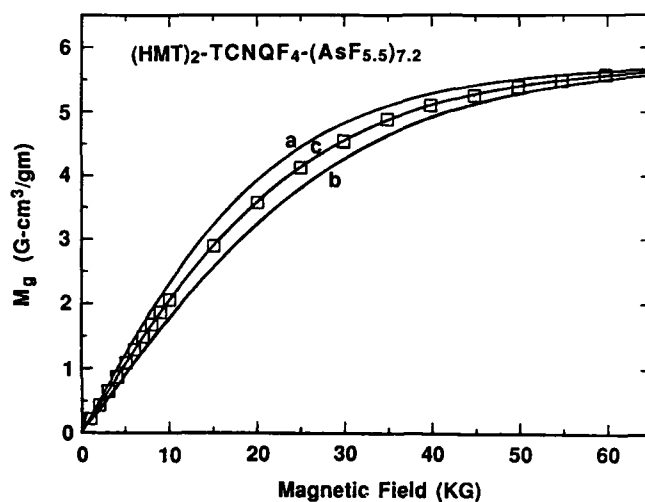


Figure 2: Magnetic field dependence of magnetization for  $(\text{HMT})_2\text{-TCNQF}_4\text{-(AsF}_{5.5})_{7.2}$  at 1.4K with theoretical curves a, b and c calculated from the Brillouin functions for magnetization with  $S = 1, 1/2,$  and  $1$  (50%) -  $1/2$  (50%), respectively.

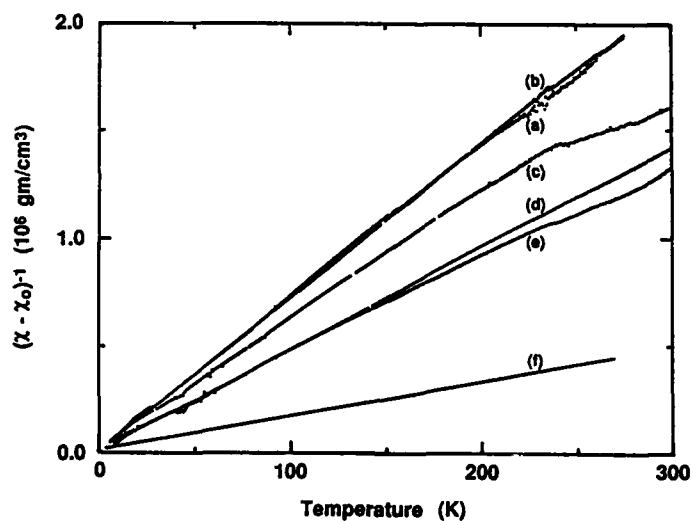


Figure 3: Temperature dependence of reciprocal magnetic susceptibility of (a)  $\text{HMT-HCHAT-(AsF}_{5.5})_{3.5}$ , (b)  $\text{HMT-(TCNE)}_{1.5}\text{-(AsF}_{5.5})_{4.1}$ , (c)  $\text{HMT-TNB-(AsF}_{5.5})_{4.4}$ , (d)  $\text{HMT-(AsF}_{5.5})_{3.4}$ , (e)  $\text{HMT-DDQ-(AsF}_{5.5})_{4.1}$ , and (f)  $(\text{HMT})_2\text{-TCNQF}_4\text{-(AsF}_{5.5})_{4.3}$

## CONCLUSION

We describe a synthetic approach to the preparation of high spin density organic solid as a probe to organic ferromagnetism utilizing an external doping process to achieve a molecular sequence of alternate donors and acceptors in different spin states for, in principle, the ground state ferrimagnets. In contrast to the irreversibility of electron oxidations of many triaminobenzene derivatives, we found that, by substituting three hindered diisopropylamino groups on benzene, stable monocationic TDIAB radicals can be obtained. The stabilization attributes to a proper degree of steric hindrance around the benzene ring without much interruption of the  $\pi$  and  $p$  orbitals interaction. In the case of HDMAB its cationic radicals can be stabilized in a strong acid medium. The observed bulk spin densities of 0.18 - 0.23 spins 1/2 per donor molecule in TDIAB-PF<sub>6</sub> and HDMAB-PF<sub>6</sub> solids are significant comparing to the diamagnetic properties normally obtained in solids of simple cationic salts of planar organic donor molecules. The results imply that a small degree of molecular spin separation due to the steric effect can readily increase sharply the paramagnetic spin density of solids.

We also found that the introduction of arsenic pentafluoride into molecular crystals disintegrates the long range order of crystal without rearranging the molecular stacking sequence in HMT complexes. In the case of the doped (HMT)<sub>2</sub>-TCNQF<sub>4</sub>, the observed bulk spin density increases with the amount of doping to a maximum of 1.6 spins 1/2 per complex when HMT molecules reach monocationic state. It then decreases slowly to 1.3 spins 1/2 per complex when most of HMT being oxidized to dicationic state. We conclude that arsenic pentafluoride serves as not only the oxidant, but also the physical molecular separator. That results in a molecular spin separation of triplet dicationic HMT spins from each other at high doping level. This concept of molecular spin separation explains the observation of static magnetic data that suggests, in the case of doped (HMT)<sub>2</sub>-TCNQF<sub>4</sub>, a high bulk spin density of 1.3 - 1.5 spins 1/2 per complex and up to 50% of the magnetization at low temperatures arising from  $S = 1$  spin triplets in the highly doped sample with dicationic HMT molecules. It also explains the observed high spin density of doped HMT-DDQ, HMT-HCHAT, HMT-TNB, and HMT-(TCNE)<sub>1.5</sub> complexes. Without the molecular spin separation, the segregated-stack complexes, such as HMT-(AsF<sub>5</sub>)<sub>3.4</sub> and HMT-DDQ-(AsF<sub>5</sub>)<sub>4.1</sub>, should instead give a low net bulk spin density with no triplet resonance after the intermolecular spin exchanges resemble to those observed in the case of HMT<sup>2+</sup>(ClO<sub>4</sub>)<sub>2</sub> crystals.<sup>15</sup>

**Acknowledgment.** The financial support for a part of this research by National Science Foundation (Grant DMR 88-22532) is gratefully acknowledged.

## REFERENCES

1. H. McConnell, *Proc. R. A. Welch Found. Conf.* **11**, 144 (1967); H. McConnell, *J. Chem. Phys.* **39**, 1910 (1963).
2. A. A. Ovchinnikov, *Dokl. Akad. Nauk. SSSR* **236**, 928 (1977); A. A. Ovchinnikov, *Theor. Chim. Acta.* **47**, 297 (1978); D. J. Klein and S. A. Alexander, *Studies in Phys. and Theo. Chem.* **51**, 404 (1987).
3. A. L. Buchachenko, *Dokl. Akad. Nauk. SSSR* **244**, 1146 (1979); N. Mataga, *Theoret. Chim. Acta.* **10**, 372 (1968); J. S. Miller, A. J. Epstein, and W. M. Reiff, *Chem. Rev.* **88**, 201 (1988).
4. R. Breslow, *Pure & Appl. Chem.* **54**, 927 (1982); R. Breslow, B. Jaun, R. Kluttz, C. Xia, *Tetrahedron* **38**, 863 (1982); T. J. LePage and R. Breslow, *J. Am. Chem. Soc.*, **109**, 6412 (1987).
5. L. Y. Chiang, D. C. Johnston, D. P. Goshorn and A. N. Bloch, *Synth. Met.* **27**, B639 (1988); L. Y. Chiang, D. C. Johnston, D. P. Goshorn and A. N. Bloch, *J. Am. Chem. Soc.* **111**, 1925 (1989).
6. J. B. Torrance, P. S. Bagus, I. Johannsen, A. I. Nazzari, S. S. Parkin and P. Batail, *J. Appl. Phys.* **63**, 2962 (1988).
7. K. Awaga, T. Sugano and M. Kinoshita, *Solid State Commun.* **57**, 453 (1986); T. Sugawara, S. Murata, K. Kimura and H. Iwamura, *J. Am. Chem. Soc.* **107**, 5293 (1985); E. Dormann, M. J. Nowak, K. A. Williams, R. O. Angus and F. Wudl, *J. Am. Chem. Soc.* **109**, 2594 (1987).
8. T. Sugawara, S. Bandow, K. Kimura, and H. Iwamura, *J. Am. Chem. Soc.*, 1984, **106**, 6450; T. Sugawara, S. Murata, K. Kimura, and H. Iwamura, *J. Am. Chem. Soc.*, 1985, **107**, 5293.
9. D. Braun, *Pure Appl. Chem.* **30**, 41 (1972).
10. L. Y. Chiang and H. Thomann, *J. Chem. Soc., Chem. Commun.* 172 (1989).
11. H. J. Backer and V. D. Baan, *Rec. Trav. Chim.* **56**, 1175 (1937).
12. F. Effenberger, E. Auer and P. Fischer, *Chem. Ber.* **103**, 1440 (1970).
13. J. Thomaidis, P. Maslak and R. Breslow, *J. Am. Chem. Soc.*, **110**, 3970 (1988).
14. K. Bechgaard and V. D. Parker, *J. Am. Chem. Soc.* **94**, 4749 (1972).
15. L. Y. Chiang, D. C. Johnston, J. P. Stokes and A. N. Bloch, *Synth. Met.* **19**, 697 (1987).
16. L. Y. Chiang and D. P. Goshorn, *Mol. Cryst. Liq. Cryst.* **176**, 229 (1989).
17. The data of Figure 2 were obtained by D. C. Johnston of Exxon Research and Engineering Co.

CHARGE TRANSFER COMPLEX OF HEXAKIS (ALKYLTHIO) BENZENE WITH  
TETRAFLUOROTETRACYANOQUINODIMETHANE (tEDTB)<sub>2</sub> TCNQF<sub>4</sub>.

CHASSEAU D.\*, ALLEAUME M.\*, BRAVIC G.\*, LAPOUYADE R.\*\*\*, MORAND J.P.\*\*,  
AMIELL J.\*\*\* and DELHAES P.\*\*\*

\* Laboratoire de Cristallographie et Physique Cristalline, URA 144 CNRS

\*\* Laboratoire de Photophysique et Photochimie Moléculaire, URA 348 CNRS et  
ENSCP Bordeaux

\*\*\* Centre de Recherche Paul Pascal CNRS

Domaine Universitaire de Bordeaux I, 33405 - TALENCE Cédex ( FRANCE ).

### Abstract

In order to evaluate the potentiality of organic donor molecules for molecular organic ferromagnets, with in principle C<sub>3</sub> molecular symmetry, as in the hexakis (alkylthio) benzene, we have prepared single crystals of the charge transfer complex of tris [ethylene dithio] benzene (tEDTB) with TCNQF<sub>4</sub>, which have been subsequently oxidized with bromine and arsenic pentafluoride gas. The stoichiometry of this complex is 2:1 and it crystallizes in the triclinic system, space group P<sub>1</sub> with the following cell parameters: a=11.515, b=11.044, c=10.460 Å, α=111.50°, β=122.50°, γ=93.82°. The crystal structure consists of columns of alternating donor dyads and acceptors monads (DDADDA). The degree of charge transfer is estimated to be 0.2-0.3 from the methods based on bond lengths. While (tEDTB)<sub>2</sub>- TCNQF<sub>4</sub> does not give a significant ESR spectrum, after treatment with the bromine or AsF<sub>5</sub> gas, a single intense line, centered around the free electron g value, appears without any evidence of either a ground or an excited triplet state.

### Introduction

In contrast to the considerable achievements that have occurred with electrical conductivity, and especially superconductivity, in organic materials, organic ferromagnets still remain a challenge. Meanwhile, several theoretical models have been proposed to realize ferromagnetic coupling in an organic solid [1]. From the structural standpoint Breslow [2], Miller et al. [1] and Yoshida et al.[3] use a donor (acceptor) component with one pair of degenerate highest occupied (lowest unoccupied) molecular orbital, to prepare mixed stacks of charge transfer (CT) complexes, whereas Torrance et al. [4] and Dormann et al. [5] explore segregated stacks of all donors (acceptors) as commonly found in electrically conducting radical ion salts.

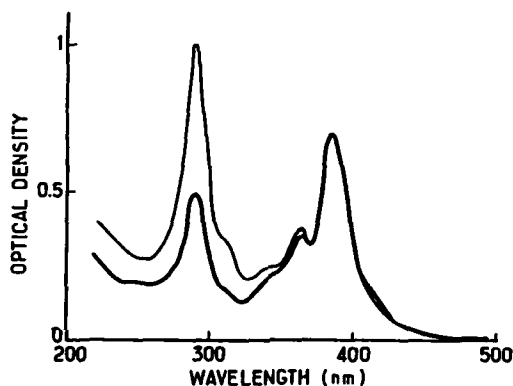
We have previously synthesized the following hexakis (alkylthio) benzenes (tEDTB, tVDTB) and tris (ethyleneoxythio) benzene (tEOTB) [6] and have already published some magnetic properties of a radical cation salt [7] and of a charge-transfer complex [8].

In order to assess the relevance of these molecules as possible precursors for molecular ferromagnets, we have now measured the physical properties at different oxidation states in solution and in the solid state of tEDTB complexed with TCNQF<sub>4</sub>. The X ray crystal structure of (tEDTB)<sub>2</sub>-TCNQF<sub>4</sub> has been refined.

### Synthesis and Molecular Composition

Acetonitrile solutions of tEDTB and TCNQF<sub>4</sub> are mixed at room temperature and the solvent is slowly evaporated. Black crystals deposit first when TCNQF<sub>4</sub> is in large excess (2 to 3 molar excess). When the mixed solution contained equimolar amount of tEDTB and TCNQF<sub>4</sub>, some tEDTB

crystallizes first and it is difficult to obtain the following black crystals of the complex free of tEDTB. Nevertheless, whatever the relative amount of tEDTB and TCNQF<sub>4</sub> is, the molecular composition of the complex remains the same: two molecules of tEDTB for one of TCNQF<sub>4</sub>, as shown by its U.V. spectrum (Fig. 1). The absence of any charge transfer band and of the radical ions at the spectroscopic concentrations used indicates a low equilibrium constant for the formation of the complex and explains the preferential crystallization of the insoluble tEDTB when the equilibrium is not shifted to the complex with an excess of the soluble TCNQF<sub>4</sub>.



— : a solution of 78 µg of (tEDTB)<sub>2</sub>-TCNQF<sub>4</sub> in 5 ml of CH<sub>3</sub>CN.  
 - - - : equimolar solution of tEDTB + TCNQF<sub>4</sub> in CH<sub>3</sub>CN (2.55 · 10<sup>-2</sup>M)

Fig. 1 - Electronic absorption spectra of the charge transfer complex (tEDTB)<sub>2</sub> - TCNQF<sub>4</sub>

#### Crystal Structure and degree of Charge Transfer

(tEDTB)<sub>2</sub> - TCNQF<sub>4</sub> crystallizes in the triclinic system, space group P1, with the following cell constants: a = 11.515(5)Å, b = 11.044(4)Å, c = 10.460(2)Å, α = 111.50 (3)°, β = 122.50(3)°, γ = 93.83(3)°, V = 983 Å<sup>3</sup>, Z = 1, D = 1.64 g.cm<sup>-3</sup> (and μ(CuKα) = 640 mm<sup>-1</sup>). Its crystal structure has been refined down to an R value of 0.037, using 3019 independent reflections [9]. The atomic numbering schemes and the bond lengths within the tEDTB donor and the TCNQF<sub>4</sub> acceptor are shown in fig 2. The TCNQF<sub>4</sub> molecule is located on a center of symmetry. No anomalous bond distances and angles are found except between the C23 -C24 atoms which are disordered as shown by the high values of their temperature factors. The six sulfur atoms of the tEDTB molecule do not deviate by more than 0.08 Å from the mean plane of the benzene ring whereas the maximum deviation of the CH<sub>3</sub> groups may reach 0.8 Å mainly for the two disordered carbon atoms which both are on the same side of the benzene plane. The TCNQF<sub>4</sub> molecule is not entirely planar, the nitrogen atoms being above (N51, 0.35 Å) and under (N52, -0.18 Å) the mean plane of the quinoid ring.



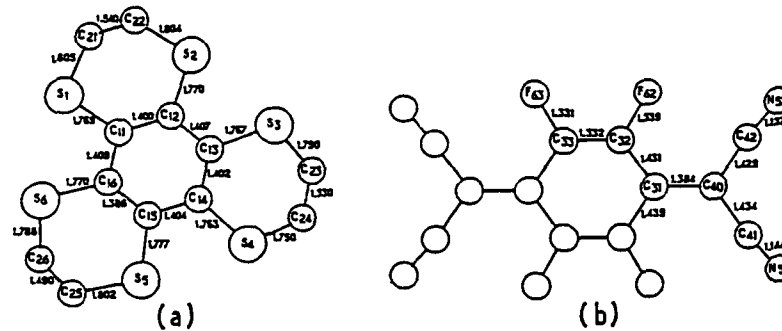


Fig. 2 - Bond lengths of tEDTB (a) and TCNQF<sub>4</sub> (b).

The crystal structure of (tEDTB)<sub>2</sub> - TCNQF<sub>4</sub>, as illustrated in fig. 3, consists of alternating donor diads and acceptor monads extending along the [111] crystallographic direction. The two molecular planes are nearly parallel; the dihedral angle between these two planes is only 1.5°. Within these stacks, the interplanar separations between two donors and between donor and acceptor are 4.19 Å and 3.34 Å respectively. The donor - acceptor interplanar separation is short for a sulfur containing donor and rather close to that observed in benzotrithiophene (BTT)<sub>2</sub> - TCNQF<sub>4</sub> (3.29 Å) [10].

On the contrary, the donor - donor separation is very large (4.19 Å), and particularly greater than in the case of the (tEDTB)<sub>2</sub> - BF<sub>4</sub> salt [7] where this distance has been found equal to either 3.75 or 3.98 Å between the two independent cations.

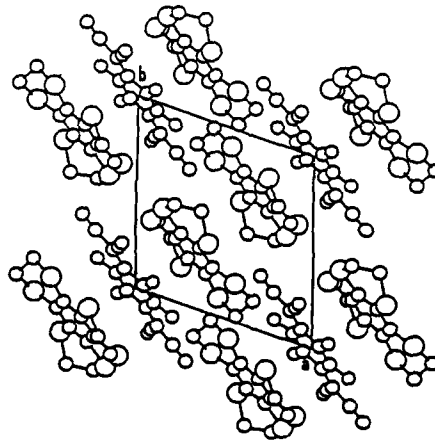


Fig. 3 - Projection of the crystal structure along the c axis.

The donor - donor and donor - acceptor molecular overlapping modes are shown in fig. 4. Within the donor diad, the tEDTB molecule is rotated by approximately  $60^\circ$  with respect to the neighboring molecule. The central benzene ring of tEDTB are stacked in such a way that the common area is rather small. The C - C bonds of tEDTB and TCNQF<sub>4</sub> are nearly parallel and one of the C - C bond of the benzene ring is superimposed on the long molecular axis of the TCNQF<sub>4</sub>.

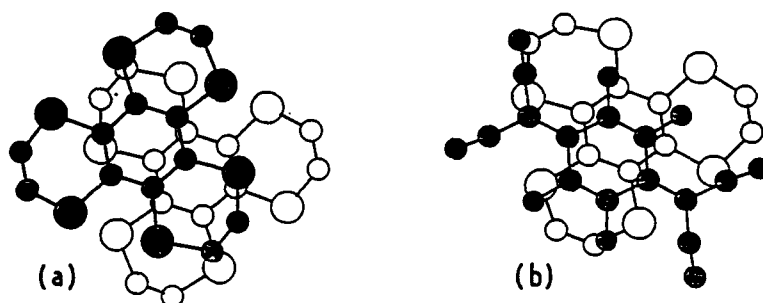


Fig. 4 - Overlapping modes  
a) between donors                      b) between donors and acceptors.

To emphasize the side-by-side interactions, the crystal structure may be described in an other way (Fig. 5).

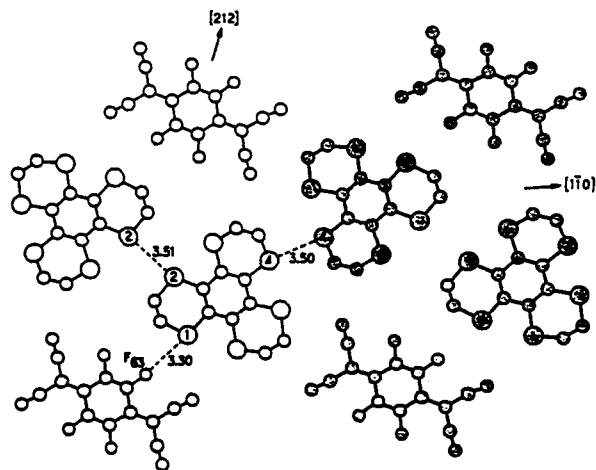


Fig. 5 - Projection of the crystal structure on the donor molecular plane.

The two tEDTB molecules, related by the short S2...S2 contact (3.51 Å), are nearly in the same plane, as well as one TCNQ<sub>4</sub> (S1...F63 = 3.30 Å); this group of three molecules repeat along the [212] direction to form a plane whose "width" is equivalent to two donor molecules. Between two adjacent planes, in the [110] direction, there is a "stair" of about 1 Å with an other sulfur-sulfur interaction S4...S4 = 3.50 Å. It has to be noticed that, although the S-S distances are the same, the strength of the interactions should be different because the angles between the S-S direction and the molecular planes are 3° [S2...S2] and 17° [S4...S4]. This hypothesis should be confirmed by the calculations of the transfer integrals.

Flandrois and Chasseau [11] and Kistenmacher et al. [12] have proposed empirical relations between the degree of charge transfer from the donor to the acceptor and the bond lengths of TCNQ<sub>4</sub> in the complex. As the bond lengths of neutral and radical anions of TCNQ<sub>4</sub> which are involved are not significantly different from those of TCNQ at the same degree of oxidation, these relations have been applied to the (tEDTB)<sub>2</sub> - TCNQ<sub>4</sub> complex; the results given by the two different relations for the degree of charge transfer are 0.25 and 0.29 respectively.

The mixed stack structure can also explain the absence of charge transfer in the infrared range (namely A following the Torrance's classification [13] characteristic of a mixed valence system and which is present in the BF<sub>4</sub> salt of tEDTB [7]).

#### E.S.R. Results

This complex presents a weak E.S.R. line which is centered at  $g = 2.0030$  (bandwidth  $\Delta H_{pp} = 7G$ ). This result is consistent with a low degree of charge transfer between tEDTB and TCNQ<sub>4</sub> moieties. After doping during one day with bromine or arsenic pentafluoride, as described by Chiang et al. [16], the e.s.r. intensity signal and the linewidth increase:  $g = 2.0095$ ,  $\Delta H_{pp} = 19G$  for bromine complex and  $g = 2.0086$ ,  $\Delta H_{pp} = 20G$  for AsF<sub>5</sub> complex. These  $g$  values are close to the  $g$  value observed for tEDTB in solution (2.0099) [7]. Furthermore, in the case of AsF<sub>5</sub> doping and by analogy with Chiang's results on hexamethoxytriphenylene compound (HMT), the molecular formula corresponds to (tEDTB)<sub>2</sub> - TCNQ<sub>4</sub> - (AsF<sub>5</sub>)<sub>4.3</sub>. E.S.R. spectrum observed down to 4K does not reveal any triplet state. In solution, the difference between the first and the second redox potential for the tEDTB compound (0.57V) is higher than for the HMT compound (0.37V) indicating that the dismutation of the radical cation in a dication and a neutral compound is less favourable for our compound. An exposure of the complex to the dopant longer than one day gave no further increase of the degree of oxidation.

#### Conclusion

We have shown that this new weak charge transfer band complex (tEDTB)<sub>2</sub> - TCNQ<sub>4</sub> presents a crystal structure with columns of alternating donors dyads and acceptors monads apparently similar to those recently found by other authors [10,15]. After doping with strong oxidizing agents we have tried without success, to find by E.S.R. spectroscopy the signature for the triplets excitons. Nevertheless this approach for the synthesis of high spin density organic solids will be pursued because we can make use of different donors belonging to this new series of C3 symmetry type molecules [6].

References

- 1 . J.S. Miller, A.J. Epstein, W.M. Reiff, Chem. Rev., **88**, 201 (1988)
- 2 . R. Breslow, Pure Appl. Chem. **54**, 201, (1982)
- 3 . Z. Yoshida and T.Sugimoto, Angew. Chem. Int. Ed. Engl., **27**, 1573, (1988)
- 4 . J.B. Torrance, S.Oostraa and A. Nazzari, Synth. Met., **19**, 709, (1986)
- 5 . E. Dormann, M.J. Nowak, K.A. Williams, R.O. Angus Jr and F.Wudl, J. Amer. Chem. Soc., **109**, 2594, (1987)
- 6 . R. Lapouyade and J.P. Morand, J. Chem. Soc. Chem. Commun., 223, (1987)
- 7 . R. Lapouyade, J.P. Morand, D. Chasseau, J.Amiell and P. Delhaes, Synth. Met., **16**, 385, (1986)
- 8 . J.P. Morand, L. Brzezinski, R. Lapouyade, J. Amiel and P. Delhaes, Mol. Cryst. Liq. Cryst., **156**, 237, (1988); J.P. Morand, L. Brzezinski, R. Lapouyade, C. Garrigou-Lagrange, J. Amiel and P. Delhaes, Mol. Cryst. and Liquid Cryst., (in press)
- 9 . D. Chasseau, M. Alléaume, G. Bravic, R. Lapouyade, Acta Cryst. C, to be published.
- 10 . T. Sugano, T. Hashida, A. Kobayashi, H.Kobayashi and M. Kinoshita Bull. Soc. of Japan (1989).
- 11 . S. Flandrois and D. Chasseau, Acta Cryst, **B33**, 2744, (1977)
- 12 . T.J. Kistenmacher, T.J. Emge, A.N. Bloch and D.O. Cowan, Acta Cryst., **B38**, 1193, (1982)
- 13 . J.B. Torrance, B.A. Scott, B.Welber, F.B. Kaufman and P.E. Seiden, Phys. Rev., **B19**, 730, (1979)
- 14 . L.Y. Chiang and H. Thomann, J. Chem. Soc. Chem. Commun., 172, (1989)
- 15 . L.Y. Chiang, D.C. Johnston, D.P. Goshorn and A.N. Bloch, J. Amer. Chem. Soc., **111**, 1925, (1989)
- 16 . L.Y. Chiang and D.P. Goshorn, Mol. Cryst. Liq. Cryst., in press as an invited paper for the Symposium of "Ferromagnetic and High Spin Molecular Based Materials", in A.C.S. Meeting, Dallas, 1989

FERROMAGNETIC INTERMOLECULAR INTERACTION AND CRYSTAL STRUCTURE  
OF  $\alpha$ -NITRONYL NITROXIDE

Kunio Awaga, Tamotsu Inabe, and Yusei Maruyama

Institute for Molecular Science, Myodaiji, Okazaki 444, Japan

ABSTRACT

The temperature dependence of the magnetic susceptibilities for several  $\alpha$ -nitronyl nitroxides have been measured. It is found that the intermolecular magnetic coupling in these radical crystals changes from antiferromagnetic to ferromagnetic depending on the substituents at  $\alpha$ -position. X-Ray crystal analysis and MO calculation have been carried out on the ferromagnetic  $\alpha$ -nitronyl nitroxide, 2-(4-nitrophenyl)-4,4,5,5-tetramethyl-4,5-dihydro-1H-imidazolyl-1-oxyl-3-oxide, revealing a two-dimensional ferromagnetic network linked by the  $N^{\delta+} \dots O^{\delta-}$  Coulomb attraction.

INTRODUCTION

The quest for organic/molecular ferromagnetism is the matter of concern now [1]. To our knowledge, there are only three metal-free organic radicals which have been confidently proved to exhibit ferromagnetic (FM) intermolecular interactions: galvinoxyl [2-4], tanol suberate [5-9], and bis(p-(octyloxy)phenyl)-carbene [10], although they do not fall into the three-dimensional FM ordered state even at low temperatures. It is characteristic that they are free  $\pi$ -radicals with strong spin polarization effect. It has been recently suggested [11,12] that the spin polarization effect stabilizes the triplet charge-transfer (CT) state and results in FM

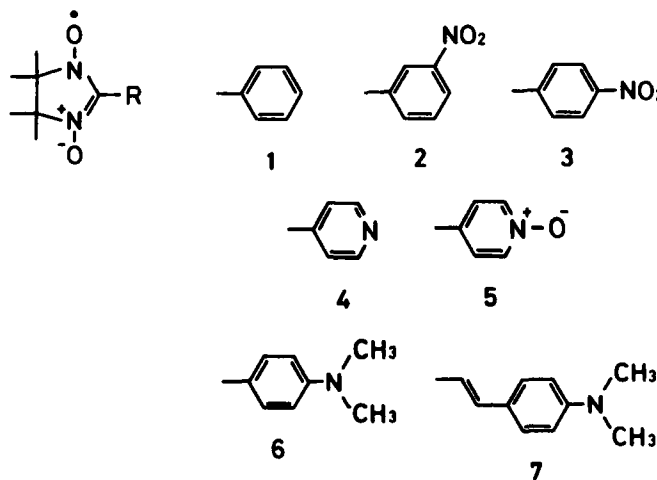


Fig. 1. The molecular structures of the  $\alpha$ -nitronyl nitroxides.

coupling, based on the MO calculations. This mechanism for stabilizing the FM intermolecular coupling, has originally been proposed by McConnell in the 1960's [13].

The stable organic radical,  $\alpha$ -nitronyl nitroxide, has an interesting molecular structure in this point of view. The unpaired  $\pi$ -electron stands close to the non-bonding electrons and, therefore, the strong spin polarization caused from the  $n$ - $\pi$  exchange interaction can be expected in this radical family. In this report, we describe the magnetic properties of several  $\alpha$ -nitronyl nitroxides 1-7 shown in Fig. 1. Furthermore, the magneto-structural correlation for the FM coupling is discussed, based on the results of the X-ray crystal analysis and the MO calculation on the FM nitroxide 3.

#### EXPERIMENTAL

The nitroxide radicals 1-7 were prepared by the reported method [14] and were purified by recrystallization from benzene solution. The elemental analyses, IR spectra and the observed Curie constants indicated that 5 and 6 crystallize with the solvent in the compositions of  $(5)_2(C_6H_6)$  and  $(6)_2(C_6H_6)$ . The radical concentrations in the other ones were estimated to be 100 % within experimental error from the Curie constants.

#### MAGNETIC PROPERTIES

The temperature,  $T$ , dependence of the paramagnetic susceptibilities  $\chi_p$  of the nitroxides 1-7 were measured over the range from 2 to 250 K, by using a Faraday balance.  $\chi_p$  of them are found to follow the Curie-Weiss law in this temperature range. The results for 1-3 [15] are shown in Fig. 2, where  $\chi_p T$

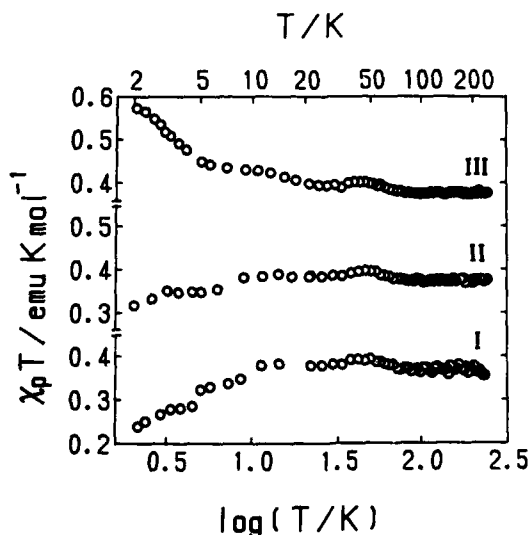


Fig. 2. The temperature dependence of the product  $\chi_p T$  for 1-3.

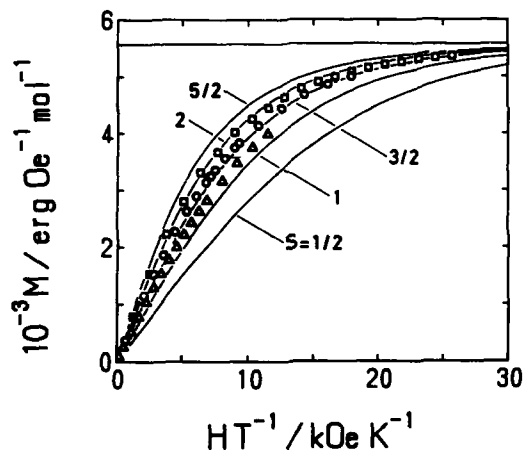


Fig. 3. The magnetization curve of 3 measured at 4.5 K (triangles), 3 K (circles), and 2 K (squares). The solid curves are theoretical ones for the  $J=S=1/2-5/2$  ( $L=0$ ) paramagnetic spin entities.

is plotted as a function of logarithms of  $T$ .  $\chi_p T$  of 1 and 2 are almost constant in the high-temperature range and decrease monotonically below about 10 K, indicating the presence of a weak antiferromagnetic (AFM) intermolecular interactions. On the other hand, the nitroxide 3 shows an opposite temperature dependence.  $\chi_p T$  of 3 increases gradually with decreasing temperature, indicating the FM coupling.

The FM coupling of 3 was firmly supported by the measurements of the field  $H$  dependence of the magnetization  $M$  at low temperatures [15]. Figure 3 shows the plots of  $M$  vs.  $H/T$ . The solid curves show the theoretical ones for the  $J=S=1/2-5/2$  ( $L=0$ ) paramagnetic spin entities. They are drawn to reach a saturation magnetization of  $M_s=5.60 \times 10^3$  erg Oe $^{-1}$  mol $^{-1}$ . The magnetization curves of 3 exhibited a more rapid saturation than that of the  $S=1/2$  spin entity. Furthermore, it is clearly shown that  $M$  comes to saturation more rapidly as the temperature decreases. These facts indicate that FM interaction, comparable to the thermal energies of this temperature range (2-4 K), operates in the crystal of 3. The magnetization at 2 K, the lower limit of the temperature measurement, almost corresponds to the theoretical one for  $S=2$  and, therefore, it is certain that the FM coupling covers more than four radicals.

The Weiss constants,  $\theta$ , for 1-7 determined from the reciprocal  $\chi_p$  vs.  $T$  plots (not shown), and are listed in Table I. As a matter of course, the nitroxide 3 gives positive one of +0.9K. The FM interaction of 3 is considered to be comparable to the thermal energy of 1 K, which is quite consistent to the results of the magnetization curve measurements. Furthermore, we observed small positive Weiss constants in 4 and 7. Through these magnetic measurements, anyhow, it is convinced that the magnetic coupling in these nitroxides changes from AFM to FM depending on the substituents, and consequently that the nitroxides 3, 4 and 7 exhibit

Table I. The Weiss constants.

	1	2	3	4	5	6	7
$\theta/K$	-1.4	-0.5	+0.9	+0.4	-3.1	0.0	+0.5 $\pm$ 0.5

weak FM interactions. This radical family could be useful to determine the factor controlling the magnetic coupling in the solid.

#### MAGNETO-STRUCTURAL CORRELATION IN THE FM NITROXIDE 3 [16]

##### Crystal Structure

The X-ray crystal analysis has been carried out on the FM radical 3. The crystal data with  $2 \times 2 \times 60^\circ$  were collected on a RIGAKU AFC-5 four-circle diffractometer with monochromatic  $\text{Mo-K}\alpha$  radiation. The crystal of 3 is found to belong to the orthorhombic  $Fdd2$  [17] space group [ $a=10.960(3)$ ,  $b=19.350(3)$ ,  $c=12.347(5)$  Å,  $Z=8$ ,  $R(F)=0.0437$  for 540 independent reflections with  $|F_o| > 3\sigma(|F_o|)$ ]. The nitroxide 3 has a twisted molecular structure, in spite of the fact that 3 can resonate with the planar quinonoid-structure. The phenyl ring is almost coplanar with the nitro group, but forms an angle of  $50.3^\circ$  with the plane of the  $\alpha$ -nitronyl nitroxide, O-N-C-N-O. In nitroxide 1, the corresponding dihedral-angle is about  $30^\circ$  [18,19], which is smaller than that in 3. The molecular distortion in 3 would be ascribed to the effect of the intermolecular interaction, as is shown later.

The projection of the crystal structure of 3 along the  $b$  axis, is shown in Fig. 4(a). There may occur weak intermolec-

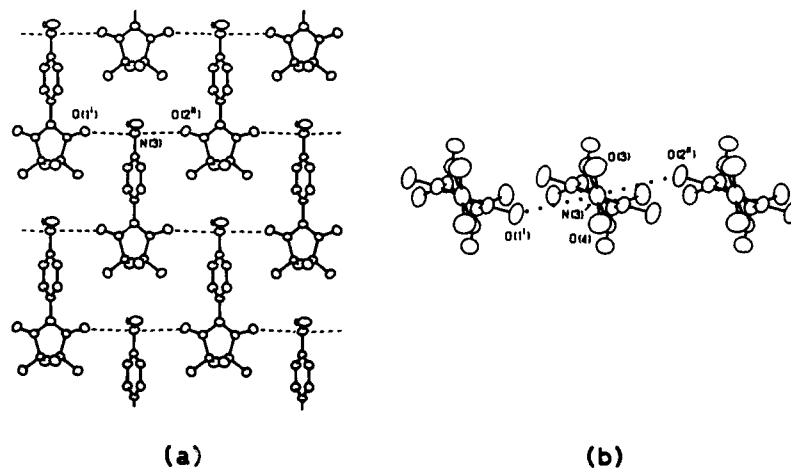


Fig. 4. (a) The projection of the structure of 3 along the  $b$  axis. (b) The molecular arrangement of 3 in the 2-D network projected to the  $ab$  plane.



ular contacts between the O-atoms (O(1) and O(2)) in the NO groups and the N-atoms (N(3)) in the NO<sub>2</sub> groups, and the nitroxide 3 forms a two-dimensional (2-D) network by these contacts. Figure 4(b) shows the intermolecular conformation in this network, which is projected to the *ab* plane. The N(3) is located at the middle point between O(1<sup>i</sup>) and O(2<sup>i+1</sup>) in the neighboring each radicals. The distance of O(1<sup>i</sup>)...N(3) or N(3)...O(2<sup>i+1</sup>) is 3.369(3) Å. The nitrophenyl plane is almost perpendicular to the O(1<sup>i</sup>)...N(3)...O(2<sup>i+1</sup>) line.

Each of the 2-D sheets are connected by the weak contacts, maybe hydrogen bondings, between O-atoms of NO and/or NO<sub>2</sub> groups and the H-atoms of phenyl rings (not shown). These contacts would also reflect the negative-charge polarization on the O-atoms. The intermolecular overlap between sheets seems to be small and, therefore, this interaction may not contribute to the FM coupling of 3.

#### MO Calculation

MO calculation has been carried out, by using an MNDO RHF-doublet method. It is found that the electronic polarization effect in 3 is so large that large positive and negative charges appear on N(3) and O-atoms, respectively. It is inferred from this calculation that this 2-D network is formed mainly by the Coulomb attraction between the negative charges on O(1<sup>i</sup>) and O(2<sup>i+1</sup>), and the positive one on N(3). These intermolecular contacts probably result in the twisted molecular structure of 3.

We consider the magnetic coupling in the 2-D network. Figure 5 shows the ground-state electronic configurations of the two neighboring radicals, R<sub>1</sub> and R<sub>2</sub>, coupled by the intermolecular CT interaction. SOMO and NHOMO are defined as the singly-occupied and the highest doubly-occupied MO, respectively. They are drawn in a spin-unrestricted picture. The intramolecular exchange interaction or the spin polarization effect makes a energy difference between the corresponding  $\alpha$  and  $\beta$  orbitals.  $\alpha$  is defined as a spin direction parallel to that of the unpaired  $\pi$ -electron. R<sub>1</sub> is assumed to have a much enhanced spin polarization effect and a small energy separation between the two frontier orbitals. In this case, the CT takes place from NHOMO- $\beta$  in R<sub>1</sub> to SOMO- $\beta$  in R<sub>2</sub> because of the energetical advantage. The CT resonance occurs without losing

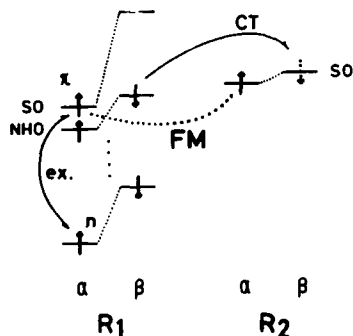


Fig. 5. FM coupling derived from the intramolecular exchange interaction and the intermolecular CT interaction.

the intramolecular exchange energies. It is worth noting that the resonance with the virtual CT state keeps the total spin multiplicity. Namely the electron transfers without changing its spin direction. This resonance results in the FM intermolecular interaction, as is shown in Fig. 5.

The  $\alpha$ -nitronyl nitroxide could have a strong spin-polarization effect as is already pointed out and, therefore, the nitroxide 3 can meet the conditions imposed on R<sub>1</sub>. Furthermore, it is indicated by the above MO calculation that the unpaired electron occupying SOMO is localized on the side of the nitronyl nitroxide and has little population in the nitrophenyl ring, whereas NHOMO and NLUMO are mainly distributed in the nitrophenyl ring. At the contact points in the 2-D network, therefore, the intermolecular overlap between SOMO's could be much smaller than those between SOMO-NHOMO and/or between SOMO-NLUMO. For these, it would be concluded that the FM interaction of 3 originates mainly in the SOMO-NHOMO and/or SOMO-NLUMO CT interactions, in addition to the strong spin polarization effect. These features resemble those in the FM organic radical, galvinoxyl [12]. The FM interaction in 3 is considered to work in the 2-D sheet through the N...O contacts.

#### REFERENCES

1. For review, see J.S. Miller, A.J. Epstein, and W.M. Reiff, *Chem. Rev.* **88**, 201 (1988).
2. K. Mukai, H. Nishiguchi, and Y. Deguchi, *J. Phys. Soc. Jpn.* **23**, 125 (1967); K. Mukai, *Bull. Chem. Soc. Jpn.* **42**, 40 (1969).
3. K. Awaga, T. Sugano, and M. Kinoshita, *Solid State Commun.* **57**, 453 (1986); *J. Phys. Chem.* **85**, 2211 (1986).
4. K. Awaga, T. Sugano, and M. Kinoshita: *Chem. Phys. Lett.* **128**, 587 (1987).
5. H. Lemaire and A. Rassat, in *The Triplet State*, (Beirut Symposium, 1967), p. 141.
6. C. Veyret and A. Blaise, *Mol. Phys.* **25**, 873 (1973).
7. G. Chouteau and C. Veyret, *J. Phys.* **42**, 1441 (1981).
8. P.J. Brown, A. Capiomont, B. Gillon, and J. Schweizer, *J. Mag. Mat.* **14**, 289 (1979); A. Benoit, J. Flouquet, B. Gillon, and J. Schweizer, *ibid*, **31-34**, 1155 (1983).
9. M. Saint Paul and C. Veyret, *Phys. Lett.* **A45**, 362 (1973).
10. T. Sugawara, S. Murata, K. Kimura, and H. Iwamura, *J. Am. Chem. Soc.* **107**, 5293 (1985).
11. K. Yamaguchi, T. Fueno, K. Nakasuji, and I. Murata, *Chem. Lett.* **1986**, 629.
12. K. Awaga, T. Sugano, and M. Kinoshita, *Chem. Phys. Lett.* **141**, 540 (1987).
13. H.M. McConnell, *Proc. Robert A. Welch Found. Chem. Res.* **11**, 144 (1967).
14. E.F. Ullman, J.H. Osiecki, D.G.B. Boocock, and R. Darcy, *J. Am. Chem. Soc.* **94**, 7049 (1972).
15. K. Awaga and Y. Maruyama, *Chem. Phys. Lett.* **158**, 556 (1989); *J. Chem. Phys.* **91**, 2743 (1989).
16. K. Awaga, T. Inabe, U. Nagashima, and Y. Maruyama, *J. Chem. Soc. Chem. Commun.* in press.
17. F. Wudl, private communication.
18. W. Wang and S.F. Watkins, *J. Chem. Soc. Chem. Commun.* **1973**, 888.
19. K. Awaga, T. Inabe, and Y. Maruyama: unpublished work.

MAGNETIC PROPERTIES OF MICROCRYSTALLINE "POLY(PHENYL-DIACETYLENES)" CARRYING RADICAL OR CARBENE CENTERS ON THE SIDE CHAINS.

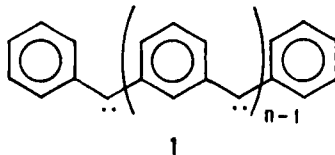
NOBORU KOGA, KATSUYA INOUE, NORIKO SASAGAWA, AND HIIZU IWAMURA  
Department of Chemistry, The University of Tokyo, 7-3-1 Hongo,  
Bunkyo-ku, Tokyo 113, Japan

ABSTRACT

1-Phenyl-1,3-butadiyne derivatives (3 and 4) carrying stable t-butyl nitroxide and diazomethyl groups, respectively, have been prepared. Mixed crystals of 3 and the corresponding hydroxylamine 2 (<1:1) polymerized in the solid state at 100°C to give black-violet microcrystals with a metallic luster. A microcrystalline sample of 4 underwent spontaneous polymerization at room temperature when crystallized to give an insoluble polymer which was then photolyzed at cryogenic temperature to generate triplet carbene centers attached to the phenyl rings of the poly(phenyldiacetylene). Some of these microcrystalline polymeric samples were responsive to a magnet at room temperature. Magnetic susceptibility measurements on the two samples revealed only weakly coupled independent spins. Hydrogen bonding between the polydiacetylene chains as estimated by X-ray crystal structure of 2 is expected to be effective for increasing the dimension of the spin alignment.

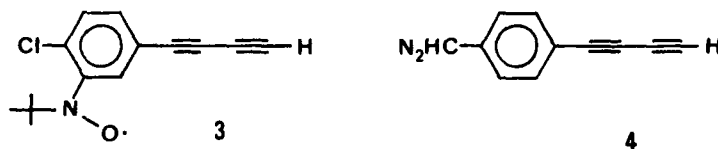
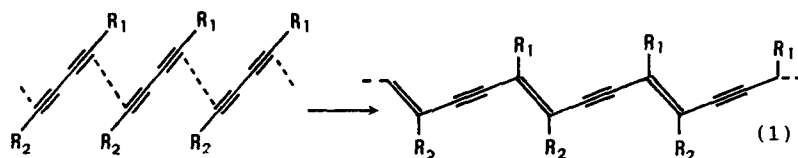
INTRODUCTION

Recent interest in high-spin organic molecules was highlighted by generation and characterization of m-phenylenetetra- and pentacarbenes (1(n = 4 and 5, respectively)). These have been demonstrated to be in ground nonet [1] and undecet [2] states, respectively, highest spin multiplicities ever reported for purely organic molecules. Whereas the higher homologues had been predicted to be of significance as models for one-dimensional organic ferromagnets [3] and are the targets of our synthetic efforts [4], the synthesis of the precursor diazo compounds becomes more and more difficult and laborious as the chain length increases. Not only there are very few straightforward synthesis for the precursors, but also it becomes difficult to have all the triplet centers generated without fail and kept intact: a prerequisite for having the expected strong exchange coupling among the carbene centers that are located on the cross-conjugated main chain. Furthermore, it is desirable for realization of usable macroscopic spins to have stable spins in place of highly reactive triplet carbenes. In order to overcome these difficulties, we have decided to modify our strategy and started to look for conjugated polymer chains to which stable radical centers are at-



tached as pendants. In this way, we may be able to construct molecules having hundreds of the electron spins and align them by bypassing the site where we are obliged to fail in generating all the radical centers and keeping them intact. For polymer chains, we pay special attention to poly(diacetylenes) out of a number of other possibilities [4]: polyacetylenes, poly(phenylenevinyls), polyphenylenes, and so on.

Some 1,3-butadiyne derivatives are known to undergo topologically controlled head-to-tail polymerization in crystals (Eq. 1)[5]. 1-Phenyl-1,3-butadiyne is one of very few examples that has a phenyl ring conjugated with the diacetylene chromophore and yet often undergoes smooth polymerization. In this paper, we report the synthesis of 1-phenyl-1,3-butadiyne derivatives **3** and **4** carrying a stable nitroxide group at the *m*-position on the phenyl ring and a *p*-diazomethyl group, respectively, their polymerization in the solid states, and some magnetic measurements of the polymers.



## RESULTS

### Synthesis

*p*-Chlorobromobenzene was coupled with 3-hydroxy-3-methyl-1-butyne in the presence of copper(I) iodide and  $\text{Pd}(\text{PPh}_3)_2\text{Cl}_2$  in triethylamine to give the phenylacetylene. The protecting group was removed by refluxing with sodium hydride in benzene. *p*-Chloroethynylbenzene was reacted with 1-bromo-3-hydroxy-3-methyl-1-butyne using copper(I) chloride and ethylamine in DMF. The hydroxyl group of the diacetylene was protected with 2,3-dihydropyran. When the *p*-chlorophenyldiacetylene ether was treated with *n*-butyllithium at  $-78^\circ\text{C}$  in anhydrous THF and then with 2-methyl-2-nitosopropane dimer, the product was not due to the metal-halogen exchange but ortho-metallation; 3-(*N*-tert-butylhydroxyamino)-4-chlorophenyldiacetylene derivative was obtained. Treatment first with *p*-toluenesulfonic acid in ethanol and then with sodium hydride in benzene gave the hydroxylamine **2** as colorless needles. It was then oxidized with Fremy's salt to give the corresponding nitroxide **3** as red crystals.

Poly(1-(p-diazomethylphenyl)-1,3-butadiyne) was obtained as follows. p-Bromobenzaldehyde ethyleneacetal was coupled with 3-hydroxy-3-methyl-1-butyne in the presence palladium diacetate to give the phenylacetylene derivative. After removal of the protecting group at the ethynyl group, the phenylacetylene was coupled with 1-bromo-3-hydroxy-3-methyl-1-butyne under the Cadiot-Chodokiewicz condition to give the doubly protected diacetylene derivative. The protecting groups were removed by the reaction first with sodium hydride in refluxing benzene and then with hydrochloric acid in aqueous dioxane. The aldehyde was converted in methanol solution to the tosylhydrazone which was then warmed with sodium methoxide in pyridine to give desired diacetylene monomer 4.

#### Topochemical Polymerization

Solid-state polymerization of hydroxylamine 2 was monitored by IR absorption on KBr discs (Figure 1). The degrees of polymerization as judged by the decrease of IR absorptions due to the H-C≡ and C=C moieties at 3250 and 2225/cm, respectively, and loss of solubilities in methanol were: 50% in 48 hr and 76% in 96 hr at 96°C. When the polymerization was carried out under oxygen, the polymer sample obtained showed ESR signals, suggesting partial conversion of the hydroxylamino group into the nitroxide. It was not possible to effect further oxidation for the purpose of obtaining fully oxidized samples.

Contrary to our expectation, 1-(3-(N-tert-butylnitroxyl)-4-chlorophenyl)-1,3-butadiyne 3 did not undergo polymerization on heating, under UV-irradiation or electron bombardment. Therefore the last recourse was made to prepare mixed crystals consisting of 2 and 3 and subject them to heat. The polymerization did take place to give black-violet microcrystals with a metallic luster when the content of 3 was lower than 50%. The rates of polymerization were often faster than that of neat crystals of 2; the reactions completed in 4 h at 50°C.

Solid-state polymerization of the diazodiacetylene 4 was spontaneous and monitored by IR absorption on KBr discs. Violet colored insoluble product was obtained. Since the polymerization reaction was so rapid that characterization of monomer

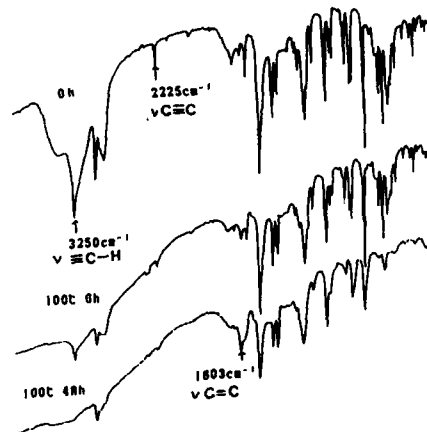


Figure 1. Polymerization of diacetylene 2 in KBr discs at 100 °C as monitored by IR absorptions.

4 required care. After removing most of pyridine, the final solvent used for the preparation of 4, the remaining solvent was replaced either with chloroform-d or 2-methyltetrahydrofuran by repeated addition and concentration of the latter solvents for the measurement of NMR and ESR spectra, respectively.

#### Crystal Structure of Hydroxylamine 2

The crystal structure of the hydroxylamine 2 as projected along the a axis and a/c diagonal is shown in Figure 2. Whereas the molecules appear to be stacked head-to-head along the crystal axis a, the nearest distance, carbons 1 and 1', between the neighboring molecules is as large as 8.00 Å. They are more closely stacked rather head-to-tail along the a/c diagonal with the distances between carbons 1 and 4' and 4 and 4' of the neighboring molecules being 4.55 and 4.72 Å, respectively. The latter columnar arrangements are bridged by intermolecular hydrogen bond between two hydroxylamino groups.

#### Thermal Analyses

The exothermicity of the solid-state polymerization of 2

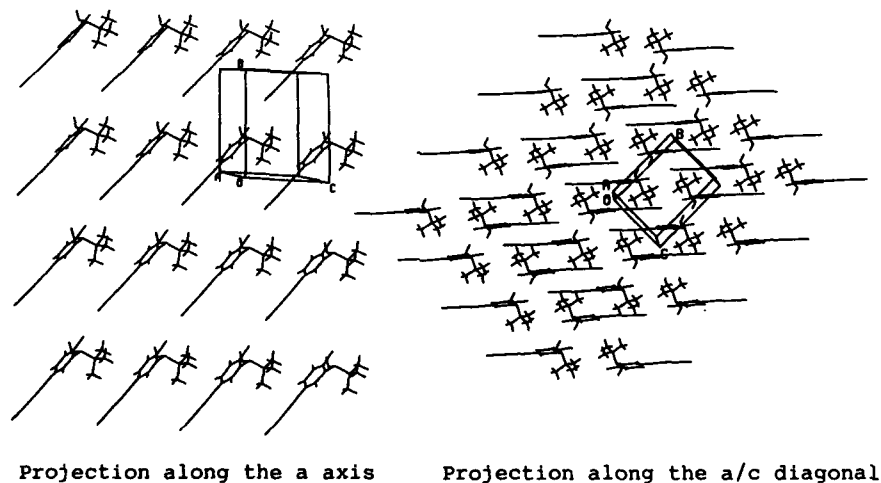


Figure 2. Two views of the unit cell for acetylene 2.

was 258.4 cal/g in good agreement with those ( $240 \pm 20$  cal/g) of other 1-phenyl-1,3-butadiynes. These values ( $\sim 65$  kcal/mol) are approximately equal to the difference of the bond enthalpies of C-C double and triple bonds, suggesting that decrease of bond orders during the polymerization process is mainly responsible for the enthalpy change.

### Photolysis

A microcrystalline sample of the polymer due to 4 was photolyzed at cryogenic temperature to generate triplet carbene centers attached to the pendant phenyl rings of the polymer.

### Magnetic Measurements

The sample obtained by cocrystallizing 2 and 3 in a 7:3 ratio showed ESR spectrum centered at  $g = 2.006$ . The magnetization curve of this sample at 4.2 K agreed nicely with the Brillouin function with  $S = 1/2$ . The  $1/\chi$  vs. temperature plots showed the Weiss temperature of +58.0 K as reproduced in Figure 3, suggesting the ferromagnetic coupling of the doublet centers. The Curie constant of the linear part of the plots showed that only 6.1% of the monomer units in the sample was the active nitroxide instead of the expected 30%!

When a rigid glass of diazodiacetylene 4 in MTHF was photolyzed at 4.6 K, it gave an ESR fine structure characteristic of triplet phenylcarbene (Figure 4):  $|D| = 0.4666$  and  $|E| = 0.0210/\text{cm}$ . The signals obeyed a Curie law in the temperature range 4.6~77 K. The magnetization curve obtained at 2.1 K after photolysis was consistent with  $S = 1$ . The  $1/\chi$  vs. T plots gave a negative Weiss temperature of -31.8 K. The Curie constant corresponds to the generation of the triplet phenylcarbene only in a few % yield.

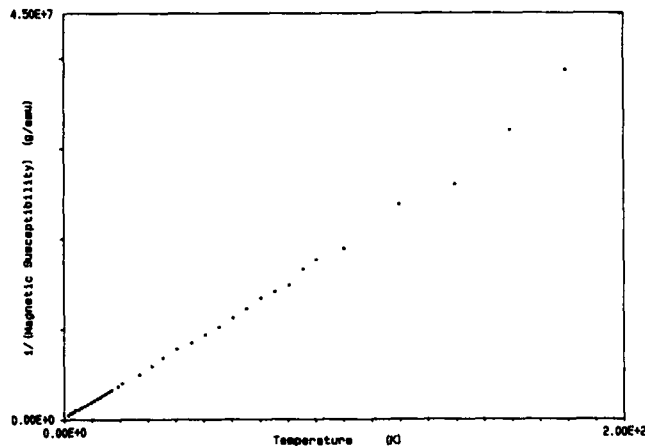


Figure 3. Temperature dependence of reciprocal magnetic susceptibility of the polydiacetylene from 2 + 3.



Figure 4. ESR fine structure due to the phenylcarbene from monomer 4.

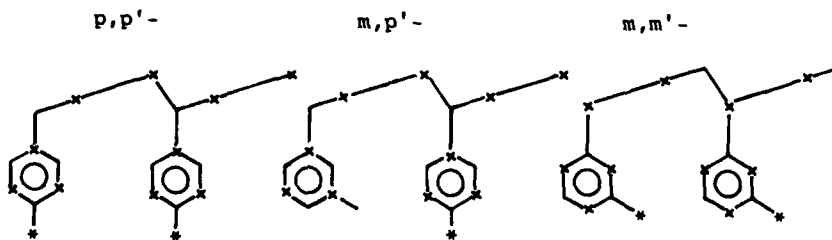
#### DISCUSSION

Conjugated polymers having stable radicals as pendants are considered to constitute a structural basis for designing and constructing high-spin organic molecules that would show interesting magnetic properties.

According to the theory of topological symmetry of alternating  $\pi$ -systems [6], spin quantum number  $S$  of the ground state is given by Eq. 2, where  $n^*$  and  $n$  are the numbers of starred and nonstarred carbon atoms, respectively. Let us take,

$$S = (n^* - n)/2 \quad (2)$$

for example, a dimer unit 5 in which radical centers are situated at  $p,p'$ -,  $m,p'$ - and  $m,m'$ -positions. Since  $n^* = 12$  and  $n = 10$  for the  $p,p'$ - and  $m,m'$ -isomers, and  $n^* = n = 11$  for the  $m,p'$ -substitution, the ground states are predicted to be triplet for the former and singlet for the latter. In other words, the exchange interactions between radical centers attached to the phenyl rings are predicted to be ferromagnetic when they are  $p,p'$  or  $m,m'$ , and the coupling is antiferromagnetic for the  $m,p'$ -isomer. In poly(1-phenyl-1,3-butadiynes), the radical centers may reside on the same positions of the repeating units to interact ferromagnetically; when the polymer in question consists of  $m$  units,  $S = (6m - 5m)/2 = m/2$ . The prediction is encouraging in that, if we are able to polymerize 1-(substituted phenyl)-1,3-butadiyne in a 1,4-fashion, all electron spins could couple ferromagnetically to generate  $S = m/2$  for the polymers consisting of  $m$  units.





According to Wegner [5], the 1,4-addition is possible if the 1,3-butadiyne molecules stack head-to-head in crystals, although the stacking may be slanted as shown in mode a of Figure 5. The empirical conditions necessary for realizing topochemically controlled head-to-tail polymerization are said to be:  $s = 3.4 \sim 4.0 \text{ \AA}$  and  $\gamma \approx 45^\circ$ . Operationally there are four modes of bonding for the polymerization of 1-substituted 1,3-butadiynes. Mode d would be predicted to be most likely for 2 by application of the principle of least motion to the triclinic crystal packing as shown in Figure 2. From the topological point of view, this is equivalent to the 1,4-addition (mode a) of head-to-head stacking.

The dark violet polymer crystals were insoluble in any organic solvents we tried. Aeration of the suspension of the polymer sample under supersonic agitation did not induce any meaningful conversion of the hydroxylamine functional group into the corresponding nitroxide although ESR signals were detected. To our dismay, however, the crystals of nitroxide 3 did not polymerize under typical conditions we tried. We therefore tried to dope the crystals of 2 with 3 and studied the mixed crystals. During the solid-state polymerization, some of the nitroxide radicals were not intact and the best sample we have so far obtained contained only 6.1 % of the theoretical concentrations. The expected superparamagnets were not obtained. However, it was encouraging that the coupling between the almost isolated radical centers was ferromagnetic ( $\theta = + 58.0 \text{ K}$ , Figure 3). We are currently pursuing oxidizing conditions for the polymer sample of 2 by electrochemistry.

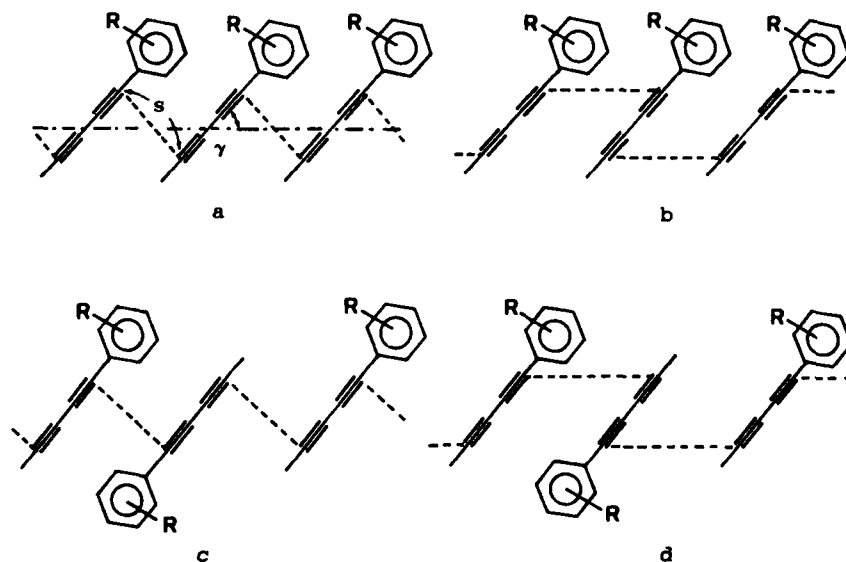


Figure 5. Two stacking and two bonding modes for the polymerization of 1-phenyl-1,3-butadiynes.

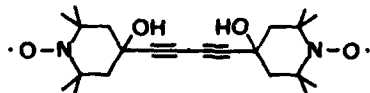
The suggested antiferromagnetic coupling ( $\theta = -31.8$  K) of the triplet centers in the photolyzed sample of the micro-crystalline polymer sample of 1-(p-diazomethylphenyl)-1,3-butadiyne **4** was discouraging. Although no crystal structural data are available, the result may be due to wrong polymerization patterns: mode b or c in Figure 5.

Basically poly(diacetylenes) are one-dimensional. One-dimensional spin alignments are said to be unstable at finite temperatures. Introduction of interchain exchange repulsion ( $J_2$ ), however weak it may be, is considered to stabilize the spin alignment. According to Tyutyulkov [7],  $T_C$  can become as high as 1190 K by introduction of  $J_2 = 0.00185$  eV. We hope such  $J_2$  values will be obtained by interchain interaction when the distance is  $0.3 \sim 0.35$  Å apart and the orientation of the overlap between the  $\pi$  moieties of the neighboring chains is appropriate [8]. In the present case, judging from the X-ray data of the precursor **2**, the hydrogen bond between the polymer chains is expected to contribute to this interchain interaction and stabilization of the spin alignment.

In 1988 Korshak and Ovchinnikov reported black powdery materials obtained by polymerization of a diacetylene carrying a pair of persistent nitroxide radicals symmetrically (**6**) [9]. A part of this sample was described to show ferromagnetic properties (spontaneous magnetization of ca. 0.022 emu G/g). Even if the expected poly(diacetylene) skeleton is formed in spite of the observed wrong crystal structure of the monomer for topochemical polymerization [10], the structure of the polymer is not consistent with our molecular design in two senses. First, radical centers are not conjugated with the main chain; they are too far apart by three saturated carbon atoms to have meaningful exchange coupling. For a second, even if there is one, since the structure is symmetric, the interaction is expected to be antiferromagnetic.

In spite of the present negative results and the above controversial data in the literature, we believe that the poly(diacetylene) skeletons have a number of merits worthy of further experimental studies. First, since the polymerization of diacetylenes is effected by heat or irradiation with electrons,  $\gamma$ -ray or UV-light in the solid state and topochemically controlled, there is fewer chance of the polymer samples being contaminated with catalysts often consisting of paramagnetic transition metals. Second, we can expect to obtain crystalline polymers that are more readily characterizable and expected to show firmer spin alignment. Third, since only the exposed part of the sample undergo polymerization, when the reaction is induced by irradiation, there is a chance of designing optomagnetic recording devices consisting only of organic polymers.

On the other hand, however, we have to be careful that the above merits can often become disadvantages as well. Since the polymerization is topochemically controlled, not all diacetylenes are amenable to the reaction. A number of other diacetylene derivatives have so far eluded our attempts to



polymerization.

Control of molecular packing in crystals, in other words crystal design, is now needed. Introduction of technology of liquid crystals or Langmuir-Blodgett membranes [12] may be of help. Second, poly(diacetylenes) are very insoluble in ordinary organic solvents, the radical centers serving as spin carriers have to be introduced in advance. Although mechanism of the polymerization does not require free radicals and topochemically controlled, there is a chance of the pendant radicals being intercepted by the polymerization reactions as observed in this study.

## EXPERIMENTAL SECTION

### X-ray Structure Determination and Other Measurements

Diffraction data were obtained on a Rigaku AFC-5R four circle diffractometer with graphite-monochromatized Mo K-radiation. Crystal data were as follows:  $C_{14}H_{14}NOCl$ , triclinic (from diethyl ether), space group P-1 (#2),  $a = 8.496(3) \text{ \AA}$ ,  $b = 10.755(5) \text{ \AA}$ ,  $c = 8.004 \text{ \AA}$ ,  $\alpha = 92.77(4)^\circ$ ,  $\beta = 106.51(3)^\circ$ ,  $\gamma = 74.85^\circ$ ,  $V = 676.6(5) \text{ \AA}^3$ ,  $Z = 2$ ,  $d_c = 1.22 \text{ g cm}^{-3}$ . 1973 Independent reflections with  $I > 3\sigma(I)$  were obtained and used in the structure analysis. The final R and  $R_w$  values were 0.081 and 0.102, respectively.

ESR spectra were obtained on a Bruker ESP 300 X-band (9.41 GHz) spectrometer attached with an Air Products Helitran LTR-3-110 cryostat.

The magnetization and magnetic susceptibility data were obtained on an Oxford Instruments magnetic susceptibility system with a 7 T superconducting magnet.

Differential scanning calorimetry was carried out on a Rigaku DPS-8151 Ver. 2.10 Thermal Analysis System.

### Materials

**1-{3-(N-tert-butyl)hydroxylamino-4-chlorophenyl}-1,3-butadiyne (2).** A mixture of 100 mg (0.26 mmol) of the protected hydroxylamine and 10 mg of pyridinium p-toluenesulfonate in 50 ml of ethanol was heated at  $55^\circ\text{C}$  for 3 hr. The reaction mixture was cooled, poured into 200 ml of water, and extracted with ether. The organic layer was dried over magnesium sulfate and concentrated in vacuo. To the benzene solution (50 ml) of the residue was added 10 mg of sodium hydride. The mixture was heated under reflux for 1 hr, cooled, filtered and the filtrate was evaporated at room temperature to yield pale yellow solids. Recrystallization from ether-hexane (1:1) gave 55 mg (86 %) of colorless triclinic crystals: mp  $140^\circ\text{C}$ ;  $^1\text{H NMR}$  (270 MHz,  $\text{CDCl}_3$ )  $\delta$  1.20 (9H, s), 2.50 (1H, s), 5.36 (1H, brs), 7.23 (2H, dd,  $J=8.2, 1.9 \text{ Hz}$ ), 7.29 (2H, d,  $J=8.2 \text{ Hz}$ ), 7.76 (1H, d,  $J=1.9 \text{ Hz}$ ). Anal. Found: C, 67.66; H, 5.86; N, 5.65; Cl, 14.18 %. Calcd for  $C_{14}H_{14}NC10$ : C, 67.88; H, 5.70; N, 5.65; Cl, 14.31 %.

**1-{3-(N-tert-butyl)nitroxyl-4-chlorophenyl}-1,3-butadiyne (3).** A 5 ml aqueous solution of 500 mg of Frey's salt was added dropwise to a mixture of 2 g of potassium dihydrogenphos-

phate, 0.1 g of potassium hydroxide, 100 mg (0.40 mmol) of 2 in water-THF (3:1). The reaction mixture was stirred at room temperature for 3 hr and then extracted with ether. The organic layer was washed with cold water, dried over magnesium sulfate, and concentrated under reduced pressure at room temperature to yield red oil. The crude product was crystallized from n-pentane-ether (10:1) to give 75 mg (76 %) of red crystals: mp 81 - 82 °C; ESR(X-band)  $g = 2.0066$ ,  $a(N) = 13.78$  G. Anal. Found: C, 68.31; H, 5.43; N, 5.71; Cl, 14.36 %. Calcd for  $C_{14}H_{13}NCIO$ : C, 68.16; H, 5.31; N, 5.68; Cl, 14.37 %.

**1-(p-Formylphenyl)-1,3-butadiyne tosylhydrazone.** Anal. Calcd for  $C_{18}H_{13}N_2O_2S$ : C, 67.06; H, 4.38; N, 8.69; S, 9.93. Found: C, 66.82; H, 4.46; N, 8.58; S, 9.85 %.

**1-(p-(Diazomethyl)phenyl)-1,3-butadiyne (4).** A mixture of 37.8 mg of sodium methoxide and 220 mg of the tosylhydrazone in 2 ml of freshly distilled pyridine was heated at 60 - 65 °C for 20 min under nitrogen atmosphere. The dark-orange-colored reaction mixture was diluted with 10 ml of cold water and treated twice with 5 ml each of n-pentane. The organic layer was washed with cold water and brine and then dried over sodium sulfate at 5 °C. The solution was concentrated under reduced pressure and kept in a refrigerator. The yield of 4 was 27 %.  $^1H$  NMR( $CDCl_3$ )  $\delta$  2.49 (1H, s), 4.97 (1H, s), 6.85 (2H, AA'BB'm), 7.44 (2H, AA'BB'm).  $\lambda_{max} = 485$  nm.

#### REFERENCES

- (a) Y. Teki, T. Takui, K. Itoh, H. Iwamura, K. Kobayashi, J. Am. Chem. Soc. **105**, 3722 (1983); (b) T. Sugawara, S. Bandow, K. Kimura, H. Iwamura, K. Itoh, J. Am. Chem. Soc. **106**, 6449 (1984); (c) T. Sugawara, S. Bandow, K. Kimura, H. Iwamura, K. Itoh, J. Am. Chem. Soc. **108**, 368 (1986); (d) Y. Teki, T. Takui, K. Itoh, H. Iwamura, K. Kobayashi, J. Am. Chem. Soc. **108**, 2147 (1986).
- I. Fujita, Y. Teki, T. Takui, T. Kinoshita, K. Itoh, F. Miko, Y. Sawaki, A. Izuoka, T. Sugawara, H. Iwamura, J. Am. Chem. Soc., 1990 (to be published).
- (a) K. Itoh, Chem. Phys. Lett. **1**, 235 (1967); (b) N. Mataga, Theor. Chim. Acta **10**, 372 (1968).
- (a) H. Iwamura, Pure Appl. Chem. **58**, 187 (1986); (b) **59**, 1595 (1987); (c) J. Phys. **49**, C8-813 (1988).
- (a) G. Wegner, Z. Naturforsch. **246**, 824 (1988); (b) Pure Appl. Chem. **49**, 443 (1977).
- A. A. Ovchinnikov, Theor. Chim. Acta **47**, 297 (1978).
- N. Tyutyulkov and S. Karabunarliev, Intern. J. Quantum Chem. **29**, 1325 (1986).
- (a) A. Izuoka, S. Murata, T. Sugawara, H. Iwamura, J. Am. Chem. Soc. **107**, 1786 (1985); (b) A. Izuoka, S. Murata,

- T. Sugawara, H. Iwamura, J. Am. Chem. Soc. 109, 2631 (1987).
- 9.(a) Yu. V. Korshak, A. A. Ovchinnikov, A. M. Shapiro, T. V. Medvedeva, V. N. Spektor, Pisma Zh. Eksp. Teor. Fiz. 43, 309 (1986); (b) YU. V. Korshak, T. V. Medvedeva, A. A. Ovchinnikov, V. N. Spektor, Nature 326, 370 (1987).
10. J. S. Miller, D. T. Clatzofer, J. C. Calabrese, A. J. Epstein, J. Chem. Soc., Chem. Commun. 322 (1988).
- 11.(a) B. Hupfer, H. Ringsdorf, H. Schupp, Makromol. Chem. 182, 247 (1981); (b) M. Engel, B. Hisgen, R. Keller, W. Kreuder, B. Reck, H. Ringsdorf, H.-W. Schmidt, P. Tschirner, Pure Appl. Chem., 57, 1009 (1985).

## ROLE OF TOPOLOGY IN SPIN ALIGNMENT OF ORGANIC MATERIALS

KOICHI ITOH, TAKEJI TAKUI, YOSHIO TEKI AND TAKAMASA KINOSHITA  
Osaka City University, Faculty of Science, Department of Chemistry, Sugimoto,  
Sumiyoshi-ku, Osaka 558, Japan

## ABSTRACT

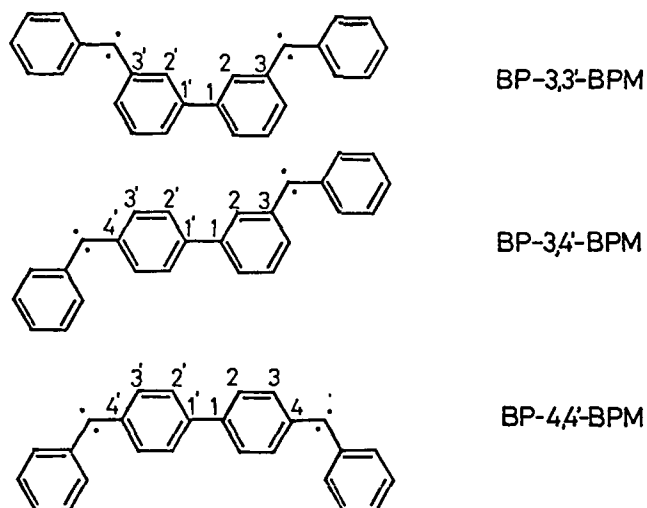
It is shown that the spin alignment in organic molecules as determined by single crystal ESR is highly dependent on the topological nature of their molecular pi electron networks. The three topological isomers of a high-spin molecule, biphenyl-*n,n'*-bis(phenylmethylene), abbreviated as BP-3,3'-BPM, BP-3,4'-BPM and BP-4,4'-BPM are taken as model compounds. BP-3,3'-BPM has a unique spin alignment for which the simple molecular orbital and valence bond methods predict different ground-state spin multiplicities. The above remarkable feature of spin alignment in organic high-spin molecule is interpreted in terms of their spin density distributions which have been determined by a single crystal ENDOR technique and compared with theoretical values calculated on the basis of a generalized Hubbard model as well as the Heisenberg model. This approach is extended to magnetic polymers in order to characterize their structure of the spin sites.

## INTRODUCTION

In recent years, much interest has been focused on ferromagnetism of organic materials, and a few polymers have been reported to exhibit ferromagnetic behaviors [1-3]. However, neither the mechanisms interpreting such behaviors nor their spin structures have been clarified. It is needed for characterization and molecular design of such organomagnetic materials, at this stage, to understand the mechanism of spin alignment characteristic of organic molecules from basic studies and to establish a method for characterizing their spin structures. The aim of this paper is to elucidate an important role of topology in spin alignment in organic materials and to demonstrate the utility of an electron-nuclear double resonance (ENDOR) technique to the determination of spin alignment not only in model high-spin molecules but also in magnetic polymers.

Since the detection of *m*-phenylenebis(phenylmethylene), the first high-spin molecule, in 1967 [4], we have synthesized and characterized a series of organic high-spin molecules as models for organic ferromagnets [5]. Very recently, an oligomer of a one-dimensional ferromagnetic polymer has been obtained with the spin multiplicity as high as undecet ( $S = 5$ ) [6]. The molecular design for most of these compounds has been based on the utilization of pi spins in topologically-degenerate non-bonding MO's (NBMO) as well as of sigma or "n" spins in the localized non-bonding orbitals on the divalent carbon atoms of carbenes.

In the present work, we have studied the spin alignment of three topological isomers of a high-spin molecule, biphenyl-*n,n'*-bis(phenylmethylene) ( $n = 3, 4$ ) which is abbreviated as BP-*n,n'*-BPM, and found a dramatic change in the ground-state spin depending on the topology of their pi electron networks. This remarkable feature of spin alignment is interpreted in terms of their spin density distributions which have been determined by a single crystal ENDOR technique and compared with theoretical values calculated on the basis of a generalized Hubbard model and the Heisenberg model. This approach is extended to magnetic polymers in order to characterize their structure of the spin sites.



#### Ground-State Spin of BP-3,3'-BPM

BP-3,3'-BPM was reported in 1978 by one of the authors [7]. This high-spin molecule is interesting because the spins on the two divalent carbon atoms couple through a biphenyl skeleton in contrast to the high-spin molecules reported so far where spins couple through a benzene ring. This alternant hydrocarbon was generated at 4.2 K or 20 K by the photolysis of its diazo precursor oriented in a single crystal of benzophenone. From the analysis of angular dependence and temperature dependence of the ESR spectra, the lowest energy levels were found to be nearly degenerate singlet, triplet and quintet states in the order of increasing energy, i.e., the singlet ground state. There are two molecular conformers L and H which are stable at low and high temperature phases, respectively. The triplet and quintet states are, respectively, located above the ground state by 20 and 60  $\text{cm}^{-1}$  for conformer L, and by 45 and 135  $\text{cm}^{-1}$  for conformer H. The spin Hamiltonian parameters of conformer L are  $D = -0.29583 \text{ cm}^{-1}$ ,  $E = 0.06032 \text{ cm}^{-1}$ , and  $g = 2.0040$  for the triplet state, and  $D = 0.10349 \text{ cm}^{-1}$ ,  $E = -0.01457 \text{ cm}^{-1}$ , and  $g = 2.0040$  for the quintet state. Similar values were also obtained for conformer H [7]. This ground-state spin is particularly interesting from the following reason.

It is widely known that from the simple molecular orbital picture by Longuet-Higgins the ground-state spin of the pi system of an alternant hydrocarbon is given by

$$S_{MO} = (1/2)(N - 2T), \quad (1)$$

if degeneracies due to geometrical symmetry do not exist, where N is the number of carbon atoms in the pi electron network and T the number of double bonds in its principal resonance structure [8].  $N - 2T$  is the number of NBMO. On the other hand, the valence bond picture by Lieb and Mattis [9] and by Ovchinnikov [10] predicts

$$S_{VB} = (1/2)(n_* - n_o), \quad (2)$$

where  $n_*$  and  $n$  are the numbers of the starred and unstarred carbon atoms, respectively. Although these predictions are the useful guiding principles for designing organic high-spin molecules as well as organic ferromagnets for their simplicity, in principle they may not necessarily agree with each other. In fact, there exists a relationship  $S_{MO} \geq S_{VB}$  [11]. BP-3,3'-BPM is the first example of such cases [7].

For BP-3,3'-BPM, we obtain  $S_{MO} = 1$  from Eq. (1) while  $S_{VB} = 0$  from Eq. (2). This means that the pi spins on each of the two divalent carbon atoms couple through biphenyl skeleton to be parallel from the MO picture, while to be antiparallel from the VB picture. Since the two NBMO's and the two localized  $n$  orbitals are nearly degenerate, the MO picture coupled with Hund's rule predicts the quintet ground state against the experiment. On the other hand, since the one center exchange integral between the orthogonal orbitals,  $n$  and  $\pi$ , is positive or ferromagnetic, the  $n$  and  $\pi$  spins on the same divalent carbon atom are expected to be parallel. As a result of this, the VB picture predicts the singlet ground state in agreement with the experiment. This interesting results are interpreted as due to a particular spin density distribution in the biphenyl skeleton using the present ENDOR experimental results described later.

#### EXPERIMENTAL

Each diazo precursor of BP- $n,n'$ -BPM was oriented in host single crystals which were grown in the dark around 6°C by slowly cooling a benzene or benzene-ethanol (1:1) mixed solution in which the guest-to-host concentration was 0.03-0.006 mole fraction. Benzophenone- $d_{10}$  was chosen as host single crystals for BP-3,3'-BPM and BP-3,4'-BPM, while 1,3-dibenzoylbenzene for BP-4,4'-BPM. Photolysis was carried out with an XBO 500 W high-pressure mercury lamp at 4.2 K except for BP-4,4'-BPM which was photolyzed at 77 K.

ESR measurements of BP-3,4'-BPM and BP-4,4'-BPM were made with a home-made spectrometer equipped with a JEOL JES K-band (25 GHz) microwave unit and with an X-band (9 GHz) Bruker ESP300 spectrometer, respectively. All the ENDOR measurements were performed with a Bruker ESR 350 spectrometer operating at X-band. For measurements of temperature dependence Oxford Variable Temperature Controller ESR910 was employed.

#### THEORETICAL

We have shown that a generalized Hubbard model [12] and the Heisenberg model [13] provide rather satisfactory and complementary descriptions for organic high-spin molecules which has so many open-shell electrons that the calculation of their electronic structure is difficult by the conventional molecular orbital or valence bond methods. In the following, these approaches are briefly described along with the parameters adopted here. An weak interaction model [7] is also given, a model which excellently interprets the interesting nature of biphenyl skeleton mentioned above.

##### Generalized Hubbard Model

For the understanding of the spin alignment in BP- $n,n'$ -BPM, we have carried out semiempirical calculation of their electronic structure using a generalized Hubbard Hamiltonian [12,14],



$$\mathcal{H} = -T \sum_{m, \sigma} a_{m, \sigma}^+ a_{m, \sigma} + (1/2) \sum_{m, \sigma} n_{m, \sigma} n_{m, \sigma} - J \sum_{k, m} [S_{zk} S_{zm} + (1/2)(S_k^+ S_m^- + S_k^- S_m^+)], \quad (3)$$

where  $a^+$  and  $a$  are the creation and annihilation operators, respectively,  $n_{m, \sigma} = a_{m, \sigma}^+ a_{m, \sigma}$ , and  $T$  is a pi electron transfer integral (i.e. minus Huckel  $\beta^{m, \sigma}$ ) between the adjacent carbon sites.  $U$  and  $J$  are the effective on-site Coulomb repulsion and the exchange integral between the  $n$  and pi electrons at the divalent carbon atoms, respectively. The sign of  $J$  should be positive (ferromagnetic), since the  $n$  and pi orbitals are mutually orthogonal on each divalent carbon atom. We have solved this model Hamiltonian by employing the unrestricted Hartree-Fock (UHF) approximation,

$$n_{m, \sigma} n_{m, \sigma} = \langle n_{m, \sigma} \rangle n_{m, \sigma} + \langle n_{m, \sigma} \rangle n_{m, \sigma} - \langle n_{m, \sigma} \rangle \langle n_{m, \sigma} \rangle, \quad (4)$$

where  $\langle \rangle$  denotes the average with respect to the spin state in question. In this calculation each  $n$  electron is assumed to be localized in each  $n$  orbital of the divalent carbon atom. We have taken here  $U/T = 1.0$  and  $J/T = 0.25$  which have been found most appropriate for high-spin molecules of alternant hydrocarbons [12], correct spin prediction being obtained for BP-3,3'-BPM.

#### Heisenberg Model

In the valence bond theory, the spin coupling is characterized by the spin Hamiltonian [15] which can be reduced to the Heisenberg Hamiltonian

$$\mathcal{H} = -2 \sum_{\langle ij \rangle} J_{ij} S_i \cdot S_j, \quad (5)$$

leaving only the spin dependent parts. This Hamiltonian has been shown to apply well to organic high-spin molecules having both unpaired pi and  $n$  electrons. In the present calculation only the nearest-neighbor interaction is taken into account where the  $n$  orbital is regarded as an independent site. For conjugated alternant hydrocarbons, the effective exchange integral between the neighboring  $p$  orbitals is normally antiferromagnetic since they form a chemical bond, while that between the  $n$  and pi orbitals is ferromagnetic since they are mutually orthogonal. We have chosen here  $J(\pi\pi) = -1.5$  eV and  $J(n\pi) / J(\pi\pi) = 0.2$  which have proved to give most satisfactory results for alternant high-spin hydrocarbons [13].

The Heisenberg Hamiltonian has exactly been solved by numerical diagonalization of the matrix derived by the use of the full basis set of the spin system  $|S_{z1} S_{z2} \dots S_{zN}\rangle$  where  $S_{zi} = \pm 1/2$ . The Lanczos method was used for the numerical diagonalization of the matrix, since this permits one to compute efficiently only the several low-lying eigenstates in order of increasing energy from the ground state.

#### Weak Interaction Model

The spin Hamiltonian for a system consisting of weakly interacting units  $a$  and  $b$  with spins  $S_1$  and  $S_2$ , respectively, may be written

$$\mathcal{H} = \mathcal{H}_a(1) + \mathcal{H}_b(2) + \mathcal{H}_{ab}(1,2), \quad (6)$$

where the first (second) term is the Hamiltonian for unit a (b) and the third term that for interaction. For  $S_1 = S_2 = 1$ , and  $g_a = g_b = g$  (isotropic), Eq. (6) can be written with the total spin  $S = S_1 + S_2$  as [7]

$$\mathcal{H} = -J [S(S+1) - 4] + g\beta H \cdot S + S \cdot D_S \cdot S \quad (7)$$

for  $S = 0, 1$  and  $2$ , where  $D_1 = (-1/2)(D_a + D_b) + D_{ab}$  and  $D_2 = (1/6)(D_a + D_b) + (1/3)D_{ab}$ .  $D_a$  ( $D_b$ ) is the spin-spin interaction tensor within unit a (b) and  $D_{ab}$  that between units a and b, and  $J$  comes from the exchange energy  $-2JS_1 \cdot S_2$  between the two units. This model fully interpretes the electronic structure of BP-3,3'-BPM [7].

On the other hand, the pi spin density  $\rho_{ai}$  on the carbon site  $i$  in unit a in the total spin state  $S$  can be expressed in terms of the corresponding spin density  $\rho_{aio}$  in the isolated unit and the Clebsh-Gordan coefficient  $C(S_1 S_2; m_1 m_2)$  for the weak interaction:

$$\rho_{ai}(S, M) = S_1^{-1} \rho_{aio}(S_1, S_1) \frac{m_1 C(S_1 S_2; m_1, M-m_1)^2}{m_1} \quad (8)$$

where  $S = S_1 + S_2, S_1 + S_2 - 1, \dots, |S_1 - S_2|$  (and the same expression holds for unit b [16]). In the case of identical spins  $S_1 = S_2 = 1$ , this expression simply becomes

$$\rho_{ai}(1,1) = (1/2) \rho_{aio}(1,1), \quad (9)$$

$$\rho_{ai}(2,2) = \rho_{aio}(1,1), \quad (10)$$

where the total pi spin density is normalized to 1 and 2 for the triplet and quintet states, respectively.

## RESULTS AND DISCUSSION

### Ground-State Spin of BP-3,4'-BPM and BP-4,4'-BPM

Figure 1 (a) shows the K-band ESR spectrum of BP-3,4'-BPM observed at 77 K after photolysis at 4.2 K. The magnetic field was applied parallel to the b-axis of a benzophenone crystal with space group  $P2_12_12_1$ . This is a pattern characteristic of the fine structure for  $S = 2$  at a high field limit.  $A_+$  and  $B_+$  correspond to the allowed transitions  $M_S = +2 \leftrightarrow +1$  and  $M_S = +1 \leftrightarrow 0$ . The ratio of the splitting between  $A_+$  to  $A_-$  and that between  $B_+$  and  $B_-$  is nearly three to one as expected. The signal intensities, resonance fields and their angular dependence were well described by the spin Hamiltonian

$$\mathcal{H} = g\beta H \cdot S + D[S_z^2 - S(S+1)/3] + E(S_x^2 - S_y^2) \quad (11)$$

with  $S = 2$ ,  $g = 2.003$ ,  $D = 0.1256 \text{ cm}^{-1}$ , and  $E = -0.0058 \text{ cm}^{-1}$ . Since the spectrum shown in Fig. 1 (a) was unchanged and no other spectrum appeared from 4.2 to 250 K, the observed quintet state was concluded to be the ground state, the other spin states being located much higher than  $10^3 \text{ cm}^{-1}$ .

On the other hand, BP-4,4'-BPM gave the X-band ESR spectrum as shown in Fig. 1 (b) which was observed immediately after photolysis at 77K with the magnetic field along the a-axis of the host crystal. This is a typical spectrum due to a triplet state where absorption line  $A_+$  was assigned to be the allowed transitions  $M_S = +1 \leftrightarrow 0$ . The signal intensities, resonance fields and their angular dependence were also well reproduced by Eq. (11) with  $S = 1$  and with the spin Hamiltonian parameters  $g = 2.003$ ,  $D = 0.0403 \text{ cm}^{-1}$ , and

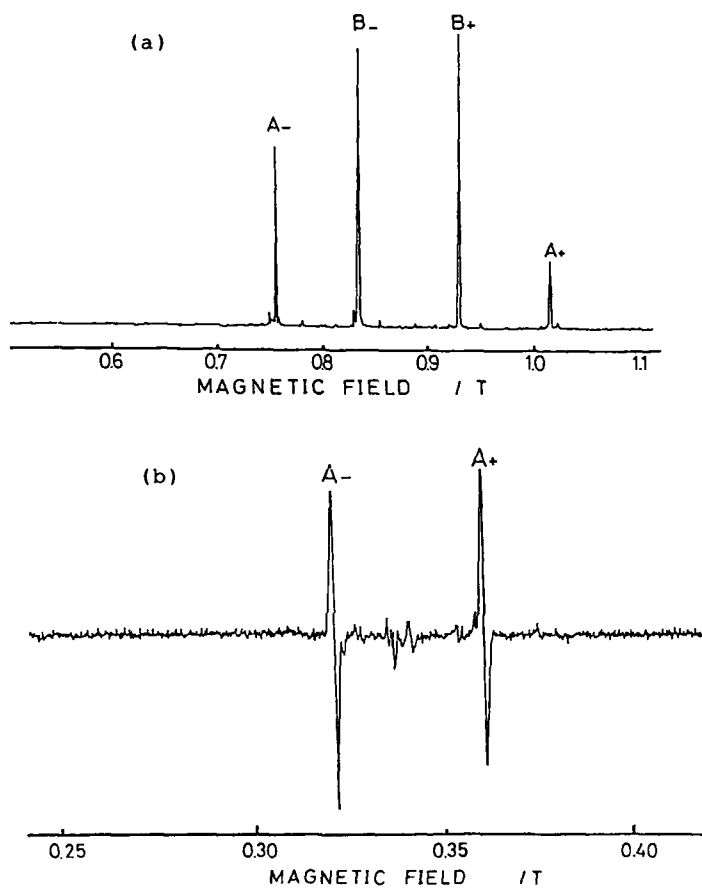


Fig. 1 ESR spectra observed at 77 K.  
 (a) K-band spectrum of BP-3,4'-BPM (H//b).  
 (b) X-band spectrum of BP-4,4'-BPM (H//a).

$E = 0.0007 \text{ cm}^{-1}$ . The small  $D$  value and the almost axial symmetry of the fine structure tensor as is evident from very small  $E$  indicate that this triplet state originates from the interaction between the two localized  $n$  spins. The temperature dependence of signal intensities suggests that this triplet is a thermally accessible excited state.

The above experimental results for the three isomers of BP- $n,n'$ -BPM have demonstrated clearly that the ground-state spin changes dramatically by a slight change of the  $\pi$  electron network, viz. by the displacement of the C-C bond only by one carbon site, showing that the spin alignment of organic molecules is highly dependent on the topological nature of  $\pi$  electron networks.

Spin Alignment in the Excited Triplet State of BP-3,3'-BPM

The dramatic change of spin alignment can reasonably be understood by the spin density distributions in these isomers which were determined by the present ENDOR experiment. We observed the proton-ENDOR spectra of BP-3,3'-BPM<sub>1</sub> with conformation L in the first excited triplet state which is located 20 cm<sup>-1</sup> above the singlet ground state as described before and thermally accessible at moderately low temperature. Figure 2 shows the ENDOR spectra observed at 34 K after photolysis at 4.2 K with the magnetic field along the a-axis of the benzophenone crystal. We obtained these spectra by monitoring the ESR transition  $M_S = +1 \leftrightarrow 0$ . The signals at the free proton frequency  $\nu_p$  came from  $M_S = 0$ , and others from +1. Hence, the signals appearing at frequencies lower than  $\nu_p$  correspond to positive hyperfine coupling constant or vice versa. Thus absolute sign of spin densities can be determined.

To facilitate the assignment, we have also measured the proton-ENDOR from the compound in which all the protons in the two end phenyl rings were deuterated. The upper and lower spectra show the proton-ENDOR of normal and deuterated BP-,3,3'-BPM, respectively. The eight lines marked by the asterisk in the upper spectrum are those common in the two spectra and, therefore, ascribable to the hydrogen atoms of the central biphenyl group, the remaining lines being assigned to those of the end phenyl groups. From the angular dependence of the 18 proton signals thus identified, we determined their hyperfine coupling tensors, which were successfully assigned to all the 18

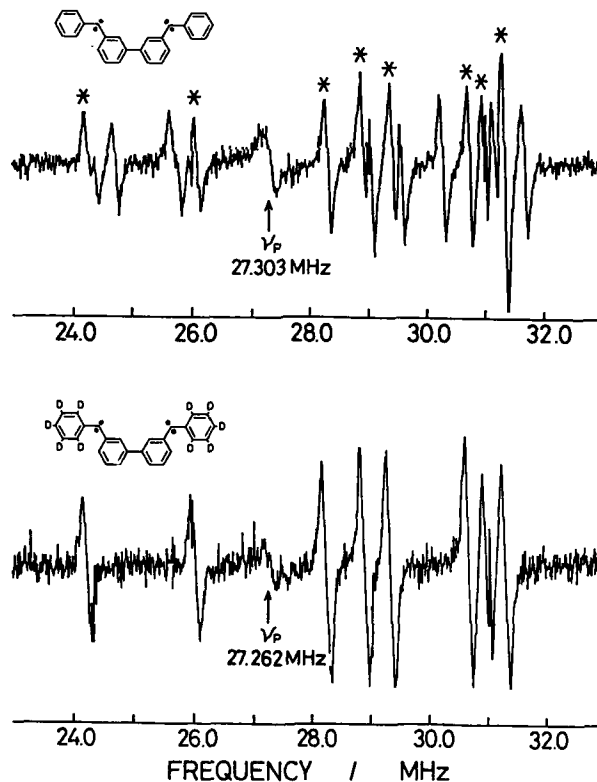


Fig. 2 Proton-ENDOR spectra of normal (upper) and deuterated (lower) BP-3,3'-BPM at 34 K.  $\nu_p$  is a free proton frequency.

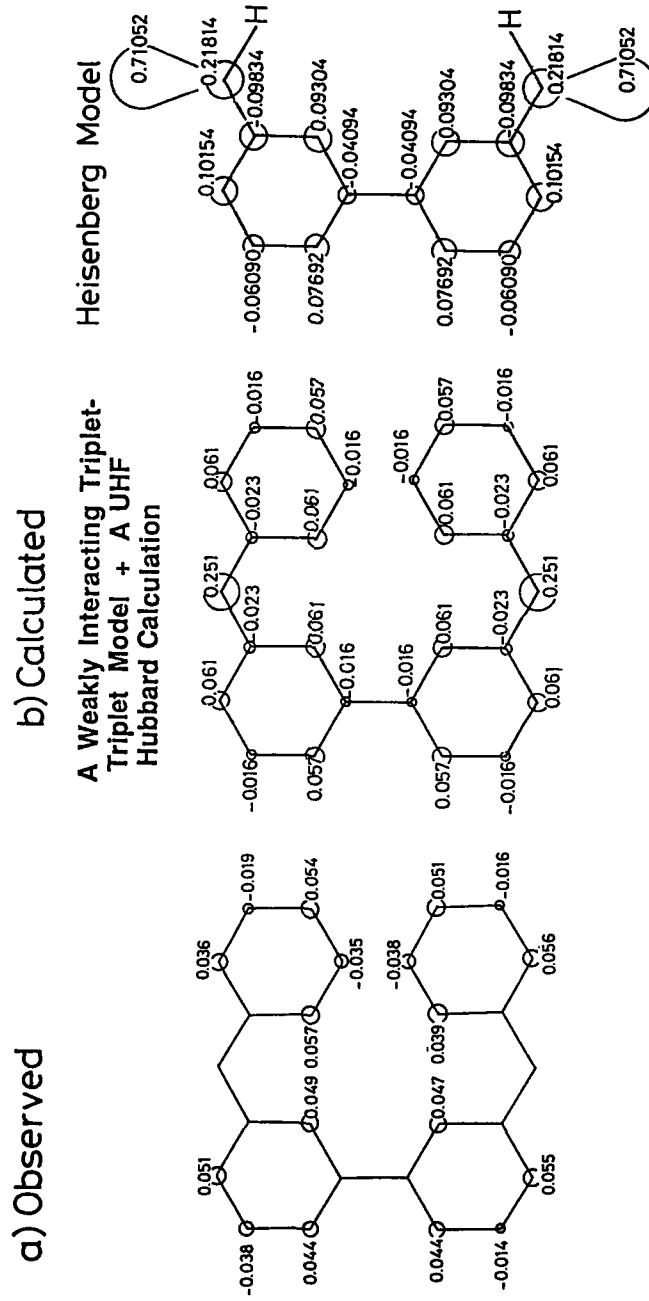


Fig. 3 Spin density distribution in the triplet excited state of BP-3,3'-BPM

hydrogen atoms in BP-3,3'-BPM. The trace of these tensors divided by 3 gives the Fermi term  $A_F$  of each hydrogen atom.

The pi spin density  $\rho_C$  on the carbon site adjacent to the hydrogen atoms was obtained from McConnell's equation  $A_F = Q \rho_C$  where  $Q = -66.9$  MHz for the excited triplet state of naphthalene [17] was used. From the Fermi terms experimentally determined by ENDOR we obtained the spin density distribution as shown in Fig. 3 (a). The area of the circle on each carbon atom is taken to be proportional to the absolute value of the spin density. The spin densities on the four carbon atoms without circles could not be obtained because of the absence of neighboring hydrogen atoms.

Figure 3 (a) shows that the spin density distribution is roughly symmetrical with respect to the center of the molecule although no center of symmetry is expected in the crystal, and that the sign of the spin density is alternately distributed within each diphenylmethylene moieties. As a result of these, the central two carbon sites of the biphenyl group, or the bridge carbons, should have the same sign which is most probably negative and small from energy considerations.

This experimental results has been confirmed by the Hubbard calculation as shown on the left side of Fig. 3 (b). Since the direct UHF calculation is difficult because of the excited state, we first calculated the spin distribution in the ground state of the diphenylmethylene moiety using Hubbard model, and then applied the weak interaction model, viz., Eq. (9). This calculation well interprets the ENDOR results, and gives small negative spin densities on both the bridge carbons as expected. The Heisenberg model also provides similar results as shown on the right side of Fig. 3 (b), although

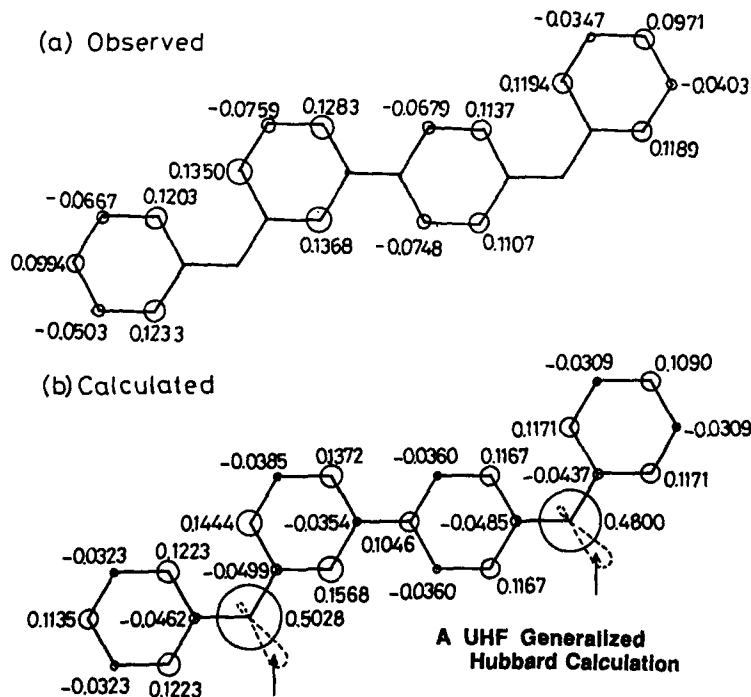


Fig. 4 Pi spin density distribution in the quintet ground state of BP-3,4'-BPM.

this calculation overestimates the spin densities because this model is the localized limit of the Hubbard model.

It is shown experimentally as well as theoretically that there are small negative spin densities on the adjacent bridge carbon atoms, resulting a node violating the spin distribution with the alternate sign which stabilizes the spin alignment owing to the polarization effect. A similar spin distribution is also expected for the quintet state from the comparison of Eqs. (9) and (10). This is the reason why the triplet and quintet states are the excited states against the simple molecular orbital prediction in which no spin correlation is taken into account. In view of this, the spin distribution in the quintet state of BP-3,4'-BPM is interesting.

#### Spin Alignment in the Quintet Ground State of BP-3,4'-BPM

In BP-3,3'-BPM the lowest spin ground state is realized since the high-spin states are unstable because of the existence of the node in the alternate spin distribution. Therefore, if the position of substitution of the divalent carbon atom is shifted by one carbon site, this node will disappear, leading to the high-spin ground state. To confirm this, we have measured the spin distribution in the quintet ground state of BP-3,4'-BPM by ENDOR. Only the result is shown in Fig. 4 (a). The spin densities derived by the UHF generalized Hubbard calculation are also given. It can be seen from these results that no node exists and completely alternate signs are realized in the spin distribution. This spin distribution interprets the high-spin ground state for BP-3,4'-BPM.

#### Characterization of Magnetic Polymers by ESR/ENDOR

Since no mechanism has been clarified for spontaneous magnetization in the magnetic polymers reported so far, it is indispensable to establish a methodology for characterizing the chemical as well as spin structures of magnetic polymers. It is shown in this section that ESR/ENDOR spectroscopy is one of the powerful tools for this purpose. We have adopted three types of condensed polynuclear aromatic hydrocarbon resins (COPNA polymers) [3], viz., pyrene/benzaldehyde (Py/BA), phenol/benzaldehyde (PH/BA), and p-hydroxybenzaldehyde (p-HBA) based polymers kindly supplied by Prof. Otani and Dr. Ota. These are possible analogues to the first proposed hypothetical ferromagnetic polymer possessing the triarylmethyl radicals as the spin site [17]. These hypothetical polymers have been proposed on the basis of the topological nature of organic molecules described in the preceding sections.

All the ESR spectra observed for the three types of polymers revealed a salient feature, viz., they are comprised of (1) the strong signal in the low field with a broad linewidth (a peak-to-peak width of 140 mT) and (2) the signal with a narrow linewidth appearing at the  $g=2$  region characteristic of doublet radical species. Lineshape analyses for the  $g=2$  signals have shown that the lineshapes of the Py/BA and PH/BA polymers are mainly Gaussian with a small amount of a Lorentzian component, whereas the lineshape of p-HBA polymers is a Lorentzian. These results suggest that there exist various degrees of the exchange interaction among the unpaired spins of each doublet species in these polymers, reflecting the inhomogeneity of the polymer structures. We have measured the temperature dependence of the ESR spectra in the range of 5 to 300 K (473 K for the Py/BA polymers). With decreasing temperature, the resonance field of the broad signal considerably shifts toward the lower magnetic field region. This low-field shift, which typically amounts to 50 mT, is interpretable in terms of an increase in short range

ordering of unpaired electron spins in the polymers of amorphous nature. Similar magnetic behavior such as spin glasses has been reported for random magnetic materials [18]. This finding suggests that the magneto-active COPNA polymers are partially comprised of organic spin glasses and that the observed broad signals may be attributed to the cooperative magnetic phenomena.

We have applied the proton-ENDOR technique to the doublet species at the  $g=2$  region as a probe for characterizing the chemical as well as magnetic structures of the magnetic polymers. It should be emphasized that such a doublet species is not a simple triarylmethyl radical unit but an oligomer composed of many triarylmethyl radical units whose spins couple mostly antiferromagnetically, leading to a net one spin, viz., a doublet state. This ENDOR study of the sharp ESR component at  $g=2$  is useful especially for studying the structure of the spin site.

Using a high-power solution-ENDOR technique, we first roughly estimated the number of the repeating unit for the Py/BA polymer soluble in organic solvents at room temperature. This is because the absence of anisotropy of hyperfine coupling constant (hfcc) in solution makes the analysis of ENDOR spectra much easier. The soluble part is composed of the polymers with relatively low degrees of polymerization. Figure 5 (a) shows a typical proton-ENDOR spectrum of the Py/BA soluble in toluene. The simulated spectrum shown in Fig. 5 (b) was obtained by the superposition of 77 proton hfcc's ranging from 0.14 to 1.1 MHz. This number of protons corresponds to an oligomer with six repeating units or a mixture of oligomers having lower

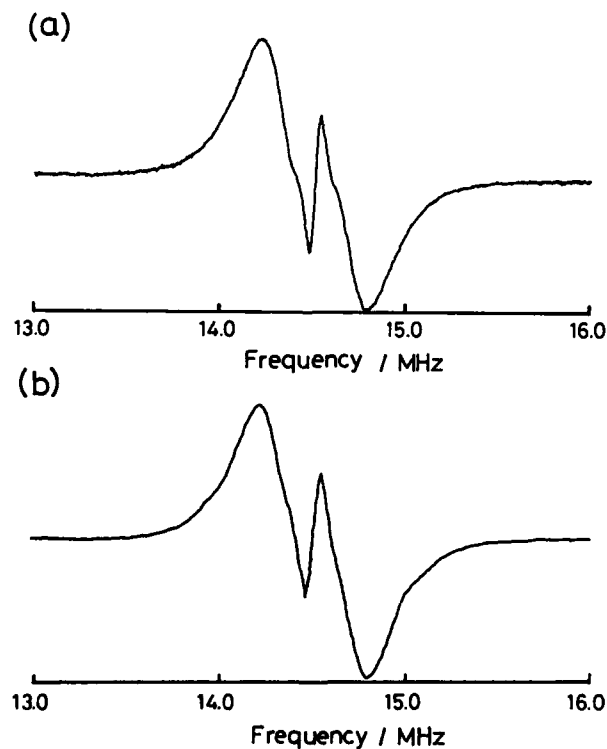


Fig. 5 Solution proton-ENDOR spectra of the PY/BA polymer in toluene.  
(a) Observed spectrum. (b) Simulated spectrum.



molecular weights with a triarylmethyl based radical as the spin site.

To identify the chemical structure in more detail on the basis of a set of hfcc experimentally determined, we have carried out a theoretical simulation according to the following procedure: We first obtained the spin density distribution for a possible chemical structure from the UHF calculation based on the generalized Hubbard model [12], where we assumed all the triarylmethyl sites to possess a single spin. Then we computed all the proton hfcc from McConnell's equation to simulate an ENDOR spectrum on the basis of a spin Hamiltonian including both hyperfine and nuclear Zeeman terms. This procedure was repeated until the best fit was obtained.

We have also applied this approach to the Py/BA polymer in the solid state. In this case the anisotropy of hfcc is taken into account, and the ENDOR spectra arising from a large number of randomly oriented molecules are summed up. The application of both the solution and solid-state ENDOR to Py/BA have led to the conclusion that the origins of the paramagnetic species giving the  $g=2.00$  signal are the triarylmethyl based radicals with various degree of polymerization. Determination of their probable molecular structure and their topological nature of pi electron network are under way.

#### Acknowledgment

The present work was supported by a Grant-in-Aid for Science Research and for Special Project Research from the Ministry of Education, Science and Culture.

#### References

1. Yu. V. Korshak, T. V. Medvedeva, A. A. Ovchinnikov, V. N. Spector, *Nature* **326**, 370 (1987).
2. J. B. Torrance, S. Oostra, Nazzari, *Synth. Met.* **19**, 708 (1987); *J. Appl. Phys.* **634**, (1988).
3. S. Otani and M. Ota, *Chem. Lett.* **1989**, 1183.
4. K. Itoh, *Chem. Phys. Lett.* **1**, 235 (1967).
5. Y. Teki, T. Takui, K. Itoh, H. Iwamura, K. Kobayashi, *J. Am. Chem. Soc.* **105**, 3722 (1983); **108**, 2147 (1986), and the references cited therein.
6. Y. Fujita, Y. Teki, T. Takui, T. Kinoshita, F. Miko, Y. Sawaki, A. Izuoka, T. Sugawara, H. Iwamura, *J. Am. Chem. Soc.*, to be published.
7. K. Itoh, *Pure Appl. Chem.* **50**, 1251 (1978).
8. H. C. Longuet-Higgins, *J. Chem. Phys.* **18**, 265 (1950).
9. E. Lieb and D. Mattis, *J. Math. Phys.* **3**, 749 (1962).
10. A. A. Ovchinnikov, *Theoret. Chim. Acta* **47**, 297 (1978).
11. D. J. Klein, C. J. Nelin, S. Alexander, F. A. Matsen, *J. Chem. Phys.* **77**, 3101 (1982).
12. Y. Teki, T. Takui, T. Kinoshita, S. Ichikawa, F. Yagi, K. Itoh, *Chem. Phys. Lett.* **141**, 201 (1987).
13. Y. Teki, T. Takui, M. Kitano, K. Itoh, *Chem. Phys. Lett.* **142**, 181 (1987).
14. I. Hubbard, *Proc. Roy. Soc.* **276A**, 238 (1963); K. Nasu, *Phys. Rev.* **B33**, 330 (1986).
15. J. H. van Vleck, *Phys. Rev.* **49**, 232 (1936); J. A. R. Coope, *Chem. Phys. Lett.* **1**, 77 (1967).
16. Teki, T. Takui, M. Kitano, K. Itoh, *Chem. Phys. Lett.*, to be published.
17. S. Morimoto, K. Itoh, F. Tanaka, and N. Mataga, *Preprints of the Symposium on Molecular Structure (Tokyo)*, 76 (1968); N. Mataga, *Theor. Chim. Acta* **10**, 372 (1968); K. Itoh, *Bussei* **12**, 636 (1971).
18. Y. Morimoto and M. Date, *J. Phys. Soc. Japan* **29**, 1093 (1970); G. Mozurkewich, H. Elliot, M. Hardiman, and R. Orbach, *Phys. Rev.* **B29**, 278 (1984).

ROLE OF HIGH-SPIN MOLECULES AS MODELS  
FOR ORGANIC FERRO- AND FERRI-MAGNETS, AND PI-TOPOREGULATED MAGNETIC POLYMERS

TAKEJI TAKUI, MAKOTO ENDOH, MASAYUKI OKAMOTO, KAZUNOBU SATOH, TOYOHIRO SHICHIRI, YOSHIO TEKI, TAKAMASA KINOSHITA AND KOICHI ITOH  
Osaka City University, Faculty of Science, Department of Chemistry, Sugimoto, Sumiyoshi-ku, Osaka 558, JAPAN

ABSTRACT

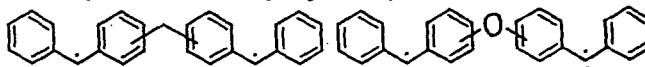
A chemical modification exploiting functional groups such as ether and methylene as bridges between high-spin assemblies has been carried out as a usable method to increase dimensionality of spin structure. Exchange interaction via an ether or a methylene bridge between two high-spin assemblies has been studied by single-crystal ESR spectroscopy. Whether it is ferromagnetic or antiferromagnetic depends upon the substituted position of the bridge, demonstrating the important role of the topological nature in spin alignment. It turns out that superexchange interaction or hyperconjugation mechanism can dominate spin alignment between high-spin assemblies. Using the criteria obtained, model compounds for units of organic ferrimagnets have been synthesized. They possess antiferromagnetically-exchange coupled heterospins and the salient features of their spin structures are characterized in terms of the spin density distribution as determined by single-crystal  $^1\text{H}$ -ENDOR (Electron-Nuclear-Double Resonance) spectroscopy.

INTRODUCTION

The quest for organic magnetism is the focus of current topics in many fields of both pure and applied science. Organic high-spin molecules have accepted increasing interest as models for synthetic organo-magnetic materials such as organic superpara-, ferro-, and ferri-magnets, and the related experimental[1-31] and theoretical work[32-53] have been done to serve their molecular design for the last two decades. Our continuing study of the high-spin molecules can date back to the detection of the first high-spin hydrocarbon, *m*-phenylenebis(phenylmethylene) in 1967 by one of the authors [1,2] and to the proposal of pi-toporegulated ferromagnetic polymers[36-38]. Our strategy for obtaining organic magnetism contains molecular design for high-spin assemblies exploiting topologically-degenerate pi non-bonding MOs[36-38,7,8,29]. An alternative approach to organic magnetism has been to utilize intermolecular charge-transfer interaction between organic electron donors and acceptors which are properly stacked in crystals. This approach has been based on the McConnell's idea[34,35] and several modifications have been proposed [9,10,13,18,28,52]. For the last two years several papers have appeared reporting synthesis of magneto-active organic materials which exhibited ferromagnetic behavior[57-61].

Most of high-spin molecules reported so far have only quasi one-dimensional spin structure. Thus it is required to extend them to polymers or macromolecules with two- or three-dimensional spin structure of magnetic ordering for obtaining synthetic organo-magnetic material, since purely one-dimensional systems can not have macroscopic magnetic properties such as ferromagnetism. There are two approaches for realizing organic ferro- and ferri-magnetic higher-dimensional spin ordering. One is to exploit molecular topological symmetry, which makes it possible to provide macromolecules with extremely large spins if they are properly designed[36-38]. The other is to utilize intra- or inter-molecular magnetic interaction between paramagnetic moieties or molecules, but little has been investigated its methodology[54-55]. Quite lately, it was suggested in the study of layered benzenoid moieties with the triplet ground state that the mode of stacking of benzene units was crucial in determining the intermolecular magnetic interactions[19].

We have attempted to utilize an intramolecular approach based on chemical modification, i.e., introduction of functional groups bridging high-spin molecules. However, no information on the magnetic interaction between high-spin molecules via some bridges has been found in the literature. We have firstly adopted, as one of the simplest models appropriate for such a study, bis(phenylmethylene)diphenylmethane (BPDM:1) in which two triplet diphenylmethylene units interact via a methylene bridge. This model tests whether hyperconjugation via a methylene bridge plays any role in spin alignment in high-spin molecules[55]. Secondly, we have chosen a group of molecules whose pi-network is broken by introduction of a hetero atom. The model compounds designed here are bis(phenylmethylene)diphenylether (BPDE:2) which include an oxygen atom bridging two ground-state triplet diphenylmethylene units.



BPDM (1)

BPDE (2)

In this paper, a basic study of the magnetic interaction between high-spin assemblies via the above two bridges is described and the role of both hyperconjugation and superexchange interaction via the bridges is discussed. This interaction is indispensable for designing and constructing macromolecules or polymers with extremely large spins and with higher-dimensional spin structures. It turned out that hyperconjugation can be a dominant interaction between high-spin assemblies and that the elegant rule derived by Longuet-Higgins for alternant hydrocarbon[32] can apply to composite systems such as BPDM(1). It was found by the syntheses and ESR detection of the model compounds of BPDE(2) that some of them were ground-state quintet. Evidently, this finding can not be interpreted of the rule by Longuet-Higgins, because his rule is unable to apply to BPDE in which pi-conjugation terminates at the bridge. The high-spin multiplicity arose from the magnetic interaction between two unit molecules via an oxygen atom bridge. The result and criteria obtained from BPDE(2) is only briefly summarized due to limitations of space. It is shown that the above-mentioned fact and all the other experimental results can fully be accounted for by a weakly interacting intramolecular triplet-triplet mechanism.

This paper also describes an application of the criteria obtained from the composite system BPDE(2) to preparation of a novel organo-magnetic molecule which is to be classified as a new category, i.e., an organic ferrimagnetic molecule, a constituent unit of possible organic ferrimagnets. This is defined as a molecule consisting of non-identical high-spin assemblies (hetero spins) being antiferromagnetically coupled with each other to yield magnetic ground states.

## EXPERIMENTAL

The composite carbenes *a,a'*-BPDM(1) were formed by the photolysis of the corresponding diazo precursors. They were synthesized from diphenylmethane *a,a'*-dicarboxylic acids via the following sequence of reactions: Friedel-Crafts, condensation with hydrazine and oxidation with activated  $MnO_2$ . We prepared deuterium labeled trisdiazo precursors of 4T4'Q-ether(3) and perdeuterated benzophenone- $d_{10}$  to reduce  $^1H$ -ENDOR spectral density and to facilitate correct assignment of  $^1H$ -ENDOR transitions. All the deuterated compounds were synthesized from perdeuterated benzene- $d_{10}$  (>99.6 atom %; Merk Sharp & Dohme Co., Inc.) as a starting material.

Single crystals of benzophenone- $h_{10}$  and  $-d_{10}$  ( $P2_12_12_1$  space group with  $Z=4$ )[62] well incorporating the corresponding diazo precursor were prepared and irradiated at liquid helium temperature with a 500W high-pressure mercury lamp. ESR measurements at K-band microwave frequencies ( $\sim 25$  GHz) were made at cryogenic temperatures in order to obtain accurate spin Hamiltonian parameters of  $g$  and fine-structure ( $D$ ) tensors.  $^1H$ -ENDOR measurements were made on a

Bruker ESP 350 spectrometer equipped with a home-made RF irradiation coil.

## RESULTS AND DISCUSSION

### Ground state and nearby excited states of a,a'-BPDM: hyperconjugation Mechanism via a methylene bridge

Figure 1 shows the fine-structure ESR spectra of 4,4'-BPDM observed at 4.2K with the external magnetic field(H) applied parallel to the crystallographic a axis of the benzophenone host crystal. Trace signals in Figure 1(a) detected in the dispersion mode was due to ground-state triplet carbenes precursors of which were by-products formed in the preparation of the magnetically-diluted mixed single crystals. With increasing the sample temperature, new signals designated by  $T_{\pm}$  ( $T_{\pm}'$ ) first appeared at 15K and subsequently those by  $A_{\pm}$  ( $A_{\pm}'$ ) and  $B_{\pm}$  ( $B_{\pm}'$ ) gained their intensity, whereas the former triplet signals were so weak that they did not contribute to the spectrum observed at 64K as seen in Figure 1(b). The lines  $T_{\pm}$  ( $T_{\pm}'$ ) were assigned to  $M_s = \pm 1$  allowed transitions of the triplet state ( $S=1$ ) and both the strong lines  $B_{\pm}$  ( $B_{\pm}'$ ) and the weak ones  $A_{\pm}$  ( $A_{\pm}'$ ) to the allowed transitions characteristic of the quintet state ( $S=2$ ), because the ratio of separation  $A_{+}-A_{-}$  to  $B_{+}-B_{-}$  is 3 : 1 and the integrated intensity of  $A_{\pm}$  to  $B_{\pm}$  is 2 : 3 to first order. The lines  $B_{\pm}$  ( $B_{\pm}'$ ) and  $A_{\pm}$  ( $A_{\pm}'$ ) correspond to the  $|M_s=0\rangle \leftrightarrow |M_s=\pm 1\rangle$  and  $|M_s=\pm 1\rangle \leftrightarrow |M_s=\pm 2\rangle$  transitions, respectively, where  $M_s$  refers to a spin sublevel of the spin-multiplet state in the high-field limit. The prime de-notes signals from the 4,4'-BPDM molecules occupying crystallographically non-equivalent sites. Since temperature dependence of the observed spectra up to 87K was completely reversible, both the quintet and triplet signals were ascribed to thermally populated states, indicating spin singlet ground states for 4,4'-BPDM (isomer I).

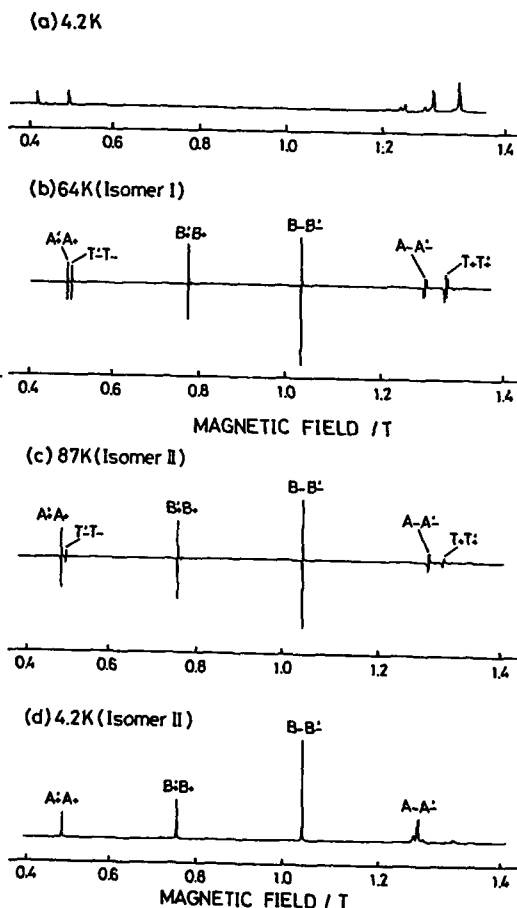


Fig. 1. ESR spectra (K-band) of 4,4'-bis(phenylmethylene)-diphenylmethane (4,4'-BPDM) observed after photolysis at 4.2K: (a) at 4.2K immediately after photolysis, (b) at 64K (isomer I) before the irreversible spectral change, (c) at 87K (isomer II) after the irreversible spectral change took place.

Figure 1(c) shows that a slight spectral change took place at 87K, which was irreversible in the process of increasing temperature. The spectrum at 87K arises from one quintet and one triplet states. It should be noted that an intensity ratio of triplet to quintet signals decreased after the irreversible change, as seen in Figure 1(c). Temperature dependence of the spectra after the change was again reversible. Figure 1(d) shows the spectrum observed at 4.2K which arises from the quintet signals alone, showing that 4,4'-BPDM (isomer II) is quintet in its electronic ground state. 4-4'BPDM before and after the change is designated as isomer I and isomer II, respectively. Complete analyses of the quintet spectrum at 4.2K gave the same spin-Hamiltonian parameters as for the quintet signals at 87K within an experimental accuracy. Detailed angular dependence of the spectra observed before and after the change gave a small difference in the fine-structure ( $D$ ) tensor, showing that the spectral change resulted from a slight irreversible change in the molecular structure of 4,4'-BPDM. The quintet ( $D_Q$ ) and triplet ( $D_T$ ) fine-structure tensors experimentally determined for each isomer coincided in direction cosines of their principal values within an experimental accuracy, and a particular relationship of  $D_Q \sim (-1/3)D_T$  has been obtained. This relationship and the appearance of one quintet and one triplet state found for both the isomers are fully interpreted by a weakly interacting triplet-triplet mechanism[6-8], concluding that the quintet and triplet signals originate from a single paramagnetic chemical species having an interacting triplet pair, viz., 4,4'-BPDM. Preliminary measurements of the quintet and triplet signal intensities as a function of temperature gave  $J_{\text{eff}} \sim +10 \text{ cm}^{-1}$  for isomer I and  $J_{\text{eff}} \sim -10 \text{ cm}^{-1}$  for isomer II, where  $J_{\text{eff}}$  denotes an effective exchange interaction between the triplet diphenylmethylene units. Thus, the effective exchange interaction changed from an antiferromagnetic ( $J_{\text{eff}} > 0$ ) to a ferromagnetic coupling ( $J_{\text{eff}} < 0$ ) via a molecular structural change of 4,4'-BPDM. The order of the spin states was reversed after the change, viz., the parallel spins belonging to one triplet moiety was ferromagnetically exchange-coupled to those belonging to the other triplet moiety after the change, yielding the highest spin multiplicity in the ground state. The small difference in the  $D$  tensor between the two isomers reveals that a conformational change such as the twisting of phenyl rings on both sides of the central methylene bridge took place, resulting in an increase in planarity of the local structure in the vicinity of methylene bridge. More planar structure favors the occurrence of a dominant hyperconjugation effect (pseudo pi mechanism) on the effective exchange interaction, inducing negative pi-spin density on the methylene carbon atom and thus aligning pi spins in the diphenylmethylene units parallel. The experimental values of the fine-structure parameters,  $D$  and  $E$ , were satisfactorily reproduced in terms of a semi-empirical calculation by the use of pi-spin densities.

Preliminary analyses of ESR spectra from 3,3'- and 3,4'-BPDM showed that singlet-quintet quantum mixing complicated their spectra, but the spectral behavior was interpretable by the weakly interacting intramolecular triplet-triplet mechanism. It was found that 3,3'-BPDM is ground-state quintet while an isomer of 3,4'-BPDM is in its singlet ground state, revealing that also for these systems the hyperconjugation effect via the methylene bridge plays an important role in establishing ferromagnetic coupling between the high-spin assemblies.

Table 1

position (a, a')	isomer	order of energy levels	magnetic coupling
4, 4'		$J$   0	Antiferromag.
		$-J$   7	
		$-2J$   5	
3, 4''		$-2J$   5	Ferromag.
		$-J$   7	
		$J$   0	
3, 3'		$J$   0	Antiferromag.
		$-J$   7	
		$-2J$   5	

Ground state and nearby excite states of a, a'-BPDE: Superexchange interaction via an oxygen atom

Table I summarizes experimental results from the model compounds, a, a'-BPDE(2) in which spins in each of the two triplet moieties interact via an oxygen atom. This table clearly

demonstrates that whether effective exchange interaction  $J_{\text{eff}}$  via an ether bridge is ferromagnetic or antiferromagnetic depends upon the substituted position of the bridge. The experimental results and values for the effective exchange interactions have been well interpreted by the Heisenberg Hamiltonian approach combined with  $180^\circ$  superexchange interaction mechanism[42].

Possible occurrence of organic ferrimagnets: a composite high-spin system possessing hetero spins

We have synthesized a prototype for organic ferrimagnetic molecules, 4-(diphenylmethylene)-4'-(m-phenylenebis(phenyl-methylene))-ether, which is abbreviated to 4T'4Q-ether (3).

Although inorganic ferrimagnetism is familiar in solid state physics, only a few reports from the experimental side have appeared as for a hybrid type of molecular based ferrimagnetism, which is comprised of magnetic transition metal ions and organic

stable doublet radicals

[63,64]. Purely organic ferrimagnetism has recently become the subject of wide interest in the research of molecular based magnetism. 4T'4Q-ether is the first example of the organic magnetic molecule with antiferromagnetically coupled hetero spins, indicating a possible occurrence of purely organic ferrimagnetism from the experimental side. The primary object of this subsection is to characterize salient features of

the spin structure of 4T'4Q-ether in terms of spin density distribution and to provide a usable physical picture for understanding of organic ferrimagnetism. For the heterospin system such as 4T'4Q-ether a weakly interacting multiplet-multiplet model predicts unusually large negative pi-spin densities on the ring carbon sites in the magnetic ground state ( $S = |S_1 - S_2| + 0$ ). Thus the most direct experimental evidence for the spin structure intrinsic to the heterospin system is to find such large negative pi-spin polarization of particular carbon sites. In the case of 4T'4Q-ether the triplet spin moiety is expected to possess large negative pi-spin distribution, in which magnitudes of negative spin densities amount to half of positive ones belonging to the triplet ground-state diphenylmethylene.

Figure 2 shows a typical single-crystal  $^1\text{H}$ -ENDOR spectrum of partially deuterated 4T'4Q-ether in its magnetic ground state ( $S = |S_1 - S_2| = 1$ ). Since the  $|M_s = -1\rangle \leftrightarrow |M_s = 0\rangle$  ESR transition was monitored, the signals appearing at frequencies higher than the free proton NMR frequency  $\nu_N$  were assigned to the protons of positive hyperfine coupling constants (hfccs), therefore, to the negative pi-spin densities on the ring carbons bonded to the corresponding protons. Straightforwardly, the five lines marked by the asterisk arise from negative pi-spin densities. It should be noted that the hfccs of the outermost marked line exceeds the largest negative hfcc of unmarked lines. Preliminary ENDOR measurements show that among the twelve ENDOR lines belonging to  $|M_s = \pm 1\rangle$  manifold the two lines give large negative pi-spin densities ( $P \sim -0.07$ ). Their absolute values nearly amounted to half of the positive ones of the constituent triplet diphenylmethylene itself. Such an

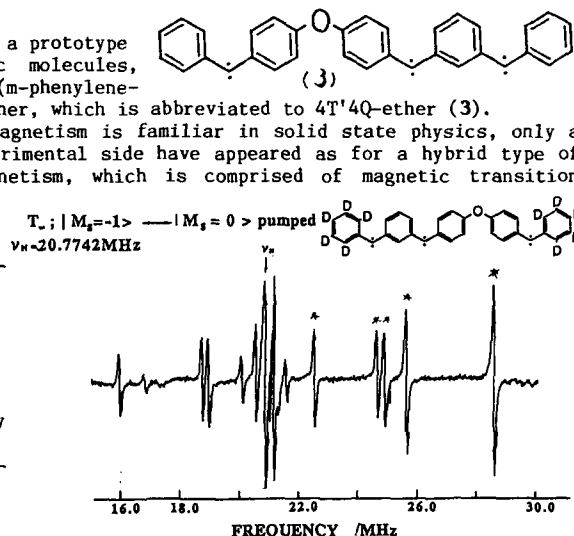


Fig. 2  $^1\text{H}$ -ENDOR spectrum of 4T'4Q-ether in benzophenone- $d_{10}$  crystal with  $H \parallel a$  at 3K.

unusually large negative spin polarization is characteristic of hetero spin systems. For 4T4'Q-ether the large negative spin polarization is expected to belong to the triplet diphenylmethylen moiety. Complete analysis is under way. The occurrence of large negative spin polarization in hetero spin systems demonstrates that organic polymers possessing antiferromagnetically-exchange coupled hetero spins can be promising candidates for organic ferrimagnets.

#### ACKNOWLEDGMENT

The present work was supported by a Grant-in-Aid for Science Research and for Special Project Research from the Ministry of Education, Science and Culture.

#### REFERENCES

1. K. Itoh, Chem. Phys. Letters, **1**, 235(1967).
2. E. Wasserman, R. E. Murray, W. A. Yager, A. M. Trozzolo and G. Smolinsky, J. Am. Chem. Soc., **89**, 5076(1967).
3. E. Wasserman, K. Scheller and W. A. Yager, Chem. Phys. Letters, **2**, 259(1968).
4. K. Reibisch, H. Kothe and J. Brickmann, Chem. Phys. Letters, **17**, 86(1972); J. Brickmann and G. Kothe, J. Chem. Phys., **59**, 2807(1973).
5. T. Takui, and K. Itoh, Chem. Phys. Letters, **19**, 120(1973).
6. K. Itoh, T. Takui, M. Asano and S. Naya, Preprints of XI. International Symposium on Free Radicals, 46(1973).
7. T. Takui, Dr. Thesis, Osaka University(1973).
8. K. Itoh, Pure & Appl. Chem., **50**, 1251(1978).
9. R. Breslow, Pure Appl. Chem., **54**, 927(1982).
10. R. Breslow, B. Jaun, R. Klutz and C.-Z. Xia, Tetrahedron, **38**, 863(1982).
11. Y. Teki, T. Takui, K. Itoh, H. Iwamura and K. Kobayashi, J. Am. Chem. Soc., **105**, 3722(1983).
12. D. E. Seeger and J. A. Berson J. Am. Chem. Soc., **105**, 5144(1983).
13. R. Breslow, P. Maslak and J. S. Thomaidis, J. Am. Chem. Soc., **106**, 6453(1984).
14. Y. Teki, Dr. Thesis, Osaka City University(1985).
15. Y. Teki, T. Takui, H. Yagi, K. Itoh and H. Iwamura, J. Chem. Phys., **83**, 539(1985).
16. G. J. Snyder and D. A. Dougherty, J. Am. Chem. Soc., **107**, 1744(1985).
17. T. Sugawara, S. Murata, K. Kimura and H. Iwamura, J. Am. Chem. Soc., **107**, 5293(1985).
18. R. Breslow, Mol. Cryst. Liq. Cryst., **125**, 261(1985).
19. A. Izuoka, S. Murata, T. Sugawara and H. Iwamura, J. Am. Chem. Soc., **107**, 1786(1985); *ibid.*, **109**, 2631(1987).
20. T. Sugawara, S. Bandow, K. Kimura, H. Iwamura and K. Itoh, J. Am. Chem. Soc., **108**, 368(1986).
21. Y. Teki, T. Takui, K. Itoh, H. Iwamura and K. Kobayashi, J. Am. Chem. Soc., **108**, 2147(1986), and references therein.
22. T. Sugawara, H. Tukada, A. Izuoka and H. Iwamura, J. Am. Chem. Soc., **108**, 4272(1986).
23. K. Awaga, T. Sugano and M. Kinoshita, J. Chem. Phys., **84**, 2211(1986); *ibid.*, Chem. Phys. Letters, **141**, 540(1987).
24. Y. Teki, T. Takui, T. Kinoshita, S. Ichikawa, H. Yagi and K. Itoh, Chem. Phys. Letters, **141**, 201(1987).
25. S. Murata, T. Sugawara and H. Iwamura, J. Am. Chem. Soc., **109**, 66(1987).
26. D. A. Dixon and J. S. Miller, J. Am. Chem. Soc., **109**, 3656(1987).
27. J. Pranata and D. A. Dougherty, J. Am. Chem. Soc., **109**, 1621(1987).
28. E. Dormann, M. J. Nowak, K. A. Williams, R. O. Angus, Jr. and F. Wudl, J. Am. Chem. Soc., **109**, 2594(1987).
29. K. Itoh, T. Takui, Y. Teki and T. Kinoshita, J. Mol. Electronics, **4**, 181(1988).
30. L. Y. Chiang, D. C. Johnston, D. P. Goshorn and A. N. Bloch, J. Am. Chem.

- Soc., **111**, 1925(1989).
31. K. Awaga and Y. Maruyama, *Chem. Phys. Letters*; **158**, 556(1989); *J. Chem. Phys.*, **91**, 2743(1989).
  32. H. C. Longuet-Higgins, *J. Chem. Phys.*, **18**, 265(1958).
  33. J. Highchi, *J. Chem. Phys.*, **38**, 1237(1963).
  34. H. M. McConnell, *J. Chem. Phys.*, **39**, 1910(1963).
  35. H. M. McConnell, *Proc. A. Robert Welch Found. Conf. Chem. Res.*, **11**, 144(1967).
  36. S. Morimoto, K. Itoh, F. Tanaka and N. Mataga, *Preprints of the Symposium on Molecular Structure(Tokyo)*, 76(1968).
  37. N. Mataga, *Theor. Chim. Acta*, **10**, 372(1968).
  38. K. Itoh, *Bussei*, **12**, 636(1971).
  39. A. A. Ovchinnikov, *Theor. Chim. Acta (Berl.)*, **47**, 297(1978); A. A. Ovchinnikov and I. A. Misurkin, *Russ. Chem. Rev.(Eng. Trans.)* **46**, 967(1977).
  40. A. L. Buchachenko, *Compt. Rend. (Dokl.) Acad. Sci. USSR*, **244**, 1146(1979).
  41. D. J. Klein, C. J. Nelin, S. Alexander, and F. A. Matsen, *J. Chem. Phys.* **77**, 3191(1982); D. J. Klein, *Pure & Appl. Chem.* **55**, 299(1983).
  42. N. Tyutyulkov, P. Schuster and O. E. Polansky, *Theor. Chim. Acta (Berl.)*, **63**, 291(1983); N. Tyutyulkov, O.E. Polansky, P. Schuster, S. Karabunarliev and C. I. Ivanov, *ibid.*, **67**, 211(1985).
  43. S. Kato, K. Morokuma, D. Feller, E. R. Davidson and W. T. Borden, *J. Am. Chem. Soc.*, **105**, 1791(1983).
  44. K. Yamaguchi, H. Fukui and T. Fueno, *Chem. Letters*, 625(1986).
  45. K. Yamaguchi, T. Fueno, K. Nakasuji and I. Murata, *Chem. Letters*, 629(1986).
  46. N. Nasu, *Phys., Rev.*, **B33**, 330(1986).
  47. H. Fukutome, A. Takahashi and M. Ozaki, *Chem. Phys. Lett.*, **133**, 34(1986).
  48. Y. Teki, T. Takui, M. Kitano and K. Itoh, *Chem. Phys. Lett.*, **142**, 181(1987); *Chem. Phys. Lett.*, submitted.
  49. K. Yamaguchi, Y. Toyoda and T. Fueno, *Synt. Metals*, **19**, 81(1987).
  50. D. J. Klein and S. A. Alexander, in *Graph Theory and Topology in Chemistry (Elsevier Science Publishers B. V., Amsterdam, 1987)*, p. 404.
  51. S. A. Alexander and D. J. Klein, *J. Am. Chem. Soc.*, **110**, 3401(1988).
  52. C. I. Ivanov, N. Tyutyulkov, G. Olblich, H. Brenzen and O. E. Polansky, *Theor. Chim. Acta*, **73**, 27(1988).
  53. J. B. Torrance, P. S. Bagus, I. Johannsen, A. I. Nazzal, S. S. P. Parkin and Batail, *J. Appl. Phys.*, **63**, 2967(1988).
  54. H. Yagi, T. Takui, Y. Teki, T. Kinoshita and K. Itoh, *Chem. Phys. Letters*, submitted.
  55. K. Akashi, T. Takui, T. Kinoshita and K. Itoh, *J. Am. Chem. Soc.*, submitted.
  56. Yu. V. Korshak, A. A. Ovchinnikov, A. M. Shapino, T. V. Medvedeva and V. N. Spector, *JETP Letters*, **43**, 399(1986); Yu. V. Korshak, T. V. Medvedeva, A. A. Ovchinnikov and V. N. Spector, *Nature*, **326**, 370(1987).
  57. J. B. Torrance, S. Oostra and A. Nazzal, *Synt. Metals*, **19**, 709(1987).
  58. A. A. Ovchinnikov, *Preprints of IUPAC 32nd Int. Symposium on Macromolecules*, 58(1988).
  59. J. S. Miller, A. J. Epstein and W. M. Reiff, *Chem. Rev.* **88**, 201(1988), and references therein.
  60. J. S. Miller, A. J. Epstein and W. M. Reiff, *Chem. Research*, **21**, 114(1988), and references therein.
  61. M. Ota, S. Otani, K. Kobayashi, A. Kojima and E. Ota, *Preprints of the 57th Annual Meeting of the Chemical Society of Japan 3D410(1988)*; M. Ota, S. Otani, K. Kobayashi and M. Igarashi, *ibid.*, 3D411(1988); H. Kamiyama, M. Ota, S. Otani and K. Kobayashi, *ibid.*, 3D412(1988); M. Ota, S. Otani and M. Igarashi, *ibid.*, 3D413(1988); *ibid.*, M. Ota, S. Otani, K. Kobayashi M. Igarashi, *Chem. Letters*, 1183(1989).
  62. E. B. Fleisher, N. Sung and S. Hawkinson, *J. Phys. Chem.* **72**, 4311(1968).
  63. A. Caneschi, D. Gatteschi, P. Rey, and R. Sessoli, *Inorg. Chem.*, **27**, 1756(1989).
  64. A. Caneschi, D. Gatteschi, J. P. Renard, P. Rey, and R. Sessoli, *Inorg. Chem.*, **27**, 1976(1989).



THERMAL STABILITY OF MAGNETIC PROPERTIES IN DEHYDROGENATED  
TRIARYLMETHANE RESINS

MICHIIYA OTA\* and SUGIO OTANI\*\*

\*Gunma College of Technology, Maebashi, Gunma 371, Japan

\*\*Faculty of Engineering, Gunma University, Kiryu-shi Gunma 376, Japan

## ABSTRACT

The stability of the magnetic properties of dehydrogenated triarylmethane resins was investigated both at room temperature and at elevated temperatures. A magnetic property different from that reported in a previous paper was found in the course of studying the reproducibility of synthesis. This new property was examined through a mechanical response of the resins to a set of permanent magnets.

## INTRODUCTION

Possibility of organic ferromagnet was proposed by McConnell [1], Mataga [2] and Itoh [3] in the 1960's. However it took until 1986 for such materials to be prepared actually as predicted. Some reports related to this object were first published by Ovchinnikov et al. [4], Torrance et al. [5], and Miller, Epstein et al. [6] in 1986 and 1987. Since then, some new organic compounds [7-9] have been so far claimed to possess the ferromagnetic properties.

It will be of interest if magnetic properties of organic compounds could be controlled by different preparation methods from the same starting material. Organic polymers may be suitable for this purpose in view of the diversity of their structure.

In the course of studying the condensed polynuclear aromatic (COPNA) resin in order for the preparation of precursors of carbon materials, we observed the magnetic hysteresis of the dehydrogenated triarylmethane resins with a vibration sample magnetometer (VSM) at room temperature. [7] The triarylmethane resins used in these experiments were prepared by heating the mixtures of aromatic compounds and aromatic aldehyde in the presence of acid catalyst. The unit structures are shown in Fig.1.

Although the origin of the magnetic property of these resins has not been clarified yet, it is difficult to explain this phenomenon as due to the presence of trace metal contamination. We think that the ferromagnetic behavior arises from the triarylmethyl structure and the present radicals formed in these resins by dehydrogenation. Hashimoto and the authors have recently reported the stable radicals evolved in the resins which has a long life time of more than 5 months in the powder under vacuum. [10] Analysis of the spin structure related to the magnetic property of the dehydrogenated triarylmethane resin is in progress by Itoh, Takui and Teki of Osaka City University [11]. The study of the stability of the magnetic properties provides helpful information on the origin of the magnetic properties.

The magnetic stability of the triarylmethane resin depends both on the preparation process itself involving dehydrogenation and on the storage environment. This paper reports the thermal stability of the magnetic properties of the dehydrogenated triarylmethane resins and the reproducibility of the dehydrogenation in the preparation process.

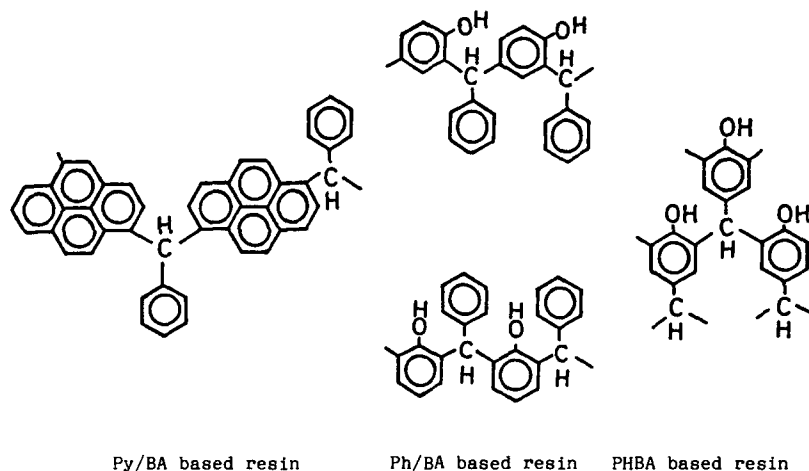


Fig.1 Typical structures of triarylmethane resins.  
(Py:pyrene, BA:benzaldehyde, Ph:phenol, PHBA:p-hydroxybenzaldehyde)

#### EXPERIMENTAL

These resins were prepared by heating the mixtures with the compositions shown in Table 1, under stirring in argon atmosphere.[7] The PHBA based resin was prepared by self-condensation and Ph/BA based resin was obtained from the mixture of phenol and benzaldehyde. These preparations required only a smaller amount of an acid catalyst than that of pyrene because of higher reactivity.

The PHBA based resin was used without purification since it was insoluble into any organic solvent. On the other hand, the pyrene based resin(abbreviated as Py/BA based resin) was purified prior to the dehydrogenation in order to remove the acid catalyst, unreacted pyrene and benzaldehyde.

The dehydrogenation was carried out by the irradiation of ultraviolet (UV) light ( $\approx 300$  nm) in the presence of a photo-oxidizing agent such as benzoquinone(BQ). In the case of PHBA based resin, after the addition of BQ which is 1.5 times in molar ratio to the structural unit of the resin, the finely powdered resin was dispersed into ca. 20 ml of cyclohexane in a quartz glass tube. Then the suspension was irradiated by UV light from a high pressure mercury lamp for 12 h at the temperature below ca. 283 K.

The Py/BA based resin mixed with BQ of 1.5 times in molar ratio to the structural unit of this resin was dissolved into ca. 20 ml of dichloromethane in a quartz glass tube. And the dichloromethane solution was irradiated by UV light for 12 h at ca. 303 K.

The magnetic properties for these dehydrogenated resins were checked qualitatively by "moving test on the water surface" and measured quantitatively with VSM.

In order to examine the stability during the preservation period, the dehydrogenated PHBA based resin in a bottle stoppered in air was kept at room temperature and after five months the resin was exposed to hydrogen chloride.

The magnetic properties of the resin immediately after preparation and after 2, 4 and 6 months were measured with VSM and compared with each other.

Table I Composition and condition for preparation of the triarylmethane resins.

Resins	Composition of raw material			Condition	
	Aro <sup>*1</sup> (mol)	Crosslinking agent	Catalyst <sup>*2</sup> (%)	Temp.(K)	Period(min)
Py/BA	Py(1)	BA(1.25)	PTS(5)	433	90
Ph/BA	Ph(1)	BA(1.25)	PTS(1)	403	90
PHBA	PHBA	---	PTS(1)	403	30

\*1 Aromatic compound, \*2 p-toluenesulfonic acid

The dehydrogenated resin preserved for 4 months was used to examine the thermal stability. After this resin was heated up to 373 and 473 K, respectively, under an inert atmosphere for 10 min, the magnetic properties of these treated resins were compared with that before heat-treatment.

#### RESULTS and DISCUSSION

The stability on storage can be seen from the change of the hysteresis loop shown in Fig. 2. The hysteresis loop of the PHBA based resin immediately after dehydrogenation( Fig. 2(a) ) showed the saturation magnetization( $I_s$ ) of 0.59 G and the coercive force( $H_c$ ) of 10 Oe. After 2 to 4 months ( Fig. 2(b) ), however,  $I_s$ ,  $H_c$  and the residual magnetization( $B_r$ ) decreased at the same time. After 6 months( Fig. 2(c) ), the loop became undetectable, and merged with a paramagnetic line. This tendency may be understood as due to the instability of the radical sites in the resin under the presence of radical scavengers such as hydrogen chloride and oxygen.

On the other hand, the hysteresis loop after heat-treatment is shown in Fig. 3 as compared with that before heating( Fig. 2(b) ), which narrowed gradually into the fine loop with raising temperature up to 473 K. This change seems to arise from the origins similar to those for the storage effect.

The instability is considered to come from the following three factors: (1) the loss of cooperative spin alignment, (2) the decrease in the radical sites due to bond rearrangement and (3) the production of free radicals through the thermal decomposition. When the resin was kept at room temperature, factors of (1) and (2) would be effective, whereas all of the three would be effective when the resin was heat-treated.

Reproducibility of the dehydrogenation process was examined on both the Py/BA based resin and the Ph/BA based resin. In the course of this experiment, other magnetic phenomena were observed: the VSM data and the result of the moving test were different from those of the previous report.[7] The result of the "moving test on the water surface"[7] was illustrated as C in Fig. 4. Although this result has not been clarified, this magnetic behavior was observed with good reproducibility.

This behavior of C in Fig. 4 was apparently different from those of A and B. The behavior characteristic of C is that the sample powders are assembled at the five points of a set of four permanent magnets which have a magnetic flux density smaller than those of the four points of B in Fig. 4.

On the other hand, when the powders were floated on the water surface and then a permanent magnet was approached toward a powder, this powder tended to be separate from the permanent magnet with some distance between

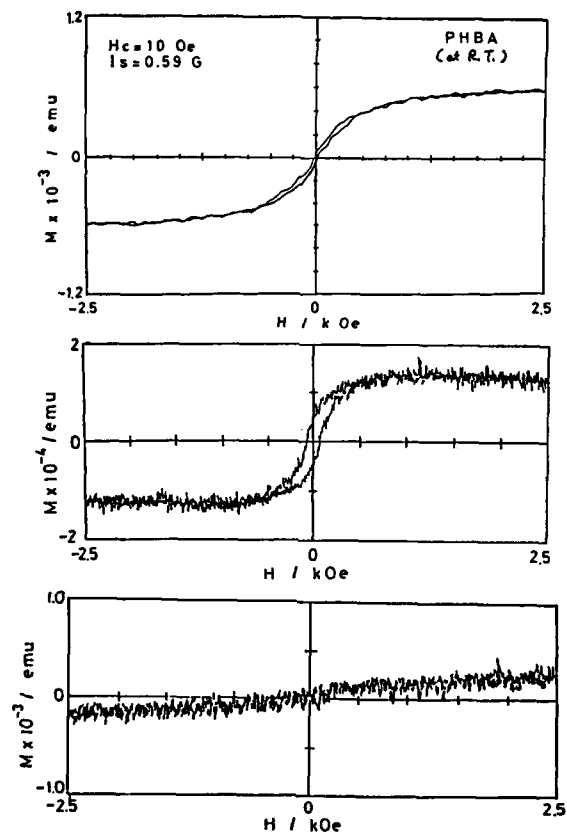


Fig. 2 Change of the magnetic property on the storage period.  
 (a) Immediately after dehydrogenation, (b) After 4 months,  
 (c) After 6 months.

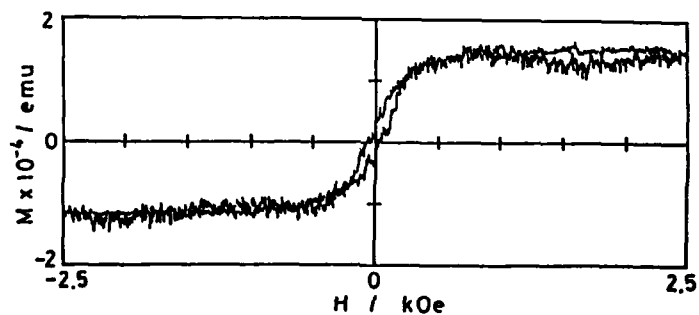


Fig. 3 Hysteresis loop with heat-treatment at 473 K for 10 min after heated at 373 K for 10 min.

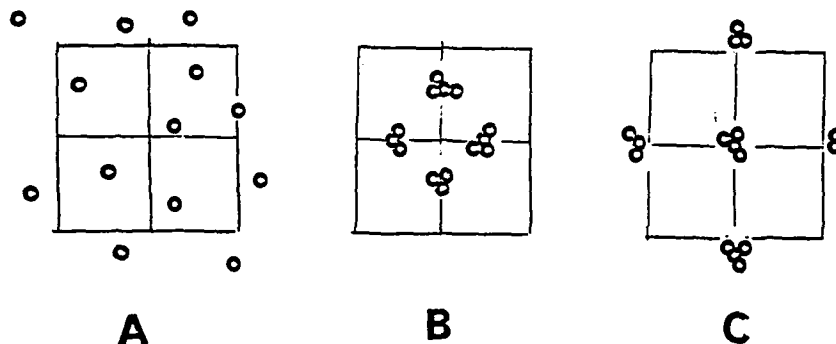


Fig.4 Classification of magnetic behavior on the basis of "moving test on the water surface".

them. According to the VSM measurement, the sample indicated the unusual magnetic curve which is thought to be obtained by the overlap of antiferromagnetic and diamagnetic components.

In general, two types of reaction path, viz., photo-exciting and photo-side reacting paths, proceed during the photo-reaction process. The former reaction path is independent of the reaction temperature during the exposure of UV light but the latter reaction path depends on the temperature. It was likely that the difference between this new phenomena and the previous ferromagnetic one[7] was attributed to the conditions on the dehydrogenation of the resin. The further elucidation about the mechanism is now in progress.

Therefore, the magnetic properties of the dehydrogenated triarylmethane resins are classified at the present stage as shown in Fig.4.

At the present time, it can not exclude the possibility that the state of the resin exhibiting the behavior of C in Fig. 4 is a complex state consisting of the mixture of a smaller amount of antiferromagnetic component and a large amount of diamagnetic one.

#### CONCLUSION

The magnetic property of the dehydrogenated triarylmethane resin was converted ferromagnetic to paramagnetic on the storage for 6 months in the presence of an oxidizing atmosphere such as hydrogen chloride and oxygen or by the heat-treatment at 473 K. We are studying the method for synthesizing the resins exhibiting B and C in Fig. 4 separately.

The authors wish to thank Prof. K. Itoh, Dr. T. Takui and Dr. Y. Teki of Osaka City University for many valuable discussions and their advice; Dr. S. Hashimoto of Gunma College of Technology for his helpful suggestions; Dr. J. S. Miller of E. I. du. Pont de Nemours and Co., Inc. for the helpful discussion, and Prof. M. Kinoshita and Dr. T. Sugano of Tokyo University for their helpful advice. A part of this study was carried out by a grant from Yazaki Memorial Foundation for Science and Technology.

REFERENCE

1. H.M.McConnell, J. Chem. Phys., 39, 1910(1963).
2. N.Mataga, Theor. Chim. Acta, 10, 372(1968).
3. S.Morimoto, K.Itoh, F.Tanaka, N.Mataga, Preprints Symp. Molec. Struc., Tokyo, P.76(1968).
4. Yu.V.Korshak, T.V.Medvedeva, A.A.Ovchinnikov and V.N.Spector, Nature, 326, 370(1987).
5. J.B.Torrance, S. Oostra and A.Nazzari, Synth. Met., 19, 709(1987).
6. J.S.Miller, J.C.Calabrese, H.Rommelmann, S.R.Chittipeddi, J.H.Zhang, W. M.Reiff and A.J.Epstein, J.Am.Chem.Soc., 109, 769(1987).
7. M.Ota, S.Otani, K.Kobayashi, M.Igarashi, Chem. Letters, 1989, 1183.
8. L.Y.Chiang, D.C.Johnston, D.F.Goshorn, R.B.Upasani and A.N.Bloch, 197th ACS international Meeting, ORGN 0100(1989).
9. H.Iwamura, Oyobutsuri, 58, 1061(1989).
10. S.Hashimoto, N.Kato, M.Ota, S.Otani, presented at the symposium on Molecular Science, Sapporo, Jpn, 1989(unpublished).
11. T.Shichiri, Y.Teki, T.Takui, K.Itoh, ibid., 1989(unpublished).

**POLYPHENOXY RADICALS: SYNTHESIS AND HOMO-POLYMERIZATION OF 2-(3,5-DI-*t*-BUTYL-4-HYDROXYPHENYL)ISOBUTYL METHACRYLATE**

RAVINDRA B. UPASANI,<sup>a,b</sup> LONG Y. CHIANG<sup>a,\*</sup> AND D. P. GOSHORNA<sup>a</sup>

<sup>a</sup> Corporate Research Laboratories, Exxon Research and Engineering Company, Annandale, New Jersey 08801

<sup>b</sup> Department of Physics, Princeton University, Princeton, New Jersey 08544

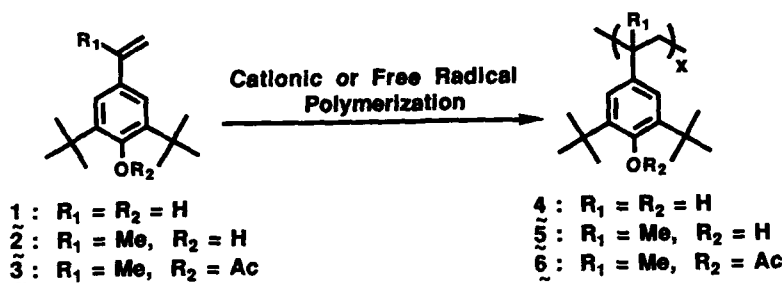
**ABSTRACT**

We evaluated the chemical stability of various polyphenoxy radicals prepared through the modified synthetic methods. The monomeric 3,5-di-*t*-butyl-4-hydroxyphenyl derivatized olefins and methacrylates were prepared in a multistep synthesis starting from 2,6-di-*t*-butylphenol. These monomers were polymerized in the presence of radical initiators at the refluxing temperature of aromatic solvents under an inert atmosphere. The most stable polyradicals were found to be highly hindered poly(DBPM) radicals.

**INTRODUCTION**

Stable polyradicals can be utilized as precursors for the preparation of potential organic ferromagnetic materials. They can be hydrazyl, nitroxyl, phenoxy, triarylmethyl, and diaryl carbene radicals. These radicals can be stabilized by a high degree of resonance and adjacent highly hindered *t*-butyl groups. The stabilization significantly decreases their reactivity toward radical coupling with bond formation. A number of polyphenoxy radicals have been synthesized and reviewed.<sup>1</sup> Generally, polyphenoxy radicals can be prepared by an oxidative reaction on the phenol moiety of polyalkenylphenols. The method of polymerization was found to depend heavily on the structure of monomers.<sup>2,3,4</sup> In the case of 2,6-di-*t*-butyl-4-vinyl phenol, the polymerization was most efficiently carried out by a cationic mechanism to give a benzyl hydrogen containing poly(2,6-di-*t*-butyl)phenols. The radicals derived from these polyphenols are not chemically stable and themselves may undergo disproportionation to result quinonemethide formation.<sup>2,5</sup> To stabilize this type of polyphenoxy radicals the removal of benzyl hydrogen is desirable. This can be achieved by replacing it with a methyl group. However, the resulting 2,6-di-*t*-butyl-4-isopropenyl phenol can not be polymerized easily.<sup>2,6</sup> Therefore, we modified the structure of 2,6-di-*t*-butyl-4-isopropenyl phenol monomer to move the polymerizable olefin away from the hindered moiety of molecules.

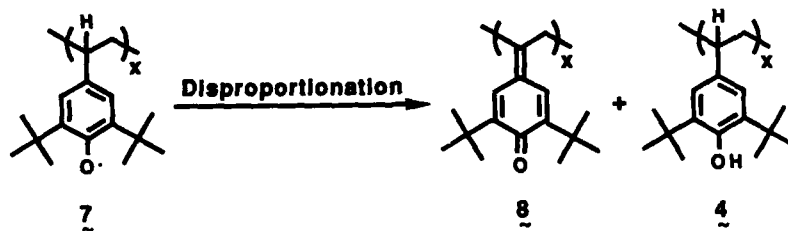
Here we report the synthesis of 3,5-di-*t*-butyl-4-hydroxy-phenyl derivatized olefins and methacrylates and their polymers. The most stable polyradicals were found to be highly hindered poly(DBPM) radicals.



**Scheme 1**

## RESULTS AND DISCUSSION

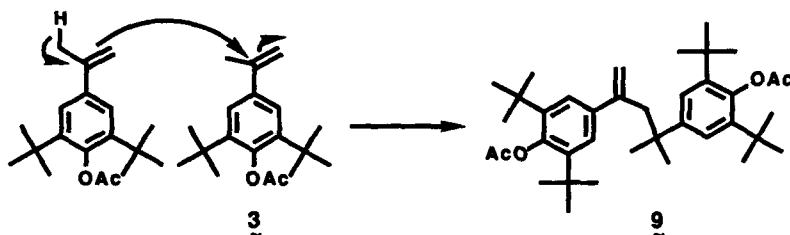
3,5-di-*t*-butyl-4-hydroxystyrene (1) was synthesized according to the literature method<sup>6</sup> starting from 2,6-di-*t*-butylphenol. As shown in Scheme 1, the polymerization reaction of 1 was carried out by a cationic method in the presence of  $BF_3 \cdot Et_2O$  in methylene chloride at  $-78^\circ C$  to give poly(3,5-di-*t*-butyl-4-hydroxystyrene) (4) with a weight average molecular weight of 5,900. Several attempts to make higher molecular weight polymers were unsuccessful. This oligomer was oxidized using various oxidation reagents, such as alkaline potassium ferricyanide,<sup>5</sup> iodine with KOH,<sup>9</sup> or lead dioxide,<sup>6,10</sup> in benzene to afford polyphenoxy radicals 7. However, due to the disproportionation reaction of polyradicals 7 as shown in Scheme 2, a sample free of quinonemethide 8 could not be obtained.



**Scheme 2**

Hence, steps were taken to modify the structure of 7 by replacing benzyl hydrogens with methyl groups to eliminate the formation of quinonemethide. This led us to prepare 3,5-di-*t*-butyl-4-hydroxy- $\alpha$ -methylstyrene<sup>11</sup> (2) and O-acetyl-2,6-di-*t*-butyl-4-

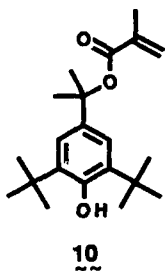




Scheme 3

isopropenylphenol (3). The monomers 2 and 3 were synthesized according to the reported method<sup>6</sup> starting from 2,6-di-*t*-butylphenol. The polymerization reaction of 3 was studied using various catalysts, such as  $\text{BF}_3\text{-Et}_2\text{O}$  and  $\text{SnCl}_4$ . However, in all cases, only a dimer 9 was isolated in fairly good yield. The dimerization mechanism of 3 is depicted in Scheme 3. The failure to obtain a polymer from compound 3 may

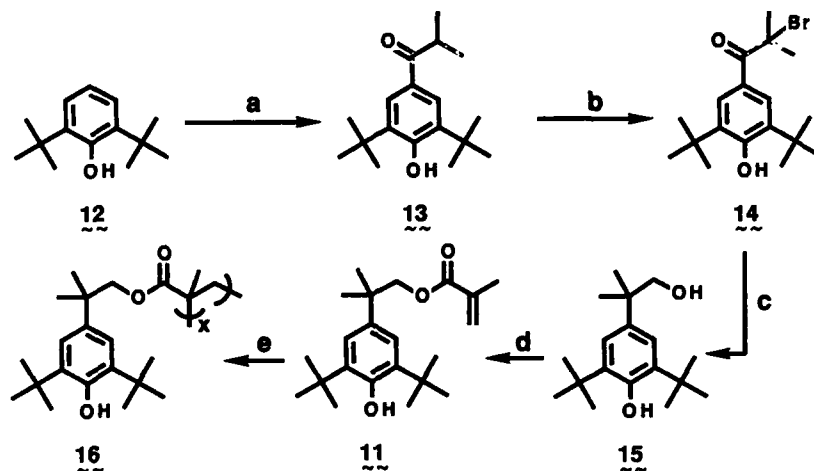
be due to the steric hindrance of monomer as confirmed by a molecular model for this polymer. To reduce the strain in the polymer chain it was decided to move the polymerizable vinyl moiety away from the hindered aromatic ring.



10

One of the potential and synthetically viable monomers is 2-(3,5-di-*t*-butyl-4-hydroxyphenyl)isopropyl methacrylate (10). However, the preliminary attempt to synthesize this monomer by reacting the corresponding (3,5-di-*t*-butyl-4-hydroxyphenyl)-isopropyl alcohol with methacryloyl chloride failed to yield 10, instead the dehydrated compound 2 was obtained as a sole

product. Therefore, we decided to move the hindered aromatic ring one more carbon away from the vinyl moiety. That resulted in a monomer structure of 2-(3,5-di-*t*-butyl-4-hydroxyphenyl)isobutyl methacrylate (11). As shown in Scheme 4, compound 11 was synthesized by a sequence of reaction starting from 2,6-di-*t*-butylphenol (12). Thus phenol 12 was allowed to react with 2-methylpropionic acid in the presence of trifluoroacetic anhydride to give the corresponding propiophenone<sup>6</sup> (13) in 92% yield. Propiophenone 13 was then brominated with  $\text{CuBr}_2$  in chloroform to afford the  $\alpha$ -bromo-derivative 14 in a nearly quantitative yield. The reduction of 14 with lithium aluminum hydride (LAH) followed by rearrangement of the resulting intermediate yielded 2-(3,5-di-*t*-butyl-4-hydroxyphenyl)isobutanol (15).<sup>8</sup> The esterification of compound 15 with methacryloyl chloride in pyridine afforded the desired monomer 11 in about 65% yield. The polymerization was carried out with purified monomer 11 using AIBN as a radical initiator in benzene to obtain white polymers of poly[2-(3,5-di-*t*-butyl-4-hydroxyphenyl)isobutyl methacrylate] (16, polyDBPM) with a weight average molecular weight of  $10^5$ .



a : 2-Methylproprionic acid / TFA; b :  $\text{CuBr}_2$  /  $\text{CHCl}_3$ -EtOAc;  
 c : LAH /  $\text{Et}_2\text{O}$ ; d : Methacryloyl chloride / pyridine; e : AIBN /  $\phi\text{H}$

#### Scheme 4

The polyphenoxy radicals of poly[2-(3,5-di-*t*-butyl-4-hydroxyphenyl)isobutyl methacrylate] (16) was prepared by an oxidation reaction of 16 with various oxidants such as potassium ferricyanide in a mixture of benzene- $\text{H}_2\text{O}$ . To ensure the removal of the residual oxidants remaining in the polyradical containing benzene solution, the solution was dried and filtered through celite prior to the solvent evaporation. The preliminary solid state magnetic susceptibility studies of the resulting polyphenoxy radicals indicate a molar Curie constant  $C_M$  corresponding to a bulk spin density of 0.16 spins 1/2 per phenoxy unit with a Curie-Weiss temperature ( $\theta$ ) of 1.0K. Even though the positive  $\theta$  seems to indicate that the interactions between these spins in solid state are ferromagnetic, but the observable spin concentration is rather dilute. Therefore, more studies are necessary to understand the nature of spin interactions in this polyradical system.

#### EXPERIMENTAL

**3,5-DI-*t*-butyl-4-hydroxystyrene (1).** Compound 1 was prepared according to the method described by Grosso.<sup>6</sup> We obtained 3,5-di-*t*-butyl-4-hydroxystyrene as low melting solids in 66% yield;  $^1\text{H NMR}$   $\delta$  1.45 (s, 18H, *t*-Bu), 5.08 (d, 1H,  $J = 10.5$  Hz, CH *trans* to phenyl), 5.23 (s, 1H, OH), 5.58 (d, 1H,  $J = 17.4$  Hz, CH *cis* to phenyl), 6.67 (m, 1H, CH), and 7.24 (s, 2H, aromatic).

**1-(3,5-Di-*t*-butyl-4-hydroxyphenyl)isobutan-1-one (13).** A mixture of 2,6-di-*t*-butylphenol (60 mmol, 12.4 g) and 2-methylpropionic acid (80 mmol, 7.1 g) were cooled to 0°C and treated with trifluoroacetic anhydride (13 ml). The mixture was stirred at room temperature for 1 hr and poured into aq. NaHCO<sub>3</sub> (300 ml). After stirring for 30 min, the precipitated solid was collected by filtration, washed thoroughly with water, and dried to afford 1-(3,5-di-*t*-butyl-4-hydroxyphenyl)isobutan-1-one (13) as white solids in 92% yield (15.4 g); mp 128-130°C (lit.<sup>7</sup> 145-7°C). <sup>1</sup>H NMR δ 1.17 (d, 6H, J = 7 Hz, CH<sub>3</sub>), 1.44 (s, 18H, *t*-Bu), 3.53 (m, 1H, CH), 5.72 (s, 1H, OH), and 7.83 (s, 2H, aromatic).

**1-(3,5-Di-*t*-butyl-4-hydroxyphenyl)-2-bromoisobutan-1-one (14).** A solution of 13 (54.3 mmol, 15 g) in chloroform (50 ml) and ethyl acetate (70 ml) was treated with an excess of CuBr<sub>2</sub> (134 mmol, 30 g) at room temperature. The resulting mixture was heated at refluxing temperature for 15 hr. It was then cooled and the insolubles filtered. The filtrate was evaporated to dryness to yield 1-(3,5-di-*t*-butyl-4-hydroxyphenyl)-2-bromoisobutan-1-one (14) as white solids (18.8 g); m.p. 138-40°C (lit.<sup>8</sup> 141-2°C). <sup>1</sup>H NMR δ 1.47 (s, 18H, *t*-Bu), 2.06 (s, 6H, CH<sub>3</sub>), 5.72 (s, 1H, OH), and 8.16 (s, 2H, aromatic).

**2-(3,5-Di-*t*-butyl-4-hydroxyphenyl)isobutan-1-ol (15).** Bromide 14 (20 mmol, 7.1 g) was dissolved in anhyd. Et<sub>2</sub>O (200 ml) and the solution was cooled to -5°C. It was then treated with lithium aluminum hydride (LAH, 45 mmol, 1M in THF). The resulting suspension was heated at refluxing temperature in an oil bath for 3 hr. After cooling to 0°C, it was treated dropwise by dil. H<sub>2</sub>SO<sub>4</sub> (10 ml in 100 ml H<sub>2</sub>O). The organic layer was separated, dried, and evaporated to obtain 15 as white solids in 95% yield (5.3 g); m.p. 147-8°C (lit.<sup>8</sup> m.p. 149-150°C). <sup>1</sup>H NMR δ 1.33 (s, 6H, CH<sub>3</sub>), 1.46 (s, 18H, *t*-Bu), 3.57 (s, 2H, CH<sub>2</sub>), 5.13 (s, 1H, OH), and 7.19 (s, 2H, aromatic).

**2-(3,5-di-*t*-butyl-4-hydroxyphenyl)isobutyl methacrylate (11).** Methacryloyl chloride (22 mmol, 2.3 g) was added dropwise to a solution of alcohol 15 (20 mmol, 5.6 g) in pyridine (14 ml) at 0°C. The pale yellow reaction mixture was then stirred at 45°C for 2.5 hr. After cooling to room temperature it was poured into ice-HCl (20 ml). The precipitated product was then extracted into Et<sub>2</sub>O. The organic layer was separated and washed with dil. NaHCO<sub>3</sub> and brine. It was then dried and evaporated to yield 2-(3,5-di-*t*-butyl-4-hydroxyphenyl)isobutyl methacrylate (11) as low melting solids in 64% yield (4.5 g); m.p. 71-73°C. <sup>1</sup>H NMR δ 1.38 (s, 6H, CH<sub>3</sub>), 1.44 (s, 18H, *t*-Bu), 1.92 (s, 3H, CH<sub>3</sub>), 4.19 (s, 2H, OCH<sub>2</sub>), 5.11 (s, 1H, OH), 5.58 (s, 1H), 6.09 (s, 1H), and 7.19 (s, 2H, aromatic).

**Polymerization of 2-(3,5-di-*t*-butyl-4-hydroxyphenyl)isobutyl methacrylate (11).** A polymerization tube was charged with 2-(3,5-di-*t*-butyl-4-hydroxyphenyl)isobutyl methacrylate (11, 5.8 mmol, 2 g), benzene (4.5 ml), and AIBN (recrystallized, 18 mg, 0.11 mmol, 1.86 mol%). The tube was degassed by the

freeze-thaw cycle and sealed at 0.1 torr. After 2 days at 70°C the thick reaction mixture was diluted with benzene (15 ml) and poured into methanol (75 ml). The precipitated product was collected by filtration, washed with methanol (20 ml), and dried to give poly[2-(3,5-di-*t*-butyl-4-hydroxyphenyl)isobutyl methacrylate] (16, polyDBPM) as white solids in 70% yield (1.4 g,  $M_w$  105,000,  $M_w/M_n = 2.64$ ); m.p. 175-80°C. Anal. Calcd for  $C_{22}H_{34}O_3$ : C, 76.3; H, 9.82. Found: C, 76.36; H, 10.01. IR  $\nu_{max}$  3634, 2948, 2886, 1727, 1473, 1435, 1236, 1150, 980, and 881  $cm^{-1}$ .  $^1H$  NMR  $\delta$  1.39-1.44 (m, 27H), 3.49 (s, 1H), 3.84 (broad, 1H), 5.1 (m, 1H), and 7.12 (s, 2H).  $^{13}C$  NMR  $\delta$  25.99, 26.26, 30.76, 34.85, 38.10, 45.36, 51.17, 122.59, 128.65, 135.73, 135.88, 136.81, 152.44, and 177.53.

**Polymerization of 3,5-di-*t*-butyl-4-hydroxystyrene (1).** A method described by Braun was used.<sup>2</sup> A solution of 3,5-di-*t*-butyl-4-hydroxystyrene (3 mmol, 700 mg) in dry  $CH_2Cl_2$  (10 ml) was treated with  $BF_3 \cdot Et_2O$  (0.12 mmol, 0.015 ml, 4 mol%) at -78°C. The mixture was then stirred at that temperature for 2 hr and more  $BF_3 \cdot Et_2O$  (0.015 ml) was added. The stirring was continued for another 15 hr. Methanol (3 ml) was added and the volatiles were removed under reduced pressure. The residue was then washed with hexane (5 X 10 ml) and dried to give poly(3,5-di-*t*-butyl-4-hydroxystyrene) (4, 530 mg,  $M_w$  5,900,  $M_w/M_n = 1.27$ ); m.p. >300°C.

**Attempted polymerization of *o*-acetyl-2,6-di-*t*-butyl-4-isopropenylphenol (3).** A solution of 3 (3 mmol, 864 mg) in dry  $CH_2Cl_2$  (10 ml) was treated with  $BF_3 \cdot Et_2O$  (0.12 mmol, 0.015 ml, 4 mol%) at -78°C. The mixture was stirred at that temperature for 15 hr. Methanol (10 ml) was added and the volatiles were removed under reduced pressure. The resulting solid was suspended in MeOH (5ml), filtered, washed with MeOH (2 ml), and dried to obtain the dimer 9 (270 mg).  $^1H$  NMR  $\delta$  1.20 (s, 6H,  $CH_3$ ), 1.33 (s, 36H, *t*-Bu), 2.33 (s, 6H,  $OCOCH_3$ ), 2.78 (s, 2H,  $CH_2$ ), 4.75 (s, 1H, CH), 5.11 (s, 1H, CH), 7.29 (m, 4H, aromatic).

**Acknowledgement.** The Financial support for this research by National Science Foundation (Grant DMR 88-22532) is gratefully acknowledged.

#### REFERENCES

1. D. Braun, *Pure Appl. Chem.*, **30**, 41 (1972).
2. D. Braun and B. Meier, *Makromol. Chem.*, **175**, 791 (1974).
3. D. Braun and W. Wittig, *Makromol. Chem.*, **181**, 557 (1980).
4. F. R. Hewgill and W. T. Smith, *J. Polym. Sci., Polym. Lett. Ed.*, **14**, 463 (1976).
5. C. D. Cook and B. E. Norcross, *J. Am. Chem. Soc.*, **78**, 3797 (1956).
6. P. Grosso and O. Vogl, *J. Macromol. Sci. Chem.*, **A23**, 1041 (1986).
7. A. Nishinaga, T. Shimizu, Y. Toyoda, T. Matura, and K. Hirotsu, *J. Org. Chem.*, **47**, 2278 (1982).
8. L. H. Schwartz and R. V. Flor, *J. Org. Chem.*, **34**, 1499 (1969).
9. K. Omura, *J. Org. Chem.*, **49**, 3046 (1984).
10. D. Braun and B. Meier, *Makromol. Chem. Suppl.*, **1**, 111 (1975).
11. D. Braun and B. Maier, *Makromol. Chem.*, **167**, 119 (1973).

## ORGANIC POLYRADICAL MODELS FOR ORGANIC MAGNETIC MATERIALS

DAVID A. MODARELLI, FRANK C. ROSSITTO, MASAKI MINATO, AND PAUL M. LAHTI\*

University of Massachusetts, Department of Chemistry, Amherst, MA 01003

### ABSTRACT

A variety of model organic high spin molecules based upon coupled phenoxy and phenylnitrene systems has been examined by semiempirical MO-CI theory. Experimental methodology using photochemical and thermal methods in solution and solid phases to generate and study phenoxy groups for investigation of these models is presented.

### INTRODUCTION

Recent interest in organic polyradicals has been part of a general interest in new magnetic molecules of potential use as information storage materials. Various types of organic or organometallic magnetic materials have been recently described.[1] We have been interested primarily in materials based upon through-bond and through-space high spin coupling of many radicals (or other high spin centers such as nitrenes) to produce very high spin polyradicals.

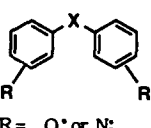
Experimental work such as Iwamura's[2] has shown that the strategy of coupling carbenes through conjugating groups -- in accordance with qualitative rules[3-5] predicting high spin coupling -- can lead to very high spin organic molecules, albeit under conditions of high dilution in crystalline or frozen solution matrix at cryogenic conditions. We wish to couple phenoxy based radicals together to form such very high spin systems. Although one gets only one spin per center -- as opposed to two per center for carbenes and nitrenes -- the greater intrinsic stability of phenoxy based systems by comparison to the more reactive high spin centers makes their synthesis attractive. Recent efforts to prepare phenoxy based polymer systems by solution oxidation of hindered phenolic systems have not yielded high spin counts.[1,6] but the reason for this failure at present is not entirely clear.

In this paper, we qualitatively summarize the application of our previously described[7-8] semiempirical computational algorithms to selected phenoxy based diradicals, and the relationship of these computations to connectivity-based models described by other workers.[3] Experimentally, we show how use of our previously developed photochemical and thermal methods[9] for solid state generation of stable phenoxyl radical centers may be extended to production of unhindered phenoxy systems under conditions where they may be readily detected and observed. *Meta* and *para*-stilbeneoxyl radicals have both been readily generated in matrix and in neat precursor matrix, studied by electron spin resonance (ESR) and ultraviolet-visible (UV-vis) spectroscopy, and their decomposition behavior in polymeric matrices elucidated. Similar experiments have been carried out for other non-*tert*-butylated phenoxy derivatives. By these and similar experiments, we hope to understand what types of phenoxy based systems are fairly robust under matrix isolation conditions (polymer matrices at room temperature and above), how efficiently our methods allow production of phenoxyl radicals under various conditions of precursor substitution and matrix type, and how plausible are the hopes of generating and partially orienting such radicals in polymeric matrix in an effort to control their magnetic interaction with one another. In addition, we have modified the preparation of poly(3,5-di-*tert*-butyl-4-hydroxystyrene), a known polymer[10] with the potential to be functionalized to derivatives which may be photochemically or thermally "developed" to produced high densities of radical sites while in the solid state.

### COMPUTATIONAL METHODS

The semiempirical molecular orbital AM1 method in the program AMPAC[11] (version 2.10) was used in all computations. Geometries were optimized using triplet wave-functions for diradicals, with either a planar constraint or full optimization. The relative energies for triplet and singlet states of the molecules were computed using the configuration interaction

Figure 1: Molecules Investigated by AM1-CI.

	X	Connectivity <sup>1</sup>	Type <sup>2</sup>	
 <p>R = O* or N*</p>	1	(none)	SF	
	2		WA	
	3	-CH=CH-	m,m'	F
	4		m,p'	WF *
	5	-(CH=CH) <sub>2</sub> -	m,m'	F
	6		m,p'	WF *
	7	-C::C-	m,m'	F
	8		m,p'	WF *
	9	-C::C <sub>2</sub> -	m,m'	F
	10		m,p'	WF *
	11	p-phenylene	m,m'	F
	12		m,p'	WF *
	13	m-phenylene	m,m'	WA
	14		m,p'	F
	15		m,m'	F
	16	=C=O	p,p'	F *
	17		m,m'	WF
	18		p,p'	WF
	19	=C=CH <sub>2</sub>	m,p'	WA
	20		m,m'	F
	21		p,p'	F
	22	-O-	m,p'	F *
	23		m,r'	WA *
	24		p,p'	SA *
	25	-NH-	m,p'	F *
	26		m,m'	WF
	27		p,p'	SA *

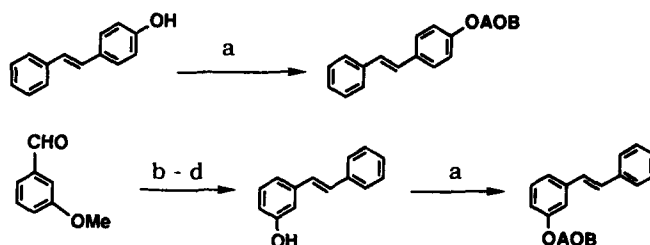
<sup>1</sup>Connectivity of the spin system. <sup>2</sup>Type refers to type of spin coupling, with F=ferromagnetic A=antiferromagnetic, S=strong, W=weak, \* = does not follow eqn. 1. (cf. ref. 12 for 22-27)

(CI) routine in AMPAC, with six or seven orbitals used in the CI active space. Results for triplet-singlet (T-S) energy gaps were not greatly affected by modest amounts of torsion up to  $-30^\circ$  about single bonds, in cases where planarity of the molecules was not enforced. Figure 1 summarizes the qualitative results of the computations, fuller details of which will be published elsewhere.[1,12]

#### EXPERIMENTAL SECTION

The synthetic routes used to prepare the stilbenoid aryloxyoxalyl *tert*-butylperoxides (AOB's) used in this study are shown schematically in Figure 2. *Para*-hydroxystilbene, phenylacetic acid, and *meta*-anisaldehyde were obtained from Aldrich Chemical Company. The general method for preparing the AOB's is described in a previous publication,[9] using the method of adding *tert*-butylperoxyoxalyl chloride to phenolic anions. NOTE THAT *tert*-butylperoxyoxalyl chloride MAY DECOMPOSE WITH POTENTIALLY HAZARDOUS VIOLENCE UNDER SOME CONDITIONS. IT SHOULD BE MADE ONLY IN SMALL (not more than two gram) QUANTITIES AND USED AS SOON AS POSSIBLE. Polymeric films were cast *in vacuo* using 10% degassed chloroform solutions of AOB precursors with polystyrene (PS, MW = 250,000) and poly-methylmethacrylate (PPMA, Aldrich medium molecular weight). Photochemical irradiations were performed with a 1000W Xenon arc lamp (Pyrex filtered for ESR). Low temperature UV-vis spectra were obtained on a Shimadzu UV-260 spectrophotometer using a special low temperature cell in an APD Cryogenics Displex circulating closed-cycle helium cryostat using Suprasil II windows; temperatures were measured by use of a gold-chromel thermocouple at the top of the cell. Low temperature ESR spectra were obtained using sealed-

Figure 2: Synthesis of Stilbene AOB Esters New to This Study.



AOB =  $-(CO)-(CO)-OO^tBu$

a. BuLi/ether, then  $Cl(COCO)OO^tBu$       b.  $PhCH_2CO_2H, Et_3N$   
 c. copper chromite, quinoline,  $200^\circ$ ,  $-CO_2$       d.  $BBr_3$

All new compounds identified by spectroscopic techniques. Adequate elemental analyses are obtained for new compounds, except for AOB esters, which tend to decompose during analysis.

in-quartz, three-fold pump-thawed samples in a Suprasil dewar at 77K (liquid nitrogen) on an IBM Instruments ESP-300 spectrometer at 9.602 GHz with computer-averaged scanning on an Aspect 3000 computer.

## RESULTS AND DISCUSSION

### Computational Findings

Qualitative connectivity based models have made predictions about the ground state (GS) spin multiplicity of diradicals for some time.[3-5] We exemplify these by use of a valence bond model, the Ovchinnikov criterion,[3] for which an alternant conjugated  $\pi$ -system with  $n_s$  starred sites and  $n_o$  unstarred sites, has multiplicity  $M$  given by equation 1. We find that this

$$M = n_s - n_o \quad (1)$$

equation gives results in accord with our computations when  $M$  is predicted to be nonzero (i.e., high spin). There is less qualitative agreement when  $M$  is predicted to be zero -- a singlet GS. In accord with the Hund rule, we sometimes find a nonzero GS to be favored by a small margin even when  $M = 0$ . Recent experimental evidence appears to favor our computations.[13] suggesting that connectivity-based predictions of singlet GS multiplicities for diradicals should be used with caution, and checked where possible by computational methods like ours.

However, we have found equation 1 quite in agreement with our computational results for  $M > 0$ , even where heteroatom radicals such as our phenoxy-based systems are used. Experiment has confirmed that heteroatom-perturbed polyradicals may still exhibit high spin GS's, despite the splitting of orbitals (increased HOMO-LUMO gap) that can exist in such systems.[13] We have shown previously that our method reproduces these results,[7-8] hence it is reasonable to extrapolate our method to yet unknown systems, especially in larger model systems for which ab initio methods are still impractical.

Our latest results indicate that coupling of nitrenes instead of radical sites does not greatly alter the qualitative predictions of equation 1 where  $M > 0$ , although a factor of two in the quantitative predicted multiplicity is observed due to each nitrene center have two instead of one unpaired electron. HS-LS energy gaps for dinitrenes and diphenoxy systems of the same connectivity with the same spacer group are fairly comparable, apparently indicating that the efficacy of a spacer group in coupling two open shell sites with a given multiplicity is to some

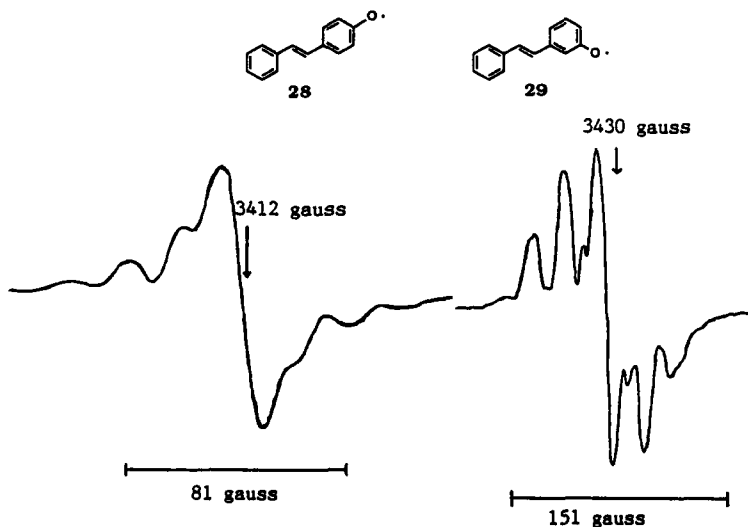
degree intrinsic to the spacer, as may be seen to come degree by the ground states shown in Figure 1. We classify the coupling as being ferromagnetic (high spin), and anti-ferromagnetic (low spin). We also note where equation 1 is not followed. For instance, the carbonyl spacer is a poor coupling spacer due to its reluctance to share the electrons in its very strong  $\pi$ -bond.[14] The coupling by spacers to yield high  $\pi$ -spin GS's are followed for both the diradical and dinitrene models. The major difference for coupled nitrenes is that the non- $\pi$  unpaired electrons in dinitrenes are only weakly coupled through the  $\sigma$ -frameworks of the models studied, hence we often compute nearly degenerate triplet and singlet states for these systems when equation 1 gives  $M = 0$  for the antiferromagnetically coupled dinitrenes.

### Experimental Findings

We find that we may readily generate observable amounts of phenoxy radical based molecules by photolysis of AOB's, both with and without radical stabilization by steric blockading. Figure 3 shows ESR spectra for **28** and **29**, generated at 77K both in 2-methyltetrahydrofuran and ethanol-pentane-ether glass. The *para* sample is deep green, the *meta* sample yellow to orange. The ESR signal and UV-vis absorbance persist until the matrix thaws. In polymeric matrix (PS or PPMA), radical generation at 77K is equally straightforward, but the ESR signal loses some resolution as expected. The lineshape of these is quite similar[10] to that noted previously in oxidation of copolymers of poly(3,5-di-*tert*-butyl-4-hydroxystyrene), **30** to the polyphenoxy radicals. This is presumably due to the poor interaction of the radical center in the stilbeneoxy radical with the ring that does not bear the oxy center, and is in accord with the lack of interaction computed by us in INDO computations.

In an effort to investigate the potential ability to use and preserve non-*tert*-butylated phenoxy systems in rigid polymer matrices, we took advantage of the characteristic UV-vis spectrum of **28**. In PPMA, **28** was made in the Displex at 13K, at which temperature it appears

Figure 3: ESR Spectra for Stilbeneoxy Radicals **28** and **29**.



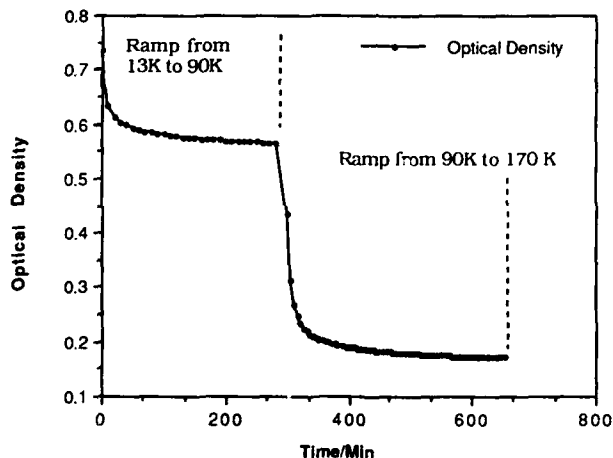
ESR spectra generated in frozen, degassed EPA glassy matrix at 77K. ESR lineshapes and widths for **28** and **29** are similar to these spectra in other frozen matrices.





to be indefinitely stable upon generation. Upon temperature ramping (maximum rate heating to various selected temperatures within 4-5 min) to 90K and 170K of this sample, the behavior of the UV-vis bands of **28** was noted as shown in Figure 4. This behavior was reproducible for different samples of **28** in PPMA and PS, as well as for 2,4,6-trichlorophenoxy similarly made. The observed sudden drop of optical density upon heating, followed by a leveling off and establishment of a constant stable concentration of radical at the new temperature, seem to us consistent with a matrix site reaction, since we are far below the softening point and glass transition temperature of the PPMA and PS matrices. We are still investigating this chemistry, but feel it plausible that at each temperature, a certain number of the leaving group *tert*-butyloxy radicals become able to attack the phenoxyl radicals by diffusion enabled through temperature rise. By the time room temperature is reached, all of the non-*tert*-butylated phenoxyl radical systems we tried were quenched by this putative process -- these included phenoxy, *meta* and *para*-stilbeneoxy, and 2,4,6-trichlorophenoxy.

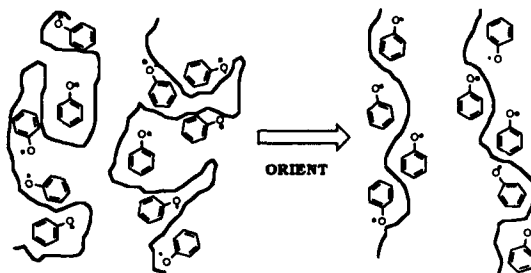
**Figure 4: Thermal Decomposition of Para-Stilbeneoxy**



However, sterically stabilized phenoxyl radicals, upon generation by AOB photolysis in PPMA or PS, proved to be quite stable at room temperature. Apparently, blocking of the reactive ortho positions with nonlabile *tert*-butyl groups allows these radicals to remain stable under these conditions, such that they may be observed by ESR or UV-vis spectroscopy. For instance, the color of 2,4,6-tri-*tert*-butylphenoxy -- photochemically generated in PPMA matrix -- persists at room temperature for many days under vacuum. In addition, the blocked radicals have substantial thermal stability, and may in solution remain fairly stable for at least 8 h at 70-80°C, under which conditions the precursor AOB's are completely decomposed within 3 h. We are at present further investigating the thermal stability of such systems in polymer matrices, and will report on this in due course.

We are also interested in generating phenoxyl radicals that are directly attached to polymer backbones, without necessarily being in conjugative through-bond spin interaction. Although conjugated polyradicals should give stronger spin-spin interactions and better

magnetic properties, we desired to investigate the degree to which fairly random assemblages of radicals attached to a polymer backbone may be oriented by stretching the polymer. In



principle, this can lead to through space spin-spin coupling between the radical sites, with improved magnetic properties. We have devised a simpler synthesis for the previously known 3,5-di-*tert*-butyl-4-hydroxystyrene **30**, [10,15] based upon simple reaction of two equivalents of the lithium ylid from methyltriphenylphosphonium bromide with 3,5-di-*tert*-butyl-4-hydroxybenzaldehyde in ether. Polymerization of **30** occurs under conditions similar to those used in the literature, [10] and is confirmed by  $^1\text{H}$ NMR and IR spectroscopy. The ESR of **30** and copolymers after solution phase oxidation is also known, [10] and will not be further described here. [10] In future work we intend to make this polymer with AOB groups attached, either through polymerizing the AOB functionalized monomer, or functionalizing after polymerization. If these can be made, photochemical or thermal generation of fairly high numbers of radical centers in the solid polymeric state-- as well as study of their magnetic properties -- may become as practical as typical solution phase phenoxy radical generation.

#### ACKNOWLEDGEMENTS

This work was supported by grants from the Office of Naval Research, the National Science Foundation (CHE 8712319), Exxon Education Foundation, and University of Massachusetts.

#### REFERENCES

1. See the proceedings of the Symposium on Ferromagnetic and High Spin Molecular Based Materials at the 197th American Chemical Society Meeting in J. S. Miller, Ed., Mol. Cryst. Liq. Cryst., **1989**, in press.
2. H. Iwamura, Pure Appl. Chem., **58**, 187(1986) and references therein.
3. A. A. Ovchinnikov, Theor. Chim. Acta, **47**, 297(1978).
4. S. A. Alexander, D. J. Klein, J. Am. Chem. Soc., **110**, 3401(1988) and references therein.
5. N. Mataga, Theor. Chim. Acta., **10**, 273(1968).
6. H. Nishide, N. Yoshioka, K. Inagaki, E. Tsuchida, Macromolecules, **21**, 3120(1988).
7. P. M. Lahti, A. R. Rossi, J. A. Berson, J. Am. Chem. Soc., **107**, 2273(1987).
8. P. M. Lahti, A. S. Ichimura, J. A. Berson, J. Org. Chem., **54**, 958(1989)
9. D. A. Modarelli, F. R. Rossitto, P. M. Lahti, Tet. Lett., **1989**, 4473,4477.
10. D. Braun, P. Tormala, W. Wittig, Makromol. Chem., **182**, 2217(1981).
11. M. J. S. Dewar, J. J. P. Stewart, Quant. Chem. Program Exchange, Program 506(1987).
12. P. M. Lahti, to be presented at 199th American Chemical Society Meeting, April, 1990; Toronto, Ontario, CANADA.
13. See citations in references 7-8.
14. A. S. Ichimura, A. R. Matlin, P. M. Lahti, J. Am. Chem. Soc., **110**, 0000(1990) in press.
15. Byproduct reactions from oxidation of these polymers is described by R. B. Upasani, L. Y. Chiang, D. P. Goshorn, these proceeding..

FERROMAGNETIC INTERACTIONS IN A SERIES OF SCHIFF-BASE METAL-ORGANIC  
POLYMERS

F. PALACIO\*, F.J. LAZARO\*, J. GARIN\*, J. REYES\* AND M.C. MORON\*\*†

\* Instituto de Ciencia de Materiales de Aragón, C.S.I.C. and  
Universidad de Zaragoza, 50009 Zaragoza, Spain.

\*\* Laboratoire des Fluorures, Faculté des Sciences, Université du  
Maine, 72017 Le Mans, France.

ABSTRACT

Magnetization and frequency dependence a.c. magnetic susceptibility measurements of the metal-organic polymers of general formula  $\{[M(C_{13}H_{17}N_3)_2]SO_4 \cdot 6H_2O\}_n$ , where  $M = Fe(II)$  or  $Co(II)$ , are indicative of superparamagnetic behavior as a consequence of the existence of strong ferromagnetic interactions in the materials. Scanning electron microscopy and X-ray dispersive spectrometry have been used to study the homogeneity in the composition of the iron polymer.

INTRODUCTION

We have recently reported on the presence of strong ferromagnetic interactions in the Schiff-base metal-organic complex polymer of formula  $\{[Fe(C_{13}H_{17}N_3)_2]SO_4 \cdot 6H_2O\}_n$  [1]. This substance was originally considered ferromagnetic because of its unusually high magnetic susceptibility at room temperature [2] and, more recently, it was described as a metamagnet with a low and temperature dependent critical field [3,4].

The organic polymer is prepared from the polycondensation of a di-aldehyde with a diamine and it is diamagnetic. The polymer is then added to an aqueous solution of the corresponding metallic salt. The presence of strong ferromagnetic interactions in the material requires the search for ferromagnetic impurities arising from the preparative process. The absence of iron oxide particles in this substance was investigated by using synchrotron radiation EXAFS and XANES techniques [4].

Previously reported Mössbauer measurements of the iron polymer [1] indicate that only a fraction of about 20% of the iron can participate in the magnetic interactions within the material. Magnetization and a.c. susceptibility experiments suggested superparamagnetism to account for the behavior of the polymer.

In this communication we study the homogeneity of the material by means of scanning electron microscopy (SEM) and X-ray dispersive spectrometry (EDX). We also offer here further evidence to support the superparamagnetic behavior of the substance studying the frequency dependence of the a.c. susceptibility at zero external magnetic field. The study is also extended to the analogous cobalt polymer.

EXPERIMENTAL DETAILS

The materials were prepared following previously described synthetic methods [1,2]. SEM and EDX experiments were performed using a Hitachi S-2300 equipment operating at 25 kV and fitted with an X-ray dispersive spectrometer EDX-LINK System AN 10000. The sample was prepared by depositing particles of the material on a copper grid overlaid by a thin gold film.

Magnetic a.c. susceptibility measurements at zero external field, were made between 4.2 K and 350 K using a computer controlled susceptometer [5]. The amplitude of the exciting field was 1 Oe and the frequency 122 Hz. Magnetization measurements between 2.4 K and 200 K were conducted using the same equipment, by integrating the voltage induced in the secondary coils when the sample was moved in the presence of an external magnetic field.

#### RESULTS AND DISCUSSION

The SEM micrographs of Fe-polymer shown in Figure 1 illustrates the morphology of the sample. In order to detect the possible presence of iron impurities, a chemical map of the iron element has been recorded by selective EDX. A chemical map of sulphur was also collected for completeness. An area of about  $100 \times 100 \mu\text{m}^2$ , selected at random, has been used for EDX analysis, each covering a volume of  $1 \times 1 \times 1 \mu\text{m}^3$ . Both iron and sulphur elements are found to be homogeneously distributed. A second chemical map performed in a different area shows the same result. Within the sensitivity of the method, the uniform distribution of the iron element in the sample is indicative of the absence of iron impurities, and consequently iron oxides, in agreement with previously reported EXAFS and XANES determinations [4]. A complete EDX analysis carried out on the same area indicates the presence of iron, sulphur, copper and gold, the last two elements coming from the way the sample was prepared for the EDX and SEM experiments.



Figure 1. SEM micrographs of the iron polymer

The frequency dependence of the magnetic susceptibility is shown in Figure 2 for the case of the iron polymer. It is observed an important dependence of both  $\chi'$  and  $\chi''$  on the measuring frequency in the sense that for increasing frequency  $\chi'$  decreases and  $\chi''$  shifts towards higher temperature. A similar behavior is observed in the case of the Co-polymer. However, Figure 3 shows that the maximum of the susceptibility curves occurs at a much lower temperature. It is worth remarking that the cobalt oxides are antiferromagnetic. This seems to indicate that the magnetic anomalies are intrinsic properties of the compound.

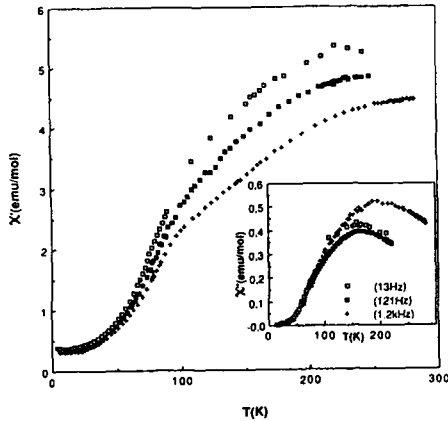


Figure 2. In-phase component of the a.c. susceptibility for the Fe-polymer at different exciting frequencies. The inset shows the out-of-phase component.

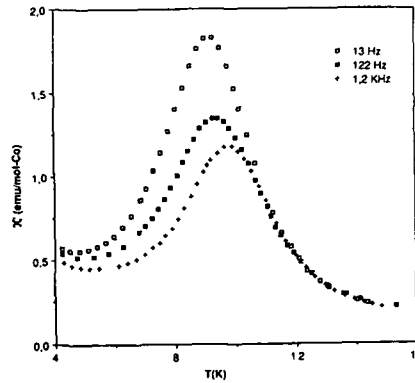


Figure 3. Temperature dependence of the in-phase component of the a.c. susceptibility for the Co-polymer at different exciting frequencies.

The field dependence of the magnetization at the constant temperature of 4.2 K is shown in Figure 4 for the case of the Fe-polymer. A similar behavior is observed in the case of the Co-polymer. The  $M(H)$  curve presents two clearly differentiated parts, namely, an irreversible (hysteretical) region for fields up to about 1500 Oe and a reversible one for higher fields. Before starting with the measurements the sample was demagnetized by field cycling. The hysteretical part of the curve was measured at a rate

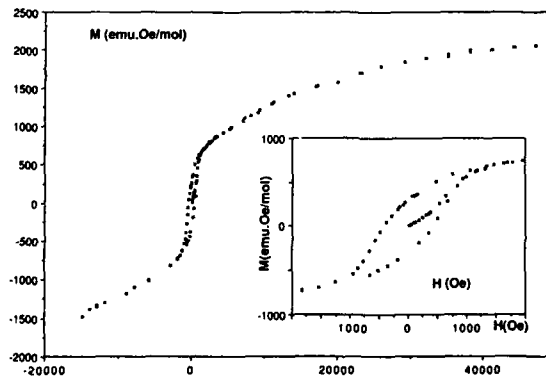


Figure 4. Field dependence of the magnetization of the iron polymer at 4.2 K.

of about 50 Oe/min, and the time needed to go from 0 to 50 kOe was 3 hours. At this temperature no appreciable time effects were found, as observed in other amorphous materials [6]. This fact could indicate a long term stability of the thermoremanent magnetization. From the high field region of the M(H) curve, a saturation magnetization of about 2300 emu.Oe/mol can be estimated. This is equivalent to 0.41  $\mu_B$  per repetitive unit of the polymer and agrees well with previously reported estimations [3]. Although this compound has a magnetic density two orders of magnitude smaller than most standard magnets, it exhibits a rather large remanence (300 emu.Oe/mol) and coercive field (420 Oe).

In conclusion, SEM and EDX determinations here reported indicate good homogeneity and, within experimental accuracy, do not show the presence of metallic oxides as impurities in these amorphous materials. Both a.c. susceptibility and magnetization measurements are consistent with the existence in the compounds of strong ferromagnetic interactions. The materials present relaxation effects consistent with superparamagnetic (or spin-glass) behavior [7], with a blocking (freezing) temperature close to room temperature for the Fe-polymer and at about 9 K for the Co one.

#### ACKNOWLEDGEMENTS

The research in Zaragoza has been supported by grant MAT88-0174, from the Comision Interministerial de Ciencia y Tecnología. The authors thank to the Laboratoire de Physique des Materiaux and to Dr. G. Legal and Dr. N. Auriault for their help with the SEM and EDX experiments. One of us (M.C.M.) wants also to acknowledge the receipt of a NATO postdoctoral fellowship.

#### REFERENCES

- † On leave from the Instituto de Ciencia de Materiales de Aragón, C.S.I.C. y Universidad de Zaragoza, 50009 Zaragoza, Spain.
1. F. Palacio, M.C. Morón, J. Garín, J. Reyes and J. Fontcuberta, *Mol. Cryst. and Liq. Cryst.*, (1989) in press.
  2. F. Lions and K.V. Martin, *J. Am. Chem. Soc.*, **79**, 2733 (1957).
  3. T. Sugano, M. Kinoshita, I. Shirotni and K. Ohno, *Solid St. Comm.*, **45**, 99 (1983).
  4. T. Sugano, M. Nomura, K. Agawa, P.L. Kieng, T. Ohta and M. Kinoshita, *Bull. Chem. Soc. Japan*, **59**, 2615 (1986).
  5. J.A. Rojo, *Ph.D. Thesis*, University of Zaragoza, Spain (1982) and C. Rillo, *Ph.D. Thesis*, University of Zaragoza, Spain (1986).
  6. J.M.D. Coey, T.R. McGuire and B. Tissier, *Phys. Rev. B*, **24**, 1261 (1981).
  7. F. Palacio, F.J. Lázaro and A.J. van Duyneveldt, *Mol. Cryst. and Liq. Cryst.*, (1989) in press.

---

PART II

---

**Organic Metals  
and Superconductors**

PREPARATION AND PROPERTIES OF ORGANIC SUPERCONDUCTOR  
 $\kappa$ -(BEDT-TTF)<sub>2</sub>[Cu(NCS)<sub>2</sub>] AND ITS RELATED MATERIALS

GUNZI SAITO

Department of Chemistry, Faculty of Science, Kyoto University,  
 Sakyo-ku, Kitashirakawa, Oiwake, Kyoto 606, Japan

ABSTRACT

$\kappa$ -(BEDT-TTF)<sub>2</sub>[Cu(NCS)<sub>2</sub>] has a two-dimensional (2D) layered structure. The compound is metallic with the room temperature conductivity of 10-40 S/cm within the 2D plane but showed a semiconductive-like anomaly between 270 and 90K. The superconducting transition was observed at T<sub>c</sub>=10.4K and T<sub>c</sub> increased by 10% on the sample of deuterated BEDT-TTF (T<sub>c</sub>=11.4K). The upper critical field, H<sub>c2</sub>, was more than 20 Tesla below 2K within the 2D plane which is more than the expected value from the simple BCS theory. The transport critical current density was estimated as 100 A/cm<sup>2</sup> (5.1K, 0 Tesla, I//b, H//c) which is an order of magnitude smaller than that obtained from the magnetization curve hysteresis. <sup>1</sup>H-NMR showed a big enhancement of the relaxation rate well below T<sub>c</sub>. The tunneling spectra showed anisotropic gap and the magnetic field penetration depth measurements strongly suggest that this system is a gapless superconductor. (BEDT-TTF)<sub>2</sub>[KHg(SCN)<sub>4</sub>] is an organic metal and showed both Shubnikov-de Haas effect and angle-dependent quantum oscillation indicating that this system has a warped 2D Fermi surface.

INTRODUCTION

Organic superconductors have attracted considerable interests and have been extensively studied chemically and physically. A particular attention has been focused on the problem of the superconducting mechanism for the past years, but still many things are to be investigated further to figure out the definite picture of the superconducting mechanism of this kind of material. Among the organic superconductors so far prepared,  $\kappa$ -(BEDT-TTF)<sub>2</sub>[Cu(NCS)<sub>2</sub>] (abbreviated to  $\kappa$ -Cu(NCS)<sub>2</sub> salt) has the highest T<sub>c</sub>, H<sub>c2</sub> and J<sub>c</sub>[1-3]. Furthermore, this compound exhibits many anomalous features in its structural, chemical and physical aspects, some of which cannot be explained by the simple BCS theory. Recent findings of the Shubnikov-de Haas (SdH) effect and angle-dependent quantum oscillation of magnetoresistance may lend a further dimension of interest to the BEDT-TTF conductors because the observation of the Fermi surface is a key to understand the metallic as well as superconducting state. We will overview our studies on the characteristic properties of  $\kappa$ -Cu(NCS)<sub>2</sub> salt and its related material, (BEDT-TTF)<sub>2</sub>[KHg(SCN)<sub>4</sub>] (abbreviated to KHg(SCN)<sub>4</sub> salt)[4].

PREPARATION

Distorted-hexagon-shaped crystals of  $\kappa$ -Cu(NCS)<sub>2</sub> salt with a typical dimension of 3x2x0.05 mm were prepared by an electrolysis of BEDT-TTF with using either CuSCN + KSCN + 18-crown-6 ether or (18-crown-6 ether)KCu(SCN)<sub>2</sub> as a supporting electrolyte



in 1,1,2-trichloroethane(TCE)[1,4]. The most developed crystal surface corresponds to the bc-plane, in which the longest crystal axis is the b-axis. The starting materials were purified as follows. KSCN was recrystallized from purified abs. EtOH twice. CuSCN was purified by treating with aq. KSCN solution three times. 18-Crown-6 ether was recrystallized from CH<sub>3</sub>CN once. Crown ether complex of KCu(SCN)<sub>2</sub> was recrystallized from acetone-water once and washed with acetone. BEDT-TTF-hg or -dg was recrystallized from CHCl<sub>3</sub>, THF, then monochlorobenzene.

By using Hg(SCN)<sub>2</sub> instead of CuSCN as a supporting electrolyte in the above electrolysis, black thick plates (1.5x0.3x0.2 mm) of KHg(SCN)<sub>4</sub> salt were grown from the mixed solvent of TCE and 10 vol% of abs. EtOH.

#### CRYSTAL STRUCTURES[5,6]

In  $\kappa$ -Cu(NCS)<sub>2</sub> salt two BEDT-TTF molecules form a dimer and the dimers are arranged almost perpendicularly to each other to form 2D layer in the bc-plane. This 2D layer is sandwiched by the insulating anion layers along the a-axis (Fig. 1). The anions form a zig-zag 1D flat polymer of -(SCN-Cu(NCS))<sub>n</sub>- along the b-axis and every polymer aligns in the same direction (Fig. 1b). So the crystal does not have an inversion center and has optical isomers (dextro- and levorotatory forms). Short atomic contacts between the terminal ethylene groups of BEDT-TTF and N and S of ligand SCN groups were observed at low temperatures. Lattice parameters are almost the same between H and D-salts (monoclinic, P2<sub>1</sub>, a=16.248(5), b=8.440(2), c=13.124(5)Å, β=110.30(3)°, V=1688.0(9)Å<sup>3</sup>, Z=2 for H salt at 298K). The unit cell parameters are very similar, especially the unit cell volume, to those of β-(BEDT-TTF)<sub>2</sub>I<sub>3</sub> (V=1687.6Å<sup>3</sup>), Tc of which is about 1/3 of that of  $\kappa$ -Cu(NCS)<sub>2</sub> salt.

In KHg(SCN)<sub>4</sub> salt 2D BEDT-TTF sheet is sandwiched by thick (6.8Å) polymer-like anion sheets, so a strong two-dimensionality due to weak interlayer coupling is expected (Fig. 2). Anion sheet has triple layered structure in which K<sup>+</sup> is linked to four SCN groups with N electrostatically to form a pyramid while Hg is coordinated to four SCN groups with S tetrahedrally (triclinic, P $\bar{1}$ , a=10.082(10), b=20.565(4), c=9.933(2)Å, α=103.70(2), β=90.91(4), γ=93.06(4)°, V=1997(2)Å<sup>3</sup>, Z=2 at 298K).

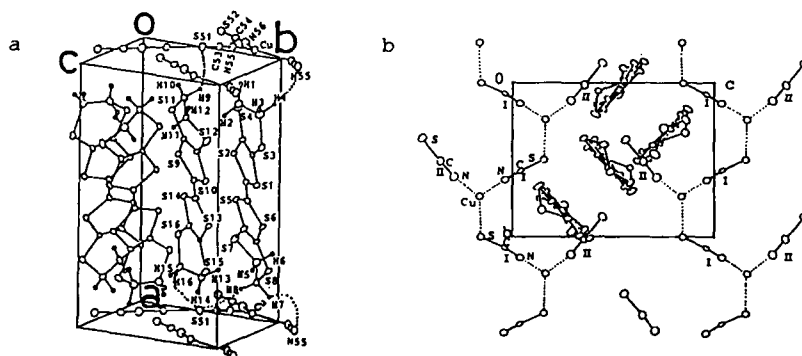


Fig.1 Crystal structure of  $\kappa$ -Cu(NCS)<sub>2</sub> H-salt at 104K (dextro-rotatory form). Dotted lines in Fig. 1a indicate short atomic contacts between BEDT-TTF and anion [5].

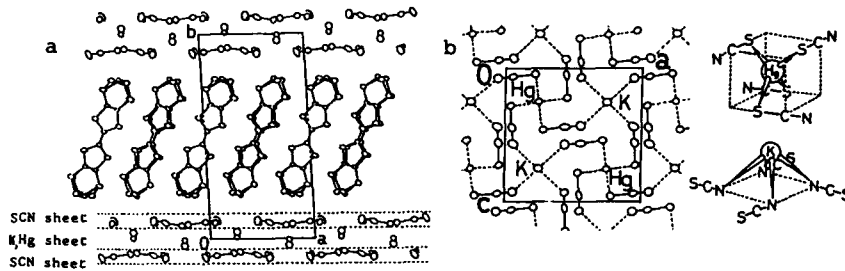


Fig.2 Crystal structure of  $\text{KHg}(\text{SCN})_4$  salt at RT, a) anion has triple-layered sheet, b) polymeric structure of anion and the schematic figures of its component clusters[6].

#### PHYSICAL PROPERTIES OF $\kappa\text{-Cu}(\text{NCS})_2$ SALT

##### $T_c$

The electrical resistivity was measured by a conventional four-probe method. The conductivity at RT was 10-40 S/cm along the b-axis and showed strong 2D anisotropy,  $\sigma_a : \sigma_b : \sigma_c = 1/600 : 1 : 1.2$ [1,2]. Though a semiconductive-like behavior was observed between 270K and 90K (Fig. 3), the constant Pauli paramagnetism in this region confirmed a metallic nature of this salt[3,7]. The enhancement of the resistivity at 90K varies from sample to sample with the ratio of  $\rho_{\text{max}}/\rho_{\text{RT}}$  in the range of 2-6. It has been also reported that most of the crystals from THF remain metallic with small temperature dependence above 100K[8]. At present the anomaly of the temperature dependence of the resistivity in this region is still unexplained.

The superconducting transition defined by the midpoint of the resistivity jump was  $T_c = 10.4\text{K}$  for the salt of BEDT-TTF-hg (H-salt). An application of pressure suppressed  $T_c$  rather rapidly with a rate  $\Delta T_c = -1.3$ [9] or  $-2\text{K/kbar}$ [10], which is larger than that of  $\beta\text{-(BEDT-TTF)}_2\text{I}_3$ .

Assuming the isotope mass ( $M$ ) of the salt as the molecular weight of donor, the  $T_c$  of the deuterated BEDT-TTF salt (D-salt) is estimated to be around 10.3K from the simple BCS equation;  $T_c \propto M^\alpha$ ,  $\alpha = -1/2$ . Although the molecular weight of BEDT-TTF-dg

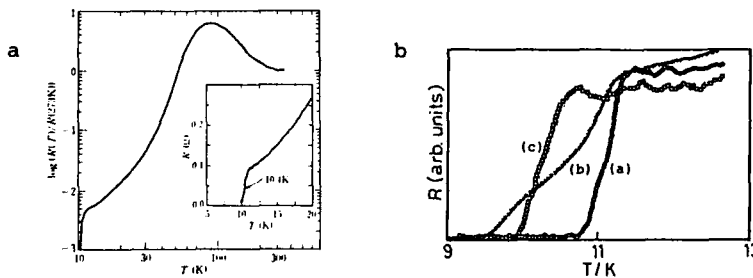


Fig.3 Temperature dependence of electrical resistivity of  $\kappa\text{-Cu}(\text{NCS})_2$  H (a) and D-salt (b). Fig. 3b demonstrates the  $T_c$  dependence on the purity of starting materials, a) most, b) moderately, and c) no purified[1,11].

(392) is heavier than that of BEDT-TTF-hg (384) and also there are almost no change in the lattice parameters between D and H-salts at RT and 104K, the  $T_c$  of the D-salt is about 10% higher than the above prediction[2]. The best purified crystal of D-salt has a  $T_c$  of 11.4K and  $T_c$  is quite sensitive to the purity of the starting materials[11]. Since the electrical contacts in the four-probe method might have the pressure effect on  $T_c$ , especially at low temperatures, we have compared the  $T_c$  of H and D-salts by the RF penetration depth measurements which are in the stress free conditions and observed that the  $T_c$  of D-salt is higher by about 0.6K than that of H-salt. The  $T_c$  difference is also confirmed by the  $H_{c2}$  measurements. One of the explanations of this inverse isotope effect, at the moment, is that the superconductivity of this salt is somewhat associated with the increase of the electron-phonon coupling in D-salt compared to the H-salt, as has been observed in the system of palladium-hydrogen[12], through the short atomic contacts between the terminal ethylenes of BEDT-TTF and ligand SCN. The  $T_c$  of the salt  $\kappa$ -Cu( $^{15}\text{NCS}$ ), in which  $^{14}\text{N}$  atoms are substituted by  $^{15}\text{N}$ , was found to be almost identical to that of  $\kappa$ -Cu(NCS) $_2$  salt within an experimental error. The isotope effect on  $T_c$  by  $^{13}\text{C}$  is underway. The structural analyses of H and D-salts in the superconducting phase are necessary toward understanding the isotope effect on  $T_c$ .

#### $H_{c2}$

The temperature dependence of  $H_{c2}$ , which is defined at the midpoint of the resistance recovery by the magnetic field, is shown in Fig. 4 where the measuring current is along the  $a^*$ -axis [2,13].  $H_{c2}$  values for  $H//b$  and  $c$ -axes are almost identical to each other between  $T_c$  and around 9K, below which  $H_{c2}//c$  exceed those for  $H//b$  slightly. It is noticeable that  $H_{c2}//a^*$  is considerably smaller than  $H_{c2}//bc$ . The anisotropy in the GL coherence length was estimated from  $H_{c2}$  near  $T_c$  as  $\xi_{a^*}(0): \xi_b(0): \xi_c(0) = 182\text{\AA}: 182\text{\AA}: 9.6\text{\AA} = 19:19:1$ . The critical field anisotropy is nearly consistent with the result of the conductivity anisotropy. The estimated  $\xi_{a^*}(0)$  is smaller than the lattice spacing along the  $a^*$ -axis, the situation of which is very similar to the 2D high  $T_c$  oxide superconductors;  $\xi_c(0) = 3.8\text{--}6.3\text{\AA}$  ( $\sim 11.6\text{\AA}$ ) and  $\xi_{ab}(0) = 23\text{--}35\text{\AA}$  were estimated in YBCO[17].

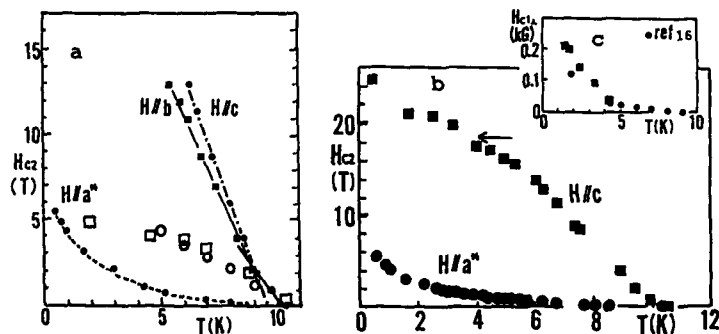


Fig. 4 Temperature dependence of  $H_c$  of  $\kappa$ -Cu(NCS) $_2$  H-salt, a)  $H_{c2}$  up to 13.5 T [2,13,14], b)  $H_{c2}$  up to 24 T where the Pauli limited value is indicated by an arrow [15] and c)  $H_{c1}$  [15,16].

It is anomalous that the temperature dependence of  $H_{c2}/c$  showed upturned behavior at low temperatures. The same non-saturating behaviors were observed in  $H_{c2}/a^*$  and  $H_{c1}$  values for  $H//a^*$  [15,16] (Fig. 4). It is also puzzling that  $H_{c2}/c$  below 4K is almost the same or larger than the Pauli limited value;  $H_{c2}(0) = 1.84T_c = 19.1$  T. These features are completely different from those of other organic superconductors so far known.

It has been pointed out in the study of oxide superconductor, YBCO, that the temperature dependence of  $H_{c2}$  determined by ac susceptibility or the onset of zero-resistance in transport measurements shows an upward curvature and  $H_{c2}$  values thus determined are not plausible, maybe due to a flux-flow effect which causes a broadening in the resistance drop with field [18]. As a more plausible way of determining the true thermodynamic  $H_{c2}$ , dc reversible magnetization measurements or the onset of resistivity drop in transport measurements have been recommended within the framework of the flux creep model.

The normal resistance recovery with magnetic field (Fig. 5) clearly shows the characteristic broadening in the resistance drop which is indicative of the existence of flux flow [14]. The  $H_{c2}$  values estimated from the onset of the resistivity drop (indicated by arrows in Fig. 5) are plotted in Fig. 4a by open squares. In the same figure,  $H_{c2}$  values estimated by the zero magnetization point in the measurements of magnetization curve by SQUID [14] (Fig. 6) are also plotted by open circles, where  $H_{c2}$  may have an experimental uncertainty indicated by arrows in Fig. 6. These data show higher  $H_{c2}$  values than the previous ones and seem to increase linearly down to 5K and then saturate at low temperatures. More precise work is underway to elucidate the flux-flow effect, and if the flux-flow effect is dominant in this 2D compound, the previously obtained  $H_{c2}$  values (underestimated) and coherence lengths (overestimated) should be modified.

### Jc

$J_c$  value was estimated from the hysteresis loop of the magnetization curve with  $H//a^*$  for aligned single crystals as  $1330$  A/cm<sup>2</sup> (50 Oe, 5K) [14], which is consistent with the value obtained for randomly oriented crystals;  $1060$  A/cm<sup>2</sup> (50 Oe, 4.9K) [3]. The critical current density was also determined by the transport measurements on a single crystal where an applied

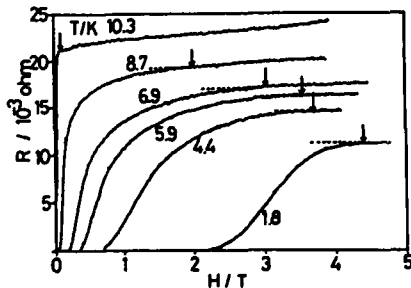


Fig. 5 Resistance recovery in magnetic fields ( $H//a^*$ ) for  $\kappa$ -Cu(NCS)<sub>2</sub> D-salt [14].

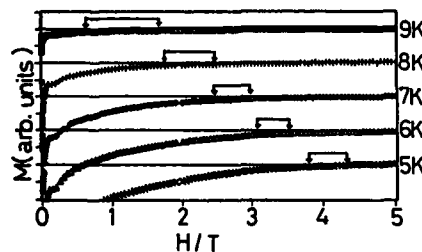


Fig. 6 Magnetization curve by SQUID for  $\kappa$ -Cu(NCS)<sub>2</sub> D-salt (13.0mg of aligned single crystals,  $H//a^*$ ) [14].

current and magnetic field are along the b and c-axes, respectively[9].  $J_c$  value thus obtained was  $100 \text{ A/cm}^2$  at 5.1K and 0T. This value is an order of magnitude smaller than those obtained by the magnetization curve hysteresis, indicating possible flux-flow effect in the magnetization curve measurements.

#### SdH Effect, Magnetic Susceptibility, ESR & NMR Measurements, etc

SdH oscillations were observed above about 8 T in the magnetoresistance curve[19] (Fig. 7). The period of the oscillations  $\Delta(1/H)=0.0015/\text{T}$  at ambient pressure gives the cross-section of the Fermi surface as  $S=0.0637\text{\AA}^{-2}$  from  $S=2\pi e/\Delta(1/H)\hbar c$ . This area corresponds to 18% of the first Brillouin zone and gives the Fermi wave number of  $k_F=0.14\text{\AA}^{-1}$  assuming an isotropic circular Fermi surface. The Fermi surface of this salt calculated by the tight-binding method based on the crystal structure at RT (Fig. 8) indicates the presence of both closed elliptical (not circular) one and warped open Fermi surface. The area of the elliptical one (18%) is in excellent agreement with that deduced from the SdH oscillations. The temperature dependence of the oscillation amplitude gives the cyclotron mass,  $m^*=3.5m_e$ . The field dependence of the oscillation amplitude gives the Dingle temperature,  $T_D=1\text{K}$ , and the relaxation rate,  $\tau=1.2\text{ps}$  from  $T_D=\hbar/2\pi k_B\tau$ . There are little differences in the SdH period between H and D-salt.

The amplitude of SdH oscillations are enhanced by the pressures and leads to the cyclotron mass of  $m^*=2.4m_e$  at 8kbar [9]. Furthermore, the SdH oscillations at high pressures indicates the coexistence of two additional small pockets, which correspond to 1 and 2% of the first Brillouin zone[20]. The origin of the additional oscillations is under investigation.

The Drude-Lorentz analysis of the polarized reflectance spectra gives the following effective mass for //b and //c, respectively;  $m^*/m_e=5.5$  and  $4.1$  for H salt[8],  $4.3$  and  $3.2$  for H salt and  $4.6$  and  $3.3$  for D salt[21]. The effective mass obtained from the optical data is not so different from that obtained from the SdH oscillation. It is noteworthy that the optical data also support the 2D nature of this salt as indicated by the ratio of the effective mass;  $m^*_b/m^*_c=1.3$  and  $1.4$  for H and D salt, respectively. A smaller effective mass along the c-axis than that along the b-axis is consistent with the conductivity anisotropy.

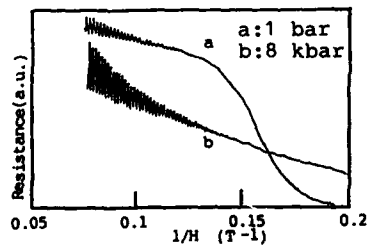


Fig. 7 Schubnikov-de Haas oscillation of  $\kappa\text{-Cu(NCS)}_2$  D-salt(H, I//a\*)[9].

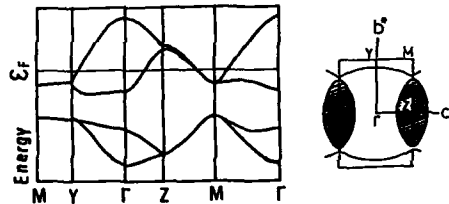


Fig. 8 Fermi surface obtained by tight-binding method[19]. Shaded regions indicate hole-like parts.

An approximately constant paramagnetic susceptibility was observed on the randomly oriented single crystals by dc magnetic susceptibility measurements[1](Fig. 9a). At 30 kOe the constant Pauli paramagnetism of  $\chi_p=4.6 \times 10^{-4}$  emu/mol at RT started to decrease gradually at around 90K to about  $4.1-4.2 \times 10^{-4}$  emu/mol below 50K where diamagnetic contribution is corrected using Pascal's law. The susceptibility decreased rapidly below 10K due to the superconducting transition. From the  $\chi_p$  at RT the density of states per formula unit for a single spin is calculated as  $N(E_F)=7.1 \text{ eV}^{-1}$  by using a relation,  $\chi_p=2\mu_B N_A N(E_F)[1-(1/3)(m/m^*)^2]$ , where the second term of the Landau diamagnetism is neglected since  $(1/3)(m/m^*)^2$  is small compared to 1. A comparative number of  $N(E_F)=7.5 \text{ eV}^{-1}$  was deduced from the optical data and a relation,  $N(E_F)=(m^*_b m^*_c)^{1/2}/(\pi a \hbar^2)$ , where  $a$  is the lattice spacing. The Fermi energy from the top of the band is also consistent between the optically obtained,  $E_F=\pi a \hbar^2/(m^*_b m^*_c)^{1/2}=0.13 \text{ eV}$  and the band calculation, 0.16 eV.

The randomly oriented crystals cooled at zero-field gave about 83% of the perfect diamagnetism at 2.0K and 50 Oe in the dc diamagnetic measurements[3]. While the same sample exhibited only 10 and 50% of the perfect diamagnetism when it is cooled at 30 and 100 Oe, respectively, indicating the flux penetration. The ac diamagnetic measurements on the randomly oriented crystals upon zero-field cooling showed almost 100% of the perfect diamagnetism below 7K at earth magnetic field[22] (Fig.9b).

The valence of Cu was assigned to be +1 since no signal assignable to  $\text{Cu}^{+2}$  was observed in ESCA at RT and ESR measurements down to 4K[7]. Due to the broadening of the ESR main signal and to the appearance of a sharp additional signal (line width  $\Delta H=10-20\text{G}$ ,  $g=2.0075$ ) an accurate estimation of  $g$ -values and  $\Delta H$  was not possible below 20K on single crystal. The ESR data were obtained by using a X-band spectrometer. The static field was perpendicular to the  $b$ -axis. The maximum (2.0095) and minimum (2.0057)  $g$ -values were observed when the field was nearly parallel to the molecular long axis and tilted to the short molecular axis by  $50^\circ$ , respectively. The  $g$ -values are independent of temperature down to 20K. The  $\Delta H$  was 59-67G at RT and increased at low temperatures. Later, Schweitzer et al. reported that their  $\kappa\text{-Cu(NCS)}_2$  salt showed much sharper line width of about 25 G at RT and decreased monotonically with temperature[23]. But we could not obtain a single crystal yet which reproduces their

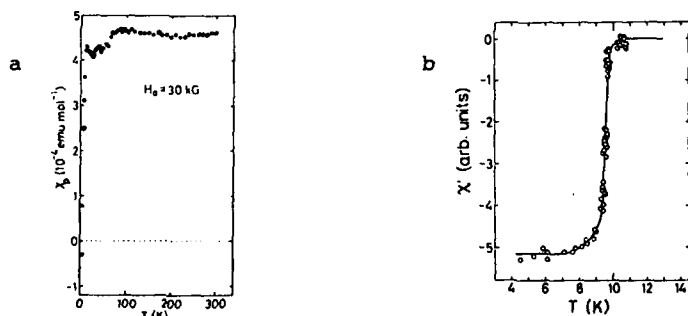


Fig. 9 Temperature dependence of dc (a,  $H=30 \text{ koe}$ ) and ac (b,  $H=\text{earth magnetic field}$ ) susceptibilities of randomly oriented single crystals of  $\kappa\text{-Cu(NCS)}_2$  H-salt[1,22].

results. Our temperature dependence of  $\Delta H$  (Fig. 10) is quite puzzling. Since the electrical resistivity increases from 270K to 90K (Fig. 3), the increase of  $\Delta H$  in this region is reasonable in terms of the increase of scattering rate of conduction electrons. While the pronounced increase below 90K, however, cannot be interpreted in terms of scattering rate since  $\Delta H$  does not follow the temperature dependence of the resistivity. So the  $\Delta H$  values are in contrast to the prediction of the Elliot formula for the spin relaxation in 2D metals,  $\Delta H \propto (\Delta g)^2 \tau_{\perp}^{-1}$ , where  $\Delta g = g - 2.0023$  and  $\tau_{\perp}$  is the interchain tunneling time.

The ESR intensity was measured with randomly oriented crystals to obtain enough intensity down to 60K where the ESR signal diminished maybe due to skin effect. The spin susceptibility of  $3.2 \times 10^{-4}$  emu/mol at RT is close to that obtained by dc susceptibility measurements. The temperature dependence of the intensity indicates the metallic nature of this salt in the measured temperature range, but again a slight decrease of intensity was observed below 90K in good accord with the dc susceptibility.

The NMR measurements are one of the most powerful methods to study the static and dynamical microscopic properties of the superconducting state. A Korringa relation,  $T_1 T = \text{constant}$ , which is characteristic of metallic nature, was observed between 77K and 10K on randomly oriented crystals [24]. The relation is plotted as a broken line in Fig. 11. From the relation between the density of state and  $T_1 T$ ,  $N(E_F) \propto \sqrt{1/T_1 T}$ ,  $N(E_F)$  of this salt is expected to be 1.28 times than that of the  $\beta$ -I<sub>3</sub> salt. An anomaly was observed in the superconducting phase. A big enhancement of  $1/T_1$  was noticed with a peak at considerably lower temperature than  $T_c$  (Fig. 11). In the measured magnetic field  $T_c$  should be around 7-8K. But the peak position which depends on the applied field was 3-4K and the peak height is about 30 times than that of the normal state at 3.28 kOe. In a typical BCS superconductor (spin singlet with finite gap),  $1/T_1$  starts to increase just below  $T_c$ , reaching a maximum at around  $T = 0.9 T_c$  with the peak height of about twice of that of the normal state, and then decreases exponentially due to finite gap opening. In the anisotropic superconductor with a gapless nature, the enhancement below  $T_c$  does not appear and the low temperature part follows a power law [25]. The latter behavior has been observed in the quasi-1D organic superconductor  $(TMTSF)_2 ClO_4$  [26]. For the anisotropic superconductors of quasi-2D a theory predicts eight types of possible superconductivity, three of which are spin singlet and the rest five are triplet [27]. However, the observed features in Fig. 11 are far from the predictions of the theory and are unexpected for usual superconductors to date.

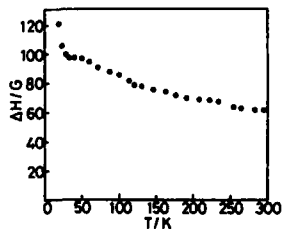


Fig. 10 ESR line width of  $\kappa$ -Cu(NCS)<sub>2</sub> H-salt [7].

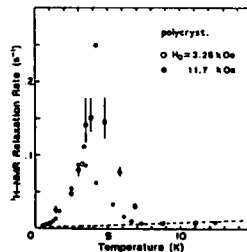


Fig. 11 <sup>1</sup>H-NMR relaxation rate  $1/T_1$  of  $\kappa$ -Cu(NCS)<sub>2</sub> H-salt [24].

The tunneling spectroscopic measurements are the direct method to obtain the superconducting gap though the experiment is quite difficult because the results are depend on the flatness of the crystal surface, crystal quality, the kinds of junction and contact between counter electrode/insulator and organics. With a junction of Au/Al<sub>2</sub>O<sub>3</sub>/κ-Cu(NCS)<sub>2</sub> salt of a face-to-face contact the tunneling spectroscopic measurements were performed[28]. No reliable spectra were obtained above 4.2K. Furthermore the obtained spectra below T<sub>c</sub> do not coincide with each other. One of the gap data gave 4.5 for the  $2\Delta_0/k_B T_c$  ( $2\Delta_0 = 4\text{meV}$ ) which is a little larger than that of the BCS ratio, 3.52, where  $2\Delta_0$  is the superconducting energy gap. The other samples showed much smaller gap structure, less than 1meV. A similar measurement for a D salt has revealed that there seem to be three different superconducting gaps, 0.8, 2.1 and 4.2meV in the tunneling spectrum. Therefore at the moment an anisotropic superconductivity is postulated for this superconductor from the tunneling spectroscopic measurements.

In order to investigate the superconducting gap the magnetic field penetration depth,  $\lambda$ , was deduced by the complex susceptibility measurements for single crystals[29]. The temperature dependence of  $\lambda$  with the ac field either parallel or perpendicular to the bc-plane showed  $[\lambda(0)/\lambda(T)]^2 = 1 - 0.8(T/T_c)^2$  or  $\lambda(T)/\lambda(0) = 1 + 0.4(T/T_c)^2$  (Fig. 12) at low temperatures. This T<sup>2</sup> dependence is completely different from the exponential temperature dependence predicted by the simple BCS theory (some theoretical and empirical predictions for conventional BCS type superconductors are compared in Fig. 12). This result strongly indicates that κ-Cu(NCS)<sub>2</sub> salt is a gapless superconductor.

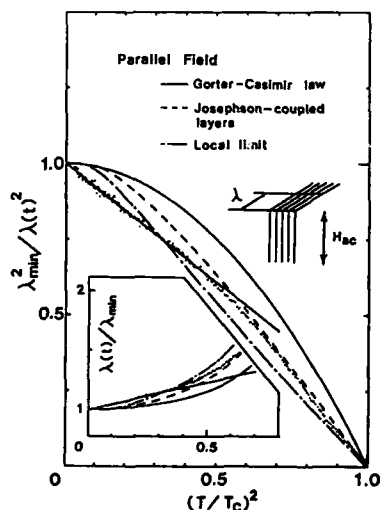


Fig. 12 Temperature dependence of penetration depth of κ-Cu(NCS)<sub>2</sub> H-salt,  $\lambda_{\min}$  is the penetration depth at the lowest temperature studied(1.5K)[29].

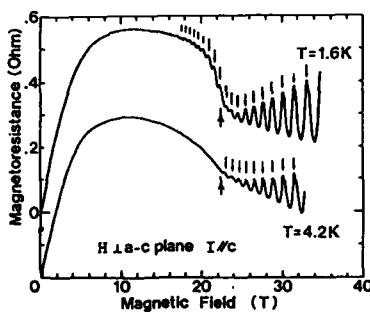


Fig. 13 Transverse magnetoresistance of KHg(SCN)<sub>4</sub> salt, the kink structure and the oscillation peaks are indicated by arrows[30].



MAGNETORESISTANCE OF  $\text{KHg}(\text{SCN})_4$  SALT[30]

The conductivity anisotropy,  $\sigma_c/\sigma_b$  is more than 2000 at 4.2K, indicates that 2D nature of this salt is much larger than  $\kappa\text{-Cu}(\text{NCS})_2$  salt. The transverse magnetoresistance (Fig. 13) increased with fields and showed saturation at around 10 T followed by a negative slope. A sharp kink was observed at around 22.5T and SdH oscillations were superposed. The amplitude of the oscillations were enhanced above the kink. The oscillation period,  $0.0015/\text{T}$  corresponds to 16% of the first Brillouin zone which is comparable to that of the closed Fermi surface in Fig. 14. The angle dependent magnetoresistance is depicted in Fig. 15 where the magnetic fields are tilted from the  $b^*$  direction in the  $a^*b^*$ -plane. The positions of the angle dependent oscillation dips are almost periodic against  $\tan \theta$  where  $\theta$  represents the angles between field and the  $b^*$ -axis. The angle dependent oscillations indicate the existence of the weakly warped cylindrical Fermi surface according to the Yamaji's model[31]. From the observed periods of  $\Delta(\tan \theta) \approx 1.5$  (magnetic fields are in the  $a^*b^*$ -plane) and  $\Delta(\tan \theta) \approx 3$  (magnetic fields are in the  $b^*c^*$ -plane) gave the Fermi wave number of  $k_{\text{Fa}} \approx 0.1 \text{ \AA}^{-1}$  and  $k_{\text{Fc}} \approx 0.05 \text{ \AA}^{-1}$ , respectively, indicating a strong anisotropy in the cross-section of the cylindrical Fermi surface in the  $ac$ -plane ( $\sim 2:1$ ).

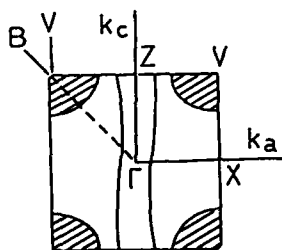


Fig. 14 Fermi surface of  $\text{KHg}(\text{SCN})_4$  salt calculated by tight-binding method by T.Mori.

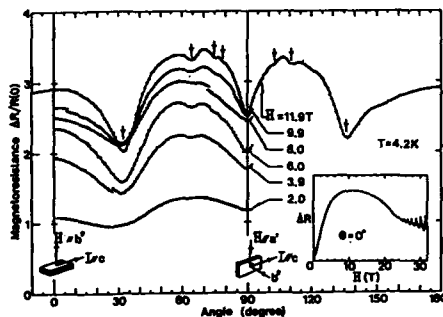


Fig. 15 Angle-dependent quantum oscillation of magnetoresistance of  $\text{KHg}(\text{SCN})_4$  salt[30], oscillation dips are indicated by arrows.

## ACKNOWLEDGEMENT

The author wishes to thank the coworkers for exciting collaborations; H.Mori (Urayama), H.Yamochi, M.Oshima, K.Oshima, N.Miura, K.Nozawa, T.Sugano, M.Kinoshita, T.Mori, H.Inokuchi, T.Inabe, Y.Maruyama, K.Kanoda, T.Takahashi, T.Osada and S.Kagoshima. This work was partly supported by the Grant-in-Aid for Scientific Research from the Ministry of Education, Science and Culture, Japan.

## REFERENCES

1. H.Urayama, H.Yamochi, G.Saito, K.Noizawa, T.Sugano, M.Kinoshita, S.Sato, K.Oshima, A.Kawamoto, and J.Tanaka, *Chem. Lett.*, **1988**, 55.
2. K.Oshima, H.Urayama, H.Yamochi, and G.Saito, *J. Phys. Soc. Jpn.*, **57**, 730(1988).
3. K.Noizawa, T.Sugano, H.Urayama, H.Yamochi, G.Saito, and K.Kinoshita, *Chem. Lett.*, **1988**, 617.
4. For reviews, G.Saito, H.Urayama, H.Yamochi, and K.Oshima, *Synth. Met.*, **27**, A331(1988), in Advances in Superconductivity, edited by K.Kitazawa and T.Ishiguro (Springer-Verlag, 1989), p107, H.Urayama, H.Yamochi, G.Saito, S.Sato, T.Sugano, M.Kinoshita, A.Kawamoto, J.Tanaka, T.Inabe, T.Mori, Y.Maruyama, H.Inokuchi, and K.Oshima, *Syn. Met.*, **27**, A393(1988); G.Saito and H.Urayama, in The Science of Superconductivity and New Materials, edited by S.Nakajima (World Scientific Pub., 1989), p60; G.Saito, in Lower-Dimensional Systems and Molecular Devices, edited by R.M.Metzger (Plenum Press, NATO-ASI Proceedings, to be published); Proceedings of the International Conference on M<sup>2</sup>S-HTSC, Stanford, 1989, to be published; Proceedings of Symposium New Developments in the Chemistry and Properties of Low-Dimensional and Conducting Solids, edited by J.M. Williams (*Mol. Cryst. Liq. Cryst.* to be published), see also papers in Proceedings of ICSM '88, *Syn. Met.*, **27** (1988) and Proceedings of ISSP-ISOS, The Physics and Chemistry of Organic Superconductors, edited by G.Saito and S.Kagoshima (Springer-Verlag, to be published).
5. H.Urayama, H.Yamochi, G.Saito, S.Sato, A.Kawamoto, J.Tanaka, T.Mori, Y.Maruyama, and H.Inokuchi, *Chem. Lett.*, **1988**, 463.
6. M.Oshima, H.Mori, G.Saito, and K.Oshima, *ibid.*, **1988**, 1159.
7. H.Urayama, H.Yamochi, G.Saito, T.Sugano, M.Kinoshita, T.Inabe, T.Mori, Y.Maruyama, and H.Inokuchi, *ibid.*, **1988**, 1057.
8. A.Ugawa, G.Ojima, K.Yakushi and H.Kuroda, *Phys. Rev. B* **38**, 5122(1988).
9. K.Oshima, T.Mori, H.Inokuchi, H.Urayama, H.Yamochi, and G.Saito, *Syn. Met.*, **27**, A165(1988).
10. K.Murata, M.Tokumoto, H.Anzai, Y.Honda, N.Kinoshita, T.Ishiguro, N.Toyota, T.Sasaki, and Y.Muto, *ibid.*, A263(1988).
11. H.Mori, S.Tanaka, H.Yamochi, G.Saito, and K.Oshima, in The Physics and Chemistry of Organic Superconductors, edited by G.Saito and S.Kagoshima (Springer-Verlag, to be published).
12. J.E.Schirber and C.J.M.Northrup, Jr., *Phys. Rev. B* **10**, 3818(1974).
13. K.Oshima, H.Urayama, H.Yamochi, and G.Saito, *Physica C* **154**, 1148(1988).
14. H.Mori, K.Nakao, I.Hirabayashi, S.Tanaka, K.Oshima, and G.Saito, in Proceedings of 2nd International Symposium on Superconductivity (Springer-Verlag, to be published).
15. K.Oshima, R.C.Yu, P.M.Chaikin, H.Urayama, H.Yamochi, and G.Saito, in Ref. 11, to be published.
16. M.Tokumoto, H.Anzai, K.Takahashi, K.Murata, N.Kinoshita, and T.Ishiguro, *Syn. Met.*, **27**, A305(1988).
17. Y.Iye, in Studies of High Temperature Superconductors, edited by A.V.Narlikar (NOVA Science Pub. Inc., 1989), p263.
18. A.P.Malozemoff, T.K.Worthington, Y.Yeshurun, and F.Holtzberg, *Phys. Rev. B* **38**, 7203(1988).
19. K.Oshima, T.Mori, H.Urayama, H.Yamochi, and G.Saito, *ibid.*

- 37, 938(1988).
20. K.Oshima (private communication).
  21. T.Sugano, H.Hayashi, M.Kinoshita, and K.Nishikida, Phys. Rev. B 39, 11387(1989).
  22. T.Sugano, K.Terui, S.Mino, K.Nozawa, H.Urayama, H.Yamochi, G.Saito, and M.Kinoshita, Chem. Lett., 1988, 1171.
  23. S.Gartner, E.Gogu, I.Heinen, H.J.Keller, T.Klutz, and D.Schweitzer, Solid State Commun., 65, 131(1988).
  24. T.Takahashi, T.Tokiwa, K.Kanoda, H.Urayama, H.Yamochi, and G.Saito, Physica c, 153-155, 487(1988); Syn. Met., 27, A319(1988); T.Takahashi, K.Kanoda, K.Sano, M.Watabe, H.Mori, and G.Saito, in Ref. 11, to be published.
  25. Y.Hasegawa and H.Fukuyama, J. Phys. Soc. Jpn., 56, 877(1987).
  26. M.Takigawa, H.Yasuoka, and G.Saito, *ibid*, 56, 873(1987).
  27. Y.Hasegawa and H.Fukuyama, *ibid*, 56, 2619(1987).
  28. Y.Maruyama, T.Inabe, H.Urayama, H.Yamochi, and G.Saito, Solid State Commun., 67, 35(1988); Y.Maruyama, T.Inabe, H.Mori, H.Yamochi, and G.Saito, in Ref. 11, to be published.
  29. K.Kanoda, T.Takahashi, and G.Saito, in Proceedings of the International Conference on M<sup>2</sup>S-HTSC, Stanford, 1989, to be published; K.Kanoda, K.Akiba, T.Takahashi, and G.Saito, in Ref. 11, to be published.
  30. T.Osada, R.Yagi, S.Kagoshima, N.Miura, M.Oshima, and G.Saito, in Ref. 11, to be published.

## SUPERCONDUCTING AND NORMAL STATE PROPERTIES OF ORGANIC METALS $\beta$ -(BEDT-TTF)<sub>2</sub>X

M. TOKUMOTO, N. KINOSHITA, K. MURATA, H. BANDO AND H. ANZAI  
Electrotechnical Laboratory, Tsukuba, Ibaraki 305, Japan

### ABSTRACT

Recent progress on the superconducting and normal state properties characteristic to the organic metals  $\beta$ -(BEDT-TTF)<sub>2</sub>X are presented. Out of a systematic study on the  $\beta$ -(BEDT-TTF)<sub>2</sub>X salts, including  $\beta$ -(BEDT-TTF)<sub>2</sub> trihalide mixed crystals, with the superconducting transition temperature ( $T_c$ ) varying from 8 K to below 1 K, empirical rules for various factors governing the  $T_c$  in this class of organic metals have been extracted. In addition to the low- and high- $T_c$  states, with  $T_c=1$  K and 8 K, respectively, a new superconducting state with  $T_c=2$  K was found in  $\beta$ -(BEDT-TTF)<sub>2</sub>I<sub>3</sub>. A particular attention is paid for the correlation between  $T_c$  and resistivity. In addition, a correlation between  $T_c$  and the anisotropy of coherence length is also considered.

### INTRODUCTION

Superconductivity of BEDT-TTF based organic metals has been found to be quite sensitive to defects, disorders and impurities. In quasi-one dimensional metals, such as (TMTSF)<sub>2</sub>X, the conduction path of electrons along the stacking donors can be seriously disturbed by the presence of defects or disorder. However, in two-dimensional system like BEDT-TTF salts, electronic conduction path forms a two-dimensional network so that the presence of point defects cannot cause a serious effect on the electrical conduction. Therefore it is not obvious why the superconductivity of BEDT-TTF based organic metals are so sensitive to the presence of non-magnetic impurities and defects. Two outstanding characteristics of the BEDT-TTF based organic superconductors, i.e. superconductivity at ambient-pressure and relatively high- $T_c$ , are advantageous features for an extensive and quantitative study of superconducting properties in these organic metals.

In this paper, we present some typical examples which exhibit the effect of defects, disorders and impurities on the superconducting properties in organic metals  $\beta$ -(BEDT-TTF)<sub>2</sub>X. A particular attention is paid to the correlation between  $T_c$  and residual resistivity, which are superconducting and normal state properties, respectively. A new 2 K state in  $\beta$ -(BEDT-TTF)<sub>2</sub>I<sub>3</sub> is examined in this context. In addition, a semi-quantitative relation between  $T_c$  and the anisotropy of coherence length is derived.

CORRELATION BETWEEN  $T_c$  AND RESISTIVITY

Here we show some typical examples where superconducting transition temperature ( $T_c$ ) and resistivity seems to be closely related with each other in  $\beta$ -(BEDT-TTF) $_2$ X, which forms an isostructural family of organic metals. An important structural feature of  $\beta$ -(BEDT-TTF) $_2$ I $_3$  is an incommensurate lattice modulation[1], which appears below 175K at ambient pressure. The presence of this incommensurate superstructure is considered to suppress its  $T_c$  from 8.1 K to 1.1-1.5 K. Another important feature in  $\beta$ -(BEDT-TTF) $_2$ I $_3$  is the presence of disordered ethylene group as designated as A-type vs. B-type[2] (or staggered vs. eclipsed[3]) at one end of the molecule and the ordered group at the opposite end. The latter additional structural disorder can possibly be eliminated, as was confirmed in  $\beta$ -(BEDT-TTF) $_2$ I $_{2.5}$ Br and  $\beta$ -(BEDT-TTF) $_2$ I $_2$ Br[4], where the former superstructure is also absent.

 $\beta$ -(BEDT-TTF) $_2$  Trihalides Mixed crystals

The best example which demonstrates a high correlation between  $T_c$  and resistivity is seen in  $\beta$ -(BEDT-TTF) $_2$  trihalide mixed crystal system. The substitution of anions in  $\beta$ -(BEDT-TTF) $_2$ I $_3$  was found to produce a series of isostructural crystals of  $\beta$ -(BEDT-TTF) $_2$ X. Complete substitution of I $_3$  with I $_{2.5}$ Br[5] and AuI $_2$ [6] was found to suppress the incommensurate superstructure and realized the high- $T_c$  state in  $\beta$ -(BEDT-TTF) $_2$ X. However, substitution of I $_3$  with asymmetric anion I $_2$ Br[7] did not give a superconductivity[8] although the "lattice pressure" model[8] predicted higher  $T_c$  and both the incommensurate superstructure and the disorder of the ethylene group were missing[4]. Partial substitution of anions corresponds to alloying in metals. It was found that we can prepare  $\beta$ -(BEDT-TTF) $_2$  trihalide mixed crystals, namely  $\beta$ -(BEDT-TTF) $_2$ (I $_3$ ) $_{1-x}$ (I $_{2.5}$ Br) $_x$ ,  $\beta$ -(BEDT-TTF) $_2$ (I $_{2.5}$ Br) $_{1-x}$ (I $_2$ Br) $_x$  and  $\beta$ -(BEDT-TTF) $_2$ (I $_2$ Br) $_{1-x}$ (I $_3$ ) $_x$ , for a wide composition range[9].

Figure 1 shows the temperature dependence of electrical resistance and superconducting transition for pure  $\beta$ -(BEDT-TTF) $_2$ X (X=I $_3$ , I $_2$ Br, I $_{2.5}$ Br) and their 1:1 mixed crystals and also for mixed crystals  $\beta$ -(BEDT-TTF) $_2$ (I $_3$ ) $_{1-x}$ (I $_{2.5}$ Br) $_x$ [10]. Temperature dependence in these figures indicates that the mixed crystals of  $\beta$ -(BEDT-TTF) $_2$ -trihalides constitute a clean alloy system, where the scattering of conduction electrons are predominantly due to phonons at temperatures above around 100 K even in high concentration (1:1) mixed crystals. The effect of alloying on the resistivity appears as a difference in the residual resistance ratio or residual resistivity at very low temperatures.

In order to study the correlation between the superconductivity and low temperature resistivity, we evaluated the residual conductivity ( $\sigma_R$ ) of each samples from the relation

$$\sigma_R = RRR \times \sigma_0(T) \quad (1)$$

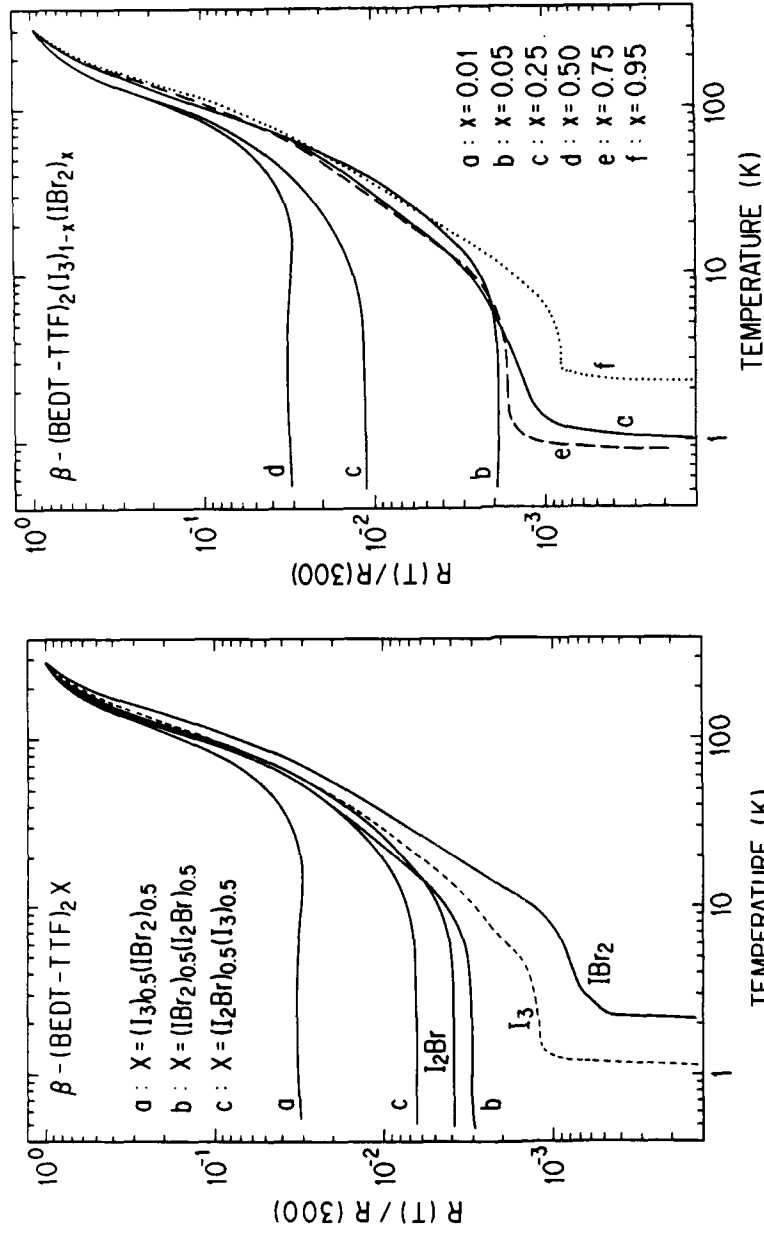


Fig. 1. Temperature dependence of electrical resistance for  $\beta$ -(BEDT-TTF)<sub>2</sub>X (X=I<sub>3</sub>, I<sub>2</sub>Br, IBr<sub>2</sub>) and their 1:1 mixed crystals  $\beta$ -(BEDT-TTF)<sub>2</sub>(I<sub>3</sub>)<sub>1-x</sub>(IBr<sub>2</sub>)<sub>x</sub> (right)[10].

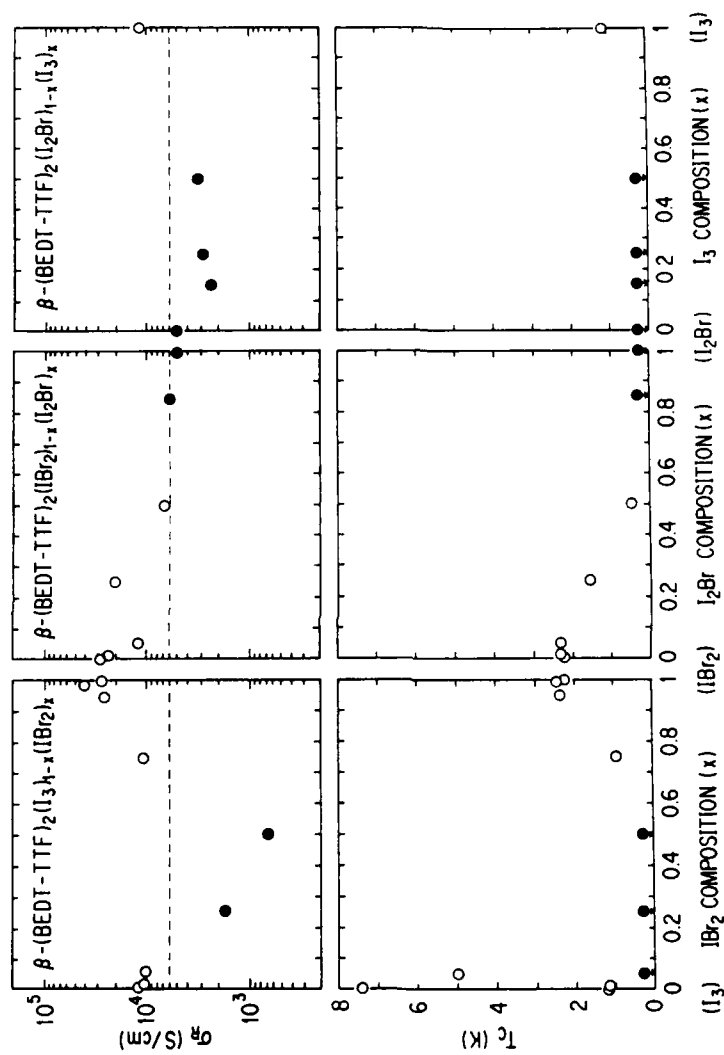


Fig. 2. Residual conductivity ( $\sigma_R$ ) and  $T_c$  in  $\beta$ -(BEDT-TTF) $_2$  trihalide mixed crystals. Samples with composition near the I $_3$  salt have two  $T_c$ 's. Closed circles indicate non-superconducting (or  $T_c < 0.5$  K) samples [10].

where RRR is the residual resistance ratio and the room-temperature conductivity,  $\sigma_0(rt)$ , was assumed to be constant, i.e. 20 S/cm[11].

Figure 2 shows the residual conductivity( $\sigma_R$ ), which is inverse of residual resistivity, and  $T_c$  in  $\beta$ -(BEDT-TTF)<sub>2</sub> trihalide mixed crystals[10]. Here we can see a clear correlation between  $T_c$  and residual conductivity( $\sigma_R$ ) for a wide range of composition, that is, as we increase the amount of substituent(x or 1-x), the residual conductivity decreases and the  $T_c$  decreases accordingly. Open circles in the figure represent superconducting samples while closed circles correspond to samples which did not show superconductivity at least down to 0.5 K. Another interesting feature shown in the upper part of the figure is the presence of a clear boundary, represented by a dashed line at  $\sigma_R=6000$  S/cm, between the superconducting and non-superconducting samples, indicating the presence of *minimum conductivity* (6000 S/cm) required for realization of superconductivity in this system. This value obtained from the above experimental results was found to be in fair agreement with a theoretical estimation based on the weak localization effect[12]. Also, this empirical rule explains why  $\beta$ -(BEDT-TTF)<sub>2</sub>I<sub>2</sub>Br does not show superconductivity.

#### High- $T_c$ (8 K) State in $\beta$ -(BEDT-TTF)<sub>2</sub>I<sub>3</sub>

The second example which shows a correlation between  $T_c$  and resistivity is  $\beta$ -(BEDT-TTF)<sub>2</sub>I<sub>3</sub> itself in which two superconducting states are known to exist at ambient pressure, i.e. the low- $T_c$  state ( $T_c=1.1-1.5$ K) and the high- $T_c$  state ( $T_c=7-8$ K). The difference between the two states is considered to be the *incommensurate lattice modulation*[1] which appears below 175K, where temperature dependence of resistance changes its slope or derivative[11,13]. Fig. 3(a) shows a temperature dependence of resistance(R), and Fig. 3(b) shows a temperature derivative of resistance(dR/dT) of  $\beta$ -(BEDT-TTF)<sub>2</sub>I<sub>3</sub>. At 175 K a crossover between the crystal structures with and without the incommensurate lattice modulation takes place. The former( $\beta_L$ ) is stable at lower temperature while the latter( $\beta_H$ ) is stable at higher temperature. And from Fig. 3(a),  $\beta_L$  state with the incommensurate superstructure seems to show higher resistance than  $\beta_H$  state without the superstructure at temperatures below 175 K.

The high- $T_c$  state without the incommensurate superstructure( $\beta_H$ ) can be realized by releasing the pressure at low temperature after cooling under pressure[14,15]. A more direct difference in resistivity between  $\beta_H$  and  $\beta_L$  states were reported by Hamzic et al.[13] in which they observed an abrupt resistance increase due to a first order structural phase transition from the metastable  $\beta_H$  state to  $\beta_L$  state when the  $\beta_H$  sample was warmed up to about 130 K, although they do not mention the difference in residual resistivity at low temperature.

A difference in residual resistivity at low temperature between the two states was reported by Ginodman et al.[16]. The result shows that the resistivity of metastable  $\beta_H$  state is much lower than that in  $\beta_L$  state at low



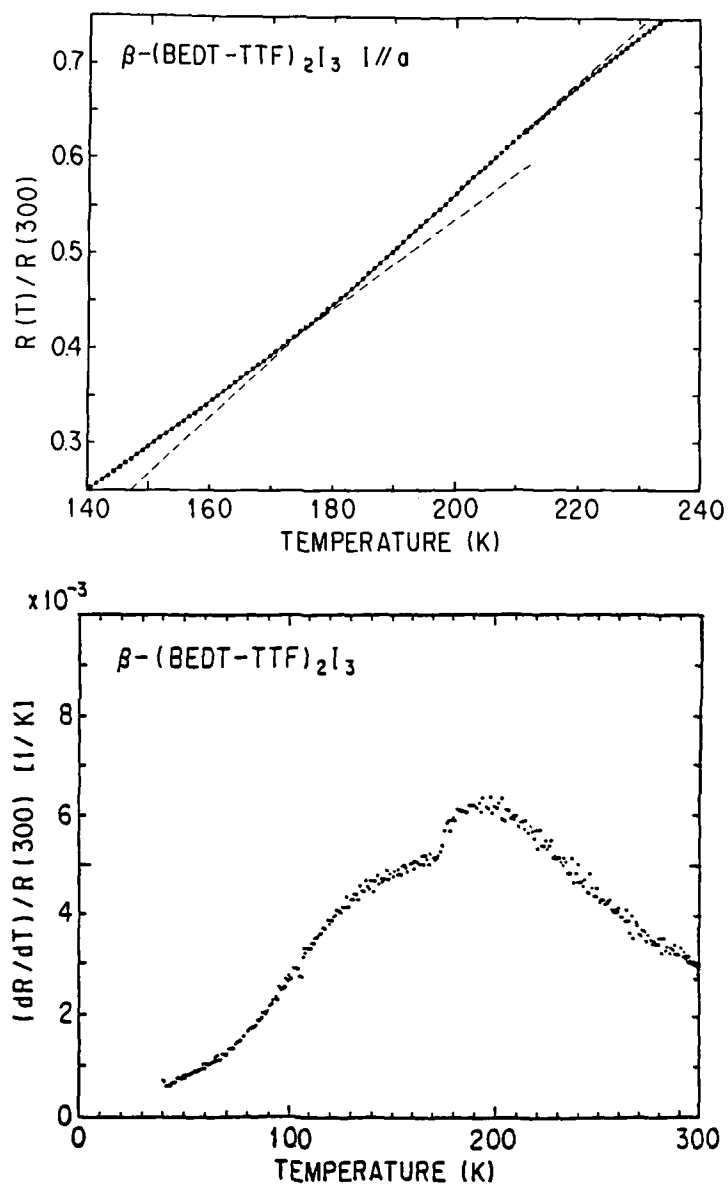


Fig. 3. (a) Temperature dependence of resistance (R) of  $\beta$ -(BEDT-TTF)<sub>2</sub>I<sub>3</sub>.  
(b) Temperature dependence of  $dR/dT$  of  $\beta$ -(BEDT-TTF)<sub>2</sub>I<sub>3</sub>.

temperatures, indicating that correlation between  $T_c$  and residual resistivity also holds in this case.

#### A New 2 K State in $\beta$ -(BEDT-TTF) $_2$ I $_3$

Recently, annealing at about 110 K was found to result in a change of the incommensurate superstructure[17]. It was also found that a new superconducting state with  $T_c=2$  K appears as a result of annealing[18,19], although its origin or structural difference responsible to the change of  $T_c$  has not been identified yet. Annealing at 110K is also accompanied by a decrease in resistance in addition to the change of incommensurate superstructure and appearance of the 2K state. Fig. 4. shows time dependence of resistance ( $i//c^*$ ) of  $\beta$ -(BEDT-TTF) $_2$ I $_3$  due to annealing. The resistance decrease by as much as 10%, indicating that the new 2 K state has lower resistivity than the original low- $T_c$  state. Fig. 5. shows temperature dependence of resistance of  $\beta$ -(BEDT-TTF) $_2$ I $_3$  before(.....) and after annealing(---). A vertical line at 106 K in the figure indicates the decrease in resistance by annealing. This annealed 2 K state with lower resistance is also metastable, and gradually goes back to the original low- $T_c$ (1.1-1.5 K) state with higher resistance when the sample is warmed up to about 120 K as seen in Fig. 5.

Now, what about the residual resistance at low temperature? Surprisingly, the temperature dependence of resistance in Fig. 5 shows that the difference in the resistance between the two states, which is as much as 10% at around 100 K, completely disappears as temperature goes down to below 40 K. More or less the same temperature dependence was observed for resistance with current flowing parallel to the conducting plane( $i//a$ )[20]. It is, however, consistent with the ESR linewidth result as shown in Fig. 6. It is well known that structural disorder in  $\beta$ -(BEDT-TTF) $_2$ X provides an additional scattering mechanism for the carriers which increases the residual (low-temperature) ESR linewidth[21]. It is also reported that in  $\beta$ -(BEDT-TTF) $_2$ I $_3$ , the linewidth in  $\beta_H$  state is much narrower than that of  $\beta_L$  state[22]. Figure 6 indicates that annealing at 100 K causes an appreciable decrease of the ESR linewidth at high temperature, but the reduction of linewidth due to annealing is much smaller at low temperatures, in contrast to the case of high- $T_c$  (8 K) state[22]. These observations seem to indicate that the change of  $T_c$  is not accompanied by the change of the low-temperature residual resistance, or scattering, in the case of 2 K superconducting state. These results suggest that we must look for other reasons which can be related to the change of  $T_c$  in this case. The reduction of the critical field anisotropy in 2 K state[20] could give us a clue to obtain a better understanding of the effect of annealing. The anisotropy of  $H_{c2}$ ,  $H_{c2//}/H_{c2\perp}$ , is reported to show a significant decrease from 20.9 to 14.5, caused by annealing[23].

It has been shown by recent magnetization measurement that an extended annealing at about 110 K results in appearance of appreciable amount of the "high- $T_c$ " state with  $T_c=7.5$  K, while the bulk 2 K state gradually loses its volume fraction[19]. The structural difference between

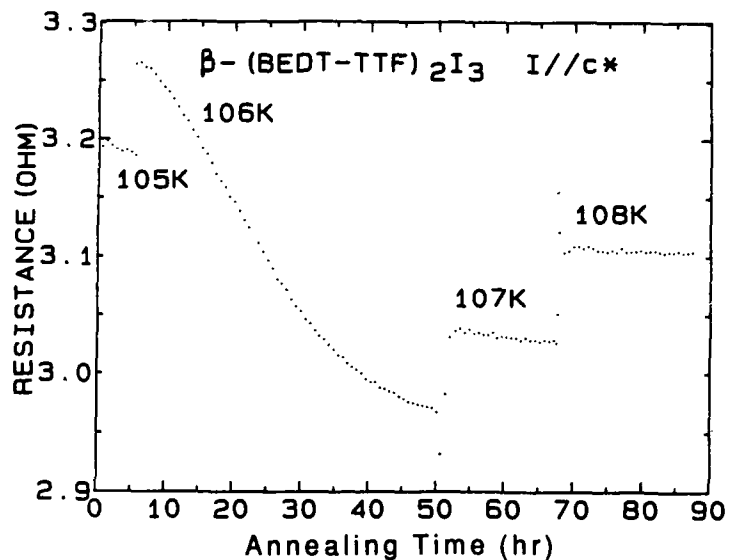


Fig. 4. Time dependence of resistance ( $i/c^*$ ) of  $\beta$ -(BEDT-TTF) $_2$ I $_3$  due to annealing.

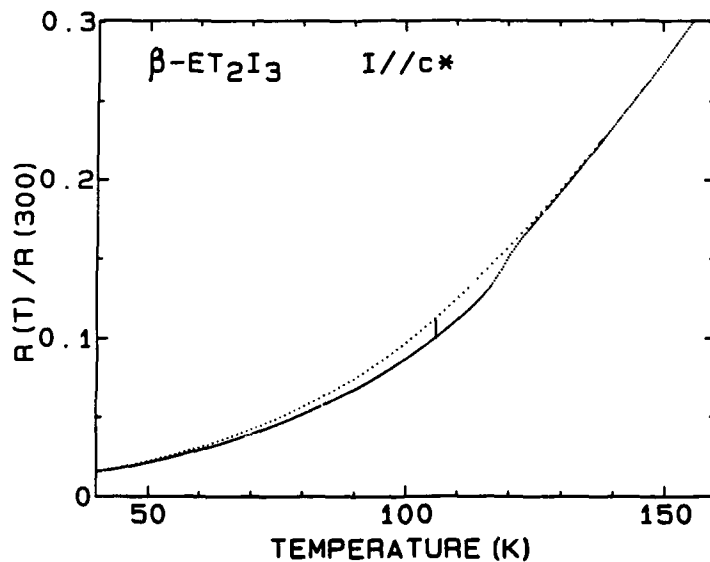


Fig. 5. Temperature dependence of resistance of  $\beta$ -(BEDT-TTF) $_2$ I $_3$  before (.....) and after annealing (---). A vertical line at 106 K in the figure indicates the decrease in resistance by annealing.

these states with different  $T_c$  has not been clarified yet, and needs further study on the superstructure and ethylene ordering.

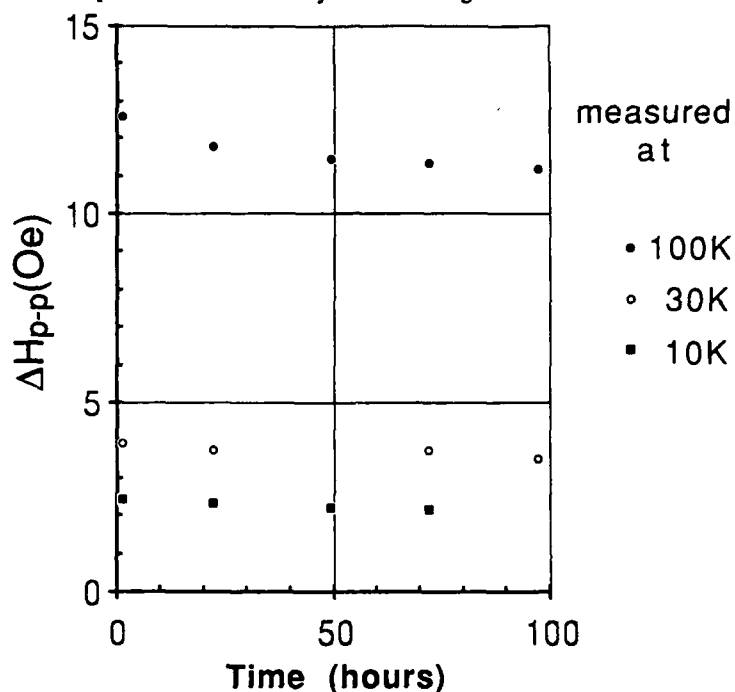


Fig. 6. Peak-to-peak ESR linewidth versus annealing time at 100 K and at low temperatures after each annealing process at 100 K.

#### ANISOTROPY IN $H_{c2}$ OR IN THE COHERENCE LENGTH

In a quasi-two-dimensional electronic system such as BEDT-TTF based organic metals, the anisotropy between in-plane and out-of-plane values of various structural and electronic parameters can, in general, play an essential role on its physical properties including superconductivity. Since a pure 2-D electronic system is not expected to show superconductivity, the introduction of interaction between conducting planes is of vital importance to establish superconductivity in such a quasi-2D metals like  $(\text{BEDT-TTF})_2\text{X}$ . It is now well known that the superconductivity in  $(\text{BEDT-TTF})_2\text{X}$  is very sensitive to the application of hydrostatic pressure. In order to clarify the relative importance between the in-plane and out-of-plane interactions, the application of hydrostatic pressure is informative but not sufficient, since it generally results in a reduction of both in-plane and out-of-plane lattice parameters. Therefore, in addition to the hydrostatic pressure experiment, an application of uniaxial pressure perpendicular to the conducting plane would eventually give us unambiguous answer.

The correlation between  $T_c$  and anisotropy is not established yet. For example, the critical field anisotropy ( $dH_{c2//}/dH_{c2\perp}$ ) showed only a small change (from 13.1 to 15.6) when  $T_c$  decreased from 6.55 K to 2.18 K by application of pressure [24,25].

It is interesting to see how  $T_c$  can correlate with the anisotropy of the superconducting coherence length, i.e.  $\xi_{//}/\xi_{\perp}$ , where  $\xi_{//}$  and  $\xi_{\perp}$  are the Ginzburg Landau coherence length  $\xi_{GL}(0)$  along and perpendicular to the conducting plane, respectively. These coherence lengths can be estimated from the temperature dependence of the upper critical field  $H_{c2}(T)$  parallel and perpendicular to the conducting plane, using the relations

$$-[dH_{c2//}/dT]_{T=T_c} = \phi_0/2\pi\xi_{//}(0)\cdot\xi_{\perp}(0)\cdot T_c \quad (2)$$

and

$$-[dH_{c2\perp}/dT]_{T=T_c} = \phi_0/2\pi\xi_{//}(0)^2\cdot T_c \quad (3)$$

where  $\phi_0 = hc/2e = 2.07 \times 10^{-7}$  gauss $\cdot$ cm $^2$  is the flux quantum. Figure 7 shows the anisotropy of the superconducting coherence length, i.e.  $\xi_{//}/\xi_{\perp}$ , in various  $\beta$ -(BEDT-TTF) $_2$ X superconductors as a function of  $T_c$  [20, 23-27].

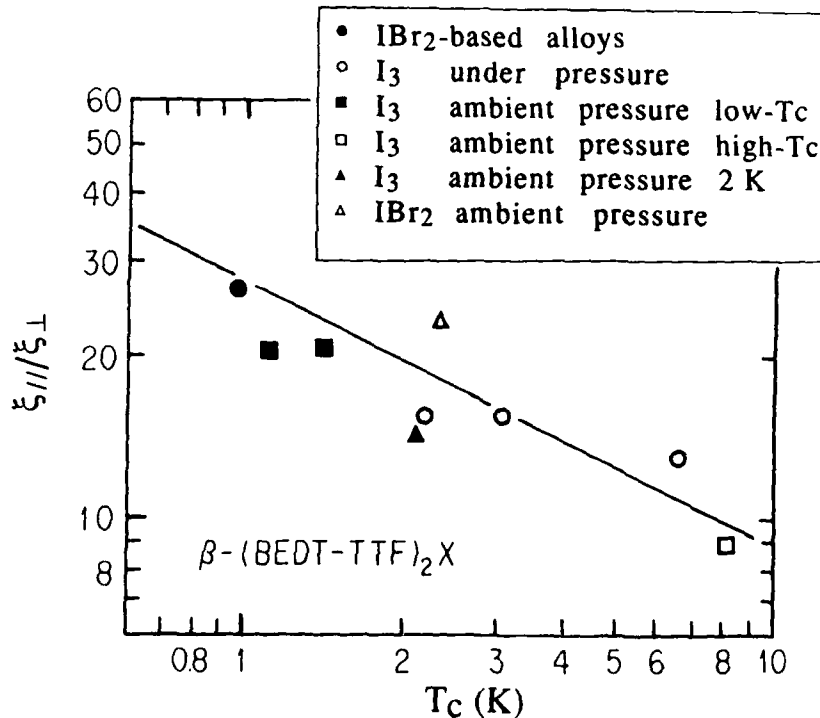


Fig. 7. The anisotropy of the superconducting coherence length,  $\xi_{//}/\xi_{\perp}$ , in  $\beta$ -(BEDT-TTF) $_2$ X superconductors as a function of  $T_c$  [20,23-29].

Although the correlation is not strict, it can be said that the ratio becomes lower for higher  $T_c$ . It is noteworthy that, most of points in the figure are within a region expressed by the following relation,

$$\xi_{\parallel}/\xi_{\perp} = (28 \pm 7)/\sqrt{T_c(K)}. \quad (4)$$

Thus, roughly speaking, the anisotropy of coherence length, or of  $H_{c2}$ , is inversely proportional to the square root of  $T_c$  for the  $\beta$ -(BEDT-TTF) $_2$ X family. The observed difference of anisotropy between 2 K state and the low- $T_c$  state is in good accord with this relation, as seen in Fig. 7.

#### SUMMARY

We have presented some typical examples which exhibit the effect of defects, disorders and impurities on the superconducting properties in organic metals  $\beta$ -(BEDT-TTF) $_2$ X. A particular attention has been paid to the correlation between  $T_c$  and residual resistivity, which are superconducting and normal state properties, respectively. A high correlation has been found in two cases, i.e.  $\beta$ -(BEDT-TTF) $_2$  trihalide mixed crystals and the high- $T_c$ ( $\beta_H$ ) state in  $\beta$ -(BEDT-TTF) $_2$ I $_3$ . A new 2 K state in  $\beta$ -(BEDT-TTF) $_2$ I $_3$  has been shown to be out of this context. It may, however, reflect the change of anisotropy, since a semi-quantitative correlation between  $T_c$  and the anisotropy of coherence length, derived in  $\beta$ -(BEDT-TTF) $_2$ X, seems to be in good accord with the observed anisotropy change.

#### Acknowledgments

The authors would like to thank Professor S. Kagoshima of the University of Tokyo, and Professor N. Toyota and Mr. T. Sasaki of Tohoku University for useful discussions through a collaborative study on the 2 K superconducting state in  $\beta$ -(BEDT-TTF) $_2$ I $_3$ .

#### References

1. T. J. Emge, P. C. W. Leung, M. A. Beno, A. J. Schultz, H. H. Wang, L. M. Soma and J. M. Williams, Phys. Rev. **B30**, 6780 (1984).
2. P. C. W. Leung, T. J. Emge, M. A. Beno, H. H. Wang, J. M. Williams, V. Petricek and P. Coppens, J. Am. Chem. Soc., **107**, 6184 (1985)
3. J. M. Williams, H. H. Wang, T. J. Emge, U. Geiser, M. A. Beno, P. C. W. Leung, K. D. Carlson, R. J. Thorn, A. J. Schultz and M. -H. Wangbo, Prog. Inorg. Chem., **35**, 51 (1987).
4. P. C. W. Leung, T. J. Emge, A. J. Schultz, M. A. Beno, K. D. Carlson, H. H. Wang, M. A. Firestone and J. M. Williams, Solid State Commun., **57**, 93 (1986)
5. J. M. Williams, T. J. Emge, H. H. Wang, M. A. Beno, P. T. Copps, L. N. Hall, K. D. Carlson and G. W. Crabtree, Inorg. Chem., **23**, 3839 (1984).

6. H. H. Wang, M. A. Beno, U. Geiser, M. A. Firestone, K. S. Webb, L. Nunez, G. W. Crabtree, K. D. Carlson, J. M. Williams, L. J. Azevedo, J. F. Kwak and J. E. Schirber, *Inorg. Chem.*, **24**, 2465 (1985).
7. H. Kobayashi, R. Kato, A. Kobayashi, G. Saito, M. Tokumoto, H. Anzai and T. Ishiguro, *Chem. Lett.*, **1985**, 1293.
8. M. Tokumoto, H. Bando, K. Murata, H. Anzai, N. Kinoshita, K. Kajimura, T. Ishiguro and G. Saito, *Synthetic Metals*, **13**, 9 (1986).
9. H. Anzai, M. Tokumoto, K. Takahashi and T. Ishiguro, *J. Cryst. Growth*, **91**, 225 (1988).
10. M. Tokumoto, H. Anzai, K. Murata, K. Kajimura and T. Ishiguro, *Synth. Metals*, **27**, A251 (1988).
11. M. Tokumoto, H. Anzai, K. Murata, K. Kajimura and T. Ishiguro, *Jpn. J. Appl. Phys.*, **26-S3**, 1977 (1987).
12. Y. Hasegawa and H. Fukuyama, *J. Phys. Soc. Jpn.*, **55**, 4265 (1986).
13. B. Hamzic, G. Creuzet and C. Lenoir, *Europhys. Lett.*, **3**, 373 (1987).
14. F. Creuzet, G. Creuzet, D. Jerome, D. Schweitzer and H. J. Keller, *J. Phys. (Paris) Lett.*, **46**, L-1097 (1985).
15. V. B. Ginodman, A. V. Gudenko, I. I. Zasavitskii and E. B. Yagubskii, *JETP Lett.*, **42**, 472 (1985).
16. V. B. Ginodman, A. V. Gudenko, L. N. Zherikhina, V. N. Laukhin, E. B. Yagubskii, P. A. Kononovich and I. F. Shegolev, *Acta Polymerica* **39**, 533 (1988).
17. S. Kagoshima, Y. Nogami, M. Hasumi, H. Anzai, M. Tokumoto, G. Saito and N. Mori, *Solid State Commun.*, **62**, 1177 (1989).
18. S. Kagoshima, M. Hasumi, Y. Nogami, N. Kinoshita, H. Anzai, M. Tokumoto and G. Saito, *Solid State Commun.*, **71**, 843 (1989).
19. M. Tokumoto, Y. Yamaguchi, N. Kinoshita and H. Anzai, in Proc. 1st ISSP Symposium on the Physics and Chemistry of Organic Superconductors (Springer-Verlag, to be published)
20. T. Sasaki, N. Toyota, M. Hasumi, T. Osada, S. Kagoshima, H. Anzai, M. Tokumoto and N. Kinoshita, *J. Phys. Soc. Jpn.*, **58**, 3477 (1989).
21. E. L. Venturini, J. E. Schirber, H. H. Wang and J. M. Williams, *Synth. Metals*, **27**, A243 (1988).
22. H. Hurdequint, F. Creuzet and D. Jerome, *Synth. Metals*, **27**, A183 (1988).
23. T. Sasaki, N. Toyota, M. Hasumi, T. Osada, S. Kagoshima, M. Tokumoto, N. Kinoshita and H. Anzai, in Proc. 1st ISSP Symposium on the Physics and Chemistry of Organic Superconductors (Springer-Verlag, to be published)
24. K. Murata, M. Tokumoto, H. Anzai, H. Bando, K. Kajimura, T. Ishiguro and G. Saito, *Synth. Metals*, **13**, 3 (1986)
25. K. Murata, M. Tokumoto, H. Anzai, H. Bando, K. Kajimura, T. Ishiguro and G. Saito, *Synth. Metals*, **19**, 151 (1987).
26. M. Tokumoto, H. Bando, H. Anzai, G. Saito, K. Murata, K. Kajimura and T. Ishiguro, *J. Phys. Soc. Jpn.*, **54**, 869 (1985).
27. M. Tokumoto, H. Anzai, H. Bando, G. Saito, N. Kinoshita, K. Kajimura and T. Ishiguro, *J. Phys. Soc. Jpn.*, **54**, 1669 (1985).
28. M. Tokumoto, K. Murata, H. Bando, H. Anzai, G. Saito, K. Kajimura and T. Ishiguro, *Solid State Commun.*, **54**, 1031 (1985).
29. M. Tokumoto, Researches of the Electrotechnical Laboratory, No. 892 (1988).

TRANSFER INTEGRALS AND BAND STRUCTURES IN (ET)<sub>2</sub>X SALTS

OLIVER H. LEBLANC, JR., MARGARET L. BLOHM, and RICHARD P. MESSMER,  
General Electric Corporate Research & Development, Schenectady, NY 12301

## ABSTRACT

Transfer integrals ( $t_{ij}$ ) between pairs of nearest neighbor ET molecules were calculated by an ab initio method. Tight-binding one-electron energy bands constructed from the  $t_{ij}$  are similar to those previously calculated by Mori and by Whangbo and their coworkers by semi-empirical, extended Hückel methods, but quite different from those found by Kübler et al. in  $\beta$ -(ET)<sub>2</sub>I<sub>3</sub> using the augmented spherical wave (ASW) method. However, all these band models are suspect. The Hubbard on-site repulsion parameter  $U$  is estimated to be about twice the band widths, indicating that a full treatment of the Hubbard hamiltonian is needed. Also, polaron effects appear to control transport except at very low temperature.

## INTRODUCTION

The (ET)<sub>2</sub>X salts [ET: bis(ethylenedithio)tetrathiafulvalene] containing ET molecules, ET<sup>+</sup> radical cations, and closed shell X<sup>-</sup> anions exhibit a variety of interesting electrical and magnetic properties, including superconductivity, which are not entirely understood theoretically[1]. Indeed, a controversy has arisen as how best to approach these solids theoretically. We describe new calculations that may shed light on some of these issues.

The crystals have structures in which the ET's are tightly packed together in planar layers sandwiched between parallel layers of X<sup>-</sup> anions. Experimental evidence suggests that electrons on the anions occupy filled orbitals well below the Fermi level, so that the electrical and magnetic properties are associated primarily with the ET's and not with the anions. Thus, the conductivity is orders of magnitude higher parallel to the ET layers than perpendicular to them, and it and other properties are more sensitive to the detailed way the ET's pack together in the layers than to the nature of the anion. The anions are therefore usually ignored in theoretical analyses.

The most extensive calculations have been carried out by Mori[2] and by Whangbo[3] and their coworkers who used the semi-empirical extended Hückel approximation to construct tight-binding one-electron bands based upon a single molecular state, the highest occupied molecular orbital (HOMO) of ET. Mixing with other ET orbitals and with orbitals on the closed shell X<sup>-</sup> anions was ignored. They have had fair success in accounting for many of the properties of (ET)<sub>2</sub>X salts with these band models.

Our calculations proceed in the same spirit, but are more elaborate. In the extended Hückel method, only overlap integrals between pairs of atomic basis functions (bfs) are actually computed; hamiltonian matrix elements are estimated as needed by multiplying the respective overlap integrals by semi-empirical constants. We have used instead an ab initio approach to calculate transfer integrals,  $t_{ij}$ 's, between nearest neighbor ET's; the required hamiltonian matrix elements are calculated exactly from the atomic bfs, with all one- and two-electron Coulomb and exchange integrals included. One-electron energy bands constructed from the  $t_{ij}$  are similar to those of Mori and Whangbo. There are a small number of subbands equal to the number of ET's per unit cell, and the Fermi level intersects 1 or 2 subbands, at most, to produce relatively simple Fermi surfaces (see Fig.1).

A very different band structure and Fermi surface was obtained for  $\beta$ -(ET)<sub>2</sub>I<sub>3</sub> by Kübler et al.[4] using the ASW method[5], which they applied to all the species in the unit cell, including the I<sub>3</sub><sup>-</sup> anion. They found many closely spaced ( $\approx 0.1$ eV), overlapping bands of various widths (up to  $\approx 1$ eV). The Fermi level intersected several of these bands, producing a complicated Fermi surface. Among the bands at the Fermi surface were partially filled I<sub>3</sub><sup>-</sup> levels, so that a fraction of the electronic charge on the anion was unbound. The



Fermi surface also intersected narrow bands located primarily in interstitial regions between molecules. These were partly filled with electrons, evidently those which had escaped from  $I_3^-$ .

These very remarkable results appear, unfortunately, to be artifacts arising from a flaw in the ASW method. It is a relatively old density-functional method[5] that employs a local-density approximation for exchange and correlation without correction for electron self-interaction. Such approximations are notorious for predicting instability in experimentally stable negative ions, grossly underestimating their binding energies[6]. The ASW method would be expected to make this error for an isolated  $I_3^-$ . And the error may have been exacerbated in the  $\beta$ -(ET) $_2I_3$  solid by the extra "muffin tin" potentials in the large interstitial spheres which Kübler placed between molecules. These artificial regions would act as efficient sinks for the stray electrons from the  $I_3^-$ .

On the basis of their complicated band structure Kübler criticized Mori's and Whangbo's use of a single molecular level in the tight-binding approximation, arguing that this is justifiable only when the separation between bands is larger than their widths. But if there really are neither  $I_3^-$  levels nor spurious interstitial levels at the Fermi energy, only partially filled ET levels, then the criticism is unwarranted, because according to our Hartree-Fock (HF) calculations, the separation between the HOMO and adjacent ET molecular levels is  $\approx 1.4$  eV, which is larger than the band widths Mori or Whangbo or Kübler or we calculate. Thus, the use of only the HOMO in the tight-binding approximation appears to be justifiable after all[7].

#### HUBBARD MODEL

A more serious objection to the one-electron band model, perhaps, is its failure to treat the very strong, localized Coulomb repulsions which are peculiar to these molecular solids. Such interactions can be discussed to lowest order in terms of the simple Hubbard model, with a hamiltonian which we write as

$$H = \sum_{\langle ij \rangle \sigma} t_{ij} b_{i\sigma}^\dagger b_{j\sigma} + U \sum_i b_{i\uparrow}^\dagger b_{i\uparrow} b_{i\downarrow}^\dagger b_{i\downarrow} \quad (1)$$

The one-electron operators in the first sum transfer electrons between Wannier orbitals corresponding to the HOMO's on ET nearest neighbors  $i$  and  $j$ . The second sum as written counts the number of ET sites occupied by an  $ET^{2+}$  dication;  $U$  is the energy of disproportionation  $2ET^+ = ET + ET^{2+}$  in the solid. The one-electron band model is obtained if the second term is ignored.

Computing values for  $t_{ij}$  and for  $U$  poses two quite different challenges. As discussed below, if the  $t_{ij}$  are computed properly, then they turn out to be sensitive only to the values of the local wave functions and potentials on molecules  $i$  and  $j$ . Thus, reasonably good values for the  $t_{ij}$  can be obtained by treating the ET molecules one pair at a time, ignoring the rest of the molecules in the crystal. This is feasible with present-day computers using *ab initio* methods, and the quality of the  $t_{ij}$  values so obtained is limited only by the size and quality of the basis set used.

$U$ , on the other hand, is more intractable, since it depends on non-local, long-range Coulomb forces which are screened in the crystal in a complicated manner. An *a priori* evaluation of it is presently hopeless, and a good estimate of it can only be obtained empirically. A reasonable value is 1.5eV, from the work of Torrance[8].

#### TRANSFER INTEGRALS

Transfer integral calculations were carried out on a Convex 220 computer, using programs from the Caltech Generalized Valence Bond (GVB) package[9], in two steps. First, a HF self-consistent-field calculation was carried out for each unique ET in the lattice using its X-ray crystal geometry and adding H atoms as needed. This produced for each ET

a set of HF MO's  $\psi^k = \sum_n c_n^k \chi_n$ , expressed in terms of atomic bfs  $\chi_n$ . Then, the GVB one- and two-electron integrals routines were used to calculate intermolecular integrals between bfs on nearest-neighbor ET molecules, and these were multiplied by the respective MO coefficients to yield the terms in eqn. 2 below. The transfer integrals were explicitly calculated with MO fillings appropriate to the case in which a neutral molecule at  $i$  switches places with a  $+1$  cation at  $j$ . Each  $t_{ij}$  computation required approximately 2 hours of cpu time on the Convex 220, of which about 90% was spent evaluating two-electron integrals.

The basis set was a minimal one consisting of 90 "single-zeta" Gaussian type orbitals. In choosing the C and S bfs we followed the suggestion of Grant[10] that the best a priori choice of bfs for computing transfer integrals are those which have long "tails" like atomic HF orbitals. For C 1s, 2s, and 2p we used the 4-Gaussian bfs which Stewart[11] obtained by fitting to HF atomic orbitals. The core electrons of S were represented by the SHC pseudopotential of Rappe et al.[12], and the S 3s and 3p by "single-zeta" contractions of the 3-Gaussian bfs which they designed to go on their pseudopotential. We chose these contractions so that the 3s-3s and 3p $\pi$ -3p $\pi$  overlap integrals of two S atoms spaced 3.60 Å apart were the same as those of the respective HF atomic orbitals[13]; this distance, twice the S Van der Waals radius, equals the typical closest S-S contact between nearest-neighbor ET's in (ET)<sub>2</sub>X salts. Huzinaga's 3-Gaussian bf[14] was used for H 1s.

Computation of the  $t_{ij}$  is complicated somewhat by the fact that the HF MO's on ET molecule  $i$  are not orthogonal to those on molecule  $j$ , whereas the Fermion operators in eqn. 1 anticommute properly only if they refer to orthogonal (Wannier) orbitals. The non-orthogonality of the HF MO's must therefore be corrected for. Using Löwdin's method[15] the  $t_{ij}$  can be expressed formally as a power series in intermolecular overlap integrals. When the overlap integrals are small, as is true here, then all terms beyond those linear in overlap integrals can be neglected, and

$$t_{ij} \approx \frac{(\beta_{ij} + \beta_{ji})}{2} - S_{ij} \frac{(\alpha_{ij} + \alpha_{ji})}{2} \quad (2)$$

Here  $S_{ij} = \int \psi_i^{\text{HOMO}}(1) \psi_j^{\text{HOMO}}(1) dv(1)$  is the overlap integral between the HOMO's on molecules  $i$  and  $j$ ,  $\beta_{ij} = \int \psi_i^{\text{HOMO}}(1) V_i(1) \psi_j^{\text{HOMO}}(1) dv(1)$  and  $\alpha_{ij} = \int \psi_i^{\text{HOMO}}(1) V_j(1) \psi_i^{\text{HOMO}}(1) dv(1)$ , where  $V_p(1)$  is an operator containing all one- and two-electron Coulomb and exchange interactions between electron 1 with the nuclei and with the other electrons in filled MO's on molecule  $p$ .

Whereas only  $S_{ij}$  need be computed in the extended Hückel approximation, the 5 integrals on the right-hand side of eqn.2 must be evaluated here to obtain  $t_{ij}$ . That all 5 must be included can be appreciated by noting that acting together they make  $t_{ij}$  behave properly as an off-diagonal element of the hamiltonian. Thus,  $t_{ij} = t_{ji}$  even though, in general,  $\beta_{ij} \neq \beta_{ji}$  and  $\alpha_{ij} \neq \alpha_{ji}$  (unless molecules  $i$  and  $j$  are symmetrically related to one another, e.g., if they are transformed into one another by an inversion). Furthermore, adding a constant to either  $V_i$  or  $V_j$  causes no change in  $t_{ij}$  - a change in one  $\beta$  term is exactly cancelled by an equal and opposite change in one of the  $S \times \alpha$  terms.

The same kind of cancellation is also remarkably complete for any potential which varies slowly over the region of the  $\psi_i^{\text{HOMO}} \psi_j^{\text{HOMO}}$  overlap. Thus, we find that a unit charge placed at any atom position of the nearest anion contributes a negligible amount (less than 1 meV) to any  $t_{ij}$  changes (of as much as 50-100 meV) in the  $\beta$ 's being almost exactly cancelled by changes in the  $S \times \alpha$  terms. This has the important effect that it makes the pairwise method of calculating  $t_{ij}$ , neglecting potentials other than  $V_i$  and  $V_j$ , an excellent approximation; long-range potentials can be ignored.

## NUMERICAL RESULTS AND DISCUSSION

We have calculated transfer integrals for a number of  $(\text{ET})_2\text{X}$  crystals. In general our results are similar to those obtained previously by Mori and by Whangbo with the much simpler extended Hückel approximation. We will discuss in detail here only our results for  $\kappa\text{-(ET)}_2\text{Cu(NCS)}_2$ , a superconductor with a  $T_c$  of 10.4K[16]. We used the 298K crystal structure data of Carlson et al.[17], and we label the ET molecules in the Table I below as they do in their Fig.1. This crystal has monoclinic symmetry ( $P2_1/c$ ). The ET layers parallel the bc crystal planes. There are 4 ET's per unit cell and 6 nearest neighbor per ET, but by symmetry only 2 distinct ET geometries ( $A=C=J=H$  and  $B=I$  in Table I) and only 6 distinct  $t_{ij}$ 's (listed in order of decreasing size). Each ET is paired closely with one ET of the opposite geometry, and these pairs (A-B) exhibit the largest  $t_{ij}$ .

ij	$\beta_{ij}$ (meV)	$\beta_{ji}$ (meV)	$S_{ij}$ $\times 10^{+3}$	$\alpha_{ij}$ (eV)	$\alpha_{ji}$ (eV)	$t_{ij}$ (meV)
A B	-207.7	-209.8	25.42	-1.742	-1.865	-162.9
A C	-100.6	-118.4	12.56	-1.407	-1.124	-93.6
B I	-115.6	-98.2	12.61	-0.962	-1.278	-92.8
B J	-84.8	-81.5	10.10	-1.003	-0.976	-73.1
B C	50.4	34.6	-4.38	-1.207	-1.004	37.6
B H	27.3	44.9	-3.57	-1.032	-1.078	32.3

The values calculated for the various terms in eqn.2 are shown in detail in Table I. The overlap integrals are sufficiently small that the leading  $\beta$  terms make the largest contribution to  $t_{ij}$  (>80%) and that higher terms in the powers series expansion for  $t_{ij}$  are completely negligible. Our results are comparable to those of extended Hückel treatment of Oshima et al.[18] and of Carlson. The former report only intermolecular overlap integrals; our four largest  $S_{ij}$  values agree with theirs to within  $\approx 20\%$ , indicating that our basis functions and theirs are similar. The latter report only  $t_{ij}$ 's; our four largest values are approximately half theirs, possibly indicating that our basis functions are less extended than theirs.

With our  $t_{ij}$ 's we compute a one-electron band structure for  $\kappa\text{-ET}_2\text{Cu(NCS)}_2$ , shown in Fig.1, virtually identical to that of Oshima[18]. The Fermi surface consists of a closed cylinder of holes about Z and an open sheet of electrons near Y. Carlson et al.[17] show a Fermi surface which, judging from their  $t_{ij}$  values, is drawn incorrectly. We can calculate some numerical values with dimensions of energy which Oshima could not; e.g., the total band width is 845 meV, the Fermi energy is located at 322 meV below the top of the band, and  $N(E_F)$ , the total density of states (both spins) at the Fermi surface, is 2.12 eV<sup>-1</sup> per ET molecule.

Recalculating the  $t_{ij}$  with small translational or rotational displacements,  $\xi$ , of ET  $i$  or  $j$ , yields a set of derivatives  $d \ln |t_{ij}| / d\xi$ , which could be used to estimate effects of lattice vibrations. For example, for the longitudinal modes in  $\kappa\text{-ET}_2\text{Cu(NCS)}_2$  we find  $d \ln |t_{ij}| / d\xi \approx 2\text{\AA}^{-1}$ . These will contribute  $\approx N(E_F) \langle (dt_{ij}/d\xi)^2 / M\Omega^2 \rangle$  to the dimensionless superconducting electron-phonon coupling constant,  $\lambda$ , where  $M$  is the ET mass (384 amu),  $\Omega$  the phonon frequency, and the brackets indicate a sum over nearest neighbors and an average over the phonon modes[1c]. The dispersion of the phonon modes is unknown.

Assuming a mean  $\Omega$  of 50K, we estimate a contribution to  $\lambda$  of  $\approx 0.3$ . We estimate a comparable value from torsional displacements. These are not insignificant contributions to  $\lambda$ , which is thought to have a value  $\approx 1$ , corresponding to strong-coupling superconductivity[1c].

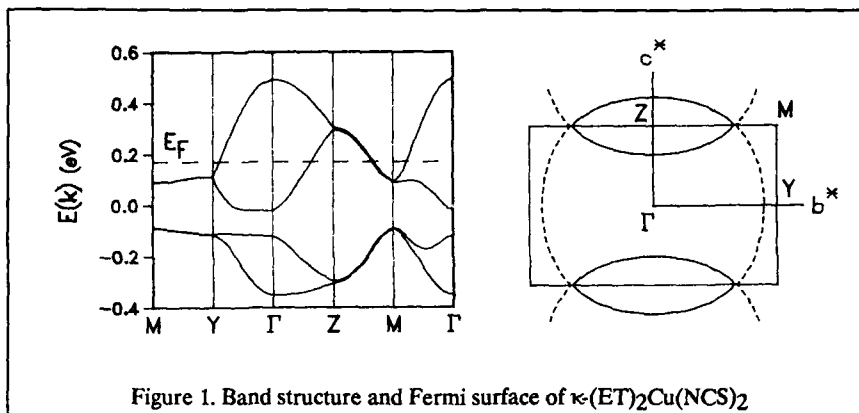


Figure 1. Band structure and Fermi surface of  $\kappa$ -(ET) $_2$ Cu(NCS) $_2$

Oshima's Fermi surface accounts remarkably well for a number of experimental observations in  $\kappa$ -ET $_2$ Cu(NCS) $_2$ . Thus, the Shubnikov-deHaas oscillations which they observed [18] below 1K have a period corresponding to a closed orbit enclosing 18% of the Brillouin zone; that agrees exactly with the area they calculated for the cylindrical part of the Fermi surface; we find a corresponding value of 17%. In addition, we can calculate for this orbit a cyclotron effective mass of  $3.6m_0$ , which agrees with their experimental value of  $3.5m_0$ . Also, Urayama et al.[19] observed an anisotropic thermoelectric power, positive along the  $c$  crystal axis and negative along the  $b$  axis, which Mori and Inokuchi[20] could explain in terms of the closed cylinder of holes and open sheet of electrons, respectively.

Other experimental data for  $\kappa$ -ET $_2$ Cu(NCS) $_2$  are predicted less well by one-electron band theory. For example, our density of states predicts a Pauli spin susceptibility of  $6.7 \times 10^{-5}$  emu/mole, whereas the ESR experimental result[19] is  $3.2 \times 10^{-4}$ , larger by a factor of 4.8. Such discrepancies in other organic metals have been attributed to enhancement of the susceptibility by the interactions represented by the  $U$  term in equation 1 above[21]. That could well be the case here; if  $U = 1.5$ eV, as estimated, then we note that it is approximately twice the one-electron bandwidth, and, thus, hardly negligible.

Fitting the electrical conductivity with the band model seems to be possible in  $\kappa$ -ET $_2$ Cu(NCS) $_2$  only at very low temperature. Conductivity is described in band theory in terms of scattering between one-electron Bloch eigenstates. This is self-consistent only when scattering is weak, i.e., only when the scattering mean free path is long compared to unit cell dimensions. Assuming a constant free path,  $\Lambda$ , using the Boltzmann transport equation, and integrating the conductivity kernel[22] over the Fermi surface, we find values of 78.9 and 77.6 S cm $^{-1}$ /Å for  $\sigma_{bb}/\Lambda$  and  $\sigma_{cc}/\Lambda$ . The observed conductivity[19] is indeed isotropic in the  $bc$  plane, within experimental error. Its magnitude near 10K is  $\approx 5000$  S cm $^{-1}$ , which is fit with a comfortably large  $\Lambda \approx 65$ Å. But the conductivity decreases rapidly with increasing  $T$ . At 30K it is already down to  $\approx 600$  S cm $^{-1}$ , which requires  $\Lambda \approx 8.4$ Å, equal to the shortest ( $b$ ) unit cell dimension. As  $T$  increases further, the conductivity goes through a minimum, then becomes nearly constant near room temperature at  $\approx 25$  S cm $^{-1}$ , which

requires  $\lambda \approx 0.3 \text{ \AA}$ , more than an order of magnitude smaller than the unit cell dimensions! Evidently, a localized, small polaron model is needed to describe carrier transport at high  $T$ [23].

#### References

1. Recent reviews: (a) J.M. Williams, H.H. Wang, T.J. Emge, U. Geiser, M.A. Beno, P.C.W. Leung, K.D. Carlson, R.J. Thorn, A.J. Schultz, *Prog.Inorg.Chem.* **35**, 51 (1987); (b) H. Inokuchi, *Angew.Chem.Int.Ed.Engl.* **27**, 1747 (1988); (c) L.N. Bulaevskii, *Adv.Phys.* **37**, 443 (1988).
2. T. Mori, A. Kobayashi, Y. Sasaki, H. Kobayashi, G. Saito, H. Inokuchi, *Chem. Lett.* **1984**, 957.
3. M.-H. Whangbo, J.M. Williams, P.C.W. Leung, M.A. Beno, T.J. Emge, H.H. Wang, *Inorg.Chem.* **24**, 3502 (1985).
4. J. Kübler, M. Weger, C.B. Sommers, *Solid State Commun.* **62**, 801 (1987).
5. A.R. Williams, J. Kübler, C.D. Gelatt, *Phys.Rev.B* **19**, 6094 (1979).
6. H.P. Shore, J.H. Rose, E. Zaremba, *Phys.Rev.B* **15**, 2858 (1977); K. Schwarz, *J.Phys.B* **11**, 1339 (1978); *Chem.Phys.Lett.* **57**, 605 (1978); J.P. Perdew and A. Zunger, *Phys.Rev.B* **23**, 5048 (1981).
7. D.R. Salahub, R.P. Messmer, F. Herman, *Phys.Rev.B* **13**, 4252 (1976).
8. J.B. Torrance, in *Low-Dimensional Conductors and Superconductors*, edited by D. Jérôme and L.G. Caron (Plenum Press, New York, 1987), p. 113.
9. R.A. Blair, W.A. Goddard III, A.F. Voter, A.K. Rappe, L.G. Yaffe, F.W. Bobrowicz, W.R. Wadt, P.J. Hay, W.J. Hunt, GVB2P5 program (unpublished); R.A. Blair, Ph.D. thesis, California Institute of Technology, 1980; W.J. Hunt, P.J. Hay, W.A. Goddard III, *J.Chem.Phys.* **57**, 738 (1972).
10. P. Grant, *Phys.Rev.B* **27**, 3934 (1983).
11. R.F. Stewart, *J.Chem.Phys.* **50**, 2485 (1969).
12. A.F. Rappe, T.A. Smedley, W.A. Goddard III, *J.Phys.Chem.* **85**, 1662 (1981).
13. E. Clementi and C. Roetti, *Atomic Data and Nuclear Data Tables* **14**, 177 (1974).
14. S. Huzinaga, *J.Chem.Phys.* **42**, 1293 (1965).
15. P.-O. Löwdin, *J.Chem.Phys.* **18**, 365 (1950).
16. H. Urayama, H. Yamochi, G. Saito, K. Nozawa, T. Sugano, M. Kinoshita, S. Sato, K. Oshima, A. Kawamoto, J. Tanaka, *Chem.Lett.* **1988**, 55.
17. K.D. Carlson, U. Geiser, A.V. Kini, H.H. Wang, L.K. Montgomery, W.K. Kwok, M.A. Beno, J.M. Williams, C.S. Cariss, G.W. Crabtree, M.-H. Whangbo, M. Evain, *Inorg.Chem.* **27**, 965 (1988).
18. K. Oshima, T. Mori, H. Inokuchi, H. Urayama, H. Yamochi, G. Saito, *Phys.Rev. B* **38**, 938 (1988).
19. H. Urayama, H. Yamochi, G. Saito, S. Sato, T. Sugano, M. Kinoshita, A. Kawamoto, J. Tanaka, T. Inabe, T. Mori, Y. Maruyama, H. Inokuchi, K. Oshima, *Synth.Met.* **27**, A393 (1988).
20. T. Mori and H. Inokuchi, *J.Phys.Soc.Japan* **57**, 3674 (1988).
21. J.B. Torrance, Y. Tomkiewicz, B.D. Silverman, *Phys.Rev. B* **15**, 4738 (1977).
22. J. Ziman, *Electrons and Phonons* (Oxford University Press, London, 1960), p. 268.
23. C.B. Duke, *Mol. Cryst.Liq.Cryst.* **50**, 63 (1979).

SPECIFIC HEAT MEASUREMENTS ON  $\kappa$ -(BEDT-TTF)<sub>2</sub>Cu(NCS)<sub>2</sub>

R. G. GOODRICH and JING-CHUN XU

Department of Physics and Astronomy, Louisiana State University, Baton Rouge, LA 70803-4001

## ABSTRACT

We have measured the specific heat of  $\kappa$ -(BEDT-TTF)<sub>2</sub>Cu(NCS)<sub>2</sub> from 4 to 14 K. The superconducting transition at 9.4 K is observed in zero applied magnetic field and in a field of 0.3 T. Both the magnitude of the change in  $C_p$  at  $T_c$  and the temperature dependence of  $C_p$  below  $T_c$  indicate a strong coupling superconductor. If the lattice specific heat is assumed to contain contributions due to the eighteen vibrational degrees of freedom, the phonon contribution to the specific heat in our temperature range can be represented by a Debye integral expression with a Debye temperature of 95 K. A model of collective modes suggesting the origin of the eighteen degrees of freedom is presented.

## INTRODUCTION

In the nine years since the discovery of superconductivity in the organic conductor (TMTSF)<sub>2</sub>PF<sub>6</sub> by Jerome, et. al [1], a considerable amount of activity has occurred to find other organic superconductors. Superconductivity now has been observed in six other TMTSF based salts (Bechgaard salts) (TMTSF)<sub>2</sub>X where X = PF<sub>6</sub>, AsF<sub>6</sub>, SbF<sub>6</sub>, TaF<sub>6</sub>, ReO<sub>4</sub>, and ClO<sub>4</sub>. In 1983 the first of a new class of organic superconductors based on the cation BEDT-TTF (ET) was discovered [2]. The ET compounds have exhibited higher transition temperatures than the TMTSF based compounds, and the discovery [3] of  $\kappa$ -(BEDT-TTF)<sub>2</sub>Cu(NCS)<sub>2</sub> with a superconducting transition near 10 K has led to a renewed interest in these systems.

In the first published measurement of the specific heat of (BEDT-TTF)<sub>2</sub>Cu(NCS)<sub>2</sub> only a small change in  $C_p$  at  $T_c$  was observed [4], and the overall temperature dependence has a different slope from what we have observed. In this measurement an A.C. technique operating between 20 and 80 Hz was used. Recently another measurement of  $C_p$  on single crystals has been reported by Andraka, et.al [5] both in zero field and in a field of 12.5 T. From these measurements it was concluded that  $\kappa$ -(BEDT-TTF)<sub>2</sub>Cu(NCS)<sub>2</sub> is a strong coupling superconductor. In both Ref. 4 and in Ref. 5 a total of 59 atoms per formula unit are assumed to be contributing to the specific heat and Debye temperatures on the order of 200 K are reported.

## EXPERIMENT

A powder of crystals of  $\kappa$ -(BEDT-TTF)<sub>2</sub>Cu(NCS)<sub>2</sub> prepared by standard techniques described by Urayama [6] and Carlson [7] were used for the measurements [8]. The a.c.

susceptibility near 1.8 MHz was measured on material prepared by the same technique between 4 and 15 K. The result is shown as the oscillator frequency shift in Figure 1. This result is indistinguishable from that reported by Gartner [9].

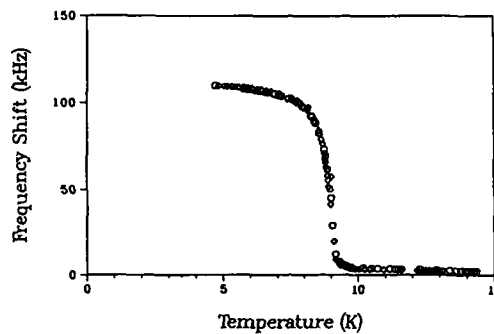


Figure 1.

A.C. susceptibility results at 1.8 Mhz.

Specific heat measurements were made using a new technique developed for small samples [10]. A 5 mg sample consisting of many small crystals was thermally attached to a bolometer consisting of a substrate, heater and thermometer. The bolometer mass was 2 mg and it was connected to a thermal reservoir with four 0.001" diameter Au(7%Cu) wires to provide a heat leak and electrical connections. Our entire system is described in Ref 7. and is approximately equivalent to an a.c. measurement system with a period of 400 S. The measurements were performed from 4 to 15 K both in zero magnetic field and in a field of 0.3 T, and data were recorded at approximately 0.05 K intervals for both sets of measurements.

## RESULTS

A discontinuity in the magnitude of  $C_p$  is apparent in the present data at the superconducting transition of  $T_c \approx 9.4$  K. Data taken with an applied field of 0.3 T shows a similar behavior with a small but measurable downward shift of the peak temperature showing that this peak is indeed due to superconductivity. In these measurements the overall scale is uncertain by  $\pm 10\%$  due to uncertainties in the sample mass and the mass of the grease used to thermally attach the sample to the bolometer. Data taken from Ref. 4 and 5 along with the present data are shown in Figure 2.

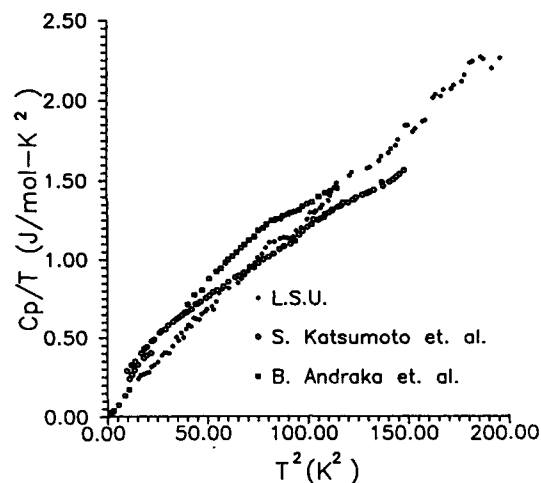


Figure 2.

Specific heat of  $\kappa$ -(BETF-TTF)<sub>2</sub>Cu(NCS)<sub>2</sub> divided by temperature vs. temperature squared in zero applied magnetic field from Ref.4 (circles), Ref.5 (squares), and the present data (stars).

### ANALYSIS

We discuss only the phonon contribution to  $C_p$  because well below  $T_c$  the electronic contribution in the superconducting state rapidly approaches zero, and above  $T_c$  it is small compared to the phonon contribution. The data for the phonon contribution to  $C_p$  were analyzed within the Debye approximation using the following expression:

$$C_p(T) = mnR(T/\Theta_D)^3 3 \int_0^{\Theta_D/T} \frac{dx x^4 e^x}{(1 - e^x)^2}$$

where  $m$  and  $n$  are both integers, the product of which corresponds to the number of independent modes contributing to the specific heat, and  $\Theta_D$  is the Debye temperature. We take  $m$  to be the number of degrees of freedom and  $n$  the number of oscillators per unit cell. In atomic systems,  $m$  is 3 for the three translational degrees of freedom for each oscillator and  $n$  is the number of atoms per unit cell. The temperature dependence of the specific heat can arise through both the  $T^3$  factor and the upper limit of the integral. At temperatures  $< 0.1\Theta_D$  the integral gives a constant value of  $1/3$  and the usual  $T^3$  behavior is observed. If we take the number of atoms per formula unit ( $n = 59$ ) to be the appropriate number of oscillators contributing to  $C_p$  with three translational degrees of freedom ( $m =$



3), then our data is fit at low temperatures with a  $\Theta_D$  of 205 K. This fit is shown in Figure 3a. It should be noticed that above 10 K the data falls appreciably below the  $T^3$  behavior of this fit.

Since the data begins to deviate from the  $T^3$  behavior with smaller values of  $C_p$  than the low temperature fit would predict near 10 K, it appears that the Debye temperature might be less than the 200 K obtained from the low temperature data. The same fit to the low temperature data can be obtained with a lower Debye temperature if the number of degrees of freedom times the number of oscillators contributing to  $C_p$  is reduced keeping  $mn/\Theta_D^3$  constant. In Figure 3b we show a fit to the data with  $mn = 18$  and a  $\Theta_D$  of 95 K. The value of 18 that we have used for this curve is uncertain by 10% due to uncertainties in both the mass of the sample and the subtraction of the heat capacity of the grease used to bind the sample.

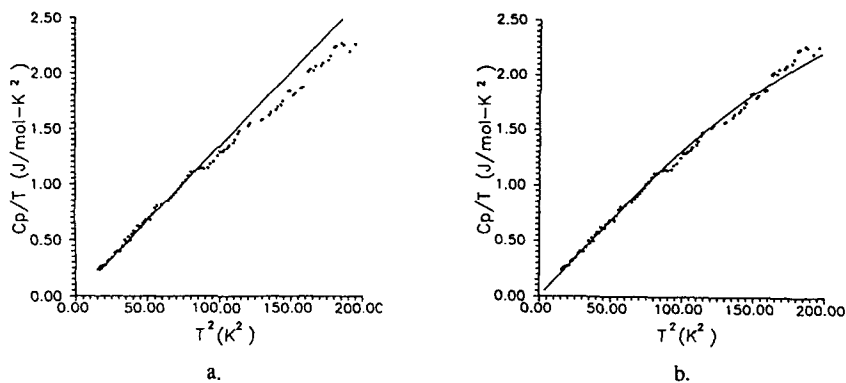


Figure 3

Specific heat of  $\kappa$ -(BETF-TTF)<sub>2</sub>Cu(NCS)<sub>2</sub> divided by temperature vs. temperature squared. In part a. the solid line is a plot of the Debye equation with  $m = 3$ ,  $n = 59$  and  $\Theta_D = 205$  K. In part b. the solid line is a plot of the Debye equation with  $m = 6$ ,  $n = 3$ , and  $\Theta_D = 95$  K.

The low values of  $mn$  and  $\Theta_D$  that give the correct temperature dependence of  $C_p$  above 10 K are indicative of collective modes of vibration for the system. As an example of one possible set of collective modes we give arguments for a value of  $m = 6$  and  $n = 3$  based on the premiss that for low energy excitations the anions and cations act as coupled rigid body oscillators. In each  $\kappa$ -(ET)<sub>2</sub>Cu(NCS)<sub>2</sub> unit cell there are two ET molecules and one Cu(NCS)<sub>2</sub> molecule. Thus, if the two ET molecules and the Cu(NCS)<sub>2</sub> molecule are each acting as rigid body oscillators, then the entire system will have 18 normal modes of vibration:  $3 \times (3 \text{ translational} + 3 \text{ rotational})$ . For this model to be an approximation for the situation in  $\kappa$ -(ET)<sub>2</sub>Cu(NCS)<sub>2</sub> the rotational energy levels must be very closely spaced into a band so that they can be continuously populated in the

temperature range of the measurement. Since the energy separation between rotational levels in a molecule is inversely proportional to the moment of inertia and both the ET and  $\text{Cu}(\text{NCS})_2$  molecules are heavy, it is not unreasonable to assume that they can be treated using a continuum approximation that averages over all of the dispersive branches with small gaps at temperatures above 1 K. In addition, we point out that the normal modes of the two ET molecules are most likely not the pure modes of the individual molecules, but rather the normal modes of the coupled system. Since the two ET molecules are in inequivalent sites in the lattice, there will be a small gap for the coupled modes due to their having different restoring forces even though they have equal masses.

This method of describing the data is similar to that used by Lord, Ahlberg and Andrews [11]. As was pointed out by Westrum and McCullough [12] measurements of specific heat do not give detailed information about the vibrational mechanisms causing the magnitude or temperature dependence of these measurements. For example, one cannot easily infer the density of states for the vibrational modes from specific heat measurements [13]. In particular, for the present measurements the value of  $\Theta_D$  we obtain is not indicative of any one branch of the vibrational spectrum, but is the result of averaging over all of the branches. On the other hand, the low value of  $mn$  is more revealing since it indicates that in the temperature region where the superconducting ordering is occurring collective vibrational modes are dominating the vibrational spectrum. If this material is a BCS superconductor, it may be one or more of these collective modes that are coupling to the conduction electron system to form Cooper pairs.

As an addenda to this argument we note that the data of Pesty et. al. [14] for  $(\text{TMTSF})_2\text{ClO}_4$  between 5 and 12 K can be reasonably well represented by the Debye equation with a value of  $mn = 15$  and  $\Theta_D \approx 70$  K. In this case it is well established that the first excited rotational level in  $\text{ClO}_4^-$  in  $(\text{TMTSF})_2\text{ClO}_4$  is populated near 24 K, the anion ordering temperature. Above 12 K the specific heat in  $(\text{TMTSF})_2\text{ClO}_4$  rises faster than the Debye equation, and is due to the thermal excitations of the rotational states of the anions. From measurements below 1 K, Pesty et. al.<sup>3</sup> note that a  $T^3$  behavior is observed with  $mn = 9$ , indicating that some of the collective modes in this compound are not excited in this low temperature range. Finally, the low temperature specific heat data [15] from a number of organic materials that contain only one molecule per unit cell with known high energy rotational excitations show a value of  $mn = 3$  as would be expected on this model.

The specific heat is rather high at  $T_c$  and our data is not sufficiently accurate to obtain the small electronic contribution to the overall curve from a fitting procedure. However, the ratio of  $T_c$  to  $\Theta_D$  is 0.099 indicating a strong coupling superconductor. Further evidence for strong coupling superconductivity comes from the fact that the specific heat in the superconducting state is back down to the phonon curve at about 70% of  $T_c$ .

rather than the weak coupling value of about 40%. The total entropy change between  $T = 0$  and  $T_c$  for either strong or weak coupling is the same. Because the data comes back to the  $T^3$  curve closer to  $T_c$ , the peak must be higher than the weak coupling case would predict.

We wish to acknowledge helpful discussions with D. A. Browne and financial assistance from the Louisiana Educational Quality Support Fund (1987-90)-RD-B-3.

#### REFERENCES

1. D. Jerome, A. Mazaud, and K. Bechgaard, *J. Physique Lett.*, **42**, L95 (1980)
2. S. S. P. Parkin, E. M. Engler, R. R. Schumaker, R. Lagier, V.Y. Lee, J. C. Scott and R. L. Greene, *Phys. Rev. Lett.*, **50**, 270 (1983)
3. H. Urayama, H. Yamochi, G. Saito, K. Nozawa, T. Sugano, M. Kinoshita, S. Sato, K. Oshima, A. Kawamoto, and J. Tanaka, *J. Chem. Lett.*, **55** (1988)
4. S. Katsumoto, S.-I. Kobayashi, H. Urayama, Hideki Yamochi, and G. Saito, *J. Phys. Soc. Japan*, **57**, 3672 (1988)
5. B. Andraka, J. S. Kim, G. R. Stewart, K. D. Carlson, H.H. Wang, and J. M. Williams, *Phys. Rev. B Rapid Communications*, to be published.
6. H. Urayama, H. Yamochi, G. Saito, K. Nozawa, T. Sugano, M. Kinoshita, S. Sato, K. Oshima, A. Kawamoto, and J. Tanaka, *Chem. Lett.* **55**, (1988)
7. K. D. Carlson, U. Geiser, A. M. Kini, H. H. Wang, L. K. Montgomery, K. Kwok, M. A. Beno, J. M. Williams, C. S. Cariss, G. W. Crabtree, M.-H. Whangbo, and M. Evain, *Inorg. Chem.* **27**, 967 (1988)
8. The authors are indebted to Margaret Blohm and Oliver LeBlanc for providing the sample.
9. S. Gartner, E. Gogu, I. Heinen, H. J. Keller, T. Klutz, and D. Schweitzer, *Solid State Commun.* (1988)
10. Jing-chun Xu and R. G. Goodrich, *Rev. Sci. Inst.*, to be published.
11. R. C. Lord, J. E. Ahlberg and D. H. Andrews, *J. Chem. Phys.* **5**, 649 (1937)
12. E. F. Westrum, Jr., and J. P. McCullough, *Thermodynamics of Crystals*, p. 59
13. J. W. Loram, *J. Phys. C:Solid State Phys.* **19**, 6113 (1986)
14. F. Pesty, P. Garoche, and A. Moradpour, *Mol. Cryst. Liq. Cryst.*, **119**, 251 (1985)
15. M. R. Madison, L. B. Coleman, J. C. Kimball, and R. M. Williams, *Phys. Rev. B*, **25**, 6146 (1982)

PRESSURE DEPENDENCE OF THE STRUCTURAL AND ELECTRONIC PROPERTIES OF ORGANIC SUPERCONDUCTORS.

CHASSEAU D.\*, GAULTIER J.\*, HOUBIB H.\*, RAHAL M.\*, DUCASSE L.\*\*,  
KURMOO M.\*\*\* and DAY P.\*\*\*

\* Laboratoire de Cristallographie et Physique Cristalline, URA 144 CNRS

\*\* Laboratoire de Physico-Chimie Théorique, URA 503 CNRS

Domaine Universitaire de Bordeaux I, 33405 - TALENCE Cédex (FRANCE).

\*\*\* Inorganic Chemistry Laboratory, University of Oxford,  
South Parks Road, OXFORD OX1 3QR (U. K.)

Abstract

The pressure dependence ( $\leq 12 \times 10^2$  MPa) of the cell parameters of  $(\text{TMTSF})_2 - \text{ClO}_4$  and  $\kappa - (\text{BEDT-TTF})_2 - \text{Cu}(\text{NCS})_2$  has been measured at room temperature. The magnitudes of the principal compressibilities calculated and the bulk modulus (B) do not vary all over the experimental pressure range for  $(\text{TMTSF})_2 - \text{ClO}_4$ , while  $k_1$  decrease slightly for  $\kappa - (\text{ET})_2 - \text{Cu}(\text{NCS})_2$  and its bulk modulus strongly increases. The directions of the principal compressibilities strongly vary with pressure for the former salt; in the latter case, the projections of the directions of the smallest and of the largest principal compressibilities remain parallel and perpendicular to the long molecular axis respectively whereas the intermediate is along the monoclinic b axis.

The crystal structures have been refined at  $4 \times 10^2$ ,  $6 \times 10^2$  and  $9.5 \times 10^2$  MPa ( $R = 0.05$ ) for  $(\text{TMTSF})_2 - \text{ClO}_4$  and at  $7 \times 10^2$  MPa ( $R = 0.095$ ) for  $\kappa - (\text{ET})_2 - \text{Cu}(\text{NCS})_2$ . The transfer integrals have been calculated for the two compounds. In  $(\text{TMTSF})_2 - \text{ClO}_4$ , both normal and transverse overlaps strongly increase with pressure; the dimerization is reduced under pressure and the two largest transverse interactions become identical. In  $\kappa - (\text{ET})_2 - \text{Cu}(\text{NCS})_2$ , the intra-dimer interaction strongly increases whereas the variations of the inter-dimer interactions may be very different.

Introduction

Since the first observation [1] of superconductivity in  $(\text{TMTSF})_2 X$  salts ( $\text{TMTSF} = \text{tetramethyltetraselenafulvalene}$ ;  $X^- = \text{PF}_6^-, \text{ClO}_4^-$ , etc), the physical properties of these compounds have been the subject of extensive studies over a wide temperature and/or pressure range. It has been the same for the organic superconductors based on the BEDT TTF donor molecule (BEDT TTF = ET = bis (ethylenedithio) tetrathiafulvalene) since the discovery of the first ambient pressure superconductor of this family in 1984 [2].

The structural properties have been extensively studied in normal conditions, sometimes at very low temperatures [3] but very rarely under high pressure. However, the high pressure ( $6.5 \times 10^2$  and  $9.8 \times 10^2$  MPa) X-ray and the low temperature and high pressure (1.7K,  $7 \times 10^2$  MPa) neutron crystal structures of  $(\text{TMTSF})_2 - \text{PF}_6$  [4,5], and high pressure ( $9.5 \times 10^2$  MPa) X-ray and the low temperature and high pressure (4.5K,  $1.5 \times 10^2$  MPa) neutron structures of  $\beta$  (BEDT-TTF) $_2 - \text{I}_3$  [6,7] have been determined.

In the present paper, we discuss the compressibilities and the pressure dependence of the crystal structures of the first ambient pressure superconductor  $(\text{TMTSF})_2 - \text{ClO}_4$  [8] and of the  $\kappa - (\text{ET})_2 - \text{Cu}(\text{NCS})_2$  salt which shows the highest transition temperature (10.5K) [9] any organic superconductor yet discovered; one particular interest is to compare the evolution of two different kinds of packing.

### Isothermal Compressibility.

a)  $(\text{TMTSF})_2\text{-ClO}_4$  (Fig. 1)

The isothermal compressibility of the  $(\text{TMTSF})_2\text{-ClO}_4$  unit cell has been measured up to  $11.5 \times 10^2$  MPa using the diamond anvil cell [4]. The pressure dependence of the cell dimensions is quasi-linear in the experimental pressure range (Tab. 1) and the ambient pressure linear compressibilities are  $k_a = 0.34 \times 10^{-4}$ ,  $k_b = 0.21 \times 10^{-4}$  and  $k_c = 0.20 \times 10^{-4}$  MPa $^{-1}$ . Cell parameters do not evolve similarly when pressure is increased as when temperature is lowered [3]. However if we only take into account the variation of the volume, its value at 100K (662.2) is nearly the same as at  $5.5 \times 10^2$  MPa (663.2), this value remains almost constant when lowering the temperature down to 7K while it continues to decrease when increasing the pressure.

P 10 <sup>2</sup> MPa	10 <sup>-3</sup>	1.2	3	4.3	5.4	7	8.2	9.6	11.5
a(Å)	7.242	7.238	7.192	7.150	7.121	7.088	7.061	7.020	6.969
b(Å)	7.662	7.652	7.621	7.596	7.580	7.555	7.540	7.519	7.480
c(Å)	13.267	13.250	13.215	13.160	13.129	13.099	13.075	13.040	12.973
$\alpha(^{\circ})$	84.51	84.53	84.51	84.53	84.56	84.61	84.57	84.61	84.67
$\beta(^{\circ})$	86.74	86.72	86.79	86.99	87.08	87.15	87.26	87.35	87.56
$\gamma(^{\circ})$	70.45	70.37	70.33	70.21	70.12	70.05	69.98	69.88	69.66
V(Å <sup>3</sup> )	690.4	687.8	687.7	669.3	663.2	656.4	651.0	643.3	631.0

Table 1: Pressure dependence of the cell parameters for  $(\text{TMTSF})_2\text{-ClO}_4$ .

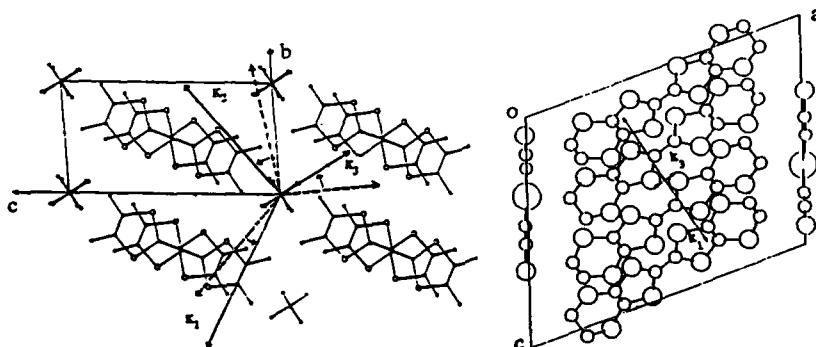


Fig. 1 - Projection of the directions of the principal compressibilities  
 a) along the normal to the molecular plane in  $(\text{TMTSF})_2\text{-ClO}_4$   
 -----  $10^1$  MPa      ———  $9.6 \times 10^2$  MPa  
 b) along b in  $\kappa$   $(\text{BEDT-TTF})_2\text{Cu(NCS)}_2$

The magnitudes and the directions of the principal compressibilities of  $(\text{TMTSF})_2\text{-ClO}_4$  have been derived from the experimental data. The observed anisotropy which is in the ratio (1; 0,51; 0,41) at 0,1 MPa does not vary up to  $11.5 \times 10^2$  MPa because the three principal compressibilities remain constant over the experimental pressure range. On the contrary, for  $(\text{TMTSF})_2\text{-PF}_6$  [4], the ratio is (1; 0,51; 0,23) at ambient pressure and (1; 0,6; 0,4) under  $12 \times 10^2$  MPa; these last values are very similar to that of  $(\text{TMTSF})_2\text{-ClO}_4$ . The direction of the largest compressibility ( $k_1$ ) is offset by  $-28^\circ$  at 0,1 MPa from the chain axis a; this offset is increased to  $35^\circ$  at  $11 \times 10^2$  MPa.  $k_2$  and  $k_3$  remain close to the TMTSF plane.

The bulk modulus  $B = k_v^{-1}$  is found to be  $B = 125 \times 10^2$  MPa at ambient pressure and remains constant. This value, compared with that observed in  $(\text{TMTSF})_2\text{-PF}_6$  ( $B = 100 \times 10^2$  MPa) indicates that  $(\text{TMTSF})_2\text{-ClO}_4$  is less compressible than  $(\text{TMTSF})_2\text{-PF}_6$ . Contrary to the present case, the values of B for the latter compound increase with pressure to reach the same value at  $12 \times 10^2$  MPa and remain nearly constant under larger pressures.

b)  $\kappa - (\text{ET})_2 - \text{Cu}(\text{NCS})_2$

The isothermal compressibility of  $\kappa - (\text{ET})_2 - \text{Cu}(\text{NCS})_2$  unit cell has been measured up to  $13 \times 10^2$  MPa. The pressure dependence of the cell dimensions is quasi linear in the experimental pressure range (Tab.2) and the ambient pressure linear compressibilities are  $k_a = 0.1 \times 10^{-4}$ ,  $k_b = 0.25 \times 10^{-4}$  and  $k_c = 0.36 \times 10^{-4}$   $\text{MPa}^{-1}$ . There is a decrease of the three parameters, which is not the case on cooling; actually, in this case, a remains constant down to 260K and increase below this temperature [12].

P 10 <sup>2</sup> MPa	10 <sup>-3</sup>	2.8	6.8	7.5	9.7	10.7	11.7	12.9
a(Å)	16.228	16.170	16.109	16.138	16.097	16.083	16.069	16.062
b(Å)	8.442	8.368	8.288	8.300	8.264	8.233	8.225	8.193
c(Å)	13.113	12.962	12.810	12.829	12.719	12.681	12.652	12.637
$\beta$ (°)	111.26	110.73	111.16	111.27	111.58	111.67	111.72	111.82
V(Å <sup>3</sup> )	1685	1640	1595	1601	1573	1560	1553	1544

Table 2. Pressure dependence of the cell parameters of  $\kappa - (\text{BEDT-TTF})_2 \text{Cu}(\text{NCS})_2$

The magnitudes and the directions of the principal compressibilities of  $\kappa - (\text{ET})_2 - \text{Cu}(\text{NCS})_2$  have also been derived from the experimental data. The observed anisotropy is in the ratio (1; 0,53; 0,17) under 0,1 MPa and (1; 0,63; 0,16) under  $13 \times 10^2$  MPa. The largest ( $k_1$ ) and intermediate ( $k_2$ ) principal compressibilities show a slight quasi linear decrease with pressure whereas the smallest one ( $k_3$ ) remains quasi constant. The direction of the smallest compressibility ( $k_3$ ) is parallel to the long axis of the molecule and corresponds to the maximum density of atoms, while the largest value  $k_1$  is in the ac plane, parallel to the transverse interactions;  $k_2$  is along the crystallographic b axis (Fig.2).

The bulk modulus B is equal to  $122 \times 10^2$  MPa at ambient pressure and increases to  $191 \times 10^2$  MPa under  $12 \times 10^2$  MPa. Its value at ambient pressure is the same as for  $(\text{TMTSF})_2\text{-ClO}_4$  but its variation under pressure is twice that of  $(\text{TMTSF})_2\text{-PF}_6$ . Thus, this compound, already very difficult to compress, becomes less and less compressible.

Crystal and electronic structures under pressure

a)  $(TMTSF)_2 - ClO_4$ :

The crystal structure has been refined at three different pressures ( $4 \times 10^2$ ,  $6 \times 10^2$  and  $9.6 \times 10^2$  MPa) down to rather good reliability factors (0.045, 0.052 and 0.063 respectively); the standard deviations do not exceed 0.02 Å for the bond lengths of the cation and  $1^\circ$  for its angles; the molecular geometry does not seem significantly modified, except the C=C bonds which are shortened by 0.06 Å from ambient pressure to  $9.6 \times 10^2$  MPa. This increase of the double bond character of these C=C bonds may be characteristic of a progressive charge localization. The  $ClO_4$  anion remains disordered at all pressures as at ambient pressure; nevertheless, according to the slight decrease of the values of the B thermal parameters of the Cl and O atoms, this disorder is reduced.

The structural evolution will be presented in comparison with the 295K, ambient pressure crystal structure described by Rindorf et al. [10].

In the following, we will only deal with the intra- and interstack interactions between cations characterized by the different  $t_{ij}$  et  $t_{ij}$  transfer integrals which have already been defined [11]. The geometrical parameters, such as the Se...Se intermolecular distances and the angles between the Se...Se directions and the molecular plane will be discussed in detail elsewhere [12].

The variations of these integrals with P is shown Fig.2.

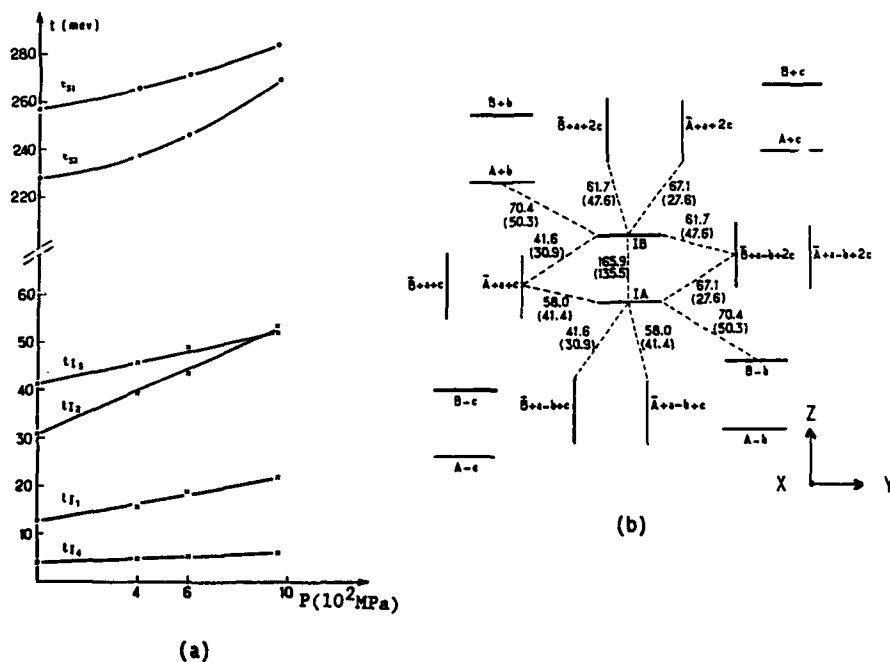


Fig.2: Transfer integrals at various pressures  
 (a)  $(TMTSF)_2 - ClO_4$  (b)  $\kappa - (ET)_2 - Cu(NCS)_2$ : (0,1 MPa) and  $7 \times 10^2$  MPa

Both intrastack  $t_s$  values increase with  $P$  especially  $t_{s2}$ . The dimerization  $t_{s1} - t_{s2}$  decreases only in the pressure range from  $6 \times 10^2$  to  $9 \times 10^2$  MPa; if we compare the temperature effects, we can say that the behaviour which corresponds to a constant dimerization is the same from 300 to 100K and from the ambient pressure to  $6 \times 10^2$  MPa; then the dimerization diminishes in both cases but not according to the same mechanism since in one case the volume, as the  $a$  parameter, does not vary ( $T$ ) and in the other ( $P$ ) it continues to decrease.

The  $t_i$  integrals do not vary with  $P$  in the same way;  $t_{14}$  remains very weak,  $t_{11}$  and  $t_{13}$  slightly increase when the augmentation of the  $t_{12}$  value is very strong. In particular, the  $t_{13}$  and  $t_{12}$  values are equal at  $9,6 \times 10^2$  MPa. In contrast with the intrastack results, the variation of the  $t_i$  values from 300 down to 100K on one hand and from  $10^{-3}$  to  $6 \times 10^2$  MPa on the other hand are quite different.

At 125K,  $t_{11} = -26$ ,  $t_{12} = -56$ ,  $t_{13} = -44$  eV while at  $6 \times 10^2$  MPa  $t_{11} = -19$ ,  $t_{12} = -44$ ,  $t_{13} = 49$  eV [13]. The negative integrals vary much more in the first case while  $t_{13}$  is constant, this result is still true if we compare with the  $9 \times 10^2$  MPa data and the difference in the two behaviours is reinforced at 7K. This difference is well measured by the  $\phi$  angle which gives, in the dispersion energy expression, the deviation from the 1D electronic character [11]; it is found that  $\phi$  is -21 at 300K, -67 at 7K but only -38 at  $9,6 \times 10^2$  MPa. The  $\phi$  angle related to the  $b$  component of the nesting vector  $q$  are shown in Fig.3 under various constraints.

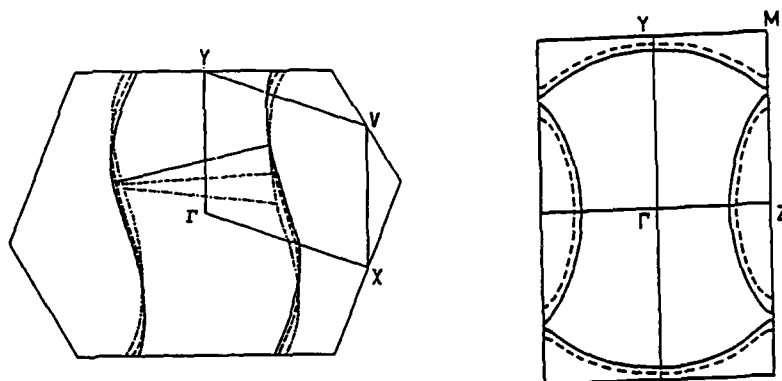


Fig.3: Fermi surfaces  
 a)  $(TMTSF)_2 - ClO_4$  b)  $\kappa - (ET)_2 - Cu(NCS)_2$

b)  $\kappa - (ET)_2 - Cu(NCS)_2$

The crystal structure has been refined at ambient pressure ( $R = 0.05$ ) and at  $7 \times 10^2$  MPa ( $R = 0.095$ ). Due to the thinness of the crystals, we have had to use a twinned crystal and this explains the rather high value of  $R$ . However we can say that the disorder of four  $CH_2$  groups found at ambient pressure still remains under pressure and that the molecules are found to be non planar in both cases.

The values of the different transfer integrals are shown in fig.2 for the two pressures. They show that all of them increase strongly by 10 to 40 meV, this augmentation may not be easily related to some special directions. For example, the variation of the intradimer integral is related to the variations of the  $Z$  value but this simple relation no longer holds for the interdimer interaction along the  $b$  axis; in that case,  $Z$  is constant but both  $X$  and  $Y$  values diminish.

If we compare now orthogonal molecules, the variations are very contrasted because the largest (40meV) as well as the smallest (10 meV)



variations may occur. For both cases, the X, Y and Z coordinates strongly vary.

The 2D character of this compound is enhanced by the pressure effect.

Under pressure, the Fermi surface is displaced isotropically and closer to the Brillouin zone edges; thus the area of the closed orbit varies from 16% at ambient pressure to 12% under  $7,5 \times 10^2$  MPa. (Fig.3).

More details and discussions about the crystallographic and electronic parameters will be given elsewhere [14], in connection with the pressure dependence of the transport properties [15].

### Conclusion

The isothermal compressibility of  $(\text{TMTSF})_2 - \text{ClO}_4$  and  $\kappa - (\text{ET})_2 - \text{Cu}(\text{NCS})_2$  has been calculated from the measurements of the cell parameters by X-ray diffraction under pressure; the results show that both compounds are not very compressible and that this character is constant for the former salt but increases for the latter.

The crystal structures have been refined at various pressures; and the transfer integrals have been calculated. In  $(\text{TMTSF})_2 - \text{ClO}_4$ , both normal and transverse overlaps strongly increase with pressure; the dimerization is reduced under pressure and the two largest transverse interactions become identical. In  $\kappa - (\text{ET})_2 - \text{Cu}(\text{NCS})_2$ , the intra-dimer interaction strongly increases whereas the variations of the inter-dimer interactions may be very different. There are only slight changes in the Fermi surfaces.

### References

1. D. Jerome, A. Mazaud, M. Ribault, K. Bechgaard, J. Phys. Lett., **41**, L95 (1982).
2. E.B. Yagubskii, I.F. Schegolev, V.N. Laukhin, P.A. Kononovich, M.V. Kartsovnik, A.V. Zvarykina, L.I. Buravov, J.E.T.P. Letters, **39**, 12 (1984).
3. B. Gallois, D. Chasseau, J. Gaultier, C. Hauw, A. Filhol, K. Bechgaard, J. Phys. (Paris), **C44**, 1071 (1983).
4. B. Gallois, J. Gaultier, C. Hauw, T. Lamcharfi, A. Filhol, Acta Cryst., **B42**, 564 (1986).
5. B. Gallois, J. Gaultier, F. Bechtel, A. Filhol, C. Vettier, Mol. Cryst. Liq. Cryst., **148**, 279 (1987).
6. V.N. Molchanov, A.P. Shibaeva, V.N. Kachinskii, E.B. Yagubskii, V.N. Simonov, B.K. Vainshtein, Dokl. Akad. Sci. Ussr, **286**, 637 (1986).
7. A.J. Schulz, H.H. Wang, J.M. Williams, A. Filhol, J. Am. Chem. Soc., **108**, 7853 (1986).
8. K. Bechgaard, K. Carneiro, M. Olsen, F.B. Rasmussen, C. Jacobsen, Phys. Rev. Lett., **46**, 852 (1981).
9. H. Urayama, H. Yamochi, G. Saito, K. Nozawa, T. Sugano, M. Kinoshita, S. Sato, K. Oshima, A. Kawamoto, Chem. Lett., **55**, (1988).
10. G. Rindorf, H. Soling, N. Thorup, Acta Cryst., **B38**, 2805 (1982).
11. L. Ducasse, M. Abderrabba, J. Hoarau, M. Pesquer, B. Gallois, J. Gaultier, J. Phys. C. Solid State Physics, **19**, 3805 (1986).
12. D. Chasseau, J. Gaultier, H. Houbib, L. Ducasse, Acta Cryst. B, to be published.
13. L. Ducasse, M. Abderrabba, B. Gallois, D. Chasseau, Synth. Met., **19**, 327 (1987).
14. D. Chasseau, J. Gaultier, M. Rahal, L. Ducasse, M. Kurmoo, P. Day to be published.
15. D. Parker, R.H. Friend, M. Kurmoo, P. Day, C. Lenoir, P. Batail, J. Phys. Condens. Matter, **1**, 4479 (1989).

THIN FILM FORMATIONS OF CHARGE TRANSFER COMPLEXES WITH  
METALLIC PROPERTIES BY VACUUM DEPOSITION METHOD

M.YUDASAKA\*, K.HIRONAGA\*, H.YAMOCHI\*\*, K.NAKANISHI\* AND G.SAITO\*\*

\*Materials Chemistry, Yokohama National University, 156 Tokiwadai,  
Hodogaya-ku, Yokohama 240, Japan\*\*Institute for Solid State Physics, 7-22-1 Roppongi, Minato-ku, Tokyo,  
Japan

## ABSTRACT

Thin films of a charge transfer complex, hepta-(tetrathiafulvalene) pentaiodide (  $TTF_7I_5$ ,  $TTF:I_{0.71}$  ), were prepared by double source evaporation of TTF and iodine. Crystalline films of  $TTF:I_{0.71}$  were obtained when substrate temperatures were kept between  $0^\circ\text{C}$  and  $25^\circ\text{C}$ . Orientation alignment of the crystalline films were affected by supply rate of iodine. By controlling the substrate temperature and the supply rate of iodine, highly oriented crystalline films were grown on mica substrates. It showed strong dichroism and anisotropic electrical properties.

## INTRODUCTION

In utilizing fine characters of organic materials, one of the most potential technics is thin film formation by vacuum deposition. Different from inorganic semiconductors such as Si and GaAs, however, organic materials have a disadvantage in evaporation methods; not a few organic materials decompose by heating before evaporation or sublimation. Polymers and charge transfer (CT) complexes are its examples. Because both polymers and CT complexes have a variety of fine properties, it is a valuable challenge to make their thin films by multi-source evaporation of starting materials (components). The authors have already shown that films of two dimensional copper phthalocyanine polymer and anthracene : pyromellitic acid dianhydride (PHDA) CT complex were available by this method; double source evaporation of Cu and tetracyanobenzene in the former case and that of anthracene and PHDA in the latter[1,2]. This study shows that thin films of  $TTF:I_{0.71}$  are formed by the double source evaporation of TTF and iodine by controlling substrate temperature and supply rate of iodine and that highly oriented  $TTF:I_{0.71}$  films can be grown on mica.

## EXPERIMENTAL

TTF was purchased from Aldrich Chem. Co.. TTF and iodine were coevaporated in a pyrex glass chamber shown in Fig.1. A crucible for TTF evaporation is also shown in Fig.1. Inner two cylinders were made of quartz; upper was for TTF and the lower was for thermocouple which detected temperature of the crucible. The two quartz cylinders were heated by the Nichrome wire wined around them. In the film formation, 1~2mg of TTF was evaporated by raising the temperature of the crucible up to  $50\sim 70^\circ\text{C}$ . Iodine was stored in an iodine source made of pyrex glass tube with one end closed and with the other end open (nozzle,  $0.2\text{mm}\phi$ ). The

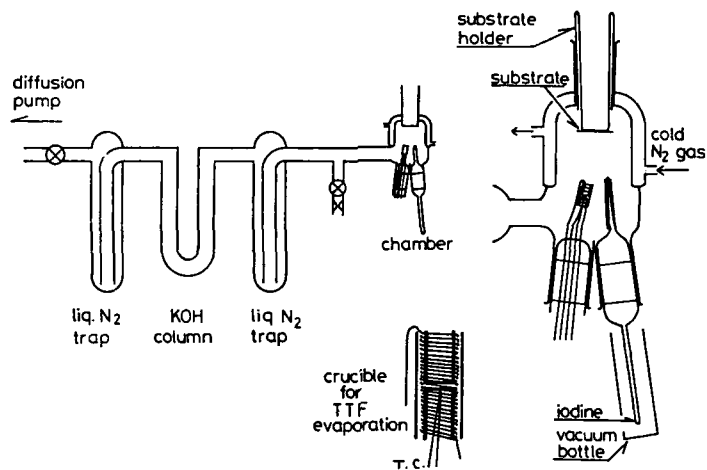


Fig.1 Schematic illustrations of equipments for TTF and iodine double source evaporation.

closed end was dipped in a heat reservoir in order to control supply rate of iodine from the nozzle. The temperature of the reservoir were changed ( $-10^{\circ}\text{C}$ ,  $0^{\circ}\text{C}$  and  $10^{\circ}\text{C}$ ) and studied about the effects of iodine supply rate on the film formation. Deposition substrates were glass plates and mica. Substrate temperatures ( $T_s$ ) were changed between  $-100^{\circ}\text{C}$  and  $30^{\circ}\text{C}$  by controlling temperatures of liquids (water or ethanol) inside substrate holder seen in Fig.1. Thus optimum  $T_s$  for the CT complex film formation could be found. Film formation rates were kept to be between several tens and several hundreds  $\text{\AA}/\text{min}$  and thickness of the deposited films was between  $0.1$  and  $1\mu\text{m}$ . Background pressure during the deposition was about  $3 \times 10^{-5}$  Torr. As is shown in Fig.1, a KOH column and two liquid nitrogen cold traps for trapping iodine.

The films were identified by infrared (IR) absorption spectra, visible absorption spectra and X-ray diffraction analyses.

Temperature dependences of the electrical conductivities were measured by four point probe methodes. The electrodes were thin films of gold evaporated under vacuum.

#### RESULTS AND DISCUSSION

Films obtained by the double source evaporation of TTF and iodine were homogeneous. In Fig.2 are shown the X-ray diffraction patterns of the films formed on glass substrates at various substrate temperatures. Iodine source temperature ( $T(I)$ ) was kept at  $0^{\circ}\text{C}$ . In Fig.2 are also given the indices of the peaks, which are determined with referring to a study of Daly and Sanz[3]. All the peaks seen in Fig.2 are those of TTF: $I_{0.71}$  crystal. (Broad peaks centered around  $24^{\circ}$  in Fig.2 are due to glass substrates.) In addition, IR and visible absorption spectra of the films are consistent with those reported before[4]. It is concluded that TTF: $I_{0.71}$  films can be formed by the double source evaporation of TTF and iodine when  $T_s$  was between  $0^{\circ}\text{C}$  and  $25^{\circ}\text{C}$ . If the substrate temperature was

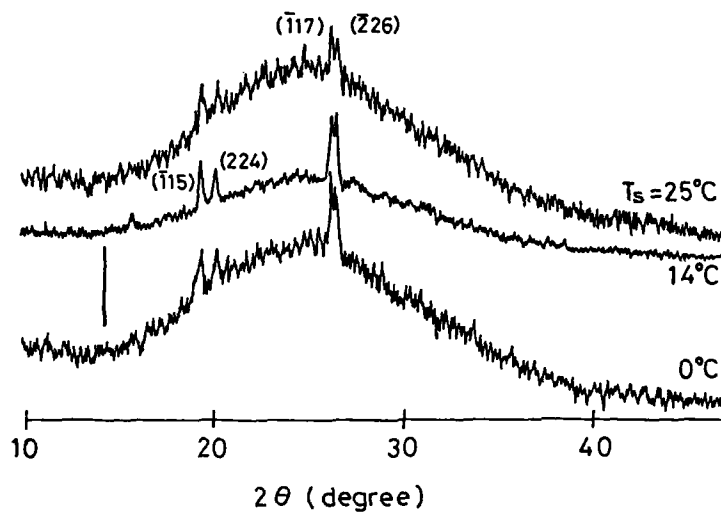


Fig.2 X-ray diffraction patterns of films deposited on glass substrates at different substrate temperatures with keeping iodine source temperature at  $0^\circ\text{C}$ .

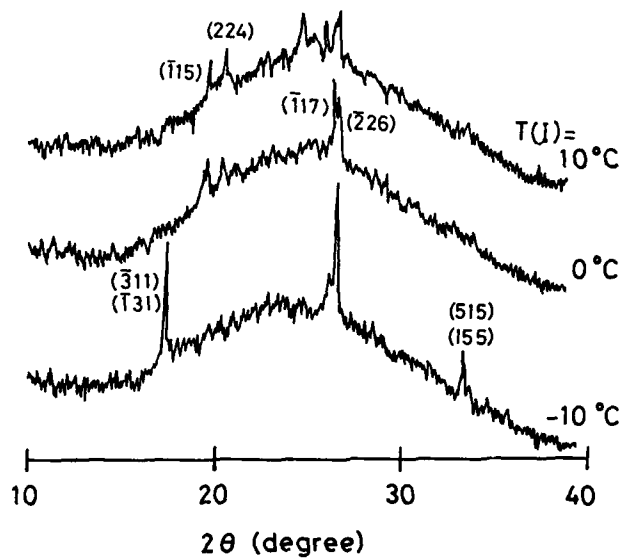


Fig.3 X-ray diffraction patterns of films deposited on glass substrates kept at  $0^\circ\text{C}$  with different temperatures of iodine source,  $T(I)$ .

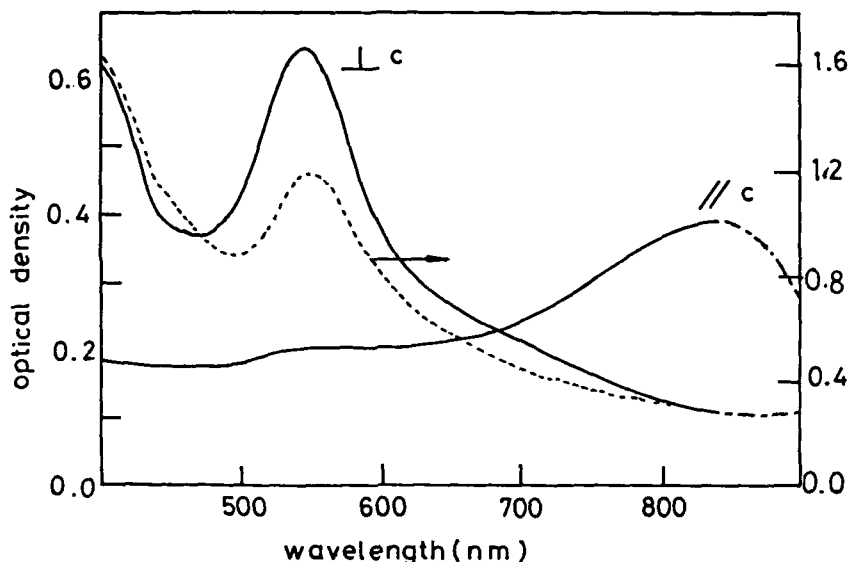


Fig.4 Polarized absorption spectra of TTF:I<sub>0.71</sub> films grown on mica substrates (14°C) with iodine source temperature kept at 0°C (solid lines) and 10°C (dotted line). In the solid line spectra, polarization directions of incident lights are considered to be parallel (indicated by "//c") and perpendicular ("⊥c") with crystal c-axis of TTF:I<sub>0.71</sub> films. In the solid line spectra, optical densities at wavelength larger than 850nm (-----) have about 20% uncertainties because of imperfect polarizing ability of polarizer.

lower than -20°C, uncomplexed TTF was contained within the film. When the substrate temperature was higher than 30°C, nothing was deposited.

It is interesting that TTF or iodine could not be deposited on the substrates with  $T_s > 0^\circ\text{C}$  when they were evaporated individually, that is, the sticking coefficients of TTF and iodine are zero when  $T_s$  is higher than 0°C. The reason why the TTF:I<sub>0.71</sub> film can be deposited on the substrates with  $T_s$  higher than 0°C may be that TTF and iodine particles make fragments of the CT complex on the substrates which are difficult to be re-evaporated from substrates due to larger masses or polarity and so on.

Although the orientations of the deposited films are independent on  $T_s$  in Fig.2, they depend on the supply rate of iodine which is apparent from Fig.3 where are shown X-ray diffraction patterns of the films obtained at different  $T(I)$  with constant  $T_s = 0^\circ\text{C}$ . A mechanism how iodine supply rate affect the film orientation can not be given definitely here; one possible explanation is that the fragments of CT complex born on the substrate are different under different iodine supply rate which leads to variation of the orientation of TTF:I<sub>0.71</sub> complex film.

The effect of iodine supply rate on the orientation of TTF:I<sub>0.71</sub> films appeared remarkably again when mica substrates were used. In Fig.4 absorption spectra of the TTF:I<sub>0.71</sub> films grown on mica kept at constant  $T_s$ , 14°C, with different  $T(I)$ , 0°C and 10°C are presented. The well

oriented film was obtained with  $T(I)=0^{\circ}\text{C}$  and it shows dichroism; two extreme polarized absorption spectra are indicated by //c and  $\perp$ c in Fig.4. Here The incident direction of light was perpendicular with the mica surface and the polarization of //c and  $\perp$ c made a right angle with each other. Comparing these absorption spectra with those in the reference [4], //c and  $\perp$ c spectra are similar to the absorption spectra of a single crystal measured with light polarized parallel with c- and b-axis, respectively. The c-axis of the film is considered to be in the same direction with the polarization direction of the //c spectrum. The absorption band around 830nm is attributed to charge transfer from a TTF<sup>+</sup> ion to a neighbouring TTF<sup>+</sup> ion within a TTF stack. The peak around 545nm is one of local excitation bands of TTF<sup>+</sup> ion[4].

On the other hand, the absorption spectra of the film obtained with  $T(I)=10^{\circ}\text{C}$  did not show any variation by changing the polarization of incident light. The spectrum is shown as dotted line in Fig.4 which has no absorption band around 830nm. This indicates that c-axis of TTF:I<sub>0.71</sub> film stands on the substrate.

For the well oriented film of TTF:I<sub>0.17</sub> obtained at  $T_s=14^{\circ}\text{C}$  with  $T(I)=0^{\circ}\text{C}$ , anisotropic electrical properties were observed. Temperature

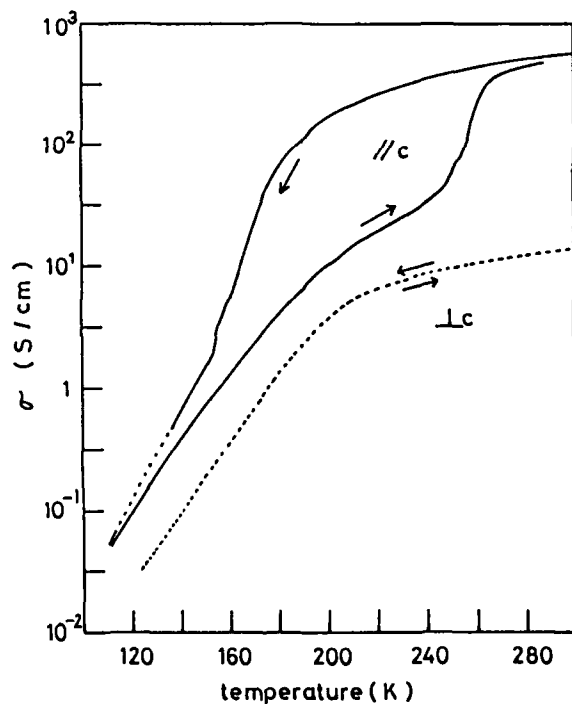


Fig.5 Temperature dependencies of electrical conductivities of TTF:I<sub>0.71</sub> films deposited on mica with substrate temperature kept at  $14^{\circ}\text{C}$  and iodine source at  $0^{\circ}\text{C}$ . The symbols, //c and  $\perp$ c, indicate that currents flow parallel and perpendicular with crystal c-axis of TTF:I<sub>0.71</sub> film, respectively.

dependence of the conductivity parallel with the c-axis is shown as curves of //c in Fig.5. The conductivities around room temperature were between 100 and 1000 S/cm ( Because of uncertainty of the film thickness, the exact value of conductivity could not be determined.) and hysteresis could be seen. These characteristics are well resemble to those of single crystals reported before[5,6]. The high conductivities are believed to be due to hole conduction through TTF columns and a transition to a less conducting state around 200°C seen in the cooling process and the hysteresis has been told to be associated with intrachain interactions[5]. On the other hand, the conductivities perpendicular with the c-axis, indicated as  $\perp c$  in Fig.5, were about 100 times smaller than those of the //c around 300K and no hysteresis could be observed. The results of the  $\perp c$  case are not against the explanation given for the //c conduction introduced above. Careful discussion is necessary on this problem which will be given in the near future.

This study can give one more example to show fruitfulness of multi-source evaporation method for organic thin film formations. Especially, the success of highly oriented film formation indicates that the films made by this method is useful for the study on the properties and for the application of organic materials.

#### ACKNOWLEDGEMENT

The authors would like to appreciate great thanks to Dr. T.Sugano for the valuable discussions on absorption spectra and crystal structure and to Prof. K.Kojima, Prof. M.Tanaka and Mr. H.Tsuyoshi for their kindness. It is a pleasure to thank Dr. T.Sekiya and his coworkers for calculating the X-ray diffraction patterns from the crystal data.

#### References

1. M. Yudasaka, K. Nakanishi, T. Hara, M. Tanaka and S. Kurita, *Synthetic Metals* **19**, 775 (1987).
2. M. Yudasaka and N. Karl, *Thin solid Films*, to be published.
3. J.J. Daly and F. Sanz, *Acta Cryst.* **B31**, 620 (1975).
4. T. Sugano, K. Yakushi and H. Kuroda, *Bull. Chem. Soc. Jpn.* **51**, 1041 (1978).
5. R.B. Somoano, A. Gupta and V. Hadeck, *J. Chem. Phys.* **63**, 4970 (1975).
6. R.J. Warmack and T.A. Callcott, *Phys. Rev. B* **12**, 3336 (1975).

SYNTHESIS, CRYSTAL STRUCTURE AND SPECTROSCOPIC STUDIES OF NEW CHARGE TRANSFER COMPOUNDS OBTAINED BY REACTION OF TTF AND THE POLYOXOANION  $[\text{Mo}_6\text{O}_{19}]^{2-}$ .

C. BELLITTO\*, D. ATTANASIO, M. BONAMICO, V. FARES, P. IMPERATORI, S. PATRIZIO.

Istituto ITSE - C.N.R., Area della Ricerca di Roma, Via Salaria Km. 29.5, C.P.10, I-00016 Monterotondo Staz., (Roma), Italy.

ABSTRACT.

Two different tetrathiafulvalene radical cation salts of the  $[\text{Mo}_6\text{O}_{19}]^{2-}$  polyoxoanion have been isolated and characterized. Compound 1 corresponds to the chemical formula  $(\text{TTF})_3[\text{Mo}_6\text{O}_{19}]$ . The crystal structure shows a 1D stack of the donor TTF molecule, and each stack fits into channels formed by the anions. Within the stack a chain of trimers is identified, the inter-trimeric distance being 3.51 Å. The I.R., electronic and XPS spectra suggest the compound to be a mixed-valence salt. The electrical conductivity at room temperature is  $\sigma = 10^{-4} \text{ } \Omega^{-1} \text{ cm}^{-1}$ . Compound 2 corresponds to the chemical formula  $(\text{TTF})_2[\text{Mo}_6\text{O}_{19}]$ . The compound consists of isolated  $(\text{TTF}^+)_2$  dimers, interspersed with the polyoxoanions. In agreement with this crystal structure the compound is a diamagnetic insulator.

INTRODUCTION.

Low-dimensional synthetic metals based on the one-electron organic donor tetrathiafulvalene, TTF, have studied extensively in the last decade [1]. Less attention has been paid to the TTF - derivatives, where the acceptor molecule is a transition metal complex or an inorganic molecular cluster, possibly in the mixed-valence state. The few examples reported in the literature show interesting electrical and magnetic properties [2,3]. Recently, we have reported a series of organic-inorganic materials made by TTF molecule and square planar inorganic metal (II) 1,2 dithio-oxalato S,S' anions [4]. With the aim of exploring this chemistry we have decided to study the reaction of several donor molecules derived from TTF with the polyoxometalates anions, having general formula  $[\text{M}_6\text{O}_{19}]^{n-}$ , where  $\text{M} = \text{Mo}, \text{W}$  and  $n = 2, 3$ . The present paper reports the preparation, the crystal structures and the spectroscopic properties of two new compounds:



EXPERIMENTAL.

Crystal Growth of  $(\text{TTF})_3[\text{Mo}_6\text{O}_9]$  (1).

A 80 cm<sup>3</sup> U-shaped glass cell with the two electrolytic compartments, separated by a sintered glass wall, porosity G4, was used. The solutions used for the electrosynthesis were previously degassed with argon. The Pt electrodes consisted of 0.5 mm diameter rods for both the anode and for the cathode. The ethylammonium salt of the Mo polyoxoanion (0.080 g) was



dissolved in acetonitrile 70 cm<sup>3</sup>, and 40 cm<sup>3</sup> of this solution was placed in the cathodic compartment. The anodic compartment contained an acetonitrile-1,1,2 trichloroethane solution (30 cm<sup>3</sup>) of neutral TTF (0.020 g) and 10 cm<sup>3</sup> of the acetonitrile solution of the inorganic salt. Electrodes were immersed in the solution, to a depth of 2.5 cm, through air tight stoppers. The synthesis was carried out at d.c. current of 1  $\mu$ A/cm<sup>2</sup> at r.t. for a month. Black shining prismatic crystals were collected at the anode. If the electrosynthesis is carried out by using the butylammonium derivative as a starting material the product isolated was mainly (TTF)<sub>2</sub>[Mo<sub>6</sub>O<sub>19</sub>].

Synthesis of (TTF)<sub>2</sub>[Mo<sub>6</sub>O<sub>19</sub>] (2).

Metathesis reaction under inert atmosphere of acetonitrile solutions of [TTF]<sub>3</sub>[BF<sub>4</sub>]<sub>2</sub> [6] and [NBu<sub>4</sub>]<sub>2</sub>[Mo<sub>6</sub>O<sub>19</sub>] [7] in 1:1 molar ratio immediately give an insoluble, black shiny microcrystalline powder. Crystals suitable for X-ray studies were prepared by a slow diffusion technique. Found : C, 11.19; H, 0.62; S, 19.88; Mo, 44.70; O, 23.60. Calcd. for C<sub>12</sub>H<sub>8</sub>S<sub>8</sub>Mo<sub>6</sub>O<sub>19</sub>: C, 11.23; H, 0.62; S, 21.98; Mo, 44.07; O, 22.03. The analysis was confirmed by the crystal structure determination (see below).

Crystal Data for (TTF)<sub>3</sub>[Mo<sub>6</sub>O<sub>19</sub>] (1).

C<sub>18</sub>H<sub>12</sub>S<sub>12</sub>Mo<sub>6</sub>O<sub>19</sub>, *M* = 1491.94, triclinic, space group *P*1, *a* = 9.961(2), *b* = 10.441(2), *c* = 10.616(2),  $\alpha$  = 72.31(1),  $\beta$  = 101.30(1),  $\gamma$  = 116.48(1)°; *V* = 939.1(3) Å<sup>3</sup>, *Z* = 1, *D<sub>c</sub>* = 2.641 g cm<sup>-3</sup>, *F*(000) = 716,  $\lambda$ (Mo-K $\alpha$ ) = 0.71069 Å,  $\mu$ (Mo-K $\alpha$ ) = 26.18 cm<sup>-1</sup>. Intensities were measured at r.t. on a Nicolet computer-controlled four-circle diffractometer in  $\theta$ - $2\theta$  scan mode,  $2\theta_{\max}$  = 65°. 6605 unique reflections with *I* > 3 $\sigma$ (*I*) were used for structure determination. The structure was solved by Patterson and Fourier methods. Full matrix least squares refinement was used (non-hydrogens anisotropic, hydrogens isotropic); weight *w* = 1/ $\sigma$ (*F<sub>o</sub>*), *R* = 0.026, *R<sub>w</sub>* = 0.033.

Crystal Data for [TTF]<sub>2</sub>[Mo<sub>6</sub>O<sub>19</sub>] (2).

C<sub>12</sub>H<sub>8</sub>S<sub>8</sub>Mo<sub>6</sub>O<sub>19</sub>, *M* = 1288.33, monoclinic, space group *C*2/*m*, *a* = 15.012(3), *b* = 11.115(2), *c* = 8.991(2) Å,  $\beta$  = 91.46(2)°; *V* = 1499.7 Å<sup>3</sup>, *Z* = 2, *D<sub>c</sub>* = 2.854 g cm<sup>-3</sup>, *F*(000) = 1224,  $\mu$ (Mo-K $\alpha$ ) = 29.98 cm<sup>-1</sup>. Intensities were collected up to  $2\theta=80^\circ$ , for a set of 2814 unique reflections with *I* > 3 $\sigma$ (*I*). Only non-hydrogen atoms were refined to *R* = 0.063, *R<sub>w</sub>* = 0.083.

RESULTS.

The compounds reported in this paper were synthesized by an electrocrystallization technique. Conversely, the compound 2 was obtained by a slow interdiffusion of an acetonitrile solution of Wudl's salt, [TTF]<sub>3</sub>[BF<sub>4</sub>]<sub>2</sub>, and of a solution of the corresponding R<sub>2</sub>[Mo<sub>6</sub>O<sub>19</sub>], where R = Et<sub>4</sub>N<sup>+</sup> or Bu<sub>4</sub>N<sup>+</sup>, in the same solvent. Both compounds are insoluble in common solvents.

Crystal Structure of [TTF]<sub>3</sub>[Mo<sub>6</sub>O<sub>19</sub>] (1).

The crystal structure consists of one-dimensional stacks of TTF units along the *b* axis, which fit into channels formed by the

polyoxoanions posed at 0,0,0. The TTF units form centrosymmetric trimers at  $1/2, 1/2, 1/2$  containing two types of independent organic molecules (A and B in the figure 1). The A and B TTF molecules are almost parallel to each other with a  $90^\circ$  rotation in a such a way that a strong overlap between the S atoms inside the trimer occurs, the S...S distances between adjacent molecules being in the range to 3.305(1) - 3.518(1) Å. The trimers are almost parallel to each other but slipped. The inter-trimer separation is 3.51 Å; however the inter-trimer S...S contacts are  $> 4.0$  Å. Only one S...S contact of 3.42 Å has been found between adjacent organic chains. Four quite strong S...O interactions of 3.00 - 3.10 Å occur between anions and cations. The hexamolybdate dianion,  $[\text{Mo}_6\text{O}_{19}]^{2-}$  shows a Lindquist structure [9]: it consists of a compact package of six distorted edge-sharing  $\text{MoO}_6$  octahedra. The three non-equivalent types of oxygens in the  $[\text{Mo}_6\text{O}_{19}]^{2-}$  anion, i.e. 12 bridging oxygens ( $\text{O}_b$ ), 6 terminal oxygens ( $\text{O}_t$ ) and one central oxygen ( $\text{O}_c$ ), form three different types of Mo-O bonds with the Mo atom: the average bond distances and bond angles are very similar to those reported in earlier studies [10,11], i.e. 1.686(3) Å for the  $\text{Mo}-\text{O}_t$ , 1.939(2) Å for the  $\text{Mo}-\text{O}_b$ , and 2.323(2) Å for  $\text{Mo}-\text{O}_c$ .

The TTF molecules are almost planar. The type A TTF molecule shows interatomic distances typical of a TTF<sup>+</sup> [12]: in fact the central carbon-carbon bond length is 1.397(4) Å and the average distance between sulfur and the central carbon atoms is 1.719(3) Å. The corresponding distances found in the type B TTF molecules are 1.373(4) Å for the central C - C and 1.730(3) Å for C - S: such distances indicate a charge  $q = +0.5$  for the type B unit.

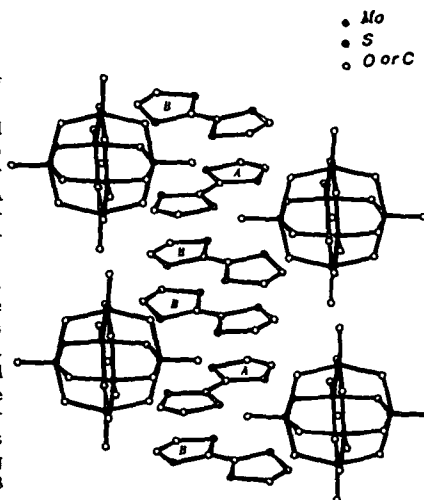


FIGURE 1

#### Crystal Structure of $(\text{TTF})_2[\text{Mo}_6\text{O}_{19}]$ (2).

The crystal structure of compound 2 is represented in fig. 2; centrosymmetrically dimerized TTF molecules lie at the centre of the unit-cell. The molecular structure of the polyoxoanions is essentially identical to that found for compound 1. The TTF<sup>+</sup> units are almost planar and coupled in nearly superimposed dimers, with a longitudinal offset of 0.5 Å, as has been found in fully oxidized  $(\text{TTF})_2[\text{Pd}(\text{S}_2\text{C}_2\text{O}_2)]$  [4]. The interplanar distance between the members of the dimer is 3.43 Å; the short S...S contacts of 3.395(5) and 3.480(5) Å suggest a significant bonding interaction. A positional disorder doubles the sites in which the dimer is located, and this is responsible for the quite high e.s.d.s. on the atomic parameters. The bond length between the central carbon atoms is 1.38(2) Å and the average distance between sulphur and the central carbon atoms is 1.72(1)

A. Therefore the degree of charge transfer cannot be assessed on the basis of these distances alone.

#### Electrical Conductivity.

Preliminary single-crystal electrical conductivity measurements on compound 1 at room temperature show a value of  $\sigma = 1 \times 10^{-4} \Omega^{-1} \text{ cm}^{-1}$ . Compound 2, on the other hand, has been found to be an insulator.

#### X-ray Photoelectron Spectra.

Table I lists the binding energies of Mo 3  $d_{3/2,5/2}$  electrons of the two TTF molybdenum salts and of related Mo(VI) polyoxometalates, as obtained from X-ray photoelectron spectra. The most important feature is that the molybdenum atoms are equivalent and the binding energy is typical of molybdenum (VI). Therefore the data suggest that in both compounds the anion is charged 2-. The S 2p spectra of both compounds have been measured. In both cases, the observed spectra show a peak corresponding to S 2p<sub>3/2</sub> and a shoulder to S 2p<sub>1/2</sub>. In compound 1, the overall f.w.h.m is > 2.0 eV, suggesting the presence of a different type of sulphur atom in agreement with the structural results.

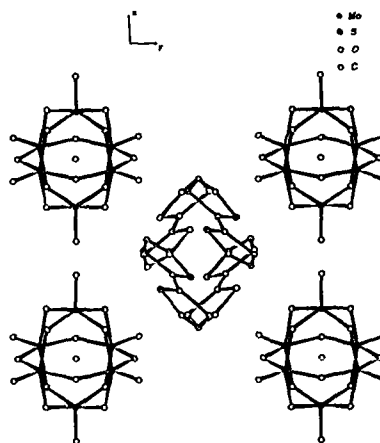


FIGURE 2

In particular, the S 2p peak analysis, obtained by deconvolution, gives two binding energy values, i.e. 164.3 and 165.5 eV (see Table I), with the intensity ratio of the deconvoluted peaks roughly 2 : 1. In compound 2 the deconvolution gives a peak at 165.8 eV, the intensity is 80% of the total area.

Table I. Electron binding energies of [TTF]<sub>n</sub>[Mo<sub>6</sub>O<sub>19</sub>], n = 2, 3.<sup>a</sup>

Compound	Mo		TTF	
	3 $d_{3/2}$	3 $d_{5/2}$	S 2p	
[NET <sub>4</sub> ] <sub>2</sub> [Mo <sub>6</sub> O <sub>19</sub> ]	235.0 (1.9)	232.0 (1.9)	-	
[TTF] <sub>2</sub> [Mo <sub>6</sub> O <sub>19</sub> ]	235.9 (1.4)	232.8 (1.4)	165.5 <sub>b</sub> (80%) <sub>b</sub>	
[TTF] <sub>3</sub> [Mo <sub>6</sub> O <sub>19</sub> ]	235.7 (1.4)	232.6 (1.4)	164.3 (66%)	165.5 (34%)

<sup>a</sup> Energies in eV; full-width at half-maximum (f.w.h.m.) are in parentheses. <sup>b</sup> Percentage of total intensity.

### Optical Spectra.

The powder electronic reflectance spectra of both compounds have been measured at room temperature. The first observation to be made is the presence of a large broad band centered at  $5970 \text{ cm}^{-1}$  in compound 1. This peak, usually labelled band A, is characteristic of mixed-valence compounds [13]. This band is absent in compound 2. In the visible region both compounds show three bands at  $11,900 \text{ cm}^{-1}$  (1.47 eV),  $19,600 \text{ cm}^{-1}$  (2.42 eV) and  $25,600 \text{ cm}^{-1}$  (3.17 eV) respectively. Further, the optical spectrum of the starting polyoxoanion  $[\text{Mo}_6\text{O}_{19}]^{2-}$  shows the first absorption band in the near ultraviolet with a maximum at  $30,769 \text{ cm}^{-1}$  (3.81 eV) [14].

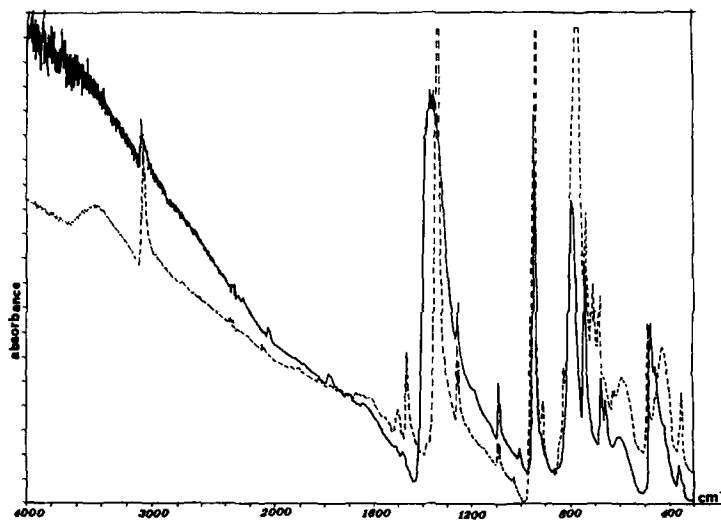


FIGURE 3. Infrared spectra of  $(\text{TTF})_3[\text{Mo}_6\text{O}_{19}]$  (—) and of  $(\text{TTF})_2[\text{Mo}_6\text{O}_{19}]$  (- - -).

### Infrared Spectra.

The IR spectra of compounds 1 and 2 in the  $4,000 - 300 \text{ cm}^{-1}$  region are reported in figure 3. For compound 1 on the tail of the lowest energy electronic band the vibrational absorption lines are superimposed. Typical vibration modes of the polyoxoanion and the donor molecules can be identified and assigned. Five IR bands can be identified as due to the  $[\text{Mo}_6\text{O}_{19}]^{2-}$  anion, i.e.  $942, 790, 597, 430, 353 \text{ cm}^{-1}$  [14]. As far as the TTF molecule is concerned, it is well known that vibrational modes in these CT compounds show a frequency shift that is dependent on the charge occupation of the molecule. The other important information comes from the presence of vibronic lines. These absorptions have been found in both compounds.

This can be related to the irregular structure in compound 1 [16] and to the presence of dimerized  $\text{TTF}^+$  in compound 2 [17]. If we compare the spectra of both compounds (see figure 3) a striking difference in the  $a_g$  mode at  $1348 \text{ cm}^{-1}$  is that in compound 1 the mode is broad, while in compound 2 it is sharp.

#### CONCLUSIONS [18].

Two new CT TTF-derivatives have been isolated and characterized.  $(\text{TTF})_3[\text{Mo}_6\text{O}_{19}]$  is a mixed-valence complex with a 1D stacking of TTF molecules. The structural motif consists of linear-chains of trimers. In projection the TTF molecules inside the trimer are staggered. The compound shows at r.t. an electrical conductivity  $\sigma = 10^{-4} \Omega^{-1}\text{cm}^{-1}$ .  $(\text{TTF})_2[\text{Mo}_6\text{O}_{19}]$  consists of isolated  $(\text{TTF}^+)_2$  dimers interspersed with the polyoxoanion. The compound is an insulator.

#### REFERENCES.

1. See for example: " Extended Linear-Chain Compounds " , ed. J.S. Miller, vol.2, ( Plenum New York 1982).
2. A. Penicaud, P.Batail, C.Perrin, C.Coulon, S.S.P. Parkin, J.B.Torrance, J.Chem.Soc., Chem.Comm. 1987, 330.
3. L.Ouahab, Thèse de doctorat d'état, (1985) Rennes France; L.Ouahab, P.Batail, C.Perrin, C.Garrigou-Lagrange, Mater. Res.Bull., 21, 1223, (1986).
4. C.Bellitto, M.Bonamico, V.Fares, P.Imperatori, S.Patrizio, J.Chem.Soc., Dalton Trans. 1989, 719.
5. V.W.Day, W.G. Klemperer, Science 228, 553, (1985).
6. M.Che, M.Fournier, J.P.Launay, J.Chem.Phys. 71, 1954, (1979).
7. F.Wudl, J.Am.Chem.Soc. 97, 1962, (1975).
8. J.L.Van der Pauw, Philips Res.Rep. 13, 1, (1958).
9. I.Lindquist, Arkiv.Kemi 5, 247, (1952); 7, 49, (1954).
10. O.Nagano, Y.Sasaki, Acta Cryst. B35, 2387, (1979).
11. a. R.Colton, B.F. Hoskins, P.Panagiotidou, Austr.J.Chem. 41, 1295, (1988);  
b. C.D.Garner et. al., J.Chem.Soc., Dalton Trans. 1978, 1582.  
c. H.R.Allcock, E.C.Bissel, E.T.Shawl, Inorg.Chem. 12, 2963, (1973).
12. T.C.Umland, S.Allie, T.Kuhlmann, P.Coppens, J.Phys.Chem. 92, 6456, (1988) and refs. therein.
13. J.B.Torrance, B.A.Scott, B.Welber, F.B.Kaufman, P.E.Seiden, Phys.Rev. B19, 730, (1979).
14. M.T. Pope, Heteropoly and Isopolyoxometalates, ( Spring Verlag, Berlin 1983), p.45.
15. C.Rocchiccioli-Deltcheff, R.Thouvenet, M.Fouassier, Inorg. Chem. 21, 30, (1982).
16. G.Maceno, et al., Synth. Metals 27, B57, (1988).
17. R.Bozio, A.Girlando, I.Zanon, C.Pecile, J.Chem.Phys. 71, 2282, (1979).
18. During the preparation of this paper we were aware of a communication describing a strictly related hexatungstate compound, i.e.  $(\text{TTF})_3[\text{W}_6\text{O}_{19}]$ ; L.Ouahab et al., J.Chem.Soc., Chem. Comm. 1989, 1068.

A NEW SYNTHETIC METAL PRECURSOR: DIMETHYLTETRATHIOTETRACENE  
AND RELATED COMPOUNDS

TOSHIO MARUO, MEGH SINGH, M. THOMAS JONES, NIGAM P. RATH, AND  
DONG MIN  
Department of Chemistry, University of Missouri-St. Louis,  
St. Louis, MO 63121

ABSTRACT

The successful synthesis of dimethyltetrathiotetracene (DMTTT) has been achieved in our laboratory and an account of the details of the synthesis has been reported. Reported herein are studies of the physical properties of DMTTT and some of its chemistry. Both 1:1 and 2:1 DMTTTX charge transfer salts have been prepared and are in the process of being characterized in our laboratory. Comparisons of physical properties and the results of studies such as single crystal x-ray diffraction, solid state ESR spectra, cyclic voltammetry and electrical conductivity are reported. To date, these comparisons reveal considerable similarity between the properties of any given DMTTT charge transfer salt and its corresponding tetrathiotetracene (TTT) charge transfer salt.

INTRODUCTION

The electron donor tetrathiotetracene (TTT) forms charge transfer salts which at room temperature possess some of the highest electrical conductivities of any known synthetic metal (e.g.  $\text{TTT}_2\text{I}_3$  where  $\sigma = 3 \times 10^3$  S/cm) [2-8]. Unfortunately, TTT and its homologs are rather insoluble and hence difficult to purify. In addition,  $\text{TTT}_2\text{I}_3$  undergoes a metal-to-insulator transition at 35K. Thus, the synthesis and characterization of a new synthetic metal precursor, dimethyltetrathiotetracene (DMTTT), and related compounds was initiated. Among the reasons for the synthesis of DMTTT are to obtain a compound with improved solubility and to investigate the question of whether a donor with symmetry  $C_{2v}$  will resist undergoing the metal-to-insulator transition better than the parent compound which has symmetry  $D_{2h}$ .

The details of the synthesis of DMTTT and its chemical characterization are presented elsewhere [1].

CYCLIC VOLTAMMETRY OF DMTTT

Cyclic voltammetric traces for DMTTT and TTT are shown in Figure 1. They demonstrate that in benzonitrile with 0.10 M  $(n\text{-C}_4\text{H}_9)_4\text{NPF}_6$  as the supporting electrolyte and Ag/AgCl as the reference electrode that both materials undergo a two step reversible one electron electrochemical oxidation where the

half wave oxidation potentials for DMITT are more negative than those observed for TIT.

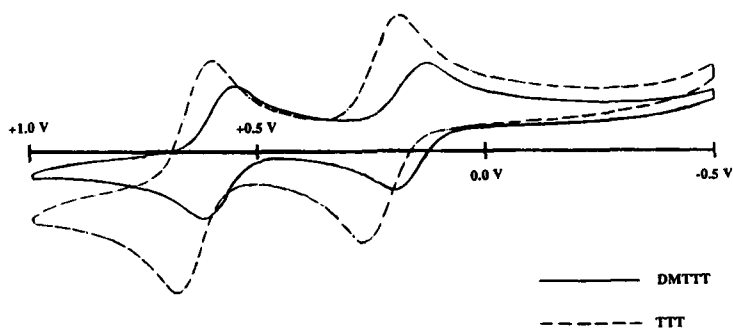


Figure 1. Cyclic Voltammograms of DMITT and TIT

#### ELECTRONIC SPECTRA OF DMITT AND DMITT<sup>+</sup> IN SOLUTION

The electronic absorption spectra DMITT and DMITT<sup>+</sup> dissolved in benzene are shown in Figure 2. The DMITT<sup>+</sup> were prepared by the addition of trifluoroacetic acid to solutions of DMITT.

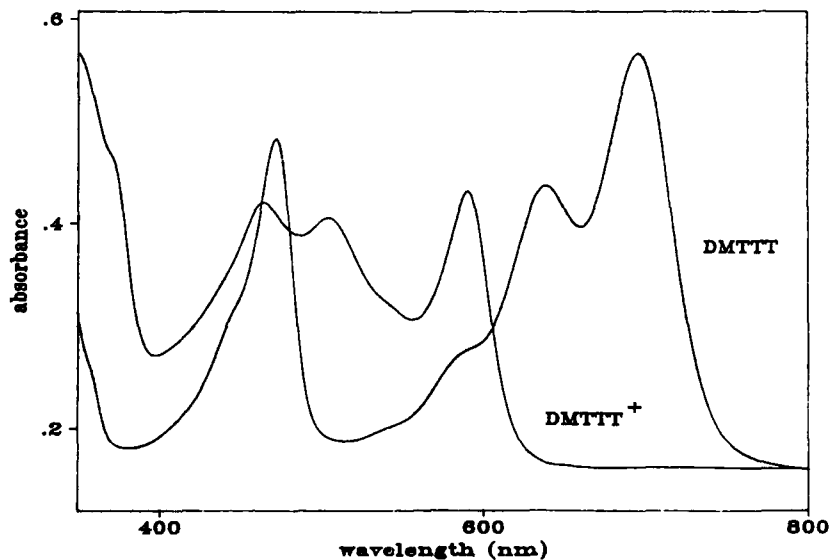


Figure 2. Electronic Absorption Spectra of DMITT and DMITT<sup>+</sup>

### SOLUBILITY OF DMTTT AND TTT

Preliminary measurements indicate that DMTTT is more soluble in monochlorobenzene than TTT which is one of the goals which we had hoped to accomplish. Quantitative measurements are underway and quantitative data will be presented when available.

### SINGLE CRYSTAL X-RAY STUDY OF DMTTT

Single crystal x-ray diffraction studies of neutral DMTTT crystallized from monochlorobenzene provide additional confirmation that DMTTT has been synthesized [9]. The important results of the single crystal x-ray diffraction study are that the DMTTT molecules stack in a pancake fashion within the crystal and that the orientation of the methyl groups alternate such that there is a local center of inversion symmetry between pairs of DMTTT molecules. In addition, one solvent molecule per unit cell is oriented approximately perpendicular to the planes of the DMTTT molecules. Note that the solvent (monochlorobenzene) molecules are disorganized and that the projection of the unit cell down the a axis shown in Figure 3 makes the solvent look as if it is 1,4-dichlorobenzene which it is not. Unit cell data are summarized in Table 1. For comparison, the corresponding information for TTT is given in Table 2 [10].

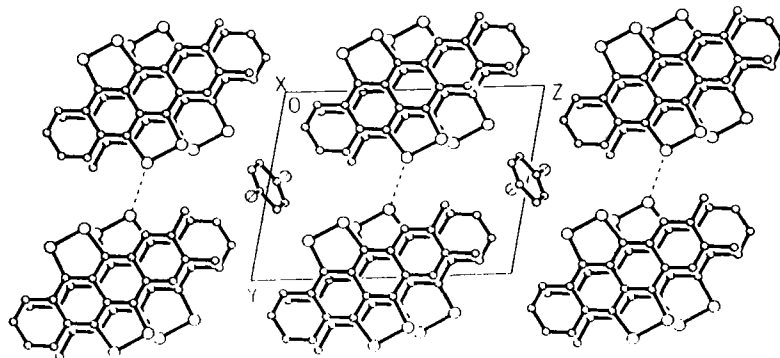


Figure 3. Projection of the bc plane of DMTTT

### PROPERTIES OF DMTTTX

The charge transfer salts DMTTTX, (X = Cl & I), have been prepared using the methods described by Masson et al [7] for the corresponding TTT salts. We have found the use of ESR spectroscopy useful to characterize these solid state salts.



Table 1. Single Crystal X-ray Diffraction Data for DMTTT  
Crystallized from Monochlorobenzene

---

$C_{20}H_{12}S_4$   $1/2C_6H_5Cl$ , Triclinic, Space Group: P1  
 $a = 7.635(1)$ ,  $b = 9.834(1)$ ,  $c = 13.214(2)$  Å  
 $\alpha = 100.39$ ,  $\beta = 101.46$ ,  $\gamma = 93.58^\circ$   
 $V = 951.43$  Å<sup>3</sup>,  $Z = 2$ ,  $\mu = 0.56$  mm<sup>-1</sup>  
 $d_c = 1.525$  g/cm<sup>3</sup>,  $R = 0.047$

---

Table 2. Single Crystal X-ray Diffraction Data for TTT  
Crystallized from Trichlorobenzene

---

$C_{18}H_8S_4$ , Triclinic, Space Group: P1 or  $\bar{P}1$   
 $a = 9.890(6)$ ,  $b = 18.226(13)$ ,  $c = 3.968(15)$  Å  
 $\alpha = 87.63$ ,  $\beta = 79.73$ ,  $\gamma = 96.48^\circ$   
 $V = 699.52$  Å<sup>3</sup>,  $Z = 2$ ,  $\mu = 5.93$  mm<sup>-1</sup>  
 $d_c = 1.65$  g/cm<sup>3</sup>,  $R = 0.13$

---

<sup>a</sup> See reference 10.

#### Esr Spectra of DMTTTX

The solid state ESR spectra of DMTTCl, DMTTI and TTTCl consist of single narrow line spectra (linewidth 11.6 - 13.8 Gauss) which partially reveal the g-tensor anisotropy and are very similar to that observed for TTT<sup>+</sup> in frozen solution reported by Jones et al [6].

#### Electrical Conductivity Measurements of DMTTI

Enough DMTTI has been synthesized and characterized to permit the measurement of its electrical conductivity. The room temperature electrical conductivity of a compressed pellet using the four probe technique is observed to be  $1 \times 10^{-3}$  s/cm. This is very close to the value reported for TTI [2].

#### **FUTURE WORK**

Plans for future work include additional work on DMTT<sub>2</sub>I<sub>3</sub> and the preparation of additional 2:1 charge transfer salts based on DMTT and a broader range of physical studies to better characterize these new materials.

Preliminary attempts to prepare dimethyltetraselenotetracene (DMTSeT) according to the scheme outline here for the synthesis of DMTTT have been successful. However, sufficient quantities have not been obtained to date to fully characterize the product which appears to be contaminated with the diseleno derivative. We will describe our work on DMTSeT more fully at a later date.

#### ACKNOWLEDGEMENTS

The partial support of this study by the University of Missouri through the Missouri Research Assistance Act and of Toshio Maruo through a Mallinckrodt Research Fellowship is gratefully acknowledged. Also acknowledged is the help of Dr. David Pipes of the Mallinckrodt Co. who kindly made the cyclic voltammetry measurements. Also gratefully acknowledged is the help of Professor Bernard Feldman of the Department of Physics at the University of Missouri-St. Louis who made the room temperature electrical conductivity measurements on DMTTTI.

#### REFERENCES

1. T. Maruo, M. Singh, and M. T. Jones, "New Synthetic Metal Precursors: Substituted Tetrathiotetracene and Related Compounds" in Lower Dimensional Systems and Molecular Devices, edited by R. M. Metzger, P. Day and G. C. Papavassiliou, NATO ASI Series B: Physics Vol. ???, Plenum Publishing Co. New York, 1990, In Press.
2. L. I. Buravov, G. I. Zvereva, V. F. Kaminskii, L. P. Rosenberg, M. L. Khidekel, R. P. Shibaeva, I. F. Shchegolev, and E. B. Yagubskii, *J. Chem. Soc. Commun.* 720 (1976); L. C. Iset and E. A. Perez-Albuerna, *Solid State Comm.* 21, 433 (1977); I. F. Shchegolev and E. B. Yagubskii, "Cation-Radical Salts of Tetrathiotetracene and Tetraselenotetracene: Synthetic Aspects and Physical Properties" in Linear Extended Chain Compounds, Vol. 2, pp. 385-434. edited by J. S. Miller, Plenum Press, NY (1982); B. Hilti, C. W. Mayer, E. Minder, K. Hauenstein, J. Pfeiffer, and M. Rudin, *Chemica* 402, 56 (1986).
3. B. Hilti, C. W. Mayer, *Helv. Chim. Acta* 61, 502 (1978).
4. B. Hilti, C. W. Mayer, G. Rihs, H. Loeliger, and P. Paltzer, *Mol. Cryst. Liq. Cryst.* 120, 267 (1985).
5. E. A. Perez-Albuerna, H. Johnson, Jr., D. J. Trevoy, *J. Chem. Phys.* 55, 1547 (1971).
6. M. T. Jones, S. Jansen, L. A. Acampora, and D. J. Sandman, *J. de Phys.* 44C, 1159 (1983).
7. M. Masson, P. Delhaes and S. Flandrois, *Chem. Phys. Lett.* 76, 92 (1980).
8. V. F. Kaminskii, M. L. Khidekel, R. B. Lyubovskii, I. F. Shchegolev, R. P. Shibaeva, E. B. Yagubskii, A. V. Zvarykina, and G. I. Zvereva, *Phys. stat. sol (a)*. 44, 77 (1977).

9. Due to the small size of the crystal, data could be collected only up to  $2\theta_{\max} = 35^\circ$ . Out of a total of 2113 data points collected 566 are observed ( $F_o > 4\sigma F_o$ ). The refinement of all the located atoms goes to  $R_o = 4.7\%$ ,  $R_w = 4.9\%$  (unit weight). Attempts to grow crystals from other solvents for additional x-ray diffraction study are underway in our laboratory.

10. O. Dideberg and J. Toussaint, Acta Cryst. B30, 2481 (1977).

TETRANITROQUINODIMETHANE (TNQ)—ELECTRON-DEFICIENT PROTOTYPE  
FOR A NEW SERIES OF ORGANIC SOLID STATE MATERIALS

DAVID J. VANDERAH, A. T. NIELSEN, R. A. HOLLINS, AND CHRIS BAUM  
Chemistry Division, Research Department, Naval Weapons Center, China Lake, CA  
93555

ABSTRACT

Recently we have synthesized several new aryl compounds substituted with two or more trinitromethyl groups. Vacuum pyrolysis of one of these— $\alpha,\alpha,\alpha',\alpha',\alpha'$ -hexanitro-*p*-xylene (*p*-HNX)—gave the title compound via 1,6-elimination of  $N_2O_4$ . Structural assignment of TNQ is based on spectral evidence (UV,  $^1H$  NMR and mass spectrometry) and conversion to the known 1,4-bis(bromodinitromethyl)benzene. Evidence for the formation of the TNQ radical anion has been obtained.

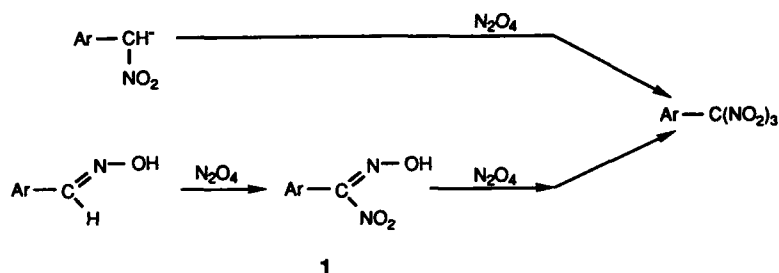
INTRODUCTION

The present work emerged from our continuing synthetic efforts on new highly nitrated energetic materials. A recent endeavor required the preparation of a nitrated benzene ring further substituted with a trinitromethyl group. Although aryl trinitromethyl compounds have been known for some time, relatively few have been reported [1-6]. Furthermore, we know of no reports of aryl rings substituted with more than one trinitromethyl group [7]. Consequently, our synthetic efforts were directed toward the preparation of new aryl compounds substituted with one, two, and three trinitromethyl groups. Although bistrinitromethyl benzenes are of marginal interest as energetic materials [6], the conversion of one such compound— $\alpha,\alpha,\alpha',\alpha',\alpha'$ -hexanitro-*p*-xylene (*p*-HNX)—to the unknown TNQ would clearly be of interest. TNQ, like its better known counterpart tetracyanoquinodimethane (TCNQ), should be a strong electron acceptor molecule and thereby form analogous charge-transfer complexes/radical anion salts. The electrical and/or magnetic properties of these complexes might be enhanced due to the stronger electron-withdrawing nature of the nitro groups of TNQ relative to the cyano groups of TCNQ.

Unsymmetrical quinoid systems substituted at one end with a dinitromethylene group are of interest in other areas, e.g., nonlinear optics [8]. Elimination processes applied to appropriate trinitromethyl-substituted aryl precursors might afford easy access to these compounds.

Synthetic methodology for the preparation of trinitromethyl groups substituted on an aryl ring is limited. As might be expected, direct substitution with nitroform (or its conjugate base) appears to have limited scope [6], due to lack of reactivity or significant side reactions. The most widely employed syntheses are those of Novikov [1,2] as outlined in Scheme 1. The reaction of excess dinitrogen tetroxide on either aryl oximes or nitronate salts of aryl nitromethanes, with heating (50 to 60°C) in the latter stages of the reaction, affords a "one pot" preparation of the trinitromethyl group. In the absence of the heating phase, dinitromethyl-substituted compounds are obtained. Alternatively, if one uses less  $N_2O_4$ , nitrolic acids, 1, are prepared.

Scheme 1



## RESULTS AND DISCUSSION

Synthesis of Trinitromethyl Compounds

For convenience, and based on results of preliminary experiments, we chose aryl oximes as our starting compounds.

The low solubility of terephthalaldehyde bisoxime, 2, in diethyl ether, forced us to modify Novikov's original procedure. The reaction of 2 with  $N_2O_4$  in either *p*-dioxane or sulfolane afforded  $\alpha,\alpha,\alpha,\alpha',\alpha',\alpha'$ -hexanitro-*p*-xylene, 3, as one of many products, eq. 1 and Table I. In addition to 3, we have identified 4 and 5 from the complex reaction mixture. The yield of 3 was substantially affected by the solvent, ranging from poor in *p*-dioxane to fair in sulfolane. An added advantage with sulfolane was that nearly pure 3 was obtained without extensive chromatography. Addition of cold water to the cooled reaction solution gave 3, contaminated only with sulfolane.

At room temperature and protected from light, 3 appears to be stable indefinitely. However, at higher temperatures 3 exhibited increased instability coupled with complex chemistry. During routine capillary melting point determination, the sample was seen to melt/decompose around 126°C. As soon as melt was observed outgassing of  $NO_2$  occurred with simultaneous resolidification. Quantitative thermal analysis (DSC/TGA) indicated loss of 4 moles  $NO_2$ /mole of 3.  $^1H$  NMR (200 MHz) analysis of the solid residue collected from the TGA experiments was consistent for an oligomer of polyphenylene-1,2-dinitrovinylene.

Table I summarizes the rest of our synthesis results. In addition to 3, we have prepared several other new compounds: *m*-HNX, 3,5, $\alpha,\alpha,\alpha$ -pentanitrotoluene, and NNM (the first trinitromethyl benzene compound).

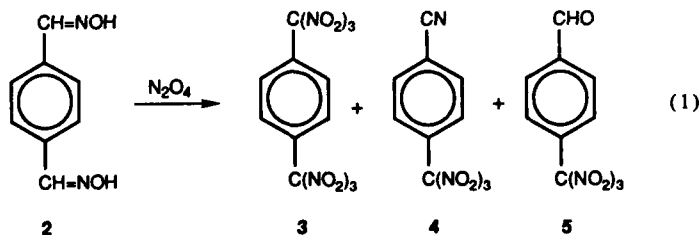


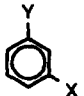
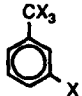
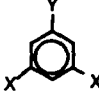
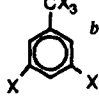

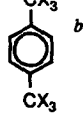
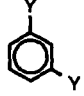
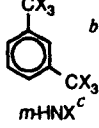
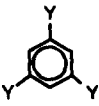
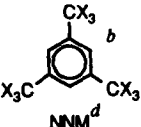


Table I. Yields of Mono-, Bis-, and Trinitromethylbenzenes in Various Solvents.

Reactant <sup>a</sup>	Product	Solvent	Yield (%)
		Et <sub>2</sub> O	20-25
		Et <sub>2</sub> O Sulfolane	20-25 45-50
		<i>p</i> -dioxane	10-20
		Et <sub>2</sub> O <i>p</i> -dioxane Sulfolane	0 3-9 18-22
		Sulfolane	15-20
		<i>p</i> -dioxane Sulfolane	0 3

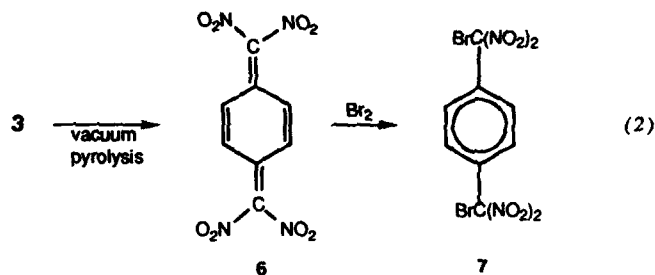
<sup>a</sup>Y = CH=NOH, X = NO<sub>2</sub>; <sup>b</sup>New compounds, <sup>c</sup> $\alpha,\alpha,\alpha,\alpha',\alpha',\alpha'$ -hexanitro-*m*-xylene (*m*-HNX) or 1,3-bis(1,1,1-trinitromethyl) benzene; <sup>d</sup> $\alpha,\alpha,\alpha,\alpha',\alpha',\alpha'',\alpha'',\alpha''$ -nonanitromesitylene (NNM) or 1,3,5-tris(1,1,1-trinitromethyl)benzene.

Mass spectral data for 3 was highly informative and helped direct our subsequent experiments in the preparation of TNQ. A molecular ion for 3 has not been observed [EI, CI (CH<sub>4</sub>, isobutane), FAB]. The highest mass spectral peak appeared at *m/z* 330 (*M*<sup>+</sup> - NO<sub>2</sub>). Prominent peaks at *m/z* 284 and *m/z* 313 (base peak) correspond to *M*<sup>+</sup> - 2 NO<sub>2</sub> and *M*<sup>+</sup> - 2 NO<sub>2</sub> + C<sub>2</sub>H<sub>5</sub>, respectively. The loss of two nitro groups from 3 corresponds to the "formal" formation of TNQ (C<sub>8</sub>H<sub>4</sub>N<sub>4</sub>O<sub>8</sub>; 284).

Due to the relatively easy loss of nitro groups from 3, important analytical data on this compound is still lacking. As a result, a sample was submitted for single crystal X-ray crystallographic analysis which confirmed our structural assignment.

### Conversion of 3 to Tetranitroquinodimethane

Vacuum pyrolysis of 3 (see experimental section) yielded TNQ, 6, as a yellow solid (UV,  $\lambda_{\text{max}}$  402 nm) [eq. 2]. The  $^1\text{H}$  NMR spectrum of 6 displayed a singlet at  $\delta$  5.96 (toluene- $d_6$ ). The stability of 6 is less than that of 3. After several days at room temperature, the still yellow solid was no longer soluble in organic solvents, presumably the result of some kind of polymerization. In polar solvents, the UV absorption at 402 nm would disappear in minutes; however, 6 displayed moderate stability in nonpolar solvents (benzene/toluene). The addition of bromine to 3 in benzene, 7 [9].



Pyrolysis of 3 in which 6 was deposited into a cold ( $-78^\circ\text{C}$ ) toluene solution containing tetrathiafulvalene (TTF), yielded a brown-purple precipitate [10], which displayed a strong maxima at 848 nm in its UV spectrum indicating the formation of the TNQ radical anion [11].

### EXPERIMENTAL

#### $\alpha,\alpha,\alpha',\alpha'$ -Hexanitro-*p*-xylene, 3

To a solution of 10.0 g (0.01 mole) of terephthalaldehyde bisoxime in 500 mL 95% aq. sulfolane at  $4^\circ\text{C}$ , 100 mL neat dinitrogen tetroxide was added over 12 h by slow distillation through an all glass connector. This was followed by a second addition of 50 mL of neat dinitrogen tetroxide all at once. The reaction flask was then heated to  $50$  to  $60^\circ\text{C}$  for 1 h. After recooling to  $3^\circ\text{C}$ , 500 mL of cold water was slowly added which gave 4.2 g (18%) of slightly impure 3 (the major impurity was sulfolane). The aq. sulfolane solution was extracted with ether (3 x 300 mL) which was combined, dried ( $\text{MgSO}_4$ ), and removed under reduced pressure to yield 18 g of a complex mixture which included a small amount of additional 3 along with 4, 5, and other reaction products. Chromatography over silica gel provided pure 3, m.p.  $120$  to  $126^\circ\text{C}$  (dec/polymerization):  $^1\text{H}$  NMR (acetone- $d_6$ )  $\delta$  8.34 (s);  $^{13}\text{C}$  NMR (acetone- $d_6$ ) 131.6, 128.0; CI MS [ $m/z$  (relative intensity)], 330 (52.8), 313 (100, base peak), 285 (44.2), 284 (68.8), 254 (43.2), 238 (34.1), 222 (22.8), 208 (41.0), 175 (11.4), 164 (15.3), 163 (10.1).

#### Tetranitroquinodimethane, 6

Fifty mg of 3 was put into a 6- x 1/2-inch glass tube with female joints at both ends. At one end a tube with a small capillary opening was attached which was, in turn, connected to a tank of argon gas. At the other end another 6- x 1/2-inch tube was attached which was wrapped with heating tape and maintained,

during the experiment, at 300°C—the "hot zone." The outlet end of the "hot zone" was connected to a U-tube which had the bottom of the U immersed in ice-water. The whole system was connected to a vacuum pump and a vacuum of 2 mm Hg was achieved with the argon valve closed. The argon valve was opened and the final vacuum was adjusted to 5 mm Hg. With the argon flowing over the sample, the tube containing the sample was heated to 50 to 70°C by means of a second heating tape. Pure **6** (<sup>1</sup>H NMR assay) accumulated between the "hot zone" and the bottom of the U-tube: <sup>1</sup>H NMR (toluene-d<sub>6</sub>) δ 5.96 (s); CI MS {m/z (relative intensity)}, 313 (83.5), 285 (100, base peak), 284 (53.4), 254 (40.5), 238 (28.9), 222 (25.4), 208 (40.0), 175 (18.5), 164 (16.8), 163 (11.0). Anal. calcd. for C<sub>8</sub>H<sub>4</sub>N<sub>4</sub>O<sub>8</sub> 284.0031, found 284.0029.

#### ACKNOWLEDGMENTS

We would like to express our appreciation to Drs. R. Gilardi, C. George, and J. Flippen-Anderson, Naval Research Laboratory, Washington, DC, for the X-ray crystallographic determination of **3**.

#### REFERENCES

1. S.S. Novikov, L.I. Khmel'nitskii, and O.V. Lebedev, *Isv. Akad. Nauk. SSSR, Otdel. Khim. Nauk.* 1659 (1960).
2. K.I. Khmel'nitskii, S.S. Novikov, and O.V. Lebedev, *Ibid.*, 1873 (1960).
3. L.A. Kaplan, *The Chemistry of Nitro and Nitroso Groups*, edited by H. Feuer, (Interscience, New York, 1970), Pt. 2, Ch. 5.
4. S.S. Novikov, L.I. Khmel'nitskii, T.S. Novikova, and O.V. Lebedev, *Khim. Getero. Soed.*, 6, 543 (1970).
5. S.S. Novikov, L.I. Khmel'nitskii, T.S. Novikova, O.V. Lebedev, and L.V. Epishina, *Ibid.*, 6, 619 (1970).
6. R. J. Spear and W.S. Wilson, *J. Ener. Mater.* 2, 61 (1984).
7. H. Feuer visited the Peking Institute of Technology, China in 1982. The preparation of a number of bistrinitromethyl aryl compounds, including 1,4- and 1,3-bis(1,1,1-trinitromethyl)benzene was alleged; private communication to A.T. Nielsen. However, this work has not appeared in the literature and these compounds are regarded as unreported.
8. D. Li, M. A. Ratner, and T. J. Marks, *J. Am. Chem. Soc.* 110, 1707 (1988).
9. G.L. Rowley and M.B. Frankel, *J. of Chem. and Eng. Data* 14, 507 (1969).
10. This material has not been fully characterized.
11. J. S. Miller and A. J. Epstein, *Angew. Chem. Int. Ed. Engl.* 26, 287 (1987)



Electron Paramagnetic Resonance Studies of Donor-Acceptor  
Salts in Polymer Media

YANG-CHENG FANN AND SUSAN ANN JANSEN

Department of Chemistry and Materials Science, Temple University,  
Philadelphia, Pa. 19122

ABSTRACT:

Charge transfer complexes, their inherent electrical conductivity, magnetic properties and donor-acceptor redox relationships have been a focus of much research in the last several years. One direction has been in the design of memory devices and applications in molecular electronics.<sup>1,2</sup> Our work has focused on analysis of such processes in a polymeric medium. Polycarbonate films of 7,7',8,8'-Tetracyanoquinodimethane (TCNQ) and o-tolidine (o-T) complexes were studied by EPR spectroscopy from 100-300K. EPR spectra and magnetic susceptibility of the dispersed charge-transfer complexes are presented and compared with the pristine materials. These studies were carried out as a function of donor/acceptor stoichiometry and concentration within the polymer matrix. Saturation studies show significant differences as the composition varies. In addition the g-tensor and linewidth are strongly dependent on temperature and composition.

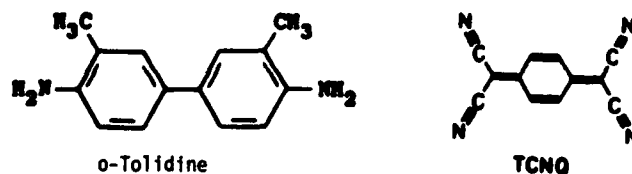
EXPERIMENTAL:

The materials studied are described in the table I below:

Table I. o-T:TCNQ	Formulation for each Salt
1:1	Pristine
1:2	1% by weight in polycarbonate
2:1	10% by weight in polycarbonate

Cyclic voltammetry, CV, (IBM EC-225) and electron paramagnetic resonance, EPR, (Bruker ER-200) and optical microscopy were used to characterize the pristine and dispersed samples.

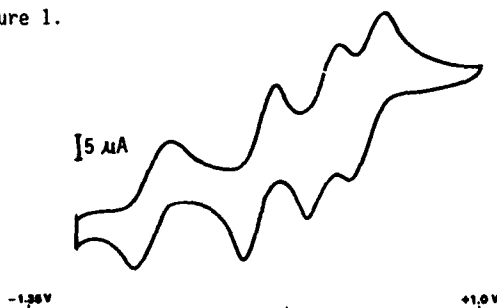
The structures for o-tolidine and tetracyanoquinodimethan are shown below:



## RESULTS AND DISCUSSION:

The CV studies have shown that the complexation of the o-T and TCNQ provides a multi-redox chemical system which can undergo a quasi-reversible four electron oxidation. Figure 1 shows the CV trace of the the pristine 1:1 complex in a 1:1 solvent mixture of THF and acetonitrile. Table II shows the redox potentials measured for the complexes listed above which are similar to those previously reported for simple complexes of TCNQ.

Figure 1.



CV trace for o-T/TCNQ measured at a scan rate of 50 mv/sec, using a glass carbon electrode in 0.1 M tetramethylammonium tetrafluoroborate. A Pt electrode was used as the reference.

Table II. Redox Potentials in volts for o-T/TCNQ Complexes.

	$E_1$	$E_2$	$E_3$	$E_4$
TCNQ	-0.28	-0.88	-	-
o-Tolidine	0.18	0.43	-	-
TCNQ-oT=1:1	-0.71	-0.15	0.19	0.41
TCNQ-oT=1:2	-0.80	-0.18	0.16	0.34
TCNQ-oT=2:1	-0.76	-0.16	0.17	0.36

EPR studies have shown the presence of two distinct magnetic species. These were resolved by a saturation/population study. The species can be described as (1) a fixed nitrogen radical and (2) an exchange coupled magnetic species. The former saturates easily and is not identifiable at high microwave power levels. The other species shows magnetic exchange as observed in many charge transfer complexes based on TCNQ and is attributed to formation of a charge transfer complex. Both species are observed in the 1% and 10% films for all stoichiometries, however the pristine powder exhibits a single exchange narrowed line. Figure 2 shows the spectra of the 1:1 complex dispersed in polycarbonate at 1%.

Our molecular orbital calculations<sup>5</sup> on the o-T component have shown that the orbital containing the unpaired electron has a large nitrogen component. Figure 3 shows the spectrum of the fixed radical obtained from spectral subtraction with the hyperfine anisotropy being as expected for a fixed nitrogen radical.

Figure 2.

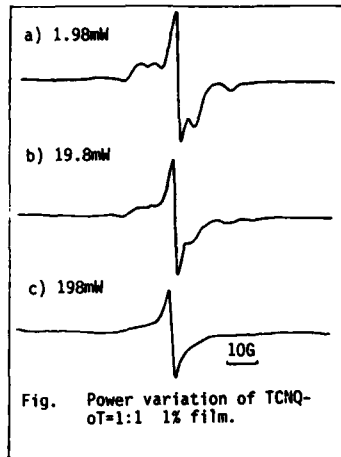


Figure 3.

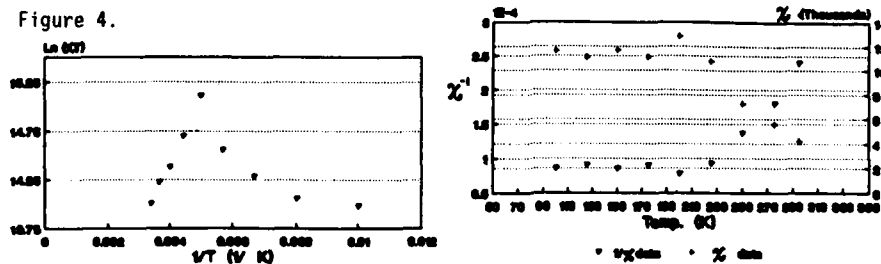


Fig. TCNQ-oT=1:1 1% film : subtraction of the low power ( 1.98 mW ) spectrum from the high power ( 198 mW ) spectrum.

The g-values measured from the 1% and 10% films are strongly power dependent and tend toward a fixed value. This dependence is believed due to differential population of two distinct magnetic species displaying extrema in relaxation properties.

Relative magnetic susceptibility measurements provide consistent information and further substantiate the conclusion that multiple magnetic species are present. The discussion here will be limited to the 1:1 complexes for the sake of brevity. At low microwave powers, 2-10 milliwatts, the magnetic susceptibility appears dominated by fixed sites and follows a Curie-type susceptibility. At high power (198 milliwatts) and low temperature an activated species appears present. Such activation, typically derived from singlet-triplet processes, have been identified in several TCNQ complexes. The activation associated with this region is ca. 0.20 eV. At roughly 200K a discontinuity in the magnetic susceptibility is observed. The effect is shown in Figure 4.

Figure 4.



Optical microscopy studies were performed to ascertain the level of mixing and miscibility of the o-T/TCNQ complex in the polycarbonate. The results of this proved very interesting. At concentrations ca. 1%, a

solid solution of the charge transfer agent and polycarbonate is formed. At higher concentrations, ca. 10%, two types of crystallites are formed within the polymeric network. In addition, these crystallites are arranged in "regularly" spaced aggregates with the spacing distance being on the order of 0.16 microns. This is described further in reference 6. Figure 5 shows the aggregate arrangement in the polycarbonate film. Figure 5.



#### CONCLUSION:

This work has demonstrated that simple charge transfer salts can be doped at significantly high concentrations in a polymeric medium without disrupting all correlated phenomena. The magnetic exchange is preserved in both the low concentration solid solution and high concentration aggregate films. Future work will focus on further characterization of the magnetic properties, explicit measurements of the resistivity within the films and elucidation of structural features on the molecular level with emphasis on structural analysis of the crystallites within the aggregates.

#### REFERENCES:

1. K. Suga, S. Fujita, and M. Fujihira, *J. Phys. Chem.* **93**, 392(1989).
2. G. Inzelt, J.Q. Chambers, J.F. Kinstle, and R.W. Day, *J. Am. Chem. Soc.* **106**, 3396(1984).
3. G. Inzelt, R.W. Day, J.F. Kinstle, and J.Q. Chambers, *J. Phys. Chem.* **87**, 4592(1983).
4. See for example: D. A. Dixon J. C. Calabrese, and J. S. Miller, *J. Phys. Chem.* **93**, 2284(1989); *ibid.*, **91**, 4344(1987); S. D. Obertelli, R. H. Friend, A. J. Moore, M. R. Bryce, and P. Bates, *Synthetic Metals*. **27**, B327(1988); M.T. Jones, S.A. Jansen, J. Roble, and G.J. Ashwell, *Mol. Cryst. Liq. Cryst.* **120**, 111(1985).
5. R. Hoffmann, *J. Chem. Phys.* **39**, 1397(1963); R. Hoffmann, and W. M. Lipscomb, *ibid.*, **36**, 3179(1962); *ibid.*, **37**, 2872(1962).
6. S. A. Jansen and Y. C. Fann, intended for *J. Phys. Chem.*

**STUDIES ON THE FORMATION OF SWITCHING AND MEMORY STORAGE  
MATERIALS CONSTRUCTED FROM METALLO-ORGANIC  
CHARGE-TRANSFER COMPLEXES**

**HAILING DUAN AND DWAIN O. COWAN**

Department of Chemistry, The Johns Hopkins University, Baltimore,  
MD 21218

**JEROME KRUGER**

Department of Materials Science and Engineering, The Johns Hopkins  
University, Baltimore, MD 21218

**ABSTRACT**

Electrochemical measurements have been employed to study the formation process of the charge-transfer complexes  $\text{Cu}^+\text{TCNQ}^-$ , a switching and memory material, in a saturated  $\text{TCNQ}/\text{CH}_3\text{CN}$  solution. These studies show that the  $\text{Cu}/\text{Cu}^+\text{TCNQ}^-(\text{s})$ ,  $\text{TCNQ}^0(\text{CH}_3\text{CN})$  system is an active-passive system corroding under diffusion control. A possible mechanism of localized corrosion-crystallization is proposed for the formation of a  $\text{Cu}^+\text{TCNQ}^-$  film in an acetonitrile solution

**INTRODUCTION**

Studies on  $\text{Cu}^+\text{TCNQ}^-$  charge-transfer complexes as a switching material have been reported for about ten years [1-6]. These materials are chemically prepared by directly reacting Cu metal with TCNQ in an acetonitrile solution. A spontaneous redox reaction is believed to occur generating the charge-transfer complexes  $\text{Cu}^+\text{TCNQ}^-$  [1]:



However, it is still unclear how the  $\text{Cu}^+\text{TCNQ}^-$  film is formed on a Cu surface, or what the mechanism is for this redox reaction. Nor is it understood how the formation process is influenced by film growth parameters. Understanding these questions will provide information for the preparation of  $\text{Cu}^+\text{TCNQ}^-$  switching materials in a controlled manner, via chemical modification and/or altering the film growth parameters, and for producing new charge-transfer complex films from different donors and/or acceptors under different conditions. This information, in turn, may help in fabricating a switching device with desired switching characteristics.

SEM studies [7] strongly indicate that the film formation process is a localized corrosion process. To study the corrosion reaction mechanism, electrochemical methods were used to measure the corrosion potential of  $\text{Cu}/\text{Cu}^+\text{TCNQ}^-(\text{s})$ ,  $\text{TCNQ}^0(\text{CH}_3\text{CN})$  system and its Tafel polarization.

## EXPERIMENTAL AND RESULTS

All the electrode potentials reported in this paper were measured vs. a Ag/AgNO<sub>3</sub> (0.01F) reference electrode [8] through a salt bridge of 0.1M tetrabutylammonium fluoroborate (TBA·BF<sub>4</sub>)/CH<sub>3</sub>CN. A Pt wire was used as the counter electrode. A Cu disc 5mm in diameter was used as the working electrode, which was mechanically polished and cleaned with high purity water and acetone before each measurement. The cell solution was 0.1M TBA·BF<sub>4</sub>/CH<sub>3</sub>CN saturated with TCNQ. TBA·BF<sub>4</sub> was used as a supporting electrolyte.

The corrosion potential vs. time curves measured on a Cu disc electrode are shown in Fig. 1. We started with a clean Cu disc electrode and measured its corrosion potential with the growing of the Cu<sup>+</sup>TCNQ<sup>-</sup> film under either static (a) or rotating (b) conditions. Two significant differences between Fig. 1(a) and (b) are: (1) the steady corrosion potential moved in a positive direction of about 300mV when the electrode was rotated; (2) the corrosion potential reached its steady state more rapidly in the rotation case (about 190 sec, comparing with 2690 sec in the static case). A more uniform, finer and tighter Cu<sup>+</sup>TCNQ<sup>-</sup> film was observed on the Cu electrode in the rotation case.

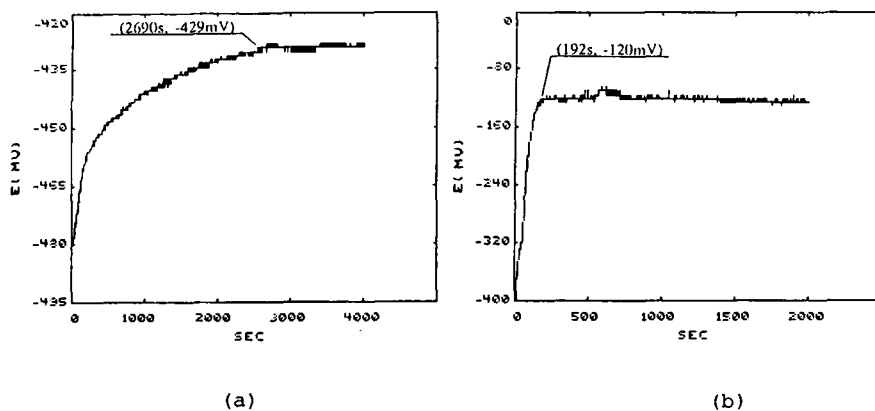


Fig. 1 Corrosion Potential vs. time measured on a Cu disc electrode in a TCNQ/CH<sub>3</sub>CN solution; (a) was measured under static condition; (b) was measured with the electrode rotating at 2000 r.p.m.

The polarization behavior of a Cu disc electrode in a TCNQ/CH<sub>3</sub>CN solution under both static and flowing conditions is shown in Fig. 2. In the static case, Fig. 2(a), the cathodic current density was limited to ca. 500 $\mu$ A/cm<sup>2</sup>, and the anodic passivation current density was about 10,000 $\mu$ A/cm<sup>2</sup> (more than one order of magnitude larger than that of the cathodic). In the rotation case (Fig. 2(b)), however, the cathodic current density was increased by more than one order of magnitude and was not limited up to the polarization of more than -500mV; in addition, the extent of anodic passivation was more obvious and the passivation current density was substantially decreased to ca. 200 $\mu$ A/cm<sup>2</sup>, a drop of almost two orders of magnitude.

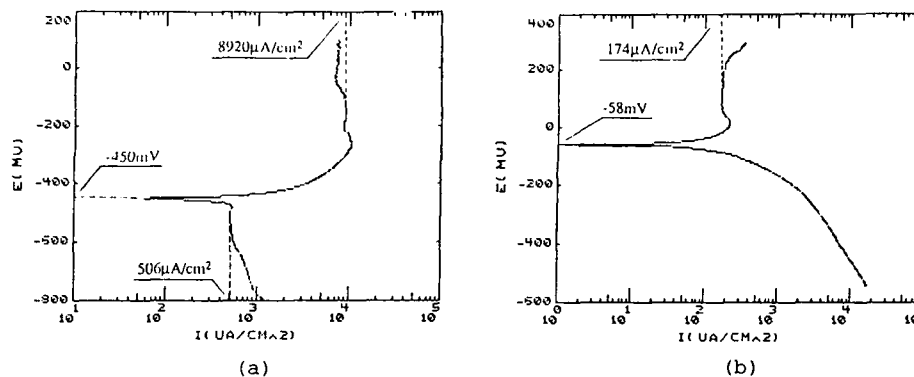


Fig. 2 Tafel polarization of a rotating Cu disc electrode in a TCNQ/CH<sub>3</sub>CN solution; (a) was measured under static condition; (b) was measured with the electrode rotating at 2000 r.p.m.

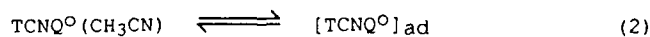
## CONCLUSIONS AND DISCUSSION

Fig. 2 shows that the cathodic diffusion is the rate limiting process for the corrosion of Cu by TCNQ in an CH<sub>3</sub>CN solution. Rotation has two effects on the formation process of a Cu<sup>+</sup>TCNQ<sup>-</sup> film: one is the elimination of the cathodic diffusion limitation (the one order of magnitude increase in the cathodic limiting current density); the other is the enhancement of the anodic passivation (the two orders of magnitude decrease in the anodic passivation current density). Both of these effects contribute to the 300mV increase in the steady corrosion potential under the rotating condition (Fig. 1). Since the decrease of the observed anodic passivation current density is caused by the reduction of the effective anodic area due to the formation of a Cu<sup>+</sup>TCNQ<sup>-</sup> film, the substantial drop of the observed anodic current density in Fig. 2(b) implies that a tighter and more uniform Cu<sup>+</sup>TCNQ<sup>-</sup> film with higher surface coverage is obtained under the rotating condition; this is consistent with our direct observations during the experiment.

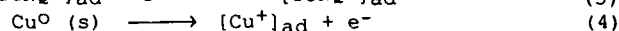
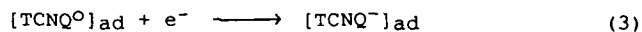
As a conclusion, the overall corrosion behavior for the Cu/Cu<sup>+</sup>TCNQ<sup>-</sup>(s), TCNQ<sup>0</sup>(CH<sub>3</sub>CN) system may be summarized as an active-passive system corroding under cathodic diffusion control. In the flowing condition, cathodic diffusion limitation is eliminated, and a tighter, finer and more uniform Cu<sup>+</sup>TCNQ<sup>-</sup> film is obtained.

Based on the electrochemical studies, we propose the following mechanism of localized corrosion-crystallization for the formation of Cu<sup>+</sup>TCNQ<sup>-</sup> charge-transfer complexes in a TCNQ/CH<sub>3</sub>CN solution (Fig. 3):

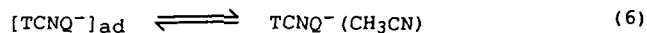
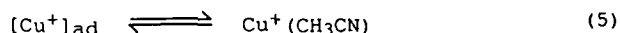
- (1) Diffusion of the oxidant TCNQ<sup>0</sup> from the bulk solution to the Cu surface (into the tight double layer); this is the rate limiting process:



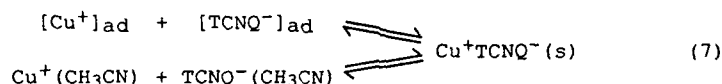
(2) Charge transfer:



(3) Diffusion of the charge transfer products into the bulk solution (perhaps as ion-pairs):



(4) Crystallization of  $\text{Cu}^+\text{TCNQ}^-$  forming a new phase:



There are two sources of  $\text{Cu}^+$  and  $\text{TCNQ}^-$  for the formation of the new phase: one is the surface migration of the redox reaction products inside the tight double layer, the other is the precipitation of the charge-transfer salt from the solution due to its low solubility. They are two competing processes. The former is favoured under flowing conditions. Crystals formed in this case tend to be needle type with larger surface coverage, while crystals formed in the latter case tend to be rectangular with lower surface coverage. These two forms of crystals have been observed in our SEM studies [7].

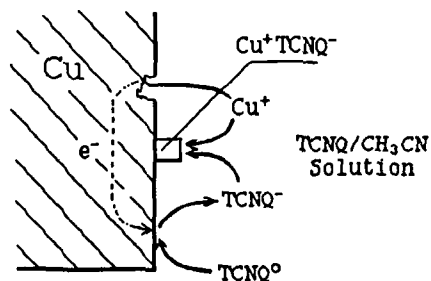


Fig. 3 Sketch of the reaction mechanism of Cu with TCNQ in an  $\text{CH}_3\text{CN}$  solution.

#### ACKNOWLEDGMENTS

We thank M. D. Mays for valuable discussions and comments on this work. We are grateful for the use of facilities of the corrosion laboratory of the Johns Hopkins University. This work was supported by the National Science Foundation-Solid State Chemistry Program grant DMR-8615305.



## REFERENCE

- 1 R. S. Potember, T. O. Poehler, and D. O. Cowan, *Appl. Phys. Lett.* 34(6), 405 (1979).
- 2 R. S. Potember, T. O. Poehler, D. O. Cowan, F. L. Carter, and P. Brant, Chapter VI, *Molecular Electronics Device*, (Marcel, Dekker, Inc., New York, 1983).
- 3 R. S. Potember, T. O. Poehler, and R. C. Benson, *Appl. Phys. Lett.* 41(6), 548 (1982).
- 4 E. I. Kamitsos, and W. M. Risen, Jr., *Mol. Cryst. Liq. Cryst.* 134, 31 (1986).
- 5 R. S. Potember, R. C. Hoffman, and T. O. Poehler, *Johns Hopkins APL Technical Digest* 7(2), 129 (1986).
- 6 H. Duan, M. D. Mays, and D. O. Cowan, *Synthetic Metals* 28, C675 (1989).
- 7 To be published.
- 8 B. Kratochvil, E. Lorah, and C. Garber, *Analy. Chem.*, 41(13), 1793 (1969).

PHYSICAL CHARACTERIZATION OF ORGANIC RADICALS  
BY LOW-FIELD EPR SPECTROMETRY

MEHDI MOUSSAVI; MARC BERANGER; DENIS DURET; NELLY KERNEVEZ and  
LILIANE SECOURGEON  
LETI, A Division of CEA. CENG 85 X 38041 GRENOBLE, FRANCE

ABSTRACT

A low-field (0.6 Gauss, 2 MHz) EPR spectrometer providing quantitative parameters is described. It gives informations such as frequency dependence of the linewidth, anisotropy of inhomogeneous line and also the values of  $T_1$ ,  $T_2$  and the magnetic susceptibility using simple hypothesis.

The behaviour of different typical  $\pi$ -systems, as well metallic as semi-conducting is compared to a radical anion salt, quinolinium bis tetracyanoquinodimethane  $Q_n(TCNQ)_2$  considered as a reference.

The materials physical characteristics will be provided by a new variable field (0.6-60 Gauss, 2-200 MHz) which is under realization, for an extended family of organic radicals.

INTRODUCTION

For reasons of sensitivity, CW EPR Spectrometry is mainly performed in the frequency range 1 to 35 GHz.

Different classes of material with exceptional spin dynamics or magnetic properties have already been developed. For such systems, an EPR study at low field becomes of high interest.

The earth field magnetometry emphasizes the need of a spectrometer in the same range to characterize the materials. The performance of the spectrometer must be optimized for the sensitivity which decreases quadratically with the frequency. The described spectrometer is automated and reduced in size (and price) in order to be used in a non specialized laboratory.

I. PRINCIPLE

Considering EPR, the electron has a spin and therefore a colinear magnetic moment. The resultant magnetic moment of the spin population can precess around the static field  $H_0$  at the Larmor frequency :  $\omega_0 = \gamma \mu_0 H_0$  (1) where  $\gamma = 1.76 \cdot 10^{11} \text{ s}^{-1} \text{ T}^{-1}$  and  $\mu_0 = 4 \pi \cdot 10^{-7} \text{ Hm}^{-1}$ . The classical arrangement to measure a resonance is known as the Bloch configuration [1].

The method we used exploits the derivative of the resonant curves. It is obtained by superimposing a dither modulation of a frequency  $\omega_N$  ( $\omega_N \ll \omega$ ) on the field. The observation via a lock-in detection of the amplitude of the response at  $\omega$ , which is modulated at  $\omega_N$ , yields a signal proportional to  $dV_S/d\omega$  or  $dV_S/dH$ , where  $V_S$  is the amplitude of the voltage present on the detection coil

The analysis of the signal is based on the extensive description given by Poole [2]. The response of a spectrometer using a resonant cavity of frequency  $\omega_0$  is related to the average power absorbed per unit volume

$$P_{\text{abs}} = \frac{1}{2} \omega_0 H_1^2 \chi''(\omega) \quad (2)$$

where  $H_1$  is the amplitude of the RF field at the sample and  $\chi''(\omega)$  is the RF susceptibility considered to be homogeneous over the whole sample volume. The final output signal of such a spectrometer may be written :

$$V(\omega) = A H_1 \chi''(\omega) P \quad (3)$$

where  $P$  is the packaging factor, and  $A$  is the scale factor of the spectrometer including the  $Q$  factor of the cavity and further amplifications in the spectrometer.

In equation (3), the signal can be related to the magnetization of the sample at the frequency  $\omega$

$$M(\omega) = H_1 \chi''(\omega) P V_S \quad (4)$$

In the homogeneous case and for a low RF field  $H_1$  as compared to the static field  $H_0$ , the absorption part of the RF susceptibility through the resonance shows a Lorentzian shape given by the solution of the Bloch equation :

$$\chi''(\omega) = \frac{\frac{1}{2} \chi_0 \omega_0 T_2}{1 + (\omega - \omega_0)^2 T_2^2} \quad (5)$$

in which  $\chi_0$  is the static susceptibility and  $T_2$  the spin-spin relaxation time.

It comes :

$$V(\omega) = \frac{A}{2} \frac{\chi_0 \omega_0 T_2 H_1 P}{1 + (\omega - \omega_0)^2 T_2^2} \quad (6)$$

The detected signal as a function of the incident RF field  $H_1$  is maximum for a value  $H_{1\max}$  which is attained [2] for :

$$H_{1\max}^2 = \frac{1}{4} (2 \gamma^2 \mu_0^2 T_1 T_2)^{-1} \quad (7)$$

Moreover for this value, the apparent peak-to-peak linewidth  $\Delta H_{pp}^0$  is broadened to  $\Delta H_{pp}$

$$\Delta H_{pp} = \frac{2}{\sqrt{3}} \Delta H_{pp}^0 = \frac{4}{3} \frac{1}{\gamma \mu_0 T_2} \quad (8)$$

the signal as then a maximum slope :

$$P_{\max} = A \frac{\omega_0}{\gamma \mu_0} H_N \chi_0 P \left(\frac{3}{4}\right)^2 \frac{\gamma^2 \mu_0^2 T_2^3}{(3 \gamma^2 \mu_0^2 T_1 T_2)^{1/2}} \quad (9)$$

where  $H_N$  is the modulation amplitude.

The slope as a function of  $H_N$  presents a maximum for a value

$$N_{N\max} = \frac{1.29}{2} \Delta H_{pp} \quad (10)$$

For this value, the apparent linewidth is :

$$\Delta H_{pp}^{obs} = 1.38 \Delta H_{pp} \quad (11)$$

in that case, the maximum slope becomes :

$$P_{\max} = A \frac{\omega_0}{\gamma \mu_0} \chi_0 P \left(\frac{3}{4}\right)^2 \frac{0.935}{2} \left(\frac{1.29}{1.38}\right) \frac{\gamma^2 \mu_0^2 T_2^2}{(3 \gamma^2 \mu_0^2 T_1 T_2)^{1/2}} \quad (12)$$

$$\text{i.e.} \quad P_{\max} = A \omega_0 \chi_0 P T_2^{3/2} T_1^{-1/2} \cdot 7.6 \cdot 10^{-2} \quad (13)$$

The optimization process will give the values of the maximum slope and associated values of  $H_1$  and  $H_N$  recalled below :

$$H_N \text{ max} = 0.86 (\gamma \mu_o T_2)^{-1} \quad (14)$$

$$H_1 \text{ max} = 0.29 (\gamma^2 \mu_o^2 T_1 T_2)^{-1/2} \quad (15)$$

Apparent values of  $T_1$  and  $T_2$  can be extracted from (14) and (15).

## II. REALIZATION

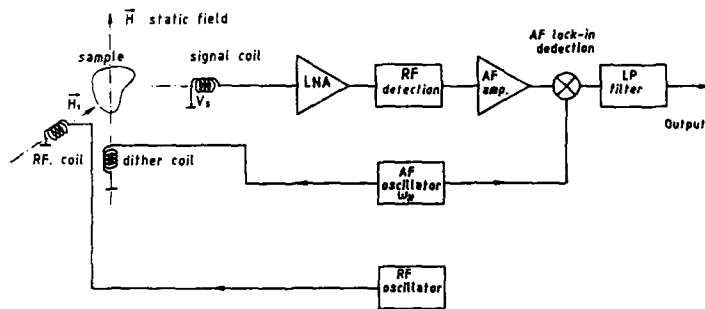


Figure 1. BLOCK DIAGRAM OF THE SPECTROMETER

The dc field is axially superimposed to the local field using high homogeneity coils driven by a control current. The resultant field excursion varies from 5  $\mu\text{T}$  to 100  $\mu\text{T}$  in five ranges, centered around 60  $\mu\text{T}$ . A low frequency dither field is added. The RF detection coil wound with Litz wire feeds a high dynamic range low-noise custom made receiver having a coherent detection thus eliminating the problem of direct coupling between the coils. The RF excitation comes from a second set of Helmholtz coils, at a fixed frequency of 1.845 MHz.

The derivative of the absorption line is observed using a commercial synchronous detection whose adjustments are commanded via the IEEE 4878 bus (EG & G 5209).

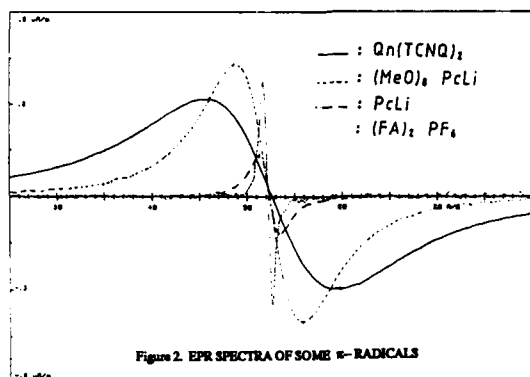
The structure is wide band and the spectrometer frequency can easily be tuned in all the useful range (0.8 - 2 MHz) or higher up to 500 MHz with little modifications.

The software provides additional facilities such as signal averaging, digital filtering, calculation of the slope and automatic plotting of networks.

The sample weights between 1 to 100 mg, depending on signal weakness, are required in a volume of 0.2  $\text{cm}^3$ . The acquisition of a spectrum lasts 1 ms (average), using a post detection time constant of 0.15 (1.6 Hz). In that case the peak to peak noise is of the order of 120  $\text{nT}\cdot\text{Hz}^{-1/2}$  for the field. The noise decreases by a factor  $N^{1/2}$  where N is the number of averages.

## III. RESULTS

Three types of systems are extensively studied: The radical ion salts (cations and anions) and the neutral radicals. Figure 2 shows typical spectra of radicals which are good candidates for EPR magnetometry.



At the present state, the spectrometer works at a unique frequency. A frequency variable EPR spectrometer in the range of 10-500 MHz is under realization, a similar tentative has been recently published [3].

Low field EPR spectrometer is quite accurate for the study of free radicals relaxation processes especially to predict the coefficient of dynamic polarization of protons (DNP) in solutions of these radicals.

The interest of free radicals is due to the hyperfine structure which induces an important separation of the energy levels at low field as shown in figure 3.

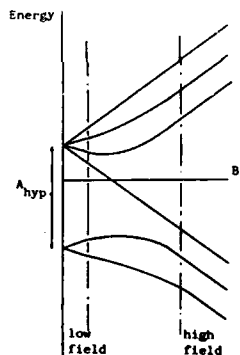


Figure 3. ENERGY LEVELS OF A FREE RADICAL

The various processes considered for the electronic spin relaxation have already been characterized at high field [4]. The effect they provide at low field on the DNP coefficient are predicted by theoretical considerations on the spin dynamic.

The field dependence relations of the linewidth are calculated for each process. We believe that the difference between the predicted and measured values of the DNP coefficient is due to the rough understanding of the electronic spin relaxation processes at low field. Our purpose is to control the EPR relaxation processes and their effects on DNP by low field EPR measurements. We expect by these means to improve considerably our prediction model of free radical DNP performance.

Preliminary experiments have already been performed at 10, 20 and 50 MHz. These first results will be published in a further communication.

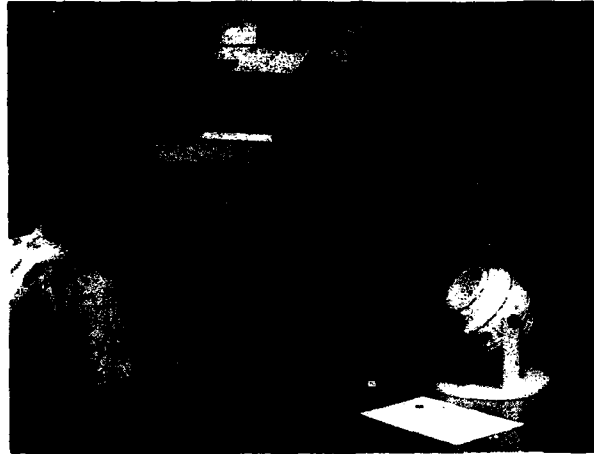


Figure 4. SPECTROMETER'S PHOTOGRAPH

#### References

- [1] F. BLOCH; W.W. HANSEN; M. PACKARD, *Phy. Rev.* 70 (1946) 474.
- [2] C.P. POOLE Jr., *Electron Spin Resonance* ed. J. Wiley (New York) 1983.
- [3] H. GEBHARDT and E. DORMANN, *J. Phys. E. Sci. Instrum.* 22 (1989) 321.
- [4] Y. AYANT; R. BESSON and A. SALVI, *J. Phys.* 41 (1975) 571.

NEW ELECTRICALLY CONDUCTING SOLIDS BASED ON  
NICKEL(II) - BIS(1,3-DITHIOLE-2-THIONE-4,5-DISELENOLATE)

A. M. KINI, M. A. BENO, S. BUDZ, H. H. WANG AND J. M. WILLIAMS  
Argonne National Laboratory, Chemistry and Materials Science  
Divisions, Argonne, IL 60439, U. S. A.

ABSTRACT

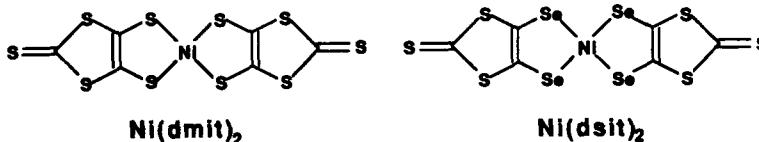
Electrochemical oxidation of the metal-organic complex, nickel(II)-bis(1,3-dithiole-2-thione-4,5-diselenolate) or simply  $[\text{Ni}(\text{dsit})_2]^{2-}$ , yields highly conducting salts, in which the stoichiometry and packing arrangement depends critically on the size of the counter-cations incorporated. Smaller counter-cations, e.g., tetramethylammonium and tetramethylphosphonium ions, yield salts with a 1:2 cation:[Ni(dsit)<sub>2</sub>] stoichiometry, while the larger tetraethylammonium ion yields a salt with 2:2 stoichiometry. In both these salts, the {Ni(dsit)<sub>2</sub>} units occur as tightly bound dimers, in which the coordination geometry of nickel is a unique, but not unprecedented square-pyramidal type. Moreover, the packing arrangement of [Ni(dsit)<sub>2</sub>]<sub>2</sub> dimer units in both (Me<sub>4</sub>N)[Ni(dsit)<sub>2</sub>]<sub>2</sub> and (Me<sub>4</sub>P)[Ni(dsit)<sub>2</sub>]<sub>2</sub> is κ-type, similar to that found in the organic superconductor with the highest-known T<sub>c</sub> (10.4 K), κ-(BEDT-TTF)<sub>2</sub>Cu(NCS)<sub>2</sub>. Both these salts possess good room temperature conductivities (σ<sub>rt</sub> = 36 and 19 S.cm<sup>-1</sup> respectively), but the temperature dependance of their conductivities is characteristic of semiconductors with small bandgaps (E<sub>g</sub> = 0.11 and 0.13 eV, respectively). The 2:2 salt (Et<sub>4</sub>N)<sub>2</sub>[Ni(dsit)<sub>2</sub>]<sub>2</sub>, on the other hand, has a substantially lower room temperature conductivity, about six orders of magnitude smaller than that of the 1:2 salts. Its structure is characterized by [Ni(dsit)<sub>2</sub>]<sub>2</sub> dimer units which are separated from each other by the tetraethylammonium cations, with no effective interaction between [Ni(dsit)<sub>2</sub>]<sub>2</sub> dimers. It is suggested that dimeric metal-dithiolene and metal-diselenolene complexes may be potential building blocks in the structural design of κ-type organic conductors and superconductors.

Introduction

Cation-radical salts derived from various tetrathiafulvalene derivatives (TMTSF, BEDT-TTF, DMET and MDT-TTF) have recently captured much interest because of the large number of organic metals and ambient pressure organic superconductors discovered among them [1]. A major milestone in the research on this class of compounds has been the discovery of ambient pressure superconductivity at 10-11 K in κ-(BEDT-TTF)<sub>2</sub>Cu(NCS)<sub>2</sub> [2]. In addition to being the organic superconductor with the highest-known superconducting transition temperature (T<sub>c</sub>), this salt also possesses the largest known negative pressure derivative of T<sub>c</sub> (-3K/kbar) [3] and, its crystal structure features tightly bound

BEDT-TTF dimers (intradimer spacing of 3.35 Å) arranged orthogonally to each other (the so-called K-type molecular packing arrangement) [4,5]. Moreover, since the superconducting salts with the highest-known  $T_c$ 's derived from unsymmetrical donors DMET and MDT-TTF also have similar molecular packing arrangements, new strategies for the structural design of organic conductors and superconductors with the K-type structures are needed, in order to achieve higher superconducting transition temperatures [6].

In our search for molecular components that are capable of forming dimeric units, the basic building blocks of K-type structures, we came across the well-precedented metal-dithiolene complexes, which have been known to form dimerized structures [7]. They have also been intensively studied because they exhibit novel electrical and magnetic properties [8]. A member of this class of compounds,  $[\text{Ni}(\text{dmit})_2]^{2-}$ , has recently yielded two superconducting salts,  $(\text{TTF})[\text{Ni}(\text{dmit})_2]_2$  [9] and  $(\text{Me}_4\text{N})[\text{Ni}(\text{dmit})_2]_2$  [10], with  $T_c = 1.62 \text{ K}$  (7 kbars) and  $5 \text{ K}$  (7 kbars) respectively. Compounds of this type offer an exceptional opportunity for chemical modifications, because the modifications can be made in terms of a) counter-cations, b) chelating metal ions and c) the organic ligand itself. Thus, a systematic study, comprising such diverse chemical modifications and the investigation of resultant solid state properties, holds considerable promise in the search for new metallic and superconducting solids. Consequently, we have prepared and studied the salts obtained by electrochemical oxidation of nickel(II)-bis(1,3-dithiole-2-thione-4,5-diselenolate) or  $[\text{Ni}(\text{dsit})_2]^{2-}$ , which is a selenium analog of  $[\text{Ni}(\text{dmit})_2]^{2-}$ , in which the four sulfur atoms bonded to Ni have been replaced by selenium atoms (see below). This substitution is expected to result in increased polarizability, bandwidths (due to the anticipated increase in orbital overlap between molecules) and also to enhance the dimensionality in the solid state.



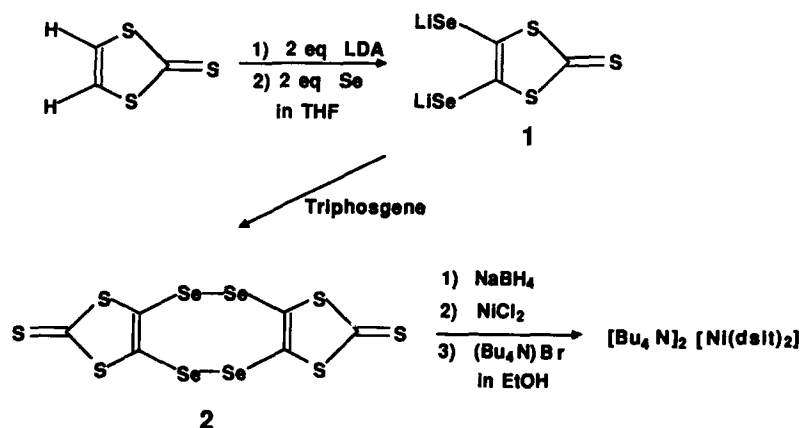
#### Preparation

Synthesis of  $(\text{Bu}_4\text{N})_2[\text{Ni}(\text{dsit})_2]$  was recently reported by Nigrey starting from commercially available 1,3-dithiole-2-thione, as shown in Scheme I [11]. According to this method, 1,3-dithiole-2-thione is first lithiated with lithium diisopropylamide in tetrahydrofuran (THF) and then elemental selenium is added, which inserts between carbon-lithium bonds, giving diselenolate 1. Removal of the solvent THF by blowing argon across it and redissolving the diselenolate 1 in methanol, followed by the



addition of  $\text{NiCl}_2$  and  $\text{Bu}_4\text{NBr}$ , furnished  $(\text{Bu}_4\text{N})_2[\text{Ni}(\text{dsit})_2]$ . Due to the extreme air/oxygen sensitivity of diselenolate **1**, this operation, in our hands, resulted in lower yields of the desired complex at the expense of side-products arising out of oxidation of the diselenolate **1**. Instead, we have found that reacting the diselenolate **1**, generated in THF, with triphosgene, or bis(trichloromethyl)carbonate, cleanly oxidizes it to selenocin **2** in nearly quantitative yields. Selenocin **2** is then converted back to the diselenolate by using an excess of sodium borohydride in absolute ethanol and is then reacted with  $\text{NiCl}_2$  and  $\text{Bu}_4\text{NBr}$  to obtain  $(\text{Bu}_4\text{N})_2[\text{Ni}(\text{dsit})_2]$  in nearly quantitative yields. The improvement in yield via this method is undoubtedly due to the reducing conditions ( $\text{NaBH}_4$ ) under which the complex is prepared. An analogous strategy, wherein the initially generated diselenolate is converted to the corresponding selenocin, and then regenerated for subsequent reaction in a different solvent, has been reported in the synthesis of a tetraselenafulvalene derivative [12].

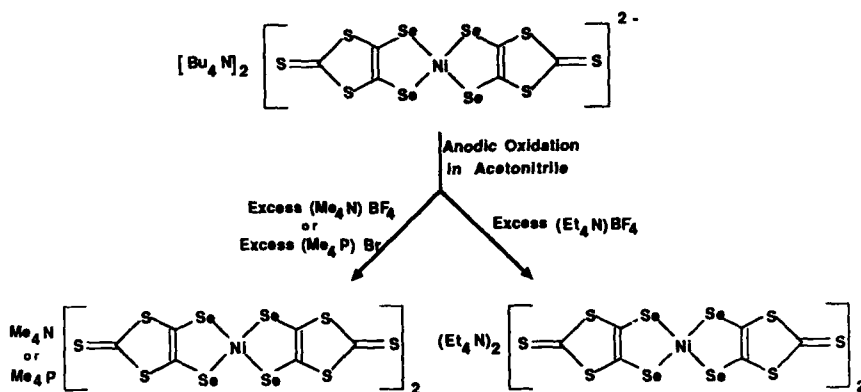
### Scheme I



Reversible, one-electron oxidation of  $(\text{Bu}_4\text{N})_2[\text{Ni}(\text{dsit})_2]$ , i.e.,  $[\text{Ni}(\text{dsit})_2]^{2-}/[\text{Ni}(\text{dsit})_2]^{1-}$  redox reaction, employing cyclic voltammetry, was demonstrated by Nigrey [11]. However, a second oxidation, i.e.,  $[\text{Ni}(\text{dsit})_2]^{1-}/[\text{Ni}(\text{dsit})_2]^0$  redox reaction, was not observed under the conditions of Nigrey's cyclic voltammetry experiment. Such an oxidation, yielding  $[\text{Ni}(\text{dmit})_2]^0$ , a formally Ni(IV) species, has been reported in the all-sulfur compound  $[\text{Ni}(\text{dmit})_2]^{2-}$  [13]. Furthermore, in the superconducting salts  $\text{TTF}[\text{Ni}(\text{dmit})_2]_2$  and  $\text{Me}_4\text{N}[\text{Ni}(\text{dmit})_2]_2$ , the overall charge on each  $[\text{Ni}(\text{dmit})_2]$  unit is  $-0.5$ , and hence they may be viewed as mixed-

valent compounds comprising  $\text{Ni}(\text{dmit})_2^{1-}$  and  $\text{Ni}(\text{dmit})_2^0$ . It is likely that such mixed-valent salts can also exist in the case of  $[\text{Ni}(\text{dsit})_2]$  and may be highly conducting. Electrochemical oxidation of  $(\text{Bu}_4\text{N})_2[\text{Ni}(\text{dsit})_2]$  in acetonitrile, in the presence of a large excess (> 10-fold) of different counter-cationic electrolytes using platinum electrodes under galvanostatic (ca.  $1\text{--}2 \mu\text{A}/\text{cm}^2$  current density) conditions, yielded black, shiny, plate-like crystals. The different counter-cationic salts employed were  $(\text{Me}_4\text{N})\text{BF}_4$ ,  $(\text{Me}_4\text{P})\text{Br}$  and  $(\text{Et}_4\text{N})\text{BF}_4$ . Crystal structure analyses (vide infra) established the compositions of the salts to be 1:2 in the case of  $(\text{Me}_4\text{N})^+$  and  $(\text{Me}_4\text{P})^+$  counter-cations, and 2:2 in the case of  $(\text{Et}_4\text{N})^+$  counter-cation.

### Scheme II



### Description of structures

Crystals of the 2:2 salt,  $(\text{Et}_4\text{N})_2[\text{Ni}(\text{dsit})_2]_2$ , were small black plates of good quality, while those of the 1:2 salts,  $(\text{Me}_4\text{N})[\text{Ni}(\text{dsit})_2]_2$  and  $(\text{Me}_4\text{P})[\text{Ni}(\text{dsit})_2]_2$ , were obtained only as small thin plates, which in most cases were twinned. The poor crystal quality of the 1:2 salts is also reflected in the final agreement factors which appear in Table I along with other relevant crystallographic data. The 1:2 salts  $(\text{Me}_4\text{N})[\text{Ni}(\text{dsit})_2]_2$  and  $(\text{Me}_4\text{P})[\text{Ni}(\text{dsit})_2]_2$  are isostructural, but the structural data for  $(\text{Me}_4\text{P})[\text{Ni}(\text{dsit})_2]_2$  were of poor quality and could not be refined to agreement factors better than ~20%. Therefore, full structural data for  $(\text{Me}_4\text{P})[\text{Ni}(\text{dsit})_2]_2$  are not included. The structures were solved with MULTAN and refined employing anisotropic temperature factors for sulfur atoms in the case of the 1:2  $(\text{Me}_4\text{N})$  salt and all non-hydrogen atoms for the 2:2  $(\text{Et}_4\text{N})$  using the UCLA crystallographic program package. Hydrogen atom positions were included in the refinements at calculated

positions, but were not refined. Positional parameters for both salts appear in Table II. Intramolecular distances and angles are given in Table III and, close intermolecular contact distances appear in Table IV. The atom numbering system and  $[\text{Ni}(\text{dsit})_2]_2$  dimer are shown in Figure 1.

Table I. Crystallographic data for  $\text{X}[\text{Ni}(\text{dsit})_2]_2$  salts.

Cation (X)	( $\text{Me}_4\text{N}$ ) <sup>+</sup>	( $\text{Me}_4\text{P}$ ) <sup>+</sup>	( $\text{Et}_4\text{N}$ ) <sub>2</sub> <sup>2+</sup>
Symmetry	orthorhombic Pbnm [No.62]	orthorhombic Pbnm [No.62]	monoclinic P2 <sub>1</sub> /c [No.14]
$M_r$	1352.68	1369.04	1538.44
<u>Unit cell parameters</u>			
a	7.410(7)	7.418(5)	6.775(3) Å
b	11.876(8)	11.942(9)	27.02(2) Å
c	38.33(3)	38.5(1)	12.973(8) Å
$\beta$			98.09(4)°
$V_c$	3372(4)	3408(12)	2351(3) Å <sup>3</sup> .
$\rho_c$ (g/cm <sup>3</sup> )	2.663(3)	2.669(9)	2.173(2)
$\mu_c$ (cm <sup>-1</sup> )	104.07	103.45	74.77
Z	4	4	2
<u>Data collection parameters</u>			
Independent			
Reflections	1466	—	3062
Refl $ F_o  > 3\sigma(F_o)$	1036	—	2243
# of Parameters	137	—	235
<u>Agreement factors</u>			
R(F)	0.101	—	0.075
wR(F <sup>2</sup> )	0.086	—	0.050
GOF	2.28	—	2.20

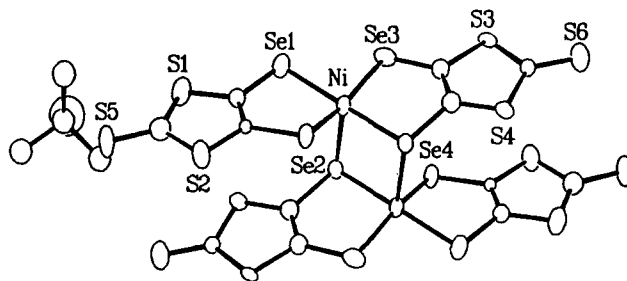


Figure 1. Dimeric  $[\text{Ni}(\text{dsit})_2]_2$  units in which the square-pyramidal coordination of Ni, by four Se atoms in a square-plane and apically by a Se atom of the next molecule, is shown. The apical Ni-Se bond lengths are 2.495(2) Å ( $\text{Et}_4\text{N}$  salt) and 2.555(7) Å ( $\text{Me}_4\text{N}$  salt).

Table II. Positional Parameters for [Ni(dsit)<sub>2</sub>] salts.

(Et<sub>4</sub>N)<sub>2</sub>[Ni(dsit)<sub>2</sub>]<sub>2</sub>

Atom	x	y	z	U <sub>eq</sub> *10 <sup>4</sup> †
Ni1	0.4159(2)	0.44488(6)	0.52392(11)	315(5)
Se1	0.2861(2)	0.46762(5)	0.67478(9)	406(5)
Se2	0.7246(2)	0.48193(5)	0.57841(9)	344(4)
Se3	0.1274(2)	0.39621(6)	0.49054(10)	518(6)
Se4	0.5804(2)	0.39905(5)	0.40772(10)	394(5)
S1	0.5039(6)	0.51838(14)	0.8753(2)	450(12)
S2	0.8835(5)	0.52811(13)	0.7995(2)	449(12)
S3	-0.0077(6)	0.33120(14)	0.2893(3)	496(13)
S4	0.3743(6)	0.33648(14)	0.2174(2)	478(13)
S5	0.0596(6)	0.2719(2)	0.1027(3)	655(16)
S6	0.8381(6)	0.5661(2)	1.0111(3)	639(16)
C1	0.516(2)	0.4948(5)	0.7510(8)	377(47)
C2	0.688(2)	0.5003(5)	0.7161(8)	452(50)
C3	0.177(2)	0.3636(4)	0.3668(8)	410(48)
C4	0.361(2)	0.3678(4)	0.3335(9)	336(44)
C5	0.131(2)	0.3110(5)	0.1962(9)	496(53)
C6	0.747(2)	0.5407(5)	0.9007(9)	454(48)
N1	0.352(2)	0.6731(4)	0.1803(8)	443(41)
C7	0.134(2)	0.6741(5)	0.1891(9)	436(48)
C8	0.058(2)	0.6305(5)	0.2424(11)	621(60)
C9	0.402(2)	0.7218(5)	0.1348(10)	519(54)
C10	0.617(2)	0.7250(7)	0.1182(11)	797(75)
C11	0.475(2)	0.6647(5)	0.2890(10)	529(55)
C12	0.433(3)	0.7031(6)	0.3688(10)	680(66)
C13	0.404(2)	0.6298(5)	0.1154(11)	622(62)
C14	0.321(2)	0.6318(5)	0.0035(11)	636(60)

(Me<sub>4</sub>N)[Ni(dsit)<sub>2</sub>]<sub>2</sub>

Atom	x	y	z	U <sub>eq</sub> *10 <sup>4</sup> †
Ni1	0.8857(6)	-0.0884(3)	-0.02371(10)	339(17)
Se1	0.9924(6)	-0.2466(3)	0.00637(10)	378(13)
Se2	0.7950(6)	0.0076(3)	0.02620(8)	390(14)
Se3	0.9432(6)	-0.1851(3)	-0.07536(10)	442(15)
Se4	0.6996(6)	0.0378(3)	-0.05161(9)	454(16)
S1	0.956(2)	-0.2979(7)	0.0876(2)	691(51)
S2	0.7562(13)	-0.0824(6)	0.1020(2)	261(29)
S3	0.895(2)	-0.0912(9)	-0.1525(2)	589(44)
S4	0.699(2)	0.1032(8)	-0.1313(2)	532(42)
S5	0.780(2)	0.0767(9)	-0.2069(2)	654(46)
S6	0.816(2)	-0.2431(10)	0.1603(3)	936(65)
C1	0.920(4)	-0.209(2)	0.0515(8)	273(88) ‡
C2	0.812(5)	-0.113(3)	0.0603(8)	419(109) ‡
C3	0.850(4)	-0.078(3)	-0.1075(8)	269(88) ‡
C4	0.761(4)	0.014(2)	-0.0993(6)	113(71) ‡
C5	0.787(5)	0.033(3)	-0.1651(8)	404(101) ‡
C6	0.847(4)	-0.209(3)	0.1184(7)	247(91) ‡
N1	0.716(7)	0.079(4)	0.2500	686(149) ‡
C7	0.721(5)	0.002(2)	0.2183(8)	493(106) ‡
C8	0.537(7)	0.130(4)	0.2500	412(151) ‡
C9	0.876(7)	0.154(4)	0.2500	436(152) ‡

† The complete temperature factor is  $\exp(-8\pi^2 U_{eq} \sin^2\theta/\lambda^2)$ , where  $U_{eq} = 1/3 \sum_{ij} U_{ij} a_i^* a_j^* a_i \cdot a_j$  in units of Å<sup>2</sup>

‡ U<sub>iso</sub>

Table III. Interatomic Distances (Å) and Angles (°) for [Ni(dsit)<sub>2</sub>] salts.(Et<sub>4</sub>N)<sub>2</sub>[Ni(dsit)<sub>2</sub>]<sub>2</sub>

Atoms	Dist.	Atoms	Dist.	Atoms	Dist.
Ni1-Se1	2.338(2)	Se4-C4	1.855(12)	S4-C4	1.741(11)
Ni1-Se2	2.337(2)	S1-C6	1.744(12)	S4-C5	1.769(15)
Ni1-Se3	2.345(2)	S1-C1	1.747(10)	S5-C5	1.631(12)
Ni1-Se4	2.350(2)	S2-C6	1.740(12)	S6-C6	1.629(11)
Se1-C1	1.875(12)	S2-C2	1.756(13)	C1-C2	1.31(2)
Se2-C2	1.904(10)	S3-C5	1.721(13)	C3-C4	1.38(2)
Se3-C3	1.902(11)	S3-C3	1.729(13)		
N1-C7	1.50(2)	N1-C11	1.551(14)	C11-C12	1.52(2)
N1-C9	1.50(2)	C7-C8	1.49(2)	C13-C14	1.48(2)
N1-C13	1.512(15)	C9-C10	1.50(2)		

Atoms	Angle	Atoms	Angle
Se1-Ni1-Se2	93.45(8)	Se1-Ni1-Se2	93.45(8)
Se1-Ni1-Se3	84.27(8)	Se1-Ni1-Se3	84.27(8)
Se1-Ni1-Se4	160.70(9)	Se1-Ni1-Se4	160.70(9)
Se2-Ni1-Se3	169.55(9)	Se2-Ni1-Se3	169.55(9)
Se2-Ni1-Se4	86.24(8)	Se2-Ni1-Se4	86.24(8)
Se3-Ni1-Se4	92.55(8)	Se3-Ni1-Se4	92.55(8)
C1-Se1-Ni1	99.3(3)	C1-Se1-Ni1	99.3(3)
C2-Se2-Ni1	99.6(4)	C2-Se2-Ni1	99.6(4)
C3-Se3-Ni1	100.0(4)	C3-Se3-Ni1	100.0(4)
C4-Se4-Ni1	99.0(3)	C4-Se4-Ni1	99.0(3)
C6-S1-C1	97.7(6)	C6-S1-C1	97.7(6)
C6-S2-C2	96.6(6)	C6-S2-C2	96.6(6)
C5-S3-C3	98.4(7)	C5-S3-C3	98.4(7)
C4-S4-C5	99.4(6)	C4-S4-C5	99.4(6)
C2-C1-S1	115.8(10)	C2-C1-S1	115.8(10)
C2-C1-Se1	125.0(9)	C2-C1-Se1	125.0(9)
C7-N1-C9	107.1(10)	C13-N1-C11	104.8(10)
C7-N1-C13	111.6(11)	C8-C7-N1	115.2(11)
C7-N1-C11	110.1(10)	N1-C9-C10	112.7(13)
C9-N1-C13	112.1(10)	C12-C11-N1	113.0(11)
C9-N1-C11	111.2(10)	C14-C13-N1	115.4(11)

(Me<sub>4</sub>N)[Ni(dsit)<sub>2</sub>]<sub>2</sub>

Atoms	Dist.	Atoms	Dist.	Atoms	Dist.
Ni1-Se1	2.342(6)	Se4-C4	1.90(2)	S4-C4	1.68(3)
Ni1-Se2	2.326(5)	S1-C1	1.76(3)	S4-C5	1.67(3)
Ni1-Se3	2.328(5)	S1-C6	1.78(3)	S5-C5	1.68(3)
Ni1-Se4	2.300(6)	S2-C2	1.69(3)	S6-C6	1.67(3)
Se1-C1	1.87(3)	S2-C6	1.77(3)	C1-C2	1.44(4)
Se2-C2	1.94(3)	S3-C3	1.76(3)	C3-C4	1.31(4)
Se3-C3	1.90(3)	S3-C5	1.75(3)		
N1-C7	1.52(4)	N1-C8	1.46(7)	N1-C9	1.48(6)

Table III (continued)

Atoms	Angle	Atoms	Angle
Se1-Ni-Se2	83.7(2)	S3-C2-Se3	123.0(17)
Se1-Ni-Se4	92.0(2)	C2-C1-S4	121.8(24)
Se1-Ni-Se3	162.5(3)	C2-C1-Se2	117.7(23)
Se2-Ni-Se4	173.7(3)	S4-C1-Se2	117.8(18)
Se2-Ni-Se3	94.9(2)	C3-C4-S2	118.9(23)
Se4-Ni-Se3	87.8(2)	C3-C4-Se1	118.2(22)
C1-Se2-Ni	100.1(9)	S2-C4-Se1	122.9(16)
C4-Se1-Ni	102.0(9)	C4-C3-S1	114.0(24)
C3-Se2-Ni	98.8(9)	C4-C3-Se4	125.7(24)
C2-Se3-Ni	99.8(9)	S1-C3-Se4	120.1(17)
C5-S <sup>-</sup> -C4	98.5(15)	S2-C5-S5	125.0(21)
C5-S1-C3	96.0(15)	S2-C5-S1	112.6(18)
C1-S4-C6	93.6(15)	S5-C5-S1	122.4(20)
C2-S3-C6	95.7(14)	S6-C6-S4	119.6(18)
C1-C2-S3	112.2(23)	S6-C6-S3	124.1(19)
C1-C2-Se3	124.5(23)	S4-C6-S3	116.2(16)
C7-N1-C7	106.0(34)	C7-N1-C9	110.3(31)
C7-N1-C8	105.5(34)	C8-N1-C9	118.6(41)

The superconducting salt  $\text{Me}_4\text{N}[\text{Ni}(\text{dmit})_2]_2$  ( $T_c = 5.0$  K, 7 kbar) has an acceptor packing mode similar to the  $\beta$ -phase BEDT-TTF salts, in which stacks of nearly equally spaced donor molecules are linked by short interstack  $\text{S} \cdots \text{S}$  interactions [10]. On the other hand, the semiconducting salt  $\text{Me}_4\text{P}[\text{Ni}(\text{dmit})_2]_2$  contains dimerized acceptor molecules, which pack almost at right angles with respect to neighboring dimer pairs [14], similar to the packing arrangement in  $\kappa$ -phase BEDT-TTF salts. Both the 1:2 salts derived from  $[\text{Ni}(\text{dsit})_2]$ ,  $\text{Me}_4\text{N}[\text{Ni}(\text{dsit})_2]_2$  and  $\text{Me}_4\text{P}[\text{Ni}(\text{dsit})_2]_2$ , exhibit the  $\kappa$ -type acceptor packing (see Figure 2) and, thus are similar to  $\text{Me}_4\text{P}[\text{Ni}(\text{dmit})_2]_2$ . The most striking difference between the structures of the  $[\text{Ni}(\text{dmit})_2]$  salt and the  $[\text{Ni}(\text{dsit})_2]$  salts is the occurrence of tightly bonded dimeric units (see Figure 1). In the latter, the Ni atom is coordinated by four Se atoms in a square-plane and also apically by a Se atom of the adjacent molecule. The intradimer interaction appears to be strong and bonding in nature in the case of  $[\text{Ni}(\text{dsit})_2]_2$  dimers, since the intradimer spacing of 2.878 Å in  $(\text{Me}_4\text{N})[\text{Ni}(\text{dsit})_2]_2$  is much shorter than the corresponding value, 3.32-3.33 Å, observed in  $\text{Me}_4\text{P}[\text{Ni}(\text{dmit})_2]_2$  [14]. The shorter intradimer spacing is even more significant in view of the larger chalcogen involved.

The larger cation  $(\text{Et}_4\text{N})^+$  gives a 2:2 salt, in which the dimeric  $[\text{Ni}(\text{dsit})_2]_2$  units are virtually isolated from each other by the counter-cations (Figure 3). This salt is also isostructural to the previously reported  $(\text{Et}_4\text{N})[\text{Ni}(\text{dmit})_2]$  [15]. The shorter intramolecular Se-Ni distances and the longer intermolecular (but intradimer) Se-Ni distance in  $[\text{Ni}(\text{dsit})_2]_2$  dimers of the 1:2 salt compared to the corresponding values in the 2:2 salt (see Tables III and IV) are noteworthy. These trends appear to be related to the formal valence of Ni in these salts.

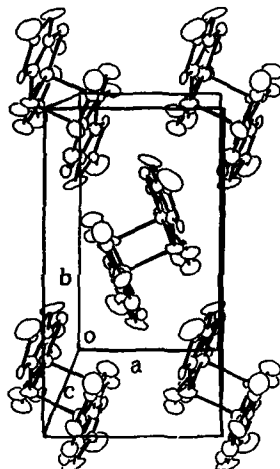


Figure 2. The acceptor packing in  $(\text{Me}_4\text{N})[\text{Ni}(\text{dsit})_2]_2$  and  $(\text{Me}_4\text{P})[\text{Ni}(\text{dsit})_2]_2$ , which is similar to that in  $\text{Me}_4\text{P}[\text{Ni}(\text{dmit})_2]_2$ .

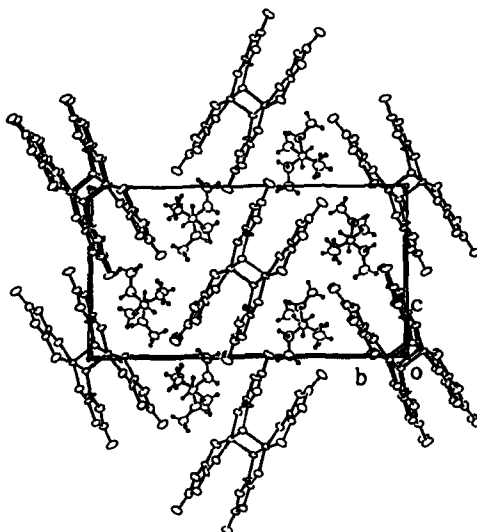
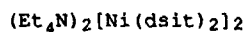


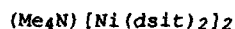
Figure 3. The acceptor packing in  $(\text{Et}_4\text{N})_2[\text{Ni}(\text{dsit})_2]_2$  showing  $[\text{Ni}(\text{dsit})_2]_2$  dimers surrounded by  $(\text{Et}_4\text{N})^+$  ions.

Table IV. Intradimer and Interdimer Distances (Å) and Angles (°) for  $[\text{Ni}(\text{dsit})_2]$  salts.

Intradimer distances and Angles					
Atoms	Dist.	Atoms	Dist.	Atoms	Dist.
Ni1-Se2	2.495(2)	Se1-Se2	3.548(3)	Se2-Se3	3.592(3)
Ni1-Ni1	3.280(4)	Se2-Se2	3.551(3)	Se3-Se4	3.711(3)

Atoms	Angle	Atoms	Angle
Se1-Ni1-Se2	94.41(8)	Se3-Ni1-Se2	95.78(9)
Se2-Ni1-Se2	94.56(8)	Se4-Ni1-Se2	104.85(8)



Intradimer Distances and Angles					
Atoms	Dist.	Atoms	Dist.	Atoms	Dist.
Ni-Se2	2.555(7)	Se1-Se2	3.478(5)	Se2-Se3	3.429(5)
Ni-Ni	3.253(9)	Se2-Se2	3.646(8)		

Atoms	Angle	Atoms	Angle
Se1-Ni1-Se2	90.4(2)	Se3-Ni1-Se2	89.1(2)
Se2-Ni1-Se2	96.5(2)	Se4-Ni1-Se2	107.0(2)

Interdimer Distances					
Atoms	Dist.	Atoms	Dist.	Atoms	Dist.
Se1-Se4	3.677(6)	Se3-S4	3.468(10)	Se4-S1	3.642(12)
Se1-Se2	3.692(6)	Se3-Se4	3.575(5)	S2-S4	3.57(2)
Se1-Se1	3.738(4)	Se3-S1	3.643(15)	S5-S5	3.31(2)

### Electrical properties

Electrical conductivities of  $(\text{Me}_4\text{N})[\text{Ni}(\text{dsit})_2]_2$  and  $(\text{Me}_4\text{P})[\text{Ni}(\text{dsit})_2]_2$ , as measured by the standard four-probe method, at room temperature are quite high,  $36 \text{ S.cm}^{-1}$  and  $19 \text{ S.cm}^{-1}$  respectively. However, the temperature dependence of the conductivities of these salts is characteristic of semiconductors. In the temperature regions of ca.100-288 K for the former and ca.150-288 K for the latter, the temperature dependence of conductivities can be fitted to the standard Arrhenius-type expression, which yields the semiconducting bandgap energies of 0.11 eV and 0.13 eV, respectively.

The 2:2 salt  $(\text{Et}_4\text{N})_2[\text{Ni}(\text{dsit})_2]_2$ , on the other hand, exhibits a much lower room temperature conductivity,  $\sigma_{\text{rt}} = 5 \times 10^{-5} \text{ S.cm}^{-1}$ , which is about six orders of magnitude smaller than that of the 1:2 salts  $(\text{Me}_4\text{N})[\text{Ni}(\text{dsit})_2]_2$  and  $(\text{Me}_4\text{P})[\text{Ni}(\text{dsit})_2]_2$ . This result can be easily understood by examining the crystal structure of



this salt. Here, the  $[\text{Ni}(\text{dsit})_2]_2$  dimer units are well separated from each other by tetraethylammonium ions. Overlap of  $[\text{Ni}(\text{dsit})_2]$  molecular orbitals to form a conduction band is not possible, and hence the conductivity is very low. The electronic conduction must be principally mediated by long-range hopping processes and accordingly, the activation energy is also quite high (0.61 eV).

#### Discussion of results

The reasons for two different stoichiometries obtained in the cases of  $(\text{Me}_4\text{N})^+$  and  $(\text{Me}_4\text{P})^+$  (1:2), and  $(\text{Et}_4\text{N})^+$  (2:2) cations are not very clear. We speculate that with the larger cations, the oxidation product tends to crystallize at the formally Ni(III) redox stage in acetonitrile. Moreover, the formally Ni(III)/Ni(IV) redox reaction may not be accessible and/or reversible in electrolytes with larger counter-cations, which is consistent with Nigrey's cyclic voltammetry results [11].

The dimeric structures  $[\text{Ni}(\text{dsit})_2]_2^{2-}$  and  $[\text{Ni}(\text{dsit})_2]_2^{1-}$  of the 1:1 and 1:2 salts, respectively, both contain a unique square-pyramidal coordination geometry around formally  $\text{Ni}^{+3}$  and  $\text{Ni}^{+3.5}$  ions. While such tightly bound dimeric structures have not been previously observed in the corresponding radical-anion salts based on  $[\text{Ni}(\text{dmit})_2]$  [13,14], they have been reported in cobalt(II)-dithiolene [16,17], iron(II)-dithiolene [18,19] complexes. The intermolecular (but intradimer) metal-chalcogen bond distances in these cobalt and iron complexes are only slightly longer (ca. 0.15-0.20 Å) than the intramolecular metal-chalcogen bond distances [19]. In the case of the three  $[\text{Ni}(\text{dsit})_2]$  complexes reported here, the lengths these two kinds of bonds also exhibit a similar trend (see Tables III and IV).

#### Concluding Remarks

Metal-dithiolene and metal-diselenolene complexes, which are capable of forming dimer units, are potential building blocks in preparation of electrically conducting and possibly superconducting solids with K-type structures. The high conductivities exhibited by  $(\text{Me}_4\text{N})[\text{Ni}(\text{dsit})_2]_2$  and  $(\text{Me}_4\text{P})[\text{Ni}(\text{dsit})_2]_2$ , which possess the K-type molecular packing arrangement, suggest that with further systematic chemical modifications, i.e., changing the counterions and the metal ions, it is likely that new metallic and superconducting salts may emerge from this class of compounds.

#### Acknowledgements

Work at Argonne National Laboratory is sponsored by the U. S. Department of Energy, Office of Basic Energy Sciences, Division of Materials Sciences, under contract W-31-109-ENG-38. S. B. is an Undergraduate Research Participant from St. Xavier College,

Chicago, IL, sponsored by the Argonne Division of Educational Programs.

#### References

1. See e.g., Proceedings of the International Conference on Science and Technology of Synthetic Metals, Santa Fe, NM, U.S.A., June 26-July 2, 1988, Synth. Metals, 27-29, (1988-1989).
2. H. Urayama, H. Yamochi, G. Saito, K. Nozawa, T. Sugano, M. Kinoshita, S. Sato, K. Oshima, A. Kawamoto, J. Tanaka, Chem. Lett. 1988, 55.
3. J. E. Schirber, E. L. Venturini, A. M. Kini, H. H. Wang, J. R. Whitworth, J. M. Williams, Physica C, 152, 157 (1988).
4. H. Urayama, H. Yamochi, G. Saito, S. Sato, A. Kawamoto, A. Tanaka, T. Mori, Y. Maruyama, H. Inokuchi, Chem. Lett. 1988, 463.
5. K. D. Carlson, U. Geiser, A. M. Kini, H. H. Wang, L. K. Montgomery, W. K. Kwok, M. A. Beno, J. M. Williams, C. S. Cariss, G. W. Crabtree, M.-H. Whangbo, M. Evain, Inorg. Chem. 27, 965 and 2904 (1988).
6. A. M. Kini, M. A. Beno, K. D. Carlson, J. R. Ferraro, U. Geiser, A. J. Schultz, H. H. Wang, J. M. Williams, in Proceedings of the First ISSP International Conference on the Physics and Chemistry of Organic Superconductors, Tokyo, Japan, August 27-30, 1989, edited by G. Saito and S. Kagoshima, (Springer-Verlag, Heidelberg), in press.
7. F. A. Cotton and G. Wilkinson, Advanced Inorganic Chemistry, 5th ed. (John Wiley & Sons, New York, 1988), p. 540.
8. L. Alcacer and H. Novais, in Extended Linear Chain Compounds, Volume 3, edited by J. S. Miller (Plenum Press, New York, 1983), p. 319.
9. L. Brossard, M. Ribault, M. Bousseau, L. Valade, P. Cassoux, C.R. Acad. Sc. Paris, Ser. II, 302, 205 (1986).
10. A. Kobayashi, H. Kim, Y. Sasaki, R. Kato, H. Kobayashi, S. Moriyama, Y. Nishio, K. Kajita, W. Sasaki, Chem. Lett. 1987, 1819.
11. P. J. Nigrey, Synth. Metals, 27, B365 (1988).
12. K. A. Lerstrup and D. O. Cowan, J. de Physique, Colloque C3, 1983, 1247.
13. L. Valade, J.-P. Legros, M. Bousseau, P. Cassoux, M. Garbauskas, L. V. Interrante, J. Chem. Soc. Dalton Trans. 1985, 783.
14. R. Kato, H. Kobayashi, H. Kim, A. Kobayashi, Y. Sasaki, T. Mori, H. Inokuchi, Synth. Metals, 27, B359 (1988).
15. L. R. Groeneveld, B. Schuller, G. J. Kramer, J. G. Haasnoot, J. Reedijk, Recl. Trav. Chim. Pays-Bas, 105, 507 (1986).
16. J. H. Enemark and W. N. Lipscomb, Inorg. Chem. 4, 1729 (1965).
17. M. J. Baker-Hawkes, Z. Dori, R. Eisenberg, H. B. Gray, J. Amer. Chem. Soc. 90, 4253 (1968).
18. W. C. Hamilton and I. Bernal, Inorg. Chem. 6, 2003 (1967).
19. A. J. Schultz and R. Eisenberg, Inorg. Chem. 12, 518 (1973).

**BRIDGED MACROCYCLIC TRANSITION METAL COMPLEXES,  
A NEW TYPE OF SEMICONDUCTING MATERIALS**

MICHAEL HANACK\*, A. HIRSCH, A. LANGE, M. REIN, G. RENZ AND P. VERMEHREN  
Institut für Organische Chemie, Lehrstuhl für Organische Chemie II der Universität  
Tübingen, Auf der Morgenstelle 18, D-7400 Tübingen, Federal Republic of Germany

**ABSTRACT**

Bridged quasi onedimensional macrocyclic transition metal complexes  $[\text{MacM}(\text{L})]_n$  using phthalocyanine (Pc), tetrabenzoporphyrine (TBP), 1,2- and 2,3-naphthalocyanines (1,2-, 2,3-Nc) as macrocycles (Mac) with  $\text{M} = \text{e.g. Fe, Ru, Co}$  and  $\text{L} = \text{e.g. pyrazine (pyz), 1,4-diisocyanobenzene (dib), tetrazine (tz)}$  exhibit interesting electrical properties. Regardless of the size of the bridging ligand after either chemical or electrochemical doping stable semiconducting compounds  $[\text{MacM}(\text{L})\text{X}_y]_n$  ( $\text{X} = \text{e.g. I, BF}_4^-, \text{ClO}_4^- \dots$ ) are formed. For the first time the complete characterization of a soluble oligomer  $[\text{MacM}(\text{L})]_n$  (Mac =  $\text{R}_4\text{Pc}$ ,  $\text{M} = \text{Ru}$ ,  $\text{L} = \text{dib}$ ) by  $^1\text{H-NMR}$  spectroscopy is reported. Some of these shish kebab complexes e.g.  $[\text{PcM}(\text{tz})]_n$ , ( $\text{M} = \text{Fe, Ru}$ ) or  $[\text{MacMCN}]_n$ ; (Mac = Pc, TBP;  $\text{M} = \text{Co, Fe}$ ) exhibit good semiconducting properties without additional external doping. Whether or not these compounds are intrinsic semiconductors will be discussed. The synthesis of oligomeric bridged mixed valence compounds  $[\text{PcM}^{3+}\text{LPcM}^{2+}\text{L}]_n$  ( $\text{M} = \text{e.g. Fe}$ ) is another target of our work. We report here about first attempts to synthesize these oligomers.

**RESULTS AND DISCUSSION**

Bridged quasi-one dimensional macrocyclic transition metal complexes linked by linear bridging ligands L containing delocalizable  $\pi$ -electrons to form stacked arrangements  $[\text{MacM}(\text{L})]_n$  have been synthesized. As macrocycles Mac phthalocyanine (Pc), tetrabenzoporphyrine (TBP), 2,3-naphthalocyanine (2,3-Nc) and 2,3-tetra-naphthoporphyrine (2,3-TNP) have been used. Fe, Ru, Co, Rh and others were taken as central metals and as bridging ligands e.g. pyrazine (pyz), diisocyanobenzene (dib), and substituted diisocyanobenzenes [1].

The characterization of the bridged macrocyclic metal compounds was done by IR spectroscopy or thermogravimetric methods. NMR studies to investigate the mechanism of formation of the bridged metal complexes have also been carried out with  $\text{PcM}(\text{Me}_4\text{dib})_2$  and  $[\text{PcM}(\text{Me}_4\text{dib})]_n$ ,  $\text{M} = \text{Fe, Ru}$  [2].

Soluble oligomers  $[\text{MacM(L)}]_n$ , namely substituted phthalocyanine oligomers  $[\text{R}_4\text{PcM(dib)}]_n$   $\text{M} = \text{Fe, Ru}$ ,  $\text{R} = \text{t-bu}$ ,  $\text{OR}'$  were synthesized. For  $[\text{t-bu}_4\text{PcRu}_4(\text{dib})]_n$  the  $^1\text{H-NMR}$  spectrum in solution was measured. From a detailed analysis of the spectrum the oligomeric bridged structure was *proved* and the chain length was shown to be in between 7 and 35  $\text{t-bu}_4\text{PcRu}$  units.

Möbbauser spectroscopy was also employed to obtain additional information about the structure of the bridged macrocyclic iron compounds. The isomer shift ( $\delta$ ) and the quadrupol splitting ( $\Delta E_Q$ ) have been measured for a variety of monomeric and polymeric phthalocyaninato-, tetranaphthoporphyrinato-, and naphthalocyaninatoiron compounds. From these data an independent proof for the hexacoordination of the bridged compounds was obtained.

The bridged systems  $[\text{MacFe(L)}]_n$ ,  $\text{Mac} = \text{Pc, TBP}$ ,  $\text{L} = \text{e.g. pyz, dib}$ , have been oxidatively doped with iodine. Incremental doping results in the formation of stoichiometric compounds  $[\text{MacM(L)}_y]_n$  which are stable up to  $120^\circ\text{C}$  [3-4]. The corresponding compounds  $[\text{PcFe(L)}_y]_n$  show at the maximum doping level conductivities  $\sigma_{\text{RT}}$  of  $10^{-2} - 10^{-1} \text{ S/cm}$ .

Electrochemical doping of  $[\text{MacM(L)}]_n$  compounds with a variety of counterions e.g.  $\text{BF}_4^-$ ,  $\text{B(Ph)}_4^-$ ,  $\text{PF}_6^-$ , and  $\text{ClO}_4^-$  is also possible leading to thermally even more stable systems ( $\sim 150^\circ\text{C}$ ) with conductivities of  $\sim 10^{-2} \text{ S/cm}$ .

The described combination of the macrocycle containing a transition metal and a bridging ligand leading to a stacked arrangement could also cause intrinsic conductivity of the bridged complexes. Exchanging e.g. pyrazine as bridging ligand against tetrazine according to MO-calculations can lead to a smaller gap between the HOMO of the  $d_{xy}$ -orbitals of the central metal atom and the LUMO of the bridging ligand, and thereby causing semi-conductive properties without additional external doping.

A higher conductivity can indeed be obtained, if instead of pyrazine e.g. tetrazine or dimethyltetrazine is used as the bridging ligand in the complexes  $[\text{PcFe(L)}]_n$  ( $\text{L} = \text{tz, me}_2\text{tz}$ ). These types of bridged systems have also been obtained with phthalocyaninoruthenium leading to  $[\text{PcRu(tz)}]_n$ . They are prepared by treating the corresponding metal macrocycles with tetrazine or dimethyltetrazine in chloroform at  $70^\circ\text{C}$ . Table 1 shows some conductivity data of monomeric and s-tetrazine bridged metal macrocycles in comparison with the corresponding pyrazine-bridged systems [5,6]. The monomers, e.g.  $\text{PcFe(tz)}_2$  show clearly an insulating behavior while the s-tetrazine bridged macrocyclic compounds show in general comparatively high conductivities up to  $0.3 \text{ S/cm}$  in case of  $[\text{2,3-NcFe(tz)}]_n$ . The difference between pyrazine and tetrazine as a bridging ligand is especially evident, if one compares the corresponding bridged systems: In all cases an increase in the powder conductivities of  $10^3 - 10^4$  is observed.

Table 1 Conductivity data of monomeric and s-tetrazine bridged metal macrocycles in comparison with the corresponding pyrazine-bridged systems

Compound	$\sigma_{RT}$ [S/cm]	$E_a$ [eV]
PcFe(tz) <sub>2</sub>	$> 10^{-9}$ <sup>a</sup>	-
[PcFe(py <sub>z</sub> )] <sub>n</sub>	$2 \times 10^{-5}$ <sup>b</sup>	-
[PcFe(tz)] <sub>n</sub>	$2 \times 10^{-2}$ <sup>b</sup>	0.20
PcRu(tz) <sub>2</sub>	$< 10^{-11}$ <sup>a</sup>	-
[PcRu(tz)] <sub>n</sub>	$1 \times 10^{-2}$ <sup>b</sup>	0.10
[PcRu(py <sub>z</sub> )] <sub>n</sub>	$1 \times 10^{-7}$ <sup>b</sup>	-
[PcRu(me <sub>2</sub> tz)] <sub>n</sub>	$4 \times 10^{-3}$ <sup>b</sup>	-
[me <sub>8</sub> PcFe(py <sub>z</sub> )] <sub>n</sub>	$9 \times 10^{-6}$ <sup>b</sup>	-
[me <sub>8</sub> PcFe(tz)] <sub>n</sub>	$1 \times 10^{-3}$ <sup>b</sup>	-
[2,3-NcFe(py <sub>z</sub> )] <sub>n</sub>	$5 \times 10^{-5}$ <sup>b</sup>	-
[2,3-NcFe(tz)] <sub>n</sub>	0.3 <sup>b</sup>	0.07

<sup>a</sup>Two-probe-technique.

<sup>b</sup>Four-probe-technique.

Table 2 Mößbauer data<sup>a</sup> of tz-bridged macrocyclic iron compounds [6]

Compound	$\delta$ [mm/s]	$\Delta E_Q$ [mm/s]
[PcFe(py <sub>z</sub> )] <sub>n</sub>	0.24	2.04
[PcFe(tz)] <sub>n</sub>	0.13	2.27
[me <sub>8</sub> PcFe(tz)] <sub>n</sub>	0.14	2.11
[(meO) <sub>8</sub> PcFe(tz)] <sub>n</sub>	0.15	2.19
[2,3-NcFe(tz)] <sub>n</sub>	0.19	1.97

<sup>a</sup>Relative to metallic iron.

Table 2 shows some Mößbauer data of tz-bridged complexes in comparison with  $[\text{PcFe}(\text{pyz})]_n$  [7]. In all cases the isomer shift of the tetrazine bridged systems is especially small, which points to a charge transfer from the iron on to the tetrazine in these systems. The electronic structure of  $[\text{PcFe}(\text{pyz})]_n$  has been studied by means of the tight-binding (LCAO) Method [8]. The band gap according to these calculations is mostly determined by the difference in energies between the LUMO of the bridging ligand and the HOMO of the transition metal  $d_{xy}$  orbital. The higher conductivities of the s-tetrazine bridged compounds  $[\text{PcFe}(\text{tz})]_n$ ,  $[\text{PcRu}(\text{tz})]_n$  and  $[2,3\text{-NcFe}(\text{tz})]_n$  are then explained by the low lying LUMO of this ligand.

Another type of bridged systems are macrocycles containing the central transition metals in the oxidation state of +III. An octahedral configuration of the metal atoms within the macrocycles is possible e.g. for Fe(III), Co(III) or Rh(III). For the formation of the corresponding bridged systems  $\text{CN}^-$ ,  $\text{SCN}^-$  or  $\text{N}_3^-$  are suitable bridging ligands [9-12].

Fig. 1 schematically shows a cyano-bridged phthalocyanine complex which can be easily synthesized e.g. from  $\text{PcCoCl}_2$  for  $M = \text{Co(III)}$ .  $\text{PcCoCl}_2$  reacts with an excess of  $\text{NaCN}$  or  $\text{KCN}$  to form the soluble  $\text{Na}[\text{PcCo}(\text{CN})_2]$  [9]. The crystal structure of this monomer is known [13] and the bisaxial coordination of the  $\text{CN}$ -groups thus proven.  $\text{HCN}$  can be cleaved from the monomer using different methods e.g. treatment with  $\text{H}_2\text{O}$  at  $100^\circ\text{C}$ . Thereby  $[\text{PcCoCN}]_n$  is directly obtained in virtually quantitative yield [9]. Other metals (e.g. Fe, Rh) and macrocycles (e.g. TBP) were used by analogy. By IR- and FIR spectroscopy, magnetic and thermographic measurements as well as by solid-state NMR investigations it was determined that these compounds possess a cyano-bridged structure [9,11]. All of the cyano-bridged macrocyclic metal complexes, but also the corresponding compounds with  $\text{SCN}^-$  as bridging ligand show comparatively high powder conductivities: for instance for  $[\text{PcCoCN}]_n$   $\sigma_{RT} = 2 \times 10^{-2} \text{ S/cm}$  ( $E_a = 0.10 \text{ eV}$ ) was measured [9]. The other bridged cyano- and thiocyanato complexes mentioned here show similar powder conductivities without additional external doping. Table 3 shows some conductivity data of cyano- and thiocyanato bridged metal macrocycles.

Table 3 Conductivity data of cyano- and thiocyanato bridged metal macrocycles

Compound	$\sigma_{RT}$ [S/cm] <sup>a)</sup>	$E_a$ [eV]
[PcFeCN] <sub>n</sub>	$6 \times 10^{-3}$	0.10
[PcCoCN] <sub>n</sub>	$2 \times 10^{-2}$	0.10
[TBPCoCN] <sub>n</sub>	$4 \times 10^{-2}$	0.11
[PcCoSCN] <sub>n</sub>	$6 \times 10^{-3}$	0.22

a) Four-probe-technique.

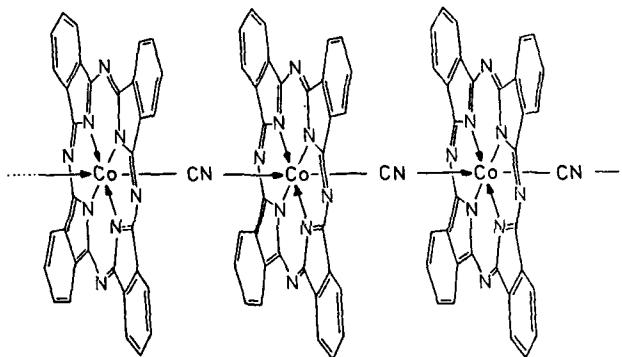


Fig. 1 Schematic structure of [PcCoCN]<sub>n</sub>

Another attempt to synthesize bridged transition metal complexes which show intrinsic semiconductive properties was carried out as follows:

Axially bridged mixed valence phthalocyaninato metal complexes which contain the central metals in the formal oxidation states of +II and +III and have cyanide and pyrazine as bridging ligand can be viewed as self doped electrically conducting compounds (Figure 2). For such an electrically neutral bridged compound is no need for any counter ion for charge compensation. A very similar class of molecules are the mixed valence compounds of the Creutz-Taube type [14].

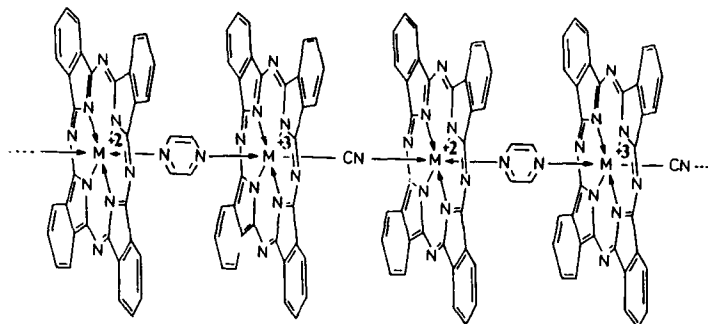


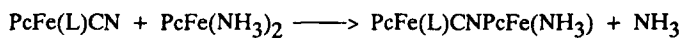
Fig. 2 Mixed valence polymer

The used ligands cyanide and pyrazine lead to a strong electronic coupling between the different charged metal centers. For such substances interesting electrical properties together with high thermal and chemical stability are expected.

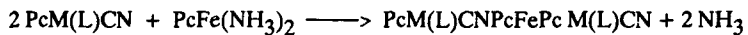
The strategy for the synthesis is the linking of axially coordinated monomeric metal(II) and metal(III) phthalocyanines (Scheme 1). The bisaxially coordinated ammonia complex  $\text{PcFe}(\text{NH}_3)_2$  could be isolated by an autoclav reaction of  $\text{PcFe}$  in liquid ammonia. Substituting of the relatively weak bonded ammonia by the stronger coordinating cyanide leads to the corresponding dimeric and trimeric systems.

Scheme 1 Synthesis of bridged mixed valence phthalocyaninato metal compounds

Dimer and trimer:



1: L = pyridine



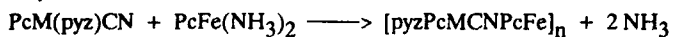
2: M = Fe, L = py

4: M = Co, L = py

3: M = Fe, L = t-bupy

5: M = Co, L = t-bupy

Polymer:



6: M = Co



The three valent monomers  $\text{PcM(L)CN}$  ( $M = \text{Fe, Co}$ ) have been synthesized by degradation reactions of the polymers  $[\text{PcMCN}]_n$  with the bases pyridine, t-butylpyridine and pyrazine. The mixed valence compounds 1 - 6 have been prepared at  $80^\circ\text{C}$  in toluene or ethanol as solvent. The reaction time is 72 h. Table 4 shows the cyanide valence frequencies and the room temperature conductivities of the mixed valence compounds 1 - 6 and the corresponding monomers  $\text{PcM(L)CN}$ . The formation of a cyano bridge leads to an increase of the CN valence frequency. This can be explained by a decrease of electron density of the antibonding  $\pi$ -orbital due to coordination to a second metal atom.

Table 4 IR data and conductivities

Compound	$\nu_{\text{CN}}[\text{cm}^{-1}]$	$\sigma_{\text{RT}}[\text{S/cm}]$
$\text{PcFe(py)CN}$	2131	$1 \times 10^{-10}$
<u>1</u>	2136	$3 \times 10^{-5}$
<u>2</u>	2135	$2 \times 10^{-5}$
$\text{PcFe(t-bupy)CN}$	2132	$6 \times 10^{-5}$
<u>3</u>	2135	$1 \times 10^{-4}$
$\text{PcCo(py)CN}$	2146	$3 \times 10^{-12}$
<u>4</u>	2150	$3 \times 10^{-8}$
$\text{PcCo(t-bupy)CN}$	2143	$2 \times 10^{-13}$
<u>5</u>	2151	$5 \times 10^{-10}$
$\text{PcCo(py)CN}$	2148	$2 \times 10^{-11}$
<u>6</u>	2152	$1 \times 10^{-6}$

Also the electrical conductivities are increasing if a bridged mixed valence compound is formed. The highest conductivities are reached if only Fe is used as central metal. In the mixed metal complexes 4, 5 and 6 charge delocalisation is less favourable.

The  $^{57}\text{Fe}$ -MöBbauer data of the compounds synthesized are given in table 5. The data for the isomer shift and quadrupole splitting of the  $\text{Fe(II)}$  centers lie in the typical range for low spin hexacoordinated phthalocyaninatoiron complexes [4,15]. This points to a similar coordination behaviour of the  $\text{PcM(L)CN}$  moiety and a N-base like

pyridine. The isomer shift of the Fe(II) center in compound **3** is comparatively small which can be related to a high decrease of electron density of the corresponding 3d-orbitals.

Table 5  $^{57}\text{Fe}$ -Mössbauer data

Compound	T [K]	$\Delta E_Q$ [mm/s]	IS [mm/s] <sup>a)</sup>	
<b>1</b> <sup>b)</sup>	M(II)	293	1.79	0.26
	M(III)		1.47	-0.05
<b>2</b> <sup>b)</sup>	M(II)	293	2.01	0.24
	M(III)		1.61	0.09
<b>3</b> <sup>b)</sup>	M(II)	293	1.98	0.11
	M(III)		1.22	0.03
<b>4</b> <sup>c)</sup>	M(II)	77	1.93	0.33
<b>5</b> <sup>c)</sup>	M(II)	293	2.01	0.23
<b>6</b> <sup>c)</sup>	M(II)	293	2.00	0.26
PcFe(py)CN <sup>c)</sup>	293	1.57	0.04	
PcFe(t-bupy)CN <sup>c)</sup>	293	1.57	0.04	
PcFe(py <sub>2</sub> )CN <sup>c)</sup>	293	1.60	0.05	
[PcFe(py <sub>2</sub> )] <sub>n</sub> <sup>c)</sup>	293	2.00	0.25	

- a) Relative to metallic iron.  
 b) Two quadrupole doublets.  
 c) One quadrupole doublet.

Further investigations are done with UV/VIS/NIR spectroscopy, X-ray powder diffraction, TGA/DTG-measurements and others. The synthesis of the mixed valence polymer [pyzPcFe(III)CNPcFe(II)]<sub>n</sub> by coupling reactions of PcFe(py<sub>2</sub>)CN with PcFe(NH<sub>3</sub>)<sub>2</sub> is in progress.

References

- [1] M. Hanack, *Chimia* 37, 238 (1983);  
M. Hanack, A. Datz, R. Fay, K. Fischer, U. Keppeler, J. Koch, J. Metz,  
M. Mezger, O. Schneider and H.-J. Schulze in T. Skotheim (ed.), *Handbook on  
Conducting Polymers*, Marcel Dekker, New York 1985.
- [2] U. Keppeler and M. Hanack, *Chem. Ber.* 119, 3363 (1986).
- [3] M. Hanack, U. Keppeler and H.-J. Schulze, *Synth. Met.* 20, 347 (1987).
- [4] B.N. Diel, T. Inabe, K.K. Jaggi, J.W. Lyding, O. Schneider, M. Hanack,  
C.R. Kannewurf, T.J. Marks and C.H. Schwartz, *J. Am. Chem. Soc.* 106, 3207  
(1984).
- [5] U. Keppeler, S. Deger, A. Lange and M. Hanack, *Angew. Chem.* 99, 349  
(1987).
- [6] A. Lange and M. Hanack, unpublished.
- [7] A. Lange, U. Keppeler and M. Hanack, *Inorg. Chem.*, in press.
- [8] E. Canadell and S. Alvarez, *Inorg. Chem.* 23, 573 (1984).
- [9] J. Metz, M. Hanack, *J. Am. Chem. Soc.* 105, 828 (1983).
- [10] M. Schwartz, W.E. Hatfield, M.D. Joestein, M. Hanack, A. Datz, *Inorg. Chem.*  
24, 4198 (1985).
- [11] M. Hanack, C. Hedtmann-Rein, A. Datz, U. Keppeler, X. Münz, *Synth. Met.*  
19, 787 (1987).
- [12] C. Hedtmann-Rein, M. Hanack, K. Peters, E.-M. Peters, H.G. v. Schnering,  
*Inorg. Chem.* 26, 2647 (1987).
- [13] M. Hanack, J. Brokken, K. Peters, *Acta Cryst.*, in press.
- [14] C. Creutz, *Prog. Inorg. Chem.* 30, 1 (1983).
- [15] F. Calderazzo, S. Frediani, B.R. James, G. Pampaloni, K.J. Remier, J.R. Sams,  
A.M. Serra, D. Vitali, *Inorg. Chem.* 21, 2302 (1982).

DISCOTIC LIQUID CRYSTALLINE PORPHYRINS: PHOTOPHYSICAL AND PHOTOELECTRICAL PROPERTIES OF LARGE-AREA CRYSTALLINE FILMS

BRIAN A. GREGG\*, MARYE ANNE FOX\*\* AND ALLEN J. BARD\*\*

\*University of Texas at Austin, Dept. of Chemical Engineering, Austin, TX 78712.

\*\*University of Texas at Austin, Dept. of Chemistry, Austin, TX 78712.

ABSTRACT

Porphyrins exhibiting discotic liquid crystalline phases have been developed in order to prepare thin, large-area, crystalline films of molecular conductors. A series of octaalkylporphyrins bearing different side chains have been synthesized including some with electron-withdrawing substituents at the meso positions. The photophysical properties of thin films of these compounds are a strong function of the film order (crystallinity). A substantial and persistent photovoltaic effect was achieved (e.g.,  $V_{oc} = 0.3$  V,  $i_{sc} = 0.4$  mA/cm<sup>2</sup> under white light, 150 mW/cm<sup>2</sup>) in capillary-filled *symmetrical* cells with indium-tin oxide electrodes. A model based on kinetically-controlled asymmetric exciton dissociation leading to photoinjection at the illuminated interface is presented to explain these results. This appears to be the first unambiguous example of a photovoltaic cell controlled entirely by interfacial kinetics. The predominance of the photoinjection process in these cells is attributed to the single-crystal-like character of the porphyrin films.

INTRODUCTION

The self-ordering properties of liquid crystals (LCs) can be used to obtain large-area arrays of ordered materials. For example, single (liquid) crystal devices covering hundreds of square centimeters are easily obtained by capillary-filling the isotropic liquid followed by slow cooling into the LC phase. If liquid crystals can be made electroactive, these inexpensive, thin, large-area devices could find a number of applications in such areas as molecular electronics, the matrix addressing of flat panel displays and the conversion of solar energy.

We describe here the photophysical and photoelectrical properties of some of the recently synthesized liquid crystal porphyrins (LCPs) [1,2]. Their properties are a strong function of the degree of crystallinity of the films [3]; this report will primarily be concerned with the most highly ordered films. The chemical structure of the LCPs is shown in Figure 1a while a schematic diagram of the columnar discotic liquid crystal phase is given in Figure 1b. Two families of LCPs have been synthesized: most of the octaesters ( $R = COOC_nH_{2n+1}$  in Figure 1a) exhibited two columnar discotic mesophases before melting to isotropic liquids [1]; in contrast, the metallo

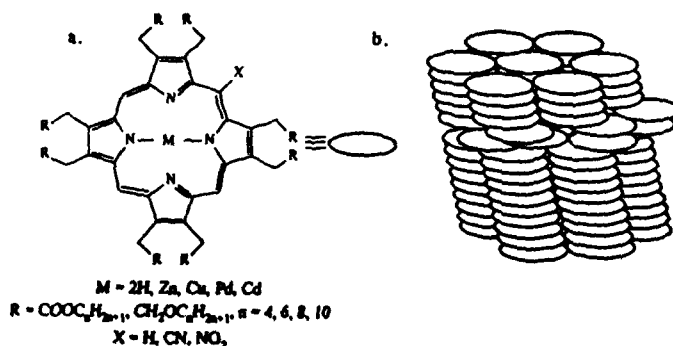


FIGURE 1. (a) General structure of the liquid crystal porphyrins. (b) Schematic diagram of a columnar discotic mesophase showing some crystal dislocations.

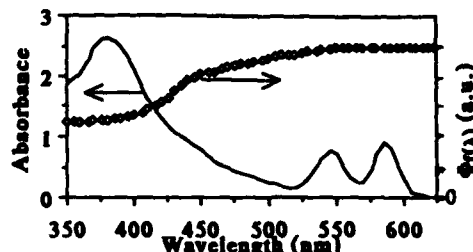


FIGURE 2. Absorption spectrum of a  $2\ \mu\text{m}$  thick capillary-filled cell of ZnOOEP and the wavelength-dependent quantum yield for fluorescence,  $\Phi_f(\lambda)$ , monitored at  $650\ \text{nm}$ .

derivatives of the octaethers ( $R = \text{CH}_2\text{OC}_n\text{H}_{2n+1}$ ) exhibited only a single mesophase while most of the free base derivatives melted directly from the solid to the isotropic liquid [2]. Two derivatives with electron-withdrawing substituents at the meso positions ( $X = \text{CN}$  and  $\text{NO}_2$ ) have also been prepared [2]. These substituents shifted the redox potentials of the material to more positive values and increased the dielectric constant of the films, thus suggesting the potential chemical versatility of such materials.

Numerous porphyrin derivatives have been extensively studied because of their unusual optical, electrical and magnetic properties [4]. The introduction of liquid crystalline derivatives may initiate the study of these materials in large-area crystalline films. Organic compounds, such as porphyrins and phthalocyanines, are highly anisotropic conductors [5]; this anisotropy is increased by the addition of the insulating aliphatic side chains on the LCP derivatives. Thus, the conductivity is much more one-dimensional in the LCPs than in the conventional porphyrin and phthalocyanine films. The ability to adjust the morphological, optical, electrical and magnetic properties by synthetic methods is one of the most promising aspects of organic materials.

#### PHOTOPHYSICAL PROPERTIES

Spin-coated films of zinc octakis( $\beta$ -octyloxyethyl)porphyrin, ZnOOEP, and its non-liquid crystalline analog zinc octaethylporphyrin, ZnOEP, have been prepared in various degrees of order ranging from amorphous to polycrystalline [3]. Increasing the order of the film led, at first, to characteristic shifts in the absorption spectra: the width of the absorption bands decreased, the Q (visible) bands shifted to lower energy by as much as  $16\ \text{nm}$  ( $469\ \text{cm}^{-1}$ ) while the B (Soret) band shifted to higher energy by up to  $20\ \text{nm}$  ( $1290\ \text{cm}^{-1}$ ). These shifts can be explained on the basis of molecular exciton theory [3,6,7]. The quantum yield for fluorescence also increased with increasing film order by a factor of ca. 17.

If the spin-coated films were heated to the isotropic phase and then cooled slowly through the LC phase to the solid, polycrystalline films were formed. More highly ordered films can be achieved by capillary-filling the LC porphyrin into a thin cell between parallel pieces of glass, leading to crystallites of ZnOOEP on the order of  $1\ \mu\text{m}$  in diameter in cells which are  $2\ \mu\text{m}$  thick. The absorption spectrum of such a capillary-filled cell is shown in Figure 2. The appearance of macroscopic crystallinity leads to spectral shifts which deviate from the pattern discussed above: the width of the absorption bands increased and both the B and the Q bands shifted towards higher energy. It is not clear whether simple (weak-coupling) exciton theory can be applied to such systems. The most dramatic change was the appearance of a wavelength dependent fluorescence quantum yield,  $\Phi_f$ , which decreased at shorter wavelengths (Figure 2). Thus, a process appeared that competes with internal conversion to the lowest singlet state. In less ordered films and in solution, internal conversion occurs with 100% efficiency. One explanation of this result is that a ring-to-ring charge transfer (RRCT) state is formed in competition with internal conversion when exciting into states lying higher in energy than the lowest excited singlet [3]. This explanation is consistent with measurements on single crystal tetracene [8] and with the photovoltaic results described below.

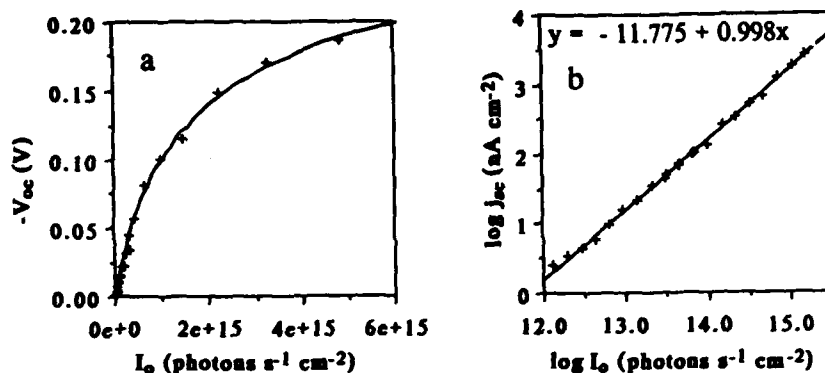


FIGURE 3. (a) Open circuit photovoltage,  $V_{oc}$ , versus incident light intensity,  $I_0$ , at 585 nm. The curve is a plot of equation 14 from reference 9. (b) Short circuit photocurrent density,  $j_{sc}$ , versus  $I_0$  at 400 nm. The line gives the best fit to the data.

#### PHOTOVOLTAIC PROPERTIES

In 1-5  $\mu\text{m}$  thick, symmetrical cells of ZnOOEP capillary-filled between two sheets of indium-tin oxide (ITO) coated glass, the porphyrin crystallites were 50 - 1000 times larger in diameter than the cell thickness [9]. The crystallites spanned the cell, thus the electrical properties are expected to more closely resemble those of single crystal cells than those of the more common evaporated (amorphous or polycrystalline) porphyrin or phthalocyanine cells. Upon illumination at open circuit with white light, these cells developed a photovoltage ( $V_{oc}$ ) in the range of -150 to -400 mV, the illuminated electrode being negative (the dark electrode was considered to be at ground). The rise and decay times of the photovoltage were less than ca. 10 ms. If the (symmetrical) cell was then illuminated from the opposite side, the illuminated electrode again charged negative, i.e., the electrons always flowed toward the light. The photovoltage increased at first with increasing incident light intensity and eventually saturated (Figure 3a).

Substantial photocurrents flowed in these devices [9]. At short circuit, under white light illumination of 150  $\text{mW}/\text{cm}^2$ , photocurrent densities ( $j_{sc}$ ) were in the range of 0.2 to 0.4  $\text{mA}/\text{cm}^2$  in 1.5 - 3  $\mu\text{m}$  thick cells. Thicker cells showed lower photocurrents. The rise and decay times of the photocurrent were less than ca. 10 ms, and, irrespective of which electrode was illuminated, the electrons flowed toward the light. The dark current in these cells was too low to measure, leading to an apparent dark resistivity,  $\rho > 10^{13} \Omega \text{ cm}$ . The photocurrent was quite stable: after a decay of ca. 15 % in the first 30 min, the photocurrent remained constant for 72 h, corresponding to the passage of ca.  $10^4$  electrons per porphyrin. The photocurrent increased linearly with incident light intensity (Figure 3b) up to  $I_0 > 10^{15} \text{ photons s}^{-1} \text{ cm}^{-2}$ . This shows that a single-photon process is involved in photocurrent production and also suggests that space charge effects [10] are unimportant, at least up to this intensity.

The photocurrent changed rapidly with applied voltage in the power curve region ( $V = 0$  to  $V = V_{oc}$ ) and eventually became a linear (ohmic) function of voltage at higher applied potentials (Figure 4a). The photocurrent in the linear region was two to three times as high for negative voltages applied to the illuminated electrode as for positive. This suggests that the mobility of electrons is two to three times as high as that of holes and, together with the insensitivity of the action spectra to voltage reversal (see below), rules out the Dember effect [11] as a mechanism for photocurrent production.

The photocurrent was a function of the wavelength of the exciting light (Figure 4b). For thin cells (ca. 1  $\mu\text{m}$ ), the photocurrent action spectrum resembled the absorption spectrum of the cell, while for thicker cells, the photocurrent showed a valley for every peak in the absorption spectrum. The action spectra changed only slightly when measured under positive, zero, or negative bias.

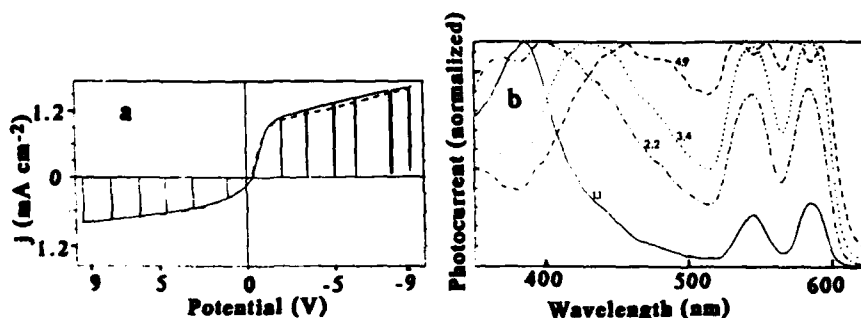


Figure 4. (a) Photocurrent-voltage curve for an LCP cell. Scan rate  $100 \text{ mV s}^{-1}$ ; white light,  $150 \text{ mW cm}^{-2}$ . Vertical lines show where the light was chopped. (b) Short circuit photocurrent versus wavelength (action spectra). The numbers on the curves give the cell thickness in  $\mu\text{m}$ .

Cells were usually assembled and tested in the presence of air, however several tests were carried out with nitrogen-saturated porphyrin and with oxygen-saturated porphyrin: the nitrogen treated cells showed slightly better properties than those exposed to air, showing that  $\text{O}_2$  is not required for the photovoltaic effect. The addition of a number of other oxidants (o- and p-chloranil,  $\text{I}_2$ , TCNQ) to the cells, had little or no effect on the photovoltaic properties. The addition of DDQ (dichlorodicyanobenzoquinone, the strongest oxidant employed) greatly increased the dark conductivity of the cells but had only a small effect on  $V_{oc}$  and  $j_{sc}$  [9].

## DISCUSSION

The occurrence of a substantial and stable photovoltaic effect in symmetrical cells was surprising. These cells showed photovoltaic characteristics comparable to some of the better organic solar cells although they were relatively thick ( $1\text{--}6 \mu\text{m}$ ) and had no apparent driving force for charge separation. Thus, we investigated the mechanism of this photovoltaic effect and developed a model which describes this behavior.

In covalently bonded (inorganic) semiconductors, the disruption of covalent bonds caused by crystal dislocations and impurities often leads to energetic states distributed throughout the otherwise forbidden bandgap. These states can be easily ionized and, in wide bandgap semiconductors such as  $\text{TiO}_2$  and  $\text{ZnO}$ , often account for the majority of the charge carriers in an otherwise intrinsic material [11]. In molecular (or van der Waals bonded) semiconductors, on the other hand, the intermolecular interactions are so weak that crystal dislocations and impurities often lead to only minor perturbations in the energy levels of the solid [12] and do not give rise to charge carriers. Thus, although the defect density and the impurity level in molecular semiconductors are often greater than those in inorganic semiconductors, the charge carrier density is often much smaller in the organic compound compared to an inorganic compound of similar bandgap.

The low charge carrier density in organic materials may prevent them from coming to equilibrium with their electrodes [13], in which case their photovoltaic properties will not be directly determined by the work functions of the contacts. In a number of cases it has been shown that only those electrode materials whose potential for oxidation is close to the potential for reduction of the organic compound, or whose potential for reduction is close to the potential for oxidation of the organic compound, can form contacts that are ohmic for electrons or holes, respectively [10,12,14]. Furthermore, it has been estimated that the formation of a blocking contact in a  $1 \mu\text{m}$  thick cell requires a charge carrier density of ca.  $10^{14} \text{ cm}^{-3}$  [9]; however, the carrier density in single crystal phthalocyanine and anthracene is ca.  $10^4\text{--}10^7 \text{ cm}^{-3}$  [13,15].

What then determines the photovoltaic properties? We suggest that, in the case of the

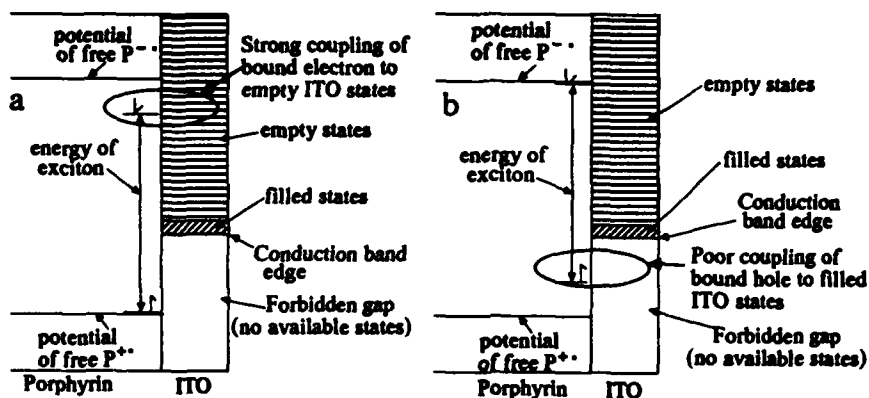


FIGURE 5. Schematic diagrams showing the proposed mechanism of asymmetric exciton dissociation. (a) The bound electron of the exciton couples strongly to the empty states of the ITO electrode leading to facile electron injection into the ITO and hole injection into the LCP. (b) The bound hole of the exciton couples only weakly to the filled states of the ITO electrode leading to a relatively slow rate of hole injection into the ITO and electron injection into the LCP.

liquid crystal porphyrins between ITO electrodes, and perhaps in other cases, the photovoltaic effect is caused by the asymmetric dissociation of excitons at the illuminated interface. Thus an exciton, upon reaching the electrode, may have a greater tendency to inject electrons into the electrode and holes into the organic material than vice versa. Such an asymmetric dissociation can be rationalized by assuming that the wave function of the bound electron (of the exciton) couples to empty conduction band states of the ITO electrode while the bound hole is isoenergetic with the forbidden gap of the ITO electrode and thus couples only weakly to filled states (Figure 5). Based on the mathematical model describing these LCP cells [9], we estimate that the injection of electrons into the ITO is twenty times more likely than hole injection at short circuit. This mechanism can adequately explain our results and those of a number of other workers [12,16-18]. To the best of our knowledge, such a mechanism for a photovoltaic effect has not previously been proposed.

A number of results from the study of single-crystal polycyclic aromatic hydrocarbons (e.g., anthracene) suggested that the dominant mechanism for photoconduction under an applied bias involved exciton migration to the surface followed by the injection of one carrier into the electrode [12,13,15,19]. Such a mechanism has rarely been invoked for porphyrin or phthalocyanine devices, which are commonly described in the same terms as inorganic semiconductors [20-24]. The predominance of the photoinjection process in these LCP cells, and its relative absence in cells made from sublimed layers of porphyrins and phthalocyanines, may be attributed to the practically single-crystal character of the LCP devices. Thus, the crystallinity of the material may be decisive in determining the mechanism of the photovoltaic effect.

Asymmetric exciton dissociation alone can not explain the thickness dependence of the photocurrent action spectra (Figure 4b). A pure interfacial process would be expected to result in action spectra that always resembled the absorption spectrum. The action spectra of thick cells suggested that photoconductivity effects were important [25] and, indeed, any photogeneration of free charge carriers in the bulk would be expected to have a large effect on the conductivity of a material which is so highly insulating in the dark ( $\rho > 10^{13} \Omega \text{ cm}$ ). Bulk photogeneration of charge carriers was also suggested by the decrease in the fluorescence quantum yield,  $\Phi_f$ , with increasing energy of excitation (Figure 2). The photogeneration of charge carriers in the bulk cannot, however, generate a steady state photovoltage or photocurrent [26]. Thus, we believe that



our results can only be explained by charge injection resulting from asymmetric exciton dissociation at the illuminated interface coupled with photoconductivity in the bulk LCP. An approximate mathematical model of these two processes has been developed which reproduces the experimental results [9]. The correct modeling of the thickness dependence of the action spectra required the assumption that the bulk photogeneration of charge carriers increased as  $\Phi_I$  decreased, in accord with our proposal of RRCT state formation in competition with internal conversion.

## CONCLUSIONS

Liquid crystal porphyrins provide a method for producing large-area, crystalline arrays of organic solid state materials. Order, or crystallinity, is of primary importance in determining the photophysical and photovoltaic properties of organic electronic devices. The photovoltaic effect in symmetrical cells containing highly-ordered LCP is postulated to be caused by the asymmetric dissociation of excitons at the illuminated electrode leading to injection of electrons into the ITO electrode and holes into the organic film. This appears to be the first example of a photovoltaic cell controlled entirely by interfacial kinetics. These results show that a substantial photovoltaic effect can be realized without the requirement for a space charge layer.

## REFERENCES

1. B. A. Gregg, M. A. Fox, A. J. Bard, *J. Chem. Soc., Chem. Commun.*, 1143 (1987).
2. B. A. Gregg, M. A. Fox, A. J. Bard, *J. Am. Chem. Soc.*, **111**, 3024 (1989).
3. B. A. Gregg, M. A. Fox, A. J. Bard, *J. Phys. Chem.*, **93**, 4227 (1989).
4. For a review, see: D. Dolphin, Ed. *The Porphyrins, Vols. I-VII*. (Academic Press, New York, 1978).
5. T. J. Marks, *Science*, **227**, 881 (1985), and references therein.
6. A. S. Davydov, *Theory of Molecular Excitons* (Plenum Press, New York, 1971).
7. M. Gouterman, D. Holten, E. Lieberman, *Chem. Phys.* **25**, 139 (1977).
8. N. Geacintov, M. Pope, H. Kallman, *J. Chem. Phys.*, **45**, 2639 (1966).
9. B. A. Gregg, M. A. Fox, A. J. Bard, *J. Phys. Chem.* in press.
10. O. H. LeBlanc, in *Physics and Chemistry of the Organic Solid State, Vol. 3*, edited by D. Fox, M. M. Labes, and A. Weissberger (Interscience, New York, 1967).
11. R. A. Smith, *Semiconductors*, 2nd Ed. (Cambridge University Press, Cambridge, 1978).
12. M. Pope, C. E. Swenberg, *Electronic Processes in Organic Solids*, (Oxford University Press, New York, 1982).
13. L. E. Lyons, in *Physics and Chemistry of the Organic Solid State, Vol. 1*, edited by D. Fox, M. M. Labes, and A. Weissberger (Interscience, New York, 1963).
14. W. Helfrich, in reference 10.
15. F. Gutmann, L. E. Lyons, *Organic Semiconductors, Part A* (Robert E. Krieger Publishing Co., Malabar, FLA., 1981).
16. H. Kallman, M. Pope, *J. Chem. Phys.*, **30**, 585 (1959).
17. K. J. Hall, J. S. Bonham, L. E. Lyons, *Aust. J. Chem.*, **31**, 1661 (1978).
18. J. S. Bonham, *Aust. J. Chem.*, **29**, 2123 (1976).
19. J. Kommandeur, *J. Phys. Chem. Solids*, **22**, 339 (1961).
20. M. Martin, J.-J. Andre, J. Simon, *Nouv. J. Chim.*, **5**, 485 (1981).
21. K. Yamashita, Y. Harima, H. J. Iwashima, *J. Phys. Chem.*, **91**, 3055 (1987).
22. F.-R. Fan, L. R. Faulkner, *J. Chem. Phys.* **69**, 3334 (1978); **69**, 3341 (1978).
23. R. O. Loutfy, J. H. Sharp, C. K. Hsiao, R. Ho, *J. Appl. Phys.*, **52**, 5218 (1981).
24. R. O. Loutfy, C. K. Hsiao, *Can. J. Phys.*, **59**, 727 (1981).
25. H. Gerischer, M. Lübke, B. Bressel, *J. Electrochem. Soc.* **130**, 2112 (1983).
26. N. F. Mott, R. W. Gurney, *Electronic Processes in Ionic Crystals*, 2nd Ed. (Dover, New York, 1964), p. 192.

LOW-DIMENSIONAL CRITICAL BEHAVIORS AND COMPETITION BETWEEN  
ORDER PARAMETERS IN THE ORGANIC METAL  $(\text{TMTSF})_2\text{ClO}_4$

F. PESTY, P. GAROCHE AND M. HERITIER  
Laboratoire de Physique des Solides,  
Associé au C.N.R.S., U.P.S., Bât 510  
91405 Orsay Cedex (FRANCE)

ABSTRACT

In low-dimensional conductors, the instability of the metallic state can lead to the formation at low temperature of a spin density wave induced by the magnetic field (FISDW). The transition results from the complex interplay between the one dimensional instability of the electronic gas and the quantization of the magnetic field's flux. This second-order phase-transition line has been investigated by measuring both specific heat and thermal conductivity along the  $c^*$  direction. The mean-field jump and the gap value have been deduced respectively from the anomaly and the exponential decay of the electronic specific heat. The coupling strength  $\lambda$  has been evaluated, and the  $\lambda > 0.3$  value indicates clearly a strong coupling behavior at high field. Below 8 teslas, the specific heat displays a double anomaly in relation with the competition between subphases. Above the second-order transition line, critical fluctuations are observed on both specific heat and lattice thermal conductivity. Along this line, one-dimensional fluctuations increase with increasing magnetic field. It is proposed that the very high field reentrance of the metal is to be related to enhancement of the 1D fluctuations.

INTRODUCTION

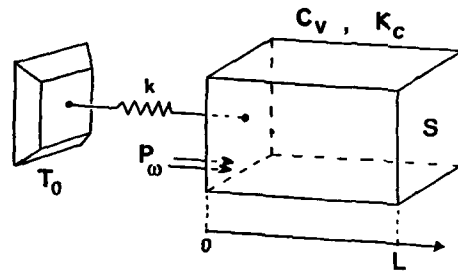
In the Bechgaard salts  $(\text{TMTSF})_2\text{X}$ , the FISDW states have been extensively studied during the past decade, from both experimental and theoretical points of view [1]. The appearance of the SDW in a moderate magnetic field (about 3 teslas) is so far understood as resulting from an orbital effect of the field which, by lowering the effective dimensionality of the electronic motion, leads at low enough temperature to the usual instability of the low-D metallic state. A description of the cascade of field induced transitions has been achieved within the "standard" model [2-6]. But number of experimental facts remain unclear. Among them, the high-field total reentrance of the metallic phase into the FISDW states [7-9], and the low-field partial ones [10], observed in the very well ordered  $(\text{TMTSF})_2\text{ClO}_4$ . Here, we will focus on the anomalous behavior of the metal-FISDW transition line in the intermediate field range.

MEASUREMENT OF THE HEAT CONDUCTION ALONG THE  $c^*$  AXIS

The 2mg single crystal, of a  $L=0.3\text{mm}$  thickness and a  $S=6.5\text{mm}^2$  cross-section area is glued onto a sapphire slab (Figure 1). The transverse direction, the  $c^*$  axis, is the least conducting one. The sample can thus be considered as resulting from the stacking of conducting planes roughly parallel to the sapphire's surface. Our basic assumption is that the planes are perfectly isothermal and that the heat conduction just takes place between neighboring planes. In such a case we are left with a purely one-dimensional

heat diffusion problem.

An experimental setup has been designed to measure simultaneously the specific heat  $c_v$  and the thermal conductivity along the  $c^*$  axis,  $K_C$  [11]. It is a combination of a.c. calorimetry [12] and Ångström's method [13]. The thermal excursion  $\delta T$  around the average temperature is chosen small enough to neglect the temperature dependence of  $c_v$  and  $K_C$ . These latter are thus considered as constant inside the bulk sample.



**Figure 1:** Sketch of the heat conduction along the  $c^*$  axis, i.e. along the magnetic field. The sample of thermal conductivity  $K_C$  and specific heat  $c_v$  is connected to the heat sink through a thermal conductance  $k$ . An a.c. heating power is applied on the  $x=0$  face.

A sinusoidal heating power  $P_\omega(t) = P_0(1 - e^{i\omega t})$  is applied on the sapphire slab, whose thermal conductance is considered as infinite at the working frequency  $\omega/2\pi$ . The sample-holder is connected to an external heat sink of temperature  $T_0$  through a thermal link of conductance  $k$ . Sample's temperature is measured using a thin-film thermometer sputtered on the sapphire slab. The temperature  $T(x,t)$  is space- and time-dependent and holds the 1D Fourier's diffusion law:

$$\frac{\partial T}{\partial t} = \frac{K_C}{c_v} \frac{\partial^2 T}{\partial x^2}, \quad \text{for } 0 \leq x \leq L,$$

where  $x$  measures the distance along  $c^*$  from the sapphire slab. The first boundary condition results from the absence of heat loss at the free edge (a reasonable assumption at low temperature):

$$\frac{\partial T}{\partial x}(L,t) = 0, \quad \text{for any } t;$$

the second boundary condition arises from the heat exchange balance:

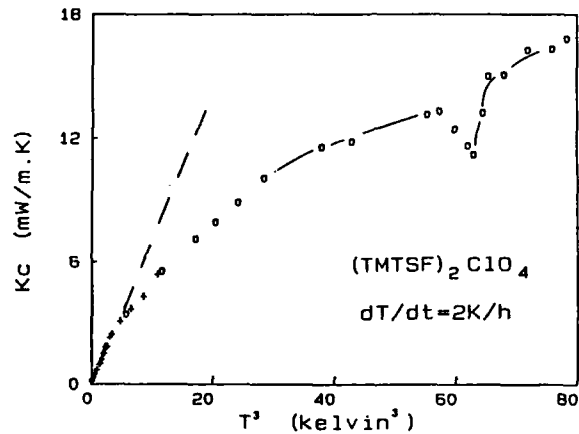
$$-K_C S \frac{\partial T}{\partial x}(0,t) = P_0 [1 - e^{i\omega t}] - k [T(0,t) - T_0].$$

The coupled equations are not analytically solvable, but a computer can easily do the job, for each set of measured parameters, at a given temperature.

The main goal here was to investigate the specific heat along

the transition line separating the metallic phase from the FISDW states, in the temperature versus magnetic field phase diagram. A 3 Hertz working frequency has been chosen. Using a digital lock-in for measuring the thermal oscillation, and a computer for its Fourier analysis, we were able to determine the thermal phase shift with a relative precision of about 0.1 degree. The simple thermal model exposed above was used to extract the thermal conductivity in the  $c^*$  direction  $K_C$  and the specific heat.

In the following we present the results obtained in the  $(TMTSF)_2ClO_4$  compound for a set of fixed fields, ranging from 5.7 to 10 teslas. It must be stressed that our diffusion method takes advantage of the thermal anisotropy of this material, and allows measurements with only one thermal contact on one face of the sample. As a consequence it allows measurements on very thin samples with a good accuracy.

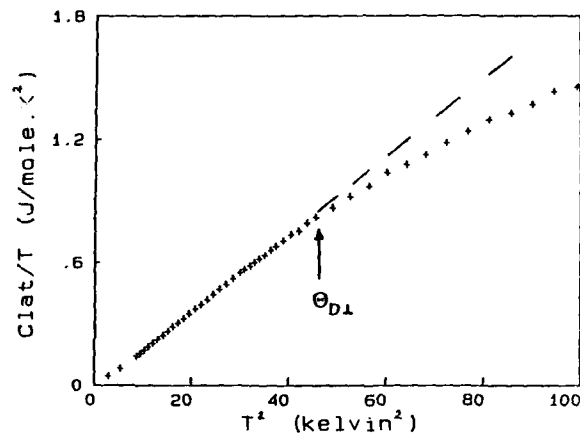


**Figure 2:** Thermal conductivity of the  $(TMTSF)_2ClO_4$  along  $c^*$ , plotted as a function of the temperature cubed, in two fixed magnetic fields: 5.7 (+) and 10 teslas (o). The dashed line features the departure from the cubic law. Cooling rate: 2 K/hour.

#### A PHONON-DOMINATED THERMAL CONDUCTIVITY

Up to now, thermal conductivity measurements in  $(TMTSF)_2ClO_4$  have only been performed above 4.2K, and along the longitudinal axis,  $a$ . Djurek et al. first found below 50K a decreasing  $K_a$  as the temperature is lowered; they reported also a strong enhancement of the heat conduction in a 5 teslas field [14]. This field-variation lead them to propose that the electrons be responsible for most of the observed thermal conduction. On the contrary, Choi et al. claimed opposite temperature and field variations [15], and attributed them to a phonon-dominated behavior. The origin of the discrepancy in the two observed temperature evolutions appeared to be related to a cooling rate effect [16]: for a rapidly cooled sample (1.2 K/min),  $K_a$  decreases monotonically, but for a much slower cooling rate of 1K/hour, it exhibits a maximum at about 10K, and then decreases. Choi's measurements appeared to rule out the field sensitivity of

$K_a$ . Thus, at least down to 6K, the thermal conductivity seems to be dominated by the lattice vibrations.



**Figure 3:** Zero-field lattice specific heat of  $(\text{TMTSF})_2\text{ClO}_4$  in a  $C/T$  vs  $T^2$  plot. The dashed line marks the departure from the cubic behavior at a temperature of about 6 kelvins.

Figure 2 displays the thermal conductivity along the  $c^*$  axis,  $K_C$ , plotted as a function of the temperature cubed, for two fixed magnetic fields: 5.7 (plus's) and 10 teslas (open circles). The sample has been cooled down at a 2 K/h rate between 30 and 15 kelvins.  $K_C$  is found to monotonically increase from 0.3 to 4.5K, aside from the regions where the metal-FISDW transition occurs: a sharp anomaly is clearly observed at  $T=4.1\text{K}$  ( $\approx 63\text{K}^3$ ) for the 10 teslas curve (Fig.2); the anomaly of the 5.7 teslas curve, at 1.2K, is invisible at this scale.

The temperature variation of  $K_C$  is approximately cubic below 1.6K, square between 1.6 and 3K, and above begins to saturate. Such a behavior can be described within a simple kinetic formalism. The thermal conductivity is generally expressed as [17]:

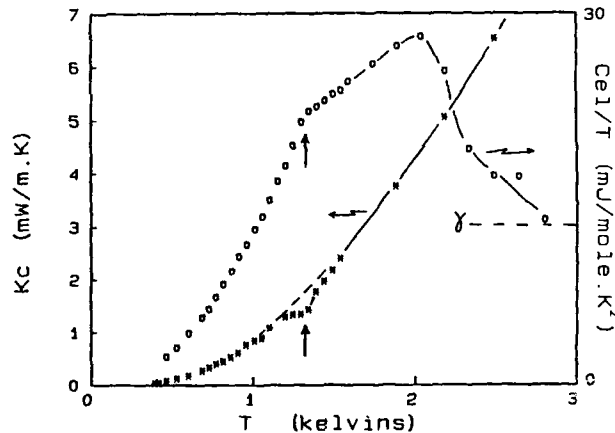
$$K = \frac{1}{3} C v \Lambda \quad (1)$$

where  $C$  is the specific heat of the thermal excitations,  $v$  their group velocity, and  $\Lambda$  their thermal mean free path. The same expression holds as well for the lattice vibration as for the electronic conduction. At low temperature, the temperature variation of  $K$  results essentially from that of  $C$ , since  $\Lambda$  is in that case temperature independent;  $v$  (Fermi velocity for electrons, sound velocity for phonons) is not expected to strongly vary with  $T$ . Thus  $K$  is expected to follow at low temperature the temperature variation of  $C$ , i.e. linear for the electrons, and cubic for the phonons.

The low- $T$  behavior displayed by the  $K_C$  curve is clearly not linear (Fig.2). On the other hand it is consistent with a thermal conduction dominated by the phonons. In particular, it is to be

related with the observed temperature evolution of the lattice specific heat,  $C_{lat}$ , shown on Fig.3 (a linear behavior, dashed line, corresponds in such a  $C/T$  vs  $T^2$  plot to a cubic law).  $C_{lat}$  follows a cubic law below 6K ( $T^2=36$ ), and a square law above [18]. This behavior is the mark of a two-dimensional lattice with a low Debye temperature  $\Theta_{D1}$  for the transverse vibration modes [19]. Such a  $\Theta_{D1}$  of about 6 kelvins is in a good agreement with the maximum in  $K_a$  observed around 10K [15,16], and the general shape of the thermal conductivity can thus be understood in the conventional way. However the  $K_C$  curve seems to display a departure from the cubic law at a temperature much lower than  $C_{lat}$  (Fig.2 and 3). It could arise from a mean free path effect: according to equation (1),  $K$  could follow a  $T$  squared-like law if  $C$  is cubic and if  $\Lambda$  varies as  $1/T$ . This is likely the case not far below  $\Theta_{D1}$ .

Other facts argue for a phonon-dominated thermal conductivity. Firstly,  $K_C$  does not change above and below  $T_C$  (Fig. 2), as opposed to the expected behavior for a phase transition toward a semi-metallic electronic ground state. Secondly, no thermal magnetoresistance is observed between 5.7 and 10 teslas (Fig.2).



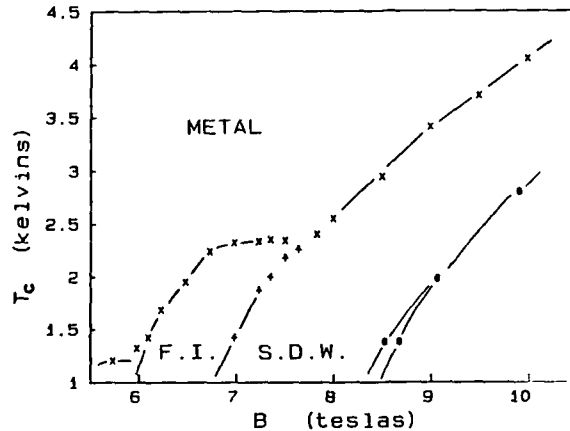
**Figure 4:** Thermal conductivity (\*, left scale) and electronic specific heat (o, right scale) versus the temperature, for a 7 teslas field. Notice the complex anomaly in  $C_{el}$ , resulting from a crossing of two transition lines, and the small anomaly in  $K_C$ , located at the lowest transition (vertical arrows).

#### AN ANOMALOUS CRITICAL BEHAVIOR

A final reason for the phonon-dominated character arises from the anomaly associated with the metal-FISDW phase transition. As it is shown on Figure 4, where both the electronic specific heat  $C_{el}$  and the thermal conductivity  $K_C$  along the  $c^*$  axis are presented as functions of the temperature. It is clear that the anomaly of  $K_C$  displays a variation opposite to that of the electronic specific heat. According to equation (1),  $K_{el}$  generally follows the same behavior as  $C_{el}$  in the vicinity of an

electronic phase transition. A reduction in the anomaly of  $K$  may result from the simultaneous decrease in the electronic mean free path due to the critical fluctuations.

Thus the observed anomaly in  $K_C$  would result in the present case from the combination of a continuous variation of  $C_{lat}$  across the electronic transition, with an abrupt decrease in the phonon mean-free-path in the vicinity of the electronic transition. This behavior demonstrates that the electronic and phonon systems are closely coupled.



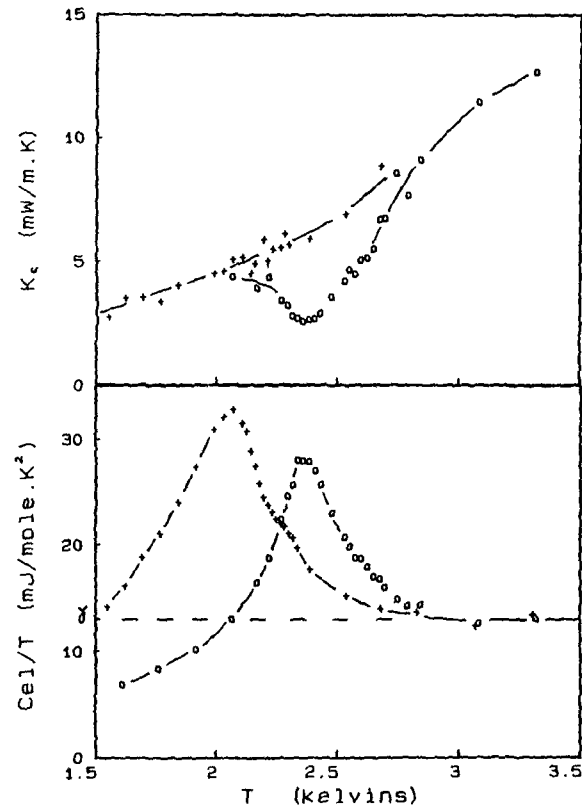
**Figure 5:** Phase diagram of  $(TMTSF)_2ClO_4$  in the intermediate-field range, as built up by specific heat (+ and x, [20]) and magnetization (black circles, [21]) measurements.

The critical behavior at the metal-FISDW second-order transition appears to be even more complex in the vicinity of the tri-critical points corresponding to the transitions between adjacent S.D.W. sub-phases. Figure 5 displays, in a temperature versus magnetic field plot, the phase diagram of  $(TMTSF)_2ClO_4$ . Plus's and cross's have been obtained from specific heat data [20] and black circles from magnetization measurements [21]. The diagram has been blown up around such a tri-critical point. At lower fields, partial reentrances of the metallic phase into the FISDW are associated with those points [10,20], illustrating the competition between neighboring sub-phases. Figure 5 displays the last of them, around 8T. The reentrance has almost disappeared, but the finite slope of the transition lines yields to complex shapes in the specific heat anomalies:  $C_{el}$  exhibits an abrupt or a smoothed jump, when a line is crossed perpendicularly or with a finite slope (for instance at 5.7T [20]), or displays a double anomaly, as shown on Figure 4 and on the lower part of Figure 6. In such a case the high-T anomaly is a jump, corresponding to the metal-FISDW second-order phase transition, whereas the low-T anomaly results from the transition to a more stable SDW sub-phase.

## QUALITATIVELY NEW BEHAVIOR AT HIGH FIELD

The 8 teslas tri-critical point of Figure 5 appears to split the phase diagram in two regions whose critical behaviors are profoundly different, and therefore this point marks a deep change in the ordering process responsible for the appearance of the FISDW.

As shown on the phase diagram of Figure 5, the low-temperature "plus" line cuts the high-temperature "cross" line at the tri-critical point. Both specific heat and thermal conductivity experiments have been performed at fixed field. With increasing temperature, the system first cuts the "plus" line, leading to the observation of a singularity on both specific heat and thermal conductivity curves: vertical arrows on Figure 4. On the contrary, the crossing of the "cross" line gives rise to the largest anomaly on the  $C_{el}$  curve, whereas the  $K_c$  curve does not display any singularity.

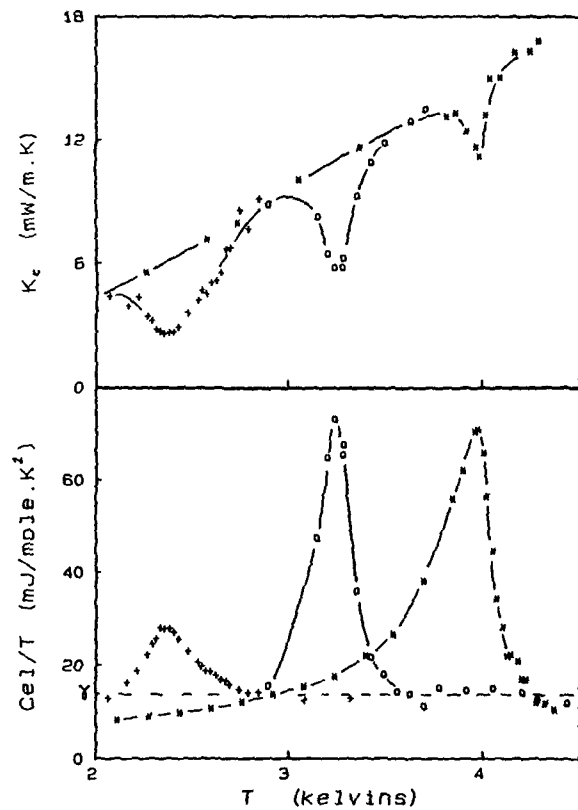


**Figure 6:** Thermal conductivity (upper curve) and electronic specific heat (lower one) versus  $T$ , at 7.5 (+) and 8 teslas (o). Note the striking behavior of  $K_c$  as compared with that of  $C_{el}$ .



Figure 6 displays an even more striking behavior: from 7.5 to 8 teslas, the amplitude of the  $K_C$  anomaly increases by one order of magnitude (upper part of Figure 6), whereas the electronic specific heat anomaly does not exhibit such a drastic evolution (lower part of Figure 6).

But just above 8 teslas, the specific heat anomaly also strongly evolves toward a qualitatively new behavior. Figure 7 shows the anomalies in  $K_C$  and  $C_{el}$  (upper and lower curves, resp.) marking the metal-FISDW transition at fields of 8 (+), 9 (o) and 10 (\*) teslas. First, note the large anomalies in  $K_C$  for all fields. Second, the specific heat jump grows very abruptly, to reach at 10 teslas a  $\Delta C/\gamma T_C$  value four times greater than the 1.43 BCS prediction. Third, both thermal conductivity and specific heat anomalies narrow as the magnetic field increases.

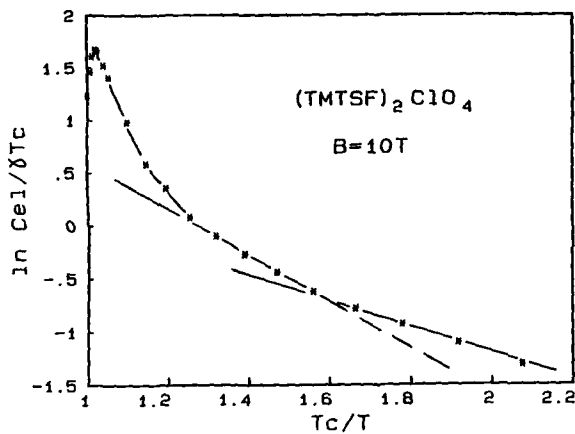


**Figure 7:** Thermal conductivity and electronic specific heat (lower curve) for  $B=8$  (+),  $9$  (o) and  $10$  teslas (\*). The anomalies in  $K_C$  and  $C_{el}$  get narrowing as  $B$  increases. Moreover, the jump  $\Delta C/\gamma T_C$  becomes much larger than the 1.43 BCS value.

## A STRONG COUPLING PHASE TRANSITION

Moreover, the strong departure of the BCS behavior concerns also the field-evolution of the energy gap which is opened at the Fermi level by the metal-FISDW transition. At 10 teslas, a  $T_c=4.1\text{K}$  critical temperature and a  $\Delta C/\gamma T_c \approx 5.7$  specific heat jump, have been determined by a mean-field analysis of the electronic specific heat anomaly [20]. The jump value ranges four times the BCS prediction of 1.43. The rapid decrease of  $C_{e1}$  below  $T_c$  results from the opening of the energy gap at  $E_F$ . This gap grows from zero, close to  $T_c$ , and becomes nearly constant at low enough temperature, where  $C_{e1}$  tends towards a pure exponential law. According to the BCS model for superconductors, the low-T electronic specific heat reads [22]:

$$\frac{C_{e1}}{\gamma T_c} \propto \exp\left(-b \frac{T_c}{T}\right), \text{ with } b = 1.44 .$$

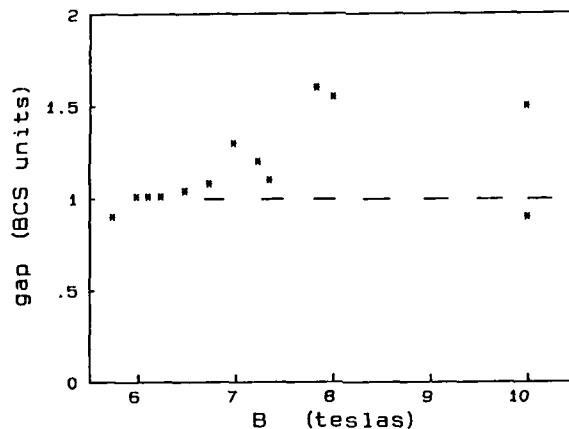


**Figure 8:** The exponential decrease of  $C_{e1}$  below the metal-FISDW transition results from the opening of an energy gap at  $E_F$ . Two gaps are extracted from the two slopes indicated on the Figure. The first one raises 1.5 times the BCS value, whereas the second is slightly smaller than the BCS value.

Figure 8 displays for a 10 teslas field the logarithm of the electronic specific heat,  $\ln(C_{e1}/\gamma T_c)$ , as a function of the inverse of the reduced temperature,  $T_c/T$ , below the critical temperature  $T_c$ . On Figure 8 two distinct linear evolutions are observed. They correspond in such a plot to two exponential regimes. The slopes give the parameters  $b_L$  and  $b_H$ , which have been used to evaluate the gap values, according to expression [23]:

$$\frac{b_{\text{exp}}}{1.44} = \frac{\Delta_{\text{exp}}(0)}{\Delta_{\text{BCS}}(0)}, \text{ with : } 2\Delta_{\text{BCS}}(0) = 3.5 k_B T_c$$

Close to  $T_C$ , all the gaps are thermally excited. As a consequence, the high-T slope on Figure 8 corresponds to a mean value of the gaps,  $\Delta_M$ , which is about 1.5 times greater than the BCS universal value. Far below  $T_C$ , thermal excitations only occur above the smallest gap, which ranges slightly below the BCS prediction:  $\Delta_m/\Delta_{BCS}=0.9$ .



**Figure 9:** Field variation of the gap, in BCS units. Notice the BCS behavior in the low-field regime, and the strong-coupling character at high field.

Figure 9 features the field evolution of the energy gap, in BCS units. Whereas the gap appears to be close to the BCS value at low field, in agreement with specific heat jump [20], it is clear that the high-field regime is not BCS-like.

The behavior of  $C_{el}$  can be compared with that of strong-coupling conventional superconductors. In order to describe those superconductors, a one-parameter model, taking into account a non-vanishing coupling constant  $\lambda$ , for the electron-phonon interaction, has been developed by Nowotny et al. [24]. For instance, they have found a value  $g=0.28$  for lead, whose jump  $\Delta C/\gamma T_C=2.7$  is only 1.9 times the BCS value [25]. According to such a model, the values that we find for the FISDW in  $(TMTSF)_2ClO_4$  at 10 teslas,  $\Delta/\Delta_{BCS}=1.5$  and  $\Delta C/1.43\gamma T_C=4$ , are coherent with a coupling strength  $\lambda$  greater than 0.3. In fact such a strong coupling, in the context of superconductors, is probably well behind the validity of the model, and as a consequence, the  $\lambda=0.3$  value must be considered as a lower limit.

#### ENHANCEMENT OF THE LOW-DIMENSIONAL CRITICAL BEHAVIOR

Close to  $T_C$ , around 8 teslas, the electronic specific heat displays a very broad anomaly (Figures 6 and 7). It is not clear whether this anomaly corresponds to a strongly fluctuating mean-field jump, or rather to a non gaussian lambda-like peak. The shape of  $K_C$  argues for this latter case. In fact, from 8 to 10 teslas, the  $T_C[\max]$  temperatures of the maxima in  $K_C$  and  $C_{el}$  are identical.

By studying the critical fluctuations above  $T_C$ , within a

gaussian model, general trends have been brought out from our data: firstly, for both  $K_C$  and  $C_{el}$ , a cross-over temperature  $T_x$  (expressed in % of  $T_C$ ) separates a 3D regime, close to  $T_C$ , from a lower-dimensional regime, above  $T_x$ . Secondly, the dimensionality  $D$  decreases from  $D=2$ , around 8 teslas, to  $D=1$  at 10 teslas. Thirdly, the  $T_x$  temperature gets closer to  $T_C$  as the field increases:  $T_x$  decreases from about 10% to 2%. As the field is increased, the shift of the cross-over temperature toward  $T_C$  leads to the increase of the one-dimensional fluctuations. Moreover, these trends do not significantly change when  $T_C[\text{max}]$  is used rather than  $T_C[\text{Mean-Field}]$ . Qualitatively, this behavior is exemplified on Figure 7 by the narrowing of both  $K_C$  and  $C_{el}$  anomalies, as the field is increased.

These experimental behaviors shed a new light on the high-field reentrance of the metallic phase [7-9]. Within the renormalized quantized nesting model [26], we propose to interpret the latter as resulting from the field-induced destabilization of the SDW ordering, due to the very same reason which is in fact responsible for its stabilization: say, the above observed one-dimensionalization of the electronic system.

#### CONCLUSION

To summarize, these low-temperature measurements of the specific heat and the thermal conductivity in the  $(\text{TMTSF})_2\text{ClO}_4$  compound give new information about the field-induced Spin-Density-Wave phase transition. The dimensionality of the fluctuations and the coupling strength of the interaction responsible for the SDW condensation have been investigated. Both the specific heat jump at  $T_C$  and the gap value deduced from the exponential decay of the electronic specific heat below  $T_C$  reveal that the high-field state must be described within the strong coupling limit:  $\lambda > 0.3$ . Moreover a large anisotropy is observed on the high-field gap. The thermal conductivity along the  $c^*$  direction has been measured using a thermal diffusivity method.

At the metal-FISDW transition, a rapid reduction of the phonon contribution is to be related with the critical fluctuations of the FISDW ordering. A cross-over from three-dimensional to lower dimensional fluctuations is observed just above  $T_C$  on both the specific heat and the thermal conductivity. As the magnetic field is increased, the evolution of the cross-over temperature leads to the extension of the one-dimensional fluctuating regime. As suggested by the renormalized quantized nesting model [26], this could be the driving force for the reentrance of the metallic phase observed at very high field [7-9]: the magnetic field always enhances the one-dimensional character of the electronic gas; this first stabilizes the SDW by improving the nesting condition, but at very high field the extension of the one-dimensional fluctuating regime renormalizes the interaction, leading to the restoration of the metallic state.

#### REFERENCES

1. For a review of experimental and theoretical results on the Bechgaard salts, see: Proc. of ICSM'88, Santa Fe, Syn. Metals 27-29 (1988-89).
2. L.P. Gor'kov and G. Lebed', J. Phys. (Paris) Lett. 45, L-433 (1984).

3. M. Héritier, G. Montambaux and P. Lederer, *J. Phys. (Paris) Lett.* **45**, L-943 (1984).
4. K. Yamaji, *Syn. Metals* **13**, 29 (1986).
5. M.Ya Azbel, P. Bak and P.M. Chaikin, *Phys. Rev.* **A34**, 1392 (1986).
6. A. Virosztek, L. Chen and K. Maki, *Phys. Rev.* **B34**, 3371 (1986).
7. J.P. Ulmet, A. khmou, P. Auban and L. Bachere, *Sol. State Commun.* **58**, 753 (1986).
8. T. Osada, N. Miura and G. Saito, *Physica* **143B**, 403 (1986).
9. M.J. Naughton, R.V. Chamberlin, X. Yan, S.-Y. Hsu, L.Y. Chiang, M.Ya Azbel and P.M. Chaikin, *Phys. Rev. Lett.* **61**, 621 (1988).
10. F. Pesty and P. Garoche, *Proceedings of Dubrovnik'89*, to be published in *Fizika (Yugoslavia)*.
11. F. Pesty and P. Garoche, to be published.
12. P.F. Sullivan and G. Seidel, *Phys. Rev.* **173**, 679 (1968).
13. A.J. Ångström, *Annln Phys.* **114**, 513 (1861).
14. D. Djurek, M. Prester, D. Jérôme and K. Bechgaard, *J. Phys.* **C15**, L669 (1982).
15. M.-Y. Choi, P.M. Chaikin and R.L. Greene, *Phys. Rev.* **B34**, 7727 (1986).
16. D. Djurek, S. Knezovic and K. Bechgaard, *Mol. Cryst. Liq. Cryst.* **119**, 161 (1985).
17. C. Kittel, *Introduction to Solid State Physics* (Wisley, 1953), 139.
18. F. Pesty, P. Garoche and K. Bechgaard, *Mol. Cryst. Liq. Cryst.* **119**, 251 (1985).
19. L. Landau and E. Lifshitz, *Statistical Physics* (Pergamon, 1980), 206.
20. F. Pesty, G. Faini and P. Garoche, *J. Appl. Phys.* **63**, 3061 (1988).
21. M. J. Naughton, J.S. Brooks, L.Y. Chiang, R.V. Chamberlain and P.M. Chaikin, *Phys. Rev. Lett.* **55**, 969 (1985).
22. J. Bardeen, L.N. Cooper and J.R. Schrieffer, *Phys. Rev.* **108**, 1175 (1957).
23. B.B. Goodman, *Compt. Rend. (France)* **244**, 2899 (1957).
24. H. Nowotny, D. Grau and O. Hittmair, *Phys. Stat. Sol.* **61**, 569 (1974).
25. J.E. Neighbor, J.F. Cochran and C.A. Shiffman, *Phys. Rev.* **155**, 384 (1967).
26. M. Héritier, F. Pesty and P. Garoche, to be published in *New Trends in Magnetism*, Eds S. Rezende and M. Cotinhio Filho (Scientific World, 1989).

HIGH MAGNETIC FIELD PHASES OF THE  $(\text{TMTSF})_2\text{X}$  ( $\text{X} = \text{ClO}_4, \text{PF}_6$ )  
CHARGE TRANSFER COMPLEXES

J. S. BROOKS<sup>a</sup>, N. A. FORTUNE<sup>a,\*</sup>, P. M. CHAIKIN<sup>b,c</sup>,  
L. Y. CHIANG<sup>c</sup>, G. MONTAMBAUX<sup>d</sup>, and Jos A.A.J. PERENBOOM<sup>e</sup>.

<sup>a</sup>Department of Physics, Boston University, Boston MA 02215

<sup>b</sup>Department of Physics, Princeton University, Princeton NJ 08544

<sup>c</sup>Exxon Research And Engineering Co. Rt. 22E, Annandale, NJ 08801

<sup>d</sup>Laboratoire de Physique des Solides, (associe au CRNS),  
Universite Paris-Sud, 91495 Orsay, France

<sup>e</sup>High-Field Magnet Laboratory, University of Nijmegen,  
Toernooiveld, NL-6525 ED Nijmegen, The Netherlands.

\* Present address: Electrotechnical Labs, Tsukuba, Japan.

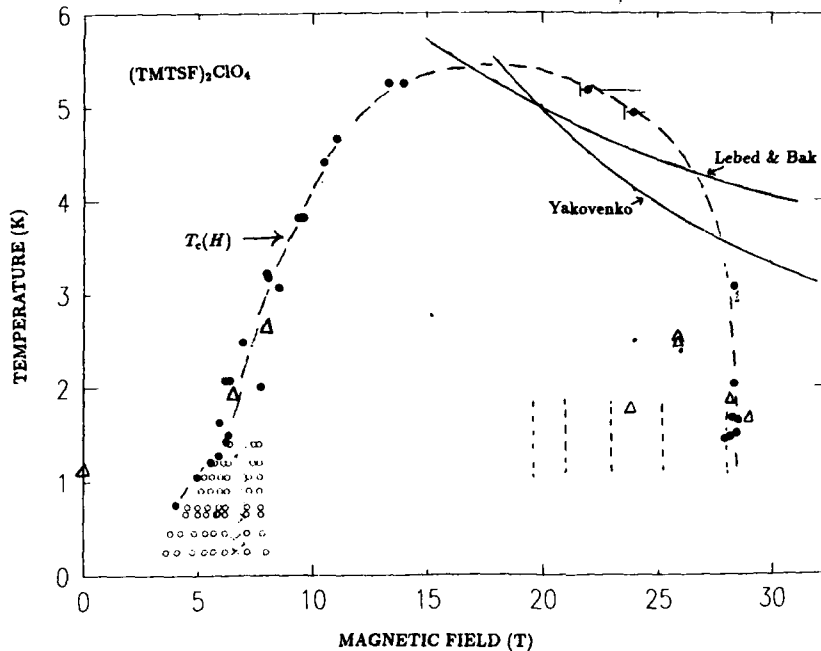
ABSTRACT

The purpose of this talk is to discuss the physical properties of the  $(\text{TMTSF})_2\text{X}$  charge transfer salts in high magnetic fields. This class of materials is of great interest since the effective lower dimensionality and the various ground states are magnetic field dependent at low temperatures. At present, the so-called "standard model" provides a good theoretical description of the low field field induced spin density wave transitions (FISDW). However the reentrance from the last FISDW back to a high field metallic state, and the coexistence of "fast oscillations" in all measured properties, is yet to be accurately described theoretically. The emphasis of this paper is on recent specific heat results which have been obtained on  $(\text{TMTSF})_2\text{ClO}_4$  in magnetic fields as high as 30 T. Here we observe both the reentrant phase transition and the fast oscillations in the specific heat. A main conclusion we draw from our measurements is that the density of states in the reentrant phase is less than it is in the low field metallic state at low temperatures.

INTRODUCTION

$(\text{TMTSF})_2\text{ClO}_4$  is an electronically anisotropic organic conductor [1]. It has an anion ordering transition at 24 K, and is superconducting below 1.3 K. In an applied magnetic field along its  $c^*$ -axis, it becomes an open orbit quasi-one dimensional metal, and at a threshold field it undergoes a second order field induced phase transition to a state with closed orbits. For increasing magnetic field, a series of field induced spin density wave (FISDW) phases appear. Above 8 tesla, the final FISDW is reached. A quantized nesting theory, the so-called "standard model" [2] has been successful in describing many of the details of the FISDW phases, but with some important exceptions. Anomalous "fast oscillations", which are periodic in inverse field, appear both below and above the threshold field [3], and there is the recently discovered reentrant behavior [4-5] which involves a transition from the final ( $n = 0$  quantum limit) FISDW state back to the lower dimensional metallic state at higher magnetic fields (about 28 tesla for temperatures below 1 K). In contrast,  $(\text{TMTSF})_2\text{PF}_6$  does not show reentrance, at least to 30 T, and has a very well defined integer quantum Hall effect [6] for each of the FISDW phases. Except for the fact that rapid oscillations are observed in  $(\text{TMTSF})_2\text{PF}_6$ , the standard model appears to be valid for this material.

Many of the topics related to these materials are presented in this Symposium, such as the critical behavior of the FISDW transitions [7], magnetization reentrance [8], and the integer quantum Hall effect and high field behavior of  $(\text{TMTSF})_2\text{PF}_6$  [9]. Therefore this paper will mainly concentrate on the new high magnetic field specific heat measurements on  $(\text{TMTSF})_2\text{ClO}_4$  [10], and the implication of these results to the developing theories which attempt to describe the phenomena of reentrance and fast oscillations.

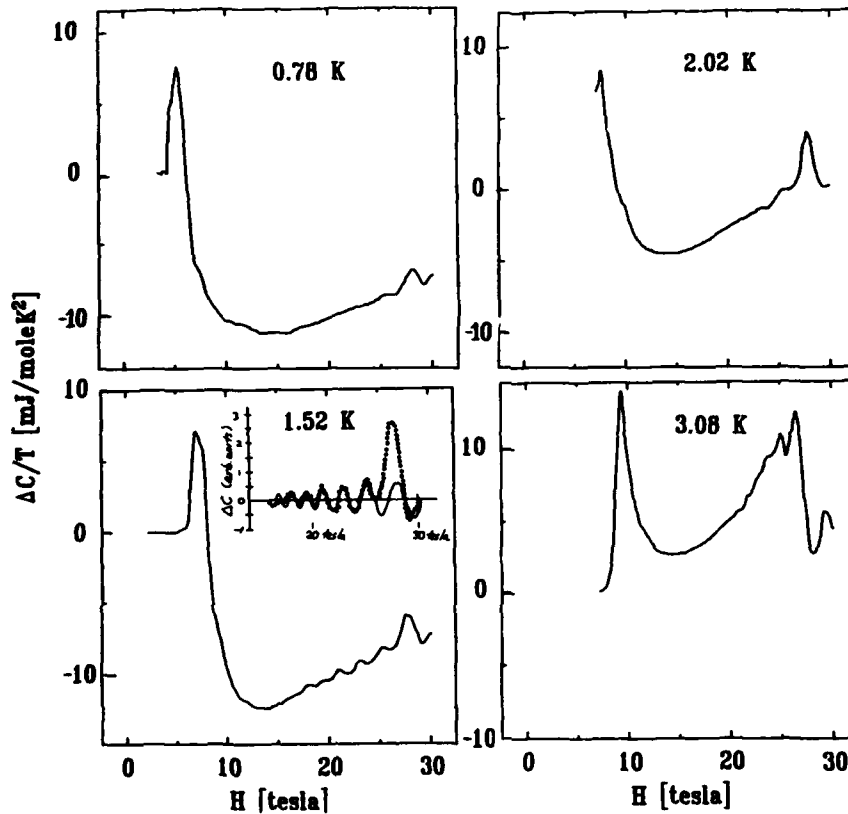


**Figure 1:** B-T phase diagram of (TMTSF)<sub>2</sub>ClO<sub>4</sub> based on our heat capacity measurements. Solid circles and dashed guide line:  $T_c(H)$ . Open circles: FISDW phases. Open triangles: phase transitions observed in temperature sweeps at constant field. Shaded region: negative Hall phase. Solid lines: Theoretical reentrant phase lines (see text). Dotted lines: position of fast oscillations. Triangles: Position of phase transitions observed in temperature sweeps at constant field, including the superconducting transition at zero field.

## RESULTS AND COMPARISON WITH THEORY

In Figure 1 we show the low temperature phase diagram of (TMTSF)<sub>2</sub>ClO<sub>4</sub> as determined from the specific heat data of Ref. [10]. The outer most phase line separating the metallic and FISDW phases  $T_c(H)$  is known to be second order in the vicinity of the cascade of FISDW transitions [11]. For magnetic fields up to 8 tesla, the standard model appears to describe well the experimental results, but the high field reentrant behavior of  $T_c(H)$  is not predicted by the model. Two new approaches to the reentrant behavior have been proposed: Yakovenko [12] predicted the reentrant behavior from a one-dimensional intrachain fluctuation model where  $T_c(H) \approx 1/H^\nu$  (where  $\nu$  is a coupling parameter of order unity), and Lebed and Bak [13] have proposed a theory based on an anion-gap model to explain both the reentrant phase line ( $T_c(H) \approx 1/H^{1/2}$  and a modulation of  $T_c(H)$  with a period of  $1/H$  (i.e. the fast oscillations). By inspection of Fig. 1, it is clear that the theoretical and experimental field dependence of  $T_c(H)$  are very far from agreement.

Specific heat measurements were carried out on ordered single crystals of (TMTSF)<sub>2</sub>ClO<sub>4</sub> with a small sample AC calorimeter. Experiments were done at both the F.B. National Magnet Laboratory in Cambridge, Massachusetts (FBNML) and at the Nijmegen High Magnetic Field Laboratory (NHFML) in the Netherlands. In Figure 2 we show some of



N.A. FORTUNE et al. (FBNML Hybrid Magnet)

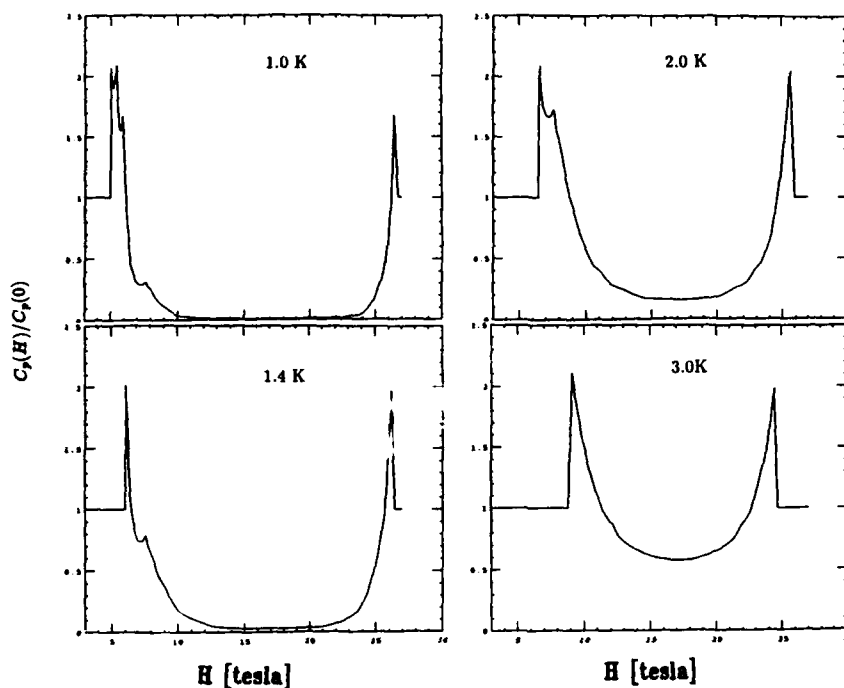
**Figure 2:** Magnetic field dependent variation of the specific heat ( $\Delta C/T$ ) of  $(\text{TMTSF})_2\text{ClO}_4$  at four temperatures from an FBNML hybrid run. Inset: Simple model of fast oscillations (solid line) to heat capacity data at 1.52 K (dots) to show relative contributions of the reentrant jump and the coexisting oscillations.

our experimental values for  $C_p(T,H)$ .

The outermost For the temperatures shown, we observe not only specific heat peaks associated with the low field threshold and FISDW phases, but additional structure at high magnetic fields: a peak which corresponds to the reentrant phase line, and a series of oscillations periodic in  $1/H$  with a temperature independent frequency of 257 tesla (most pronounced in our 1.52 K data). We further note that there is a local minimum in the specific heat near 15 T which is higher than the low field value at 3.08 K, but which drops significantly with respect to the low field value at low temperatures. Finally, we see that the size of the reentrant jump becomes substantially less than the threshold and FISDW jumps at low temperatures. Similarly, the value of the specific heat in the reentrant phase falls below the low field value at lower temperatures.

Montambaux [14] has recently provided an expression for the magnetic field dependent

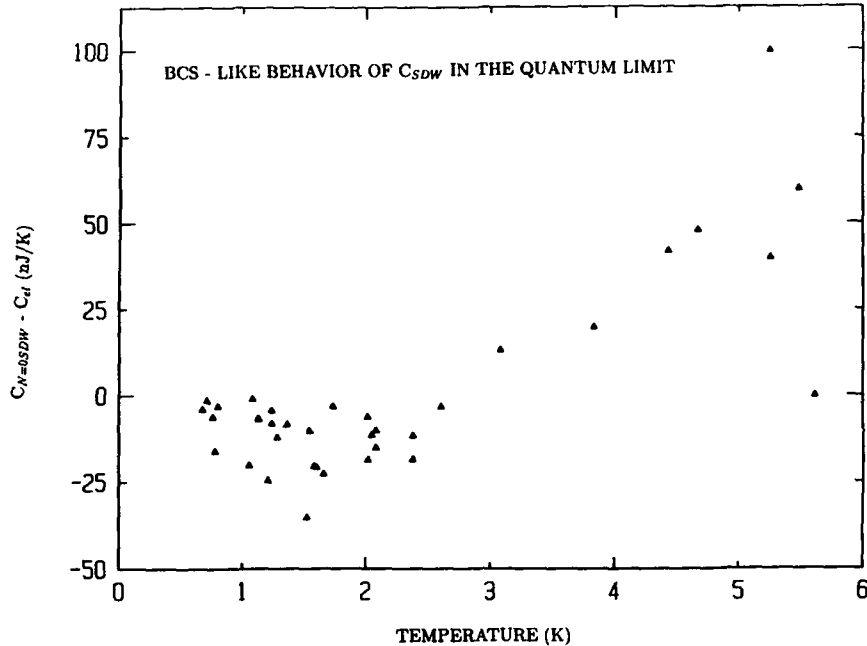




**Figure 3:** Calculated magnetic field dependent specific heat (after Montambaux [14])

specific heat: under the assumption that the entire  $T_c(H)$  phase line is second order, the magnetic field dependent specific heat  $C_p(T,H)$  will go like  $\exp(-T_c(H)/T)$  which is just a BCS-like description of a transition where a gap (proportional to  $T_c(H)$ ) opens at the metallic-to-SDW transition. Additionally, a comparison of the specific heat jump along  $T_c(H)$  with the electronic specific heat in the form  $\Delta C/1.43\gamma T$  gives a measure of the coupling. Previous workers [11] have reported that this value may be as much as 400% higher than the weak coupling value ( $\approx 1$ ) above 8 tesla along  $T_c(H)$ . Our independent measurements are in quantitative agreement with this result. In Figure 3 we show the predictions of Montambaux's model, based on the shape of the phase diagram, and the assumption that the density of states below the threshold field and above the reentrant transition are the same (i.e.  $\gamma_n = \gamma_{reentrant}$ ).

The general agreement between the measured and calculated  $C(H,T)$  is satisfactory, but with one important difference. Our results strongly suggest that the density of states in the reentrant phase is reduced from the low field value. We draw this conclusion from both the reduced size of the jump, and the smaller specific heat above the reentrant transition. We note however, that the reentrant "BCS" value is not too far from unity [10], and this is strong evidence that  $T_c(H)$  is second order along the reentrant line. It is instructive to examine the temperature dependence of the final FISDW state and the reentrant state. Although systematic temperature dependent specific heat measurements are yet to be carried out in the quantum limit, we are able to treat the several data we have with some degree of confidence. Our point of reference is the normal state specific heat below threshold field, which we take as the low field metallic state. In our analysis,



**Figure 4:** Variation of the specific heat with respect to the normal state for the  $N = 0$  phase near 15 tesla.

we identify two different positions on the phase diagram where we can investigate the temperature dependence of the specific heat relative to the normal state. The first is along a constant field line near the center of the last FISDW phase, where we expect a thermally activated behavior, and the second is above the reentrant line. Our results are shown in Figures 4 and 5. In Fig. 4, the activated behavior of the last FISDW phase is clear, and a simple analysis of the results yields a SDW gap of about 10 K which is consistent with a BCS gap for a transition temperature of 5.5 K, in agreement with  $T_c(H)$  at  $H = 15$  T. In Fig. 5, we show a similar analysis for the reentrant data taken from Fig. 2, presented in terms of the difference in the density of states between the normal state ( $\gamma_n$ ) below the threshold field and the reentrant state ( $\gamma_{reentrant}$ ) above the reentrant jump.

Although the data is incomplete, the temperature dependence clearly indicates a reduction with decreasing temperature. It has been pointed out recently [15] that for a reentrant phase boundary similar to the prediction, of for instance, Yakovenko (see Fig. 1), there would be a thermally activated behavior of the specific heat in this range of field below the theoretical phase line since below this phase line, the SDW state would remain. It is apparent that we observe a temperature dependent density of states in the reentrant field range, but we cannot conclude at this point with any certainty that it is thermally activated (i.e. that there is a gap).

The "fast oscillations" observed in the specific heat are of the same frequency in  $1/H$  as those seen in other transport [16] and magnetization results [4]. What is remarkable is that the relative size of the oscillations in the specific heat signal is comparable to the reentrant transition signal, and that it seems that the oscillations may continue to higher

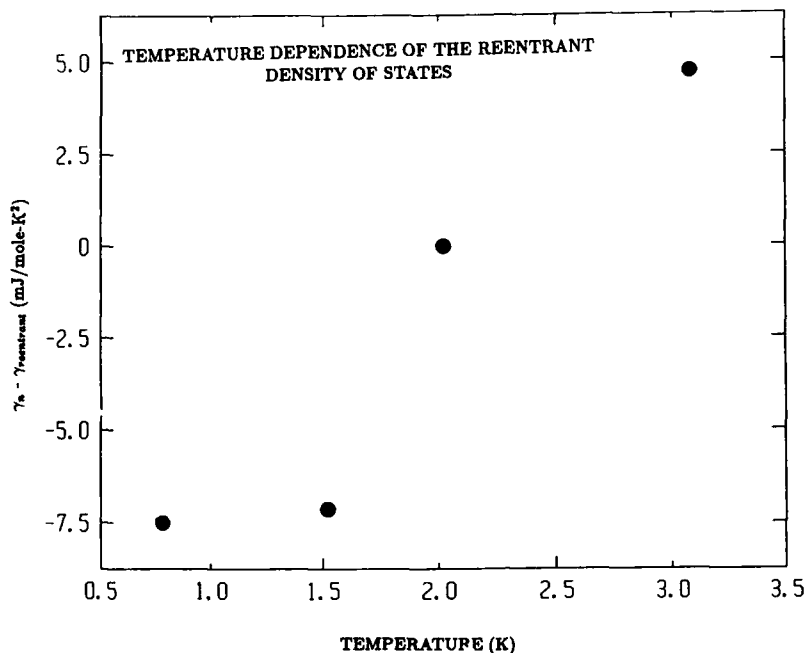
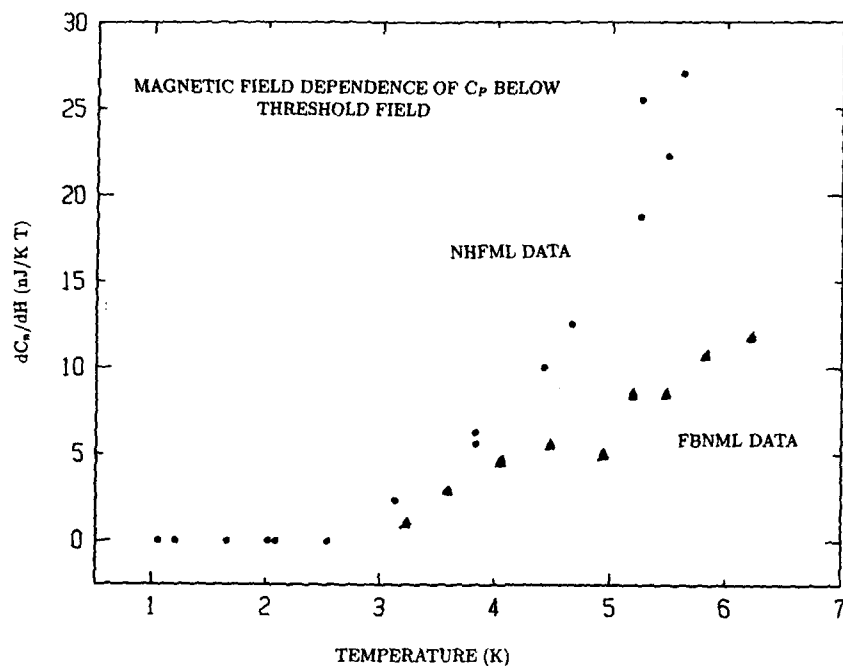


Figure 5: Variation of the reentrant density of states near 30 tesla.

fields beyond the reentrant phase boundary. Although there have been several theoretical treatments of the origin of these oscillations [17], an explanation which is consistent with all experiments is yet to be found. The fast oscillations have been observed in both  $(\text{TMTSF})_2\text{ClO}_4$  and  $(\text{TMTSF})_2\text{PF}_6$ . This brings into question whether or not anion ordering (which does not occur in  $(\text{TMTSF})_2\text{PF}_6$ ) is connected with the phenomenon. As is the case in previous studies, we observe that the magnitude of the oscillations in the specific heat are largest at intermediate temperatures between 5 K and 1 K. It is interesting to note the similar oscillations observed in the same field range in the magnetization [4] have an explicit "reversed sawtooth" form which is similar to the shape of the FISDW signals. This would imply that the two phenomena may share the same magnetic field dependent relationship between the fermi level and the field induced energy gaps. In our analysis, as indicated in the inset in Fig. 2, we find that the fast oscillations in the specific heat may be modeled as standard quantum oscillations with an effective mass of unity (one electron mass). This demonstrates that the density of states associated with the oscillations is not small. Another point of interest is the magnetic field dependent normal state specific heat below threshold field. For temperatures below about 2.5 K, none was observed. However, at higher temperatures there was the onset of an approximately linear magnetic field dependent specific heat in the normal state. In Figure 6 we show this behavior for two independent experiments. At present we have no explanation for this behavior.

Finally, we return to a discussion of the anion-gap model [13] which predicts both a reentrant phase line and fast oscillations, the latter of which arises from a competition between two SDW states with different transition temperatures. A plot of the normalized



**Figure 6:** Temperature dependence of the magnetic field dependent specific heat below threshold field.

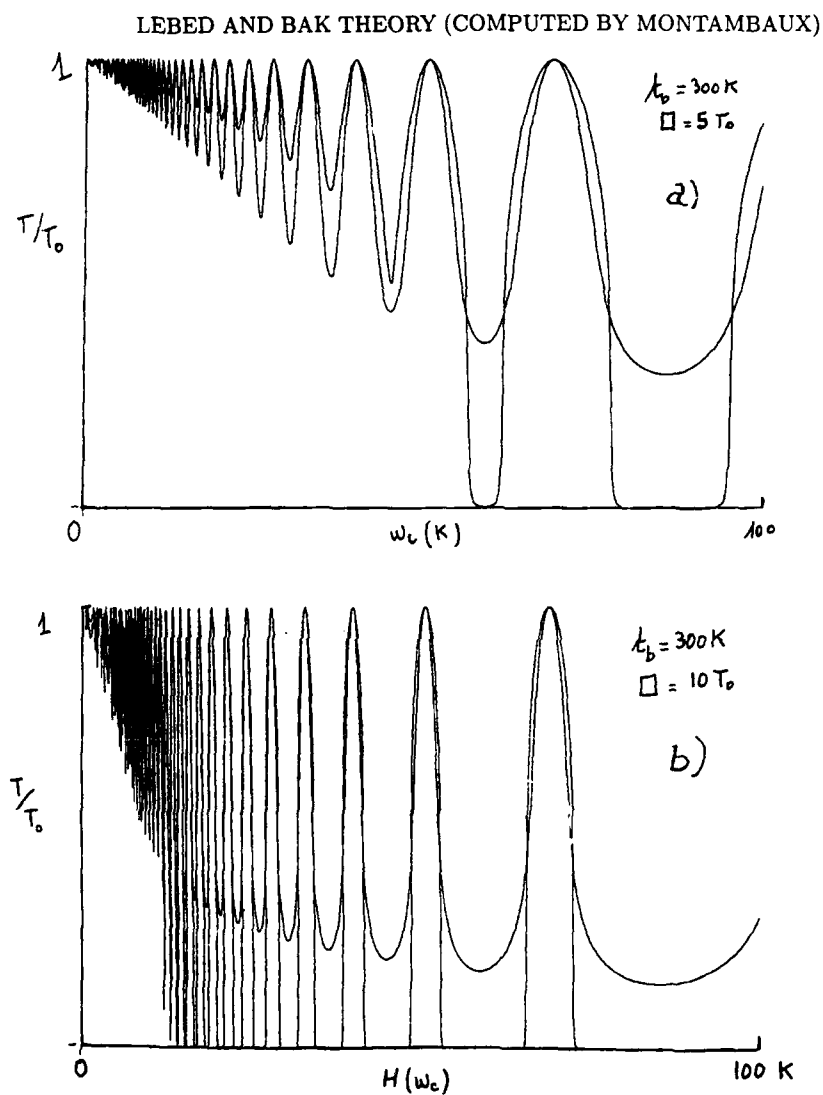
transition temperature vs the cyclotron frequency and the magnetic field energy for two different values of the anion gap are shown in Figure 7. By comparison with Figure 1, there still seems to be a considerable difference between theory and experiment, and further theoretical and experimental work in the quantum limit is needed.

#### CONCLUSIONS

In conclusion, we have measured the specific heat of  $(\text{TMTSF})_2\text{ClO}_4$  in the quantum limit, and have observed both the reentrant phase transition and fast oscillation phenomena. We find that although the phase boundary  $T_c(H)$  appears to be second order at reentrance in reasonable agreement with a "BCS" model, the density of states in the reentrant phase is temperature dependent. We also find that the density of states associated with the fast oscillations is comparable to the reentrant density of states over an intermediate range of temperature. We note that although recent theories for the quantum limit behavior yield qualitative similarities to experiments, further theoretical and experimental work (especially at higher magnetic fields) is needed to explain satisfactorily the reentrant and fast oscillation phenomena in  $(\text{TMTSF})_2\text{ClO}_4$ .

#### ACKNOWLEDGEMENTS

We wish to acknowledge the staff of the F.B. National Magnet Laboratory (Supported by the NSF) and the staff of the High-Field Magnet Laboratory at Nijmegen where various stages of this work were carried out. We thank M.J. Graf, D. Althof, A. G. Swanson, and M. Lu for their contributions to various stages of this work. This work is supported by the NSF at BU under DMR88-18510 and at Princeton under DMR 88-22532. We



**Figure 7:** Prediction of the phase diagram from the anion-gap model from Lebed and Bak. Fig. 7a. Transition temperature vs cyclotron frequency for an anion gap of 5 times  $T_0$ . Fig. 7b Transition temperature vs magnetic field for an anion gap of 10 times  $T_0$ .

also acknowledge travel support from NATO grants 335188 (BU/Nijmegen) and 19189 (Princeton/Orsay).

## REFERENCES

1. See review articles by M. Ribault, P. M. Chaikin, G. Montambaux, M. Heritier in NATO ASI Series, Low Dimensional Conductors and Superconductors, ed. by D. Jerome and L. G. Caron, (Plenum Press, New York, 1987).
2. L. P. Gor'kov, A. G. Lebed, J. de Phys. Lett. **45**, L433 (1984), P. M. Chaikin, Phys. Rev. **B31**, 4770 (1985), M. Heritier, G. Montambaux and P. Lederer, J. Physique Lett. **45**, L-943 (1984), G. Montambaux, M. Heritier and P. Lederer, Phys. Rev. Lett. **55**, 2078 (1985), K. Yamaji, J. Phys. Soc. Japan **54**, 1034 (1985), M. Ya Azbel, Per Bak and P. M. Chaikin, Phys. Lett. **A117**, 92 (1986), K. Maki, Phys. Rev. **B33**, 4826, (1986)..
3. H. Schwenk, et al., Phys. Rev. Lett. **56**, 667 (1986), T. Osada, N. Miura, and G. Saito, Solid State Commun. **60**, 441 (1986); Physica **143B**, 403 (1986), J. P. Ulmet et al., Physica **143b**, 400 (1986); X. Yan et al., Phys. Rev. **B36** 1799(1987)..
4. M.J. Naughton *et al.*, Phys. Rev. Lett. **55**, 969 (1985).
5. R. V. Chamberlin *et al.*, Phys. Rev. Lett. **60**, 1189 (1988).
6. S. T. Hannahs *et al.*, Phys. Rev. Lett. **63**, 1988(89); J. R. Cooper *et al.* Phys. Rev. Lett. **63**, 1984(89).
7. P. Garoche, F. Pesty, and M. Heritier, these proceedings.
8. M. J. Naughton, these proceedings.
9. S. T. Hannahs *et al.* these proceedings.
10. N. A. Fortune *et al.* to be published, and PhD Thesis, Boston University, 1989.
11. F. Pesty and P. Garoche, in "Lower-Dimensional Systems and Molecular Devices", R. M. Metzger Ed., (NATO-ASI, Plenum Press), to be published..
12. V. M. Yakovenko, Z.E.T.F. **93**, 627 (Soviet Physics JETP **66**, 355) (1987).
13. A. G. Lebed and P. Bak, preprint.
14. G. Montambaux, ISSP Symposium on Low Dimensional Conductors and Superconductors, Tokyo 1989 (Springer Verlag, 1989).
15. P. Garoche, private communication..
16. X. Yan *et al.*, Synth. Met. **27 B**, 145(1988).
17. K. Yamaji, Physica **143B+C**, 439(1986); J. Phys. Soc. Jpn. **55**, 1424(1986), M. Ya. Azbel, P.M. Chaikin, Phys. Rev. Lett **59**, 582(1987), T. Osada and N. Miura, Solid State Commun. **69**, 1169(1989).

## MAGNETIC EVIDENCE FOR REENTRANT FIELD-INDUCED SPIN DENSITY WAVES

M.J. NAUGHTON,<sup>+</sup> R.V. CHAMBERLIN,<sup>#</sup> X. YAN,<sup>x</sup> P.M. CHAIKIN<sup>\*,@</sup>  
AND L.Y. CHIANG,<sup>@</sup>

<sup>+</sup> State University of New York at Buffalo, Buffalo, New York 14260

<sup>#</sup> Arizona State University, Tempe, Arizona 85287

<sup>x</sup> University of Pennsylvania, Philadelphia, PA. 19104

<sup>\*</sup> Princeton University, Princeton, New Jersey 08544

<sup>@</sup> Exxon Research & Engineering, Annandale, New Jersey 08801

## ABSTRACT

High magnetic field (to 31T) d.c. magnetization measurements on the quasi-one dimensional organic conductor (TMTSF)<sub>2</sub>ClO<sub>4</sub> yield thermodynamic evidence for the reentrance of a metallic phase from the magnetic field-induced spin density wave state. The H-T phase diagram developed previously from magnetotransport measurements is reproduced from 8 to 26 tesla. The reentrance occurs as a sharp collapse of M(H) to (near) zero magnetization in the high field metal phase. For fields above 27 tesla, deHaas-van Alphen-like oscillations appear, similar to earlier resistance data, as well as other features possibly signifying multiple transitions in the very high field regime.

## INTRODUCTION

(TMTSF)<sub>2</sub>ClO<sub>4</sub> is the most studied of the many quasi-one dimensional metals known as the Bechgaard salts, which were the first organic superconductors.<sup>1</sup> Many other interesting phenomena have been observed in these materials in the past ten years, including the quantized Hall effect, Hall effect sign changes as a function of magnetic field, the Schubnikov-deHaas effect, magnetic field-induced spin density waves (FISDW), oscillatory magnetoresistance anisotropy, nonlinear conductivity, and the subject of this paper, the reentrance of the low field metal phase out of the FISDW phase in very large magnetic fields. All these effects owe their occurrence in this material to the highly anisotropic crystal structure, which allows one to consider it quasi-one, -two, or -three dimensional, depending on temperature, magnetic field (strength and direction), pressure, etc. Perhaps the least understood and most interesting of these effects is the reentrant phase.

While a convergence of theoretical efforts<sup>1</sup> in the past five years has left us with a good (i.e. consistent with data) understanding of the emergence of the FISDW states for magnetic fields below 10T, the situation is much less clear above 10T (see references for a description of the FISDW transitions below 10T). The last of the SDW transitions occurs at 7.5T to a semimetallic state which appears to be stable all the way out to 26T at low temperature (T<1K). By stable, we mean there are no more transitions in this region: the Hall effect is constant and the magnetization is linear.<sup>2</sup> The magnetoresistance  $\rho_{xx}$  (along the highest conducting axis) in this phase exhibits a broad minimum probably related to the expected zero resistance regime of the QHE.

Previous experiments have shown, however, that the FISDW system, which was formed in a high magnetic field, is destroyed by

an even higher field. These were magnetoresistance and Hall effect measurements, with some additional information regarding the H-T phase diagram coming from earlier magnetization data.<sup>3</sup> This reentrance was completely unexpected, and remains unexplained, although some theoretical papers have been written which may prove to have the answer.<sup>4,5</sup> Not only was the reentrance surprising, it was also unverified from thermodynamic measurements, in that initially, all data was from magnetotransport, which are often difficult to interpret on their own. We present here magnetization data from magnetic field and temperature sweeps which give thermodynamic evidence for the discussed reentrant phase.

#### EXPERIMENTAL

The experiments were performed in the hybrid magnet at the National Magnet Laboratory at M.I.T. and a <sup>3</sup>He cryostat. Magnetization measurements were taken on two samples, with simultaneous magnetoresistance measurements taken on two others, all grown at Exxon. Further experimental details can be found elsewhere.<sup>2,3</sup> The samples' cooling rate through the anion ordering transition at 24K was 13mK/min to assure well relaxed samples. All data presented is from the two magnetometer samples, but we note that all transition temperatures and fields to be discussed were shared by the two resistance samples as well.

#### RESULTS

In Fig. 1 we show the magnetization  $M$ , which in these experiments is a capacitance/magnetic field ratio<sup>6</sup>, versus field  $H$  at  $T=0.7K$ , for both sample #1 and #2. This data includes a background component which is typically a small, linear, isotropic term that varies somewhat from experiment to experiment, and is not believed to be representative of the sample magnetization. The magnetization in the metallic state at low fields (below 4T), therefore, is essentially zero on the scale shown. The threshold field for the FISDW states is seen as a slight paramagnetic rise at  $\sim 4T$ , followed by several other paramagnetic jumps at each subphase. Above the final SDW transition at 7.5T, we see a linear diamagnetic-tending region (between 8T and  $\sim 15T$ ). At this point, the sample magnetization crosses  $M=0$ , becomes net diamagnetic<sup>2</sup>, and deviates from linearity, tending toward saturation near 23T. This is the regime (8-25T) where the Hall effect is essentially constant.

At 23-24T, we observe a slight diamagnetic rise or jump in both samples, apparently signalling the onset of what has been called the very high field transition (VHFT)<sup>2</sup>. This is soon followed by a sharp collapse of  $M$  toward zero magnetization at  $H=(26.0\pm 0.5)T$ , which we interpret as the reentrance into the metallic phase. We note that the field axis for sample #2 has been scaled by  $\cos(25.4^\circ)$  to correct for a sample misalignment. Hence we are plotting for this sample  $M$  versus the component of  $H$  parallel to  $c^*$ . We also note that both samples show the FISDW and the reentrant transitions at equivalent field values. Above 26T, there appear to be further magnetooscillations, which we interpret as deHaas-van Alphen oscillations, based on our previous evidence of very large deHaas-Schubnikov (resistance) oscillations<sup>7</sup> in the same field regime.



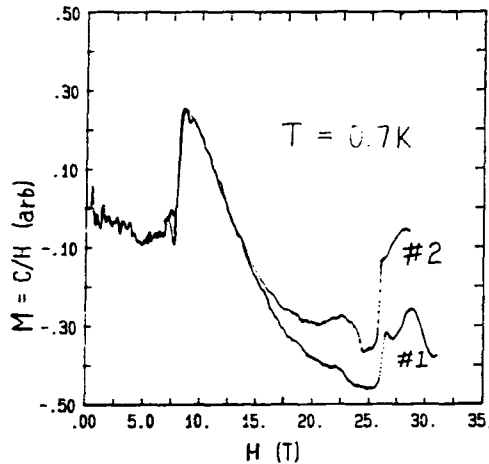


Fig. 1 Magnetization of samples #1 and #2, showing reentrant transition near 26T, followed by dHvA-type oscillations.

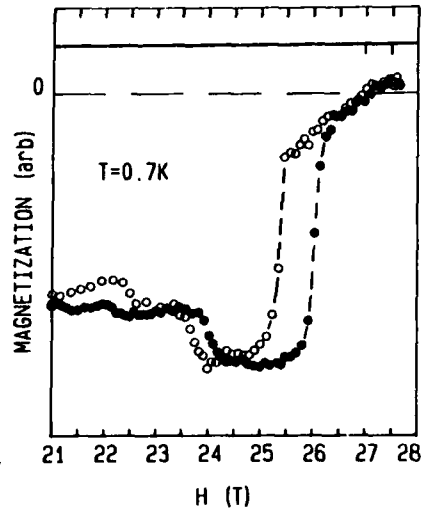


Fig.2 Expanded view of  $M(H)$  for sample #2 at reentrance. Solid symbols: upsweep, open symbols: downsweep.

In Fig. 2, we show raw data of an expanded view of the high field behavior of sample #2. The apparent first order nature of the transition is reflected by the pronounced hysteresis upon field sweep direction. Both samples showed this hysteresis effect. Magnetoresistance data for this transition shows an oscillation at the same field as the diamagnetic rise (24T), followed by a very large rise in  $\rho_{xx}$  where  $M \rightarrow 0$ , followed further by the SDH oscillations. Meanwhile the Hall resistance  $\rho_{xy}$  collapses along with the magnetization.<sup>2,3</sup>

We have taken magnetic field sweeps similar to Fig. 1 at several temperatures, to follow the evolution of this phase transition in H-T space. These are presented in Fig. 3, where we show raw data for sample #1 only. The small arrows mark the field positions of the last SDW transition, while the x's denote the reentrance field values. Here we see the critical field for the reentrance decreasing as well as the effect diminishing with increasing temperature, consistent with our previous transport data.<sup>3</sup> We also can clearly see a region of dHvA oscillations above the reentrance, although they have a somewhat complicated appearance. There is also some evidence for yet another phase transition at the highest fields, where M has a large diamagnetic shift. At this point, we have made no determination on this aspect of our data.

Finally, in Fig. 4, we show constant magnetic field temperature sweeps for field values of 15T, 19T, and 21,22,23,... 31T, and temperatures below 10K. Here we have plotted the sample #1 magnetization versus T, where we have constructed the y-axis to represent both the fields at which data was recorded and  $M(T)$ . That is, we have offset each trace by an amount proportional to

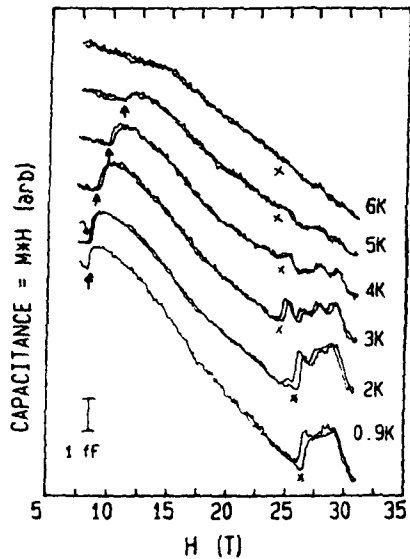


Fig. 3 Raw data ( $M \cdot H$ ) at several temperatures. Arrows mark the last FISDW, x's mark reentrance.

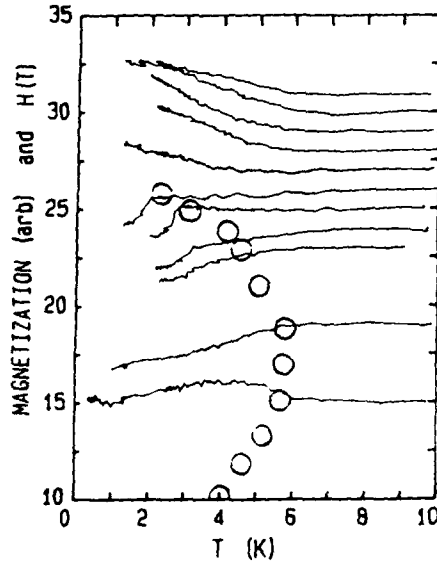


Fig. 4 Magnetization at several constant field values. Open symbols denote previous phase diagram.<sup>3</sup>

the field at that trace, so that, for example, the  $H=15T$  data is drawn with its  $M=0$  at  $y=15T$ , etc. In this manner, we can construct the phase diagram for the FISDW-metal boundary. The solid circles are from our transport phase diagram.<sup>3</sup> One can see immediately that the magnetization data is in very good agreement with the published data.

There is one more aspect to the data in Fig. 4 we wish to address. This concerns the five traces at the top of the figure, representing temperature sweeps between  $H=27T$  and  $H=31T$ . While we have indicated that the system has reentered the metallic state, it is an unusual metal. The magnetoresistance  $\rho_{xx}$  is very large and thermally activated, but the Hall resistance is very small. But from temperature sweeps similar to those in Fig. 4, there were no indications of phase transitions above  $26T$  down to  $T=0.6K$ . Hence the conclusion that the high field state is the same as the low field, metal, phase (One can move from  $1K, 1T$  to  $1K, 31T$  by going around the FISDW phase diagram without crossing any phase boundaries). The data here in Fig. 4, however, show a slight paramagnetic rise at the highest fields, and below  $5-6K$ . This could be due to isolated spins in the "metal" (Curie paramagnetism), which of course would be most prominent at low temperatures, or possibly of some unknown origin. In fact, these data ( $27T$  to  $31T$ ) do not have a  $1/T$  dependence, and do seem to discontinuous derivatives  $dM/dT$  near  $5-6K$ . Whether or not this is an artifact will require further study.

## CONCLUSIONS

With magnetization measurements from constant magnetic field temperature sweeps and constant temperature field sweeps, we have verified the reentrant nature of the H-T phase diagram for  $(\text{TMTSF})_2\text{ClO}_4$ . The magnetization, like the Hall resistance, is small at fields above and below the FISDW regime. This is consistent with the low field, nonmagnetic metal being reentrant at very high fields. However, the large magnetoresistance and temperature-dependent magnetization in this high field ( $H > 26\text{T}$ ) regime is difficult to ascribe to such a metal. Further experimental information, such as recent specific heat experiments,<sup>1</sup> as well as a more complete understanding of the high magnetic field properties of a quasi-one dimensional metal, may help to unravel the physics beneath this discovery.

In particular, more information is needed as to the nature of the reentrant phase. Are the FISDW and reentrant metal states at high field separated by a 1st or 2nd order phase transition? Since the threshold line at low fields is known to be 2nd order<sup>2</sup> we expect the reentrant line to be likewise, unless there is more than one transition above 25T, or there exists a multicritical point at lower fields. Our magnetization data presented here suggest a discontinuous (1st order) transition. However, this measurement is also much more sensitive to 1st order transitions, while the specific heat measurements of Refs. 8 and 9 more readily detect 2nd order transitions. Magnetocaloric effect measurements would be useful in clarifying this particular question. An interesting and thermodynamically intriguing scenario would be that the cascade of FISDW subphases seen below 10T individually reappear above 25T, with a final reentrant metallic phase at the highest fields. A series of measurements in the 30-40T range are under development.

## ACKNOWLEDGEMENTS

We would like to thank M.Ya. Azbel, O.H. Chung, M.Chaparalla, and P. Garoche for helpful comments and assistance.

\* Supported by the National Science Foundation, DMR88-22532.

## REFERENCES

- <sup>1</sup> See reviews in *Physics and Chemistry of Quasi-One Dimensional Materials*, ed. by S. Tanaka and K. Uchinokura, Yamada Conf. XV, *Physica* **143B** (1986); and *Low Dimensional Conductors and Superconductors*, ed. by D. Jerome and L.G. Caron, NATO ASI Series (Plenum Press, New York 1987).
- <sup>2</sup> R.V. Chamberlin, M.J. Naughton, X. Yan, L.Y. Chiang, S.Y. Hsu, and P.M. Chaikin, *Phys. Rev. Lett.* **60**, 1189 (1988).
- <sup>3</sup> M.J. Naughton, R.V. Chamberlin, X. Yan, S.Y. Hsu, L.Y. Chiang, M.Ya. Azbel, and P.M. Chaikin, *Phys. Rev. Lett.* **61**, 621 (1988); and *Synth. Metals* **22**, F327 (1989).

- <sup>4</sup> V.M. Yakovenko, Zh. Eksp. Teor. Fiz. 93, 627 (1987) [Sov. Phys. JETP 66, 355 (1987)].
- <sup>5</sup> A.G. Lebed and P. Bak, (unpublished).
- <sup>6</sup> J.S. Brooks, M.J. Naughton, Y.P. Ma, P.M. Chaikin, R.V. Chamberlin Rev. Sci. Instrum. 58, 117 (1987).
- <sup>7</sup> X. Yan, M.J. Naughton, L.Y. Chiang, P.M. Chaikin, Phys. Rev. B36, 1799 (1987)
- <sup>8</sup> J.S. Brooks, N.A. Fortune, M. Graf (these proceedings).
- <sup>9</sup> F. Pesty, P. Garoche, K. Bechgaard, Phys. Rev. Lett. 55, 2495 (1985), and these proceedings and F. Pesty, P. Garoche, M. Heritier, in "The Physics and Chemistry of Organic Superconductors", Eds. G. Saito and S. Kagoshima (Springer Verlag, 1990).

## SOUND PROPAGATION IN CDW AND SDW

ATTILA VIROSZTEK\* AND KAZUMI MAKI\*\*

\* University of Virginia, Department of Physics, Charlottesville, VA 22901

\*\*University of Southern California, Department of Physics, Los Angeles, CA 90089-0484

## ABSTRACT

We present a microscopic theory of the sound propagation in quasi one dimensional charge density wave (CDW), spin density wave (SDW) and field induced spin density wave (FISDW). First, we consider the ideal situation that the phase correlation length in the CDW or the SDW is infinite. In this limit due to the diffusion pole at  $i\omega = Dq^2$  in a variety of correlation functions the sound propagation depends on a) what is the ratio  $\omega/Dq^2$  and b) if the CDW (or the SDW) is pinned or unpinned where  $D$  is the diffusion constant. Second, when the CDW (or the SDW) is unpinned, the phason starts to participate in the screening of the ionic potential. However, since the unpinned part is strongly inhomogeneous, the contribution of the phason term depends on the wave vector of  $q$  of the sound wave like  $(1 + (Lq)^2)^{-1}$  where  $L$  is the Fukuyama-Lee-Rice coherence length. The present theory accounts for a variety of features observed in sound propagation in quasi-one dimensional CDW systems like  $NbSe_3$  and  $TaS_3$ .

## INTRODUCTION

The Fröhlich conduction is seen in number of quasi-one dimensional CDW and SDW systems [1]. One of its manifestations is the electromechanical effect (i.e. the softening of the elastic constant associated with depinning of CDW or SDW) first established in CDWs in  $TaS_3$  and  $NbSe_3$  by Brill et al [2] and others [3]. In general, Young's modulus (or the longitudinal sound velocity) increases upon entrance into a CDW [2,3] or a SDW [4]. Then when an electric field exceeding the threshold field  $E_T$  is applied Young's modulus starts decreasing with increasing electric field  $E$  [2,3] though the latter behavior has not been seen in a SDW yet. On the other hand, the shear modulus does not exhibit any anomaly at the CDW transition [5]. However, application of  $E$  exceeding  $E_T$  decreases the shear modulus [5]. More recently, Xiang and Brill [6] observed the strong frequency dependence in this softening in Young's modulus of CDWs in  $NbSe_3$  and  $TaS_3$ . The observed softening  $\Delta Y = Y(o) - Y(E)$  decreases like  $\omega^{-\alpha}$  with  $\alpha \approx \frac{3}{4}$ . This frequency dependence is consistent with an early experiment by Jericho and Simpson [7] who saw only small depinning anomaly at  $\omega \approx 10$  MHz.

We have shown earlier [8] within mean field analysis of the Fröhlich Hamiltonian for the quasi-one dimensional CDW that the ionic potential in a CDW is screened by both the quasi-particle and the phason. However, when the CDW is pinned the phason cannot participate in the screening. Therefore, in a pinned CDW the increase in the sound velocity is due to the decrease in the quasi particle density in the CDW. On the other hand, when the CDW is completely depinned, by an electric field, both the quasi-particle and the phason participate in the screening resulting in the sound velocity same as in the normal state [8,9]. Though this theory describes both the observed temperature and the field dependence of Young's modulus in  $TaS_3$  and  $NbSe_3$  quite well, the theory fails completely to describe the observed behavior of the shear modulus. The shortcoming of the above theory is clear. The theory is valid only in the collisionless limit, while most of experiments are done in the hydrodynamic limit.

More recently we have succeeded in incorporating the effect of the quasi-particle

damping into the theory. Since the details of this theory will be published shortly elsewhere [10], we shall review the main results in the following. In spite of remarkable success of this theory, which describes both the temperature and the field dependence of both Young's modulus and the shear modulus, the theory cannot account for the frequency dependence of the softening [6] observed in  $TaS_3$  and  $NbSe_3$ , since the phason contribution depends only on  $(\omega/Dq^2)$  and it is fairly constant when the flexural modes are excited. So far, we assumed implicitly that both the pinned CDW and the sliding CDW are more or less homogeneous. On the other hand, it is known that the spatial correlation of the phase of the order parameter in a pinned CDW decreases exponentially like [11]

$$\langle \phi(\vec{x}) \phi(\vec{y}) \rangle \propto e^{-|\vec{x}-\vec{y}|/L} \quad (1)$$

where  $L$  is the Fukuyama-Lee-Rice coherence length [12,13]. Now, if we assume that the same spatial correlation persists even when the CDW starts sliding since the depinning takes place randomly, this will give the wave vector  $q$  dependence of the softening

$$\Delta Y/Y(o) = (Y(o) - Y(E))/Y(o) \propto (1 + (Lq)^2)^{-1} \quad (2)$$

where  $E > E_T$ .

This relation accounts not only the frequency dependence reported by Xiang and Brill [6] but also the earlier relation found by Xiang and Brill

$$\Delta G/G \propto E_T \quad (3)$$

where  $G$  is the shear modulus since  $L^{-2} \propto E_T$  in the weak pinning limit [13,14].

#### PHONON PROPAGATOR

First, we shall consider the homogeneous case. Also, we limit ourselves to the SDW, since the result for the CDW is very similar to the one in the SDW. The phonon propagator is then given by [15]

$$\omega_q^2 D^{-1}(\omega, q) = \omega^2 - \omega_q^2 (1 - g^2 \Pi(\omega, q)) \quad (4)$$

and

$$\Pi(\omega, q) = \langle [n, n] \rangle = \langle [n, n] \rangle_0 - \frac{1}{2} U \langle [n, \delta \Delta] \rangle_0^2 \left( 1 - \frac{1}{2} U \langle [\delta \Delta, \delta \Delta] \rangle_0 \right)^{-1} \quad (5)$$

where  $n$  and  $\delta \Delta$  are the electron density operator and the fluctuation of the SDW order parameter,  $U$  is the on site Coulomb potential and  $\langle \rangle_0$  means the retarded product obtained in the absence of interaction between fluctuations. The first term in Eq(5) is the quasi-particle term while the second term is the phason term. Quite an analogous expression for  $\Pi$  is obtained for a CDW [8,10].

The retarded products in Eq(5) is evaluated within standard method [10]. The impurity scattering is incorporated in terms of the frequency and the vertex renormalisation. In the limit  $\omega, \zeta = vq, \Gamma_1, \Gamma_2 \ll \Delta_0$ , the retarded products are evaluated as [10]

$$\langle\langle n, n \rangle\rangle_0 = 2N_0(1 - f_1)Dq^2(Dq^2 - i\omega)^{-1} \quad (6)$$

$$\langle\langle n, \delta\Delta \rangle\rangle_0 = iN_0\zeta\Delta^{-1} \begin{cases} f_1 - i\omega f_2(Dq^2 - i\omega)^{-1} & \text{for } T \simeq T_C \\ f_1 - i\omega(1 - f_1)(Dq^2 - i\omega)^{-1} & \text{for } T \simeq 0 \end{cases} \quad (7)$$

$$1 - \frac{1}{2}U\langle\langle \delta\Delta, \delta\Delta \rangle\rangle_0 =$$

$$\frac{1}{2}UN_0\zeta^2(2\Delta)^{-2} \times \begin{cases} f_1 - i\omega f_2(Dq^2)^{-1} & \text{for } T \simeq T_C \\ f_1 - \omega(1 - f_1)(Dq^2 - i\omega)^{-1} - i\omega\Gamma\zeta^{-2} & \text{for } T \simeq 0 \end{cases} \quad (8)$$

where  $f_1$  is the condensate density which reduces to the superfluid density in the BCS theory in the clean limit

$$\Gamma\dot{p} = 2\Gamma_2 f_2 \simeq 2\pi\Delta^2 T^{-1} f(\Delta) f(-\Delta) \left[ 1 + (\Gamma/2\pi\Delta) \ln(4\pi\Delta/\Gamma) \right] \quad (9)$$

and

$$D \approx D_0(1 - f_1) \left[ 2f(\Delta) + f_2 \right]^{-1} \quad (10)$$

where  $f(\Delta) = (1 + e^{\beta\Delta})^{-1}$  is the Fermi distribution function and  $D_0 = v^2/(2\Gamma_2)$  is the diffusion constant in the normal state. The diffusion constant  $D$  defined in Eq(10) decreases with the temperature and vanishes like  $T^{\frac{1}{2}}$  as  $T$  approaches 0K.

The sound velocity and the attenuation coefficient are determined from the pole of the phonon propagator as

$$C/C_0 = 1 - \frac{1}{2}g^2 \text{Re}\Pi(\omega, q) \quad (11)$$

$$\alpha = g^2 (C_0 q/C) \text{Im}\Pi(\omega, q) \quad (12)$$

where  $C_0$  is the bare sound velocity. The corresponding elastic constant is given approximately by  $C^2$ . It is very important to consider the pinned SDW and the unpinned SDW separately.

### Pinned SDW

When the SDW is pinned, we neglect the second term in Eq(5) as the phason does not contribute to the screening. Then we obtain

$$C/C_0 = 1 - \lambda(1 - f_1)(Dq^2)^2 [(Dq^2)^2 + \omega^2]^{-1} \quad (13)$$

$$\alpha = 2\lambda(1 - f_1)Dq^2\omega [(Dq^2)^2 + \omega^2]^{-1} \quad (14)$$

where  $\lambda = g^2 N_0$ . In the limit  $\omega \ll Dq^2$  Eqs(13) and (14) reduce to

$$C/C_0 = 1 - \lambda(1 - f_1) \quad (15)$$

$$\alpha = 2\lambda(1 - f_1) \omega(Dq)^{-1} \quad (16)$$

where Eq(15) reproduces the earlier collisionless limit result [8]. In the other limit  $\omega \gg Dq^2$ , we obtain

$$C/C_0 = 1 - \lambda(1 - f_1)(Dq^2/\omega)^2 \quad (17)$$

$$\alpha = 2\lambda(1 - f_1)Dq^2/\omega \quad (18)$$

In this limit, the quasi-particle contribution becomes almost negligible and the sound velocity hardly changes at the SDW transition.

#### Unpinned SDW

When the SDW is unpinned by an electric field, it is necessary to include the second term in Eq(5). Then in the high temperature region ( $T \simeq T_c$ ) we obtain

$$C/C_0 = 1 - \lambda(Dq^2)^2 X^{-1} \left\{ 1 + \omega^2 X^{-1} (f_1 + 2f_2 + f_1(f_1 + f_2)^2 \omega^2 Y^{-1}) \right\} \quad (19)$$

$$\alpha = 2\lambda Dq^3 \omega X^{-1} \left\{ 1 - f_1 - f_2 + f_2 \omega^2 X^{-1} (1 + (f_1 + f_2)^2 \omega^2 Y^{-1}) \right\} \quad (20)$$

where

$$X = (Dq^2)^2 + \omega^2, \quad Y = (f_1 Dq^2)^2 + (f_2 \omega)^2 \quad (21)$$

In particular for  $\omega \ll Dq^2$ , we obtain

$$C/C_0 = 1 - \lambda = \mathcal{C}_N/C_0 \quad (22)$$

and

$$\alpha = 2\lambda\omega(1 - f_1 - f_2)(Dq)^{-1} \quad (23)$$

while for  $\omega \gg Dq^2$

$$C/C_0 = 1 - \lambda(D_0 q^2/\omega^2) \left[ 1 + (3 + (1 + f_1/f_2)^2) f_1 \right] \quad (24)$$

and

$$\alpha = 2\lambda Dq^3 \omega^{-1} (1 - f_1 + (f_1 + f_2)^2 f_2^{-1}) \quad (25)$$

Again Eq(22) reproduces the collisionless limit result [8,9]. At low temperatures ( $T \ll T_c$ ) we obtain

$$C/C_0 = 1 - \lambda \quad (26)$$



$$\alpha = 2\lambda q \omega \Gamma \dot{\phi} / \zeta^2 \quad (27)$$

Therefore, at low temperatures, the sound velocity decreases whenever the SDW is depinned. Further, this decrease is independent of  $\omega/Dq^2$ .

$$C_{pin} - C_{unpin} = \lambda C_0 \quad (28)$$

The crossover temperature between the high temperature and low temperature behavior is given by  $\omega \Gamma \dot{\phi} / \zeta^2 \approx f_1$ .

### INHOMOGENEOUS DEPINNING

So far, we assumed that the depinning takes place uniformly all over the sample. However, a variety of experiments suggest that it is quite inhomogeneous. A small portion of the SDW starts moving generating a characteristic narrow band noise at the domain boundary. In such a situation, the phason term in Eq(5) acquires an extra momentum dependence, which reflect the size of the sliding domain. If we further assume that the size of this domain for  $E$  not too large compared with  $E_T$  is still controlled by  $L$  the Fukuyama Lee Rice length, the extra momentum dependence is given by  $(1 + (Lq)^2)^{-1}$ .

Both the sound velocity and the attenuation coefficient of unpinned SDW (or CDW) are now given by

$$C/C_0 = 1 - \lambda \left( 1 - f_1 + f_1 (1 + (Lq)^2)^{-1} \right) \quad (29)$$

$$\alpha = 2\lambda \left[ (1 - f_1) - f_2 (1 + (Lq)^2)^{-1} \right] \omega / Dq \quad (30)$$

where we assumed  $\omega \ll Dq^2$ .

The present result account for the frequency dependence of Young's modulus and the attenuation coefficient in the depinned CDW's in  $TaS_3$  and  $NbSe_3$  observed by Xiang and Brill [6]. Further, the related expression in the limit  $\omega \gg Dq^2$  at low temperatures

$$C_{pin} - C_{unpin} = \lambda C_0 (1 + (Lq)^2)^{-1} \quad (31)$$

account for the relation established between the change in the shear modulus  $G$  and the threshold electric field in  $TaS_3$  by Xiang and Brill [5].

$$(G_{pin} - G_{unpin}) / G_{pin} \propto E_T \quad (32)$$

since in the weak pinning limit we obtain [14]

$$E_T^W = (4 - D) / (4D) \left[ (Q/en) \alpha \eta^{-1} v^2 N_0 \right] L^{-2} \quad (33)$$

where  $\alpha = \pi^2/3$ ,  $\eta = v_2 v_3 / v^2$  the anisotropy coefficient,  $Q = 2p_F$  and  $D$  here is the dimension of the CDW (or the SDW).

Therefore, we interpret that Xiang and Brill is not measuring the frequency dependence but the momentum dependence of the depinned portion of the CDW. Perhaps this will provide a new probe to study both the  $T$  and  $E$  dependence of the coherence length  $L$  (i.e. the size of the sliding domains).

## ACKNOWLEDGEMENTS

We have benefitted from correspondence and discussion on their work with J. W. Brill and X. D. Xiang. The present work is supported by the National Science Foundation under grant No. DMR86-11829 and by the U.S. Department of Energy under grant No. DEF605-84-ER45113.

References

1. See for reviews on CDW: P. Monceau, *Electric Properties of Inorganic One Dimensional Materials II*, edited by P. Monceau (Reidel, Dordrecht 1985), p.139; G. Grüner and A. Zettl, Phys. Report 119 117 (1985)
2. J. W. Brill and W. Roark, Phys. Rev. Lett. 53 846 (1984);  
J. W. Brill and W. Roark, and G. Minton, Phys. Rev. B 33 6831 (1986)
3. G. Mozurkewich, P. M. Chaikin, W. G. Clark, and G. Grüner, Sol. State Commun, 56 421 (1985)
4. P. M. Chaikin, T. Tiedje and A. N. Bloch, Sol. State Commun 41 739 (1982)
5. X. D. Xiang and J. W. Brill, Phys. Rev. B 36 2969 (1987);  
X. D. Xiang and J. W. Brill, Phys. Rev. B 39 1290 (1989)
6. X. D. Xiang and J. W. Brill, Phys. Rev. Lett 63 1853 (1989)
7. M. H. Jericho and A. M. Simpson, Phys. Rev. B 34 1116(1986)
8. K. Maki and A. Virosztek, Phys. Rev. B 36 2910 (1987)
9. Y. Nakane and S. Takada, J. Phys. Soc. Jpn. 54 977 (1985)
10. A. Virosztek and K. Maki , Phys. Rev. B 41 (in press)
11. K. B. Efetov and A. I. Larkin, Zh, Eksp. Teor. Fiz. 72 2350 (1977);  
[Sov. Phys. -JETP 45 1236 (1977) ]
12. H. Fukuyama and P. A. Lee, Phys. Rev. B 17 535 (1978)
13. P. A. Lee and T. M. Rice, Phys. Rev. B 19 3970 (1979)
14. K. Maki and A. Virosztek, Phys. Rev. B 39 9640 (1989)
15. A. Virosztek and K. Maki, Phys. Rev. B 37 2028 (1988);  
K. Maki and A. Virosztek Phys. Rev. B 41 (in press)

## SOUND VELOCITY STUDY OF BECHGAARD SALTS $(\text{TMTSF})_2\text{PF}_6$ AND $(\text{TMTSF})_2\text{ClO}_4$

X. D. Shi<sup>(1,2)</sup>, L. Chiang<sup>(3)</sup>, R. Upasani<sup>(3)</sup>, P. M. Chaikin<sup>(2,3)</sup>

<sup>(1)</sup> Dept. of Physics, Univ. of Pennsylvania, Phila. , PA 19104

<sup>(2)</sup> Dept. of Physics, Princeton Univ. , Princeton, NJ 08544

<sup>(3)</sup> Exxon Research and Eng. Co. , Route 22 East, Annandale, NJ 08801

### Abstract

We have studied the elastic properties of the Bechgaard salts  $(\text{TMTSF})_2\text{PF}_6$  and  $(\text{TMTSF})_2\text{ClO}_4$  through their Spin Density Wave (SDW) and anion ordering transitions. Using a vibrating reed technique to measure the sound velocity and attenuation, we observed a large softening of sound velocity immediately above the SDW transition temperature, 12K, of  $(\text{TMTSF})_2\text{PF}_6$  followed by a large hardening below the transition. The softening results from a strong dependence of  $T_c$  on stress in the most conducting direction, while the hardening results from the loss of screening from the conduction electrons and yields a value for the long wavelength electron-phonon coupling constant. The anion ordering transition at 24K in  $(\text{TMTSF})_2\text{ClO}_4$  is marked by a hardening of the lattice that is considerably larger than expected from the lattice constant changes. Our most interesting finding, however, is the observation of a series of steps in the sound velocity as the Field Induced Spin Density Wave (FISDW) transitions are crossed by increasing the magnetic field at low temperatures. The fact that the sound velocity steps are small at the beginning of the cascade of transitions and increase with field, even as extrapolated to low temperature, is an unexpected result from present theory and may indicate a more direct coupling of the lattice stiffness to the SDW order parameter.

The Bechgaard salts,  $(\text{TMTSF})_2\text{X}$  where X are anions such as  $\text{PF}_6$ ,  $\text{ClO}_4$ , etc, have been of great interest for the past decade because of the richness of physical phenomena they have presented [1-5]. They provide an unique opportunity for the study of interacting electron systems in reduced dimensions. Although they represented the first organic superconductors, Spin Density Wave (SDW) transitions and magnetic Field Induced Spin Density Wave (FISDW) transitions have proven to be the most interesting and unusual properties for these systems. Numerous experiments and calculations have shown that they are extremely anisotropic and have only open orbits at their Fermi surfaces. In  $(\text{TMTSF})_2\text{PF}_6$  at ambient pressure, a Peierls like instability leads to a SDW ground state with a  $T_c$  of 12K [7].  $(\text{TMTSF})_2\text{ClO}_4$  is metallic and superconducting at low temperature, and application of a magnetic field (much larger than that required to destroy the superconductivity) perpendicular to the most conducting plane has dramatic effects on its electronic properties. The field reduces the effective dimensionality of the electron gas to one and leads to a density wave instability. The competition between the magnetic length and the SDW wavelength introduces a cascade of FISDW transitions [2,3,4].

Elastic measurements are very sensitive probes of second order phase transitions. There are thermodynamic relationships which relate the change in an elastic constant

to the specific heat and the derivative of the transition temperature with respect to the conjugate stress [12]. Further, studies on charge density wave (CDW) systems [10,11] indicate that information about the reduction of the density of states and the electron-phonon coupling is provided by elastic measurements, as well as information about the pinning of the density waves. Models that explain the behavior of the sound velocity and attenuation for SDW systems are largely based on analogies with the CDW systems.

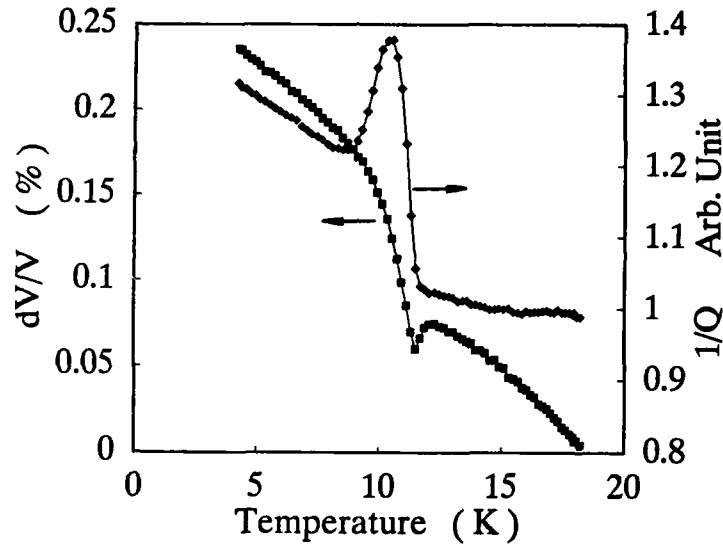


Fig. 1. Change in the sound velocity and the reciprocal quality factor for the flexural resonance near the spin density wave transition in  $(\text{TMTSF})_2\text{PF}_6$ .

The  $(\text{TMTSF})_2\text{PF}_6$  sound velocity and attenuation data (with detailed technique described in ref.14) are shown in figure 1. For all of the measurements we report in this paper the modes measured are the first and/or second flexural modes which would yield information about Young's modulus in an isotropic sample. The frequencies used are typically in the KHz range. The data resemble previous studies on  $(\text{TMTSF})_2\text{PF}_6$  [6], save for the dip preceding the 12K SDW transition. The rather abrupt increases in both the sound velocity and sound attenuation indicate a very accurate measurement of the onset temperature of the transition. The transition temperature and the overall temperature dependence are found not affected by magnetic fields up to 8 Tesla. The temperature dependence of the sound velocity is also similar to what has been observed in many CDW systems [8,9,13]. Although there have been many attempts to understand the dip which precedes the transition in the CDW systems [17], they have to date eluded satisfactory explanation. One simple interpretation is that the dip is a slightly smeared version of the abrupt softening that accompanies any second order phase transition. The thermodynamic relation is: [12]

$$\frac{\Delta B}{B^2} = -\left(\frac{\Delta C_p}{T_c}\right)\left(\frac{dT_c}{dP}\right)^2 \quad (1)$$

where B is the bulk modulus and P is the pressure. While (1) is most appropriate for an isotropic system, for our anisotropic system, the bulk modulus is approximated by

the Young's modulus, and the hydrostatic pressure  $P$  replaced by  $\sigma_a$ , the the uni-axial stress in a-direction. The dip above the transition temperature corresponds to  $\sim 315$  ppm change. If we take the  $\gamma$  value measured for  $(\text{TMTSF})_2\text{ClO}_4$  [4,15], and assume a BCS-like transition, we have

$$\frac{\Delta C_p}{T_c} = 1.43\gamma = 15\text{mJ/molK}^2 \quad (2)$$

From (1) and (2) we get  $dT_c/d\sigma_a = 3\text{K/kbar}$ , which is about 4 times larger than the result of hydrostatic pressure measurement,  $dT_c/dP = 0.7\text{K/kbar}$  [1]. The result suggests that this is a viable explanation and that the discrepancy may come from an underestimate of the specific heat jump or, more likely, that  $T_c$  is a more sensitive function of elongation than volume change.

Below the SDW transition temperature the sound velocity is seen to increase and saturate as temperature is lowered. The similar effect in CDW systems is attributed to the reduced screening by conduction electrons [6,11]. In the metallic state a lattice deformation is accompanied by a change in the local electron density due to the electron phonon coupling (with coupling constant  $g$ ), and the electron density change then reduces the energy of the distortion again through the electron-phonon interaction. This second order effect is proportional to  $g^2/E_f$  or more precisely to the low frequency long wavelength electron polarization function, which is the density of states at the Fermi energy in its simplest form. The usual result is: [6,11]

$$\frac{\delta V}{V} = g^2 N(0)/2 = \lambda/2 \quad (3)$$

where  $\lambda$  is the dimensionless electron phonon coupling constant, and  $\delta V$  is the extrapolated zero temperature sound velocity change due to the SDW transition.  $\lambda$  for the SDW transition in  $(\text{TMTSF})_2\text{PF}_6$  is thus determined to be 0.005.

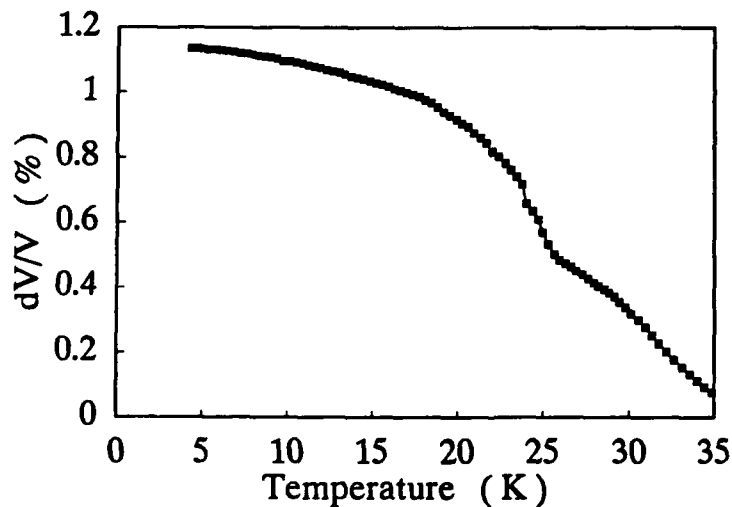


Fig. 2. Change in the sound velocity through the anion ordering transition in  $(\text{TMTSF})_2\text{ClO}_4$ .

In figure 2 we show the sound velocity change in the vicinity of the anion ordering transition of  $(\text{TMTSF})_2\text{ClO}_4$ . The increase in the sound velocity through this transi-

tion is larger than the comparable hardening observed for the Fermi surface instability driven transitions associated with SDW and CDW formations. It is also considerably larger than the change observed in the lattice constants at this anion ordering transition [16]. It is worth of pointing out that for cooling rates ranging from 1K/minute to 0.01K/minute, the temperature dependences of the sound velocity below 24K are not noticeably changed. The critical fields of the FISDW transitions, however, are shifted about 0.5 Tesla to higher fields for samples with the faster cooling rate, indicating that the scatterings of the electrons by the anions are very crucial to the formation of the FISDW's.

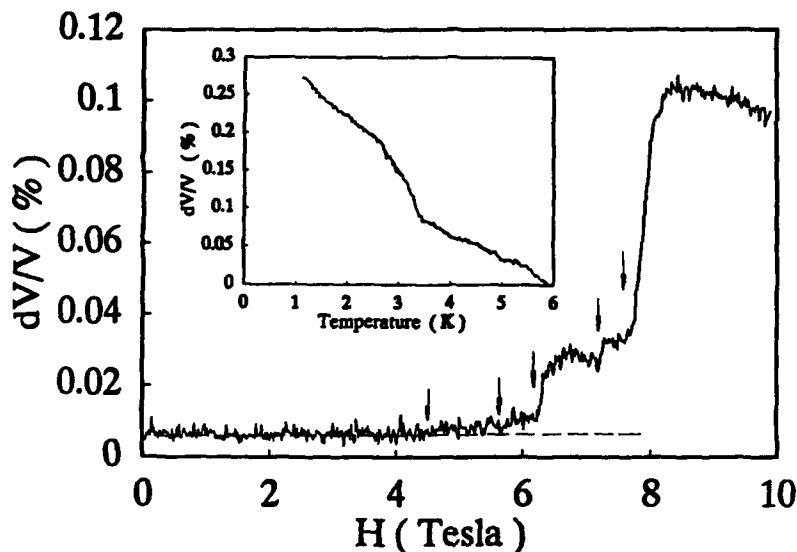


Fig. 3. Magnetic field dependence of the sound velocity in  $(\text{TMTSF})_2\text{ClO}_4$  at 0.7K. Arrows indicate the five field induced spin density wave transitions observed at this temperature. The inset shows the temperature dependence of the sound velocity change at a field of 10 Tesla.

In figure 3, we show the magnetic field dependence of the sound velocity for  $(\text{TMTSF})_2\text{ClO}_4$  at 0.7K where the FISDW transitions are clearly observable. The inset shows the temperature dependence for an applied field of 10 Tesla. The samples were cooled at a rate of 10 mK/minute through the anion ordering transition. At  $T=0.7\text{K}$ , we identify a cascade of transitions from the sound velocity as indicated by the arrows. There are five transitions observed including the "Ribault" transition for a relaxed sample (the third arrow). Significant changes in sound velocity are seen only for the transitions with fields higher than 6 Tesla. We have measured the temperature dependence of the sound velocity in different fixed magnetic fields as well as the magnetic field dependence of the sound velocity at different fixed temperatures. Extrapolation to  $T=0\text{K}$  shows that the field dependence of sound velocity at  $T=0\text{K}$  will be steplike with the height of each step increasing progressively with the field.

We now contrast this result with our expectations from the conventional picture of sound velocity changes at density wave transitions as suggested in equation (3) above. The softening of the sound velocity in the metallic state relates naively to the density of

states at the Fermi surface. In this case we would expect the zero temperature sound velocity to harden by the amount given in equation (3) as soon as we enter a state with vanishing density of states at the Fermi surface. According to our understanding of the FISDW, as soon as the magnetic field exceeds a threshold value and an SDW state is entered, we are in a situation where  $E_f$  always sits in a gap. It remains in a gap as the succession of SDW states progress in increasing field. We therefore should expect a vanishing density of states independent of which FISDW state we are in. In this picture, at  $T=0$  the sound velocity vs field should show a step at the lowest field induced transition and remain at this value as field is increased. Although we have only extrapolations to indicate the  $T=0$  behavior, the experimental results clearly show that the lower field transitions have small steps in sound velocity and that the hardening increases for the higher field transitions.

In actuality it is not the density of states which is relevant to the screening of the phonons, but rather whether the electron density can respond to the lattice deformations. Thus an unpinned CDW screens and softens the sound velocity as well as the normal metal, even though the density of states at  $E_f$  is zero [10]. The FISDW is considerably more complicated. There is a gap at  $E_f$ , but the resistivity should be zero (theoretically, at  $T=0$ ) due to the Quantum Hall Effect (QHE). Whether this allows effective screening is a question which must be addressed. However, the steplike increase in sound velocity would still be unusual unless the higher field states were more effectively pinned, either in a density wave or a QHE sense, than the lower field states.

Phenomenologically the hardening of the sound velocity qualitatively resembles the magnetization data, which suggests that there is another mechanism at work, where the sound velocity is probing the condensation energies of the FISDW's. The ratios of the steps, however, are more like the expected ratios of the gaps in the different phases than like the magnetization steps.

In conclusion, we have measured the sound velocity and attenuation in Bechgaard salts  $(\text{TMTSF})_2\text{PF}_6$  and  $(\text{TMTSF})_2\text{ClO}_4$ . The temperature dependence of the sound velocity in  $(\text{TMTSF})_2\text{PF}_6$  at the 12K SDW transition can be well accounted for by theories of normal metal-insulator transitions. For the FISDW in  $(\text{TMTSF})_2\text{ClO}_4$ , the magnetic field dependence of sound velocity is not well understood and the existing theory can not explain the behavior. We suggest that the hardening of the sound velocity is an indication of the condensation energy of the different FISDW states. In experiments to higher fields in  $(\text{TMTSF})_2\text{ClO}_4$ , we have observed the rapid oscillations seen in many other measurements as well as the reentrant transition, but further experiments are required to quantify these results.

We would like to thank R.C. Yu for technical help during the experiment and K. Maki and J. Brill for many helpful discussions. This work is supported by NSF under DMR 88-22532.

## References

- [1] D.Jerome and H.J.Schultz, *Adv. Phys.* 31, 299 (1982)
- [2] M. Heritier, G.Montambaux and P. Lederer, *J. Physique Lett.* 45 L943 (1984)
- [3] N.J.Naughton, J.S.Brooks, L.Y.Chiang, R.V.Chamberlin, and P.M. Chaikin, *Phys. Rev. Lett.* 55, 969 (1985)
- [4] F.Pesty, P.Garoche and K.Bechgaard, *Phys. Rev. Lett.* 55, 2495 (1985)
- [5] N.J.Naughton, R.V.Chamberlin, X.Yan, S.-Y. Hsu, L.Y.Chiang M.Ya.Azbel, and P.M.Chaikin, *Phys. Rev. Lett.* 61, 621 (1988)

- [6] P. M. Chaikin, T. Tiedje and A.N. Bloch, *Solid St. Commun.* 41, 739 (1982)
- [7] K. Bechgaard, C.S. Jacobsen, K. Montensen, H.J. Pedersen and N. Throup, *Solid St. Commun.* 33, 1119 (1980)
- [8] J.W. Brill and W. Roark, *Phys. Rev. Lett.* 53 846 (1984)
- [9] X.D. Xiang and J.W. Brill, *Phys. Rev. Lett.* 63, 1853 (1989)
- [10] Kazumi Maki and Attila virosztek, *Phys. Rev.* B36, 2910 (1987)
- [11] M.J. Rice, *Low Dimensional Cooperative Phenomena* (edited by H.J. Keller), p.23, Plenum Press, New York (1975)
- [12] L.R. Testardi, *Phys. Rev.* B12, 3849 (1975)
- [13] M. Barmatz, L.R. Testardi and F.J. Di Salvo, *Phys. Rev.* B12, 4367 (1975)
- [14] T. Tiedje, R.R. Haering and W.N. Hardy, *J. Acoust. Soc. Am.* 65(5) 1171 (1979)
- [15] F. Pesty and P. Garoche, *Low Dimensional Systems and Molecular Devices* (Edited By R. M. Metzger), NATO-ASI, Plenum Press
- [16] C. Gaonach, G. Creuzet and C. Noguera, *J. Physique* 48, 107 (1987)
- [17] Y. Nakane *J. Phys. Soc. Jpn.* 55, 2235 (1986)



SOUND VELOCITY MEASUREMENTS IN  $(\text{TMTTF})_2\text{X}$   
SALTS,  $\text{X} = \text{ReO}_4, \text{AsF}_6, \text{SbF}_6$

S.E. Brown\* and H.H.S. Javadi, Los Alamos National Laboratory, Los Alamos, N.M.  
87545

R. Laversanne, Centre de Recherche Paul Pascal, CNRS, Domaine Universitaire de  
bordeaux I, 33405 Talence Cedex, France

ABSTRACT

Young's modulus  $E$  measurements using the vibrating reed technique are reported for salts of the  $(\text{TMTTF})_2\text{X}$  series, where  $\text{X} = \text{ReO}_4, \text{SbF}_6, \text{AsF}_6$ . All three exhibit softening of the modulus at the structureless transition, with the largest effect in the material with the non-centrosymmetric anion  $\text{ReO}_4$ . The behavior is typical of quadratic coupling to an order parameter plus effects from fluctuations. There is a large stiffening of  $E$  below the anion ordering temperature of  $(\text{TMTTF})_2\text{ReO}_4$ .

INTRODUCTION

The charge transfer salts  $(\text{TMTCF})_2\text{X}$  ( $\text{C} = \text{Se}, \text{S}$ ) consist of flat molecules of TMTCF which are stacked in a zig-zag pattern to form a conducting path along the stacking direction. A complete charge transfer occurs from the conducting stacks to the counterions  $\text{X}$ , which are positioned in structural cavities and separate the sheets of TMTCF stacks from each other. A combination of interactions in these highly tunable systems leads to a wide variety of low temperature phases, including the formation of charge/spin density waves (CDW/SDW), superconductivity (SC), spin-Peierls (SP) and anion ordering (AO). Some of the phase transitions are linked to the type of counterion, which has two varieties: non-centrosymmetric [dipolar,  $(\text{SCN}^-; \text{NO}_2^-; \dots)$ ], or tetrahedral ( $\text{ReO}_4^-; \text{ClO}_4^-; \dots$ ]), or centrosymmetric [octahedral ( $\text{PF}_6^-; \text{AsF}_6^-; \text{SbF}_6^-; \dots$ ), or single ions ( $\text{Br}^-; \dots$ )]. For example, the salts with non-centrosymmetric anions are observed to order at various temperatures. However, despite the concentrated effort of many researchers, some questions concerning the transitions remain unanswered. The importance of electron-electron as compared to electron-phonon interactions in driving some of these instabilities is still controversial. An outstanding question regarding the TMTTF salts is the role of charge localization in the competition between different instabilities.

Perhaps related to the more localized nature of  $(\text{TMTTF})_2\text{X}$  (compared to the selenium analogs) is the observation of a "structureless transition" (SLT) in several species (e.g.  $\text{AsF}_6, \text{SbF}_6$ , and  $\text{ReO}_4$ ). The accepted signature of the SLT is a sharp change in slope of the conductivity and thermopower but no observed change in the

magnetic susceptibility [1]. Below the SLT the conductivity is activated, reminiscent of many systems with Peierls instabilities [2], although no evidence for a structural transition has been found in x-ray scattering [3] or infrared spectroscopy [4] experiments. However, more recent x-ray studies suggest that more thorough investigations are in order [5].

The observed distinction between charge and spin degrees of freedom (as suggested by the substantial effect of the structureless transition on the charge transport properties but not on the magnetic susceptibility) can only be understood in a correlated electron picture [6]. Recently, Caron and Bourbonnais [7] offered a unified theory for both TMTTF and TMTSF salts. In this theory, important parameters include the the dimensionality crossover temperature ( $T_x$ ), and the temperature of the resistivity minimum ( $T_\rho$ ), which has been used to characterize the strength of localization in each salt. For example,  $T_\rho$  ( $X = \text{SbF}_6$ )  $\sim$  170K and  $T_\rho$  ( $X = \text{AsF}_6$ )  $\sim$  220K [8], indicating stronger localization in the latter that in turn leads allows the electron-phonon interaction to lead to a spin-Peierls ground state.

The theory of Caron and Bourbonnais does not describe the SLT; however, it has been speculated to be a  $q = (0,0,0)$  displacement of the anion sublattice with respect to the organic stacks [9],[10]. In this case, a quadratic coupling of elastic moduli to the order parameter is expected, and the temperature dependence of the elastic constants provide thermodynamic evidence of the order of the transition. Also of interest is the strength of the coupling and how do the fluctuations effect the sound velocity and losses.

Here we present measurements of the Young's Modulus for three salts of the (TMTTF)<sub>2</sub>X type:  $X = \text{ReO}_4$ ,  $\text{SbF}_6$ , and  $\text{AsF}_6$ . In the case of the  $\text{ReO}_4$  salt, there is an AO transition at 160K and a structureless transition at 220K. The  $X = \text{SbF}_6$  ( $\text{AsF}_6$ ) salt has a SLT at 160K (100K), and was measured primarily to contrast the behavior in systems with both types of counterion lattices. The measurements in all three materials display substantial softening at the SLT temperature, with the largest effect in the salt with the noncentrosymmetric anion, (TMTTF)<sub>2</sub>ReO<sub>4</sub>. Comparing the effects in the  $\text{AsF}_6$  and  $\text{SbF}_6$  material, we find that the greater softening in  $\text{AsF}_6$ , which has the SLT at a lower temperature, implying that the strength of the electron-electron interaction may be significant, because  $T_\rho$  is larger in the former.

## EXPERIMENTAL

The Young's modulus experiments were carried out in a vibrating reed configuration. The brittle crystals grow with the stacking direction (a axis) much longer than the other directions, making conventional ultrasound experiments extremely difficult. During the measurements, the sample is resonantly driven in a bending mode with one end fixed and the other free [11]. The fixed end is grounded, while the free end is coupled electrostatically to a nearby electrode ( $\sim$  0.5 mm)

driven at audiofrequencies. The motion is capacitively detected at a second electrode using a radiofrequency carrier that is amplitude modulated at the frequency of vibration.

Assuming that the sample is approximated by a rectangular bar, Young's modulus is related to the resonant frequency by

$$f_n = t/l^2(E/\rho)^{1/2}\beta_n, \beta_n = (0.162, 1.01, 2.83, \dots), \quad (1)$$

with  $t$  the thickness,  $l$  the length,  $E$  the modulus and  $\rho$  the mass density.  $\beta_n$  is a multiplicative constant that depends on the number of nodes  $n$ . Clearly, any changes of the resonant frequency with temperature can arise from geometric effects as well as from  $E$ :  $f_1 \sim w^{1/2}(t/l)^{3/2}E^{1/2}$ , with  $w$  the width of the bar.

#### RESULTS AND DISCUSSION

Ambient temperature values of the modulus have been calculated from measured resonant frequencies and appear in Table 1. The variation between samples in the case of the  $\text{ReO}_4$  and the  $\text{SbF}_6$  salts probably results from a nonuniform cross-section in each of the samples. Geometric uncertainties are great, and therefore we quote the values in the table to  $\pm 25\%$ . There is the additional complication that arises from stress cracks in the crystals upon cooling and warming. There was less reproducibility and evidence for crack formation when the anion ordering temperature of  $(\text{TMTTF})_2\text{ReO}_4$  was crossed. Also included in the table is some data from previous experiments on  $(\text{TMTSF})_2\text{PF}_6$  [12]. There is no apparent reason why the selenium-based salts should have a smaller modulus. Although the uncertainties are large, our measurements indicate that the modulus is larger when the counterion is centrosymmetric, and suggests that the materials are softer above an anion ordering instability. We note more data on a larger number of materials is necessary to support that speculation.

Table 1. Young's modulus  $E$  at ambient temperature ( $10^{11}$  dynes/cm<sup>2</sup>)

X	$\text{ReO}_4$	$\text{SbF}_6$	$\text{AsF}_6$	$(\text{TMTSF})_2\text{PF}_6^a$
$E$ (S1) <sup>b</sup>	2.2	3.4	3.2	1.5
(S2)	2.6	3.7	N/A	

<sup>a</sup>from Ref [12].

<sup>b</sup>S1 and S2 refer to different samples.

The relative changes in Young's modulus appear in Fig. 1 and Fig. 2 for all three materials. Each of them show an anomaly at the SLT; in addition there is an extremely large effect at the first order anion ordering temperature for

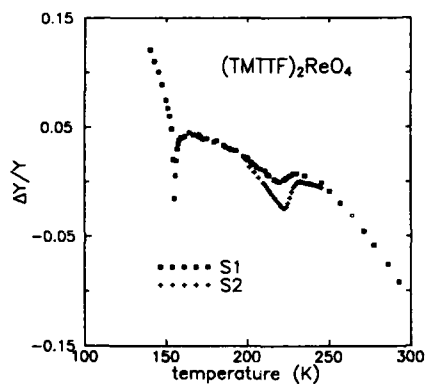


Fig. 1. Change in Young's modulus vs. temperature for  $(\text{TMTTF})_2\text{ReO}_4$ . S1, S2 refer to different samples.

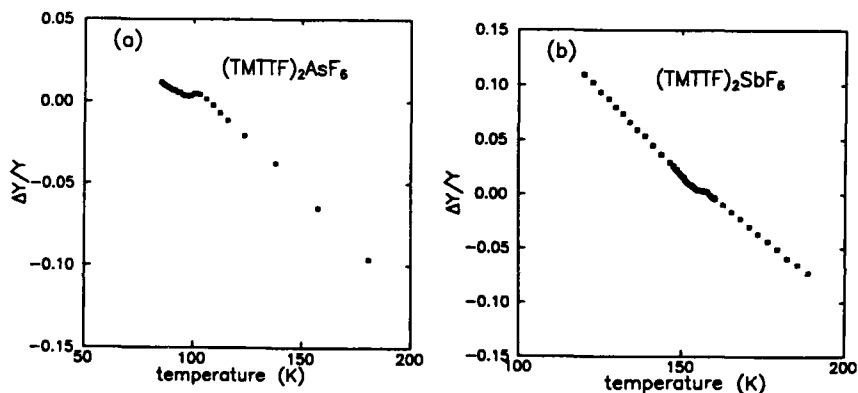


Fig. 2. Change in Young's modulus vs. temperature for (a)  $(\text{TMTTF})_2\text{AsF}_6$  and (b)  $(\text{TMTTF})_2\text{SbF}_6$ .

$(\text{TMTTF})_2\text{ReO}_4$  that will be discussed in more detail below.

Sample dimension changes with temperature have not been used to normalize the data in Fig's. 1 and 2. However, using numbers from the x-ray data for  $(\text{TMTTF})_2\text{PF}_6$  [13] and  $(\text{TMTTF})_2\text{ReO}_4$  [14], we estimate that approximately 35% of the variation at 300K is from thermal expansion, giving, approximately 300 ppm/K stiffening of the modulus below room temperature.

The effect of the structureless transition is observable for all three materials, with a softening of the Young's modulus characteristic of continuous transitions, occurring over a temperature range 5–10K wide. The amount of softening is largest for the  $\text{ReO}_4$  salt (3%), followed by the  $\text{AsF}_6$  salt (2%) and the  $\text{SbF}_6$  (0.5%). Below the transition, there is a small continuous stiffening in each material. The essential

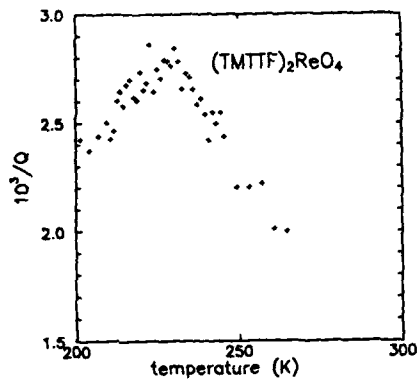


Fig. 3. Reciprocal quality factor vs. temperature near the structureless transition of  $(\text{TMTTF})_2\text{ReO}_4$ .

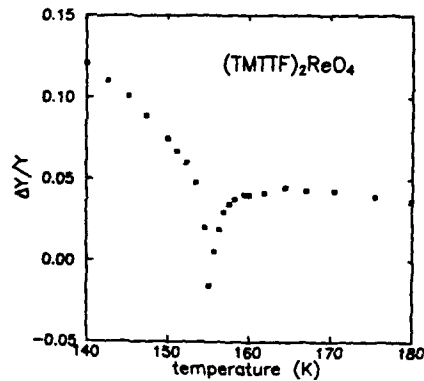


Fig. 4. Change in modulus near the anion ordering temperature for  $(\text{TMTTF})_2\text{ReO}_4$ .

features reproduced for two samples each of the  $\text{ReO}_4$  and  $\text{SbF}_6$  materials. In the former, the details of the shape of the anomaly near to the transition varied between samples as shown in Fig. 1. It may be attributable to a frequency dependence from relaxation effects, as the sample with the sharper features resonated at 1400 Hz, whereas the other resonated at 4 kHz. Another obvious possibility is a sample dependence arising from inhomogeneities or cracks. We observed no significant difference between two samples of the  $\text{SbF}_6$ , with resonant frequencies of 2.5 kHz and 4 kHz.

The quality factor  $Q$  data of Fig. 3 provides evidence that the difference between the two  $\text{ReO}_4$  samples is relaxational, because there is a peak near the transition. The data was taken from the response of the sample with sharper features in Fig. 1. It is representative of all of the samples we studied, with the highest loss near the SLT, although the sample plotted had the highest  $Q$  at 300K and therefore exhibited that trend more clearly than the other samples. The data suggests that fluctuation effects from the SLT persist to high temperatures, with no evidence for losses induced by coupling to domain walls below the transition.

Finally, we discuss the anion-ordering transition of  $(\text{TMTTF})_2\text{ReO}_4$ , identified as a  $q = (1/2, 1/2, 1/2)$  superstructure [15]. It has the typical strong stiffening that appears below a first-order transition. The weak temperature dependence above the transition is characteristic of the AO transition, having been previously observed in  $(\text{TMTSF})_2\text{FSO}_3$  and  $(\text{TMTSF})_2\text{F}_2\text{PO}_2$  [16]. The first of those materials had a sharp dip in the modulus, similar to that observed here. The dip also occurs at the first order lock-in transition in the inorganic charge-density wave material  $2\text{H-TaSe}_2$  [17] and may be associated with nucleation (Fig. 4).

## CONCLUSIONS

We have measured the temperature dependence of the Young's modulus along the stacking direction in three charge transfer salts  $(\text{TMTTF})_2\text{X}$ ,  $\text{X} = \text{ReO}_4$ ,  $\text{SbF}_6$ , and  $\text{AsF}_6$ . Each of the materials exhibit a softening at the "structureless transition", providing the first thermodynamic evidence that we know of for the transition. The observation of an associated broad loss peak has the implication that fluctuations for the SLT in the  $\text{ReO}_4$  material persist over a broad temperature range. More measurements are necessary to correlate the acoustic losses to signatures of localization in the transport measurements. However, the work presented here would indicate that the localization effects observed in the  $(\text{TMTTF})_2\text{X}$  variety of salts is linked directly to the SLT. Any comprehensive theory which describes the localization phenomena should include a description of the SLT.

## ACKNOWLEDGEMENT

Work at Los Alamos National Laboratory was performed under the auspices of the U.S. Department of Energy.

\*Present address, Department of Physics, University of Florida, Gainesville, FL 32611.

## REFERENCES

1. C. Coulon, *J. Physique Colloq.* **44**, C3-885 (1983).
2. C. Coulon, S.S.P. Parkin, and R. Laversanne, *Mol. Cryst. Liq. Cryst.* **119**, 325 (1985).
3. C. Coulon, S.S.P. Parkin, and R. Laversanne, *Phys. Rev.* **B31**, 3583 (1985).
4. R. Laversanne, J. Amiel, C. Coulon, C. Garrigon-Lagrange, and P. Delhaes, *Mol. Cryst. Liq. Cryst.* **119**, 317 (1985).
5. T. Granier, B. Gallois, A. Fritsch, L. Ducasse, C. Coulon (preprint, 1989).
6. See, for example, Ref. [3].
7. L.G. Caron and C. Bourbonnais, *Physica* **453**, 1438 (1986).
8. C. Coulon, P. Vaca, T. Granier, and B. Gallois, *Synth. Met.* **27**, B449 (1988).
9. J.P. Pouget, in *Low-Dimensional Conductors and Superconductors*, ed. by D. Jerome and L.G. Caron (Plenum Press, New York, 1986).
10. S. Brazovskii and V. Yakovenko, *J. Physique Lett.* **46**, L-111 (1985).
11. M. Barmatz, J.J. Leamy, and H.S. Chen, *Rev. Sci. Instrum.* **42**, 885 (1971).
12. P.M. Chaikin, T. Tiedje, and A.N. Bloch, *Solid State Commun.* **41**, 739 (1982).
13. T. Granier, B. Gallois, L. Cucasse, A. Fritsch, and A. Filhol, *Synth. Met.* **24**, 343 (1988).
14. S.S.P. Parkin, J.J. Mayerle, and E.M. Engler, *J. Physique Colloq.* **44**, C3-1105 (1983).
15. J.P. Pouget, R. Moret, R. Comes, K. Bechgaard, J.M. Fabre, and L. Giral, *Mol. Cryst. Liq. Cryst.* **79**, 129 (1982).
16. R.C. Laco, P.M. Chaikin, F. Wudl, S.D. Cox, and J. Brennan, *Mol. Cryst. Liq. Cryst.* **119**, 155 (1985).
17. M. Barmatz, L.R. Testardi, and F.J. Di Salvo, *Phys. Rev.* **B12**, 4367 (1975).

QUANTUM HALL EFFECT AND RAPID OSCILLATIONS IN  $(\text{TMTSF})_2\text{PF}_6$  UNDER PRESSURE

S. T. HANNAHS<sup>a</sup>, J. S. BROOKS<sup>a</sup>, W. KANG<sup>b</sup>, P. M. CHAIKIN<sup>b,c</sup>,  
L. Y. CHIANG<sup>c</sup>, AND R. UPASANI<sup>b,c</sup>

<sup>a</sup>Department of Physics, Boston University, Boston MA 02215

<sup>b</sup>Department of Physics, Princeton University, Princeton NJ 08544

<sup>c</sup>Exxon Research And Engineering Co. Rt. 22E, Annandale, NJ 08801

ABSTRACT

We present magnetotransport data and the phase diagram derived from them for  $(\text{TMTSF})_2\text{PF}_6$  under sufficient pressure that the zero field Spin Density Wave (SDW) is suppressed and the material is superconducting. Application of a large magnetic field perpendicular to the conducting plane then leads to the cascade of Field Induced Spin Density Wave (FISDW) transitions. The transitions are in good agreement with the Standard model for these transitions and in contrast to the more complicated behavior seen in the  $\text{ClO}_4$  salt. In addition Hall and longitudinal resistivity indicates a behavior much closer to that observed in conventional Quantum Hall devices than in the  $\text{ClO}_4$  salt or previous studies of  $\text{PF}_6$ . We do observe the "rapid" Schubnikov de Haas like oscillations in magnetoresistance at high field similar to those seen in  $\text{ClO}_4$ , even though in the present case there is no evidence for anion ordering as some theories would require.

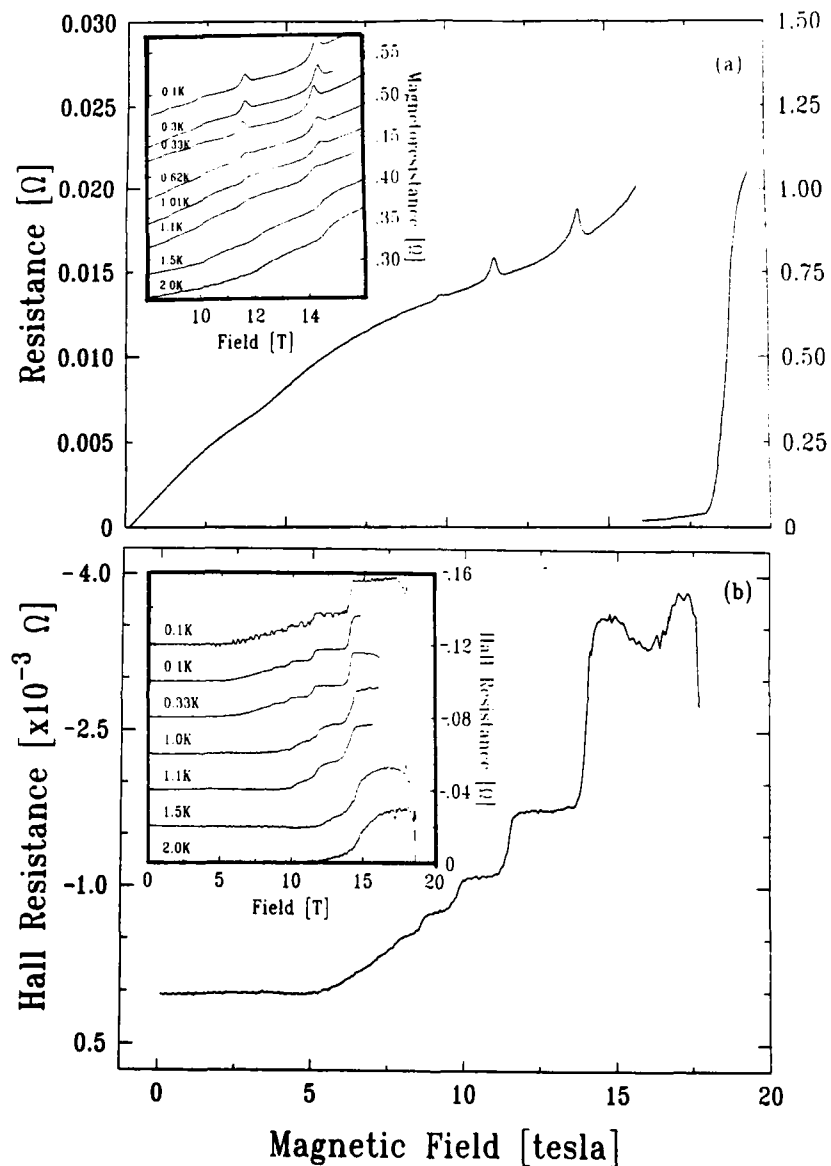
The integer and fractional quantum Hall effects (QHE) have been previously reported only in quantum wells formed in semiconductor heterostructures [1] and in a few weakly coupled layers. [2] The only bulk materials which have shown QHE-like behavior are the Bechgaard salts  $(\text{TMTSF})_2\text{X}$  [3] where X is the anion  $\text{ClO}_4$ ,  $\text{ReO}_4$ , or  $\text{PF}_6$ . Theoretical work has shown that there should be a QHE associated with the field induced spin density wave (FISDW) states [4] and experimental observation of the QHE [5-6] in these salts has been suggested. However, the interpretation has been complicated by anomalies and additional transitions which question the basic theoretical understanding of these materials. We have made measurements of the transport properties of  $\text{PF}_6$  under pressure. These are in almost complete agreement with expectations for a system undergoing a series of FISDW transitions to states with filled Landau bands exhibiting QHE. [7]

Previous studies on  $(\text{TMTSF})_2\text{ClO}_4$  have found instead of the regular progression of Hall steps  $n, n-1, \dots, 1, 0$  there were intervening phases where the Hall resistance ( $\rho_{xy}$ ) changed sign, [8] there was not a transition from  $n=1$  to 0 but rather apparently [6] from  $n=1$  to  $n=1/3$ , there was no evidence for the  $n=0$  state anywhere in the phase diagram, and there was a reentrance of the metallic state at high field. [9]

The material  $(\text{TMTSF})_2\text{PF}_6$  differs from the other  $(\text{TMTSF})_2$ salts,  $\text{ClO}_4$  and  $\text{ReO}_4$ . The anions are centrosymmetric and thus there can be no anion ordering transition and below 12 K at ambient pressure there is the formation of a SDW phase. This SDW phase can be suppressed by application of hydrostatic pressure exceeding a critical pressure  $P_c$ . This results in a metallic (and below 1 K a superconducting) phase. Upon application of a magnetic field greater than some threshold FISDW behavior is observed. [10]

We used a miniature BeCu pressure clamp with a Fluorinert fluid for pressures of 7 to 12 kbar. A loss of approximately 2 kbar is expected on cooling to 4.2K. Samples were mounted in a conventional six probe configuration for longitudinal and  $\rho_{xy}$  measurements. Gold leads were attached to the samples with silver paint. Experiments were carried out at the Francis Bitter National Magnet Laboratory.

We show in Fig. 1a low temperature data for the magnetoresistance ( $\rho_{xx}$ ) of  $(\text{TMTSF})_2\text{PF}_6$  at 10.5 kbar for fields up to 20 T. The  $\rho_{xx}$  data show the threshold field, and remarkably sharp structure at the onset of each FISDW phase. The Hall signal, obtained by subtraction, are shown in Fig. 1b. The data show a negligible  $\rho_{xy}$  in the metallic state at low field, a sharp upturn in  $\rho_{xy}$  at the threshold field, followed by a series of steps



**Figure 1:** Magnetoresistance and Hall resistance of  $(\text{TMTSF})_2\text{PF}_6$  vs. magnetic field for different temperatures. a) Original trace of mixed magnetoresistance and Hall signal at 0.1 K. The inset shows the temperature evolution of the corrected magnetoresistance. b) Hall signal (note the negative sign) at 0.1 K. The inset shows the temperature evolution.

for each FSDW phase and finally a large fluctuation in the Hall signal above 18 tesla.



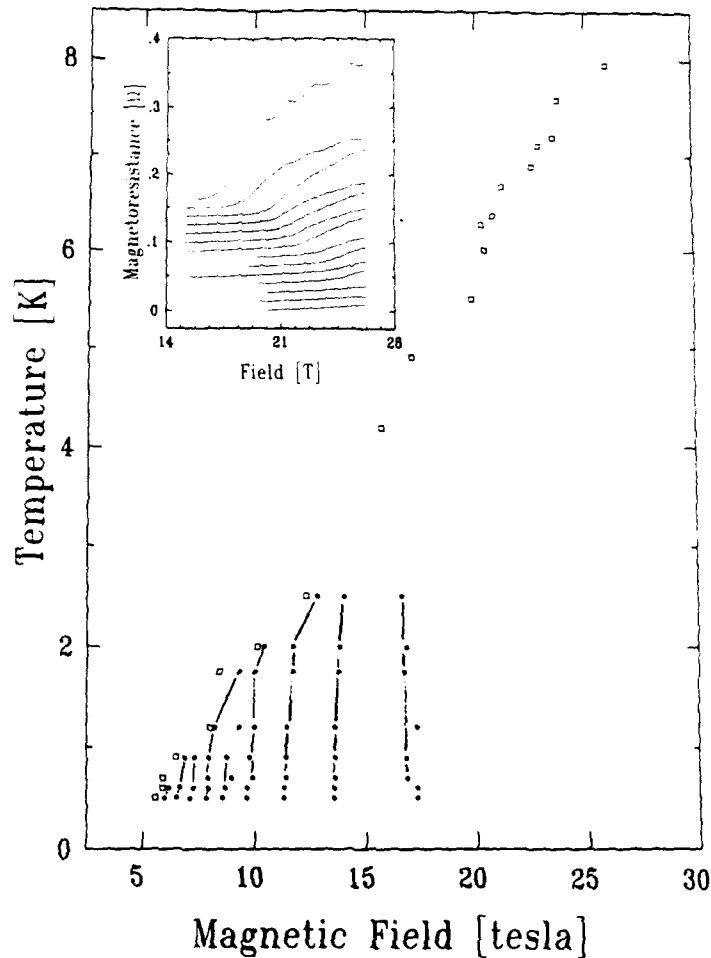
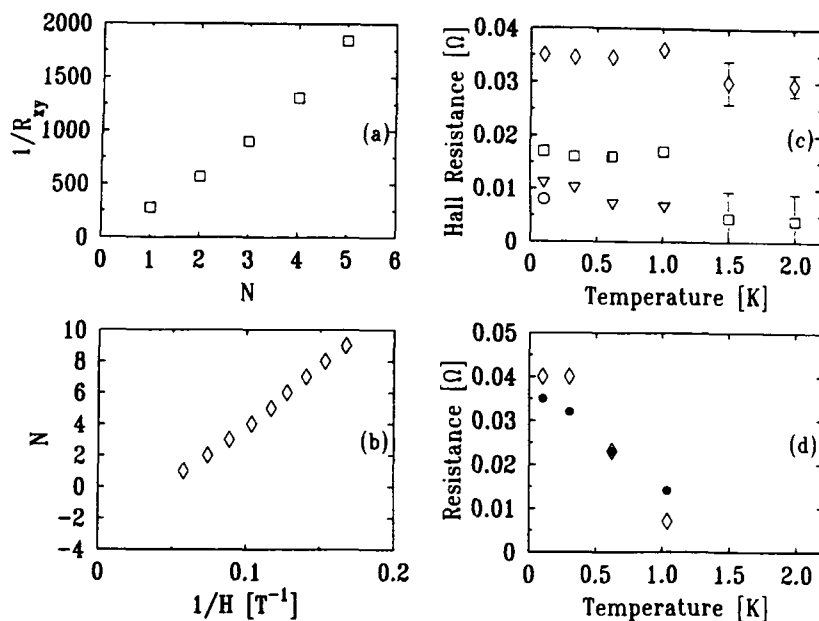


Figure 2:  $B$ - $T$  phase diagram produced from the magneto-resistance. Threshold field and phase boundary are represented by squares. Inset: magneto-resistance measurements used to determine the phase boundary at high temperatures.

$\rho_{xx}$  increases by 2 orders of magnitude and a subtraction to obtain the Hall signal is difficult. From many measurements on many samples we believe that  $\rho_{xy}$  is close to zero in this phase. The inset in Fig. 1b shows the temperature evolution of the shapes and magnitudes of the Hall plateaus. A phase diagram is shown in Fig. 2. The inset shows the threshold region at high temperatures. A small ( $\approx 3\%$ ) hysteresis in the transition positions was observed depending on magnetic field sweep direction.

In Fig. 3 we show field and temperature dependencies. Fig. 3a refers to the plot of the Hall conductance *vs.* step index showing clearly the integer ratio of the steps. Deviations from integer behavior in the low field limit are due to the approach of the FISDW phase line to the threshold field, (*i.e.* the steps have not yet reached their low temperature limit). Fig. 3b shows the relation of the transition field to its index. Fig. 3c shows the temperature dependence of the Hall steps and Fig. 3d shows the corresponding



**Figure 3:** a) Plot of  $1/R_{xy}$  vs. FISDW phase index at low temperatures. The solid line is a linear fit to the  $i = 1$  and 2 values. b) Plot of FISDW transition index vs. inverse field at low temperatures. The line is a fit to all points. Note the negative intercept of -3.5. c) Temperature dependence of the  $i = 1$  and  $i = 2$  Hall plateaus: diamonds,  $i = 1$ ; squares,  $i = 2$ ; triangles,  $i = 3$ , and circle,  $i = 4$ . d) Temperature dependence of the magnetoresistance peaks for  $i = 1$  (diamonds) and 2 (circles).

temperature dependence of  $\rho_{xx}$  transition peaks.

A comparison with the integer quantum Hall effect is clear: 1) we observe eight transitions, five of which have measurable Hall signals in consecutive integer ratio, 2) The peaks in  $\rho_{xx}$  are coincident with the onset of each step. That the QHE alone will not explain all of the data is evident from the temperature dependence of the Hall steps and the negative intercept of the  $1/H$  plot in Fig. 3b. These discrepancies are due to the existence of the FISDW's which make the gap, and the  $T$  and  $B$  dependence of the Fermi surface and number of carriers.

Previous studies of the phase diagram for  $\text{ClO}_4$  [9] and  $\text{PF}_6$  [11] are similar but with important differences. The quasi-dhva frequency of the FISDW states is about 74 T at 10.5 kbar in contrast to 31 T in  $\text{ClO}_4$ . The FISDW subphases are much less temperature dependent than in  $\text{ClO}_4$  and there is no indication of reentrance in either the low field [12] or high field regions. There are no phases between the consecutive integer phases, no sign reversals in  $\rho_{xy}$ , and no fractional phase after the  $n = 1$  phase. For the first time a transition is seen from the  $n = 1$  to an FISDW state with an activated resistance which can be identified by its Hall coefficient, and field and temperature dependence as the  $n = 0$  state.

The series of magneto-oscillations ("rapid oscillations") [13] shown in Fig. 4 for  $\text{PF}_6$  and previously in both transport and thermodynamic properties of the  $\text{ReO}_4$  and  $\text{ClO}_4$  salts are not yet understood. The quasi-frequency of the oscillations shown in Fig. 4 is

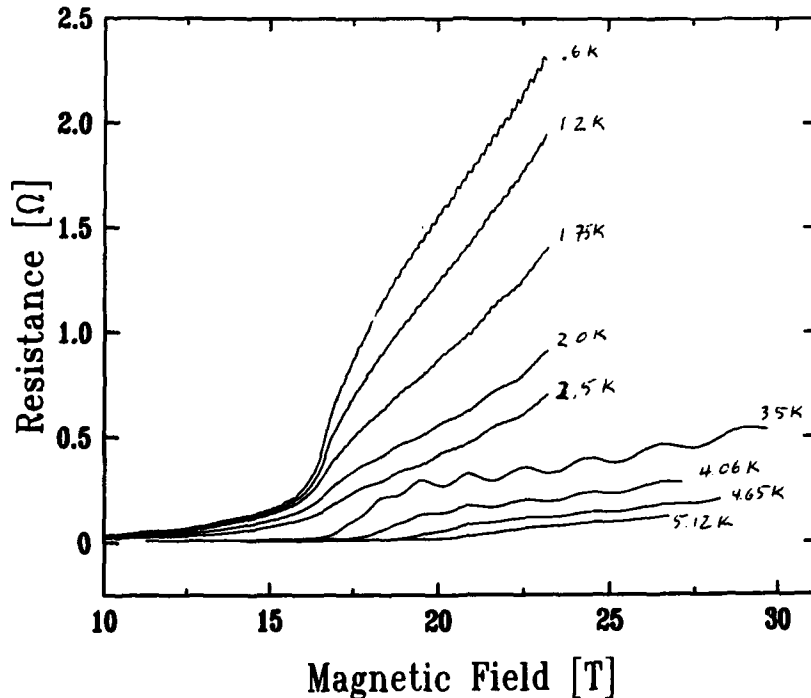


Figure 4: "Rapid" oscillations in the magnetoresistance of  $\text{PF}_6$ .

30T. The oscillation amplitude is quite temperature dependent, with a maximum at 3K. These oscillations have been also been seen at pressures below the superconducting threshold  $P_c$ , though they are small compared to the large resistance of the SDW state. They have been interpreted as due to the effects of anion ordering, magnetic breakdown through the anion ordering gap or from the existence of edge states. [14] That we observe them in the  $\text{PF}_6$  salt where the centrosymmetric anions preclude an ordering transition eliminates any explanation involving anion ordering. Virtually all of the models of the rapid oscillations predict that their frequency is proportional to the  $b$  axis bandwidth  $t_b$ . The quasi-frequency of the FISDW's on the other hand is proportional to the area of the unnnested part of the Fermi surface which for a simple bandstructure varies as  $t_b^2/E_f$ . Our values of the FISDW, and rapid frequencies from four separate measurements (all at room temperature pressures of about 10 kbar) are 72.6, 263; 64.9, 262; 74.1, 283; and 60.7, 291 tesla respectively. Thus at least in this small range any correlations are not evident.

The above observations are based on investigation of nearly half a dozen samples. A variable in our measurements has been the absolute value of the Hall plateaus. Here, for  $n = 1$ , we expect a value of  $h/2e^2$  (corresponding to a value of  $12.9 \text{ k}\Omega/\square/\text{layer}$  for a spin degeneracy of two due to the SDW formation [4]). We simply model the system as a parallel electric circuit so that the measured resistances are layer resistances divided by the number of layers. There can be considerable uncertainty in estimating the number of layers, and sample cracks, and imperfect contacts would cause non-ideal current paths within the sample. However, we consistently find a value of  $6.4 \pm .3 \text{ k}\Omega/\square/\text{layer}$ , a factor of 2 less than  $h/2e^2$  and similar to the value found in  $\text{ClO}_4$ .

Finally we consider the possibility of reentrance from a final SDW state above the

last transition back into a 1-d metallic state, as is the case for  $\text{ClO}_4$ . [9] In the present data for  $\text{PF}_6$   $\rho_{xx}$  increases very rapidly at the  $n = 0$  transition and is thermally activated in this state.  $\rho_{xy}$  is near zero in this phase and heating reveals a phase boundary must be crossed to enter the metallic state. These observations constitute our main evidence for the existence of the  $n = 0$  state. In contrast, for  $\text{ClO}_4$   $\rho_{xx}$  does not rise significantly after the  $n = 1$  plateau, and  $\rho_{xy}$  increases to a larger value. The material remains a semi-metal and has been suggested as being in the FQHE state. At much higher field the reentrant transition is reached. Then  $\rho_{xy}$  collapses, and  $\rho_{xx}$  increases rapidly, and is thermally activated. Theoretical work on the very high field phases of these materials is relatively new. [15] An estimate for the reentrance field is the frequency of the FISDW transitions. For  $\text{ClO}_4$  it is 31 T (28 T actual) and for  $\text{PF}_6$  it would be around 65 to 90 T for the pressures we have studied. In Fig. 2, it is clear that to 27T there is no evidence for reentrance.

In conclusion, we observed an unambiguous integer quantum Hall effect in a bulk material. The QHE is no longer the exclusive domain of two dimensional semiconductor devices. We have also found evidence for the complete cascade of field induced spin density wave transitions and have observed the previously unseen semiconducting state indicating the theoretical high field limit. Thus it appears that the standard model for these transitions is experimentally well confirmed at least for one material and pressure.

We wish to thank the staff of the Francis Bitter National Magnet Laboratory, R. Guertin and S. Bloom, for experimental help and G. Montambaux for many interesting and useful discussions. This work is supported by the NSF at BU under DMR88-18510 and at Princeton under DMR 88-22532.

#### REFERENCES

1. K. von Klitzing, G. Dorde and M. Pepper, *Phys. Rev. Lett.* **45**, 494, (80);  
D. C. Tsui, H. L. Stormer and A. C. Gossard, *Phys. Rev. B* **25**, 1408 (82).
2. H. L. Stormer, *et al.*, *Phys. Rev. Lett.* **56**, 85 (86).
3. D. Jerome, and H. J. Schultz, *Adv. in Phys.* **31**, 299 (82).
4. D. Poilblanc, *et al.*, *Phys. Rev. Lett.* **58**, 270 (87).
5. M. Ribault, *et al.*, *J. Phys. Lett.* **44**, L-953 (83);  
P. M. Chaikin *et al.*, *Phys. Rev. Lett.* **51**, 2333 (83).
6. R. V. Chamberlin *et al.*, *Phys. Rev. Lett.* **60**, 1189 (88).
7. S. T. Hannahs *et al.*, *Phys. Rev. Lett.* **63**, 1988 (89); S. T. Hannahs *et al.*, *Bull. Am. Phys. Soc.* **34**, 740 (89); J. R. Cooper *et al.*, *Phys. Rev. Lett.* **63**, 1984 (89).
8. M. Ribault, *Mol. Cryst. Liq. Cryst.* **119**, 91 (85).
9. M. J. Naughton *et al.*, *Phys. Rev. Lett.* **61**, 621 (88).
10. J. F. Kwak, J. E. Schirber, R. L. Greene, and E. M. Engler, *Phys. Rev. Lett.* **46**, 1296 (81) and *Mol. Cryst. Liq. Cryst.* **79**, 121 (81).
11. J. F. Kwak *et al.*, *Phys. Rev. Lett.* **56**, 972 (86); M. Ribault, *et al.*, *Physica* **143b**, 393 (86); L. Brossard, *et al.*, *Physica* **143b**, 406 (86).
12. G. Montambaux *et al.*, *Phys. Rev. B* **39**, 885 (89).
13. H. Schwenk *et al.*, *Phys. Rev. Lett.* **56**, 667 (86), T. Osada, N. Miura, and G. Saito, *Solid State Commun.* **60**, 441 (86); *Physica* **143B**, 403 (86), J. P. Ulmet *et al.*, *Physica* **143b**, 400 (86), X. Yan *et al.*, *Phys. Rev. B* **36**, 1799 (87).
14. K. Yamaji, *Physica* **143B+C**, 439 (86); *J. Phys. Soc. Jpn.* **55**, 1424 (86), M. Ya. Azbel, P. M. Chaikin, *Phys. Rev. Lett.* **59**, 582 (87), T. Osada and N. Muiira, *Solid State Commun.* **69**, 1169 (89).
15. V. M. Yakovenko, *Z.E.T.F.* **93**, 627 (87) [*Soviet Physics JETP* **60**, 355 (87)].

ANGULAR DEPENDENCE OF THE MAGNETORESISTANCE IN  $(\text{TMTSF})_2\text{ClO}_4$ 

M.J.NAUGHTON,\* O.H.CHUNG,\* L.Y.CHIANG+, S.T.HANNAHS,\* J.S.BROOKS#  
 \* State University of New York at Buffalo, Buffalo, N.Y. 14260  
 + Exxon Research and Engineering, Annandale, N.J. 08801  
 x Francis Bitter National Magnet Lab, M.I.T., Cambridge, MA 02139  
 # Boston University, Boston, MA 02215

## INTRODUCTION

We discuss recent low temperature results on the magnetoresistance of  $(\text{TMTSF})_2\text{ClO}_4$  in the low field metallic and the moderate field FISDW phases. From constant field rotations in a plane perpendicular to the highest conducting  $a$ -axis, we observe oscillatory resistance behavior along certain orientations at all fields measured. While at odds with usual considerations of resistance anisotropy due to the crystal structure, this feature may be consistent with the recent predictions of Lebed and Bak[1,2], wherein the oscillatory electron trajectories along the  $b^*$  and  $c^*$  directions become commensurate near particular "magic" orientations in the magnetic field. We compare our preliminary data with the Lebed-Bak model, finding some qualitative agreement.

## EXPERIMENTAL

The crystals used were synthesized at Exxon, and were from the same batch as those used in previous experiments. Four  $25\mu\text{m}$  Au wires were attached with Ag paint along one  $a$ - $c$  face and two along the other, to allow for magnetoresistance and Hall effect configurations. Low temperature contacts were  $\sim 2\Omega$ , the excitation current was  $100\mu\text{A}$  at 17Hz, and standard checks for sample heating and d.c. equivalence were employed. The experiments were performed at the National Magnet Laboratory at MIT in an 8-T horizontal field magnet and top-loading dilution refrigerator. Most data were taken at  $T=(75\pm 10)$  mK. *In situ* sample orientation was determined potentiometrically, with the top-loading probe rotated externally. The angular resolution for this experiment was approximately  $0.5^\circ$ , with reproducibility of  $\pm 2^\circ$ . The sample cooling rate was approximately 0.1 K/min below the anion ordering at 24K, yielding only moderately relaxed samples. Two samples were monitored, exhibiting qualitatively similar behavior; all data presented is for one sample. This sample was oriented by eye with its needle  $a$ -axis perpendicular to H to within  $\pm 5^\circ$ . The room temperature resistivity was  $\sim 300\mu\Omega\text{-cm}$ , while the residual resistivity ratio (RRR) was  $\rho_{300\text{K}}/\rho_{1\text{K}}=380$  (neglecting superconductivity), which we take as further evidence for a partially relaxed ground state (other samples from this batch typically have RRR values  $\sim 10^3$  in the fully relaxed state, i.e. cooling rates below 10mK/min.)

One motivation for this work was to extend previous FISDW angular dependence studies[3] to lower temperatures, in order to test the prediction due to Lebed[1] of a lowering of the FISDW critical (threshold) field at certain orientations of H in the  $b^*$ -

$c^*$  plane. Briefly stated,  $(TMTSF)_2ClO_4$  is a very anisotropic quasi-one dimensional (Q1-D) metal that retains enough 2-D character at low temperature to suppress the Peierls-type instabilities typical of Q1-D materials. A magnetic field applied normal to the quasi-2-D layers, however, drives the system back toward 1-D, and leads to the formation of a density wave, the FISDW. The fact that there is a critical threshold field at all (greater than zero), however, is due to the small but finite 3-D character at low temperatures as well (i.e. a nonzero bandwidth along the third direction,  $c^*$ ). What Lebed has observed is that at special orientations of the field, electron motion in the  $b^*-c^*$  plane becomes bounded and periodic: the 3-D effect is eliminated, the system becomes 2-D and the threshold field reduces to zero. The experimental limitations on observing this effect are related to the absolute temperature, crystal quality (including defects and anion order), and angular resolution.

## RESULTS

The magnetoresistance of  $(TMTSF)_2ClO_4$  was measured for several orientations  $\theta$  of the magnetic field, to determine the angular dependence of  $H_c$  on  $\theta$ , which in the 2-D case is a simple  $1/\cos\theta$  law. Here we define  $\theta$  as the angle between the field  $H$  and the sample  $c^*$  axis, in the  $b^*-c^*$  plane, as shown in the inset to Fig. 1. In the region  $-55^\circ < \theta < 55^\circ$ , we found no deviations from 2-D behavior, and hence no evidence of the oscillatory critical field of Lebed, similar to our result at 0.8K in Ref. [3]. Likewise, the oscillation fields identifying the higher field FISDW states appeared to follow the standard 2-D behavior. However, this aspect of our study was not done in great detail. Small deviations in temperature can cause significant changes in the phase diagram for the FISDW states[4], and a complete study of the threshold field angle dependence will require better angular resolution and more thorough studies.

Instead, we have concentrated here on sample rotations in a fixed magnitude and direction magnetic field. Previous studies of the normal metallic state magnetoresistance have noted an unusual anisotropy  $\rho_{b^*}/\rho_{c^*}$ , in light of the known band structure, including deviations from 2-D behavior [5,6,7]. In Fig. 1(a) we show our data for  $R_{xx}(\theta)$  at several fixed field values between 3T and 7T. There are some features of note. First, there is a clear resistance minimum near  $c^*$  (or possibly  $c'$ ) for fields of 3T, 4T and 5T, with a weak minimum near  $b'$  (where  $c^*$  is determined as  $b' \pm 90^\circ$ ). In following the resistance at  $\theta=0$  with increasing field, we note a small magnetoresistance relative to that at  $b'$ . At the higher fields (6T and 7T), we are well into the FISDW regime, and the resistance along  $c^*$  has increased dramatically. At 6T, there is no longer a minimum at  $\theta=0^\circ$ , due most likely to hysteresis of the FISDW transitions with respect to field sweep direction. This hysteretic effect is also very pronounced near  $\theta=0^\circ$  at  $H=7T$ , where an inflection point is observed (note the scale change for the 7T data). We have also made a small correction to each trace in Fig. 1(a) to compensate for a reactive component to the detected

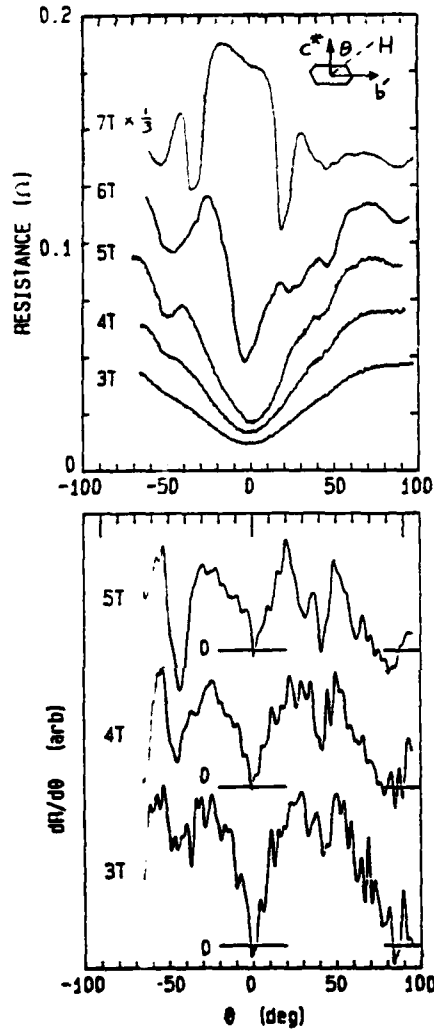


Figure 1. (a) Rotations at fixed field at  $T=75\text{mK}$ , showing oscillatory resistance in the metal phase in the range  $40^\circ \leq (\pm\theta) \leq 50^\circ$ . (b) derivative of three traces in (a), showing in more detail that the position (in  $\theta$ ) of the anomaly is independent of the magnetic field strength.

voltage. This correction amounts to less than 5% at all fields).

Second, we detect a slight oscillation in  $R(\theta)$  at 3T, near  $\theta = \pm(48 \pm 5)^\circ$ , which becomes more pronounced as field is increased. By 5T, we see a well developed maximum near  $\theta = \pm 40^\circ$  and the minimum again at  $\pm(48 \pm 5)^\circ$ . What is the origin of this resistance oscillation? An obvious candidate might be that we are simply passing through the FISDW oscillations, including the lowest field transition at the threshold field discussed above, as angle is swept. Recall that from previous studies, the only component of  $H$  that matters for FISDW formation is that parallel to  $c^*$ . Hence, starting at  $\theta=0^\circ$  and rotating toward  $\theta=\pm 90^\circ$  is equivalent to sweeping the field component along  $c^*$  from  $H_{\text{max}}$  to zero, with the added complication of picking up an increasing component of the  $b$ -axis magnetoresistance. For the 5T rotation, the resistance minimum occurs at  $H(c^*) = H \cdot \cos\theta = 5T \cdot \cos 48^\circ = 3.3T$ .

However, from magnetoresistance versus field measurements on this sample at fixed angle  $\theta=0$  ( $H//c^*$ ), the FISDW states appear only above a threshold field of 3.5T. This implies that the resistance oscillation is NOT due to the FISDW in the usual way, and must be of some other origin. Actually, stronger evidence for this conclusion is given by the 3T and 4T rotations, where  $H(c^*) = 3T \cdot \cos(48 \pm 5)^\circ = 2.01T \pm 0.20T$  and  $H(c^*) = 4T \cdot \cos(48 \pm 5)^\circ = 2.67T \pm 0.26T$ : well below any observed magnetic fields for the FISDW's (The lowest observed threshold field for this material is 2.95T at  $T=11\text{mK}$  [8]). In Fig. 1(b), we plot the resistance derivative  $(dR/d\theta) \cdot \text{sgn}(\theta)$  for some of the data in Fig. 1(a), in order to accentuate the observed anomalous oscillation. At all fields shown, there is a sharp minimum at

$\theta=0^\circ$ , and broader minima at  $\theta=\pm(48\pm5)^\circ$  (for presentation purposes, the derivatives have been scaled as follows: 3T:4T:5T :: x5:x2:x1). We note also that in Fig. 1(b) there are maxima in the derivatives at  $\theta=\pm(25\pm5)^\circ$ , which appear to be derived from inflection points in the raw data at these angles in Fig. 1(a).

In Fig. 2 we have plotted data similar to that in Fig. 1(a), but for higher magnetic field, 7.9T. At this field, several FISDW oscillations are observed, again with an inflection point at  $c^*$ , and distinct minima at  $\pm b'$  ( $\theta=\pm 90^\circ$ ). Upon close observation, we also detect shallow minima at  $\theta=\pm(48\pm5)^\circ$ , as in the lower field cases, although the large resistance changes incurred in passing through the FISDW transitions during the rotation make this assignment very difficult. Nonetheless, it appears possible that the anomalous oscillations persist. In an attempt to compare the magneto-resistance from these sample rotations with that obtained in the traditional manner, we have plotted in Fig. 3 the sample resistance in Fig. 2 versus  $H(\theta)\cos\theta = R/c^*$ , and  $R$  versus  $H$  for  $H/c^*$ . In Fig. 3, we essentially see a one-to-one correspondence for each FISDW state, verifying the predominantly two dimensional nature of the transitions.

#### DISCUSSION

In the theories due to Lebed, [1] and Lebed and Bak, [2] particular anomalous features are expected at angles  $\theta$  such that

$\tan\theta = (m/n) b\sin\gamma/c^*$ , where  $m$  and  $n$  are integers, and  $b, c^*$  and  $\gamma$  are unit cell parameters. At these angles, electron motion in the  $b$  direction is

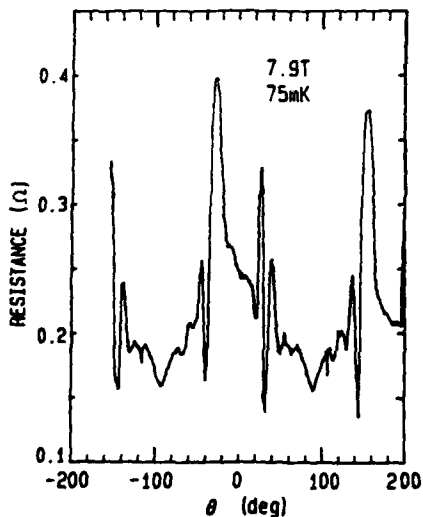


Figure 2. Rotation diagram 7.9T. Large oscillations are due to FISDW transitions. Note distinct minima at  $\theta=\pm 90^\circ$ , corresponding to  $\pm b'$ .

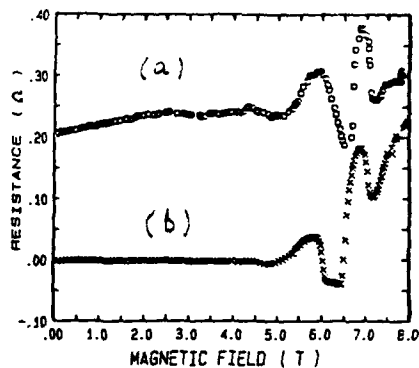


Figure 3. Comparison of (a) an angle sweep at fixed field 7.9T, and (b) a field sweep at fixed angle  $\theta=0^\circ$ , showing predominantly 2-D behavior.



periodic and commensurate with the periodic motion along  $c^*$ . Using published crystallographic data, the lowest order "magic" angle would occur for  $m=n=1$  or at  $\theta_1=28.7^\circ$ , while the two next order angles are for  $m=1, n=2$  ( $\theta_2=15.2^\circ$ ) and  $m=2, n=1$  ( $\theta_3=47.5^\circ$ ). The two  $n=1$  ( $m=1,2$ ) angles correspond well with the maxima and minima in Figs. 1 and 2, although a direct interpretation of the features is lacking. From Lebed's idea of the FISDW threshold field having a local minimum at these special angles, we would expect this to be manifest as a rise in resistance at  $\theta_i$ ,  $i=1,2,3,\dots$  (i.e. the FISDW state is more resistive than the metallic phase). However, without a detailed knowledge of the dependence of  $\sigma_{xx}$  on a varying field along  $b'$  with fixed field along  $c^*$ , we do not know whether to expect a rise or drop in  $R_{xx}$  in Fig. 1. So the observed oscillation may be related to the SDW threshold field. In the theory of Lebed and Bak, however, fine structure in the metallic state is predicted, again due to commensurate motion at the same magic angles  $\theta_1, \theta_2$ , etc. We have reproduced two of their theoretical curves in Fig. 4 along with our data from Fig. 1 at  $H=5T$  (trace a). Traces (b) and (c) are

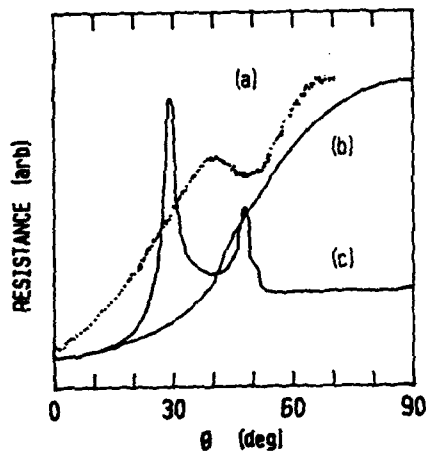


Figure 4. (a) data from Fig. 1 at  $H=5T$ , scaled for comparison to theoretical predictions of Ref. [2]; traces (b)  $H=2T$ ,  $T=0.4K$ , and (c)  $H=4T$ ,  $T=0.4K$ .

theoretical magnetoresistances at  $H=2T$  and  $H=4T$ , both at  $T=0.4K$ , and we have scaled our data arbitrarily for this comparison. Although the vertical axis is arbitrary for all three curves, some qualitative comparisons can be made. One is that the strong field dependence for oscillation amplitudes in the theory is similar to that in the data of Fig. 1. Another is the angles where the oscillations or resonances appear. Our data has a maximum in trace (a) where trace (c) has a local minimum, while the converse is true as well. The maxima in trace (c) and largest slope changes in (b) occur at the magic angles  $\theta_1=28.7^\circ$  and  $\theta_3=47.5^\circ$ . While this comparison may be dubious, we believe at the very least it warrants further investigation. Also, there is other independent data which shows similar oscillatory magnetoresistance near these special angles in the FISDW state, [9] again with a resistance minimum near  $\theta_3$ . Their data, however, shows one broad resistance maximum centered near  $\theta_1$  in the metallic state resistance, similar to the data of Refs. 6 and 7. We see no distinct features at  $\theta_1$ , save for a slight slope change, seen best in the derivatives in Fig. 1(b).

## CONCLUSIONS

From constant magnetic field sample rotations at  $T=75\text{mK}$  in the crystal  $b^*-c^*$  plane, we have observed a pronounced resistance oscillation in  $R_{xx}$  in  $(\text{TMTSF})_2\text{ClO}_4$ . This oscillation is present at ambient fields above and below that of the well known threshold field for field-induced spin density wave formation, and so is not related to the FISDW in any trivial manner. We have detected no anomalies in the threshold field angular dependence as predicted by Bak. In addition, we have compared the orientational dependence of the observed resistance oscillation with a recent prediction due to Lebed and Bak, where sharp "resonances" in commensurability between electron motion along the  $b^*$  and  $c^*$  axes are proposed to occur, leading to new effects in the magnetoresistance. We find some qualitative agreement between theory and experiment, in that the observed resistance versus orientation curve has an extremum (minimum) at a predicted "magic" angle, where otherwise no notable features are expected.

If the observed anomalous magnetoresistance is a reflection of this "magic" angle commensurability, we might expect a strong dependence on sample quality, especially anion ordering. Since the low temperature mean free path this system essentially scales with the 24K anion ordering order parameter, the predicted effects may become more pronounced for cooling rates slower than those used in this study (superconductivity and FISDW occur only for slowly cooled, well ordered samples, and the s.c.  $T_c$  and sharpness of the FISDW transitions improve with longer cooling rates below 24K). Such further studies are under way.

## REFERENCES

1. A.G. Lebed, Zh. Eksp. Teor. Fiz. **43**, 137 (1986) [Sov. JETP Lett. **43**, 174 (1986)].
2. A.G. Lebed and P. Bak, Phys. Rev. Lett. **63**, 1315 (1989).
3. X. Yan, M.J. Naughton, O.S. Cheema, R.V. Chamberlin, S.Y. Hsu, L.Y. Chiang, P.M. Chaikin, Sol. State Commun. **66**, 905 (1988).
4. M.J. Naughton, J.S. Brooks, L.Y. Chiang, R.V. Chamberlin, P.M. Chaikin, Phys. Rev. Lett. **55**, 969 (1985) and M.J. Naughton, R.V. Chamberlin, X. Yan, S.Y. Hsu, L.Y. Chiang, M. Ya. Azbel, P.M. Chaikin, Phys. Rev. Lett. **61**, 621 (1988).
5. J.F. Kwak, J.E. Schirber, R.L. Greene, E.M. Engler, Mol. Cryst. Liq. Cryst. **79**, 111 (1982).
6. R. Brusetti, K. Bechgaard, G. Lonzarich, R.H. Friend, J. Phys. (Paris) **44**, C3-1055 (1983).
7. K. Murata, H. Bando, K. Kajimura, T. Ishiguro, H. Anzai, Mol. Cryst. Liq. Cryst. **119**, 131 (1985).
8. P.M. Chaikin, J.S. Brooks, R.V. Chamberlin, R. Goshorn, D.C. Johnston, M.J. Naughton, X. Yan, Physica **143 B**, 383 (1986).
9. G.S. Boebinger, G. Montambaux, M. Kaplan, R.C. Haddon, S.V. Chichester, L.Y. Chiang (unpublished).

## ELECTRON TUNNELING IN CHARGE-DENSITY AND SPIN-DENSITY WAVES

X. Z. HUANG and K. MAKI  
University of Southern California, Department of Physics,  
Los Angeles, California 90089-0484

## ABSTRACT

First we calculate the tunneling density of states of quasi-two dimensional charge density waves (CDW) or spin density waves (SDW) in the presence of impurity scattering. Second, we consider the tunneling current between two CDWs or two SDWs. We point out the existence of new contribution, which gives rise to the a.c. current when one CDW is sliding relative to the other one.

## INTRODUCTION

There are accumulating evidences that most of the CDW observed in the quasi-one dimensional compounds like NbSe<sub>3</sub> and TaS<sub>3</sub> are two or three dimensional. For example both the impurity concentration dependence of the threshold field [1] and the resistivity anomaly of orthorhombic TaS<sub>3</sub> near the transition temperature [2] indicate that the CDW in o-TaS<sub>3</sub> is three dimensional. A similar analysis of the CDWs in NbSe<sub>3</sub> indicates that they are two dimensional [3]. We have shown earlier [4] that both the tunneling density of states and the large ratio of  $2G/k_B T_c = 11.4 \sim 14.4$  (where  $G$  is the apparent energy gap) observed by the electron tunneling experiment [5,6] can be accounted for by quasi-two-dimensional model with imperfect nesting. For definiteness we take the quasi-particle spectrum [7]

$$\begin{aligned} E(\mathbf{p}) &= -2t_a \cos(ap_1) - 2t_b \cos(bp_2) - \mu \\ &\simeq v(p_1 - p_F) - 2t_b \cos(bp_2) - \epsilon_0 \cos(2bp_2) \end{aligned} \quad (1)$$

where we neglect the third transfer integral  $t_c$  for simplicity. Further we simplify Eq.(1) following Yamaji [8] and Hasegawa and Fukuyama [9]

$$\epsilon_0 = -\frac{1}{4} t_b^2 \cos(ap_F) (t_a \sin^2 ap_F)^{-1} \quad (2)$$

For the simple nesting vector  $Q = (2p_F, \pi/b, \pi/c)$  the last term in Eq.(1) gives rise to the imperfect nesting. If we assume that  $\epsilon_0$  increases linearly with the external pressure, the present model describes very well both the pressure dependence of the CDW transition temperature observed in NbSe<sub>3</sub> [10] and that of the SDW transition temperature in (TMTSF)<sub>2</sub>PF<sub>6</sub> [11].

## DENSITY OF STATES

Within mean field theory the single particle Green's function in the CDW is given by

$$G^{-1}(\omega_n, \mathbf{p}) = i\omega_n - \eta - \xi\rho_3 - \Delta\rho_1 \quad (3)$$

where  $\omega_n$  is the Matsubara frequency

$$\begin{aligned} \xi &= v(p_1 - p_F) - 2t_b \cos(bp_2) \\ \eta &= \epsilon_0 \cos(2bp_2) \end{aligned} \quad (4)$$

and  $\rho_i$ 's are the Pauli matrices operating on the spinor space consisting of the right going and the left going electrons. We also have quite similar Green's function for a SDW [12]. In the presence of impurity scattering both  $\omega_n$  and  $\Delta$  in Eq.(3) have to be replaced by  $\bar{\omega}_n$  and  $\bar{\Delta}$  respectively where

$$\bar{\omega}_n = \omega_n + \frac{1}{2}(\Gamma_1 + \Gamma_2)((\bar{\omega}_n + i\eta)[(\bar{\omega}_n + i\eta)^2 + \bar{\Delta}^2]^{-\frac{1}{2}}) \quad (5)$$

$$\bar{\Delta} = \Delta - \frac{1}{2}\Gamma_1 \bar{\Delta} [(\bar{\omega}_n + i\eta)^2 + \bar{\Delta}^2]^{-\frac{1}{2}} \quad (6)$$

where  $\Gamma_1$  and  $\Gamma_2$  are the forward and the backward scattering rate due to the impurity scattering and  $\langle \dots \rangle$  means the average over  $p_2$  [13]. Unlike in a superconductor the impurity suppresses both the CDW and the SDW. Therefore we assume in the following  $\Gamma_i/\Delta_0 < 0.1$ , where  $\Delta_0$  is the order parameter at  $T = 0K$ . Solving the gap equation we obtain

$$\begin{aligned} -\ln\left(\frac{\Delta_0}{\Delta_{00}}\right) &= \frac{1}{2}(\Gamma_1 + \Gamma_2) \int_0^\infty dz ((z - i\eta)X) \langle (z - i\eta)X^3 \rangle \\ &\quad + \frac{1}{2}\Gamma_1 \int_0^\infty dz (X) \langle (z - i\eta)X^2 \rangle \\ &\simeq \frac{\pi}{4}\Gamma\Delta_0^{-1} \quad \text{for } \epsilon_0/\Delta_0 \ll 1 \end{aligned} \quad (7)$$

where  $X = [(z - i\eta)^2 + \Delta^2]^{-\frac{1}{2}}$  and  $\Gamma = \Gamma_1 + \frac{1}{2}\Gamma_2$  and  $\Delta_{00}$  is the order parameter at  $T = 0K$  of the clean system. In the absence of the scattering, the single particle density of states is obtained as [4]

$$N(E)/N_0 = \langle (E - \eta)[(E - \eta)^2 - \Delta^2]^{-\frac{1}{2}} \rangle \quad (8)$$

$$\begin{cases} \frac{1}{2}(\Delta\epsilon_0)^{-\frac{1}{2}} [ (|E| + \Delta + \epsilon_0) \Pi\left(-\frac{|E| - \Delta + \epsilon_0}{2\Delta}, r\right) - \Delta K(r) ] \\ \text{for } \Delta - \epsilon_0 < |E| < \Delta + \epsilon_0 \end{cases} \quad (8a)$$

$$\begin{cases} \frac{1}{2}(E^2 - (\Delta - \epsilon_0)^2)^{-\frac{1}{2}} [ (|E| + \Delta + \epsilon_0) \Pi\left(-\frac{2\epsilon_0}{|E| + \Delta - \epsilon_0}, r_1\right) \\ - \Delta K(r_1) ] \\ \text{for } |E| > \Delta + \epsilon_0 \end{cases} \quad (8b)$$

where  $r = \frac{1}{2} \left[ \frac{E^2 - (\Delta - \epsilon_0)^2}{\Delta\epsilon_0} \right]^{\frac{1}{2}}$ ,  $r_1 = r^{-1}$  and  $K$  and  $\Pi$  are the complete elliptic integral of the first kind and the third kind respectively. Here we assume  $\epsilon_0 < \Delta$ . In the presence of the

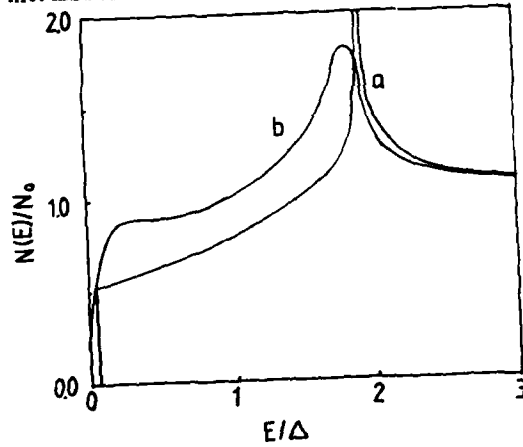


Fig.1  
Electron density of states  
 $N(E)$  is shown for  
a) the clean limit  $\Gamma/\Delta = 0$   
and b)  $\Gamma/\Delta = 0.1$ .

impurity scattering ( $\Gamma/\Delta = 0.1$ ), the logarithmic singularity at  $|E| = \Delta + \epsilon_0$  is broadened. Further there is nonvanishing density of states for  $|E| < \Delta - \epsilon_0$ . These are shown in Fig.1

### TUNNELING CURRENT BETWEEN TWO CDWS OR SDWS

We shall consider here at  $T = 0K$  for simplicity. The tunneling current between two CDWs consists of two terms in general

$$J_{\text{CDW-CDW}}(E) = |T|^2 \int_0^E dE' \{ N(E')N(E-E') + \cos(\phi)M(E')M(E-E') \} \quad (9)$$

where  $\phi = \phi_1 - \phi_2$  is the phase difference between two CDW's order parameters and

$$M(E)/N_0 = \Delta \left( |(E-\eta)^2 - \Delta^2|^{-\frac{1}{2}} \right) = \begin{cases} \frac{1}{2} \left( \frac{\epsilon_0}{\Delta} \right)^{\frac{1}{2}} K(r) & \text{for } \Delta - \epsilon_0 < |E| < \Delta + \epsilon_0 \\ \frac{1}{2} \Delta [E^2 - (\Delta - \epsilon_0)^2]^{-\frac{1}{2}} K(r_1) & \text{for } |E| > \Delta + \epsilon_0 \end{cases} \quad (10)$$

The related conductance is given by

$$g_1(E) = |T|^2 \frac{\partial}{\partial E} \left[ \int_0^E dE' N(E')N(E-E') \right] \quad (11)$$

and

$$g_2(E) = |T|^2 \frac{\partial}{\partial E} \left[ \int_0^E dE' M(E')M(E-E') \right] \quad (12)$$

which are shown in Fig.2. Here we correct an error in our earlier numerical analysis [4]. Though  $g_1(E)$  has the logarithmic singularity at  $E = 2\Delta$ ,  $g_1(E)$  experiences a jump without singularity at  $E = 2(\Delta + \epsilon_0)$ . The behavior of  $g_2(E)$  is very similar to  $g_1(E)$  except for  $|E| > 2(\Delta + \epsilon_0)$ , it takes negative value. As for the contribution of the  $g_2$

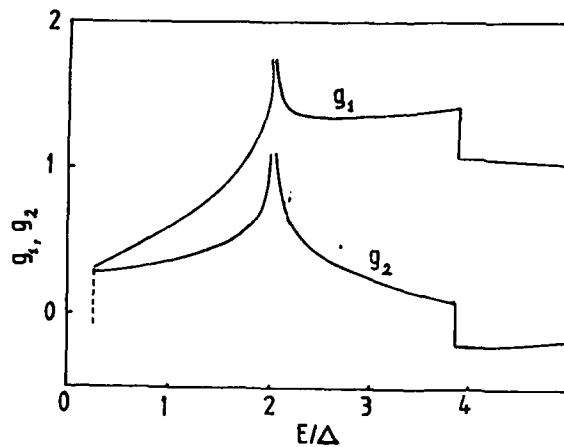


Fig.2  
The tunneling conductance  $g_1(E)$  and  $g_2(E)$  are shown as functions of  $E=eV$ .

term to the tunneling conductance, we can think of three limiting cases: a) Ideal case;

b) Random case; c) Sliding case. In the first case we assume that  $\phi_i$ 's in each CDW has the correlation length (Efetov-Larkin-Fukuyama-Lee-Rice length [14,15]) more extended than the tunneling junction. Then we will have  $\phi = 0$ . In the second case the correlation length is much shorter and therefore no coherent current due to  $g_2$ . In the third case when one or both of CDWs are driven by the external current, the correlation length may be increased. In such a situation  $\phi$  is given by  $\phi = Q(v_1 - v_2)t$  with  $v_1$  and  $v_2$  the sliding velocities of two CDWs, and the tunneling current develops an a.c. component.

#### CONCLUDING REMARKS

We have reanalysed the density of states and the tunneling current associated with quasi-two-dimensional CDWs and SDWs. The detection of the tunneling associated with  $g_2$  will provide a new insight into the CDW or SDW dynamics.

#### ACKNOWLEDGEMENT

This work is supported by the National Science Foundation under Grant No. DMR 86-11829.

#### REFERENCES

- [1] P.-L. Hsieh, F. de Cizto, A. Janossy, and G. Grüner, *J. Phys.* **44** C3-1749 (1983)
- [2] K. Maki, to be published
- [3] K. Maki and A. Virosztek, *Phys. Rev.* **B39** 9640 (1989)
- [4] X. Z. Huang and K. Maki, *Phys. Rev.* **B40** 2575 (1989)
- [5] A. Fournel, J. P. Sorbier, M. Konczykowski, and P. Monceau, *Phys. Rev. Lett.* **57** 2199 (1986)
- [6] T. Ekino and J. Akimitsu, *Jpn. J. Appl. Phys.* **26** suppl. 625 (1987)
- [7] K. Yamaji, *J. Phys. Soc. Jpn.* **51** 2787 (1982)
- [8] K. Yamaji, *Synth. Met.* **13** 29 (1986)
- [9] Y. Hasegawa and H. Fukuyama, *J. Phys. Soc. Jpn.* **55** 3978 (1986)
- [10] A. Brigg, P. Monceau, M. Nuñez-Regueiro, J. Peyrard, M. Ribault, and J. Richard, *J. Phys (Paris)* **42** 1453 (1981)
- [11] D. Jérôme and H. Schulz, *Adv. Phys.* **31** 299 (1981); R. L. Greene and P. M. Chaikin, *Physics B126* 431 (1984)
- [12] K. Maki and A. Virosztek, *Phys. Rev.* **B41** (in press)
- [13] K. Maki and A. Virosztek, *Phys. Rev.* **B39** 2511 (1989)
- [14] K. B. Efetov and A. I. Larkin, *Zh. Eksp. Teor. Fiz.* **72** 2350 (1977) [*Sov. Phys.-JEPT* **45** 1236 (1977)]
- [15] H. Fukuyama and P. A. Lee, *Phys. Rev. B* **17** 535 (1978); P. A. Lee and T. M. Rice, *Phys. Rev. B* **19** 3970 (1979)

---

PART III

---

## Organic Conducting Polymers

## FIBERS OF CONDUCTING POLYMERS: HIGH ELECTRICAL CONDUCTIVITY COMBINED WITH ATTRACTIVE MECHANICAL PROPERTIES

ALEJANDRO. ANDREATTA\*, S. TOKITO\*\*, P. SMITH\*\*\* and A.J. HEEGER\*\*\*\*  
Institute for Polymers and Organic Solids, University of California, Santa Barbara,  
CA 93106

\*Materials Department

\*\*Permanent address: Department of Materials Science and Technology, Kyushu  
University, Kasuga-shi, Fukuoka 816, JAPAN,

\*\*\*Chemical and Nuclear Engineering Department

\*\*\*\*Physics Department

### ABSTRACT

We present a summary of our recent results on the electrical and mechanical properties of fibers made from poly(2,5-dimethoxy-p-phenylene vinylene), PDMPV and poly(2,5-thienylene vinylene), PTV, using the precursor polymer methodology, and from polyaniline, PANI, using the method of processing as polyblends with poly-(p-phenylene terephthalamide), PPTA, from sulfuric acid. The solubility of both PANI and PPTA in  $H_2SO_4$  presents a unique opportunity for co-dissolving and blending PANI and PPTA to exploit the excellent mechanical properties of PPTA and the electrical conductivity of PANI; we summarize the electrical and mechanical properties of such composite fibers. For PDMPV and PTV fibers, we find a strong correlation between the conductivity and the tensile strength (and/or modulus), and we show from basic theoretical concepts that this relationship is an intrinsic feature of conducting polymers.

### 1. INTRODUCTION

In conjugated polymers, the  $\pi$ -bonding leads to  $\pi$ -electron delocalization along the polymer chains and to the possibility of relatively high charge carrier mobility,  $\mu$ , which is extended into three dimensional transport by the interchain electron transfer interactions.<sup>1</sup> The high density of redox sites within the  $\pi$ -electron system (essentially one per monomer) offers the additional advantage of a relatively high density,  $n$ , of carriers (charge  $e$ ) through doping. Thus, high electrical conductivity,  $\sigma = ne\mu$ , is possible. As a result of the same intrachain  $\pi$ -bonding and relatively strong interchain electron transfer interactions, the mechanical properties (Young's modulus and tensile strength) of conjugated polymers are potentially superior to those of saturated polymers, such as polyolefins. Moreover, because of these two features, it may be possible to achieve exceptional mechanical properties with aligned conjugated polymers at lower chain lengths than required for their saturated counterparts.<sup>2</sup> Thus, conjugated polymers are of special interest because of the potential of a unique combination of electrical and mechanical properties.<sup>3</sup>

Since the electrical and mechanical properties are currently limited by defects and structural disorder, improvement in material quality that will enable the exploration of intrinsic properties has become an important goal of conducting polymer research.<sup>3</sup> It has been long recognized, however, that conjugated polymers tend to be insoluble and infusible. Thus, the question to be answered is whether or not processing methods can be developed that will lead to chain



extended and chain aligned materials of sufficient quality. Significant progress has been made; the addition of long alkyl side chains<sup>4</sup> has opened opportunities for processing from solution or from the melt. However, the relatively bulky side chains decrease the  $\pi$ -electron density (and thus the carrier density) and the interchain coupling, thus making it more difficult to achieve the structural coherence needed to obtain high carrier mobility and exceptional mechanical properties.

A promising strategy to approach the intrinsic mechanical and electrical properties is through the use of the versatile precursor route which involves the preparation of a processible precursor polymer and subsequent conversion of the precursor polymer to the conjugated polymer.<sup>5,6</sup> The significant advantage of this route is that the saturated precursor polymers can be processed from solution prior to the thermal conversion to the conjugated final product. The precursor polymers may, therefore, be drawn prior to and during the thermal conversion process so as to yield oriented, homogeneous conjugated polymers.

Poly(*p*-phenylenevinylene), PPV, and its derivatives can be prepared from a precursor polymer, a polyelectrolyte, which is soluble in water.<sup>6</sup> The dimethoxy-derivative of PPV, poly(2,5-dimethoxy-*p*-phenylenevinylene), PDMPV, has been prepared via a similar precursor route to PPV and exhibited high conductivities after doping. However, the commonly used aqueous solutions of the PDMPV precursor polymer tend to form gels, and the gradual elimination of the sulfonium group in the solid precursor cannot be avoided even at room temperature; both effects make subsequent processing into highly oriented films and fibers difficult. Recently, the Kyushu University group<sup>7</sup> succeeded in the preparation of dense PDMPV film from a new precursor polymer which is soluble in common organic solvents, easily processible, and stable even at 100 °C. Similarly, poly(2,5-thienylene vinylene) (PTV) is one of the larger class of poly(arylenevinylene) polymers which is attractive as a conjugated polymer and which can be synthesized via the precursor polymer route. As with PDMPV, the Kyushu University group<sup>8,9</sup> and Murase et al.<sup>10</sup> have found that PTV can be prepared through a new precursor polymer which is soluble in common organic solvents and chemically stable.

An alternative strategy is to identify stable conjugated polymer systems that can be processed. Of this class, polyaniline (PANI) is certainly a promising example. The use of concentrated acids<sup>11</sup> as solvents for PANI has specific advantages in that both the salt and the base form can be completely dissolved at room temperature, with polymer concentrations ranging from extremely dilute to more than 20% (w/w) in concentrated protonic acids such as H<sub>2</sub>SO<sub>4</sub>, CH<sub>3</sub>SO<sub>3</sub>H, and CF<sub>3</sub>SO<sub>3</sub>H. Perhaps more important is the fact when precipitated from acid solution, PANI comes out in the conducting (protonated) emeraldine salt form.<sup>11</sup> Although the ability to process conducting polyaniline from solution represents genuine progress, fibers and films made from these solutions have mechanical properties which are not adequate for many applications due mainly to the low molecular weight of the polyaniline used.<sup>12</sup> Fibers with significantly enhanced mechanical properties have been obtained by blend processing polyaniline with the rigid chain polymer poly-(*p*-phenylene terephthalamide), PPTA.<sup>13</sup> It is well known that PPTA is processed from solutions in concentrated H<sub>2</sub>SO<sub>4</sub> to yield one of the strongest and stiffest fibers commercially available.<sup>14</sup> The process takes advantage of the fact that PPTA is a rod-like polymer that exhibits a liquid crystalline phase at high solution concentrations which facilitates the formation of highly oriented structures.<sup>15</sup>

In this review, we present a summary of our recent results on the electrical and mechanical properties of fibers made from PDMPV<sup>16</sup> and PTV<sup>17</sup> using the precursor polymer methodology, and from PANI using the method of processing as polyblends with PPTA from sulfuric acid.<sup>13</sup>

## II. Experimental Methods and Techniques

### A. Preparation of Precursor Polymers for PDMPV and PTV

The preparation of the precursor polymer and conversion to the conjugated polymer are summarized in Figure 1a (PDMPV) and 1b (PTV). Details on the synthesis of the precursor polymer and the conversion to the conjugated polymer are presented elsewhere.<sup>16,17</sup>

Differential scanning calorimetric (DSC) measurements of the polymer were carried out using a Mettler DSC 30, with the sample under nitrogen. The DSC thermogram of the PDMPV precursor polymer indicated a glass transition at 110°C, well-separated in temperature from the -195°C needed for thermal elimination of the methoxy leaving groups (Scheme 1a). For the PTV precursor polymer, the glass transition is at 50°C, again, well-separated in temperature from the elimination of methoxy leaving groups, which occurred at 188°C.

### B. Preparation of the PANI/PPTA Blends<sup>13</sup>

The synthesis of the polyaniline used in this study was reported elsewhere<sup>8,9</sup>. Poly (p-phenylene terephthalamide) with inherent viscosity of 7.43 dl/g was obtained from DuPont as Kevlar<sup>®</sup> powder.

A stock solution of 2 wt% PPTA in sulfuric acid was prepared by mixing 3.76 g of PPTA in 100 ml of 98% H<sub>2</sub>SO<sub>4</sub> (Fisher). The mixture was mechanically stirred overnight to yield a homogeneous solution. This solution was also used to produce the 100% PPTA fibers. Polyaniline was weighed into a vial and concentrated H<sub>2</sub>SO<sub>4</sub> was subsequently added. The mixture was stirred until the polyaniline dissolved and the solution was homogeneous. An amount of 2wt% PPTA stock solution was added to yield a desired specific PANI/PPTA ratio. The mixture was mechanically stirred for 5 to 12 hours at room temperature, and then allowed to stand for 24 hours before spinning, to let the trapped air escape. In all cases, optically homogeneous solutions were obtained. Since the concentration of PPTA in the solutions was maintained at 1.5wt% (which is below the onset of the formation of the lyotropic phase: typically at 6-8 wt% PPTA<sup>11</sup>), these polyblend fibers were spun from isotropic solutions.

### C. Fiber Spinning. Drawing and Conversion of PDMPV<sup>16</sup> and PTV<sup>17</sup>

Details on the fiber spinning of the purified precursor polymers are given elsewhere.<sup>16,17</sup> For PDMPV and PTV, the precursor polymers were dissolved into chloroform. The solutions were spun using a high precision syringe pump (Sage Instruments, model 355). The viscous solutions were pumped at a speed of 0.013 ml/min through a needle with diameter of 0.5 mm into hexane; the resulting precursor fibers were taken up onto a bobbin at a speed of 30 cm/min. The

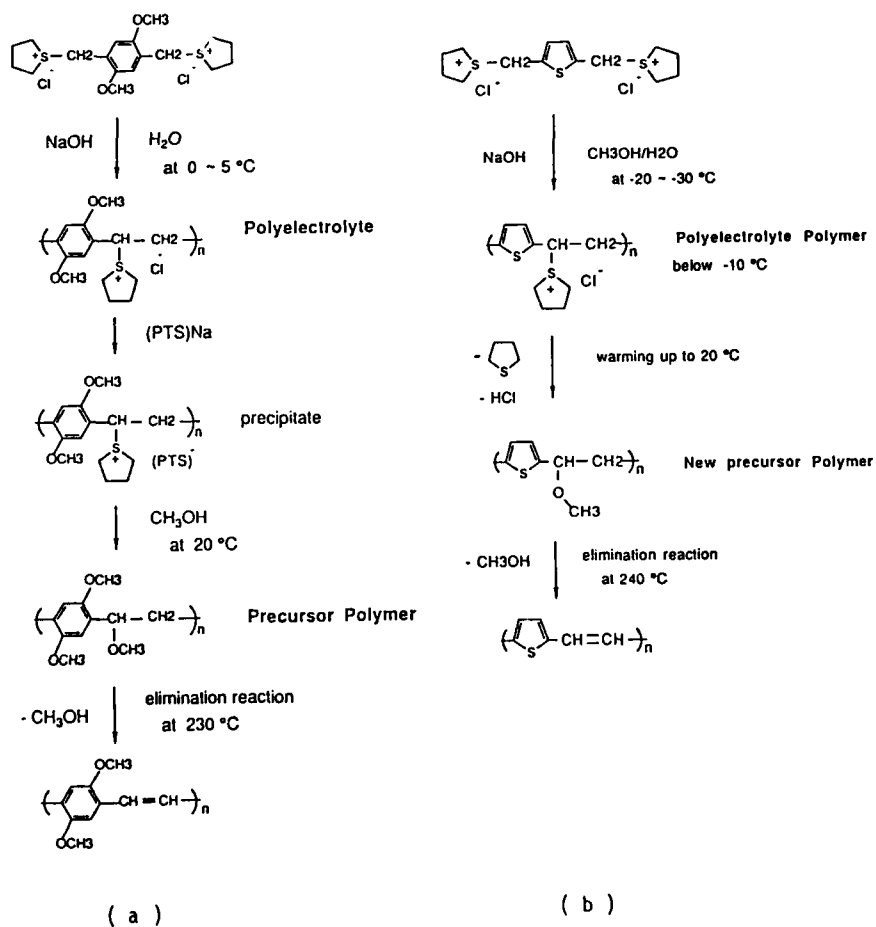


Figure 1

a: Synthesis of poly(2,5-dimethoxy-p-phenylenevinylene) from precursor polymer soluble in organic solvents.

b: Synthesis of poly(2,5-thienylene vinylene) from precursor polymer soluble in organic solvents.

precursor polymers were dried in a vacuum oven overnight; uniform pale yellow fibers were obtained with diameters of 50 -100  $\mu\text{m}$ . The drawing of the precursor fiber and conversion to fibers of the conjugated polymer were carried out using a temperature controlled, continuous drawing, tube furnace system.<sup>16,17</sup>

The PDMPV and PTV fibers were doped by exposure to the vapor pressure (approximately 1 mm Hg) of iodine at room temperature. Electrical measurements were carried out using the conventional four-probe method. The electrical conductivity was monitored *in-situ* during the doping; measurements were continued over a period of about an hour until the conductivity reached the steady state value.

#### D. PANI/PPTA Fiber Spinning<sup>13</sup>

The polymer blend solutions were wet spun into 1N  $\text{H}_2\text{SO}_4$  using a high precision syringe pump. Monofilaments were collected onto a take-up spool; applied tension was applied to elongate the fiber during coagulation. The draw down ratio (take up speed/extrusion speed) invariably was as high as possible, for the production of continuous fibers; and it was increased from 7 to 20 with increasing PPTA concentration in the solution. Extrusion speed varied from 0.12 to 0.3 m/min and the windup speed from 1.8 to 4.2 m/min.

The fibers were prevented from drying on the bobbin by continually spraying them with deionized water; this procedure impeded the open structure of the wet spun fibers from collapsing and allowed removal of the residual  $\text{H}_2\text{SO}_4$ . Subsequently, the fibers were washed with running deionized water for 48 hr. Half of the bobbin was then submerged in 1.5N HCl for 12 hr. This allowed the acid to penetrate the fibers and homogeneously protonate them to the conducting emeraldine salt form (partial reduction of the emeraldine salt occurs during the washing; the HCl treatment restores PANI to the fully protonated form). Finally, the bobbin was placed in an oven and the fibers dried under vacuum at 50°C while maintained at constant length by the bobbin. The pure PPTA fibers were spun with the same method. The pure polyaniline solution was dry-jet wet spun into a 1N  $\text{H}_2\text{SO}_4$  solution. Washing, HCl treatment, and drying was carried out as described for the blend fibers.

### III. RESULTS

#### A. PANI/PPTA

Wide angle X-ray patterns of the composite fibers consisted of superimposed reflections from the two components, indicating that PANI and PPTA segregated during the coagulation.<sup>13</sup> In Figure 2 (inset), the conductivity vs volume fraction of PANI is shown on a log-log plot; the results indicate that over a relatively wide range of concentrations, the conductivity follows a simple power law,

$$\sigma = \sigma_0 f^{\alpha} \quad (1)$$

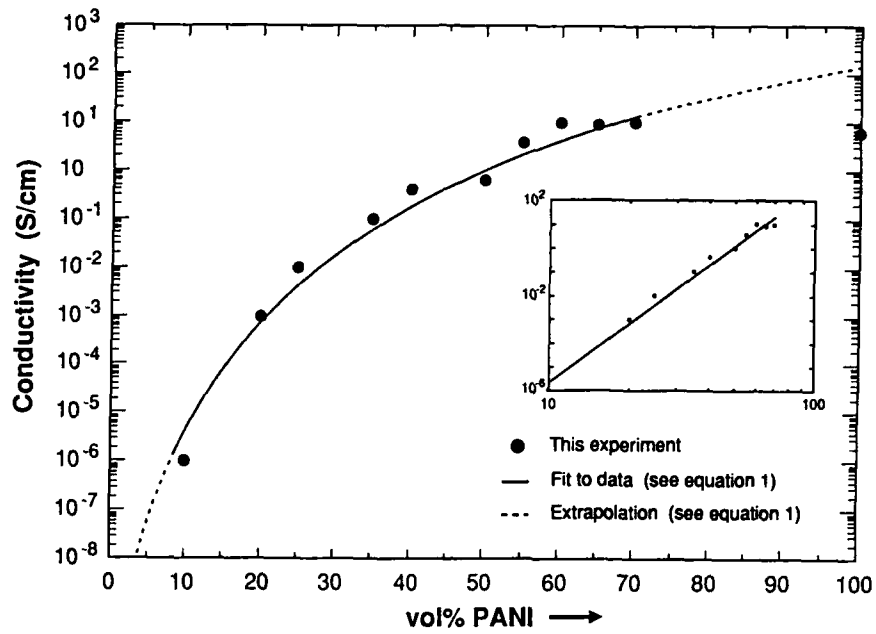


Figure 2: Conductivity versus volume fraction of PANI in the fiber; the inset shows the same data on a log-log plot.

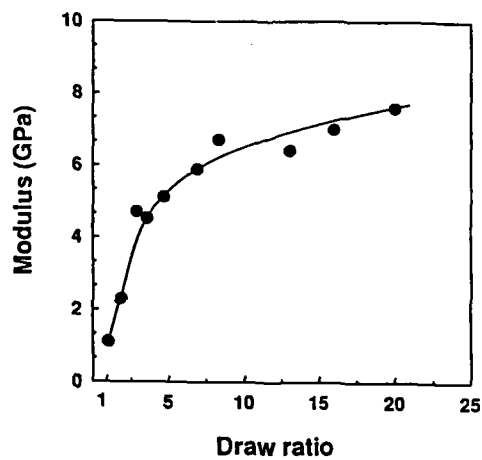


Figure 3: Relationship between draw ratio and modulus of PTV fibers.

where  $f$  is the weight fraction of PANI. The solid curve in Figure 2 shows the power law fit to the experimental data with  $\alpha=8.3$  and  $\sigma_0=1.2 \times 10^{-14}$ ; the conductivity varies with fractional concentration of conducting polymer (from 10-70 % PANI) according to equation 1 over a range of values spanning nearly seven orders of magnitude.

In the context of percolation theory,<sup>18</sup> at sufficiently dilute concentrations such that there are no connected paths, the conductivity would be zero. As the concentration of conducting polymer is increased above the percolation threshold, the conductivity would become finite and increase as the connectivity (i.e. the number of conducting paths) increases. In contrast, the data presented in Figure 2 show no indication of a well-defined percolation threshold. Attempts to estimate a value for the percolation threshold ( $f_p$ ) by fitting the data to the form  $\sigma = \sigma_0(f - f_p)^\alpha$  lead to the conclusion that  $f_p$  is below a few tenths of a percent. By contrast, classical percolation theory for a three-dimensional network of conducting polymer globular aggregates in an insulating matrix predicts a percolation threshold at a volume fraction  $f_p=0.16$ .<sup>18</sup> Percolation at  $f_p=0.16$  has been observed for conducting polymer composites.<sup>19</sup>

On the other hand, for rod-like structures with length  $L$  and diameter  $d$  (e.g. a more fibrillar conducting network), the percolation threshold is determined by the excluded volume per fibril ( $\approx \pi L^2 d$ ).<sup>20</sup> With  $N$  fibrils per unit volume, the percolation threshold is given by  $f_p \approx N \pi L^2 d = N \pi L d^2 (L/d) = f_{fib}(L/d)$  where  $f_{fib}$  is the volume fraction of conducting material in the fibrillar network. Thus, the onset of conductivity would occur at  $f_{fib} = f_p(d/L) \ll f_p$ . The analogous percolation of molecularly dispersed rods was observed<sup>21</sup> for polydiacetylene in solution in toluene, where the onset of gelation (i.e. the formation of a connected mechanical network) occurs at a volume fraction of only 0.04%. Since PPTA precipitates from sulfuric acid at a lower water content (at  $\approx 10$  wt%) than PANI (at  $\approx 25$  wt%), the PPTA comes out of solution first and forms a mechanically connected network. That structure may serve to assemble the conducting PANI along the pre-existing connected paths, thereby leading to the kind of fibrillar conducting pathways that would decrease the percolation threshold to  $f_p \ll 0.16$ .

## B. PTV<sup>17</sup>

The Young's modulus and the tensile strength of the PTV fibers were measured at room temperature. Figure 3 shows the Young's modulus plotted against draw ratio; Figure 4 displays the tensile strength plotted against draw ratio. The modulus of the undrawn, converted PTV fiber was 1.1 GPa. Values of the Young's modulus of 7 GPa and of the tensile strength of 0.5 GPa were obtained for fibers which had been drawn to 20 times their initial length.

The tensile strength of 0.5 GPa is identical to the value as reported for highly stretched PPV film prepared by a heated roll method<sup>22</sup> and comparable to the values obtained with stretched *trans*-polyacetylene films.<sup>23</sup> The modulus, however, was lower than the values reported for stretched PPV films<sup>22</sup> and for stretched polyacetylene<sup>23</sup> films.

The conductivities of the iodine-doped PTV fibers were measured at room temperature. The conductivity rapidly increased after the PTV fibers were exposed on iodine vapor, approaching maximum values after about 1 hour. Figure 5 shows the conductivity plotted against the draw ratio. The undrawn PTV fiber exhibited a conductivity of 80 S/cm. As expected, the conductivity was

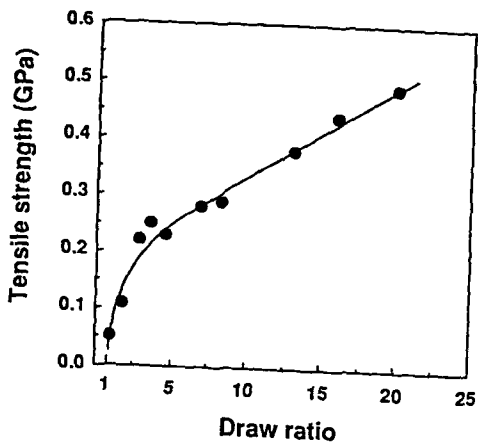


Figure 4:  
Relationship between draw ratio and tensile strength of PTV fibers.

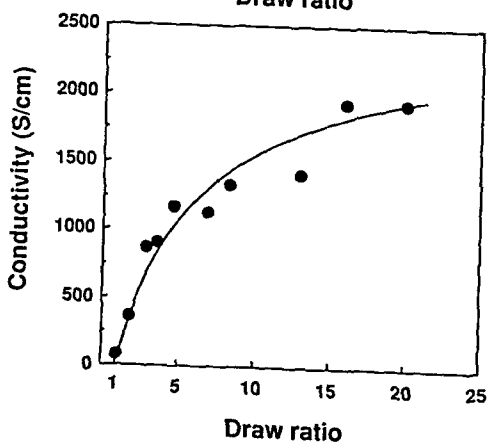


Figure 5:  
Relationship between draw ratio and conductivity of PTV fibers.

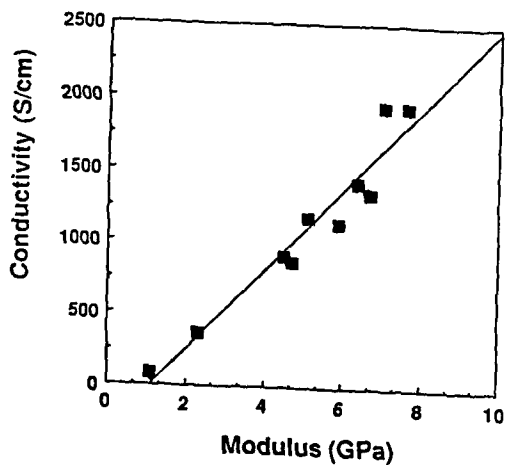


Figure 6:  
Correlation between modulus and conductivity of PTV fibers.

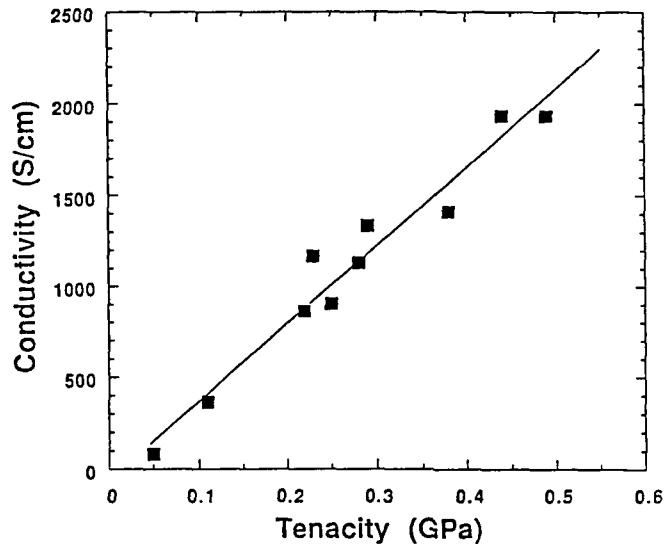


Figure 7: Correlation between tensile strength and conductivity for PTV fibers.

found to increase with the draw ratio; the maximum conductivity of 2000 S/cm was obtained at the maximum draw ratio. This value was 20 times higher than that of an undrawn fiber and comparable to that of an oriented film reported by Murase et al.<sup>10</sup> The relationship between the conductivity and the draw ratio was similar to that for the modulus and tensile strength (and draw ratio), indicating a strong correlation between conductivity and the mechanical properties.

This correlation between the structural dependence (as induced by the draw ratio) of the mechanical and electrical properties are illustrated more clearly by Figures 6 and 7, where the conductivity of drawn/converted PTV samples is plotted against, respectively, the modulus and the tensile strength. In both cases, an essentially linear relationship is found.

The many complex molecular processes that simultaneously occur in the drawing/conversion process need to be carefully optimized so that their time scales are in harmony. The critical parameters for process optimization are the degree of pre-conversion, deformation rate, process-temperature profile, conversion-catalyst concentration, and residence time. Obviously, in this initial study of PTV, we have not developed a fully balanced set of processing parameters. This is illustrated by the modest orientation indicated by the X-ray patterns.<sup>16</sup> Nevertheless, the current materials have a Young's modulus of 7 GPa, a tenacity of 0.5 GPa and a conductivity of 2000 S/cm; a combination of properties which are adequate for conductive textile applications. It should be clear that further optimization of the inter-related processing variables will undoubtedly result in materials of superior quality.



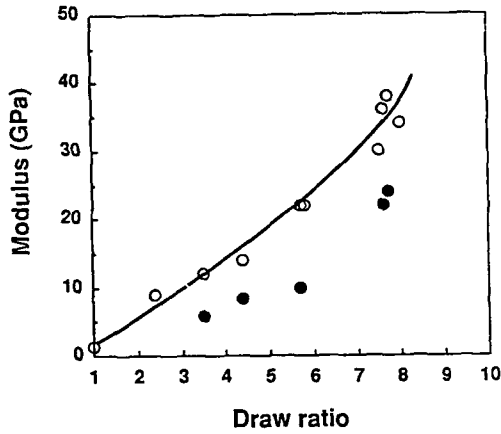


Figure 8:  
Young's modulus as a function of the draw ratio for PDMPV fiber (open circles) and for PDMPV fiber doped with iodine (closed circles).

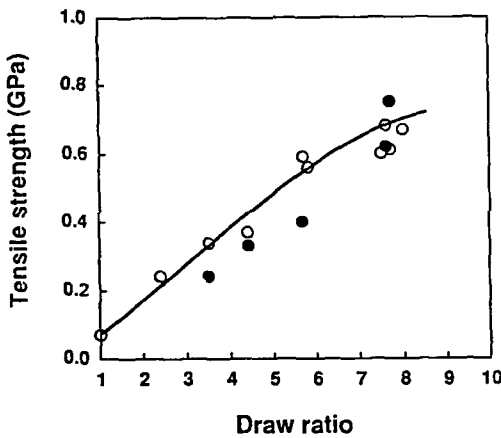


Figure 9:  
Tensile strengths as a function of the draw ratio for PDMPV fiber (open circles) and for PDMPV fiber doped with iodine (closed circles).

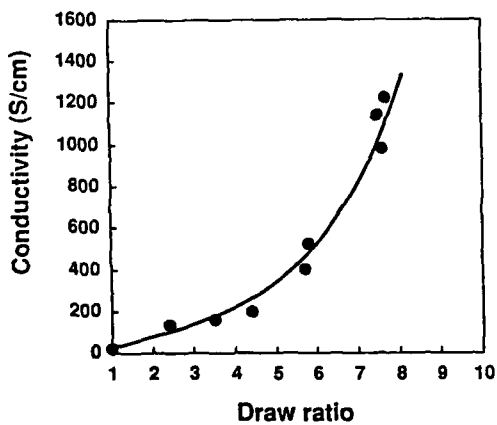


Figure 10:  
Electrical conductivity as a function of the draw ratio of PDMPV fiber.

### C. PDMPV<sup>16</sup>

The Young's modulus and the tensile strength of PDMPV fibers are shown versus draw ratio in Figures 8 and 9. The undrawn PDMPV fiber exhibited relatively poor mechanical properties: the modulus and tensile strength were 1.3 GPa and 0.07 GPa, respectively. Figures 8 and 9 reveal that fibers which had been drawn to 8 times their initial length had a Young's modulus as high as 35 GPa and a tensile strength of 0.7 GPa. The effects of doping on the mechanical strength are also displayed (filled circles in Figures 8 and 9). The data presented on these graphs indicate that doping caused only a moderate reduction of the modulus and essentially no loss of tensile strength.

Figure 10 shows the conductivity plotted against draw ratio. The undrawn PDMPV fiber exhibited a conductivity of 20 S/cm, with a gradual increase of conductivity seen up to a draw ratio of 5. At draw ratios greater than 5, the conductivity increased dramatically, as reported for stretched films<sup>15</sup> (although different in detail, since in ref. 15 the unstretched films were already about 30% converted). At a draw ratio of 8, the conductivity was 1200 S/cm, 60 times higher than that of the undrawn material.

Figures 11 and 12 show the relationship between Young's modulus and electrical conductivity (Figure 11) and between the tensile strength and electrical conductivity (Figure 12) for drawn PDMPV fibers. In both cases, a strong correlation is observed.

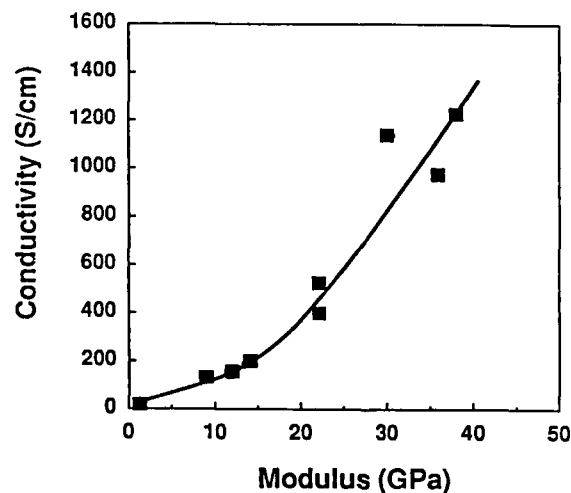


Figure 11: Electrical conductivity as a function of Young's modulus for PDMPV fiber.

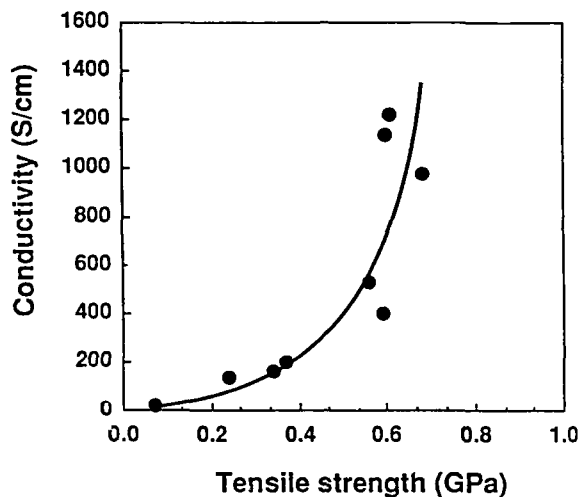


Figure 12: Electrical conductivity as a function of the tensile strength for PDMPV fiber.

#### IV. DISCUSSION

Although the electrical conductivity of conducting polymers is enabled by intra-chain transport, in order to avoid the localization inherent to one-dimensional systems, one must have the possibility of interchain charge transfer.<sup>1,3</sup> The electrical transport becomes essentially three-dimensional (and thereby truly metallic) so long as there is a high probability that an electron will have diffused to a neighboring chain between defects on a single chain. For well-ordered crystalline material in which the chains have precise phase order, the interchain diffusion is a coherent process. In this case, the condition for extended transport is that<sup>1,3</sup>

$$L/a \gg (t_0/t_{3d}) \quad (2)$$

where  $L$  is the coherence length,  $a$  is the chain repeat unit length,  $t_0$  is the intra-chain  $\pi$ -electron transfer integral, and  $t_{3d}$  is the inter-chain  $\pi$ -electron transfer integral. An analogous argument can be constructed for achieving the intrinsic strength of a polymer. If  $E_0$  is the energy required to break the covalent main-chain bond and  $E_{3d}$  is the weaker interchain bonding energy (from Van der Waals forces and hydrogen bonding for saturated polymers), then the requirement is coherence over a length  $L$  such that<sup>2,3</sup>

$$L/a \gg E_0/E_{3d} \quad (3)$$

In this limit the large number ( $L/a$ ) of weak interchain bonds add coherently such that the polymer fails by breaking the covalent bond. The direct analogy between

equations 2 and 3 is clearly evident. In fact, for conjugated polymers,  $E_0$  results from a combination of  $\sigma$  and  $\pi$  bonds (the latter being equal to  $t_0$ , see eqn. 2) and  $E_{3d}$  is dominated by the interchain transfer integral,  $t_{3d}$ . Thus, equations 2 and 3 predict that quite generally the conductivity and the mechanical properties will improve in a correlated manner as the degree of chain alignment is increased, with each approaching intrinsic values when the inequalities of equations 2 and 3 are satisfied. These predictions are in general agreement with the data obtained from PTV and PDMPV as shown in Figures 6, 7, 11, and 12. In both PTV and PDMPV, a strong correlation is observed, suggesting that major improvements in electrical conductivity can be anticipated as the materials are further improved such that the mechanical properties approach their intrinsic values. However, until a more quantitative understanding of the implied relationships is attained, extrapolation to the intrinsic electrical conductivity is not possible.

## V. CONCLUSIONS

We have demonstrated that blend fibers of polyaniline and poly (p-phenylene terephthalamide) can be derived from solutions in concentrated sulfuric acid. A minor amount of PPTA significantly improved the mechanical properties of PANI fibers while retaining the conductivity of pure polyaniline. These results indicate, therefore, that processing PANI/PPTA from concentrated sulfuric acid represents a viable method for producing polyblend fibers with mechanical properties in the textile range and with moderate levels of electrical conductivity. In this study, the concentration of PPTA was below the onset of the formation of the lyotropic phase; we anticipate that results obtained with lyotropic systems will exhibit improved properties.

Oriented PDMPV fibers exhibited excellent mechanical properties (modulus and strength were 35 GPa and 0.7 GPa, respectively) and high electrical conductivity ( $\sigma \approx 1200$  S/cm after iodine doping). The mechanical properties were retained after doping; the modulus only decreased to 25 GPa, and the tensile strength remained essentially unchanged. In the case of PTV, orientation of fibers resulted in both improved mechanical properties and high conductivity; the current materials have a Young's modulus of 7 GPa, a tenacity of 0.5 GPa and a conductivity of 2000 S/cm.

We have shown that the modulus and tensile strength derive from a combination of the intra-chain interactions (e.g. strength of chemical bonding, chain conformation, etc.) and inter-chain interaction (e.g. van der Waals forces, interchain transfer interactions, chain conformation, etc.). In conjugated polymers, these same features (band conduction within a polymer chain and efficient electron transfer between polymer chains) determine the carrier mean free path, and thus, the electrical conductivity. Therefore, we conclude that the mechanical and electrical properties of conjugated polymers are intrinsically linked, and we anticipate that in general as the tensile strength (and/or modulus) improve with improved chain orientation, the electrical conductivity will show corresponding improvements until both approach their respective intrinsic theoretical values.

**Acknowledgement:** The research on PDMPV and on PTV was supported by the office of Naval Research (N00014-83-K-0450). The synthesis of the polyaniline used in this study was funded through a MRG grant from the National Science

Foundation (NSF-DMR87-03399). The polyblend fiber spinning and the mechanical and electrical measurements were supported jointly by DARPA-AFOSR and monitored by AFOSR under contract no. F49620-88-C-0138.

References:

1. S. Kivelson and A.J. Heeger, *Synth. Met.* **22**, 37 (1988).
2. Y. Termonia and P. Smith, in "The Path to High Modulus Polymers with Stiff and Flexible Chains", edited by A.E. Zachariades and R.S. Porter (Marcel Dekker, New York, 1988) p. 321.
3. A.J. Heeger, *Faraday Discuss. Chem. Soc.* **88**, 1 (1989).
4. a. K.Y. Jen, R. Oboodi and R. Elsenbaumer, *Polym. Materials: Sci. Eng.* **53**, 79 (1985).  
 b. M.J. Nowak, S.D.D. Rughooputh, S. Hotta, and A.J. Heeger, *Macromolecules*, **20**, 212 (1987).  
 c. S.D.D. Rughooputh, S. Hotta, A.J. Heeger and F. Wudl, *J. Polym. Sci., Polym. Phys. Ed.* **25**, 1071 (1987).  
 d. M.J. Nowak, D. Spiegel, S. Hotta, A.J. Heeger and P. Pincus, *Macromolecules*, **22**, 2917 (1989).  
 e. M. Sato, S. Tanaka and K. Kaeniyama, *J. Chem. Soc. Chem. Commun.*, **295**, 873 (1986).
5. J.H. Edwards and W.J. Feast, *Polym. Commun.*, **21**, 595 (1980).
6. a. D.R. Gagnon, J.D. Capistran, F.E. Karasz and R.W. Lenz, *Polym. Bull.*, **12**, 93 (1984).  
 b. I. Murase, T. Ohnishi and M. Hirooka, *Polym. Commun.*, **25**, 327 (1984).
7. T. Momii, S. Tokito, T. Tsutsui and S. Saito, *Chem. Lett.*, 1201 (1988).
8. S. Yamada, S. Tokito, T. Tsutsui and S. Saito, *J. Chem. Sci., Chem. Commun.*, 1448 (1987).
9. S. Tokito, H. Murata, T. Tsutsui and S. Saito, *Polymer*, to be published (1989).
10. I. Murase, T. Ohnishi, T. Taniguchi and M. Hirooka, *Polym. Commun.*, **28**, 229 (1987).
11. A. Andreatta, Y. Cao, J.C. Chiang, A.J. Heeger and P. Smith, *Synth. Met.*, **26**, 383 (1988).
12. Y. Cao, A. Andreatta, A.J. Heeger and P. Smith, *Polymer*, (in press), (1989).
13. A. Andreatta, A.J. Heeger and P. Smith, *Polym. Commun.*, (in press), (1989).
14. H. Blades, U. S. Pat. 3,767,756 (1973), 3,869,429 (1975), 3,869,430 (1975).
15. M. Lewin and J. Preston, ed., *Handbook of Fiber Science and Technology*, (Marcel Dekker, Inc., New York, NY, 1985), Vol III, part A, chapter 9.
16. S. Tokito, P. Smith and A.J. Heeger, *Polymer* (in press).
17. S. Tokito, P. Smith and A.J. Heeger, *Synth. Met.* (in press).
18. R. Zallen, *The Physics of Amorphous Solids*, (John Wiley, New York, 1983), Ch.4.
19. S. Hotta, S.D.D.V. Rughooputh and A.J. Heeger, *Synth. Met.* **22**, 79 (1987).
20. I. Balberg, C.H. Anderson, S. Alexander and N. Wagner, *Phys. Rev. B* **30**, 3933 (1984).
21. a. M. Sinclair, K.C. Lim and A.J. Heeger, *Phys. Rev. Lett.* **53**, 3933 (1985).  
 b. A. Kapitulnik, K.C. Lim, S.A. Casalnuovo and A.J. Heeger, *Macromolecules*, **19**, 676 (1986).
22. J.M. Machado and F.E. Karasz, *Polym. Preprints*, **30**, 154 (1989).
23. K. Akagi, M. Suezaki, H. Shirakawa, H. Kyotani, M. Shimomura and Y. Tanabe, *Synthetic Metals*, **28**, D1 (1989).

## THE POLYANILINES: A NOVEL CLASS OF CONDUCTING POLYMERS

ALAN G. MACDIARMID\* AND ARTHUR J. EPSTEIN\*\*

\*Department of Chemistry, University of Pennsylvania, Philadelphia, PA 19104-6323

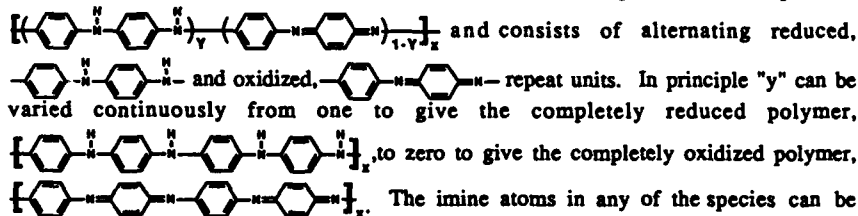
\*\*Department of Physics and Department of Chemistry, The Ohio State University, Columbus, Ohio 43210-1106

### ABSTRACT.

The synthesis of polyaniline in its fully oxidized, fully reduced and selected average intermediate oxidation states is described together with the synthesis of a self-protonic acid doped polyaniline. The processing of polyaniline films and fibers by thermal stretching to give conductivities up to ~100 S/cm is reported. Both doped and undoped polyaniline fibers have tensile strengths approaching those of commercial polymers.

### INTRODUCTION

The term "polyaniline" as commonly employed today [1,2] refers to a class of polymers consisting of up to 1,000 or more (ring-N-) repeat units which can be considered as being derived from a polymer, the base form of which has the generalized composition



protonated in whole or in part to give the corresponding salts, the degree of protonation of the polymeric base depending on its oxidation state and on the pH of the aqueous acid.

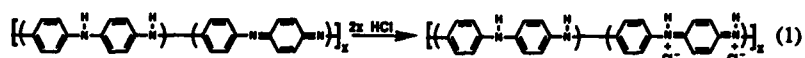
The terms "leucoemeraldine", "emeraldine" and "pernigraniline", used in the following discussion will refer to the different oxidation states of the polymer where  $y = 1, 0.5$  and  $0$  respectively, either in the base form, e.g. emeraldine base or in the protonated salt form, e.g. emeraldine hydrochloride [1,2]. It seems highly likely that the true average emeraldine oxidation state where  $y$  is exactly equal to  $0.5$  may never have been synthesized from aniline. The term "emeraldine" in the following discussion will therefore refer to an average oxidation state where  $y$  is approximately equal to  $0.5$  in the generalized formula of the polyaniline bases given above.

### SYNTHESIS OF POLYANILINE IN THE EMERALDINE OXIDATION STATE

The partly protonated emeraldine hydrochloride salt can be synthesized easily as a partly crystalline black-green precipitate (dark green by transmitted light) by the oxidative polymerization of aniline,  $(\text{C}_6\text{H}_5)\text{NH}_2$ , in aqueous acid media by a variety of oxidizing agents, the most commonly used being ammonium peroxydisulfate,  $(\text{NH}_4)_2\text{S}_2\text{O}_8$ , in aqueous HCl [1,3]. As noted in a later section, we have recently shown that the pernigraniline oxidation state

is first formed and that this is subsequently converted to the emeraldine oxidation state. It can be deprotonated by aqueous ammonium hydroxide to give an essentially amorphous black-blue (dark blue by transmitted light) "as-synthesized" emeraldine base powder with a coppery, metallic glint having an average oxidation state corresponding approximately to that of the ideal emeraldine oxidation state. The  $^{13}\text{C}$  [4] and  $^{15}\text{N}$  NMR [5,6] spectra of emeraldine base are consistent with its being composed principally of alternating oxidized and reduced reduced repeat units.

The emeraldine base form of polyaniline was the first well established example [1,7-9] of the "doping" of an organic polymer to a highly conducting regime by a process in which the number of electrons associated with the polymer remain unchanged during the doping process. This is accomplished by treating emeraldine base with aqueous protonic acids and is accompanied by a 9 to 10 order of magnitude increase in conductivity (to 1 - 5 S/cm; compressed powder pellet) reaching a maximum in ~ 1M aqueous HCl with the formation of the fully protonated emeraldine hydrochloride salt, viz.,



If the fully protonated i.e. ~50% protonated emeraldine base should have the above dication i.e. bipolaron constitution as shown in equation 1, it would be diamagnetic. However, extensive early magnetic studies [10] show that it is strongly paramagnetic and that its Pauli (temperature independent) magnetic susceptibility increases linearly with the extent of protonation. These observations and other earlier studies [7-9] show that the protonated polymer is a polysemiquinone radical cation, one resonance form consisting

of two separated polarons being  $\left[ \left( \text{C}_6\text{H}_4 \right)_n \left( \text{C}_6\text{H}_4 \right)_m \right]_x^{\cdot+}$ . It can be seen from the alternative resonance form where the charge and spin are placed on the other set of nitrogen atoms that the overall structure is expected to have extensive spin and charge delocalization.

Emeraldine hydrochloride may also be deposited by "in-situ adsorption polymerization" in a few minutes as strongly adhering films on a variety of substrates such as natural and synthetic fibers and textiles, [11] plastic, glass, silver chloride pellets etc. [12] by immersing the substrate in a freshly mixed acidic aqueous solution of aniline and oxidizing agent such as ammonium peroxydisulfate. As noted in a later section, the pernigraniline oxidation state is first formed and is then converted to the emeraldine oxidation state. It is believed that a reactive intermediate, possibly an oligomeric radical cation of aniline is first adsorbed which subsequently polymerizes [11]. The emeraldine hydrochloride films are deprotonated instantly by ammonium hydroxide to give corresponding films of the emeraldine base. Such films, because they react so rapidly with a variety of reagents and because their electronic and IR spectra can be easily obtained, are useful in rapidly screening reactions of the polymer.

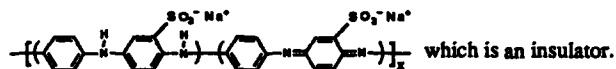
#### SELF-PROTONIC ACID DOPED POLYANILINE

It is well known that other strong protonic acids such as  $\text{R-SO}_3\text{H}$  ( $\text{R}$ = organic group) besides HCl dope polyaniline according to equation 1. It has recently been found [13] that emeraldine base reacts with fuming  $\text{H}_2\text{SO}_4$ . A hydrogen atom on the ( $\text{C}_6\text{H}_4$ ) rings is replaced by a  $-\text{SO}_3\text{H}$  group thus making  $\text{R}=(\text{polyaniline chains})$ . The proton from the  $\text{SO}_3\text{H}$  groups then protonates the  $-\text{N}=\text{N}-$  groups resulting in a "self-doped" polymer ( $\sigma \sim 0.1 \text{ S/cm}$ ; 4-probe, compressed pellet) in which the protonic acid (dopant) is part of the polymer itself,

viz.,  $\left[ \left( \text{C}_6\text{H}_3(\text{SO}_3^-) \right)_n \left( \text{C}_6\text{H}_4 \right)_m \right]_x^+$ . This polymer differs remarkably from conventionally protonated emeraldine base in that its conductivity remains unchanged when

equilibrated with aqueous acid in the pH range 0 to 7. Emeraldine hydrochloride for example is essentially deprotonated even at pH 4-5 where its conductivity is very small; at pH 7 it is an insulator. The concentration of the  $-\text{SO}_3^-$  group and hence of the protons in the "volume" of a chain is  $\sim 1-10$  molar. This is 8-9 orders of magnitude higher than the proton concentration of a neutral aqueous solution of pH = 7 with which, for example, it could be in equilibrium. This "enhanced proton concentration effect" is responsible for the high conductivity even when the polymer is in equilibrium with a mildly acid or neutral solution.

When treated with, for example, aqueous NaOH solution, the polymer readily dissolves forming the corresponding sodium salt,



## LEUCOEMERALDINE AND PERNIGRANILINE OXIDATION STATES

### Synthesis

Leucoemeraldine, the completely reduced form of polyaniline,

$\left[ \text{C}_6\text{H}_4\text{NH}(\text{C}_6\text{H}_4\text{NH})_2\text{C}_6\text{H}_4 \right]_x$ , was first synthesized in 1910 [14,15]. It can be conveniently prepared as an analytically pure, off-white powder by the reduction of emeraldine base, [14,15] the most commonly used reducing agents being phenyl hydrazine or hydrazine [16]. Similarly to emeraldine base, free-standing films can be cast from NMP solutions [16].

Pure pernigraniline, the completely oxidized form of polyaniline,

$\left[ \text{C}_6\text{H}_4\text{N}^+(\text{C}_6\text{H}_4\text{N}^+) \right]_x$ , has recently been synthesized for the first time [17]. It was reported in 1910 [14,15] to be formed in an impure state by the oxidation of emeraldine base but that it was unstable and rapidly decomposed, especially when wet. Synthesis of the analytically pure dark purple, partially crystalline powder has been accomplished by the controlled oxidation of emeraldine base with  $m\text{-Cl}(\text{C}_6\text{H}_4)\text{C}(\text{O})\text{OOH}/\text{N}(\text{C}_2\text{H}_5)_3$  in NMP containing a trace of  $\text{CrCl}_3$ . Free-standing, lustrous, copper-colored films can be cast from this solution and subsequently leached in a methanol/acetone mixture to remove excess oxidizing agent.

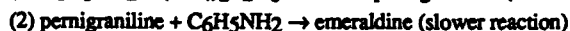
We have found recently that polyaniline in the pernigraniline oxidation state is the first formed product in the common method of synthesizing the emeraldine oxidation state involving the oxidative polymerization of aniline by acidic (HCl) aqueous  $(\text{NH}_4)_2\text{S}_2\text{O}_8$  [12]. This is the case both for the *in-situ* deposition of polyaniline as thin films on substrates as described in a previous section and for the synthesis of the polymer as a bulk powder.

When the synthesis is carried out at  $\sim 0^\circ\text{C}$  using excess aniline [1,2] the initial oxidation potential of the reaction system increases from  $\sim 0.66\text{V}$  (vs. SCE) immediately after mixing the reactants to  $\sim 0.75\text{V}$  after  $\sim 3$  minutes where it stays essentially constant for approximately 6 minutes whereupon it decreases rapidly to  $\sim 0.45\text{V}$ , a potential characteristic of the emeraldine oxidation state [18] in this medium during the next  $\sim 10$  minutes. The temperature increases noticeably during this latter period. The above times and potentials are, of course, dependant on the temperature at which the reaction is studied. Treatment of the *in-situ* deposited films when the potential of the system is  $\sim 0.75\text{V}$  with aqueous alkali gives electronic and I/R spectra characteristic of pernigraniline base. If the reaction mixture at this potential is poured into aqueous NaOH solution, pernigraniline base powder is obtained as confirmed by spectroscopic studies.

Our working hypothesis at the present time to rationalize the above observations is as follows: The potential at which aniline commences to undergo electrochemical oxidation in



aqueous acid is  $-0.7V$  (vs. SCE) [19]. The potential of the  $-0.05M$  solution of  $(NH_4)_2S_2O_8$  in  $1M$  aqueous  $HCl$  before adding aniline is  $-1.05V$  and that of pernigraniline and emeraldine bases in  $1M$   $HCl$  are  $0.83V$  [20] and  $0.43V$  [18] respectively. It therefore appears not unreasonable that the  $[(NH_4)_2S_2O_8 + HCl]$  system employed might be expected to produce, at least initially, polyaniline in its highest oxidation state i.e., the pernigraniline oxidation state. Furthermore, it seems highly likely that pernigraniline, if formed in the presence of excess aniline, would oxidatively polymerize the aniline to the emeraldine oxidation state while it, itself was reduced and also converted to the emeraldine oxidation state. If this should be the case, then the final polymer product having the emeraldine oxidation state would be formed under the experimental conditions employed by two different mechanisms:



Thus part of the final polymer formed in the emeraldine oxidation state would come from the pernigraniline state which had undergone reduction in step 2 and part would come from the aniline which had been polymerized in step 2. This is qualitatively consistent with the observed bimodal molecular weight distribution curve [21,22] for emeraldine base synthesized in the usual way. The presence of a bimodal molecular weight distribution curve in a polymer suggests that the polymer may have been formed by two different reaction pathways.

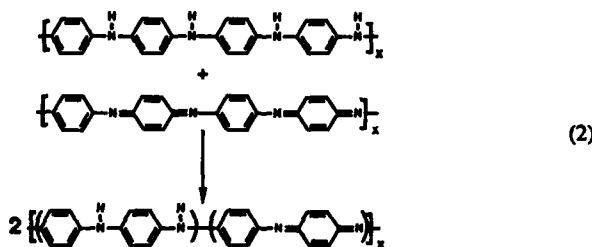
The above conclusions are consistent with the observation that when a film of pernigraniline polymer formed by *in-situ* polymerization on conducting glass was placed in a fresh solution of aniline in  $1M$  aqueous  $HCl$  that its potential fell within  $\sim 2$  minutes to  $-0.43V$ , characteristic of the emeraldine oxidation state, consistent with step 2 above. The electronic spectrum of the resulting film was identical to that of emeraldine.  $HCl$ .

In summary, experimental evidence at the present time strongly suggests that aniline undergoes oxidative polymerization in the commonly used  $[(NH_4)_2S_2O_8 + HCl]$  medium to give at first polyaniline in its highest (pernigraniline) oxidation state and that as the concentration of the oxidizing agent,  $(NH_4)_2S_2O_8$  is decreased by the reaction occurring in step 1, the polymer in the pernigraniline oxidation state then reacts more extensively with the excess aniline according to step 2.

The fact that the two extreme members of polyaniline bases - the completely reduced and completely oxidized - have been synthesized should now make it easier to interpret future systematic studies of intermediate members of the series.

#### Reaction of Leucoemeraldine with Pernigraniline

It has recently been observed [23] that the completely reduced base form of polyaniline, (leucoemeraldine), spontaneously reduces, and is itself oxidized, when its solution in NMP is mixed with an NMP solution of the completely oxidized base form of polyaniline, (pernigraniline). The reaction which occurs when equimolar solutions are mixed is given by equation 2.



Under the experimental conditions employed, equilibrium appears to be attained at room temperature in ~14 hours. The electronic spectra of a solution of pure leucoemeraldine and of mixtures of leucoemeraldine and pernigraniline at various molar ratios in NMP were examined after ~14 hours. They are shown in Figure 1.

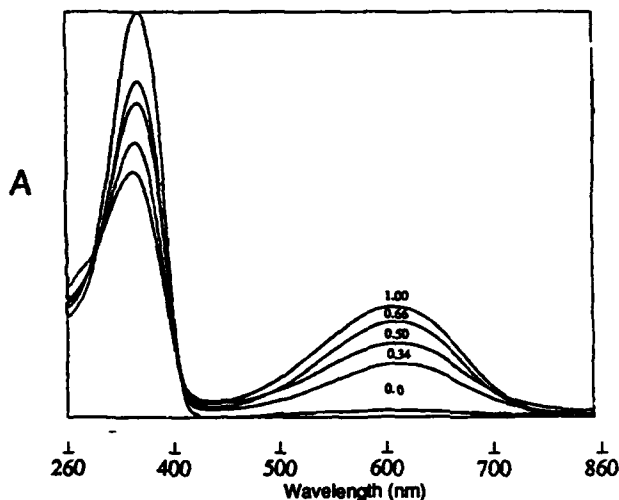


Figure 1 - Electronic spectra (A = absorbance) of leucoemeraldine and pernigraniline in NMP in molar ratios (pernigraniline/leucoemeraldine) of: 0.34; 0.50; 0.66 and 1.00 after ~14 hours. (0.0 = pure leucoemeraldine).

It can be noted that a peak at ~633nm (1.96eV) grows continually with increasing concentration of pernigraniline. This peak is virtually absent in pure leucoemeraldine base. The peak at 343nm (3.61eV) characteristic of leucoemeraldine base decreases with increasing concentration while at the same time an absorption at 327nm (3.79eV) characteristic of emeraldine base begins to appear. The spectrum containing the equilibrated mixture of a 1:1 initial ratio of leucoemeraldine and pernigraniline bases is identical to that of pure emeraldine base in NMP. A set of two isosbestic points is observed at the two points where the spectra of leucoemeraldine base and emeraldine base cross each other. The invariant position of the 633 nm absorptions in all spectra and the isosbestic point set can be interpreted at the present time in one or the other of the two different ways outlined below: (1) no evidence is obtained for the formation of discrete electronic states in NMP solution, such as the postulated [14,15] protoemeraldine ( $\gamma = 0.75$ ) oxidation state, intermediate between the leucoemeraldine and emeraldine oxidation states. This leads to the conclusion that leucoemeraldine base is converted in one step, involving no intermediate species, to emeraldine base, i.e. the system consists of a physical mixture of leucoemeraldine base and emeraldine base molecules or of long segments of leucoemeraldine and emeraldine bases in the same molecule. This is qualitatively consistent with cyclic voltammetry/spectroscopic studies of oligomers and of *solid* polyaniline which suggest that polyaniline may exist locally in only three discrete oxidation states although the average oxidation state of the bulk polymer may be intermediate between them, [24] or (2) the 633nm peak is characteristic of a chromophore associated with one oxidized repeat unit surrounded on each side by a reduced repeat unit, e.g.

$\text{---}[\text{C}_6\text{H}_4\text{---NH---C}_6\text{H}_4\text{---NH}]_x\text{---}[\text{C}_6\text{H}_4\text{---N}^+\text{---C}_6\text{H}_4\text{---N}^+]_y\text{---}$  whose concentration increases as the molar ratio of pernigraniline is increased. Emeraldine base, which contains this

chromophore, would of necessity have this peak in its absorption spectrum but it would not be uniquely characteristic of emeraldine base but instead would be common to a continuous series of *average* oxidation states of polyaniline bases ranging from oxidation states greater than leucoemeraldine base to, and including emeraldine base. Preliminary studies of average oxidation states intermediate between emeraldine and pernigraniline bases suggest that as the number of oxidized repeat units increase past the emeraldine oxidation state that they begin to interact giving rise to a continuum of different electronic states.

## STRUCTURAL MODIFICATION BY PROCESSING

"As-synthesized" emeraldine base is soluble in N-methyl pyrrolidinone, NMP [25], and in concentrated H<sub>2</sub>SO<sub>4</sub> [14,15,26]. However, the term "soluble" must be used with caution since it is not clear how much of the polymer in, for example, a viscous ~20 weight % NMP "solution", is in "true" solution. It has been known for some time that emeraldine base is readily solution-processible [25,27] and that it may be cast as free-standing, flexible, coppery-colored films from its solutions in NMP. These films can be doped with ~1M aqueous HCl to give the corresponding flexible, lustrous purple-blue films ( $\sigma \sim 1-4 S/cm$ ) of emeraldine hydrochloride [25].

Exhaustive extraction at room temperature under nitrogen of "as-synthesized" essentially amorphous emeraldine base, first with tetrahydrofuran, THF, then with NMP results in the removal of ~20 weight% of oligomeric material and impurities [21,28,29]. The resulting "processed" emeraldine base powder has an excellent elemental analysis, and is up to ~50% crystalline (orthorhombic) [30,31]. It is insoluble in NMP and in concentrated sulfuric acid under the same experimental conditions in which the "as-synthesized" emeraldine base powder is "soluble" in these solvents. Increased crystallinity, not unexpectedly, tends to result in decreased solubility.

It is interesting to note that the above partly crystalline emeraldine base powder can be repeatedly interconverted to its amorphous form, and then back to its crystalline form. For example, protonation with HCl to give the corresponding emeraldine hydrochloride ( $\sigma \sim 18 S/cm$ ; 4-probe compressed pellet) followed by deprotonation with NH<sub>4</sub>OH results in the amorphous form. Treatment of this amorphous form with THF, in which it is essentially insoluble results in some solvation of the polymer giving it sufficient mobility to rearrange at least in part back to the more thermodynamically stable, partly crystalline form.

A solution of the amorphous "processed" emeraldine base in NMP exhibits a bimodal molecular weight distribution (by g.p.c.; polystyrene standard), the maximum molecular weight fraction corresponding to approximately 325,000 [21,29]. Lower molecular weights in concentrated H<sub>2</sub>SO<sub>4</sub> solution of emeraldine base synthesized in a slightly different manner have also been reported [26]. Partly crystalline films of the insoluble protonated polymer are formed when thin layers of these concentrated H<sub>2</sub>SO<sub>4</sub> solutions are exposed to air [26].

## Oriented Films

Oriented, partly crystalline emeraldine base films are obtained by simultaneous heat treatment and stretching of films formed from "as-synthesized" emeraldine base containing a plasticizer such as NMP [32,33]. Samples are observed to elongate by up to 400% when held above the glass transition temperature [ $\geq 110^\circ C$ ] [32,33]. The resulting films have an anisotropic x-ray diffraction and optical response, with a misorientation of only a few degrees [31]. Oriented polyaniline may also be obtained by evaporating (in the present of a heat lamp) a

solution of emeraldine base in NMP on polyethylene, polyacetylene or other substrates while the substrate is being mechanically stretched [34].

### Oriented Fibers

Fibers of emeraldine base can be formed by drawing a ~20 weight % "solution" of any form of amorphous emeraldine base in NMP in a water/NMP solution [28]. They can be thermally stretch oriented up to 400% in a similar manner to emeraldine base films [28]. X-ray diffraction studies show directional enhancement of the Debye-Scherrer rings. They differ from the oriented, partly crystalline fibers prepared from solutions of emeraldine base in concentrated sulfuric acid [26] by coagulation in water in that they consist of undoped polymer. Doping with 1M aqueous HCl results in a significant increase in the conductivity parallel to the direction of stretching (to 40 - 170 S/cm; Av. 85 S/cm) [28] similar to that observed with fibers formed from concentrated H<sub>2</sub>SO<sub>4</sub> solution [26]. If desired, the emeraldine base "solution" in NMP may also be drawn in aqueous HCl which results in direct formation of the doped fiber.

The thermally stretch oriented base fibers have tensile strengths [366(best), 318 (av.)MPa; initial modulus, 8.6 (best), 8.1 (av.)GPa; 1 inch gauge length] which falls within the lower limit of the tensile strengths of commercial fibers (tensile strengths: Nylon 6, 200-905; Nylon 66, 231-985; polyesters, 236--1,165 MPa). Doping of such fibers with 1M HCl reduces the tensile strength somewhat [176 (best), 150 (av.) MPa; initial modulus, 5.0 (best), 4.6 (av.) GPa]. This is possibly caused by the somewhat reduced degree of observed crystallinity [28]. These early results suggest that further work will result in tensile strengths of the doped polymer at least equal to that of commercial fibers.

### CONCLUSIONS

Although extensive advances have been made during the last four years in obtaining an understanding of the fundamental electronic, magnetic, spectroscopic, transport and theory relating to this large and diverse area of conducting polymers it is apparent that the field has not yet been clearly delineated. The fact that aniline is a relatively inexpensive compound, that its polymerization can be readily accomplished by simple chemical procedures and that some of its conducting derivatives apparently exhibit good thermal and environmental stability strongly suggest it may have many good technological uses. The richness of the chemistry, electrochemistry, and physics of the polyanilines indicates they will continue to serve as a focus for challenging interdisciplinary research in the future.

### ACKNOWLEDGEMENTS

The authors wish to thank Messrs. P.B. Friese and S.K. Manohar in particular for their invaluable assistance in preparing the manuscript. Most of the work reported by the authors was supported by the Defense Advanced Research Projects Agency through a contract monitored by the Office of Naval Research.

### REFERENCES

1. J-C. Chiang and A.G. MacDiarmid, *Synth. Met.* **13**, 193 (1986).
2. A.G. MacDiarmid, J-C. Chiang, A.F. Richter, N.L.D. Somasiri and A.J. Epstein, Conducting Polymers, edited by L. Alcacer (Reidel Publications, Dordrecht, 1987).

3. J-C. Chiang, Ph.D. dissertation, University of Pennsylvania, (1987).
4. S. Kaplan, E.M. Conwell, A.F. Richter and A.G. MacDiarmid, *Synth. Met.* **29**, E235 (1989).
5. A.F. Richter, A. Ray, K.V. Ramanathan, S.K. Manohar, G.T. Furst, S.J. Opella, A.G. MacDiarmid and A.J. Epstein, *Synth. Met.* **29**, E243 (1989).
6. A. Ray, Ph.D. dissertation, University of Pennsylvania, (1989).
7. A.G. MacDiarmid, J-C. Chiang, A.F. Richter and A.J. Epstein, *Synth. Met.* **18**, 285 (1987).
8. P.M. McManus, S.C. Yang and R.J. Cushman, *J. Chem. Soc. Chem. Commun.* 1556 (1985).
9. G.E. Wnek, *Synth. Met.* **15**, 213 (1986).
10. A.J. Epstein, J.M. Ginder, F. Zuo, R.W. Bigelow, H.S. Woo, D.B. Tanner, A.F. Richter, W-S. Huang and A.G. MacDiarmid, *Synth. Met.* **18**, 303 (1987); J.M. Ginder, A.F. Richter, A.G. MacDiarmid and A.J. Epstein, *Solid State Commun.* **63**, 97 (1987).
11. R.V. Gregory, W.C. Kimbrell and H.H. Kuhn, *Synth. Met.* **28**, C-823 (1989).
12. S.K. Manohar, A.G. MacDiarmid and A.J. Epstein, *Bull. Am. Phys. Soc.* **34**, 582 (1989); S.K. Manohar, A.G. MacDiarmid and A.J. Epstein, 1989, unpublished observations.
13. J. Yue, A.J. Epstein and A.G. MacDiarmid, to be published (1989).
14. A.G. Green and A.E. Woodhead, *J. Chem. Soc. Trans.* **27**, 2388 (1910).
15. A.G. Green and A.E. Woodhead, *J. Chem. Soc. Trans.* **101**, 1117 (1912).
16. J. Masters, S.K. Manohar, A. Ray, A.G. MacDiarmid and A.J. Epstein, unpublished results; A. Ray Ph.D. dissertation, University of Pennsylvania, (1989).
17. Y. Sun, A.G. MacDiarmid and A.J. Epstein, unpublished observations, (1989).
18. W-S. Huang, A.G. MacDiarmid and A.J. Epstein, *J. Chem.Soc., Chem. Commun.*, **1784**, (1987).
19. W-S. Huang, B.D. Humphrey and A.G. MacDiarmid, *J. Chem. Soc. Faraday Trans. 1* **82**, 2385 (1986).
20. Y. Sun, A.G. MacDiarmid and A.J. Epstein, unpublished observations, (1989).
21. A.G. MacDiarmid, G.E. Asturias, D.L. Kershner, S.K. Manohar, A. Ray, E.M. Scherr, Y. Sun, X. Tang and A.J. Epstein, *Polymer Preprints* **30-1**, 147 (1989).
22. X. Tang, Y. Sun and Y. Wei, *Makromol. Chem., Rapid Commun.*, **829**, 9 (1988).
23. J.G. Masters, Y. Sun, A.G. MacDiarmid and A.J. Epstein, unpublished observations (1989).
24. L.W. Shacklette, J.F. Wolfe, S. Gould and R.H. Baughman, *J. Chem. Phys.* **88**, 3955 (1988).
25. M. Angelopoulos, G.E. Asturias, S.P. Ermer, A. Ray, E.M. Scherr, A.G. MacDiarmid, M. Akhtar, Z. Kiss and A.J. Epstein, *Mol. Cryst. Liq. Cryst.* **160**, 151 (1988).
26. A. Andreatta, Y. Cao, J-C. Chiang, A.J. Heeger and P. Smith, *Synth. Met.* **26**, 383 (1988).

27. M. Angelopoulos, A. Ray, A.G. MacDiarmid and A.J. Epstein, *Synth. Met.* **21**, 21 (1987).
28. X. Tang, E. Scherr, A.G. MacDiarmid and A.J. Epstein, *Bull. Am. Phys. Soc.* **34**, 583 (1989).
29. X. Tang, A.G. MacDiarmid, A.J. Epstein and Y. Wei, unpublished observations, (1989).
30. M.E. Jozefowicz, R. Laversanne, H.H.S. Javadi, A.J. Epstein, J.P. Pouget, X. Tang and A.G. MacDiarmid, *Phys. Rev. B, Rapid Commun.* **39**, 12958 (1989).
31. A.J. Epstein and A.G. MacDiarmid, Electronic Properties of Conjugated Polymer, editors H. Kuzmany, M. Mehring and S. Roth, Springer-Verlag, Berlin (1989) in press.
32. K.R. Cromack, M.E. Jozefowicz, J.M. Ginder, R.P. McCall, A.J. Epstein, E.M. Scherr and A.G. MacDiarmid, *Bull. Am. Phys. Soc.* **34**, 583 (1989).
33. E.M. Scherr, A.G. MacDiarmid and A.J. Epstein, unpublished observations, (1989).
34. N. Theophilou, A.G. MacDiarmid, D. Djurado, J.E. Fischer and A.J. Epstein, Electronic Properties of Conjugated Polymers, edited by H. Kuzmany, M. Mehring and S. Roth, Springer-Verlag, Berlin, (1989) in press.

## POLYANILINE: AN OLD POLYMER WITH NEW PHYSICS

A.J. EPSTEIN\* and A.G. MACDIARMID\*\*

\*The Ohio State University, Department of Physics and Department of Chemistry, Columbus, OH 43210-1106

\*\*University of Pennsylvania, Department of Chemistry, Philadelphia, PA 19104

### ABSTRACT

Polyanilines have been known for over one hundred years. Recent studies of this chemically flexible polymer have demonstrated unusual electronic phenomena in both the insulating forms and the conducting forms. Studies of both forms show that the origins of the electronic phenomena are substantially different than those observed in polyacetylene and related earlier studied conjugated carbon backbone polymers. Unusual aspects include the formation of massive polarons upon photoexcitation in the insulating forms. These polarons have unusual time dynamics associated with the roles of ring-flipping and ring-conformation in the polymer system. A new model for the effects of electron lattice coupling via ring rotation has been introduced. The "metallic" form of the polymer shows that the metallic state is associated with the ordered regions of the doped polymer. The roles of localization are important in leading to the formation of a textured, granular metal. At low temperatures for emeraldine salt, and at higher temperatures for derivatized polyanilines, localization is important. Potential new technologies based on the polyanilines, including optical information storage, controlled microwave absorption, and use of a self-protonating derivative that is soluble in aqueous media are noted.

### INTRODUCTION

The polyanilines differ substantially from earlier studied polyacetylene, polythiophene, polypyrrole, polydiacetylene and other recently studied electronic polymers [1, 2] in that their electronic structure is based on the overlap of alternating nitrogen atoms and C<sub>6</sub> rings [3-6], Fig. 1. The presence of the nitrogen atoms provides a degree of chemical flexibility absent in most other electronic polymers, the ability to add or remove protons and pseudoprotons at the nitrogen sites, in addition to the ability to oxidize or reduce the backbone polymer [7]. A schematic illustration of the idealized structure of the well-characterized limiting states of the polyaniline system are summarized in Fig. 1. Leucoemeraldine base (LEB), emeraldine base (EB), and pernigraniline base (PNB) are insulators while the emeraldine salt (ES) polymer is conducting. The conducting form can be achieved by oxidation of LEB, protonation of EB, or protonation and reduction of PNB. The ability to prepare these materials in oriented films [8] and fibers [9] and of known crystallinity and crystal structures [10] has advanced the quantitative studies of this field.

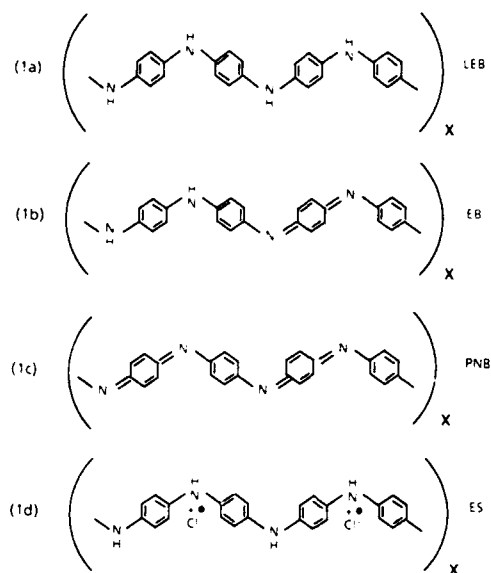
## ELECTRONIC STRUCTURE AND CHARGED DEFECT STATES

The electronic structure of the LEB form can be considered as derived from the overlap of the six  $C_6$  molecular orbitals and the nitrogen  $p_z$  orbital, resulting in seven energy bands [3-6]. As a result, the valence and conduction bands of the LEB form and also for the EB form are extremely asymmetric resulting in a loss of charge conjugation symmetry in this polymer. The energy bandwidths and absolute energies are sensitive to the overlap of the para carbon  $p_z$  orbitals with the adjacent nitrogen ( $p_z$ ) orbitals.

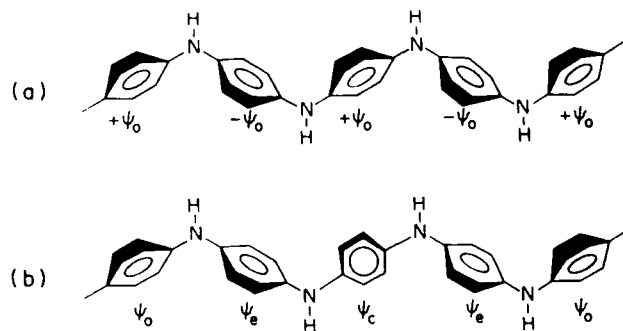
Extensive spectroscopic, photoinduced spectroscopic, and photoinduced electron spin resonance studies have been carried out for the insulating LEB, EB, and PNB polymers on time scales with time resolutions ranging from picoseconds through hours [11-18]. The results differ dramatically from the results of earlier similar studies for polyacetylene, polythiophene, etc. In particular, the oscillator strength for the photoinduced infrared active vibrations (IRAV) is much smaller than the oscillator strength for the photoinduced electronic transitions. Analysis leads to the conclusion that the photoinduced polarons are massive ( $m_p > 50-100 m_e$ ) [12].

For the simplest polyaniline, LEB, exposure of the sample to bandgap (3.6 eV) illumination leads to the formation of two photoinduced absorptions at 0.75 eV and 2.8 eV. A model has been developed to account for this behavior [5, 15]. The bandgap for LEB has its origin in the  $n-n^*$  gap of  $C_6$  and not in a Peierls distortion. Electron-lattice coupling is introduced via dependence on the ring torsion angle of the transfer integral between N-H and the ring sites. The lattice energy is then assumed to depend primarily on the steric interactions between adjacent phenyl rings. This differs substantially from the usual model of a Peierls gap originating from the effects of bondlength modulation on the electronic energy structure. A Hückel Hamiltonian has been used to gauge the important ramifications of the ring torsion angle and steric hindrance [5]. It is found that hole polarons are self-localized due to changes in local ring torsion angles, Fig. 2. This hole polaron has an electronic structure that corresponds to the photoinduced electronic transitions in LEB. In contrast, negative polarons are not expected to be strongly localized because of the weak coupling of the antibonding  $C_6$  orbitals to the nitrogen  $p_z$ . Both the  $P^+$  and  $P^-$  are modified by the presence of quinoid groups (as in partially oxidized leucoemeraldine or also in EB), Fig. 3. In particular, the quinoid acts as a trap for the  $P^-$  to form a  $P^-_q$ , while the  $P^+$  is also trapped at the quinoid for the  $P^+_{BQ}$ . Positive and negative charges may also be bound together to form excitons [19, 20] with negative charge centered at the quinoid group and positive charge distributed on neighboring benzenoids, Fig. 3. The temperature dependence of the relaxation times support that

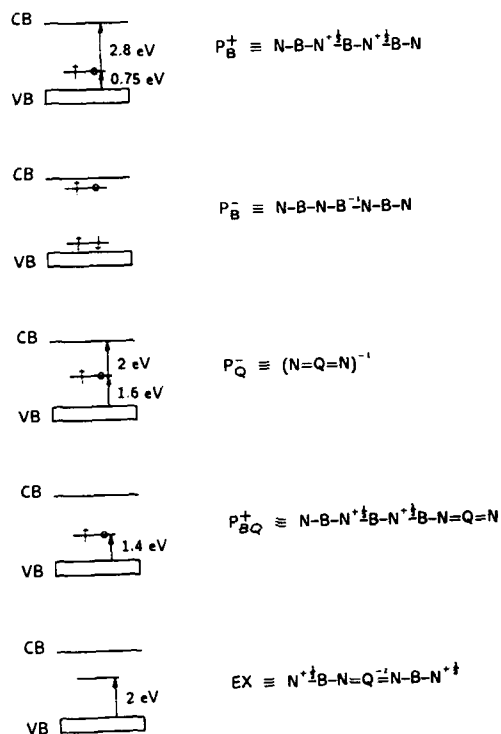




1. (a) Leucoemeraldine base (LEB or polyphenyleneamine); (b) emeraldine base (EB or polyphenyleneamineimine); (c) pernigraniline base (PB or polyphenyleneimine); (d) emeraldine salt (ES).



2. (a) Sketch of a segment of a leucoemeraldine base chain showing the phenyl rings rotated by  $\pm \psi_0$  out of the plane formed by nitrogens; (b) representation of a ring-rotational hole polaron in LB where the center phenyl ring and the end phenyl rings rotate toward the nitrogen plan to new ring angles  $\psi_c$  and  $\psi_e$  [Ref. 5].



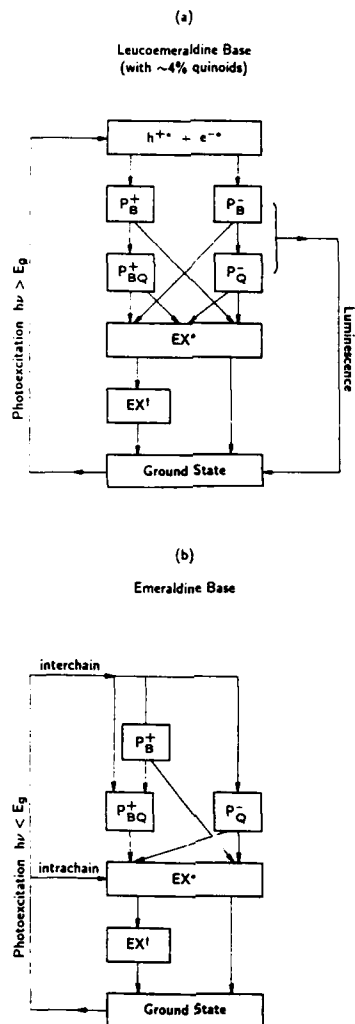
3. Schematic definition of defect states  $P_B^+$ ,  $P_B^-$ ,  $P_Q^-$ ,  $P_{BQ}^+$ , and EX with approximate energy level diagrams. B denotes a benzenoid ring, Q a quinoid ring, and N represents either an amine nitrogen (adjacent to B) or an imine nitrogen (adjacent to Q). Note that the charge distributions of the defects are expected to be more delocalized than those schematically shown here for simplicity. The splitting for  $P_B^-$  is expected to be no more than a few tenths of an electron-volt [Ref. 15].

these new electronic states involve changes in the ring torsion angles; there is then very slow relaxation of the photoexcited states back to the ground state. For low temperatures, a significant component of the photoinduced polarons are essentially permanent providing a novel means for optical information storage due to redistribution of the IR through UV oscillator strength upon exposure of the polymer to external light [21]. Figure 4 shows a schematic representation of the evolution of the photoinduced states for leucoemeraldine base with a small percentage of quinoid groups and also for the emeraldine base polymer [15].

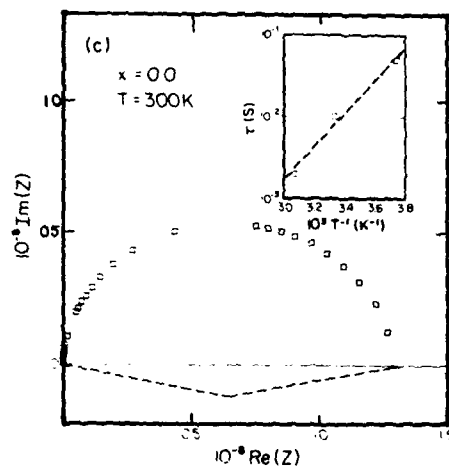
#### DOPING OF POLYANILINE

The emeraldine base polymer is insulating with conductivity  $\sim 10^{-10}$  S/cm. Extensive audio frequency conductivity and dielectric constant studies as a function of protonation at the low protonation level shows that the temperature dependent audio frequency ( $10^1 - 10^5$  Hz) conductivity varies as  $f^s$  with  $s \sim 0.9$  for  $x = [H^+]/[N] = 0$ , decreasing with increasing  $x$  [22]. For frequencies greater than  $10^3$  Hz the dielectric constant agrees with the  $T$  independent dielectric constant measured by microwave techniques. At lower frequencies and higher temperatures, dielectric constant increases. A Cole-Cole analysis shows the presence of primarily a single thermally activated relaxation process in these materials with a small dispersion in relaxation rates, Fig. 5. These results support that in the low protonated regime, the measured conductivity is that of hopping of charge among positive polaron and bipolaron states in the emeraldine polymer. The characteristic relaxation time  $\tau$  obtained from the Cole-Cole plot is temperature dependent. Assuming a simple Arrhenius expression for  $\tau$ , Fig. 5 inset,  $\tau = \tau_0 \exp(E_a/k_B T)$ ,  $\tau_0 = 1.6 \times 10^{-10}$  s and  $E_a \sim 0.5$  eV. The  $\tau_0$  and  $E_a$  are suggestive of the important role of the flipping of rings [23] in the charge conduction mechanisms.

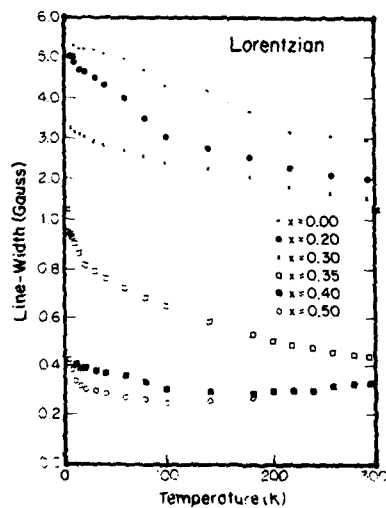
For higher protonation levels, the conductivity varies markedly with protonation level. Extensive study of the temperature and electric field dependence of the conductivity as well as temperature dependence of thermopower as a function of  $x$  shows that the conductivity varies as  $\exp[-(T_0/T)^2]$  with  $T_0$  decreasing with increasing  $x$  [24]. The thermopower changes sign with increasing  $x$  and is proportional to  $T$  for  $x \sim 0.5$ . The transport properties have been analyzed in terms of formation of a granular polymeric metal with charging energy limited tunneling between the small granules. The size of these islands was estimated as  $\sim 200 \text{ \AA}$  [24]. Recent x-ray diffraction studies confirm the presence of ordered regions in the emeraldine salt of order  $100-150 \text{ \AA}$  size [10]. Correlation of the Pauli susceptibility



4. Schematic representation of a model for photoproduction and relaxation of defect states in (a) LB for above-gap photoexcitation; and (b) EB for below-gap photoexcitation [Ref. 15].



5. Imaginary impedance at varying frequencies for a temperature of 300 K and for unprotonated ( $x=0.0$ ) emeraldine polymer. The inset presents  $\log_{10}\tau$  [determined from the maximum of plots of  $\text{Im}(Z)$  vs  $\text{Re}(Z)$ ] vs  $T^{-1}$  for the unprotonated emeraldine polymer. The dashed line indicates the center of curvature for the Cole-Cole analysis; the dashed line in the inset is the best fit to an Arrhenius expression [Ref. 22].

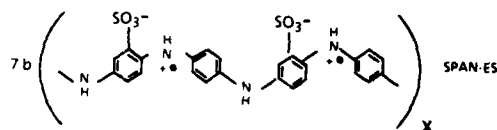
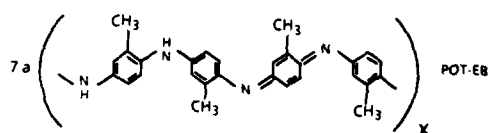


6. Temperature dependence of the linewidth of the Lorentzian component of the ESR signal for "emeraldine" salts of different protonation levels. Note the change in the vertical scale [Ref. 27].

versus protonation level, together with the degree of crystallinity versus protonation level, lead to the conclusion that protonation of the amorphous material leads to spinless charge sites while protonation in the ordered regions leads to a "metallic polaron lattice" [10]. Extensive microwave frequency conductivity and dielectric constant studies of the emeraldine polymer as a function of protonation level support the phase segregation of the polymer into metallic islands and an insulating background with localization prevailing within the metallic islands at low temperatures [25]. In view of the presence of barriers within the metallic islands as well as between the metallic islands, the phrase "texture in metallic islands" was introduced to describe the delicate role of temperature on the interplay between localization and delocalization [25]. The large controllable loss tangent in emeraldine leads to potential application in absorption of electromagnetic radiation [25]. The increase in the measured spin susceptibility at low temperatures beyond the value of the Pauli susceptibility may be a reflection of this increasing localization with decreasing temperature [26]. The narrow electron spin resonance line for highly protonated samples is in accord with the metallic behavior at high temperatures [27]. The decreasing linewidth with decreasing temperature again agrees with reduced scattering of the delocalized electrons with decreasing temperature, Fig. 6. However, as indicated in Fig. 6, the linewidth increases again below 100K likely reflecting the role of increasing localization. It is noted that samples with the highest order in crystallinity have the weakest susceptibility temperature dependence for  $T > 100\text{K}$ .

#### DERIVATIZATION OF POLYANILINE: POT-ES AND SPAN-ES

The ability to derivatize polyaniline at the  $C_6$  ring positions opens the opportunity to tailor the properties of the polyaniline system. Figure 7 shows two such successful derivatives, poly(*o*-toluidine) [POT] and sulfonated polyaniline [SPAN]. Extensive study of the crystal structure of the emeraldine hydrochloride salt of POT shows that it is of similar crystallinity to ES with increased separation between the polymer chains [28]. Combined magnetic susceptibility, conductivity, thermopower, electron spin resonance, and microwave conductivity and dielectric constant studies show that although the emeraldine hydrochloride form of POT has the same polaron band optical signature, the charge transport is dominated by electron localization. The increasing separation between chains combined with the similar degree of order to ES leads to the conclusion that the increased localization is due to the decrease interchain bandwidth caused by the larger  $\text{CH}_3$  on the  $C_6$  rings [29].



7. (a) Poly(orthotoluidene) (emeraldine base form); (b) sulfonated polyaniline (self-doped salt form).

The recently reported [30] sulfonation of polyaniline results in the formation of a self-protonated conducting polymer, Fig. 7b. Without any external counterion present the polymer is in the conducting emeraldine salt state with conductivity  $\sim 0.03$  S/cm. The conductivity of this polymer is independent of pH for pH between zero and seven, in contrast to the behavior of the parent emeraldine. An insulating form of the polymer can be formed by reaction with NaOH to form the sodium salt. The sulfonated polyaniline is very soluble in basic aqueous media, making it attractive for technological applications.

#### SUMMARY

The polyaniline family of polymers show physical phenomena distinctly different from those for polyacetylene and polythiophene families due to the presence of the  $C_6$  rings. The variation of behavior with protonation and oxidation depends upon the degree of local order in the samples. The polarons formed in the lightly doped or undoped samples are massive due to the ability of the  $C_6$  rings to rotate.

This work was supported in part by the Defense Advanced Research Projects Agency through a contract monitored by the U.S. Office of Naval Research.

## REFERENCES

1. See, for example, Proceedings of the International Conferences on Synthetic Metals, Santa Fe, NM, June 1988 [Synth. Met. 27 (1988); 28, 29 (1989)]; Kyoto, Japan, June, 1986 [Synth. Met. 17-19 (1987)]; Albano Terme, Italy, June 1984 [Mol. Cryst. Liq. Cryst. 117-121 (1985)].
2. See, for example, T. Skotheim (ed.), Handbook of Conducting Polymers, Vols. 1 and 2, Dekker, New York (1986).
3. D.S. Boudreaux, R.R. Chance, J.F. Wolf, L.W. Shacklette, J.L. Brédas, B. Thémans, J.M. André, R. Silbey, J. Chem. Phys. 85, 4584 (1986).
4. S. Stafstrom, J.L. Bredas, A.J. Epstein, H.S. Woo, D.B. Tanner, W.S. Huang, A.G. MacDiarmid, Phys. Rev. Lett. 59, 1464 (1987).
5. J.M. Ginder, A.J. Epstein, and A.G. MacDiarmid, Solid State Commun. 72, 987 (1989), and to be published.
6. M.C. dos Santos and J.L. Bredas, Phys. Rev. Lett. 62, 2499 (1989); see also M.C. dos Santos and J.L. Bredas, Synth. Met. 29, E321 (1989).
7. A.G. MacDiarmid and A.J. Epstein, J. Chem. Soc., Faraday Trans., in press. A.J. Epstein and A.G. MacDiarmid, Proc. Winter School on Electronic Processible Polymers, Kirchberg, Austria (H. Kuzmany, M. Mehring and S. Roth, Ed., Springer-Verlag, Berlin, 1989), p. 282.
8. K.R. Cromack, M.E. Jozefowicz, J.M. Ginder, R.P. McCall, A.J. Epstein, E. Scherr, A.G. MacDiarmid, Bull. Am. Phys. Soc. 34, 583 (1989), and to be published.
9. X. Tang, E. Scherr, A.G. MacDiarmid, A.J. Epstein, Bull. Am. Phys. Soc. 34, 583 (1989), and to be published; A. Adreata, Y. Cao, J.C. Chiang, A.J. Heeger, and P. Smith, Synth. Met. 26, 383 (1988).
10. M.E. Jozefowicz, R. Laversanne, H.H.S. Javadi, A.J. Epstein, J.P. Pouget, X. Tang, A.G. MacDiarmid, Phys. Rev. B 39, 12,958 (1989).
11. M.G. Roe, J.M. Ginder, P.E. Wigen, A.J. Epstein, M. Angelopoulos, A.G. MacDiarmid, Phys. Rev. Lett. 60, 2789 (1988).
12. R.P. McCall, J.M. Ginder, M.G. Roe, G.E. Asturias, E.M. Scherr, A.G. MacDiarmid, A.J. Epstein, Phys. Rev. B 39, 10,174 (1989).
13. R.P. McCall, M.G. Roe, J.M. Ginder, T. Kusumoto, A.J. Epstein, G.E. Asturias, E.M. Scherr, A.G. MacDiarmid, Synth. Met. 29, E433 (1989).
14. Y.H. Kim, S.D. Phillips, M.J. Nowak, D. Spiegel, C.M. Foster, G. Yu, J.C. Chiang, A.J. Heeger, Synth. Met. 29, E291 (1989); S.D. Phillips, G. Yu, Y. Cao, and A.J. Heeger, Phys. Rev. B 39, 10,702 (1989).
15. R.P. McCall, J.M. Ginder, H.J. Ye, J.M. Leng, S.K. Manohar, J.G. Masters, G.E. Asturias, A.G. MacDiarmid, and A.J. Epstein, Phys. Rev. B (1990), in press.
16. M.G. Roe, J.M. Ginder, T.L. Gustafson, M. Angelopoulos, A.G. MacDiarmid, A.J. Epstein, Phys. Rev. B 40 (15 Aug. 1989).
17. M.G. Roe, J.M. Ginder, R.P. McCall, K.R. Cromack, A.J. Epstein, T.L. Gustafson, M. Angelopoulos, A.G. MacDiarmid, Synth. Met. 29, E425 (1989).



18. F. Zuo, R.P. McCall, J.M. Ginder, M.G. Roe, J.M. Leng, A.J. Epstein, G.E. Asturias, S.P. Ermer, A. Ray and A.G. MacDiarmid, *Synth. Met.* **39**, E445 (1989).
19. A.J. Epstein, J.M. Ginder, F. Zuo, R.W. Bigelow, H.S. Woo, D.B. Tanner, A.F. Richter, W.S. Huang, and A.G. MacDiarmid, *Synth. Met.* **18**, 303 (1987).
20. C.B. Duke, E.M. Conwell, and A. Paton, *Chem. Phys. Lett.* **131**, 82 (1986).
21. R.P. McCall, J.M. Ginder, and A.J. Epstein, to be published.
22. F. Zuo, M. Angelopoulos, A.G. MacDiarmid, and A.J. Epstein, *Phys. Rev. B* **39**, 3570 (1989).
23. S. Kaplan, E.M. Conwell, A.F. Richter, and A.G. MacDiarmid, *Macromolecules* **22**, 1669 (1989); *Synth. Met.* **29** E235 (1989); *Polymer Preprints* **29**, 58 (1988).
24. F. Zuo, M. Angelopoulos, A.G. MacDiarmid, A.J. Epstein, *Phys. Rev. B* **36**, 3475 (1987).
25. H.H.S. Javadi, K.R. Cromack, A.G. MacDiarmid, and A.J. Epstein, *Phys. Rev. B* **39**, 3579 (1989); H.H.S. Javadi, *Microwave Journal*, 162 (Feb., 1989).
26. J.M. Ginder, A.F. Richter, A.G. MacDiarmid and A.J. Epstein, *Solid State Commun.* **67**, 97 (1987).
27. H.H.S. Javadi, R. Laversanne, A.J. Epstein, R.K. Kohli, E.M. Scherr, and A.G. MacDiarmid, *Synth. Met.* **29**, E439 (1989).
28. M. Jozefowicz, et al., to be published.
29. Z. Wang, H.H.S. Javadi, A. Ray, A.G. MacDiarmid, and A.J. Epstein, submitted.
30. J. Yue, A.J. Epstein and A.G. MacDiarmid, submitted.

## THE 0.9 eV ABSORPTION BAND OF POLYANILINE: A MORPHOLOGICALLY SENSITIVE ELECTRONIC ABSORPTION

D. ZHANG, J.-H. HWANG, S. C. YANG

Department of Chemistry, University of Rhode Island, Kingston, RI 02881

### INTRODUCTION

The optical absorption spectra of polyaniline in the visible and UV spectral regions have been characterized before. The electrically conductive form has a band gap absorption at 3.8 eV and polaron absorptions at 2.9 and 1.5 eV [1,2]. An additional electronic absorption band at 0.9 eV was found to be also related to the existence of polaron. The assignment of this transition has yet to be made. Epstein and co-workers [3] have found a photo-induced absorption band at 0.9 eV by photo-exciting emeraldine base (insulator) with 2.0 eV light. It is not known yet whether these two 0.9 eV transitions belong to the same set of electronic energy levels of polaron, or they belong to two different electronic systems but are coincidentally have the same transition energy.

In this communication we present a comparative study of the 0.9 eV band and the 2.9 and 1.5 eV bands in polyaniline samples of different morphology. We will show that although the 0.9 eV band is, like the other two bands, due to the existence of polarons, it is far more sensitive to the micro-environment of polyaniline than the other polaron bands. Using template molecules to control the morphology, we are able to alter the micro-environment around polyaniline molecule, we found the 0.9 eV band splits into two bands in samples in which the molecular aggregation of polyaniline were likely to have been altered, while the other two bands are unaffected by these changes. We propose that the experimentally observed morphological sensitivity of the 0.9 eV band may be explained by assigning the 0.9 eV band as an inter-molecular charge transfer absorption involving a charge transfer complex of two neighboring polyaniline molecules.

### RESULTS AND DISCUSSION

#### The 0.9 eV band is sensitive to the electrode used for electrochemical polymerization

Thin polyaniline films with thickness ranging from 100 to 300 nm were prepared by anodic oxidation on a tin oxide coated glass in 1.5 M aniline dissolved in 3 M HCl solution. The electrolysis was potentiostatically controlled at +0.65 V vs saturated calomel electrode (S.C.E.). Platinum was used as counter electrode.

Two types of tin oxide coated glass were used as working electrode. Glass coated with fluoride doped tin oxide ( $\text{SnO}_2:\text{F}$ ) was made by PPG Industries. This transparent electrode is trademarked as NESA and has approximately 25 ohm/square surface resistivity. The glass coated with antimony doped tin oxide ( $\text{SnO}_2:\text{Sb}$ ) was purchased from Delta Technology. This glass has about 100 ohm/square surface resistivity. Examining by scanning electron microscope, the bare electrode surface of  $\text{SnO}_2:\text{F}$  contains micro-crystalites of 100 to 200 nm dimension and the surface appears to be rocky at a magnification of x50 K. The  $\text{SnO}_2:\text{Sb}$  surface appears to be smooth under the same scale of magnification.

When thin films (50 nm) of polyaniline were electrochemically deposited on these two kinds of surfaces, the first layer morphology of polyaniline (PAN) is different for these two kinds of substrate. PAN/ $\text{SnO}_2:\text{F}$  appears to be clinging to the micro-crystalites like ivy vines. The first layer morphology of PAN/ $\text{SnO}_2:\text{Sb}$

is composed of 100 nm length fibers that anchor their end at sparsely spaced surface nucleation sites. When the polymers are grown sufficiently thick (more than 200 nm), the morphology on both kinds of sample is the same network morphology with short fibers (100 to 150 nm in length, 80 nm diameter) which form network.

The visible absorption spectra of these two types of samples have exactly the same pH and potential dependence, but the Near IR spectra in the 5000 - 10,000  $\text{cm}^{-1}$  region are very different. The 0.9 eV band for  $\text{SnO}_2:\text{Sb}$  (see fig. 1a) is split into two bands at 0.7 and 1.1 eV for  $\text{SnO}_2:\text{Sb}$  (see fig. 1b). This splitting does not appear to be dependent on the film thickness.

We will not comment on what are the possible difference in the interaction of the surface with the polymer that brings about the change in the 0.9 eV band, except noting that we suspect that there is a difference in polymer stacking at the nucleation stage of the electro-polymerization. The difference in micro-environment might be propagated to the fibers so that the mode of aggregation of polyaniline molecules are different in these samples. In the following we will describe a more controlled way to modify the molecular aggregation in polyaniline to further explore our suspicion that the 0.9 eV band is sensitive to polymer morphology and the mode of aggregation of polyaniline.

#### Modification of polyaniline molecular aggregation: Electrochemical synthesis of polyaniline-polyanion complexes:

In this section we describe methods for modifying PAN molecular aggregation by forming molecular complex with polyanions such as polyacrylic acid (PAA) and poly(4-styrenesulfonic acid) (PSSA). These polymer complexes are formed by replacing small molecular weight acids used in dissolving aniline monomers by polymeric acids [4]. In reference 4 we reported that the morphology of these polyaniline-polyacid complexes are dramatically different from that of the electrochemically synthesized pure PAN samples. The PAN-PAA complex form long (2 - 3 micron) needles with about 100 nm diameter. PAN-PSSA complex are packed globulets with diameter of 150 to 200 nm. This is in contrast with the un-complexed PAN whose morphology consists of network built from short (150 nm) fibers of 80 to 100 nm diameter.

Elemental analysis of the samples indicate that there are 30 % (mole percent of monomers) and 50% of polyanions included in PAN-PAA and PAN-PSSA complexes respectively. The polyacids are sufficiently entangled in the fiber so that they are not dissolvable by washing with either acidic or basic aqueous solutions.

We have previously described this method of morphological modification as an application of the "molecular template" concept to the control of polymer aggregation during the polymerization of conducting polymers [4]. The idea is to use polymeric acids as template molecules to bind aniline monomers to form aniline-template complex (AN-TEMP) then polymerize aniline molecules in these AN-TEMP complexes. The molecular aggregation of the resulting polyaniline-TEMP polymer complexes is strongly controlled by the configuration of the AN-Temp complexes. In the following we will discuss how the configurations of the AN-Template complex can be different for two cases where Template = PAA and PSSA. We will show that the AN-PAA complex have a relatively extended linear configuration while the AN-PSSA complex has a random coil configuration.

Consider a titration process to form AN-PAA complex. When aniline is added drop by drop into an aqueous solution of PAA (M.W. = 90,000) the following changes to PAA occur:

- (1) Initial addition of aniline, which is a base, to PAA solution causes ionization of the carboxylic acid group of PAA and the formation of free anilinium ions.
- (2) Additional amount of aniline causes the PAA backbone to extend to more linear configuration because of the coulombic repulsion between the increasing

number of negatively charged carboxylate groups. As the titration progresses, the remaining protons become harder to ionize.

(3) At a sufficient degree of ionization, PAA is no longer able to lose the remaining carboxylic proton to form more anilinium ions. Additional aniline molecules are now hydrogen-bonded to those now unionizable protons on PAA. There are also some additional anilinium ions territorially bond to PAA because of counter ion condensation. The resulting AN-PAA complex will have a relatively linear and extended configuration.

Next we examine the configuration of AN-PSSA complex. Since the sulfonic group is a strong acid, the added AN molecules will almost fully ionize the acid to form anilinium ions ( $\text{AN.H}^+$ ) and polystyrene sulfonates ( $\text{PSS}^-$ ). However there are two interactions between  $\text{AN.H}^+$  that helps attaching  $\text{AN.H}^+$  to  $\text{PSS}^-$ .

- (1) Hydrophobic interaction between the aromatic rings in AN and in styrenesulfonate group promotes stacking of these aromatic rings.
- (2) Ion pairing between the positive charge on  $\text{AN.H}^+$  and the negative charge on the sulfonate group further helps to stabilize the hydrophobically aggregated complex.

The resulting AN-PSSA complex has a random coil configuration because the ion-pair formation effectively shields the coulombic repulsion between the ionized sulfonate groups so chain extension is minimal

When these AN-TEMP complexes are electrochemically polymerized, the PAN-PAN aggregation is modified depending on the configuration of the aniline-template complex. The AN molecules in extended chain AN-PAA tends to polymerize into stiff chain polyaniline-polyacrylic acid complex (PAN-PAA). It is likely that such kind of extended-chain PAN-PAA complex would aggregate parallel along the molecular axis to form long and straight fibers. Comparatively, the random coil configuration of the precursor AN-PSSA complex makes it possible to join the monomers which are at a large distance along the PSSA backbone but are brought to contact by the folding chain of the  $\text{AN.H}^+$ - $\text{PSS}^-$  complex. Polymerization of aniline in such a random coil complex will cause substantial entanglement of PAN and PSSA polymer chains to form globular morphology.

The 0.9 (0.7/1.1) eV absorption band of morphologically modified polyaniline:

The Near IR absorption spectra of PAN samples described in the previous section were measured, and we found that the 0.9 eV band is sensitive to the mode of aggregation of PAN molecules. Thin film PAN-PAA and PAN-PSSA polymer complexes were electrochemically deposited on both types of tin oxide electrodes. The template molecules appear to exert sufficient influence on the mode of aggregation in PAN to overwhelm the influence of the substrate. Therefore samples of (PAN-PAA)/ $\text{SnO}_2(\text{Sb})$  and (PAN-PAA)/ $\text{SnO}_2(\text{F})$  both show single NIR absorption band at 0.9 eV in the conductive state. Their spectra looks very similar to that of  $\text{SnO}_2(\text{Sb})$  in Fig. 1a The conversion of double-band absorption in PAN/ $\text{SnO}_2(\text{F})$  to a single-band in (PAN-PAA)/ $\text{SnO}_2(\text{F})$  can not be simply explained as an effect of dilution of PAN by adding polymer PAA, because in a more diluted (PAN-PSSA)/ $\text{SnO}_2(\text{F})$  sample the double band returns and the spectrum looks like that shown for PAN/ $\text{SnO}_2(\text{F})$  in figure 1b.

A hypothesis: The 0.9 eV absorption band of the conductor form is an inter-molecular charge transfer absorption involving polarons.

Intermolecular charge transfer absorption has been well documented in small-molecule charge transfer complexes [5,6]. A classic example is the  $\text{I}_2$ :benzene complex whose charge transfer absorption involves mixing of the filled pi orbital of benzene and the empty antibonding sigma orbital of  $\text{I}_2$ . The

intensity and the position of the charge transfer band are sensitively dependent on the symmetry and the spatial overlap of the electron donor and acceptor orbitals in A:B complex. When A and B are two neighboring polymer molecules, the spatial overlap of the donor and acceptor orbitals could be sensitive to how A and B molecules are aggregated. It is, therefore, possible to observe sensitive morphological dependence of intermolecular charge transfer in solid polymer samples.

We now postulate that the 0.9 eV (0.7, 1.1 eV) transition is an intermolecular charge transfer absorption band involving two neighboring polymer chains A and B<sup>+</sup>. We further suggest that A is a reduced leucoemeraldine segment and B<sup>+</sup> is a polaron containing segment. The optical transition are between levels that are derived from mixing of a partially empty polaron molecular orbital of B<sup>+</sup> and a filled orbital from the valence band of A.

This postulation should be directly tested by either measuring the polarization of absorption transition moment in aligned samples or to verify the loss of this NIR band upon dispersing the polymer in solvents. Before such experiments are performed, we can only offer somewhat less direct support by observing that this postulation is consistent with other experimental details which will be discussed in the following section.

Observation of two stages in electrochemical oxidation induced polaron band intensity growth:

Jozefowicz et al [7] reported that polyaniline samples may have a crystalline portion and an amorphous portion. The relative content of these phases is dependent on sample preparation and method of synthesis. In a sample that contains largely microscopic fibers such as the samples that yields NIR spectra shown in Figure 1, the crystalline phase is likely to be in the core portion of the fiber, the amorphous portion is likely to be at the surface (peripheral) of the fiber and at the junction between fibers to form networks. In the core region a polaron segment B<sup>+</sup> is likely to be in contact with a donor segment A. Therefore it will have not only the 2.9 eV and the 1.5 eV polaron absorption bands of B<sup>+</sup>, but also the 0.9 eV (or the 0.7, 1.1 eV pair) transition of A:B<sup>+</sup> molecular complex. Most of the B<sup>+</sup> molecules at the peripheral of a fiber would be surrounded by solvent molecules to form solvated ions (B<sup>+</sup>:S), so is unable to find nearby chains to form A:B<sup>+</sup> and these polarons will have the 2.9 eV and the 1.5 eV absorption but will not have the 0.9 eV intermolecular absorption.

If a polyaniline sample indeed has these two phases, what effects on spectro-electrochemistry that we should expect to observe? In an electrochemical oxidation in aqueous solution the oxidation potential, E<sub>1/2</sub>, for injection of polaron into leucoemeraldine is dependent on the ease of swelling and the lattice energy for inserting solvated counter anion (Cl<sup>-</sup>: nH<sub>2</sub>O). Therefore one would expect that the E<sub>1/2</sub> will be at higher potential in the fiber core than in the solvated free polymer chains. The consequence of such a differentiation of oxidation potential is that the 1.5 eV transition of B<sup>+</sup> will start to grow at a lower electrochemical potential than that of the 0.9 eV transition of A:B<sup>+</sup>. Such an apparent two-stage growth is seen in figures 1a and 1b. For example, in fig. 1a, the 1.5 eV band (12,500 cm<sup>-1</sup>) starts to grow in intensity at -0.3 V but the 0.9 eV band do not start to grow until at -0.2 V. Although the part of 1.5 eV band intensity increase between -0.4 to -0.2 V is a relatively small percentage of the maximum intensity at +0.4 V, the difference in the starting potential of this band is clearly shown in figure 1.

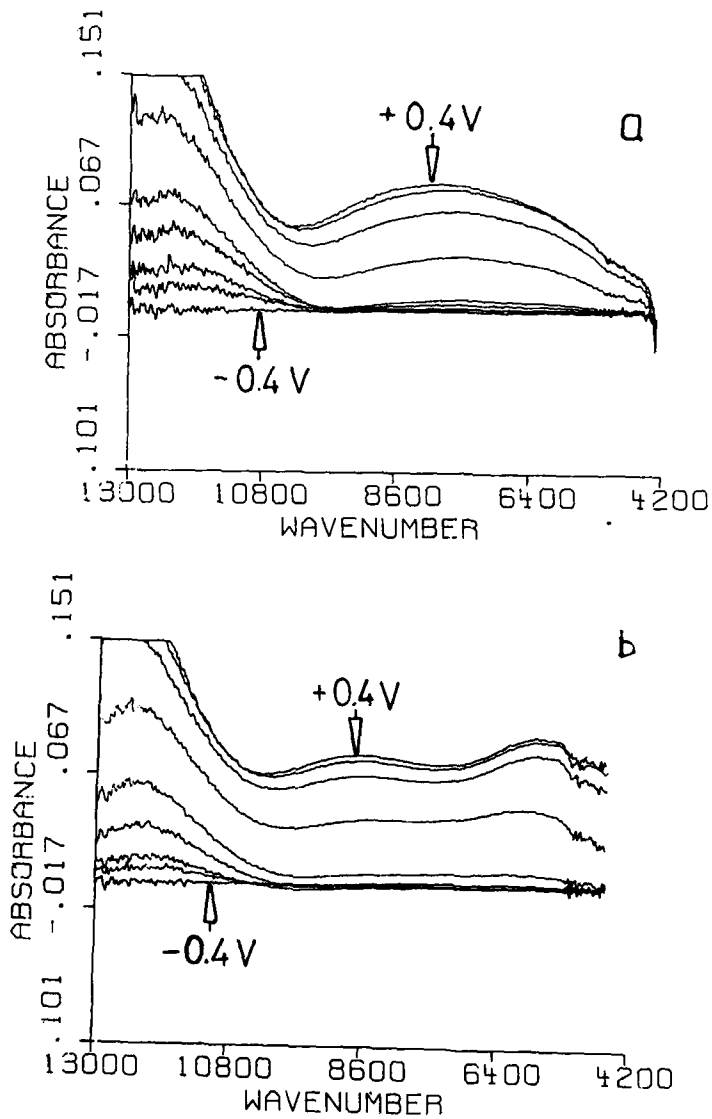


Fig. 1 Optical absorption spectrum of polyaniline measured by in-situ control of electrochemical potential of polyaniline coated on two different tin oxide substrates: (a) PAN/SnO<sub>2</sub>:Sb (b) PAN/SnO<sub>2</sub>:F.

## SUMMARY

We have shown that the 0.9 eV (0.7, 1.1 eV) absorption band of the conductive form of polyaniline sample is sensitive to the morphology of polyaniline. Using different polyanions as templates for aniline polymerization, we were able to obtain samples of polyaniline-polyanion complexes with different morphology. The differences in morphology are rationalized as due to differences in the molecular aggregation in these samples. We suggest that the changes in 0.9 eV band in these samples is related to different modes of aggregation between neighboring chains of polyaniline, and we postulate that the 0.9 eV absorption band is an intermolecular charge transfer absorption band. The assumption of inter-molecular transition is found to be consistent with the observation of two-stage charge injection observed in our spectroelectrochemical studies. At present, the assignment of 0.9 eV band as *inter-chain charge transfer* absorption is still largely hypothetical, the author wish that this communication will stimulate further testing of the hypothesis.

## ACKNOWLEDGMENT

This work is supported in part by a contract administered by the Office of Naval Research from DARPA, and by NSF under grant CHE-8216482.

## REFERENCES:

1. S. Stafstrom, J. L. Bredas, A. J. Epstein, H. S. Woo, D. B. Tanner, W. S. Huang and A. G. MacDiarmid, *Phys. Rev. Lett.*, 59 (1987) 1464.
2. R. J. Cushman, P. M. McManus and S. C. Yang, *J. Electroanal. Chem.*, 291 (1986) 335.
3. M. G. Roe, J. M. Ginder, P. E. Wigen, A. J. Epstein, M. Angelopoulos and A. G. MacDiarmid, *Phys. Rev. Lett.*, 60 (1988) 2789.
4. J. H. Hwang and S. C. Yang, *Synth. Metal.*, 29 (1989) E271.
5. R. S. Drago, "Physical Methods in Chemistry", p.115-123, (Saunders, 1977).
6. W. Kauzmann, "Quantum Chemistry", p. 687, (Academic Press, 1959).
7. M. E. Jozefowicz, R. Laversanne, H. H. S. Javadi, A. J. Epstein, J. P. Pouget, X. Tang and A. G. MacDiarmid, *Phys. Rev. B*, 39 (1989) 12958.

## AQUEOUS COLLOIDAL DISPERSIONS OF POLYANILINE PARTICLES

STEVEN P. ARMES\* AND MAHMOUD ALDISSI, Materials Science and Technology Division, Los Alamos National Laboratory, P. O. Box 1663, Los Alamos, NM 87545  
\*Presently at University of Sussex, School of Chemistry and Molecular Sciences, Brighton BN1 90J, United Kingdom

## ABSTRACT

Colloidal polyaniline has been prepared in acidic aqueous media by a modified chemical polymerization of aniline in the presence of a tailor-made polymeric surfactant. The surfactant which acts as a steric stabilizer used in this study is derivatized poly(vinyl alcohol-co-vinyl acetate). This surfactant contains pendant aniline units which participate in the aniline polymerization, resulting in the formation of sterically-stabilized polyaniline particles which have a non-spherical "rice-grain" morphology.

It is shown that this novel form of polyaniline is more processable than the bulk powder that is normally obtained from a conventional chemical synthesis. The solid-state conductivity of solution-cast films or compressed pellets of these dispersions is surprisingly high ( $\approx 1$  S/cm), despite the presence of the insulating outer layer of chemically-grafted stabilizer.

## INTRODUCTION

Intractability is typical of conjugated polymers because of the aggregated character associated with strong interchain interactions. To take advantage of this property, in the preparation of conducting polymers as colloidal dispersions seemed to be an excellent approach toward processability. Since 1986 several groups have described the preparation of spherical sub-micronic polypyrrole colloidal particles in aqueous media [1-6]. The particles are sterically-stabilized by an outer layer of physically adsorbed polymeric surfactant such as methylcellulose, poly(vinyl alcohol-co-vinyl acetate), poly(vinyl pyrrolidone), poly(vinyl pyridine-co-butyl methacrylate), etc. Most of our initial attempts to produce colloidal polyaniline particles by analogous methods have resulted in macroscopic precipitation due to inefficient adsorption of the stabilizer, although in certain cases a low yield of colloidal polyaniline has been reported [7,8]. To achieve colloidal stability of polyaniline particles and avoid the problems associated with physical adsorption/desorption, we employed another synthetic approach which consisted of graft copolymerization of aniline onto the appropriate polymeric surfactant. In a recent preliminary communication [9] we described the preparation of colloidal polyaniline particles using a tailor-made random copolymer poly(2-vinyl pyridine-co-*p*-aminostyrene) as a polymeric surfactant. Preparation of the latter and evidence of grafting were described recently [10]. In this paper, we describe the preparation and characterization of polyaniline colloids using the derivatized poly(vinyl alcohol-co-vinyl acetate) as a steric stabilizer in the graft copolymerization process.



## EXPERIMENTAL

Commercially available poly(vinyl alcohol-co-vinyl acetate), PVA, whose vinyl alcohol/vinyl acetate ratio is 88/12 and nominal molecular weight is 25,000 or 125,000 was dissolved with stirring at 130° C in DMF under argon. Triethylamine and a DMF solution of *p*-nitrobenzoyl chloride (1-6 mol% relative to the PVA base monomer) were added in turn to the reaction solution and esterification allowed to proceed for 16-24 hrs. An 8-10 mole excess of phenylhydrazine (based on *p*-nitrobenzoyl chloride) was then added to the reaction solution and its temperature was raised to reflux for 16-24 hrs. The reaction product was purified by repeated precipitation from water/acetone or water/THF solvent/non-solvent mixtures.

The synthesis which utilized potassium iodate to oxidize aniline was carried out as follows: potassium iodate (0.90 g) and stabilizer (0.4 - 1.0 g) were dissolved together in 100 ml of 1.2 M hydrochloric acid at room temperature. The solution was allowed to age for 0 to 30 min. to insure a maximum yield of the oxidation reaction of the *p*-aminostyrene moiety in the copolymer. Aniline (1.0 ml) was injected into the stirred reaction mixture and allowed to react for 2 days. At the end of this period the reaction medium turned dark green. The dispersion was centrifuged at 18,000 rpm for 2 hrs, the supernatant decanted, and the dark green sediment redispersed in 1.25 M HCl via ultrasonics.

The graft copolymer steric stabilizer was characterized by gel permeation chromatography (GPC), and NMR. Polyaniline colloids were characterized using a wide range of techniques including electron microscopy, cyclic voltammetry and Raman, uv-visible absorption and X-ray photoelectron spectroscopies. Conductivity measurements as a function of temperature and pressure were performed on films cast from the colloidal dispersions.

## RESULTS AND DISCUSSION

### Oxidant/Stabilizer Compatibility

The oxidation/polymerization of aniline in the presence of the derivatized PVA stabilizer was attempted using several oxidants that are typically used for the synthesis of bulk polyaniline. Recently, Pron *et al.* [11] reported that potassium iodate could be used over a wide range of reaction conditions to produce good quality bulk polyaniline powder. We found that this oxidant did not cause precipitation of the stabilizer; as a consequence it became the reagent of choice for the preparation of colloidal polyaniline.

### Molecular Weight and Composition of the Stabilizer

Gel permeation chromatographs of the underivatized commercial PVA and the chemically modified version indicated significant chain scission occurred as a result of the grafting process of *p*-aminostyrene. This degradation is undesirable because in some cases the derivatized PVA did not produce stable colloidal dispersions of polyaniline, particularly when PVA (25,000) was used as the starting material. This is presumably due, at least in part, to its lowered molecular weight. We have determined  $M_w$  and

$M_w/M_n$  of PVA (25,000) and PVA (125,000) before and after grafting of *p*-aminostyrene. For PVA (25,000), the values are 31,900 and 22,700 before and after grafting respectively. No change in the polydispersity index was observed (2.3). For PVA (125,000), the values are 101,800 and 40,200. The polydispersity index increased from 1.9 to 2.4 due to grafting.

We have determined the mol% of grafted pendant aniline groups onto PVA by means of  $^1\text{H}$  NMR. Both PVA starting materials consisted of 88 mol% PVA and 12 mol% poly(vinyl acetate). The resulting grafted amount was 1.7 mol% for PVA (25,000) and 1.8 mol% for PVA (125,000).

#### Spectroscopic Evidence for Grafting of polyaniline

The polymerization of aniline by  $\text{KIO}_3$  (and other oxidants such as ammonium persulfate) in acid solutions proceeds via a short-lived anilinium radical cation intermediate which has an absorption peak  $\lambda_{\text{max}}$  at 525 nm (Fig. 1). If  $\text{KIO}_3$  is added to an acidic solution containing the polymeric stabilizer, a similar absorption peak is observed. In a control experiment, an underivatized poly(vinyl alcohol-co-vinyl acetate)/ $\text{KIO}_3/\text{HCl}$  solution showed no absorption peak under identical conditions. Thus, we conclude that the observed absorption peak is due to the oxidation of the pendant aniline groups. An absorption spectrum of colloidal polyaniline is shown in Fig. 1 for comparison. The latter spectrum is identical to that of the electrochemically-synthesized polyaniline film. In our preparative procedure for the synthesis of colloidal polyaniline, the aniline monomer is added last to a stirred solution containing  $\text{KIO}_3$  and the stabilizer. Since it is clear that the pendant aniline groups grafted onto PVA are activated under these conditions, we believe that these moieties inevitably participate in the aniline polymerization and constitute sites for the grafting of polyaniline onto the stabilizer's chain.

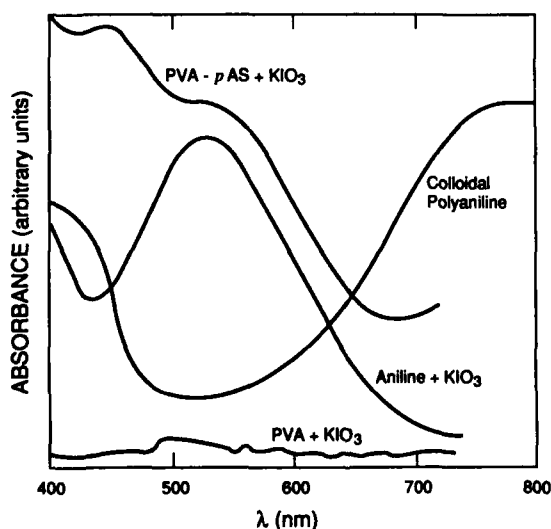


Fig. 1. Spectroscopic evidence for grafting of polyaniline

### Colloids Morphology

Examination of the dried-down dispersions by scanning and transmission electron microscopies revealed a morphology which consisted of "rice grain" particles. The length of the particles was  $150 \pm 50$  nm and their width was  $60 \pm 10$  nm. Fig. 2 shows a transmission electron micrograph of the dispersions in which individual particles can be seen clearly. Because steric stabilization by the polymeric surfactant takes place during polymerization of aniline, aggregation is limited to particles in the sub-micronic range. Although the shape of the particles is non spherical (unlike polypyrrole), scanning tunneling microscopy revealed that any given colloidal polyaniline particle is composed of much smaller ones whose shape is spherical-like. The morphology using this latter technique will be discussed elsewhere [12].

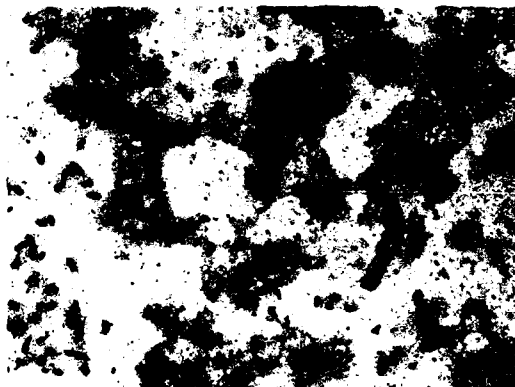


Fig.2. Transmission electron micrograph of polyaniline colloidal particles (magnification 18,000).

### Conductivity

Four-probe conductivity measurements were performed on pellets of the dark green powder obtained by drying the colloidal dispersions. Room temperature conductivity was in the range 0.5-2.0 S/cm. This conductivity is comparable to that of bulk polyaniline prepared chemically or electrochemically despite the presence of the non-conducting component which is the PVA-based polymeric surfactant. Scanning tunneling microscopy [12] indicated the absence of surfactant chains where there is contact between the conducting components once the solvent is removed. This allows for the hopping of charge carriers between the colloidal particles. Conductivity measurements as a function of pressure and temperature [13] indicated that conduction is pressure-dependent and occurs via a variable-range hopping mechanism.

### Stability of Polyaniline Colloids

We have observed that the colloidal stability of polyaniline/PVA dispersions is not as good as that of the previously reported polyaniline/poly(vinyl pyridine) systems [9]. In fact, precipitation starts to occur after a few weeks upon standing. Chain scission which occurs during the derivatization process and results in lower molecular weights than that of the starting PVA material might cause the relative colloidal instability. A better stability of the dispersions with PVA (125,000) than that of the dispersions with PVA (25,000) supports the above assumption.

Air-stability of polyaniline colloids is usually excellent and similar to that of bulk polyaniline. When monitored over several months, room temperature conductivity remains constant.

Thermogravimetric analysis data of bulk and colloidal polyaniline in air (prepared under similar conditions) showed that decomposition of the colloids follows a similar trend to that of the bulk polymer. For both materials, the gradual weight loss attains a value of approximately 10% at 150° C. However, the weight loss beyond this temperature is higher than for the bulk polymer. This could be due to shorter polyaniline grafts than in the bulk form and possibly to less interchain interaction resulting from the distribution of the grafting sites. The effect of such degradation on conductivity has not been determined yet.

### Structure of the Colloids

We have determined the weight fractions of the various elements by microanalysis. What is of interest to us are the weight fractions of chlorine and iodine species that are due to the oxidation process, which results in their incorporation as counter-ions, and the iodine and chlorine to nitrogen ratios. In one specific example, the analysis gave 6.91, 7.84, and 20.28 weight% for nitrogen, chlorine and iodine respectively. Raman spectroscopy showed that iodine species were in the form of mostly  $I_3^-$  and a small amount of  $I_5^-$ . At a first approximation, we will consider that iodine exists in the form of triiodide ions only. In this case, iodine accounts for 20 mol% of the total doping and the rest is due to chlorine ions. The ratio of the combined dopant ions to that of nitrogen (based on one nitrogen atom for each aniline monomer unit) is approximately 50 mol%. This means that there is a counter-ion for each 2 aniline repeat units. However, the actual amount of iodine involved in the doping process is probably less than the value given above because (i) secondary ion mass spectroscopy analysis (SIMS) indicated that there is a small amount of iodine that reacted with the backbone forming C-I bonds, and (ii) X-ray photoelectron spectroscopy indicated that triiodide ions might have formed a complex with the stabilizer..

### CONCLUSIONS

Chemical grafting of polyaniline onto the backbone of the polymeric surfactant is so far the only way to obtain colloidal forms of the conducting polymer. It is interesting to note that a small percentage of grafts of polyaniline yielded a conducting colloid. The chemical grafting technique offers the advantage, compared to physical adsorption in the case of polypyrrole, of forming more stable materials in which desorption of the

steric stabilizers does not take place. Such a technique could be generalized for the derivatization and use of other polymeric surfactants toward better colloidal stability and ease of film formation.

#### Acknowledgments

The authors wish to thank J. F. Smith and R. Sebring (SEM and TEM), Dr. Van Ooij (SIMS), S. Agnew (Raman), S. Cisneros (TGA) and M. Coburn (NMR). This project was partly funded by the Office of Basic Energy Sciences, U. S. Department of Energy.

#### References

1. R. B. Bjorklund and B. Liedberg, *J. Chem. Soc., Chem. Commun.*, 1293 (1986).
2. S. P. Armes and B. Vincent, *J. Chem. Soc., Chem. Commun.*, 288 (1987).
3. S. P. Armes, J. F. Miller and B. Vincent, *J. Coll. Interface Sci.* 118(2), 410 (1987).
4. S. P. Armes, M. Aldissi and S. F. Agnew, *Synth. Met.* 28, C837 (1989).
5. S. P. Armes and M. Aldissi, accepted for publication in *Polymer*.
6. N. Cawdery, T. M. Obey and B. Vincent, *J. Chem. Soc., Chem. Commun.*, 1189 (1989).
7. J. F. Miller, B.Sc. Thesis, University of Bristol, UK, 1987.
8. E. C. Cooper, Ph.D. Thesis, University of Bristol, UK, 1988.
9. S. P. Armes and M. Aldissi, *J. Chem. Soc., Chem. Commun.*, 88 (1989).
10. S. P. Armes and M. Aldissi, *Proceedings of the ACS Division of Polymeric Materials: Science and Engineering*. 6Q, 751 (1989).
11. A. Fron, F. Genoud, C. Menardo and M. Nechtschein, *Synth. Met.* 24, 193 (1988).
12. M. Hawley, S. P. Armes and M. Aldissi, manuscript in preparation.
13. M. Aronson, S. P. Armes and M. Aldissi, manuscript in preparation.

## V<sub>2</sub>O<sub>5</sub> XEROGELS AS HOSTS FOR CONDUCTIVE POLYMERS. INTERCALATIVE POLYMERIZATION OF ANILINE, PYRROLE AND 2,2'-BITHIOPHENE.

Chun-Guey Wu<sup>(a)</sup>, Henry O. Marcy<sup>(b)</sup>, Donald C. DeGroot<sup>(b)</sup> and Carl R. Kannewurf<sup>(b)</sup>,  
Mercouri G. Kanatzidis<sup>(a)</sup>

(a) Department of Chemistry and Center for Fundamental Materials Research, Michigan State University, East Lansing MI 48824 (b) Department of Electrical Engineering and Computer Science, Northwestern University, Evanston, IL 60208.

### ABSTRACT

Intercalative polymerization of aniline, pyrrole and 2,2'-bithiophene in vanadium oxide xerogels results in electrically conductive novel materials which are composed of alternating monolayers of metal-oxide and conductive polymers. The driving force for this intercalation is redox chemistry. The conductivity type in these materials is a function of the polymer/V<sub>2</sub>O<sub>5</sub> xerogel ratio. Low ratios result in xerogel-based charge transport, while high ratios favor polymer-based charge transport properties. Chemical, spectroscopic and electrical data on the intercalative polymerization products of aniline, pyrrole and 2,2'-bithiophene with V<sub>2</sub>O<sub>5</sub> xerogels are presented.

### INTRODUCTION

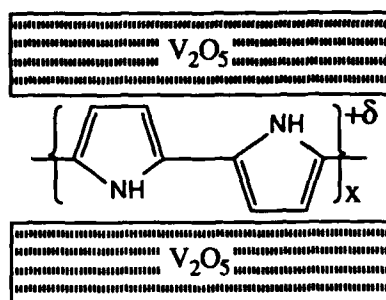
Progress in elucidating the real structure of conducting polymers [1] such as polypyrrole (Ppy), polyaniline (Pani), and polythiophene (Pth) thus far has been hampered by their invariably amorphous nature. The lack of structural data on electrically conductive polymers, inhibits the development of a theoretical understanding of charge transport processes in these materials. Although the availability of single crystals of conductive polymers is not in sight, it would be extremely desirable if at least partially oriented systems could be synthesized. One interesting approach would be to produce such polymers in restricted environments (e.g. the gallery space of a layered solid or the channel space of a microporous material). Recently, the intercalation of conductive polymers into layered inorganic host structures such as FeOCl [2,3] and V<sub>2</sub>O<sub>5</sub>·nH<sub>2</sub>O xerogels [4,5] was accomplished by the *in-situ* intercalative polymerization of appropriate monomers to yield layered materials containing monolayers of conductive polymers inserted in the intralamellar space of the host. Other layered materials [6] and three dimensional matrices such as zeolites have also been used to encapsulate conducting polymers [7].

It has been proposed that layered organic/inorganic hybrid materials may give rise to a new properties not possible from either component separately [8]. When intercalated, the polymers can be thought of as being ordered at least perpendicular to the stacking direction. These materials are interesting because they are molecular composites of two electrically active but chemically diverse components: organic conductive polymers and inorganic metal-oxide bronzes [9]. Here we report further chemical, spectroscopic and electrical data on the intercalative polymerization products of aniline, pyrrole and 2,2'-bithiophene with V<sub>2</sub>O<sub>5</sub> xerogels.

### RESULTS AND DISCUSSION

The idea behind intercalative polymerization is that if a host matrix is capable of oxidizing an oxidatively polymerizable molecule, intercalation of the polymer product could occur. V<sub>2</sub>O<sub>5</sub> is an excellent host choice because of its exceptionally high redox potential. Crystalline orthorhombic V<sub>2</sub>O<sub>5</sub> however, is not amenable to intercalation because of significant O---V

interactions between layers. Sol-gel prepared  $V_2O_5 \cdot nH_2O$  is an excellent redox host material because of the intercalated water which keeps the metal-oxide layers apart and allows for facile guest penetration [10]. The intercalative polymerization reactions of the monomers usually are done by (a) refluxing the xerogel in acetonitrile solutions of the monomer, (b) xerogel reaction with monomer/water or  $CH_3CN$  mixtures and (c) monomer reaction with water-swollen  $V_2O_5 \cdot nH_2O$  xerogels. X-ray diffraction shows that complete intercalation occurs, and the resulting black shiny products have a layered turbostratic structure as depicted in scheme (A). The interlayer distance of the products is larger than that of the pristine xerogel, which is consistent with intercalation. Both free-standing films and powders of these materials can be obtained.



Scheme (A)

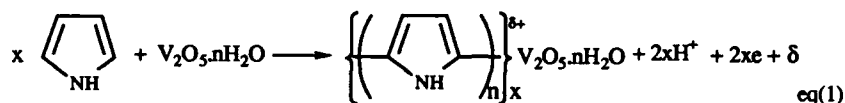
Table (I) summarizes the different intercalation compounds synthesized thus far, and their corresponding interlayer separation. The intercalative polymerization is usually accompanied by deintercalation of a water monolayer (approx. 2.8 Å). The magnitude of the interlayer expansion observed in these materials is consistent with a polymer orientation in which the planar cyclic aromatic rings are primarily perpendicular to the metal-oxide slabs.

The formation of the conductive polymer inside the host's gallery space is confirmed by the FT-IR spectra of these compounds which clearly show characteristic vibrations of the corresponding polymers in the 1000-1600  $cm^{-1}$  region. The FT-IR spectra are similar with those of bulk conductive polymers. The intercalated conductive polymers can be easily isolated from these materials by dissolving the host layers of vanadium oxide with aqueous 50% HCl or 2% NaOH solutions. As with bulk conductive polymers, the degree of polymerization of the intercalated polymers in these materials is currently unknown.

The reaction of toluidine (4-methylaniline) with  $V_2O_5 \cdot nH_2O$  does not yield a conductive polymer, which is consistent with the inability of toluidine to polymerize oxidatively. As expected, 2,6-dimethylaniline (DMAN) intercalatively polymerizes to yield  $\{poly-(DMAN)\}_{0.40}V_2O_5 \cdot 0.50H_2O$ , which possesses a slightly larger interlayer distance of 14.55 Å. Also, while the use of N-methylpyrrole did result in intercalative polymerization, as expected, 2,5-dimethylpyrrole did not.

During intercalative polymerization, the vanadium oxide framework is reduced to form  $V^{4+}$  centers. The unpaired electrons in these  $d^1$  centers are fairly localized (small polarons) and hop between the vanadium sites giving the layers a finite thermally activated n-type conductivity [11]. Assuming all the electrons removed by oxidation from the monomers are transferred to  $V_2O_5$ , the degree of reduction of the  $V_2O_5$  framework should be  $2x + \delta$  (according to eq(1)). Therefore the  $V_2O_5$  framework qualifies as a bronze, and the  $(Polymer)_x V_2O_5 \cdot nH_2O$  materials can be viewed as polymer bronzes. From a conductive-polymer viewpoint, the  $[V_2O_5]^{(2x+\delta)}$ -portion of the compound can be regarded as the dopant. Furthermore, the alternating monolayers

of conductive polymer chains and vanadium oxide qualify these materials as molecular organic/inorganic microcomposites.



**Table I.** Interlayer Spacings, Thermoelectric Power and Conductivity Data for (Polymer)<sub>x</sub>V<sub>2</sub>O<sub>5</sub>·nH<sub>2</sub>O Materials, Prepared by Intercalative Polymerization

Formula	d-Spacing (Å)	Seebeck coeff* μV/K	Carrier type	σ Ω <sup>-1</sup> cm <sup>-1</sup> at 300 K
V <sub>2</sub> O <sub>5</sub> ·nH <sub>2</sub> O (n~1.6)	11.55(1)	>-350	n	10 <sup>-5</sup>
(Pani) <sub>0.06</sub> V <sub>2</sub> O <sub>5</sub> ·1.0H <sub>2</sub> O	13.92(2)	-300	n	10 <sup>-4</sup>
(Pani) <sub>0.21</sub> V <sub>2</sub> O <sub>5</sub> ·0.56H <sub>2</sub> O	13.92(2)	-120	n	10 <sup>-3</sup>
(Pani) <sub>0.37</sub> V <sub>2</sub> O <sub>5</sub> ·0.62H <sub>2</sub> O	13.94(2)	-60	n	10 <sup>-2</sup>
(Pani) <sub>0.44</sub> V <sub>2</sub> O <sub>5</sub> ·0.5H <sub>2</sub> O	13.94(2)	-30	n	0.1
(Ppy) <sub>0.22</sub> V <sub>2</sub> O <sub>5</sub> ·0.68H <sub>2</sub> O	11.44(2)	-280	n	10 <sup>-3</sup>
(Ppy) <sub>0.26</sub> V <sub>2</sub> O <sub>5</sub> ·0.36H <sub>2</sub> O	16.60(2)	-180	n	10 <sup>-3</sup>
(Ppy) <sub>0.32</sub> V <sub>2</sub> O <sub>5</sub> ·0.48H <sub>2</sub> O	14.56(2)	-70	n	10 <sup>-2</sup>
(Ppy) <sub>0.44</sub> V <sub>2</sub> O <sub>5</sub> ·nH <sub>2</sub> O	11.44(2)	--	-	10 <sup>-3</sup>
(Ppy) <sub>0.64</sub> V <sub>2</sub> O <sub>5</sub> ·0.50H <sub>2</sub> O	14.55(2)	+15	p	0.5
(C <sub>8</sub> H <sub>4</sub> S <sub>2</sub> ) <sub>0.08</sub> V <sub>2</sub> O <sub>5</sub> ·0.60H <sub>2</sub> O	14.55(2)	-50	n	10 <sup>-2</sup>
(C <sub>8</sub> H <sub>4</sub> S <sub>2</sub> ) <sub>0.20</sub> V <sub>2</sub> O <sub>5</sub> ·0.65H <sub>2</sub> O	14.57(2)	-	-	--
(C <sub>8</sub> H <sub>4</sub> S <sub>2</sub> ) <sub>0.44</sub> V <sub>2</sub> O <sub>5</sub> ·0.54H <sub>2</sub> O	14.70(2)	-3**	p	0.2

\* Value at room temperature

\*\* The behavior of this material is unusual. The Seebeck coefficient is slightly negative at 300 K but quickly crosses to positive values and remains positive down to the lowest temperature measured (~100 K)

The electron paramagnetic resonance (EPR) spectra of (polymer)<sub>x</sub>V<sub>2</sub>O<sub>5</sub>·nH<sub>2</sub>O show broad (ΔH<sub>pp</sub>~150-200 G) isotropic signals centered around g~1.96 which arise from interacting d<sup>1</sup> vanadium centers. The typical narrow EPR signals arising from static defects in conducting polymers are not observed in these materials, suggesting that the unpaired spins on such static defects are magnetically coupled to the proximal unpaired spins in the V<sub>2</sub>O<sub>5</sub> layers. Therefore, the magnetic behavior of these polymer bronzes is dominated by the paramagnetic V<sub>2</sub>O<sub>5</sub> layered network. The absence of the typical signal observed for these conductive polymers suggests antiferromagnetic exchange between the unpaired density on the polymer backbone and that in the V<sub>2</sub>O<sub>5</sub> slabs. The EPR signal of the polymers [12] returns only after the polymer is separated by dissolving the host matrix. These data show that separation to a polymer and a V<sub>2</sub>O<sub>5</sub> phase does not occur significantly in these materials. Consistent with the EPR data, variable temperature magnetic susceptibility data suggest that these compounds are paramagnetic obeying Curie-Weiss law.

#### Charge Transport Measurements.

The electrical properties of these materials depend strongly on the polymer/V<sub>2</sub>O<sub>5</sub> ratio. Figure 1 shows a comparison of variable temperature electrical conductivity data of several



(polymer)<sub>x</sub>V<sub>2</sub>O<sub>5</sub>·nH<sub>2</sub>O materials, as well as pristine V<sub>2</sub>O<sub>5</sub>·1.6H<sub>2</sub>O and Na<sub>0.40</sub>V<sub>2</sub>O<sub>5</sub>·nH<sub>2</sub>O. The latter was used as a model compound for the reduced state of the vanadium oxide matrix in these materials with interference from the intercalated polymer. Conductivity data for all samples are shown in Table I. The decrease in conductivity with temperature for all samples, indicates thermally activated behavior, as is typical for most conductive polymers [1] and V<sub>2</sub>O<sub>5</sub> bronzes [9]. The reason for this is interparticle contact resistance in the case of conductive polymers and semiconductivity in the case of vanadium bronzes. Thus far, we have found that compounds with high polymer/V<sub>2</sub>O<sub>5</sub> ratio show higher conductivities than corresponding samples with low ratio. Since both the polymer and the V<sub>2</sub>O<sub>5</sub> portions in these materials are potentially capable of charge transport, it is important to determine which would be the preferred charge transport medium. The type and mechanism of charge transport will be different through the various chemical components i.e. polymer, vanadium oxide. If the V<sub>2</sub>O<sub>5</sub> portion is the preferred conduction medium (lowest resistivity) then n-type semiconducting behavior is expected. However, if the polymer section dominates the charge transport then p-type conductivity for polypyrrole and polythiophene, and either n-type or p-type conductivity (depending on the degree of protonation) for polyaniline is expected [13]. Furthermore, charge transport in these conductive polymers is intrinsically metal-like. It should be noted that ionic conductivity is not a significant contributor to the charge transport properties of the (polymer)<sub>x</sub>V<sub>2</sub>O<sub>5</sub>·nH<sub>2</sub>O materials.

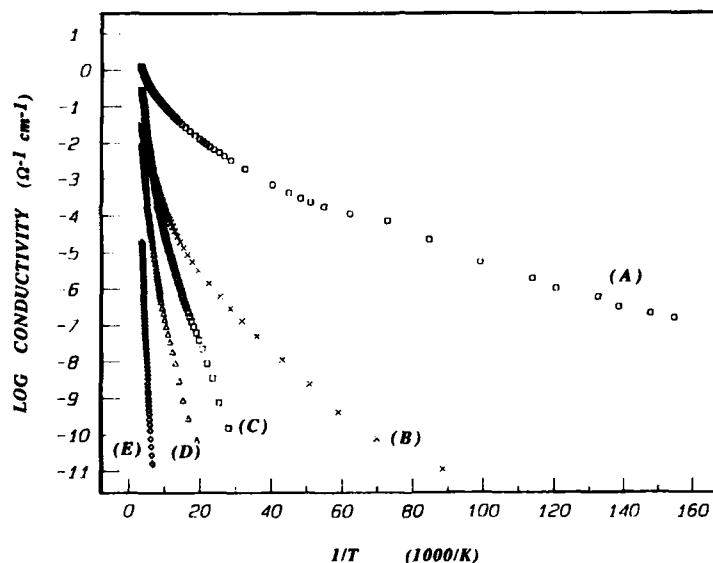


Figure 1. Four probe electrical conductivity data of films of (A) (Ppy)<sub>0.64</sub>V<sub>2</sub>O<sub>5</sub>·0.5H<sub>2</sub>O, (B) (C<sub>8</sub>H<sub>4</sub>S<sub>2</sub>)<sub>0.44</sub>V<sub>2</sub>O<sub>5</sub>·0.54H<sub>2</sub>O, (C) (Pani)<sub>0.44</sub>V<sub>2</sub>O<sub>5</sub>·0.5H<sub>2</sub>O and (D) Na<sub>0.40</sub>V<sub>2</sub>O<sub>5</sub>·1.0H<sub>2</sub>O and (E) vanadium oxide xerogel.

Unlike electrical conductivity measurements, thermoelectric power (TEP) measurements are not subject to interparticle contact resistance effects and could provide more reliable answers to questions of charge transport. TEP data obtained from these materials also show a systematic trend, consistent with the conductivity data. The Seebeck coefficient (S) tends to be small and positive for the polypyrrole and polythiophene samples with high polymer content. The corresponding samples with lower polymer content show large and negative S values. Samples with the lowest polymer content have the most negative S values. As the polymer content increases, the Seebeck coefficient becomes less negative until, after a polymer/V<sub>2</sub>O<sub>5</sub>·nH<sub>2</sub>O threshold ratio, it turns small and positive. Figure 2 shows representative variable temperature TEP data for (Ppy)<sub>x</sub>V<sub>2</sub>O<sub>5</sub>·nH<sub>2</sub>O (x=0.64, 0.22). In the case of (polyaniline)<sub>x</sub>V<sub>2</sub>O<sub>5</sub>·nH<sub>2</sub>O, the Seebeck coefficient is large and negative, when x is low and decreases with falling temperature,

consistent with semiconductive character. The model compound  $\text{Na}_{0.40}\text{V}_2\text{O}_5 \cdot 1.0\text{H}_2\text{O}$  is a n-type semiconductor and shows a large negative Seebeck coefficient which decreases with decreasing temperature. In high polyaniline/ $\text{V}_2\text{O}_5 \cdot n\text{H}_2\text{O}$  ratios the Seebeck coefficient is smaller, negative, but it increases toward zero at low temperatures, consistent with metal-like behavior. Room temperature TEP data are shown in Table I.

The charge transport data presented here indicate that in compounds with high polymer/ $\text{V}_2\text{O}_5$  ratio the charge transport occurs primarily through the polymer section while in compounds with low polymer/ $\text{V}_2\text{O}_5$  ratio the inorganic network is primarily responsible for the conductivity.

The dependence of electrical properties on the polymer/ $\text{V}_2\text{O}_5$  ratio probably reflects the variation in the average distance between polymer chains in the intralamellar region of the vanadium oxide host. Low polymer/ $\text{V}_2\text{O}_5$  ratios will result in long interchain distances thus making interchain electron (or hole) transport less favorable. In this case, charge transport through the polymer is inhibited to the point that it becomes more favorable to transport charge through the  $\text{V}_2\text{O}_5$  network, thus giving rise to n-type semiconducting characteristics. This is supported by the fact that alkali metal bronzes of these xerogels such as  $\text{Na}_{0.40}\text{V}_2\text{O}_5 \cdot 1.0\text{H}_2\text{O}$  and  $\text{K}_x\text{V}_2\text{O}_5 \cdot n\text{H}_2\text{O}$ , exhibit conductivity and thermoelectric power very similar to low polymer/ $\text{V}_2\text{O}_5$  ratio materials [14]

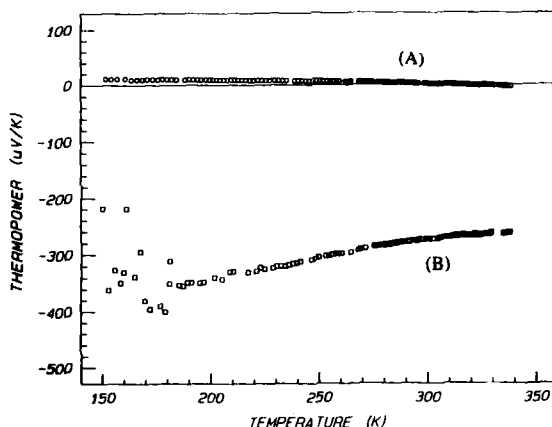


Figure 2. Variable temperature thermoelectric power data for (A)  $(\text{Ppy})_{0.64}\text{V}_2\text{O}_5 \cdot 0.5\text{H}_2\text{O}$ , (B)  $(\text{Ppy})_{0.22}\text{V}_2\text{O}_5 \cdot 0.68\text{H}_2\text{O}$ . Electrical contacts were made using gold wire [15].

**Acknowledgement.** Financial support from the Center Fundamental Materials Research of Michigan State University and the NSF for a Presidential Young Investigator Award is gratefully acknowledged. At Northwestern University support was provided by ONR; this work made use of Central Facilities supported by NSF through the Materials Research Center.

#### REFERENCES

- [1] (a) "Proceedings of the International Conference on Science and Technology of Synthetic Metals (ICSM'88)" Aldissi, M. (ed) *Synth. Met.* 1989, 27-29, references therein. (b) Skotheim, T.A. (ed) in "Handbook of Conductive Polymers", Marcel Dekker: New York, Vol. 1,2, 1986 (c) Marks, T. J. *Science*, 1985, 227, 881-889

- [2] (a) Kanatzidis, M. G.; Tonge, L. M.; Marks, T. J.; Marcy, H. O.; Kannewurf, C. R. *J. Am. Chem. Soc.* **1987**, *109*, 3797-3799 (b) Kanatzidis, M. G.; Marcy, H. O.; McCarthy, W. J.; Kannewurf, C. R.; Marks, T. J. *Solid State Ionics* **1989**, *32/33*, 594-608 (c) Kanatzidis, M. G.; Hubbard, M.; Tonge, L. M.; Marks, T. J.; Marcy, H. O.; Kannewurf, C. R. *Synth. Met.* **1989**, *28*, C89-C95
- [3] Wu, C.-G.; Kanatzidis, M.G.; Marcy, H.O.; DeGroot, D.C.; Kannewurf, C.R. submitted for publication
- [4] (a) Kanatzidis, M.G.; Wu, C.-G.; Marcy, H.O.; Kannewurf, C.R. *J. Am. Chem. Soc.* **1989**, *111*, 4139-4141 (b) Wu, C.-G.; Kanatzidis, M.G.; Marcy, H.O.; DeGroot, D.C.; Kannewurf, C.R. *Polym. Mat. Sci. Eng.* **1989**, *61*, 969-973. (c) Wu, C.-G.; Kanatzidis, M.G.; Marcy, H.O.; DeGroot, D.C.; Kannewurf, C.R. NATO Advanced Study Institute "Lower Dimensional Systems and Molecular Devices" R. M. Metzger, Ed. Plenum Press, Inc. 1989 in press
- [5] Wu, C.-G.; Marcy, H.O.; DeGroot, D.C.; Kannewurf, C.R.; Kanatzidis, M.G. submitted for publication
- [6] Brandt, P.; Fischer, R. D.; Martinez, E.S.; Calleja, R. D. *Angew. Chem. Int. Ed. Engl.* **1989**, *28*, 1265-1266
- [7] (a) Bein, T.; Enzel, P. *Synth. Met.* **1989**, *29*, E163-E168 (b) Enzel, P.; Bein, T. *J. Phys. Chem.* **1989**, *93*, 6270-6272 (c) Enzel, P.; Bein, T. *J. Phys. Chem.* **1989**, *93*, 6270-6272
- [8] Day, P. *Phil. Trans. R. Soc. Lond. A* **1985**, *314*, 145-158
- [9] (a) Hagemuller, P in "Non-stoichiometric Compounds, Tungsten Bronzes, Vanadium Bronzes and Related Compounds" Bevan, D.J.; Hagemuller, P. (eds), Vol. 1, Pergamon Press, Oxford 1973
- [10] (a) Aldebert, P.; Baffier, N.; Legendre, J.-J.; Livage, J. *Revue Chim. Min.* **1982**, *19*, 485-495. (b) Masbah, H.; Tinet, D.; Crespin, M.; Erre, R.; Setton, R.; Van Damme, H. *J. Chem. Soc., Chem. Commun.* **1985**, 935-936 (c) Gharbi, N.; Sanchez, C.; Livage, J.; Lemerle, J.; Nejem, L.; Lefebvre, J. *Inorg. Chem.* **1982**, *21*, 2758-2765.
- [11] (a) Bullot, J.; Gallais, O.; Gauthier, M.; Livage, J. *Appl. Phys. Lett.* **1980**, *36*, 986-988. (b) Sanchez, C.; Babonneau, F.; Morineau, R.; Livage, J.; Bullot, J. *Philos. Mag. [Part] B* **1983**, *47*, 279-290. (c) Bullot, J.; Cordier, P.; Gallais, O.; Gauthier, M.; Livage, J. *J. Non-Cryst. Solids* **1984**, *68*, 123-134.
- [12] (a) Schärli, M.; Kiess, H.; Harbeke, G.; Berlinger, W.; Blazey, K. W.; Müller, K. A. *Synth. Met.* **1988**, *22*, 317-336
- [13] Javadi, H.H.S.; Laversanne, R.; Epstein, A.J.; Kohli, R.K.; Scherr, E.M.; MacDiarmid, A.G. *Synth. Met.* **1989**, *29*, E439-E444
- [14] Wu, C.-G.; Marcy, H.O.; DeGroot, D.C.; Kannewurf, C.R.; Kanatzidis, M.G. work in progress
- [15] Although not critical for the data in curve (B), the data in curve (A) must be corrected for the contribution of the gold thermopower. This correction will shift the data by a small amount (ca. 1-2  $\mu$ V depending on the temperature) toward more positive values, thus bringing the entire curve (A) on the positive scale of the plot.

CHEMICAL AND PHYSICAL PROPERTIES OF SOLUBLE PART OF EMERALDINE:  
COMPARISON WITH INSOLUBLE EMERALDINE.

R. LAVERSANNE\* and P. VACA‡

\*Centre de Recherche Paul Pascal, CNRS, Château Brivazac, F-33600 Pessac FRANCE

‡Laboratoire CPMOH, Université de Bordeaux I, F-33405 Talence FRANCE

## ABSTRACT

A preliminary physical study of the soluble part of emeraldine is presented. The electrical and magnetic properties of this low weight material are very similar of those of the pristine emeraldine salt. These results emphasize the possible role of short chain species in the conduction mechanism of polyaniline. In order to clarify this point, previous magnetic investigations on insoluble emeraldine salts are revisited. It appears that the fit of the magnetic susceptibility temperature dependence of polyaniline with a Curie law plus a Pauli term might not be justified at low temperature. A  $T^{-\alpha}$  law with  $\alpha = 0.75$  gives a better fit suggesting a behavior similar to the one found in Random Exchange Heisenberg Antiferromagnetic Chain (REHAC).

## INTRODUCTION

Among conducting polymers, Polyaniline (PANI) has been of special interest because of its ability to encover insulator to conductor transition upon protonation [1, 2]. The partly oxidized form of PANI called emeraldine [3], shows an electrical conductivity increasing from  $10^{-10} \text{ Scm}^{-1}$  in the base form up to  $5 \text{ Scm}^{-1}$  for 50% protonation [1, 4]. Numerous studies have been performed to tentatively elucidate the conduction mechanism in this polymer [5]. Yet controversy is still alive upon the existence of *metallic islands* in emeraldine salts [6]. On the one hand the defenders of this picture have proposed that a Pauli susceptibility can be deduced from magnetic measurements [7]. Moreover studies on transport properties [8], where an  $\exp(-(T/T_0)^{1/2})$  law is demonstrated for electrical conductivity, as well as microwave measurements [9] may be interpreted in agreement with this model.

On the other hand the opponents to this model [10-12] give several arguments against a true metallic behavior. The electrical conductivity of emeraldine salt is too low compared to other polymers with genuine metallic conductivity, and can almost be reached with oligomers as short as eight units [10]. The temperature dependence of the electrical conductivity is understandable in terms of hopping of rather localized charges [11] and the disordered nature of this polymer should always be kept in mind when describing its properties [12].

Besides, in a recent study on a crystalline emeraldine salt [13], a Pauli susceptibility has been seen at high temperature from EPR measurements, while at lower temperature the susceptibility becomes temperature dependent. This has been interpreted as the onset of a homogeneous metallic behavior at high temperature, destroyed by disordered induced localization at low temperature.

In the first part of this paper we describe an experimental study of the low weight species obtained as a soluble part of emeraldine base. Electrical conductivity and EPR are described at room temperature for values of protonation level ranging between 0% and 50%. These results are compared with those previously obtained upon protonation for the insoluble part of the base. In a second part a new interpretation of the magnetic behavior of insoluble emeraldine salts is given in light of the results found on short chains species. The validity of the decomposition of the magnetic susceptibility of insoluble emeraldine salts into a Pauli term plus a Curie law over the whole temperature range is then discussed.

## SOLUBLE PART OF EMERALDINE

### Experimental

Emeraldine base has been prepared by ammonium persulfate oxidation in pH = 0 medium as previously described [14]. Care has been taken to avoid exposure of the material to the air. Extraction of the soluble part of the polymer has been done through suspension of the base powder in THF and sonication for 5 min. Filtration and subsequent washing of the powder gave the insoluble part of the material. Evaporation of the combined dark blue solutions gave the so called soluble part of emeraldine. Salts of different protonation levels have been obtained by suspension in aqueous solution of determined pH according to published values [14].

Two probe conductivity measurements have been performed at room temperature on compressed pellets using a HP 4194 A impedance analyser between 100 Hz and 40 MHz, the high frequency measurements being used to check the quality of the contacts. ESR experiments have been done on powder, in vacuum sealed quartz tubes using a Varian X band spectrometer. Care has been taken to avoid saturation of the signal and absorption of the microwaves (very low sample mass and very low power output). Absolute values of the spin susceptibility have been obtained using a weighed sample of DPPH as a reference. Nevertheless a large degree of inaccuracy is usual in these determinations. X-ray diffraction patterns have been obtained on powdered samples in Lindemann tubes using an Inel curved detector and the Cu  $K_{\alpha}$  radiation.

### Results

The IR spectrum of the soluble part of PANI is reported in Fig. 1. The main features of the IR spectrum of emeraldine base are present as compared to published data [10]. Moreover the sharpness of the peaks is in agreement with the presence of short chains species. The elemental analysis shows that oxygen is present in the sample. Such a point has to be related with the extracting of benzoquinone from air exposed samples of emeraldine [15]. This could be at the origin of the weak band visible around  $1680\text{ cm}^{-1}$  on the IR spectrum. Finally, a mass spectroscopy analysis using FAB technique has failed to detect any mass higher than 863 in the soluble material.

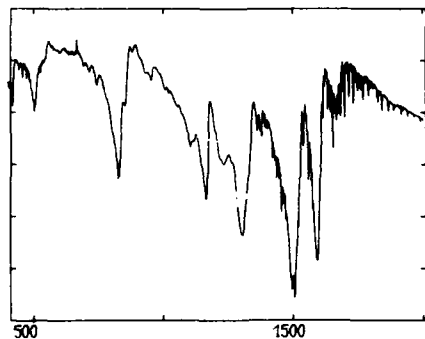


Fig. 1 : IR spectrum of soluble part of emeraldine base (KBr pellet).

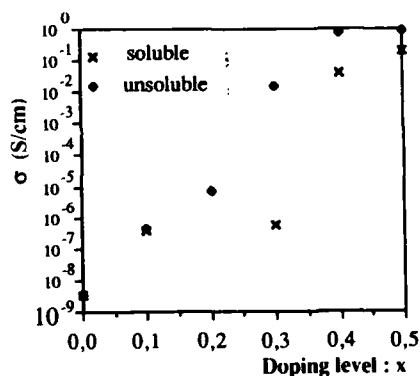


Fig. 2. Variation of the room temperature electrical conductivity with protonation for soluble and insoluble emeraldine

The room temperature electrical conductivity measurements for both the soluble and insoluble parts of emeraldine are plotted as a function of the doping level  $x$  in Fig. 2. The maximum value of the conductivity, found for  $x = 0.5$  is of the same order of magnitude for both materials and is only slightly smaller than the conductivity usually found in emeraldine. However for lower doping levels a striking difference appears between soluble and insoluble materials. While

conductivity of insoluble samples decreases smoothly with  $x$ , a threshold is seen on the conductivity vs. protonation curve for the soluble part of emeraldine,  $\sigma$  changing by more than 4 orders of magnitude around  $x = 0.3$ . The frequency dependence of the room temperature conductivity is the same for all the samples, and remains resistive up to 1 MHz.

X-Ray diffraction pattern of the soluble base is presented in Fig. 3. The deduced parameters are similar to those of EB-II obtained through THF washing and recrystallization in NMP [16]. Moreover this sample exhibits a higher crystallinity than that found for EB-II samples. Nevertheless it should be noted that the crystallinity of the sample is highly dependent upon the experimental conditions, as expected for crystallization of samples through solvent evaporation.

Spin susceptibility has been measured at room temperature as a function of protonation for the soluble emeraldine. The results are shown in Fig. 4. A rapid increase of the susceptibility is observed around  $x = 0.25$  as already found for ES-II [16]. This onset of the magnetic susceptibility around  $x = 0.25$  has to be compared with the threshold effect seen on the electrical conductivity. Nevertheless it should be noted that the jump occurs at slightly different protonation levels

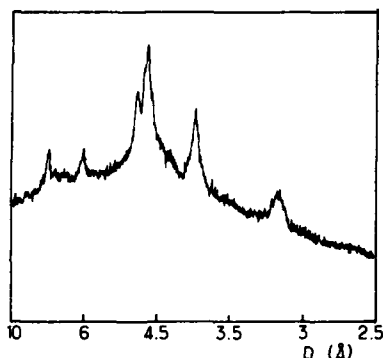


Fig. 3 : X-Ray diffraction pattern of a powdered sample of soluble part of emeraldine base.

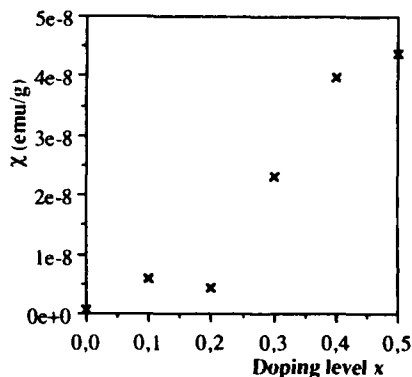


Fig. 4 : Variation of the room temperature spin susceptibility of soluble part of emeraldine with protonation.

### Discussion

The presence of short chains species in polyaniline has been supposed for a long time [14]. Washing the emeraldine base has been the usual way to remove these low molecular weight materials from the polymer. This soluble material has long been considered as impurities and discarded. However the high conductivity of oligomers has been evidenced through direct synthesis of phenyl-capped octaaniline [17].

Our results clearly show that the short chains species extracted through light solvent solubilization of emeraldine are conducting materials. The room temperature electrical conductivity of the  $x = 0.5$  protonated material is almost the same as the one obtained for classical insoluble emeraldine salt although lower than that of highly crystalline sample [13] or of high molecular weight polymer [18]. The magnetic behavior is reminiscent of that of insoluble emeraldine [19], as far as room temperature results are concerned. Moreover the crystallinity of the soluble base is comparable or higher than that of the insoluble one.

One conclusion which can be drawn from the above results is that the soluble part of emeraldine is a material that is worth studying more deeply. It presents high conductivity in the protonated form, good crystallinity and the solubility needed for processing. This material has to be compared with soluble polyaniline obtained by new oxidative routes [20, 21].

Moreover these results, and their similarity with the results obtained for pristine emeraldine, suggest that the electronic properties of polyaniline could be at least partly due to short chains species embedded in an insulating polymer as already proposed from spin dynamic studies [12, 22]. This does not preclude a material in which the so called short chains species are in fact part of longer chains but would be isolated by chemical defects. It should be noted that in such picture the size of the conducting segments is not expected to change during protonation. The

onset of electrical conductivity above a threshold around  $x = 0.3$  in soluble emeraldine could be accounted for by percolation process between conducting chains of finite size.

#### MAGNETIC PROPERTIES OF INSOLUBLE EMERALDINE REVISITED

The description of polyaniline as a genuine metal is mainly based on the decomposition of the magnetic susceptibility of emeraldine salts into a sum of Curie and Pauli terms [6, 7]. This observation has been deduced from static magnetic measurements in which the Pauli susceptibility of the base has been supposed to be zero in order to precisely estimate the diamagnetic susceptibility [6]. However the classical decomposition ( $\chi = C/T + \chi_p$ ) has never been perfect, and an unconventional behavior of the number of Curie spins has been proposed, with  $C$  being temperature dependent [6]. Temperature dependence of the number of spins has been observed in other experiments on insoluble emeraldine salts [8], as well as on the highly crystalline material [13].

One way to avoid the problem of determining the core value is to perform dynamic measurements. ESR experiments on emeraldine salts have been performed between 4K and 300K and recently published [19]. The Curie and Pauli components of the susceptibility are well visible on a plot of the product  $\chi T$  versus temperature as presented in Fig. 5 for the insoluble emeraldine base and for the corresponding  $x = 0.5$  salt. It can be seen that both the salt and the base exhibit a non zero slope of the product  $\chi T$ . Moreover the values of the slope, namely  $\chi_p$ , are very similar for the base and for the  $x = 0.5$  salt. Finally at low temperature both curves diverge from the linearity and drop to smaller values. A similar behavior is observed for all the salts with intermediate protonation levels. In particular the ratio between the Pauli and the spin susceptibility remains similar for all the protonation levels including the base (see Table I).

Protonation level	$\chi_{\text{Pauli}}/\chi_{\text{Spin}}$	$\alpha$
0.	0.8	0.78
0.2	0.4	0.53
0.3	0.5	0.82
0.4	0.6	0.62
0.5	0.5	0.73

Table I: Variation of the ratio of the Pauli over spin susceptibility and  $\alpha$  (see text) for different protonation levels of insoluble emeraldine.

The discrepancies outlined above lead to the following questions:

- Why is there a change in the number of Curie spins with temperature ?
- How can we conciliate Pauli susceptibility and insulating material as emeraldine base ?
- Why does not the ratio of Pauli over Curie susceptibilities change with protonation ?

Answers at the first question have been given within the framework of the *metallic islands* model [7]. The two other are much more difficult to address. In fact the discrepancy could arise from the hypothesis that the susceptibility may be decomposed over the whole temperature range into two terms, one of which being temperature independent.

Fig. 6 is a log-log plot of the spin susceptibility versus temperature for emeraldine base and  $x = 0.5$  salt. For both samples the experimental points can be fitted with a straight line of slope  $\alpha = 0.75$ . Similar behavior is observed for other protonation levels, the observed values of  $\alpha$  being summarized in Table I. Such a behavior is reminiscent of the so called REHAC systems (Random Exchange Heisenberg Antiferromagnetic Chains) [23] in which the thermodynamics of the spins is governed by a random distribution of the exchange related to microscopic disorder. This model has been developed for charge transfer salts where disorder is due to unsymmetrical anions. In polyaniline disorder is known to be present in the structure. Antiferromagnetic exchange has been supposed in order to explain the rather low ESR linewidth of this material especially at low temperature [19]. Therefore a susceptibility governed by random exchange is not excluded in this material. Finally it should be noted that such model is not in contradiction with the proposal of a *textured metallic islands* model proposed to describe transport properties [9]

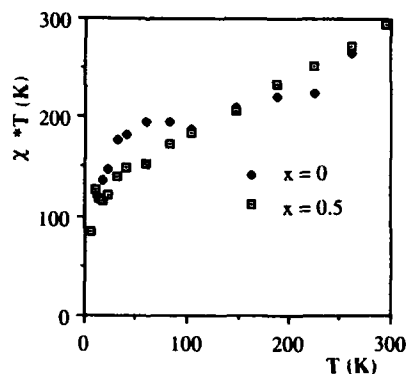


Fig. 5 : Product  $\chi*T$  versus temperature for two insoluble emeraldine samples.

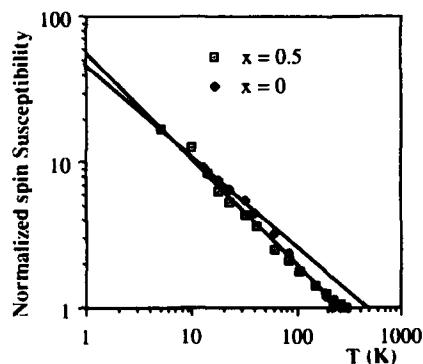


Fig. 6: Log-Log plot of the temperature dependence of the spin susceptibility of two insoluble emeraldine samples. The lines are guides for the eyes.

#### Conclusion

This study of the soluble part of emeraldine has shown that high electrical conductivity can be achieved in a low weight compound extracted from polyaniline. This should initiate more study on this material. Moreover it introduces some doubt about the validity of the decomposition of the susceptibility into Pauli plus Curie terms over the whole temperature range. At low temperature a  $T^{-\alpha}$  law fits better the experimental data, suggesting that exchange and disorder should be considered when describing the exciting properties of emeraldine. This point deserves to be confirmed by further experimental as well as theoretical studies.

#### Acknowledgements

The authors are indebted to Dr. C. Coulon and Dr. A.J. Epstein for fruitful discussions.

#### REFERENCES

1. R. de Surville, M. Josefowicz, L.T. Yu, J. Périchon and R. Buvet, *Electrochim. Acta*, **13**, 1451 (1968).
2. A.G. MacDiarmid, J.C. Chiang, M. Halpern, W.S. Huang, S.L. Mu, N.L.D. Somasiri, W.Wu and S.I. Yaniger, *Mol. Cryst. Liq. Cryst.*, **121**, 173 (1985)
3. E.M. Genies and C. Tsintavis, *J. Electroanal. Chem.*, **200**, 127 (1986)
4. J.C. Chiang and A.G. MacDiarmid, *Synth. Metal.*, **13**, 193 (1986)
5. For a recent review, see Proceedings of the International Conference on Science and Technology of Synthetic Metals (ICSM '88) Santa Fe, NM, USA June 26-July 2, 1988, in *Synth. Metal.*, **22**, E141-E457 (1989).
6. A.J. Epstein, J.M. Ginder, F. Zuo, R.W. Bigelow, H.S. Woo, D.B. Tanner, A.F. Richter, W.S. Huang and A.G. MacDiarmid, *Synth. Metal.*, **18**, 303 (1987).
7. J.M. Ginder, A.F. Richter, A.G. MacDiarmid and A.J. Epstein, *Solid State Comm.*, **63**, 97 (1987).



8. F. Zuo, M. Angelopoulos, A.G. MacDiarmid and A.J. Epstein, *Phys. Rev. B*, **36**, 3475 (1987).
9. H.H.S. Javadi, K.R. Cromack, A.G. MacDiarmid and A.J. Epstein, *Phys. Rev. B*, **39**, 3579 (1987).
10. F. Wudl, R.O. Angus Jr., F.L. Lu, P.M. Allemand, D.J. Vachon, M. Nowak, Z.X. Liu and A.J. Heeger, *J. Amer. Chem. Soc.*, **109**, 3677 (1987)
11. A.P. Monkman, D. Bloor, G.C. Stevens, J.C.H. Stevens and P. Wilson, Proceedings of the International Conference on Science and Technology of Synthetic Metals (ICSM '88) Santa Fe, NM, USA June 26-July 2, 1988, in *Synth. Metal.*, **29**, E277 (1989).
12. M. Nechstein, F. Genoud, C. Menardo, K. Mizoguchi, J.P. Travers and B. Villeret, *ibid*, p E211.
13. C. Fite, Y. Cao and A.J. Heeger, *Solid State Comm.*, **70**, 245 (1989)
14. A.G. MacDiarmid, J.C. Chiang, A.F. Richter, N.L.D. Somasiri and A.J. Epstein in *Conducting Polymers*, edited by L. Alcacer (D. Reidel Publishing Co., The Netherlands, 1987), p. 105.
15. A. Ray, G.E. Asturias, D.L. Kershner, A.F. Richter, A.G. MacDiarmid and A.J. Epstein, Proceedings of the International Conference on Science and Technology of Synthetic Metals (ICSM '88) Santa Fe, NM, USA June 26-July 2, 1988, in *Synth. Metal.*, **29**, E141 (1989).
16. M.E. Jozefowicz, R. Laversanne, H.H.S. Javadi, A.J. Epstein, J.P. Pouget, X. Tang and A.G. MacDiarmid, *Phys. Rev. B*, **39**, 12958 (1987).
17. F.L. LU, F. Wudl, M. Nowak and A.J. Heeger, *J. Amer. Chem. Soc.*, **108**, 8311 (1986)
18. A.G. MacDiarmid, G.E. Asturias, D.L. Kershner, S.K. Manohar, A. Ray, E.M. Scherr, Y. Sun, X. Tang and A.J. Epstein, *Polymer Preprints*, **30**, 147 (1989)
19. H.H.S. Javadi, R. Laversanne, A.J. Epstein, R.K. Kohli, E.M. Scherr and A.G. MacDiarmid, Proceedings of the International Conference on Science and Technology of Synthetic Metals (ICSM '88) Santa Fe, NM, USA June 26-July 2, 1988, in *Synth. Metal.*, **29**, E439 (1989)
20. M. Inoue, R.E. Navarro and M.B. Inoue, *Synth. Metal.*, **30** (1989)
21. S. Li, H. Dong and Y. Cao, Proceedings of the International Conference on Science and Technology of Synthetic Metals (ICSM '88) Santa Fe, NM, USA June 26-July 2, 1988, in *Synth. Metal.*, **29**, E329 (1989).
22. K. Mizoguchi, M. Nechstein, J.P. Travers and C. Menardo, *ibid*, p E417
23. L.N. Bulaevskii, A.V. Zvarykina, Y.S. Karimov, R.B. Lyubovskii and I.F. Shchegolev, *Sov. phys. JETP*, **35**, 384 (1972)  
G. Theodorou and M.H. Cohen, *Phys. Rev. B*, **16**, 4104 (1977)  
L.C. Tippie and W.G. Clark, *ibid*, **23**, 5854 (1981)

POLYANILINE AS A REVERSIBLY SWITCHABLE ELECTROCHROMIC MATERIAL

WOAN-RU SHIEH\*, SZE C. YANG\*, CHARLES MARZZACCO#, JYUN-HUEI HWANG\*

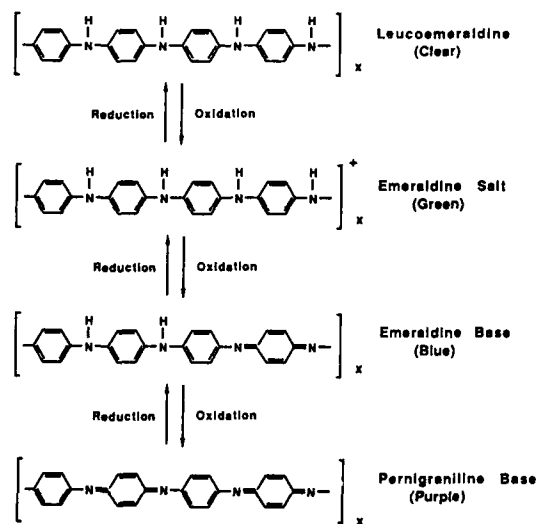
\*Department of Chemistry, The University of Rhode Island, Kingston, RI 02881

#Department of Physical Sciences, Rhode Island College, Providence, RI 02908

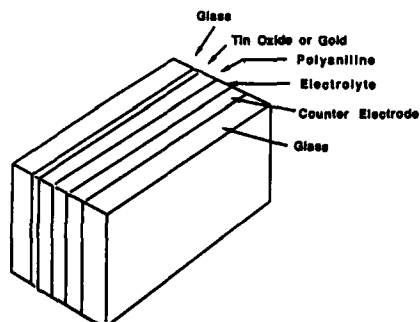
INTRODUCTION

Polyaniline is an interesting electrochromic material because its color can be changed from clear to green, to blue, and to purple by electrochemical oxidation[1]. The structural transformations associated with these color changes are shown in Scheme I. One of the possible applications for polyaniline is to use it as the active material in electrochromic windows.

An electrochromic window is a multi-layered device (Scheme II) with the structure of a transparent rechargeable battery. A practical electrochromic window needs to have long color-cycling lifetime and good durability under solar radiation. This is a severe requirement because all layers of materials in Scheme II and interfaces between layers have to be durable under



Scheme I Oxidation and Reduction of Polyaniline



Scheme II Diagram of An Electrochromic Window

such electrochemical and photochemical stress.

In this communication we report an initial study towards the construction of a polyaniline-based electrochromic window. We concerned ourselves with only half of the device shown in Scheme II, which consists polyaniline coated on tin oxide glass. We tested such a half-cell in an aqueous electrolyte to see if this part of the electrochromic device can be made durable enough for electrochromic applications and to find useful designing principles for constructing good devices. Our tests were confined to switching between the clear and the green colors of polyaniline because its purple form is known to have limited electrochemical stability[2].

## RESULTS AND DISCUSSION

### Electrochemical Stability of Polyaniline

Thin film polyaniline was polymerized from acidic aniline monomer solution (1.5 M aniline in 3 M HCl solution) by potentiostatic (0.65 V vs. S.C.E.) electrochemical oxidation. Tin oxide coated on glass was used as a transparent working electrode and platinum was used as a counter electrode. Details of the synthesis and the optical spectra of polyaniline films have been reported in reference 1. During the electro-polymerization, a thin film of polyaniline (about 500 nm in thickness) adheres to tin oxide electrode surface. For convenience in the following discussion we designate the sample as S-type polyaniline/SnO<sub>2</sub> which denotes polyaniline synthesized by potential static electrolysis and coated on a SnO<sub>2</sub> coated glass transparent electrode.

To test the electrochromic cycling lifetime, this half-cell is immersed in 0.1 M HCl or a pH buffered solution, and the electrochemical potential of polyaniline is potentiostatically controlled by a saturated calomel reference electrode (S.C.E.). Charging capacity was determined by measuring the area enclosed in periodically measured cyclic voltammograms.

Figure 1 shows the charging capacity as the potentials were cycled continuously between 0.4 V and -0.2 V vs. S.C.E. at a scan rate of 10 mV/sec. The cell was cycled for 10<sup>5</sup> times continuously (which took 700 hours). The charging capacity is essentially constant throughout the test except for a slight decrease during the first 10<sup>4</sup> cycles. After this initial period the charging capacity curve is flat all the way to the end of the test.

These data show that polyaniline is electrochemically stable at these two color states. During 10<sup>5</sup> cycles of test, the polymer molecules did not degrade by reacting with their neighboring polymer molecules, the electrolyte, or the contacting electrode surface. Neither did it undergo conformational or physical phase transitions that would result in loss of reversibility in electrochromic transformations.

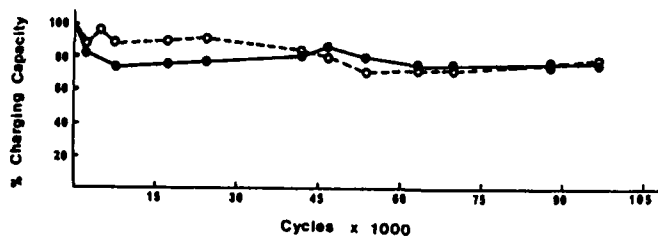


Figure 1. Charging capacity as a function of the number of clear-green electrochromic cycles. The samples, S-type polyaniline/SnO<sub>2</sub>, were either exposed to simulated solar radiation (○---○) or shielded from light (●—●).

### Photochemical Stability of Polyaniline

A high pressure xenon arc lamp was used to irradiate the sample while it is electrochemically cycled. Since the tests were performed in an aqueous electrolyte, the radiation passed through water before reaching the test cells (path length : 5.5 cm). The spectral distribution of radiation[3] shining upon the polymer film simulates the solar radiation for March at 34° north latitude (in the wavelength range of 300 nm to 900 nm)[4]. The result of the test for an irradiated sample is plotted in Figure 1 to compare with the color cycling test in dark. This comparison shows that there is no loss of charging capacity in irradiated samples during the same  $10^5$  cycles (700 hours) of tests. The implication is that although polyaniline absorbs solar radiation, it does not undergo any irreversible photochemical reaction. The observed photochemical stability is not surprising because the strong electron-phonon interaction present in conducting polymer provides an extremely efficient pathway to quench any electronically excited state created by absorption of radiation energy.

### The Polyaniline/Electrode Interface

Our test cells consist not only the electrochromic polymer, polyaniline, but also an polyaniline/SnO<sub>2</sub> interface. The fact that such sample passed a test shown in Figure 1 implies that the interface between polyaniline and SnO<sub>2</sub> electrode in this sample was durable enough to withstand electrochemical cycling and solar radiation. This does not mean that all the factors that influence the quality of the interface are understood. In fact, the factors are poorly understood and that sometimes leads to an "apparent" lack of reproducibility of the durability of the interface. There are, however, some factors in the synthesis of polyaniline we found to be controllable and have reproducible influence on the durability of the electrochromic device. An example will be shown here that involves using an electrochemical synthesis method slightly different from that of the S-type cell mentioned before.

As the aforementioned S-type cells, these samples were also made by electrochemical polymerization of aniline except that the electrochemical potential was not held at a static value as in the S-type sample, instead the potential was cycled between +0.7 V and -0.2 V vs. S.C.E. with a scan rate of 10 mV/sec. We denote these half-cells as C-type samples for they were made by cycling the electrochemical potential. Similar charging capacity tests were performed on the C-type samples and the results are shown in Figure 2. In contrast to the nearly perfect retention of charging capacity for the S-type samples, the C-type sample lost about 40% of its charging capacity within the initial 15,000 cycles (which corresponds to the "work-in" period for the S-type sample). After this initial loss, the charging capacity stayed constant throughout the rest of this test which lasted for  $10^5$  cycles.

Because we have just shown in Figure 1 that polyaniline molecules are

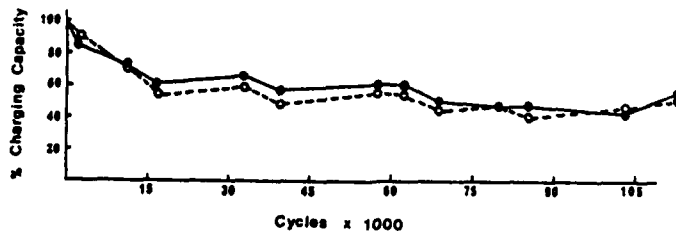


Figure 2. Charging capacity of C-type polyaniline film coated on tin oxide glass. The testing condition was the same as that for Figure 1 except that the cycling potential was from 0.4V to 0V.

electrochemically and photochemically stable, it is unlikely that the polymer would become chemically unstable just because the method of synthesis is slightly changed (potential cycling vs. potentiostatic). Furthermore, if the C-type polymer is more reactive, then the degradation should continue as the test goes on; it would be difficult to explain why the reactivity should stop after the initial period of cycling. The initial loss of charging capacity is not due to chemical transformation of the polymer into any non-switchable form because the UV-VIS spectra (data not shown) did not reveal any new band as the test progressed, and the absorption bands were still those of polyaniline. The only observed change in spectra was that as the charging capacity decreased the absorption intensity decreased proportionally, which signifying a loss of polyaniline from the electrode. Indeed, in a few tests we found that portions of polyaniline film detached from the electrode, which implies that poor adhesion of small portion of the polymer might be the cause of the initial decay. Nonetheless, the interfaces became durable after the loosely adhered polymer was removed.

Our study shows that the initial loss of charging capacity is due to



(A)



(B)

Figure 3. Scanning electron micrograph of first S-type polyaniline layer coated on tin oxide glass (A) and first C-type polyaniline layer coated on tin oxide (B).

loss of adhesion of polyaniline on tin oxide substrate rather than a chemical or physical transformation of an intact polyaniline film. The electrochromic film becomes less dense by loosing small particles of polyaniline from the electrode surface. After the initial loss of a portion of polyaniline film, the remaining adhered portion of the film retains its charging capacity in a way quite similar to that of the S-type cell.

In order to understand the reason for the differences in the interfacial adhesion, we examined the morphology of the polyaniline/SnO<sub>2</sub> interface using scanning electron microscopy (Figure 3). The polymer morphologies at the interface are different for these two types of samples. The first layer of polyaniline in S-type samples have about 150 nm diameter fibers[5], sparsely anchoring on tin oxide surface (figure 3A). However, the morphology of C-type sample is formed by packing globules of polyaniline with about 200 to 300 nm diameters (Figure 3B). We believe the difference in void space at the interface of these two types of samples is the reason for the difference in performance. The S-type samples have enough void space at the interface for polymer fibers to swell and contract during the color switchings; but the C-type samples are packed densely at the interface so strain is developed when polyaniline swells and contracts during each color-switching cycle. In the initial "work-in" period a portion of polyaniline lost adhesion due to this cycling induced strain at the interface.

Polyaniline swells and contracts in a color-switching cycle because of the hydrophilicity of the polymer changes as the color is changed. The clear-state, although partially protonated, is less hydrophilic than the green-colored state which has additional positive charges on the polymer backbone (the polarons, see scheme I). Therefore, polyaniline swells when the color turns to green and contracts when it turns to clear.

If the "breathing space" at the interface is indeed important as we proposed, a sample with densely packed interfacial morphology would have adhesion problem even if it is made by potentiostatic electrolysis similar to the S-type polyaniline/SnO<sub>2</sub> cell. One example is by substituting the SnO<sub>2</sub> electrode with a gold electrode as shown in Figure 4. The first layer exhibits a much denser formation than those grown on tin oxide. Gold surface appears to be a better electrode catalyst for forming nucleation sites for polyaniline to grow into fibers; a higher surface density of nucleation sites leads to a denser first-layer morphology. Figure 5 shows the test results of such an S-type film on gold. The charging capacity could be maintained for more than  $2.4 \times 10^5$  cycles, indicating that both the interface and the polymer were quite durable. There was, however, a small but discernible initial loss of charging capacity during the initial 15,000 cycles. Although

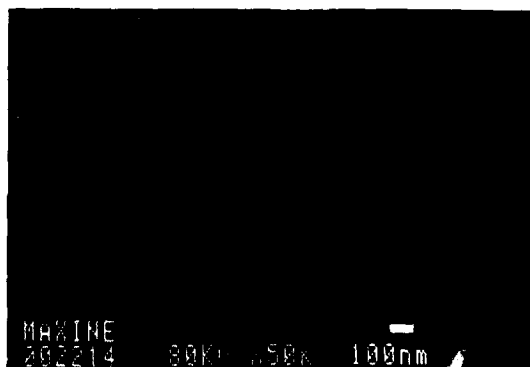


Figure 4. Scanning electron micrograph of first layer S-type polyaniline film electrochemically grown on gold electrode.

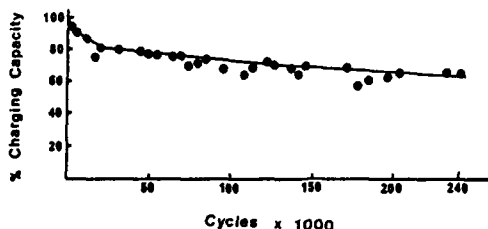


Figure 5. Charging capacity of S-type polyaniline film coated on gold. The test was performed in 0.1 M acetate buffer, pH 5, containing 1 M KCl with a scan rate of 100 mV/sec and potential range of 0.25V to -0.2V.

the extent of loss for S-type polyaniline/gold is less than for C-type polyaniline/SnO<sub>2</sub>, the patterns are similar: during the initial work-in period, "breathing room" is created by shedding off excess polyaniline at the interface, as the strain is relieved the charging capacity levels off and maintains at a constant value in the subsequent cycles.

#### SUMMARY

This study shows that polyaniline is both electrochemically and photochemically stable enough to be used as electrochromic material for clear-to-green color switching. This study also shows that if the polyaniline/electrode interface is densely packed to leave insufficient "breathing space" for the polymer to swell and contract during color switching, the density of polyaniline at the interface will be re-adjusted during the initial electrochemical cycles by losing some polymer fibers to relieve the strain.

From this study we learned a useful guideline for making good polyaniline/electrode interface for electrochromic applications. There is an optimum density of polyaniline fibers at the interface: the packing of polyaniline fibers should be dense enough to get fast charge transfer between the electrode and the polymer, but not too dense to cause strain when the fibers swell and contract during the electrochromic cycles. The scanning electron microscopy can be used as a diagnostic tool for such interfaces.

#### ACKNOWLEDGMENT

This work is supported in part by PPG Industries and by Office of Naval Research from DARPA. We thank Ms. Grace Ordonio and Mr. Michael Marsella for technical assistance.

#### REFERENCES

1. R. J. Cushman, P. M. McManus, S. C. Yang, *J. Electroanal. Chem.* **291**, 335 (1986).
2. D. E. Stilwell, Su-Moon Park, *J. Electrochem. Soc.* **136**(3), 688 (1989).
3. K. Y. Kondratyev, *Radiation in the Atmosphere*, edited by J. V. Miegham (Academic Press, New York, 1969), p. 123.
4. The average global radiation were obtained from (a). South Florida Test Service Inc., Miami, Florida; 750 Watt/m<sup>2</sup> at 34° north latitude for March in 1988. (b). *Solar Radiation*, edited by N. Robinson (Elsevier Publishing Company, Inc., New York, 1966), p. 158; 690 Watt/m<sup>2</sup> at 25° N. latitude.
5. D. Zhang, J. H. Hwang, S. C. Yang, *Synthetic Metals* **22**, E251 (1989).

## MOISTURE EFFECTS IN THE CONDUCTING POLYMER, POLYANILINE

J.P. TRAVERS, C. MENARDO and M. NECHTSCHIEIN  
DRF/SPh/DSPE (UPR CNRS 216), Centre d'Etudes Nucléaires de Grenoble,  
85 X, 38041 Grenoble-Cédex (FRANCE)  
S.K. MANOHAR and A.G. MACDIARMID  
Department of Chemistry, University of Pennsylvania, Philadelphia,  
PA 19104-6323 (USA)

## ABSTRACT

Water content as well as conductivity have been measured as a function of water vapour pressure on polyaniline and poly-N-methylaniline samples. It is shown that i) absorption is governed by the acid protons of the polymers and ii) enhancement of conductivity needs the existence of protonated imines. It is concluded that moisture favours conductivity through an increase of the interchain transfers.

## INTRODUCTION

Among conducting polymers, polyanilines (PANI) have attracted a considerable interest during the last five years. This class of electroactive polymers offer the unique situation in which the conductivity depends upon both the oxidation state, as in standard conducting polymers, and the protonation level [1-3]. In particular, number of works have been devoted to the study of the Insulator-to-Conductor transition which takes place on the emeraldine form upon protonation, while the oxidation level is held constant. Several results have been obtained which support the assumption of a phase segregation mechanism : protonation proceeds via the formation of fully protonated conducting islands embedded in an unprotonated insulating matrix [4-5]. Spin dynamic studies have suggested that conducting islands could consist of only one polymer chain and that the DC conductivity could be controlled by the interchain hoppings [6-7].

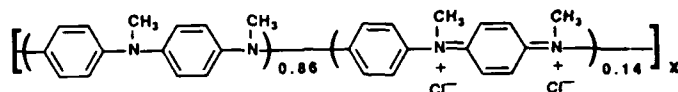
In addition, to oxidation and protonation, hydration has been shown also to control the transport properties [8]. For instance the conductivity can be increased by an order of magnitude when water is absorbed in the polymer. Several assumptions have been proposed to explain the role of moisture, invoking either a granular scale mechanism [9]- the role of water would consist of decreasing the insulating barriers between conducting grains- or a microscopic mechanism [10-11]- involving a role of the acid protons at the polymer chain level-.

In this paper, we present a comparative study of the water absorption process, and the induced effects on the conductivity, in the parent polyaniline and the substituted poly-N-methylaniline (PNMA). The aim of the experiments was to follow the behaviour of conductivity variation versus moisture content with respect to a modification of the acid-base properties of the polymer. We, first, report experimental determination of water absorption isotherms and we establish a relation between the water absorption and the protonation level, which holds for both compounds. Then, we present conductivity measurements upon hydration. Finally, the different models are discussed to the light of the present results.



## EXPERIMENTAL

PANI samples were chemically prepared using  $(\text{NH}_4)_2\text{S}_2\text{O}_8$  in 1M HCl using the detailed method previously described [12]. The samples were washed, equilibrated in pH = 10  $\text{NH}_4\text{OH}$  solution, dried under vacuum, then equilibrated in HCl solutions of a given pH and dried again. PNMA samples were chemically synthesized from N-Methyl-aniline using  $(\text{NH}_4)_2\text{S}_2\text{O}_8$  in 1M HCl at room temperature [13]. The powder is then filtered and equilibrated in 1M HCl for 48 hours in order to obtain the salt form (PNMAS). After heating at 90-100°C under vacuum, PNMAS is deprotonated and transformed into the base form (PNMAB) whose elemental analysis corresponds to the following form :



Spectroscopic characterisations have been reported elsewhere [13].

## WATER ABSORPTION PROCESS

Measurements of the water content of PANI and PNMA samples were performed by weight uptake as a function of water vapor pressure (wvp) with a Sartorius 4201 microbalance. The wvp, as settled by the temperature of a water bath, was maintained constant for 5 hours before every measurement for the absorption process to reach equilibrium.

In Fig. 1. we compare the water absorption isotherms obtained on three samples : PANI emeraldine salt (pH ~ 0), PANI emeraldine base (pH ~ 10) and PNMAS (pH ~ 0). The water content is scaled in water molecules per monomer unit and the wvp is normalized to the saturating vapor pressure at room temperature ( $P \approx 17.6$  Torrs at 20°C). The data obtained on PNMAS are located between those collected on fully protonated and unprotonated PANI. At a relative wvp of 0.5 there are about 0.5 and 0.3 water molecules absorbed per ring in PANI (pH ~ 0) and in PNMAS, respectively. This amount is much far too large to be accounted for by a surface process (surface area of about 40  $\text{m}^2/\text{g}$  [14]).

Using NMR techniques, it has been previously determined that for a given wvp, the amount of absorbed moisture in PANI is composed of two parts : a) a protonation independent contribution of about 0.07  $\text{H}_2\text{O}$  per ring and b) a contribution proportional to the protonation level [14]. The first one was attributed to the surface absorption. The second one indicates that water absorption is mainly a bulk process directly connected to the acid sites. It was, then, proposed that water absorption proceeds via the formation of hydrogen bonds between water molecules and acid protons [14]. Furthermore, water absorption in the protonated leucoemeraldine PANI was shown to obey the same law [15]. Therefore, one can wonder if water absorption in PNMAS is driven by the same mechanism.

To answer this question, let us compare the water uptake of different PANI samples and of a PNMAS sample at a wvp of 8 Torrs ( $P/P_0 \approx 0.45$ ) as a function of the protonation level, X. The determination of X was made either by elemental analysis of the chlorine, or by titration studies of acid species or by both methods. For PNMAS, both techniques yield  $X \approx 0.20$  to 0.22. The data, for all the samples, are reported on the same diagram

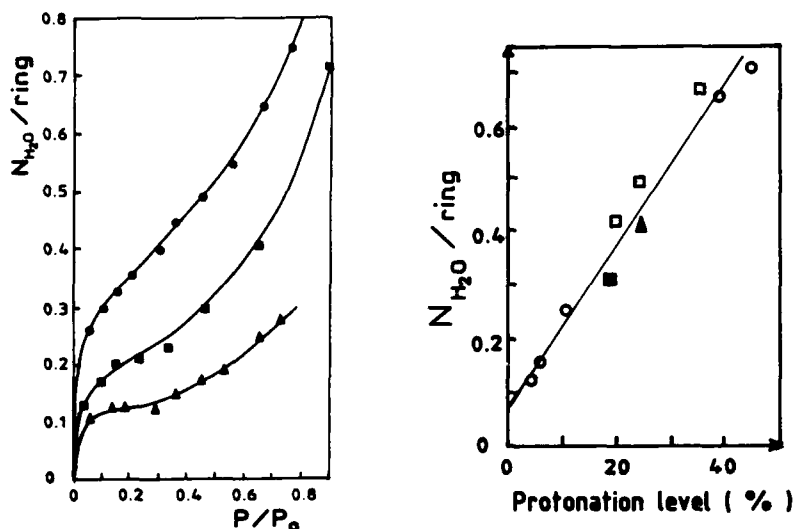


Fig. 1. Concentration of absorbed water molecules vs relative water vapor pressure (wvp) in : emeraldine PANI pH  $\sim 0$  ( $\bullet$ ) and pH  $\sim 10$  ( $\blacktriangle$ ) and PNMAS ( $\blacksquare$ ).  $P_0$  is the saturating vapor pressure at 20°C (solid lines are guides for the eyes).

Fig. 2. Concentration of absorbed water molecules at a wvp = 8 Torr vs protonation level : emeraldine PANI ( $\circ$ ,  $\square$ ), leucoemeraldine PANI ( $\blacktriangle$ ) and PNMAS ( $\blacksquare$ ) (solid line is a guide for the eyes).

in Fig. 2. It appears that all data can be fitted by only one straight line. This result strongly suggests that in PNMAS as well as in PANI, water absorption is a microscopic process driven by the presence of acid protons.

#### CONDUCTIVITY MEASUREMENTS

Four probe DC conductivity ( $\sigma$ ) was measured on 100 to 400  $\mu\text{m}$  thick compressed pellets. The samples were mounted on a tight cell which enabled us to make vacuum and to introduce a controlled wvp. After application of a given wvp, the  $\sigma$  variation was monitored as a function of time using a computerized experimental setup. Due to the water diffusion phenomena inside the pellet, the steady state value of  $\sigma$  was reached after a time going from 2 to 24 hours, according to the pellet thickness [10]. The steady state values measured on two emeraldine samples ( $X = 0.11$  and  $X = 0.22$ ) and on a PNMAS sample ( $X \approx 0.20$ ) are compared in Fig. 3 as a function of the wvp. Apart from the difference in the absolute values of  $\sigma$ , due to the low value of the oxidation level of PNMAS ( $y = 0.15$ ), two characteristic features can be observed : a) in emeraldine PANI,  $\sigma$  increases with increasing wvp, as already observed [8] while b) the PNMAS conductivity does not depend on the wvp and, therefore, on the water content.

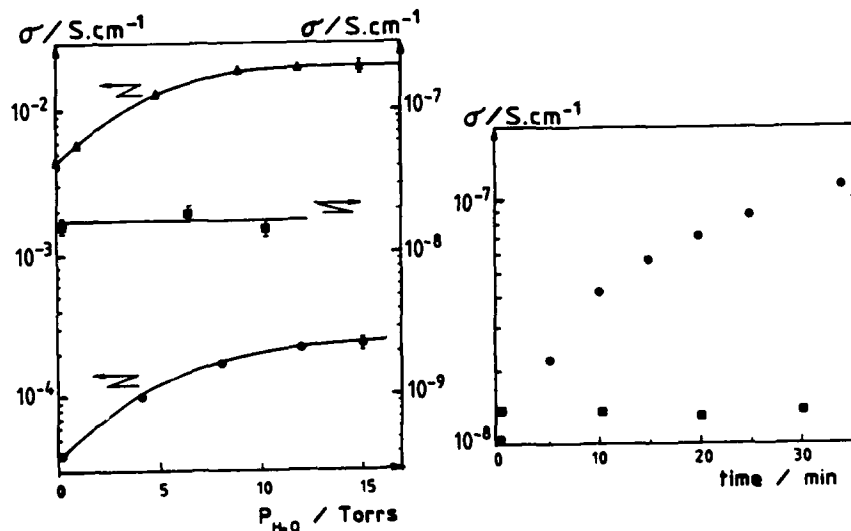


Fig. 3. Steady state conductivity vs water vapor pressure in : emeraldine PANI with protonation level  $X = 0.11$  (●) and  $X = 0.22$  (▲), PNMA (■). (Solid lines are guides for the eyes).

Fig. 4. Conductivity vs time after setting a given water vapor pressure : wvp = 6.5 Torr on emeraldine PANI with  $X = 0.04$  (●), wvp = 9.2 Torr on PNMA (■).

In order to clarify the influence of the absolute value of  $\sigma$ , we performed a measurement on a lightly protonated ( $X \approx 0.04$ ) emeraldine PANI sample whose conductivity was similar to that one of PNMA (about  $10^{-8}$  S.cm<sup>-1</sup>). In Fig. 4 is presented the time evolution of  $\sigma$  in this sample after application of a pressure of 6.5 Torr, as well as the  $\sigma$  evolution of a PNMA sample under a pressure of 9.2 Torr. The conductivity of the PANI sample increases, while it remains approximately constant in the PNMA one, in full agreement with the previous results.

#### DISCUSSION

We have to face the following question. Why does the presence of water favours conduction in PANI and has no effect in PNMA, even though the absorption process is roughly the same ?

First, it is necessary to specify the nature of the absorption sites in both compounds. By titration studies, it has been shown that the acid sites in emeraldine PANI are composed of a majority of imine sites ( $-NH^+$  in the bipolaronic picture) with a pKa value of 5.5 and a minority of amine sites ( $-NH_2$ ) with a pKa value of 2.5 [16]. In particular, in lightly protonated emeraldine PANI samples equilibrated in pH > 3 solutions ( $X = 0.04, 0.11$  and  $0.22$ ) the acid species are essentially imine sites. In PNMA the situation is somewhat different. The imine sites are, here,

replaced by  $\text{-N}^+\text{CH}_3\text{-}$  species which cannot release protons. Titration studies of PNMAS have shown that only one acid function actually exists with a pKa value of 2.2, which signifies that the acid species are exclusively amine sites. Thus, one is led to the evidence that the *enhancement of the conductivity in presence of water molecules requires the presence of imine acid species.*

We now discuss the models which were proposed to account for the observed effects, to the light of our results. One of them [9] is based on the "granular metal" picture invoked for emeraldine PANI [4]. Energy barriers between metallic grains, or islands, are supposed to account for the observed temperature dependence of PANI conductivity. In this picture, water absorption is assumed to take place only at the grain surface, so that the dielectric constant of the collected moisture between the grains decreases the energy barriers and gives rise to an increase of the macroscopic conductivity. However, this model fails to account for the bulk aspect of the absorption process as well as the behaviour of PNMAS. If we assume that the structure of PNMAS is similar to that of PANI, the moisture effect on the intergrain energy barriers should be qualitatively the same as for PANI, in contradiction with experiment.

The alternative models assume a microscopic point of view for the role of water in the conduction process [10-11]. The common basic idea for these mechanisms is that the presence of water molecules favours local fluctuations of the number of protons bound to the nitrogen atoms so that electronic transfers which would not be possible in a fixed configuration become now possible. In their model, Travers et al [10] attempt to explicit this idea, and estimate quantitatively the different possible mechanisms. The calculations were made assuming that  $\text{pKa}(\text{imines}) < \text{pKa}(\text{amines})$ ; hence, the amine species were assumed to play the major role. Later, this assumption was shown to be wrong [16]. So, the conclusions of this model have to be reconsidered. Besides, Focke et al [11] proposes a mechanism which involves only imine species: the water molecules assist the charge transfer between protonated and unprotonated imine moieties, through the release and the fixation of protons. This mechanism takes into account the main experimental results (the microscopic nature of the absorption and the particular role of the acid imine species) and thus, accounts for the opposite behaviours of PANI and PNMAS. In principle, this mechanism could be invoked for both intrachain and interchain processes. However, it was stated by spin dynamics studies that observed conductivity is limited by interchain charge transfers [7]. Therefore, it is more efficient for the process of conductivity enhancement to proceed by interchain rather than by intrachain transfers.

Finally, as a conclusion, we propose that water molecules favour conduction via a microscopic mechanism which increases the interchain conductivity. It is interesting to analyze this statement to the light of conclusions derived from spin dynamics studies. Mizoguchi et al [7] conclude that conducting islands, as proposed by Epstein et al [4] do exist in emeraldine PANI and are only composed of a single polymer chain. In such a picture, the two types of mechanisms - microscopic and granular - which have been previously discussed may be somewhat reconciled.

#### REFERENCES

1. R. de Surville, M. Josefowicz, L.T. Yu, J. Perichon and R. Buvet *Electrochim. Acta* **13**, 1451 (1968)

2. J.P. Travers, J. Chroboczek, F. Devreux, F. Genoud, M. Nechtschein, A. Syed, E.M. Genies and C. Tsintavis, *Mol. Cryst. Liq. Cryst.* **121**, 195 (1985)
3. J.C. Chiang and A.G. MacDiarmid, *Synth. Met.* **13**, 193 (1986)
4. A.J. Epstein, J.M. Ginder, F. Zuo, R.W. Bigelow, H.S. Woo, D.B. Tanner, A.F. Richter, W.S. Huang and A.G. MacDiarmid, *Synth. Met.* **18**, 303 (1987) ; J.M. Ginder, A.F. Richter, A.G. MacDiarmid and A.J. Epstein, *Sol. St. Comm.* **63**, 97 (1987)
5. M. Hemle, C. Mayer, M. Mehring, M. Nechtschein and A. Pron in Electronic Properties of Conjugated Polymers, ed. by H. Kuzmany, S. Roth, M. Mehring (Springer Verlag, 1989)
6. M. Nechtschein, F. Genoud, C. Menardo, K. Mizoguchi, J.P. Travers and B. Villeret, *Synth. Met* **29**, E 211 (1989)
7. K. Mizoguchi, M. Nechtschein, J.P. Travers and C. Menardo *Phys. Rev. Lett.* **63**, 66 (1989)
8. M. Nechtschein, C. Santier, J.P. Travers, J. Chroboczek, A. Alix and M. Ripert, *Synth. Met* **18**, 311 (1987)
9. H.H.S. Javadi, M. Angelopoulos, A.G. MacDiarmid and A.J. Epstein *Synth. Met* **26**, 1 (1988)
10. J.P. Travers and M. Nechtschein, *Synth. Met* **21**, 135 (1987)
11. W.W. Focke, G.E. Wnek and Y. Wei, *J. Phys. Chem.* **91**, 5813 (1987)
12. A.G. MacDiarmid, J.C. Chiang, A.F. Richter, N.L.D. Somanisi, A.J. Epstein in Conducting Polymers, ed. by L. Alcacer (Reidel Pub, Dordrecht, Holland, 1987) p 107
13. S.K. Manohar, A.G. MacDiarmid, K.R. Cromack, J.M. Ginder and A.J. Epstein, *Synth. Met.* **29**, E 349 (1989)
14. A. Alix, V. Lemoine, M. Nechtschein, J.P. Travers and C. Menardo *Synth. Met* **29**, E 457 (1989)
15. A. Alix, Thesis, Grenoble (1989)
16. C. Menardo, M. Nechtschein, A. Rousseau and J.P. Travers *Synth. Met* **25**, 311 (1988)

## SPECTROSCOPIC AND MOLECULAR WEIGHT STUDIES OF POLYTOLUIDINES

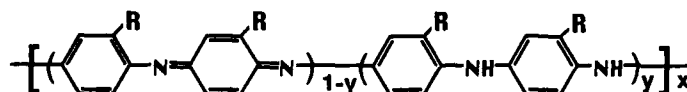
Y. Wei,\* K. F. Hsueh and S. Nagy  
 Department of Chemistry, Drexel University, Philadelphia, PA 19104  
 A. Ray, A. G. MacDiarmid and J. Dykins  
 Department of Chemistry, University of Pennsylvania, Philadelphia, PA 19104-6323  
 A. J. Epstein  
 Departments of Chemistry and Physics, Ohio State University, Columbus, OH 43210  
 G. E. Wnek  
 Department of Chemistry, Rensselaer Polytechnic Institute, Troy, NY 12180

### ABSTRACT

Poly(*o*-toluidine) and poly(*m*-toluidine) in base form have been characterized by infrared and <sup>1</sup>H NMR spectroscopy. Assignments of the proton NMR signals have been facilitated by the use of model compounds. The distinction between benzenoid and quinoid methyl resonances in the NMR permits a semi-quantitative estimation of the oxidation states of the polytoluidines. Infrared studies are consistent with a polyaniline-type backbone having pendant methyl groups. Field desorption mass spectrometry (FD-MS) was employed for estimation of the molecular weight of poly(*o*-toluidine). Gel-permeation chromatography of the same sample showed a bimodal elution pattern, suggesting that the FD-MS technique detects only the lower molecular weight fraction of the polymer. Despite this inherent limitation, FD-MS yields the interesting information that the polymer contains chains of both odd and even numbers of repeat units, necessitating the coexistence of different oxidation states in the base form of the polymer.

### INTRODUCTION

Recently, there have been many reports on the synthesis, electrochemistry and electronic properties of alkyl ring-substituted polyanilines.[1-3] Like the unsubstituted polyaniline, these polyaniline derivatives also exhibit reasonably high electrical conductivities upon doping with protonic acids, well-behaved electrochemistry and good environmental stability. Furthermore, their solubilities in organic solvents were found to be generally higher than that of polyaniline.[1,2] However, very few studies have been reported on the structural characterization and the molecular weights of these polymers. It is proposed that the structures of these polymers in their base (undoped) form could be represented by the following general formula:



where R is H for polyaniline, CH<sub>3</sub> for polytoluidines, and CH<sub>3</sub>CH<sub>2</sub> for polyethylanilines, etc. The value of y represents the oxidation state of the polymers, which could be estimated by elemental analysis or by chemical titrations.[4] The polymers are in the "pernigraniline", "emeraldine" and "leucoemeraldine" oxidation states when y has values of 0, 0.5 and 1.0, respectively.

In this communication, we report the spectroscopic and molecular weight studies of the base form of poly(*o*-toluidine), poly(*m*-toluidine) and poly(*o*-ethylaniline), by means of infrared, proton NMR, and field desorption mass spectroscopy (FD-MS), and by gel-permeation chromatography (GPC).

## EXPERIMENTAL

The polymers were synthesized by oxidation of the appropriate monomers in an acidic (1.0 M HCl) aqueous solution with  $(\text{NH}_4)_2\text{S}_2\text{O}_8$  as oxidant and were converted to their base form by treating with aqueous ammonia solution, following the previously reported procedures.[1] The base form of poly(*o*-toluidine) was further treated with a hydrazine aqueous solution to give a reduced form whose oxidation state was close to that of the leucoemeraldine.

Infrared spectra of the polymer-KBr pellets were recorded on a Perkin-Elmer Model 1610 FTIR spectrometer. Proton NMR spectra were recorded on an IBM Bruker WM 250 FTNMR spectrometer. For the NMR measurements, deuterated dimethyl sulfoxide ( $\text{DMSO-d}_6$ ), chloroform ( $\text{CDCl}_3$ ) and methylene chloride ( $\text{CD}_2\text{Cl}_2$ ) were employed as solvents and tetramethylsilane (TMS) as internal standard. Dilute solutions of the polymers (0.1-1% w/v) were used to ensure the maximum dissolution of the polymers, and various relaxation delays were used to validate the reliability of the signal integrations. Assignments of the proton NMR signals were made by the use of the model compounds which were either purchased from Aldrich or prepared in our laboratories.[5]

Gel-permeation chromatography was performed on a Waters GPC Model IIA equipped with a Model 590 programmable solvent delivery module, a differential refractometer as detector, and a Ultrastyrigel linear THF-packed column which had a tangent number of ca. 7,000 plates per column with an acetone marker. For a typical procedure, 50 mg of poly(*o*-toluidine) base were dissolved in 25 mL of 1-methyl-2-pyrrolidinone (NMP, HPLC grade from Aldrich) followed by filtering through a 0.5 mm filter. Temperatures of both the GPC column and detector were kept at 35 °C. NMP was used as elutant with a flow rate of 0.4 mL/min. Monodispersed polystyrene standards (Waters) with molecular weight ranging from 1,800 to 2,700,000 were used for the molecular weight calibration and a tetramer of aniline for a further correction.[6]

## RESULTS AND DISCUSSION

The infrared spectra of poly(*o*-toluidine) and poly(*m*-toluidine) show similar characteristics of that of polyaniline, e.g. the stretching vibration band of C=N in the quinoidal units of all the polymers appears at about 1600  $\text{cm}^{-1}$ . However, the out-of-plane aromatic C-H bending absorptions of the polytoluidines appear at about 810 and 870  $\text{cm}^{-1}$ , which are indicative of the 1,2,4-trisubstitution of the benzene ring, whereas the spectrum of polyaniline shows one band at ca. 830  $\text{cm}^{-1}$  because of the 1,4-disubstitution pattern.[2,7] The results are consistent with the proposed structure of the polytoluidines.

The proton NMR spectrum of polyaniline (Figure 1a) shows one broad peak at ca. 6.96 ppm, which is assigned to the aromatic protons. The -NH- protons generally give broad signals in the range of ca. 8.2-8.6 ppm. The signals of the aromatic protons in polytoluidines appear at ca. 6.6-6.8 ppm with a small shoulder at ca. 7.1-7.5 ppm as shown in Figure 1b. Based on the NMR spectral data of the model compounds (Table 1, entries 6 and 7), the -NH- proton signals in the polytoluidines could be "buried" under the aromatic signals. The overall pattern of the aromatic signals in the spectra of the polytoluidines are quite similar to that of the combination of the two forms of the model compounds, indicating that the polymers consist of both aryl and quinoidal units. It should be noted that the methyl substituent in the polytoluidines gives two signals at 2.08 and 2.18 ppm, which could be assigned to the protons of the methyl groups on the phenyl and quinoidal rings, respectively. These assignments were made based on a comparison with the model compounds and were further confirmed by the NMR spectrum of poly(*o*-toluidine) at the "leucoemeraldine" oxidation state (i.e.  $y \sim 1$ ) in which only one strong signal of the methyl protons was observed at ca. 2.08 ppm. The ratio ( $3 \pm 0.3$ ) of the aryl methyl to the quinoidal methyl groups for poly(*o*-toluidine), estimated from the integration and a computer curve fitting of the proton signals, indicates that the oxidation state of the polymer was close to that of the emeraldine ( $y=0.5$ ). Both poly(*o*-toluidine) and poly(*m*-toluidine) show essentially identical infrared and proton NMR spectra, suggesting that they have the same

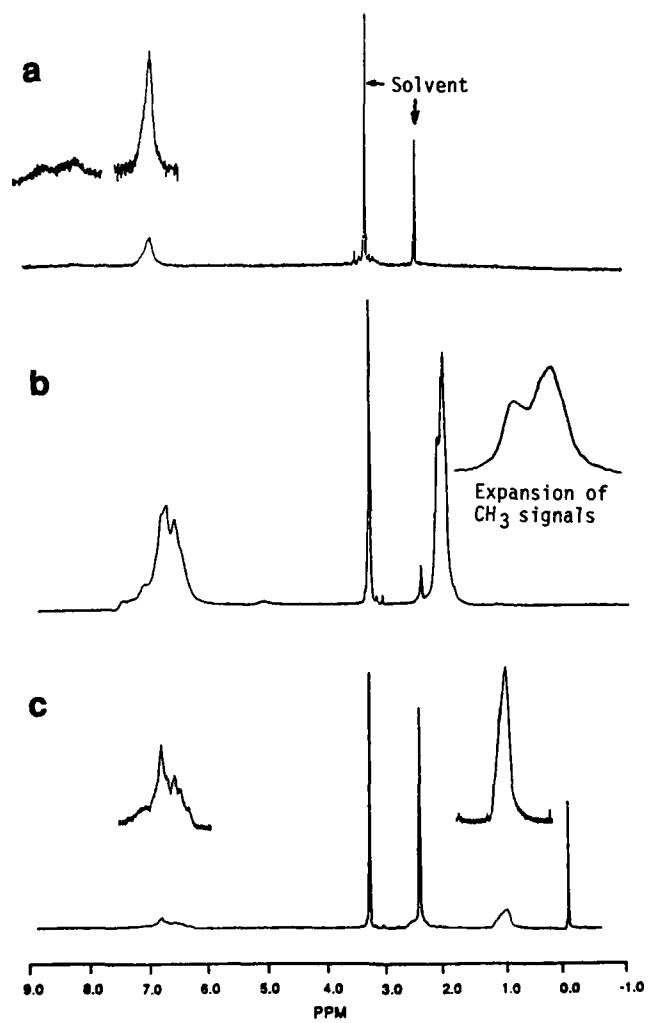


Figure 1. Proton NMR spectra of the base form of (a) polyaniline, (b) poly(*o*-toluidine) and (c) poly(*o*-ethylaniline) in DMSO-d<sub>6</sub>.



chemical structure. The proton NMR spectrum (Figure 1c) of poly(*o*-ethylaniline) is similar to those of the polytoluidines in the aromatic region. A broad signal at ca. 1.05 ppm is assigned to the methyl protons. The methylene proton signals are overlapped with the signal of the water in DMSO solvent, at ca. 2.5 ppm, which have been resolved with CDCl<sub>3</sub> or CD<sub>2</sub>Cl<sub>2</sub> as solvent. The NMR results are summarized in Table 1.

Table 1. Proton NMR spectral data of polyaniline, alkyl ring-substituted polyanilines, and model compounds.

No. Model Compound <sup>a</sup> and Polymer	Chemical Shift in ppm (Solvent: DMSO-d <sub>6</sub> )			
	-NH <sub>2</sub>	-NH-	Aromatic Protons	-CH <sub>3</sub>
1 Ph-NH-Ph-NH-Ph	-	7.90	6.69-7.19	-
2 Ph-N=Q=N-Ph	-	-	6.76-7.46	-
3 Ph-NH-Ph-NH <sub>2</sub>	4.75	7.44	6.54-7.11	-
4 Ph-NH-Ph-N=Q=N-Ph-NH <sub>2</sub>	5.53	8.40	6.60-7.28	-
5 Polyaniline	-	8.2-8.6	~6.96	-
6 ( <i>o</i> -Me)Ph-NH-Ph-NH-Ph( <i>o</i> -Me)	-	6.78	~6.6-6.8; ~6.9-7.1	2.14
7 ( <i>o</i> -Me)Ph-N=Q=N-Ph( <i>o</i> -Me)	-	-	~6.95	2.20
8 Poly( <i>o</i> -toluidine) and Poly( <i>m</i> -toluidine)	~5.1 <sup>b</sup>	-	~6.6-6.8; ~7.1-7.5	2.08, 2.18
9 Poly( <i>o</i> -ethylaniline) <sup>c</sup>	-	-	~6.6-6.7; ~7.1	~1.05

a. Ph = Aryl ring; Q = quinoidal ring. b. The signals may be attributed to the end group (-NH<sub>2</sub>). c. The methylene proton signal appeared at ca. 2.5 ppm.

Figure 2 shows the field desorption mass spectrum of poly(*o*-toluidine) in the mass range of 200-5,000 amu. No clear features are detected above ca. 3,000 amu. The spectrum consists a series of maxima, with the largest one at 1257 amu. The spacing between any two maxima is ca. 100-110 amu. The possible constituent units of poly(*o*-toluidine), [-(CH<sub>3</sub>)C<sub>6</sub>H<sub>3</sub>N=] for a quinoidal imine unit and [-(CH<sub>3</sub>)C<sub>6</sub>H<sub>3</sub>NH-] for an aryl amine unit, have molar masses of 104.13 and 105.14, respectively. For a most simplified situation, each maximum is separated from its neighbor by a mass approximately corresponding to a one-ring-one-nitrogen, i.e. a monomer unit. As shown in Figure 2a, a distribution of chain length from ca. 3 to ca. 25 monomer units were detected, with the most frequent chain length being ca. 12 monomer units. The expansions of the spectrum are given in Figures 2b and 2c. Each maximum is surrounded by a series of satellite peaks, which could be resulted from the ion-molecule and fragmentation reactions and/or from distributions of the oxidation states of the polymer for the given chain lengths, besides the normal isotope distributions. It should be noted that in the spectrum both odd and even numbers of chain lengths are detected, with no obvious preference for either. This observation seems to support the mechanism proposed for the polymerization of aniline and its derivatives<sup>8</sup> in which the growing polymer chain end adds one monomer at each growth step. Similar FD-MS results were obtained for poly(*o*-ethylaniline).

The molecular weight data obtained by the current FD-MS technique, unfortunately, are limited because of the small detection range. Parallel molecular weight measurements on the same poly(*o*-toluidine) sample were made using GPC technique. The chromatogram of the polymer in NMP shows a bimodal elution pattern. With polystyrene calibration and the correction by the tetramer of aniline,<sup>[6]</sup> the GPC peak molecular weights of the polymer are ca. 3,500 and 67,000 for the lower and higher molecular weight fractions, respectively. The lower molecular weight fraction is believed to be related to the information obtained from FD-MS but the higher molecular weight fraction is well beyond the detection limit of the FDMS technique.

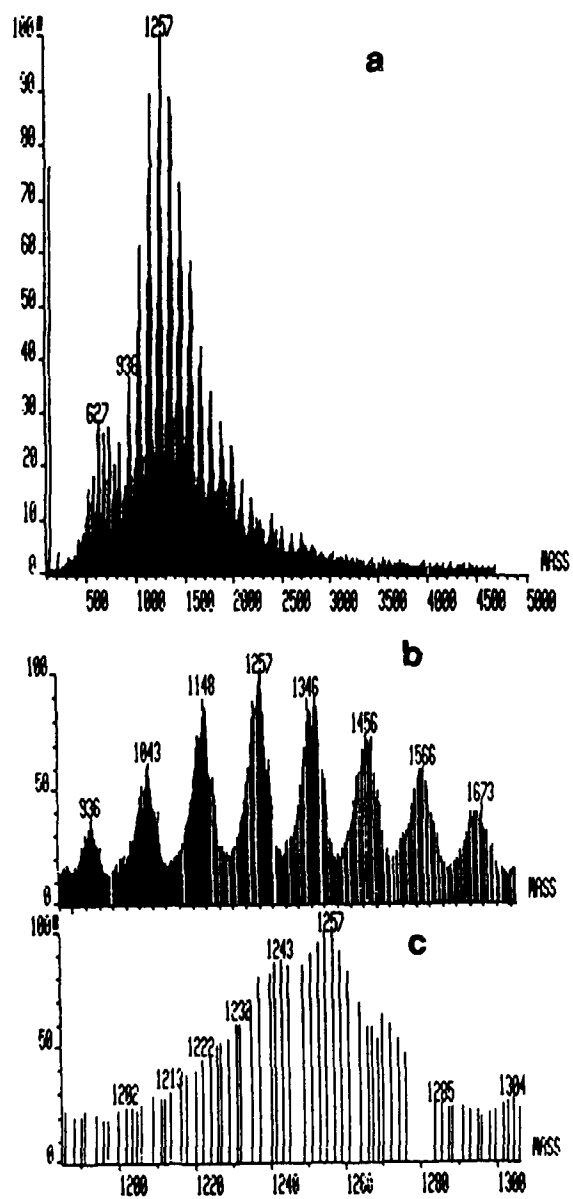


Figure 2. Field desorption mass spectra (FD-MS) of the base form of poly(o-toluidine) (a) and its expansions in the vicinity of the largest mass peak. (b) and (c)

The discrepancy in the lower molecular weight region between the FD-MS and GPC techniques might be attributed to the lack of a suitable calibration in GPC and to that only relatively short polymer chains were desorbed and detected in the FD-MS method. Further research is in progress in our laboratories to improve the accuracy of the molecular weight determination using both techniques.

**ACKNOWLEDGMENT** This work was supported in part by the Defense Advanced Research Projects Agency through a grant monitored by the Office of Naval Research. Y.W. is also grateful to the Donors of the Petroleum Research Fund, administered by the American Chemical Society for partial support of this research.

#### REFERENCES

1. Y. Wei, W.W. Focke, G.E. Wnek, A. Ray, and A.G. MacDiarmid, *J. Phys. Chem.* **93**, 495 (1988).
2. L. X. Wang, X.B. Jing, S.L. Ni, and F.S. Wang, *Zhongguo Kexue (Chinese Science)*, **B(2)**, 129 (1989).
3. S.L. Wang, F.S. Wang, X.H. Ge, *Synth. Met.* **16**, 99 (1986); M. Leclerc, J. Guay, and L. H. Dao, *Macromol.* **22**, 649 (1989).
4. A.G. MacDiarmid, J.C. Chiang, A.F. Richter, N.L.D. Somasiri, in *Conducting Polymers*, L. Alcazar Ed., Reidel Publisher, Dordrecht, Holland, 1987.
5. Y. Wei, K.F. Hsueh, R. Hariharan, A. Ray, A.G. MacDiarmid, and G.E. Wnek, unpublished results.
6. X. Tang, Y. Sun and Y. Wei, *Makromol. Chem., Rapid Commun.* **9**, 829 (1988).
7. R.M. Silverstein, G.C. Bassler and T.C. Morrill, *Spectrometric Identification of Organic Compounds*, 4th Ed., Wiley, NY, 1981.
8. Y. Wei, X. Tang and Y. Sun, *J. Polym. Sci., Polym. Chem. Ed.* **27**, 2385 (1989); *J. Phys. Chem.* **93**, 4878 (1989).

ELECTRICALLY CONDUCTIVE COMPOSITE OF POLYANILINE AND  
POLY(p-PHENYLENE-TEREPHTHALAMIDE)

XIAN-TONG BI, C. WANG AND J.S. BAO

Institute of Chemistry, Academia Sinica, Beijing 100080, China.

ABSTRACT

The improvement of the processibility and mechanical properties of polyaniline (PAN) by processing a concentrated sulfuric acid solution of the mixture of chemically prepared conductive PAN powders and poly(p-phenylene-terephthalamide) (PPTA) in different weight ratios are presented.

The concentrated sulfuric acid solution of PAN and PPTA were processed to films and threads, they are liquid crystalline conductive polymer composite sites, the electrical conductivities of the composites are between  $10^{-4}$ - $10^{-1}$  s/cm.

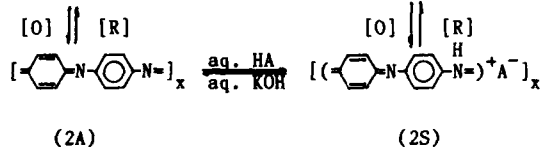
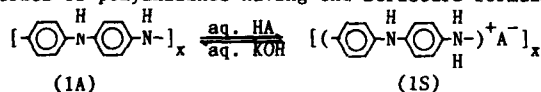
PAN enhanced the tensile strength of PPTA, but does not effect the elongation. The morphology of the PPTA/PAN composite surfaces are fiberlike texture.

INTRODUCTION

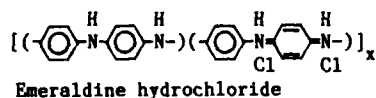
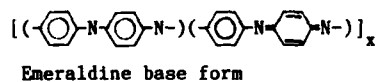
In recent years, the study of para-aromatic polyamide has become a very attractive subject. Due to the semi-rigid chain in polymers, poly(p-phenylene-terephthalamide) can form anisotropic liquid crystalline solution [1-5]. Fibers with high tensile strength and high modulus can be obtained by dry-jet wet-spinning of this kind of polymer solution.

PPTA is a kind of lyotropic liquid crystalline polymer, if we can prepare a composite of conductive liquid crystalline polymer from polyaniline and poly(p-phenylene-terephthalamide), then a new material can be obtained.

Polyaniline has been discussed in many papers during the past 120 years [6-9]. A series of polyanilines having the structure formulae [10] :



or [11] :



The 2S form and the emeraldine hydrochloride form are electrical conductive polyaniline and all of the rest are insulators. The polyaniline powder can be processed to self-supported film, but the processibility and mechanical properties are very poor.

In order to improve the processibility and mechanical properties of polyaniline, we have studied the electrochemical polymerization of aniline in the polyurethane matrix to form electrically conductive composites [12,13], which had the same electrical conductivity as polyaniline and the mechanical properties of pure polyurethane films. Our previous work showed that the composite retained the mechanical properties of the matrix material.

In this paper, we report the chemical oxidative polymerized aniline to form liquid crystalline electrical conductive composites by means of mixing the concentrated sulfuric acid solution of polyaniline with the concentrated sulfuric acid solution of poly(p-phenylene-terephthalamide).

## EXPERIMENTAL

### Synthesis of poly(p-phenylene-terephthalamide) (PPTA)

#### Starting materials:

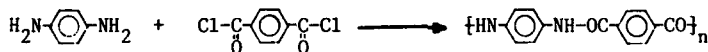
p-phenylenediamine: commercial 1,4-phenylenediamine was purified by vacuum distillation, white solids, m.p. 140-141 °C.

Terephthaloyl chloride: terephthaloyl chloride was prepared from terephthalic acid and thionyl chloride and purified by twice vacuum distillation, white solids, m.p. 83-84 °C.

N-methyl pyrrolidone: purified by vacuum distillation.

CaCl<sub>2</sub> ; HCl ; H<sub>2</sub>SO<sub>4</sub> : used as received.

#### Synthesis:



details of the synthesis were described in our previous paper [14].

### Synthesis of polyaniline (PAN)

#### Starting materials:

Aniline : commercial product was purified by distillation, b.p. 183-185°C.  
HCl ; (NH<sub>4</sub>)<sub>2</sub>S<sub>2</sub>O<sub>8</sub> : commercial products, used as received.

#### Synthesis :

Protonated polyaniline was synthesized by the oxidative polymerization of 0.5 M aniline in 3M aqueous HCl solution by (NH<sub>4</sub>)<sub>2</sub>S<sub>2</sub>O<sub>8</sub>. The composition of PAN by elemental analysis is C<sub>12</sub>H<sub>9.45</sub>N<sub>2</sub>Cl<sub>1.45</sub>.

### Preparation of conductive composite of PPTA/PAN.

PPTA was dissolved in conc. H<sub>2</sub>SO<sub>4</sub> at 50-60 °C by stirring, the concentration was about 10-15 % . The conc. H<sub>2</sub>SO<sub>4</sub> solution of PAN was added to the conc. H<sub>2</sub>SO<sub>4</sub> solution of PPTA at a weight ratio of PPTA: PAN = 4:1, 3:1, 2:1, and kept the concentration of PPTA in total H<sub>2</sub>SO<sub>4</sub> not less than 8 %, and stirred continuous for 5 hrs. Threads were made by passing the mixed

sulfuric acid solution through a syringe to a warm water bath, and drawn for orientation.

### Characterization

Electrical conductivity measurement : four point probe method was used.

Mechanical properties : tensile strength and elongation at break point were obtained on a Instron-1122 material testing machine. Room temperature tested at a draw speed of 10 mm/min.

X-ray diffraction : Wide angle X-ray diffraction patterns were taken on a Rigaku(made in Japan) X-ray diffraction apparatus, CuK radiation, 40 KV, 30 mA.

SEM : Hitachi-S-530 scanning electron microscope.

### RESULTS AND DISCUSSION

#### 1, Liquid crystallinity of PPTA/PAn composite

Column 2 and 3 of table I show that the cross-polarized light became weaker as the quantity of PAn increased to PPTA:PAn=2:1 in the concentrated sulfuric acid solution. The reason is due to the greenish black PAn affects the transparency of the sample, and the PAn has no effect on the liquid crystallinity of PPTA. Also, the cross-polarized light microscope picture of the sample PPTA:PAn=2:1 is shown on figure 1.

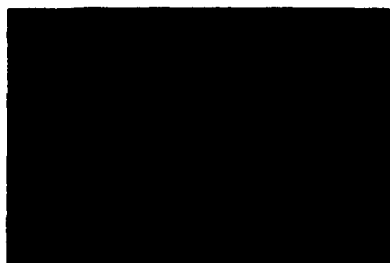


Figure 1.  
Cross-polarized light microscopy  
of liquid crystalline PPTA/PAn  
composite:

PPTA/PAn=2:1 (wt./wt.)  
Polarizer at +90°

$\eta_{inh}$ of PPTA	PPTA/PAn (wt./wt.)	Liquid crystallinity (polarized light)	Tensile strength of the threads (N/mm <sup>2</sup> )	Elongation at break of the threads (%)	Electrical conductivity (s/cm)
3.41	4/1	strong	12.5	4.0	$1.5 \times 10^{-4}$
	3/1	strong	20.1	4.0	$2.6 \times 10^{-3}$
4.26	pure PPTA	strong	41.2	4.0	$10^{-10}$
	4/1	strong	---	---	$1.3 \times 10^{-4}$
	3/1	strong	41.5	4.0	$2.4 \times 10^{-3}$
	2/1	weak	44.8	4.0	$2.3 \times 10^{-1}$

Table I. Liquid crystallinity, mechanical properties and electrical conductivity of PPTA/PAn

## 2, Mechanical properties of PPTA/PAn composite

(1) Tensile strength : The tensile strength of thread form PPTA ( $\phi=0.2$  mm.) increase with the amount of PAn (Table I. column 4), especially for the PPTA component with low  $\eta_{inh}$ . So we think that the PAn has a reinforcing effect to PPTA.

(2) Elongation at break : there are no effects of PAn on the elongation of PPTA threads (Table I, column 5), even when the ratios of PPTA/PAn are changed. These results show that the PAn has no effect on the orientation of the polymer chain of PPTA.

## 3, Electrical conductivity of PPTA/PAn composite

Obviously, the electrical conductivity of the composites are due to the effect of the small particles of PAn which are smoothly distributed in the PPTA matrix. The electrical conductivity of the composite with the weight ratio of PPTA:PAn=2:1 is  $2.3 \times 10^{-1}$  s/cm, which is one order of magnitude less than the pure PAn. This is due to many holes appearing in the composite, and we will discuss this phenomena later in the section of morphology. The electrical conductivity increased with the increasing amount of PAn in PPTA (Table I, column 6).

## 4, X-ray diffraction (WAXD) of PPTA/PAn composite

There is a strong peak at  $2\theta=22.8^\circ$  (Figure 2, a and a') of pure PPTA[14], and a strong peak at  $2\theta=25.1^\circ$  of pure PAn (Figure 2, b). Figure 2,c shows strong peak at  $2\theta=22.7^\circ$  and a less strong peak at  $2\theta=25^\circ$ , which coincide with PPTA and PAn. The peak at  $2\theta=28^\circ$  in 2a' is (006) of powdered PPTA, this peak became flat in oriented fiber 2a. We think that the composites are physically mixed with each other, no chemical bonding between the two compositions.

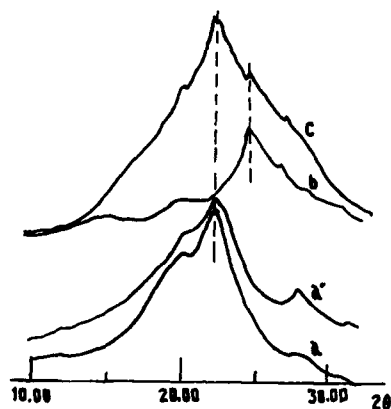


Figure 2, Wide angle X-ray diffraction pattern of PPTA/PAn composite

a -PPTA fiber  
a' PPTA powder  
b -PAn  
c -PPTA/PAn

## 5, Morphology of PPTA/PAn composite

Surface morphology of PPTA threads after drawn in  $50^\circ\text{C}$  aqueous HCl solution present fiber like orientation (Figure 3, a ). The PPTA/PAn composite thread surface also has fiber like oriented surface morphology (Figure 3, b).

The morphology of the cross-section of PPTA/PAn show that there are many holes in the composite (Figure 3, c ). Obviously, there are two reasons: (1) Air bubbles generated during the mechanical stirring for mixing the two components; (2) The holes were generated by the diffusion of the sulfuric

acid after the threads formed and were layed in the aqueous HCl solution.

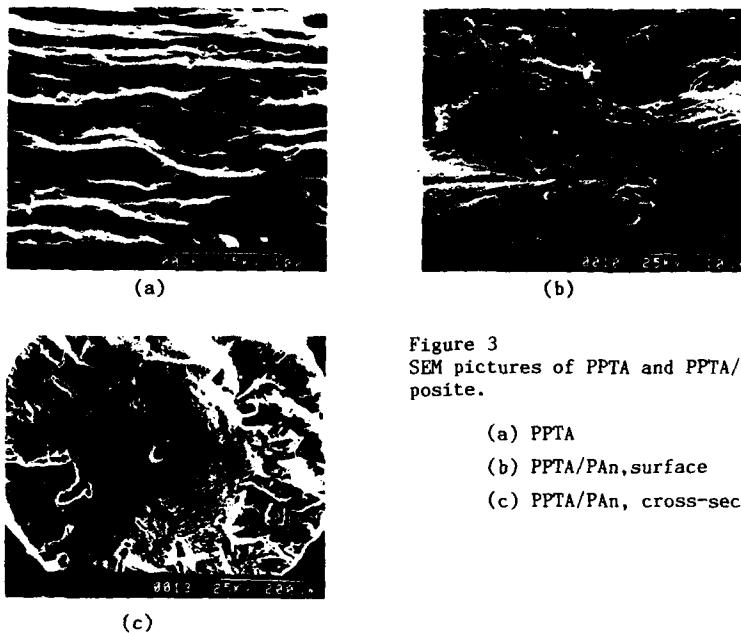


Figure 3  
SEM pictures of PPTA and PPTA/PAN composite.

- (a) PPTA
- (b) PPTA/PAN, surface
- (c) PPTA/PAN, cross-section

#### CONCLUSION

- 1, The concentrated sulfuric acid solution of PPTA and PAN mixtures are electrical conductive and liquid crystalline composites.
- 2, The electrical conductivity of the composite PPTA: PAN=2:1 (wt./wt.) is equal to  $2.3 \times 10^{-1}$  s/cm, which is one order of magnitude less than the pure PAN.
- 3, PAN has reinforcement effect to the tensile strength of PPTA, but no effect to the elongation at break of PPTA.
- 4, The wide angle X-ray diffraction showed that PPTA and PAN are mixed with each other only, there is no chemical bonding between them.
- 5, The SEM picture showed that the surface morphology of PPTA/PAN threads are fiberlike oriented.

#### ACKNOWLEDGEMENTS

This work was supported by the Director's Fund of the Institute of Chemistry, Academia Sinica.

#### REFERENCES

- [1] H. Blades, U.S.P. 3,767,756(1972); *ibid.*, 3,869,429(1975).
- [2] 菊地哲野, J. of Texture Mechanics Society(Japan) 27, 722 (1974).
- [3] T.S.Sokolowa, S.G. Efimowa, A.B.Woloxena, et al., *Him. Woloi na.* 1, 26 (1974).
- [4] *ibid.*, 5, 71(1975).



- [5] S.X. Chen C.F. Lung, S.R. Hu and M.Xu, *Polym.Commun.* 1, 1(1979).
- [6] A.G. Green and A.E.Woodhead, *J. Chem. Soc.* 2388(1910).
- [7] R.de Surville, M. Josefowicz, L.T. Yu, et.al., *Electrochim. Acta* 13, 1451 (1968).
- [8] J.C.Chiang and A.G. MacDiarmid, *Synth. Metals* 13, 193 (1986).
- [9] J.P. Travers, J. Chro'aczek, F. Devreux et.al. , *Mol. Cryst. Liq. Cryst.*, 121, 195 (1985).
- [10] A.G.MacDiarmid, J.C,Chiang and M.Halpern, et. al. *Mol. Cryst. Liq. Cryst.* 121, 173 (1985).
- [11] A.G. Macdiarmid, J.C. Chiang, A.F. Richter and A.J. Epstein, *Synth. Metals* 18 285 (1987).
- [12] Q.Peí and X.T.Bi, *Synth. Metals* 30, 351 (1989).
- [13] Q.Peí and X.T.Bi, *J. Appl. Polym. Sci.* 38, 1819 (1989).
- [14] J.S. Bao, C.C. Xu and Q.H. Zhang, *Polym. Commun. (Chinese Chemical Society)* , 3, 235 (1985).

## OPTICAL STUDIES OF POLYANILINES: EFFECTS OF ALKYL RING-SUBSTITUTION AND SOLVENT ENVIRONMENT

ANJAN RAY\*, ALAN G. MACDIARMID\*, JOHN M. GINDER\*\* and ARTHUR J. EPSTEIN\*\*

\* Department of Chemistry, University of Pennsylvania, Philadelphia, PA 19104

\*\*Department of Physics, The Ohio State University, Columbus, OH 43210.

## ABSTRACT

Methyl and ethyl ring-substituted polyaniline derivatives have been synthesized and characterized by UV-visible-near IR spectroscopy. Optical spectra of the base forms in DMF solution suggest that the torsion angle between adjacent rings is increased by steric hindrance due to the alkyl groups in the substituted polymers, leading to blue shifts in the ~4 eV ("bandgap") and ~2 eV ("exciton") absorptions and an accompanying decrease in the relative intensity of the "exciton" band.

The methyl ring-substituted derivative, poly(o-toluidine), is shown to exhibit solvatochromism. The "exciton" absorption shifts from 2.03 eV in pure NMP to 2.19 eV in CH<sub>2</sub>Cl<sub>2</sub>, accompanied by a loss in intensity relative to the "exciton" absorption. The phenomenon is attributed to the presence of a more "rod-like" state in NMP as compared to a more "coil-like" state in CH<sub>2</sub>Cl<sub>2</sub>.

The effects of alkyl substituents on acetic acid solution spectra of "emeraldine" salt will be discussed with respect to polaron band formation in these systems.

## INTRODUCTION

Substituted polyanilines have attracted considerable recent attention [1,2] due to their good environmental stability and processability. Whereas unsubstituted polyaniline ("emeraldine") base can only be dissolved in high boiling solvents such as N-methylpyrrolidinone (NMP) and dimethylsulfoxide (DMSO), the N-substituted and ring-substituted bases are often soluble in common volatile solvents.

The electronic spectra of alkyl ring-substituted polyanilines has already been shown to depend primarily on the steric effects of alkyl substituents [1]. We extend the argument here to cover the phenomenon of solvatochromism in the base form of the ring-methyl derivative, poly(o-toluidine). A modified valence-effective Hamiltonian (VEH) technique based on a polaron band model [3] is used to examine the effect of alkyl ring-substitution on the electronic spectrum of the conducting "emeraldine" salt form.

## EXPERIMENTAL

Aniline, o-toluidine and o-ethylaniline were polymerized by (NH<sub>4</sub>)<sub>2</sub>S<sub>2</sub>O<sub>8</sub> chemical oxidation of the corresponding monomers. The poly(o-alkylaniline) salts thus obtained were then deprotonated in air to yield the corresponding base forms using aqueous NH<sub>4</sub>OH as reported previously [1]. All samples used had a C+H+N total of at least 99% by weight, as determined by elemental analyses.

UV/Visible spectra were recorded at room temperature on a Perkin-Elmer Lambda 4C or a Lambda 9 spectrophotometer at a scan rate of 120 nm/min. Approximately saturated polymer solutions were prepared, filtered through a 0.2μm micropore filter and then diluted by visual estimate such that maximum absorbances did not exceed 2.0.

For the solvatochromism study, samples of a given batch of poly(o-toluidine) base were dissolved in pre-mixed solvent mixtures consisting of varying proportions (from 100:0 to 0:100)

of NMP and  $\text{CH}_2\text{Cl}_2$ . Reversibility of the data after changing solvents was verified by obtaining a spectrum in  $\text{CH}_2\text{Cl}_2$  solution, evaporating the solvent and redissolving the residue in NMP - a spectrum identical to poly(*o*-toluidine) base which had been dissolved directly in NMP was obtained.

In order to study "doped" solutions in 80% aqueous acetic acid, a sample of the base form of a given polymer was dissolved and diluted as described above and spectra recorded every 1-2 hours until no change was observed between scans. The time taken for "equilibration" in this respect varied between samples but was generally ~10-15 hours.

## RESULTS AND DISCUSSION

The UV/visible/near-IR spectra of the base forms of polyaniline, poly(*o*-toluidine) and poly(*o*-ethylaniline) in DMF solution have been found to consist of two absorption bands [1]. The first absorption at 311-330 nm (3.99 - 3.76 eV) is assigned to the "bandgap" (i.e.  $\pi\text{-}\pi^*$ ) transition and the second, at ~2 eV is attributed to the formation of an exciton [1, 4]. Both bands show *hypsochromic* shifts as the series  $\text{R} = \text{H}, \text{CH}_3, \text{C}_2\text{H}_5$  is traversed (Table 1). Also, the ratio of the maximum absorbance of the "bandgap" absorption to that of the "exciton" band *increases* from ~1.1 to ~1.5 to ~1.8 respectively. These trends indicate an increase in the bandgap brought about by a *decrease* in the extent of conjugation, which results from an increase in the torsion angle between adjacent rings. A narrowing of bandwidths is also expected to occur as a consequence. This argument is consistent with cyclic voltammetry and conductivity trends reported earlier [1] and also with theory [3,4].

Table 1. Optical absorption maxima<sup>a</sup> of poly(*o*-alkylanilines)

	DMF solution		Aqueous 80% Acid Solution		
	"Bandgap" nm (eV)	"Exciton" nm (eV)	"Bandgap" nm (eV)	"Shoulder" <sup>b</sup> nm (eV)	"Signature" nm (eV)
R = H	330 (3.76)	620 (2.00)	340 (3.65)	~420 (2.95)	785 (1.58)
R = $\text{CH}_3$	316 (3.92)	610 (2.03)	326 (3.80)	~402 (3.08)	822 (1.51)
R = $\text{C}_2\text{H}_5$	310 (4.00)	600 (2.07)	316 (3.92)	407 (3.05)	834 (1.49)

(a)  $\lambda_{\text{max}}$  values reported are reproducible to  $\pm 2$  nm. (b) Except for  $\text{R}=\text{Et}$ , where it is distinct, the shoulder is visually estimated ( $\pm 5$  nm).

### Poly(*o*-toluidine) base: solvatochromism

Care must be taken to confine comparative discussions of base spectra to a given solvent. As shown in Figure 1, the position of the "exciton" peak of poly(*o*-toluidine) base is extremely sensitive to solvent composition - the  $\lambda_{\text{max}}$  for this is found to vary from 566 nm (2.19 eV) in neat  $\text{CH}_2\text{Cl}_2$  to 610 nm (2.03 eV) in pure NMP. In contrast, the "bandgap" peak changes only marginally (314 to 317 nm). Thus, as anticipated from their different molecular origins, the two peaks respond differently to changes in solvent.

The ratio of intensities (denoted  $A_b/A_e$ ) of the "bandgap" to the "exciton" peaks also changes as a function of solvent composition, the exciton becoming relatively *more* intense as it moves to *lower* energies with increasing NMP content. It is to be noted that the changes in intensity were not accompanied by any significant changes in peak widths and could thus be used as an estimate of the oscillator strengths of the absorptions. The changes in energy and relative intensity of the exciton band in going from NMP to  $\text{CH}_2\text{Cl}_2$  for poly(*o*-toluidine) base follow the same trend that is seen for this band when one proceeds from unsubstituted polyaniline to the more bulky *o*-alkyl substituents in DMF solution [1]. The phenomenon is therefore strongly suggestive of a conformation-related process, more sensitive to *local* changes (as reflected in the

"exciton" peak) than to extended effects (since the "bandgap" absorption is essentially unaffected).

Solvatochromism in conjugated polymers has been noted previously, notably in polydiacetylenes [5] and poly(3-alkylthiophenes) [6]. In all cases, the phenomenon has been attributed to a transition between "rodlike" and "coil-like" states, the former being thermodynamically more stable as a result of greater conjugation. In solvents that interact readily with the polymer, the increased entropy of solvation of the polymer promotes formation of the coil-like state, causing loss of planarity, consequent decreased conjugation in parts of the polymer chain and hence shifting related absorption bands to higher energies. Thus a "poorer" solvent for a given polymer is more likely to favor a conjugated "rodlike" state and is expected to show transitions at lower energies. In accordance with this argument, it follows that  $\text{CH}_2\text{Cl}_2$  interacts to a greater extent with poly(o-toluidine) base than does NMP. This is also consistent with our finding that while polyaniline ("emeraldine") base is more soluble in polar solvents, e.g. NMP, DMF, etc., the reverse trend is observed for poly(o-toluidine) base, which is more soluble in  $\text{CH}_2\text{Cl}_2$ ,  $\text{CHCl}_3$ , etc. An additional contribution to the observed solvatochromic phenomena could arise from the interaction of the charged excited state of the 2 eV peak with a more polar solvent such as NMP.

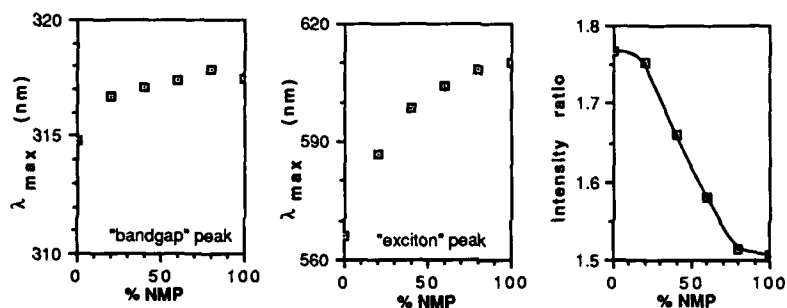


Figure 1: Dependence upon solvent composition of peak positions of "exciton" peak, "bandgap" peak and their relative intensities in the UV/visible spectrum of poly(o-toluidine) in NMP- $\text{CH}_2\text{Cl}_2$  mixtures.

#### Spectra of Doped Forms in Aqueous 80% Acetic Acid

Whereas, for both solution and solid-state spectra, the base forms of the polyanilines exhibit two peaks in the electronic spectrum in the range 280-900 nm (4.43-1.38 eV), the protonated salt forms show three bands in this region. The dissolution of the "emeraldine" base form of polyaniline in 80% aqueous acetic acid to yield intense green solutions of the protonated polymer is a complex process [7]. The low-energy band, initially at ~670 nm (1.85 eV) when the polymer base is dissolved in acetic acid, shifts progressively with time to an "equilibrium" value of ~785 nm (1.58 eV) while the high-energy band at ~3.65 eV and the pronounced shoulder at 2.9 eV remain essentially unchanged. This has been attributed [7] to hydrolysis of excess oxidized units in the polymer backbone.

Electronic spectra of the polymers in 80% aqueous acetic acid are compared in Fig. 2. The following trends are noted (Table 1) in traversing the series  $R = \text{H}, \text{CH}_3, \text{C}_2\text{H}_5$ :

(i) the high-energy peak (termed "bandgap") moves to *higher* energies; (ii) the "shoulder" absorption, which is somewhat harder to precisely locate, also moves to *higher* energies; (iii) the strong low-energy band ("signature") shifts to significantly *lower* energies. These observations can be analyzed using a model based on valence-effective Hamiltonian (VEH) calculations by Stafstrom et al. [3] which envisages the formation of a polaron lattice from extended interaction of semiquinone units. Figure 3 (a-c) shows the generalized band structure for aniline, its fully reduced ("leucoemeraldine") polymer and the polaron band created in the gap by oxidation of this reduced polyamine.

Examination of the dimeric repeat unit (Fig. 3, inset) used for the construction of the lattice suggests that an increase in the angle  $\phi$  by which the ring is twisted out of the plane of the C-N bond will decrease the transfer integral (which is directly proportional to  $\cos \phi$ ) between the lone pair and the aromatic  $\pi$ -system, affecting bandwidths as well as average band energies. The HOMOs in both the polyamine form and the "doped" polaron-lattice form arise from antibonding combinations of nitrogen and benzene orbitals. Thus, a larger ring twist angle (smaller transfer integral) leads to a qualitative narrowing of bands [Fig. 3[(c)  $\rightarrow$  (d)].

From Fig. 3[(c) and (d)] in this simplified picture, increased  $\phi$  may be expected to lead to these effects: (i) The "bandgap" (HOMO  $\rightarrow$  LUMO)  $c \rightarrow d$  transition will shift to *higher*

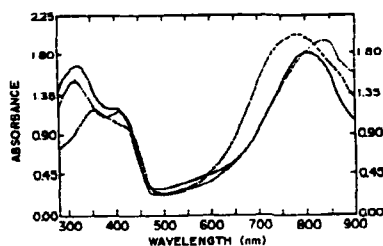


Figure 2: Electronic spectra of poly(o-alkylaniline) salts in aqueous 80% acetic acid. Table 1 shows peak listing.

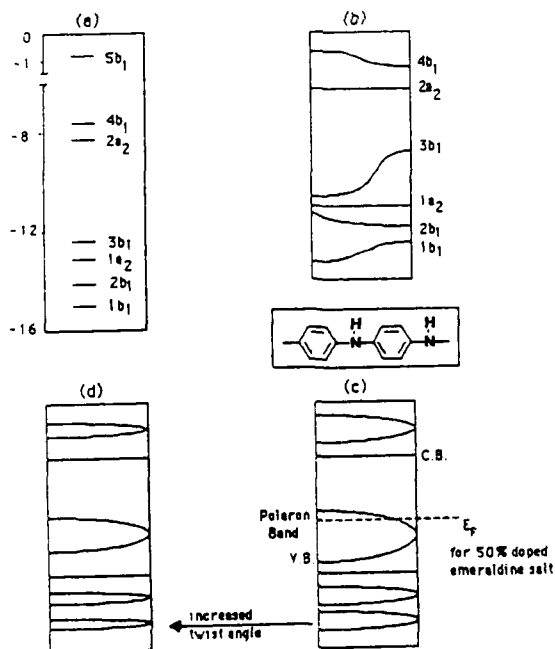


Figure 3: Qualitative band diagrams for polyaniline: (a) Aniline molecular orbitals, (b) bands for leucoemeraldine,  $(-C_6H_4NH-)_x$ , (c) bands for dimeric repeat unit (inset), showing Fermi level for half-filled polaron band, (d) Increased torsion angle decreases overlap integral, causing bandwidths to decrease.

energies; (ii) The  $b \rightarrow c$  transition, a "signature" of the presence of the polaron band, will move to lower energies; (iii) The  $a \rightarrow c$  "shoulder" will also decrease in energy but less so than the "signature" peak since the "a" band is very flat.

The experimental observations (Fig. 2, Table 1) agree with the first two expectations but are inconsistent with the behavior of the "shoulder": a monotonic decrease from  $R = H$  to  $Me$  to  $Et$  is not seen for the "shoulder". While the position of this shoulder is generally difficult to estimate, the anomaly may also be due to (i) electronic effects of the alkyl substituent on the energy of band "a"; (ii) breaking of the twofold symmetry of each ring about its 1, 4-axis when an alkyl group is introduced or (iii) a combination of both these factors.

#### ACKNOWLEDGEMENTS

The authors are grateful to Mr. James G. Masters and Dr. Yen Wei for helpful discussions. Financial support from the Defense Advanced Research Projects Agency, through a contract monitored by the office of Naval Research, is gratefully acknowledged.

#### REFERENCES

1. Y. Wei, W.W. Focke, G.E. Wnek, A. Ray and A.G. MacDiarmid, *J. Phys. Chem.* **93**, 495 (1989).
2. M. Leclerc, J. Guay and L.H. Dao, *Macromolecules* **22**, 641 (1989); J.W. Chevalier, J.Y. Bergeron and L.H. Dao, *Polymer Commun.* **30**, 308 (1989).
3. S. Stafstrom, J.L. Bredas, A.J. Epstein, H.S. Woo, D.B. Tanner, W.S. Huang and A.G. MacDiarmid, *Phys. Rev. Lett.*, **59**, 1464 (1987).
4. E.M. Conwell, C.B. Duke, A. Paton and S. Jeyadev, *J. Chem. Phys.* **88**, 3331 (1988).
5. G.N. Patel, R.R. Chance and J.D. Witt, *J. Chem. Phys.* **70**, 4387 (1979).
6. O. Ingnas, W.R. Salaneck, J.E. Osterholm and J. Laakso, *Synth. Met.* **22**, 395 (1988).
7. G.E. Asturias, R.P. McCall, A.G. MacDiarmid and A.J. Epstein, *Synth. Met.* **29**, 157 (1989).

INFRARED REFLECTION-ABSORPTION STUDY OF THE ANILINE  
ELECTROPOLYMERISATION ON STAINLESS STEEL

F. GAILLARD, G. BOUYSSOUX AND S.N. KUMAR\*

Département de Chimie Appliquée et Génie Chimique, CNRS-URA 417  
Université Claude Bernard LYON, 69622 Villeurbanne Cedex, France.

\*Laboratoire de Physique de la Matière, Institut National des Sciences  
Appliquées de Lyon, 69621 Villeurbanne Cedex, France.

ABSTRACT

Polyaniline (PANI) films were grown on 304 L steel and studied by FTIR spectrometry. The spectra of the films formed carry evidence for quinonic/aromatic alternating structure involving head-to-tail coupling. The coupling is quite independent of the thickness of the polymeric layer. The quinonic/aromatic ratio can be varied when the film is subjected to further dedoping treatments (electrochemical reduction or KOH immersion).

INTRODUCTION

The polyaniline family of polymers is attracting increasing interest owing to its applications in electrochromic, organic storage and micro-electronic devices [1,2]. In addition, PANI obtained by electropolymerisation on metals are known to act as a good intermediate film for strong adhesion of subsequent coatings, such as, varnish, glue etc. [3]. The properties dealing with adhesion are highly dependent on surface chemistry of the relevant treated substrates. Consequently, a detailed chemical characterisation is required. For this purpose the best suited spectro-metric tools seem to be photoelectron (XPS and UPS) and Fourier transform infrared (FTIR) spectrometries [4,5]. In this paper, results dealing with surface characterisation by FTIR of aniline electropolymerised on 304L stainless steels are presented. Such results are to be considered in conjunction with our recent XPS data [6].

EXPERIMENTAL

The PANI films were grown electrochemically on 304L stainless steel substrates by electropolymerisation of aniline in an aqueous solution containing sodium sulfate as the supporting electrolyte. The 304L substrates were solvent degreased and some of them anodised in nitric acid solution in order to form a chromium enriched oxide film, about 20 nm in thickness [7]. The electropolymerisation solution contained 0.1 M aniline in a 0.5 M solution of Na<sub>2</sub>SO<sub>4</sub> with the final pH adjusted to 1.0 by the addition of H<sub>2</sub>SO<sub>4</sub>. Films were grown either at constant voltage or constant current density.

The FTIR spectra were obtained using a Nicolet 740 spectrometer, at a resolution of 4 cm<sup>-1</sup>. Using a DTGS detector and a reflexion-absorption device (70° incidence angle) each spectrum is made from 256 scans.

RESULTS

The narrow scan spectra shown in Fig. 1 are relative to PANI prepared chemically by (NH<sub>4</sub>)<sub>2</sub>S<sub>2</sub>O<sub>8</sub> method (a) and by electropolymerisation on 304L (b). The main bands respectively correspond to : i) C-C stretching of quinoid (A) and benzoid (B) structures, ii) C-N stretching for aromatic amines (C), iii) band referred to by MacDiarmid et al. as 'electronic like band' and considered as a measure of the degree of delocalisation of electrons [8] (D) and iv) C-H out of plane bending on 1,4 substituted ring (E).

The spectrum of chemical PANI exhibits a band near  $1450\text{ cm}^{-1}$  which gives evidence for the presence of N-N bonds and then head-to-head coupling [9]. The structure of PANI on 304 L steel is mainly alternating quinoid/benzoid, involving head-to-tail coupling in the 1-4 position.

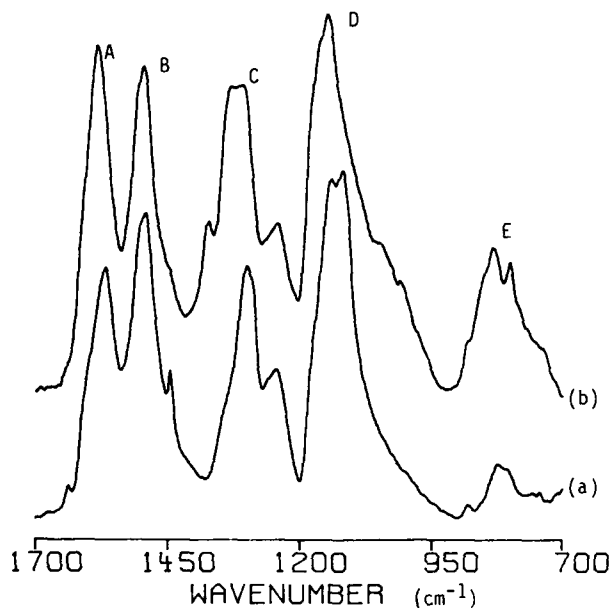


Fig.1:FTIR spectra of chemical (a) and electropolymerised (b) PANI.

The effect of total electrical charge ( $Q$ ) used for film formation (by galvanostatic mode) is shown Fig. 2. One can detect the presence of PANI for values of  $Q$  greater than  $10\text{ mC}\cdot\text{cm}^{-2}$ . This observation is consistent with the existence of an induction time before film growth, as confirmed by electrochemical data, x-ray emission spectrometry [10] and XPS [6] measurements. During the growth process, the chemical composition of polymeric film appears as quite constant.

A slight shape modification of the band E is to be noted, for the thickest films, which would be consistent with additional substitution on rings as assessed from XPS results [11].

The spectra in Fig. 3 show the effect of immersing in KOH solution (b) or electrochemically reducing in HCl solution (c) of the PANI film prepared at  $700\text{ mV/SCE}$  (a). The loss of conductivity when passing from (a) to (c) is associated to: i) a decrease of the quinoid form with respect to the benzoid form, the former being predominant in oxidised PANI [4], ii) decrease of the C-N band, which is in agreement with the conclusions of some authors who reported an increase of this peak with doping [14], iii) large decrease of the band at about  $1160\text{ cm}^{-1}$ , taken as representative for conductivity and related to the abundance of the quinoid form [14]. Finally, the background in the  $4000\text{ cm}^{-1}$  region (not shown here), linked to conductive properties of the polymer [4,12], decreases from (a) to (c).



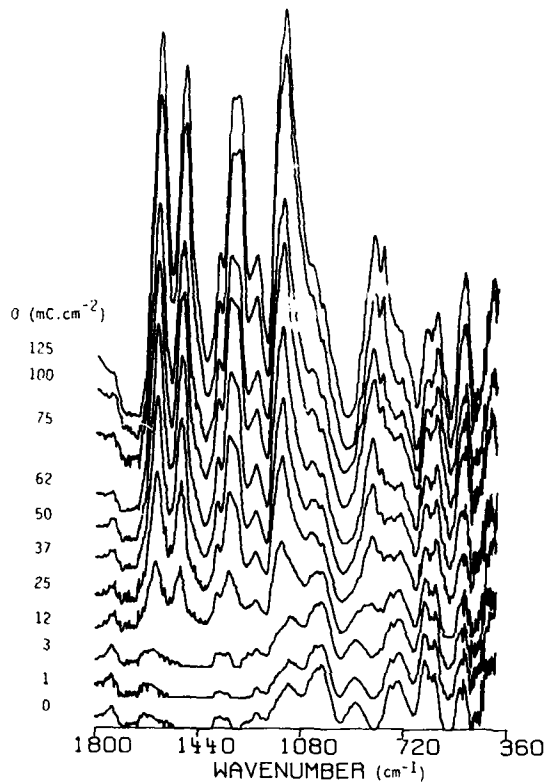


Fig.2 : Influence on the PANI covered 304 L steel surface composition of the electrical charge used for the electrochemical process.

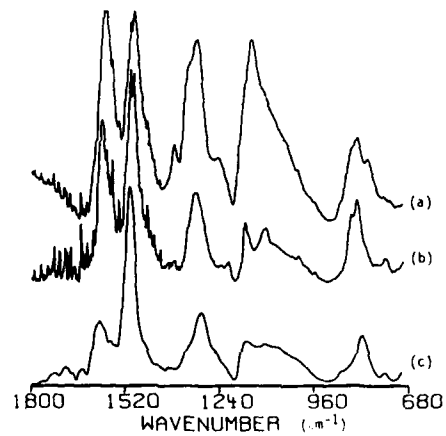


Fig.3 : Effects on a PANI film (a) of immersing in KOH solution (b) or electrochemically reducing in HCl solution (c)

## CONCLUSION

The examples considered in this paper show that the thickness of the PANI films can be monitored by varying the electrochemical conditions for film formation (electrical charge), this without modification of the overall film chemical composition. Conversely, this composition is modified by KOH immersion and electrochemical reduction. The modification of bands in the range 800-1400  $\text{cm}^{-1}$  can be related to the doping process (protonation/deprotonation or electron loss of N atoms). The variation of the conducting properties of PANI films according to the chemical or electrochemical treatments are also clearly evidenced with the evolution of C-C stretching of quinoid and benzoid structure and the band shape near 1160  $\text{cm}^{-1}$ . In the fields of research in adhesion and metal-polymer interaction, such ability, coupled with analysis techniques such as XPS and FTIR, can be of great help to understand the mechanisms involved.

## Acknowledgements

The authors wish to thank the UNIREC Company (Centre Commun de Recherche de la Sidérurgie Française) for the FTIR experiments performed during the secondment of one us (F.G.).

## References

1. A.G. MacDiarmid, J.C. Chiang, M. Halpern, W.S. Huang, S.L. Mu, N.L.D. Somasiri, W. Wu and S.I. Yaniger, *Mol.Cryst.Liq.Cryst.* **121**, 173 (1985).
2. E.M. Genies, A.A. Syed and C.Tsintavis, *Mol.Cryst.Liq.Cryst.* **121**, 181 (1985).
3. G. Bouyssoux, F. Gaillard, A. Roche, International Symposium on Trends and New Applications in Thin Films, (Société Française du Vide, Strasbourg, France, 1987) pp. 369-373.
4. H. Neugebauer, N.S. Sariciftci, H. Kuzmany, A. Neckel, *Mikrochim. Acta [Wien]* **1**, 265 (1988).
5. A. Volkov, G. Tourillon, P.E. Lacaze, J.E. Dubois, *J. Electroanal. Chem.* **115**, 279 (1980).
6. S.N. Kumar, F. Gaillard, G. Bouyssoux, *Synth. Metals*, in press.
7. F. Gaillard, Thesis, Lyon, France, 1987.
8. W.R. Salaneck, B. Lidberg, O. Inganäs, R. Orlandsson, I. Lundström, A.G. MacDiarmid, M. Halpern, N.L.D. Somasiri, *Mol. Cryst.Liq. Cryst.* **121**, 191 (1985).
9. T. Ohsaka, Y. Ohnuki, N. Oyama, G. Katagiri, K. Kamisako, *J. Electroanal. Chem.* **161**, 399 (1984).
10. D. Mazella, F. Gaillard, G. Bouyssoux, A. Roche, M. Romand, 2ème Congrès International sur l'Adhésion et les Adhésifs, (ADHECOM, Bordeaux, France, 1989) pp. 41-49.
11. S.N. Kumar, G. Bouyssoux, F. Gaillard, presented at the European Conference on Applications of Surface and Interface Analysis (ECASIA 89) Antibes, France, 1989.
12. J. Tang, X. Jing, B. Wang, *Synth. Metals* **24**, 231 (1988).

## EVALUATION OF THIN FILM CAPACITORS FABRICATED FROM HETEROGENEOUS POLYPYRROLE BASED LANGMUIR-BLODGETT FILMS

R. B. Rosner and M. F. Rubner\*

Department of Materials Science and Engineering, Massachusetts Institute of Technology, Cambridge, Massachusetts 02139, USA

### ABSTRACT

The electrical properties of Langmuir-Blodgett films of conducting polypyrrole were investigated in an effort to elucidate the molecular architecture of these multilayer films and determine the mechanism of conduction. Values of the dielectric constant and transverse conductivity recorded as a function of frequency were determined from electrical measurements performed on devices made with the conductive polymer. The highly anisotropic nature of the conductivity as well as the frequency dependence demonstrated by both the conductivity and dielectric constant provide evidence for a highly ordered molecular structure in which the conductive and insulative components of the multilayer film form an organized, layered structure. Even greater control of the electrical and structural properties has been achieved through the fabrication of a thin film superlattice in which the conducting polymer and an insulating derivative were deposited as alternating bilayers. The properties of the superlattice were close to those predicted for an inhomogeneous, mixed media.

### INTRODUCTION

The desire to control the order and molecular and supermolecular organization of thin films of conducting polymers has recently stimulated interest in utilizing the Langmuir-Blodgett (LB) technique to process these novel materials. Towards this goal, our group has developed a number of different approaches that can be used to manipulate electrically conductive polyheterocycles, such as poly(3-alkylthiophenes) and polypyrroles, into LB films [1,2]. In the case of the polypyrroles, electrically conductive monolayers are created by polymerizing pyrrole monomer in the presence of a surface active pyrrole at the air-water interface of the LB trough. The resultant mixed monolayers are then transferred into multilayer thin films using the standard LB vertical transfer technique. When 3-octadecanoyl pyrrole (3-ODOP) is used as the surface active molecule, the multilayers are comprised of well ordered domains of insulating 3-ODOP and partially ordered domains of electrically conductive polypyrrole. In this paper, we discuss the electrical properties of these heterogeneous multilayers in the form of thin film capacitors.

### EXPERIMENTAL

The synthesis of the surface active pyrrole molecules, 3-octadecyl pyrrole (3-ODP) and 3-octadecanoyl pyrrole (3-ODOP), used in this study as well as information on monolayer formation and manipulation have been described in detail in previous publications [1]. Transverse conductivities and dielectric measurements were made on films deposited onto platinum coated glass slides. Two methods were employed in making the electrical contacts to the top of the film; one involving an array of aluminum electrodes; the second a mercury drop. In the former case, a series of aluminum electrodes 0.02 and 0.04 cm<sup>2</sup> in area and 500 Å thick were evaporated onto the surface of the film. By comparing equal thickness capacitors created with two different top electrode sizes it was possible to better evaluate the quality of the devices. In most cases, the capacitance of the multilayer thin films was found to scale directly with the size of the top electrode. A physical contact was made to the top aluminum electrodes with a

fine gold wire. The second type of contact was produced by simply resting a small drop of mercury on the film surface and dipping a gold wire into that drop. Capacitance measurements were made on the metal/LB film/metal sandwich structures via an HP Model 4275A impedance analyzer. Measurements of the transverse conductivity indicate that the LB films are reversibly ohmic up to field strengths of about  $10^6$  V/cm. Measurements on all samples were made under ambient conditions in air.

It should be noted that we have found that the specific details concerning the electrical behavior of the thin film capacitors, such as the magnitude of the conductivity anisotropy, dielectric constant, transverse conductivity and frequency dependence of these latter two parameters are very much dependent on the type of top electrode used and the environment that the samples are exposed to during manipulation and measurement (air versus dry box). This reflects both the environmental stability of the conducting polymer and the nature of the interface established by the polymer/electrode interaction. The basic trends discussed in this paper, however, are common to all of the samples evaluated to date.

## RESULTS AND DISCUSSION

Figure 1 displays the transverse conductivity and dielectric constant of a polypyrrole/3ODOP multilayer thin film as a function of frequency. This particular film was evaluated in the form of a Pt/LB film/Al sandwich type capacitor. As can be seen, the dielectric constant displays a strong frequency dependence. At low frequencies, the dielectric constant is very large (around 150), it then drops to an apparent plateau in the range between  $10^4$  and  $10^5$  Hz with a value of about 50 and finally decays to values less than 5 in the MHz range. Similar samples measured in a dry box develop a clearly defined plateau region extending from  $10^2$  to  $10^5$  Hz over which the dielectric constant is about 250.

The large dielectric constant of this heterogeneous LB film at low frequencies is due to the accumulation of space charges at the interfaces of conducting and insulating domains. The molecular organization for this film is best described as domains of conducting polypyrrole chains sandwiched between domains of the insulating surface active 3ODOP molecules. Thus, carriers move through the polypyrrole domains, most likely via the hopping of positively charged bipolarons, until they encounter an interface with an insulating region of the film at which point they become trapped. At low frequencies, the movement of these species, and possibly ions, across their respective domains is fast enough to allow them to easily follow the oscillating electric field. With progressively higher frequencies, however, the motion of some of the less mobile species is frozen out thereby eliminating their contribution to the dielectric constant.

The transverse conductivity is seen to increase in a linear fashion with increasing frequency, eventually reaching a level of about  $10^{-5}$  S/cm in the MHz domain. This type of conductivity relaxation is very common in insulating or semiconducting polymeric systems whose charge transport is dominated by hopping or tunneling mechanisms involving localized charge carriers [3]. Transport across the film thickness in this case requires that carriers move through insulating domains of the 3ODOP molecules. Since there are no extended band states available to the carriers they must hop or tunnel between localized defect states within the insulating layers. This type of behavior inevitably results in a conductivity at higher frequencies that is larger than the DC conductivity. From the slope of this plot, it can be shown that the log of the conductivity varies as the frequency raised to the 0.82 power, which is quite close to that predicted by the Austin-Mott analysis for the hopping of charges between localized states [4]. In the low frequency regime, the transverse conductivity decreases and eventually approaches the value obtained by DC measurements ( $\sigma_{DC} = 10^{-10}$  S/cm). It should be noted that the DC in-plane conductivity of this system is about  $10^{-2}$  S/cm. This exceptionally large conductivity anisotropy ( $>10^8$ ) is due to the highly anisotropic structure created by the LB deposition process.

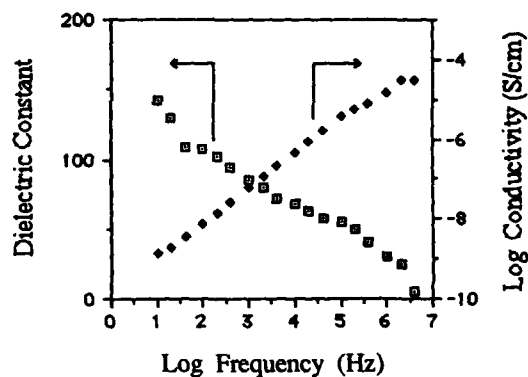


Figure 1. Dielectric constant and transverse conductivity of a polypyrrole/3-ODOP multilayer thin film as a function of frequency.

The ability to construct LB films from electrically conductive polypyrroles opens the door to the fabrication of a number of new thin film structures with novel molecular architectures and superstructures. By controlling the structure of the LB film at the molecular and supermolecular level, it should be possible to tailor the electrical properties of the capacitors fabricated from them. In order to enhance the conductivity anisotropy of the polypyrrole LB films and to study the influence of molecular organization on their electrical properties, organic superlattices comprised of layers of electrically conductive polypyrrole/3ODOP alternating with layers of electrically insulating 3ODP monomer were fabricated. To accomplish this, bilayers of polypyrrole/3ODOP and 3ODP monomer were alternately transferred onto either glass slides or platinum coated glass slides using two LB troughs operating simultaneously. The transfer ratios of the monomer onto polymer layer and polymer onto monomer layer were both close to unity indicating excellent transfer of both components. Superlattice structures containing up to 20 bilayers of each component were easily fabricated into stepped LB films. This represents the first time that such novel molecular organizations have been fabricated.

The in-plane conductivities of these new superlattice films reach levels as high as  $10^{-1}$  S/cm, whereas the transverse conductivity is less than  $10^{-12}$  S/cm. The conductivity anisotropy of these superlattice films is therefore greater than  $10^{11}$  and at least three orders of magnitude greater than the multilayers fabricated directly from polypyrrole/3ODOP. Thus, the addition of alternating insulating layers into the LB film dramatically restricts the conductivity across the film thickness. These films are therefore ideal for capacitor measurements.

An organic superlattice of the type mentioned above was constructed by transferring bilayers of the conducting and insulating materials onto a platinum coated glass slide in a stepped configuration. Steps of 10, 18, 26, 34, 42 and 50 layers were created on the substrate electrode as illustrated in Figure 2. Each conducting layer was sandwiched between a bilayer of the insulating surface active 3ODP monomer so as to create insulating layers about 50 Å thick alternating with conducting layers about 90 Å thick. An array of aluminum top electrodes was deposited onto the LB film to complete the capacitor. The entire superlattice assembly was isolated from the top and bottom electrodes by a bilayer of the insulating monomer which was deposited onto the platinum coated slide before deposition of the superlattice and finally over the completed LB film. The sample was stored under vacuum for one week prior to the deposition of the top electrodes to remove all residual water. Dielectric measurements were made at 100 kHz by contacting the top electrodes with gold wires.

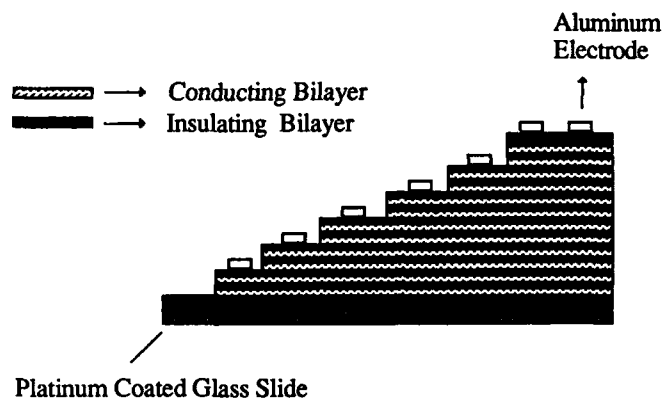


Figure 2. Stacking sequence and electrode configuration of the polypyrrole/3ODOP-3ODP alternating layer superlattice.

By depositing steps with different film thicknesses, it is possible to readily evaluate the quality of the deposition process and the uniformity of the resultant multilayer film. The capacitance of a high quality film should depend inversely on film thickness as indicated by equation 1 given below. In this equation,  $C$  is the film capacitance,  $T_{\text{oxide}}$  is the thickness of the aluminum oxide layer which develops when the upper electrodes are exposed to air,  $T_{\text{LB}}$  is the average thickness of a monolayer,  $A$  is electrode area and  $\epsilon_0$  and  $\epsilon_{\text{LB}}$  are the dielectric constants of the oxide and LB film respectively.

$$1/C = \frac{T_{\text{oxide}}}{A \epsilon_0 \epsilon_{\text{oxide}}} + \frac{T_{\text{LB layer}} (\# \text{ Layers})}{A \epsilon_0 \epsilon_{\text{LB}}} \quad (1)$$

Figure 3 displays the inverse capacitance versus number of layers plot for this new superlattice thin film. The linear relationship observed between  $1/C$  and the number of layers deposited clearly demonstrates that a well defined layer structure has been established. The slope of this curve gives a dielectric constant of about 8.7 for the superlattice assembly (at 100 kHz). In addition, the intercept of  $1.2 \times 10^8$  1/F is very close to the expected value of  $2.7 \times 10^8$  1/F which is calculated based on the presence of a 50 Å layer of native oxide on the Al electrode ( $\epsilon_{\text{ox}}=7$ ) and the 100 Å thick layer of 3-ODP ( $\epsilon=2.7$ ) used to isolate the superlattice from the electrodes. Thus, this completely new supermolecular organization behaves as a classical multilayer LB film.

A dielectric constant of 8.7 (at 100 kHz) is consistent with the heterogeneous nature of this system. When two materials with different dielectric constants and different electrical conductivities are mixed together, the final effective dielectric constant of the mixed system can be calculated using a modified version of the well known Clausius-Mossotti equation [5].

Using this equation and a value for the dielectric constant of the conducting phase of  $\epsilon=55$  (at 100 kHz) as determined from the polypyrrole/3ODOP multilayer and  $\epsilon=2.7$  for the 3ODP insulating phase, a value determined from a pure multilayer of the 3ODP monomer, one would expect the superlattice film to exhibit a dielectric constant of about 11.5. This value is very

close to the actual value obtained for this film of 8.7. The fact that the dielectric constant is lower than theoretically predicted may simply reflect the highly anisotropic nature of the LB film. Similar calculations [6] that take into account the layered stacking of the different phases predict an effective dielectric constant of about 6.6 for this particular film. Thus, the lower dielectric constant of the superlattice film is a simple consequence of the two phase nature of the alternating layer structure.

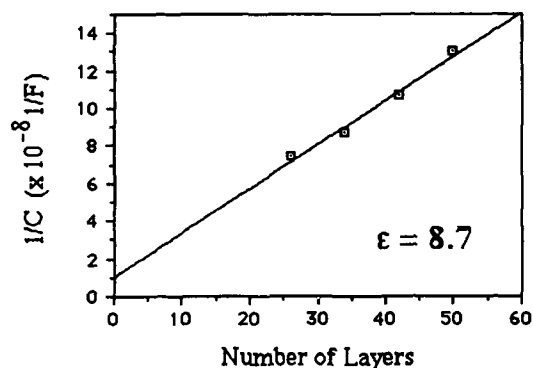


Figure 3. Inverse capacitance versus the number of layers transferred plot of the polypyrrole/3ODOP-3ODP alternating superlattice.

## CONCLUSIONS

Langmuir-Blodgett multilayer thin films containing electrically conductive polypyrroles have been shown to exhibit enormous conductivity anisotropies and large dielectric constants (at low frequencies). The unusual electrical properties of these new thin films are a direct consequence of their multilayer structures and heterogeneous molecular organizations.

## ACKNOWLEDGEMENTS

The authors are grateful to Dr. Enid Sichel for her invaluable contributions to this work. The assistance of Dr. Keith Hong and Ms. Josephine Cheung is also gratefully acknowledged. Partial support of this research was provided by the National Science Foundation, the MIT Center for Materials Science and Engineering and the U. S. Army Electronics Technology and Devices Laboratory (via the Army Research Office Scientific Services Program administered by Batelle).

## REFERENCES

- (a) K. Hong, M.F. Rubner, *Thin Solid Films*, **160**, 187 (1988).
  - (b) K. Hong, M.F. Rubner, *Thin Solid Films*, *in press*.
  - (c) K. Hong, R.B. Rosner, M.F. Rubner, *Chemistry of Materials*, *in press*.

2. (a) I. Watanabe, K. Hong, M.F. Rubner, I.H. Loh, *Synth. Met.* **28**, C473 (1989).  
(b) I. Watanabe, K. Hong, M.F. Rubner, *J. Chem. Soc., Chem. Commun.* **1989**, 123.  
(c) I. Watanabe, K. Hong, M.F. Rubner, *Thin Solid Films*, in press.  
(d) I. Watanabe, K. Hong, M.F. Rubner, submitted to *Langmuir*.
3. A.J. Epstein in *Handbook of Conducting Polymers*, Edited by T.A. Skotheim (Marcel Dekker Publishers, New York, 1986) p. 1041.
4. I.G. Austen and N.F. Mott, *Adv. Phys.* **18**, 41 (1969).
5. R. Landauer in *Electronic Transport and Optical Properties in Inhomogeneous Media*, Edited by J.C. Garland and D.B. Tanner (American Institute of Physics, New York, 1978) p 2.
6. Results to be published.



## HETEROCYCLIC POLYMERS AND COPOLYMERS WITH CONTROLLED OPTOELECTRONIC PROPERTIES

JOSE P. RUIZ, KASINATH NAYAK, ANDREW D. CHILD, DENNIS S. MARYNICK\*  
AND JOHN R. REYNOLDS\*

Center for Advanced Polymer Research, Department of Chemistry,  
The University of Texas at Arlington, Arlington, Texas 76019-0065

### ABSTRACT

A series of aromatic polymers and copolymers have been investigated that contain a combination of 2,5-thienylene and 1,4-phenylene linkages. 1,4-Bis-(2-thienyl)phenylene monomers have been prepared with a variety of substituents on the 2,5-phenylene positions. Subsequent oxidative polymerization of these monomers, both chemically and electrochemically, yield a family of polymers containing a thiophene-phenylene-thiophene repeat unit. Theoretical modeling, using both PRDDO and *ab initio* methods, has been used to correlate the thiophene-phenylene torsional angles with band gaps. In addition, polymer band structure has been investigated using the Extended Hückel method.

### INTRODUCTION

During the past decade, a significant amount of effort has been directed towards the architectural modification of electrically conductive polymers. This work has been stimulated by a variety of emerging potential applications [1]. Much of the research has been aimed at improving both the physical and electronic properties of these polymers. Notable among these are solution and melt processability, environmental stability, mechanical integrity and controllable conductive and optical properties.

One conjugated polymer of interest arises when both phenylene and thiophene moieties are incorporated into the polymer backbone. Synthetic efforts which have been pursued include the incorporation of sulfur into a polymer consisting of phenylene and diketone [2] or acetylene [3] units to form a completely alternating thiophene/phenylene backbone; the random incorporation of phenylene and thiophene repeat units [4] utilizing a Grignard reaction; and the utilization of monomeric bis-thienylphenylene which can be electrochemically polymerized to form polymers with bithiophene/phenylene repeat units [5-7].

In this work, we present the synthesis of a series of 1,4-bis(2-thienyl)-2,5-disubstitutedphenylenes and their polymerization using both chemical and electrochemical oxidative polymerizations. The electrochemical, spectroscopic and electrical properties of these polymers are correlated with theoretical calculations demonstrating the utility of theory in helping to direct experimentation.

### RESULTS AND DISCUSSION

#### Monomer Preparation

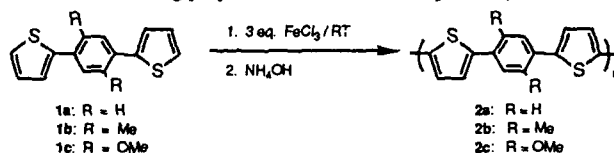
The monomers, 1,4-bis(2-thienyl)benzene, **1a**, and 1,4-bis(2-thienyl)-2,5-dimethylbenzene, **1b**, were prepared from the corresponding 1,4-diiodobenzene derivative [8] and 2-thienyl magnesium bromide with a nickel catalyst. The reaction of 2-thienyl copper with 1,4-diiodo-2,5-dimethoxybenzene in refluxing pyridine [9,10] yielded a crystalline product 1,4-bis(2-thienyl)-2,5-dimethoxybenzene, **1c**, after recrystallization in methanol.

### Electron Density Theoretical Calculations for the Monomers

Initial PRDDO UHF calculations on the monomeric radical cation of monomer 1a yield the maximum positive spin populations on the outer  $\alpha$ -carbons with spin densities of 0.797e and 0.744e respectively. In addition, significant amount of spin populations are found on the  $\beta$ -sites of the thiophene moieties, and the ortho and para positions of the central phenylene ring. In the case of system 1b, although a substantial amount of positive spin is found on the external  $\alpha$ -carbons, (0.796e and 0.589e respectively), there are high positive spin densities predominantly distributed on other sites. In the case of system 1c, the highest amount of positive spin is obtained on the extreme  $\alpha$ -sites, with values of 0.697e and 0.688e. These results lead us to conclude that, in that the external  $\alpha$ -sites are the least sterically blocked and all contain a high spin density, oxidative coupling polymerization will proceed predominantly at these positions. The distribution of measurable spin populations at other sites on the thiophene rings suggests that the copolymers may contain some fraction of  $\alpha$ - $\beta$  and /or  $\beta$ - $\beta$  linkages.

### Chemical Polymerization

Directed by the above spin density calculations, the polymerization of a series of monomers having the general structure 1, has been carried out using both electrochemical and chemical methods. Chemical polymerization was effected utilizing  $\text{FeCl}_3$  as outlined in Equation 1. The resulting polymers, all bluish-black in color, precipitate from the reaction in the oxidized, conductive form. The polymers were subsequently compensated to the insulating forms by stirring in aqueous ammonium hydroxide. Orange, yellow and brick red polymers were obtained for the insulating polymers 2a, 2b and 2c, respectively.



### Structural Properties

The structure and the purity of the monomers and the polymers were fully analyzed using IR,  $^1\text{H}$  and  $^{13}\text{C}$  NMR. The integrity of the thiophene and phenylene moieties, and the substitution patterns expected for essentially  $\alpha$ - $\alpha$  coupling, are maintained throughout the syntheses. Elemental analyses were used to confirm these findings.

### Polymer Physical Properties

Similar to the analogously substituted polymers with thiophene backbones, these polymers are insoluble in common organic solvents. Thermogravimetric analysis showed all three polymers to be quite thermally stable and exhibit an onset of degradation in the neighborhood of 390 °C in the reduced form in nitrogen. These are comparable to the corresponding series of polymers with the complete thiophene backbone. These polymers leave about 60 % char residue even after heating up to 1000 °C.

### Electrochemical Polymerization and Analysis

All three monomers were electropolymerizable in acetonitrile to yield electroactive polymers. Monomer 1c exhibits an oxidation with an onset potential of 0.90 volts (versus  $\text{Ag}/\text{Ag}^+$ ) as shown in Figure 1. A corresponding small reductive peak is observed on the reverse scan and is assigned to the reduction of electrodeposited polymer formed during oxidation. Subsequent scans produced increasing anodic and cathodic currents and a decrease

in the oxidation onset potential to 0.50 volts. This can be attributed to polymer oxidation as the polymer deposited on the electrode is switched from the neutral to the conducting state. Further electropolymerization is evident as the monomer is continually oxidized on the conducting film. The effect of overoxidation was examined by switching the potential at 1.40 volts during a scan. Complete loss of polymer electroactivity is observed at this potential as no cathodic current is detected on the return scan. Subsequent scanning leads to decay of the anodic current as the polymer becomes insulating. Similar results were observed for monomers, 1b and 1c, and their corresponding polymers, 2b and 2c.

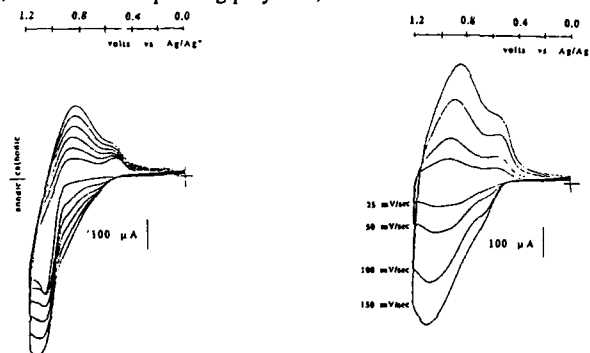


Figure 1. Cyclic voltammograms of 1,4-bis(2-thienyl)-2,5-dimethoxybenzene (1c) and poly[1,4-bis(2-thienyl)-2,5-dimethoxybenzene] (2c). (.1M TBAClO<sub>4</sub> in acetonitrile)

#### Conformational Details

Total energy optimizations were performed, at the PRDDO level [11-13], using internal bond stretches and angle bend variations in order to determine the equilibrium ground state geometries of the monomers of the thiophene and phenylene rings. Upon coupling the two units of thiophenes to the phenylene moiety at its para positions, geometry optimizations were performed to estimate the interring bond distances and the corresponding torsional angles between the phenylene moiety and thiophene moieties. For comparison, the Modified Neglect of Differential Overlap method (MNDO) within the CHEMX program [14] was also employed to obtain the minimum energy conformations. For the system 1a, the interring distance ( $r$ ) and the torsional angle ( $\phi$ ) about the inter ring bond were calculated to be 1.47Å and 24.3° respectively, with a barrier to rotation ( $\Delta E$ ) of 3.1 kcal/mol. In case of system 1b, it was found that  $r=1.48\text{Å}$  and  $\phi=63^\circ$ ; the increased twist angle clearly being due to the steric interaction of the methyl group with the sulfur atom. The barrier to rotation was calculated to be 15.8 kcal/mol. For the system 1c, the optimized torsional angle ( $\phi$ ) was found to be 40° and  $r=1.474\text{Å}$  with a  $\Delta E$  of 3.5 kcal/mol. Thus it is evident that the phenylene-bithiophene copolymers do not represent planar systems. In case of system 1a we carried out the MNDO calculations within the CHEMX program [15], which predicted the perpendicular conformation (a rotation of 90° between the phenylene and thiophene units) to be 4.1 Kcal/mol more stable than the planar form.

Very recently a number of studies [16-23] have appeared leading to a controversy concerning the relative stabilities of the aromatic and quinoid forms of the polythiophene and its derivatives. It is thus quite interesting to explore such alternate features in case of the copolymers of the phenylene and bithiophene systems. Initial optimizations of the aromatic monomeric systems suggest that these copolymers do represent essentially nonplanar backbones. Since it is obvious that the aromatic and quinoid structures may coexist, we extended our studies to estimate the stabilities between the aromatic and quinoid forms of these systems using the PRDDO method and the thermodynamic cycle arguments developed earlier [23]. These calculations clearly indicate a strong preference for the aromatic forms of all of the polymers considered here.

### Band Structure Calculations

The band structures of the one dimensional polymer chain of alternating phenylene and bithiophene were calculated using the extended Hückel theory within the tight binding approximation [24-25]. A representative band structure of polymer 2c is shown in Figure 2.

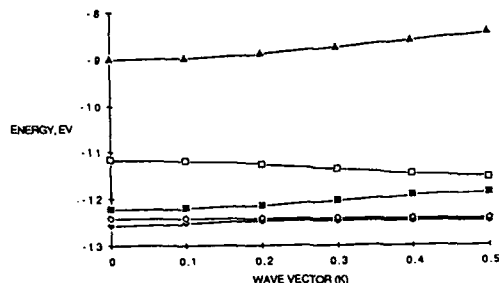


Figure 2. Band structure of poly[1,4-bis(2-thienyl)-2,5-dimethoxybenzene] (2c)

A repeat unit consisting of a phenylene connected to thiophenes at the *para* positions was considered for our calculations. The geometric parameters required such as bond lengths and bond angles were obtained from our PRDDO calculations. Due to the large size of the unit cell, the lattice sums were carried out only to the first nearest neighbor. The present calculations include all the valence atomic orbitals of H, C, O, and S atoms. The atomic parameters required for the computations were obtained from the literature [24-26].

The estimated quantities of interest are the band gaps and band widths of the highest occupied valence bands of these polymers. The band structures were obtained within the first half of the first Brillouin zone with wave vector ( $k$ ) (where  $k = 2\pi/a$ ,  $a$  being the primitive vector) ranging from 0.0 to 0.5k with an increment of 0.1. In the case of system 2a in its most stable conformational state, the band gap ( $E_g$ ) and band width ( $E_{bw}$ ) are found to be 2.03 and 0.43 eV respectively. The corresponding values calculated for polythiophene are 1.73 and 1.17 eV [27]. In the case of system 2b, the band gap and band widths are found to be 2.58 and 0.13eV respectively. For system 2c the values of  $E_g$  and  $E_{bw}$  are 2.18 and 0.36 eV respectively. In general, the electronic properties of 2a and 2c are found to be intermediate between those of polyparaphenylene and polythiophene. From detailed analysis of the highest occupied valence bands (HOVB) of 2a, it is found that the HOVB originates from the  $\pi$  orbitals of the phenylene ring and sulfur atoms. In the case of the substituted copolymers, there is loss of conjugation due to nonplanarity of the backbones and the states in the HOVB are more localized on the individual rings. This partly explains the flatness or the nondispersive characteristics of the HOVBs of these substituted polymers.

### Optoelectrochemistry

A spectroscopic analysis of the polymers gave an onset of the  $\pi$ - $\pi$  transition of 2.2, 2.75 and 2.2 eV for polymers 2a, 2b and 2c respectively. This is shown in Figure 3 for polymer 2c. These polymers, unlike 3-substituted polythiophenes, exhibit strong modifications of the band gap upon the incorporation of alkyl and alkoxy groups. This phenomenon is observed in substituted poly(p-phenylene) due to the steric interactions of the substituent groups with the adjacent phenyl rings.

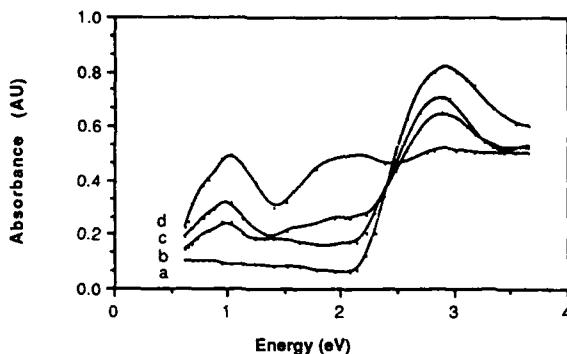


Figure 3. Optoelectrochemical Spectra of poly[1,4-bis(2-thienyl)-2,5-dimethoxybenzene] (2c) at varied applied potentials. a) 0.0 V, b) 1.2 V, c) 1.8 V, d) 2.2 V.

Partial oxidation of the polymers, using applied potentials lower than that of the polymer oxidation potential, resulted in the emergence of two new low energy transitions between 0.5 and 2.0 eV. This is indicative of the formation of bipolaronic species on the polymer chain upon oxidation and is observed for each system.

#### Conductivity of the Polymers

The neutral polymers isolated were oxidized to the conductive form by using  $\text{NOPF}_6$  and  $\text{I}_2$ . Upon oxidation the color of the polymers changed from the insulating forms of orange, yellow and brick red for 2a, 2b and 2c, respectively to bluish black for the 2a and 2c polymers and a very dark green for 2b. Pressed pellet conductivities between 0.1 to 2.0  $\text{Scm}^{-1}$  were observed for 2a and 2c while 2b exhibited a conductivity of  $10^{-6}$ .

#### CORRELATION OF RESULTS

Spin calculations have indicated that the most probable locations for coupling are the external 5 and 5' positions of the thiophene rings in the monomers studied (1a, 1b and 1c) although other sites may be reactive. The structural analysis supports these calculations as  $\alpha$ - $\alpha$  coupling was observed exclusively. This can be attributed to both the relatively low steric hindrance and high spin populations at these sites.

The theoretically preferred conformation of the monomers indicates that the substituent groups interact with the adjacent rings forcing the rings out of planarity. This phenomenon is demonstrated by the higher observed band gap of the dimethyl substituted polymer relative to the unsubstituted polymer. This large twist angle also shortens the conjugation length and is responsible for the low conductivity exhibited by the dimethyl substituted polymer. The dimethoxy substituted polymer's conductivity and band structure is a function not only of twist angle, but also of the electron donating ability of its substituents. The methoxy chains increase the electron density in the ring system and compensate for the steric effects creating the large twist angle. This balance between steric and electron donating effects enable the dimethoxy substituted polymer to exhibit electronic properties similar to the unsubstituted system.

## ACKNOWLEDGEMENT

This work was supported by grants from the Defense Advanced Research Projects Agency, monitored by the Office of Naval Research, the Texas Energy Research in Applications Program, the Robert A. Welch Foundation and Rockwell International.

## REFERENCES

1. J.R. Reynolds, *Chemtech.*, **18**, 440 (1988).
2. K.L. Power, T.R. Vries, E.E. Havinga, E.W. Meijer and H.J. Wynberg, *Chem. Soc., Chem. Comm.*, 1432 (1988).
3. W. Braeke, *J. Polym. Sci.*, **10**, 975 (1972).
4. W. Czerwinski, N. Nucker and J. Fink, *Synth. Met.*, **25**, 71 (1988).
5. R. Danieli, R. Ostoja, M. Tiecco, R. Zamboni and C. Taliani, *J. Chem. Soc., Chem. Comm.*, 1473 (1986).
6. T. Mitsuhashi, S. Tanaka and K. Kaeriyama, *Makromol. Chem.*, **189**, 1755 (1988); *J. Chem. Soc., Chem. Comm.*, 764 (1987).
7. S. Tanaka, K. Kaeriyama and T. Hiraide, *Makromol. Chem., Rapid Comm.*, **9**, 743 (1988).
8. H. Suzuki, K. Nakamura and R. Goto, *Bull. Chem. Soc. Jpn.*, **39**, 128 (1966).
9. Y. Ogata and K. Nakajima, *Tetrahedron*, **20**, 2751 (1964).
10. M. Nilsson and C. Ullenius, *Acta Chem. Scand.*, **24**, 2379 (1970).
11. T.A. Halgreen, W.N. Lipscomb, *J. Chem. Phys.*, **58**, 1569 (1973).
12. D.S. Marynick, W.N. Lipscomb, *Proc. Nat. Acad. Sci.*, **79**, 1341 (1982).
13. D.S. Marynick, F.U. Axe, C.M. Kirkpatrick and L. Throckmorton, *Chem. Phys. Lett.*, **92**, 406 (1982).
14. CHEMX: This software package was obtained from Chemical Design Inc. Sigmex Limited, West Sussex, England 1988.
15. S. Hotta, M. Soga and N. Sonoda, *Synth. Met.*, **26**, 267 (1988).
16. J. L. Brédas, B. Théman, J. M. André, A.J. Heeger and F. Wudl, *Synth. Met.*, **11**, 343 (1985).
17. J. L. Brédas, A. J. Heeger and F. Wudl, *J. Chem. Phys.*, **85**, 4673 (1986).
18. J. L. Brédas, *Synth. Met.*, **17**, 115 (1987).
19. A.K. Bakhshi, C.M. Liegener, J. Ladik and M. Seel, *Synth. Met.*, **30**, 79, (1989).
20. M. Kertesz and Y.S. Lee, *J. Phys. Chem.*, **91**, 2690 (1987).
21. Y.S. Lee, M. Kertesz, *J. Quantum Chem. Symp.*, **21**, 163 (1987).
22. Y.S. Lee, M. Kertesz, *J. Chem. Phys.*, **88**, 2609 (1988).
23. K. Nayak, D.S. Marynick, *Macromolecules* submitted.
24. M.H. Whangbo and R. Hoffmann, *J. Am. Chem. Soc.*, **100**, 6093 (1978).
25. M.H. Whangbo, R. Hoffmann and R.B. Woodward, *Proc. R. Soc. A.*, **366**, 23 (1979).
26. D. Bhaumik, J.E. Mark, *J. Polym. Sci., Polym. Phys. Ed.*, **21**, 1111 (1983).
27. J. Ruiz, K. Nayak, D.S. Marynick, J.R. Reynolds, *Macromolecules*, **22**, 1231 (1989).

SYNTHESIS, STRUCTURE, INFRARED SPECTRA, AND IODINE DOPING OF  
UNSUBSTITUTED POLYAZINES

WILLIAM B. EULER and BENJAMIN C. GILL  
Department of Chemistry, University of Rhode Island, Kingston, RI 02881

ABSTRACT

Polyazines,  $-\text{[N-CH-CH=N]}_x-$ , are environmentally stable conjugated polymers that can be doped with iodine into an electrically conductive state. These polymers are prepared by the condensation of glyoxal and glyoxal dihydrazone with acid catalysis. IR spectra of the undoped polymers, independent of the synthetic conditions, exhibit a broad band centered around  $3240\text{ cm}^{-1}$  indicative of the presence of OH groups in the polymer. Solid state NMR spectra show that the OH groups are covalently bound to the polymer chain so that the polymer chain has a number of defect and/or cross-linking sites present. The polymer can be doped with iodine into a poorly conducting state. Iodine doping introduces one new vibrational band into the IR spectra at  $1490\text{ cm}^{-1}$ , associated with a bipolaronic charge carrier.

INTRODUCTION

We have recently reported [1] the physical and chemical properties of permethyl polyazine,  $-\text{[N-C(CH}_3\text{)-C(CH}_3\text{)-N]}_x-$ . Permethyl polyazine forms in the all trans conformation as demonstrated by both IR [1] and solid state NMR spectroscopy [2]. Iodine doping of permethyl polyazine gives a conducting powder with room temperature pressed pellet conductivities of  $0.1\text{ }\Omega^{-1}\text{cm}^{-1}$  for the most heavily doped material [1,3]. Because it is known that methyl groups inhibit the conductivity in polyacetylenes [4], we undertook the synthesis and doping of the unsubstituted polyazine,  $-\text{[N-CH-CH=N]}_x-$  (PAZ), with hopes of improving the conductivity properties of this class of materials. We have found that the synthetic conditions leading to PAZ introduces defect sites that are probably tetrahydroxypiperazines and  $\alpha$ -amino alcohols. Because of the loss of conjugation from the defects, these polymers can only be doped into a poorly conductive state, about  $1 \times 10^{-6}\text{ }\Omega^{-1}\text{cm}^{-1}$  for the most heavily doped powders at room temperature.

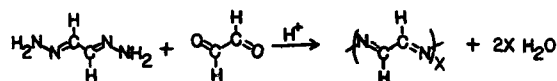
## EXPERIMENTAL

Polyazine is prepared by the acid catalyzed (acetic acid) condensation of equimolar amounts of glyoxal (obtained from Aldrich as a 40% aqueous solution) and glyoxal dihydrazone (prepared by adding glyoxal to excess hydrazine hydrate) and stirring at room temperature or at reflux for at least 24 hours. Solvents used were methanol, ethanol, n-propanol, and n-butanol with only minor differences in the IR spectra of the products obtained. Doping was accomplished by stirring a chloroform solution of iodine with the polymer for 24 hours.

IR spectra were obtained between 600 and 4000  $\text{cm}^{-1}$  as KBr pellets on a Perkin-Elmer 281B instrument. Conductivities were measured at room temperature on pressed pellets using the vanderPauw technique using an instrument built by Research Specialties (Chicago, IL) [1].

## RESULTS

Polyazines are formed by the acid catalyzed condensation between an  $\alpha,\beta$ -dicarbonyl and an  $\alpha,\beta$ -dihydrazone:



Mechanistically, this reaction should proceed by addition of the amine to the carbonyl followed by elimination of water to form the imine bond. For permethyl polyazine the reaction scheme behaves as described but for the unsubstituted polymer there is clear evidence for incomplete dehydration. The elemental analysis of PAZ has a high oxygen content and the IR spectrum of the polymer has a broad and intense band centered at 3240  $\text{cm}^{-1}$  due to an OH vibrational mode. Solid state NMR shows that this OH group must be covalently bound to the polymer chain [5].

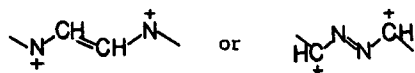
The top spectrum in Figure 1 shows the IR response of the undoped PAZ below 1800  $\text{cm}^{-1}$ . All of the peaks are broad, probably due to two reasons. First, there may be a relatively wide distribution of molecular weights, leading to a number of similar but not identical vibrational transitions. Second, the presence of defect sites interrupts the chain, thus leading to a number of new structures not found in the conjugated part of the chain.





Despite the presence of defects, PAZ readily reacts with iodine. However, the amount of iodine that can react with PAZ appears to maximize at about 0.3 iodine atoms per repeat unit, similar to polyacetylene [7], which is significantly less than the 1.4-1.5 iodine atoms per repeat unit that permethyl polyazine can accommodate [1]. The maximum conductivity at the highest doping level is about  $1 \times 10^{-6} \Omega^{-1}\text{cm}^{-1}$ . This very low value for the conductivity is consistent with the presence of a large number of defects in the polymer which impede the mobility of the charge carrier. An ionic charge carrier is also a possibility.

The IR spectra of the doped and undoped species are similar, as shown in Figure 1. The major vibrational bands are unaffected by the doping indicating that the polymer backbone structure has not been disrupted. A new band appears at  $1490 \text{ cm}^{-1}$  that grows in intensity with increased doping level. A similar absorption occurs in the iodine doped permethyl polyazines [3] and this was attributed to a bipolaronic charge carrier:



A similar structure is expected to form in the unsubstituted polyazine upon oxidation. There is no IR evidence that the defect sites participate in the oxidation process. Further investigations of the UV-Vis spectra to confirm the presence of the bi-polaron and charge transport processes in these materials is in progress.

#### REFERENCES

1. C.R. Hauer, G.S. King, E.L. McCool, W.B. Euler, J.D. Ferrara, and W.J. Youngs, *J. Am. Chem. Soc.* **109**, 5760 (1987).
2. W.B. Euler and J. E. Roberts, *Macromolecules*, in press.
3. W.B. Euler, *Sol. State Commun.* **68**, 291 (1988).
4. J.C.W. Chien, G.E. Wnek, F.E. Karasz, and J.A. Hirsch, *Macromolecules* **14**, 479 (1981).
5. B. Chaloner-Gill, C.J. Cheer, J.E. Roberts, and W.B. Euler, manuscript in preparation.
6. Y. Cao and S. Li, *J. Chem. Soc. Chem. Commun.* **1988**, 937.
7. N.S. Murthy, G.G. Miller, and R. H. Baughman, *J. Chem. Phys.* **89**, 2523 (1988).

GENERATION OF STABLE RADICAL CATIONS (POLARONS) AND DICATIONS (BIPOLARONS)  
ON MODEL THIOPHENE OLIGOMERS

Denis FICHOV and Gilles HOROWITZ  
Laboratoire des Matériaux Moléculaires - C.N.R.S. - 2, rue Henry Dunant  
94320 - Thiais, France

ABSTRACT

Oxidative doping of individual thiophene oligomers nT (n = 3 to 6) with FeCl<sub>3</sub> in dilute CH<sub>2</sub>Cl<sub>2</sub> solution generates the corresponding radical cations (polarons) nT<sup>•+</sup>, as evidenced by in-situ visible/near infrared absorption and electron spin resonance spectroscopies. The nT<sup>•+</sup> species in solution progressively precipitate as conducting ( $\sigma_{300K} = 10^{-1}-10^{-2}$  S/cm) and strongly paramagnetic radical cation salts (g = 2.003,  $\Delta H_{pp} = 4-8$  G). The conductivity of the 6T<sup>•+</sup> salt is weakly temperature dependent, with an activation energy of 32 meV above 100 K and a tendency to level off at lower temperatures. In the case of the sexithienyl radical 6T<sup>•+</sup>, further doping results in the quantitative conversion into the dication 6T<sup>++</sup> (bipolaron).

INTRODUCTION

It is now well-admitted that the doping process of conjugated polymers leads to the formation of charged localized defects called polarons and bipolarons. In the case of polythiophene (PT), a nondegenerate ground state polymer, experimental studies have shown that at low doping levels ( $\approx 0.5$  mol%) singly charged hole polarons are the dominant species while at higher doping levels ( $> 5$  mol %) they recombine to form the more stable hole bipolarons [1]. Numerous theoretical approaches have also been proposed to account for these observations, as that carried out by Bertho and Jouanin in the framework of the Hückel approximation [2]. Recently, Brédas et al. presented VEH (Valence effective hamiltonian) band-structure calculations on doped PT as a function of the doping level using model oligomers such as the hexamer (6T) for the geometry optimization of the systems [3]. Nevertheless, even if long thiophene oligomers are good qualitative approximations for the corresponding neutral and doped PT geometries, they remain hypothetical systems which may behave quite differently as synthesized molecules. In sharp contrast with the polymer, they have a finite structure and do not possess any structural disorder (side chains, conjugation interruptions) susceptible to influence their electronic properties.

We have recently synthesized long oligothiophenes (nT, with n up to 10) [4] and studied their optical [5] and electrical [6] properties in the form of thin solid films as a function of the chain length. These compounds represent a compromise between small molecules and macromolecules. They remain very slightly soluble in organic solvents up to the hexamer and can then be studied in dilute solutions ( $\approx 10^{-2}$  mole.l<sup>-1</sup>).

In order to check whether or not real thiophene oligomers behave similarly to PT and could thus be considered as model systems for PT on both the experimental and theoretical levels, we have performed FeCl<sub>3</sub>-doping experiments on 3T, 4T, 5T and 6T in dilute CH<sub>2</sub>Cl<sub>2</sub> solutions. We report in this article on the successive generation of the corresponding radical cations nT<sup>•+</sup> (polarons) and dications nT<sup>++</sup> (bipolarons) as followed by in-situ optical absorption (400-3000 nm) and electron spin resonance (ESR). The electrical conductivity of the 6T<sup>•+</sup> radical cation salt in the solid state has been studied as a function of temperature down to 15 K in order to investigate its transport properties. Finally, in the particular case of 6T, clear-cut spectroscopic evidences of the polaron-bipolaron

( $6T^+ \rightarrow 6T^{++}$ ) transition are presented.

#### EXPERIMENTAL

3T is commercially available (Aldrich) and 4T, 5T and 6T were synthesized according to known procedures [7]. Solutions of the various nT oligomers ( $10^{-5}$  mole.l<sup>-1</sup>) in spectrophotometric grade CH<sub>2</sub>Cl<sub>2</sub> were prepared under argon atmosphere. Upon doping by the progressive addition of a controlled quantity of anhydrous FeCl<sub>3</sub> in CH<sub>2</sub>Cl<sub>2</sub> ( $10^{-3}$  mole.l<sup>-1</sup>), the nT solutions turns to different colours typical of organic radicals and the optical and ESR spectra were immediately recorded. A black solid slowly precipitates, which corresponds to the [nT<sup>••</sup>, FeCl<sub>4</sub><sup>-</sup>] cation radical salts. Its electrical conductivity as a function of temperature was measured over the 12-300 K range in the form of a pressed pellet (10 tons).

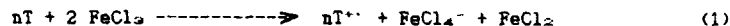
Absorption spectra were recorded with a Varian Cary 2415 UV-VIS-NIR spectrophotometer monitored by a Varian DS 15 Data Station. Spectra were corrected from the solvent absorption by the Varian Multiscan program. All spectra were recorded up to 3.0 μm but no absorption was observed in the 2.0-3.0 μm; thus, this spectral range is not presented here.

ESR spectra were taken at room temperature on a Varian E3 spectrometer at a frequency of 9.08 GHz, with a 16 G magnetic field modulation amplitude, and a 3 mW incident microwave power. The magnetic field was centered at 3.225 kG, i.e. in the g=2.003 region where the narrow ESR signals of organic radicals are expected. Nevertheless, if paramagnetic Fe(III) ions are present in the solution, they also give a signal around g=2, but with a much broader linewidth ( $\Delta H_{pp}$ =400-600 G).

#### RESULTS AND DISCUSSION

The chemical oxidation of aromatics into radical cations by Lewis acids or protic acids as the oxidant is a well-known technique and a 100% conversion can be easily obtained by a proper choice of the reagent [8]. In particular, the oxidation potential of the π-electron molecule should be relatively small, the electron affinity of the oxidant relatively large and the solvent should be of maximum polarity in order to stabilize the ionic reaction product. On the other hand, the stability of the nT<sup>••</sup> radicals increases with the chain length n owing to the increasing degree of resonance along the conjugated π-system. As a matter of fact, coupling reactions of the nT<sup>••</sup> radicals into dimer or trimer-type products become less and less favourable as n increases and the generated nT<sup>••</sup> becomes more and more stable.

As we discuss it elsewhere [4a], the chemical generation of the radical cation nT<sup>••</sup> can be summarized as follows:



The optical spectra of the 3T, 4T, 5T and 6T solutions after doping by a stoichiometric quantity of FeCl<sub>3</sub> (two moles of FeCl<sub>3</sub> per mole of nT as deduced from equation 1) are shown in Fig.1(a-d). For the sake of clarity, the spectra of the neutral molecules are not drawn; the fundamental π-π\* transition bands of 3T, 4T, 5T and 6T in CH<sub>2</sub>Cl<sub>2</sub> have their respective maxima at 350, 388, 403 and 432 nm and do not exhibit any vibronic structure.

The most striking general feature of all nT<sup>••</sup> optical spectra is the appearance in the visible and near-infrared regions of very narrow and well-resolved absorption bands, which contrast greatly with the usual

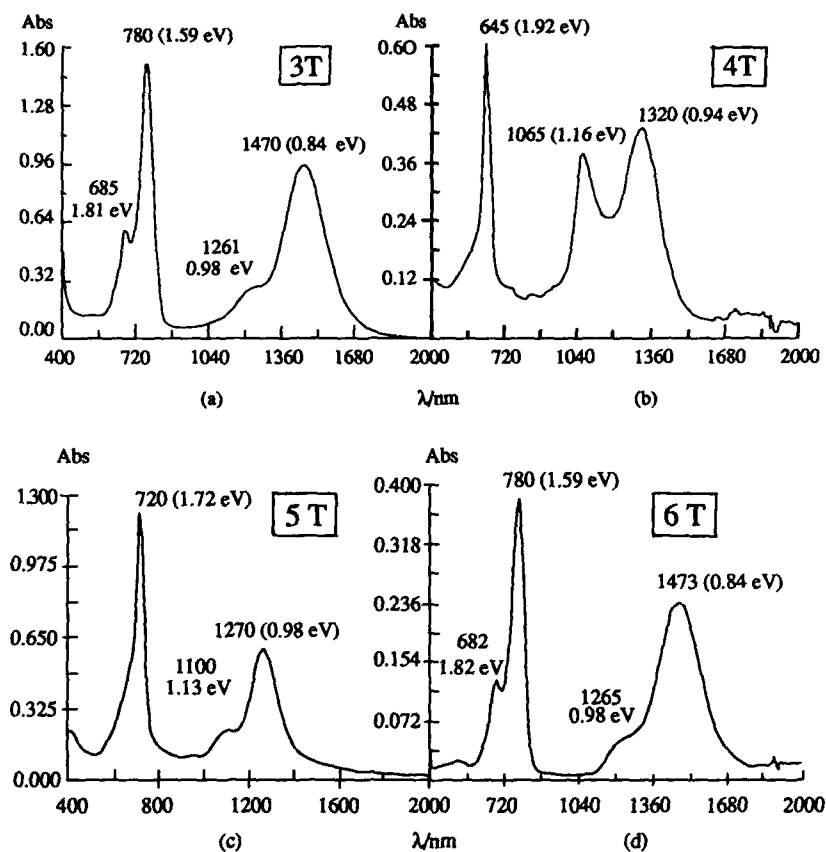


Figure 1 - Visible and near infrared absorption spectra of the  $nT^+$  radical cations in  $CH_2Cl_2$  solution as obtained by  $FeCl_3$  oxidation of the respective  $nT$ : (a) 3T, (b) 4T, (c) 5T, and (d) 6T.

broad spectra of doped polythiophenes. This arises from the unique chain length of the molecules in the solution together with their homogeneous and highly symmetrical spin and charge distribution along the chains. A second remarkable point is the perfect similarity of both 3T and 6T spectra (compare Fig. 1a and 1d). This simply shows that the 3T<sup>+</sup> radical, which is the shortest molecule in this study, is too unstable to be observed at room temperature and dimerizes immediately into the more stable sexithienyl. This basic observation was the starting point of a new synthesis of 6T (4a). Two types of bands are observed on every spectrum, in the visible (band 1) and the NIR (band 2) regions respectively. Each of them shows a fine structure, with a narrow and intense peak maximum accompanied by a shoulder of weaker intensity on the high energy side. An increased chain length results in a red shift of every absorption band, as expected. All spectroscopic data are summarized in Table 1.

	4T	5T	6T
Band 1	620 (2.00)	660 (1.88)	682 (1.82)
	645 (1.92)	720 (1.72)	780 (1.59)
Band 2	/	1100 (1.13)	1265 (0.98)
	1065 (1.16)	1270 (0.98)	1473 (0.84)
	1320 (0.94)*		
Band 3	/	/	908 (1.36)
	/	/	1003 (1.24)

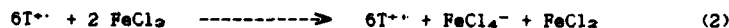
\* tentatively attributed to the 8T<sup>++</sup> dication.

Table 1 - Absorption peak maxima (nm/eV) of nT<sup>++</sup> radical cations (Bands 1 and 2) and 6T<sup>++</sup> dication (Band 3) in CH<sub>2</sub>Cl<sub>2</sub> as obtained by FeCl<sub>3</sub>-doping of nT oligomers in solution at room temperature.

The free radical character of the oxidized species in solution was confirmed by ESR measurements which show for all nT<sup>++</sup> species an intense and narrow ( $\Delta H_{pp} \approx 4-8$  G) Lorentzian signal centered at  $g=2.003$ . No hyperfine structure has been found yet. This signal, which is typical of an organic radical, is superimposed to a much broader one ( $\Delta H_{pp} \approx 400-600$  G) of much weaker intensity and also centered around  $g=2$ , characteristic of the paramagnetic FeCl<sub>4</sub><sup>-</sup> ion. On the other hand, if no particular precaution against O<sub>2</sub> is taken, the ESR signal intensity decreases by only 50% after 24 hours in open air, which is a good indication of the stability of the radical in CH<sub>2</sub>Cl<sub>2</sub>.

When FeCl<sub>3</sub> is quantitatively added to 6T to form 100% of 6T<sup>++</sup>, (as checked by the complete extinction of  $\pi-\pi^*$  transition band of neutral 6T at 432 nm) a black precipitate appears progressively. The solid material is strongly paramagnetic and exhibits a sharp ESR signal ( $\Delta H_{pp} = 4$  G) centered at  $g=2.003$  together with a broad and intense signal due to the Fe(III) ions in high concentration, very likely in the form of FeCl<sub>4</sub><sup>-</sup> counter-anions. This solid can be (partially) dissolved back in CH<sub>2</sub>Cl<sub>2</sub>. The optical spectrum of the solution is similar to that of the radical cation 6T<sup>++</sup> (see Fig. 1d) indicating unambiguously that it corresponds to the radical cation salt [6T<sup>++</sup>, FeCl<sub>4</sub><sup>-</sup>]. The conductivity  $\sigma$  of 6T<sup>++</sup> was measured on pressed pellets of the powder down to a temperature of 15 K. An Arrhenius plot of  $\sigma$  is shown in Fig. 2. The conductivity is only weakly temperature dependent, with an activation energy of 32 meV above 100 K and a tendency to level off at lower temperatures. This behavior, together with the relatively high value of  $\sigma$ , can be compared to what is observed on doped polythiophene.

An excess of FeCl<sub>3</sub> does not oxidize further the 4T<sup>++</sup> and 5T<sup>++</sup> radical cations. On the contrary, if an excess of FeCl<sub>3</sub> is added to the 6T<sup>++</sup> radical cation in solution, both Band 1 and Band 2 progressively vanish while a new structured band (Band 3) appears at intermediate energies revealing two isosbestic points at 823 and 1135 nm respectively as shown in Fig. 3. This new species in solution is diamagnetic, as shown by the simultaneous disappearance of the in-situ narrow ESR signal. From these data, we conclude that 6T<sup>++</sup> is oxidatively converted into the dication 6T<sup>+++</sup>, according to equation (2):



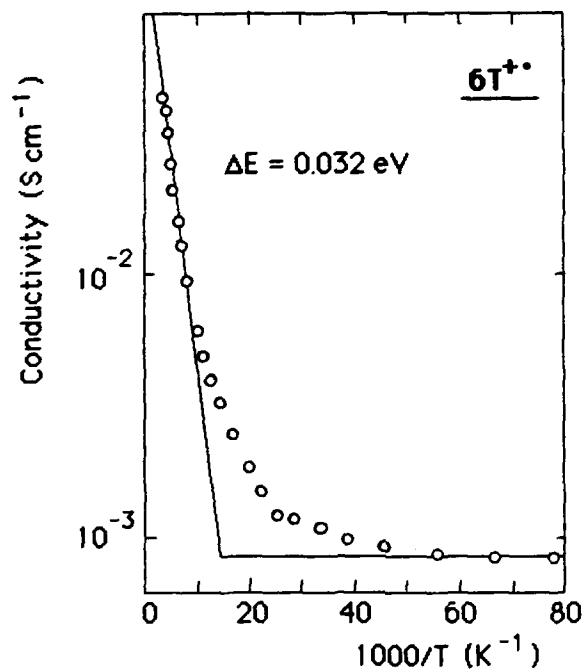


Figure 2 - Conductivity  $\sigma$  versus  $T^{-1}$  of a pressed pellet of the  $[6T^{\bullet\bullet}, FeCl_4^-]$  radical cation salt.

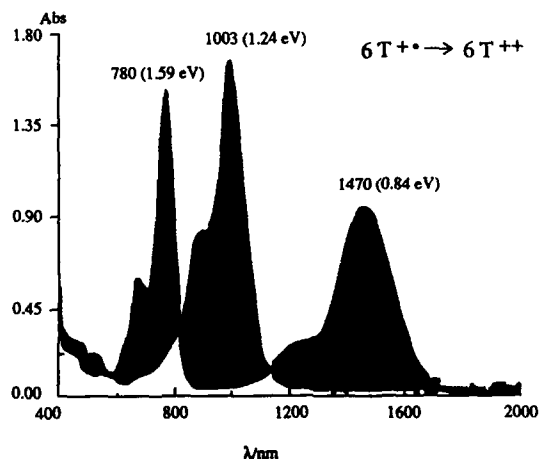


Figure 3 - Absorption spectra of the radical cation  $6T^{\bullet\bullet}$  (Bands 1 and 2) and of the dication  $6T^{++}$  (Band 3) in  $CH_2Cl_2$ , showing the two isosbestic points of the  $6T^{\bullet\bullet} \rightarrow 6T^{++}$  interconversion.

The fact that neither  $4T^{+}$  nor  $5T^{+}$  can be further oxidized in the presence of an excess of oxidant is very likely due to a too high second oxidation potential.  $6T$  would then be the shortest oligothiophene which can be oxidized into a stable dicationic form  $6T^{2+}$ .

## REFERENCES

- [1] (a) T.-C. Chung, J.H. Kaufman, A.J. Heeger and F. Wudl, *Phys. Rev. B* 30, 702 (1984). (b) K. Kaneto, Y. Kohno and K. Yoshino, *Mol. Cryst. Liq. Cryst.* 118, 217 (1985).
- [2] D. Bertho and C. Jouanin, *Phys. Rev. B* 35, 626 (1987).
- [3] S. Stafström and J.L. Brédas, *Phys. Rev. B* 38, 4180 (1988).
- [4] (a) D. Fichou, G. Horowitz and F. Garnier, in press. (b) Z. Xu, D. Fichou, G. Horowitz and F. Garnier, *J. Electroanal. Chem.* 267, 339 (1989).
- [5] (a) D. Fichou, F. Garnier, F. Charra, F. Kajzar and J. Messier, in "Organic Materials for Nonlinear Optics", eds. R. Hahn and D. Bloor, Royal Society of Chemistry, London, pp.176 (1989).
- [6] (a) G. Horowitz, D. Fichou and F. Garnier, *Solid State Commun.* 70, 385 (1989). (b) G. Horowitz, D. Fichou, X. Peng, Z. Xu and F. Garnier, *Solid State Commun.*, in press.
- [7] (a) J. Kagan and S. Arora, *Heterocycles*, 20, 1937 (1983). (b) J. Kagan and S. Arora, *Tetrahedron Lett.*, 24, 4043 (1983).
- [8] G. Vincow, in "Radical Ions", eds. E.T. Kaiser and L. Kevan, (Interscience, New-York, 1968), pp. 151.



PHOTOLUMINESCENCE AND ODMR STUDIES OF PRISTINE AND  
PHOTODEGRADED POLY(3-HEXYLTHIOPHENE) FILMS AND SOLUTIONS

L. S. SWANSON,\* J. SHINAR,\* L. R. LICHTY,\* AND K. YOSHINO\*\*

\*Ames Laboratory - USDOE and Physics Department, Iowa State University,  
Ames, IA 50011-3020

\*\*Department of Electrical Engineering, Faculty of Engineering, Osaka  
University, Osaka 565, Japan.

ABSTRACT

The photoluminescence (PL) and optically detected magnetic resonance (ODMR) spectra of poly(3-hexylthiophene) in solutions of  $CCl_4$ , toluene, and  $CH_2Cl_2$ , and films cast from these solutions, are described and discussed. In solution, the PL yield is 7%, and increases with increasing temperature. In oxygen-free, protected films cast from these solutions, the room-temperature yield is ~0.7%, the spectra is red shifted by ~0.5eV, and strong peaks at 1.52, 1.69, and 1.86eV appear. In films and  $CH_2Cl_2$  solutions, the ODMR is resolvable into narrow and broad components, and its intensity  $\Delta I/I$  is  $\sim 5 \times 10^{-5}$  at room temperature. A strong photoinduced oxidation process quenches the PL upon exposure to  $O_2$  but not water, at a rate possibly limited by  $O_2$  diffusion.

INTRODUCTION

The photoexcitations in polythiophene (PT) and its 3-alkyl derivatives, a prototypical weakly nondegenerate ground state  $\pi$ -conjugated polymer, have been the subject of numerous studies [1-13]. Thus, the nonradiative decay channels of photogenerated  $e-h$  pairs into polarons within a few picoseconds, and of polarons into bipolarons within a few milliseconds, are well established [1,2,4,9,13]. Similar processes are observed during oxidative p-doping [3,8]. Yet the nature of the radiative decay processes is still not well understood. The observations of anisotropic photoluminescence (PL) in stretch oriented films [6] and an enhanced PL yield of ~7% in dilute solutions vs. films [11] provide strong evidence that the radiative channel is intrachain, and enhanced by conformational defects [10,15-18] that reduce the conjugation length. Yet while previous studies of Kaneto and coworkers [5-7,14] provided evidence that the PL is due to exciton decay, recent optically detected magnetic resonance (ODMR) measurements support the polaron-to-band channel [19-21]. This work, while not offering a conclusive verdict on this issue, provides additional results on poly(3-hexylthiophene) (P3HT) relevant to this problem. In particular, the temperature dependence of the PL and ODMR spectra in solutions and films is described, as well as the photoinduced oxidation process, which quenches the PL and the ODMR.

EXPERIMENTAL PROCEDURE

Free standing films of P3HT were prepared as described elsewhere [14,15]. These films were stored in the dark, but not in vacuo. Thus, to clean the films from physisorbed oxygen, the free standing films were dissolved in  $CCl_4$ , toluene, or  $CH_2Cl_2$ , and the solution was then degassed by several cooling-pumping cycles. Clean films were then deposited by casting onto quartz substrates, in vacuo or a protective inert atmosphere, and sealed in quartz tubes. Degassed solutions were also sealed in quartz tubes.

To obtain either PL or ODMR signals and spectra, the samples were placed in the quartz dewar of an Oxford He gas-flow cryostat, enabling temperature control from 4-300K, inside an optically accessed X-band microwave cavity. The PL was excited by 4765Å photons from a Pockels-cell

stabilized Ar<sup>+</sup> laser chopped at 500Hz. The excitation intensity incident on the sample was usually kept below 10mW to prevent sample heating. The PL spectra were measured by dispersing the emission through either a high resolution 1m SPEX monochromator, or a low resolution 0.25m Schoeffel monochromator, and detecting it with a cooled RCA C31034 photomultiplier tube. The ODMR was lockin detected from the modulated PL intensity resulting from microwave chopping, as the dc magnetic field was swept through the resonance.

#### EXPERIMENTAL RESULTS AND DISCUSSION

##### Photoinduced oxidation

The decay of the total PL intensity  $L$  of solution-cast films exposed to  $O_2$  is shown in Figure 1. As clearly seen from the inset of Figure 1, which plots  $\log(L/L_0)$  vs.  $t$ , the PL decreases with a distribution of decay times. The asymptotic slope, however, yields a constant  $\tau \approx 1800s$ , suspected to be determined by the rate of diffusion of  $O_2$  into the film. It should be noted that the PL of films pre-exposed to  $O_2$  for prolonged periods exhibited a qualitatively similar response to photoexcitation. This behavior, and the lack of any decline in the PL intensity of protected films (top trace in Figure 1), clearly shows that the oxidation is photoinduced. Although the decay of the PL in  $O_2$  was previously reported [12], its photoinduced nature was not apparent. The photooxidation-induced quenching of the PL is probably due a process similar to that occurring during  $I_2$  doping-induced quenching of the PL [7]. It is suspected that both are due to a transformation from a coil or helical conformation to a rod-like one [22], which increases the conjugation

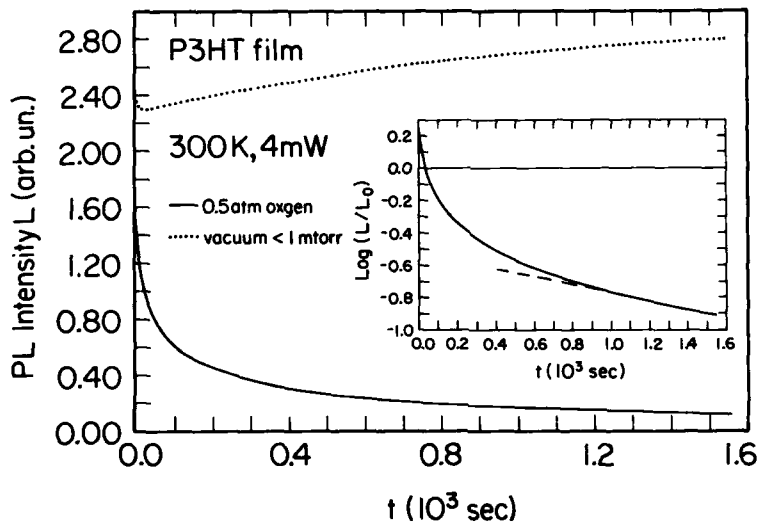


Figure 1. The time dependence of the total photoluminescence (PL) intensity  $L$  of oxygen-free, protected P3HT films (dotted line), and clean films exposed to  $O_2$  (solid line). Inset: Semi-log plot of photooxidation-induced decay of the PL; the asymptotic slope is  $1/\tau = 5.6 \times 10^{-4} s^{-1}$ .

length. An increase in the effective conjugation length decreases the PL intensity [10,11,16,17]. Such a doping-induced transformation has indeed been observed in a solution of poly(3-butylthiophene) doped with  $\text{NOSbF}_6$  [23].

It should be noted that exposure to water did not result in an observable effect on the PL.

A close examination of the time dependence of L in protected films (top trace in Figure 1) reveals a slight increase of L with exposure. Since heating effects are ruled out [24], it is suggested that photogenerated defects (possibly including bondbreaking) cause this slight increase of L with exposure.

#### Photoluminescence in Solutions and Films

The PL spectra of oxygen-free, sealed dilute solutions of P3HT in  $\text{CH}_2\text{Cl}_2$ , at  $T = 200, 240,$  and  $300\text{K}$ , corrected for monochromator and detector response, is shown in Figure 2. Since the onset of absorption in  $\text{CH}_2\text{Cl}_2$  solutions occurs at  $-2.3\text{eV}$  [9], reabsorption effects are not significant. As clearly seen, the spectrum becomes red-shifted with decreasing temperature. In addition, the yield, which is  $\sim 7\%$  at  $300\text{K}$ , decreases to  $\sim 2\%$  at  $200\text{K}$ . It thus appears that the conjugation length increases, and with it the yield of non-radiative channels (e.g., interchain hopping and consequent generation of bipolarons), as the temperature decreases [4,11]. Since these effects are temperature dependent, they are probably due to a decrease in dynamically induced conformational defects.

The PL yield of oxygen-free, sealed films cast from these solutions is  $\sim 0.7\%$  at room temperature. The peaks in the PL spectra are more pronounced in these films. Although the spectrum is qualitatively similar to the previously published spectra of unprotected films [19,20], with peaks split by  $\sim 0.17\text{--}0.19\text{eV}$ , the relative intensities of these peaks is not the same. The main peak is observed at  $1.69\text{eV}$ , with secondary peaks at  $1.52$  and  $1.86\text{eV}$ . The  $\sim 0.17\text{eV}$  splitting of the peaks corresponds to the C-C stretch vibration. The PL thus includes contributions from phonon

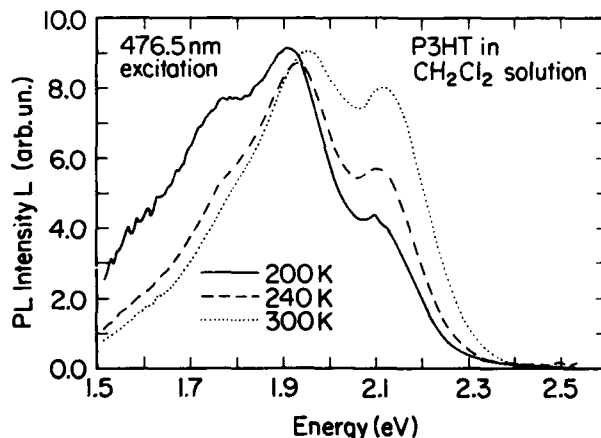


Figure 2. The Photoluminescence spectra of a dilute solution of poly(3-hexylthiophene) in methylene chloride at 200, 240, and 300K, corrected for monochromator and detector response.

sidebands of the high-energy peak. The role of these contributions will be discussed in a future publication [24].

#### ODMR in Films and Solutions

The total-PL ODMR spectrum of an oxygen-free, sealed solution-cast film, at (nominally) 20K, excited by  $\sim 10\text{mW}$  at 488nm, and lockin detected from the chopped X-band microwaves, is shown in Figure 3. It is

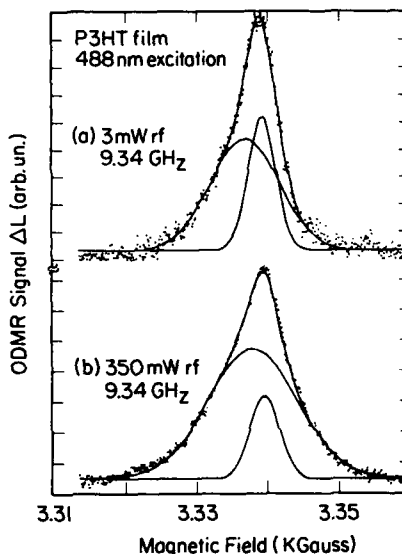


Figure 3. The total-photoluminescence X-band ODMR, at 20K, of an oxygen-free, solutions-cast poly(3-hexylthiophene) film. The ODMR is clearly the sum of two gaussian lines. The 12G FWHM of the narrow line, at  $g = 2.0019$ , is independent of microwave power. The FWHM of the broad line, at  $g = 2.0032$ , increases from 12G at  $\sim 1\text{mW}$  to 15G at  $\sim 350\text{mW}$ .

noteworthy that the ODMR is essentially the same as that of unprotected (and thus partially oxidized) films published previously [19-21]. Two gaussian components are clearly observable: A wide line at  $g = 2.0032 \pm 0.0005$ , and a narrow line at  $g = 2.0019 \pm 0.0005$ . The FWHM of the narrow line is  $\sim 5$  gauss, independent of the microwave power up to  $\sim 350\text{mW}$ . The width of the broad line increases from 12 gauss at  $\sim 1\text{mW}$  to 15 gauss at  $\sim 350\text{mW}$ . It should be noted that the ODMR components are definitely gaussian. All attempts to fit the observed resonance to a combination which included a Lorentzian line resulted in a poorer fit.

$\Delta L/L$  decreases with increasing temperature, but the ODMR is still clearly observable at 300K, where  $\Delta L/L = 5 \times 10^{-5}$  in both films and solutions. This contrasts with the temperature dependence of the ODMR in unprotected films, where it was not observable above 150K. In addition, the ODMR, while unobservable in solutions of P3HT in toluene, was clearly detectable in  $\text{CCl}_4$  solvents at 300K. However, it decayed below the detection limit within a few minutes, and consequently no ODMR spectrum could be obtained. It is interesting to note that although the ODMR rapidly decayed, the PL spectrum remained unchanged. The nature of this behavior is not clear at present.

Although the ODMR was unobservable in toluene solutions, and rapidly decayed in  $\text{CCl}_4$  solutions, it was clearly observable, and stable, in  $\text{CH}_2\text{Cl}_2$  solutions. The total-PL spectrum in this solution is essentially

identical to that of films. This result provides additional evidence that the ODMR is due to an intrinsic intrachain process, and is unrelated to any defect or interchain coupling.

#### SUMMARY AND CONCLUDING REMARKS

The photoluminescence (PL) and optically detected magnetic resonance (ODMR) of poly(3-hexylthiophene) (P3HT) films and solutions was described and discussed. In solutions and solution-cast films exposed to oxygen, a photoinduced oxidation process quenches the PL at room temperature. In oxygen-free  $\text{CH}_2\text{Cl}_2$  solutions of P3HT, the PL yield is ~7% at 300K, but decreases, and the spectrum becomes red-shifted, upon cooling. This is apparently due to a decrease in dynamically-induced conformational defects. The resulting increase in the effective conjugation length consequently increases the yield of non-radiative shunt processes, e.g., decay of polarons into bipolarons. In oxygen-free films cast from solution, the PL yield is ~0.7% and the spectrum is red-shifted by ~0.5eV, apparently due to similar processes. The ODMR of the oxygen-free films and solutions in  $\text{CH}_2\text{Cl}_2$  is essentially identical to that previously described in unprotected, partially oxidized films [19-21]. This provides further evidence that the ODMR is due to intrinsic, intrachain processes, apparently polaron-to-band transitions [19-21], and not related to any defect or interchain coupling. Further studies, which would include the spectral dependence of the ODMR and the ODMR spectra of separate PL bands, should reveal the contributions, if any, of other processes, notably exciton decay. These studies are currently underway and will be published later [24].

#### ACKNOWLEDGEMENTS

We thank Profs. Z. V. Vardeny and T. J. Barton for valuable discussions. Ames Laboratory is operated for the USDOE by Iowa State University under contract no. W-7405-Eng-82.

#### REFERENCES

1. A. J. Heeger, S. Kivelson, J. R. Schrieffer, and W.-P. Su, *Rev. Mod. Phys.* **60**, 781 (1988).
2. Z. Vardeny, E. Ehrenfreund, O. Brafman, M. Nowak, H. Schaffer, A. J. Heeger, and P. Wudl, *Phys. Rev. Lett.* **56**, 671 (1986).
3. J. H. Kaufman, N. Colaneri, J. C. Scott, and G. B. Street, *Phys. Rev. Lett.* **53**, 1005 (1984).
4. R. H. Friend, D. D. C. Bradley, and P. D. Townsend, *J. Phys. D* **20**, 1367 (1987).
5. K. Kaneto, F. Uesugi, and K. Yoshino, *J. Phys. Soc. Jap.* **56**, 3703 (1987).
6. K. Kaneto, F. Uesugi, and K. Yoshino, *Sol. St. Comm.* **65**, 783 (1988).
7. S. Hayashi, K. Kaneto, and K. Yoshino, *Sol. St. Comm.* **61**, 249 (1987).
8. M. J. Novak, S. D. D. V. Rughooputh, S. Hotta, and A. J. Heeger, *Macromol.* **20**, 965 (1987).

9. D. Spiegel and A. J. Heeger, *Polymer Comm.* **29**, 266 (1988).
10. O. Inganas, W. R. Salaneck, J.-E. Osterholm, and J. Laakso, *Syn. Met.* **22**, 395 (1988).
11. J. R. Linton, C. W. Frank, and S. D. D. V. Rughooputh, *Syn. Met.* **28**, C393 (1989).
12. J. L. Sauvajol, B. Chenouni, S. Hasoon, and J. P. Lere-Porte, *Syn. Met.* **28**, C293 (1989).
13. G. S. Kanner, Z. V. Vardeny, and B. C. Hess, *Phys. Rev. Lett.* (submitted).
14. K. Kaneto and K. Yoshino, *Syn. Met.* **28**, C287 (1989).
15. K. Yoshino, S. Nakajima, M. Onoda, and R. Sugimoto, *Syn. Met.* **28**, C349 (1989).
16. B. Themans, W. R. Salaneck, and J. L. Bredas, *Syn. Met.* **28**, C359 (1989).
17. O. Inganas, G. Gustafsson, and W. R. Salaneck, *Syn. Met.* **28**, C377 (1989).
18. M. J. Winokur, D. Spiegel, Y. Kim, S. Hotta, and A. J. Heeger, *Syn. Met.* **28**, C419 (1989).
19. B. C. Hess, J. Shinar, Z. V. Vardeny, E. Ehrenfreund, and F. Wudl, in *Nonlinear Optical Properties of Polymers*, edited by A. J. Heeger, J. Orenstein, and D. R. Ulrich, (*Mater. Res. Soc. Proc.* **109**, Pittsburgh, PA 1988), p. 363.
20. B. C. Hess, J. Shinar, Q.-X. Ni, Z. Vardeny, and F. Wudl, *Syn. Met.* **28**, C365 (1989).
21. B. C. Hess, J. Shinar, X. Wei, and Z. V. Vardeny, *Phys. Rev. Lett.* (submitted).
22. C. X. Cui and M. Kertesz, *Phys. Rev. B* **40**, 9661 (1989).
23. J. P. Aime, F. Bargain, M. Schott, H. Eckhardt, G. G. Miller, and R. L. Elsenbaumer, *Phys. Rev. Lett.* **62**, 55 (1989).
24. L. S. Swanson, J. Shinar, and K. Yoshino, to be published.

## HELICAL CONFORMATIONS OF CONDUCTING POLYMERS

MIKLOS KERTESZ AND CHANGXING CUI

Department of Chemistry, Georgetown University, Washington DC 20057.

## ABSTRACT

Helical conformations of polymers occur due to a variety of factors, some of which are electronic in origin. We briefly review the situations in which there is an electronic driving force towards a helix including a case that might be called a helical Peierls distortion. Energetics and geometries of helical conformations of polythiophene and polypyrrole are also analyzed.

## EXPERIMENTAL EVIDENCES OF HELICAL CONDUCTING POLYMERS

There is ample evidence for the existence of helical conformations for conducting polymers in their undoped and doped states [1-8]. For instance in the solid state x-ray diffraction shows that doped poly(3-methylthiophene) (PMeT) is in a coil conformation. Small angle neutron-scattering experiments on poly(3-butylthiophene) indicate that it has a coil or helical conformation in solution, and upon doping it becomes rodlike. The existence of such a coil structure has been confirmed recently for doped polypyrrole and polythiophene by scanning tunneling microscopy [3,4]. For polyacetylene helical conformation has also been found by x-ray diffraction. Theoretical calculations show that helical structures of various conducting polymers are energetically close and even sometime more stable than planar conformations [5-8]. As shown below polyketone (PK) and polyisocyanide (PIC) which have small band gaps also have helical conformations [9].

## WHAT DRIVES A POLYMER TOWARDS A HELICAL CONFORMATION?

We briefly summarize the factors influencing the formation of helical conformations for polymers. Hydrogen bonding in biopolymers often drive the formation of a helix [10]. Lone-pair repulsions are responsible for helical conformation for a group of inorganic and organic polymers such as polyethylene, polymeric sulfur and poly(oxymethylene) [8]. Crystal packing plays an important role in the helical conformation of HgS. Side group repulsions in some polymers such as  $(CF_2)_x$  are responsible for their spiral conformation [11]. Structural crowding is very important in the helical conformation of polythiophene and polypyrrole [12]. Other helical polymers have been considered in R. Hoffmann's group [13]. In this work we show that in the case of polyketone and polyisocyanide there is a new type of driving force towards a helix, which is similar to Peierls-like distortion.

## METHODS

We have employed a solid state version of the Modified Neglect of Diatomic Overlap (MNDO) band theory [14] and one of its recent version: MNDO-AM1 [15] in the bond distance and bond

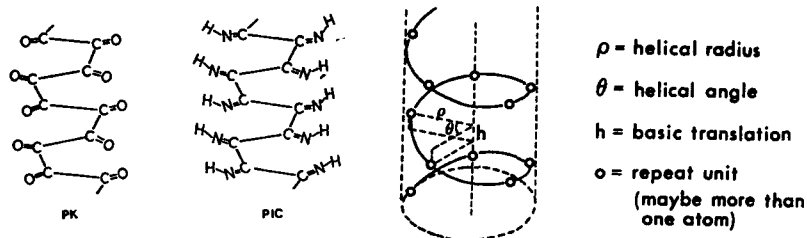


Fig. 1. Helical structures of PK and PIC.

Fig. 2. Parameters to describe a helix.

angle calculations for PK, PIC, polythiophene (PT), polypyrrole (PPy). The MNDO approach produces reasonable geometries for many organic and inorganic molecules and polymers without using vast amounts of computer time. Recent studies show that the predictions of geometries of number of organic and inorganic  $\sigma$ -bonded helical polymers are in overall agreement with experiments [8]. A screw axis of symmetry has been taken into account in order to simplify the calculations. More details about a screw axis of symmetry in polymeric band calculations can be found elsewhere [10]. Extended Huckel Theory (EHT) [16] approach is used for the calculation of the band gap and torsional potentials for PK, PIC, PT, PPy and their derivatives.

#### HELICAL PEIERLS DISTORTION

The two polymers which are used here to illustrate the helical Peierls distortion are PK and PIC, which are shown in Fig. 1. The distortion coordinate for these polymer is helical angle ( $\theta$ ) as shown in Fig. 2.

Fig. 3a presents the torsional potential curve, the total energy of PK per repeat unit (CO) as a function of helical angle, as calculated by the MNDO-AM1 crystal orbital approach together with the EHT torsional potential curve obtained by performing EHT energy calculations on the MNDO-AM1 optimized PK structures at various helical angles. In agreement with our *ab-initio* calculations for tetraketone, the MNDO-AM1 approach predicts that PK has a helical conformation with a helical angle of about  $120^\circ$ . The helical conformation is more stable than the planar zigzag conformation by 2.1 kcal/mole at the MNDO-AM1 level while the EHT estimates stabilization energy of 1.8 kcal/mole upon the formation of the helix.

Fig. 3b shows the EHT band gap of PK as a function of the helical angle. It is well known that *ab-initio* and MNDO approaches overestimates the band gap for semiconductors such as PA. However, the EHT approach gives reasonable band gaps. The band gap increases with decreasing helical angle. When the band gap is around the maximum, the total energy of PK reaches the minimum.

For the purpose of comparison, the total energy and band gap of *all-trans* PA as a function of bond length alternation  $\delta r = r(\text{C-C}) - r(\text{C=C})$  are shown in Fig. 3c and 3d, respectively. The AM1 energy in kcal/mole for PK around the planar zigzag structure is quadratic with respect to the change of the helical angle  $\delta\theta$  (in



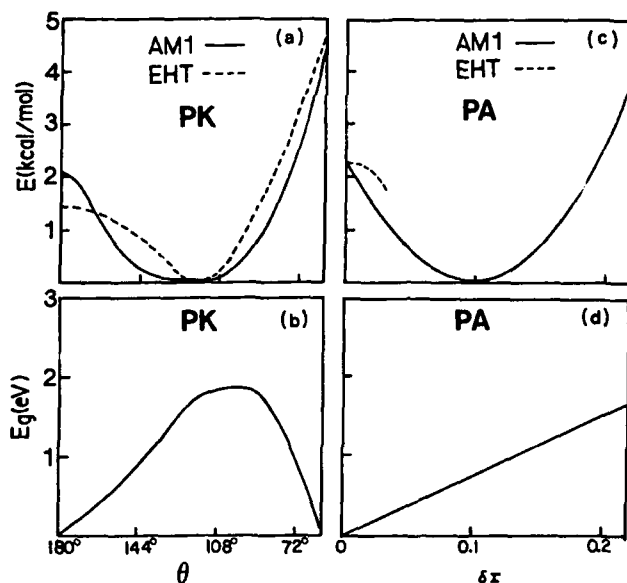


Fig. 3 (a) Torsional potential curve of PK by the MNDO-AM1 and EHT approaches. (b) Band gap of PK as a function of helical angle by the EHT approach based on the MNDO-AM1 geometry. (c) Total energy of all-trans PA as a function of bond alternation  $\delta r$  by the MNDO-AM1 method. (d) Band gap of all-trans PA as a function of bond alternation  $\delta r$  by EHT based on the MNDO-AM1 geometry.

degree) [ $E(\delta\theta) = -20.31 - 0.005(\delta\theta)^2$ ]. However, the AM1 energy for PA due to bond alternation is linear [ $E(\delta r) = 15.91 - 41\delta r$ ] around the structure with no bond alternation ( $\delta r=0$ ) since the first derivative of energy with respect to the bond alternation  $\delta r$  is  $-41$  kcal/Å at the MNDO-AM1 level. The force toward the formation of the bond alternation of PA is attributed to symmetry breaking in form of a bond order alternation wave (BOAW) [17]. The BOAW, which is unique for PA, leads to nonzero first derivative of the energy with respect to the bond alternation in a self consistent field (SCF) theory such as MNDO while the mixing of the different symmetry crystal orbitals (those close to  $k = \pi/a$ ) around the Fermi level are responsible for the lowering of the total energy and opening up a gap. For PK at the planar zigzag conformation there is no force which is comparable to that for PA. The only way to lower the total energy of PK is to couple the out-of plane vibrational states with the electronic states. Such vibrations lead to the mixing of  $\sigma$  and  $\pi$  bands and lower the total energy of PK. The analysis of the total EHT energy as a function of the distortion parameter for PA is known to yield [17,18]  $E_{PA} = E(0) - k(\delta r)^2 \ln \delta r$ . For PK the total EHT energy is very similar to that of PA at this non-SCF level of theory.

The band structures of PK for planar and helical conformations at the optimal helical conformation are shown in Fig. 4. The bands cross in the planar conformation at  $E_c$ . According to Peierls' theorem there is no one-dimensional metal and such a system has to be unstable. [18] The major inter-

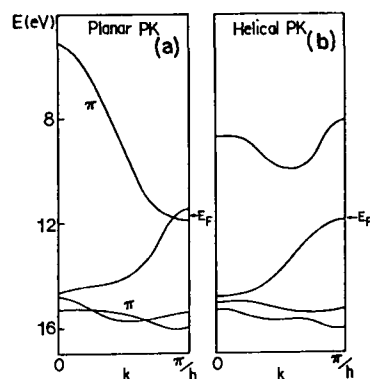


Fig. 4. Band structures of PK with planar (a) and helical (b) conformations by the EH. Both are based on MNDO-AM1 fully optimized geometries.

action which is linear in the distortion parameter ( $\theta$ ) is the interaction of the  $\pi$ -orbital ( $2p_y$ ) with the  $\sigma$ -type  $2p_x$  orbital ( $Z$  is the axis of polymer).

For PIC, the torsional potential curve and band structure as a function of helical angle are similar to those of PK, and are not given here. The optimized geometrical parameters for PK and PIC at the MNDO-AM1 CO level are listed in Table I, along with available experimental data [9]. Both PK and PI have been experimentally demonstrated to be in helical conformations.

#### HELICAL CONFORMATIONS OF PT, PPy AND THEIR DERIVATIVES

It is known from experiments and theoretical calculations that bithiophene has two conformations, an anti and a syn [19, 20]. The importance of the coexistence of two stable conformations of bithiophene and its derivatives is that it leads to various stable forms of the corresponding polymers.

Fig. 5 shows the torsional potential curve of PT. Two minima have been located on the energy surface. The first corresponds to the planar zigzag (anti) conformation. The second is a helical conformation with a large helical radius. A completely planar syn conformation is impossible since the molecule would coil back onto itself. A helical angle of  $35^\circ$  is obtained at the minimum, and the coil structure at the minimum is shown in Fig. 5(c).

Table I. Optimized geometrical parameters of PK and PIC by the MNDO-AM1 crystal orbital approach.

polymer	R(C-C) <sup>a</sup>	R(C-X) <sup>a</sup>	$\alpha$ (CCC) <sup>b</sup>	$\tau$ (CCCC) <sup>c</sup>	$h^d$	(expt) <sup>e</sup>	$\theta^e$ (expt) <sup>e</sup>
PK	1.510	1.225	115.2	91.6	1.13		119.0
PIC	1.506	1.277	112.0	75.6	1.01(1.05)		98.1(90)

a) bond length in Å b) bond angle in degrees c) dihedral angle in degrees d) translation in Å e) helical angle in degrees.

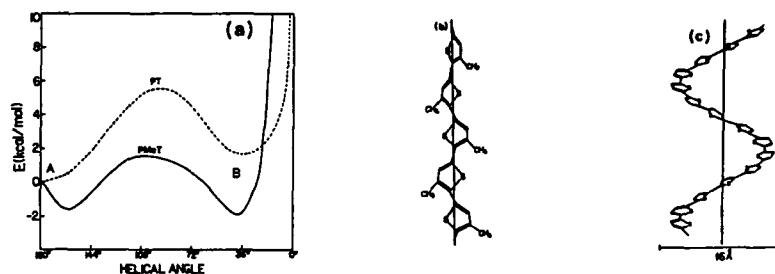


Fig. 5. (a) Torsional potential curve of PT (dashed line) and PMeT (solid line) (the energy relative to anti conformation) calculated by EHT based on the MNDO fully optimized geometry. A and B correspond to the anti (rod-like) and syn (coil) conformations, respectively. (b) Structure B. (c) Structure A.

Similar results have been obtained for PPy its derivatives. Optimized geometrical parameters are listed in Table II. The energy gap of these polymers as a function of  $\theta$  has a minimum at the A (planar or nearly planar) conformation, but conformation B has also a small gap [12]. This observation is related to the thermochromism of these compounds [12,21].

Table II. Summary of Geometrical Parameters of Undoped PT, PMeT, PPy and PMePy at Two Stable Conformations.

polymer	band gap <sup>a</sup>	$C_a-C_a^b$	$XC_aC_aX^c$	$\theta^d$	$R^e$	Energy <sup>f</sup>
PT (rod)	1.70	1.446	180.0	180.0	2.4	0.0
PT (coil)	1.76	1.446	17.6	35.0	7.8	1.6
PMeT (rod)	1.88	1.450	158.2	159.9	3.7	0.4
PMeT (coil)	1.92	1.451	26.2	42.7	8.5	0.0
PPy (rod)	1.51	1.454	180.0	180.0	2.5	0.0
PPy (coil)	1.38	1.452	10.9	40.0	7.5	2.2
PMePy (rod)	1.55	1.457	180.0	180.0	3.8	0.0
PMePy (coil)	1.86	1.455	40.7	52.2	6.3	3.9

a) In eV b) Interring bond distance in Å c) Dihedral angle in degrees d) Helical angle in degrees e) Helical radius in Å f) Energy relative to the most stable conformation (in kcal/mol).

#### ACKNOWLEDGMENTS

This work has been supported by the National Science Foundation through a grant (DMR-8702148).

## REFERENCES

- [1] F. Garnier, G. Tourillon, J.Y. Barraud, and H. Dexpert, *J. Mater. Sci.* **22**, 2687(1986).
- [2] J.P. Aime, F. Bargain, M. Schott, H. Eckhardt, G.G. Miller and R.L. Elsenbaumer, *Phys. Rev. Lett.* **62**, 55(1989).
- [3] R. Yang, K.M. Dalsin, D.F. Evans, L. Christensen, and W.A. Hendrickson, *J. Phys. Chem.* **62**, 23(1989)
- [4] L. Christensen, W.A. Hendrickson, R. Yang, and D.F. Evans, *Polymer Preprints*, **30**, 100(1989).
- [5] M.L. Elert and C.T. White, *Phys. Rev.* **B28**, 1013(1983).
- [6] B.K. Roa, J.A. Darsey, and N.R. Kestner, *Phys. Rev.* **B31**, 1178(1985).
- [7] F.S. Bates and G.L. Baker, *Macromolecules*, **16**, 1013(1983).
- [8] C.X. Cui and M. Kertesz, *J. Am. Chem. Soc.* **111**, 4216(1989).
- [9] B.R. Mordecai, *Chem. Rev.* **75**, 177(1975); F. Millich, *J. Polymer Sci.* **15**, 207(1980).; G. Wulff, *Angew. Chem. Int. Ed. Engl.* **28**, 21(1989).
- [10] A.G. Walton and J. Blackwell, *Biopolymer*, (Academic Press, New York, 1973).
- [11] P. Desantis, E. Giglio, A.M. Liquori and A. Repanonti, *J. Polymer Sci.* **A1**, 1383(1963).
- [12] C.X. Cui and M. Kertesz, *Phys. Rev.* **B40**, 9661(1989).
- [13] C. Zheng, R. Hoffmann, and D.R. Nelson (to be published).
- [14] M.J.S. Dewar, W. Thiel, *J. Am. Chem. Soc.* **99**, 4899, 4907(1977); J.J.P. Stewart, *QCPE Bull*, **5**, 62(1985); *MOSOL Manual*; USAF, (Colorado, Springs, 1984); Y. Lee and M. Kertesz, *J. Chem. Phys.* **88**, 2609(1988).
- [15] M.J.S. Dewar, E.G. Zoebisch, E.F. Healy, J.J.P. Stewart, *J. Am. Chem. Soc.* **107**, 3902(1985).
- [16] R. Hoffmann, *J. Chem. Phys.* **39**, 1397(1963); M.H. Whangbo, R. Hoffmann, *J. Am. Chem. Soc.* **100**, 6093(1978).
- [17] M. Kertesz, *Adv. Quantum Chem.* **15**, 161(1982).
- [18] R.E. Peierls, *Quantum Theory of Solid*, (Oxford University Press, London, 1955).
- [19] V. Barone, F. Leli, N. Russo, and M. Toscano, *J. Chem. Soc., Perkin Trans. II*, **1986**, 907.
- [20] P. Bucci, M. Longeri, C.A. Verracini, and L. Lunazzi, *J. Am. Chem. Soc.*, **96**, 1305(1974).
- [21] S.D.D.V. Rughooputh, S. Hotta, A.J. Heeger, and F. Wudl, *J. Polym. Sci. Polymer Phys. Ed.* **25**, 1071(1987).

### RESONANT RAMAN SCATTERING OF POLY-3-ALKYLTHIOPHENES

C. BOTTA, S. LUZZATI, A. BOLOGNESI, M. CATELLANI, S. DESTRI and R. TUBINO\*

Istituto di Chimica delle Macromolecole, CNR, via Bassini 15  
20133 Milano

\* and Istituto di Fisica, Università di Sassari, via Vienna 2.

#### ABSTRACT

We report Raman scattering measurements on poly-3-heptylthiophene and poly-3-undecylthiophenes both on resonance and preresonance conditions. We have studied different samples as solutions, solution cast films and electrosynthesized as grown films. Our results indicate that the vibrational frequency of the mode which is strongly coupled to the  $\pi - \pi^*$  electronic transition is sensible to "small" torsions between thiophene rings, which do not necessarily interrupt completely the conjugation path.

#### INTRODUCTION

The strong interaction between the electronic structure and the backbone conformation seems to be a fundamental feature of conjugated polymers. For polyacetylenes and other conducting polymers, this leads to non linear excitations (viz. solitons, bipolarons and polarons)[1]. Polyalkylthiophenes (PAT hereafter) are a class of non degenerate ground state conjugated polymers which are supposed to have the same trans planar backbone conformation and  $\pi$  electronic structure of polythiophene (PT) [2]. These materials seem particularly interesting for studying the interaction between the electronic structure and the backbone conformation. In fact the presence of the side chain substituent leads to thermochromic and solvatochromic effects which monitor the coupling of the electronic structure of  $\pi$  - electrons to the conformational changes [3-5].

PATs have been already studied by a number of photoexcitation spectroscopies like photoluminescence [6,7] and photoinduced absorption [8]. We report here resonant Raman scattering results which provide novel informations on the photophysics of these systems.

#### EXPERIMENTAL

The monomers were synthesized by the Wittig reaction between 3-thiophenecarbox-aldehyde and hexyl- or decyl-thiophenylphosphonium bromine salt followed by reduction of the resulting double bond. We have studied both chemically and electropolymerized samples. The electropolymerization has been carried, at room temperature and at 5 °C, with .1 M monomer and 0.001 M  $Bu_4NClO_4$  electrolyte in nitrobenzene with currents ranging from 1 to 10 mA/cm<sup>2</sup>.

Poly-3-heptylthiophene has been also chemically polymerized by using iron trichloride as reported in the literature [9]. The characterization of the chemically synthesized PAT (CC7) has

been performed by NMR, GP chromatography, IR absorption, X-ray diffraction and will be reported elsewhere. CC7 has a molecular weight  $M_n = 15900$  (87 numeral average monomers per chain) and a polydispersity  $M_w/M_n = 3.1$ . Its X-ray diffraction pattern and I.R. absorption spectra are in substantial agreement with those reported for poly-3-hexylthiophenes [10].

The Raman spectra are obtained with excitation in the visible region using an Ar<sup>+</sup> and an He-Ne laser; the power impinging the sample is kept  $\approx 1$  mW. We have used a flat field Jasco trs300 polychromator with a 512 intensified diode array (EG&G 1420) interfaced to a XT286 PC IBM by an EG&G 1461 microprocessor. In the NIR region we have done the Raman spectra with a Bruker Fourier transformer spectrometer (IFS66 + FRA106), working with a Nd-Yag laser (1064 nm) with a power emission kept lower than 200 mW.

## RESULTS AND DISCUSSION

Fig.1 shows the visible absorption spectra performed at room temperature with a Cary 2300 spectrophotometer. 14EC7, 25EC7 and 4EC11 are electropolymerized samples of poly-3-heptyl and poly-3-undecyl thiophene. Both absorption and Raman spectra are performed directly on the as grown films over indium tin oxide quartz plate electrodes. CC7S and CC7F are respectively a  $1 \times 10^{-3}$  M chloroform solution and a solution cast film of the chemically coupled poly-3-heptylthiophene. CC7F absorption maximum (2.49 eV) shifts, upon dissolution, to higher energy (2.83 eV in CC7S) due to the existence in solution of rotational conformers which reduce the mean conjugation path. Our solvatochromic effect is very similar to what have been found for other PATs [3,4]. By cooling CC7F we have found that

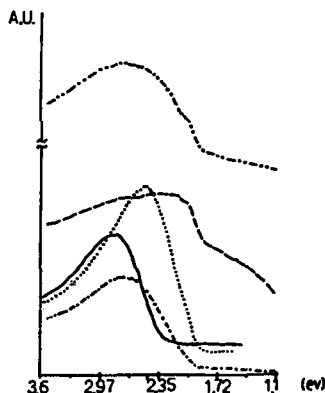


Fig.1 Absorption spectra of 14EC7-----;4EC11-.-.-.- ; CC7F ..... ;CC7S ———— ; 25EC7-.-.-.- ;(see text).

the shoulder at 2.58 eV decreases with a redistribution of the oscillator strength to lower energies. We confirm that the thermochromic effect, under room temperature, turns out to be detectable down to about 200 °K [11] (CC7F abs. maximum converges to 2.47 eV at 200 °K). We have also used a very ordered sample, LBCC7, which is a mixed 20 layers Langmuir Blodgett film over a silicon substrate formed by 2 parts of arachidic acid : 1 part of CC7. Its reflection minimum is at 2.34 eV.

Fig. 2a and 2b show the Raman spectrum of a CC7F sample obtained at 80 °K with the 454.52 nm exciting wavelength. The bands frequencies are listed in table I where we have labeled by  $\mu_1$  the modes which give overtones and combinations. It can be seen that the Raman features are very similar to poly-3-methylthiophene (PMT) [12] and the number of vibrational modes is much higher than in polythiophene (PT) [13].

Our results show that the bands frequencies do not depend on the alkylic chain length and, with the exception of  $\mu_1$  and

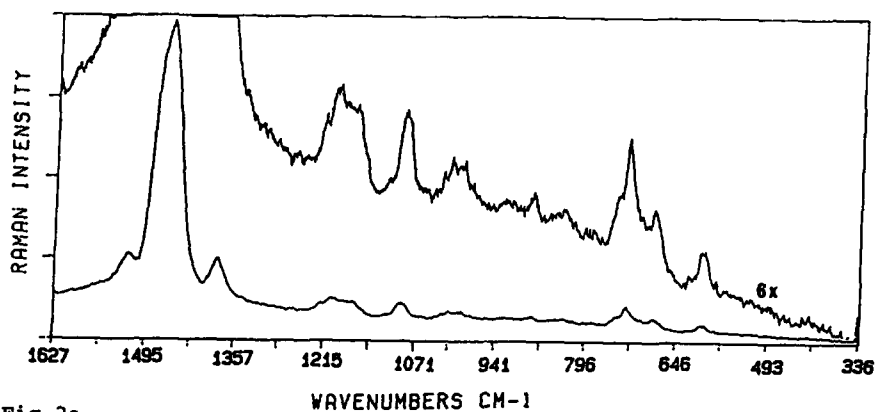


Fig. 2a

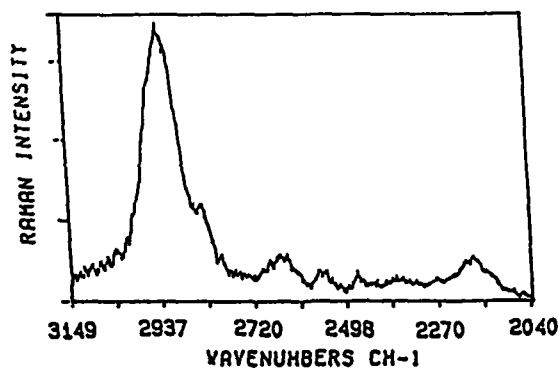


Fig. 2b

Fig. 2 CC7F Raman spectra in the fundamental (2a) and first overtone region (2b). Exciting wavelength : 452.52 nm ; T = 80 K

TABLE I

Raman Modes of poly-3-heptylthiophene CC7F  
(in  $\text{cm}^{-1}$ ), excitation wavelength : 454.52 nm  
(vs=very strong, s=strong, m=middle, w=weak, vw=very weak)

(resolution = $4 \text{ cm}^{-1}$ )		(resolution = $8 \text{ cm}^{-1}$ )	
		observed	(calculated)
599 w	1022 vw	2186 w	$\mu_6 + \mu_1$ (2191)
680 w	1092 m $\mu_3$	2474 w	$\mu_6 + \mu_2$ (2474)
727 m $\mu_1$	1169 m	2566 w	$\mu_6 + \mu_3$ (2556)
740 w	1199 m $\mu_4$	2660 m	$\mu_6 + \mu_4$ (2663)
831 vw	1219 w	2840 m	$\mu_6 + \mu_5$ (2848)
884 vw	1384 s $\mu_5$	2928 s	$2\mu_6$ (2928)
995 w	1464 vs $\mu_6$		
1010 w $\mu_2$	1522 m		

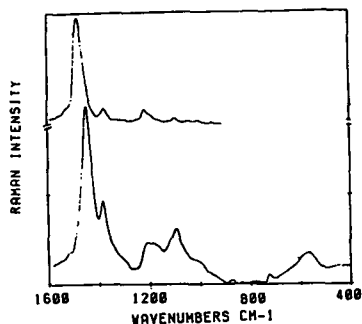


Fig.3 Raman spectra at 1064 nm of CC7S (upper) and CC7F (lower).

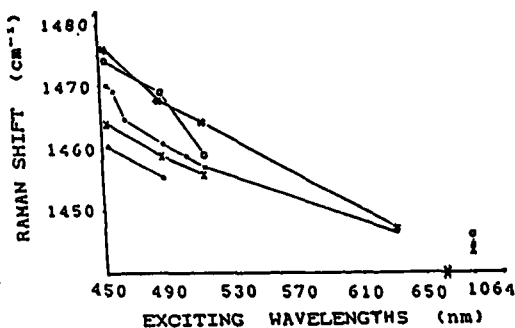


Fig.4 C=C stretching frequency dispersion of \* 14EC7; o 25EC7; • 4EC11; x CC7F; Δ LBCC7; ◊ CC7S.

$\mu_6$ , they do not shift with the exciting wavelength. By comparing the results in resonant and in preresonant condition (fig. 2, 3) we can assert that  $\mu_1$  and  $\mu_6$  are both coupled to the  $\pi - \pi^*$  transition.  $\mu_1$  is a backbone mode which by analogy to PT can be assigned to a symmetric thiophene rings bending [13];  $\mu_6$  is the backbone mode which is mostly coupled to the electronic transition containing thus an important contribution of C=C stretching. It is not possible to rule out other resonant enhancements but we have the evidence that  $\mu_1$  are  $A_g$  modes because they combine in overtones. It is difficult to distinguish between backbone and side chains modes because there are several side chains vibrational frequencies ranging from  $1400 \text{ cm}^{-1}$  to  $800 \text{ cm}^{-1}$  [14]. The luminescence background decreases with temperature but it is so high in solution that, in order to obtain a spectrum of CC7S, it has been necessary to excite in the NIR region. Passing from 293 °K to 80 °K there is a shift of  $\approx 4 \text{ cm}^{-1}$  of the entire spectrum to higher frequencies, which is probably due to the lattice contraction. We have found that, unlike PT and similarly to PMT [12], the C=C stretching frequency decreases with the exciting wavelength. This dispersion is plotted in fig. 4 for all the samples. It is evident that this behaviour is sample dependent and it is coherently related to the distribution of conjugation lengths as monitored by the absorption spectra. The tight relation in conjugated polymers between conjugation lengths and C=C stretching dispersion is well established and it has been extensively studied in trans polyacetylene [15]. Fig. 5 and fig. 6 show how the C=C stretching band is affected by the selective enhancement of different conjugation lengths, both by changing the exciting wavelength (fig. 5) or by taking samples with different abs. spectra at a fixed wavelength (fig. 6).

Our results show that the mode which is strongly coupled to the electronic transition exhibits a very different behaviour from PT. It is known that in PT the C=C stretching frequency is not sensitive to the conjugation length. For thiophene oligomers



longer than trimers, this frequency converges to the value of the polymeric chain ( $\approx 1460 \text{ cm}^{-1}$ ) [16]. PATs electronic

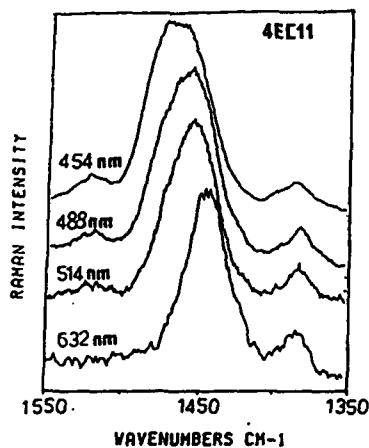


Fig.5 C=C stretching exciting wavelength dependence

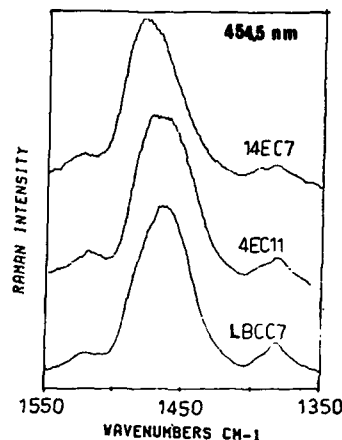


Fig.6 C=C stretching sample dependence at 454 nm

structure is not affected by the alkylic side chains. Therefore if the same PT trans-planar backbone conformation is supposed, the C=C stretching mode should not be shifted for conjugation lengths longer than 3 thiophene rings. Thus we cannot reasonably understand our results in the frame of a discontinuous model, where the backbone is supposed to be in a planar conformation and localized rotations interrupt the conjugation paths [4].

A good knowledge of PAT conformation seems to be crucial for understanding the thermochromic and solvatochromic effects [3,4] and for the understanding of our Raman scattering data. PATs conformation is not well established because it is difficult to obtain direct and clear informations from X-ray diffraction due to the presence in these samples of a low number of diffraction lines [10,17].

It is interesting to notice that upon dissolution we observe an upper shift of  $\approx 30 \text{ cm}^{-1}$  of the C=C stretching frequency (see fig. 3). The presence in solution of rotational conformers suggests that the torsion between thiophene rings should be responsible for the band dispersion. The backbone chain should be affected by a loss of planarity at a short range scale (less than 3 monomers). In order to test the importance of backbone rotations we have measured some additional Raman spectra on thiophene oligomers (T3 and T5) both in solid state and in solution. In fact thiophene oligomers are in trans planar conformation when in the solid state, but oligomers shorter than the hexamer (T6) can be dissolved in organic solvents. We have found that the  $1461 \text{ cm}^{-1}$  C=C stretching frequency of T3 and T5 increases upon dissolution in chloroform of  $3 \text{ cm}^{-1}$  for T3 and  $12 \text{ cm}^{-1}$  for T5. We have thus confirmed that thiophene backbone rotations shift upwards the C=C stretching vibrational frequency.

We can conclude that Raman scattering data bring novel informations on PATs conformation. The vibrational frequency of

the mode which is strongly coupled to the  $\pi - \pi^*$  transition is sensible to "small" torsions between thiophenes rings, which do not necessarily interrupt completely the conjugation path. Our results seem to indicate that PAT backbone conformation is affected by a loss of planarity at a short range scale (less than 3 monomers).

## REFERENCES

1. Handbook of Conducting Polymers, edited by T.J. Skotheim (Marcel Dekker, New York, 1986).
2. W.R. Salaneck, O. Inganas, B. Thémans, J.O. Nilsson, B. Sjogren, J.E. Osterholm, J.L. Brédas and S. Svensson, *J. Chem. Phys.* **89**, 4613 (1988).
3. S.D.D.V. Rughooputh, S. Hotta, A.J. Heeger and F. Wudl, *J. of Polymer Sci. Polymer Phys.*, **25**, 1071 (1987).
4. O. Inganas, W.R. Salaneck, J.E. Osterholm and J. Laakso, *Synth. Met.*, **22**, 395 (1988).
5. K. Yoshino, S. Nakajima, D.H. Park and R. Sujimoto, *Jpn. J. Appl. Phys.*, **27**, L454, (1988).
6. K. Yoshino, S. Nakajima, D.H. Park and R. Sujimoto, *Jpn. J. Appl. Phys.*, **27**, L716, (1988).
7. J.R. Linton, C.W. Frank, S.D.D.V. Rughooputh, *Synth. Met.*, **28**, C393, (1989).
8. D. Spiegel, P. Pincus and A.J. Heeger, *Synth. Met.*, **28**, C385, (1989).
9. S. Hotta, M. Soga, N. Somoda, *Synth. Met.*, **26**, 267 (1988).
10. M.J. Winokur, D. Spiegel, Y. Kim, S. Hotta and A.J. Heeger, *Synth. Met.*, **28**, C419, (1989).
11. M. Sundberg, O. Inganas, S. Stafstrom, G. Gustafsson and B. Sjogren, *Solid State Comm.*, **71** (6), 435, (1989).
12. E.F. Steigmeier, H. Auderset, W. Kobel and D. Baeryswyl, *Synth. Met.*, **18**, 219, (1987).
13. M. Akimoto, Y. Furukawa, H. Takeuchi, I. Harada, Y. Soma, M. Soma, *Synth. Met.*, **15**, 353, (1986).
14. F.R. Dollish, W.G. Fately, and F.F. Beutty, Characteristic Raman frequencies of Organic Compounds, (John Wiley, 1974).
15. D.B. Fitchen, *Mol. Cryst. Liq. Cryst.*, **83**, 1127 (1982).
16. Y. Furukawa, M. Akimoto and I. Harada, *Synth. Met.*, **18**, 151, (1987).
17. W. Porzio, private communication.

HALL EFFECT AND MAGNETORESISTANCE IN UNDOPED  
POLY(3-HEXYLTHIOPHENE).

Azar Assadi, Christer Svensson and Magnus Willander.

Dept. of Physics and Measurement Technology, Linköping University, S-581 83  
Linköping, Sweden.

ABSTRACT.

We report studies of transport properties of thin films of undoped poly(3-hexylthiophene) (P3HT) fabricated by spinning a polymer solution onto oxidised silicon or glass. The film thicknesses were on the order of 1000 Å. We studied magnetoresistance, the effect of magnetic field on field effect mobility and Hall effect.

Transverse magnetoresistance was measured on films on glass. A positive anomalous magnetoresistance with a saturation value of about 0.1 % was found. Transverse magnetoresistance was also studied by measuring the change of a field effect mobility with magnetic field. This measurement was performed using the field effect transistor structure. An initial mobility of  $6.5 \times 10^{-5} \text{ cm}^2/\text{Vs}$  was reduced by about 15 % in a transverse magnetic field.

We also carried out Hall effect measurements on films on glass using a Van der Pauw contact configuration. The measured Hall mobility was  $2.17 \times 10^{-5} \text{ cm}^2/\text{Vs}$ . Finally we measured the temperature dependence of the Hall mobility and found it follow the  $\exp(T^{-1/4})$  law of variable range hopping.

INTRODUCTION

Many conjugated polymers show high electrical conductivity, which is associated with the high degree of delocalisation of the  $\pi$  electrons. The detailed mechanism of charge transport is however not well understood. Presently, the general assumption is that transport occurs through a hopping mechanism, similar to what is believed to be the transport mechanism in amorphous inorganic semiconductors [ 1 ]. In the case of poly(3-hexylthiophene) the charge carriers are assumed to be polarons (or possibly also bipolarons)[ 2 ], [ 3 ], so that hopping is expected to occur between polaron or bipolaron states.

As magnetoresistance and Hall effect have been successfully used to provide information about the transport mechanism in amorphous and crystalline semiconductors, we have performed such experiments on P3HT films. The results of these investigations can then be compared to previous results from field effect measurements [ 4 ] , [ 5 ] and hopefully contribute further to our knowledge of the transport mechanisms in semiconductor P3HT.

#### EXPERIMENTAL

The P3HT used was synthesised by Neste Oy as reported previously [ 6 ]. The polymer was dissolved in chloroform (20 mg/ml) and the solution was spin coated onto the substrates. This method of preparation of the polymer has been used for all samples. The film thickness measured by a Dektak 3030 surface profile measuring system was 700-1000Å.

The substrates used were either glass substrates (for magnetoresistance and Hall effect measurements) or heavily boron doped and oxidised silicon wafers (<100> axis)(for field effect measurements). The silicon wafer, acting as a gate, was covered with thermally grown oxide film (3000 Å thick) and 2 finger shaped gold electrodes, acting as source and drain, see also [ 4 ].

The glass substrate samples were used for magnetoresistance and Hall effect measurements. In both cases we used a Van-der-Pauw electrode configuration. The electrodes were made by evaporated gold, connected to gold wires by silver epoxy. The contacts between the polymer and gold wires had low resistance, and did not require any further treatment. Small contact resistance is important in minimising noise for the Hall voltage measurement. The magnetoresistivity measurements were done at room temperature for magnetic fields up to 0.4 T. Hall effect measurements were performed by the usual Van-der-Pauw method, at a constant magnetic field of 0.25 T, at room temperature. Then the sample was slowly cooled down to 77° K and at every 10 degree interval the measurement was performed again in order to obtain the temperature dependence.

The field effect mobility of the film was measured in the same way as reported before [4 ], using the field effect samples. In these series of experiments we studied the field effect mobility in the channel under different external DC magnetic fields up to 0.4 T and at room temperature. The mobility was evaluated from the field effect transistor characteristic using drain voltages of 0-4 V and gate voltages of 1-3 V.

## RESULTS AND DISCUSSION

One result of the magnetoresistance measurements is shown in Fig. 1. Several other samples show similar results. The curve in Fig. 1 is clearly characterized as a steep increase and then saturation. Saturation occurs at a magnetic field of the order of 0.1 T with a saturation value of about  $1 \times 10^{-4}$ .

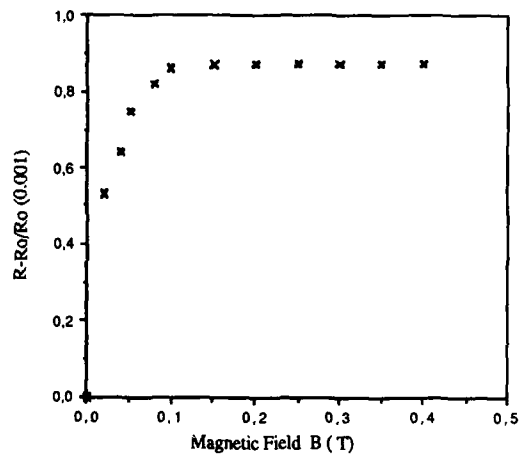


Fig.1 Positive magnetoresistance  $\Delta R/R_0$  as function of magnetic field B.

This result resembles the positive part of magnetoresistance observed in amorphous silicon and germanium [ 7 ], also called anomalous magnetoresistance (AMR). A similar behaviour has been observed in lightly doped polyacetylene [ 8 ]. Both the magnitude of our effect and the magnetic field values are similar to the referred results.

AMR has been successfully explained on the basis of a variable range hopping model using two different models [ 9 , 7 , 10 ]. Both models is based on the assumption of both singly and doubly occupied gap states, which in our case should correspond to polarons and bipolarons. Movaghar and Schweitzer [ 9 ] propose that hopping may occur with spin flip and that AMR is controlled by a magnetic field dependent spin flip relaxation time. Kurobe [ 10 ] propose that the positive AMR is caused by a decreased probability for hops

to an occupied state with a magnetic field induced spin alignment. Our result thus indicates that the conduction mechanism in P3HT is variable range hopping among polarons and bipolarons.

We also investigated the effect of magnetic field on the field effect mobility. The result of one of these measurements is shown in Fig. 2. Again, we see a similar behaviour as for the magnetoresistance, but with a considerably larger saturation value of about 15%. This is a very large value compared to any other magnetoresistance results. A possible explanation for this might be the larger charge carrier density in the channel, which may increase the probability for hops including bipolarons (doubly occupied states in Kurobe's model).

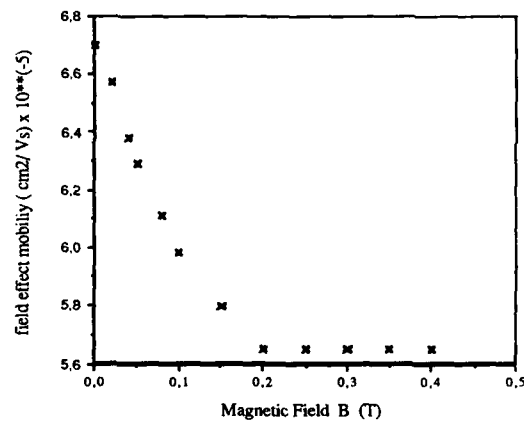


Fig.2 Variations of field effect mobility due to the external magnetic field B.

Finally, we investigated the Hall mobility and its temperature dependence. The measured value of Hall mobility at room temperature was  $2.11 \times 10^{-5} \text{ cm}^2/\text{Vs}$  while the field effect mobility of a similar film was  $6.2 \times 10^{-5} \text{ cm}^2/\text{Vs}$ . A lower value of Hall mobility is expected for the variable range hopping conduction mechanism [ 11 ], although it is not so easy to predict the magnitude of the difference (the theory in [ 12 ] may be used but parameter values are lacking). The temperature dependence of the Hall mobility is demonstrated in Fig. 3. The general behaviour resembles the previous results on the temperature dependence of the field effect mobility of P3HT [ 5 ].

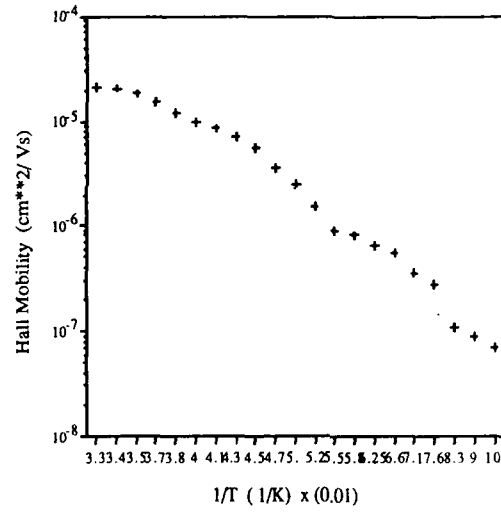


Fig. 3 Hall mobility of the charge carriers v.s. inverse temperature.

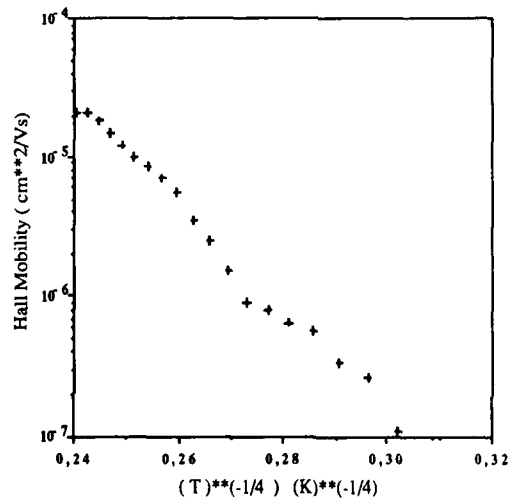


Fig. 4 Hall mobility of charge carriers v.s.  $T^{-1/4}$ .

The fast changing part of the curve again indicates a hopping model of conduction. At higher temperatures, the situation becomes more complicated as we approach the glass transition temperature of the polymer and therefore expect conformational changes [5, 4]. In Fig.4 we have plotted again the  $\log(\text{mobility})$  data versus  $T^{-1/4}$ . As expected, this indicates a straight line for variable range hopping (also for Hall mobility [11]).

#### ACKNOWLEDGEMENTS.

We are grateful to Dr. J. E. Österholm at Neste Oy for preparing the P3HT. This work is supported by National Board for Technical Development, Sweden.

#### REFERENCES.

1. R. Colson and P. Nagels, Philosophical Magazine B, Vol. 38 No.5 , (1978).
2. G. Harbeke, D. Baeriswyl, K. Kiess and Kobel, Phys. Scr. (1986).
3. M. Lögdlund, R. Lazzaroni, S. Stafström, W. R. Salaneck and J.-L. Bredas, Phys. Rev. Letters, 17 (1989).
4. A. Assadi, C. Svensson, M. Willander and O. Inganäs, Appl. Phys. Lett., 53 195-197 (1988).
5. J. Paloheimo, E. Punkka, H. Stubb and P. Kuivalainen, in R. M. Metzger, ed., Proc. of NATO Advanced Study Institute on Lower Dimensional Systems and Molecular Devices, Spetses, Greece, 1989.
6. O. Inganäs, W. R. Salaneck, J. E. Österholm and J. Lookso, J. Synth. Met., 22 395 (1988).
7. M. Mehra, R. Shyam and P. C. Mathur, Thin Solid Films, 100 81-109 (1983).
8. H. Isotalo, P. Kuivalainen, H. Stubb, J. E. Österholm, Mol. Cryst. Liq. Cryst. 171-180 (1985).
9. B. Movaghar and L. Schweitzer, J. Phys. C, 11 125 (1978).
10. A. Kurobe and H. Kamimura, J. Non-Cryst. Sol., 59&60 41-44 (1983).
11. T. Datta, Applied Phys. Comm., 3 1-31 (1983).
12. B. Movaghar, B. Pohlmann and G. Würtz, J. Phys. C, 14 5127-5137 (1981).



INSULATOR-METAL TRANSITION AND CONDUCTION  
PROCESSES IN TRANS-POLYACETYLENE

ESTHER M. CONWELL, HOWARD A. MIZES AND SURENDAR JEYADEV  
Xerox Webster Research Center, Webster, NY 14580

ABSTRACT

We show by calculations for a chain of stage-1 (16.7%) potassium-doped  $(\text{CH})_x$  that the metallic state is obtained by adding to the Su-Schrieffer-Heeger Hamiltonian the Coulomb potential of the doping ions and solitons on other chains. Good agreement with the measured Pauli susceptibility is obtained. Adding interchain coupling is found to lead to essentially the same density of states.

INTRODUCTION

Undoped trans-polyacetylene,  $(\text{CH})_x$ , has very low conductivity and a gap of  $\sim 1.8$  eV. Doping causes the conductivity  $\sigma$  to rise, very rapidly up to a concentration  $y \sim 1\%$  and then less rapidly as  $y$  increases further. The Pauli susceptibility  $\chi_p$  is quite small for  $y$  up to  $\sim 4$  to 6%, the value being sample dependent. Beyond that range  $\chi_p$  shows a sharp increase with increasing  $y$  [1], taken to be the signature of an insulator-metal transition. Indeed very high values of  $\sigma$ ,  $\sim 10^6$  ohm $^{-1}$ cm $^{-1}$ , are found in some  $(\text{CH})_x$  samples [2].

Despite the high  $\chi_p$  and  $\sigma$  in samples doped beyond the transition, the conductivity generally behaves in non-metallic fashion, increasing with increasing temperature. This raises the question as to whether highly doped  $(\text{CH})_x$  is really metallic or, more exactly, because doping is known to be inhomogeneous, whether there are any metallic regions in the doped samples. It is clear that the inconsistent behavior of  $\chi_p$  and  $\sigma$  results from the inhomogeneous doping.  $\chi_p$  measurements reflect the energy level spacing around the Fermi energy  $E_F$  in the metallic regions, while the  $\sigma$  measurements are likely to be dominated by the nonmetallic regions. Although in most samples  $\sigma$  drops by orders of magnitude from  $T=300\text{K}$  down to 4K, say, there are some heavily doped samples for which  $\sigma$  decreases less than an order of magnitude in this range and also varies little with  $T$  at the low temperatures. The latter feature in particular indicates that in these samples there is no gap within the doped regions and that barriers due to high resistance are small enough to be transversed by tunneling. Indeed, very good fits to  $\sigma$  vs.  $T$  have been found using Sheng's theory [3] of thermal-fluctuation-induced tunneling between metallic particles embedded in an insulator [2]. Although strong

doubts have been expressed as to the detailed applicability of the Sheng theory, the fit to the theory has yielded barrier heights and widths that appear reasonable [2]. For samples whose  $\sigma$  changes by less than an order of magnitude from 4 to 300K the barriers are, of course, small compared to  $kT$  at 300K. It is not surprising then that for some of these samples  $\sigma$  is found to decrease with increasing  $T$  in a small range below 300K [4], indicating the presence of phonon scattering. Although optical phonons have too high energy to scatter in this temperature range, there is no reason why acoustic phonon scattering should not be operative in  $(CH)_x$ . We conclude that there is good evidence for the existence of genuinely metallic regions in some heavily doped  $(CH)_x$  samples.

#### ORIGIN OF METALLIC NATURE

The question of what makes polyacetylene metallic has been considered by many workers. Early work attributed the metallic nature to randomness of the dopant distribution destroying the gap at high concentrations [5]. It is by now well documented, however, that the impurity ions are well ordered in the heavily doped regions [6]. For Na-doped  $(CH)_x$ , in particular, the regular arrangement of ions, plus the small value of  $\chi_p$  below 6%, was attributed to the existence of a soliton lattice in the dopant-rich phase at those concentrations [1, 7]. This led to the proposal [7] that the insulator-metal transition constitutes a phase transition from a soliton to a polaron lattice, the latter being metallic because it has a half-filled band. The idea that the metallic state is a polaron lattice has been espoused more recently on the ground that the VEH band structure for the polaron lattice case, calculated with geometry determined by MNDO, leads to good agreement with the observed optical absorption of  $(CH)_x$  [8].

Several arguments have been advanced against a polaron lattice. It has been shown that, to the accuracy of the SSH Hamiltonian, the polaron lattice is unstable with respect to the undimerized lattice [9]. Also, in a one-dimensional system the half-filled polaron band is unstable towards a Peierls distortion that opens a gap at the Fermi energy. Undoped  $(CH)_x$  is, of course, sufficiently one-dimensional that it becomes a semiconductor by precisely this mechanism. The arrangement of  $(CH)_x$  chains is altered by doping [6] but interchain spacing is not decreased and it is therefore expected that interchain coupling remains much the same, leaving the Peierls distortion a most likely prospect. Lögdlund et al, arguing for the existence of a polaron lattice in poly (3-hexyl-thiophene), have suggested that the interaction with the dopant ions is what prevents the Peierls distortion [10]. If the interaction with the dopant ions were strong enough to accomplish this, it is clearly inadmissible to neglect their potential in

calculating the band structure for the polaron lattice, as has been done in Ref. 8. It will be shown below that the ion potential has a strong effect on the energy levels, in fact giving rise to the insulator-metal transition in a soliton lattice.

On the evidence that the intensities of the three doping-induced infrared absorption lines (IRAV), established as being due to solitons at low concentrations, increase more or less linearly with  $y$  in K-doped  $(\text{CH})_x$  up to the maximum possible doping [11], we conclude that electrons or holes donated to the chains go into soliton states at all concentrations [12, 13]. For a long, heavily doped chain an energy level calculation using the SSH Hamiltonian [14] results in soliton states spreading over a large portion of the energy gap, but there is still a sizeable gap remaining between the highest filled state and the conduction band edge, or, in the case of p-type material, between the lowest empty state and the valence band edge. In what follows we will speak of donor-doped samples for specificity, but the results apply to acceptor-doped samples with the obvious modifications. We have found, in calculations for 8.33% Na-doped  $(\text{CH})_x$ , that the addition to the SSH Hamiltonian of the potential due to the doping ions and charged solitons on other chains results in changes of the spacing of the levels such that, for long enough chains, the remaining gap, between the top soliton level and the lowest conduction band levels, is only a few  $kT$  at room temperature, small enough to yield [13] the  $\chi_p$  measured for this material [1]. To determine whether inclusion of the Coulomb potential due to the ions and off-chain solitons can yield a metal, in agreement with experiment, we have carried out similar calculations for stage-1 potassium-doped  $(\text{CH})_x$ . This is the best case for such a test of our theory because the structure and the charge transfer to the chains are reasonably well known, unlike the case of iodine doping where the relative abundance of  $I_3^-$  and  $I_5^-$  is not known.

In what follows we review briefly the method of calculation and the structure of stage-1 K-doped  $(\text{CH})_x$ . We then discuss the results of the band structure calculations for a single chain and the effect on the energy levels of interchain coupling.

#### SINGLE CHAIN CALCULATIONS

In stage-1 K-doped  $(\text{CH})_x$ , each K ion column is at the center of four  $(\text{CH})_x$  chains, as shown in Fig. 1, arranged on a square of side  $5.98\text{\AA}$  [6]. Thus there are two chains/ion column. The spacing between ions is  $3a$ ,  $a$  being the average spacing between C-H's [6]. There are thus 6 sites between soliton centers. Because x-rays do not give the location of an ion relative to the C-H's on an adjacent chain we calculated for two different arrangements. In both arrangements the ions were arranged symmetrically with respect to the two

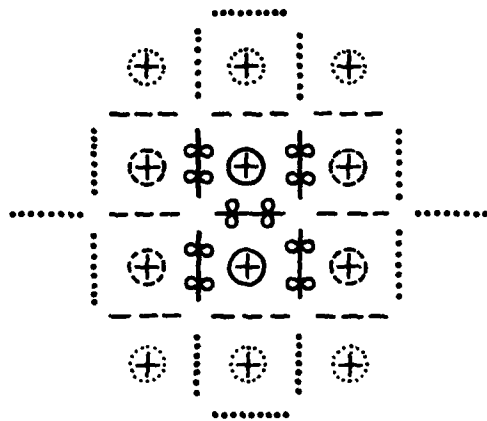


Fig. 1 Lattice of stage-1 K-doped  $(\text{CH})_x$  viewed along the chains. Solid lines indicate the ion columns and  $(\text{CH})_x$  chains in the first shell with respect to the chain at the center, dashed lines those in the second shell and dotted lines those in the third shell. Locations of the  $n$  orbitals between which transfer integrals were calculated are indicated.

chains but the soliton centers were opposite the ions in one arrangement (asymmetric with respect to the chains) and halfway between ion centers in the other (symmetric).

As noted earlier, we used the electronic part of the SSH Hamiltonian [14] plus the Coulomb potential  $V_c$  due to the ions and off-chain solitons, calculated as will be described below. The presence of  $N_s$  solitons on the chain was incorporated by taking the displacement of each lattice site as

$$u_n = -(-1)^n u_0 \prod_{j=1}^{N_s} \tanh\left(\frac{n-jb-n_c}{\ell}\right) \quad (1)$$

where  $u_0$  is the displacement in the perfectly dimerized chain,  $b$  the number of spaces between soliton centers and  $\ell$  the number of sites in the half-length of a soliton. The quantity  $n_c$  is chosen to allow for  $\sim\ell$  sites between the center of the first (or last) soliton and the end of the chain.

For the calculation of the Coulomb potential  $V_c$  the ions and solitons were considered arranged in shells containing equal numbers of positive and negative charges, as indicated in Fig. 1. The screening employed in the calculations was sufficiently effective that charges beyond the third shell had negligible effect. To calculate that screening, the other chains were represented by a metallic cylinder that fills all space beyond the nearest neighbor distance [13]. Within this cylinder the inverse screening length  $\kappa_3$  was taken as the metallic value

$$\kappa_3^2 = (4ne^2 \eta(E_F) N_0)^{1/2} \quad (2)$$

Here  $\eta(E_F)$  is the number of states per unit energy per C atom and  $N_0$  the number of C atoms/cm<sup>3</sup>. The value of  $\eta(E_F)$  was obtained from the measured  $\chi_p$  [13]. This imposes a self-consistency requirement on the calculation: the output  $\eta(E_F)$ , i.e. the value obtained from the calculated energy levels, must equal the value of  $\eta(E_F)$  used in Eq. (2) to calculate  $\kappa_3$ .

Calculation of  $V_c$  was carried out numerically for a chain of 104 sites, with 16 solitons, surrounded by similar chains. We note that 104 sites is within the coherence length found by x-rays for stretched Shirakawa or Naarmann-Theophilou (CH)<sub>x</sub> [15]. With the ion columns shorter than the chain length, the potential is found to be a well of average depth 5eV and variations along the chain of < 1eV. The self-consistent value of  $\eta(E_F)$  was found to be 0.09 states/eV C-atom, in good agreement with the measurements for the metallic state [1]. The calculated energy levels for the symmetric arrangement of the solitons are shown in Fig. 2 plotted as a function of  $fV_c$  for  $0 \leq f \leq 1$ , to show how the levels evolve with the introduction of  $V_c$ . For  $f=0$  there are the 16 soliton levels in the gap, which has increased to  $\sim 3$ eV due to the removal of conduction and valence band states to make soliton states. The remaining gap between the filled soliton band and the conduction band edge is only  $\sim 0.25$  eV. As  $f$  increases from zero, 16 localized levels split off from the bottom of the valence band and a number of levels split off from the top of the conduction band. For  $f=1$  there is no longer a gap at the Fermi energy and the wave functions of the levels around  $E_F$  are delocalized. The material is clearly metallic. We note that the small gap between the second and third level below  $E_F$  is not seen in the asymmetric soliton arrangement, which otherwise gives quite similar energy levels.

#### EFFECT OF INTERCHAIN COUPLING

It is seen that the gaps between levels are of the order of tenths of an eV. Since interchain coupling in the undoped (CH)<sub>x</sub> lattice has been estimated to be of that order [16], it is important to look at the corrections to the single chain energies due to this coupling. For this purpose we assumed an infinite lattice

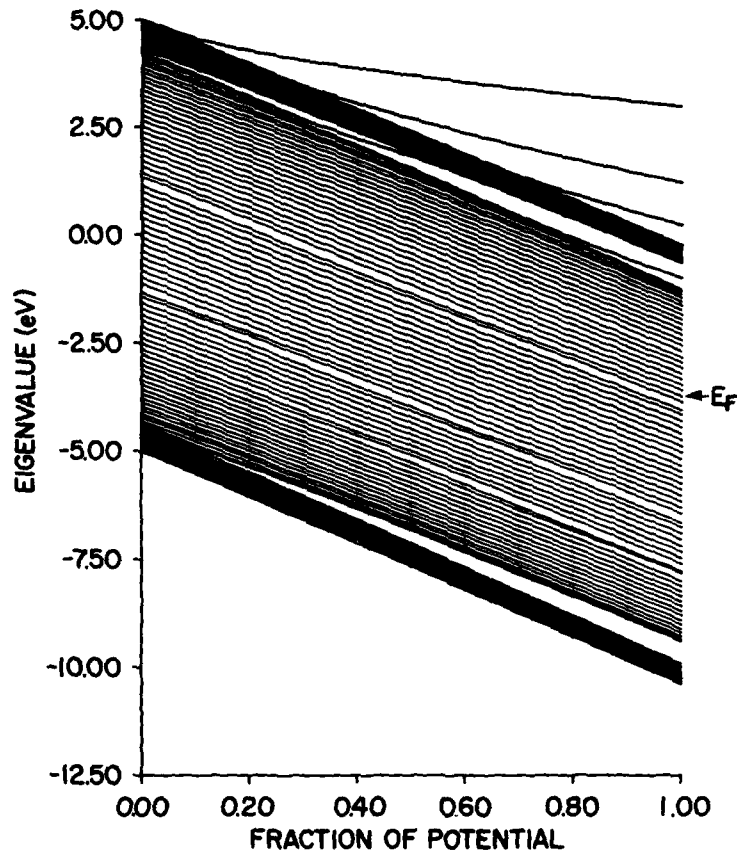


Fig. 2 Calculated eigenvalues for the symmetric arrangement of solitons plotted as a function of  $fV_c$ ,  $0 \leq f \leq 1$ , for a chain length of 104 sites (16 solitons).

perpendicular to the chains; this allows well-defined  $k$  values in the perpendicular direction. We added to the Hamiltonian the term

$$H' = \sum_{j \neq i} \sum_{n=1}^N \sum_{n'=1}^N t_{ijn'} [C_{in}^+ C_{jn'} + H.c.] \quad (3)$$

where the subscript  $i$  refers to the  $n$ 'th site on the  $i$ 'th chain. For the tetragonal structure of stage-1 K-doped  $(\text{CH})_x$  we took  $j$  to run over the four nearest neighbor chains to the  $i$ 'th chain (see Fig. 1). The transfer integrals  $t_{in;jn'}$  are comparable in magnitude to those obtained in undoped  $(\text{CH})_x$  because the distances between pairs of C's are comparable or shorter.

The single-chain wavefunction for an energy level  $E_s$  may be written, for the  $i$ 'th chain,

$$\Psi_i(E_s) = \sum_{n=1}^N a_{in}(E_s) |n\rangle \quad (4)$$

where the set of  $a_{in}(E_s)$  has been determined as described in the last section. With Eqs. (3) and (4), first order perturbation theory gives for the shift  $\Delta E_s$  in the energy level  $E_s$  due to interchain coupling

$$\Delta E_s = \sum_{j \neq i} \sum_{n=1}^N \sum_{n'=1}^N [a_{in}^*(E_s) a_{jn'}(E_s) t_{in;jn'} e^{i\mathbf{k}\cdot\mathbf{d}} + H.c.] \quad (5)$$

where  $\mathbf{d}$  is the vector distance between site  $n$  on chain  $i$  and  $n'$  on chain  $j$ .

The interactions included in the summation of Eq. (5) were those between each of the two inequivalent  $n$  orbitals on a given chain (see Fig. 1) and the three or five closest orbitals on each of the four nearest neighbor chains. This requires evaluation of  $t_{in;jn'}$  for 28 different pairs, although only 7 of these are unique. In the absence of information from x-rays, we calculated for the symmetric arrangement and chose the atoms on the chains in the horizontal sides of the square unit cell to lie in the same plane as the atoms on the chains in the vertical sides. With so many different pairs included in the calculations the choice of arrangements should not have much effect on the final result. To evaluate  $t_{in;jn'}$  it is convenient to express each  $n$  orbital as a sum of two perpendicular orbitals with orientation chosen so that one part of each pair forms a  $\sigma$  bond and the other a  $\pi$  bond [17, 18]. By means of parameters given by Harrison [17, 19]  $t_{in;jn'}$  may then be expressed as a function of the orientation of the  $n$  orbitals at the two sites and the vector  $\mathbf{d}$  joining the two. For the relatively large  $d$  values with which we are concerned, the transfer integrals should decay exponentially. Values taken from Harrison's parametrization of transfer integrals for C  $n$  orbitals gave the decay as  $[\exp(-1.70d)]$  for  $d$  given in  $\text{\AA}$ . Further details of the calculation of the  $t_{in;jn'}$  will be given in a future publication.

We evaluated  $\Delta E_s$ , using Eq. (5), for 1,024  $k$  values throughout the Brillouin Zone. To obtain the density of states the energy values were sorted into 1,000 intervals or bins. The results are shown in Fig. 3. It is seen that over all the properties of the density of states are quite similar to those seen at the right hand side of Fig. 2. The differences can be attributed to the fact that interchain coupling is more effective for the lower energy levels. This is a result of the smaller number of nodes, i.e., the smaller number of sign reversals, in the lower energy wavefunction, which makes it more likely that contributions to  $\Delta E_s$  of near neighbors will add up in phase. Thus we see in Fig. 3 that the discrete nature of the levels is retained in the upper part of the conduction band, the spikes correlating well with individual levels in Fig. 2. The lower valence band levels, as expected, are more continuous, with, for example, the gap of Fig. 2 between the band of localized levels centered at -10 eV and the next higher valence band levels wiped out. The material is still metallic. At  $E_F$  and within a volt above  $E_F$  the density of states is continuous although spiky. A very small gap is still seen two levels below  $E_F$ . Such a gap could be wiped out by thermal vibrations at all but the lowest temperatures. In any case, as noted earlier, it is not seen in the asymmetric soliton arrangement, and we do not know the correct arrangement for this material.

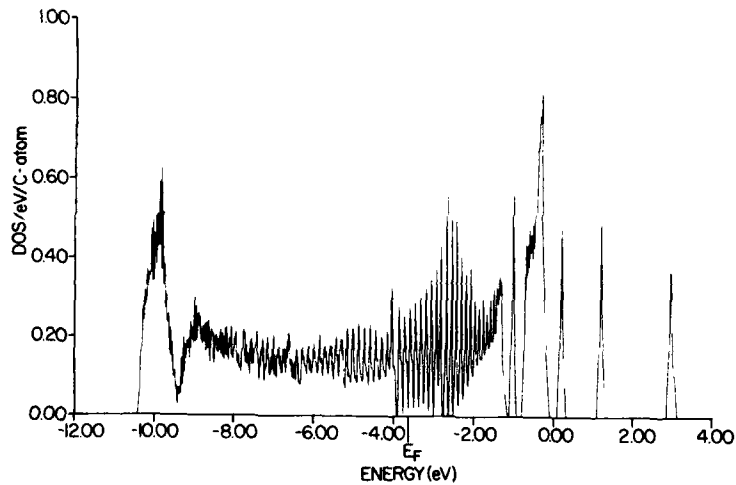


Fig. 3 Density of states vs. energy corrected for interchain coupling for the 104 site stage-1 K-doped chain with the symmetric arrangement of solitons.



## CONCLUSIONS

We believe our model has accounted for metallic behavior in stage-1 K-doped  $(\text{CH})_x$ , thus in the heavily K-doped samples of Ref. 4. The features that result in metallic behavior are the strong overlap of electron wavefunctions on adjacent solitons, whose centers are only 6 sites apart, and the deep potential well due to the large ion concentration, 16.67%. Incorporation of interchain coupling leads to a density of states similar, except for some spreading, to what was obtained for the single chain. Scattering by acoustic modes cannot be neglected in the metallic regions.

## REFERENCES

1. F. Moraes, J. Chen, T.-C. Chung and A.J. Heeger, *Synth. Met.* **11**, 271 (1985).
2. See, for example, Th. Schimmel, G. Denninger, W. Riess, J. Voit, M. Schwoerer, W. Schoepe and H. Naarmann, *Synth. Met.* **28**, D11 (1989).
3. P. Sheng, *Phys. Rev.* **B21**, 2180 (1980).
4. This behavior has been found for 12-14% K-doping by J. Ghanbaja, J.F. Mâreché, E. McRae and D. Billund, *Solid State Commun.* **60**, 87 (1986) and Y. W. Park, C. Park, Y.S. Lee, C.O. Yoon, H. Shirakawa, Y. Suezaki and K. Akagi, *Solid State Commun.* **65**, 147 (1986). It has also been found for doping by  $\text{AsF}_5$ ,  $\text{FeCl}_3$ , I and  $\text{SnCl}_5$ .
5. E.J. Mele and M.J. Rice, *Phys. Rev. B* **23**, 5397 (1981).
6. R.H. Baughman, L.W. Shacklette, N.S. Murthy, G.G. Miller and R.L. Elsenbaumer, *Mol. Cryst. Liq. Cryst.* **118**, 253 (1985) and references therein.
7. S. Kivelson and A.J. Heeger, *Phys. Rev. Lett.* **55**, 308 (1985).
8. S. Stafström and J.-L. Brédas, *Phys. Rev. B* **38**, 4180 (1988).
9. H.-Y. Choi and E.J. Mele, *Phys. Rev. B* **34**, 8750 (1986).
10. M. Lögdlund, R. Lazzaroni, S. Stafström, W.R. Salaneck and J.-L. Brédas, *Phys. Rev. Lett.* **63**, 1841 (1989).
11. D.B. Tanner, G.L. Doll, A.M. Rao, P.C. Eklund, G.A. Arbuckle and A.G. MacDiarmid, *Synth. Met.* **28**, D141 (1989).

12. E. Conwell and S. Jeyadev, *Phys. Rev. Lett.* **61**, 361 (1988).
13. E.M. Conwell, H.A. Mizes and S. Jeyadev, *Phys. Rev. B* **40**, 1630 (1989).
14. W.P. Su, J.R. Schrieffer and A.J. Heeger, *Phys. Rev. B* **22**, 2099 (1980).
15. D. Djurado, J. Ma, N. Theophilou and J.E. Fischer, *Synth. Met.* **30**, 395 (1989).
16. D. Moses, A. Feldblum, E. Ehrenfreund, A.J. Heeger, T.-C. Chung and A.G. MacDiarmid, *Phys. Rev. B* **26**, 3361 (1982).
17. W.A. Harrison, *Electronic Structure and the Properties of Solids* (W.H. Freeman and Co., San Francisco, 1980).
18. J.C. Slater and G.F. Koster, *Phys. Rev.* **94**, 1498 (1954).
19. W.A. Harrison, *Phys. Rev. B* **31**, 2121 (1985).

## DETERMINATION OF CORRELATION PARAMETERS IN $\pi$ -CONJUGATED POLYMERS

J. TINKA GAMMEL,\* D.K. CAMPBELL,\* E.Y. LOH, JR.,\* S. MAZUMDAR,\*\* and  
S.N. DIXIT\*\*\*

\*Theoretical Division and Center for Nonlinear Studies Los Alamos National Laboratory,  
Los Alamos, NM 87545

\*\*Department of Physics, University of Arizona, Tucson, AZ 85721

\*\*\*Lawrence Livermore National Laboratory, Livermore, CA 94550

### ABSTRACT

Using exact finite-size diagonalizations of extended Peierls-Hubbard Hamiltonians for systems of up to 15 sites, we study the excited state spectra of models for the finite oligomer analogs of *trans*- and *cis*-polyacetylene. We use a novel "phase randomization" technique and a variety of other methods to extract maximal information from these small systems. For several electron-phonon couplings in the expected range, we discuss the extent to which we are able to find consistent values of the Hubbard on-site ( $U$ ) and nearest-neighbor ( $V$ ) correlation parameters such that the band gap, the  $2^1A_g$  state, optical phonon frequency, and the optical absorptions for charged and neutral solitons and dimers occur in the experimentally expected ranges. Our results suggest that these correlation parameters are in the intermediate coupling regime ( $U \simeq 2.5t_0$ ), beyond the range of perturbation theory.

### INTRODUCTION

Recent interest in novel low-D materials - *e.g.*, high-temperature superconducting copper oxides, "heavy-fermion" and charge-density wave systems, halogen-bridged transition-metal chains, and organic synthetic metals and superconductors - has stimulated the theoretical study of competing electron-electron (e-e) and electron-phonon (e-p) interactions in reduced dimensions. It is essential in these new materials to capture the essence of both e-p and (strong) e-e interactions and to represent faithfully their synergetic, or competing, effects. To this end, variants of the extended Peierls-Hubbard (ePH) Hamiltonian have been widely used.<sup>1</sup> In contrast to the relative simplicity of independent-electron theories, the correlated electron systems described by these Hamiltonians are difficult to treat adequately. In the present article we adopt one technique - exact diagonalization using the Lanczos method<sup>2</sup> combined with a novel "phase randomization" technique<sup>3</sup> - which, at least in the case we treat here, appears to allow us to sail the narrow channel between the Scylla of exponential growth of the number of states in any exact many-body basis and the Charybdis of the failure of mean-field theories to capture correctly the effects of e-e interactions in reduced dimensions.

We focus on the 1-D ePH Hamiltonian in the context of *trans*-polyacetylene ( $(CH)_x$ ). Of the novel, low-D materials, it has the simplest idealized structure. Thus the hope of modeling (and understanding) it within the geometrically and quantum chemically simple (single chain, single molecular orbital, nearest neighbor, tight-binding) ePH Hamiltonian is greatest. In spite of this, the correct parameters for modeling  $(CH)_x$  remain a matter of much debate.<sup>1</sup> For a broad range of parameters, including those of the "SSH" model<sup>4</sup>, we present results for (1) the self-consistent lattice distortion, (2) the longitudinal optical phonon mode ( $\omega_{LO}^2$ ), and (3) the optical absorption properties (optical gap ( $E_g$ ) and bandwidth ( $W$ )), all as functions of the strength of the e-e and e-p interactions. Comparing with the appropriate experimental values allows us to infer an internally consistent set of parameters, which we can then use to determine whether other observables - such as the soliton absorptions and the triplet gap - are consistent with experiment; at present, this part of the work is still in progress. We stress that obtaining fits to many different observables with a single set of physically plausible parameters is essential to any true understanding of *trans*- $(CH)_x$ , or more generally any member of the class of low-D materials.

## MODEL AND METHOD

In the context appropriate to *trans*-(CH)<sub>x</sub>, the ePH Hamiltonian takes the form<sup>1</sup>

$$H = \sum_{\ell} (-t_0 + \alpha \Delta_{\ell}) B_{\ell, \ell+1} + \frac{1}{2} K \sum_{\ell} (\Delta_{\ell} - a_0)^2 + U \sum_{\ell} n_{\ell \uparrow} n_{\ell \downarrow} + V \sum_{\ell} n_{\ell} n_{\ell+1}. \quad (1)$$

Here  $c_{\ell \sigma}^{\dagger}$  ( $c_{\ell \sigma}$ ) creates (annihilates) an electron at site  $\ell$ ;  $n_{\ell \sigma} = c_{\ell \sigma}^{\dagger} c_{\ell \sigma}$ ,  $n_{\ell} = n_{\ell \uparrow} + n_{\ell \downarrow}$ ;  $B_{\ell, \ell+1} = \sum_{\sigma} (c_{\ell \sigma}^{\dagger} c_{\ell+1 \sigma} + c_{\ell+1 \sigma}^{\dagger} c_{\ell \sigma})$ ;  $t_0$  is the hopping integral for the uniform chain;  $\alpha$  is the e-p coupling describing the modification of the hopping between adjacent sites due to the distortion of the underlying discrete chain;  $\Delta_{\ell}$  is the projection along the chain axis of the relative displacement between the (CH) units at sites  $\ell$  and  $\ell+1$ ; and  $K$  represents the cost of distorting the "lattice" of (CH)<sub>x</sub> moieties.  $a_0$  is defined to be the value needed in order that in the uniform ground state  $\Delta_{\ell} = (-1)^{\ell} \Delta_0$ . Without this constraint  $t_0$  is renormalized; further, the value of  $a_0$  is important in the calculation of the phonon modes and has a  $1/N$  effect (large here) on calculations for excited geometries. The Coulomb repulsions among electrons are parameterized with the conventional Hubbard  $U$  and  $V$ .

Exact diagonalization studies are made feasible by the Lanczos method,<sup>2</sup> which in essence involves generating a basis in which the Hamiltonian is tridiagonal, and which we have discussed in this context elsewhere.<sup>3</sup> For small clusters, the lattice-size dependence in numerical calculations is large. The importance of the Jahn-Teller/non-Jahn-Teller distinction for small system size  $N$  is familiar from the finite cyclic polyenes (bagelenes), where  $4N+2$  rings do not dimerize; benzene, for example, has equal bond lengths. For  $U=V=0$ , one can show that "complex-phase-averaging"<sup>3</sup> - just using Bloch's theorem to construct units of size  $MN$  from units of size  $N$  by averaging over complex phase boundary conditions (b.c.'s)  $\psi(N+1) = e^{i\phi} \psi(1)$ ,  $\phi = 2\pi\ell/M$ ,  $\ell = 1, \dots, M$  on the smaller units - exactly captures the long chain behavior. However, for the half-filled band systems we are currently considering, in the strongly correlated ( $U \rightarrow \infty$ ) limit, all measurable quantities become independent of  $\phi$  and the complex-phase-averaging scheme becomes ineffective. We have found a "scaled-hopping" phase randomization (amplitude b.c. averaging) technique to be effective in this regime.<sup>3</sup>

The value of the self-consistent adiabatic lattice distortion is found by minimizing the total energy. At fixed  $K$ , to find the ground state lattice distortion we use the Lanczos procedure iteratively to calculate the new guess at the minimum energy dimerization from the expectation value of the bond charge (the self-consistency condition)  $K(\Delta_{\ell} - a) = -\alpha \langle B_{\ell, \ell+1} \rangle$  (appropriately averaged over b.c.'s). For uniform dimerization, one can reverse the question and consider instead the dimerization as the independent variable, the spring constant then being determined self-consistently. For parameter space searches, this greatly reduces the computation, as no iteration is needed. This procedure fails, of course, when the dimerization vanishes. By calculating the phonon vibrational frequencies around this equilibrium dimerization, we gain additional insight into the competition between e-e and e-p interactions and additional constraints on possible parameters values.

To calculate the phonon dispersion relation, we need to evaluate the dynamical matrix:  $D_{\ell, \ell'} = \partial^2 E / \partial y_{\ell} \partial y_{\ell'}$ . Phonon eigenmodes  $y_{\ell}^q$  and eigenfrequencies  $\omega_q^2$  are found from  $D_{\ell, \ell'} y_{\ell}^q = M \omega_q^2 y_{\ell}^q$ . Here we are interested only in the LO ( $q=0$  longitudinal optical) mode of the uniform ground state, and thus we need only evaluate the total energy  $E[\Delta]$  at three different  $\Delta$  near the equilibrium geometry, as  $y_{\ell}^{LO} = [(-1)^{\ell} \Delta/2]$  is an eigenmode. This requires minimal additional computation beyond finding the ground state.

For studies of the optical absorption we need the current operator,  $J_q$ ,

$$J_q = \frac{i}{\sqrt{N}} \sum_{\ell} e^{-iq(\ell+1/2)} (t_0 - \alpha \Delta_{\ell}) \sum_{\sigma} (c_{\ell+1 \sigma}^{\dagger} c_{\ell \sigma} - c_{\ell \sigma}^{\dagger} c_{\ell+1 \sigma}). \quad (2)$$

The problem of calculating the optical absorption coefficient

$$\alpha(\omega) = \frac{1}{\omega} \sum_m | \langle m | J_q | 0 \rangle |^2 \delta(\omega - (E_m - E_0)) \quad (3)$$

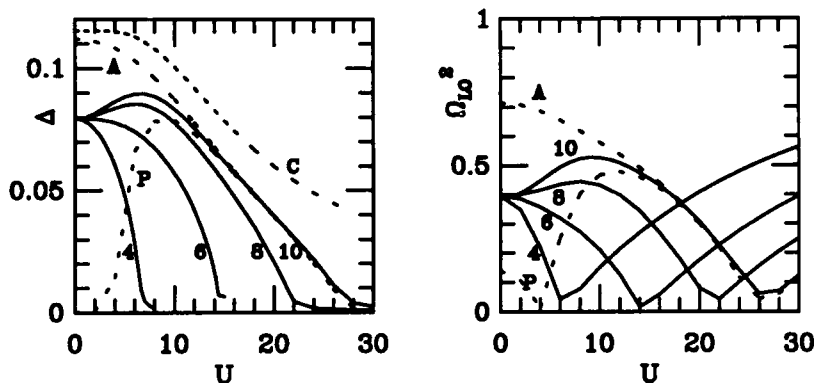


Fig. 1 (left). Self-consistent dimerization ( $\Delta$ ) as a function of Hubbard  $U$  for several  $N$  with  $48/N$  ( $50/N$  for 10 sites) different phase b.c.s summed (solid lines). The counter-intuitive increase of  $\Delta$  with  $U$  can be seen on systems as small as 8-sites. For comparison, the results for the 10-site chain (C) and the 10-site ring with periodic (P) and anti-periodic (A) boundary conditions, where finite-size effects obscure the enhancement, are also shown (dashed lines).

Fig. 2 (right). Complex-phase-averaged LO mode frequency as a function of Hubbard  $U$  and system size. The results for the 10-site ring with periodic (P) and anti-periodic (A) boundary conditions are also shown (dashed lines). Note the LO mode frequency tracks the dimerization shown in Fig. 1.

within a Lanczos scheme reduces to finding the spectral weight of  $J_q|\psi_0\rangle$ .<sup>3</sup>

Though there are pathologies — including violation of the f-sum rule and difficulties both with physical interpretation of the geometry<sup>5</sup> and with phase-randomization — that arise when we attempt to define  $\alpha(\omega)$  on a closed  $N$ -site ring for  $q = 0$ , we will study  $q = 0$  as well as the smallest allowed nonzero momentum value,  $q = 2\pi/N$ .

## DETERMINATION OF POLYACETYLENE PARAMETERS

To begin our discussion, it is useful to recall how the parameters are determined in the conventional SSH model<sup>4</sup> of *trans*-(CH)<sub>x</sub>, which corresponds to (1) with  $U = V = 0$ . Since this is a single-electron theory, it can be solved analytically for the uniformly dimerized ground state. One finds that the bandwidth is given by  $W = 4t_0$ , the optical gap by  $E_g = 4\alpha\Delta$ , and that the dimerization  $\Delta$  is determined by the self-consistency condition  $K = (2/\pi)(K(\delta) - E(\delta))/\delta^2$ , where  $\delta = \alpha\Delta/t_0$  and  $E$  and  $K$  are the complete elliptic integrals. Fitting to  $W = 10\text{eV}$ ,  $E_g = 1.4\text{eV}$ , and  $\Delta = .086\text{\AA}$  yields the conventional SSH parameters  $t_0 = 2.5\text{eV}$ ,  $\alpha = 4.1\text{eV/\AA}$ , and  $K = 21\text{eV/\AA}^2$ . For these single-electron parameters, we have previously<sup>3</sup> analyzed the effects of non-zero  $U$  and  $V$  as functions of system size on several experimental observables. To illustrate our approach, we mention briefly some of the salient results.

It is well known that the Hubbard  $U$  counterintuitively initially increases dimerization for weak e-p coupling. In Fig. 1 we show the dimerization as a function of  $U$  for various lattice sizes with the b.c. averaged over several complex phases ("complex-phase-averaged"). This figure illustrates the convergence of the Lanczos technique with system size, as well as the effects of periodic, anti-periodic, and chain versus complex-phase-averaged b.c.s. Complex-phase-averaging yields a behavior for 10 sites that is nearly converged to the value inferred for the infinite case, whereas any single b.c. yields this behavior only after (considerable) extrapolation. Thus complex-phase-averaging eliminates many of the problems involved in determining what extrapolation scheme to use.

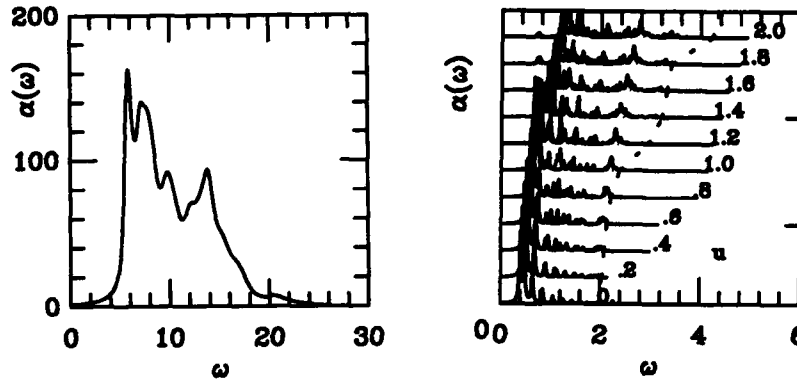


Fig. 3 (left). The phase randomized optical spectrum obtained using the "scaled-hopping" approach for 12-site rings at intermediate coupling ( $U = 10eV$ ) and  $\Delta = 0.086\text{\AA}$ .  
 Fig. 4 (right). Optical absorption spectra for a range of  $u$  at  $v = 0$  and  $\delta = .2$  for 8 and 6 sites complex phase randomized. The outer band edge  $w$  (dashed line) is indicated.

However, for non-uniform geometries the problem of extrapolation remains. (Complex-phase-averaging the ground state on a odd chain corresponds at  $U = V = 0$  to finding the (high-density) soliton lattice.)

In the case of phonon vibrational frequencies it is unclear how to formulate a "phase randomization" technique to determine full dispersion relations, especially for non-uniform ground states. Thus we can obtain only limited information about the full dispersion curve.<sup>3</sup> However, for the LO mode frequency of the uniform ground state, complex-phase-averaging can be used to advantage. Fig. 2 shows the LO mode frequency as a function of  $U$  and system size. Note that this mode tracks the dimerization, as can be seen by comparing Figs. 2 and 1.

Turning to optical absorption, Fig. 3 shows how phase-randomization yields non-sparse spectra that correspond to those of the infinite system, in contrast to the sparse spectra of finite rings with fixed b.c.'s. Further, this spectrum establishes that our phase-randomized Lanczos technique produces results consistent with expectations based on strong- and weak-coupling arguments.<sup>3,6</sup>

The above results suggest that the phase-randomized results on systems as small as 8 sites provide reasonable estimates of the behaviors of observables in the infinite system limit. Hence we can use systems of this (manageable) size to carry out an exhaustive parameter search. Our procedure is to span the dimensionless parameter space:  $t_d \equiv .5$ ,  $\alpha_d \equiv .5$ ,  $\delta = \alpha\Delta/t_0$ ,  $u = U/2t_0$ , and  $v = V/2t_0$ ; determining  $k = Kt_0/2\alpha^2$ ,  $e_g = E_g/2t_0$ ,  $w = W/2t_0$ , and  $\Omega_{LO}^2 = \omega_{LO}^2/(4K/M)$ . To date we have completed for 6 sites with 8 phases and 8 sites with 6 phases a search over  $\delta = .05, .10, .20$ ,  $v = 0, .2, \dots, 2$ , and  $u = v, v + .2, \dots, 3$ . In Fig. 4 we show the optical absorption spectra for a range of  $u$  at  $v = 0$  and  $\delta = .2$ . Note a spurious absorption within the gap is seen. It is related to an optically forbidden peak in the dimer, and is a consequence of the phase b.c.'s. The Lanczos method does not reliably give outer band edges; thus, the band edge  $w$ , shown by the dotted line in Fig. 4, was determined by defining the edge of the band to be where the absorption had fallen to 1% of its maximum. Note even at  $u = v = 0$  this can differ considerably from the actual band edge. The dependence of  $e_g$  and  $\Omega_{LO}^2$  on input dimensionless parameters are shown in Figs. 5 and 6. The gap does appear to scale with  $U - V$ , as predicted by strong coupling. However, we have not carried the search to large enough  $U$  to verify this in detail. For  $U \approx 2V$ , the gap appears to depend on  $U - 2V$  as expected from decoupled dimer arguments. For  $U > 2V$  insofar as it can be accurately determined, the ratio band/gap is remarkably insensitive to parameters, with  $w/e_g \approx 5$ . Note  $\Omega_{LO}^2$  is roughly independent of  $U, V$  for  $U \gg 2V$ . This can be understood by the argument that fixing the dimerization fixes the effective e-p coupling, which determines

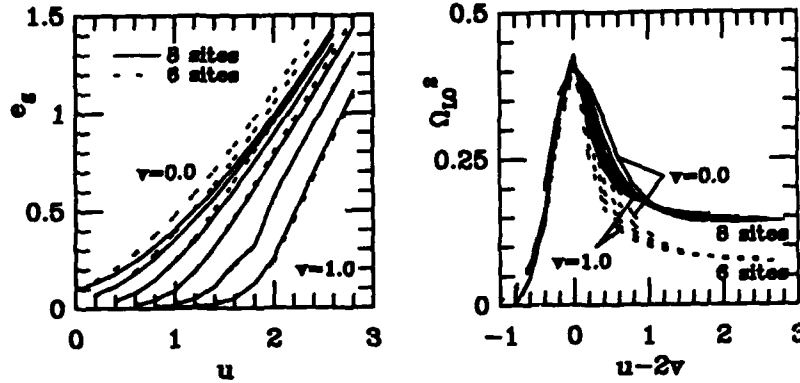


Fig. 5 (left). The dependence of  $e_g$  on input dimensionless parameters.

Fig. 6 (right). The dependence of  $\Omega_{LO}^2$  on input dimensionless parameters.

the strength of the Kohn anomaly. The maximum  $\Omega_{LO}^2$  can be understood in terms of the competition between the SDW and CDW states:  $\Omega_{LO}^2$  is maximal as  $V \rightarrow U/2$ , consistent with the dimerization increasing as one approaches this phase boundary. For  $V > U/2$ ,  $V$  rapidly destroys dimerization, and the  $\Omega_{LO}$  mode goes soft.

To determine the parameters describing  $trans-(CH)_x$ , we scale each of these dimensionless data points to the actual gap and dimerization to determine the dimensional parameters. If the bandwidth and LO phonon frequency then agree with their actual values, we accept these as possible parameters. However, although SSH used for the alternating component of the dimerization along the chain  $\Delta = .086\text{\AA}$ , even this simple fact is not carved in stone. More recent structural data<sup>7</sup> suggest values as low as  $.022\text{\AA}$ . The appropriate value of the bandwidth  $W$  is also unclear, as experimental spectra never cutoff cleanly. It is "generally agreed" that  $\Delta = .03\text{\AA}$ ,  $W = 10\text{eV}$ , and  $E_g = 1.8\text{eV}$  are the values to use. The vibration spectra of  $trans-(CH)_x$  is complicated by the zig-zag geometry. Though it has an appreciable isotope effect indicating considerable C-H stretch mixing, the C=C stretch at  $\bar{\nu}_{LO} = \omega_{LO}/(2\pi c) = 1450\text{cm}^{-1}$  in  $trans-(CH)_x$  is considered to be the mode corresponding most closely to the single LO mode of the theoretical 1-D chain.<sup>8</sup> The triplet absorption at  $E_g^T = 1.4\text{eV}$ , and the  $S^\pm/S^0$  optical and infrared absorptions have also been identified. We are currently considering how well the inferred parameters match these data on non-uniform geometries. Listed in Table I are our results to date for the possible parameters describing  $trans-(CH)_x$ .

## CONCLUSIONS AND OPEN ISSUES

The phase randomization modified exact diagonalization allows for reasonable extrapolations from 8 site systems, for which an exhaustive parameter search can be carried in reasonable time. Our current estimates of the parameters modeling  $trans-(CH)_x$  are shown in the Table 1. Clearly much work remains. The parameter search needs to be repeated on 10 and 12 site systems as the approximate allowed parameters ranges are refined. Dependences of the inferred parameters on experimental inputs need to be understood, and a prescription for defining what is meant by the bandwidth needs to be agreed upon. Surprisingly,  $\omega_{LO}^2$  does not significantly restrict  $U, V$  for fixed  $U - 2V$ . The amplitude mode formalism for analysing the LO mode should also be incorporated. The analyses of solitons and triplet optical gap for the inferred parameters need to be performed with an appropriate phase randomization technique. Since intrinsic defects can be viewed as  $1/N$  effects, it may prove very difficult to extrapolate non-uniform geometries to large systems.

Table I: Parameters scaled to  $\Delta = .03\text{\AA}$ ,  $W = 10\text{eV}$ , and  $E_g = 1.8\text{eV}$  having  $\bar{\nu}_{LO}$  near  $1450\text{cm}^{-1}$ .

$\delta$	$u$	$v$	$t_0$ eV	$\alpha$ eV/ $\text{\AA}$	$U$ eV	$V$ eV	$K$ eV/ $\text{\AA}^2$	$\bar{\nu}_{LO}$ $\text{cm}^{-1}$	$W$ eV
.05	0.2	0.0	6.8	11.3	2.7	0.0	84.	1638.	7.4
.05	0.4	0.0	5.0	8.3	4.0	0.0	61.	1279.	5.6
.05	0.6	0.2	5.0	8.4	6.0	2.0	68.	1447.	5.7
.05	0.8	0.4	6.1	10.1	9.7	4.9	89.	1757.	6.1
.05	1.0	0.4	3.7	6.2	7.4	3.0	54.	1261.	7.3
.05	1.2	0.6	4.8	7.9	11.4	5.7	75.	1620.	6.6
.05	1.4	0.6	2.9	4.8	8.0	3.4	45.	1118.	10.9
.05	1.6	0.8	3.9	6.4	12.3	6.2	64.	1518.	6.8
.05	2.0	1.0	3.5	5.8	13.9	7.0	61.	1484.	12.8
.10	1.2	0.0	1.9	6.4	4.6	0.0	76.	1484.	11.7
.10	1.4	0.2	1.9	6.2	5.2	0.7	78.	1563.	12.0
.10	1.6	0.2	1.2	4.0	3.8	0.5	49.	1239.	7.8
.10	1.6	0.4	1.8	6.1	5.9	1.5	81.	1648.	12.4
.10	1.8	0.4	1.1	3.7	4.0	0.9	48.	1249.	6.0
.10	1.8	0.6	1.8	6.1	6.6	2.2	85.	1746.	10.5
.10	2.0	0.6	1.1	3.6	4.3	1.3	48.	1291.	5.7
.10	2.0	0.8	1.9	6.2	7.5	3.0	91.	1868.	10.6
.10	2.2	0.8	1.1	3.6	4.8	1.7	51.	1370.	6.0
.10	2.4	1.0	1.2	3.9	5.6	2.3	57.	1502.	6.9
.20	3.0	0.0	0.5	3.2	2.8	0.0	45.	1474.	4.9
.20	3.0	0.2	0.5	3.2	2.9	0.2	48.	1515.	4.7
.20	3.0	0.4	0.5	3.2	2.9	0.4	51.	1573.	4.1

We would like to thank Alberto Girlando, Eugene Mele, Anna Painelli, Doug Scalapino, and Zoltan Soos for several valuable discussions. Computational support was provided by the CMS and CNLS at Los Alamos National Laboratory, by the Computational Sciences Division of the U.S. DOE at the NMFEC at Livermore, and by the DOE's Supercomputing Access Program at the Air Force Supercomputer Center.

## REFERENCES

1. For a recent review of the ePH Hamiltonian applied to  $(CH)_x$ , see: D. Baeriswyl, D. K. Campbell, and S. Mazumdar, to be published in *Conducting Polymers*, edited by H. Kiess (Springer, New York, 1990).
2. See, e.g., the section on Lanczos diagonalization in S. Pissanetsky, *Sparse Matrix Technology* (Academic, London, 1984).
3. D. K. Campbell, J. Tinka Gammel, and E. Y. Loh, Jr., to be published in the Proceedings of the Anniversary Adriatico Research Conference on Strongly Correlated Electrons, Trieste, Italy, July 18-21, 1989.
4. W.P. Su, J.R. Schrieffer, and A.J. Heeger, Phys. Rev. Lett. **42**, 1698 (1979); Phys. Rev. B **22**, 2099 (1980).
5. P. F. Maldague, Phys. Rev. B **16**, 2437 (1977).
6. S. K. Lyo and J.-P. Gallinar, J. Phys. C **10**, 1693 (1977).
7. J.C.W. Chien, F.E. Karasz, and K. Shimamura, Makromol. Chem. Rapid Commun. **3**, 655 (1982).
8. E. Ehrenfreund, Z. Vardeny, O. Brafman, and B. Horovitz, Phys. Rev. B **36**, 1535 (1987).



## OPTICAL SPECTROSCOPY OF THE CHARGE ACCUMULATION LAYER IN MIS STRUCTURES WITH POLYMERIC INSULATOR AND SEMICONDUCTOR LAYERS

J. H. BURROUGHES and R. H. FRIEND,  
Cavendish Laboratory, Madingley Road, Cambridge CB3 0HE, UK.

### ABSTRACT

Metal-Insulator-Semiconductor (MIS) and MISFET structures constructed with polyacetylene prepared by the Durham precursor route provide convenient systems for the investigation of charge storage and transport in this polymer. The charge accumulation layer is particularly easy to form, and is of particular interest because charge is introduced into the polymer without compensation by chemical dopants. Charge is stored in soliton-like excitations of the chain, and we are able to characterise these from optical measurements of their electronic excitations. We find that the nature of the soliton-like states is very sensitive to the structure of the polyacetylene at the interface between the insulator and polyacetylene, and we report here the properties of devices formed with various organic polymers as the insulator layers which we contrast with those formed with silicon dioxide.

### INTRODUCTION

The use of conjugated polymers as the active semiconductors in device structures has been limited by the difficulties of processing the polymer to a suitable form. It is with the development of polymers which can be solution-processed, either in the form of a precursor polymer as is the case with Durham-route polyacetylene [1], or which are intrinsically soluble as is the case with poly(3-alkyl thienylenes), that fabrication of these devices has become feasible. We have used Durham route polyacetylene for this work [2,3]; others have used poly(3-alkyl thienylenes) and similar materials [4-9].

The device physics of conjugated polymers is intrinsically different to that of three-dimensionally bonded inorganic semiconductors because the fundamental electronic excitations of the chain are self-localised excitations which take the form of solitons in the *trans* isomer of polyacetylene, and more generally as polarons. Thus, charge injected onto the polymer chains causes local chain relaxation to form these excitations, and the description of all aspects of the operation of such devices is controlled by their excitations and motion. These self-localised excitations of the chain pull energy levels away from the band edges to create gap states, which for the limiting case of the soliton in polyacetylene are of the character of non-bonding  $p_z$  states and lie at mid-gap [10]. Two clear consequences of this behaviour are, firstly, that charge mobilities are often low for materials where charge transport across the device requires many inter-chain transfers, and secondly, that there are novel electro-optical properties associated with the electronic and vibrational excitation of the self-localised states. In our work with Durham polyacetylene we have been able to characterise the 'mid-gap' optical transition from the soliton level to the band edge, the 'translation' IR active modes, and the Raman-active amplitude mode of the soliton [2,3,11]. These electro-optic effects are large, and we consider that there are several potential areas for applications based on these phenomena.

The MIS structure allows the possibility of band bending at the insulator-semiconductor interface through the Fermi level to produce a surface charge layer which may be the same carrier sign as the majority carriers (accumulation layer) or as the minority carriers (inversion layer). Durham polyacetylene as prepared is an extrinsic semiconductor with a concentration of p-type carriers in the range  $10^{16}$  to  $10^{17}$   $\text{cm}^{-3}$ , as determined from C(V) measurements of Schottky barrier diodes in reverse bias [2] and from thermopower [12]. It is considered that the dopants responsible for these carriers are probably the catalyst residues at the chain ends of the precursor polymer [2]. MIS structures therefore form an accumulation layer of positive charge carriers at the semiconductor-insulator interface for negative gate voltages and move to a regime of depletion for small positive biases. Formation of an inversion layer at large negative biases is seen for three-terminal MISFET structures [2], where the negative charge can be directly injected from the source and drain contacts if these have a suitably low work function, but is not readily observed in two-terminal MIS structures for which negative charge can only be formed by thermal excitation of electron-hole pairs and removal of the positive charge through to the bulk semiconductor. This process is slow in most semiconductors, and we can expect that it is particularly so here since

geminate recombination of thermally-generated electron-hole pairs is very efficient for charge pairs diffusing in one dimension, and charge separation will require inter-chain charge motion [13]. We have, therefore, chosen to use the accumulation layer of positive charge carriers as the standard regime of operation for these devices. We emphasise that, in contrast to the depletion regime where the carriers that are depleted are present as a result of the extrinsic doping, the charges present in the accumulation layer are present without any associated dopants, and we thus have a system for study that is free of the effects of disorder and Coulomb potentials that are always present for doped polymers.

For reasons of convenience we have made extensive use of silicon dioxide as the insulator layer in the MIS device, and this is conveniently grown on a silicon substrate which can provide the gate contact, usually in the form of a heavily-doped thin (400 nm) layer just underneath the silicon dioxide layer [2,11,13]. We can carry out optical measurements on the accumulation layer; modulation of light transmitted through the structure by the gate voltage allows measurement of the soliton to band-edge transition, found to peak at around 0.8 eV, and of the IR-active translation modes of the soliton, but we are restricted by the transmission of the silicon substrate to a lower limit of around 1000  $\text{cm}^{-1}$  and an upper limit set by the silicon absorption edge at 1.1 eV.

In this paper we report measurements we have made on devices fabricated with polymeric insulators as the insulator layers; these include PMMA, poly(methylmethacrylate), and polyimide. These materials allow optical measurements over a wider spectral range, up to and above the absorption edge in polyacetylene. We have also found from the optical characteristics of the solitons formed in the accumulation layer for these devices that the polyacetylene at the insulator interface is significantly better ordered than for the structures which use silicon dioxide as the insulator layer.

#### DEVICE FABRICATION

The requirement for an insulator suitable for use in an MIS device is that it form films free of defects, especially pin-holes, and that the product of the relative dielectric constant,  $\epsilon_r$ , and the dielectric breakdown field,  $E_b$ , be high. Both polyimide and PMMA satisfy these requirements, though the maximum values of  $\epsilon_r E_b$  are considerably lower than obtained with silicon dioxide. Polyimide has the advantage that after spin-coating from solution, the film is then heat-treated to render it insoluble, so that it is not affected by further treatment with solvents such as those used for the Durham precursor. In contrast, PMMA remains soluble after deposition, and devices were fabricated with PPMA applied on top of the previously-converted polyacetylene film.

The polyimide precursor solution (PI<sup>TM</sup> supplied by Brewer Science Inc.) was spin-coated onto a thin (300 nm) aluminium film previously deposited onto a spectroil substrate. Imidisation was carried out using the prescribed heat treatment, to give a polyimide film of thickness 360 nm. Polyacetylene (440 nm) was then deposited on top in the usual way and capped with a semi-transparent film of gold.

For the PPMA devices, the polyacetylene was deposited onto a spectroil substrate previously coated with a semitransparent (20 nm) gold film. PMMA was then spin-coated at 2000 r.p.m. from solution in 2-butanone (1:100); two layers were applied, and each was heated at 60°C under vacuum to remove all traces of solvent. This procedure gave a total thickness of the PMMA layer of about 450 nm. Finally, the PPMA layer was capped with thin evaporated layers of 20 nm chromium and 10 nm gold.

#### ELECTRICAL CHARACTERISATION

The formation of accumulation, depletion and inversion layers may be demonstrated through the behaviour of the device capacitance with respect to the bias voltage. The measured capacitance,  $C$ , is that of the series combination of the insulator capacitance,  $C_i$ , and the capacitance of the active region of the semiconductor,  $C_d$ , and is given by  $C = C_i C_d / (C_i + C_d)$ . Since  $C_d$  is large for the accumulation and inversion layers,  $C$  is equal to the geometric capacitance of the insulating layer, but  $C$  falls to a lower value for movement of the depletion layer. The variation of  $C$  with bias voltage in the depletion regime has been modelled by Goetzberger and Nicollian [14] for the case of a p-type semiconductor as

$$\left(\frac{C_i}{C}\right)^2 - 1 = \left(\frac{C_i}{A}\right)^2 \frac{2(V-V_0)}{qN_A \epsilon_r \epsilon_0} \quad (1)$$

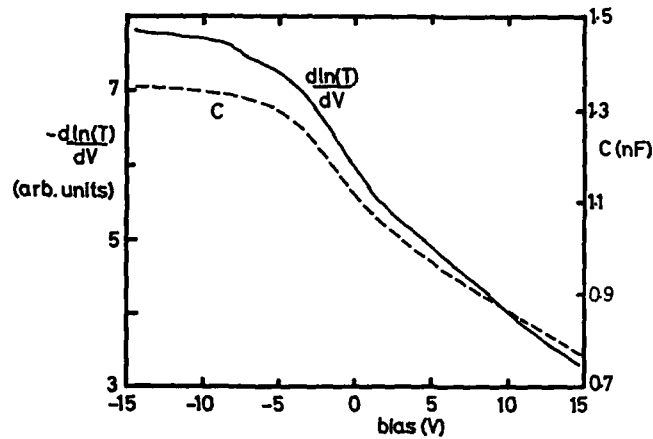


Figure 1 Differential capacitance,  $C$ , and differential of  $\log(\text{optical transmission})$  with gate voltage, as a function of bias voltage for an MIS structure with polyimide as insulator. Transmission was measured at 0.59 eV.

where  $A$  is the device area,  $\epsilon_r$  the relative dielectric constant of the semiconductor (taken here to be 6),  $N_A$  the acceptor concentration and  $V_f$  the flat-band voltage.

The experimental variation of  $C$  with bias voltage shows the formation of accumulation for negative gate voltages and of depletion for positive voltages. Figure 1 shows results for a polyimide device; for negative bias the capacitance approaches the geometric capacitance of the polyimide layer, and from analysis of the capacitance in the depletion regime using equation 1, we obtain values for  $N_A$  of  $3.3 \times 10^{16} \text{ cm}^{-3}$  and  $V_f$  of 0.7 V. Similar results are obtained with the PMMA devices; for those used for the optical measurements discussed below, a value of  $N_A$  of  $2.1 \times 10^{16} \text{ cm}^{-3}$  was found. These values of  $N_A$  are the same as those found with devices based on silicon dioxide.

#### ELECTRO-OPTICAL PROPERTIES

Both the MIS structures used here were designed to allow measurements of optical transmission through the device. We have used the same procedures to measure the modulation of the optical transmission due to the presence of charge in the accumulation layer as previously developed [2], by detecting the modulation of the optical transmission at the frequency of modulation of the gate voltage. The advantage of using these polymers in place of the silicon/silicon dioxide structures is that we can explore a wider range of the spectrum, and can probe not only the formation of the mid-gap absorption due to soliton to band edge transitions, but also the changes in the absorption at the band edge.

#### Soliton to Band-Edge Transitions

Figure 2 shows the response for the PMMA structure in the range 0.4 to 0.9 eV, and figure 3 shows the response of the polyimide device over the range 0.5 to 2.0 eV. With formation of the accumulation layer, achieved for negative gate voltages, both devices show the formation of an absorption band, peaked at 0.55 eV. Furthermore, as shown in figure 1 the strength of this band

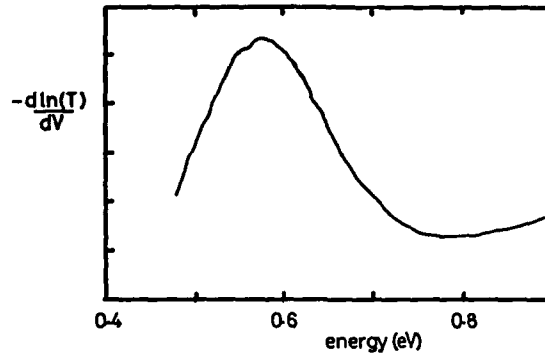


Figure 2 Differential of  $\log(\text{optical transmission})$  with gate voltage, as a function of photon energy for an MIS structure with PMMA as insulator. Measurements were made at 1 kHz.

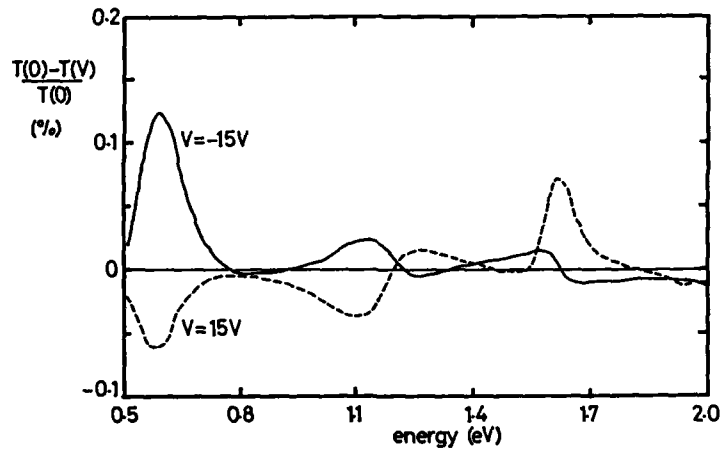


Figure 3 Difference in optical transmission at gate voltage 0 and at gate voltage  $V$  as a function of photon energy for an MIS structure with polyimide as insulator. Values of  $V$  are indicated.

scales with the differential capacitance of the device. We attribute this to optical transitions between the soliton states created to store the injected charge in the accumulation layer and the band edges. We note that this band is found at the same energy as for photoexcited solitons in unoriented Durham polyacetylene [12], but is considerably lower than the 0.8 eV found for MIS devices which use silicon dioxide as insulator [2,3]. We have also been able to measure the optical cross-section,  $\sigma$  per injected charge from the ratio of  $\partial \ln(T)/\partial V$  and  $\partial Q/\partial V$ , as shown for the polyimide device in figure 1. We find a value for  $\sigma$  of  $1.6 \times 10^{-15} \text{ cm}^2$  at the peak of the mid-gap absorption band; this is considerably higher than the value of  $1.2 \times 10^{-15} \text{ cm}^2$  found for the silicon/silicon dioxide devices.

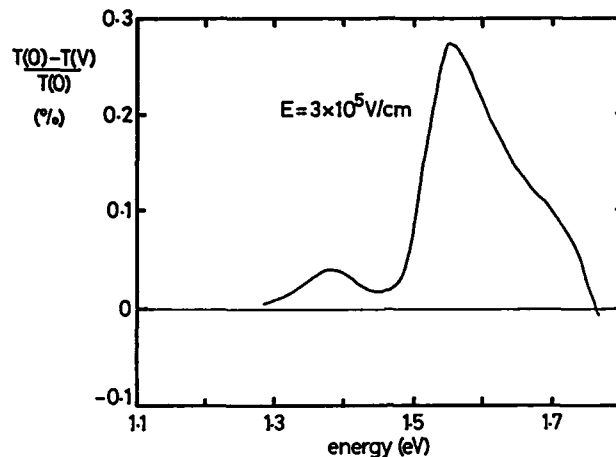


Figure 4 Electromodulation of optical transmission for a structure of 480 nm polyacetylene sandwiched between semitransparent gold electrodes.

We consider that the differences in the optical response between the devices built with silicon dioxide and with these polymeric insulators lies in the structure of the polyacetylene at the interface with the insulator. For the case of the silicon dioxide insulator, this surface layer to which the charge accumulation layer is confined is considerably more disordered than the bulk material, and this has the effect of modifying the electronic structure of the chains. We have shown previously that this disorder can be modelled through an increase in the value of the Peierls-like gap parameter,  $\Delta$  [3]. Within this model, the energy of the soliton to band-edge transition scales as  $\Delta$ , and the optical cross-section for this band is proportional to the width of the soliton which in turn scales inversely with  $\Delta$ . Further evidence for the variation in the soliton characteristics with differing levels of disorder is obtained from the IR-active translational modes of the soliton [2,3]. In contrast to the devices with silicon dioxide as insulator, those built with polymeric insulators show the same spectroscopic characteristics due to the injected carriers as are seen in photoexcited polyacetylene [12] and we conclude that the structure of the surface of the polymer is similar to the bulk. There is a distinction between the two types of structure: for the PPMA device, the active surface is the free surface of the polyacetylene film, which is subsequently coated with PMMA, whereas for the polyimide device the active polyacetylene surface is the bottom surface formed onto the polyimide layer.

For modulation of the gate voltage in the depletion regime, as seen for the modulation from 0 to +15 V in figure 3, the modulation of the optical transmission is of the opposite sign. This is as expected for the build up of space charge density in the device by depletion of the extrinsic carriers. The peak at 0.55 eV is as seen for movement of the depletion layer in Schottky diodes [2] and is again at the same energy as that due to photoexcited carriers [12].

#### Band Edge Modulation

The spectrum shown in figure 3 extends above the band edge of the polyacetylene and well into the region of the interband  $\pi$ - $\pi^*$  transitions. We expect to see a contribution to the electromodulation spectrum due to the bleaching of the interband  $\pi$ - $\pi^*$  transitions. Since the energy of the soliton to band edge transitions for the accumulation layer charge for this device is the same as that for photoexcited charges [12], we can expect to see bleaching of the  $\pi$ - $\pi^*$  absorption at the same energies. The bleaching due to the photoexcited charges shows an onset at about 1.8 eV and a peak at just over 2 eV. However, in the region of the band edge, the electromodulation experiment will also pick up a contribution due to electromodulation, EM, of the band edge absorption. We have measured this directly on a sandwich structure of gold/polyacetylene/gold, as shown in figure 4. We have checked that the electromodulation signal scales as  $E^2$  where  $E$  is the

applied electric field. This spectrum shows rather less structure than that seen for more ordered polyacetylene at high energies, but is similar at the band edge though the features are shifted to higher energies [15,16]. The spectrum is dominated by a broad positive absorption feature which peaks at 1.55 eV and which switches sign to give bleaching at 1.7 eV. In addition we see a weaker absorption feature which peaks at 1.35 eV, similar to the low energy feature seen at 1.28 eV in Shirakawa polyacetylene [16].

The spectrum for the polyimide device in figure 3 shows clear evidence for both  $\pi$ - $\pi^*$  bleaching (absorption) for accumulation (depletion) due to charge movement and also for EM, which in the energy range 1.2 to 1.7 eV is of opposite (same) sign for accumulation (depletion). Thus for depletion, the peak at 1.6 eV is due primarily to EM, whereas for accumulation in the same energy range the signal switches sign from absorption due to EM to bleaching due to  $\pi$ - $\pi^*$  bleaching at higher energies. The response at 1.15 eV is less easily assigned. Multiple interference effects might be responsible, with the structure behaving as a Fabry-Perot etalon, with modulation of the condition for constructive interference or the finesse by the applied field, and the 1.15 eV feature appearing as the tail of the 0.55 eV feature. However, the absorption coefficient at this energy is probably too large to allow strong interference effects. The variation of  $\partial \ln(T)/\partial V$  with bias voltage, V, at 1.15 eV is also different from that shown in figure 1 for the response at 0.59 eV. We find that it takes a low and constant value in accumulation, but rises to reach a peak at +5 V bias before falling away at higher positive biases. This behaviour confirms that the 0.55 and 1.15 eV features do not share a common origin.

#### REFERENCES

1. J. H. Edwards and W. J. Feast, *Polymer Commun.* **21**, 595 (1980).
2. J. H. Burroughes, C. A. Jones and R. H. Friend, *Nature* **335**, 136 (1988).
3. J. H. Burroughes, C. A. Jones, R. A. Lawrence and R. H. Friend, in Conjugated Polymeric Materials: Opportunities in Electronics, Optoelectronics and Molecular Electronics, edited by J-L Brédas and R. R. Chance, proceedings of NATO-ARW, Mons, Belgium, September 1989 (in press).
4. H. Tomozawa, D. Braun, S. Phillips, A. J. Heeger and H. Kroemer, *Synthetic Metals*, **22**, 63 (1987); **28**, 687 (1989).
5. F. Garnier and G. Horowitz, *Synthetic Metals* **18**, 693 (1987).
6. F. Garnier, G. Horowitz and D. Fichou, *Synthetic Metals* **28**, 705 (1989).
7. H. Koezuka and A. Tsumara, *Synthetic Metals* **28**, 753 (1989).
8. A. Assadi, C. Svensson, M. Willander and O. Inganäs, *Appl. Phys. Lett.* **53**, 195 (1988).
9. J. Paloheimo, E. Punkka, P. Kuivalainen, H. Stubb and P. Yli-Lahti, *Acta Scandinavica, Electrical Engineering Series*, No. E1 64, 178 (1989).
10. W. P. Su, J. R. Schrieffer and A. J. Heeger: *Phys. Rev. Lett.* **42**, 1698 (1979); *Phys. Rev. B* **22**, 2099 (1980); **B28**, 1138(E) (1983).
11. R. A. Lawrence, J. H. Burroughes and R. H. Friend, *Springer Series on Solid State Sciences*, **91**, 127 (1989).
12. P. D. Townsend and R. H. Friend, *Phys. Rev. B* **40**, 3112 (1989).
13. R. H. Friend, D. D. C. Bradley and P. D. Townsend, *J. Phys. D* **20**, 1367 (1987).
14. A. Goetzberger and E. H. Nicollian, *Appl. Phys. Lett.* **9**, 12 (1966).
15. R. Worland, S. D. Phillips, W. C. Walker and A. J. Heeger, *Synthetic Metals* **28**, D663 (1989).
16. S. D. Phillips, R. Worland, G. Yu, T. Hagler, R. Freedman, Y. Cao, V. Yoon, J. Chiang, W. C. Walker and A. J. Heeger (preprint 1989).

REVERSIBLE PHOTOPRODUCTION OF STABLE CHARGED DEFECTS IN  
TRANS-POLYACETYLENE

CAROLYN F. HOENER\*

Laboratory of Chemical Biodynamics, Lawrence Berkeley Laboratory, Berkeley, CA

ABSTRACT

Photoproduction and photodepletion of stable charged defects in *trans*-polyacetylene were observed, at low temperatures, by monitoring the IR signature of these defects: absorptions at 1368, 1289, 640  $\text{cm}^{-1}$  (1053, 600  $\text{cm}^{-1}$  for  $(\text{CD})_x$ ). These absorptions could be observed at long times (two to several hundred minutes) after photolysis, only when the sample was protected from photolysis by the probe beam, by blocking  $\nu > 2,300 \text{ cm}^{-1}$ .

The location of these absorptions and the temperature dependence of their intensities were similar to those of previously observed photoinduced defects reported to have much shorter lifetimes ( $\tau = \text{ms}$ ). The stable defects reported here can be produced at much lower photolysis energies ( $\nu > 5,000 \text{ cm}^{-1}$ ) than transient-photoinduced defects ( $\nu > 9,000 \text{ cm}^{-1}$ ). A mechanism for the photoproduction of stable defects, involving a two-photon process catalyzed by existing neutral defects, is proposed to explain this low onset.

The slow decay of these defects observed when the sample is kept in the dark is attributed to photoinduced depletion by blackbody irradiation. This process was slow enough to allow the wavelength dependence of photodepletion (observed at  $2,800 < \nu < 8,000 \text{ cm}^{-1}$ ) to be studied. The photodepletion was fastest near  $4,500 \text{ cm}^{-1}$ , suggesting that the defects possess an electronic absorption (with a peak near  $4,500 \text{ cm}^{-1}$ ) similar to that observed directly for the transient-photoinduced defects.

INTRODUCTION

Linear polyacetylene has two structural isomers; *cis*- and *trans*-; both exhibit bond-alternation. In the *trans*- isomer the bond-alternation arises from a mixing of molecular orbitals, in the  $\pi$  system, which lowers the energy of the filled orbitals while raising the energy of the unoccupied orbitals. In the *cis*- isomer this effect is fortified by the fact that adjacent bonds are inequivalent, this provides an additional reason for one bond to be double and the next single resulting in a larger band-gap.

The bond positions in the *trans*- isomer are equivalent. Thus, end-effects or other external forces can determine opposite directions of bond-alternation at either end of a length of chain, creating a "misfit region"[1] in the middle. These misfit regions, in which bond lengths do not alternate, extend over an odd number of carbons. Thus, neutral misfit regions contain unpaired electrons and can be detected with EPR.

The unpaired electron in this non-bond-alternating defect is in a non-bonding  $\pi$  orbital (of the defect moiety - divorced from the electronic structure of the surrounding polymer) located near the center of the *trans*-polyacetylene band-gap. This partially filled orbital provides the lowest energy position for both introduced electrons and holes. Thus, when polyacetylene is chemically doped, similar non-bond-alternating defects are formed to accommodate the introduced charges.

\*Present address: Department of Chemistry, University of Texas at Austin, Austin, TX

The molecular vibrations of charged defects are accompanied by the movement of the excess charge. This greatly magnifies the defects IR absorption coefficients, allowing for the detection of very low defect concentrations. Charged defects which extend over an even number of carbons contain one unpaired electron and (like uncharged defects which extend over an odd number of carbons) can be detected with EPR.

Charged defects extending over an odd number of carbons have an even number of electrons, and thus no unpaired spin. Odd-carbon defects have an unusual relationship between spin and charge, they poses either one or the other. In this respect these misfit regions can be viewed as solitary waves, excursions from the usual spin-charge relationship (in the bond-alternating polymer) to the unusual phase and back.

The size and energy of all non-bond-alternating defects is determined by a balance of forces: the energy gained from mixing (tendency to bond-alternation) counterbalanced by the need to accommodate excess charge or structural abnormalities. The unique definition of the defects' size and energy give them particle-like properties. Regions with both solitary wave and particle-like properties (odd-carbon defects) are known as solitons. Charged defects which extend over an even number of carbons are known as polarons.

Absorption spectroscopy is the main source of information about the electronic structure of polyacetylene and its defects. The band-gap absorption of the *trans*- isomer has an onset at  $11,000\text{ cm}^{-1}$  and a maximum at  $15,700\text{ cm}^{-1}$  [2]. There is a shoulder on this edge at  $12,000\text{ cm}^{-1}$  which is assigned to the promotion of a polymer valance-band electron into a neutral soliton [3]. Absorptions with peaks between  $4,000\text{ cm}^{-1}$  and  $7,300\text{ cm}^{-1}$  have been observed in doped polyacetylene [4]; the location of this peak varies with the extent of doping and different sample preparations.

Photophysics should be another important source of information about the electronic properties of polyacetylene and its structural defects. The formation of defects, to accommodate introduced charges, provides a stabilization energy of more than half the band-gap energy. Su and Schrieffer predicted [5] that photoinduced electron-hole pairs would be accommodated as two bond-alternation defects before they recombined. Electron-hole pairs on a single chain are expected to form charged solitons while electron-hole pairs on separate chains should form charged polarons.

The vibrational and electronic absorptions of photoinduced charged defects have been detected. However, these absorptions have been observed on two time-scales (ms [6] and ps [7]), and can be produced with sub-band-gap ( $\nu > 9,000\text{ cm}^{-1}$ ) photolysis. The interpretation of these results is further complicated by a second, unrelated, electronic absorption (near  $11,000\text{ cm}^{-1}$  [8]) and a lack of definitive (or consistent with expectation) EPR results [9]. Several alternative mechanisms have been proposed to explain these results [10]. Yet, the system remains a puzzle.

The detection of the vibrational absorptions of charged defects at long times after mid-band-gap photolysis, reported herein, introduces both a third time-scale and a new onset frequency. Rather than simply complicating matters, this result may provide the additional information needed to understand several of the previous results.

## EXPERIMENTAL

Relatively thick films of polyacetylene were prepared by the popular Shirakawa method [11], cut into one inch discs and sandwiched between two CsI windows. The windows, with sample, were mounted at the end of the cold tip in an Air Products closed-cycle Joule-Thomson helium refrigerator (Displex, model CS202). This cryostat could cool the sample to 10 K. Temperatures between 10 and 200 K could be maintained by the use of a 20 W resistance heater mounted on the cold tip. The



temperature was monitored at the cold tip with a iron-doped gold/chromel thermocouple.

The cryostat was mounted in the beam path of an IBM IR/44 IR spectrometer, such that the sample could be rotated 90° for photolysis. The IR probe beam was filtered with an Optical Coatings Laboratory cut-on filter which blocked all light above  $\nu = 2,400 \text{ cm}^{-1}$ . Spectra were taken from 400 to 2,300  $\text{cm}^{-1}$  at 2  $\text{cm}^{-1}$  resolution, averaging 200 scans. These spectra took less than 2 minutes to record.

A General Electric "Chill Chaser"™ heat lamp was used as a near-IR photolysis source. The light was collected with a reflective shade and an aluminum foil cone. It was directed through filters and onto the sample by 1" diameter glass tubes lined with reflectorized mylar. The various filters and filter combinations were used to select photolysis frequencies. The power passed by each filter was measured with a Scientech volume absorbing disc calorimeter (#38-0101).

A circular variable filter (Optics Coating Laboratory) was used to photolyze at frequencies between 2,800 and 5,200  $\text{cm}^{-1}$  with a 0.12  $\mu$  band-width and a typical power throughput of 4 mW. Narrow band-pass (typically 1,000  $\text{cm}^{-1}$ ) filters from Optics Coating Laboratory were used in the 5,800 to 10,700  $\text{cm}^{-1}$  range. A Corning Glass 2-60 filter and 1" water filter combination passed 200 mW between 7,500 and 16,500  $\text{cm}^{-1}$ ; a 5 mm thick germanium plate passed 300 mW below 5,500  $\text{cm}^{-1}$ . A camera shutter was used for short, timed photolyses.

## RESULTS AND DISCUSSION

The difference spectra in figure 1 was obtained by subtracting the absorbance spectrum taken of an undoped polyacetylene sample immediately after photolysis with  $\nu < 5,500 \text{ cm}^{-1}$  from the spectrum obtained after subsequent photolysis with 7,600  $< \nu < 16,500 \text{ cm}^{-1}$ . The observed increase in IR absorption at 1368, 1289, 640  $\text{cm}^{-1}$  (1053, 600  $\text{cm}^{-1}$  for  $(\text{CD})_x$ ) indicates the production of charged defects. The new IR absorptions (the charged defects) could be removed by photolysis with  $\nu < 5,500 \text{ cm}^{-1}$ . The changes were completely reversible; the IR absorptions could be cycled in and out for days without any change in the range of intensity.

Various photolysis frequency ranges were tried: the maximum depletion of these IR absorptions was obtained with  $\nu < 5,500 \text{ cm}^{-1}$  light, and the maximum increase was obtained with photolysis at 7,600 - 16,500  $\text{cm}^{-1}$ . IR absorptions could be produced, in a sample which had been photolyzed at  $\nu < 5,500 \text{ cm}^{-1}$ , with photolysis frequencies  $> 5,000 \text{ cm}^{-1}$ . The IR absorptions produced by photolysis at 7,600 - 16,500  $\text{cm}^{-1}$  decrease slowly when the sample is left in the dark. The rate of depletion can be enhanced by photolysis with  $\nu > 3,000 \text{ cm}^{-1}$ . The maximum initial rate of depletion was obtained with photolysis near 4,500  $\text{cm}^{-1}$ .

Both photo-production and depletion take place at photolysis frequencies between 5,000  $\text{cm}^{-1}$  and 9,000  $\text{cm}^{-1}$ . During long photolyses at these frequencies a steady-state is reached where the rates of photo-production and depletion are equal. Figure 2b shows the growth of photoinduced IR absorption at 1368  $\text{cm}^{-1}$  during photolysis near 5,800  $\text{cm}^{-1}$  in a sample which had been prepared by photolyzed at  $\nu < 5,500 \text{ cm}^{-1}$ . The depletion of the IR absorptions caused by photolysis at 7,600 - 16,500  $\text{cm}^{-1}$  during photolysis near 5,800  $\text{cm}^{-1}$  is shown in figure 2a. A steady-state value is approached in both curves at long photolysis times.

No change in IR absorbance was observed in spectra taken after photolysis at various frequencies when the 2,400  $\text{cm}^{-1}$  cut-on filter was removed from the probe beam. The establishment of a steady-state IR absorption intensity characteristic of photolysis by the probe beam, during the time it takes to turn the cryostat and record a spectrum, could account for this. If probe-beam photolysis was a factor in the experiments where photoinduced defects were found to have millisecond-lifetimes,

this may explain why no change was observed in the spin density during photomodulated EPR experiments, in the absence of an IR probe beam.

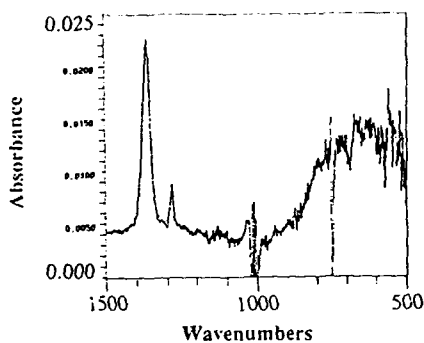


Figure 1

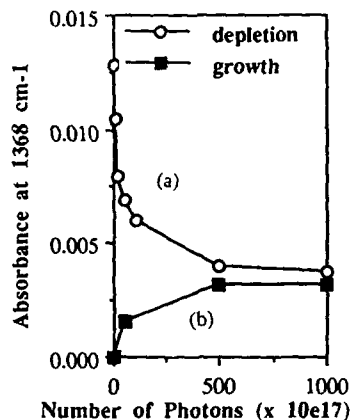


Figure 2

The photoinduced IR absorptions decays even when the sample is kept in the dark. The shape of this decay curve is similar to the curve for photodepletion. The number of black-body photons in the photodepletion frequency range (from the room temperature sample chamber) that reach the sample is sufficient to account for this decay.

Qualitative EPR experiments revealed a persistent increase in the number of unpaired spins under the photolysis conditions which produce the IR absorptions which indicate charged defects, and a decrease in unpaired spins under conditions which deplete the IR absorptions. The magnitude of this effect was  $\approx 2$  times greater at 4 K than at 77 K. This is consistent with the assertion that the same defect is responsible for both the unpaired spin and charge. A quantitative study of the number of defects, temperature and photolysis frequency dependence will be necessary to determine the one to one correspondence is needed to definitively link the spin and charge to the same defect.

In the absence of contradictory EPR data the stable photoinduced IR active defects are assumed to possess spin and are referred to as charged polarons. This proves convenient for distinguishing defects with different electronic structures. Neutral solitons have a half filled orbital  $12,000 \text{ cm}^{-1}$  above the polymer valence band. The lowest unoccupied orbitals of positively charged solitons and polarons are  $7,300$  and  $4,500 \text{ cm}^{-1}$  above the polymer valence band, respectively. The highest occupied orbitals in negatively charged solitons and polarons are at  $8,400$  and  $11,200 \text{ cm}^{-1}$  above the polymer valence band, giving rise to absorptions at  $7,300$  and  $4,500 \text{ cm}^{-1}$ , respectively.

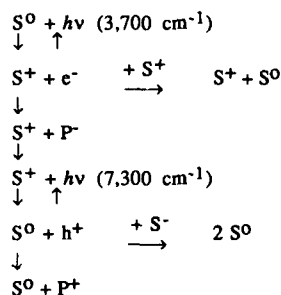
#### Photoproduction Mechanism

The transition involving the promotion of an electron from a neutral soliton to the polymer conduction band should occur near  $3,700 \text{ cm}^{-1}$ . (This transition has never been observed.) Upon the removal of an electron a neutral soliton is converted to a positive soliton. The electron, a single charge, will be accommodated by the formation of a negative polaron, if it does not combine with a positive or neutral soliton first. If photons of sufficient energy are available an electron can be promoted to the positive soliton, leaving a hole in the polymer valence band. This

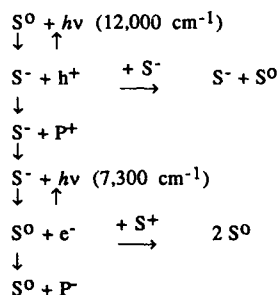
hole will be accommodated by the formation of a positive polaron, unless it encounters a negative or neutral soliton first.

The limiting step in this cycle is the low transition probability for the promotion of an electron from a neutral soliton to the polymer conduction band. A more efficient cycle (cycle B) involves the conversion of a neutral soliton to negative soliton and back. In this process a hole and an electron, which can relax to form two oppositely charged polarons, are produced. The minimum photolysis energy required for either cycle is minimum frequency absorbed for the higher energy transition. The absorption maxima for the higher energy transitions in cycles A and B are 7,300 and 12,000  $\text{cm}^{-1}$ , given the typical widths of these electronic states photoproduction onsets of 5,000 and 9,000  $\text{cm}^{-1}$  are reasonable. These onsets correspond to those observed for stable- and transient-photoinduced defects.

Cycle A

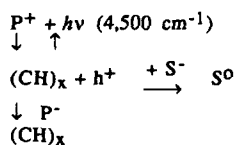
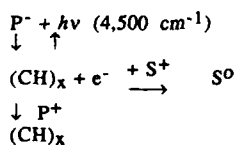


Cycle B



#### Photodepletion Mechanism

The electronic absorptions associated with the photoinduced polarons result in their neutralization and the production electrons or holes. Once the charge has been removed from an even carbon region it will revert back to a bond-alternating form. The photoinduced electrons and holes either reform charged polarons or are trapped by structural defects. Since not all charges revert to polarons, the defects are depleted by photoexcitation.



The quantum yield for the formation of charged polarons from electrons and holes depends on the likelihood of their encountering a suitable length of trans-polyacetylene relative to that of encountering structural defects. This is determined by the concentration of defects, their mobility, and the mobility of the electrons and holes. These factors lead to a very complicated kinetics model. Qualitatively, the rate of polaron production should decrease with increasing defect concentration, and the rate of polaron depletion should decrease with decreasing defect concentration. This is consistent with experiment.

## REFERENCES

1. L. Salem, The Molecular Orbital Theory of Conjugated Systems. (W. A. Benjamin Inc., Reading MA, 1974), p. 518
2. S. Etemad, A. J. Heeger, A. G. MacDiarmid, *Ann. Rev. Phys. Chem.* **33**, 443, (1982)
3. S. Etemad, G. L. Baker, C. B. Roxlo, B. R. Weinberg, J. Orenstein, *Mol. Cryst. Liq. Cryst.* **117**, 275, (1985)
4. H. Fujimoto, J. Tanaka, M. Tanaka, *Bull. Chem. Soc. Jpn* **56**, 671, (1983)
5. W. P. Su, J. R. Schrieffer, *Proc. Natl. Acad. Sci.* **77**, 5626, (1980)
6. G. B. Blanchet, C. R. Fincher, T. C. Chung, A. J. Heeger, *Phys. Rev. Letts.* **50**, 1938, (1983)
7. L. Rothberg, T. M. Jedju, S. Etemad, G. L. Baker, *Phys. Rev. Lett.* **57**, 3229, (1986)
8. J. Orenstein, G. L. Baker, *Phys. Rev.* **B49**, 1043, (1982)
9. J. D. Flood, A. J. Heeger, *Phys. Rev.* **B28**, 2356, (1983)
10. a) J. Orenstein, Ch. 36, The Handbook of Conducting Polymers, T. Skotheim Ed. (M. Dekker, New York, 1986) b) N. F. Colaneri, R. H. Friend, H. E. Schaffer A. J. Heeger, *Phys. Rev.* **B38**, 3960, (1988)
11. T. Ito, H. Shirakawa, S. Ikeda, *J. Polym. Sci., Poly. Chem. Ed.* **12**, 11, (1974)

TEMPERATURE DEPENDENCE OF THE PICOSECOND PHOTOCURRENT IN  
STRETCHED TRANS-POLYACETYLENE FILMS WITH BELOW GAP EXCITATION

A. D. WALSER\*, R. DORSINVILLE\*, R. TUBINO\*\* and R. R. ALFANO\*

\*Institute for Ultrafast Spectroscopy and Lasers

Electrical Engineering Department

The City College of New York, 138th St. and Convent Ave. N.Y., N.Y. 10031

\*\*Istituto di Fisica dell'Universita', Via Vienna 2, Sassari and Istituto di Chimica delle  
Macromolecole, CNR, Italy

ABSTRACT

The temperature dependence of the picosecond photocurrent with below gap excitation (1.06  $\mu\text{m}$ ) has been measured for a highly oriented form of trans-polyacetylene. The 1-d picosecond photocurrent is independent of temperature. The 3-d picosecond photocurrent is temperature dependent with an activation energy of 63 meV. These results demonstrate the photoproduction of nonlinear charged carriers (solitons and polarons) at energies that are below the principal interband absorption edge.

INTRODUCTION

Trans-polyacetylene (trans-(PA)) is a linear polymer consisting of weakly coupled chains of CH units. Trans-(PA) has a twofold degenerate ground state which is believed to lead to mobile topological chain distortions or kinks called solitons which are responsible for many of the interesting properties of the polymer<sup>1-4</sup>. According to the Su, Schrieffer and Heeger (SSH) model, solitons can be photogenerated in transpolyacetylene when an incident photon excites an e-h pair, and the lattice then distorts around the photogenerated charged carriers leading to a soliton-antisoliton ( $S^+S^-$ ) pair. This model stimulated a host of experiments to challenge or prove the existence of solitons<sup>5-16</sup>. The results of photoinduced experiments and simultaneous electrical conductivity and ESR measurements confirmed the predictions of Su and Schrieffer and also established the reversed spin-charge relation of the soliton model<sup>5,6</sup>. Theoretical calculations using the SSH or Takayama et al. (TLM) models have shown that the energy to create a soliton at rest ( $E_s$ ) was less than one-half the single particle gap ( $\Delta$ ). Therefore, direct photoproduction of soliton pairs at energies well below the principle interband absorption edge is possible as shown experimentally by Blanchet et al.<sup>8</sup>.

The role played by nonlinear charge carriers such as solitons and polarons in the photoconductive response of trans-(PA) has been studied by several groups by comparing the excitation profile of the photoinduced absorption to that of the photoconductive response of the polymer<sup>9-14</sup>. The similarity between the two profile is generally considered as evidence that charged solitons play a crucial role in the photocurrent of trans-(PA). However, most of the past photoconductive experiments were performed with above gap ( $\hbar\omega > 2\Delta$ ) excitation where the charged soliton pairs are generated indirectly via electron-hole pairs. The photoconductive response of trans-(PA) with below gap excitation has received relatively little attention. In addition, there is strong evidence both from photoinduced absorption measurements and recent picosecond photoconductive measurements in trans-(PA) that the nature and characteristics of the charged carriers in trans-polyacetylene change rapidly with time. We have recently suggested, based on our temperature dependent picosecond photoconductive measurements in stretched samples, that the soliton like properties of photogenerated carriers in trans-(PA) are maintained only when they travel along the chains and for a duration of time shorter than the time required for the carriers to hit the end of the segment of the chain on which they have been created (for few picoseconds). For carriers drifting across the chains, even the first step of their random walk motion will take place by phonon assisted hopping between neighboring chains. In this paper we have extended our recent picosecond temperature dependent photoconductive measurements in trans-(PA) with above gap excitation to include below gap excitation. Below gap ( $\hbar\omega < 2\Delta$ ) excitation has allowed us to reduce the generation of pairs and isolate the possible contribution of charged solitons /polarons to the photo-

current. A study of the photoconductive response as a function of temperature was carried out to help determine the nature of the charged carriers.

## RESULTS

The highly oriented trans-polyacetylene films were obtained from Enichem Res. Lab. (Italy). The films (20  $\mu\text{m}$  thick) were attached by pressure to copper electrodes of a microstrip line. The details of the microstrip switch are given elsewhere<sup>9</sup>. For temperature measurements the sample was mounted on a cold finger of a nitrogen Dewar. The samples were excited by 1.06  $\mu\text{m}$  (1.17 eV), 25-30 ps pulses from a YAG laser. A half wave plate suited for the 1.06  $\mu\text{m}$  optical pulse was used to change its polarization with respect to the chain direction of the polymer. The excitation energy was approximately 36  $\mu\text{J}$  (10 Hz repetition rate) and the applied bias was approximately 400 V.

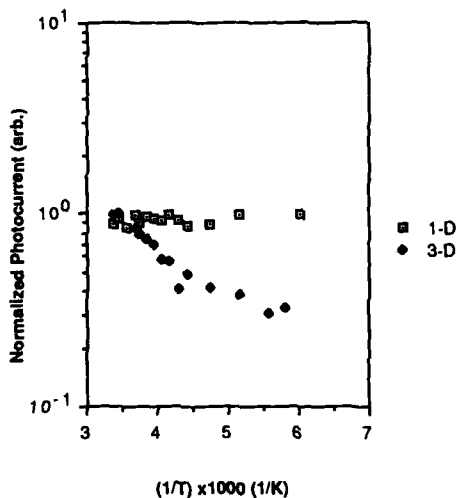


Figure 1. Semilogarithmic plot of the temperature dependence of the picosecond photoconductive response of trans-(PA) with below gap excitation.

Figure 1 shows a semi-logarithmic plot of the fast photoconductive response as a function of temperature for the 1-d and 3-d case. The polarization of the excitation pulse was kept perpendicular to the stretching direction for both cases to keep the penetration

depths identical and to obtain the strongest signal. In the 1-d configuration (electric field parallel to the chain) the fast photocurrent is practically independent of the temperature between 300 and 160 K. In the 3-d configuration (electric field perpendicular to the chain) the photocurrent decays with temperature between 300 and 200 K. The activation energy ( $E_a$ ) in this region is approximately 0.063 eV. This response is very similar to that obtained for above gap excitation<sup>9</sup>. Below 200 K there is a change of slope. This may be explained by assuming that the phonon activated hopping becomes relatively inefficient at low temperature and that tunneling through the barrier becomes the main mechanism for charge transfer between neighboring chains. Another possible explanation is that the change in slope is due to the contribution from misaligned chains.

## DISCUSSION

With oriented samples we are able to separate the contribution of charged carriers moving along from those moving across the polymer chains. The temperature dependence of the transient picosecond photoconductive response of stretched trans-(PA) in the 1-d and 3-d configurations for below gap excitation is very similar to our previous measurements with above gap excitation<sup>9</sup>. The similarity of these two measurements imply that they arise from the same mechanism (solitons and polarons). For above gap excitation, the photogeneration of charged soliton pairs occur indirectly via an electron-hole pair. In the case of below-gap excitation the photogeneration of the nonlinear charged carriers is direct. The energy gap ( $E_g$ ) for trans-(PA) is approximately 1.8 eV. With an excitation energy of 1.17 eV (1.06  $\mu\text{m}$ ) one would expect that the photoconductive response would not occur except as a result of two photon absorption or through band-tailing. However, measurements of the photoconductivity under pressure have shown<sup>16</sup> that the absorption edge for trans-(PA) does not arise from static disorder or the associated band-tailing effect known in amorphous semiconductors. Two photon absorption cannot be totally ruled out, but earlier experimental results such as the observation of a threshold near the soliton pair creation energy strongly suggest that the photocurrent at 1.17 eV is due to direct excitation of the charged carriers<sup>17</sup>.

We previously reported<sup>9</sup> that with above gap ( $h\nu > 2\Delta$ ) excitation the picosecond photocurrent of stretched trans-(PA) was temperature independent in the 1-d configuration (electric field parallel to stretching direction) and temperature dependent in the 3-d configuration (electric field perpendicular to the stretching direction). The temperature independence of the transient photocurrent in the 1-d configuration, violates both band conduction and hopping conduction since both are strongly dependent on temperature. It therefore seems reasonable to assume that the photogenerated carriers have unusual properties which are maintained only when traveling along the chain. It has been shown through theoretical analysis that the mobility of solitons do not depend much on temperature between 70 and 300 K. The explanation for the temperature dependence of the picosecond photocurrent in the 3-d configuration is as follows. For carriers produced on the chain, the first step of their random walk motion would take place by phonon assisted hopping, giving rise to perpendicular hopping conductivity. In this case only polarons will be available to carry current because a single soliton can not jump from one chain to another and a simultaneous jump of a soliton/antisoliton pair is very unlikely. Thus one is led to conclude that the 63 meV activation energy ( $E_a$ ) observed for the perpendicular picosecond photocurrent, represents the activation energy for a polaron to hop between neighboring chains.

The activation energy ( $E_a$ ) in the 3-d configuration for below gap ( $E_a=63$  meV) and above gap ( $E_a=43$  meV) excitations are of the same order of magnitude. The roughly equal value of the activation energy for both above and below gap excitation coupled with previous and present data strongly suggest that the charged carriers for both cases are the same. Also with below-gap excitation we have minimized the contribution of free electrons and holes to the transient photocurrent.

## CONCLUSION

We have presented the first experimental study of the picosecond photoconductive response with below gap excitation of the highly oriented stretched trans-polyacetylene polymer. We have found that the transient 1-d PC with below gap excitation is temperature independent as in our previous study with above gap excitation. And the transient 3-d PC with below gap excitation is temperature dependent as in the case with above gap excitation. The activation energy of the 3-d PC with below gap excitation is 63 meV. We have shown that the charged carriers that participate in the picosecond PC with above gap excitation are the very same carriers that are generated with below gap excitation. These results are further evidence that charged solitons and polarons probably play an important role in the transient photoconductive response of trans-(PA); and that these nonlinear carriers can be photogenerated by below gap excitation.

This work is supported in part by NASA grant 449521 and NSF grant RII-88-02964.

## REFERENCES

1. S. Etemad, A. J. Heeger, and A. G. MacDiarmid, *Annu. Rev. Phys. Chem.* **33**, 443-469 (1982).
2. W. P. Su, J. R. Schrieffer, and A. J. Heeger, *Phys. Rev. Lett.* **42**, 1698 (1979), and *Phys. Rev. B* **22**, 2099 (1980).
3. M. J. Rice, *Phys. Lett.* **71A**, 152 (1979).
4. H. Takayama, Y. R. Lin-Lin, and K. Maki, *Phys. Rev. B*, **21**, 2388 (1980).
5. J. Orenstein and G. Baker, *Phys. Rev. Lett.* **49**, 1043 (1982).
6. Z. Vardeny, J. Strait, D. Moses, T. T. Chung and A. J. Heeger, *Phys. Rev. Lett.* **49**, 1657 (1982).
7. C. V. Shank, R.L. Fork, J. Orenstein, and G. L. Baker, *Phys. Rev. Lett.* **49**, 1660 (1982).
8. Graciela B. Blanchet, C. R. Fincher, T. C. Chung, and A. J. Heeger, *Phys. Rev. Lett.* **50**, 1938 (1983).
9. A. Walser, A. Seas, R. Dorsinville, R. R. Alfano, and R. Tubino, *Solid State Communications*, **67**, 333 (1988).
10. R. Dorsinville, S. Krimchansky, R. R. Alfano, J. L. Birman R. Tubino and G. Dellepiane, *Solid State Communications*, **56**, 857 (1985).
11. R. Dorsinville, M. Szalkiewicz, R. Tubino, J. L. Birman, and R. R. Alfano, *Synthetic Metals*, **17**, 509 (1987).



12. R. Tubino, R. Dorsinville, A. Seas, J. Birman and R. R. Alfano, *Phys. Rev. B*, **38**, 8318, (1988).
13. M. Sinclair, D. Moses, R. H. Friend, and A. J. Heeger, *Phys. Rev. B*, **36**, 4296 (1987).
14. Gracia B. Blanchet, C. R. Fincher, and A. J. Heeger, *Phys. Rev.*, **51**, 2132 (1983).
15. L. Rothberg, T. M. Jedju, and G. L. Baker, *IEEE J. of Quant. Electron.*, **24**, 311 (1988).
16. D. Moses, A. Feldblum, E. Ehrenfreund, and Heeger, *Phys. Rev.*, **26**, 3361 (1982)
17. L. Lauchlan, S. Etemad, T. C. Chung, A. J. Heeger, and A. G. MacDiarmid, *Phys. Rev. B*, **24**, 3701 (1981).

THE EFFECTS OF CONJUGATION LENGTH AND SUBSTITUENTS ON THE  
CONDUCTIVITY OF OXIDATIVELY DOPED *p,p'*-DISUBSTITUTED  
DIPHENYLPOLYENES

Linda S. Sapochak, David W. Polis, Art N. Bain, Paul Bryson, Larry R. Dalton,\* and C.W. Spangler\*\*

\*Department of Chemistry, University of Southern California, Los Angeles, California 90089-0482.

\*\*Department of Chemistry, Northern Illinois University, DeKalb, Illinois, 60115.

Abstract

It has been demonstrated that the oxidative doping of  $\alpha,\omega$ -diphenylpolyenes generates polaronic and/or bipolaronic intermediates which can be directly observed by optical spectroscopy. Furthermore, the absorption frequencies have been shown to correlate with conjugation length and the nature of the substituents. Species are stabilized by donor substituents and destabilized by acceptor substituents. We now report conductivity and ESR studies on iodine doped  $\alpha,\omega$ -diphenylpolyenes, containing donor *p,p'*-disubstituents. The implications of these studies can provide insight into electrical conductivity and optical nonlinearity of doped organic materials.

Introduction

Polymeric systems with delocalized  $\pi$ -electrons as potential electroactive materials with conductive or optical nonlinearity properties have been extensively studied in the past decade [1]. Reports that polyacetylene could attain high conductivities upon doping created an overwhelming interest in the field [2]. More recent concern involves elucidation of the roles of inter- versus intrachain charge transport, as well as the influence and nature of the midgap species (polarons, bipolarons, solitons) on conductivity and non-linear optical enhancement.

In the past few years, Spangler and coworkers have demonstrated that a series of phenyl-capped polyenes could be oxidatively doped in solution to form midgap species, observed by optical spectroscopy [3]. Doping studies with excess  $\text{SbCl}_5$  showed that as  $n$  increases from 3 to 6, and as the electron donating ability of the para-substituent is increased ( $\text{H} < \text{Me} < \text{MeO} < \text{Me}_2\text{N}$ ), the transition energies of the midgap species in the absorption spectra are decreased (see Table I) [4]. It was established that upon doping, bipolarons were more stable in solution than polarons by noting the decay of electron spin resonance signals [5]. More recently, they have shown that polaronic and bipolaronic formation can be controlled selectively with varying concentrations of dopant [6].

In this paper, we will report conductivity measurements and electron spin resonance data for iodine doped *N,N*-dimethylamino and methoxy-*p,p'*-

disubstituted diphenylpolyenes with varying conjugation lengths. From the data we can infer that intermolecular interactions and packing dominate the measured conductivities.

### Experimental

The synthesis of the p,p'-disubstituted diphenylpolyenes is given elsewhere [7]. Two series of compounds were investigated, the dimethylamino (Me<sub>2</sub>N) and methoxy (MeO) disubstituted compounds with varying conjugation lengths of n=3, 4, 5, and 6, where n is the number of -CH=CH- repeat units. All samples were doped in an I<sub>2</sub> chamber which was swept with nitrogen and sealed for 24 hours, after which the samples were placed in a 50 °C oil bath under full vacuum for 5 hours. Solid state doping experiments with other oxidizing agents, such as SbCl<sub>5</sub> and nitrosyl salts are currently in progress. Materials were doped as powders and then pressed into pellets (pressure of 20,000 psi for 3 minutes) and all samples were transferred into an inert atmosphere glove box for conductivity measurements. The measurements were obtained with an Alessi collinear 4-point probe (1.0 mm probe tip spacing), a Keithley model 220 programmable current source, and a Keithley model 617 electrometer. The bulk conductivity was calculated and correction factors were included to take into account the geometry of the samples [8,9]. Electron spin resonance data were obtained at room temperature in the presence of air using an IBM-Bruker ER200D for both doped and undoped samples.

### Results and Discussion

From the previous doping studies, it might be expected that high conductivities would be attained for the material with the best delocalization stabilization (e.g. EDG=Me<sub>2</sub>N, n=6). However, this may not be a practical prediction due to the fact that conductivity is a macroscopic measurement, and the effects of conjugation length and substituents on the delocalization stabilization were established on a microscopic level.

All samples exhibited color change from yellow, orange, or brown to purple, green, or blue upon oxidation with iodine. This corresponds to a bathochromic shift to lower energy, in agreement with the solution doping studies. The conductivities of the iodine doped diphenylpolyenes in this study are shown in Table II. The highest value observed was  $5 \times 10^{-2} \Omega^{-1} \text{cm}^{-1}$  for the EDG=Me<sub>2</sub>N, n=3 polyene. Neither series show significant correlation between conductivity and conjugation length. The effect of the EDG on the conductivity indicates that in general, polyenes with EDG=Me<sub>2</sub>N show slightly higher conductivities than polyenes with EDG=MeO. The conductivities of all samples were stable in air with no significant decrease in the measured values over time.

The electron spin resonance data suggests that differences do exist between the conducting states of the EDG=Me<sub>2</sub>N series versus the EDG=MeO series. Compounds with Me<sub>2</sub>N substituents display an ESR signal in the undoped state, which is probably due to trace impurities formed from amine oxidation in air, a routine problem with aromatic amines [10]. This signal

exhibits the effects of  $g$ -anisotropy which is clearly seen in the ability to distinguish between the  $g_{\perp}$  and  $g_{\parallel}$  contributions (Figure 1). It is expected that upon the formation of polarons via doping that the  $g$ -anisotropy would become averaged. Indeed this is what is observed for the doped sample; the signal is an order of magnitude larger in intensity than that of the undoped material, which indicates significant amounts of polaron formation upon doping. The signal is also narrower as a result of the averaging of the  $g$ -anisotropy which corresponds to the movement of the electrons (Figure 2). The  $g$ -factors for the EDG= $\text{Me}_2\text{N}$  series are all very close to the free electron value of 2.0023.

The EDG= $\text{MeO}$  series do not give rise to an ESR signal in the undoped state. Upon doping an almost perfectly symmetrical ESR signal is displayed which is slightly broader and an order of magnitude smaller in intensity than seen in the  $\text{Me}_2\text{N}$  series (Figure 3). The  $g$ -factors are farther away from the free electron value (e.g. 2.0035), indicating more localized electronic character.

Table I

EDG-C <sub>6</sub> H <sub>4</sub> -(CH=CH) <sub>n</sub> -C <sub>6</sub> H <sub>4</sub> -EDG		
EDG	n	Absorption Spectra (nm)
H	5	564, 612
Me	5	590, 650
MeO	5	640, 692, 760
Me <sub>2</sub> N	5	658, 714, 776
H	6	615, 685
Me	6	640, 700
MeO	6	676, 728, 816
Me <sub>2</sub> N	6	700, 752, 832

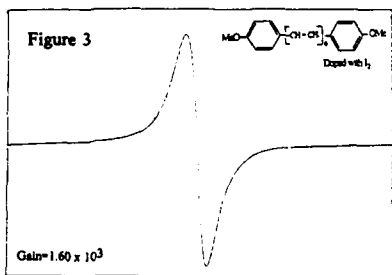
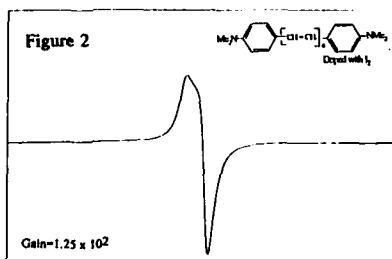
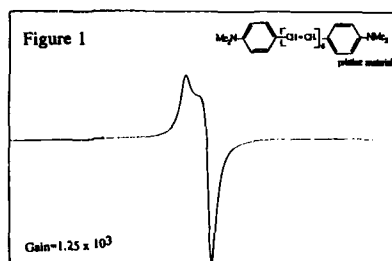
EDG = electron donating group

Table II MEASURED CONDUCTIVITY

Substituent	n	$\sigma$ ( $\Omega^{-1} \text{cm}^{-1}$ )
Me <sub>2</sub> N	6	$1 \times 10^{-3}$
	5	$2 \times 10^{-3}$
	4	$1 \times 10^{-4}$
	3	$5 \times 10^{-2}$
MeO	6	$1 \times 10^{-4}$
	5	$6 \times 10^{-4}$
	4	$9 \times 10^{-3}$
	3	$2 \times 10^{-6}$

### Conclusions

These studies indicate that there is no significant effect on measured conductivities for the  $N,N$ -dimethylamino and methoxy- $p,p'$ -disubstituted diphenylpolyenes with varying substituents and/or conjugation length. It



appears that the major factor contributing to conductivity is the packing and the intermolecular interactions between the molecules in the solid state. Although preliminary investigation into the packing and solid state nature of selected polyenes has been accomplished by Spangler and coworkers, a complete picture into the nature of the solid state of the compounds included in this report has not been achieved at this time [11].

Electron spin resonance allows a microscopic view of the electronic states formed by doping. Polaron formation is confirmed by ESR for both the Me<sub>2</sub>N compounds and the MeO compounds, and it is apparent that polaronic species play a major role in the conductivity of these doped materials. The relative number of spin species formed upon doping is obviously lower in the MeO series than in the Me<sub>2</sub>N series, and this may contribute to the lower conductivities in the MeO series.

It is interesting to note that even on the timescale of the ESR experiment (nanoseconds), that the electrons do not move fast enough in the doped materials to average out all g-anisotropy. Hence, it can be predicted that the formation of midgap species will not contribute to the non-linearity of these materials, because the timescale of an NLO experiment is even shorter (femto-picoseconds), and the movement of the electrons would be too slow to make any contribution to the delocalization. Measurements of the third order susceptibilities of the pristine and doped materials is in progress.

#### Acknowledgements

This work was funded by the Air Force Office of Scientific Research under contracts F49620-87-C-0100 and F49620-88-C-0071 and the National Science Foundation under grant DMR-88-15508.

#### References

1. A.J. Heeger, A.J. Orenstein, and D.R. Ulrich, *Nonlinear Optical Properties of Polymers, Part II* (Materials Research Society, Pittsburgh, PA, 1988).
2. H. Shirakawa, E.F. Louis, A.G. MacDiarmid, C.K. Chiang, and A.J. Heeger, *J. Chem. Soc. Chem. Commun.* **578** (1977).
3. C.W. Spangler, E. Nickel, and T.J. Hall, *Polymer Preprints*, **28**, 543 (1987).
4. C.W. Spangler, L. Sapochak, and B. Gates, in *Organic Materials for Nonlinear Optics*, edited by R. Hann and D. Bloor (Royal Society of Chemistry, Oxford, 1989), p. 57.
5. C.W. Spangler, P. Bryson, and L.R. Dalton, to be published.
6. C.W. Spangler and K. Havelka, to be presented at the 1990 ACS Spring Meeting, Boston, MA.
7. C.W. Spangler, R. McCoy, A. Dembek, L. Sapochak, and B. Gates, *J. Chem. Soc. Perkin Trans.* **1**, 151 (1989).
8. A. Uhler Jr., *The Bell System Technical Journal*, **105** (1955).
9. F.M. Smits, *The Bell System Technical Journal*, **711** (1958).
10. Morrison and Boyd, *Organic Chemistry*, 3rd ed., (Allyn and Bacon, Inc., Boston, 1977), p. 730.
11. T.J. Hall, S.M. Bachrach, C.W. Spangler, L.S. Sapochak, C.T. Lin, H. W. Guan, and R.D. Rogers, *Acta Cryst.* **C45**, 1541 (1989).

## THERMALLY ACTIVATED CHARGE HOPPING TRANSPORT STUDIES IN A $\Sigma$ -CONJUGATED POLYMER

L. Samuel and P.N. Sanda

T.J. Watson Research Center, IBM Corporation, P.O. Box 218, Yorktown Heights,  
NY 10598

R.D. Miller and D. Thompson

Almaden Research Center, IBM Corporation, San Jose, CA 95120

### ABSTRACT

Time of flight (TOF) and thermally stimulated current (TSC) measurements were performed on poly(methylphenylsilane) (PMPS), poly(ethyl-p-methoxyphenylsilane) (PMeOPhEtS) and poly(ethylphenylsilane) (PEtPhS), to study the mechanism of inter-chain charge hopping transport. The value of the hole mobility at a given electric field and temperature varied with the substituent side groups. The activation energies, which were assigned to the hopping transport, ranged between 0.1-0.3eV and were dependent on the applied electric field. The nature of this dependence also varied with the substituent side groups. In the TSC spectra, a well defined current peak was observed in the temperature range between 100K-160K. The peak temperature was dependent both on the electric field and the heating rate. For a constant electric field and heating rate it was also dependent on the side groups, in a manner which was consistent with the results obtained by TOF. When the samples were exposed to high doses of UV radiation, a secondary peak at  $\sim$ 180K was observed, which was attributed to surface defect sites produced by the UV exposure.

### INTRODUCTION

Polysilanes are photoconducting polymers [1,2], consisting of a  $\sigma$ -conjugated Si backbone, and two organic substituents attached to each Si atom. These substituent side groups have a major influence on the spectral properties of the polymer [3-7] and its electronic structure [8-10]. Charge transport in polysilanes is believed to involve fast transport along the polymer chain and thermally activated hopping transport between the chains. Although it is suggested [11,12] that the energy states correlated with the hopping transport are associated with segments in the polymer backbone, the substituent side groups of the polymer also play a role in determining the transport properties of these polymers.

Thermally stimulated current (TSC) measurements and time of flight (TOF) spectroscopy were performed on polymethylphenylsilane (PMPS), poly(ethyl-p-methoxyphenylsilane) (PMeOPhEtS) and polyethylphenylsilane (PEtPhS) to study the mechanism of charge hopping transport in these materials and learn about the influence of the substituent side groups on that process.

## EXPERIMENTAL

The polymers were prepared from purified dichloro-organosilane monomers with different substituents according to the desired polysilane. The monomers were polymerized using sodium dispersion. Chlorodimethylphenylsilane was used for end capping. The details of the syntheses are discussed in Ref.13. The polymer samples, 4-7 $\mu\text{m}$  thick, were cast from the polymer solution in toluene (6-10% weight ratio), using a doctor blade. The coating was applied to an aluminized Mylar substrate, which served as the bottom electrode. The top Al electrode, which was vapor deposited, was semitransparent in the UV (60% transmission at 337nm) and blocking for hole injection. The electric field, which was applied across the sample by positively biasing the top electrode, ranged from 5V/ $\mu\text{m}$  to 80V/ $\mu\text{m}$ .

For the TSC measurements, the sample was illuminated at 80K by a UV pulsed laser under an applied electric field. The illumination energy was controlled by neutral density filters and by the number of the laser pulses. After illumination, the sample's temperature was ramped linearly in time, while the sample was held in the dark. The current induced by the transport of the holes through the sample towards the bottom electrode was monitored by an electrometer connected in series.

TOF measurements were performed on the same samples, using the conventional procedures.

## RESULTS AND DISCUSSION

In the TSC measurements, charge carriers are photogenerated in the top  $\sim 500\text{\AA}$  of the sample [2] by the field assisted dissociation of the photexcited electron-hole pairs. Upon illumination at 80K, these charge carriers, which are known to be holes [2], are pinned at the hopping states near the surface. When the temperature is ramped, an increase in the current is observed, due to the increasing mobility of the holes. Depletion of the charge carriers leads to the observed decrease in the current at higher temperatures. The overall spectrum consists of a current peak at temperature  $T_m$ , which depends both on the applied electric field and heating rate.

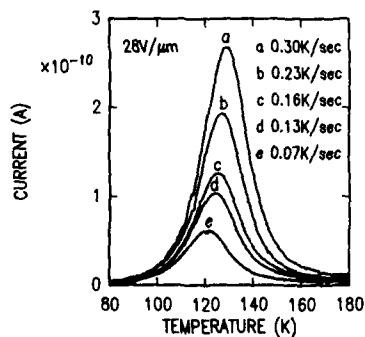


Figure 1. TSC spectra of PEtPhS measured at 28V/ $\mu\text{m}$

Figure 1 shows some TSC spectra for PEtPhS at a constant electric field of  $28\text{V}/\mu\text{m}$  and heating rates ranging between  $0.07\text{K}/\text{sec}$  to  $0.30\text{V}/\text{sec}$ . Similar spectra, with  $T_m$  ranging between  $100\text{-}160\text{K}$  were also observed for PMPS [14] and PMeOPhEtS. The activation energies assigned to the thermally activated hopping transport are derived from the slope of the line fitted to the curve of  $\ln(R/T_m^2)$  vs.  $1/kT_m$ , where  $R$  is the heating rate,  $T_m$  is the current peak temperature, and  $k$  is Boltzmann constant [15].

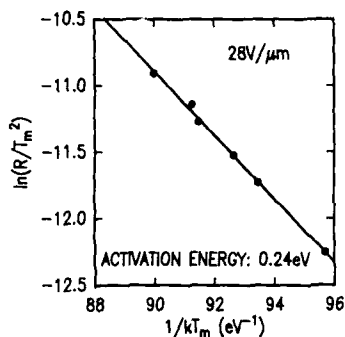


Figure 2.  $\ln(R/T_m^2)$  vs.  $1/kT_m$  for PEtPhS at  $28\text{V}/\mu\text{m}$ .

Figure 2 shows the plot of  $\ln(R/T_m^2)$  vs.  $1/kT_m$  for measurements performed on PEtPhS at  $28\text{V}/\mu\text{m}$ . The values of the field dependent activation energies obtained from TSC measurements were similar to those measured by the TOF technique.

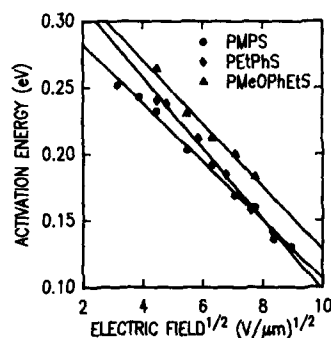


Figure 3. Activation energy vs. electric field for various polysilanes.

Figure 3 shows the field dependence of the activation energies for the various polysilanes studied. The activation energies ranged between  $0.1\text{-}0.3\text{eV}$  for electric fields of  $5\text{V}/\mu\text{m}\text{-}80\text{V}/\mu\text{m}$ . In each case the curve seems to fit a square root dependence of the activation energy on the electric field. However, both the slope of the line fitted to the curve, as well as the extrapolated value of the activation energy at zero electric field, vary with the substituent side groups. Figure 4 shows the Arrhenius plots of the mobility for the various polysilanes, measured at an electric field of  $20\text{V}/\mu\text{m}$ .



As can be seen in Figure 4, PMeOPhEtS has the lowest mobility of the polysilanes studied, which is consistent with its higher activation energy.

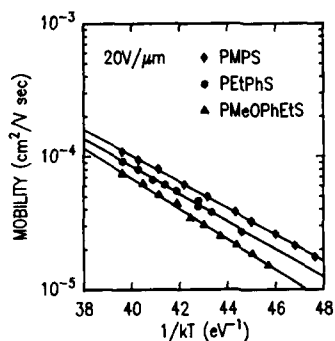


Figure 4. Arrhenius plot of the mobility for various polysilanes.

This result is also consistent with the observed shift of the current peak ( $T_m$ ) in the TSC spectra of PMeOPhEtS to higher temperatures, relative to the other polysilanes measured at the same electric field and heating rate.

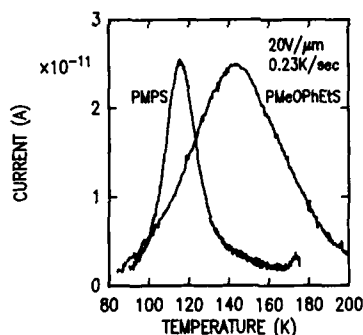


Figure 5. TSC spectra of PMPS and PMeOPhEtS at  $20\text{V}/\mu\text{m}$  and  $0.23\text{K}/\text{sec}$ .

Figure 5 shows TSC spectra of PMPS and PMeOPhEtS recorded at  $20\text{V}/\mu\text{m}$  and  $0.23\text{K}/\text{sec}$ . The lower mobility and the increase in the activation energy of the later, which lead to the decrease in the depletion rate of the charge carriers, may account for the significant shift in the peak temperature by  $\sim 30\text{K}$ .

A significant decrease in the hole mobility, coupled with an increase in the activation energy associated with the hopping transport has been reported upon doping PMPS with molecules [11,12] with lower oxidation potential. These experimental results were described in terms of "trapping" of the holes by the electron-donor type dopants. Similar decrease in the hole mobility following doping of lower oxidation potential species has been observed also in molecularly doped systems [16]. Likewise, the decrease in the

mobility of P<sub>MeOPhEtS</sub> may be associated with the decrease in the oxidation potential of P<sub>MeOPhEtS</sub> (0.63V) relative to P<sub>MPS</sub> (0.78V) [17].

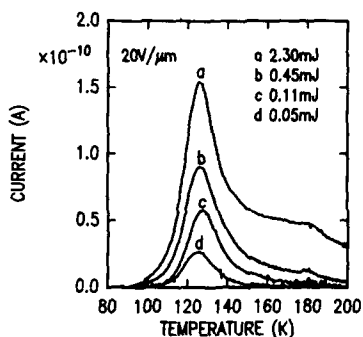


Figure 6. Filling of photodegradation-induced traps in P<sub>MPS</sub> at 20V/ $\mu$ m.

For samples which were exposed to irradiation doses of 1mJ, a secondary peak at  $\sim$ 180K was observed in the TSC spectra. The temperature of the peak increased with the heating rate, but was independent of the electric field. An activation energy of  $\sim$ 0.5eV was associated with that peak. The dependence of the intensity and the structure of the secondary peak on the radiation dose suggests that this peak is associated with surface defect sites produced by the UV exposure. Figure 6 shows some TSC spectra measured at 20V/ $\mu$ m and illumination energies ranging between 0.05mJ to 2.30mJ. The filling fraction of the trapping states associated with these sites increased with illumination energy, but decreased with electric field. Photodegradation effects, which may be related to breaking of Si-Si bonds in the polymer backbone, have been observed also in ESR measurements [18] and by luminescence spectroscopy [19].

In summary, thermally activated charge hopping transport in polysilane has been studied in P<sub>MPS</sub>, P<sub>PhEtS</sub> and P<sub>MeOPhEtS</sub>, using TSC and TOF spectroscopies. An influence of the substituent side groups on the charge hopping transport has been observed by both methods. The activation energies associated with this transport ranged between 0.1-0.3eV for electric fields of 5V/ $\mu$ m-80V/ $\mu$ m for all the polysilanes measured. However, their explicit dependence on the electric field varied with the side groups, as well as the values of the hole mobility for a given temperature and electric field.

#### REFERENCES

1. M. Fujino, Chem. Phys. Lett. **136**, 451 (1987).
2. R.G. Kepler, J.M. Zeigler, L.A. Harrah and S.R. Kurtz, Phys. Rev. B, **35**, 2818 (1987).
3. G.E. Johnson and K.M. McGrane in "Photophysics of polymers", ACS symposium series 358, Washington D.C., 1987, Chap. 36, p.499.
4. R.D. Miller, D. Hofer, J.F. Rabolt and G.N. Fickes, J. Am. Chem. Soc., **107**, 2172 (1985).

5. P. Trefonas III, R. West, R.D. Miller, D. Hofer, *J. Polym. Sci. Polym. Sci. Ed.* **21**, 823 (1983).
6. J.F. Rabolt, D. Hofer, R.D. Miller and G.N. Fickes, *Macromolecules*, **19**, 611 (1986).
7. J.R.G. Thorne, R.M. Hochstrasser and J.M. Zeigler, *J. Phys. Chem.*, **92**, 4275 (1988).
8. K. Takeda, H. Teramae and N. Matsumoto, *J. Am. Chem. Soc.*, **108**, 8186 (1986).
9. L.A. Harrah and J.M. Zeigler, *Macromolecules*, **20**, 603 (1987).
10. K. Takeda, M. Fujino, K. Seki and H. Inokuchi, *Phys. Rev. B*, **36**, 8129 (1987).
11. M.A. Abkowitz, K.M. McGrane, F.E. Knier and M. Stolka, to be published in *Molec. Cryst. & Liq. Cryst. J.*
12. M.A. Abkowitz, M. Stolka, R.J. Weagley, K. McGrane and F.E. Knier, *Syn. Met.*, **28**, C553 (1989).
13. P. Trefonas III, P.I. Djurovich, X.H. Zhang, R. West, R.D. Miller and D. Hofer, *J. Polym. Sci. Polym. Lett. Ed.*, **21**, 819 (1983).
14. L. Samuel, P.N. Sanda and R.D. Miller, *Chem. Phys. Lett.*, **159**, 227 (1989).
15. I. Chen and J.H. Slowik, *Sol. State Comm.*, **17**, 783 (1975).
16. J. Mort and G. Pfitser in "Electronic properties of polymers", edited by J. Mort and G. Pfitser (John Wiley & Sons publishers, 1982) Chap. 6, p.230.
17. A.F. Diaz, D. Thompson, M. Baier, J. Nelson and R.D. Miller, unpublished results.
18. A.J. Kinley, T. Karatsu, G.M. Wallraff, R.D. Miller, R. Sooriyakumaran and J. Michl, *Organometallics*, **7**, 2567 (1988).
19. J.M. Zeigler and L.A. Harrah, *J. Polym. Sci. Polym. Lett. Ed.*, **25**, 205 (1987).

## BAND-TO-BAND TRANSITIONS IN POLY (PHENYL METHYL SILANE)\*

R. G. KEPLER AND J. M. ZEIGLER  
Sandia National Laboratories, Albuquerque, NM 87185

## ABSTRACT

We have measured the quantum efficiency for carrier generation as a function of photon energy and the electroabsorption spectrum in poly (phenyl methyl silane). The experimental data are consistent with a band gap of about 4.6 eV. A strong absorption peak which is observed at 3.7 eV is shown to be an exciton band.

## INTRODUCTION

Polysilanes are silicon backbone polymers with two side groups, typically carbon based, attached to each silicon atom [1]. It has recently been found that these materials exhibit a wide variety of interesting electronic properties, many of which are very similar to those of  $\pi$ -conjugated polymers and molecular crystals. They typically absorb strongly in the UV and many exhibit a high quantum efficiency for fluorescence [2]. In the solid state they tend to be excellent photoconductors [3,4] and have exhibited unusually high nonlinear optical coefficients for materials which are transparent in the visible [5].

It is now well established that these interesting properties result from the  $\sigma$  electrons which are delocalized on the silicon backbone but our understanding of the states of these electrons is still rudimentary.

In this paper we report measurements of the quantum efficiency for charge carrier generation in poly (phenyl methyl silane) for photon energies from 3.65 eV to 5.65 eV and of the electroabsorption spectrum from 3.25 eV to 5.2 eV. The experimental results indicate that the free carrier band gap is about 4.6 eV. The electroabsorption spectrum exhibits a feature consistent with a band gap of 4.6 eV and shows that the strong absorption peak at 3.7 eV results from the formation of an exciton in an electronic transition with a change in polarizability of about  $3 \times 10^{-23}$  cm<sup>3</sup>.

## EXPERIMENTS

Poly (phenyl methyl silane) is a silicon chain with a phenyl and a methyl group attached to each silicon atom in stereochemically random fashion. The material

\* This work performed at Sandia National Laboratories supported by the U. S. Department of Energy under contract number DE-AC04-76DP00789.

used in these experiments was prepared by the method of Zeigler [6] and the molecular weight was such that a molecule consisted of a chain of about 3800 silicon atoms.

In a previous publication [3], we reported on many of the photoconductive properties of this material. For the charge carrier generation experiments reported on in this paper, samples a few micrometers thick were cast from toluene solution on a quartz substrate which had been coated with a vacuum-evaporated, semi-transparent aluminum film. An aluminum electrode about 10 mm in diameter was then evaporated on top of the polymer film. The light source for these experiments was a pulsed dye laser with a pulse width of about 5 ns and the light was incident on the sample through the quartz plate and the semi-transparent aluminum electrode. The number of carriers generated by a single pulse of light was determined by measuring the amount of charge displaced on the electrodes and the number of photons incident on the sample was determined by measuring the energy in the light pulse by reflecting a known fraction of the beam into a detector.

The experimental results are shown in Figure 1. Also shown in this figure for reference is a typical optical density curve obtained on a much thinner sample and the wavelength dependence for carrier generation reported in reference 3. The quantum efficiency for carrier generation in the energy range 3.5 eV to 4.0 eV was found to be lower in these experiments than that reported in reference 3, presumably because a different electrode material was used and these experiments were conducted in a vacuum rather than in air. Therefore the reference 3 data were normalized to the present data at 3.75 eV for this graph.

Samples for the electroabsorption experiments were prepared by spin casting from toluene solution a thin poly (phenyl methyl silane) film onto a quartz substrate onto which a 15 nm layer of aluminum had been vacuum deposited. Another 15 nm aluminum electrode of total area  $0.91 \text{ cm}^2$  was then vacuum deposited on top of the polymer film. Gold pads, approximately 100 nm thick, were then deposited onto the thin aluminum electrodes to allow mechanical contact with gold wires. The light source was a high pressure xenon arc and the light was passed through a monochromator with a spectral resolution of 0.06 nm. The intensity of the light transmitted by the sample and the two electrodes was measured with a photomultiplier and the modulation of the transmitted light intensity induced by an applied electric field was measured with a lock-in amplifier. The sample capacitance between the two electrodes was measured to be 22.5 nf. In other measurements we had found that the dielectric constant is about 3 and therefore the calculated sample thickness was 107 nm. The maximum modulation voltage applied was 7.3 volts rms at 1 kHz providing a modulation electric field of  $6.8 \times 10^{-5} \text{ V/cm}$ .

The experimental results at room temperature are shown in Figure 2 where  $\Delta T/T$  is plotted as a function of photon energy.  $\Delta T$  is the change in transmission induced by the electric field and T is the transmission of the sample. Also shown in the figure for reference is the optical density of the sample versus photon energy. The maximum optical density of the sample was 1.23 at 3.7 eV.

In Figure 3 we have plotted the magnitude of the signal observed at the two positive peaks in Figure 2, at 3.54 and 4.68 eV, versus the applied voltage squared. These results show that the signal observed varied as the square of the applied electric field.

The derivative of the optical absorption spectrum with respect to photon energy is plotted versus photon energy, along with the electroabsorption spectrum shown in Figure 2, are shown in Figure 4. The magnitude of the derivative spectrum was normalized to the magnitude of the electroabsorption spectrum at 3.54 eV.

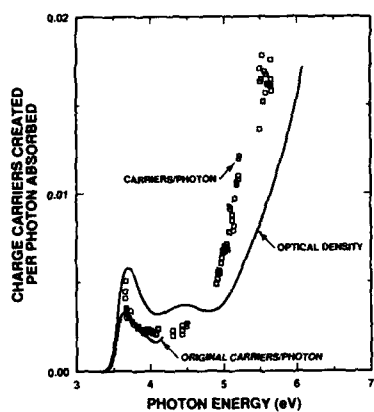


FIG. 1 The quantum efficiency for carrier generation versus photon energy. Also shown is the absorption spectrum on an arbitrary scale and data from reference 3 normalized to match the present data at 3.75 eV.

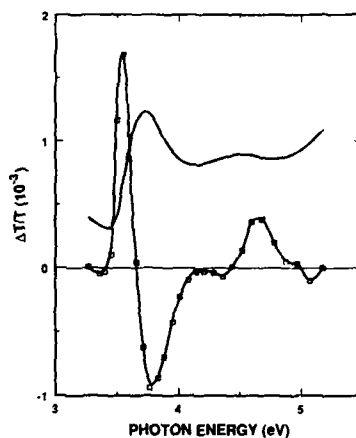


FIG. 2 The electroabsorption spectrum of poly(phenyl methyl silane) is shown as the open squares. The solid line was drawn through the data to guide the eye. Also shown is the optical density of the sample used. The maximum optical density was 1.23 at 3.7 eV.

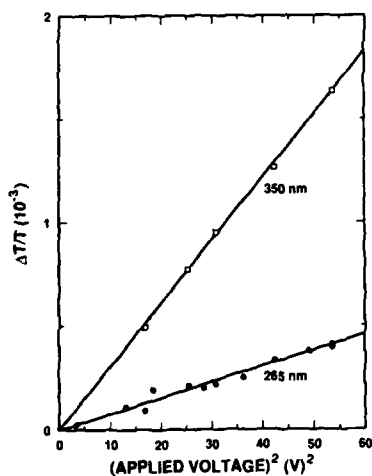


FIG. 3 The electric field dependence of the electroabsorption signal. The signal intensity at the two positive peaks shown in Figure 2 is plotted as a function of the square of the applied voltage.

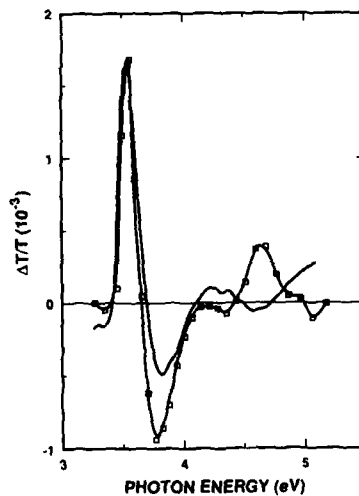


FIG. 4 The electroabsorption spectrum, solid square data points with a solid line drawn through them, is compared to the derivative of the absorption spectrum, solid line with no data points. The derivative of the absorption spectrum was normalized to the electroabsorption spectrum at 3.54 eV.

## DISCUSSION

In our earlier work [3], we concluded that carrier generation in the vicinity of the strong absorption peak at 3.7 eV resulted from excitons, which were created by absorbed photons, diffusing to the vicinity of the sample surface and injecting carriers into the sample from the surface or the electrode. An exciton diffusion length of 50 nm was deduced from the data, a value which is in excellent agreement with estimates of the diffusion length based on exciton-exciton annihilation experiments [7]. If these conclusions are accepted, it raises the question of the magnitude of the free carrier band gap. This line of reasoning lead to the experiments which resulted in the data presented in Figure 1. The strong increase in carrier generation quantum efficiency which appears to begin in the vicinity of 4.6 eV suggests that the free carrier band gap is 4.6 eV.

These results are very reminiscent of the results obtained on molecular crystals [8] and polydiacetylene [9] and suggested that electroabsorption experiments might prove fruitful. In these materials it has been found that the lowest energy electronic transition is an exciton band. The electroabsorption spectrum in this region results from a Stark shift of this transition and thus follows the first derivative of the absorption band. The optical transitions which result in the generation of free carriers tend to be quite weak but they show up strongly in the electroabsorption spectrum because a large change in polarizability results from the transition.

Figure 4 shows that the electroabsorption spectrum of poly (phenyl methyl silane) in the vicinity of the first electronic transition agrees quite well with the first derivative of the absorption coefficient showing that it results from a Stark shift of the absorption peak. If we assume that the polymer molecules are randomly oriented in the amorphous film, the change in the absorption coefficient  $\alpha$  becomes

$$\Delta\alpha = (1/10) \Delta p F^2 \delta\alpha/\delta E.$$

$\Delta p$  is the change in the polarizability parallel to the chain axis resulting from the transition and is assumed to be the only significant component of the polarizability tensor,  $F$  is the applied electric field plus the Lorentz field and is parallel to the direction of propagation of the light in our experiment, and  $E$  is the energy of the photons. From our experiments, we have calculated that  $\Delta p$  for the first electronic

transition in poly (phenyl methyl silane) is  $1.7 \times 10^{-22} \text{ cm}^3$ , which seems to be a reasonable value when compared to the values obtained for molecular crystals.

The peak in the electroabsorption spectra which occurs at 4.68 eV is clearly not the result of a Stark shift of an obvious absorption band. Presumably it arises from a weak electronic transition which results in a large change in polarizability and thus is consistent with the hypothesis that the free carrier band gap is about 4.6 eV.

## CONCLUSIONS

Measurements of the quantum efficiency for carrier generation as a function of photon energy in poly (phenyl methyl silane) indicate that the band gap for carrier generation is about 4.6 eV. Electroabsorption measurements tend to confirm this conclusion.

## ACKNOWLEDGEMENTS

The technical assistance of P. M. Beeson is gratefully acknowledged.

## REFERENCES

1. R. D. Miller and J. Micht, *Chem. Rev.* **89**, 1359 (1989).
2. L. A. Harrah and J. M. Zeigler, *Macromolecules* **20**, 601 (1987).
3. R. G. Kepler, J. M. Zeigler, L. A. Harrah and S. R. Kurtz, *Phys. Rev. B* **35**, 2818 (1987).
4. M. Abkowitz, F. E. Krier, H. -J. Yuh, R. J. Weagley and M. Stolka, *Sol. St. Comm.* **62**, 547 (1987).
5. F. Kajzar, J. Messier and C. Rosilio, *J. Appl. Phys.* **60**, 3040 (1986); J. C. Baumert, G. C. Bjorklund, D. H. Jundt, M. C. Jurich, H. Looser, R. D. Miller, J. Rabolt, R. Sooriyakumaran, J. D. Swalen and R. J. Twieg, *J. Appl. Phys. Lett.* **53**, 1147 (1988).
6. J. M. Zeigler, *Poly. Prepr. Am. Chem. Soc. Div. Polm. Chem.* **27** (1), 109 (1986).
7. R. G. Kepler and J. M. Zeigler in *Proc. of the International Workshop "Advances in Silicon Based Polymer Technology,"* edited by J. M. Zeigler and G. Fearon, to be published; R. G. Kepler and J. M. Zeigler, *Mol. Cryst. and Liq. Cryst.* **175**, 85 (1989); R. G. Kepler, *Synth. Met.* **28**, C573 (1989).
8. See for example L. Sebastian, G. Weiser and H. Bassler, *Chem. Phys.* **61**, 125 (1981).
9. L. Sebastian and G. Weiser, *Phys. Rev. Lett.* **46**, 1156 (1981); Y. Tokura, Y. Oowaki and T. Koda, *Chem. Phys.* **88**, 437 (1984).



THE DOPING OF POLY-p-PHENYLENE SULFIDE AND ITS OLIGOMERS:  
A SPECTROSCOPICAL STUDY

P. PIAGGIO, D. GIRIBONE, C. CUNIBERTI AND G. DELLEPIANE  
Università di Genova, Istituto di Chimica Industriale, Corso  
Europa 30, 16132 Genova, Italy

ABSTRACT

It is shown that the spectra of poly-p-phenylene sulfide doped at low doping level with different doping agents exhibit features similar to those already observed in polyacetylene and can be qualitatively interpreted in terms of the Amplitude Mode Theory.

INTRODUCTION

Poly-p-phenylene sulfide (PPS) is a processable polymeric material with interesting properties of chemical, physical and thermal stability [1,2]. The capability of this polymer to become conductive upon doping with strong oxidants has stimulated several studies on the physical and chemical modifications responsible of the change in its electrical conductivity [3-7]. Powerful tools for these studies are provided by electronic and vibrational spectroscopies, which also enable to compare the behaviors of different chemical classes of conducting polymers on the basis of the theoretical models developed for conjugated chains.

Spectroscopical studies of PPS doping have been carried out mostly for the reaction with gaseous  $\text{AsF}_5$  [3,4,6,8]. Less data are available for other dopants in the vapour phase like  $\text{SbF}_5$ ,  $\text{SO}_3$  [7] or for the doping reactions with  $\text{AlCl}_3$ ,  $\text{FeCl}_3$ ,  $\text{TaF}_5$  in solution [9]. These data, often contradictory, have been explained by different models so that the origin of electrical conduction in PPS is still a controversial problem.

It is our opinion that these difficulties derive from the following general problems connected with the spectroscopy of conducting polymers:

- the best polymer samples for conductivity studies often are the worst ones for spectroscopy work; moreover they are always opaque in the conductive state
- the reactivity of both dopants and doped polymers is very high and causes a great instability of the materials. Moreover in the case of PPS only very recently a reliable assignment of the vibrational spectrum and its dependence on the sample crystallinity has been proposed [10].

To reach a better understanding of all the problems connected with the doping of PPS selected samples of the polymer as well as of simple related molecules have been doped with  $\text{TaF}_5$  and the spectral changes in the VIS, NIR and IR regions have been carefully analysed. Some comparative results from doping with other oxidizing agents are also reported.

## RESULTS

The spectra of PPS films lightly doped in  $\text{CH}_3\text{NO}_2$  solutions of  $\text{TaF}_5$  show a broad asymmetric band in the NIR with the maximum at 1250 nm (Fig.1) and less intense peaks in the IR around 1550 and 1040  $\text{cm}^{-1}$  (Fig.2).

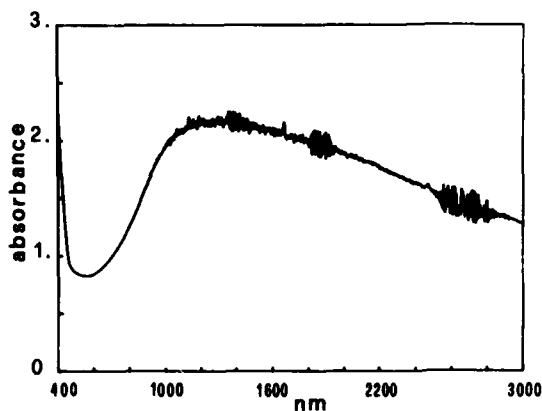


Fig.1. Electronic absorption of PPS doped with  $\text{TaF}_5$ .

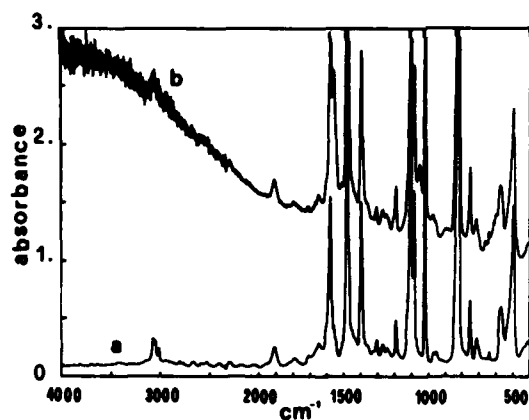


Fig.2. Infrared spectra of pristine (a) and  $\text{TaF}_5$  doped (b) PPS.

All these bands disappear after exposure of the doped sample to air and the original spectrum of the undoped material is obtained in a very short time. Instead, by working in Ar atmosphere or in the vacuum the intensity of all these doping induced bands decreases with the same decay law.

The very low doping degree of these samples is inferred from the fact that the bands of pristine PPS remain nearly unchanged and that no appreciable absorption characteristic of Ta derivatives is observed. This fact clearly shows that the intrinsic transition moment of all the observed doping induced bands is very high, especially that associated to the electronic transition in the NIR region.

Very similar results are obtained upon doping PPS films with a  $\text{FeCl}_3/\text{CH}_3\text{NO}_2$  solution or with  $\text{SbF}_5$  vapours. Also by light doping of a thin film of PPS with  $\text{AsF}_5$  vapour features similar to those just described [4] are observed. The frequencies of the IR bands associated to the strong NIR absorption, observed for different dopants, are summarized in Table I.

TABLE I - Frequencies of IR bands induced by different doping agents ( $\text{cm}^{-1}$ ).

Frequency	$\text{TaF}_5$	$\text{FeCl}_3$	$\text{SbF}_5$	$\text{AsF}_5$ [4]
$\omega_1$	1550	1560	1550	1547
$\omega_2$	1045	1040	1040	1048

At present, even though a detailed analysis of the minor differences observed with different dopants cannot be performed, all the data appear to be consistent with the activation of a peculiar state of the polymer which, regardless of the nature of the doping agent, originates identical spectroscopic signals that is a strong broad absorption covering the NIR region and two weaker and sharper bands in the IR at about 1550 and 1040  $\text{cm}^{-1}$ . The first stages of the reaction with  $\text{TaF}_5$  in  $\text{CH}_3\text{NO}_2$  solution have been studied in the VIS-NIR region for selected low molecular weight molecules related to the chemical structure of PPS. From these spectra, shown in Fig.3, it is apparent that all the molecules containing at least one  $-\text{S}-\phi-\text{S}-$  unit can originate strong absorption bands in the visible region. On the contrary no band in this region is observed for phenyl-thioether. Observations in the IR region for this solutions are prevented by the strong absorptions of  $\text{CH}_3\text{NO}_2$ .

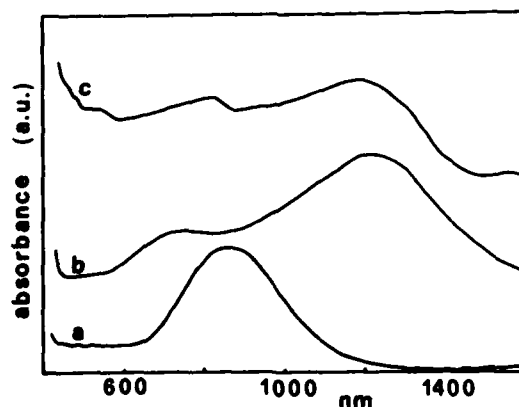


Fig.3. Electronic absorptions of PPS oligomers  $\phi-\text{[S}-\phi\text{]}-\text{Br}$  doped with  $\text{TaF}_5$ : (a)  $n = 2$ , (b)  $n = 3$ , (c)  $\bar{n} = 10$ .

The study of the doping of powdered samples of both PPS and oligomers by spectroscopical methods has been found to be very difficult. In such cases indeed, being the doping very fast because not so limited by dopant diffusion as in the case of films, only opaque samples are obtained. Moreover, the reactivity of the dopants with KBr, nujol, halocarbons and moisture prevents the standard technique of sampling. Highly doped PPS samples are well known to "deactivate" after air exposure or chemical treatments [3]. The NIR absorption bands disappear and the IR spectrum shows several new bands superimposed to the pristine polymer, modified to more or less extent, depending on both the dopant nature and the sample history. This behavior is consistent with several possible mechanisms of "deactivation" of the charged defects. The comparison of the spectra of samples doped in solution and in the gas phase shows that an excess of dopants is usually present in the latter case. Due to the highly hygroscopic nature of these molecules a fast reaction with moisture occurs and the spectra show a continuum below  $3600\text{ cm}^{-1}$ , characteristic of amorphous systems with charged highly polarizable H-bonds [11]. Such spectral features have been sometimes considered an evidence of the presence of free carriers in doped polymers [7]. The growth of a similar continuum in the infrared is also observed for the reaction of  $\text{TaF}_5$  powder with moisture.

PPS films heavily doped with  $\text{TaF}_5/\text{CH}_3\text{NO}_2$  solution show a slow decrease of the doping induced bands in air with a slow growing up of the bands characteristic of the OH bond (Fig.4). The reaction of PPS with  $\text{TaF}_5$ , on the contrary, causes an evident degradation of the polymeric material with the release of gaseous products. The characterization of these systems is as yet a matter of study.

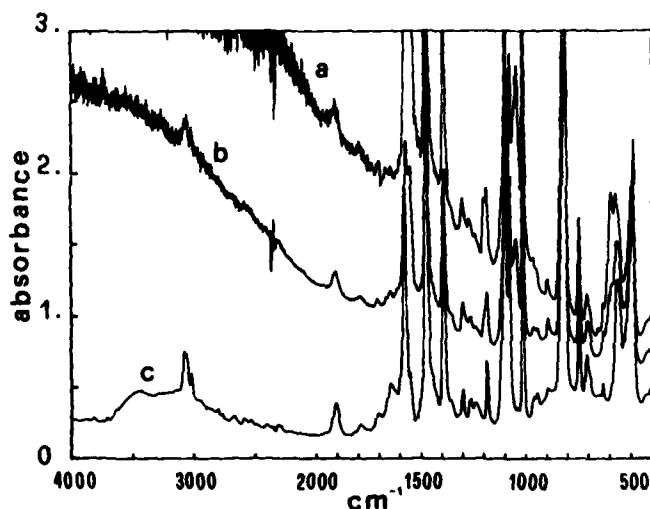


Fig.4. Decay of the infrared absorptions of heavily doped PPS films exposed to air. (a) as doped, (b) 6 days, (c) 33 days.

All these facts indicate that by doping PPS with TaF<sub>5</sub> solutions it is possible to obtain a material showing doped induced bands of high intensity without appreciable modifications of the characteristic bands of the polymer. These conditions can not be achieved in the case of doping with pure dopants.

Since in this paper we want to illustrate the most general spectroscopic aspects of doping in PPS, we shall not report here the detailed analysis carried out on the effect of both crystallinity and chain orientation but just stress the fact that doping is most effective in amorphous material and that no dichroic effect in doped induced bands of highly oriented samples has been detected.

#### CONCLUSIONS

As previously discussed, we have been able to measure the spectrum of PPS doped in such a way that a few new strong absorptions arise superimposed on the bands of the pristine material. Independently of the doping agent, a strong and broad absorption appears around 1250 nm accompanied by two infrared bands at about 1550 and 1040 cm<sup>-1</sup>. The whole original spectrum is fully restored upon decay of the induced bands. From all these observations we can infer that the bands induced in PPS are originated by some "activation" mechanism in analogy to what happens in polyacetylene. In this case for instance the vibrational spectra have been interpreted on the basis of the Amplitude Mode Theory [12] which accounts for the different electron-phonon coupling exhibited by the pristine and doped material and predicts a one to one correspondence between the Raman active modes and the infrared doping-induced modes. This correspondence is found to hold also for PPS whose two strong Raman bands appears at 1572 and 1075 cm<sup>-1</sup> [10].

On the basis of the above theory, the amount of the shift of the frequency of one IR activated band with respect to the frequency of its Raman correspondent depends on the change of the involved electron-phonon coupling constant in the polymer backbone due to the charge defects. For PPS, in contrast with polyacetylene, these shifts are small in agreement with the smaller delocalization expected for this polymer. Moreover, the fact that the defect is here much more localized than in polyacetylene is also confirmed by the NIR data on the doped oligomers.

#### Acknowledgements

This work was supported by the Italian Ministry of Public Education.

References

1. S.Z.D. Cheng, Z.Q.Wu and B. Wunderlich, *Macromolecules* 20, 2802 (1987).
2. P.L. Carr and I.M. Ward, *Polymer* 28, 2070 (1987).
3. L.W. Shacklette, R.L. Elsenbaumer, R.R. Chance, H. Eckhardt, J.E. Frommer and R.H. Baughman, *J. Chem. Phys.* 75, 1919 (1981).
4. T.C. Clarke, K.K. Kanazawa, V.Y. Lee, J.F. Rabolt, J.R. Reynolds and G.B. Street, *J. Polym. Sci. Polym. Phys. Ed.* 20, 117 (1982).
5. J. Tsukamoto and K. Matsumura, *Japan. J. Appl. Phys.* 23 L584 (1984).
6. J.E. Frommer, R.L. Elsenbaumer, H. Eckardt, R.R. Chance, *J. Polym. Sci. Polym. Lett. Ed.* 21, 39 (1983).
7. K.F. Schoch, J.F. Chance and K.E. Pfeffer, *Macromolecules* 18, 2389 (1985).
8. P. Piaggio, C. Cuniberti, G. Dellepiane, G. Capannelli, *Synth. Metals* 29, E61 (1989).
9. J. Tsukamoto, S. Fukuda, K. Tanaka, T. Yamabe, *Synth. Metals* 17, 673 (1987).
10. P. Piaggio, C. Cuniberti, G. Dellepiane, E. Campani, G. Gorini, G. Masetti, M. Novi, G. Petrillo, *Spectrochim. Acta*, 45A, 347 (1989)
11. G. Zundel, in The Hydrogen Bond, edited by P. Schuster, G. Zundel and C. Sandorfy (North-Holland Publishing Co., New York, 1976), pp.683-766.
12. B. Horovitz, *Solid State Comm.* 41, 729 (1982).

---

PART IV

---

**Non-linear Optical Properties of  
Organic Molecules and Polymers**

NONLINEAR OPTICAL POLYMERS:  
CHALLENGES AND OPPORTUNITIES IN PHOTONICS

A.F. Garito and J.W. Wu, Dept. of Physics, University of Pennsylvania, Philadelphia, PA 19104  
G.F. Lipscomb and R. Lytel, Lockheed Palo Alto Research Lab. O-9720, B-202, Palo Alto, CA  
94304

ABSTRACT

In polymer structures, highly correlated virtual excitations of the  $\pi$ -electrons are responsible for the exceptionally large nonresonant nonlinear optical responses observed. Extremely large resonant nonlinear optical responses are also achievable in certain  $\pi$ -electron systems, which can be treated as optical Bloch systems. In addition to their obvious scientific importance, these large optical nonlinearities potentially make possible the implementation of powerful, new nonlinear optical devices and systems. After a description of nonlinear optical processes in polymers, two examples are presented. First, saturable absorption and optical bistability in ultrathin organic polymer films are described, illustrative of resonant third order processes. Saturable absorption studies of glassy polymer films consisting of quasi two-dimensional conjugated disc-like structures of silicon naphthalocyanine demonstrate that on-resonance the system behaves as an optical Bloch system with a linear absorptivity coefficient  $\alpha_0$  of  $1 \times 10^5 \text{ cm}^{-1}$  and an intensity dependent refractive index  $n_2$  of  $1 \times 10^{-4} \text{ cm}^2/\text{kW}$  in the wavelength range of standard laser diodes. A resonant nonlinear optical response of  $\pi$ -electron excitations provides the nonlinear interaction essential to the onset of bistability. Electronic absorptive optical bistability is observed on a nanosecond time scale in a nonlinear Fabry-Perot interferometer employing the saturably absorbing naphthalocyanine film as the nonlinear optical medium. As a second example, the nonresonant second order process of linear electrooptic effects in poled polymer films, is discussed. For such a second order nonlinear optical process, the broken global centrosymmetry is achieved by electric field poling of a thin polymer film. With high electrooptic coefficients of 10-50 pm/V and low dielectric constants of 3-4, poled polymers have potentially great advantages over inorganic crystals as electrooptic materials. As one device illustration, the application of poled polymers in electrooptic waveguide operations is presented.

1. INTRODUCTION

Organic and polymeric materials and devices have been the center of intense scientific and engineering investigations for many years due both to the outstanding primary nonlinear optical and electrooptic properties of certain conjugated  $\pi$ -electron systems and to the success in creating new nonlinear optical and electrooptic materials with suitable secondary properties that include high



optical transparency, low dielectric constant, and thermal, mechanical, and oxidative stabilities.[1] As a result of fundamental progress in the field, the microscopic origin and mechanism for second order and third order electronic excitation processes are fairly well understood, and recent advances toward efficient device designs and architectures now allow implementation of organic polymers into prototype electrooptic and nonlinear optical devices. Primary among the many important nonlinear optical properties of polymers is the ability to change the refractive index by applying dc or optical electric fields either through second order processes such as the nonresonant linear electrooptic effect, or through resonant third order processes such as nonlinear absorption and dispersion. Basic concepts and key results for each process are reviewed by way of recent studies of electrooptic effects in aligned polymer waveguides[2] and absorptive optical bistability in glassy polymer films.[3] These studies are particularly noteworthy because of possible applications in optical communications and signal processing.

Section 2 addresses the microscopic description of nonlinear optical processes in organic polymer systems, emphasizing that each nonlinear optical process is explained in terms of the corresponding molecular hyperpolarizability. For the particular case of the linear electrooptic effect, the quantum mechanical expression of the microscopic, molecular hyperpolarizability,  $\beta_{ijk}(-\omega; 0, \omega)$ , is given explicitly, where the Bogoliubov-Mitropolsky method of averages is employed to avoid secular divergences. The discussion then turns to a resonant third order optical process of nonlinear absorption and dispersion, where a real population of excited state occurs, and the change in population of the ground and excited states causes a change in the refractive index. A Bloch susceptibility is introduced for later use in the discussion of optical bistability.

Section 3 addresses linear and nonlinear optical excitation properties of an optically active molecule embedded in a glassy polymer matrix. The linear optical properties of a conjugated  $\pi$ -electron structure in a random glassy polymer can be understood in terms of linear response theory, where the surrounding glassy matrix is treated as a thermal bath and a source of stochastic forces in broadening the absorption line shape. A glassy polymer below the glass transition temperature is in an extremely highly viscous, amorphous, random structure that can be modeled as a collection of low excitation energy two-level-systems (TLS).[4] After a general theory of lineshape function of an optical excitation is briefly described in section 3.1, the line broadening of an optical site in an amorphous matrix is calculated in section 3.2 as a specific example of the general theory introduced in section 3.1. Once the physical model for linear optical excitations is clearly identified, the nonlinear optical excitations associated with the individual homogeneous lines are studied. When the incident light frequency is on resonance with the optical eigenfrequency of the system, the intensity dependent refractive index,  $n_2$ , can be obtained from the Bloch susceptibility through saturable absorption measurements as described in section 3.3. In particular, the observed saturable absorption behavior for the first cases of pure glassy polymer and polymer alloy ultrathin films are presented.

In section 4, optical bistability, one example of third order nonlinear optical processes, is discussed as the quantum optical realization of a first order phase transition occurring far from equilibrium. Nonequilibrium systems in steady states far from equilibrium may exhibit instabilities

which are analogous to phase transitions in thermodynamic equilibrium systems. When an open atomic system is driven far from equilibrium by an external source, it may jump from an initial stationary state of independent atomic motion to a macroscopic ordered state of cooperative motion. The discontinuous transition occurs because of the presence of nonlinear interactions between the atoms and the external field.[5] A major physical realization of such instability phenomena is bistable transmission in a nonlinear optical system where an external coherent optical field resonantly drives a nonlinear optical material contained in an optical cavity to new nonequilibrium stationary states of broken symmetry.[6] After the general features of nonequilibrium phase transition are briefly described, an analogy is made between a nonlinear optical random glassy polymer contained in a Fabry-Perot resonator and a two-dimensional Ising spin system. A nonlinear interaction between the optical field with a disc-like optically active polymer gives rise to a nonequilibrium phase transition. Experimental observation of the absorptive bistability in glassy polymer thin films is presented.[3][7]

In section 5, the second order nonlinear optical properties of poled polymers is presented. Thin films of glassy polymers can be easily formed by spin coating on an optical substrate. For a second order material, a noncentrosymmetric structure is required at both the microscopic molecular and the global macroscopic level. In particular, organic  $\pi$ -electron systems asymmetrically substituted with donors and acceptors have emerged as exceptionally promising electrooptic materials, offering substantial advantages in electrooptic response, speed, fabricability and flexibility over conventional inorganic crystals. In order to get a large nonlinear optical response at the molecular level, a long chain of conjugated  $\pi$ -electrons is preferred, since strong electron-electron correlations in delocalized  $\pi$ -electrons along the chain axis are found to be important in determining the nonlinear optical responses of conjugated structures. Also in order to achieve a broken global symmetry, the thin film must first be aligned by electric field poling. After the electro-optical responses of organic polymers are compared with those of inorganic crystals, prototype electrooptic operations, such as waveguide modulation, are demonstrated in section 5.2.

## 2. NONLINEAR OPTICAL PROCESSES IN ORGANIC POLYMERS

### 2.1 Nonresonant linear electrooptic susceptibility

The macroscopic nonlinear optical properties of organic molecular and polymer structure in condensed states are best described starting from the individual response of isolated molecular, or polymer chain, units. In a lattice gas approximation, if the nonlinear optical susceptibility of an isolated molecule is known, then the susceptibility of the macroscopic ensemble of molecules is determined by the orientational distribution function of individual units. The macroscopic frequency-dependent second order susceptibility  $\chi_{ijk}^{(2)}(-\omega_3; \omega_1, \omega_2)$ , for example, can be expressed in terms of molecular hyperpolarizability,  $\beta_{ijk}(-\omega_3; \omega_1, \omega_2)$ , as

$$\chi_{ijk}^{(2)}(-\omega_3; \omega_1, \omega_2) = N_u \sum_{s=1}^c R_{im}^s R_{jn}^s R_{ko}^s f(\omega_3)_{m'i} \beta_{i'j'k'}^s(-\omega_3; \omega_1, \omega_2) \times f(\omega_1)_{j'n} f(\omega_2)_{k'o} \quad (2.1)$$

where  $R^S$  is the Euler matrix connecting the molecular axes to the macroscopic lab. coordinates, and  $f(\omega)$  stands for the local field corrections. The description of the macroscopic nonlinear optical response is thus reduced to an understanding of the microscopic hyperpolarizability and knowledge of the orientational distribution of the molecular units in the condensed phase. The fact that the intramolecular interaction energy is much stronger than the intermolecular interaction energy in organic molecular crystals, liquids, solutions, and polymer thin films means that the starting point for understanding the macroscopic nonlinear optical properties of these various condensed phases lies in an accurate description of the microscopic response from an isolated molecular unit. In a nonresonant regime, a quantum mechanical perturbative expansion of the response function is allowed, leading to an analytic expression for each nonlinear optical process. For the important case of the linear electrooptic effect with  $\omega_1 = 0$ ,  $\omega_2 = \omega$ ,  $\omega_3 = \omega$ , the microscopic hyperpolarizability  $\beta_{ijk}(-\omega; 0, \omega)$  is given by the following expression.

$$\begin{aligned} \beta_{ijk}(-\omega; 0, \omega) = & \frac{1}{2!} \frac{(-e)^3}{\hbar^2} \sum_{n1 n2} \left\{ \frac{(x_i)_{gn1} (\bar{x}_j)_{n1n2} (x_k)_{n2g}}{(\omega_{gn1} - \omega)(\omega_{gn2} - \omega)} \right. \\ & + \frac{(x_i)_{gn1} (\bar{x}_k)_{n1n2} (x_j)_{n2g}}{(\omega_{gn1} - \omega) \omega_{gn1}} + \frac{(x_i)_{gn1} (\bar{x}_i)_{n1n2} (x_k)_{n2g}}{\omega_{gn1} (\omega_{gn2} - \omega)} \\ & + \frac{(x_k)_{gn1} (\bar{x}_i)_{n1n2} (x_j)_{n2g}}{(\omega_{gn1} + \omega) \omega_{gn2}} + \frac{(x_j)_{gn1} (\bar{x}_k)_{n1n2} (x_i)_{n2g}}{\omega_{gn1} (\omega_{gn2} + \omega)} \\ & \left. + \frac{(x_k)_{gn1} (\bar{x}_j)_{n1n2} (x_i)_{n2g}}{(\omega_{gn1} - \omega)(\omega_{gn2} + \omega)} \right\} \quad (2.2) \end{aligned}$$

where  $(x_i)_{n1n2}$  is the transition matrix  $\langle n1 | x_i | n2 \rangle$  between the electronic state  $|n1\rangle$  and  $|n2\rangle$ , and  $(\bar{x}_i)_{n1n2} = (x_i)_{n1n2} - (x_i)_{gg}$ . The molecular hyperpolarizability  $\beta_{ijk}(-\omega; 0, \omega)$  is obtained from a quantum mechanical perturbation theory, where the induced polarization is expanded in the eigenfunction of electronic states of the molecule up to the second power of the fine structure constant,  $\alpha = e^2/\hbar c$ . In an electrooptic process where the incoming and the outgoing light frequency are identical, the Bogoliubov-Mitropolsky method of averages[8] is required to avoid a secular divergences coming from the vanishing denominator. The microscopic nonlinear optical susceptibilities for second order processes as well as third order processes have been explicitly calculated by the direct sum over states method based on self consistent field configuration interaction theory for a variety of quasi-one and -two dimensional conjugated structures.[9] The microscopic origins and mechanisms for second order and third order virtual electronic excitation

have been described in detail in the cited references, especially the important role of many-body correlations within the  $\pi$ -electron states.

### 2.2 Resonant intensity dependent refractive index

The optical response of a  $\pi$ -electron system to resonant incident light is described by the Bloch susceptibility.[10] As the light frequency approaches one of the  $\pi$ -electron optical excitations, the response function is resonantly enhanced, and the perturbation theory employed to describe the nonlinear optical response off resonance no longer holds. In a resonant optical excitation, a real population of the excited state and an associated depletion of the ground state occurs, which depends on the incident light intensity. Since the response function depends on the light intensity, it represents a third order nonlinear optical process at a lowest nonvanishing order. The quantum mechanical description of resonant excitation in the form of the optical Bloch equations is applicable to  $\pi$ -electron systems resonant with an applied optical field.

$$\begin{aligned}\frac{du}{dt} &= -\Delta v - \frac{u}{T_2} \\ \frac{dv}{dt} &= \Delta u + \kappa \epsilon w - \frac{v}{T_2} \\ \frac{dw}{dt} &= -\kappa \epsilon v - \frac{w-w_{eq}}{T_1}\end{aligned}\quad (2.3)$$

where  $u$  and  $v$  are the real and imaginary part of the induced polarization and  $w$  is the population difference between the excited state and the ground state, and  $\Delta = \omega - \omega_a$ , is the difference between the incident optical frequency,  $\omega$ , and atomic resonance frequency,  $\omega_a$ . In steady state, the complex susceptibility  $\chi(\omega)$  of a Bloch system is expressed as

$$\chi(\omega) = \frac{\alpha_0 c}{4\pi\omega} \frac{\Delta + i}{1 + \Delta^2 + I/I_s} \quad (2.4)$$

where  $I_s$  is the threshold intensity for saturation and  $\Delta = (\omega - \omega_a)T_2$  is redefined as a dimensionless number. As appears in the denominator, the dipole moment induced in an optical Bloch system is a nonlinear function of the incident light intensity, which allows definition of the intensity dependent refractive index,  $n_2$ , as follows.

$$n_2 = -\frac{\alpha_0 \lambda}{4\pi I_s} \frac{\Delta}{(1 + \Delta^2)^2} \quad (2.5)$$

From this expression, we see that the nonlinear refractive index  $n_2$  can be obtained through saturable absorption measurements.

### 3. OPTICAL EXCITATIONS IN RANDOM GLASSY POLYMERS

One of the major studies reviewed in this paper is the investigation of optical bistability in random glassy polymers resonantly driven by intense laser fields through the intensity dependent refractive index. In sections 3.1 and 3.2, we first address the linear optical excitations of glassy polymer ultrathin films consisting of quasi-two dimensional, disc-like, structures randomly distributed in a glassy matrix. A major result is that the optical absorption consists of an inhomogeneous, site-broadened band of very many narrow homogeneous lines from the on-site excitations of the conjugated discs. A physical model by Anderson, Halperin, and Varma,[4] for the linear optical excitations of random glass media is an insightful approach that focuses on the microscopic mechanisms for broadening of optical excitations. The nonlinear optical excitations in random glassy media and an experimental study of the intensity dependent refractive index are presented in section 3.3.

#### 3.1 Lineshape function

A physical picture of the linear optical excitations of  $\pi$ -electrons in optical sites randomly distributed inside a polymer matrix is necessary for the proper understanding of nonlinear optical processes. The emission spectrum of an isolated molecule has a narrow bandwidth corresponding to the excited state lifetime for an optical transition. Optical line broadening occurs when an optical site is disturbed by its interaction with other excitations in the polymer matrix which acts as a heat reservoir as well as a source of low energy excitations (TLS). In another words, the bath is not just a heat reservoir but a source of interactions which should be considered explicitly to determine the effects on the optical excitations.

In general, the lineshape function,  $F(\omega)$ , is defined as the Fourier transform of the auto-correlation of dipole moments.

$$F(\omega) = \frac{1}{2\pi} \int dt \exp(i\omega t) \text{Tr}\{\rho_{xx}(t)\} \quad (3.1)$$

where  $\rho$  is the density matrix of the entire system composed of the molecular sites and the bath, and the problem of lineshape change through interactions with other excitations comes down to solving the density matrix of a statistical mechanical system undergoing an irreversible process.[11] In this case, because of the presence of the interaction between the dipoles and the bath, the eigenstate of the entire system is not simply the product of the eigenstates of the dipoles and the bath. This means that the density matrix of the entire system is not a simple product of the density matrices of the dipoles and the bath. The optical response of the entire system, however, comes only from the optical dipoles and not from the bath, which allows us to use the projection operator method,[12][13] a well known technique in solving irreversible statistical mechanical

problems. The bath is assumed to be always in a thermal equilibrium canonical ensemble; that is, the density matrix of the bath is given by the canonical distribution. With standard procedures to solve the average value of an operator in the projection operator method, and to identify the imaginary part of the lineshape function  $F(\omega)$  as the linewidth broadened by the interaction of optical dipoles with the thermal bath, the homogeneous line width (FWHM) is given as

$$\Delta\omega = \frac{2\pi}{\hbar} \sum_{p'p} \rho_p \frac{b}{p} | \langle fp' | T(\omega_i + \omega_p) | fp \rangle - \langle ip' | T(\omega_i + \omega_p) | ip \rangle |^2 \delta(E_{p'} - E_p) \quad (3.2)$$

where  $|f\rangle$  and  $|i\rangle$  are the excited and ground states of the molecule,  $|p\rangle$  and  $|p'\rangle$  are the thermal bath states,  $\rho_p$  is the occupation probability of the bath state  $|p\rangle$ , and  $T$  satisfies the Lippman-Schwinger equation

$$T(\omega) = V + V \frac{1}{\omega - H_0} T(\omega) \quad (3.3)$$

Once the interaction Hamiltonian  $V$  is known,  $\Delta\omega$  can be obtained to the same order by perturbative expansion in  $V$  of the Lippman-Schwinger equation.

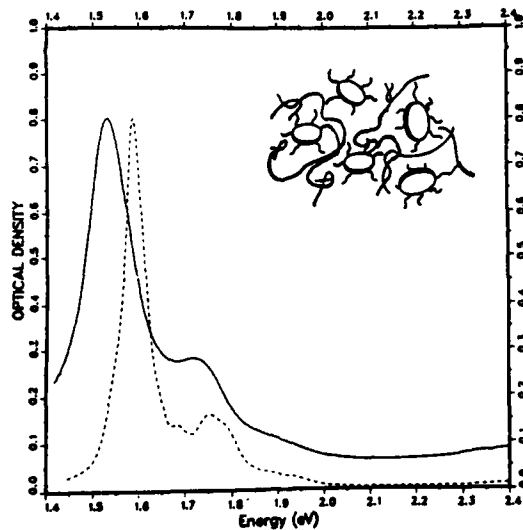


Figure 1. Linear absorption spectra of a pure SINC (solid curve) and a solid solution film of SINC in PMMA (dashed curve). The large oscillator strength Q-band absorption peaks at 1.53 eV (810 nm) in the pure SINC film and 1.60 eV (774 nm) in the SINC:PMMA solid solution film.[3]

### 3.2 Linear optical properties

Random glassy polymer films consisting of quasi-two dimensional disc-like structure of SINC (silicon naphthalocyanine) (Figure 1) are directly formed by standard spin coating technique onto optical substrates. The linear absorption spectra in Figure 1 of a pure SINC film and of a solid solution film of SINC in PMMA each exhibit an intense electronic excitation (Q band) centered in the near infrared region having an exceptionally large linear absorptivity coefficient  $\alpha_0$  of  $1 \times 10^5 \text{cm}^{-1}$ . The local point group symmetry is  $D_{4h}$ , and the Q-band excitation corresponds to the  $1^1A_g \rightarrow 1^1E_u$   $\pi$ -electron transition.

The Q-band appears as a Gaussian-shaped, inhomogeneous band consisting of many narrow homogeneous lines. The observed large linewidth of the Q-band is primarily due to inhomogeneous site broadening associated with variations in the local environment in the polymer matrix. Each line of the series of narrow, homogeneously broadened, resonances contained in the Gaussian envelope is approximated by a Lorentzian function, and the width of each line is determined by coupling to the phonons of the amorphous material surrounding each optical site. The coupling is mediated by an ensemble of non-interacting two-level systems (TLS) contained in the amorphous surroundings which flip-flop at low energies (meV) between two eigenstates as they emit or absorb acoustic phonons.[4] The Hamiltonian of the thin film on a substrate is expressed as

$$H = H_0 + H_{12} + H_{23}, \quad (3.4a)$$

$$H_0 = \epsilon_0 \psi_0^\dagger \psi_0 + \epsilon_1 \psi_1^\dagger \psi_1 + \frac{1}{2} E \sigma^z + \sum_q \hbar \omega_q (n_q + \frac{1}{2}), \quad (3.4b)$$

$$H_{12} = \frac{1}{2} \sum_\alpha V_0^\alpha \psi_0^\dagger \psi_0 \sigma^\alpha + \frac{1}{2} \sum_\alpha V_1^\alpha \psi_1^\dagger \psi_1 \sigma^\alpha, \quad (3.4c)$$

$$H_{23} = \frac{1}{2} \sum_\alpha f^\alpha \epsilon \sigma^\alpha, \quad (3.4d)$$

where  $H_0$  is the non-interacting Hamiltonian of the optical site, TLS, and the phonons;  $H_{12}$  the electrostatic dipole interaction between the optical sites and TLS; and  $H_{23}$  the interaction between TLS and the phonons. With the TLS and phonons as a thermal bath, we can write the phonon emission process, for example, as  $|ip\rangle = |\psi_0 \uparrow n_q\rangle$ ,  $|ip'\rangle = |\psi_0 \downarrow n_q + 1\rangle$ ,  $|fp\rangle = |\psi_1 \uparrow n_q\rangle$ ,  $|fp'\rangle = |\psi_1 \downarrow n_q + 1\rangle$ . With the Lippman-Schwinger equation expanded to second order in the interaction Hamiltonian  $H_{12} + H_{23}$ , the optical linewidth can then be expressed in terms of the TLS lifetime (or flip-flopping rate). An important finding is that the TLS-mediated coupling results in a characteristic temperature dependent linewidth  $T^{1+\delta}$  ( $0 < \delta < 1$ ) observed experimentally,[14] which is to be compared to  $T^7$  behavior for an optical single crystal.[15]

### 3.3 Saturable absorption

Saturable absorption is a resonant nonlinear optical phenomenon in which the absorption coefficient decreases for an increased incident light intensity. At a low incident light intensity, the absorption coefficient of an optical system is related to the imaginary part of the linear refractive index, which in turn is related to the linear susceptibility of the system in an electromagnetic field. According to linear response theory, a Lorentzian susceptibility results when a stochastic force, either an electromagnetic fluctuation manifested as a spontaneous decay, or a thermal bath responsible for a temperature dependent line shape function, is approximated to be near Markovian, or has a short memory. A Markovian stochastic force disturbs the time-correlation of

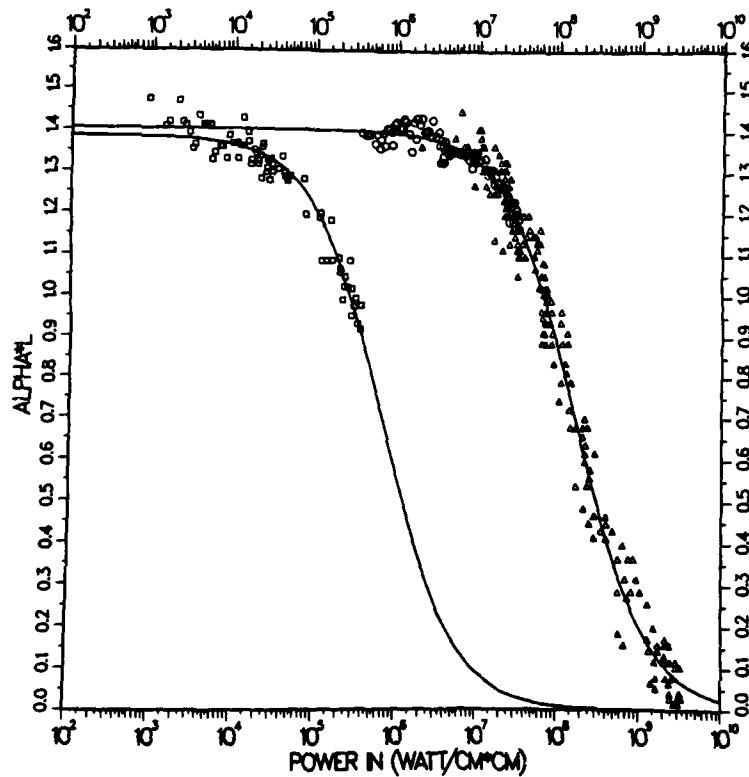


Figure 2. Saturable absorption at absorption maxima (see Figure 1) and least squares fit. Squares are data for pure SINC film at pulse width  $\tau_p = 10$  ns and wavelength  $\lambda = 813$  nm; circles, pure SINC film at  $\tau_p = 30$  ps and wavelength  $\lambda = 813$  nm; and triangles, SINC:PMMA solid solution film at  $\tau_p = 30$  ps and wavelength  $\lambda = 770$  nm.  $\alpha_0 L$  is reflection calibrated, and the low intensity limit is  $\alpha_0 L = 1.40$ . [3]



dipole moments leading to a finite relaxation time. But a basic underlying assumption of linear response theory is that the interaction of the system with the external field is small, thus allowing a perturbative expansion of the response function. However, when the perturbing field is very intense, or the interaction of the system with the perturbing external field becomes comparable to the unperturbed Hamiltonian of the system, the response of the system becomes large and the approximation taken in linear response theory is no longer valid. The resonant interaction of a system with an intense coherent optical field can be described in terms of a Bloch equation, and as shown in Eq.(2.4) the threshold intensity is the same for the real and imaginary part of the susceptibility. This allows us to determine the intensity dependent refractive index  $n_2$  from saturable absorption experiments that measure the imaginary part of the Bloch susceptibility.

The Q-band of the quasi-two dimensional SINC discs is easily saturable at fast timescales ( $10^{-9}$  -  $10^{-12}$  sec) as shown in Figure 2. The change in the absorption is reproducible through many cycles of increased and decreased incident light intensity. Data points for 10 ns are more scattered owing simply to power fluctuations in the Nd:YAG pump laser used. Each solid line in Figure 2 is a least squares curve for Bloch type saturable absorption

$$\alpha(I) L = \frac{\alpha_0 L}{1 + I/I_s} + \alpha_B L \quad (3.5)$$

where  $I_s$  is the threshold intensity for saturation,  $\alpha_0 L$  the low intensity linear absorption, and  $\alpha_B L$  the unsaturable background absorption. Importantly,  $\alpha_B L$  was found to be zero for both the pure and solid solution polymer films, even up to an intensity of  $4\text{GW}/\text{cm}^2$  for 30 ps pulses in the solid solution film. In the case of the pure SINC film, the saturation threshold intensities are  $100\text{MW}/\text{cm}^2$  and for  $440\text{kW}/\text{cm}^2$  for 30 ps and 10 ns pulses, respectively. The threshold intensity for 10 ns pulse is lower than that for 30 ps pulse, but this trend saturates for pulse durations near  $10\ \mu\text{s}$ . This behavior is characteristic of a Bloch system. For a light pulse with a pulse width much shorter than the excited state radiative decay time, what actually counts is the total number of incident photons because all of the incoming photons can be stored in the excited state. In the case of a long pulse with a pulse width longer than the radiative decay time, saturable absorption is a balanced, steady state of absorption and emission, and, therefore, there is not much difference between a long pulse and a much longer pulse.

For solid solution SINC:PMMA films, the value of  $I_s$  is the same for a given pulse width as that of the pure SINC film. This experimental finding that the saturable absorption behavior is identical for both pure SINC and solid solution SINC:PMMA films results from absence of any positional and orientational long range order. The SINC optical sites are independent, and there is no phase coherence between sites. Thus, the on-site  $\pi$ -electron excitations in the Q-band of the individual SINC sites are responsible for the large resonant nonlinear optical behavior of the SINC films. From the saturable absorption results, the nonlinear refractive index  $n_2$  (Eq.2.5) for the SINC films is  $1 \times 10^{-4} \text{cm}^2/\text{kW}$  which is comparable to that for GaAs.[16]

#### 4. OPTICAL BISTABILITY IN RANDOM GLASSY POLYMERS

##### 4.1. Optical bistability as a first order phase transition

Optical bistability can be generally understood as a quantum optical analog of a first order phase transition of a thermodynamic equilibrium system, and the two dimensional Ising spin system in an external magnetic field has an almost identical formal analogy to optical bistability. According to mean field theory for a ferromagnet in a magnetic field, the Ginzburg-Landau potential  $F(\phi)$  can be expanded in terms of the magnetization, or order parameter,  $\phi$ . [17]

$$F(\phi) = -H\phi + \frac{(kT-J\gamma)}{2} \phi^2 + \frac{kT}{12} \phi^4 + \dots \quad (4.1)$$

where  $H$  is the external magnetic field,  $J$  the coupling constant, and  $\gamma$  the number of nearest neighbor spins. The state equation for a ferromagnet in an external field is determined by minimizing the potential  $F(\phi)$  with respect to  $\phi$ .

$$H = k(T-T_c)\phi + \frac{kT}{3} \phi^3 \quad (4.2)$$

where the critical temperature  $T_c = J\gamma/k$ . Below  $T_c$ , a first order phase transition takes place, and the magnetization shows hysteresis behavior upon increase and decrease of the external field  $H$ .

Certain nonlinear optical systems may exhibit a similar phase transition from a disordered fluorescent state to a macroscopic ordered, coherent state when resonantly driven by a coherent optical field. The output field intensity of the optical system shows hysteresis behavior upon change of the incident light intensity. A quantum optical instability, however, is not a phase transition in a thermodynamic equilibrium system in which a Gibbs ensemble can be introduced and a thermodynamic potential defined. Instead, optical bistability is one example of a phase transition that occurs far from equilibrium, where a nonlinear interaction between the system and external field is essential in causing bistability. The major example is the nonlinear optical response of an optical Bloch system to a coherent optical field, where the Bloch susceptibility,  $\chi(\omega)$ , was introduced in section 2.2. In contrast to a thermodynamic phase transition, the absence in a nonequilibrium system of a thermodynamic potential, such as a free energy, makes it difficult to describe a phase transition far from equilibrium. In a quantum optical system, such as the optical Bloch system, however, a generalized Ginzburg-Landau potential can be defined through a Fokker-Planck equation which is equivalent to a Maxwell-Bloch equation describing a resonant nonlinear optical process in the Bloch system contained in a Fabry-Perot cavity. In a slowly varying envelope approximation (SVEA), the Maxwell-Bloch equation reduces to a set of Langevin equations. In an absorptive case where the incident light frequency,  $\omega$ , the cavity resonance

frequency,  $\omega_c$ , and the atomic resonance frequency,  $\omega_a$ , are identical, the equation of motion of the system can be further reduced to a single Langevin equation.

$$\frac{dx}{dt} = y - x - \frac{2Cx}{1+x^2} + F(t) \quad (4.3)$$

where  $x$  is the transmitted output optical field amplitude, the incident coherent optical field  $y$  is the external field,  $C$  is the cooperativity of the nonlinear optical system (in analogy to temperature in an equilibrium system). In order to understand (i) the phase transition behavior, (ii) the temporal change of the order parameter  $x$  upon the change of the external field  $y$ , and (iii) the effects of fluctuations, we need to find the Fokker-Planck equation for the probability density function, which allows us to introduce a generalized Ginzburg-Landau potential similar to the thermodynamic potential in an equilibrium statistical mechanical system.

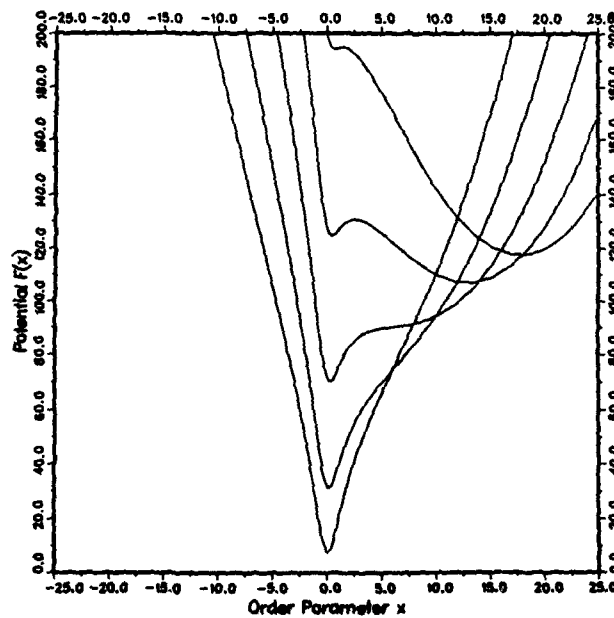


Figure 3. Ginzburg-Landau potential for optical bistability ( $C=20$ ) with various input field amplitude [7]

$$\frac{\partial f(x, \tau)}{\partial \tau} = -\frac{\partial}{\partial x} K(x)f(x, \tau) + \frac{1}{2} \frac{\partial^2}{\partial x^2} Q(x)f(x, \tau) \quad (4.4)$$

with

$$K(x) = y - x - \frac{2Cx}{1+x^2} \quad (4.5)$$

$$Q(x) = q \left( \frac{x}{1+x^2} \right)^2 \quad (4.6)$$

When the system is kept in a stationary state, the bistable transmission of a nonlinear optical system as a function of the input intensity can be described by the generalized Ginzburg-Landau potential,  $F(x)$ . [6]

$$F(x) = \frac{2}{q} \left\{ \frac{1}{2} (x-y)^2 + C \ln(1+x^2) \right\} \quad (4.7)$$

where the transmitted output optical field amplitude  $x$  is the order parameter, and  $q$  is a measure of the stochastic force (such as spontaneous decay) which tends to destroy the macroscopic long range order of the microscopic optical dipole moments.

The Ginzburg-Landau potential for  $C = 20$  is plotted in Figure 3 as an example. At a low input amplitude, the output amplitude (order parameter) is near zero, say  $x_1$ , and as the input intensity is increased, a new local minimum of the potential  $F(x)$  starts to appear at another positive value of order parameter, say  $x_2$ , greater than the original value  $x_1$ . For a large enough input amplitude, the potential  $F(x)$  at this new value of order parameter,  $x_2$ , becomes the global minimum, but the system still assumes the order parameter  $x_1$  corresponding to the local minimum, because the potential barrier is high enough to prevent the system from leaking through to the global minimum  $x_2$ . Once the input amplitude exceeds the threshold value corresponding to the disappearance of the local minimum with the order parameter value  $x_1$ , the nonlinear Fabry-Perot switches over to the high transmission state having a new order parameter  $x_2$ , and stays there. When the above process is reversed, that is, as the input amplitude is decreased, the potential  $F(x)$  shows a similar behavior upon change of the input intensity. But this time the roles of  $x_1$  and  $x_2$  are reversed because the system is already in a state with the order parameter value  $x_2$ ; that is, in a highly transmittant state. As the input amplitude is further decreased, the potential  $F(x)$  at the order parameter  $x_1$  starts to become a local minimum and evolves to the global minimum, but the system remains in the high transmittant state until the local minimum at  $x_2$  disappears. Thus, the nonlinear Fabry-Perot can assume two different macroscopic optical states depending on the history of the preparation of the given input amplitude. The state equation corresponding to Eq.(4.7) is

$$y = x + \frac{2Cx}{1+x^2} \quad (4.8)$$

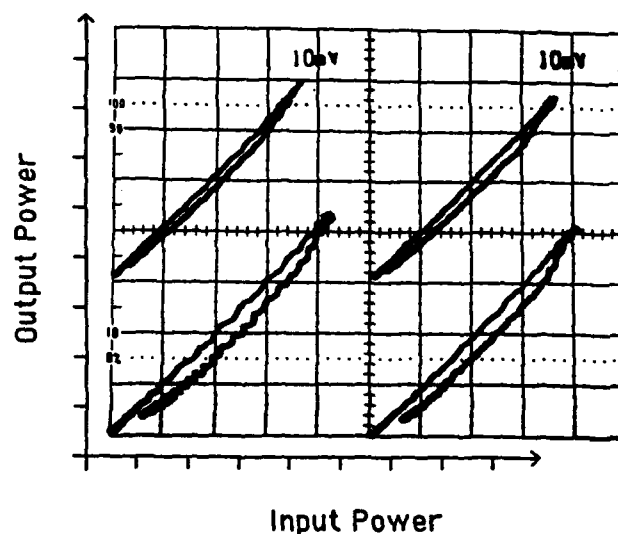


Figure 4. Absorptive optical bistability observed for SINC film etalon with pulse width  $\tau_p = 40$  ns and wavelength  $\lambda = 799$  nm.[3]

A nonlinear optical system of sufficiently large cooperativity  $C$  is analogous to an Ising spin system at a temperature below  $T_c$ . The transmitted output field amplitude  $x$  (order parameter) can then be either in a low, or in a high, transmittance state for a given incident light intensity and can exhibit hysteresis as the incident light field  $y$  (external field) is increased and decreased.

#### 4.2. Absorptive optical bistability in random glassy polymers

Based on the unusually large resonant nonlinear refractive index  $n_2$  of the SINC films, absorptive optical bistability was observed at nanosecond timescales in Fabry-Perot etalons containing the films as the active medium. Figure 4 shows the bistable hysteresis behavior typically observed for incident single mode, nanosecond pulses tuned near the maximum saturable absorption. These data are for a pure SINC ultrathin film with 40 ns pulses at wavelength 799 nm with incident light intensity of  $160 \text{ kW/cm}^2$ . The driving field is resonant with a narrow saturable absorption line within the Q-band envelope and a single mode of the Fabry-Perot cavity. Due to the resonant conditions, the medium is suddenly bleached beyond a critical driving field, and each optical site is then collectively coupled through the cooperative dipole radiation field within the cavity. The high critical field of the macroscopic ordered state cannot be supported by the cavity, and stimulated emission of coherent monochromatic light suddenly occurs from the macroscopic state. As the field within the cavity decreases, the system returns to the initial low transmission

state but via a different path because the cooperative field effectively acts as an internal coercive field, resulting in the observed bistable hysteresis.

The bistable loop does not show a sharp, high contrast, switching on and switching off. According to the Ginzburg-Landau description of optical bistability of section 4.1, the magnitude of the hysteresis depends on a number of relevant physical parameters. Among these, the cooperativity  $C$  is the most important factor in determining the size of the hysteresis loop. In our experiment, the value of  $C$  is relatively low at about 10, which results in the observed low contrast loop. Current experiments in our laboratory are focused on this issue, and measurements are being performed as a function of film thickness, optical density, cavity length, and pulse width.

## 5. ELECTROOPTIC POLED POLYMERS FOR INTEGRATED OPTICS

### 5.1. Comparison of electrooptic poled polymers and inorganic crystals as nonlinear optical materials

Electrooptic polymers offer potentially significant advantages over conventional inorganic electrooptic crystals, such as  $\text{LiNbO}_3$  and GaAs, in several key areas of integrated optics technology, as summarized in Table 1. The most striking advantage, and the main reason for the intense interest in these materials, is due to the intrinsic difference in the electrooptic mechanism. Unlike inorganic ferroelectric crystals, where the electrooptic response is dominated by phonon contributions, the electrooptic effect in certain organic materials arises from the electronic excitations on individual molecular sites, yielding extremely large electrooptic coefficients with little dispersion from dc to optical frequencies and, additionally, low dielectric constants. Poled polymer organic materials have been developed which exhibit electrooptic coefficients nearly twice as large as that of  $\text{LiNbO}_3$ [18] coupled with a dielectric constant nearly an order of magnitude smaller. The low dielectric constant is essential to the success of high bandwidth modulators due to the resulting lower velocity mismatch between the RF and optical waves, and could lead to an improvement of more than a factor of 10 in the bandwidth-length product over current  $\text{LiNbO}_3$  devices.

The microscopic molecular origin of the second order nonlinear susceptibility,  $\chi^{(2)}$ , and linear electrooptic coefficient,  $r$ , in organic materials is now well understood theoretically [19][20] and experimentally[21]-[24], and the materials are ready for device implementation. The materials research effort in recent years has centered on the inclusion of the nonlinear optical moiety in a guest/host or polymer system with appropriate linear optical, mechanical and processing properties and the artificial creation of the desired symmetry through electric field poling.[25][26] These materials can then be simply and rapidly spun coat into high quality thin films, processed with standard photolithographic techniques and poled quickly and efficiently. In addition, channel waveguides and integrated optic circuits can be defined by the poling process itself[2] or by a variety of well understood micro-machining techniques. These processes represent a considerable increase in fabrication flexibility and processing simplicity over current titanium indiffused  $\text{LiNbO}_3$

Table 1 Comparison of Ti:LiNbO<sub>3</sub> and Electrooptic Polymers in Integrated Optics Technologies.

<u>PHYSICAL &amp; DEVICE PROPERTIES</u>	<u>Ti:Lithium Niobate</u>	<u>Electrooptic Polymers</u>
Electrooptic coefficient (pm/V)	32	10-50
Dielectric constant	28	4
Loss (dB/cm @ l=1.3 mm)	0.1	0.2-0.5
Space-bandwidth product (GHz-cm)	10	120
Crystal Growth Temperature, °C	1000	NA
Waveguide Processing Temperature, °C	1000	150-200
Waveguide Processing Time	10 hr.	10 min.
Multiple Layers Possible	No	Yes
Fabrication & processing	difficult	simple
Packaging	expensive	UNKNOWN
Maturity	30 years	10 years

waveguide technology, which requires processing at temperatures approaching 1000°C after expensive and difficult crystal growth. A serious limitation of LiNbO<sub>3</sub> modulators is the velocity mismatch between the electrical wave traveling down the electrodes and the optical wave traveling down the optical waveguide. The RF field from the electrodes extends into the dielectric material and thus travels with a velocity  $v = c/\sqrt{\epsilon_{eff}}$  where  $c$  is the free space velocity of light and  $\epsilon_{eff}$  is the effective dielectric constant of the waveguide structure. For LiNbO<sub>3</sub>  $\epsilon_{eff}$  is 38, while for the poled polymer films  $\epsilon_{eff}$  is typically 3 - 4. The light, however, travels down the waveguide with a velocity  $v = c/n$ , where  $n$  is the index of refraction of the waveguide material, which for LiNbO<sub>3</sub> is 2.2 and for the poled polymer films 1.57. Thus, the optical and electrical waves traveling down the device structure gradually get out of phase with each other, and for a given device interaction length there is a maximum frequency,  $f_c$ , at which the device can be driven. The high speed modulation limit of the material can be estimated by the bandwidth length product given by [27]:

$$f_c L = \frac{1}{c(\sqrt{\epsilon_{eff}} - n)} \quad (5.1)$$

For  $\text{LiNbO}_3$ ,  $f_c L$  is 9.6 GHz-cm for a standard Mach Zehnder configuration, while for the electrooptic poled polymer films  $f_c L$  can be as high as 150 - 200 GHz-cm. Thus, for this new class of materials the primary limitation of  $\text{LiNbO}_3$  for high speed modulation in the 20 - 40 GHz range is effectively removed. The limiting factor for the poled polymer films will probably be RF loss in the electrodes, which increases as the square root of the drive frequency.

### 5.2. Poled Polymer Waveguides

Integrated optic devices based on electrooptic polymers can be fabricated by spinning the material into high quality thin films on optical substrates. As spun, the films are isotropic and thus exhibit no linear electrooptic effect. In addition to inducing a non-centrosymmetric structure to achieve a macroscopic electrooptic effect, a second major feature must be achieved in the material to enable the fabrication of integrated optic circuits. Channel waveguides must be formed to confine and guide the light from one active element of the integrated optic circuit to another range is effectively removed. For  $\text{LiNbO}_3$ ,  $f_c L$  is 9.6 GHz-cm for a standard Mach Zehnder configuration, while for the electrooptic poled polymer films  $f_c L$  can be as high as 150 - 200 GHz-cm. Thus, for this new class of materials the primary limitation of  $\text{LiNbO}_3$  for high speed modulation in the 20 - 40 GHz range is effectively removed. The limiting factor for the poled polymer films will probably be RF loss in the electrodes, which increases as the square root of the drive frequency. Electric field poling has been extensively studied as a means to partially align nonlinear optical molecules in an inert polymer matrix to induce a macroscopic electrooptic coefficient.[25] Figure 5 illustrates a new, powerful method, by which channel waveguides can be fabricated by the poling process itself.[2] An electrode pattern, defining the channel waveguides, is deposited on an optical substrate and covered with a buffer layer, to isolate the active waveguide layer from the electrode. The buffer material must be chosen to have an index lower than the guiding layer and to be compatible with the required processing. The electrooptic polymer is spun directly onto the lower buffer layer, and different buffer layers are often used with different nonlinear polymers. A metal ground plane is then deposited directly onto the nonlinear polymer for poling using standard photolithographic techniques. The nonlinear layer is then poled by applying an electric field above the polymer glass transition temperature and cooling the sample to room temperature under the influence of the field. The degree of alignment induced and the resultant electrooptic coefficient can be calculated based on a statistical average of the molecular susceptibilities. In this case only those regions of the polymer film defined by the electrode pattern are poled.

Since most organic nonlinear optical molecules also possess an anisotropic microscopic linear polarizability, the poled region becomes birefringent. The poled regions are uniaxial, with  $n_e$  oriented along the direction of the poling field. Consequently, TM waves propagating along the device structure will experience a greater refractive index in the poled regions than in the unpoled regions, and so can be confined in the lateral dimension. Thus, by applying the poling fields using electrodes patterned to define the waveguide network, including both active and passive sections,



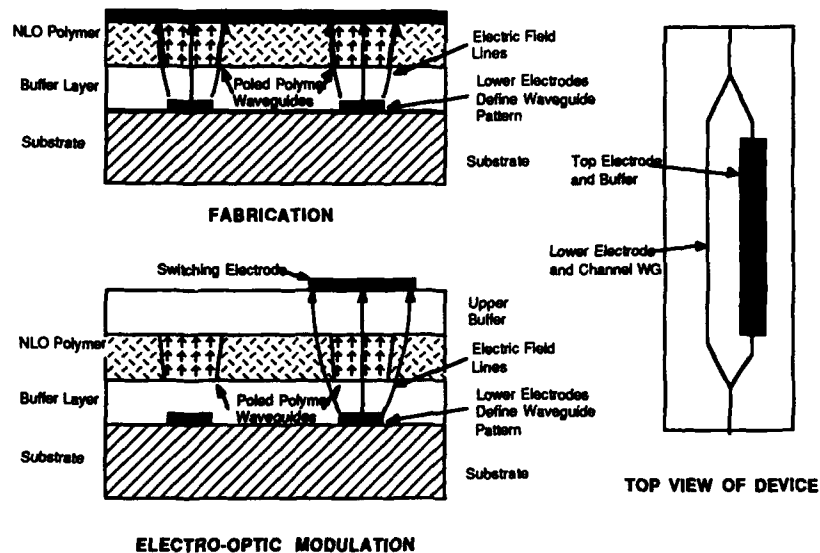


Figure 5. Fabrication of Channel Waveguide by Electric Field Poling.

no further patterning of the polymer layer is required in order to form the channel electrooptic waveguide structures. The devices are then completed by etching off the poling electrode, applying an upper buffer layer and depositing the patterned switching electrodes, as shown in Figure 5. The switching electrodes are positioned to address only the sections of the guide desired to be active. A photograph of a section of poled waveguide is shown in Figure 6. The region on the left is unpoled and the light fans out and is clearly unguided. The region on the right has been poled, and the light is clearly guided and confined to the waveguide region. Using this technique, poled polymer channel waveguides have been fabricated, and modulators, couplers, and bends in electrooptic polymer films have been demonstrated.

## 6. CONCLUSION

In summary,  $\pi$ -electron excitations in low dimensional conjugated structure are responsible for the large resonant and nonresonant nonlinear optical responses of polymeric systems. A SINC film behaves as an easily saturable, optical Bloch system with unusually large values for the linear absorptivity coefficient  $\alpha_0$  of  $1 \times 10^5 \text{ cm}^{-1}$  and intensity dependent refractive index  $n_2$  of  $1 \times 10^{-4} \text{ cm}^2/\text{kW}$ . The  $n_2$  value is the largest observed to date for a conjugated structure and is the basis for the electronic absorptive bistable behavior in random glassy polymer films mediated by the nonlinear electronic excitations occurring within the quasi-two dimensional disc-like SINC structures. Electrooptic effects, such as waveguide operations, are demonstrated in polymer channel waveguides fabricated by electric field poling process. With high electrooptic coefficients

of 10-50 pm/V and low dielectric constants of 3-4, poled polymers have potentially great advantages over inorganic crystals as electrooptic materials.

## 7. ACKNOWLEDGEMENTS

This research was generously supported by the U.S. Air Force Office of Scientific Research and the U.S. Defense Advanced Research Projects Agency Grant No. F49620-85-C-0105. We gratefully acknowledge the scientific contributions of Drs. R.A. Norwood, P. Kalyanaraman, J. Sounik of Hoechst Celanese, and Dr. K. Aron of Lockheed.

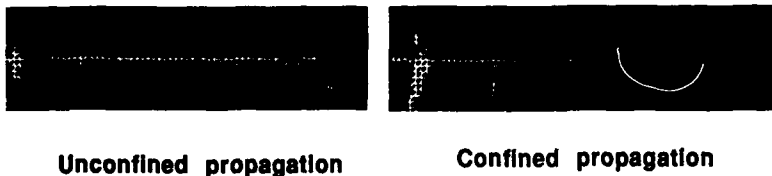


Figure 6. Photograph of a Poled Polymer Waveguide.

## 8. REFERENCES

- [1] See for example, *Organic Materials for Nonlinear Optics*, Hann, R.A. and Bloor, D. ed., Roy. Soc. Chem., London (1989)
- [2] Thackara, J.I., Lipscomb, G.F., Stiller, M.A., Ticknor, A.J., and Lytel, R., *Appl. Phys. Lett.* **52**, 1031 (1988)
- [3] Wu, J.W., Heflin, J.R., Norwood, R.A., Wong, K.Y., Zamani-Khamiri, O., Garito, A.F., Kalyanaraman, P., and Sounik, J., *J. Opt. Soc. Am.* **B6**, 707 (1989)
- [4] Anderson, P.W., Halperin, B.I., and Varma, C., *Philos. Mag.* **25**, 1 (1972)
- [5] Nicolis, G. and Prigogine, I., *Self-Organization in Non-Equilibrium Systems: From Dissipative Structures to Order Through Fluctuations*, Wiley, New York (1977)
- [6] Bonifacio, R. and Lugiato, L.A., *Phys. Rev. Lett.* **40**, 1023 (1978)
- [7] Wu, J.W., Ph.D. dissertation, University of Pennsylvania, University Microfilms International, Ann Arbor, Michigan (1989)
- [8] Orr, B.J. and Ward, J.F., *Mol. Phys.* **20**, 513 (1971)
- [9] Heflin, J.R., Wong, K.Y., Zamani-Khamiri, O., and Garito, A.F., *Phys. Rev.* **B38**, 1573 (1988)
- [10] See, for example, Gibbs, H.M., *Optical Bistability - Controlling Light with Light*, Academic, New York (1985)

- [11] Kubo, R., in Stochastic Processes in Chemical Physics, ed. Shuler, K.E., *Advances in Chemical Physics*, Prigogine, I. and Rice, S.A. eds. Wiley, New York (1969) vol. 15
- [12] Zwanzig, R., *J. Chem. Phys.* **33**, 1338 (1960); *Phys. Rev.* **124**, 983 (1961)
- [13] Burns, M.J., Liu, W.K., and Zewail, A.H. in Springer Series in Chemical Physics, vol. 3: Spectroscopy and Excitation Dynamics of Condensed Molecular Systems, North-Holland, New York (1983)
- [14] Volker, S. and Macfarlane, R., *IBM J. Res. Develop.* **23**, 547 (1970)
- [15] McCumber, D.E. and Sturge, M.D., *J. Appl. Phys.* **34**, 1682 (1963)
- [16] See, for example, Gibbs, H.M., *Optical Bistability - Controlling Light with Light*, Academic, New York (1985)
- [17] Landau, L.D. and Lifshitz, E.M., *Statistical Physics*, Part 1, 3rd ed. Pergamon, Oxford (1978)
- [18] See, for example, Nonlinear Optical Properties of Polymers, MRS Symposium Proceedings, Vol. 109, A.J. Heeger, J. Orenstein and D.R. Ulrich eds., 1988.
- [19] Lalama, S.J. and Garito, A.F., *Phys. Rev.* **A20** 1179 (1979).
- [20] See, for example, Pugh, D. and Morley, J.O. in reference 1.
- [21] Singer, K.D. and Garito, A.F., *J. Chem. Phys.* **75**, 3572 (1981).
- [22] Teng, C.C. and Garito, A.F., *Phys. Rev. Lett.* **50**, 350 (1983).
- [23] Lipscomb, G.F., Garito, A.F., and Narang, R.S., *Appl. Phys. Lett.*, **38**, 663 (1981).
- [24] Lipscomb, G.F., Garito, A.F., and Narang, R.S., *J. Chem. Phys.*, **75**, 1509 (1981).
- [25] Singer, K.D., Sohn, J.E., and Lalama, S.J., *Appl. Phys. Lett.* **49**, 248 (1986), and Singer, K.D., Kuzyk, M.G., and Sohn, J.E., *J. Opt. Soc. Am.* **B4**, 968 (1987).
- [26] Williams, D.J., in Nonlinear Optical Properties of Organic Molecules and Crystals, Vol. 1, Chemla, D. and Zyss, J. ed., Academic Press, NY (1987), p. 405.
- [27] Krotky, S.K. and Alferness, R.C. in Integrated Optical Circuits and Components, Hutchenson, L.D. ed., Marcel Dekker Inc., New York, 1987, p.203.

## NEW SECOND-ORDER NONLINEAR OPTICAL ORGANIC CRYSTALS

D.S. DONALD, L.-T. CHENG, G. DESIRAJU, G.R. MEREDITH AND F.C. ZUMSTEG  
 E.I. du Pont de Nemours & Co., Central Research and Development Department,  
 Experimental Station, Wilmington, DE 19880-0328

## ABSTRACT

The design of molecular crystals with specific optical properties, which are thought to arise from constituent molecules' polarizability properties, is a desirable but currently unachievable goal. One can partially achieve this goal by choosing compounds with specific molecular attributes and empirically determining the manner in which these are translated into crystal properties. Besides the fact that there are no certain rules for prediction of crystal packing arrangements, there is also a problem in specifying molecular properties from what are today incomplete polarizability structure-property relationships. We have, realizing these limitations, identified new molecular crystals by a nonlinear optical (powder-SHG) scouting-screening program from lists of compounds chosen because of desirable molecular properties. Examination of successful materials has revealed interesting, new alignment motifs. Some of these materials, a set of halogen and cyano derivatives of aromatic compounds, are described relating properties and structures of molecules and crystals. In particular, the orientation directing influence of intermolecular halogen-cyano interactions and the use of heterocyclic compounds to improve transparency in the near infrared and in the blue and near ultraviolet spectral regions are demonstrated.

## INTRODUCTION

Recent activity in the design and selection of organic materials for second-order nonlinear-optical (NLO) applications, such as second harmonic generation (SHG), has produced a variety of techniques for generating the, by now, well known requisite asymmetrically aligned ensembles [1]. An oriented-gas model is often used to relate microscopic-molecular and macroscopic-crystalline dielectric properties [1, 2]. In this model molecules are thought to have some molecule-specific polarizability attributes (which may be more realistically considered to be those of molecules in the condensed phase, as opposed to molecules in vacuum), and, in addition to being polarized by the Maxwellian electric fields, are mutually polarized by fields arising from polarization of neighbors. Disregarding anisotropy of local-field corrections  $f$ , the second-order NLO susceptibility tensor is approximated as the volume-normalized, local-field corrected, orientational average of second-order hyperpolarizability tensor

$$\chi^{(2)} \approx (N/V) \langle \beta \rangle_{\text{orientation}} f f f \quad (1)$$

Straightforward geometric considerations of a crystal's sublattices allow an understanding of the gross features of  $\chi^{(1)}$  and  $\chi^{(2)}$ . For example, if two molecular sublattices exist whose sites are related by an inversion center,  $\langle \beta \rangle$  and the nonlinearity vanish. In other cases interferences intrinsic to orientational averaging of polar odd-rank tensors reduce the degree of projection of the molecular nonlinearity to the macroscopic level. Obviously for each crystal class there are optimal molecular orientations on the sublattices. These optimal orientations depend on the nature of the molecular  $\beta$ , particularly on the effective dimensionality of polarizability. Many of the molecular examples described below have high symmetry with a well defined dipole and charge-transfer axis. It is expected that they can be reasonably described, then, as 1-D nonlinearly polarizable entities (with higher dimensionality linear polarizability).

Strategies to effect good alignment have included reduction of crystal symmetry by occlusion [3], inclusion complexation [4] and alignment associated with a strong, directing intermolecular interaction such as hydrogen bonding [5]. Such techniques have been somewhat successful, but the prediction of crystal structure from considerations of the molecular structure of organic materials is still highly problematical. It will be shown below that halogen-cyano

## 4 - Chlorobenzonitrile Crystals

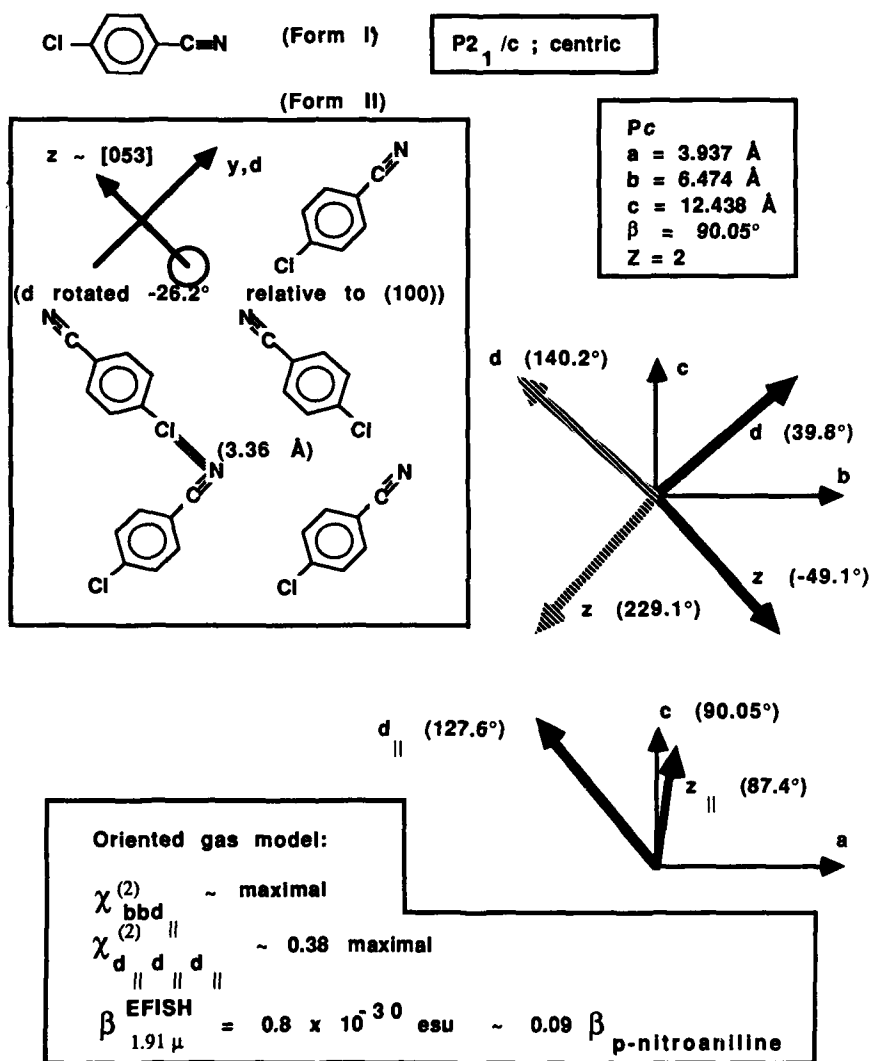


Figure 1. Summary of the crystal structures of 4-chlorobenzonitrile, molecular orientations and their influence on  $\chi^{(2)}$ .

interactions offer an alternative, advantageous intermolecular directing factor.

The materials design and selection processes are further complicated when additional requirements such as transparency in the near infrared, for example around the 1.3 and 1.55 micron wavelengths associated with optical communications applications, or transparency in the blue and near ultraviolet, for applications employing frequency doubled light from compact, efficient and inexpensive diode lasers which lase in the 0.8-0.9 micron wavelength range. These restrictions dictate the absence of hydrogens in the former case and the need for polarizable and polar structures, while still maintaining transparency in the visible, in the latter case. Obviously the utilization of hydrogen bonding potential as a selection criterion is of little use if near IR transparency is a requirement.

The incorporation of heteroatoms in organic structures can be advantageous for both of the aforementioned applications. Most organic heterocycles contain fewer hydrogens than their carbon analogs and indeed many are hydrogen free. In addition, the substitution of heteroatoms for carbon generally results in a hypsochromic shift in the UV spectrum. A further improvement in the ability to select potential NLO candidates meeting these criteria would be to use some structural feature or features analogous to hydrogen bonding that would influence crystal packing properties in a more or less predictable way, even if only within a restricted class of compounds. The intermolecular halogen-cyano interaction is one such feature.

## RESULTS AND DISCUSSION

The well known intermolecular aromatic chlorine-chlorine close interaction in many organic crystals is one potentially useful orientation directing feature [6]. A search of the Cambridge Crystal Data Base revealed that a similar halogen-cyano close interaction is also pervasive [7]. In the course of screening a wide variety of organic materials by the powder SHG method we have found an unusually large fraction of such compounds to exhibit activity. The directing influence of the interaction is illustrated in the crystal structures of the 4-halobenzonitriles [7] as outlined in Figures 1 and 2.

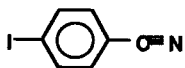
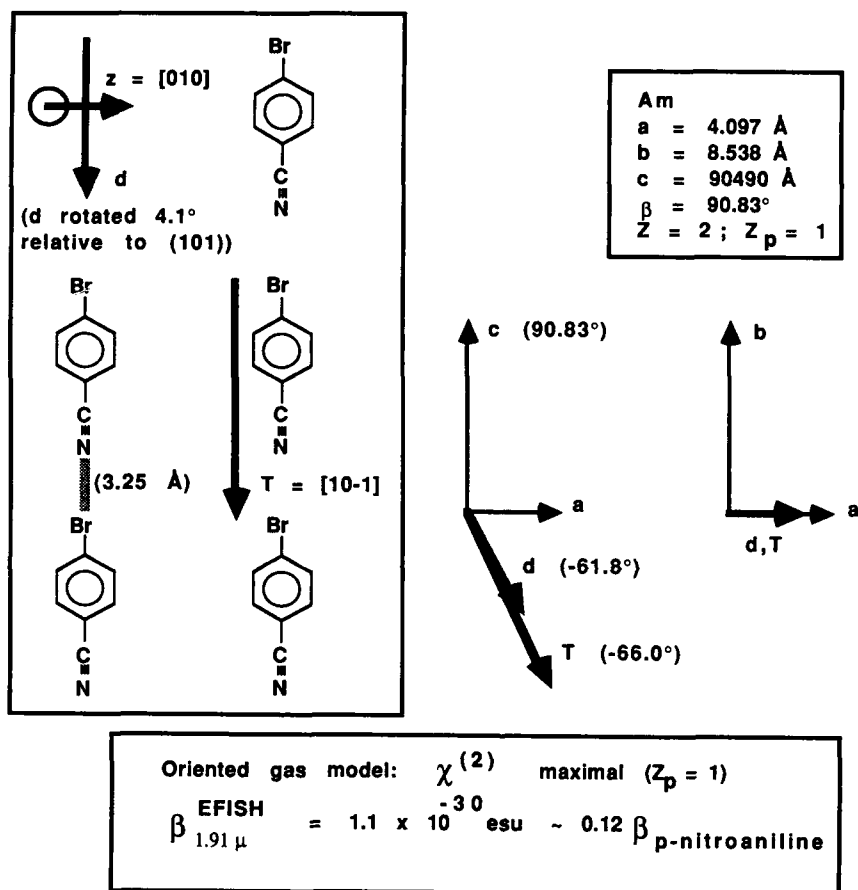
### 4-Halobenzonitrile Structures

The 4-chloro- (Form I), 4-bromo- and 4-iodo-benzonitrile crystals (CBN, BBN and IBN, respectively) exhibit similar structures: linear arrays of molecules, with close contacts between halogen and nitrogen atoms on neighboring molecules, form a primary alignment motif. This motif is best exemplified by BBN (Figure 2). In BBN the importance of this interaction is indicated by the fact that the 3.25 Å Br-N contact is particularly short. The arrays of this primary motif are organized in higher, secondary structures. For BBN the arrays are rigorously parallel, resulting in an interesting NLO crystal, and for CBN (Form I) and IBN the arrays are rigorously antiparallel, resulting in centrosymmetric structures with no significant second-order NLO value. Since the BBN structure has only one sublattice, according to Eq. (1) the projection of  $\beta$  into  $\chi^{(2)}$  is perfect. According to the charge-transfer mechanism of second-order nonlinearity [1] the hyperpolarizability can be approximated to be one-dimensional, in this case along the molecular dipole  $d$ .  $\chi^{(2)}$  <sub>ddd</sub> then is maximal. The mixed polarization components such as  $\chi^{(2)}$  <sub>e'ee</sub> or  $\chi^{(2)}$  <sub>ee'e</sub> can be maximum, in contrast to crystals with interfering sublattices, for sets of angles where perpendicular projecting unit vectors  $e$  and  $e'$  fulfill the requirement  $(e \cdot d)^2 (e' \cdot d) = 2/\sqrt{27}$  (i.e. make angles of 35.26° and 54.74° with  $d$ ).

As an aside we note that for BBN, and CBN (Form II) as described below, though the angle of the unit cell in these monoclinic structures is very close to 90°, the optics of these crystals are not close to optics of orthorhombic systems. In the ac planes the principle linear polarizability axes are not constrained to be parallel to the a or c axes nor is there a symmetrical distribution of these molecular axes about them. Thus the principal indicatrix axes will not necessarily fall along the a or c axes as required in orthorhombic crystals.

In addition to the centrosymmetric antiparallel-linear-chains crystal structure, CBN has exhibited a subtly formed, more stable polymorph as depicted as Form II in Figure 1. A zig-zag

## 4 - Halobenzonitrile Crystals (continued)



I2/a ; centric

Figure 2. Summary of the crystal structures of 4-bromobenzonitrile and 4-iodobenzonitrile, molecular orientations and their influence on  $\chi^{(2)}$ .

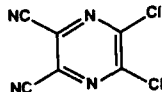
chain motif appears. When projected onto (100) the sequence of molecules in the chains is seen to alternate between members of the two sublattices. Though there are two sublattices, all molecules are rotated  $26.2^\circ$  (downward) out of this plane as measured around the shorter in-plane molecular axis  $z$  (because the glide plane is perpendicular to the  $b$ -axis). The orientation of projections of the longer in-plane molecular axes  $y$ , which are also the dipole axes, onto (010) is identical for both sublattices. A one-dimensional hyperpolarizability model predicts that the mixed polarization element,  $\chi_{bbll}^{(2)}$  ( $d_{||}$  is the projection of  $d$  onto (010)), is nearly maximal in this class since  $d$  projects at  $39.8^\circ$  and  $50.2^\circ$ , respectively, onto the  $b$ -axis and into the glide plane (as above, maximum occurs at  $35.26^\circ$  and  $54.74^\circ$ ).

The molecular hyperpolarizabilities  $\beta^{EFISH}$  as determined in solutions by dc-electric-field-induced second-harmonic generation (EFISH) with 1.91 micron radiation [8] show the influence of the increased electron donating strength of bromine compared to chlorine. The use of such a long wavelength for EFISH studies makes possible the observation of the influence of chemical structure on hyperpolarizability. Shorter wavelength experiments result in dispersion-enhanced values which are more strongly affected by variations in the actual energies of the lower lying electronic excitations rather than the global molecular properties. In this nondispersively enhanced regime the halo-cyano-aromatics here and below compare modestly to the well known nonlinear *p*-nitroaniline compound. These values may be used with Eq. (1) to estimate crystal nonlinearities.

The similarity of structures among the 4-halobenzonitriles argues for the importance of the directing influences of specific intermolecular interactions. However, the secondary structures, while quite closely related [7], have drastically different consequences for second-order nonlinearity in this systematic and closely related set of compounds. Thus while one sees benefits in affecting local intermolecular alignment, the prospect of global design and control of crystal packing seems dim given the subtle nature of the differences. As stated above and to be further demonstrated below, though, the halo-cyano interaction seems to provide a positive tendency for NLO-useful alignment which can be exploited.

#### Halo-dicyano-pyrazine Compounds and Structures

In the course of the SHG powder screen we have found a class of halogen and cyano-containing heterocycles in which the halo-cyano close interaction appears to be a significant influence in the crystal packing behavior as indicated both by high incidence of activity and preliminary structure determinations. In addition, a few of the members of this class also meet the criteria of visible and near IR transparency.



Solution UV:  $\lambda_{max}^{CH_2CN}$  304 nm( $\epsilon$  8,300), 253 nm( $\epsilon$  11,700),  
211 nm( $\epsilon$  26,900)

Diffuse reflectance UV: No absorption beyond 380 m $\mu$

Near infrared transparent: No absorption from 2.5 to 4.0  $\mu$ m

Powder SHG: 500 x Quartz

$\beta^{EFISH}$  at 1.91  $\mu$ m:  $1.7 \times 10^{-30}$  esu ( $\mu = 4.4 \times 10^{-18}$  esu)

Single crystal structure: monoclinic  $P2_1$ (No. 4)

Figure 3. Properties of 2,3-dichloro-5,6-dicyanopyrazine (DCDCP).



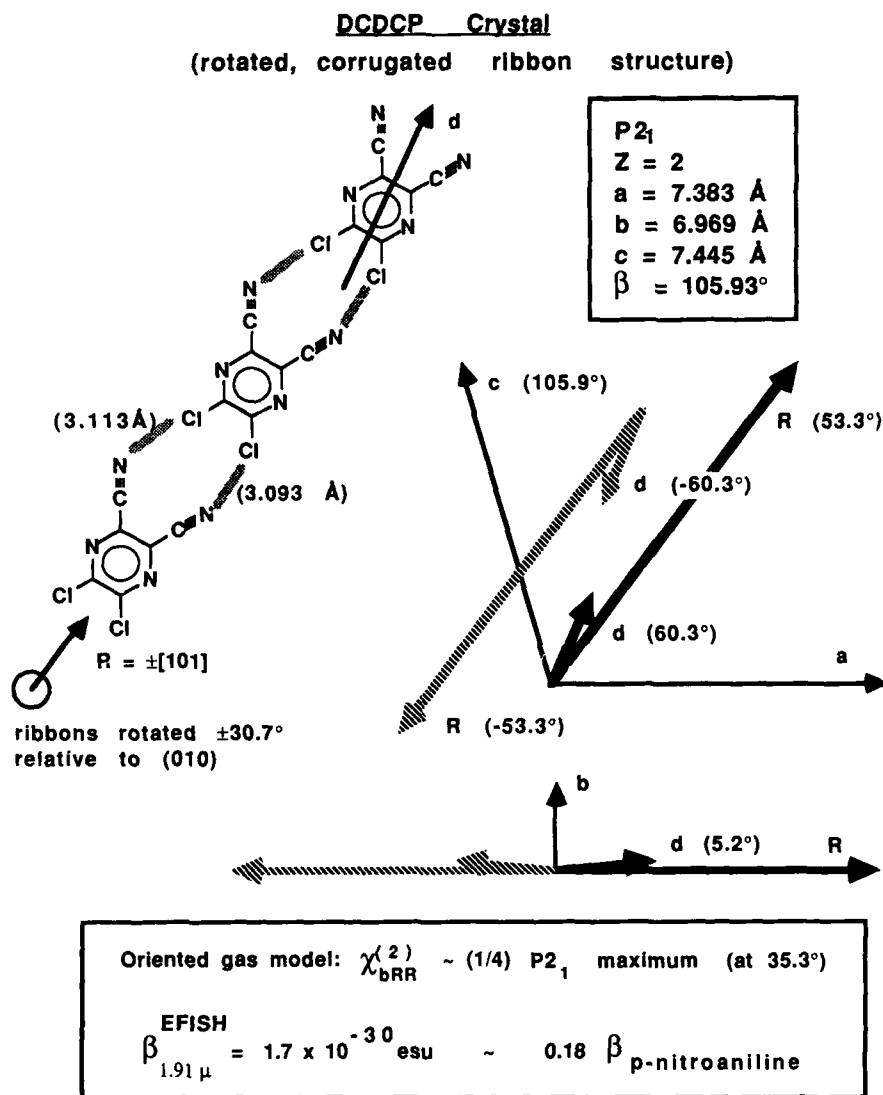


Figure 4. Summary of the crystal structure of DCDCP, molecular orientations and their influence on  $\chi^{(2)}$ .

Figure 3 shows some pertinent properties of one interesting member of this class of halo-cyano pyrazines: 2,3-dichloro-5,6-dicyanopyrazine (DCDCP) [9, 10]. The crystal structure is portrayed in Figure 4. A primary motif, molecular ribbons formed by close approach of both chlorine atoms of a molecule to the two nitrogen atoms of the cyano groups of its neighbor, is emphasized. The 3.1 Å contact angles are among the smallest known (compare Figure 1). Each ribbon consists of molecules related by a [101] translation  $R$ . The molecular dipoles are tilted  $7.0^\circ$  and  $5.2^\circ$  from  $R$  as measured in the orthogonal  $ac$  and  $bR$  planes. The ribbons are rotated  $30.7^\circ$  about  $R$  relative to the  $ac$  plane. Each ribbon consists exclusively of molecules from one of the two sublattices. The sublattices are related by the two-fold screw axes which lie parallel to the  $b$  axis. The ribbons are thus exactly antiparallel. The  $5.2^\circ$  tilt ( $\theta$ ) of the dipoles relative to the  $ac$  planes creates the polar structure which allows nonvanishing nonlinearity. Since in the 1-D hyperpolarizability model  $\chi_{bRR}^{(2)} \propto \cos^2\theta \sin\theta$ , which as noted above is maximized at  $35.3^\circ$ , in DCDCP it is nearly (1/4) of the maximum achievable in this class (which is one of the preferred classes for maximizing these projections [1]). Even though the tilt angle is small a substantial fraction of achievable susceptibility is created due to the relatively slow fall-off of these susceptibilities with deviation from optimal. Further, we note that the molecular nonlinearity compares favorably to the well known value for *p*-nitroaniline in the nondispersive regime.

One of the chlorine atoms in DCDCP is very readily replaced by nucleophiles [10]. This is illustrated in Figure 5 wherein the nucleophiles are variously substituted amines. This seemed a good strategy to pursue since amines are recognized as stronger donors and would be expected to enhance molecular hyperpolarizability. The incidence of SHG activity is very high in products of this type.

The structure of one of these in its crystal is shown in Figure 6. In this crystal's structure ( $P2_1$ ,  $a = 8.843$  Å,  $b = 8.323$  Å,  $c = 11.404$  Å,  $\beta = 101.48^\circ$ ,  $Z = 2$ ) the lone chlorine appears to be shared nearly equally between the two cyano groups with again a rather short 3.31 Å contact between the chlorine (Cl1) and the nitrogen (N4) of one of the cyano groups of a neighboring molecule. The packing is a variation of the DCDCP case, again with antiparallel molecular ribbons being the dominant feature.

The dibromo analog of DCDCP behaves in a completely analogous way as shown in Figure 7.

Although a single crystal X-ray structure of DBDCP is not yet available, the structure of a bromo analog of the chloro compound shown in Figure 6 has been obtained ( $P2_1$ ,  $a = 8.934$  Å,  $b = 8.294$  Å,  $c = 11.474$  Å,  $\beta = 101.63^\circ$ ,  $Z = 2$ ) and the packing is the same. In fact the bromo-cyano (Br1-N4, Figure 8) contact distance is slightly shorter in this case, being 3.23 Å as compared to 3.31 Å in the chloro analog.

The importance of the halogen-cyano interaction from a purely phenomenological point of view is exemplified by the observation that in all comparisons examined to date the substitution of a cyano for the last remaining halogen on these structures, thus eliminating the possibility of any halo-cyano interaction, results in a complete loss of SHG activity. These compounds are readily prepared by displacement of a cyano group in tetracyanopyrazine (TCP) as illustrated in Figure 9 [10,11].

The structures of the products of the displacement of a chloro, bromo or cyano group by the action of a primary amine on DCDCP, DBDCP or TCP have been depicted as only one of two possible tautomeric forms that are possible for compounds of this type. Indeed, in all crystal structures that we have obtained to date the form with the hydrogen on the exocyclic nitrogen has been observed (Figure 10). However, any solution measurements made on these compounds must take this possibility into account. Of course the dichloro- and dibromodicyanopyrazines do not exhibit this potential ambiguity.

In the process of measuring  $\beta^{EFISH}$  it became apparent that the potential for mixtures resulting from tautomeric shifts in solution could severely compromise the results. Since we wish to correlate crystal activity with crystal structure and molecular hyperpolarizability, we have begun a study of the tautomericly immobilized versions of the primary amino substitution products. These are readily prepared by simply using a secondary amine instead of the primary amine in the reactions shown in figures 5, 7 and 9. An example wherein *N*-methyl-4-chloroaniline was allowed to react with DCDCP is shown in Figure 10. An almost

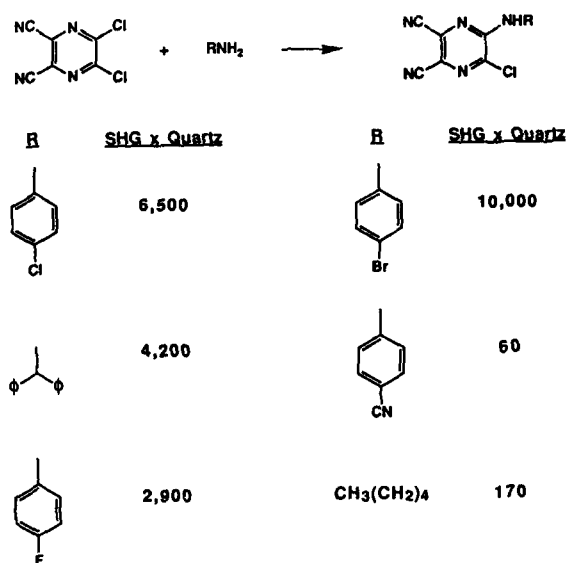


Figure 5. Amine derivatives of DCDCP and their powder SHG behavior.

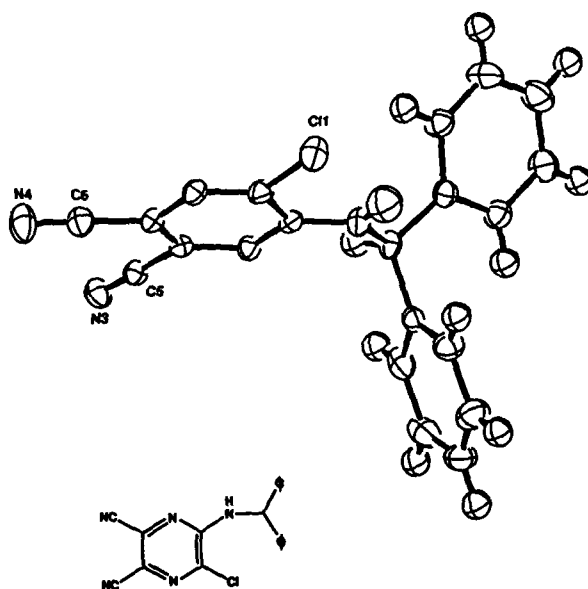


Figure 6. Structure of a DCDCP derivative.

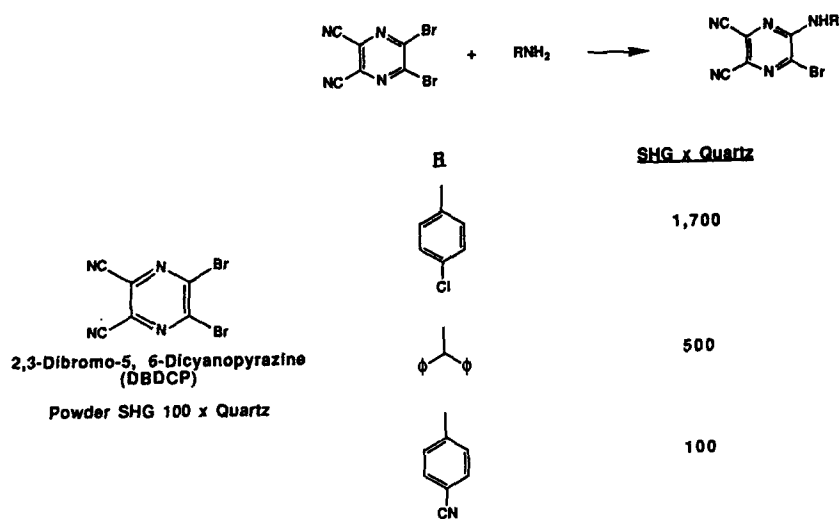


Figure 7. Amine derivatives of DBDCP and their powder SHG behavior.

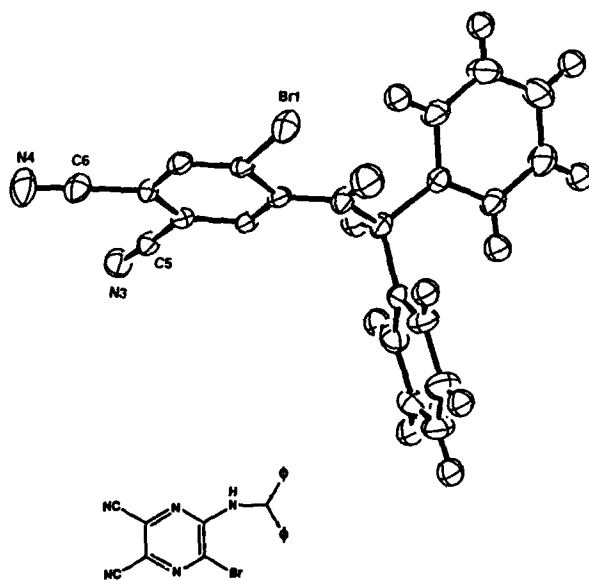
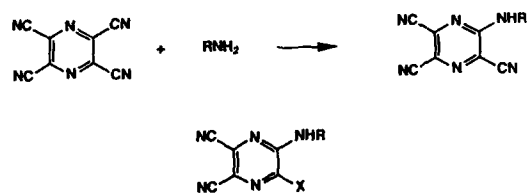


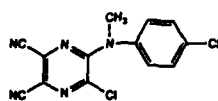
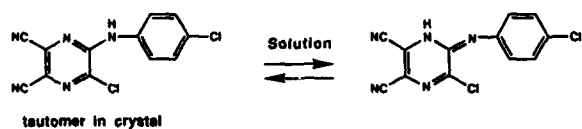
Figure 8. Structure of a DBDCP derivative.



X	R	SHG x Quartz
Cl		6,500
Br		1,700
CN		0
Cl		10,000
Br		4
CN		0
Cl		60
Br		100
CN		0

Figure 9. Variation of molecular alignment in crystals with chloro replacement in the amino derivatives of DCDCP as monitored by powder SHG.

#### Tautomeric Mobility and $\beta$ Determination



$$\beta_{\text{EFISH}} = 3.0 \times 10^{-30} \text{ esu}$$

$$\mu \beta = 1.8 \times 10^{-47} \text{ esu}$$

Figure 10. Tautomeric mobility in amine derivatives of DCDCP.

identical value of the "mu-beta" product for this compound and an unblocked analog suggests that in the solvent employed, N-methylpyrrolidinone, the tautomer with the exocyclic hydrogen is strongly favored. The possibility that both tautomers have the same value of  $\beta^{\text{EFISH}}$  cannot be ruled out, but this seems unlikely.

These EFISH results indicate that the influence of amino substitution might not increase molecular nonlinearity substantially above the levels of the DCDCP parent (Figure 4). When the increased molecular volume is considered, the more relevant volume normalized hyperpolarizabilities which occur in Eq. (1) are probably equal to or less than DCDCP.

However,  $\beta^{\text{EFISH}}$  nearly as large as p-nitroaniline have been achieved in nonblocked structures where electron donating groups are attached to the amine. A clearer picture without the uncertainty of tautomeric interference will require similar blocked structures. Given the relatively high SHG results shown by this class of materials, the influence of the primary amine substituents (and other modifications not listed here) on crystal packing and crystal optics is beneficial, warranting further work to characterize these crystals.

#### SUMMARY

The presence of an intermolecular halogen-cyano orientation directing interaction has been discussed in relation to achieving molecular alignment which favorably projects molecular second-order nonlinear polarizability to the macroscopic scale, as modelled in the simple oriented-gas picture. Crystals of the 4-halobenzonitriles display a linear, primary molecular-packing motif which, though highly desirable for this purpose, is overshadowed by the influence of secondary structure. This demonstrates the fragileness of crystal structure prediction. Empirically, though, optimized structures occur in 4-bromobenzonitrile and 4-chlorobenzonitrile (Form II). Extension of the search to heterocycles has revealed the interesting class of halo-dicyanopyrazines. The parent compound, 2,3-dichloro-5,6-dicyanopyrazine, exhibits a crystal packing dominated by ribbons of molecules coupled through the halo-cyano interaction. The secondary packing of these ribbons is rigorously antiparallel, but nonlinearity is achieved through a rotation of molecules out of the ribbons. Even so a nonlinearity within a factor of four of the optimum results. Bromo, primary amine and other substitution effects were investigated. The facile chemistry, high incidence of substantial SHG activity in powder tests and the increased transparency in the blue (due to heteroatoms) and near infrared (due to low or zero content of hydrogens) make this class appealing for further investigation.

#### References

1. D.S. Chemla and J. Zyss, editors, Nonlinear Optical Properties of Organic Molecules and Crystals (Academic Press, New York, 1987).
2. G.R. Meredith, *SPIE Proc.* **824**, 126 (1987).
3. I. Weissbuch, M. Lahav, L. Leiserowitz, G.R. Meredith and H. Vanherzeele, *Chem. Mater.* **1**, 114 (1989).
4. W. Tam, D.F. Eaton, J.C. Calabrese, I.D. Williams, Y. Wang and A.G. Anderson, *Chem. Mater.* **1**, 128 (1989).
5. M.C. Etter and G. M. Frankenbach, *Chem. Mater.* **1**, 10 (1989).
6. G.R. Desiraju, in Organic Solid State Chemistry, edited by G.R. Desiraju (Elsevier, New York, 1987), p. 519.
7. G.R. Desiraju and R.A. Harlow, *J. Am. Chem. Soc.* **111**, 6757 (1989).
8. G.R. Meredith, H. Hsiung, S.H. Stevenson, H. Vanherzeele and F.C. Zumsteg, in

Organic Materials for Nonlinear Optics, edited by R.A. Hahn and D. Bloor (The Royal Society of Chemistry, London, 1989), p. 97.

9. D.S. Donald, U.S. Patent No. 3,879,394 (22 April 1975).
10. D.S. Donald and O.W. Webster, in Advances in Heterocyclic Chemistry, Vol. 41, edited by A.R. Katritzky (Academic Press, New York, 1987), p.1.
11. D.S. Donald, U.S. Patent No. 3,814,757 (4 June 1974); U.S. Patent No. 3,928,351 (23 December 1975).

SYNTHESIS, THERMAL BEHAVIOR, AND SECOND-ORDER  
NONLINEAR OPTICAL PROPERTIES OF CONJUGATED, ACCEPTOR/DONOR COMPOUNDS

JAMES F. WOLFE,\* SUSAN P. ERMER,\* STEVEN M. LOVEJOY,\* DORIS S. LEUNG,\* KENNETH P. ARON,\* GLENN A. HANSEN,\* AND STEVEN P. BITLER\*\*

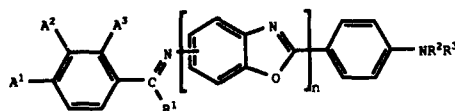
\*Lockheed Missiles & Space Co., Inc., 3251 Hanover St., Palo Alto, CA 94304  
\*\*SRI International, 333 Ravenswood Ave, Menlo Park, CA 94025

ABSTRACT

New noncentrosymmetric compounds having both electron-accepting and electron-donating substituents on a conjugated, aromatic heterocyclic structure were synthesized and their spectroscopic, thermal, and solubility properties were determined. D.C. electric field-induced second harmonic generation (EFISH) experiments were performed to provide values of the second-order nonlinear optical susceptibility/dipole moment product  $\beta\mu$ . Long alkyl substituents were required in heterocycle-containing compounds for sufficient solubility to conduct EFISH analysis. 2,4-Dinitro-substitution on these imine-linked materials gave the highest  $\beta\mu$  in the series.

INTRODUCTION

Our overall objective of this work has been to develop the capability of synthesizing and evaluating materials for applicability in second-order nonlinear optical devices. The material of choice, when processed into a device, must have an optimized combination of both nonlinear optical activity and stability of performance. In other words, the nonlinear optical moiety must have not only a high microscopic nonlinear optical susceptibility, but it must also be processible and thermally stable structurally, be capable of high degrees of orientation, and maintain its orientation with time. Our approach has been to study the effect of the nature and position of substituents on the second-order nonlinear optical susceptibility in a homologous series of compounds that allow the adjustment of these secondary, but just as necessary, characteristics. We have given the name ALHD compounds to this series because of the four components common to each, namely, electron-Acceptor, Linking group, Heterocycle, and electron-Donor. The compounds synthesized in this study have the following general structure:



where  $A^1$ ,  $A^2$ , and  $A^3$  are either H or electron-accepting groups such as nitro, cyano, or dicyanoethenyl.  $R^1$  is either H or methyl, and  $R^2$  and  $R^3$  are either H, methyl, n-hexyl, n-octadecyl, or phenyl. The heterocyclic moiety for this study was a benzoxazole unit ( $n=1$ ), although ALD compounds, i.e.,  $n=0$ , were prepared for comparison. The linking group is an imine moiety in all cases.

RESULTS AND DISCUSSION

Synthesis

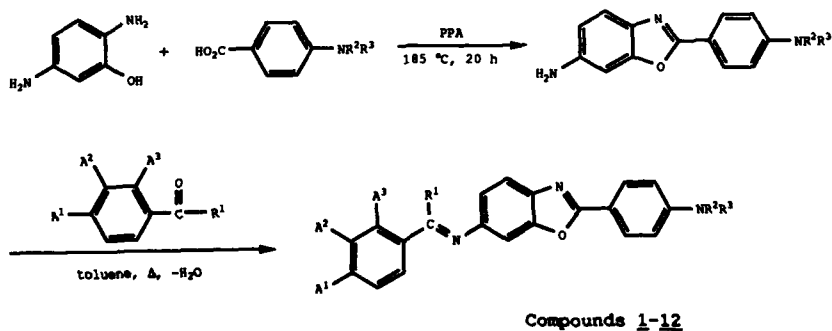
The specific compounds synthesized are shown in Table I. The general method used to prepare compounds 1-12 is shown in Scheme 1. Compound 13 was prepared in an analogous fashion by condensing p-nitrobenzaldehyde with 5-amino-2-[(4-(dimethylamino)phenyl)benzoxazole]. Compounds 14-20 were prepared in toluene by Schiff base condensation of the appropriate aldehyde or ketone



Table I. NLO compounds synthesized and their  $\beta_{11}$  values.

Compound #	A <sup>1</sup>	A <sup>2</sup>	A <sup>3</sup>	R <sup>1</sup>	R <sup>2</sup>	R <sup>3</sup>	n	Attachment <sup>a</sup>	$\beta_{11}$ (cm <sup>5</sup> D/esu) <sup>b</sup>
<u>1</u>	NO <sub>2</sub>	H	H	H	C <sub>6</sub> H <sub>13</sub>	H	1	6	400
<u>2</u>	NO <sub>2</sub>	H	NO <sub>2</sub>	H	C <sub>6</sub> H <sub>13</sub>	H	1	6	4590
<u>3</u>	H	NO <sub>2</sub>	H	H	C <sub>6</sub> H <sub>13</sub>	H	1	6	355
<u>4</u>	CN	H	H	H	C <sub>6</sub> H <sub>13</sub>	H	1	6	
<u>5</u>	DCNV <sup>c</sup>	H	H	H	C <sub>6</sub> H <sub>13</sub>	H	1	6	2440
<u>6</u>	NO <sub>2</sub>	H	H	CH <sub>3</sub>	C <sub>6</sub> H <sub>13</sub>	H	1	6	
<u>7</u>	NO <sub>2</sub>	H	H	H	C <sub>18</sub> H <sub>37</sub>	H	1	6	
<u>8</u>	NO <sub>2</sub>	OH	H	H	C <sub>18</sub> H <sub>37</sub>	H	1	6	
<u>9</u>	NO <sub>2</sub>	H	NO <sub>2</sub>	H	C <sub>18</sub> H <sub>37</sub>	H	1	6	- <sup>d</sup>
<u>10</u>	NO <sub>2</sub>	H	H	H	CH <sub>3</sub>	CH <sub>3</sub>	1	6	- <sup>e</sup>
<u>11</u>	NO <sub>2</sub>	H	NO <sub>2</sub>	H	CH <sub>3</sub>	CH <sub>3</sub>	1	6	- <sup>e</sup>
<u>12</u>	CN	H	H	H	CH <sub>3</sub>	CH <sub>3</sub>	1	6	- <sup>e</sup>
<u>13</u>	NO <sub>2</sub>	H	H	H	CH <sub>3</sub>	CH <sub>3</sub>	1	5	- <sup>e</sup>
<u>14</u>	NO <sub>2</sub>	H	H	H	C <sub>6</sub> H <sub>5</sub>	H	0	-	
<u>15</u>	NO <sub>2</sub>	H	H	CH <sub>3</sub>	C <sub>6</sub> H <sub>5</sub>	H	0	-	
<u>16</u>	NO <sub>2</sub>	H	H	H	CH <sub>3</sub>	CH <sub>3</sub>	0	-	
<u>17</u>	NO <sub>2</sub>	H	NO <sub>2</sub>	H	CH <sub>3</sub>	CH <sub>3</sub>	0	-	- <sup>d</sup>
<u>18</u>	H	NO <sub>2</sub>	H	H	CH <sub>3</sub>	CH <sub>3</sub>	0	-	200
<u>19</u>	CN	H	H	H	CH <sub>3</sub>	CH <sub>3</sub>	0	-	
<u>20</u>	DCNV	H	H	H	CH <sub>3</sub>	CH <sub>3</sub>	0	-	- <sup>d</sup>

<sup>a</sup> refers to attachment position on heterocyclic ring. <sup>b</sup> x 10<sup>30</sup>, measured at 1.06  $\mu$ m. <sup>c</sup> DCNV-2,2-dicyanoethyl. <sup>d</sup> absorption is too high at 532 nm for EFISH measurements using 1.06  $\mu$ m as the fundamental. <sup>e</sup> insufficient solubility in 1,4-dioxane at RT for EFISH measurements.



Scheme 1. Synthesis of ALHD compounds with 2,6-benzoxazole substitution

with the corresponding N,N-dimethyl or N-phenyl diamine. The final condensation to form compounds 6 and 15 ( $R^1 = \text{CH}_3$ ) required several days of reaction over molecular sieves. This lower reactivity was in contrast to the rest of the series in which  $R^1$  is H, which gave high yields in overnight reactions. All compounds were characterized by <sup>1</sup>H-nmr, UV-vis spectroscopy, and elemental analysis and were consistent with the assigned structures. Detailed procedures and analyses are given in the Experimental section.

Compounds 10-13 ( $R^2, R^3 = \text{CH}_3$ ) exhibited only limited solubility in common organic solvents. For example, 11 was soluble only to the extent of 0.88 mmol/L in toluene at 25 °C. In contrast, those compounds with n-octadecyl substituents were approximately four times more soluble on a molar basis (e.g., 9 had a solubility of 3.2 mmol/L in toluene at 25 °C.) Compounds 1-6

showed comparable solubility to the  $C_{18}$  compounds with the advantage of a greater weight per cent of the molecule being nlo active.

#### Thermal Analysis

Thermogravimetric analysis was performed on the ALHD compounds; initial weight loss occurred between 250 and 300 °C. Differential scanning calorimetry confirmed this level of stability with decomposition exotherms in the same temperature range. Compounds 7, 8, and 9 showed novel behavior by exhibiting multiple endotherms below the melt endotherm. For example, 7 undergoes crystal to crystal phase transitions at 95 and 104 °C, and a crystalline to an enantiotropic smectic A phase transition at 137 °C before melting to the isotropic phase at 182.5 °C. An example of a typical DSC thermogram is given in Figure 1. Compounds 1-6 did not display thermotropic behavior.

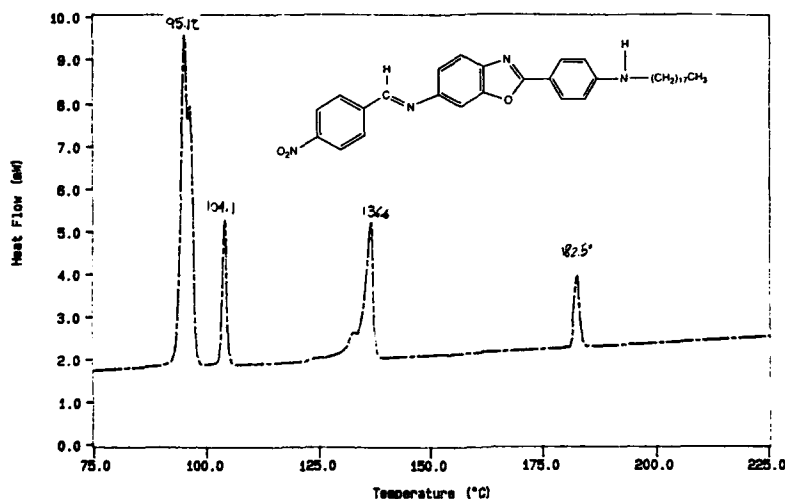


Figure 1. DSC Thermogram of Compound 7

#### EFISH Analysis

A standard technique for accurate and rapid evaluation of the molecular second-order nonlinear optical susceptibility  $\beta$  and  $\beta_{\mu}$  for noncentrosymmetric compounds is d.c. electric field-induced second harmonic generation (EFISH). For this measurement the material of interest is dissolved in an appropriate solvent and probed with the pulsed output of a laser (normally in the near infrared) for generation of the second harmonic in the visible while a d.c. electric field is applied across the sample. [1] The electric field serves to orient the solute molecules in the solution so that the macroscopic centrosymmetric nature of the sample is broken. An infinite dilution extrapolation method was carried through on several of our materials dissolved in 1,4-dioxane, which itself is nonpolar and possesses a low d.c. induced second harmonic susceptibility.

The values reported in Table I were among our first EFISH measurements taken. The fundamental wavelength at 1.06  $\mu\text{m}$  leads to a second harmonic at 0.532  $\mu\text{m}$ , which, for our orange and red samples, clearly lies in the region of molecular absorption. Although the dispersive nature of  $\beta$  is well known [2], we rigorously accounted for the absorption at 0.532  $\mu\text{m}$  and thus the current measurements serve to both assess our materials' nonlinear optical susceptibility, as well as to form an internal ranking. Future measurements, nevertheless, will be performed at a fundamental frequency whose second harmonic will be red-shifted off any molecular absorptions.

Clearly the nonlinear optical susceptibility/dipole moment product  $\beta\mu$  for the most highly optically nonlinear ALHD materials is comparable to such materials as Disperse Red 1, which we also measured as a standard and obtained a value of  $4500 \times 10^{-30} \text{ cm}^5 \text{ D/esu}$ . For device applications, the  $\beta\mu$  measurement is of value as a prediction of a nonlinearity/poling-efficiency figure of merit.

#### CONCLUSIONS

A series of noncentrosymmetric dipolar compounds was synthesized that shows a wide range of the molecular second-order nonlinear optical susceptibility/dipole moment products,  $\beta\mu$ . We found that 2,4-dinitro substitution in these imine-containing materials increases this figure of merit nearly two-fold over the dicyanoethenyl moiety (compare 2 with 5) and tenfold compared with the analogous 4-nitro derivative. We found little difference in  $\beta\mu$  between meta- and para-nitro substitution, which suggests that inductive effects may override resonance effects in these nonplanar ALHD compounds. The additional molecular length provided by the benzoxazole unit doubled the  $\beta\mu$  value, if we compare the measurements on Compound 3 with 18. Molecular volume effects will have to be weighed against orientability and orientation stability in these systems.

We need to measure the  $\beta\mu$  value (at 1.9  $\mu\text{m}$ ) for Compound 17, for which we might observe a tenfold increase over 18 if the same relationship as seen between Compounds 1 and 2 holds. We plan to continue our EFISH analysis for the remaining compounds in Table I and confirm these observed trends by additional EFISH analysis using 1.9  $\mu\text{m}$  as the fundamental wavelength.

#### EXPERIMENTAL PROCEDURES

All chemicals were purchased from Aldrich Chemical Company and were used as received. Reduction of 2-amino-5-nitrophenol by  $\text{SnCl}_2$  in concentrated hydrochloric acid [3] gave 2,5-diaminophenol dihydrochloride. Alkylation of 4-aminobenzoic acid or ethyl 4-aminobenzoate and subsequent saponification [4] provided 4-(hexylamino)- and 4-(octadecylamino)benzoic acids. 5- and 6-Amino-2-[4-(dimethylamino)phenyl]benzoxazole were prepared by the condensation of the appropriate diaminophenols and 4-(dimethylamino)benzoic acid in polyphosphoric acid (PPA) [5]. Compounds 1-20 were synthesized by one of two methods (A or B). An example of each method is given below. The physical properties and elemental analyses of the prepared compounds are shown in Table II.

Melting points (mp) were determined on a Mel-Temp II capillary melting point apparatus utilizing a digital thermometer and are uncorrected. Differential Scanning Calorimetry (DSC) was performed using a Dupont 1090 Differential Scanning Calorimeter and a Perkin Elmer 7 Series Thermal Analysis system. Proton Nuclear Magnetic Resonance ( $^1\text{H}$  NMR) spectra were obtained at room temperature (RT) on a Bruker MSL-200 and Varian XL-300 and XL-400 NMR spectrometers using residual solvent resonances as internal references unless otherwise noted. Chemical shifts are reported in parts per million (ppm). Ultraviolet-visible (UV-vis) spectra were measured on a Hewlett Packard 8450A and Varian Cary 219 Spectrometer. Elemental microanalyses were performed by Galbraith Laboratories (Knoxville, TN) and Desert Analytics (Tucson, AZ).

EFISH measurements were taken on samples having concentrations of  $1.0 \times 10^{-4}$  to  $5.0 \times 10^{-3} \text{ M}$  of the ALHD compound in 1,4-dioxane. An alignment field of 5000 volts was applied across a 1.5 mm spacing with an electrode configuration that ensured a constant field pattern across the interaction region. The fundamental wavelength (1.06  $\mu\text{m}$ ) was blocked before the detectors by appropriate filters and dielectric mirrors, and the second harmonic was detected in a standard photomultiplier arrangement. The results in all cases were referenced to the  $d_{11}$  value for quartz.

Table II. Physical properties of synthesized compounds

Compound #	Method	Yield <sup>a</sup>	mp (°C)	λ <sub>max</sub> (nm)		λ <sub>max</sub> (nm) <sup>c</sup>	Molecular Formula			Calculated			Found		
				<sup>b</sup>	<sup>d</sup>		% C	% H	% N	% C	% H	% N			
1	A	68	162	411 (2.48)	399 (2.77)		C <sub>26</sub> H <sub>26</sub> N <sub>4</sub> O <sub>3</sub>	70.57	5.92	12.66	70.63	5.72	12.74		
2	A	61	181	453 (1.70)	427 (1.75)		C <sub>26</sub> H <sub>25</sub> N <sub>5</sub> O <sub>5</sub>	64.06	5.17	14.37	64.23	5.05	14.35		
3	A	82	168	d	d		C <sub>26</sub> H <sub>26</sub> N <sub>4</sub> O <sub>3</sub>	70.57	5.92	12.66	70.86	5.80	12.68		
4	A	58	150	396 (3.02)	382 (3.88)		C <sub>27</sub> H <sub>26</sub> N <sub>4</sub> O	76.75	6.20	13.26	76.76	6.20	13.25		
5	A	57	230	444 (2.52)	419 (2.82)		C <sub>30</sub> H <sub>27</sub> N <sub>5</sub> O	76.09	5.75	14.79	76.25	5.63	14.83		
6	B	11	172	d	d		C <sub>27</sub> H <sub>28</sub> N <sub>4</sub> O <sub>3</sub>	71.03	6.18	12.27	71.08	6.19	12.29		
7	A	81	181 <sup>e</sup>	416 (2.00)	399 (2.86)		C <sub>38</sub> H <sub>50</sub> N <sub>4</sub> O <sub>3</sub>	74.72	8.25	9.17	73.57	8.18	8.98		
8	A	90	161 <sup>e</sup>	426 (2.49)	406 (2.94)		C <sub>38</sub> H <sub>50</sub> N <sub>4</sub> O <sub>4</sub>	72.81	8.04	8.94	71.94	8.38	8.73		
9	A	88	149 <sup>e</sup>	454 (1.50)	428 (1.43)		C <sub>38</sub> H <sub>49</sub> N <sub>5</sub> O <sub>5</sub>	69.59	7.53	10.68	68.17	7.53	10.63		
10	A	89	272	418 (1.08)	402 (0.94)		C <sub>22</sub> H <sub>18</sub> N <sub>4</sub> O <sub>3</sub>	68.38	4.70	14.50	68.70	4.67	14.65		
11	A	90	248	461 (1.13)	429 (1.77)		C <sub>22</sub> H <sub>17</sub> N <sub>5</sub> O <sub>5</sub>	61.25	3.97	16.23	61.19	3.95	16.17		
12	A	76	276	399 (3.12)	d		C <sub>23</sub> H <sub>18</sub> N <sub>4</sub> O	75.39	4.95	15.29	74.50	5.00	15.03		
13	A	90	276	d	d		C <sub>22</sub> H <sub>16</sub> N <sub>4</sub> O <sub>3</sub>	68.38	4.70	14.50	68.88	4.63	14.56		
14	B	78	174-175.5 <sup>f</sup>	429 (1.83)	425 (1.88)		C <sub>19</sub> H <sub>15</sub> N <sub>3</sub> O <sub>2</sub>	72.49	5.17	12.68	72.26	5.17	12.56		
15	B	63	138.5-139.5	422 (0.53)	412 (0.50)		C <sub>20</sub> H <sub>17</sub> N <sub>3</sub> O <sub>2</sub>								
16	B	51	221-223 <sup>g</sup>	446 (1.88)	441 (1.87)		C <sub>15</sub> H <sub>15</sub> N <sub>3</sub> O <sub>2</sub>								
17	B	61	212.5-213.5 <sup>h</sup>	503 (1.79)	487 (1.66)		C <sub>15</sub> H <sub>14</sub> N <sub>4</sub> O <sub>4</sub>								
18	B	75	158-159 <sup>i</sup>	395 (1.64)	388 (1.59)		C <sub>15</sub> H <sub>15</sub> N <sub>3</sub> O <sub>2</sub>								
19	B	67	199-201 <sup>j</sup>	414 (2.07)	411 (2.07)		C <sub>16</sub> H <sub>15</sub> N <sub>3</sub>								
20	B	43	188-191	486 (2.21)	467 (2.15)		C <sub>19</sub> H <sub>16</sub> N <sub>4</sub>	75.98	5.37	18.65	75.70	5.37	18.66		

<sup>a</sup> Yield of imine-forming reaction after recrystallization.

<sup>b</sup> λ<sub>max</sub> for n-π\* transition in toluene, ε × 10<sup>-4</sup> in parentheses.

<sup>c</sup> λ<sub>max</sub> for n-π\* transition in acetonitrile, ε × 10<sup>-4</sup> in parentheses.

<sup>d</sup> λ<sub>max</sub> for n-π\* transition appears as shoulder to or is hidden under the π-π\* transition.

<sup>e</sup> Compounds exhibit multiple endotherms prior to melting, smectic A phase to isotropic melt is listed.

<sup>f</sup> lit. [10] 178-179 °C.

<sup>g</sup> lit. [7] 220-222 °C.

<sup>h</sup> lit. [8] 193 °C (monohydrate).

<sup>i</sup> lit. [9] 169-170 °C.

<sup>j</sup> lit. [7] 198-200.5 °C.

6-Amino-2-[4-(hexylamino)phenyl]benzoxazole. PPA (82.61 g, 77.81% P<sub>2</sub>O<sub>5</sub>) and 2,5-diaminophenol dihydrochloride (6.36 g, 32.3 mmol) were placed in a 100 mL three-neck flask equipped with a mechanical stirrer and gas inlet. The mixture was heated to 70 °C with stirring under dry N<sub>2</sub> to remove HCl then carefully under reduced pressure (aspirator then vacuum pump) until clear. The solution was heated to 185 °C after the addition of 4-(hexylamino)benzoic acid (7.10 g, 32.1 mmol) and P<sub>2</sub>O<sub>5</sub> (32.00 g) and maintained at that temperature for 20 h. After cooling to 100 °C, the reaction mixture was poured into 400 mL of water with vigorous stirring. Solid NaOH was added to neutralize the solution, and the resulting solid was collected by filtration, washed with water, and dissolved in dichloromethane. This solution was washed with 5% aqueous NaOH and saturated aqueous NaCl, then dried with anhydrous MgSO<sub>4</sub>, filtered, and roto-evaporated to give 9.82 g (98%) crude pink-brown solid. Flash chromatography (99/1 CH<sub>2</sub>Cl<sub>2</sub>/methanol) and recrystallization from toluene yielded the product, 6.00 g (60%): mp 129.5-131.5 °C.

6-Amino-2-[4-(octadecylamino)phenyl]benzoxazole. Prepared as above from 2,5-diaminophenol dihydrochloride and 4-(octadecylamino)benzoic acid in 29% yield: mp 127 °C (DSC).

4-(2,2-Dicyanoethenyl)benzaldehyde. Terephthalaldehyde mono-(diethyl acetal) (10.00 g, 48.0 mmol), malononitrile (3.33 g, 50.4 mmol), and triethylamine (1 mL) were dissolved in ethanol (80 mL) and heated with stirring at 60-65 °C for 105 min. The reaction solution was cooled to RT, then roto-evaporated. Chloroform (25 mL), water (25 mL), and trifluoroacetic acid (25 mL) were added, and the mixture was allowed to stir overnight at 0-25 °C. After roto-evaporation, the residue was extracted into dichloromethane, and the solution was dried over anhydrous MgSO<sub>4</sub>, filtered, and roto-evaporated to give a yellow solid. Recrystallization from ethyl acetate gave the product, 5.36 g (61%): mp 154-155 °C (lit.[6] 154 °C); <sup>1</sup>H NMR (acetone-d<sub>6</sub>) δ 8.13-8.22 (m, 4H, aromatic H), 8.47 (s, 1H, ethenyl H), and 10.16 (s, 1H, CHO).

Method A: 6-[[[4-(2,2-Dicyanoethenyl)phenyl]methylene]amino]-2-[4-(hexylamino)phenyl]benzoxazole (5). Into a 250 mL flask equipped with a Dean-Stark trap, reflux condenser, and magnetic stir bar were placed 6-amino-2-[4-(hexylamino)phenyl]benzoxazole (1.30 g, 4.20 mmol), 4-(2,2-dicyanoethenyl)benzaldehyde (0.77 g, 4.20 mmol), and toluene (100 mL). The reaction mixture was stirred at reflux overnight, then the toluene/water azeotrope was removed by distillation until only 10 mL of solvent remained. The red crystals that formed upon cooling the solution to RT were collected by filtration, washed with ice-cold toluene, recrystallized from toluene, and dried under reduced pressure at RT overnight to give the product, 1.13 g (57%): mp 230 °C; <sup>1</sup>H NMR (CDCl<sub>3</sub>) δ 0.89 (t, 3H, J=6.59 Hz, CH<sub>3</sub>), 1.28-1.73 (m, 8H, aliphatic H), 3.18 (dt, 2H, J=6.87 and 5.07 Hz, HNCH<sub>2</sub>), 4.11 (br s, 1H, HNCH<sub>2</sub>), 6.65 (d, 2H, J=8.79 Hz, 4-(hexylamino)phenyl ring H), 7.28 (dd, 1H, J=7.93 and 1.12 Hz, benzoxazole ring H(5)), 7.44 (d, 1H, J=1.41 Hz, benzoxazole ring H(7)), 7.66 (d, 1H, J=8.52 Hz, benzoxazole ring H(4)), 7.77 (s, 1H, ethenyl H), 7.96-8.06 (m, 6H, 4-(2,2-dicyanoethenyl)phenyl and 4-(hexylamino)phenyl ring H), and 8.57 (s, 1H, imine H); UV-vis λ<sub>max</sub> (toluene) 341 and 444 nm (ε=5.01 X 10<sup>4</sup> and 2.52 X 10<sup>4</sup>), (acetonitrile) 339 and 419 nm (ε=5.14 X 10<sup>4</sup> and 2.82 X 10<sup>4</sup>); Anal. Calcd. for C<sub>30</sub>H<sub>27</sub>N<sub>5</sub>O: C, 76.09; H, 5.75; N, 14.79. Found: C, 76.25; H, 5.63; N, 14.83.

Method B: N,N-Dimethyl-N'-[[2,2-dicyanoethenyl]phenyl]methylene]-1,4-benzenediamine (20). N,N-Dimethyl-1,4-phenylenediamine (1.33 g, 9.77 mmol), 4-(2,2-dicyanoethenyl)benzaldehyde (1.78 g, 9.77 mmol), toluene (100 mL), and 4 Å molecular sieves (6 g) were stirred together overnight at RT with the exclusion of light. Dichloromethane (100 mL) was added to the reaction mixture, and it was filtered through a 5 cm bed of silica gel. The bed was washed with further portions of dichloromethane until the filtrate was nearly colorless. Roto-evaporation of the filtrate gave a crude red solid that was re-

crystallized twice from 2-propanol to yield the product, 1.26 g (43%): mp 188-191 °C;  $^1\text{H}$  NMR (acetone- $d_6$ )  $\delta$  3.02 (s, 6H,  $\text{N}(\text{CH}_3)_2$ ), 6.77-6.85 and 7.36-7.44 (two m, 4H, 4-(dimethylamino)phenyl ring H), 8.10-8.20 (m, 4H, 4-(2,2-dicyanoethyl)phenyl ring H), 8.37 (s, 1H, ethenyl H), and 8.78 (s, 1H, imine H); UV-vis  $\lambda_{\text{max}}$  (toluene) 324 and 486 nm ( $\epsilon=2.18 \times 10^4$  and  $2.21 \times 10^4$ ), (acetonitrile) 319 and 467 nm ( $\epsilon=2.52 \times 10^4$  and  $2.15 \times 10^4$ ); Anal. Calcd. for  $\text{C}_{19}\text{H}_{16}\text{N}_4$ : C, 75.98; H, 5.37; N, 18.65. Found: C, 75.70; H, 5.37; N, 18.66.

#### ACKNOWLEDGEMENTS

Some of the initial syntheses of compounds 7-13 were sponsored by AFOSR Contract No. F49620-85-0015 at SRI International. Thermal analyses were conducted by Martha Steiner, LMSC. We thank Prof. Anselm Griffin, U. of Southern Mississippi, for his analysis of the liquid crystalline nature of some of the ALHD compounds. Dr. Bitler's current address is Landec Labs, Menlo Park, CA 94025.

#### REFERENCES

1. See, for example, J.L. Oudar, J. Chem. Phys. 67, 446 (1977); K.D. Singer, J.E. Sohn, L.A. King, H.M. Gordon, H.E. Katz, and C.W. Dirk, J. Opt. Soc. Am. B6, 1339 (1989).
2. C.C. Teng and A.F. Garito, Phys. Rev. B28, 6766 (1983).
3. F. Kehrman and G. Betsch, Chem. Ber. 30, 2096 (1897).
4. J.D. Albright, V.G. DeVries, E.E. Largis, T.G. Miner, M.F. Reich, S.A. Schaffer, R.G. Sheperd, and J. Upešlacis, J. Med. Chem. 26 (10), 1378 (1983).
5. J.F. Wolfe, B.H. Loo, R.A. Sanderson, and S.P. Bitler, in Nonlinear Optical Properties of Polymers, edited by A.J. Heeger, J. Orenstein, and D.R. Ulrich (Mater. Res. Soc. Proc. 109, Pittsburgh, PA 1988) pp. 291-300.
6. L.K. Maslil, G.S. Nikol'skaya, M.N. Umetskaya, and A.A. Tikhomolov, Zh. Anal. Khim. 38 (2), 269 (1983) [J. Anal. Chem. USSR 38 (2), 215 (1983)].
7. R. Gawinecki and F. Muzalewski, Pol. J. Chem. 58 (10-12), 1091 (1984).
8. F. Sachs and R. Kempf, Chem. Ber. 35, 1224 (1902).
9. V.A. Bren', V.I. Minkin, and K.A. Tskhadadze, Zh. Org. Khim. 12 (4), 830 (1976) [J. Org. Chem. USSR 12 (4), 833 (1976)].
10. R. Gawinecki and F. Muzalewski, Pol. J. Chem. 56 (6), 1177 (1980).

**NOVEL PHOTOCHROMIC ZWITTERIONS FOR MULTIFREQUENCY DATA STORAGE**

G. J. ASHWELL\*, E. J. C. DAWNAY, A. P. KUCZYNSKI AND M. SZABLEWSKI  
Centre for Molecular Electronics, Cranfield Institute of  
Technology, Cranfield, Bedford MK43 0AL, UK

**ABSTRACT**

Z- $\beta$ -(N-alkyl-4-pyridinium)- $\alpha$ -cyano-4-styryldicyanomethanide (R-P3CNQ) and its quinolinium analogue (R-Q3CNQ) are photochromic. Their LB films show sharp charge transfer bands at 495 nm (C<sub>16</sub>H<sub>33</sub>-P3CNQ), 565 nm (C<sub>16</sub>H<sub>33</sub>-Q3CNQ) and 614 nm (C<sub>8</sub>H<sub>17</sub>-Q3CNQ) with half widths at half maximum of 27, 22 and 37 nm respectively. They show interesting nonlinear optical properties and have the potential to store three bits per pixel when addressed at these wavelengths.

**INTRODUCTION**

7,7,8,8-Tetracyano-p-quinodimethane undergoes substitution reactions with (i) primary and secondary amines to give materials of general formula R'R"N-C(CN)=C<sub>6</sub>H<sub>4</sub>=C(CN)<sub>2</sub> and (R'R"N)<sub>2</sub>C=C<sub>6</sub>H<sub>4</sub>=C(CN)<sub>2</sub> [1] and (ii) picolinium, quinaldinium and lepidinium salts to give the zwitterionic derivatives D<sup>+</sup>-CH=C(CN)-C<sub>6</sub>H<sub>4</sub>-C(CN)<sub>2</sub><sup>-</sup> where D<sup>+</sup> is a heterocyclic cation (see Figure 1) [2-7]. The zwitterionic ground state is substantiated by the bond lengths and segmented molecular geometry: the N-methyl-2-pyridinium analogue has dihedral angles of 36.1 and 5.0° between the plane through the -CH=C(CN)- bridge and the donor and acceptor planes respectively [8]. It has a large second order hyperpolarisability but intermolecular dipole-dipole interactions cause the crystal structure to be centrosymmetric. The molecules overlap in a head-to-tail manner with a spacing of 3.54 Å between the pyridinium ring and -C(CN)<sub>2</sub> group. For second harmonic generation (SHG) it is necessary to suppress this arrangement and the LB deposition of three amphiphilic congeners has provided non-centrosymmetric Z-type films.

In this work the photochromic switching and nonlinear optical properties of the zwitterionic LB films are reported. Our main interest was aroused by the narrow photochromic absorption bands and their conceivable use in a multifrequency memory device. To store several bits per pixel demands insignificant overlap of the bands in order that they may be independently addressed. There are few suitable materials: the spiropyrans which have narrow J-bands at ~600 nm [9,10] and the D<sup>+</sup>-CH=C(CN)-C<sub>6</sub>H<sub>4</sub>-C(CN)<sub>2</sub><sup>-</sup> zwitterions [3] which show sharp charge transfer bands at 495, 565 and 614 nm.

\*To whom correspondence should be addressed.

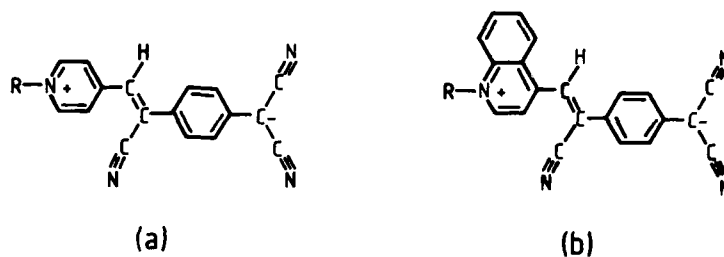
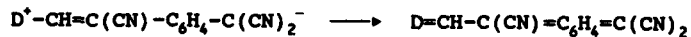


Figure 1. Molecular structures of (a) Z- $\beta$ -(N-alkyl-4-pyridinium)- $\alpha$ -cyano-4-styryldicyanomethanide (R-P3CNQ) and (b) Z- $\beta$ -(N-alkyl-4-quinolinium)- $\alpha$ -cyano-4-styryldicyanomethanide (R-Q3CNQ).

#### PHOTOCHROMISM

Photochromism was reported as early as in the 19th century [11] and it results from reversible changes in the molecular structure [12] or charge distribution [13,14] during irradiation. The zwitterions bleach when irradiated at the frequency of the charge transfer band [3,4] and, in solution, the bleaching and recolouration of R-P3CNQ follow first order kinetics. The molecule also exhibits electrochromic behaviour and the spectra of the bleached forms are independent of the method of switching. This implies that both processes involve reduction/oxidation and we postulate that the photobleaching entails charge transfer from the  $-\text{C}(\text{CN})_2^-$  group to the positively charged pyridinium ring followed by a molecular rearrangement to the neutral quinonoid form.



The mechanism is analogous to the photo-induced charge transfer in  $\text{Cu}^+\text{TCNQ}^-$  [13] but attempts to verify it have been hampered by the low solubility of the zwitterion. Nevertheless, we regard the alternative explanations, outlined below, as less plausible. (i) Photoisomerisation is feasible but we note that the low energy photochromic transitions are inconsistent with those normally associated with sterically hindered cis forms. (ii) Dimerisation (or polymerisation) of the ethylene bridge may occur but it is unlikely that it would be reversible. (iii) Protonation of the  $-\text{C}(\text{CN})_2^-$  group causes bleaching but this is dismissed because the addition of base to acidified solutions induces rapid recolouration whereas the photochromically switched solutions are unaffected.



## PHOTOCHROMIC LB FILMS

LB films of the zwitterions were deposited on hydrophilically treated silica slides using an alternate-layer Nima Technology Langmuir-Blodgett trough. Most homomolecular films are Y-type (centrosymmetric) but, in this work, interlayer repulsions between the negative charges on the terminal  $-\text{C}(\text{CN})_2^-$  groups suppress the customary antiparallel alignment, causing Z-type deposition.

The  $\text{C}_8\text{H}_{17}$ -Q3CNQ and  $\text{C}_{16}\text{H}_{33}$ -Q3CNQ films have different structures with areas per molecule of 28 and 50  $\text{\AA}^2$  respectively at 25  $\text{mN m}^{-1}$ . They also exhibit distinctive spectra in which the charge transfer band is shifted from 614 to 565 nm (Figure 2). This is attributed to a change in molecular tilt which causes the transition to alter from an intermolecular to intramolecular band [6]. In contrast, the  $\text{C}_8\text{H}_{17}$ -P3CNQ and  $\text{C}_{16}\text{H}_{33}$ -P3CNQ films have identical spectra with charge transfer bands at 495 nm. The bands at 495, 565 and 614 nm have half widths at half maximum of 27, 22 and 37 nm respectively. They are photochromic but, unlike the solutions, the bleached films do not recolour. Thus, they may be used for optical data storage as write once read many memory materials and as there is little direct overlap at the three wavelengths which correspond to the absorption maxima, it is plausible that the bands may be independently switched. In a multicomponent configuration the films have the potential to store three bits per pixel but this needs to be verified.

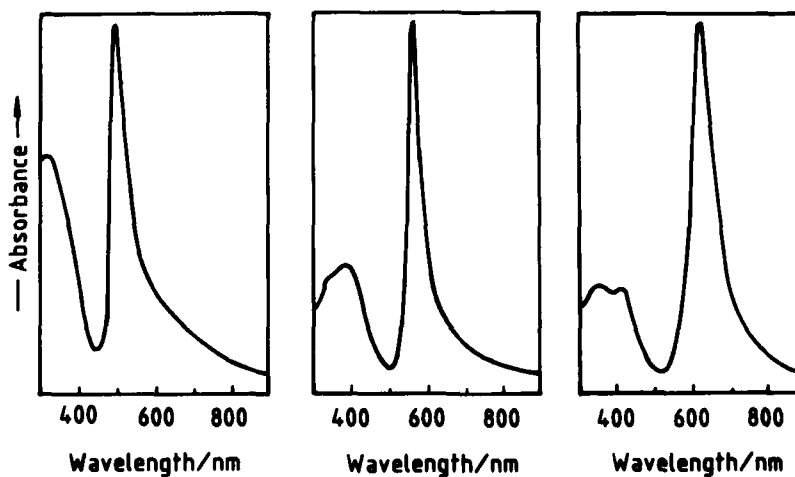


Figure 2. LB film spectra of, from left to right,  $\text{C}_{16}\text{H}_{33}$ -P3CNQ ( $\lambda_{\text{max}}$ , 495 nm),  $\text{C}_{16}\text{H}_{33}$ -Q3CNQ ( $\lambda_{\text{max}}$ , 565 nm) and  $\text{C}_8\text{H}_{17}$ -Q3CNQ ( $\lambda_{\text{max}}$ , 614 nm). The charge transfer bands have absorbances of 0.020 per monolayer.

The spectra of  $C_{16}H_{33}$ -P3CNQ and  $C_{16}H_{33}$ -Q3CNQ indicate that the photochromic charge transfer bands may be tuned by substitution. For back charge transfer the 70 nm red shift from 495 to 565 nm is consistent with the pyridinium cation being a weaker electron acceptor than quinolinium. The wavelength is dependent upon the difference between the ionisation energy and electron affinity of opposite ends which crudely approximates to the difference between the reduction potentials of the cation and TCNQ derivatives from which the zwitterions were synthesised (see Figure 3).

#### SECOND HARMONIC GENERATION

Molecules with high second order hyperpolarisabilities, e.g. the hemicyanine [15] and merocyanine [16] dyes, have donor and acceptor groups located at opposite ends of an extended  $\pi$ -electron bridge. The zwitterions, reported here, have similar molecular structures and exhibit interesting nonlinear optical properties. SHG studies were performed on LB films of  $C_{16}H_{33}$ -Q3CNQ using a pulsed Nd:YAG laser ( $\lambda$ , 1.064  $\mu\text{m}$ ; repetition rate, 5 Hz; pulse width, 10 ns; pulse energy, < 1 mJ) at an incident angle of 45° with a Y-cut quartz plate as reference.

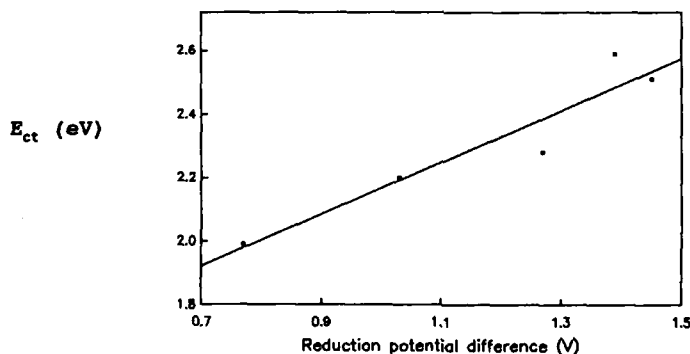


Figure 3. Energy of the charge transfer band (in eV) versus the difference between the half wave reduction potentials (in V) of the TCNQ derivative and cation (see text):  $C_{16}H_{33}$ -Q3CNQ(benz) ( $\lambda_{max}$ , 623 nm);  $C_{16}H_{33}$ -Q3CNQ ( $\lambda_{max}$ , 565 nm);  $C_{16}H_{33}$ -Q3CNQ(Br<sub>2</sub>) ( $\lambda_{max}$ , 545 nm);  $C_{16}H_{33}$ -P3CNQ ( $\lambda_{max}$ , 495 nm);  $C_{16}H_{33}$ -Q3CNQ(F<sub>4</sub>) ( $\lambda_{max}$ , 480 nm). These analogues have 2,3-benz, 2,5-dibromo and 2,3,5,6-tetrafluoro substituents at the acceptor end (see [4]).

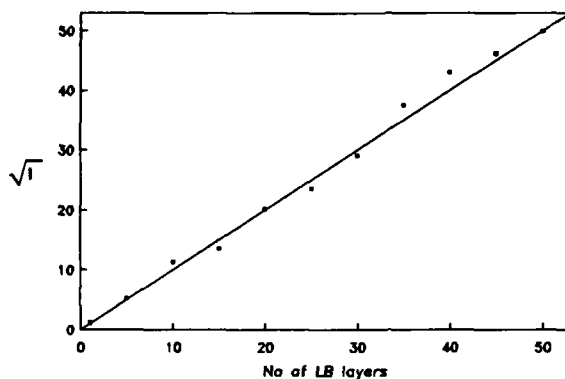


Figure 4. Square root of the SH intensity (arbitrary units) of  $C_{16}H_{33}$ -Q3CNQ versus the number of LB layers.

The non-centrosymmetric films of  $C_{16}H_{33}$ -Q3CNQ show strong SHG and, consistent with theory, the intensity increases quadratically with the number ( $n$ ) of layers (Figure 4). The SH signal generated by the monolayer,  $I_{(1)} = I_{(n)}/n^2$ , is similar to the value obtained for a monolayer of hemicyanine, E-N-docosyl-4-(2-(4-dimethylamino-phenyl)ethenyl)pyridinium bromide. The hemicyanine dye was chosen for comparison because it has a high second order nonlinearity ( $\beta$ ) of  $200 \times 10^{-30} \text{ cm}^5 \text{ esu}^{-1}$  at  $1.064 \mu\text{m}$  [15]. It forms centrosymmetric Y-type films and only odd numbers of layers show any appreciable SHG. In contrast the  $C_{16}H_{33}$ -Q3CNQ films are Z-type and the SH signal increases as  $n^2$ .

A detailed analysis of the data will be reported elsewhere together with the properties of several substituted analogues.

#### ACKNOWLEDGEMENTS

We acknowledge the SERC for supporting this work (research grants GR/E/88974 and GR/F/45813) and for providing studentships to EJCD, APK and MS. We are also grateful to Dr Simon Allen for helpful discussions concerning the design of the SHG apparatus.

#### REFERENCES

1. W.R. Hertler, H.D. Hartzler, D.S. Acker and R.E. Benson, *J. Amer. Chem. Soc.* **84**, 3387 (1962).

- 2 G.J. Ashwell, UK Patent Appl. 8907311.8 (31 March 1989).
- 3 G.J. Ashwell, Thin Solid Films, in the press (1989).
- 4 G.J. Ashwell, E.J.C. Dawney, A.P. Kuczynski, M. Szablewski, I.M. Sandy, M.R. Bryce, A.M. Grainger, M. Hasan, A.T. Jones, R.C. Thorpe, N.A. Bell and R.A. Broughton, J. Chem. Soc. Faraday Trans., in the press (1989).
- 5 G.J. Ashwell, A.P. Kuczynski and M. Szablewski in Proceedings of the NATO-ASI Conference on Low-Dimensional Materials and Device Materials, edited by R.M. Metzger, Plenum Press, to be published.
- 6 R.M. Metzger, N.E. Heimer and G.J. Ashwell, Mol. Cryst. Liq. Cryst. 107, 133, (1984).
- 7 S. Akhtar, J. Tanaka, R.M. Metzger and G.J. Ashwell, Mol. Cryst. Liq. Cryst. 139, 353 (1986).
- 8 Determined from the atomic coordinates in [6].
- 9 J. Miyazaki, E. Ando, K. Yoshino and K. Morimoto, Eur. Patent Appl. EP 193931 A2 (1986); US Patent 4737427A (1988).
- 10 E. Ando, J. Miyazaki, K. Morimoto, H. Nakahara and K. Fukuda, Thin Solid Films 133, 21 (1985); E. Ando, J. Hibino, T. Hashida and K. Morimoto, *ibid.*, 160, 279 (1988).
- 11 E. Ter Meer, Annalen, 181, 1 (1876).
- 12 H.G. Heller, IEE Proceedings, 130, 209 (1983).
- 13 R.S. Potember, R.C. Hoffman and T.O. Poehler, Johns Hopkins APL Technical Digest 7, 129 (1986) and references therein.
- 14 T. Nagamura, K. Sakai and T. Ogawa, J. Chem. Soc. Chem. Commun. 1035 (1988).
- 15 I.R. Girling, N.A. Cade, P.V. Kolinski, J.D. Earls and G.H. Cross, Thin Solid Films, 132, 101 (1985).
- 16 A. Dulcic and C. Flytzanis, Opt. Commun. 25, 402 (1978); I.R. Girling, N.A. Cade, P.V. Kolinski and C.M. Montgomery, Electronics Lett. 21, 169 (1985).

ELECTRO-OPTIC AND NONLINEAR OPTICAL PROPERTIES OF  
2,6-DIBROMO-N-METHYL-4-NITROANILINE (DBMNA) CRYSTALS

AJAY NARATA, KEITH A. HORN, AND JAMES T. YARDLEY  
Allied-Signal, Inc., Engineered Materials Sector  
Columbia Turnpike, Morristown, New Jersey 07962

ABSTRACT

We report a new organic nonlinear optical crystal, 2,6-dibromo-N-methyl-4-nitroaniline (DBMNA). The refractive indices of DBMNA were measured at several wavelengths between 500 and 1100 nm and fit to a single oscillator Sellmeier equation. Second harmonic Maker fringe data yielded  $d_{33}$  values through comparison with y-cut crystalline quartz. We also report measurements of the electro-optic coefficients,  $(n_a^3 r_{13} - n_c^3 r_{33})$ ,  $r_{42}$ , and  $r_{51}$  at several wavelengths. We find good agreement between the observed dispersion and that predicted by the simple two level dispersion model. However, the second order susceptibility is not well described by a single tensor component hyperpolarizability.

INTRODUCTION

The intrinsically large second order nonlinearities and low dielectric constants associated with organic materials have generated significant interest in their use for parametric frequency generation and high speed electro-optic devices [1]. In this work, we present the structure, refractive indices, nonlinear optical properties and linear and quadratic electro-optic properties of single crystal DBMNA, a new organic nonlinear crystal. The electro-optic coefficients are modeled by a fit to the two level dispersion equation, from which a non-resonant  $\chi^{(2)}$  is obtained.

CRYSTAL GROWTH AND STRUCTURE

DBMNA was prepared by the reaction of bromine with N,N-dimethyl-4-nitroaniline in methanol at reflux. Clear yellow rhombohedral b-platelet single crystals were grown with typical dimensions of  $2 \times 2 \times 0.2 \text{ mm}^3$ . Single crystal X-ray diffraction showed that DBMNA belongs to the orthorhombic space group Fdd2, point group mm2, with unit cell parameters of  $a=11.745(1) \text{ \AA}$ ,  $b=29.640(2) \text{ \AA}$ ,  $c=10.807(2) \text{ \AA}$ , and  $Z=16$ . Powder X-ray diffraction patterns showed that crystals grown from acetonitrile, ethanol, and methylene chloride all belong to the same space group. The unit cell contains four identical groups of four molecules defined by  $C_{2v}$  symmetry, each related to the other by simple translations. The approximate charge transfer axis, amino to nitro, of each molecule is  $71^\circ$  off the c-axis in the a-c plane, yielding a net polar vector along the c-axis. Figure 1 shows an ORTEP plot and a projection along the crystallographic a-axis. Further details of the crystal structure are given in Reference [2].

ABSORPTION AND REFRACTIVE INDEX MEASUREMENTS

The optical absorption spectrum of single crystal DBMNA was measured from 200 nm to 2500 nm. The absorption spectrum was recorded at room temperature using unpolarized light propagating along the b-axis. These data indicate that the title compound is essentially transparent from 500 nm to 1500 nm with weak infrared overtone bands occurring in the near infrared. Using a thin polycrystalline sample, the peak of the charge transfer absorption band was found to occur at  $430 \pm 2 \text{ nm}$ . This is red shifted from the maximum of 360 nm measured in acetonitrile solution.

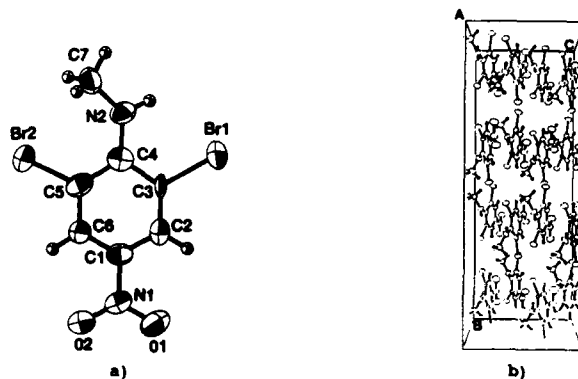


Figure 1. a) ORTEP plot and b) projection along the crystallographic a-axis of the unit cell of DBMMA.

The refractive indices of single crystal DBMMA were measured as a function of wavelength using two separate techniques. The measurements at 632.8 nm and 810 nm were performed using a Brewster's angle technique for biaxial crystals [3]. The angular dependence of the reflected p-polarized light from each face was measured and the individual refractive indices were obtained from the three independently measured Brewster's angles. The refractive indices at 532 nm and 1064 nm were determined from the second harmonic Maker fringe data [4].

A single oscillator Sellmeier equation [5] was used to describe  $n_x$ ,  $n_y$ , and  $n_z$

$$n^2 - 1 = A / (\lambda_0^{-2} - \lambda^{-2}) + B \quad (1)$$

where  $A$  is proportional to the oscillator strength,  $\lambda_0$  is the wavelength of the oscillator, and  $B$  accounts for the nondispersive contribution from all other oscillators. The experimentally measured refractive indices and corresponding Sellmeier coefficients are given in Table I. For orthorhombic crystals belonging to point group  $mm2$ , the crystallographic axes  $a$ ,  $b$ , and  $c$  lie parallel to the principal axes  $x$ ,  $y$ , and  $z$ , respectively.

Table I. Refractive Indices of DBMMA and Corresponding Sellmeier Coefficients

$\lambda$ (nm)	$n_x$	$n_y$	$n_z$
514.5	2.18 <sup>a</sup>	1.72 <sup>a</sup>	1.54 <sup>a</sup>
532	2.12	-	1.53
632.8	1.90 ± 0.06 <sup>b</sup>	1.62 ± 0.04 <sup>b</sup>	1.48 ± 0.03 <sup>b</sup>
810	1.81 ± 0.06 <sup>b</sup>	1.59 ± 0.04 <sup>b</sup>	1.46 ± 0.03 <sup>b</sup>
1064	1.82	-	1.47
$A$ ( $10^{-6}$ nm <sup>-2</sup> )	4.10	1.23	0.68
$\lambda_0$ (nm)	430	430	430
$B$	1.22	1.21	0.96

a) Extrapolated from the single oscillator Sellmeier fits.

b) Error estimated from the inaccuracy in determining precise minima in the Brewster's angle measurements.

## SECOND HARMONIC GENERATION

Second harmonic Maker fringe data were obtained using both 1064 nm and 1620 nm fundamental wavelengths [6]. The second harmonic intensity from each DBNBA crystal was compared to the second harmonic Maker fringe data obtained from a y-cut crystalline quartz slab under identical experimental conditions. Figure 2 shows the Maker fringe data of DBNBA corresponding to the nonlinear optical coefficient,  $d_{33}$ , at 1064 nm. The values of the nonlinear optical coefficient,  $d_{33}$ , and the coherence length,  $l_c$ , are

$$\begin{aligned} d_{33} (1064 \text{ nm}) &= 9.1 \times 10^{-9} \text{ esu} & l_c (1064 \text{ nm}) &= 5 \mu\text{m} \\ d_{33} (1620 \text{ nm}) &= 1.3 \times 10^{-9} \text{ esu} & l_c (1620 \text{ nm}) &= 40 \mu\text{m} \end{aligned}$$

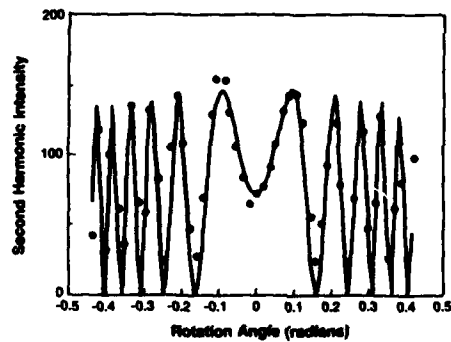


Figure 2. Second harmonic Maker fringe data corresponding to  $d_{33}$  of DBNBA ( $\lambda = 1064 \text{ nm}$ ).

## ELECTRO-OPTIC MEASUREMENTS

Orthorhombic crystals belonging to point group  $mm2$  have five nonzero, independent electro-optic coefficients,  $r_{11}$ ,  $r_{13}$ ,  $r_{23}$ ,  $r_{33}$ ,  $r_{42}$ , and  $r_{51}$  [7]. The refractive indices obtained from solving the general equation of the index ellipsoid are approximately given by

$$\begin{aligned} n_x &\sim n_a - \frac{1}{2} n_a^3 r_{13} E_z - \frac{1}{2} n_a^3 \left[ \frac{1}{n_a^2} - \frac{1}{n_c^2} + (r_{13} - r_{33}) E_z \right]^{-1} r_{51}^2 E_x^2 \\ n_y &\sim n_b - \frac{1}{2} n_b^3 r_{23} E_z - \frac{1}{2} n_b^3 \left[ \frac{1}{n_b^2} - \frac{1}{n_c^2} + (r_{23} - r_{33}) E_z \right]^{-1} r_{42}^2 E_y^2 \\ n_z &\sim n_c - \frac{1}{2} n_c^3 r_{33} E_z + \frac{1}{2} n_c^3 \left[ \frac{1}{n_a^2} - \frac{1}{n_c^2} + (r_{13} - r_{33}) E_z \right]^{-1} r_{51}^2 E_x^2 \\ &\quad + \frac{1}{2} n_c^3 \left[ \frac{1}{n_b^2} - \frac{1}{n_c^2} + (r_{23} - r_{33}) E_z \right]^{-1} r_{42}^2 E_y^2 \end{aligned} \quad (2)$$

The electric field induced phase retardation in DBNBA was measured using a standard AC modulated Senarmont compensator with lock-in detection. Sinusoidal fields of up to 50 kV/cm at 1 kHz were applied to the crystal using two different electrode geometries. Thin film slit type nickel electrodes (electrode gap = 100  $\mu\text{m}$ , electrode dimensions = 5 x 9  $\text{mm}^2$ , thickness = 750  $\text{\AA}$ ) were photolithographically defined on quartz substrates for field application along the a and c axes.

For fields along the b-axis, samples were sandwiched between two indium tin oxide coated pyrex substrates (ITO thickness = 300 Å). An argon ion laser operating at 514.5 nm, a He-Ne laser operating at 632.8 nm, and a diode laser operating at 810 nm were used as the probe beams. For all measurements, the probe beam was propagated parallel to the b-axis and was linearly polarized at 45° with respect to the a and c axes. Details of the corrections to the electric field arising from thickness variations between crystals are given in Reference [8]. The crystal morphology and electrode configuration allowed for the determination of the magnitudes of  $(n_a^3 r_{13} - n_c^3 r_{33})$ ,  $r_{42}$ , and  $r_{51}$ . Table II gives the values of the electro-optic coefficients at each wavelength. These values were determined using the refractive index data from Table I.

Table II. Electro-optic Coefficients of DBMMA Versus Wavelength

$\lambda$ (nm)	$ n_a^3 r_{13} - n_c^3 r_{33} $ (pm/V)	$ r_{42} $ (pm/V)	$ r_{51} $ (pm/V)
514.5	148	86	83
632.8	32 <sup>a</sup>	20.4 <sup>a</sup>	41.4 <sup>a</sup>
810	18.3 <sup>a</sup>	11.5 <sup>a</sup>	31 <sup>a</sup>

a) Average values of measurements taken from two different crystals.

#### DISCUSSION

From the measured electro-optic coefficients and refractive indices we may deduce the corresponding second order nonlinear optical susceptibilities using the relation [9]  $\chi_{ijk}^{(2)} = -n_i^2 n_j^2 r_{ijk}/2$ . We may attempt to understand the observed dispersion in susceptibility by noting that, in an independent molecular response model, we may write [10]

$$\chi_{ijk}^{(2)} = (16/V_0) f_i f_j f_k \sum_{PQR} W_{ijkPQR} \beta_{PQR} \quad (3)$$

where  $V_0$  is the unit cell volume,  $f_i$  are local field factors,  $\beta_{PQR}$  is the molecular hyperpolarizability for molecule-defined axes P, Q, and R, and the weighting factors  $W_{ijkPQR}$  are

$$W_{ijkPQR} = \frac{1}{4} \sum_l \lambda_{iP}^{(l)} \lambda_{jQ}^{(l)} \lambda_{kR}^{(l)} \quad (4)$$

with the sum  $l$  over the four inequivalent molecular orientations within the crystal and with  $\lambda_{iP}^{(l)}$  representing the direction cosine for molecular axis P along crystal axis i for molecule  $l$ .

For molecules of the nitroaniline type, second harmonic generation and electro-optic experiments on single crystals [10, 11, 12] and poled polymer [9] films suggest that the principal contribution to the nonlinearity arises from the electronic degree of freedom. A simple two-level model has been applied to show the correspondence between the second harmonic and electro-optic measurements and to predict the dispersion in second-order nonlinearity. In simplest form, this model gives a single non-zero hyperpolarizability of the form [13]

$$\beta_{333}^{(2)} = (\beta_{333}^{(2)})_0 \Omega^{(2)}(\omega, \omega_{10}) \quad (5)$$

where the dispersion function is  $\Omega^{(2)}(\omega, \omega_{10}) = \omega_{10}^2 (\omega_{10}^2 - \omega^2/3) (\omega_{10}^2 - \omega^2)^{-2}$  for optical



angular frequency  $\omega$  and molecular transition frequency  $\omega_{10}$ . Here  $\Omega$  is defined so that  $\Omega^{BO}(0, \omega_{10}) = 1$ . Thus in this model, we may write  $\chi_{ijk}^{BO} = (\chi_{ijk}^{BO})_0 \Omega^{BO}(\omega, \omega_{10})$ . We have fit the observed susceptibilities (or linear combinations thereof) to this expression for each wavelength with parameters  $(\chi_{ijk}^{BO})_0$  (or appropriate combination) and  $\omega_{10}$  ( $= 2\pi c/\lambda_{10}$ ). The resulting best fit values are listed in Table III. Figure 3 shows the observed susceptibilities and the fits. Overall, it is clear that the functional form of the dispersion given by Equation (5) is obeyed quite well. The resonant frequencies obtained, expressed in terms of wavelength, (426, 462, and 457 nm) are in reasonable accord with the experimentally observed wavelength of peak absorbance (430 nm). Thus these data demonstrate the electronic nature of the electro-optic response of this crystal and support the validity of the two-level model for describing the electro-optic response of nitroanilines.

Table III. Two Level Dispersion Model Fit to Electro-optic Coefficients of DBNMMA

Electro-optic Coefficient (pm/V)	Second Order Susceptibility (pm/V)	$(\chi^{BO})_0$ (pm/V)	$\lambda_{10}$ (nm)
$n_a^3 r_{13} - n_c^3 r_{33}$	$\begin{pmatrix} \chi_{13}^{BO} & \chi_{33}^{BO} \\ -n_a & -n_c \end{pmatrix}_0$	4.5	457
$r_{42}$	$(\chi_{42}^{BO})_0$	15.8	462
$r_{51}$	$(\chi_{51}^{BO})_0$	59.5	426

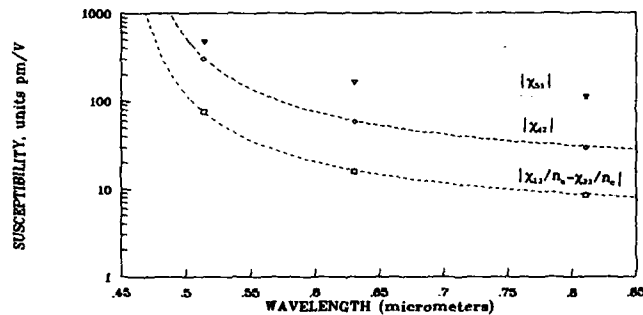


Figure 3. Experimental electro-optic susceptibilities and best fits as a function of wavelength.  $(\chi_{42}^{BO})_0$ ,  $(\chi_{51}^{BO})_0$ , and  $(\chi_{13}^{BO}/n_a - \chi_{33}^{BO}/n_c)$ .

We may investigate further the relationship between the observed electro-optic response and the molecular response by a more detailed examination of Equations 3-5. From the known crystal geometry, the direction cosines  $\lambda_{ij}^{(l)}$  may be explicitly determined. Using standard assumptions concerning local field factors, we may deduce values for  $(\beta_{EES}^{BO})_0$  for each of the three measured susceptibilities (or linear combination thereof). The results give (in cgs units normally used for describing molecular hyperpolarizabilities)  $(\beta_{EES}^{BO})_0 = 22.6 \times 10^{-30}$  esu,  $44.2 \times 10^{-30}$  esu, and  $3.7 \times 10^{-30}$  esu extrapolated from  $\chi_{51}$ ,  $\chi_{42}$ , and  $(\chi_{13}/n_a - \chi_{33}/n_c)$  respectively. The large inconsistency in these numbers suggests that molecular hyperpolarizabilities in addition to  $\beta_{EES}$  must make significant contributions to the observed electro-optic response. Preliminary calculations suggest that inclusion of an additional single independent contribution of the form  $(\beta_{EET}^{BO})_0 = (\beta_{ETE}^{BO})_0 = (\beta_{TEE}^{BO})_0$  provides for a more satisfactory agreement between theory and experiment.

We may examine the observed dispersion in the second order susceptibility  $\chi_{33}^{SBO}$  in a similar way. The simple two-level model suggests that we may write [13, 14]  $\chi_{ijk}^{SBO} = (\chi_{ijk}^{SBO})_0 \Omega^{SBO}(\omega, \omega_{10})$  where the dispersion function is defined by  $\Omega^{SBO}(\omega, \omega_{10}) = \omega_{10}^4 (\omega_{10}^2 - 4\omega^2)^{-1} (\omega_{10}^2 - \omega^2)^{-1}$  and is defined so that  $\Omega^{SBO}(0, \omega_{10}) = 1$ . A fit for the two data points gives  $(\chi_{33}^{SBO})_0 = 0.6$  pm/V and (expressed in terms of wavelength)  $\lambda_{10} = 504$  nm. Again the expected dispersion is observed with a transition frequency in accord with the observed absorption spectrum and with the corresponding transition frequencies found from the electro-optic response. On the basis of a simple single- $\beta$  model, we would expect [15]  $(\chi_{33}^{BO})_0 \sim 4(\chi_{33}^{SBO})_0$ . This is clearly not consistent with the electro-optic results unless  $\chi_{13}^{BO} > \chi_{33}^{BO}$ . These results also suggest that additional electronic hyperpolarizabilities are important in this system.

#### CONCLUSIONS

We have measured the second order nonlinear optical coefficient,  $d_{33}$ , and the corresponding coherence lengths,  $l_c$ , at 1064 nm and 1620 nm. We have also made the first known measurements of the quadratic electro-optic effect in an organic crystal, yielding the coefficients  $r_{42}$  and  $r_{51}$ , as well as the linear effect at several wavelengths between 500 and 1000 nm. It has been shown that the electro-optic response of DBNMMA can be well described by the two level dispersion model. However a single tensor component hyperpolarizability cannot adequately account for the magnitude of the electro-optic coefficients.

#### REFERENCES

- [1] D.S. Chemla and J. Zyss, Eds., Nonlinear Optical Properties of Organic Molecules and Crystals, Vols. 1 and 2. (Academic Press, New York, 1987).
- [2] K.A. Horn and A. Nahata, *Acta Cryst.*, submitted for publication.
- [3] C.H. Grossman and A.F. Garito, *Mol. Crystal Liq. Crystal* **168**, 255 (1989).
- [4] K.D. Singer, PhD thesis, University of Pennsylvania, 1981.
- [5] M. Born and E. Wolf, Principles of Optics. (Pergamon, Oxford, England, 1980), p. 96.
- [6] J. Jerphagnon and S.K. Kurtz, *J. Appl. Phys.* **41**, 1667 (1970).
- [7] I.P. Kaminow, Introduction to Electro-Optic Devices. (Academic Press, New York, 1974), pp. 44-51.
- [8] K.A. Horn, A. Nahata, and J.T. Yardley, *IEEE J. Quantum Electron.*, submitted for publication.
- [9] K.D. Singer, M.G. Kuzyk, and J.E. Sohn, *J. Opt. Soc. Am. B* **4**, 968 (1987).
- [10] J. Zyss and D.S. Chemla, Nonlinear Optical Properties of Organic Molecules and Crystals Vol. 1, ed. by D.S. Chemla and J. Zyss (Academic Press, New York, 1987) p.100.
- [11] K. Sutter, C. Bosshard, M. Ehrensperger, P. Günter, and R.J. Twieg, *IEEE J. Quantum Electron.* **24**, 2362 (1988).
- [12] G.F. Lipecomb, A.F. Garito, and R.S. Narang, *J. Chem. Phys.* **75**, 1509 (1981).
- [13] Ref. 10, p.71.
- [14] D. Pugh and J.O. Morley, Nonlinear Optical Properties of Organic Molecules and Crystals Vol. 2, ed. by D. Chemla and J. Zyss (Academic Press, New York, 1987) p.205-206.

## QUADRATIC NONLINEAR OPTICAL PROPERTIES OF DIVA CRYSTAL

T. WADA, C. H. GROSSMAN, S. YAMADA, A. YAMADA, A. F. GARITO<sup>a)</sup> AND H. SASABE  
 Frontier Research Program (RIKEN), Wako, Saitama 351-01, Japan

### ABSTRACT

New organic nonlinear optical crystal : dicyanovinyl anisole (DIVA) has been grown from vapor by low pressure sublimation and from saturated solution by solvent evaporation. Crystallographic structure and quadratic nonlinear optical properties were investigated. Molecular orientation in DIVA crystal with space group  $P2_1$  is favorable for the highest possible value of bulk phase-matchable coefficient. Both type I and type II phase matched second harmonic generation (PMSHG) were observed from naturally grown faces of single crystals. Efficient PMSHG was achieved at a fundamental wavelength of 812 and 1064 nm. The efficient type I PMSHG coefficient was determined as  $d_{\text{eff}} = 4.9 \times 10^{-8}$  esu = 40 x ( $d_{11}$  of  $\alpha$ -quartz) at a wavelength of 1064 nm. Blue light generation was demonstrated by both PMSHG and sum-frequency mixing of the 812 nm laser with 1064 nm.

### INTRODUCTION

Organic molecules which have conjugated  $\pi$ -electron systems exhibit various photoresponses: photoconductive, photovoltaic, photocatalytic behavior, and so on. Nowadays remarkable interest has been focused on organic single crystals because it has been found to possess unique opto-electronic properties in a crystalline state, such as ultrafast electron motion in polydiacetylene crystals, superconductive phenomena in charge transfer complexes and large second order nonlinear optical effects in intramolecular charge transfer compounds. It has been established experimentally and theoretically that organic intramolecular charge transfer compounds have anomalously large optical nonlinearity [1] and show ultrafast response [2]. After the demonstration of the powder test by Kurtz et al., a large number of organic molecules have been found to possess second order optical nonlinearity. However, only a few of them, for example 2-methyl-4-nitroaniline, urea, methyl-(2,4-dinitrophenyl)-aminopropanate (MAP), N-(4-nitrophenyl)-(L)-prolinol and 3-methyl-4-nitropyridine-1-oxide (POM), could be crystallized in high quality and investigated on phase matched second harmonic generation (PMSHG) properties. Systematic ideas of molecular design have succeeded to some degree in the enhancement of microscopic second order nonlinear optical susceptibility ( $\beta$ ). On the other hand, molecular orientation in the crystalline state significantly influences the macroscopic second order susceptibility. Several approaches have been taken to control the molecular orientation; from the chemistry side, chemical modification was applied, such as introducing steric hindrance, hydrogen bonding, a chirality etc. and/or reducing the electrostatic dipole-dipole interaction; from the physics side poling techniques were applied to align nonlinear optically active molecules in polymer matrix. However, crystal engineering of organics is untouched area and lack of knowledge for crystal growth and crystal fabrication. One of the key issues for development of new nonlinear optical organic crystals is to establish the crystal fabrication of organic molecules for nonlinear optical measurements.

<sup>a)</sup> Permanent address: Department of Physics, University of Pennsylvania, Philadelphia, PA 19104

In this paper, we will present the quadratic nonlinear optical properties of DIVA crystals and the demonstration of blue light generation by PMSHG and sum-frequency mixing (SFM).

#### CRYSTAL GROWTH AND CHARACTERIZATION

On searching for new organic structures that possess nonlinear optical properties, cyano and dicyanovinyl compounds were found to show PMSHG and have a large SHG coefficient and a short cut-off wavelength comparable with that of POM [3],[4]. New organic optical nonlinear compounds which possess a methoxy group as an electron donor and a dicyanovinyl group as an electron acceptor were investigated and the crystallographic structure of ortho- and para-methoxy-benzalmalono-nitrile was determined by an X-ray diffraction method [5]. Both of them were found to have a monoclinic unit cell. The para-substituted compound is centrosymmetric with space group  $P2_1/a$ , whereas the ortho-substituted compound is a non-centrosymmetric structure with space group  $P2_1$ . Polar substituents were introduced to one side of a benzene ring. This highly anisotropic structure resulted in non-centrosymmetric stacking in the crystalline state as shown in Fig. 1.

Several conventional techniques, *i. e.*, vapor sublimation growth, slow solvent evaporation from a saturated solution and cooling method, are available to grow single crystals of DIVA. After pumped down to  $10^{-4}$  Pa, the pressure of sublimation tube was set at  $10^2$  Pa back-filled with argon gas and sealed. The bottom of the tube was heated up to 70 °C while the top was allowed to remain at room temperature. In the region between the top and the bottom, high quality crystals were grown in 1-2 days. Plate shape crystals were obtained depending on the conditions: temperature gradient and inner pressure and so on. Typical size is  $1 \times 2 \times 10$  mm<sup>3</sup>. Larger crystals were grown from solution by slow solvent evaporation. Approximately 36 grams of DIVA was dissolved in 100 ml of acetone at room temperature. The slow evaporation from saturated solution was performed under constant nitrogen gas flow. Typical size is  $10 \times 10 \times 5$  mm<sup>3</sup>. The single crystals up to  $15 \times 15 \times 10$  mm<sup>3</sup> in size were grown from acetone solution by cooling method. No evidence of polymorphism was found by X-ray diffraction method.

#### QUADRATIC NONLINEAR OPTICAL PROPERTIES

The methoxy groups ( $OCH_3$ ) are nearly aligned along the crystallographic b-axis, while the dicyano groups have approximately 55° direction cosine to this axis. Therefore, the molecular dipole moments have a common polar axis in the b-direction. In the a-c plane the dicyano groups point in the opposite directions, and the projection in this plane is centrosymmetric. With this type of molecular orientation we would expect to find large off-diagonal SHG tensor components like  $d_{21}$ ,  $d_{23}$  and  $d_{25}$  but smaller diagonal components like  $d_{22}$ . According to the analysis done by Zyss et al.[6], this molecular orientation in DIVA crystal with space group  $P2_1$  is favorable for the highest possible value of bulk phase-matchable coefficient.

High precision measurements were performed on the vapor grown crystals to determine the  $d_{22}$  SHG tensor component and the efficient type I PMSHG coefficient. For both Maker fringe and PMSHG experiments, the SHG intensity polarized along the b-axis was measured as a function of crystal rotation about the same b-axis. The  $d_{22}$  Maker fringes were generated

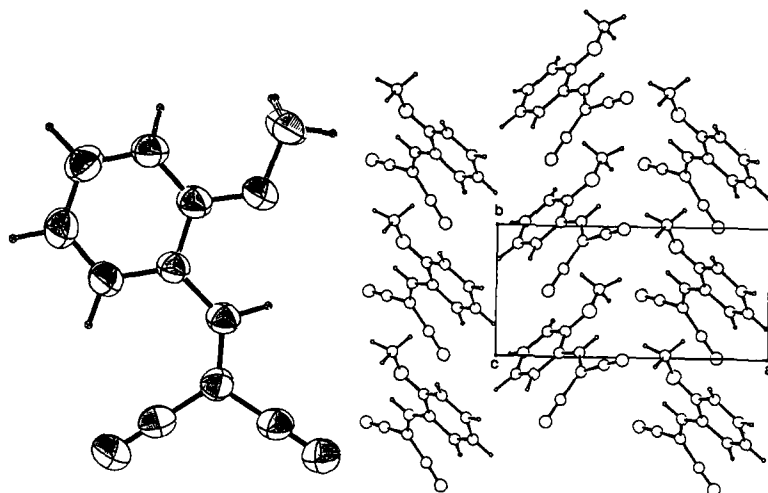


Fig. 1 The molecular structure of DIVA and the projection along the c-axis showing a net dipole alignment along the crystallographic b-axis.

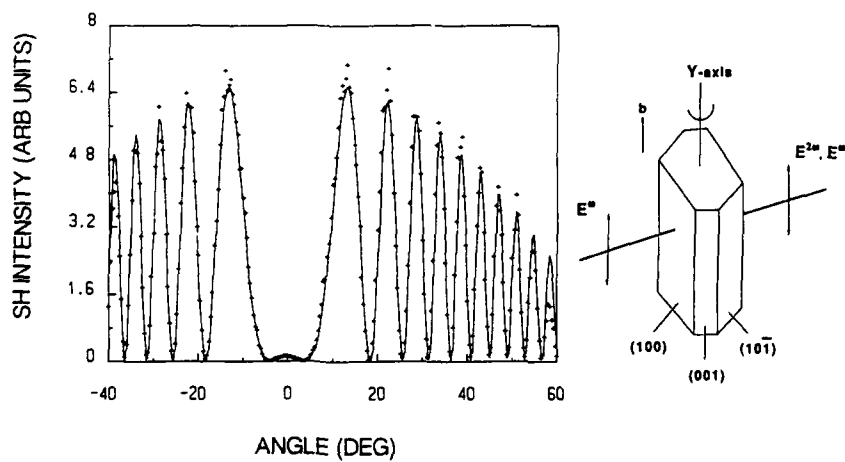


Fig. 2 Maker Fringe SHG at a wavelength of 1064 nm with the fundamental and second harmonic polarized along the principal Y-axis.

when the fundamental was incident in the crystal a-c plane and polarized along the b-axis. The results are shown in Fig. 2 along with the calculated curve. The value of  $d_{22}$  is  $2.6 \times 10^{-8}$  esu =  $20 \times (d_{11}$  of  $\alpha$ -quartz).

#### PHASE MATCHED SECOND HARMONIC GENERATION

On studies of the solution grown crystals, we observed both type I and type II PMSHG for laser light incident into the naturally grown crystal faces [4] Fig. 3. This eliminates the difficulty and time consuming task of cutting and polishing the organic crystals which have poor mechanical strength. Type I phase matching was observed from unfocused Q-switched Nd:YAG laser incident at  $30^\circ$  from the normal of the (100) face at a wavelength of 1064 nm. In this case, the fundamental was polarized in the a-c plane and the second harmonic along the b-axis. Type II PMSHG was observed near normal incidence in the (001) face with the fundamental polarized at  $45^\circ$  from the b-axis and the second harmonic polarized along the b-direction. Type I PMSHG was stronger than the type II and the conversion efficiency was measured using an unfocused incident beam. The incident beam had a peak power of 150 kW and the measured SHG was 300 W. In the limit  $n^\omega$  approaches  $n^{2\omega}$ , the PMSHG power is given by

$$P^{2\omega} = \frac{(8\pi)^5 (d_{\text{eff}})^2 L^2 (P^\omega)^2}{\pi c \lambda^2 w^2 (n+1)^6}$$

where L is the crystal length,  $\lambda$  the fundamental wavelength, w the beam radius, n the refractive index and  $P^\omega$  the fundamental power. With L = 0.5 mm, n = 1.65, w = 3 mm and  $P^\omega = 150$  kW the calculated PMSHG power is 407 W which is in good agreement with the measured value.

PMSHG was generated at the specific PM angle, the same angle as in the solution grown crystal case, with the fundamental incident in the a-c plane and also polarized in the a-c plane. Figure 4 shows the observed and calculated SHG intensity as a function of angle around the PMSHG position. From the amplitude of the fitted curve, we calculated the efficient PMSHG coefficient (a combination of  $d_{21}$ ,  $d_{23}$ ,  $d_{25}$  and direction cosines) with the result of  $d_{\text{eff}} = 4.9 \times 10^{-8}$  esu =  $40 \times (d_{11}$  of  $\alpha$ -quartz) [7].

#### BLUE LIGHT GENERATION BY QUADRATIC EFFECTS OF DIVA CRYSTAL

The practical application of quadratic effects in nonlinear crystals is frequency conversion of a commercial laser source; especially efficient quadratic nonlinear optical crystals are needed for frequency up-conversion of a diode laser in order to increase the memory densities of an optical disk and to open new applications as a visible laser. There are several approaches to get blue laser based on diode laser. One case is a direct frequency doubling of diode laser itself. The other is SFM of the tunable radiation of a diode laser with near-infrared laser obtained from diode laser pumped YAG laser which is now commercially available. In case of organic crystals they have large nonlinear optical coefficient arising from large second order nonlinear optical susceptibilities and low refractive indices, though, they have narrow optical transparent region. The investigation on optical parametric effects was limited so far to urea [8] and POM [9]. We demonstrated blue light generation by both PMSHG and SFM in DIVA crystals. Blue laser light (406 nm) was obtained by type I PMSHG from DIVA crystals at a fundamental

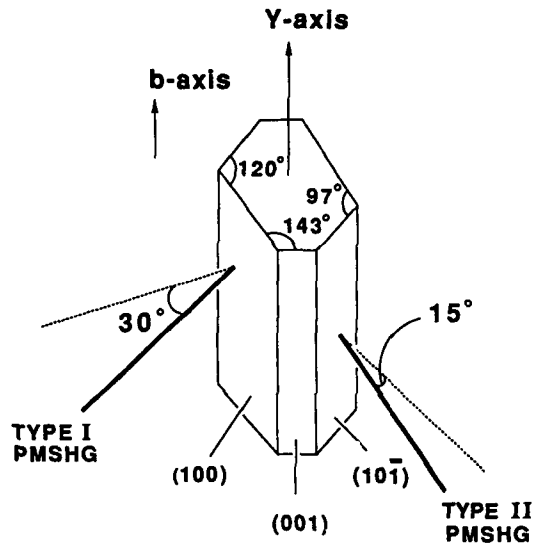


Fig. 3 DIVA crystal morphology; type I and type II PMSHG.

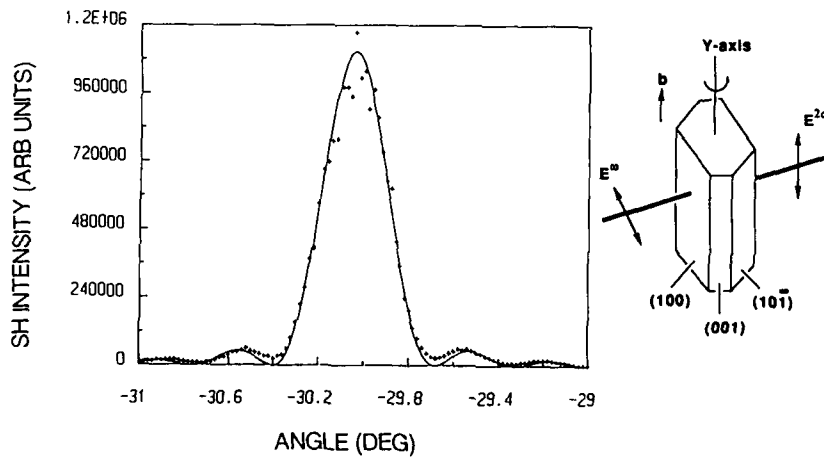


Fig. 4 Angular dependence of type I PMSHG at a wavelength of 1064 nm with the fundamental polarized in the a-c plane.

wavelength of 812 nm which was generated through high pressure  $\text{CH}_4$  gas as a first anti-Stokes Raman line. Phase matched angle is  $13.6^\circ$  from the normal of the (100) face. Type I sum-frequency mixing of 812 nm laser beam with 1064 nm was achieved under almost collinear configuration. Blue laser light (461 nm) was generated at about same PMSHG angle at 812 nm but coupling angle is about  $2^\circ$  perpendicular to the plane of incidence. Detailed investigation on coefficient and conversion efficiency will be published separately. This result demonstrates that DIVA crystals are applicable to frequency up-conversion of a diode laser in which the wavelength of oscillation is around 840 nm.

## REFERENCE

- [1] A. F. Garito, K. D. Singer and C. C. Teng, in "Nonlinear Optical Properties of Organic and Polymeric Materials", edited by D. J. Williams, ACS Symp. Ser. #233, (ACS, Washington DC, 1983) p.1
- [2] G. M. Carter, J. V. Hryniewicz, M. K. Thakur, Y. J. Chen, and S. E. Meyler, *Appl. Phys. Lett.* **49**, 998 (1986).
- [3] Y. Mori, M. Okamoto, T. Wada, and H. Sasabe, *Mat. Res. Soc. Symp. Proc.*, **109** 345 (1988).
- [4] C. H. Grossman, T. Wada, S. Yamada, A. Yamada, A. F. Garito, and H. Sasabe, *IQEC'88 Technical Digest*, (1988) p.134
- [5] T. Wada, S. Yamada, Y. Matsuoka, C.H. Grossman, K. Shigehara, H. Sasabe, A. Yamada, and A. F. Garito, in "Nonlinear Optics of Organics and Semiconductors", edited by T. Kobayashi, *Springer Proceedings in Physics*, **36**, 292 (1989).
- [6] J. Zyss and J. L. Oudar, *Phys. Rev.* **A26**, 2028 (1982).
- [7] C. H. Grossman, T. Wada, S. Yamada, A. Yamada, H. Sasabe, and A. F. Garito, in "Nonlinear Optics of Organics and Semiconductors", edited by T. Kobayashi, *Springer Proceedings in Physics*, **36**, 214 (1989).
- [8] J. Halbout, S. Blit, W. Donaldson, and C. L. Tang, *IEEE J. Quant. Electron.*, **QE-15**, 1176 (1979).
- [9] J. Zyss, I. Ledoux, R. B. Hierle, R. K. Raj, and J. Oudar, *IEEE J. Quant. Electron.*, **QE-21**, 1286 (1985).



FERROELECTRICITY OF CHIRAL COMPOUNDS IN HIGHLY ORDERED  
SMECTIC PHASES

STANISLAW WRÓBEL<sup>\*</sup>, MATTHIAS PFEIFFER, ASHÓK M. BIRADAR<sup>+</sup>  
AND WOLFGANG HAASE

*Institut für Physikalische Chemie, Technische Hochschule Darmstadt,  
Petersenstr. 20, D-6100 Darmstadt, Federal Republic of Germany*

ABSTRACT

Measurements of the complex electric permittivity for the Sm C<sup>\*</sup> and for three highly ordered smectic phases: Sm I<sup>\*</sup>, Sm J<sup>\*</sup> and Sm K<sup>\*</sup> of 4-(2-methylbutyl)-phenyl-4'-(octyloxy)-(1,1')-biphenyl-4-carboxylate (8OSI) have been done in the frequency range from 5 Hz to 13 MHz. For the first three chiral phases the Goldstone mode was found with temperature independent critical frequencies,  $\nu_c = 1.5\text{ kHz}$  and the relaxation time  $\tau_G = 106\ \mu\text{s}$  - for the Sm C<sup>\*</sup> phase, and  $\nu_c = 1\ \text{kHz}$  and  $\tau_G = 160\ \mu\text{s}$  - for the Sm I<sup>\*</sup> one. In two highly ordered smectics, i.e. Sm J<sup>\*</sup> and Sm K<sup>\*</sup> with inter-layer correlations, the Goldstone mode seems to be suppressed. By applying a D.C. bias field of 1.4 kV/cm the Goldstone mode has been suppressed and shifted towards higher frequencies in both the Sm C<sup>\*</sup> and Sm I<sup>\*</sup> phase. For the Sm J<sup>\*</sup> phase the Goldstone mode is very weak and practically insensitive to the bias field used. In the Sm K<sup>\*</sup> phase there is no Goldstone mode like relaxation, and the only contribution to electric permittivity comes from the fast molecular motion connected with reorientation of molecules about their long axis.

INTRODUCTION

Ferroelectric liquid crystals (FLCs) were theoretically predicted by R. B. Meyer and the first substance exhibiting ferroelectric properties (DOBAMBC) was synthesized in 1975 [1]. Ferroelectric properties of thermotropic liquid crystals are due to both the molecular structure (chirality of polar molecules) and the quasi-crystalline structure of tilted smectics (Sm C<sup>\*</sup>, Sm I<sup>\*</sup>, Sm F<sup>\*</sup>, Sm J<sup>\*</sup>, Sm G<sup>\*</sup>, Sm K<sup>\*</sup> and Sm H<sup>\*</sup>). The spontaneous polarization within a smectic layer is proportional to the vector product of the unit vector along the layer normal ( $\vec{z}_0$ ) and the director ( $\vec{n}$ ),

$$P_s \sim (\vec{z}_0 \times \vec{n}) \quad (1)$$

Because of chirality of molecules the tilted smectics form helicoidal structure and z is the axis of the helix. Fluctuations of the  $\phi$ -angle, the angle in the layer plane which gives the pitch, create a signal in the dielectric spectrum, the Goldstone mode. However, it is known that in highly ordered tilted smectics with strong inter-layer correlations ( $S_J$ ,  $S_G$ ,  $S_K$  and  $S_H$ ) the helicoidal structure is

suppressed [2,3].

FLCs exhibit the spontaneous polarization between 1 and  $\sim 300$  nC/cm<sup>2</sup>, which is very small in comparison with classical ferroelectrics. However, the existence of spontaneous polarization within the layers allows one to induce electro-optic effects with switching times in ms and  $\mu$ s region depending on temperature, phase structure and so on.

The electric permittivity tensor of the Sm C\* phase, having a helicoidally arranged polarization vector, has the following form in the layer normal frame:

$$\hat{\epsilon}_{xyz} = \begin{Bmatrix} \epsilon_{xx} \cos^2 \varphi + \epsilon_{yy} \sin^2 \varphi, & (\epsilon_{yy} - \epsilon_{xx}) \sin \varphi \cos \varphi, & \epsilon_{xz} \sin \varphi \\ (\epsilon_{yy} - \epsilon_{xx}) \sin \varphi \cos \varphi, & \epsilon_{xx} \sin^2 \varphi + \epsilon_{yy} \cos^2 \varphi, & -\epsilon_{xz} \cos \varphi \\ \epsilon_{zx} \sin \varphi, & -\epsilon_{zx} \cos \varphi, & \epsilon_{zz} \end{Bmatrix} \quad (2)$$

where  $\varphi = \frac{2\pi}{L_0} z$  is an angle of rotation of the polarization vector, and  $L_0$  is in turn the pitch of the helix. For our experimental conditions one can assume that  $z \gg L_0$ , and (2) can be averaged out and one arrives at:

$$\langle \hat{\epsilon}_{xyz} \rangle = \begin{Bmatrix} \epsilon_{\perp} & 0 & 0 \\ 0 & \epsilon_{\perp} & 0 \\ 0 & 0 & \epsilon_{\parallel} \end{Bmatrix} \quad (3)$$

where  $\epsilon_{\perp} = \frac{1}{2} (\epsilon_{xx} + \epsilon_{yy})$  and  $\epsilon_{\parallel} = \epsilon_{zz}$ . Thus one obtains the diagonal dielectric tensor, the principal components of which can be measured for chiral SmC\* phase by using weak A.C. fields.

After applying a bias D.C. field, which unwinds the helix, the dielectric tensor (2) undergoes a transformation and has the form:

$$\hat{\epsilon} = \begin{Bmatrix} \epsilon_{xx} & 0 & 0 \\ 0 & \epsilon_{yy} & \epsilon_{yz} \\ 0 & \epsilon_{zy} & \epsilon_{zz} \end{Bmatrix} \quad (4)$$

where  $\epsilon_{ij}$  are the components of the dielectric tensor in the frame, the z axis of which coincides with the layer normal. It is worth noting that  $\epsilon_{ij}$  can be easily expressed by the diagonal tensor elements defined in the director frame.

Application of a bias field to chiral smectics can unwind the helix. It follows, that their dielectric and optical properties can be modified, which is very important from the application point of view.

Unwinding of the helicoidal structure of a chiral smectic exhibits a threshold behaviour [1],

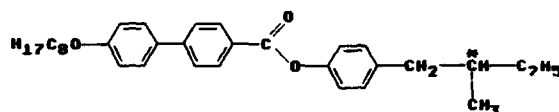
$$E_C = \frac{\pi k \Theta}{4 P_0 L_0^2} \quad (5)$$

where  $\Theta$  is the tilt angle and  $k$  is the twist elastic constant. It is known from the dielectric and electro-optical studies of CE 8 [4,5] and CE 3 [4] that these FLC's exhibit rather short pitch and small spontaneous polarization. Thus their threshold

field is high as has also been found for the sample under investigation, which has a similar molecular structure to CE 8 and CE 3.

## EXPERIMENTAL

BOSI sample has been obtained as a gift from E. Merck Company, Darmstadt. Its chemical formula is:



Phase transition temperatures obtained by us by means of polarizing microscopy are the following:

I-171.8-BP-171.8-Ch-170.2-S<sub>A</sub>\*-130.5-S<sub>C</sub>\*-79.7-S<sub>I</sub>\*-73.3-S<sub>J</sub>\*-61.9-S<sub>K</sub>\*.

where temperatures are in °C. In literature there were some doubts about the structures of the S<sub>J</sub>\* and S<sub>K</sub>\* phases [2,6,7]. Our X-ray investigations are being done.

Dielectric measurements for all chiral smectic phases of BOSI have been performed in the frequency range from 5 Hz to 13 MHz by using HP 4192A impedance analyzer being under computer control. The  $\epsilon_1^*$  complex electric permittivity component has been measured versus temperature at 53 frequencies evenly spaced on the logarithmic scale. To suppress the Goldstone mode in the S<sub>C</sub>\* and S<sub>I</sub>\* phases an internal bias voltage of +35 V (E = 14 kV/cm) has been used.

As a parallel plate condenser gold-plated glass electrodes, properly shaped and guarded and separated by 25  $\mu$ m mylar spacers, were used. The active surface of the condenser's plates was 0.78 cm<sup>2</sup>. Calibration of the condenser was performed by measuring temperature dependences of the capacity and loss factor of the air- and toluene-filled cell between 22 and 65 °C. The calculated parameters were then extrapolated to higher temperatures.

The sample of BOSI was introduced into the cell by means of capillary action, at few degrees above the clearing point. After checking under the polarizing microscope the quality of filling in the gaps between the active and guard electrode, the sample holder was put into a "thermal aluminium box", which was thermally isolated and placed between the magnet poles. The planar alignment of the S<sub>C</sub>\* phase (the so-called book-shelf geometry) was achieved by a slow cooling rate ( $-\frac{dT}{dt} = -2^\circ/\text{min}$ ) of the sample from its Ch phase to the S<sub>C</sub>\* one in the presence of the magnetic field of 1.2 T. The alignment in the S<sub>C</sub>\* phase was not affected after switching off the magnet. It means that the orientation was stabilized by the surface effect. The same procedure was used by us in the case of mixtures [8-10]. One should explain that in the book-shelf geometry the helix axis is parallel to the electrodes, i.e. perpendicular to the measuring electric field.

## RESULTS AND DISCUSSION

Dielectric properties of FLCs are very important from the application standpoint. Due to this fact some mixtures showing room temperature  $S_C^*$ ,  $S_I^*$  and  $S_F^*$  phases have been investigated [8-10]. In this paper we are dealing with a single chiral component showing - in addition to the  $S_C^*$  and  $S_I^*$  ferroelectric phases - two highly ordered smectics, namely,  $S_J^*$  and  $S_K^*$  ones.

Taking into account the molecular structure of 8OSI possessing two polar groups:  $OC_8H_{17}$  and  $CO_2$ , one can calculate the perpendicular component of the dipole moment as equal to:  $\mu_{\perp} = 2.1$  D. This component should give the contribution to spontaneous polarization in the tilted smectics. However, in the case of 8OSI there might be a weak coupling between the chiral center and the dipole moments.

As is seen from Fig. 1, in the  $S_C^*$  phase there is a relaxation process in the frequency range from 1 Hz to  $10^5$  Hz, centred around 1.5 kHz ( $\tau_G \approx 106 \mu s$ ). As the critical frequency is practically temperature independent, and the dispersion and absorption processes show up only in the chiral phases, the relaxation observed is the Goldstone mode. In addition, by applying a bias field of 14 kV/cm a tremendous decrease of the absorption peak is observed like for other FLCs [10,11]. It is worth noting that the critical frequency is shifted towards higher frequencies. The same effect has been observed for CEB [5], which is a similar molecule to 8OSI, but does not have an oxygen atom in the non-chiral side chain. The alkoxy group has most probably very small influence on the ferroelectric properties of 8OSI. Such a conclusion can be drawn by comparing the dielectric spectra of CEB [5] and 8OSI (Fig.1), which are about the same in their intensity and temperature and frequency dependences.

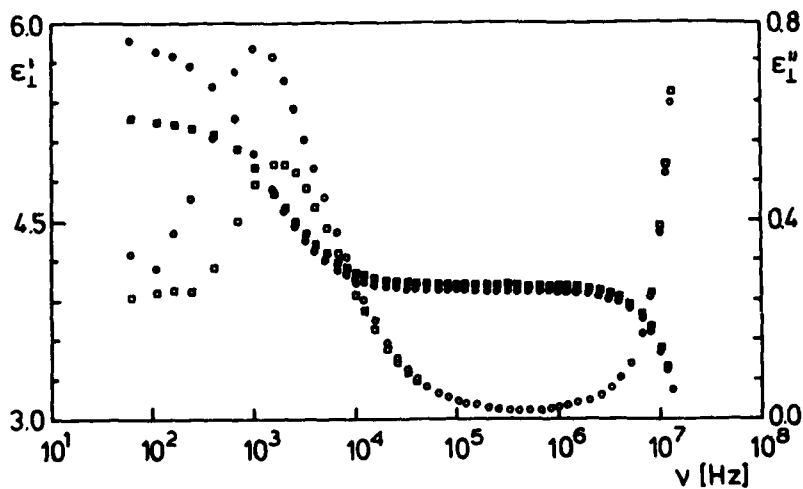


Fig. 1. Frequency dependences of the  $\epsilon'_1$  electric permittivity and the  $\epsilon''_1$  dielectric losses obtained in the  $S_C^*$  phase of 8OSI, at  $T = 84.03^\circ C$ .  
( $\bullet$  -  $\epsilon'_1(\nu)$  and  $\circ$  -  $\epsilon''_1(\nu)$  - bias off;  $\blacksquare$  -  $\epsilon'_1(\nu)$  and  $\square$  -  $\epsilon''_1(\nu)$  - bias on)

Our measurements were extended to the highly ordered smectic phases where it was possible to observe the Goldstone mode contribution. In Fig. 2 one can see the Goldstone mode dielectric spectrum obtained for the  $S_{1^*}$  phase. As is seen the absorption peak is shifted towards lower frequencies (ca. 1 kHz,  $\tau_G \approx 160 \mu s$ ). Its position does not change with temperature within the  $S_{1^*}$  phase. As is seen the influence of the D.C. bias field is also tremendous in this phase. It means that the helicoidal structure is in the  $S_{1^*}$  phase very well developed.

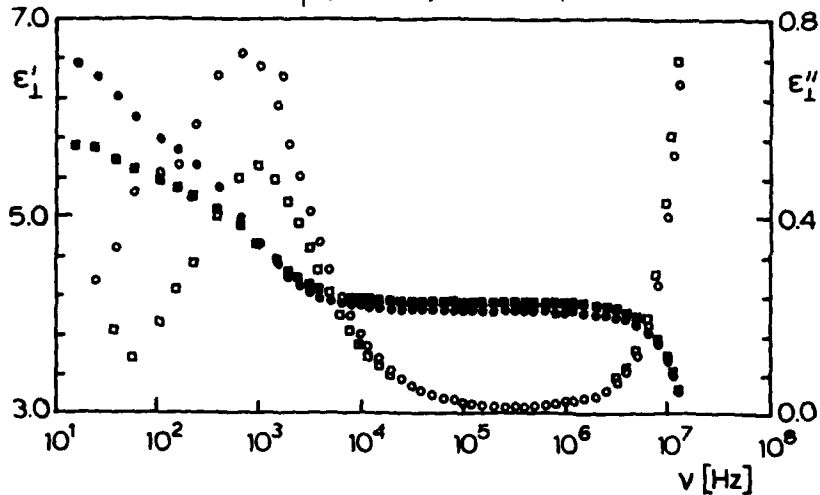


Fig. 2. Dispersion ( $\epsilon'_1(\nu)$ ) and absorption ( $\epsilon''_1(\nu)$ ) curves obtained for the Goldstone mode in the  $S_{1^*}$  phase without bias field ( $\bullet - \epsilon'_1$ ,  $\circ - \epsilon''_1$ ) and with bias field  $E = 14$  kV/cm ( $\blacksquare - \epsilon'_1(\nu)$ ,  $\square - \epsilon''_1(\nu)$ ), at  $T = 77.92^\circ\text{C}$ .

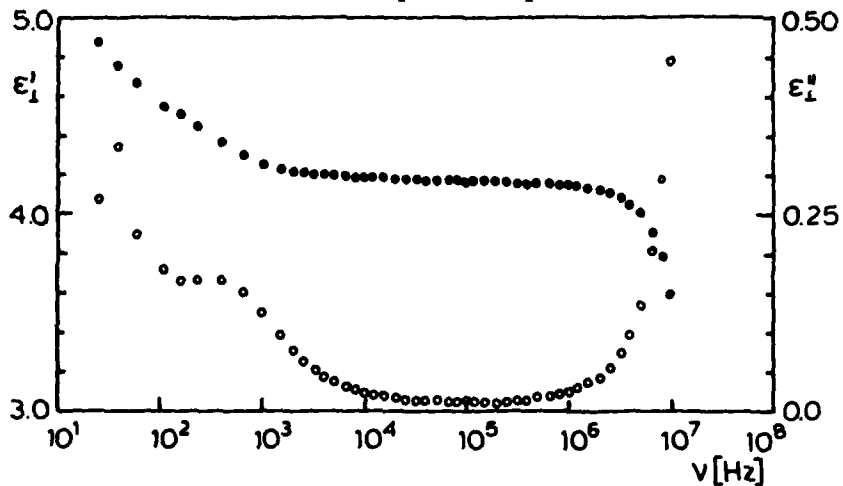


Fig. 3. Dispersion ( $\bullet - \epsilon'_1(\nu)$ ) and absorption ( $\circ - \epsilon''_1(\nu)$ ) curves acquired for the  $S_{1^*}$  phase of 8OSI, at  $T = 77.4^\circ\text{C}$ . Little shoulder centred around 0.8 kHz is a residual Goldstone mode contribution.

On the other hand in the  $S_{J^*}$  phase there is only a weak absorption peak connected with the Goldstone mode ( Fig. 3 ). This means that the Goldstone mode is strongly suppressed in the  $S_{J^*}$  phase due to - most probably - strong inter-layer correlations, which do not allow for a pitch development. This effect has been suggested before [2] and found, recently, for CE 8 [4] by optical studies. One should add that in the  $S_{K^*}$  phase there is no contribution from the Goldstone mode. The only molecular contribution to the  $\epsilon_{\parallel}$  electric permittivity in this phase comes from the reorientation about the long axis which is not restricted by both the hexatic structure inside the layers and the inter-layer correlations.

#### ACKNOWLEDGEMENTS

The authors thank E. Merck Company, Darmstadt, for putting the 80S1 sample at their disposal. Financial support by Fonds der Chemischen Industrie is highly appreciated. S. W. would like to thank the President of the Technische Hochschule Darmstadt and the Hessisches Ministerium für Wissenschaft und Kunst for financial assistance.

#### Permanent addresses:

\*S. Wróbel, Institute of Physics, Jagellonian University, Reymonta 4, 30-059 Kraków, Poland;

+A. M. Biradar, National Physical Laboratory, Dr. K.S. Krishnan Road, New Delhi - 110012, India.

#### REFERENCES

1. R.B. Meyer, L. Liebert, L. Strzelecki and P. Keller, *J. de Phys. Lett.* **36**, 69 (1975).
2. G.W. Gray and J.W. Goodby, *Smectic Liquid Crystals*, Leonard and Hill, Glasgow and London 1984.
3. W. Kuczyński and H. Stagemeyer, *Ferroelectrics* **5**, 553 (1989).
4. M.F. Bone, D. Coates, A.B. Davey, *Mol. Cryst. Liq. Cryst.* **102**, 331 (1984).
5. R.J. Cava, J.S. Patel and E.A. Rietman, *J. Appl. Phys.* **60**, 3093 (1986).
6. D. Brok, A. Aharony, R.J. Birgeneau, K. Evans-Lutterodt, J.D. Litster, P.M. Horn, G.B. Stephenson and A.J. Tajbakhsh, *Phys. Rev. Lett.* **57**, 98 (1986).
7. A.J. Leadbetter, J.P. Gaughan, B. Kelly, G.W. Gray and J.W. Goodby, *J. Phys. (Paris), Colloq.* **3**, **40**, p.C1 (1979).
8. A.M. Biradar, S. Wróbel and W. Haase, *Phys. Rev. A* **39**, 2693 (1989); *Liquid Crystals* **5**, 1227 (1989).
9. A.M. Biradar, S. Wróbel and W. Haase, *Ferroelectrics* (in print).
10. S. Wróbel, A.M. Biradar and W. Haase, *Ferroelectrics* **100**, ..... (1989).
11. M. Glogarowa, J. Fousek, L. Lejcek and J. Pavel, *Ferroelectrics* **58**, 161 (1984).

LANGMUIR-BLODGETT FILMS OF POTENTIAL UNIDIMENSIONAL ORGANIC  
RECTIFIERS #

ROBERT M. METZGER \* AND CHARLES A. PANETTA\*\*

\* Department of Chemistry, The University of Alabama, Tuscaloosa, Alabama, 35487-0336,  
USA

\*\* Department of Chemistry, The University of Mississippi, University, MS 38677, USA

ABSTRACT

The progress of the Organic Rectifier Project (ORP) is reviewed. Several molecules of the type D- $\sigma$ -A (D=organic one-electron donor,  $\sigma$  = covalent saturated bridge, A = organic one-electron acceptor) have been synthesized, to test the Aviram-Ratner Ansatz that they could be one-molecule thick rectifiers of electrical current. Many of these molecules ( $\sigma$ = urethane) self-assemble as Langmuir-Blodgett films; the cyclic voltammetry peaks confirm that these molecules preserve the good D and A characteristics. Calculations confirm that the zwitterionic state D<sup>+</sup>- $\sigma$ -A<sup>-</sup> is much below the state D- $\sigma$ -A<sup>+</sup>, as expected. Preliminary tests of electrical rectification have failed. With the installation of a new scanning electron microscope, the Aviram-Ratner Ansatz will soon be put to a final and definitive test.

INTRODUCTION

The Organic Rectifier Project (ORP) is inspired by the Ansatz of Ari Aviram, Mark A. Ratner, and coworkers [1-3] that a single organic molecule D- $\sigma$ -A could rectify electrical current, because the zwitterionic state D<sup>+</sup>- $\sigma$ -A<sup>-</sup> should lie maybe 1 eV above the neutral ground state D- $\sigma$ -A, but 3 to 4 eV lower than the zwitterionic state D<sup>+</sup>- $\sigma$ -A<sup>-</sup>. This asymmetry would allow facile electron conduction from the A end through the molecule to the D end. If the molecule were to be placed between two conventional metallic layers M<sub>1</sub> and M<sub>2</sub>, then the device M<sub>1</sub>|D- $\sigma$ -A|M<sub>2</sub> (where | denotes an interface) would be a rectifier of electrical current of molecular dimensions. This rectifier, if realized, would be one of the most dramatic advances of the infant field of molecular electronics. Such a rectifier would have high speed (> 1 ns), but a working length (5 nm) much smaller than conceivable for Si or GaAs devices.

The progress of the ORP [4-25] has been summarized elsewhere [5,8,10,16,19-21,23,25], and is here reviewed again; for more details, see Ref. [25].

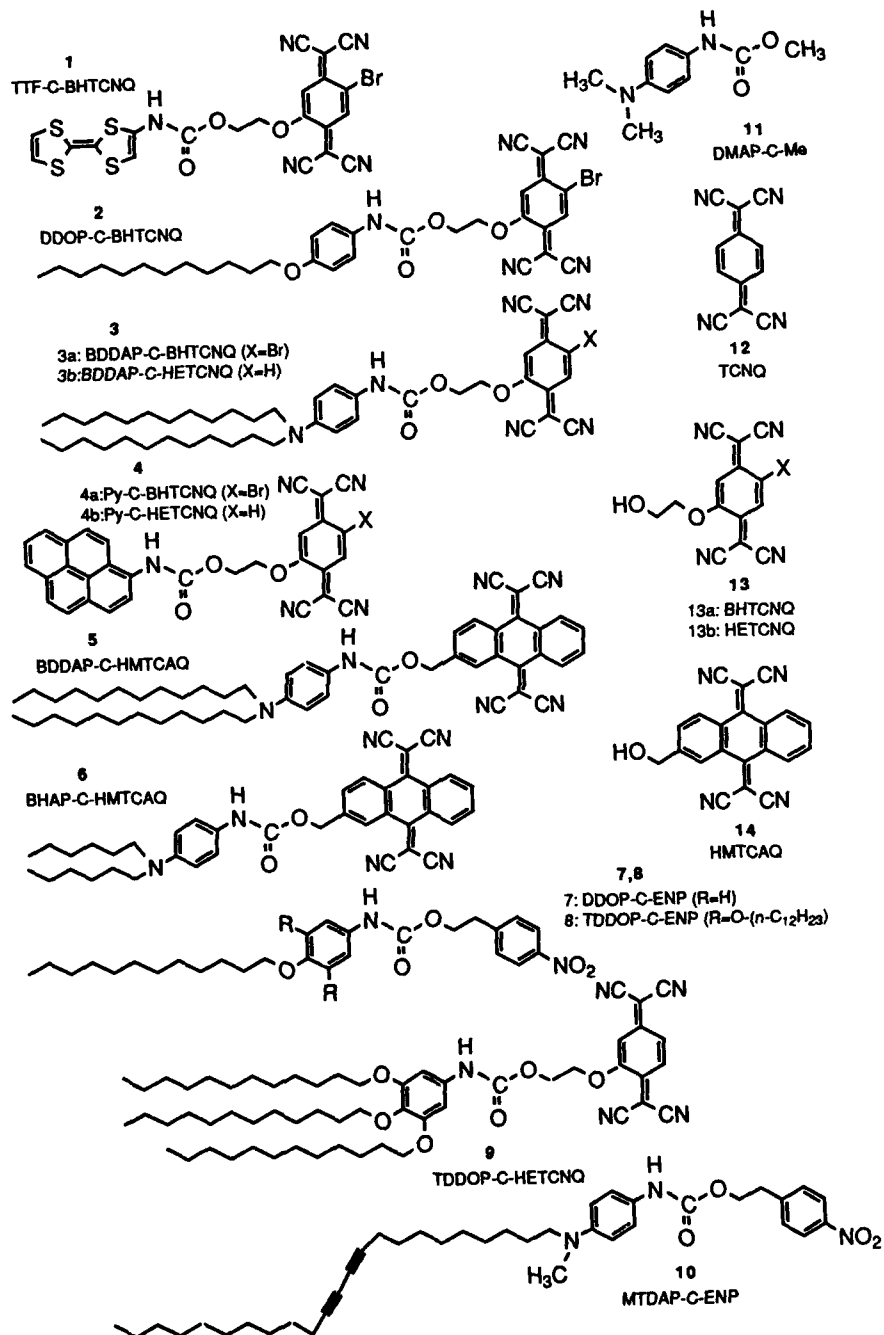
METHODS FOR ASSEMBLY OF D- $\sigma$ -A MOLECULAR DEVICES

Until the recent advent of the scanning tunneling microscope (STM: *vide infra*) there was no way of addressing electronically a single molecule; thus one had to find a method to assemble and test a one-molecule thick D- $\sigma$ -A rectifier. The three methods that seemed promising were (i) the Langmuir-Blodgett technique [26-32], (ii) the covalent bonding of molecules to silanized electrodes [33], or (iii) the covalent bonding of silanized molecules to hydroxyl-coated electrodes [34]. Full monolayer coverage of a surface is claimed by (i) and (iii), but not by (ii). The ORP chose the LB method. This often required the attachment of "greasy chains" to the D end, at the possible price of speedy electron transfer through the saturated chain; chains as short as possible were sought.

Table I shows which D- $\sigma$ -A molecules (1-10) form LB monolayers. (Molecules 7-10 are part of a study to combine rectification properties with possible non-linear optical behaviour of D- $\sigma$ -A molecules coupled to a polydiacetylene backbone). A typical pressure-area ( $\Pi$ -A) isotherm is shown in Fig. 1.

OTHER REQUIREMENTS FOR RECTIFICATION

- Of course, there are several other requirements which must be satisfied for a D- $\sigma$ -A rectifier:
- (i) **electronic:** in the device M<sub>1</sub>|D- $\sigma$ -A|M<sub>2</sub> the work function of the metal M<sub>1</sub> must be as close as possible to the ionization potential I<sub>D</sub> of the donor end D (i.e. I<sub>D</sub> must be low); the work





**Table I.**  
Pressure-Area isotherm data for Pockels-Langmuir films.  $\Pi_c$  and  $A_c$  are the pressure and molecular area, respectively, at the collapse point. \$ indicates that the film makes Z-type LB multilayers (substrate at 22°C, film at 5°C).

Molecule	No.	Type	T K	$\Pi_c$ mN/m	$A_c$ $\text{\AA}^2$	Ref.
TTF-C-BHTCNQ	1	strong D strong A	292	12.7	134±50	[5]
DDOP-C-BHTCNQ	2	weak D strong A	292	20.2	50±1	[7]
BDDAP-C-BHTCNQ	3a	medium D strong A	293	47.3	57±1	[15]
Py-C-BHTCNQ	4a	medium D strong A	283	28.2	53±1	[7]
BDDAP-C-HMTCAQ	5	medium D weak A	293	22.3	58±1	[15]
BHAP-C-HMTCAQ	6	medium D weak A	293	35.8	42±1	[16]
DDOP-C-ENP	\$ 7	weak D weak A	278	23.7	38±1	[24]
TDDOP-C-ENP	\$ 8	weak D weak A	278	34.0	76±1	[24]
TDDOP-C-HETCNQ	\$ 9	weak D strong A	283	47.5	54±1	[24]
MTDAP-C-ENP	\$ 10	weak D weak A	278	16.5	63±1	[23]

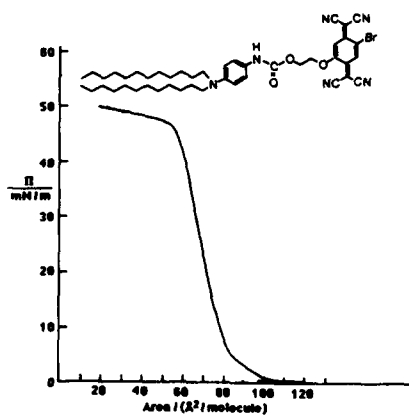


Fig. 1. Pressure-Area isotherm for BDDAP-C-BHTCNQ, 3a [15].

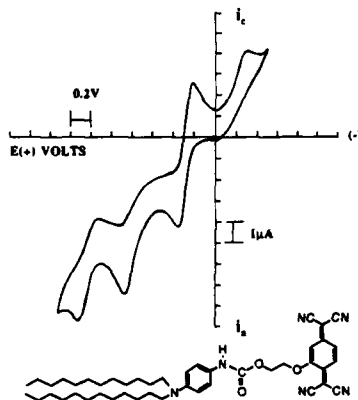


Fig. 2. Cyclic voltammogram for BDDAP-C-HECTNQ, 3b [25].

function of the metal  $M_2$  must be as close as possible to the electron affinity  $A_A$  of the acceptor end A (i.e.  $A_A$  must be high); the current flow must be tunneling through the bond system, not through space (and no electrical shorts through defects must exist)

- (ii) speed: the electron transfer will be faster, the larger the difference  $I_{D-A}$ , but if this difference is too large, then the increased Franck-Condon geometry reorganization of the molecule will slow down the electron transfer [35,36] (Marcus inverted region [37]).

#### OXIDATION AND REDUCTION PROPERTIES OF D- $\sigma$ -A MOLECULES

In Table II are shown the solution oxidation and reduction potentials of one donor (11), several acceptors (12-14), and several D- $\sigma$ -A molecules; the data show conclusively that these molecules do indeed preserve the good electron donating (accepting) ability of the D (A) end. A typical cyclic voltammogram is shown in Fig. 2.

Futhermore, MNDO semi-empirical molecular orbital calculations have shown [20] that molecules very similar to 1-6 preserve the electronic properties of the D and A ends, as expected, and that the difference between the zwitterionic excitation energies  $I_{D-A}$  (for D- $\sigma$ -A to D $^+$ - $\sigma$ -A $^-$ ) and  $I_{A-D}$  (for D- $\sigma$ -A to D- $\sigma$ -A $^+$ ) remains large. Thus, the D- $\sigma$ -A molecules studied in Table I, and particularly BDDAP-C-BHTCNQ, (which has the highest collapse pressure  $\Pi_c$ , and the highest slope of  $\Pi$  versus A) should be a good candidate for a molecular rectifier.

Table II.  
Solution oxidation and reduction potentials, obtained by cyclic voltammetry at a Pt electrode, and quoted in Volts vs SCE.

Molecule	No.	Oxid.(1)		Oxid.(2)		Red.(1)		Red.(2)		Ref.	
		$D \rightarrow D^+$	$D^+ \rightarrow D^{++}$	$A \rightarrow A^-$	$A^- \rightarrow A^{--}$	$E_p$	$E_{1/2}$	$E_p$	$E_{1/2}$		
<b>Donor:</b>											
DMAP-C-Me	11	a	0.58	0.55	-	--	-	-	-	-	[12]
<b>Acceptors:</b>											
TCNQ	12	b	-	-	-	-	0.19	-	-0.35	[38]	
TCNQ	12	c	-	-	-	-	0.11	0.13	-0.46	-0.43	[24]
BHTCNQ	13a	b	-	-	-	-	0.305	-	-0.170	[7]	
HETCNQ	13b	b	-	-	-	-	0.107	-	-0.398	[17]	
HMTCAQ	14	b	-	-	-	-	-	-0.372	-0.333	[9]	
<b>D-<math>\sigma</math>-A:</b>											
DDOP-C-ENP	7	c	1.42	1.39	-	-	-1.16	-1.13	-	-	[24]
TDDOP-C-ENP	8	c	1.17i	-	-	-	-1.12	-1.15	-	-	[24]
MTDAP-C-ENP	10	c	0.57	0.54	-	-	-1.09	-1.06	-	-	[25]
BHAP-C-HMTCAQ	6	c	0.63	0.60	-	--	-	-	-0.39	-0.36	[25]
DDOP-C-BHTCNQ	2	d	-	1.21	-	-	-	0.25	-	-0.07	[7]
TDDOP-C-HETCNQ	9	c	1.02i	-	-	-	0.10	0.07	-0.50	-0.47	[24]
BDDAP-C-HETCNQ	3b	e	0.66i	-	1.10	-	0.02	-	-0.49i	-	[25]
Py-C-HETCNO	4b	e	1.04	1.01	1.18	1.15	0.11	0.08	-0.32	-0.35	[25]

#### Footnotes:

- (a) Solvent: CH<sub>3</sub>CN. Reference electrode: SCE. A peak at 0.37 V (return scan) grows with successive cycles, and is indicative of dimer or polymer formation [12].
- (b) Solvent: CH<sub>3</sub>CN. Reference electrode: SCE.
- (c) Solvent: CH<sub>2</sub>ClCH<sub>2</sub>Cl. Reference electrode: Ag|AgCl. An offset correction of 0.15 V has been applied to convert the values to V vs. SCE.
- (d) Solvent: CH<sub>3</sub>CN. Reference electrode: Ag|AgNO<sub>3</sub>. An offset correction of 0.320 V has been applied to convert the values to V vs. SCE.
- (e) Solvent: CH<sub>2</sub>ClCH<sub>2</sub>Cl. Reference electrode: Ag|AgCl. An offset correction of 0.19 V has been applied to convert the values to V vs. SCE.

## FTIR AND MONOLAYER THICKNESS DATA

In addition, preliminary Fourier transform infrared (FTIR) spectra have been obtained for monolayer and multilayer LB films on Al substrates [19-21, 23, 24]. Monolayer thicknesses have also been determined by X-ray diffraction and ellipsometry [24].

## TESTS OF RECTIFICATION

Crude tests of rectification, using a Hg drop over the D- $\sigma$ -A monolayer which had been transferred atop a metal-coated substrate, failed [7], as did efforts to detect rectification in sandwiches Al | BDDAP-C-BHTCNQ | Al, in which the overlap of Al over Al was kept to about 0.5 mm<sup>2</sup>: in all cases either open circuit conditions were attained, or else the ohmic resistivity of the underlying Al was measured [19]. Clearly, the defects (domain boundaries, etc.) of single monolayers prevented a realistic test of rectification by macroscopic probes.

A test by scanning tunneling microscopy (STM) suggested [20,21] that rectification had been attained for a monolayer of BDDAP-C-BHTCNQ, 5a, deposited on a Au and Ag-coated mica substrate and probed by a W tip (similar rectification had been claimed for a H-bonded ortho-quinone-catechol molecule [39]). However, later testing revealed that the "rectification signal" could also be observed in the absence of any molecule, albeit at a much higher bias voltage, and all claims of rectification were withdrawn ("Notes in proof" in [20, 21]).

One week ago, a Digital Instruments Nanoscope II STM was installed in our laboratory, and we intend to measure carefully the currents across D- $\sigma$ -A monolayers using a large variety of substrates and tips. Thus we have high hopes of determining, once and for all, whether rectification by a single organic molecule (organized in an LB film) can be observed.

Fujihira and co-workers demonstrated rectification in an electrochemical cell by shining light on a LB monolayer: this is an LB monolayer photodiode [40,41].

## CONCLUSION

It has been shown that organic donors and acceptors can be coupled within the same covalently bonded D- $\sigma$ -A molecules, and that these can form monolayers at the air-water interface; these D- $\sigma$ -A monolayers can be transferred quantitatively to solid substrates as LB films. What still remains to be shown is that these D- $\sigma$ -A molecules can act as rectifiers of electrical current; there is ample hope that such a test can be done by STM, thus avoiding the problem of electrical shorts due to defects at macroscopic domain edges in LB films.

## REFERENCES

- # Supported by the National Science Foundation, Grant DMR-88-01924
- [ 1 ] A. Aviram, M. J. Freiser, P. E. Seiden, and W. R. Young, U.S. Patent US-3,953, 874 (27 April 1976).
  - [ 2 ] A. Aviram and M. A. Ratner, Chem. Phys. Lett. **29**, 277 (1974).
  - [ 3 ] A. Aviram, P. E. Seiden, and M. A. Ratner, in *Molecular Electronic Devices*, F. L. Carter, ed. (Dekker, New York, 1982) page 5.
  - [ 4 ] R. M. Metzger and C. A. Panetta, J. Phys. (Les Ulis, Fr.) Colloque **44**, C3-1605 (1983).
  - [ 5 ] R. M. Metzger and C. A. Panetta, in *Molecular Electronic Devices*, Vol. II, F. L. Carter, ed. (Dekker, New York, 1987) page 1.
  - [ 6 ] C. A. Panetta, J. Baghdadchi, and R. M. Metzger, Mol. Cryst. Liq. Cryst. **107**, 103 (1984).
  - [ 7 ] R. M. Metzger, C. A. Panetta, N. E. Heimer, A. M. Bhatti, E. Torres, G. F. Blackburn, S. K. Tripathy, and L. A. Samuelson, J. Molec. Electronics **2**, 119 (1986).
  - [ 8 ] R. M. Metzger, C. A. Panetta, Y. Miura, and E. Torres, Synth. Metals **18**, 797 (1987).
  - [ 9 ] E. Torres, C. A. Panetta, and R. M. Metzger, J. Org. Chem. **52**, 2944 (1987).
  - [ 10 ] R. M. Metzger and C. A. Panetta, in *Proc. of the Eighth Winter Conference on Low-Temperature Physics, Cuernavaca, Mexico*, 81 (1987).
  - [ 11 ] R. K. Laidlaw, Y. Miura, C. A. Panetta, and R. M. Metzger, Acta Cryst. **C44**, 2009 (1988).

- [12] R. K. Laidlaw, Y. Miura, J. L. Grant, L. Cooray, M. Clark, L. D. Kispert, and R. M. Metzger, *J. Chem. Phys.* **87**, 4967 (1987).
- [13] R. K. Laidlaw, J. Baghdadchi, C. A. Panetta, Y. Miura, E. Torres, and R. M. Metzger, *Acta Cryst.* **B44**, 645 (1988).
- [14] Y. Miura, R. K. Laidlaw, C. A. Panetta, and R. M. Metzger, *Acta Cryst.* **C44**, 2007 (1988).
- [15] R. M. Metzger, R. R. Schumaker, M. P. Cava, R. K. Laidlaw, C. A. Panetta, and E. Torres, *Langmuir* **4**, 298 (1988).
- [16] R. M. Metzger and C. A. Panetta in Organic and Inorganic Lower-Dimensional Materials. NATO ASI Series, Vol. B168, edited by P. Delhaes and M. Drillon (Plenum, New York, 1988) page 271.
- [17] Y. Miura, E. Torres, C. A. Panetta, and R. M. Metzger, *J. Org. Chem.* **53**, 439 (1988).
- [18] Y. Miura, C. A. Panetta, and R. M. Metzger, *J. Liquid Chrom.* **11**, 245 (1988).
- [19] R. M. Metzger and C. A. Panetta, *J. Mol. Electronics* **5**, 1 (1989).
- [20] R. M. Metzger and C. A. Panetta, *J. Chim. Phys.* **85**, 1125 (1988).
- [21] R. M. Metzger and C. A. Panetta, *Synth. Met.* **28**, C807 (1989).
- [22] R. M. Metzger, R. K. Laidlaw, E. Torres, and C. A. Panetta, *J. Cryst. Spectr. Res.* **19**, 475 (1989).
- [23] R. M. Metzger and C. A. Panetta in Molecular Electronics - Science and Technology, edited by A. Aviram and A. Bross (New York Engineering Foundation), in press.
- [24] R. M. Metzger, D. C. Wisner, R. K. Laidlaw, M. A. Takassi, D. L. Mattern, and C. A. Panetta, *Langmuir*, accepted and in press.
- [25] R. M. Metzger and C. A. Panetta, in Lower-Dimensional Systems and Molecular Electronics. NATO ASI Series, edited by R. M. Metzger and P. Day (Plenum, New York, in press)
- [26] See e.g. G. L. Gaines, Jr. Insoluble Monolayers at Liquid - Gas Interfaces (Interscience, New York, 1966).
- [27] K. B. Blodgett, *J. Am. Chem. Soc.* **57**, 1007 (1935).
- [28] K. B. Blodgett and I. Langmuir, *Phys. Rev.* **51**, 964 (1937).
- [29] H. Kuhn, D. Möbius, and H. Bücher in Techniques of Chemistry. Vol. I - Physical Methods of Chemistry - Part V - Determination of Thermodynamic and Surface Properties A. Weissberger and B. W. Rossiter, eds. (Wiley - Interscience, New York, 1972) page 577.
- [30] H. Kuhn, *Pure Appl. Chem.* **51**, 341 (1979).
- [31] H. Kuhn, *Pure Appl. Chem.* **53**, 2105 (1981).
- [32] See e. g. *Thin Solid Films* Vols. **68** (1980), **99** (1983), **132-134** (1985), **159-160** (1987).
- [33] R. W. Murray, *Acc. Chem. Res.* **13**, 135 (1980).
- [34] R. Maoz, L. Netzer, J. Gun, and J. Sagiv, *J. Chim. Phys.* **85**, 1059 (1988).
- [35] L. T. Calcaterra, G. L. Closs, and J. R. Miller, *J. Am. Chem. Soc.* **105**, 670 (1983).
- [36] J. R. Miller, L. T. Calcaterra, and G. L. Closs, *J. Am. Chem. Soc.* **106**, 3047 (1984).
- [37] R. A. Marcus, *Disc. Faraday Soc.* **22**, 21 (1960).
- [38] J. R. Anderson and O. Jorgensen, *J. Chem. Soc. Perkin Trans. I*, 3095 (1979).
- [39] A. Aviram, C. Joachim, and M. Pomerantz, *Chem. Phys. Lett.* **146**, 490 (1988).
- [40] M. Fujihira, K. Nishiyama, and H. Yamada, *Thin Solid Films* **132**, 77 (1985).
- [41] M. Fujihira and Y. Yamada, *Thin Solid Films* **160**, 125 (1988).

L.B. FILMS EXHIBITING COOPERATIVE SPIN TRANSITION, FOR 2D MOLECULAR MEMORY DEVICES.

P. CORONEL, A. RUAUDEL-TEIXIER, A. BARRAUD  
CEA-IRDI-DESICP-DLPC-SCM, CEN.Saclay, 91191 Gif sur Yvette Cedex (France)  
O. KAHN  
Laboratoire Chimie Organique, Université Paris-Sud, URA-CNRS 420, 91405 ORSAY Cedex

ABSTRACT

Molecular electronics requires materials of molecular size exhibiting switching or memory properties. The Langmuir-Blodgett method (L.B.) and its variants provide controlled fabrication of molecular films one molecule thick and their transfer onto solid supports. In these 2D monolayers, molecules are highly organized, so that complex organizations aimed at specific properties can be built. One of these, a semi-amphiphilic complex made of two NCS and two amphiphilic phenantrolines in a cis position, exhibits a spin transition around -20 °C. It switches from high spin ( $S = 2$ ) at room temperature to low spin ( $S = 0$ ) at low temperature. The transition does not follow the expected thermal Boltzmann statistics, but is rather steep, pointing out molecular cooperation. The L.B. film exhibits a hysteresis about 4 °C in width, while the parent 3D compound exhibits a hysteresis of less than 0.2 °C, but a much sharper transition. This apparently contradictory behaviour is ascribed to the high impurity content and the multicrystallinity of the L.B. film in association with high intermolecular coupling. Because of its intrinsic properties this new material is a breakthrough on the way to magnetic memories at the molecular scale for molecular electronics.

INTRODUCTION

One of the challenges of molecular chemistry is the use of molecular assemblies for data processing at the molecular scale<sup>1</sup>. This requires molecular assemblies tailored to exhibit specific functions. The Langmuir-Blodgett method and its associated solid state chemistry are one of the most powerful tools to build up such molecular edifices and adjust their properties<sup>2</sup>. The versatility of this method has already been demonstrated by active molecular assemblies in various fields<sup>3,4,5,6</sup>.

This work is an attempt to make a new molecular edifice for magnetic memories at the molecular scale. The driving idea is based on the observation of spin transitions in 3D bulk crystals of complexes of transition ions: in some cases the thermally induced spin transition between high-spin and low spin states is very sharp with a hysteresis effect<sup>7</sup>. For instance  $\text{Fe}^{\text{II}}(\text{phen})_2(\text{NCS})_2$  (compound 1), in which phen means 1-10 phenantroline, exhibits a very sharp spin transition<sup>8</sup> at 174 K, with a temperature hysteresis width of 0.15 K.

We designed a similar compound,  $\text{Fe}^{\text{II}}(\text{R}_2\text{R}'\text{-phen})_2(\text{NCS})_2$  (compound 2) in which the phenantroline ligand is substituted with three long aliphatic chains in order to render it amphiphilic (R is  $-\text{C}_{17}\text{H}_{35}$ , R' is  $-\text{OC}_{18}\text{H}_{37}$ ). The cis complex is shown in fig. 1. Such an amphiphilic compound is well suited to form superimposed monomolecular layers by the Langmuir-Blodgett method. In these lamellar structures the planes containing the active parts of the compound are separated and decoupled from one another by the aliphatic chains, which form a fatty layer about 20 Å thick<sup>9</sup>. In these films, the intermolecular coupling is hence two dimensional (2D) instead of 3D. The aim of this work is to check one of these molecular assemblies (compound 2) for spin transition and

intermolecular cooperativity and compare the results with those from the parent 3D compound (compound 1).

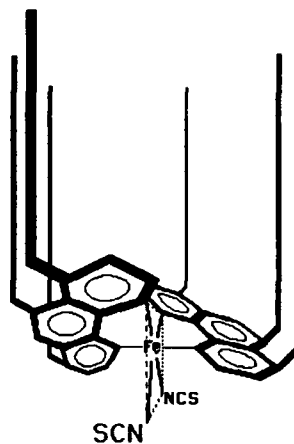


Fig. 1 : Steric configuration of compound 2.

#### SAMPLE PREPARATION

The synthesis of compound 2 has been described elsewhere<sup>10</sup>. The molecules were spread at the surface of pure Millipore water (reverse osmosis + deionization) in a Langmuir trough 0,4 m<sup>2</sup> in size made of special, non porous PTFE (ATEMETA trough, model LB 105). 40 to 200 monolayers were transferred at 32 mN/m onto calcium fluoride and fused silica slides, at a speed of 5 mm/min. on the up stroke and 10 mm/s on the down stroke. The transfer ratio was close to unity during the up stroke and zero during the down stroke (Z type deposition<sup>9</sup>). The Z structure of the L.B. film was confirmed by X-ray diffraction measurements which gave a period of 28 Å along the normal to the substrate.

Light scattering measurements showed that the deposited films were of high quality.

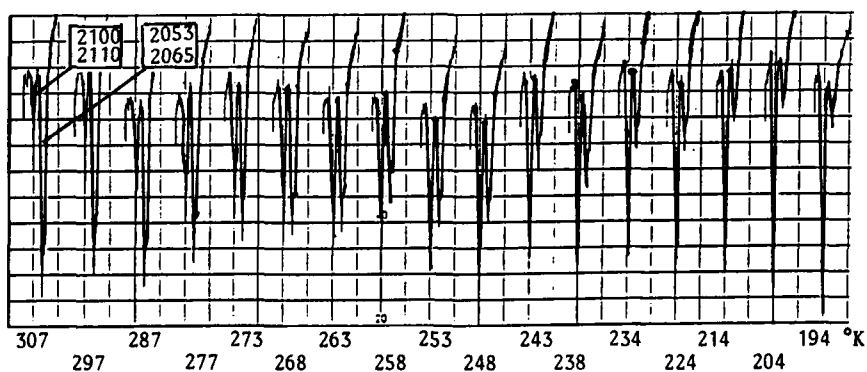


Fig. 2 : Infrared absorption spectra of LB monolayers of compound 2 transferred onto a CaF<sub>2</sub> substrate at various temperatures (cooling). Each spectrum exhibits two doublets, one growing at the expense of the other upon cooling.

## EXPERIMENTAL RESULTS

Since the amount of material is less than  $1 \mu\text{g}/\text{cm}^2$  per layer, no direct magnetic measurement could be performed. However the magnetic behaviour of the samples could be followed by infrared spectroscopy in the  $2200$  to  $2000 \text{ cm}^{-1}$  range, by examination of the absorption bands corresponding to the stretching modes of the  $\text{C}\equiv\text{N}$  bond of the NCS ligands. At room temperature, compound 2 exhibits a doublet at  $2053$  and  $2065 \text{ cm}^{-1}$ , characteristic of a high spin ( $S = 2$ ), cis structure. It also exhibits a much weaker doublet, at  $2100$  and  $2110 \text{ cm}^{-1}$ , characteristic of a low spin ( $S = 0$ ), cis structure (the assignment of these bands has been discussed elsewhere<sup>10</sup>).

In fig. 2 is shown the evolution of the absorption spectra as temperature is lowered. The main feature of this set of spectra is the increase of the low spin doublet at the expense of the high spin one at low temperature. Fig. 3 shows the results in the form of a plot of the molar fraction of the high spin species versus temperature (full line). The behaviour of the parent 3D compound is shown in dotted line for comparison. This figure clearly points out a spin transition around  $260 \text{ K}$ , which extends over a temperature range of about  $60 \text{ K}$ .

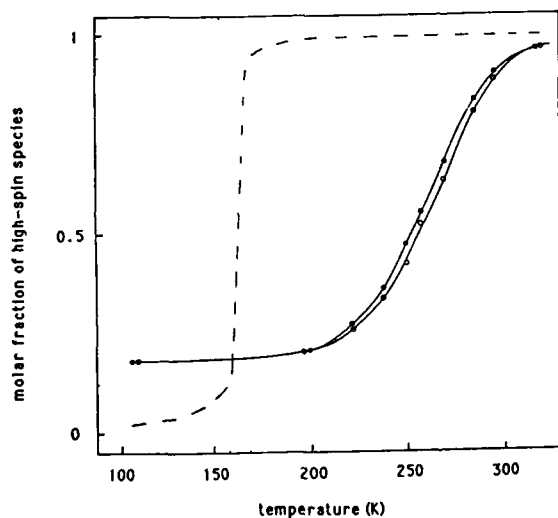


Fig. 3 : Molar fraction of high spin species (HS), i.e.  $\text{H.S./total}$ , vs temperature upon cooling ( $\bullet$ ) and warming ( $\circ$ ). Solid line : compound 2. Dotted line : parent 3D compound 1.

The four main features to be remembered from this figure are :

- i - a slope higher than the one expected from a simple Boltzmann thermal distribution, indicative of intermolecular positive cooperativity.
- ii - a transition nevertheless smoother than that of the parent 3D compound.
- iii - a hysteresis effect much larger (ca  $4 \text{ K}$ ) than the one exhibited by the parent 3D compound ( $0.15 \text{ K}$ )\*.
- iv - a transition temperature definitely different from that of the parent 3D compound.

Some of these features seem contradictory and hence will be discussed below.

\* The sample holder was designed to provide thermal exchange on both sides, along all the perimeter of the  $35 \times 10 \times 2 \text{ mm}$   $\text{CaF}_2$  slides, and the precision on temperature measurements was  $0.1 \text{ K}$ .

## DISCUSSION

Features i, ii and iii are clearly indicative of molecular positive cooperation. The behaviour of an assembly of identical molecules submitted to intermolecular coupling can be very easily understood and modelled by the behaviour of an amplifier looped with positive feedback (fig. 4a). At low feedback rate, the slope of the transfer characteristics increases (gain increases) as positive feedback is increased (fig. 4e). No hysteresis is observed.

At higher feedback rate, the gain increases to infinity and the transfer characteristics exhibits a vertical portion (fig. 4d). However even in this case there is no hysteresis yet. If positive feedback is further increased, the transfer characteristics remains vertical, but a hysteresis loop shows up (fig. 4c), the width of which increases with feedback (fig. 4f).

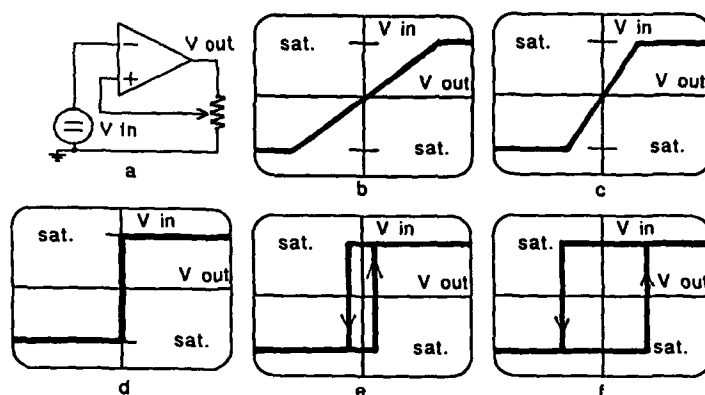


Fig. 4 : The transfer characteristics of a linear amplifier with positive feedback can be used to model curves of fig. 3.

- a : diagram of the model amplifier.
- b : transfer characteristics of the amplifier without feedback.
- c : transfer characteristics of the amplifier with moderate positive feedback.
- d : transfer characteristics of the amplifier at critical positive feedback.
- e : transfer characteristics of the amplifier above critical positive feedback.
- f : transfer characteristics of the amplifier far above critical positive feedback.

From this it is clear that hysteresis is indicative of very high intermolecular positive cooperativity and coupling. But hysteresis is incompatible with a smooth transition (feature ii). Agreement can nevertheless be found between features ii and iii if notice is taken that each LB monolayer is not single crystalline, but made of a compact array of small 2D crystallites or domains of various sizes. If it is supposed that the transition temperature of each domain varies with its environment or size (this has been shown to occur in 3D compounds by finely grinding large grains<sup>11</sup>), the transition curve is the sum of many sharp transitions occurring at various temperatures. Hysteresis is of course preserved, but the transition is spread over a wide temperature range. This effect may be further enhanced by a non-negligible fraction (estimated to ca 30 %) of  $(R_2R'phen)_3Fe^{II}$  (counter ion<sup>-</sup>)<sub>2</sub> complex which is still present in the spreading solution<sup>10</sup> and acts as an inert impurity which weakens mechanical intermolecular coupling at random positions.



In spite of this impediment to intermolecular cooperativity, the width of the hysteresis loop points out an intermolecular coupling much larger than in the parent 3D compound, which exhibits only narrow hysteresis. From the changes in bond length measured in similar 3D compounds<sup>12,13</sup>, it seems likely that the intermolecular coupling is mechanical. Nevertheless, a molecular array giving rise to so high an intermolecular influence is not easy to imagine, especially because structure determination is not straightforward in L.B. films.

The reason for the large shift (90 K) in the transition temperature is not clear yet : it may originate in a local environment or structure slightly different in the 3D and 2D systems. It may also originate in the electron withdrawing effect of the ether function born by R', which modifies the ligand field via the  $\pi$  electron cloud of phenantroline.

#### CONCLUSION

This 2D array of Fe<sup>II</sup> magnetic complex built up by the L.B. method has been shown to exhibit :

1. temperature induced spin transition ( $S = 2$  to  $S = 0$ ) near room temperature.
2. very high positive intermolecular cooperativity in spite of its high impurity content.

This is a breakthrough on the way to magnetic memories at the molecular scale, because : i. this new material can be made one molecule thick, ii. it can very simply give rise to superimposed memory structures, and iii. its hysteresis loop is wide enough for accommodating simple temperature control.

#### REFERENCES

- 1 - See for instance report ARAGO 7 : "Electronique Moléculaire. Perspectives en Traitement Moléculaire de l'Information", collective report from OFTA, Masson publ., Paris (1988).
- 2 - A. Barraud, J. Chim. Phys. et Phys. Chim. Biol., **89**, 1121 (1988).
- 3 - D. Möbius, Ber. Bunsenges. Phys. Chem., **82**, 848 (1978).
- 4 - E. Polymeropoulos, D. Möbius, H. Kuhn, Thin Solid Films, **68**, 173 (1980).
- 5 - C. Lecornte, C. Baudin, F. Berleur, A. Ruau-del-Teixier, A. Barraud, M. Momenteau, Thin Solid Films, **133**, 103 (1985).
- 6 - M. Vandevyver, J. Chim. Phys. et Phys. Chim. Biol., **85**, 1033 (1988).
- 7 - E. König, Chem. Rev., **85**, 219 (1985).
- 8 - P. Gütlich, Struct. Bonding, **44**, 83 (1981).
- 9 - G.L. Gaines Jr., Insoluble Monolayers at liquid-gas interfaces, Interscience publ., 1966.
- 10 - A. Ruau-del-Teixier, A. Barraud, O. Kahn and P. Coronel, Thin Solid Films, **160**, 107 (1988).
- 11 - E.W. Müller, H. Spiering and P. Gütlich, Chem. Phys. Letters, **93**, 567 (1982).
- 12 - E. König and K. Watson, Chem. Phys. Letters, **6**, 457 (1970).
- 13 - J. Takemoto, B. Hutchinson, Inorg. Chem., **12**, 705 (1973).

**EFFECTS OF MOLECULAR RIGIDITY ON ELECTRIC FIELD INDUCED ALIGNMENT AND ORIENTATIONAL STABILITY OF DIPOLAR CHROMOPHORE COMPOSITES****H.E. KATZ, M.L. SCHILLING, G. WASHINGTON, C.W. DIRK, W.R. HOLLAND, T. FANG, AND K.D. SINGER**

AT&amp;T Bell Laboratories 1D-250, 600 Mountain Avenue, Murray Hill, NJ 07974 and Princeton, NJ 08540

**ABSTRACT**

The relationship between the supramolecular conformational structure of assembled chromophores and their susceptibility to electric field poling is of interest for maximizing the bulk alignment achievable in an electro-optic material. We have employed solution phase dielectric constant measurements to investigate possible enhancements in dipolar susceptibility as a function of connectivity and state of aggregation in rationally synthesized chromophore assemblies, including conformationally defined head-to-tail oligomers. On the other hand, conformationally unrestricted, highly dipolar azo dyes behave as relatively isolated molecules even when present in supersaturated solutions and in close proximity on polymer chains.

**INTRODUCTION**

The 4-amino-4'-(2,2-dicyanovinyl)azobenzene (DCV) chromophore has been utilized in the fabrication of polymeric materials with large, stable optical nonlinearities (1). These materials display larger second order nonlinear optical responses relative to corresponding nitro-substituted azo dye materials by virtue of the higher  $\beta$  value associated with DCV-substituted donor-acceptor compounds (2). In principle, it should also be possible to enhance the bulk hyperpolarizability by increasing the electric field orientability of the active moieties. This could be accomplished via designed molecular assembly in which individual chromophore dipole moments are additive (3). This would be in contrast to conformationally unrestricted aggregation in which dipole moments would tend to align antiparallel and electric field poling would be less efficient.

We have evaluated head-to-tail assemblies of cyanovinyl chromophores for enhanced orientability relative to individual chromophore moieties. These pseudodimeric and higher oligomeric chromophore chains are unique because they incorporate strongly electron donating and accepting groups in segments whose relative conformations are defined. Dipole moment measurements were carried out on the pseudodimers and on appropriate smaller model compounds. Enhancements in effective dipole moment were observed, and are in agreement with those predicted from x-ray crystallography of close analogues. According to preliminary

data, a tetrameric sample is sufficiently extended in a PMMA film to allow the fabrication via poling of an electro-optic and birefringent film.

In order to explore the possibility of undesigned aggregation affecting the electric field orientability of a nonlinear optical chromophore, we first performed concentration-dependent dielectric measurements on liquid solutions containing DCV dyes. Data were obtained on both monomeric and polymeric DCV solutes over a wide range of concentrations. While phase separation of monomeric solutes and thickening of polymer solutions occurred at concentrations near the apparent limiting concentration for particle-free film formation, no significant deviations from linearity were observed in any plots of capacitance versus concentration as long as mixtures were homogeneous.

## EXPERIMENTAL

Monomeric dye esters 1 and 2 (mp 140 and 125 deg C respectively) were synthesized from the corresponding aniline esters according to the published procedure (4). A random copolymer containing equimolar amounts of methyl and DCV ester monomer subunits was also prepared as previously reported. Anilines and azo dyes containing cyanovinylcarboxamide linkages (compounds 3, 4, 7, 8, and 10) were synthesized by Knoevenagel condensation of cyanoacetamides with amino- or aminophenylazo-substituted benzaldehydes. These precursors were prepared by conventional functional group transformations. Polymers of general structure 11 where the diamond represents a chromophore have also been prepared by these methods.

Dipole moments were determined by differentiating equation 1 (5) where  $[s_i]$  is the concentration of the  $i^{\text{th}}$  species expressed in terms of its mass fraction  $w$ ,  $\alpha$  is the linear polarizability, and  $f_i$  and  $f_i'$  are local field factors, differentiating with respect to solute mass fraction, and solving the resulting equation using the slopes of the plots of dielectric constant versus weight fraction of substrate as the value for  $d\epsilon/dw$  assuming Onsager local fields. (6) The random error associated with this procedure is on the order of 5%.

## RESULTS

In order to observe the dielectric behavior of extremely concentrated solutions of monomeric DCV, an equimolar mixture of 1 and 2 was used. These derivatives were selected so that each would inhibit the crystallization of the other, permitting higher total dye concentrations to be reached in solution. A mixture of the two dyes that had been

concentrated from dioxane solution had a much lower and broader melting range than either pure compound, and retained solvent much more tenaciously as well, evidence of poor crystallinity in the mixture. While dioxane solutions  $>0.5$  mol/kg in DCV could not be prepared from either 1 or 2 alone, a 0.75 mol/kg solution of the equimolar mixture was homogeneous at room temperature long enough for a dielectric constant determination. Plots of dielectric constant versus concentration of the 1-2 mixture or of the copolymer in dioxane were linear up to this maximum concentration.

Dipole moments of various monomeric and "dimeric" chromophoric compounds are reported in Table I. Those of the azo dyes were measured in chloroform, in which the random experimental error at 95% confidence is 1 Debye, and the others were obtained in dioxane, where the 95% confidence limit is about 0.2 Debye. The dipole moment of a tetrameric sample of 11 with chromophores like those in 3 was  $16.5 \pm 1$  D.

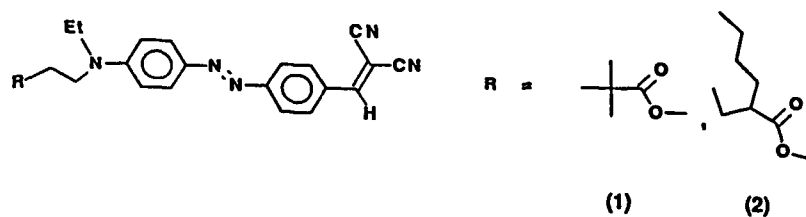
## DISCUSSION

The contribution of dipolar molecules in a liquid to the dielectric constant arises predominantly from the orientational response of the dipoles to the applied electric field. Thus, a parallel may be drawn to electric field poling in polymer films, in which orientation of dipoles is achieved by the application of a (much higher) electric field (7). In both cases, the degree of orientation depends on the free energy difference among alignments of an individual dipole with or against the field, taking into account any possible effects of field screening by the local medium. The amount of bulk dipole alignment, recorded in the present experiments as contributions to capacitance and in the nonlinear optics case as second harmonic generation or electro-optic activity, is proportional to the density of dipoles in the sample, as long as the dipoles may be regarded as isolated.

However, if there is a special concentration-dependent screening of the applied field from individual dipoles or the formation of antiparallel aggregates of dipoles, then the observed orientation should be diminished relative to that expected from an ensemble of isolated dipoles. No such reduction in dielectric constant is observed at the high concentrations examined here, short of catastrophic precipitation, most likely because there is no aggregation of the dyes in the solutions, or possibly because any such aggregation is either not antiparallel, or is compensated by a medium-induced increase in the ground-state dipole moment of the orientable chromophores.

Both of the dimeric compounds included in Table I exhibit higher dielectric responses than would have been expected from uncorrelated mixtures of the respective "monomers" in the same solvents. The theoretical dipole moment for an uncorrelated pair of species having dipole moments  $\mu_1$  and  $\mu_2$  would be  $(\mu_1^2 + \mu_2^2)^{1/2}$ , which is the equivalent of the dipole moment of a dimer whose segments are at  $90^\circ$  angles. Since the dimers discussed here

Table I



$$\frac{\epsilon - 1}{4\pi} = \sum_i [s_i] \left( \alpha_i f_i + \frac{\mu_i^2 f_i}{3kT} \right)$$

eq 1

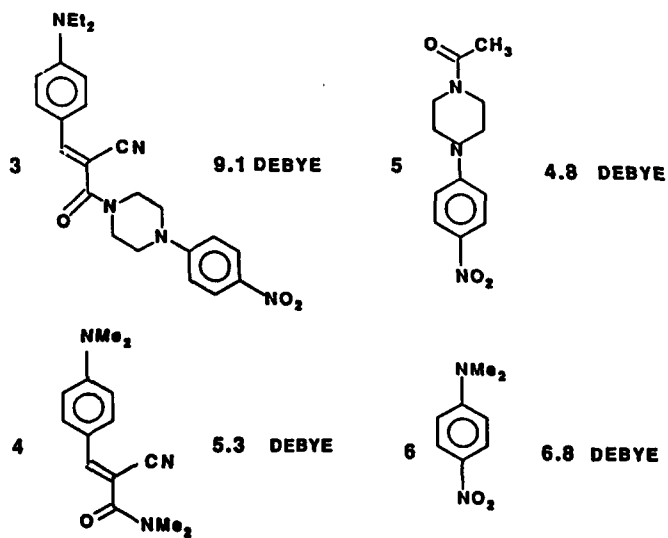
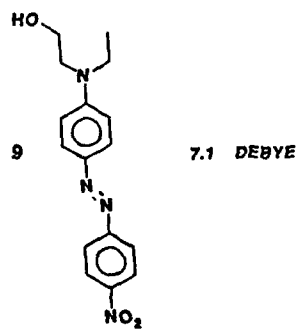
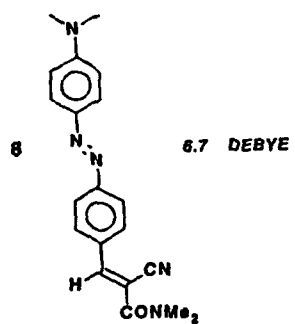
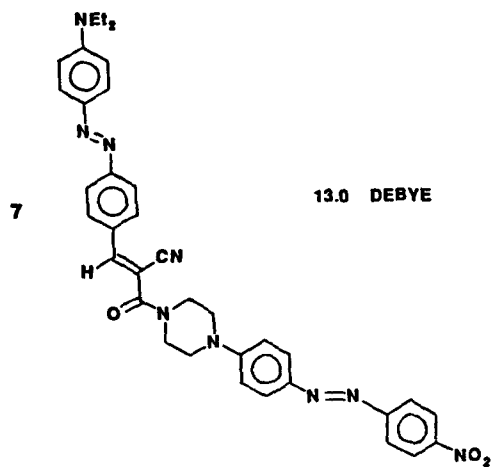
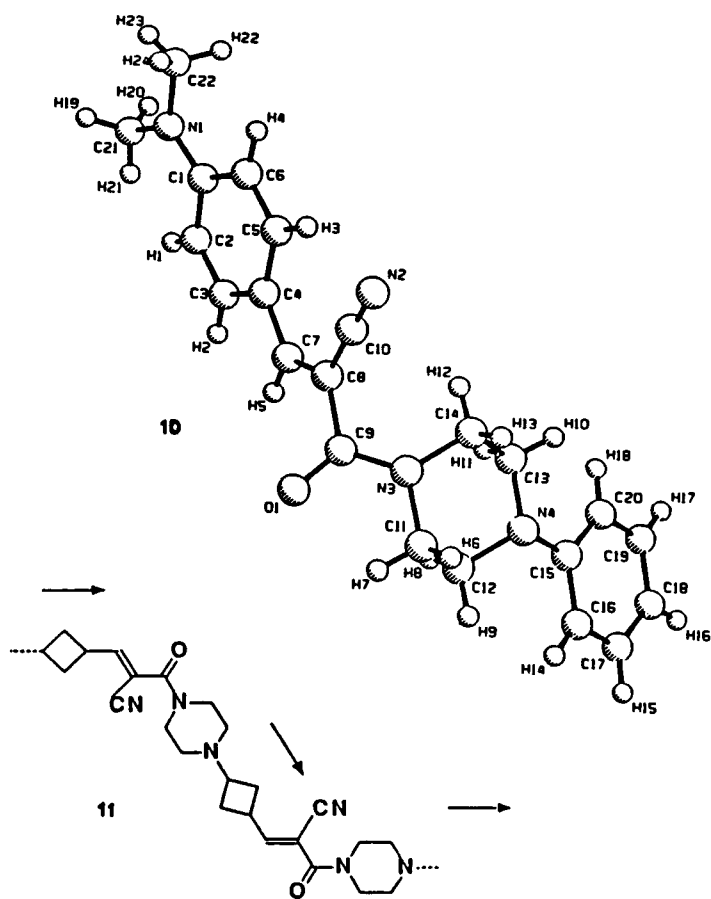


Table I (continued)





incorporate enforced  $110^\circ$  linkages, as indicated by the crystal structure of compound 10, enhanced dipole moments would be expected and are observed. The precise magnitude of enhancement depends on the negative contribution assignable to the moment of the piperazine-carbonyl bond, which is approximately 2 Debye, but is otherwise in agreement with the vector sum of the moments calculated on the basis of the x-ray structure. The enhancements amount to 0.5-2 Debye for compound 3 and 3 Debye for compound 7. The expected dielectric response from four unattached acceptor-substituted anilines such as 5-8 would be ca. 11 D, significantly less than the 16.5 D measured for a head-to-tail tetramer. Thus, doubled-back conformations available to the tetramer are disfavored relative to the more desirable extended forms. Poling of this tetramer as a 10% "solution" in PMMA gave a material with orientation commensurate with an extended conformation, based on preliminary electro-optic and birefringence measurements. The stability of the orientation was greater than for simple azo dyes as well. Thus, it is possible that dipole moment additivity and enhanced orientability observed for these compounds in liquids can be exploited with higher oligomers in polymer films.

#### REFERENCES

1. K.D. Singer, M.G. Kuzyk, W.R. Holland, J.E. Sohn, S.J. Lalama, R.B. Comizzoli, H.E. Katz, and M.L. Schilling. *Appl. Phys. Lett.* 53, 1800 (1988).
2. H.E. Katz, K.D. Singer, J.E. Sohn, C.W. Dirk, L.A. King, H.M. Gordon. *J. Am. Chem. Soc.* 109, 6561 (1987).
3. D.J. Williams, H.K. Hall, et al. *Macromolecules*, 20, 716, 722 (1987); C.S. Willand, D.J. Williams. *Ber. Bunsen. Phys. Chem.*, 91, 1304 (1987).
4. M.L. Schilling, H.E. Katz, D.I. Cox. *J. Org. Chem.* 53 5538 (1988).
5. C.J. Bottcher, "Theory of Electric Polarization" (Elsevier, Amsterdam 1952).
6. L. Onsager. *J. Am. Chem. Soc.* 58, 1456 (1936).
7. K.D. Singer, M.G. Kuzyk, J.E. Sohn. *J. Opt. Sci. Am. B.* 4, 968 (1987).



## THE EFFECT OF MATRIX ATTACHMENT ON THE THIRD ORDER NONLINEAR OPTICAL PROPERTIES OF DYES

DAVID W. POLIS, MAMOUN M. BADER, AND LARRY R. DALTON  
Department of Chemistry, University of Southern California, Los Angeles, CA  
90089-0482

### ABSTRACT

In order to discern the source of the third order nonlinear optical (NLO) phenomenon both morphological and electronic considerations are required. A series of styrene copolymers with varying amounts of p-aminostyrene or p-chloromethylstyrene were prepared as anchoring sites for chemically reactive electrophilic and nucleophilic dyes. For comparison, the same dyes were incorporated into composites of polycarbonate. Preliminary degenerate four wave mixing results for all materials indicate that the copolymeric support allowed incorporation of greater amounts of electroactive units, versus composites, and hence allowed high third order nonlinear responses ( $\chi^{(3)}/\alpha$  of approximately  $10^{-13}$  esu cm). Third order NLO responses were absent in some composite systems due to limited solubility and/or phase separation difficulties.

### INTRODUCTION

Rigid rod ladder polymers and their third order NLO properties have been extensively studied [1]. Also, NLO properties of ladder oligomer units incorporated into polyethers with large spacer groups have been investigated in attempts to minimize absorption and solubility problems associated with the rigid rod systems [2]. These studies have raised questions as to what the morphological dependence is on the NLO phenomenon.

There have been many examples of composites incorporating electroactive units exhibiting second and third order NLO properties [3]. Also, it has been established that polymers with long pendant groups incorporating an electroactive unit can display liquid crystalline behavior and can be poled to yield materials with enhanced second order NLO properties [4]. This is a clear indication of morphological dependencies on the second order NLO effect. We are interested in understanding whether polymers with pendant electroactive groups attached close to the polymer chain display third order NLO behavior and whether this behavior is enhanced in comparison to randomly distributed molecules in composite films.

This study utilized both electrophilic and nucleophilic polymers to facilitate attachment of a wide variety of electrophilic and nucleophilic dyes possessing chemically reactive amino, or halo substituents. Initial NLO results for incorporated and composite materials of 7-nitrobenzo-2-oxa-1,3-diazole (E1, Figure 1) will be discussed. Also, limitations to both procedures for dye incorporation will be addressed.

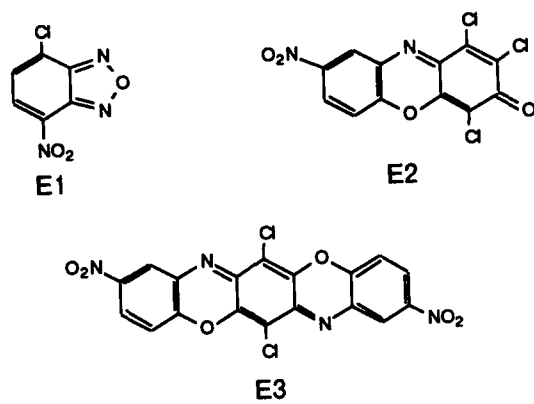


Figure 1. Electrophilic Dyes

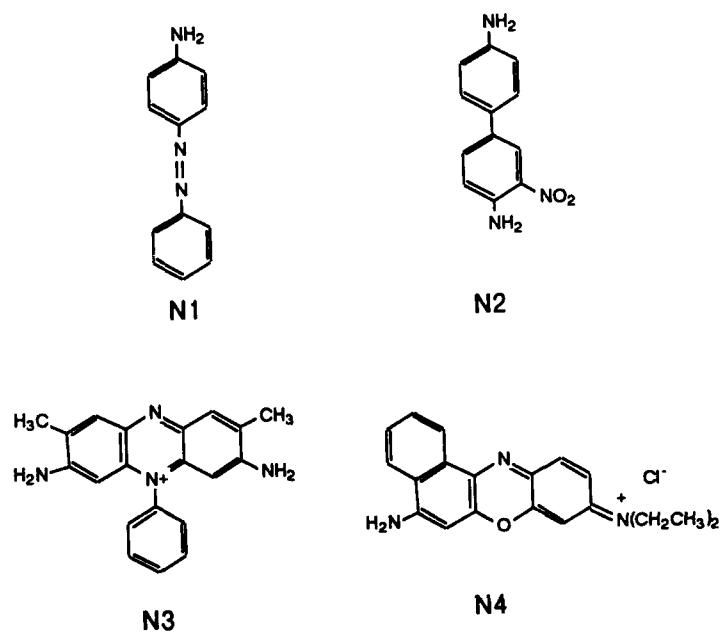


Figure 2. Nucleophilic Dyes

## EXPERIMENTAL

### Materials

Nucleophilic polymers were synthesized from styrene and between 5 to 75 molar percent *p*-aminostyrene. The polymerizations were performed in bulk using 2,2'-azobisisobutyronitrile (AIBN) initiator. Precipitation of the polymers from chloroform into methanol afforded pure powders. The molecular weight of the polymers was determined to be in the range of 100,000 a.m.u. by gel permeation chromatography, against a polystyrene standard. An electrophilic polymer was synthesized from styrene and 5 molar percent *p*-chloromethylstyrene. The polymerization and purification was identical to that described above for the nucleophilic polymers. The polymer compositions are listed in Table 1.

A wide variety of electrophilic and nucleophilic dyes were available for study and are shown in Figures 1 and 2. The electrophilic dyes were attached to the nucleophilic polymers in boiling tetrahydrofuran (THF) solution in the presence of excess sodium acetate. Similarly, the nucleophilic dyes were attached to the electrophilic polymer in boiling THF solution in the presence of excess potassium carbonate and a trace of potassium iodide. The polymers were then precipitated into methanol and washed thoroughly with methanol/water mixtures before drying.

The complete synthetic details and characterization of these materials is currently underway [5].

Table 1. Backbone Polymer Compositions (molar percent)

Polymer ID	Classification <sup>a</sup>	Sty%	PAS% <sup>b</sup>	CMS% <sup>b</sup>
1	N	95	5	—
2	N	80	20	—
3	N	70	30	—
4	N	33	66	—
5	N	25	75	—
6	E	95	—	5

a) N = nucleophilic, E = electrophilic

b) PAS = *p*-aminostyrene, CMS = chloromethylstyrene

### NLO measurements

The third order susceptibilities reported here were measured by degenerate four wave mixing (DFWM) employing a variation of this technique by Hellwarth and coworkers [6] which permits the measurement of all the tensor components of the third order susceptibility including the fast and slow components which give the acoustic velocity and damping coefficients. A phase conjugation geometry for DFWM was employed in which all four beam polarizations were varied to give independent data. The three input beams were formed from 532 nm laser pulses (derived from 5 Hz repetition rate mode locked pulses from a Quantel Model YG471-C Nd:YAG laser frequency doubled to 532 nm) having energies of approximately 2 mJ and durations of approximately 25 psec.

### RESULTS AND DISCUSSION

The preliminary NLO data are summarized in the Table 2 below. The most obvious result from these measurements occurs in the 7-nitrobenzo-2-oxa-1,3-diazole (E1) case. At low incorporation (5 molar percent) the copolymeric and composite systems showed no measurable NLO response. It was not possible to incorporate more than 10% of E1 into composites due to phase separation problems, however, copolymeric incorporation at 20 and 30 molar percent yielded materials which did give a third order NLO signal which, within the error of the measurement, remained relatively small and constant.

At very high incorporation of E1, 66 and 75 molar percent, insolubility of the copolymer resulted.

Table 2. Third Order Susceptibilities for Systems Studied

Polymer support	Dyes	Composite	$\chi^{(3)}/\alpha^a$
Polycarbonate <sup>b</sup>	E1	Yes	not measurable.
Polycarbonate	E2	Yes	$3.9 \times 10^{-13}$
Polycarbonate	E3	Yes	--- <sup>c</sup>
Polycarbonate	N3	Yes	not measurable
Polycarbonate	N4	Yes	not measurable
Polymer 1	E1	No	not measurable
Polymer 2	E1	No	$0.55 \times 10^{-13}$
Polymer 3	E1	No	$0.72 \times 10^{-13}$
Polymer 4 and 5	E1	No	--- <sup>d</sup>
Polymer 6	N1	No	not measurable
Polymer 6	N2	No	not measurable

a) in units of e.s.u. cm b) Nominal 5 to 10% dye incorporation  
c) Strong signal which changes due to photochemistry d) insoluble

By attaching the E1 dye to the *p*-aminostyrene copolymer the group at carbon number 2 in the dye moiety was changed from chlorine to amino. In order to test whether the dye had changed significantly upon attachment and this new species was giving rise to the NLO behavior, model compounds were prepared (Figure 3). Incorporation of these dyes into polycarbonate was again nominal (5 to 10%), and these samples showed no measurable third order NLO response.

Interestingly, high nonlinear responses were seen for the ladder oligomers E2 and E3 incorporated into polycarbonate. The five ring oligomer (E3) gave a very strong signal, however, it diminished with time and could not be measured accurately. The three ring compound (E2) in polycarbonate also gave a third order NLO response of approximately  $4 \times 10^{-13}$  esu cm ( $\chi^{(3)}/\alpha$ ). Initial attempts to incorporate this dye into nucleophilic polymers have been successful, and NLO measurements are under way [5].

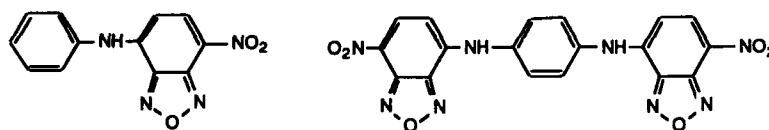


Figure 3. Model Compounds for the 7-nitrobenzo-2-oxa-1,3-diazole (E1)

## CONCLUSIONS

It is possible to incorporate a large amount of an electroactive dye which has potential third order NLO behavior as a pendant group on a *p*-amino-styrene/styrene copolymer. Incorporation of dyes in this fashion has the advantage over composite formation in allowing high concentrations of electroactive units to be introduced into samples without the problems of insolubility and phase separation. Also, the utility of this procedure may possibly be extended to many dye systems which have potential third order NLO behavior and which possess chemically reactive electrophilic or nucleophilic groups.

Morphological considerations may be key to understanding the NLO phenomenon. Certainly, knowledge into the mechanisms of the NLO phenomenon (inter- or intramolecular) is essential in designing the perfect NLO material. By monitoring these differences in the fashion in which electroactive units are arranged in a polymer matrix, we will eventually answer these and other pertinent questions.

**ACKNOWLEDGEMENTS**

This work was funded by the Air Force Office of Scientific Research under contracts F49620-87-C-0100 and F49620-88-C-0071 and the National Science Foundation under grant DMR-88-15508. We are also indebted to Dr. R. W. Hellwarth, X. F. Cao, and J. P. Jaing for the DFWM experiments.

**REFERENCES**

1. L. R. Dalton, J. Thomson, and H. S. Nalwa, *Polymer* **28**, 543 (1987); L.-P. Yu, L. R. Dalton, *Synthetic Metals* **29**, E463 (1989).
2. L.-P. Yu, and L. R. Dalton, *J. Amer. Chem. Soc.* **111**, 8699 (1989).
3. S. R. Flom, G. C. Walker, L. E. Lynch, L. L. Miller, and P. F. Barbara, *Chem. Phys. Lett.* **154**(3), 193 (1989).
4. J. E. Sohn, K. D. Singer, S. J. Lalama, and S. J. Kuzyk, *Polym. Mater. Sci. Eng.* **55**, 532 (1986).
5. M. Bader, D. W. Polis, M. R. McLean, and L. R. Dalton, to be published.
6. X. F. Cao, J. P. Jaing, D. P. Bloch, R. W. Hellwarth, L.-P. Yu, and L. R. Dalton, *J. Appl. Phys.* **65**(12), 15 (1989).

## SEMIORGANICS: A NEW CLASS OF NLO MATERIALS

P.R. NEWMAN\*, L.F. WARREN\*, P. CUNNINGHAM\*, T.Y. CHANG\*, D.E. COOPER\*,  
G.L. BURDGE\*\*, P. POLAK-DINGELS\*\*, and C.K. LOWE-MA\*\*\*

\* Rockwell International Science Center, Thousand Oaks, CA 91360

\*\* Laboratory for Physical Sciences, College Park, MD 20740

\*\*\* Naval Weapons Center, China Lake, CA 93555

Recent results indicate that certain organic molecules whose electronic structures are characterized by extended pi-molecular orbitals can exhibit significant second and third order nonlinear optical (NLO) effects [1]. Unfortunately, this same arrangement which leads to the NLO effects, can also result in essentially one-dimensional bonding coordination. This in turn means that crystals grown from these materials do not readily form good three-dimensional optical-quality crystals, but rather tend to form needles. In addition, pure organic crystals are usually bonded by weak van der Waals forces, often resulting in poor mechanical properties. Indeed, organic impurities are frequently incorporated into these systems during crystallization resulting in poor crystallinity, spurious absorptions, and low damage thresholds. This is particularly true in the case of polymeric NLO materials, where impurities result from the polymerization steps and/or starting materials.

SEMIORGANICS

A new approach to high performance, optical quality organic-based NLO materials is to consider compounds in which a polarizable organic molecule is stoichiometrically bonded within an inorganic host forming either an organic/inorganic salt (e.g., LAP [2]) or an organic ligand/metal ion complex. Although such systems have been known for many years, we are the first to examine them for their NLO properties and have coined the term "semiorganics" to refer to them. With semiorganics, the organic component is chosen to possess high molecular hyperpolarizability by virtue of extended pi-orbitals and is bonded chemically within a surrounding inorganic host. The bonding scheme of this inorganic species is three dimensional and can lead to the growth of large optical-quality three-dimensional crystals. The stoichiometric nature of the chemistry associated with these materials results in a much purer material, leading to reduced absorption.

NLO Polarizability in Semiorganics

Intuitively, one might expect that to first-order, the characteristics of a semiorganic crystal would be described essentially as diluting the effective hyperpolarizability as a result of the decrease in volume fraction of the organic NLO component. Also, it would appear to limit the extent of intermolecular pi interactions by breaking up the organic units. In actual fact, many semiorganic systems have a polymeric character which retains extensive pi molecular orbital interactions between the organic components. Recent theoretical and experimental results in pure conjugated organic polymer systems, however, show that the large hyperpolarizabilities associated with these molecules saturate as the number of monomer units reaches about twenty.

In the case of the semiorganics, there are evidently some mitigating circumstances. The intervening inorganic atoms, or more precisely the bonds to these atoms, are in turn polarizable by the large short range dipole fields which result from the initial polarization of the organic component by an external field. This added polarizability apparently compensates to some extent for the reduction in hyperpolarizability due to the reduced volume fraction of the organic component. Consequently,

the dielectric constant of the near surround affects both  $\chi^{(2)}$  and  $\chi^{(3)}$  as shown by the following [3]:

$$\begin{aligned}\chi^{(2)} &= \frac{1}{3} (\epsilon + 2) \cdot \left( \sum_k \rho_{0,1} \beta_k \right) : \frac{1}{3} (\epsilon + 2) \frac{1}{3} (\epsilon + 2) \\ \chi^{(3)} &= \frac{1}{3} (\epsilon + 2) \cdot \left( \sum_k \rho_{0,1} \gamma_k \right) : \frac{1}{3} (\epsilon + 2) \frac{1}{3} (\epsilon + 2) \frac{1}{3} (\epsilon + 2) \\ &\quad + \chi^{(2)} \cdot [(\epsilon + 2)^{-1} \cdot \chi^{(2)}]_1 + [(\epsilon + 2)^{-1} \cdot \chi^{(2)}]_2 .\end{aligned}$$

#### Theoretical Calculations of NLO Properties

In an effort not so much aimed at calculation of precise values, but rather to derive a predictive methodology, we have set out to calculate by semi-empirical methods the NLO properties of some selected semiorganic materials. In particular, we wish to appreciate the effect of the inorganic surroundings upon the nonlinear susceptibilities of the organic molecules within the crystal. Our approach begins with calculation of bond polarizabilities, which are then used to calculate net hyperpolarizabilities for the combined semiorganic molecule. The calculation of the polarizability and hyperpolarizabilities has been facilitated through the use of the MOPAC program (fifth edition) available through the Quantum Chemistry Library. Following this, we then calculate the net polarization for all molecules in the unit cell by performing a self consistent dipole sum over all the molecules. Finally, the conversion from hyperpolarizabilities to the NLO susceptibilities is achieved by using the Lorentz approximation in which we sum up the contribution to the polarization from the interior of a sphere which is chosen large enough to contain many unit cells, but small enough not to worry about surface depolarization effects. We have calculated the (hyper)polarizabilities for prototype semiorganic molecules (*vide infra*), and the reduction to the susceptibilities is in progress.

#### SEMIORGANIC CRYSTALS

Synthetically, relatively simple nonabsorbing organic molecules with appreciable  $\beta$  values were selected based on SHG powder data [1]. The molecules either form ions, e.g., by protonation, or acted as coordinating ligands to (colorless) metal ions to form complexes; these are designated as type 1 and type 2 semiorganics, respectively. For each organic molecule, a variation of inorganic counterions and/or metal ions were investigated to enable us to screen a great number of semiorganic systems with regards to crystal growth and habit (i.e., optical quality). Three prototype compounds were studied more extensively; they are type 2 semiorganics: zinc tris(thiourea) sulfate, its cobalt(2+)-doped analog, and (4-nitropyridine-N-oxide) mercury chloride.

#### Zinc Tris(Thiourea) Sulfate

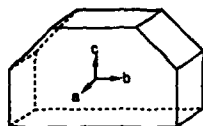
$Zn(TU)_3SO_4$  crystallizes in the noncentrosymmetric orthorhombic space group  $Pca2_1$  (point group  $mm2$ ) from aqueous solution as water-clear block-like crystals with an external morphology as shown in Figure 1. Crystals approaching 20 mm on a side have been grown by Cleveland Crystals, Inc. The x-ray structure determination shows a zinc ion tetrahedrally coordinating three planar thiourea molecules and one oxygen from a sulfate [4]. There is also extensive inter- and intramolecular hydrogen bonding between thiourea N-H's and the sulfate O's, and this feature most likely gives rise to the noncentrosymmetry.



## INDICES MEASURED BY AUTOCORRELATION TECHNIQUE @ 600 nm

$$n_a \sim n_c = 1.782, n_b = 1.701 \text{ (NEARLY UNIAXIAL)}$$

CRYSTAL SYMMETRY: ORTHORHOMBIC  $Pca2_1$  \*  
POINT GROUP:  $mm2$



## UNIT CELL DIMENSIONS \*

$$a = 11.12 \text{ \AA}, b = 7.77 \text{ \AA}, c = 15.49 \text{ \AA}$$

\* G. D. Andreotti, et al., Acta Cryst. **B24**, 683 (1968)

Figure 1  $Zn(TU)_3SO_4$  crystal properties.

The optical transmission spectrum of  $Zn(TU)_3SO_4$ , presented in Figure 2, shows transparency from about 350 nm to about 1 micron. The shallow absorption at 1 micron appears to be an N-H stretch overtone and should disappear upon deuteration of the material (e.g., in  $KD^*P$ ). Refractive indices of  $Zn(TU)_3SO_4$  over the range 570–640 nm were measured by observing the propagation delay for a picosecond optical pulse through a known crystal thickness. The crystal is essentially uniaxial, with indices in the crystallographic a and c-axes being equal within experimental error at 1.782, while the b-axis is 1.701 (at 600 nm). Figure 1 summarizes these data.

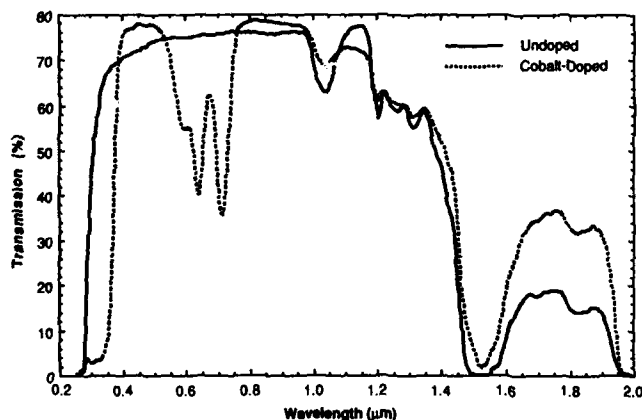


Figure 2 Transmission spectra of  $Zn(TU)_3SO_4$  and the cobalt(2+) doped crystals.

Second harmonic generation (SHG) was observed in  $Zn(TU)_3SO_4$  crystals, and we used the Maker fringe technique to determine the second order NLO coefficients. It was not necessary to have the crystal cut for exact phase matching; the sample was rotated along the z(c)-axis to vary the coherence length while the polarization vector for the fundamental radiation was perpendicular to the z-axis. The fundamental radiation source was a cw mode-locked Nd:YAG laser. The  $d_{36}$  NLO coefficient for KDP was measured as a standard. The  $mm2$  point group of  $Zn(TU)_3SO_4$  gives rise to five nonzero second order NLO tensor coefficients, three of which were measurable with the particular samples and are listed in Table 1.

Table 1  
Second-Order NLO Coefficients for  $\text{Zn(TU)}_3\text{SO}_4$

Nonlinear Optical Coefficient	Rotation Axis	Polarization Vector	Magnitude Relative to $d_{36}$ of KDP
$d_{24}$	Y	$45^\circ$ to Y	2.5
$d_{32}$	Z	Y	3.6
$d_{33}$	Y	Z	0.60

$\text{Zn(TU)}_3\text{SO}_4$  also exhibits a  $\chi^{(3)}$  response by degenerate four-wave mixing (DFWM) using a pulsed (8 ns) doubled Nd:YAG (532 nm) laser; details of these measurements have been made elsewhere [5]. Analysis of the phase conjugate reflectivity vs pump beam intensity yields a nonresonant  $\chi^{(3)}$  value - 0.10 times that of the  $\text{CS}_2$  reference; the response was at least as fast as the pulse. The observed (unoptimized) damage threshold of this material at this wavelength was  $\sim 18.5 \text{ J/cm}^2$ .

An enhancement of  $\chi^{(3)}$  of this compound was observed when we "doped" with cobalt ions during the crystallization process. This resulted in pale blue crystals due to incorporation of tetrahedrally coordinated  $\text{Co}^{2+}$ . ( $\text{Zn(TU)}_3\text{SO}_4$  and the cobalt analog are isomorphous). At  $10^{-3}$  mole fraction, the Co-doped single crystal gives the transmission spectrum shown in Figure 2, where the absorptions between 550 and 750 nm are due to the cobalt. Preliminary DFWM measurements at 565 nm using a pulsed (ns) dye laser shows a complex power vs reflectivity behavior with an approximate  $\chi^{(3)}$  value - 1.5 times that of  $\text{CS}_2$ , more than an order of magnitude greater than that of the undoped crystal [5]. While the exact mechanism of this resonance enhancement is presently unknown, it is probably due to internal atomic transitions associated with the transition metal ion. Further studies are currently underway.

#### (4-Nitropyridine-N-Oxide) Mercury Chloride

The centrosymmetric triclinic (space group  $P\bar{1}$ )  $(\text{NPO})\text{HgCl}_2$  crystallizes as large optically clear yellow blocks from solutions containing mercuric chloride and 4-nitropyridine-N-oxide. The crystal gives the transmission spectrum shown in Figure 3, and exhibits a moderate (nonresonant) phase conjugate reflectivity by DFWM at 532 nm corresponding to a  $\chi^{(3)}$   $\sim 0.5$  times that of  $\text{CS}_2$  [5].

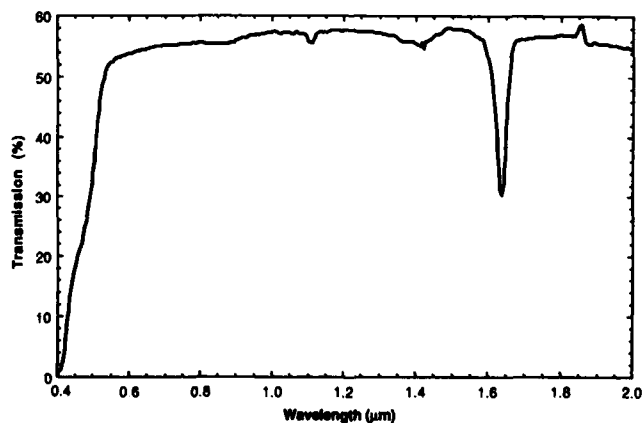


Figure 3 Transmission spectrum of a  $(\text{NPO})\text{HgCl}_2$  crystal.

To more fully understand the potential NLO-structure relationship, a single crystal x-ray diffraction study of  $(\text{NPO})\text{HgCl}_2$  was carried out. The molecular arrangement of the molecules is comprised of sheets of NPO molecules held together in a three-dimensional array by mercury atoms bridging through the N-oxides. A key feature of  $(\text{NPO})\text{HgCl}_2$  which apparently gives rise to its  $\chi^{(3)}$  response is the strong intermolecular communication between the organic moieties as a result of the bridging mercury chloride chains. The pi frameworks of the NPO molecules are, in effect, linked via the mercury chlorides into an extended three-dimensional molecular orbital network which is highly polarizable.  $\text{Zn}(\text{TU})_2\text{SO}_4$ , on the other hand, exhibits hydrogen bonding which is less effective in extending thiourea pi orbitals than the mercury chlorides with NPO, and thus a lower  $\chi^{(3)}$  response is observed.

In conclusion, we have demonstrated, for the first time, significant nonlinear optical effects, in two prototype semiorganic crystalline materials. The chemistry associated with this class of compounds is such that there is tremendous flexibility in "designing" new systems, potentially leading to increased optical response. Additional resonant enhancement of the nonlinear response obtained through substitutional doping, may allow additional mechanisms for optimization. Finally, to maximize the effectiveness of our crystal growth program, we are pursuing the development of a generalized predictive methodology that will allow calculation of relative nonlinear optical characteristics from chemical composition, and crystallographic geometry.

#### ACKNOWLEDGEMENT

We wish to acknowledge the assistance of Professor Truman O. Woodruff, formerly of Michigan State University, for providing direction in the theoretical modeling studies, and of Gretchen Kennedy of Cleveland Crystals for semiorganic crystal growth.

#### REFERENCES

- [1] D.J. Williams, ed., Nonlinear Optical Properties of Organic and Polymeric Materials, ACS Symp. Ser. 233, Am. Chem. Soc., Washington, D.C., 1983.
- [2] D. Eimerl, S. Veisko, L. Davis, F. Wang, G. Loiacono, and G. Kennedy, *IEEE J. Quantum Elec.* 25, 179 (1989).
- [3] D. Bedeaux and N. Bloembergen, *Physica* 69, 57 (1973).
- [4] G.D. Andreotti, L. Cavalca, and A. Musatti, *Acta Cryst.* B24, 683 (1968).
- [5] T.Y. Chang, M.D. Ewbank, R.A. Vazquez, L.F. Warren, and P.R. Newman, presented at the 1989 Opt. Soc. Am. Fall Meeting, Orlando, FL, Oct. 16, 1985.

FUSED, THREE-RING DONOR-ACCEPTOR MOLECULES AS POTENTIAL  
MATERIALS FOR EFFICIENT SECOND HARMONIC GENERATION

MALCOLM R. McLEAN, MAMOUN BADR and LARRY R. DALTON\*  
Department of Chemistry  
ROBERT L. S. DEVINE and WILLIAM H. STEIER  
Department of Electrical Engineering, University of Southern California  
Los Angeles, CA 90089-1062

ABSTRACT

A series of fused three-ring compounds have been synthesized and characterized for their possible use as organic crystals for second-harmonic generation. Polymer films doped with these compounds were aligned via corona poling and their second order non-linear optical properties compared with layers doped with stilbene like molecules. Values of  $\mu\beta_0$  have been obtained and the effects of different heteroatoms and substituents on  $\lambda_{\text{max}}$  and on  $\mu\beta_0$  were examined. An X-ray diffraction crystal structure on one member of the series, 1,2,4-Trichloro-8-nitro-phenoxazin-3-one (Compound 1), revealed a centrosymmetric crystal habit in a  $P2_1/n$  space group, with  $a = 9.829(3)$ ,  $b = 8.300(2)$  and  $c = 15.542(4)$  Å. Final  $R(F) = 0.0939$  for 754 reflections where  $I > 3\sigma(I)$ .

INTRODUCTION

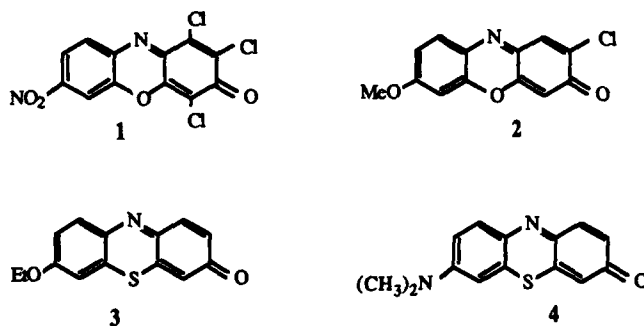
Recent activity in the study of nonlinear optical (NLO) organic molecules has concentrated on either polyene- or azo-type dyes. Very large values of the second order hyperpolarizability,  $\beta$ , have been obtained, with the corresponding expectation of high  $\chi^{(2)}$  values for either electro-optic or second-harmonic generation (SHG) applications. The successful exploitation of these high  $\beta$  values has, however, encountered several difficulties. In the case of thin-film electro-optic applications using doped polymers, problems such as relaxation of the molecular orientation are well known. For SHG applications, utilization of bulk organic crystals is the most common approach. There are two fundamental problems which must be overcome here, however, before a useful crystal can be obtained. The first is to obtain a non-centrosymmetric crystalline structure, which is a necessary condition for the crystal to exhibit second-order NLO properties. Unfortunately, approximately 85% of known second-order NLO molecules crystallize in a centrosymmetric structure (in fact, this value can be extended to all known crystal structures of organic materials). Even if this condition is satisfied, however, the crystal must be phase-matchable if useful intensities of the second harmonic are to be obtained. [1]

DISCUSSION

In the search for useful materials for such applications we are currently studying a series of fused, three-ring aromatic compounds. Rationale for interest in such systems stems from the fact that some dyes, such as

merocyanine and disperse red 1 (DR1) have high  $\beta$  values. Unfortunately, merocyanine, which possesses the highest  $\beta$  value to date, is unstable and decomposes on exposure to the atmosphere, while DR1 is prone to thermal decomposition. This instability would appear to be due to the presence of a stilbene type linkage (merocyanines) and an azo linkage (DR1). Our aim was to design molecules with dye-type characteristics (i.e., sharp and strong absorption bands in the visible region) but with in-built robustness as a foil against degradation. Thus, the linkage must be incorporated into the molecule, i.e., use rings instead of double bonds. To this end we chose to concentrate on fused, 3-ring aromatic systems, some of which are already utilized in established dye molecules (i.e., Compound 4 = methylene violet). Precedent for their durability came from our own experience with ladder polymers such as PQL, PTL, BBB and BBL which exhibit exceptional thermal and photo stability. [2] The compounds of interest incorporate oligomeric units of ladder polymers with known dye structures such as phenoxazine. In addition, the present series contains the same terminal group as merocyanine (carbonyl), which should enhance the attainment of high  $\beta$  values.

We are currently investigating the following four oligomers:



#### EXPERIMENTAL

Compounds 1-3 were synthesized in-house, according to literature methods [3], via condensation reaction of the appropriate monomers in refluxing acetic acid or ethanol. Purification was achieved by sublimation, recrystallization or column chromatography. Compound 4 is a commercially available dye (methylene violet) and was used as received. Compounds were characterized by <sup>1</sup>H NMR, UV-Visible and fourier transform infrared spectroscopy and elemental analysis (e.g. Compound 1 calc.. C = 41.71%, H = 0.88% N = 8.11%, actual C = 42.05%, H = 0.97%, N = 7.89%). Initial measurement of the  $\beta$  value of 1 looked promising, with a value comparable to MNA, but, more importantly, with minimal thermal or atmospheric degradation. This prompted us to perform an X-ray diffraction crystal structure on 1, to confirm the assigned structure and to investigate whether 1 crystallizes in a non-centrosymmetric form, essential for bulk  $\chi^{(2)}$ .

### Crystal Data

The orange-red crystal (0.6 x 1.04 x 0.8 mm) used in the structural analysis was grown by vapor diffusion from a saturated solution of Compound 1 in benzene with hexane as a co-solvent. Data were collected on a Nicolet/Syntex diffractometer utilizing Mo K $\alpha$  radiation. A data set consisting of 1740 reflections was collected, of which 754 satisfied the  $I > 3\sigma(I)$  criteria. These reflections were used in the refinement, which was solved with the SHELX84 program. The unit cell consisted of four molecules of 1 and contained a crystallographic center of symmetry. 1 therefore crystallizes in a centrosymmetric space group, in this case  $P2_1/n$ , and is not expected to exhibit a bulk  $\chi^{(2)}$ . A full description of the crystal study will be presented at a later date [4], however, the relatively high R-factor ( $R = 0.0939$ ) is due to broad peak widths, themselves the result of disorder in the crystalline matrix.

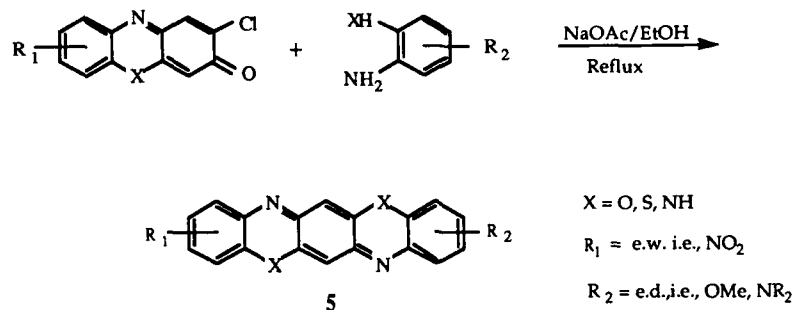
### Trends in $\mu\beta_0$ Values

Values of  $\mu\beta_0$  were obtained using solvatochromism, and the observed trends in  $\mu\beta_0$  were confirmed by second-harmonic generation studies on corona-poled doped polymer films. Polyvinylacetate was used as a matrix, hence allowing in-situ poling due to its low glass transition temperature. General trends in  $\mu\beta_0$  values will be discussed below.

The substitution of the stronger electron donating group, di-methyl amino, for ethoxy, i.e., Compounds 4 vs 3, resulted in an increase of  $\mu\beta_0$  from 105 to 250 x 10<sup>-30</sup> D-esu, illustrating the general trend of increasing values with stronger electron donating groups. More important is the overall magnitude of the signals (for comparison, p-NA has  $\mu\beta_0$  approx. = 55 x 10<sup>-30</sup> D-esu). A second trend is seen between 2 and 3 where the main difference in structure is the heteroatom, sulfur in 3 and oxygen in 2. The respective values for  $\mu\beta_0$  are 250 vs. 75, therefore the choice of bridging heteroatom is very important in maximizing the  $\beta$  value. It should be noted that this is a preliminary study, nonetheless we feel that the trends and approximate magnitudes of the signals are well-defined.

### CONCLUSION

The three-ring systems examined have demonstrated high  $\mu\beta_0$  values, comparable in magnitude to MNA, but with much improved thermal and photo stability. 1 crystallizes in a centrosymmetric space group, and given the similarities in structures it is likely that 2, 3 and 4 also will. Therefore we are examining their attachment as pendant groups to a polymer backbone. We are also examining different substituents and compounds where the backbone is expanded to a five-ring system. The following scheme demonstrates the general utility of the condensation reaction utilized in forming a series of fused five-ring donor-acceptor compounds.



It is also possible to incorporate more exotic substituents such as tricyanoethylene (e.w.) and disubstituted thiophene rings (e.d.). Such substituents are expected to markedly increase  $\beta$  values. This is a preliminary communication of  $\mu\beta_0$  values, a full manuscript is in preparation. [5]

#### ACKNOWLEDGEMENTS

This research was supported by the Air Force Office of Scientific Research through contract Number F49620-87-C-0100 and F49620-88-C-0071 and by National Science Foundation grant DMR-88-15508. The authors wish to thank Jin-an Feng, whose work contributed to this article.

#### REFERENCES

- [1]. I. Ledoux, D. Josse, P. Vidakovic, J. Zyss, *Opt. Eng.* 25, 2 (1986).
- [2]. See, for example, F. Coter, Y. Belaish, D. Davidov, L.R. Dalton, E. Ehrenfreund, M.R. McLean and H.S. Nalwa, *Syn. Metals* 29, E471 (1989).
- [3]. R.L. Mital and S.K. Jain, *J. Chem. Soc. (C)*, 1875 (1971).
- [4]. M.R. McLean, M. Badr, J. Feng and L.R. Dalton, manuscript in preparation.
- [5]. R.L.S. Devine, W.H. Steier, M.R. McLean, M. Badr and L.R. Dalton, manuscript in preparation.

## OPTICAL AND MAGNETIC PROCESSES AND THE SIDE CHAINS OF DIACETYLENIC MATERIALS

DANIEL J. SANDMAN, GREGORY P. HAMILL, MARK LEVINSON,  
PHILIP G. ROSSONI, AND ELIZABETH A. YOST

GTE Laboratories Incorporated, 40 Sylvan Road, Waltham, Massachusetts 02254

GEORGIA C. PAPAETHYMIU

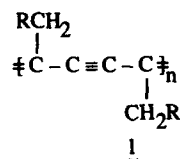
Francis Bitter National Magnet Laboratory, Massachusetts Institute of Technology,  
Cambridge, Massachusetts 02139

### ABSTRACT

Similarities in the molecular energy levels of alkylcarbazoles and aliphatic nitroxides motivate the detailed study of 4,4'-(butadiyne-1,4-diyl)-bis-(2,2,6,6-tetramethyl-4-hydroxypiperidin-1-oxyl) (4) as a precursor to a ferromagnetic polymer. A more convenient synthetic route to 4 is reported, and an X-ray-induced transformation of the  $\beta$ -phase of 4 to the  $\alpha$ -phase has been observed. The magnetic properties of 4 and derived polymers have been studied using a SQUID system. The observed level of ferromagnetism found in samples of polymerized 4 is comparable to the amount of trace iron materials detected in these samples.

### INTRODUCTION

The polydiacetylenes (PDA, 1) are the best known class of polymers available as macroscopic polymer single crystals [1-3]. Associated with the PDA



conjugated backbone is an intense visible absorption which manifests a degenerate third-order nonlinear susceptibility ( $\chi^{(3)}(\omega)$ ) greater than  $10^{-10}$  esu at transparent wavelengths with a temporal response in the femtosecond regime [4-5].

The numerous roles of side groups (R in 1) in PDA structure, spectroscopy, and processes have been discussed [6]. The role of side group polarizability in the crystal structure - solid state spectroscopy relationship is of particular interest [5,7-9], and has been offered [9] as a reason that poly-DCH (1a), with a polarizable carbazole side chain, absorbs at lower energy than other fully polymerized PDA single crystals. The results of both electroreflectance [10] and photoconductivity



[11] studies in poly-DCH have been interpreted [10,11] to imply a significant coupling of the carbazole group to the  $\pi$ -electrons of the PDA chain.

Additional motivation for further inquiry into electronic interactions between the PDA conjugated backbone and side groups comes from reported values of the crystal dipole strengths,  $D$ , a measure of the intensity of a spectral transition. For poly-DCH [12],  $D = 1.93 \text{ \AA}^2$ , while reported [12,13] values for other PDA fall in the range  $D = 1.66\text{--}1.76 \text{ \AA}^2$ . This reported modest enhancement of the intensity of the PDA excitonic transition is reminiscent of enhancements of molecular transitions in conformationally rigid  $\beta,\gamma$ -unsaturated ketones [14] and homoconjugated styrenes [15] where the intensity enhancement has been attributed [16] to mixing of locally excited states of the interacting chromophores.

N-Ethylcarbazole (**2**) is a useful model for the side group energy levels ( $I_G$ , vertical ionization energy;  $E_1$ , solution radiation potential;  $\lambda_{\max}$ , position of maximum absorption of lowest energy electronic transition) of poly-DCH [17], and this data is summarized in Table 1. Also given in Table 1 are analogous data for 2,2,6,6-tetramethylpiperidin-1-oxyl (**3**), a cyclic nitroxide [18,19]. Nitroxides are of

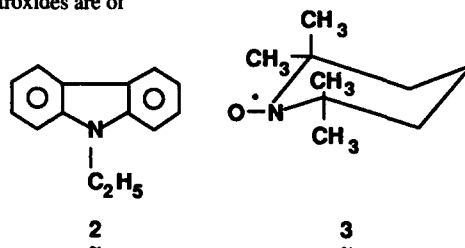


Table 1

Energy levels of side chain model compounds

Model Compound	$I_G$ (eV)	$E_1$ (V vs SCE)	$\lambda_{\max}$ (nm); $\Delta E$ (nm)
N-Ethylcarbazole ( <b>2</b> )	7.29	+1.12	344 ; 3.61
2,2,6,6-tetramethyl-piperidin-1-oxyl ( <b>3</b> )	7.31	+0.57	437 ; 2.74

interest as PDA side groups pursuant to the initial reports [20,21] that polymerization of 4,4'-(butadiyne-1,4-diyl)-bis-(2,2,6,6-tetramethyl-4-hydroxypiperidin-1-oxyl) (**4**) leads to a ferromagnetic material. Analogous to the line of reasoning which suggests that electronic interactions might occur between a carbazole group and the PDA backbone in poly-DCH, the similarity of the molecular energy levels of **2** and **3** leads to the speculation that in an ideal case, a nitroxide could also be involved in electronic interactions with the PDA backbone leading to a modified electronic structure and possibly ferromagnetism. Alternatively, in an ideal case, ferromagnetism might arise via interactions among the paramagnetic nitroxide groups with no significant participation of the PDA electronic structure. It must be emphasized, however, that the currently reported nitroxide-substituted diacetylenes are far from ideal, especially with respect to

solid state reactivity. An energy level diagram of PDA electronic structure showing the energy levels of a nonconjugated side group [11,12] is shown in Figure 1. In Figure 1, the highest occupied molecular orbital (HOMO) would be doubly occupied for a carbazole and singly occupied for a nitroxide.

In initial work [20,21], the polymerization of **4** at 80–100°C to give a polymer formed by either a 1,2 addition polymerization of only one acetylenic group or a 1,4 nontopochemical addition [21] was reported. The resultant polymer lacked long-range order and exhibited a spontaneous magnetization of only 0.1% of the theoretical value, although a variation from sample to sample was noted [21]. Monomeric **4** in these studies belonged to space group  $P_{ccn}$  [21] and is termed the  $\alpha$ -phase. The polymerization was also termed "explosive" [23]. Subsequently, Chinese investigators [24,25] reported heating samples of **4** of undefined crystallographic phase for 48 and 480 hours. They reported a spontaneous magnetization corresponding to 0.7% of the sample and observed magnetic hysteresis.

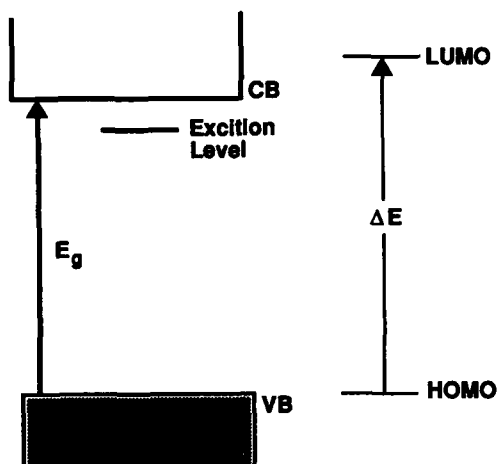


Figure 1. PDA electronic structure and relative disposition of side chain energy levels.

In contrast to these reports, the isolation of a polymorphic form of **4** ( $\beta$ -phase) was reported [26]; heating this material at about 90°C for 17 hours led only to a reduced moment.

The reports [27] of thermal and photochemical decomposition of stable nitroxides with structural elements similar to those of **4** rendered the suggestion [21] of polymerization of **4** with retention of structural elements rather curious. Nevertheless the reports that, in contrast to diaryl nitroxides which exhibit planar



groups [28], representative cycloaliphatic nitroxides [29–31] exhibit geometries in which the nitroxide nitrogen is in a pyramidal geometry led to the notion that the variation in properties of the thermolysis products of 4 could involve the presence of higher energy conformers of 4, such as those shown in Figure 2. However, an examination of the literature [32] revealed that the barrier for nitrogen inversion in nitroxides was probably too small to allow isolation of such higher energy conformers.

The remainder of this article details our studies of the synthesis of 4 of its characterization by X-ray diffraction, and the magnetic properties of 4 and the product of its thermal polymerization.

## EXPERIMENTAL SECTION

### Materials Synthesis and Characterization

Compound 4 was synthesized either as previously described [33] or by Hay coupling [34] of 4-ethynyl-4-hydroxy-2,2,6,6-tetramethylpiperidin-1-oxyl 5 [29]. Single crystals of the  $\alpha$ -phase of 4 were obtained by crystallization of 4 and its bis-piperidinol (6) precursors [35] in a 3.74:1 molar ratio from aqueous methanol, and single crystals of the  $\beta$ -phase were obtained from ethyl acetate.

Electronic spectra were recorded on a Varian Cary 17 spectrophotometer in methanol solution using 1.0 cm cells. Compound 4 exhibited the following:  $\lambda_{\text{max}}$  (nm), eV,  $\epsilon$  : 435, 2.85, 19.6; 240, 5.17, 5000. Our extinction coefficients are significantly higher than previously reported [25]. Compound 5 exhibited the following  $\lambda_{\text{max}}$  (nm),  $\epsilon$  : 437 (9), 240 (1900). Raman spectra of 4 and 6, recorded on solid samples, exhibited triple bond shifts at 2244 and 2254  $\text{cm}^{-1}$ , respectively, in general agreement with a previous report [26].

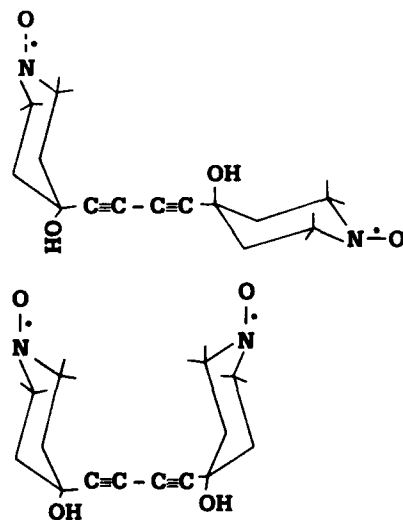


Figure 2. Higher energy conformations of 4.

### Magnetic Characterization

Magnetic moments of polymerized materials were measured in magnetic fields up to  $\pm 5$  T at temperatures of 2.0 and 4.8 K using a SQUID magnetometer system with a superconducting magnet (Quantum Designs). Samples were contained in teflon capsules that exhibited maximum moments at 2 K of  $4 \times 10^{-5}$  emu above 0.1 T, and no hysteresis within the experimental resolution of  $\sim 10^{-6}$  emu. Magnetic moment was recorded as the magnetic field was swept from 0 to 5 T, then to  $-5$  T, and back to 0. The time required for a complete sweep was about 4 hr.

Magnetic moments of monomeric samples were also measured on SQUID systems at either the Francis Bitter National Magnet Laboratory (6–300 K, 0.5 T) or at GTE Laboratories (4.6–300 K, 0.5 and 1.0 T).

## RESULTS AND DISCUSSION

### Synthesis and Thermal Characterization of 4

The synthesis of 4 was accomplished by the two methods summarized in Figure 3. The pertungstate oxidation of 6 [33] requires a reaction time of 1.5 months, and unreacted 6 is always detectable in such reaction mixtures and in samples of 4 synthesized via this procedure. Accordingly, we chose to also synthesize 4 by Hay coupling [34] 5. Note that the stereochemical relationship of the substituents in the 4 position of 5, established by X-ray crystallography [29], is not maintained in 4.

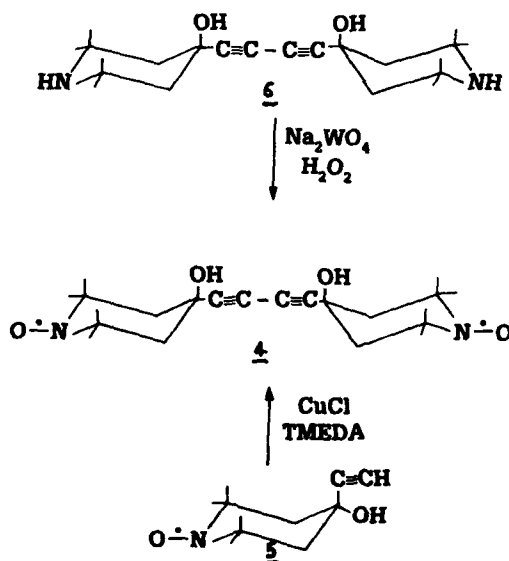


Figure 3. Synthetic routes to 4.

The sensitivity of 4 to heat is apparent from previously reported work [20,25,26], but the dependence of decomposition temperature on heating rate is not apparent. Using differential scanning calorimetry when 4 is heated at a rate of 2°C/min, a decomposition temperature of 139°C is observed, while a decomposition temperature of 160°C is found with a heating rate of 13°C/min.

### X-Ray Diffraction of 4

Single crystals of the  $\alpha$ - and  $\beta$ -phase of 4 were obtained as described in the Experimental Section. Table 2 lists the lattice constants of our samples obtained from single-crystal photographs, along with those reported in the literature [21,26].

In the course of these studies, it was observed that  $\text{CuK}\alpha$  radiation induces a transformation of polycrystalline (but not single crystals) samples of  $\beta$ -4 to the  $\alpha$ -phase. This transformation is not observed with  $^{60}\text{Co}$  gamma radiation. These experiments are described in more detail elsewhere [36].

Table 2  
Crystal data for the phases of 4

	$\alpha$ -Phase		$\beta$ -Phase	
a	19.2425Å <sup>a</sup>	19.08(11)Å <sup>b</sup>	14.265Å <sup>c</sup> (100 K)	14.38(7)Å <sup>b</sup>
b	16.2402	16.11(6)	8.079(3)	8.115(5)
c	14.1883	14.25(14)	18.865(2)	18.53(12)
Space Group	P <sub>ocn</sub>	P <sub>ocn</sub>	P <sub>ca</sub> <sup>2</sup> 1	P <sub>ca</sub> <sup>2</sup> 1
Z	8	8	4	4
Habit	Needles	Needles	Parallelepiped	Needles and Prism

a. *Nature*, 326, 370 (1987)

b. Present work

c. *J. Chem. Soc., Chem. Commun.* 332 (1988)

### Magnetic Properties of 4

The magnetic moment of a sample of  $\beta$ -4 synthesized by Hay coupling was studied using a SQUID system from 6 to 300 K at 0.5 T. The data obtained was treated according to the Curie-Weiss law,  $\chi = C/T - \theta$ . For this experiment,  $\theta = -1.2^\circ$  and the effective moment  $\mu_{\text{eff}} = 2.84 \sqrt{\chi T} = 2.40$  Bohr magnetons, comparable to the earlier report [26].

As noted in the Synthesis Section, 4 is inevitably contaminated by 6 when prepared according to Rozantsev [33]. In view of the various roles played by impurities in the observed properties of both diacetylenes and organic ion-radical solids [37], it is conceivable that differences in the impurity levels found in samples of 4 prepared in different laboratories might account for the differences in magnetic properties reported for polymerized 4 [20,21,23-26]. Accordingly we characterized a sample of 4 isolated from a pertungstate oxidation [33] by spectral and magnetic

methods. Its magnetic moment was 86.5% that of the sample of  $\beta$ -4 described above, and spectroscopic analysis suggested the presence of 87%–89% of 4.

#### Polymerization of 4

While it is unlikely that "polymerization" is the best term for the process which occurs on heating of 4, we will nevertheless use that term. Samples of 4 which were characterized as in the preceding paragraph were heated under vacuum in an oil bath kept at 100°C for 48–480 hours [24]. Weight loss varied in each experiment. For example, one monomer sample of the material which was 87% 4 lost 76% of its weight after 480 hours heating, while another lost 62% in the same time period. The FTIR spectrum of our polymerized material is in excellent agreement with a reported spectrum [25]. Raman spectra, obtained using both 632.8 and 514.6 nm as wavelengths of excitation of polymerized 4 heated for either 48 or 480 hours, yield no evidence for the presence of either a PDA, graphitic carbon, or unreacted 4.

#### Magnetic Properties of Polymerized 4

For samples of 4, synthesized by either method [33,34] used in this work, thermal polymerizations result in loss of magnetic moment compared to 4, and no evidence for reproducible ferromagnetism was observed in samples of polymerized 4 measured after 48 and 240 hours of heating as described above.

Magnetization data vs field at 2 K for a sample of 87% 4 heated for 480 hours is shown in Figure 3; a hysteresis is revealed. Since the moment observed is less than 1% that of the initial moment of 4, it was deemed appropriate to analyze the sample for iron. X-ray fluorescence analysis revealed the presence of iron at the 1–10 ppm level. Since the data in Figure 4 reveal a moment at low fields which can be accommodated by that level of iron, we conclude that polymerized 4 does not make a significant contribution.

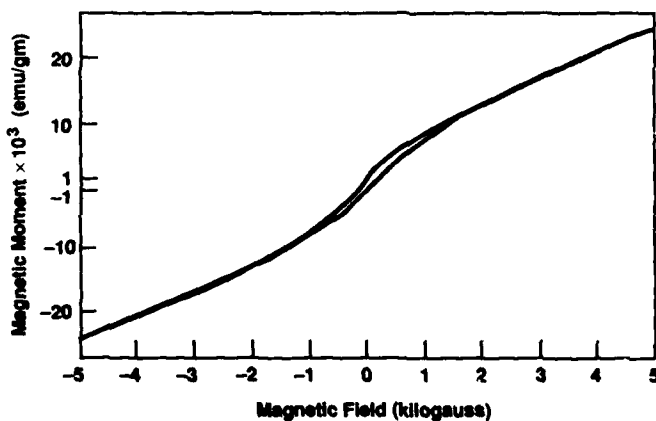
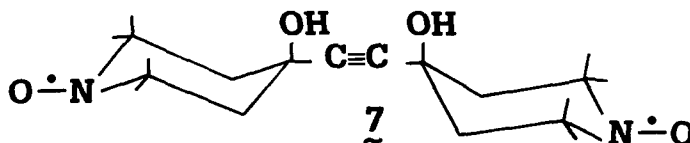


Figure 4. Magnetic moment vs magnetic field at 2 K for a polymerized (480 hr) sample of 87% 4.

## CONCLUSIONS

A new, more convenient synthesis of **4** has been achieved, and the  $\alpha$  and  $\beta$  phases of this compound have been identified by single-crystal X-ray diffraction. An unusual X-ray-induced transformation of the  $\beta$  to  $\alpha$  phase has been observed in polycrystalline samples of **4**.

The magnetic properties of the products of thermal polymerization of **4** have been studied, and the results offer no evidence for intrinsic organic ferromagnetism in contrast to previous studies [20,21,23-25]. The presence of impurities, especially in various preparations of **4**, was discussed above. Additionally, the monoacetylene, **7** [38], identified by melting point and mass spectrum, was isolated in low yield in one experiment in the present work. In view of the recognition herein that various impurities can be present in samples of **4**, those claiming that "thermally polymerized **4**" leads to an intrinsic organic ferromagnetic material have not provided sufficient information to allow their experimental results to be reproduced. The magnetic hysteresis, displayed in Figure 3, can be explained by the presence of traces of iron.



Progress in ferromagnetic polymers in general and those based on diacetylenic materials in particular will require better defined materials than those available at present.

## ACKNOWLEDGMENTS

The authors thank Dr. S. Hankin, D.R. Hammond, D. Carrill, and F.X. Pink for furnishing, respectively, infrared and Raman spectra, differential scanning calorimetry data, mass spectrometry, and X-ray fluorescence data.

## REFERENCES

1. D.J. Sandman, ed., *Crystallographically Ordered Polymers*, American Chemical Society Books, Washington, D.C. (1987).
2. D. Bloor and R.R. Chance, eds., *Polydiacetylenes*, Martinus Nijhoff, Nordrecht, Boston (1985).
3. H.-J. Cantow, ed., *Polydiacetylenes*, *Advances in Polymer Science*, Vol. 63, Springer Verlag, Berlin, Heidelberg (1984).

4. G.M. Carter, M.K. Thakur, J.V. Hryniewicz, Y.J. Chen, and S.E. Meyler, in [1], pp. 168–176.
5. D.J. Sandman and Y.J. Chen, *Polymer*, **30**, 1027 (1989).
6. D.J. Sandman, presented at the 9th International Conference on the Chemistry of the Organic Solid State, Como, Italy (July 2–7, 1989).
7. D.J. Sandman and Y.J. Chen, *Synthetic Metals*, **28**, D613 (1989).
8. M. Schott and G. Wegner, *Nonlinear Optical Properties of Organic Molecules and Crystals*, ed. D.S. Chemla and J. Zyss, Academic Press, 1987, Vol. 2, pp. 3–49.
9. R.J. Hood, H. Müller, C.J. Eckhardt, R.R. Chance, and K.C. Yee, *Chem. Phys. Lett.* **54**, 295 (1978).
10. L. Sebastian and G. Weiser, *Chem. Phys.* **62**, 447 (1981).
11. K. Lochner, H. Bässler, L. Sebastian, G. Weiser, G. Wegner, and V. Enkelmann, *Chem. Phys. Lett.*, **78**, 366 (1981).
12. M.E. Morrow, K.M. White, C.J. Eckhardt, and D.J. Sandman, *Chem. Phys. Lett.*, **140**, 263 (1987).
13. H. Eckhardt, C.J. Eckhardt, and K.C. Yee, *J. Chem. Phys.* **70**, 5498 (1979).
14. D.J. Sandman, K. Mislow, W.P. Giddings, J. Dirlam, and G.C. Hanson, *J. Am. Chem. Soc.* **90**, 4877 (1968).
15. D.J. Sandman and K. Mislow, *J. Am. Chem. Soc.*, **91**, 645 (1969).
16. A. Moscowitz, *Proc. Roy. Soc., Ser. A*, **297**, 16, 40 (1967).
17. D.J. Sandman and G.P. Ceasar, *Israel J. Chem.*, **27**, 293 (1986).
18. I. Morishima, K. Yoshikawa, T. Yonezawa, and H. Matsumoto, *Chem. Phys. Lett.*, **16**, 336 (1972).
19. W. Sümmerrmann and U. Deffner, *Tetrahedron*, **31**, 593 (1975).
20. Y.V. Korshak, A.A. Ovchinnikov, A.M. Shapiro, T.V. Medvedeva, and V.N. Spektor, *JETP Lett.*, **43**, 399 (1986).
21. Y.V. Korshak, T.V. Medvedeva, A.A. Ovchinnikov, and V.N. Spektor, *Nature*, **326**, 370 (1987).
22. D.J. Sandman, B.S. Elman, G.P. Hamill, C.S. Velazquez, and L.A. Samuelson, *Mol. Cryst. Liq. Cryst.*, **134**, 89 (1986).



23. A.A. Ovchinnikov and V.N. Spektor, *Synthetic Metals*, 27, B615 (1988).
24. Y. Cao, P. Wang, Z. Hu, S. Li, L. Zhang, and J. Zhao, *Solid State Commun.*, 68, 817 (1988).
25. Y. Cao, P. Wang, Z. Hu, S. Li, L. Zhang, and J. Zhao, *Synthetic Metals*, 27, B625 (1988).
26. J.S. Miller, D.T. Glatzhofer, J.C. Calabrese, and A.J. Epstein, *J. Chem. Soc., Chem. Commun.*, 322 (1988).
27. E.G. Rozantsev and V.D. Sholle, *Synthesis*, 401 (1971).
28. X. Solans, S. Gali, C. Miravittles, and M. Font-Altaba, *Acta Crystallogr.*, B34, 2331 (1978).
29. M. Cygler, *Acta Crystallogr.*, B35, 195 (1979).
30. R.P. Shibaeva and L.P. Rozenberg, *J. Struct. Chem.*, 15, 845 (1974).
31. L.D. Arutyunyan and R.P. Shibaeva, *Dokl. Akad. Navk SSSR*, 215, 881 (1974).
32. V. Barone, P.L. Cristinziano, F. Leij, and A. Pastore, *J. Molecular Structure*, 90, 59 (1982).
33. E.G. Rozantsev, *Theoretical and Experimental Chem.*, 2, 316 (1966).
34. A.S. Hay, *J. Org. Chem.*, 27, 3320 (1962).
35. W.B. Lutz, S. Lazarus, and R.I. Meltzer, *J. Org. Chem.*, 27, 1695 (1962).
36. G.P. Hamill, E.A. Yost, and D.J. Sandman, to be published.
37. D.J. Sandman, *J. Crystal Growth*, 82, 111 (1988).
38. V.V. Pavlikov, V.V. Muravev, A.B. Shapiro, S.Z. Taitis, and E.G. Rozantsev, *Izv. Akud. Navk SSSR, Ser. Khim.*, 1200 (1980).

## INVESTIGATIONS OF A NEW REVERSIBLE STRAIN INDUCED CHROMIC TRANSITION IN POLYDIACETYLENE ELASTOMERS

R. A. Nallicheri and M. F. Rubner\*

Department of Materials Science and Engineering, Massachusetts Institute of Technology, Cambridge, Massachusetts 02139, USA

### ABSTRACT

In-situ visible dichroism/tensile elongation studies of segmented polyurethanes containing conjugated polydiacetylene chains within their hard segment domains have revealed a new reversible mechanochromic transition that manifests itself as a color change from blue to yellow during tensile elongation. This unusual strain induced transition, found in an elastomer whose hard segment structure is derived from hexamethylene diisocyanate and 5,7-dodecadiyne-1,12 diol, closely resembles the thermochromic transition also exhibited by this same material. The color change and the associated shift in the position of the polydiacetylene absorption band to higher energies is not simply an order-disorder transition but reflects a strain induced reorganization of the hard domain structure. It has been found that this blue to yellow transition is reversible as long as the material is not strained beyond about 300%. This represents the first reversible, mechanically induced chromic transition in a cross-polymerized diacetylene containing polymer.

### INTRODUCTION

The optical properties of polydiacetylenes are known to be very sensitive to the molecular environment of their conjugated polymer backbones. Variations in backbone planarity and/or the level of stress experienced by the backbone can result in significant changes in the energy, shape and breadth of the absorption bands characteristic of these materials [1]. Thus, the electronic states of the conjugated backbone are strongly coupled to its conformation. As a result of this strong coupling, the polydiacetylenes exhibit a wide variety of chromic transitions that can be induced by temperature, stress or solvent changes.

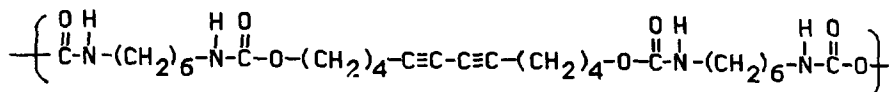
In this paper, we discuss a new reversible strain induced chromic transition observed during the tensile elongation of a polyurethane-diacetylene segmented copolymer. In such materials, the fully extended polydiacetylene chains reside exclusively in phase separated hard domains dispersed throughout a soft elastomeric matrix. Consequently, any changes in the electronic states of the conjugated backbone are a direct result of changes in the molecular organization of the hard domains. Previous work has demonstrated that these materials exhibit thermochromic behavior [2] and that their mechanical properties can be controlled systematically by varying the level of diacetylene cross-polymerization within the hard domains [3]. These new elastomers therefore exhibit an unusual collection of mechanical and optical properties that can be directly traced to their two phase microstructures.

### EXPERIMENTAL

Details concerning the synthesis, structure and characterization of the polyurethane diacetylene segmented copolymers can be found in our previous publications [2-4]. The elastomers are designated by the monomers used to synthesize them. For example HDI-5,7-2000 refers to an elastomer synthesized from HDI (hexamethylene diisocyanate), 5,7-dodecadiyne-1,12-diol and poly(tetramethylene oxide) PTMO of molecular weight 2000. Figure 1 displays the hard and soft segment structures (which alternate along the polymer chain) of the

HDI-5,7 based segmented copolymers as well as an illustration of diacetylene polymerization within the hard domains. Samples for mechanical and optical testing were prepared by a static solvent casting technique in which a 75% toluene and 25% THF solution containing the elastomer was allowed to slowly evaporate in a confined chamber (typically two days) under a flow of nitrogen. The casting solvent greatly influences the morphology of polyurethanes and hence the same casting solvent composition was consistently used for a particular elastomer. All samples were annealed at 90°C for 45 minutes to improve ordering. The diacetylene groups of the HDI-5,7-2000 samples were partially polymerized by exposure to 0.08 Mrads of electron beam radiation generated from a Van de Graff electron accelerator operated at 2.6 MeV. A comparison of the stress-strain curves of the irradiated materials with those of the as-prepared elastomers revealed no differences thereby confirming a low level of diacetylene cross-polymerization.

#### hard segment structure



#### soft segment structure

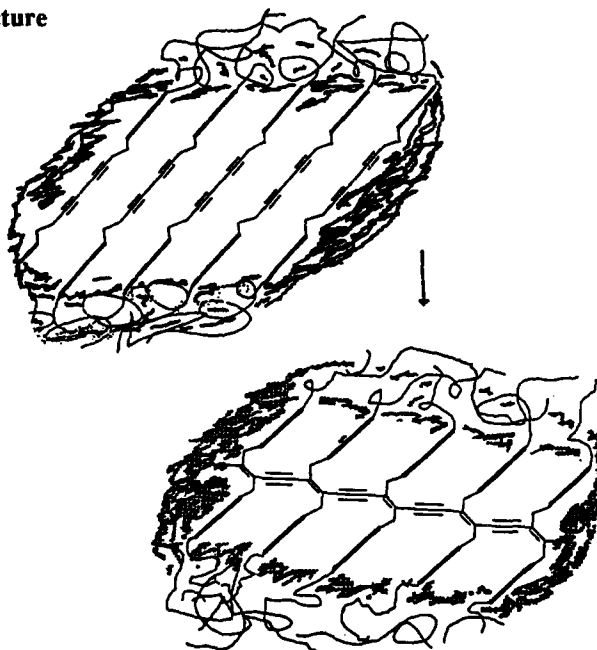
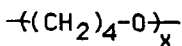


Figure 1. Hard and soft segment structures of the HDI-5,7 based segmented copolymers. Illustration shows diacetylene polymerization within a phase separated hard domain.

Tensile testing was done at room temperature on an Instron model 1122, using elastomeric or pneumatic grips to prevent slippage of the samples. Visible Absorption Spectroscopy was performed with an Oriel Instaspec System 250 multi-channel analyzer. This instrument, which

is capable of measuring a complete visible spectrum in 41 milliseconds, was programmed to take spectra continuously at specified time intervals. Visible spectroscopy and tensile testing were performed simultaneously to study the changes in the absorption spectra as a function of strain. To accomplish this a halogen lamp was placed behind the sample which was mounted in the Instron. A liquid light guide positioned in front of the sample was used to collect and transmit the signal to the multichannel analyzer. When polarized light was required, a polarizer was placed between the lamp and the sample. The absorption spectra were measured in the stretched state and after relaxation to zero stress with light polarized parallel (PP) and perpendicular (NP) to the stretch direction. Hence for each strain level there are four spectra - two in the stretched state (with PP light and with NP light) and two in the relaxed state. When examining the absorption spectra of these elastomers as a function of strain it should be borne in mind that a part of the decrease in intensity is a result of a decrease in the sample thickness which accompanies the elongation of the sample. Dichroic ratios were calculated by taking the ratio of the area under the absorption curve due to light polarized parallel to the stretch direction, to the area under the absorption curve due to light polarized perpendicular to the stretch direction. The region between 425 and 700 nm was considered. A limitation of using this wavelength range is that at high strain levels, a significant portion of the polymer spectrum shifts outside of the range of detection of the spectrophotometer, and thus its contribution to the area (both horizontal and vertical spectra) is not reflected in the data. Thus, high strain values of the dichroic ratio are best used for comparison purposes.

## RESULTS AND DISCUSSION

Figure 2 shows the visible spectra of HDI-5,7-2000 recorded with vertically polarized light (parallel to stretch direction) as a function of increasing strain levels. The spectra recorded with horizontally polarized light (normal to stretch direction) at similar strain levels are also presented in Figure 2. The absorption spectrum in the unstretched state exhibits an excitonic peak at 620 nm followed by a large, broad absorption band centered at about 570 nm. The breadth of this latter band indicates that the polydiacetylene backbones experience a variety of different molecular environments within the hard domains thus giving rise to a distribution of excitation energies.

As the elastomer is stretched, the absorption band observed in vertically polarized light shifts dramatically to higher energies and decreases in intensity. During this process, the material changes from a blue color to a yellow color. Specifically, it can be seen that the original excitonic peak moves to higher energies and is gradually eliminated while a new higher energy absorption band centered initially at about 500 nm (at 55 % strain) begins to grow in intensity, broaden and also shift to higher energies. The emergence of a new absorption band suggests that the color change is a result of a strain induced phase transition within the hard domains. The shifting of each absorption band to higher energies with increasing strain level is a direct result of the stress that is transmitted to the hard domains during tensile elongation.

In sharp contrast, the absorption band revealed by horizontally polarized light rapidly decreases in intensity with increasing strain and only shifts to higher energies at very large strains. The very weak intensity of this latter band at high strains relative to the intensity of the absorption band observed with vertically polarized light indicates that the fully extended polydiacetylene chains are preferentially orienting into the stretch direction. Thus, during stretching, the hard domains containing the polydiacetylene chains undergo a mechanically induced phase transition and become oriented with their long axes pointing into the stretch direction. Since the hard segments are perpendicular to the long axis of the hard domains, it appears that the hard segments become oriented transverse to the stretch direction during this process. The polydiacetylene chains that do not initially orient into the stretch direction apparently do not experience high stress levels as indicated by the initial insensitivity of the energy of the excitonic peak observed with horizontally polarized light to strain level.

Figure 3 contains the spectra recorded in the relaxed, unstrained state after stretching the polymer to the indicated strain levels. These spectra provide information on the reversibility of the mechanochromic transition and the level of residual orientation remaining in the film. Focusing on the spectra generated with vertically polarized light, it can be seen that the strain

induced optical transition is essentially reversible up to strains of about 300%. In fact, the original absorption band recovered after relaxation from the stretched state has shifted to slightly lower energies and exhibits a less intense higher energy peak. This would suggest that stretching to low strains (< 300%) actually improves the ordering of the polydiacetylene chains within the hard domains. Relaxation from higher strains, on the other hand, reveals the co-existence of two well defined phases; a blue phase centered at 624 nm and a yellow phase centered around 510 nm. As the strain level increases, the yellow phase grows at the expense of the blue phase. Note, however, that even after stretching to strains as high as 635%, where the blue phase is essentially nonexistent, relaxation to the unstrained state leads to the re-establishment of small but significant amount of this phase. Similar trends were observed with horizontally polarized light as indicated in Figure 3.

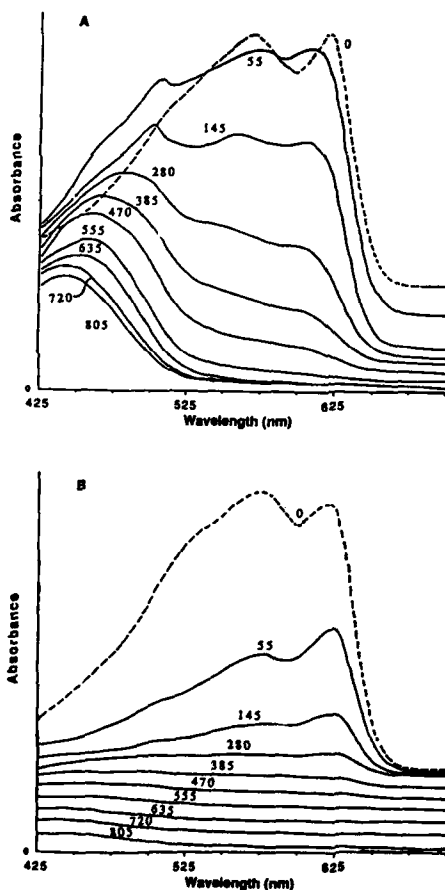


Figure 2. Visible absorption spectra of HDI-5,7-2000 recorded as a function of strain with vertically polarized light (A) and horizontally polarized light (B). Numbers indicate strain levels (spectra have been arbitrarily offset along the absorption axis for clarity).

From these data, it is possible to calculate a dichroic ratio which gives an indication of the level of polydiacetylene orientation developed during and after stretching. The dichroic ratio of HDI-5,7-2000 in the stretched state reaches a maximum value of about 5.7 at 300% strain,

implying that the system develops its highest state of polydiacetylene chain alignment in this strain region. Beyond 300% strain there is a decrease in the dichroic ratio which can be attributed to a stress induced disruption of the hard domains. The level of residual orientation remaining after relaxation from the stretched state was found to increase slowly with increasing strain level but remain relatively small; the dichroic ratio was about 1.5 after stretching to 300% strain where maximum orientation in the stretched state was observed. Thus, once released from the stretched state, the polydiacetylene chains, or more specifically the hard domains that they are contained in, quickly relax to a near isotropic state.

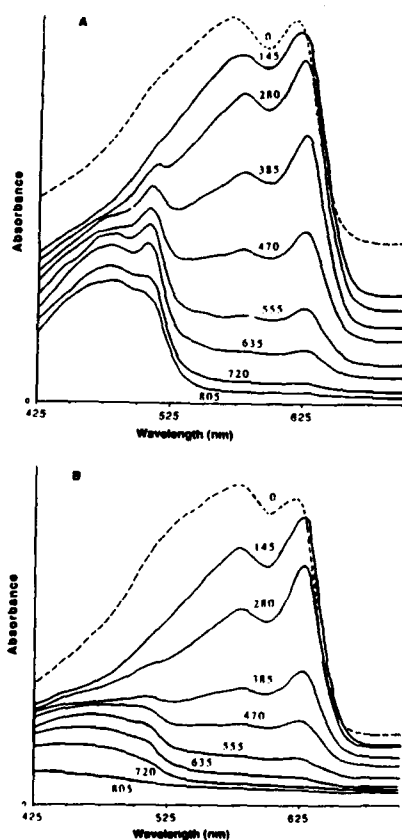


Figure 3. Visible absorption spectra of HDI-5,7-2000 recorded in the relaxed state as a function of strain with vertically polarized light (A) and horizontally polarized light (B). Numbers indicate strain levels before relaxation (spectra have been arbitrarily offset along the absorption axis for clarity).

The mechanically induced optical transition of this segmented copolymer is very similar to the thermochromic transition exhibited by all of the HDI-5,7-based elastomers [2]. Typically, these materials change in color from blue to yellow at temperatures greater than 90°C. The spectral changes associated with the thermochromic transition also involve the elimination of the original blue phase absorption band and the development of a new yellow phase absorption with a peak at 510 nm. In this latter case, however, the absorption band of the yellow phase (at

room temperature) is unusually narrow and exhibits well defined vibronic sidebands. Clearly, the mechanically induced transition is also accompanied by disordering at high strain levels.

The thermochromic transition of these materials has been attributed to a conformational rearrangement of the methylene groups attached to the polydiacetylene backbone which takes place without changes in the hydrogen bonding of the side chains [2,5]. Given the similarities in optical properties, it is reasonable to conclude that mechanical stress induces the same kind of hard domain molecular reorganization as the thermal process. A clue to the types of conformational changes induced by either heat or stress in the polydiacetylene-elastomers is provided by recent NMR studies [6] of the thermochromic transition of poly(ETCD). This particular polydiacetylene has a sidegroup structure very similar to the HDI-5,7-based elastomers (there are four methylene groups between the polydiacetylene backbone and the urethane group). In this case, the thermochromic transition has been shown to involve a gauche to trans conformational transition of the methylene groups in the poly(ETCD) sidegroups.

## CONCLUSION

Visible spectra recorded during the tensile elongation of a segmented polyurethane containing polydiacetylene chains within its hard domains have revealed a new mechanically induced phase transition that is responsible for the blue-to-yellow color change observed during stretching. This mechanochromic transition is nearly reversible as long as the strain on the elastomer does not exceed 300%. The mechanically induced phase transition is very similar to the thermally induced phase transition exhibited by this material suggesting a common molecular origin. Thus, either thermal or mechanical energy can be used to drive the molecular reorganization within the hard domains that is responsible for changes in the electronic states of the polydiacetylene conjugated backbones.

## Acknowledgements

This work was supported in part by the Office of Naval Research and the Naval Air Development Center. The authors are grateful to Dr. K. Wright of the High Voltage Research Laboratory at MIT for irradiation of the samples used in this study.

## REFERENCES

1. See for example, D. Bloor and C. L. Hubble, *Chem. Phys. Lett.* **56**, 89 (1978).
2. M. F. Rubner, *Macromolecules* **19**, 2129 (1986).
3. R. A. Nallicheri and M.F. Rubner, *Macromolecules*, in press.
4. M.F. Rubner, *Macromolecules* **19**, 2114 (1986).
5. M. F. Rubner, C. Velazquez, D. J. Sandman, *Macromolecules* **20**, 1296 (1987).
6. H. Tanaka, M. A. Gomez, A. E. Tonelli, M. Thakur, *Macromolecules* **22**, 1208 (1989).

**SYNTHESIS AND PROPERTIES OF A FULLY CONJUGATED  
POLYDIACETYLENE : POLY(1,4-BIS (3-QUINOLYL)-1,3-BUTADIYNE).**

SATYA S. TALWAR, MANJUNATH B. KAMATH AND K. N. BABU  
Department of Chemistry, Indian Institute of Technology, Powai, Bombay, India 400 076.

**ABSTRACT**

Synthesis of a new fully conjugated polydiacetylene i.e. poly(1,4-bis(3-quinoly)-1,3-butadiyne) is described. Reflectance spectra of partially polymerised samples and the polymer are reported. The spectra show long wavelength absorption band at 750 nm. with the visible absorption edge above 800 nm. DC electrical conductivity measurements on pristine and Iodine doped Poly-DQ are reported. The results are discussed in terms of side group - backbone electronic interactions.

**INTRODUCTION**

Synthesis of new polydiacetylenes(PDAs) and study of their properties continue to be an active area of investigation[1]. Much of the recent interest in polydiacetylenes is related to their linear, nonlinear optical properties[2] and conductivity behaviour[3]. Polydiacetylenes exhibit one of the highest third order nonlinear coefficient and a fast response, which has potential applications in electro-optics and all optical communication system[4].

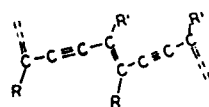


FIG. 1 PDA CHAIN

Polydiacetylenes have a highly conjugated backbone consisting of an alternate sequence of single, double and triple bonds (Fig.1). Although electronic properties of these polymers are primarily dominated by the  $\pi$ -conjugated backbone, the substituent pendant groups (R and R') markedly influence the electronic, optical and other physical properties of polydiacetylenes.

Polydiacetylenes are one dimensional semiconductors and their optical spectra are characterised by a sharp excitonic peak followed by an interband transition[3]. However the position of these spectral features is sensitive to the crystalline phase organisation of the substituent groups. An understanding of the nature and origin of these changes is relevant to design of suitable nonlinear optical materials[5].

Two kinds of substituent effects on the electronic and optical properties may be distinguished. Property changes may arise due to modifications in the geometry and planarity of the conjugated backbone induced by the crystalline phase organisation of the side group. Another kind of interaction becomes possible when the substituent group is in formal  $\pi$ -conjugation with the backbone. Such substituents could affect the spectral and electronic conduction properties through  $\pi$ -electronic interaction of the substituent group and the backbone[6].

Relatively few polydiacetylenes with substituent groups in formal  $\pi$ -conjugation with backbone have been reported. This has been partly due to lack of solid state reactivity in many precursor diacetylenes(DAs)[7,8]. Recently there has been considerable interest in synthesis and polymerisation of diacetylenes with  $\pi$ -conjugating groups. Some success in synthesis of such PDAs' and study of their properties have been reported[1,6,9,10].  $\pi$ -conjugating substituent



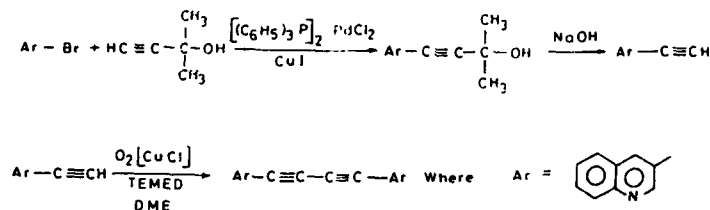
may have the following effects on the properties of PDA due to electronic coupling :

- \* PDA electronic spectra and electronic structure may be perturbed.
- \* Extended  $\pi$ -conjugation per repeat unit may cause enhanced polarisability and enhanced nonlinear optical response.
- \* Electrical conduction may be altered since the doping of substituent group may get transmitted to backbone.

The extent of substituent-backbone electronic interaction depends on the orientation of the  $\pi$ -system of the conjugating group with respect to planar backbone. Recent reports suggest varying degrees of conjugation[*vide infra*]. We have been involved in the synthesis of DAs' and PDAs' with  $\pi$ -conjugating substituents and study of properties of such PDAs'[11]. In this study, we report the synthesis of the title compound, its optical spectra and electrical conduction behaviour.

### EXPERIMENTAL METHODOLOGY

The diacetylene 1,4-bis(3-quinolyl)-1,3-butadiyne (DQ) was synthesised as in Scheme 1. Details of the synthesis will be published elsewhere. The extent of polymerisation was determined by gravimetric method by extracting out the monomer with methylene chloride. Reflection spectra of polymerised polycrystalline samples were recorded on Shimadzu UV 260 UV-visible spectrophotometer with diffuse reflectance accessory. Raman spectra of solid samples were recorded on JobinYvon Ramnor HG2S using Argon Laser excitation frequency at 4880 Å. Conductivity measurements were done on polycrystalline pellets using two probe method.



SCHEME.1 SYNTHETIC ROUTE FOR HETEROARYL DIACETYLENES.

### RESULTS AND DISCUSSION

DQ crystallises as long needles which pick up slight blue colour on exposure to ambient light and temperature conditions. Single crystal X-ray study[12] showed that planar DA molecules pack in stacks along 'a' axis with a repeat distance of 4.807 Å and an inclination of 47.5° as shown in Fig.2. DQ undergoes polymerisation on heating and on exposure to UV-visible and actinic radiation to form a deep blue polydiacetylene. The thermal polymerisation behaviour is summarised in Fig.3. Thermal polymerisation exhibits an induction period but no such induction period was observed in photochemical and  $\gamma$ -radiation polymerisation. It is noteworthy that despite suitable molecular packing parameters, a maximum of 25% polymer conversion was obtained in all the three modes of polymerisation. The PDA could be obtained by extracting out the monomer from a partially polymerised sample with methylene chloride. The extracted

polymer is a highly reflecting copper colored mass of very fine needles. XRD measurements indicated high degree of crystallinity. PDA crystals were too thin for single crystal X-ray structure determination.

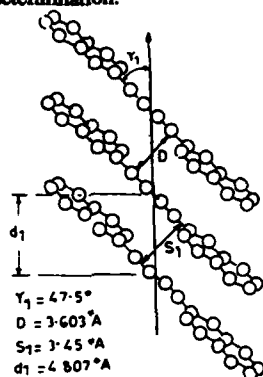


FIG. 2. STACKING ARRANGEMENT OF DQ ALONG A-AXIS

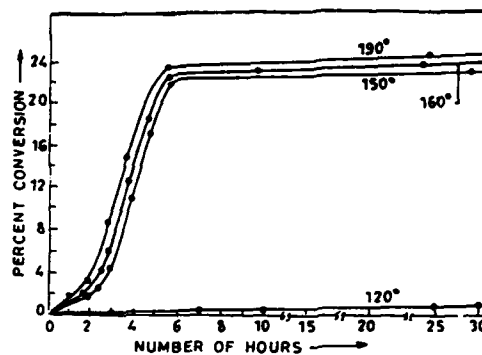


FIG. 3. PLOTS OF POLYMER CONVERSION WITH ANNEALATION TIME OF DQ.

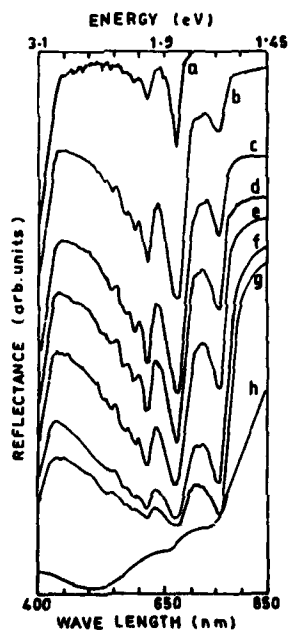


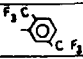
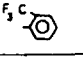
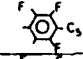
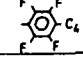

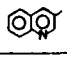
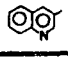
FIG. 4. REFLECTANCE SPECTRA OF PARTIALLY POLYMERISED (THERMAL,  $160^\circ\text{C}$ ) SAMPLES OF DQ (a-g: 0, 1, 2, 5, 1, 4, 7, HR) AND MONOMER FREE POLY DQ (h)

The reflection spectra of partially polymerised (thermal) diacetylene and monomer free PDA are shown in Fig. 4. In the initial stages of polymerisation a long wavelength band at 670 nm was observed and as the polymerisation progressed, a longer wavelength band at ca. 750 nm gained in intensity. The reflection spectra of the monomer free polymer shows long wavelength absorption at ca. 750 nm with the absorption edge above 800 nm. The changes in reflection spectra with polymerisation suggest two phases of PDA. This point needs further exploration. Poly DQ shows the longest wavelength optical transition of all known PDAs reported. Recent optical spectral data on aryl substituted polydiacetylenes is summarised in Table 1. The origin of this large red shift in poly DQ is of considerable interest. Structure spectra relationship and specially the 'blue-red' thermochromic changes has been the subject of several recent investigations and comment [13]. These changes have been understood in terms of the polarisability of side groups and the mechanical stress of the side group structural organisation on the backbone-geometry and conformation. We feel that red shift in poly-DQ is too large to be accounted by the above environmental facts alone and it is a consequence of conjugative interaction of the quinolyl groups with the backbone causing an extension of the backbone conjugation. Laser raman spectra of poly DQ recorded with 480.0 nm excitation showed only a single peak at  $2190 \text{ cm}^{-1}$  for the triple bond stretching frequency. This is the highest value of  $\gamma_{\text{C}\equiv\text{C}}$

reported for polydiacetylenes [14]. Band gap calculations of unsubstituted and phenyl substituted PDAs showed a reduction of the band gap in substituted PDAs and the gap was found to reduce with planar orientation of the side group with respect to the backbone[6]. Probably similar situation prevails in poly DQ.

A closer study of the data in Table 1 also suggests that a more extended  $\pi$ -conjugating substituent, like the quinolyl or the cabozolyl tend to orient better of conjugation than a phenyl substituent. A comparison of the spectral data for CPDO, QPDO and that for Poly-DQ suggests that a 'linear' orientation (as in 2 or 3 Quinolyl-) of the aryl substituent is more suitable for  $\pi$ -conjugation than a 'cross-linked' aryl group as in CPDO. These considerations are important in molecular and crystal engineering of DA and PDA.

TABLE I  
OPTICAL SPECTRA OF SOME POLYDIACETYLENES

SUBSTITUENTS R	R'	ABREVA- -TION	$\lambda_{\text{max}}^a$ (nm) (ev)	ABS. EDGE(nm) (ev)	$\phi^b$ ORIENTATION OF AROMATIC RING
$(\text{CH}_2)_4\text{OCONHC}_6\text{H}_5$	R	TDCU-A (BLUE)	646 <sup>c</sup> (192)	697 (178)	-
		TDCU B (RED)	544 <sup>c</sup> (228)	620 (20)	-
$\text{CH}_2\text{OSO}_2\text{C}_6\text{H}_4\text{CH}_3$	R	PTS	614 <sup>c</sup> (202)	713 (174)	-
	R	DF MDP	574 <sup>c</sup> (216)	670 (185)	66.8 <sup>c</sup>
	R	-	579 <sup>c</sup> (214)	659 (188)	-
	R	-	590 <sup>c</sup> (210)	653 (190)	-
	R	BTFP	620 <sup>c</sup> (200)	697 (178)	58.6 <sup>c</sup>
	$\text{CH}_2\text{OH}$	CPDO	674 <sup>d</sup> (184)	800 (155)	-
	$\text{CH}_2\text{OH}$	QPDO	700 <sup>e</sup> (177)	850 (145)	-
	R	POLY DQ	756 <sup>e</sup> (164)	832 (149)	-

FOOT NOTES a) Longest wavelength maxima.

b) Angle between zig-zag backbone plane and phenyl ring plane.

c) From ref.9 d) From ref. 6 e) Present work

DC conductivity measurements of the polycrystalline Poly-DQ pellets showed it to be an intrinsic insulator. Doping with  $I_2$  showed high iodine uptake and enhanced conductivity, the maximum conductivity observed was  $1.8 \times 10^{-7}$  S/cm. Temperature dependence measurements of doped samples indicate it to be a semiconductor with a band gap of 0.66 eV (Fig.5). Typical conductivities for iodine doped polydiacetylene films with non-conjugated side groups are in the range  $10^{-9}$ [16]. Polydiacetylenes with conjugated side groups have been reported to show both enhanced  $I_2$  doping and enhanced conductivities. Thus  $I_2$  doped poly 1,4-bis(3-acetamidophenyl)-1,3-butadiene (m-AAPB) films showed a maximum conductivity of  $4.8 \times 10^{-2}$  S/cm. Maximum conductivity for the iodine doped pellet for m-AAPB was  $1.1 \times 10^{-4}$  S/cm. The role of aryl side groups in enhancing conductivity needs further exploration.

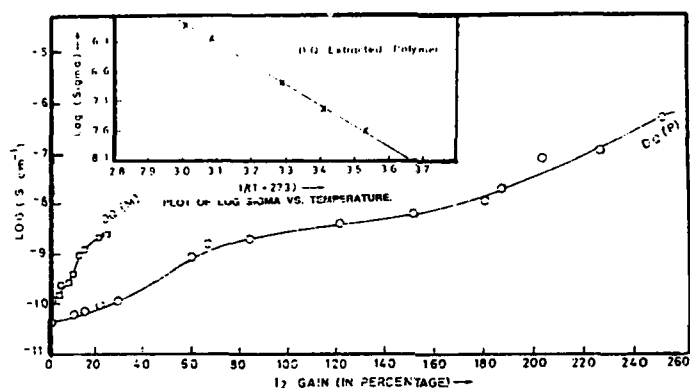


FIG. 5 VARIATION IN CONDUCTIVITY OF DQ (MONOMER), DQ (POLYMER) WITH IODINE INTAKE.

In conclusion we have reported the synthesis of a polydiacetylene with  $\pi$ -conjugating substituents which are oriented in a manner causing enhanced conjugation as indicated by the optical spectra. This polydiacetylene shows longest wavelength absorption of all the polydiacetylenes reported so far. Poly DQ is crystalline, can be doped to high dopant levels and doping leads to enhanced conductivity. The nature of electronic perturbation caused by a large aromatic side groups need to be explored further. Interchain interactions may become important in the class of polydiacetylenes with formally conjugated aryl groups as the substituent aromatic planar ring and the zig-zag backbone may lie in the same plane.

#### ACKNOWLEDGEMENTS

This work was partially supported by a grant from Board of Nuclear Studies of the Department of Atomic Energy, Government of India. Valuable discussions and help in preparation of this manuscript of A. Sarkar and P. Sekher is gratefully acknowledged.

## REFERENCES

1. H. Matsuda, H. Nakanishi, T. Hosomi and M. Kato, *Macromolecules* **21**, 1238 (1988).
2. G. M. Carter, Y. J. Chen, M. F. Rubner, D. J. Sandman, M. K. Thakur and S. K. Tripathy in *Nonlinear Optical Properties of Organic Molecules and Crystals*, vol. 2, edited by D. S. Chemla and J. Zyss (Academic Press, New York, 1987), p. 85.
3. D. Bloor, *Phil. Trans. R. Soc. Lond.* **A314**, 51 (1985).
4. A. F. Garito, C. C. Teng, K. Y. Wong and O. Zammani 'Khamiri, *Mol. Cryst. Liq. Cryst.* **106**, 219 (1984).
5. D. J. Sandman and Y. J. Chen, *Polymer* **30**, 1027 (1989).
6. S. B. Clough, S. Kumar, X. F. Sun, S. Tripathy, H. Matsuda, H. Nakanishi, S. Okada and M. Kato, *Chem. Abst.* No.135131 Z, 111, (1989).
7. S. Talwar, M. Kamath, Kalyan Das and U. Sinha, *Polymer Commun.*(in press).
8. G. Wegner, *J. Polym. Sci., Part B* **9**, 133 (1971); Y. Ozcayir, J. Asrar and A. Blumstein, *Mol. Cryst. Liq. Cryst.* **110**, 1424 (1984); J. Tsibouklis, A. R. Wernick, A. J. Shand and G. H. W. Millburn, *Chemtronics* **3**, 211 (1988); G. H. W. Millburn, A. R. Wernick, J. Tsibouklis, E. Bolton, G. Thomas and A. J. Shand, *Polymer* **30**, 2115 (1989); J. J. Meyerle and M. A. Flandro, *Acta Crystallogr., Sect. B : Struct. Crystallogr. Crystl. Chem.* **34**, 1374 (1978).
9. Y. Tokura, T. Koda, A. Itsubo, M. Miyabayashi, K. Okuhara and A. Ueda, *J. Chem. Phys.* **85**, 99 (1986).
10. H. Matsuda, H. Nakanishi, S. Kato and M. Kato, *J. Polym. Sci. Polym. Chem.* **25**, 1663 (1987).
11. P. K. Khandelwal and S. S. Talwar, *J. Polym. Sci. Polym. Chem. Ed.* **21**, 3073 (1983); M. B. Kamath, Ph.D Dissertation, I.I.T., Bombay (1989).
12. Kalyan Das, U. C. Sinha, M. B. Kamath and S. S. Talwar, *Acta Crystallogr., C* (in press).
13. Reference 5 and references therein.
14. D. N. Batchelder and D. Bloor in *Advances in Infrared and Raman Spectroscopy*, Vol. II, edited by R. J. H. Clark and R. E. Hester (Wiley Heyden, New York, 1984) p. 133.
15. K. N. Babu and S. S. Talwar (unpublished work).
16. K. Se, H. Ohnuma and T. Kotako, *Macromolecules* **17**, 2126(1984).

## ORGANIC POLYMER SEMICONDUCTOR SUPERLATTICES

Samson A. Jenekhe<sup>1</sup> and Wen-Chang Chen  
 Department of Chemical Engineering, University of Rochester  
 Rochester, New York 14627

Abstract

We describe the synthesis and study of the first organic polymer semiconductor superlattices designed as periodic block conjugated copolymers,  $(-A_xB_y-)_m$ . The observed variation of electronic spectra and wavelength of the lowest energy absorption maxima with block length  $y$  are interpreted in terms of quantum confinement size effects predicted for semiconductor superlattices. The periodic block conjugated copolymers were synthesized by a two-step strategy that ensure strict control of sequence, block length and periodicity. It is suggested that organic semiconductor superlattices provide a rational and systematic approach to the molecular engineering of electronic, optical, nonlinear optical, and electro-optical properties in polymeric materials and hold promise for molecular electronics and molecular photonics.

Introduction

Our interest in the "molecular engineering" of polymeric materials with specified or novel electronic, linear optical, nonlinear optical, and electro-optical properties [2-9] recently led to the concept of organic semiconductor superlattices [2-4,6]. A semiconductor superlattice is a periodic structure [10-17],  $(-A_xB_y-)_m$ , consisting of alternating layers ( $x$  and  $y$ ) of two semiconductors with unit cells A and B and different bandgaps  $E_g^A$  and  $E_g^B$  ( $E_g^A > E_g^B$ , say). In such a periodic structure, the small gap semiconductor (B) forms a series of square potential wells and the large gap semiconductor (A) forms a series of potential barriers in the direction of the periodicity. The height of the potential wells formed depend primarily on the magnitude of the gap difference,  $\Delta E_g = E_g^A - E_g^B$ . In a superlattice (SL) structure the barrier thickness ( $d_A$ ) is small enough for charge carriers in adjacent wells of width ( $d_B$ ) to interact; otherwise, the periodic structure is a multiple quantum well (QW). Superlattices and quantum well structures have been widely studied in inorganic semiconductors where the barrier thickness, well width, and number of layers ( $m$ ) of the repeating unit cell of the periodic structure can be precisely controlled by thin film deposition processes, such as molecular beam epitaxy (MBE) or metal-organic chemical vapor deposition (MOCVD) [11-17].

The possible experimental approaches to organic semiconductor superlattices might include Langmuir-Blodgett (LB) and vapor phase thin film deposition processes. However, although these two techniques are conceptually analogous to the MBE and MOCVD processes, they do not appear adequate for preparing true semiconductor superlattices without the prior design of the SL and QW structures into the macromolecular chains. Since polymers are periodic structures by nature, the required SL or QW structure,  $(-A_xB_y-)_m$ , is thus a multiblock conjugated copolymer containing sufficiently long blocks ( $x > 1$  and  $y > 1$ ) of repeating unit cells A and B of the conjugated homopolymers  $(-A-)_m$

and  $(-B-)_m$ , with energy gaps  $E_g^A$  and  $E_g^B$ . Some examples of the proposed organic polymer semiconductor superlattices are shown in Figure 1. All the homopolymers of A and B of Figure 1 are well known conjugated polymers, with bandgaps of the order 1-3 eV,

except perhaps the polyalkyne,  $(-C\equiv C-)_m$ . The alternating conjugated copolymers,  $(-AB-)_m$  ( $x=y=1$ ), in Figure 1 are also known except those involving benzo[c]thiophene. Although block copolymerization and block copolymers constitute a well developed field of

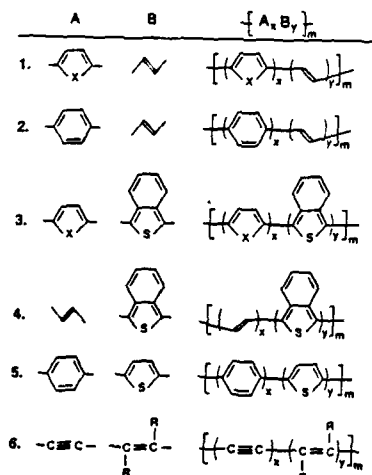


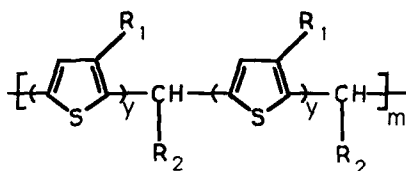
Figure 1. Some proposed organic Semiconductor Superlattices.

polymer science[18,19], experimental synthesis of the periodic block conjugated copolymers will require novel copolymerization or synthetic techniques that will allow strict sequence and block length control. The related random block conjugated copolymers,  $(-A-)_m (-B-)_m$ , which can be more readily synthesized by conventional methods are not strictly superlattices but are also of interest to investigate the effect of disorder on electronic localization/delocalization phenomena[20-21].

The block copolymer structures in Figure 1 have a sufficient  $\Delta E_g$  to permit formation of semiconductor quantum wells and superlattices along the chain direction as the copolymer block lengths, particularly the block length of the small bandgap moiety, increases. One of the important properties of semiconductor superlattices and quantum wells is the phenomena of quantum size effects on electronic and optical properties [11, 14, 16, 17]. The phenomena arise from the spatial confinement of charge carriers in semiconductor structures of small size. Among the predicted quantum size effects in semiconductor superlattices that one can expect to also hold in these proposed organic semiconductor superlattices include: (1) the effective superlattice bandgap  $E_g^s$  ( $E_g^A > E_g^B \geq E_g^B$ ) will decrease as the well width ( $d_B$  or  $y$ ) increases or alternatively, the  $\lambda_{max}$  of the lowest energy absorption band will increase with increasing  $y$ ; (2) there will be new structure in the electronic absorption spectrum due to excitonic excitations or discrete quantum states in the valence and conduction bands.

Here we explore the possibility of synthesizing semiconductor superlattices and quantum wells in organic polymers and observing the associated quantum size effects. In particular, we consider the block conjugated copolymers  $(-A_y B_x-)_m$ , i.e.  $x=y$ , where A is an aromatic thiophene ring and B is its quinoid isomer. In this case  $(-A-)_m$  is poly(2,5-thiophene)(PT) with  $E_g^A$  of 2.1 eV and  $(-B-)_m$  is the quinoid isomer of PT which

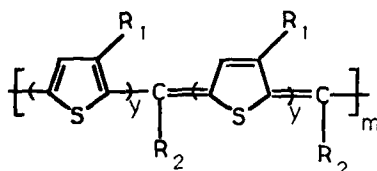
has a calculated  $[22]E_g^B$  of  $\sim 0.5$  eV. We use a two-step synthetic approach [2-4,6] involving nonconjugated precursor polymers that are subsequently converted to the block conjugated copolymers. This synthetic strategy ensures the necessary strict sequence and block length control and periodicity in the final block conjugated copolymer structures. The actual structures are shown below.



1A  $y=1$ ,  $R_1 = \text{CH}_3$ ,  $R_2 = \text{Ph}$

2A  $y=2$ ,  $R_1 = \text{H}$ ,  $R_2 = \text{PhOCOCH}_3$

3A  $y=3$ ,  $R_1 = \text{H}$ ,  $R_2 = \text{Ph}$



1B  $y=1$ ,  $R_1 = \text{CH}_3$ ,  $R_2 = \text{Ph}$

2B  $y=2$ ,  $R_1 = \text{H}$ ,  $R_2 = \text{PhOCOCH}_3$

3B  $y=3$ ,  $R_1 = \text{H}$ ,  $R_2 = \text{Ph}$

### Experimental

The synthesis and characterization of the precursor polymers 1A, 2A, 3A, and related homopolymers and copolymers is described elsewhere [5-7]. The dehydrogenation of the precursor polymers 1A, 2A, and 3A to yield 1B, 2B, and 3B respectively will also be described in detail elsewhere [23]. At least four different reagents were used to effect the dehydrogenation reactions at room temperature (25°C): (1) concentrated sulfuric acid (96%); (2) concentrated sulfuric acid (96%)/tetramethyl sulfone (sulfolane) at various ratios; (3)  $\text{HBF}_4$ /diethyl ether (15:85); (4) dilute solutions of  $\text{SbCl}_5$  in dichloromethane (DCM) in which the mole ratio of precursor polymer repeating units to the Lewis acid is less than 1. The detailed characterization of the dehydrogenated materials, i.e. 1B, 2B, 3B, and related periodic and random block conjugated copolymers will be described elsewhere [23], including proton NMR, FTIR, elemental analysis, thermal analysis, and electronic spectra.

### Results and Discussion

The molecular structure of 1B, 2B, and 3B were established by two different lines of evidence. First, spectroscopic (NMR and electronic spectra) evidence of complete dehydrogenation were combined with the already established structures of the precursor polymers. A second approach is the direct determination of the structures of 1B, 2B, and 3B from NMR, FTIR, electronic spectra, and elemental analysis. Both approaches showed that the materials prepared have the proposed structures. For example, the precursor polymer 3A has a characteristic methine proton resonance at 5.95 ppm (TMS) and a UV-Vis absorption maximum at 372 nm (27,700/M.cm) in tetrahydrofuran. Both can be used to follow the progress of dehydrogenation in solution till their complete disappearance upon exhaustive dehydrogenation. The proton NMR spectrum of 3B in deuterated sulfuric acid/deuterated sulfolane was readily assigned to the proposed structure (Figure 2). It is especially important that 6 proton resonances (with 2 protons each) were observed due to the six different thiophene rings per repeating unit of 3B. This suggests that the aromatic and quinoid blocks in 3B are not equivalent.



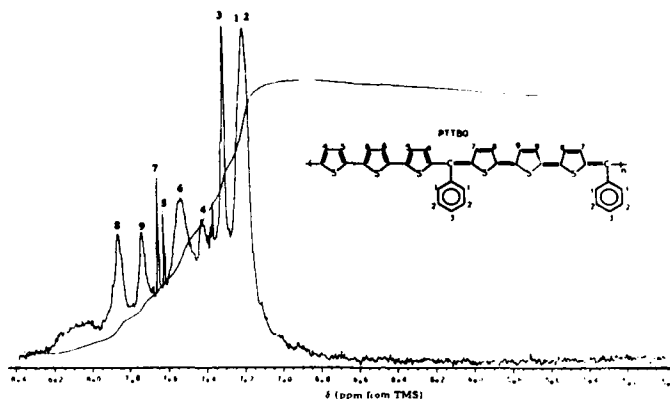


Figure 2. Proton NMR spectrum of 3B.

The solution electronic absorption spectra of 1B, 2B, and 3B in sulfuric acid are shown in Figure 3. The spectrum of 1B has an absorption maximum at 465 nm ( $\epsilon=20,000/\text{M}\cdot\text{cm}$ ) with a shoulder at  $\sim 600\text{nm}$  and the long wavelength absorption edge at about 710nm ( $\sim 1.75\text{ eV}$ ). In the case of 2B two sharp absorption bands appear at 562nm and 706nm and a third at 642 nm, all with  $\epsilon \sim 20,000\text{--}30,000/\text{M}\cdot\text{cm}$ . The lowest energy absorption band in the spectrum of 2B has a sharp absorption edge at about 760nm ( $\sim 1.63\text{ eV}$ ). The spectrum of 3B has two sharp bands at 578 nm and 928 nm with smaller peaks at 699nm and 837nm, all with  $\epsilon \sim 16,000\text{--}45,000/\text{M}\cdot\text{cm}$ . The low energy absorption edge of 3B is 1050nm ( $\sim 1.18\text{ eV}$ ).

The key features of the electronic spectra to be explained are: (1) the observed progressive spectra red shift as the copolymer block length  $y$  increases from 1 to 3; (2) the remarkable multiband structure of the spectra at copolymer block lengths of 2 and 3. There is no evidence that the sulfuric acid solvent has doped the copolymers in Figure 3. Even if current ideas such as solitons, polarons, and bipolarons in conjugated polymers can be invoked, they fail to explain the multiband structure in the absorption spectra of the block copolymers ( $y=2$  and 3) and the significant spectra red shift.

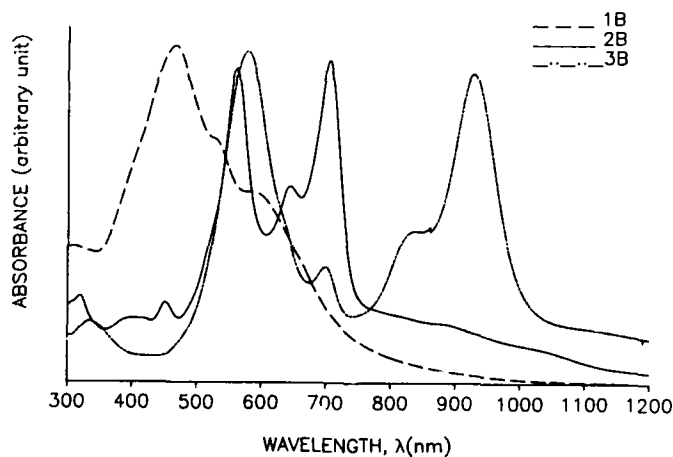


Figure 3. Electronic absorption spectra of 1B, 2B, and 3B.

Our results can be satisfactorily explained if we assume the formation of quasi-one-dimensional superlattices and quantum wells in the block copolymers 2B and 3B. In this scenario, the spectrum of the alternating copolymer 1B is not unusual and is similar to typical spectra of other alternating copolymers or conjugated homopolymers. This is consistent with a barrier thickness ( $d_A \sim 3-4 \text{ \AA}$ ) too small or insufficient to confine charges to a potential well that is equally too thin ( $d_B \sim 3-4 \text{ \AA}$ ). Furthermore, the sizes of A and B are comparable to the "interface" separating them which is  $-C(R)=$  or about  $3\text{ \AA}$ . If we take the size of a thienyl ring plus a C-C or C=C bondlength to be  $d_0 \approx 4\text{ \AA}$ , then  $d_A \approx d_B = yd_0$  and hence when  $y=2$ ,  $d_A = d_B = 8\text{ \AA}$  and when  $y=3$ ,  $d_A = d_B = 12\text{ \AA}$ . As the copolymer block length increases above 1 it becomes meaningful to talk about and expect formation of block segment bandgaps  $E_{gb}^A$  and  $E_{gb}^B$  which are not necessarily identical with the constituent homopolymer bandgaps  $E_g^A$  and  $E_g^B$ . Absorption bands due to these two characteristic energies of block conjugated copolymers,  $E_{gb}^A$  and  $E_{gb}^B$ , are expected to appear in the electronic spectra even if the repeating unit of the periodic structure is unity ( $m=1$ ) provided the block length is large enough. Assuming the large gap block constitute both end groups of the copolymer, then  $m=1,2,3,\dots$  respectively define the number of quantum wells in the periodic structure. A large  $m$  and a small  $d_A$  define a superlattice in a copolymer structure. In addition to the primitive two-band structure due to  $E_{gb}^A$  and  $E_{gb}^B$ , quantization of the conduction and valence bands due to the potential barrier  $\Delta E_g = E_{gb}^A - E_{gb}^B$  should lead to additional absorption bands with energies between the two block segment bandgaps. These essential features of expected absorption spectra of QW and SL structures in the block copolymers are observed at block length  $y=2$  and 3.

A further feature of the electronic spectra that suggests their interpretation in terms of quantum size effects is the spectra red shift as the block length was increased from 2 to 3. The effective bandgap decreased from 1.63eV for 2B to 1.18eV for 3B. Figure 4 shows the variation of the lowest energy absorption band maximum with  $y$  is linear between 1 to 3.

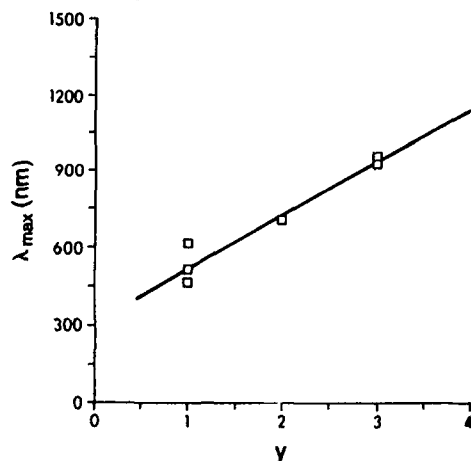


Figure 4. The variation of lowest energy  $\lambda_{max}$  with  $y$ .

The successful preparation of organic polymer semiconductor superlattices and observation of quantum size effects in their electronic spectra show that block conjugated copolymers provide a rational approach to the molecular engineering of electronic, optical, nonlinear optical, and electro-optical properties in synthetic organic polymers. The organic semiconductor superlattices exhibit very large cubic optical nonlinearities [9b, 9c] and have important implications for the feasibility of molecular electronic devices [24]. Important future directions of our work on organic semiconductor superlattices will include the preparation of larger block length periodic copolymers ( $y > 3$ ), preparation of LB films of the superlattices, and synthetic approaches to those in Figure 1.

This research was supported by the Naval Air Development Center under contract no. N62269-87-C-0261 to Honeywell Inc., by the University of Rochester, and by grants from the General Electric Foundation and Amoco Foundation.

#### References and Notes

1. To whom correspondence should be addressed.
2. S.A. Jenekhe, *Nature*, **322**, 345-347 (1986).
3. S.A. Jenekhe, *Macromolecules*, **19**, 2663-2664 (1986).
4. S.A. Jenekhe, In: Proc. Workshop held at Sintra, Portugal, July 28-31, 1986, L. Alcacer, ed., *Conducting Polymers*, p. 149 (D. Reidel Publishing Co., Dordrecht, 1987).
5. S.A. Jenekhe and M.K. Hansen, U.S. Patent 4,694,062, Sept. 15, 1987; U.S. Patent, 4,711,946, Dec. 8, 1987.
6. S.A. Jenekhe, U.S. Patent 4,717,762, Jan. 5, 1988; U.S. Patent 4,758,634, July 19, 1988.
7. S.A. Jenekhe, *Macromolecules*, in press; (b) S.A. Jenekhe, in preparation; (c) S.A. Jenekhe and W.C. Chen, in preparation.
8. A.K. Agrawal and S.A. Jenekhe, *Chem. Mater.*, submitted.
9. (a) S.K. Lo, S.A. Jenekhe and S.T. Wellinghoff, *Advances in Nonlinear Polymers and Inorganic Crystals, Liquid Crystals, and Laser Media*, Proc. SPIE, **824**, 162 (1987); (b) S.A. Jenekhe, S.K. Lo and S.R. Flom, *Appl. Phys. Lett.*, **54**, 2524 (1989); (c) S.A. Jenekhe, W.C. Chen, S.K. Lo and S.R. Flom, *Appl. Phys. Lett.*, submitted.
10. L. Esaki and R. Tsu, *IBM J. Res. Dev.* **14**, 61-65 (1970).
11. L. Esaki, in: L.L. Chang, and K. Ploog (eds.), *Molecular Beam Epitaxy and Heterostructures*, 1-36 (Martinus Nijhoff Publishers, Dordrecht, 1985).
12. L. Esaki and L.L. Chang *Phys. Rev. Lett.* **33**, 495-498 (1974).
13. G.A. Sai-Halasz, L.L. Chang, J.M. Welter, C.A. Chang and L. Esaki, *Solid State Commun.* **27**, 935-937 (1978).
14. R. Dingle, *Festkorperprobleme* **15**, 21-48 (1975).
15. R. Dingle, A.C. Gossard and W. Wiegmann, *Phys. Rev. Lett.* **34**, 1327-1330 (1975).
16. G.H. Dohler, in: T. Tsakalacos, (ed.), *Modulated Structure Materials*, 509-535, (Martinus Nijhoff Publishers, Dordrecht, 1984).
17. G.H. Dohler, *Scientific American* **249**, 144-151 (1983).
18. G. Reiss, G. Hurtrez, and P. Bahadur, *Encycl. Polym. Sci. Eng.*, vol. 2, 324-434 (John Wiley, New York, 1985).
19. A. Noshay and J.E. McGrath, *Block Copolymers* (Academic Press, New York, 1977).
20. S. Das Sarma, A. Kobayashi and R.E. Prange, *Phys. Rev. Lett.* **58**, 1280-1283 (1986).
21. P.W. Anderson, *Phys. Rev.* **109**, 1492-1505 (1958).
22. M. Kertesz and Y.S. Lee, *Synthetic Metals* **28**, C545-C552 (1989).
23. W.C. Chen and S.A. Jenekhe, in preparation.
24. F.L. Carter, ed., *Molecular Electronic Devices II* (Marcel Dekker, New York, 1987).

## LARGE CUBIC NONLINEAR OPTICAL PROPERTIES OF ORGANIC SEMICONDUCTOR SUPERLATTICES

Samson A. Jenekhe\*, Wen-Chang Chen\*, Saukwan Lo\*\* and Steven R. Flom\*\*\*

\*Department of Chemical Engineering, University of Rochester Rochester, New York 14627

\*\*Honeywell Systems and Research Center Minneapolis, Minnesota 55418

\*\*\*Department of Chemistry, University of Minnesota, Minneapolis, Minnesota 55455

### Abstract

We have measured extremely large second hyperpolarizabilities ( $\gamma_{xxxx}$ ) in solutions of two recently prepared organic polymer semiconductor superlattices. These block copolymers are of alternating aromatic and quinoidal moieties and structurally differ by a side group substituent. The values observed are  $1.6 \times 10^{-29}$  esu for the parent copolymer (PBTBQ) and  $3.7 \times 10^{-30}$  esu for its acetoxy derivative (PBTABQ). The corresponding values of  $\chi^{(3)}$  are estimated to be  $2.7 \times 10^{-7}$  esu and  $4.5 \times 10^{-8}$  esu. The measurements, made by picosecond degenerate four wave mixing at 532 nm, showed that the dynamics of the larger  $\chi^{(3)}$  valued copolymer were faster than the 30 ps resolution of the instrument while the derivative exhibited a slower response. The large magnitude and rapid response of the cubic optical nonlinearities in these novel materials suggest their potential for further development and photonic device applications.

### Introduction

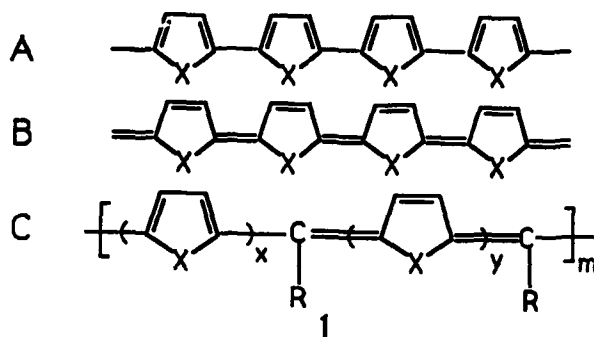
The origins of large nonlinear optical (NLO) responses and the development of materials for application in photonic devices is the focus of much of the current interest in the third order NLO properties of conjugated polymers<sup>1-9</sup>. These NLO properties are macroscopically characterized through measurements of the third order electric susceptibility tensor,  $\chi^{(3)}$ . Magnitudes typically observed in most of the currently known conjugated polymers range from about  $10^{-12}$  to  $10^{-9}$  esu when probed using nonresonant conditions. This range is insufficient for most proposed, practical device applications.<sup>10</sup>

Several strategies can be followed to increase the third order NLO response. Near resonant or resonant enhancement increases the magnitude of  $\chi^{(3)}$ . For example, the three photon enhanced  $\chi^{(3)}$  of polyacetylene was recently<sup>9</sup> measured to be about  $10^{-8}$  esu at  $2.1 \mu\text{m}$  ( $\sim 0.6$  eV). Other approaches being pursued to further enhance the magnitude of  $\chi^{(3)}$  include derivatization of existing NLO polymers<sup>8</sup> and preparation of new conjugated polymer structures that might enhance  $\chi^{(3)}$  by optimization of the currently known critical molecular parameters or offer new mechanisms of optical nonlinearity. Here the focus will be the NLO properties of a new type of conjugated polymer structure.

Much recent research has shown that conjugated polymers can be effectively modeled as quasi-one-dimensional semiconductors<sup>11-14</sup>. Recently<sup>15-17</sup>, periodic multiblock conjugated copolymers were proposed as quasi-one-dimensional *organic semiconductor superlattices* that may exhibit novel electronic, linear optical, electro-optical, and nonlinear optical properties. These structures have chemical formulas of  $(A_x B_y)_m$ , where A and B are the repeating units of conjugated homopolymers  $(A)_m$  and  $(B)_m$  with different band gaps,  $E_g^A$  and  $E_g^B$ . It should be pointed out that the electronic and NLO properties of

alternating conjugated copolymers,  $(AB)_m$  (i.e.  $x=y=1$ ) have been investigated and include the polyphenylene vinylenes<sup>18</sup> and polythiophene vinylenes<sup>19</sup>. The NLO properties of copolymers for which  $x>1$  and  $y>1$  have not been previously investigated.

The only prior experimental investigation of block conjugated copolymers of this kind of structure was by Jenekhe<sup>20</sup> who studied the electronic spectra of thin films of structure **1C** below. The initial preparation of members of **1C** by halogen dehydrogenation of precursor polymers<sup>20,21</sup> in the solid state yielded insoluble materials that were difficult to process and characterize. Note that when  $X=S$ , **1A** is aromatic poly(2,5-thiophene) which has a band gap of 2.1 eV and **1B** is its quinoid isomer which has a calculated<sup>22</sup> band gap of  $\sim 0.5$  eV. We have recently prepared and characterized several soluble copolymers, **1C**, by a new synthetic method<sup>15</sup>. These new periodic block copolymers have a mixed quinoidal and aromatic character



In this paper we present our measurements of the third order NLO properties of two organic polymer superlattices with the structure **1C**. The two block conjugated copolymers are derivatives of poly( $\alpha$ -[5,5'-bithiophene]-block- $\alpha$ -[5,5'-bithiophenequinodimethane]). The first copolymer is referred to as PBTBQ and has the structure **1C** with  $x=y=2$ ,  $X=S$  and  $R$ =phenyl. The second copolymer, referred to as PBTABQ, differs from PBTBQ only in the side group radical  $R$ =*p*-acetoxyphenyl. Since the acetoxy side group in PBTABQ is an electron donor it was anticipated that measurable differences in the linear and nonlinear optical properties would be observed. The synthesis and characterization of these copolymers are described elsewhere<sup>15</sup>.

### Experimental

Figure 1 shows the electronic absorption spectra of PBTBQ and PBTABQ in concentrated sulfuric acid solution. Both spectra have peaks in the visible and the near infrared. The spectrum of PBTABQ is shifted to the red relative to the spectrum of PBTBQ. The observed spectral maxima and the associated molar (repeating unit) extinction coefficients are  $\lambda_{max}=537\text{nm}$  ( $\epsilon=8.5 \times 10^4 \text{M}^{-1}\text{cm}^{-1}$ ) and  $702\text{nm}$  ( $\epsilon=2.5 \times 10^4 \text{M}^{-1}\text{cm}^{-1}$ )

for PBTBQ and  $\lambda_{max}=562\text{nm}$  ( $\epsilon=6.0 \times 10^4 \text{M}^{-1}\text{cm}^{-1}$ ) and  $706\text{nm}$  ( $\epsilon=6.2 \times 10^4 \text{M}^{-1}\text{cm}^{-1}$ ) for PBTABQ. The substitution of the acetoxy group in PBTABQ for the hydrogen has a significant effect on the linear absorption spectrum.

The third-order NLO properties of PBTBQ and PBTABQ in sulfuric acid solutions were measured using degenerate four wave mixing (DFWM). A diagram of the DFWM apparatus is shown in figure 2. Single pulses from a hybrid active/passive mode-locked Nd:YAG laser are amplified and doubled to 532nm. The 30 ps FWHM, 200  $\mu\text{J}$  pulses are beam split and overlapped spatially and temporally in the sample. The incident intensity

and the phase conjugate intensity are monitored by photodiodes 2 and 3 respectively. The phase conjugate intensity in the small signal limit<sup>23</sup> is

$$I_{\text{conj}} \propto \frac{|\chi^{(3)}|^2}{n^4} I_{\text{inc}}^3 \left[ \frac{1-e^{-\alpha L}}{\alpha} \right]^2 e^{-\alpha L} \quad (1)$$

In this equation  $\chi^{(3)}$  is the third order susceptibility,  $n$  is the refractive index,  $I_{\text{inc}}$  is the total intensity incident on the sample,  $\alpha$  is the sample absorption coefficient and  $L$  is the sample length.

The dependence of the phase conjugate intensity on the incident intensity is measured and fit to a cubic plus linear expression. Direct evaluation of the proportionality constant is avoided through comparison of the least square cubic coefficients,  $C^{(3)}$ , resulting from identical experiments using a reference and the sample in question as shown in equation 2,

$$|\chi_{\text{sample}}^{(3)}| = |\chi_{\text{ref}}^{(3)}| \left[ \frac{C_{\text{sample}}^{(3)}}{C_{\text{ref}}^{(3)}} \right]^{1/2} \left[ \frac{n_{\text{sample}}}{n_{\text{ref}}} \right]^2 \left[ \frac{L_{\text{ref}} \alpha_{\text{sample}}}{(1-e^{-\alpha L}) e^{-\alpha L/2}} \right] \quad (2)$$

The reference used is  $\text{CS}_2$  since its copolarized  $\chi_{\text{xxxx}}^{(3)}$  at 532nm is known to be  $6.8 \times 10^{-13} \text{esu}^{24}$ . The  $\alpha L$  products in the denominator of equation 2 refer to the absorption

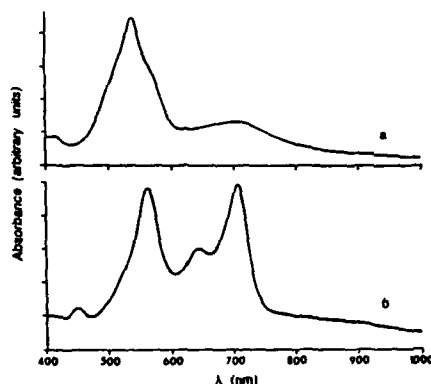


Figure 1. Solution electronic absorption spectra of PBTBQ (a) and PBTABQ (b).

coefficient and length of the sample. The configuration averaged second hyperpolarizability,  $\langle \gamma \rangle$  is deduced from the concentration dependence of the sample  $\chi^{(3)}$  through use of equation 3,

$$\chi_{ijkl}^{(3)} = L \sum_m N_m \langle \gamma_{ijkl}^m \rangle \quad (3)$$

Here  $L$  is the local field correction factor assumed to be the same as that of the pure solvent and equal to  $\{(n^2+2)/3\}^4$ , again  $n$  is the refractive index and  $N_m$  is the number density of the  $m^{\text{th}}$  species. The subscripts  $i, j, k,$  and  $l$  recognize the tensor nature of both the macroscopic susceptibility and microscopic hyperpolarizability. Equation 3 also allows a means to estimate, as a means of comparison to other studies,  $\chi^{(3)}$  for the pure, isotropic, noninteracting sample provided its refractive index and density are known.

In these experiments the two measured tensor elements are  $\chi_{xxxx}^{(3)}$  and  $\chi_{xyyx}^{(3)}$ . They are measured via rotation of the half wave plate in the path of the probe beam, coupled with the polarizer before the conjugate detector shown in figure 2. In isotropic samples, it can be shown that only two of the nonresonant tensor elements are independent. Hellwarth<sup>25</sup> demonstrated from symmetry arguments using the Born-Oppenheimer approximation, separating the electronic motions from nuclear, that the relationship between the electronic tensor elements in isotropic solution is such that

$$\chi_{xxxx}^{(3)el} = 3\chi_{xyyx}^{(3)el} = 3\chi_{xyxy}^{(3)el} = 3\chi_{xxyy}^{(3)el} \quad (4)$$

Further, Hellwarth<sup>25</sup> gave an approximate relation for the molecular response elements which has been experimentally<sup>26,27</sup> shown to hold for liquids and solutions.

$$\chi_{xxxx}^{(3)mol} = (4/3)\chi_{xyyx}^{(3)mol} = (4/3)\chi_{xyxy}^{(3)mol} = -2\chi_{xxyy}^{(3)mol} \quad (5)$$

The total response, ignoring excited state, thermal, and acoustic contributions, using parallel polarizations for all three beams is

$$\chi^{(3)exp} = \chi^{(3)el} + \chi^{(3)mol} \quad (6)$$

under these conditions, measurement of the experimental ratio,

$$r = \chi_{xyyx}^{(3)} / \chi_{xxxx}^{(3)} \quad (7)$$

allows one to calculate the fraction of the response that is due to electronic processes,

$$f_e = 1.8 - 2.4r \quad (8)$$

$r$  ranges from 1/3 to 3/4. Measurements of ratios less than 1/3 or greater than 3/4 indicate that thermal, acoustic, or excited state processes are contributing significantly to the observed signal. Measurements of ratios between 1/3 and 3/4 do not necessarily guarantee that the mechanism of the observed nonlinear response is limited to the molecular and electronic responses; however, when these polarized measurements are coupled with measurements of the time response of the nonlinearity, the mechanism of the nonlinear response as well as its magnitude can be identified. In the experiments, the time response of the  $\chi^{(3)}$  is evaluated by performing multiple experiments such as those above at different arrival times of the back pump beam.

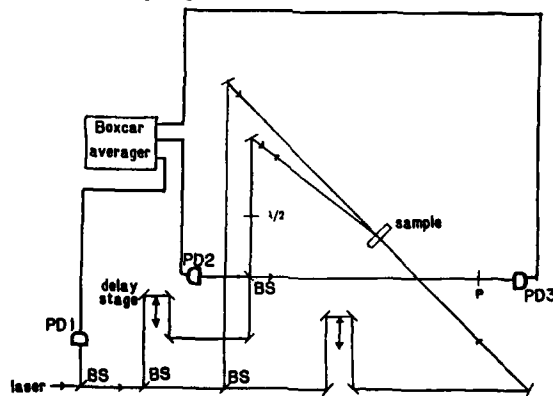


Figure 2. Optical arrangement for DFTM experiments.

### Results and Discussion

The measured second hyperpolarizability,  $\langle \gamma_{xxxx} \rangle$  of PBTBQ and PBTABQ is shown in table I along with the polarization ratio. The estimated value of  $\chi_{xxxx}^{(3)}$ , shown in

table I was calculated from the measured hyperpolarizability via equation 3 using an estimated density of  $1.6\text{g}/\text{cm}^3$  for both PBTBQ and PBTABQ and a calculated<sup>28-30</sup> index of refraction also shown in table I. The measured  $\langle\gamma_{xxxx}\rangle$  values and the estimated values

for  $\chi_{xxxx}^{(3)}$  are among the largest ever reported for an organic polymer, resonant or nonresonant. The extremely large optical nonlinearities observed in these organic superlattices are believed to be due to a combination of factors: (1) a large  $\pi$ -electron

Table I. Third-Order NLO Properties of Organic Superlattices

Superlattice	IC	X	x	y	R	n	$\gamma_{xxxx}$ (esu)	$\chi_{xxxx}^{(3)}$ (esu)	r	$f_e$
PBTBQ	S	2	2		Ph	1.811	$1.60 \times 10^{-29}$	$2.73 \times 10^{-7}$	0.39	0.86
PBTABQ	S	2	2		-PhOOCCH <sub>3</sub>	1.762	$3.70 \times 10^{-30}$	$4.49 \times 10^{-8}$	0.41	0.82

delocalization structure; (2) resonance enhancement; (3) the regular A/B asymmetry in the superlattice structure that enhances the anharmonicity of the electronic potential; and (4) the large polarizability of the quinoid structure relative to the aromatic.

Another important observation and one that will be more extensively explored in the future is that the polarization resolved NLO measurements differ by as much as a factor of six between PBTBQ and PBTABQ. The primary difference between the two structures is the presence of the electron donating acetoxy group away from the principal conjugated backbone. If one can assume that this small side group has little effect on the overall conformation of the polymer in solution then this structure-property relationship would seem to imply that substitution of an electron accepting group for the acetoxy would yield still larger values for the third order NLO coefficients. We plan to test this idea.

The polarization and time dependence of the configuration averaged hyperpolarizability support the inferences drawn above. The ratio of equation (7), the response with the probe beam cross polarized with respect to the pump beams versus the copolarized response, and the fractional electronic response calculated via equation (8), are also shown in table I. The ratios, r, deviate significantly from the .33 value expected if the response were entirely electronic. The fractions calculated as though the excitations were nonresonant are reasonable and show that there is a component to the response that is not due to nonresonant electronic response.

The dynamics of the response, demonstrates that: (1) In both cases the response rises immediately within the 30 ps resolution of the experiment; (2) In both cases the decay of the signal is rapid and decays to zero within 200 ps; (3) in the case of PBTBQ, the signal is completely symmetric and indistinguishable from the response of CS<sub>2</sub>, i.e. the decay of the response is faster than the resolution of the apparatus; (4) PBTABQ has a slower decay as well as a pulse limited component. In addition, the time dependence in the crossed polarized configuration is always pulse limited and nonzero which indicates that thermal and acoustic mechanisms have little to do with the observed magnitude of  $\langle\gamma\rangle$  and  $\chi^{(3)}$ . It appears that the electronic mechanism is dominant in the NLO response of these copolymers. Though there are some smaller amplitude molecular alignments and/or excited state contributions to the signal, it is clear from the rapidity of the response that these are not the major processes giving rise to the large values of  $\langle\gamma\rangle$  and  $\chi^{(3)}$  observed. The slower decay and smaller fraction electronic response exhibited by PBTABQ is probably due to an excited state decay rather than molecular alignments.

In either case the origin of the extremely large values observed for the third order NLO coefficients of these organic superlattices is largely associated with electronic processes, in both the ground and excited states. Their large magnitude and rapid response together with the molecular architectural possibilities make this class of organic polymer superlattices promising candidates for further material development and possible photonic device applications.



We acknowledge the support of this research by the Naval Air Development Center under contract no. N62269-87-C-0261. Work at the University of Rochester was also supported by the University of Rochester and an equipment grant from the General Electric Foundation. The technical assistance and helpful discussions of D.J. Rogers is appreciated.

#### References

1. P.N. Prasad and D.R. Ulrich, eds., Nonlinear Optical and Electroactive Polymers, (Plenum Press, New York, 1988).
2. A.J. Heeger, J. Orenstein and D.R. Ulrich, eds., Nonlinear Optical Properties of Polymers, *Materials Research Soc., Proc.*, vol 109, (Pittsburgh, PA, 1988).
3. D.S. Chemla and J. Zyss, eds., Nonlinear Optical Properties of Organic Molecules and Crystals, vols. 1 and 2, (Academic Press, New York, 1987).
4. D.J. Williams, ed. Nonlinear Optical Properties of Organic and Polymeric Materials, ACS Symp. Series, no. 233, (Am. Chem. Soc., Washington, DC 1983).
5. D.N. Rao, J. Swiatkiewicz, P. Chopra, S.K. Ghosal and P.N. Prasad, *Appl. Phys. Lett.*, **48**, 1187 (1986).
6. (a) P.N. Prasad, J. Swiatkiewicz and J. Pflieger, *Mol. Cryst. Liq. Cryst.* **160**, 53 (1988). (b) M.-T. Zhao, B.P. Singh and P.N. Prasad, *J. Chem. Phys.*, **89**, 5535 (1988).
7. S.K. Lo, S.A. Jenekhe and S.T. Wellinghoff, Advances in Nonlinear Polymers and Inorganic Crystals, Liquid Crystals, and Laser Media, Proc. SPIE, **824**, 162 (1987).
8. S.A. Jenekhe, S.K. Lo and S.R. Flom, *Appl. Phys. Lett.*, **54**, 2524 (1989).
9. W.-S. Fann, S. Benson, J.M.J. Madey, S. Etamad, G.L. Baker and F. Kajzar, *Phys. Rev. Lett.*, **62**, 1492, (1989).
10. D.R. Ulrich, *Mol. Cryst. Liq. Cryst.*, **160**, 1 (1988).
11. T.A. Skotheim, ed., Handbook of Conducting Polymers, vols. 1 and 2, (Marcel Dekker, New York, 1986).
12. A.J. Heeger, *ibid.*, vol.2, p. 729.
13. J. Simon and J.-J. Andre, Molecular Semiconductors, (Springer, New York, 1984).
14. S.A. Jenekhe, S.T. Wellinghoff and J.F. Reed, *Mol. Cryst. Liq. Cryst.*, **105**, 175 (1984).
15. S.A. Jenekhe and W.C. Chen, in: Mater. Res. Soc. Proceedings Vol. 173; (this volume).
16. S.A. Jenekhe, *U.S. Patent* 4,717,762, Jan. 5, 1988.
17. S.A. Jenekhe, *U.S. Patent* 4,758,634, July 5, 1988.
18. B.P. Singh, P.N. Prasad and F.E. Karasz, *Polymer*, **29**, 1940 (1988).
19. K.Y. Jen, H. Eckhardt, T.R. Jow, L.W. Shacklette and R.L. Elsenbaumer, *J. Chem. Soc. Chem. Commun.*, 1988, 215 (1988).
20. S.A. Jenekhe, *Nature*, **322**, 345 (1986).
21. S.A. Jenekhe, *Macromolecules*, **19**, 2663 (1986).
22. M. Kertesz, Y.S. Lee, *Synthetic Metals*, **28**, C545 (1989).
23. Y. R. Shen, The Principles of Nonlinear Optics, (J. Wiley and Sons, New York, 1984) p. 247.
24. (a) N.P. Xuan, J. L. Ferrier, J. Gazengel, and G. Riviere, *Opt. Commun.* **51**, 433 (1984); (b) M.D. Levenson and N. Bloembergen, *J. Chem. Phys.* **60**, 1323 (1974).
25. R.W. Hellwarth, *Prog. Quantum Electron.* **5**, 1 (1977).
26. (a) J. Etchepare, G. Grillon, J.P. Chamberet, G. Hamoniaux and A. Orszag, *Opt. Commun.*, **63**, 329 (1987); (b) J. Etchepare, G. Grillon, G. Hamoniaux, A. Antonetti and A. Orszag, *Revue Phys. Appl.*, **22**, 1749 (1987); (c) J. Etchepare, G. Grillon, A. Antonetti and A. Orszag, *Physica Scripta*, **T23**, 191 (1988).
27. F.W. Deeg and M.D. Fayer, *J. Chem. Phys.*, **91**, 2269 (1989).
28. A. Bondi, Physical Properties of Molecular Crystals, Liquids, and Glasses, (Wiley, New York, 1968), Chapt. 14.
29. A.A. Askadskii, *Pure Appl. Chem.*, **146**, 19 (1976).
30. D.W. Van Krevelen, Properties of Polymers: Their Estimation and Correlation with Chemical Structure, (Elsevier, New York, 1976), Chapt. 10.

## SYNTHESIS AND SECOND-ORDER NONLINEAR OPTICAL PROPERTIES OF NEW COUMAROMETHACRYLATE-METHYLMETHACRYLATE COPOLYMERS

R.A. HENRY,\* J.M. HOOVER,\* A. KNOESEN,\*\* S.T. KOWEL,\*\* G.A. LINDSAY,\* AND M.A. MORTAZAVI\*\*

\*Chemistry Division, Research Department, Naval Weapons Center, China Lake, CA 93555-6001

\*\*Organized Research Program on Polymeric Ultrathin Film Systems, Department of Electrical Engineering and Computer Science, University of California, Davis, CA 95616

### ABSTRACT

The synthesis and second-order nonlinear optical (NLO) properties of a new family of optically nonlinear coumarin dye-containing polymers is reported. Polymerizable coumaromethacrylate (CMA) monomers having various alkyl spacers ( $C_2$  to  $C_5$ ) between the polymerizable group and the chromophore were prepared and copolymerized with methacrylate (MMA) and other vinyl monomers. The CMA copolymers had high chromophoric content (up to  $18 \times 10^{20}$ ) and glass transitions as high as  $132^\circ\text{C}$ . Spin cast films were prepared on BK7 substrates and oriented by corona-onset poling at elevated temperatures (COPET). The poled CMA copolymer films were characterized for spectroscopic absorption and second harmonic properties. A comparison of the nonlinear optical properties of poled CMA-MMA copolymers to poled guest-host systems is made. Relative to guest/host systems, CMA-MMA copolymer films exhibit larger and much more stable second-order nonlinear optical properties.

### INTRODUCTION

Second-order NLO polymers have recently been the subject of extensive research. This interest is largely due to their broad spectrum of unique and useful electrical, optical, thermal, and physical properties. In general, they may have very large molecular hyperpolarizabilities ( $\beta \sim 100 \times 10^{-30}$  esu or more) [1], high optical clarity, ultra-fast response times ( $\sim 10^{-14}$  s or less) [2], and robust mechanical integrity. In addition, many may be conveniently and inexpensively processed into thin film geometries, oriented by electric field poling, and integrated with microelectronics. Alternatively, some second-order NLO polymers may be processed using Langmuir-Blodgett (L/B) monolayer deposition techniques to yield more highly ordered, ultrathin, multilayer NLO films [3-5]. Consequently, these materials are attractive for a variety of applications including optical communications and computing components, frequency doublers for lasers, and laser resistant surfaces.

Two basic approaches exist for the synthesis of optically nonlinear polymers. One approach is to prepare guest-host materials by simply dissolving polarizable moieties (chromophores or dyes as the guest) in a polymeric host. The other approach is to synthesize polymers that have chromophores chemically attached as either pendent or main-chain substituents. These polymers may usually be molecularly oriented by one of the two techniques mentioned above. Additionally, these materials may be completely thermoplastic (soluble and reprocessable) after poling or L/B deposition, or crosslinked to further inhibit chromophore mobility [6].

Polymers that have chemically attached chromophores have several distinct advantages over guest-host materials. These advantages include higher chromophore densities ( $N$  chromophore molecules/cm<sup>3</sup> polymer), reduced mobility and enhanced orientational stability of the chromophore [7], and improved optical, thermal, and mechanical properties.

The attachment or substitution of chromophores onto polymers is often complicated by limited reactivity of the chromophores and/or the polymer. The result is often poor control over the extent of reaction and less than effective substitution of the polymer with chromophores. Polymerizable chromophores are an attractive alternative if the chromophore does not act as a polymerization inhibitor (e.g., a free radical scavenger). Coumarin dye-containing methacrylate monomers provide such an alternative. They have sufficient reactivity to yield polymers and copolymers of high molecular weight, high optical clarity, and high degrees of chromophore incorporation.

Our laboratory has been successful at synthesizing a variety of coumarin dye-containing methacrylate monomers and NLO polymers in which the chromophore is incorporated as a side-chain. These materials have a number of interesting properties that are described below in more detail.

#### EXPERIMENTAL PROCEDURE

A variety of CMA monomers have been synthesized in which the alkyl "spacer" between the chromophore and the methacrylate group was varied from ethyl to pentyl and the configuration of the electron-donating amine group was changed from normal alkyl to cyclic as shown in Figure 1 below. The synthesis of these monomers is thoroughly described in a patent disclosure [8] and will not be discussed here. The CMA monomers were used as synthesized after purification by column chromatography.

Styrene and *t*-butylstyrene comonomers were purified by passing them through an activated alumina column and degassing under reduced pressure. The other reagents used (MMA, chlorobenzene, and benzene) were purified by distillation from finely ground calcium hydride.

The CMA monomers and comonomers (if any) were dissolved in mixed solvents (ca. 5-10% by weight monomer) containing ca. 25% benzene and 75% chlorobenzene. The solutions were refluxed for ca. 16 hours under a nitrogen atmosphere with ca. 1% (by weight to monomer) azobisisobutyronitrile (AIBN) as the initiator.

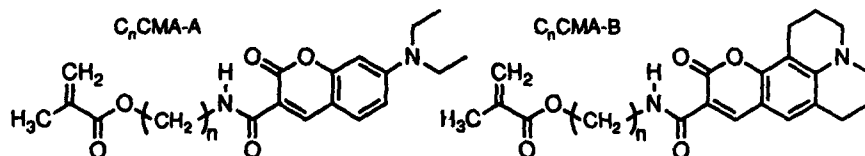


Figure 1. Coumaromethacrylate Monomers C<sub>n</sub>CMA-A and C<sub>n</sub>CMA-B.

The polymers were isolated by precipitation in hexane and purified by preparative gel permeation chromatography (GPC) in chloroform using styragel columns. This technique removed all measurable amounts of unsubstituted dye (monomer) from the copolymers. The final products were dried under reduced pressure above their glass transition temperature ( $T_g$ ) for several hours.

The polymers were thermally characterized by differential scanning calorimetry (DSC) and thermal gravimetric analysis (TGA) at 10°C/min. Spectroscopic characterizations were performed in chloroform using 80 MHz, proton, nuclear magnetic resonance (NMR), and ultra-violet/visible (UV/Vis) techniques.

The molecular weights of the polymers were determined by analytical GPC in tetrahydrofuran (THF) with low-angle laser light scattering (LALLS) detection. In some cases only relative molecular weights were determined (based on polystyrene standards).

The samples for NLO characterization were prepared by spin-casting and/or draw-casting chlorobenzene and/or cyclohexanone solutions of the polymers on glass (BK7) microscope slides. The films were dried slowly and completely in a series of room temperature and oven temperature steps. A noncentrosymmetric orientation of molecular dipoles was introduced into the films by COPET [8-10].

The poled films were characterized for second-order optical nonlinearity using second harmonic generation (SHG) at 532 nm. The source was a polarized and filtered Nd-YAG laser. A molecular dipole order parameter ( $\Phi$ ) was also determined for these films using UV/Vis absorbance data as previously described [9].

## RESULTS AND DISCUSSION

Table I summarizes the comonomer (backbone), chromophore number density ( $N$ ) in chromophores/cm<sup>3</sup>, the  $T_g$ , and the weight and number-average molecular weights for four CMA copolymers. All four samples had solution UV/Vis absorbance maxima of 419 nm with full-width-half-maxima of 44 nm as shown in Figure 2. These coumarin-based chromophores were observed to be very narrow oscillators and to have no significant absorbance at 532 nm. Together, these factors permit the measurement of nonresonance-enhanced  $\chi^{(2)}$ s from SHG measurements at 532 nm and provide a large window of transparency in the visible spectrum.

Table I. Characteristics of Several CMA Copolymers.

Sample	Backbone	Dye Type	$N/10^{20}$	$T_g$ (°C)	$\langle M_w \rangle / \langle M_n \rangle$
1220-30	PMMA	C <sub>2</sub> CMA-A <sup>a</sup>	9.8	116	20k/14k
1220-32	PMMA	C <sub>5</sub> CMA-A	7.7	92	31k/18k
1220-29	PTBS	C <sub>2</sub> CMA-A <sup>a</sup>	7.6	132	29k/17k
1220-31	PTBS	C <sub>5</sub> CMA-A	6.1	100	24k/14k

<sup>a</sup> C<sub>2</sub> CMA-A, calculated  $\mu = 5.02$  Debye,  $\beta = 20.7 \times 10^{-30}$  esu; private communication with R. F. Kubin, Naval Weapons Center, China Lake, CA.

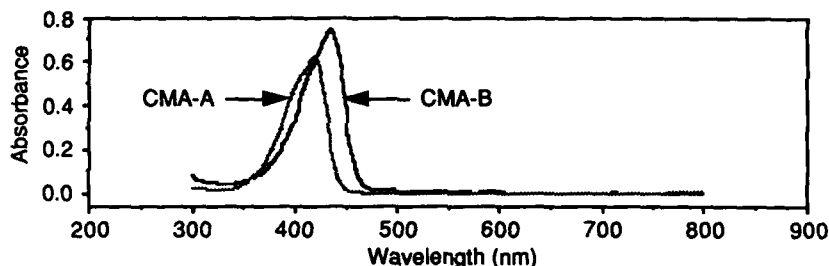


Figure 2. UV/Vis Spectrum of CMA-A and CMA-B Copolymers.

The chemical attachment of chromophores to polymers restricts the mobility of the chromophores and improves their solubility in the polymers to which they are attached. A limited mobility of the chromophores is important to the preservation of molecular dipole alignment once it has been accomplished by electric field poling. Good solubility of the dye in the polymer is important to the achievement of high chromophore concentrations while maintaining good physical and optical properties. Poor solubility can result in multiphase materials with poor optical properties.

The immobilization of chromophores in polymers is a function of chemical and electronic constraints placed on the chromophore through specific interactions (e.g., hydrogen-bonding or acid-base interaction) and covalent bonding with the polymer. The greatest immobilization should occur when the chromophore is covalently bonded to the polymer at opposite ends and the polymer is below its  $T_g$ . Examples of this situation would include main-chain chromophore polymers [11,12] and cross-linked polymers in which the chromophore is held at opposite ends. Polymers with chromophore side-chains would provide less constraint and dyes in guest/host systems would have the greatest mobility. The results of accelerated aging experiments to determine chromophore mobility are summarized below in Figures 3 and 4.

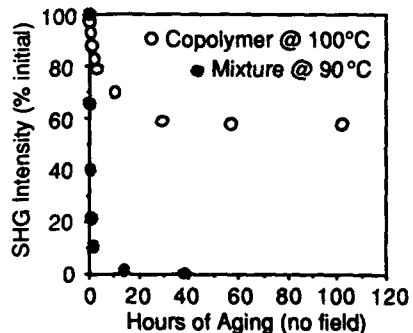


Figure 3. Accelerated Aging of Poled Films of P(MMA-C<sub>2</sub>CMA-A) and PMMA + C<sub>2</sub>CMA-A model.

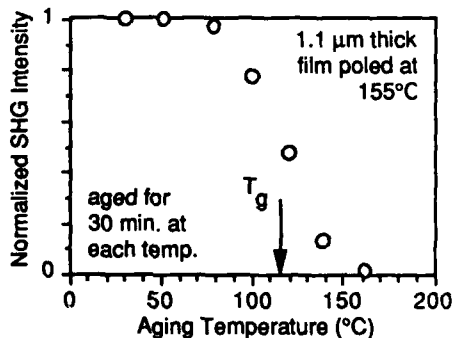


Figure 4. Aging of Poled P(MMA-C<sub>2</sub>CMA-A) Film.

In Figure 3, guest/host (mixture) and copolymer films of similar thickness, chromophore density and poling conditions were aged in an oven and periodically removed for SHG measurements. In Figure 4, the sample was aged for 30-minute

periods at increasingly higher temperatures with SHG measurements between temperature increases of the oven.

As judged from SHG measurements, it is clear that the CMA copolymer is much more orientationally stable at slightly elevated temperatures than the guest/host system of its model compound in PMMA. The chemical structure of the model compound was the same as that of a CMA monomer with no vinyl unsaturation. From the data in Figure 4, we can see that aging of the copolymer does not result in the complete loss of molecular polarization and NLO properties until it is done at temperatures well above the  $T_g$ . These data suggest that orientational stability of the chromophores in CMA copolymers is enhanced by attachment to the polymer and additionally by hydrogen bonding intermolecular attractions. Complete relaxation of poled order is not observed until sufficient time and thermal energy is provided to overcome the molecular attractions present.

Additional evidence for the presence of molecular interactions that assist in the immobilization of coumarin chromophores in PMMA may be found in the results summarized by Figure 5. When copolymer films were poled at increasingly higher temperatures, optimum poling (as judged by SHG) was not observed until the  $T_g$  was exceeded by ca. 50°C. This indicates again that sufficient time and thermal energy must be provided to obtain optimum dipole alignment and overcome any restraining interactions.

In any dipole-containing material, the possibility of dipole aggregation and the loss of effective noncentrosymmetry must be considered. Such aggregation has been proposed to explain the behavior of some Langmuir-Blodgett films in which the dipoles may be in close proximity. Side-chain chromophore polymers are unlikely to show such effects especially when the dipoles are moderately separated. This appears to hold for CMA copolymers when  $N$  is kept below  $1 \times 10^{21}$  chromophores/cm<sup>3</sup> as shown in Figure 6.

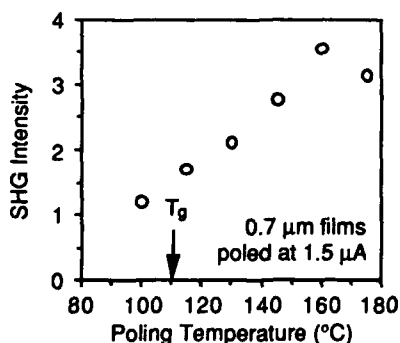


Figure 5. Poling of C<sub>2</sub>CMA-A/MMA Copolymers.

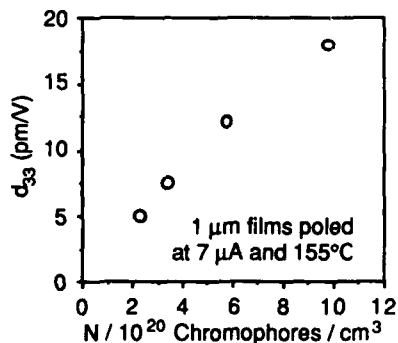


Figure 6. SHG vs. CMA Content for C<sub>2</sub>CMA-A/MMA Copolymers.

A nearly linear relationship is observed for SHG as a function of  $N$  for a series of C<sub>2</sub>CMA-A/MMA copolymers that had similar thicknesses and poling conditions. When this result is considered along with their high optical clarity, the presence of scattering crystallites or deleterious aggregates may be ruled-out with some confidence.

## CONCLUSION

From the discussions above, we may conclude that the study of these interesting CMA copolymers provides insight into several aspects of polymer science that must be considered for the success of developmental research on future generations of NLO polymers. These polymers should have strong specific interactions between the chromophore(s) and the backbone to promote solubility of the chromophore(s) (high N numbers), inhibit aggregation, and aid immobilization. They should have chromophores that are sufficiently asymmetric to assist in the suppression of crystallinity and scattering losses. They should have chromophores that are sufficiently narrow oscillators such that large frequency windows of transmission are available, and sufficiently strong oscillators such that large molecular polarizabilities are present.

## REFERENCES

1. K.D. Singer, J.E. Sohn, L.A. King, H.M. Gordon, H.E. Katz, and C.W. Dirk, *J. Opt. Soc. Am.*, **6(7)**, 1339 (1989).
2. M.A. Mortazavi, D. Yankelevich, A. Dienes, A. Knoesen, S.T. Kowel, and S. Dijaili, *Appl. Opt.*, **28(5)**, 3278 (1989).
3. R.C. Hall, J.M. Hoover, and G.A. Lindsay, Navy Case No. 70969 (January 1988).
4. B.L. Anderson, R.C. Hall, B.G. Higgins, G.A. Lindsay, P. Stroeve, and S.T. Kowel, *Syn. Metals*, **28**, D683 (1989).
5. R.C. Hall, G.A. Lindsay, B.L. Anderson, S.T. Kowel, B.G. Higgins and P. Stroeve, Nonlinear Optical Properties of Polymers, edited by A.J. Heeger, J. Orenstein and D.R. Ulrich (Mater. Res. Soc, Pittsburgh, 1988) p. 351.
6. B. Reck, M. Eich, R.J. Twieg, C.G. Willson, D.Y. Yoon, and G.C. Bjorkland, *SPIE Proceedings* 1147-08, 1989.
7. K.D. Singer, M.G. Kuzyk, W.R. Holland, J.E. Sohn, S.J. Lalama, R.B. Comizzoli, H.E. Katz, and M.L. Schilling, *Appl. Phys. Lett.*, **53**, 1800 (1988).
8. R.A. Henry, J.M. Hoover, and G.A. Lindsay, Navy Case No. 72263 (October 1989).
9. M.A. Mortazavi, A. Knoesen, S.T. Kowel, B.G. Higgins, and A. Dienes, *J. Opt. Soc. Am.*, part B, **6(4)**, 733 (1989).
10. A. Knoesen, M.A. Mortazavi, S.T. Kowel, A. Dienes, and B.G. Higgins, "Corona-Onset Poling of Nonlinear Molecularly Doped Films," in Digest of Topical Meeting on Nonlinear Optical Properties of Materials (Opt. Soc. Am., Washington, D.C., 1988) p. 24.
11. J.W. Fischer, R.A. Henry, J.M. Hoover, G.A. Lindsay, and J.D. Stenger-Smith, Navy Case No. 72224 (September 1989).
12. J.W. Fischer, R.A. Henry, J.M. Hoover, G.A. Lindsay, and J.D. Stenger-Smith, *Makromol. Chem. Rapid Commun.*, Submitted October 1989.

## SYNTHESIS AND CHARACTERIZATION OF THIRD ORDER NONLINEAR OPTICAL MATERIALS

L. P. YU\*, M. CHEN\* and L. R. DALTON\*, X. F. CAO\*\*, J. P. JIANG\*\* and R. W. HELLWARTH\*\*

\*Department of Chemistry, University of Southern California, Los Angeles, CA-90089;

\*\*Department of Electrical Engineering and Physics, University of Southern California, Los Angeles, CA-90089.

### ABSTRACT

New polymers incorporating a variety of electroactive moieties with defined  $\pi$ -electron conjugation lengths have been synthesized and characterized by degenerate four wave mixing (DFWM) techniques. The  $\chi^{(3)}/\alpha$  values for these materials varied from  $10^{-12}$  to  $10^{-13}$  esu cm. This work has identified several promising structures with nonlinear optical activity including organometallic and purely organic materials. The preparation of composite materials has also permitted the measurement of  $\chi^{(3)}/\alpha$  as a function of the electroactive unit concentration.

### INTRODUCTION

Nonlinear optical (NLO) properties of polymers is a rapidly growing research field because of the many practical applications of polymeric materials in optoelectronic devices.<sup>1</sup> Polyconjugated materials like polydiacetylene, polyacetylene and polythiophene have been heavily investigated.<sup>1-3</sup> But the inherent deficiencies of these materials, such as poor solubility, poor thermal and environmental stability and high optical absorption losses, prevent their use in practical applications. Therefore, new materials must be found. Both theory and experiment have demonstrated that polymers with limited conjugated length can manifest NLO effects as large as polymers with extended polyconjugation.<sup>4-6</sup> It has been recognized that electron delocalization and charge transfer contribute to NLO effects, and that polymers with electron clouds of enhanced anharmonicity are expected to give rise to large NLO effects.<sup>3,7</sup> Therefore, it is reasonable to test different materials with different kinds of constituents for optical nonlinearities. Such materials would include those containing transition metals and polymers with ionic or with charge separated

.....  
Abbreviations: Fourier Transform Infrared (FTIR), Nuclear Magnetic Resonance (NMR), Ultraviolet/visible (UV/vis), Gel Permeate Chromatography (GPC), Differential Scanning Calorimeter (DSC), Dimethylformamide (DMF), Dimethylsulfoxide (DMSO).



species. With this in mind, we have extended our research to a broader survey of conjugated electroactive units. Here we report part of our effort in the synthesis and characterization of new materials exhibiting large optical nonlinearities.

### EXPERIMENTAL

**Polymer 1.** This polymer was synthesized through a precursor polymer.<sup>6</sup> The mixture of prepolymer (0.904 g, 1.97 mmol) with nitrobenzene (20 mL) and benzoyl chloride (3 mL) was refluxed for 4 hrs. The reaction mixture was poured into methanol (50 mL) and the red precipitate was collected by filtration and washed with methanol until the filtrate becomes colorless, yielding polymer 1 (1.09 g, 83%). <sup>1</sup>H NMR (DMSO-d<sub>6</sub>) δ 1.6, (broadened, 6H), 3.9, (broadened, 4H), 6.5-8.2 (broadened, 18H) ppm.

Anal. Calcd. for (C<sub>37</sub>H<sub>28</sub>N<sub>2</sub>Cl<sub>2</sub>O<sub>6</sub>)<sub>n</sub>: C, 66.56, H, 4.20, N, 4.20, Cl, 10.64%. Found: C, 66.12, H, 3.87, N, 3.75, Cl, 11.45%.

**Polymer 2.** The mixture of monomer (1,6-di(1-ethyl,2-methyl-quinolidine-6-oxy) pentane diiodide) (1.00g, 1.36 mmol) with triethyl orthofomate (0.739 g, 5.44 mmol) and pyridine (15 mL) was refluxed for one hr. The mixture was poured into THF. The precipitate was collected and washed with cold methanol. The final product was dried at 40°C under vacuum overnight, yielding polymer 2 (0.73g, 85%). <sup>1</sup>H NMR (DMSO-d<sub>6</sub>) δ 1.4, (t, J=9.0 Hz, CH<sub>3</sub>- of ethyl), 1.8, (broadened, -(CH<sub>2</sub>)<sub>3</sub>-), 3.0, (s, overlapped with water side band, 2-methyl), 4.3, (broadened, -OCH<sub>2</sub>-), 5.0 (broadened, -CH<sub>2</sub>- of ethyl), 6.5 (broadened, =CH-), 7.0-9.0, (multiple, aromatic protons).

Anal. Calcd. for (C<sub>119</sub>H<sub>145</sub>N<sub>8</sub>O<sub>8</sub>)<sub>5</sub>5H<sub>2</sub>O: C, 56.26, H, 6.11, N, 4.41%. Found: C, 56.43, H, 5.78, N, 4.40%.

**Polymer 3.** The mixture of monomer<sup>11</sup> (1.00 g) and AIBN (0.003g) was added to toluene (20 mL) in a tube. The solution was frozen and thawed twice under vacuum to remove oxygen and was then sealed. The sealed tube was immersed in a oil bath at 70°C overnight. The reaction solution was poured into ether and the polymer was collected by filtration and washed with ether. The product was then dried at room temperature under vacuum overnight, yielding polymer 3 (0.3 g, 30%).

Anal. Calcd. for (C<sub>30</sub>H<sub>32</sub>N<sub>4</sub>O<sub>3</sub>)<sub>0.3</sub>H<sub>2</sub>O: C, 71.79, H, 6.50, N, 11.17%. Found: C, 71.94, H, 6.54, N, 11.22%.

**Polymer 4.** Squaric acid (0.91 g, 7.98 mmol) was dissolved in 20 mL hot butanol and then N-methylpyrrole (0.65 g, 7.98 mmol) was added. The mixture was refluxed for 2 hrs. The dark blue precipitate was collected and washed with water and ethanol, dried at 50°C under vacuum yielding polymer 4 (1.16, 80%).

Anal. Calcd. for (C<sub>55</sub>H<sub>40</sub>N<sub>7</sub>O<sub>10</sub>)<sub>5</sub>H<sub>2</sub>O: C, 63.03, H, 4.68, N, 9.36%. Found: C, 63.07, H, 4.87, N, 9.65%.

Polymer characterization and DFWM experiments have been described in previous works.<sup>6, 12</sup>

### RESULTS AND DISCUSSION

The following materials (polymers and small molecules) have been synthesized and characterized by DFWM techniques (See Fig. 1).

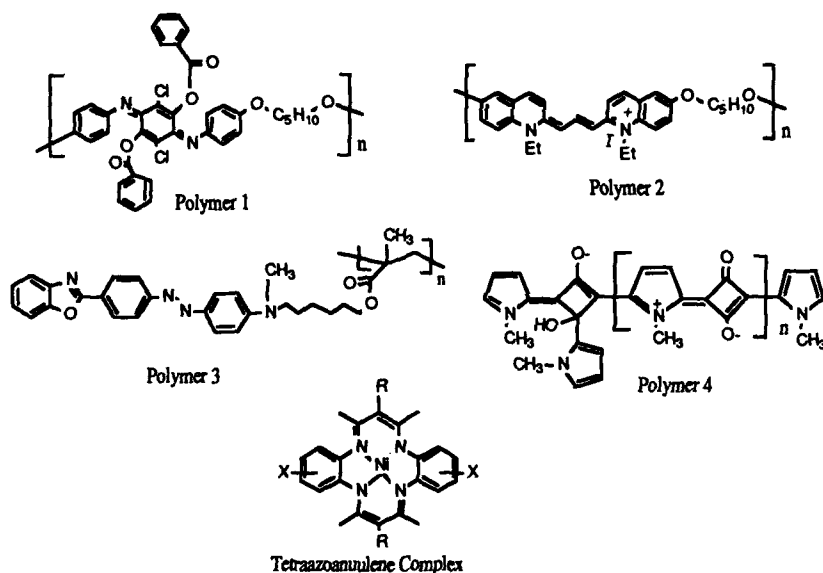
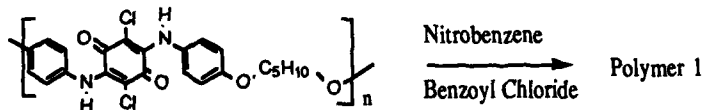


Fig. 1: Structures of NLO active materials.

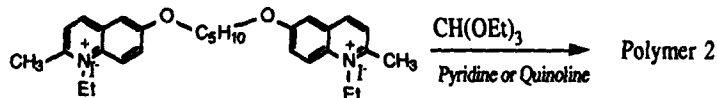
Polymer 1 is synthesized following reaction scheme 1.



Scheme 1: Synthesis of polymer 1.

The polymer structure has been confirmed by FTIR,  $^1\text{H}$  NMR,  $^{13}\text{C}$  NMR, UV/vis spectroscopic studies and elemental analysis. Fig. 2a shows the UV/vis spectrum of polymer 1. Sharp absorptions at ca. 479, 515 and 567nm can be found. Polymer 1 is fully soluble in DMF, DMSO and 1-chloronaphthene and optical quality films can be cast from these solutions. GPC measurements in DMF show that the weight average molecular weight,  $\langle M_w \rangle$ , is about 20,000 using polystyrene as a standard. This polymer is thermally stable up to 480°C.

Polymer 2 is synthesized through a well known cyanine dye formation reaction (see scheme 2).



Both pyridine and quinoline can be used as solvents. Since these solvents are not good solvents for the final products, the materials we obtained are not high molecular weight polymers. Elemental analysis showed that they have only about three repeat units. They are partially soluble in DMF, DMSO and *m*-cresol. The films can be cast from solution or from mixed solution with polycarbonate on glass slides.  $^1\text{H}$  NMR spectra shows that a broad peak at 6.5 ppm attributed to methine proton appears and the 2-methyl peak of the monomer decreased dramatically. FTIR spectra show similar features with those of model compound, 6,6'-dimethoxy-quinolidine cyanine. Fig. 2b shows the Uv/vis spectrum of polymer 2 in which absorptions appear at 540, 580 and 640 nm.

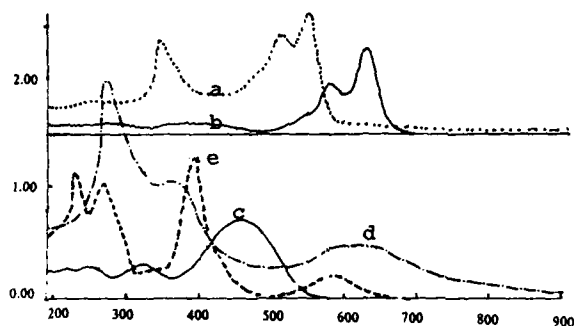


Fig. 2: Uv/vis spectra of a). Polymer 1, b). Polymer 2, c). Polymer 3, d). Polymer 4 and e). Tetraazoanulene nickel complex.

Polymer 3 is synthesized by a free radical polymerization of the corresponding  $\alpha$ -vinyl monomer.<sup>11</sup> The final polymer has MW of 4000 to 10000 (polystyrene as standard).  $^1\text{H}$  NMR,  $^{13}\text{C}$  NMR, FTIR, Uv/vis spectroscopic data and elemental analysis results confirm the structure proposed. Fig. 2c gives the Uv/vis spectrum of polymer 3. This polymer is thermally stable up to 300°C as shown by TGA studies. DSC shows  $T_g$  at 40°C and no liquid crystal transitions have been observed between 0°C-200°C.

Polymer 4 is a known polymer which was synthesized by Treibs and Jacob<sup>8</sup> with only three repeat units. We modified the synthesis procedure and obtained a polymer with a repeat units larger than five. The elemental analysis results suggest that each squaric acid unit is associated with one water molecule. TGA and DSC studies support this assumption. A weight loss of 7% accompanied by an endothermic process were observed between 50-140°C. It is partially soluble in DMF and *m*-cresol and forms blue solutions. FTIR spectra show absorption at 1775  $\text{cm}^{-1}$ (s) due to the carbonyl group of the squaric acid unit, absorption at 1640  $\text{cm}^{-1}$  (vs) due to the vinyl group in the squaric acid unit and methyl absorption is observed around 2890  $\text{cm}^{-1}$ . Fig. 2d is the Uv/vis spectrum of this polymer in which the lowest absorption band appears around 610 nm. This polymer is very interesting because it can have many resonance structures in which the charge separated structure is the most likely one.<sup>8</sup>

Tetraazoannulene complexes are synthesized according to a known procedure.<sup>9</sup> We are interested in these compounds because they contain transition metals (Ni can be replaced by Cu and Fe etc.) and they are soluble in common organic solvents. They can be derivatized by different substituents both at the R and X positions, which provide opportunity for incorporating them into polymer backbone. Fig. 2e shows the Uv/vis spectrum of compound with R=X=H, in which a window around 530 nm can be seen. This is an advantage for DFWM measurements, usually performed at 532 nm.

All these materials have been demonstrated NLO active by DFWM experiments. Table 1 summarizes the results for these materials.

Table I. NLO properties of Polymers 1-4 and Tetraazoannulene Nickel complex.

Materials	$\chi^{(3)}/\alpha$ (esu. cm) $\times 10^{13}$ at $\lambda=532$ nm
polymer 1	0.37
polymer 2	9.00*
polymer 2 in polycarbonate 10%	0.86
polymer 3	8.50*
polymer 4 in polycarbonate 10%	0.90
complex in polycarbonate 10%	2.45

\* Permanent grating has been observed in high pulse energy.

Fig. 3 shows a typical plot of the DFWM signal pulse energy versus the delay time of the backward pump beam B for polymer 1. From Fig. 3, we can see an extremely fast NLO process at zero delay time, which might be attributed to an electronic excitation contribution, and a slower process which might arise from thermal contributions. Polymers 2 and 4 show similar signal patterns. It can be noted from Table I. that polymer 2 and polymer 4 have similar  $\chi^{(3)}/\alpha$  values in polymer matrix which they are larger than polymer 1 and, in this case, might mean that the charge species and/or longer conjugation make significant contributions. The results in Table I are comparable with those of polyconjugated polymer systems such as polyacetylene and polythiophene. It demonstrates that high third order NLO effect can be observed in polymer systems with moderate conjugation lengths. In Table I, the  $\chi^{(3)}/\alpha$  value for tetraazoannulene nickel complex is very high and is comparable to those of phthalocyanine complexes.<sup>10</sup> We are now trying to incorporate this complex into a polymer backbone so that the processibility of the materials can be improved.

## CONCLUSION

The processibilities of NLO polymers can be improved by introduction of flexible chain to link electroactive unit. The polymers so obtained with moderate conjugation lengths can manifest optical nonlinearities as large as polymers with extended polyconjugations.

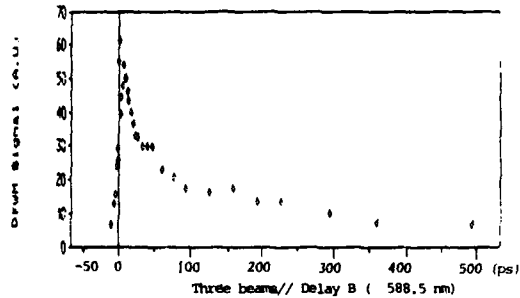


Fig. 3: Plot of DFWM signal as a function of delay time.

#### ACKNOWLEDGEMENTS

This work was supported by Air Force Office of Scientific Research contracts F49620-87-C-0100 and F49620-88-C-0071 and by National Science Foundation grant DMR-88-15508.

#### REFERENCES

1. A. J. Heeger, J. Orenstein and D. R. Ulrich. Eds. Nonlinear Optical Properties of Polymers. Symposium Proceedings; Materials Research Society, 1989, vol. 109.
2. L. Yang, R. Dorsiville, Q. Z. Wang, W. K. Zou, P. P. Ho, N. L. Yang, R. R. Alfano, R. Zamboni, R. Danieli, G. Ruani, and C. Taliani. *J. Opt. Soc. Amer. B* 1989, vol. 6, 753.
3. S. A. Jenekhe, S. K. Lo, and S. R. Flom. *Appl. Phys. Lett.* 1989, 54, 2524.
4. C. P. de Melo and R. Silby. *Chem. Phys. Lett.* 1988, 140, 537.
5. J. R. Heflin, K. Y. Wong, O. Z. Khamir and A. F. Garito. *Phys. Rev.*, 1988, B38 1573.
6. L. P. Yu and L. R. Dalton. *J. Amer. Chem. Soc.*, 1989, 111, 8699.
7. P. N. Prasad, E. Perrin and M. Samoc. *J. Chem. Phys.*, 1989, 91, 2360.
8. A. Treibs and K. Jacob. *Liebigs Ann. Chem.*, 1966, 699, 153.
9. D. A. Place, G. P. Ferrara, J. J. Harland and J. C. Dabrowiak. *J. Heterocyclic Chem.* 1980, 17, 439.
10. L. P. Yu, R. Vac, L. R. Dalton and R. W. Hellwarth. *SPIE proceedings*, 1989, vol. 1147.
11. M. Chen, L. P. Yu and L. R. Dalton. (in preparation).
12. X. F. Cao, J. P. Jiang, D. P. Bloch, R. W. Hellwarth, L. P. Yu, and L. R. Dalton. *J. Appl. Phys.*, 1989, 65, 5012.

NONLINEAR OPTICAL PROPERTIES OF TWO THIOPHENE-BASED  
POLYCONJUGATED SYSTEMS: PHOTOINDUCED ABSORPTION AND THIRD  
HARMONIC GENERATION SPECTROSCOPY

R. Zamboni, C. Taliani, G. Ruani, and A.J. Pal  
Istituto di Spettroscopia Molecolare, CNR, Via de' Castagnoli, 1, 40126 Bologna, Italy  
F. Kajzar  
CEA-IRDI, DEIN-LPEM, CEN/Saclay, 91191 Gif-sur-Yvette Cedex, France

ABSTRACT

Nonlinear optical properties of two thiophene-based conjugated polymers (PTT and PDTB) were studied by the photoinduced absorption spectroscopy and the third harmonic generation spectroscopy. The results obtained with these two methods are used to estimate the value of  $\chi^{(3)}$  in these materials. Resonant  $\chi^{(3)}$  are  $(2.0 \pm 0.2) \times 10^{-11}$  e.s.u. and  $(1.0 \pm 0.1) \times 10^{-11}$  e.s.u. for PTT and PDTB, respectively.  $\chi^{(3)}$  is shown to be related to the width of the optical gap through a sixth-power law. In PTT a vibronic structure due to the C=C stretching mode appears in the  $\chi^{(3)}$  spectrum.

INTRODUCTION

Recent studies on polyacetylene  $(CH)_x$  and polythiophene (PT) have shown that conjugated  $\pi$ -electron systems manifest high cubic susceptibilities [1,2] as well as ultrafast response time [3]. Soliton and polaron/bipolaron dynamic has been proposed as the primary factor that gives rise to the optical nonlinearity in  $(CH)_x$  and PT respectively. With the aim to study the relation between the molecular structure and the nonlinear optical properties (NLO), we have focused our attention on fused-thiophene-ring polyconjugated systems with non-degenerate ground state. Two new conducting polymers have been electrochemically synthesized, polythieno(3,2-b)thiophene (PTT; Fig. 1, left) and poly[1,4-di(2-thienyl)benzene] (PDTB; Fig. 1, right).



Figure 1: Structure of polythieno(3,2-b)thiophene (left) and poly[1,4-di(2-thienyl)benzene] (right).

The polymers have been synthesized in the form of amorphous thin films and the NLO properties have been investigated by the photoinduced absorption (PA) and wave-dispersive  $\chi^{(3)}$  third harmonic generation (THG) measurements.

## EXPERIMENTAL

Thin films of PDTB and PTT were prepared and reduced to the neutral state electrochemically [4,5]. High-quality free-standing films were detached from the electrode after swelling with suitable solvents. The thickness of the samples used for the NLO experiments ( $\approx 2500$  Å) was measured by means of a surface profiler TENCOR INSTRUMENTS mod. Alpha-step 200, with an accuracy of approximately 100 Å.

For PA measurements, the films were scratched off from the electrode, powdered, mixed with KBr, and pressed in pellets. The PA spectra were performed with a modified FTIR spectrometer (Bruker mod. 113v), in which a laser beam with photon energy above the energy gap was used to excite the neutral polymers.

THG measurements were performed by transmission as a function of the incident light wavelength (from 1.907 to 1.064  $\mu\text{m}$ ). The laser was a Q-switched Nd-Yag 13 ns pulse-duration coupled with a Quantel dye laser (TDLIII) and with a Raman shifter cell filled with  $\text{H}_2$ . A silica substrate provides the internal standard which is used as calibration.

## RESULTS AND DISCUSSION

### Third Harmonic Generation

The calibrated THG measurements on the two thin films of PTT and PDTB as a function of the incident photon energy in the 1.064-1.907  $\mu\text{m}$  fundamental wavelength range are shown in Figure 2. The results show that these polymers are highly nonlinear; in fact, we observe a three-photon resonant  $\langle \chi^{(3)}(-3\omega; \omega, \omega, \omega) \rangle$  of  $(2.0 \pm 0.2) \times 10^{-11}$  e.s.u. for PTT and  $(1.0 \pm 0.1) \times 10^{-11}$  e.s.u. for PDTB. Non resonant values are approximately a factor of 4 lower in both polymers.

Since these polymers have a substantially different optical bandgap (i.e.  $E_g(\text{PTT}) = 2.0$  eV and  $E_g(\text{PDTB}) = 2.3$  eV), we compare the dependence of  $\chi^{(3)}$  vs.  $E_g$  with the predicted dependence on the inverse of the sixth-power of the optical gap, as reported in detail in ref 6. The agreement is quite good.

The oscillations observed in the PTT THG spectrum (fig. 2, top) are separated by 1325  $\text{cm}^{-1}$  and can be interpreted as resonance enhancements due to the excited state vibronic levels of the  $\nu_{c=c}$  stretching mode. In fact, this mode is at 1292  $\text{cm}^{-1}$  in the lowest electronic excited state of the TT monomer[7].

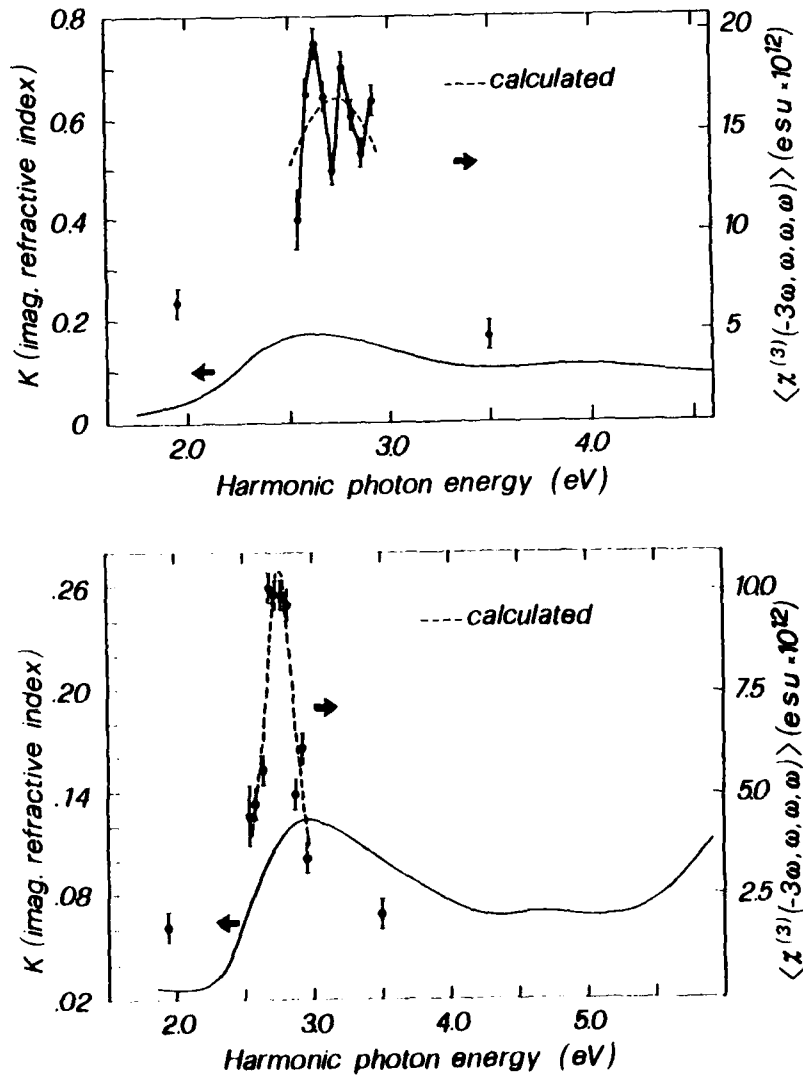


Figure 2  $\chi^{(3)}(-3\omega, \omega, \omega, \omega)$  spectra of PTT (top) and PDTB (bottom).  
 The broken curves represent calculated values;  
 lower solid lines represent the imaginary part of the refractive index.



Both the measured and the calculated  $\chi^{(3)}$  values are comparable to the values found for other systems with similar conjugation lengths, but about three orders of magnitude smaller than the one-photon resonant  $\langle \chi^{(3)}(-\omega; \omega, -\omega, \omega) \rangle$  obtained by optical Kerr effect [8]. The difference could be accounted for by the different origin of these two susceptibilities, the former (THG) being a purely electronic and coherent process connected with the polarization of the electronic cloud whereas the latter is influenced by other non-coherent phenomena (heating, level population changes) and may be dominated by them.

#### Photoinduced Absorption

The generation of electron-hole pairs by photoexcitation above the gap in semiconducting one-dimensional systems with non-degenerate ground state gives rise to new metastable electronic states (bipolarons). These states are accessible by one photon absorption. The optical absorption due to these states is very similar to that observed in the chemically-doped polymers [9]. The nonlinear refractive index associated to the shift of the oscillator strength from  $\pi-\pi^*$  transition to the near infrared transition has been proposed to be the cause of resonant nonlinear optical properties in conjugated one-dimensional systems [10].

The PA process can be described as a four-photon process by  $\chi^{(3)}(-\omega_2; \omega_1, -\omega_1, \omega_2)$  (see Fig. 3). Following this approach, we have measured the PA spectra of PTT and PDTB (Fig. 4) and we have determined  $\chi^{(3)}(\text{PA})$  values of  $1.5 \times 10^{-2}$  for PTT and  $7.7 \times 10^{-2}$  for PDTB (for more details, see ref. 11).

One should note that the very large  $\chi^{(3)}(\text{PA})$  values obtained by PA measurements involve a very slow response time, that is in the order of milliseconds. In fact, due to intrinsic experimental conditions of the PA measurements, we specifically select, among the distribution of photoexcited species, those species that have a lifetime which is in the same order of magnitude of the modulation frequency of the laser excitation. In view of this,  $\chi^{(3)}(\text{PA})$  derived from the shift in the oscillator strength is characteristic of photoexcited species that have a lifetime of hundreds of milliseconds.

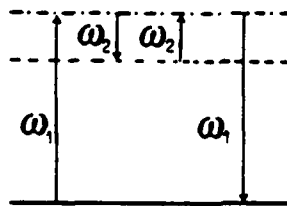


Figure 3: Schematic representation of PA as a four-photon process.

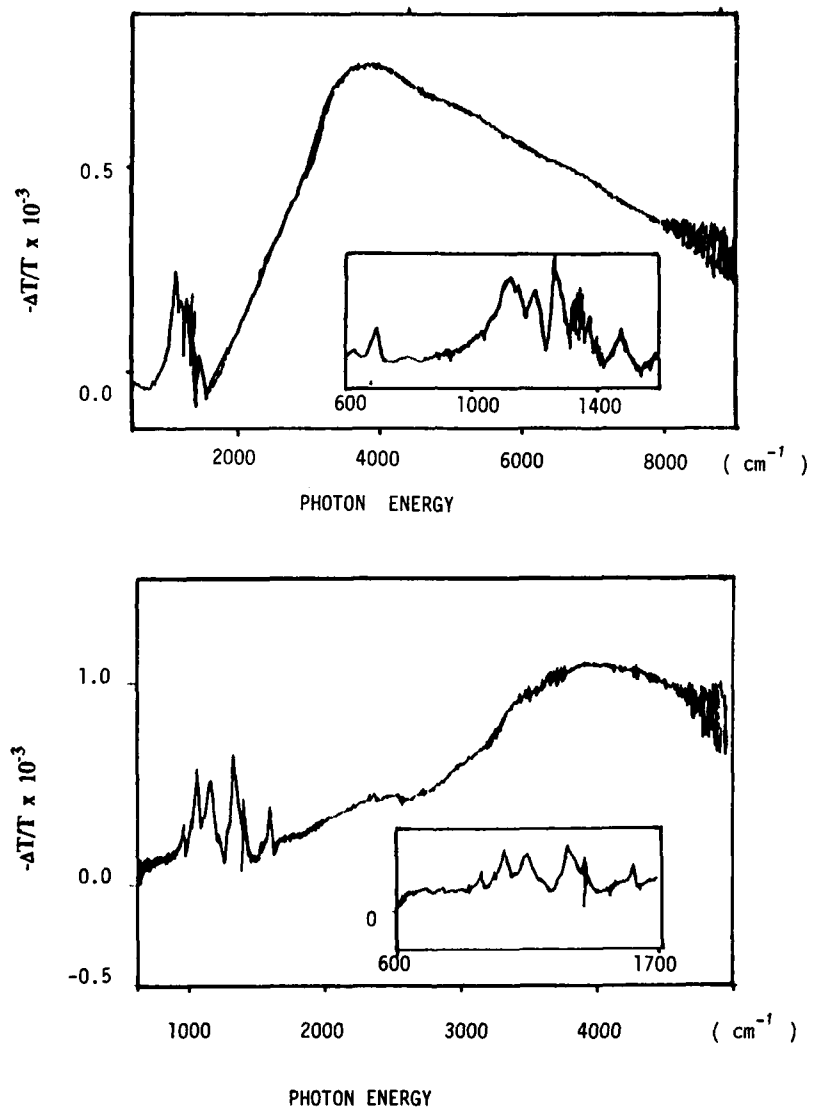


Figure 4: Photoinduced absorption spectra of PTT (top) and PDTB (bottom).

In conclusion, we have measured the third-order nonlinear susceptibility of two new polyconjugated systems with two different methods: wave-dispersed THG and PA. The large difference between the so-obtained values is mainly due to the fact that the  $\chi^{(3)}$ (PA) is measured in the millisecond timescale instead of the nanosecond timescale for THG processes. Nevertheless, we can conclude that both processes are related to intrinsic instability in the polyconjugated one-dimensional systems due to charge-phonon interaction.

#### ACKNOWLEDGMENTS

The authors wish to thank Dr. P. Ostoja for the SEM measurements, and G. Pizzochero, S. Guerri, G. Tasini, and P. Mei for valuable technical assistance.

#### REFERENCES

1. F. Kajzar, S. Etemad, G.L. Baker, and J. Messier, *Synth. Met.* **17**, 563 (1987).
2. F. Kajzar, J. Messier, C. Sentein, R.L. Elsenbaumer, and G.G. Miller, *Proceed. of SPIE Conf., San Diego, August 6-11, 1989* (in press).
3. P.N. Prasad, in Nonlinear Optical Effects in Organic Polymers, edited by J. Messier, F. Kajzar, P.N. Prasad, and D. Ulrich (Kluwer, Dordrecht, 1989), p. 351.
4. R. Danieli, C. Taliani, R. Zamboni, G. Giro, M. Biserni, M. Mastragostino, and A. Testoni, *Synth. Met.* **13**, 325 (1986).
5. R. Danieli, P. Ostoja, M. Tiecco, R. Zamboni, and C. Taliani, *J. Chem. Soc., Chem. Commun.* 1473 (1986).
6. F. Kajzar, G. Ruani, C. Taliani, and R. Zamboni, submitted to *J. Chem. Phys.*
7. F. Bertinelli, A. Brillante, P. Palmieri, and C. Taliani, *J. Chem. Phys.* **66**, 51 (1977).
8. L. Yang, R. Dorsinville, Q.Z. Wang, W.K. Zou, P.P. Ho, N.L. Yang, R.R. Alfano, R. Zamboni, R. Danieli, G. Ruani, and C. Taliani, *J. Opt. Soc. Am. B* (in press).
9. C. Taliani, R. Danieli, R. Zamboni, G. Ruani, and P. Ostoja, in Springer Series in Solid State Sciences, Vol. 76, edited by H. Kuzmany, M. Mehring, and S. Roth (Springer-Verlag, Heidelberg, 1987), p. 322.
10. A.J. Heeger, D. Moses, and M. Sinclair, *Synth. Met.* **15**, 95 (1985).
11. G. Ruani, A.J. Pal, R. Zamboni, C. Taliani, and F. Kajzar, *Proceed. NATO-ARW, Mons, September 3-8, 1989* (in press).

ROTATIONNAL DIFFUSION OF CHROMOPHORES INSIDE A GLASSY POLYMERIC FILM  
STUDIED BY ELECTROOPTICAL INTERFEROMETRY

MEYRUEIX R. AND MIGNANI G.

Rhône-Poulenc Recherches, 85 avenue des Frères Perret, B.P. 62,  
69192 SAINT FONS CEDEX - France

ABSTRACT

Perot Fabry interferometry under oblique incidence provides a powerful tool for the determination of the complex values of the independent components of the tensors  $\chi^2(-\omega; \omega, 0)$  and  $\chi^3(-\omega; \omega, 0, 0)$  of poled films. Deorientation of Disperse Red One chromophore in a poled film can be followed by the decrease with time of two order parameters. In the short term regime, the relaxation times of this process are spread over a broad spectrum. By comparing the chromophore dynamics in PMMA, PS and SAN at different temperatures, it appears that free volume and secondary transition concepts cannot fully explain the chromophore behavior. Chromophore dipole/Polymer dipole interactions are invoked in order to explain the slow deorientation rate in SAN.

Introduction

Poled polymers films containing conjugated charge transfert chromophores appear to be very promising for application in emerging guided wave integrated technologies [1]. The additive acentric order required for second order non linear optical (NLO) processes is usually achieved by poling the film above the glassy temperature  $T_g$  and freezing the induced polar order of the chromophores at  $T < T_g$  [2,3]. It is now well established that deorientation occurs in the glassy state over periods of months [4-6]. This residual mobility is usually interpreted as a consequence of the dynamics processes by which glassy polymers undergo physical aging [6,7].

In the first part of this paper, we present an electrooptical (E/O) method for the measurement of the complex components of the tensors  $\chi^2(-\omega; \omega, 0)$  and  $\chi^3(-\omega; \omega, 0, 0)$  of a poled film. Two order parameters of the chromophores can be measured. A simplified version of this method is used in the second part to compare the dynamics of the Disperse Red One (DR1) azo dye in PMMA, PS and Poly(Styrene Acrylonitrile) (SAN).

E/O Measurement of order parameters of NLO chromophores in a poled polymeric film

In the case of monodimensional CT chromophores, the quadratic susceptibility  $\chi^2$  is related to the microscopic static value of the hyperpolarisability  $\beta_{uuu} = \beta$  by the relation [3] :

$$\chi^2_{ijk}(\omega_1, \omega_2) = \beta_{uuu} Q(\omega_1, \omega_2) \langle \cos(i,u) \cos(j,u) \cos(k,u) \rangle \quad (1)$$

Where  $Q(\omega_1, \omega_2)$  describes the wavelength dependence of  $\beta$ . Eq.(1) shows that NLO effects provide a powerful method of measurement of the order parameters  $\rho_{ijk} = \langle \cos(i,u) \cos(j,u) \cos(k,u) \rangle$  of the dopant. In one of the earliest work, Blumenfeld et al. [4] have studied the deorientation of NLO azodyes in PMMA by linear electrochromism. Other have used second harmonic generation [5,6,8,15], Mach Zender interferometry [3,9,13], polarimetry [7,10], attenuated total reflection [11] or Perot Fabry interferometry with continuously varying wavelength [12].

In our Perot Fabry under oblique incidence method (PFOI), the sample is a plane 4-layered media : glass substrate/thin conducting layer (Au or  $\text{SnO}_2$ )/polymer film/Au. This sample is illuminated under incidence  $i$  by s and p polarized waves (Fig.1).

The alternating voltage  $\Delta V$  ( $\Omega = 0,5 \text{ Hz}$ ) applied to the poled film modulates its two independent dielectric principal values  $\epsilon_{11}$  and  $\epsilon_{33}$  at the frequency  $\Omega$  according to :

$$\Delta \epsilon_{ii} = 2 \chi_{i i 3} \cdot \frac{(\Delta V)}{L} \quad i = 1 \text{ and } 3 \quad (2)$$

and at  $2\Omega$  according to

$$\Delta \epsilon_{ii} = 3 \chi_{i i 33} \frac{(\Delta V)^2}{L} \quad i = 1 \text{ and } 3 \quad (3)$$

These variations of the dielectric constant of the film modulate the intensity transmission factor  $T$  ( $T = T_s$  or  $T_p$ )

$$\frac{L}{2} \frac{\Delta T}{\Delta V} = \chi'_{i 13} \frac{\partial T}{\partial \epsilon'_{11}} + \chi''_{i 13} \frac{\partial T}{\partial \epsilon''_{11}} + \chi'_{i 33} \frac{\partial T}{\partial \epsilon'_{33}} + \chi''_{i 33} \frac{\partial T}{\partial \epsilon''_{33}} \quad (4)$$

$$\frac{L^2}{3} \frac{\Delta T}{(\Delta V)^2} = \chi'_{i 133} \frac{\partial T}{\partial \epsilon'_{11}} + \chi''_{i 133} \frac{\partial T}{\partial \epsilon''_{11}} + \chi'_{i 333} \frac{\partial T}{\partial \epsilon'_{33}} + \chi''_{i 333} \frac{\partial T}{\partial \epsilon''_{33}} \quad (5)$$

In Eq. (4) and (5) the superscripts ' and " refer to, respectively, the real and the imaginary parts of the tensor components. The next step is to compute the partial derivatives of  $T$ .

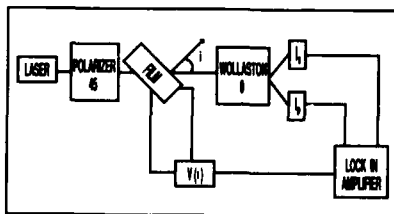


Fig.1 PFOI experimental set up  
The transmitted intensities  $I_x$  and  $I_y$  are modulated by the alternating voltage  $V$  applied to both faces of the film.

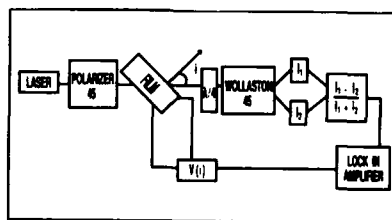


Fig.2 Polarimetric version of PFOI  
The signal is proportional to the phase shift between s and p waves.

The transmission coefficient  $T$  of the 4-layered sample is entirely determined by the thickness and the complex dielectric tensor of each layer. Under the applied voltage, the film becomes uniaxial (optical axis along the film normal) and light propagates through an anisotropic absorbing layered medium.

Since  $s$  and  $p$  waves are in principal dielectric planes of the film, there is no coupling between ordinary ( $s$ ) and extraordinary ( $p$ ) modes of propagation in the film (see [17] for detailed calculations). So we have :

$$\text{For } s \text{ polarization : } \epsilon_{t_{11}} = \epsilon_{11} \quad (6)$$

$$\text{For } p \text{ polarization : } \frac{\sin^2 i}{\epsilon_{33}} + \frac{\epsilon_{t_{11}} - \sin^2 i}{\epsilon_{11}} = 1 \quad (7)$$

At this point,  $T_s$  and  $T_p$  and their partial derivatives are computed by standard numerical methods [17].

The thickness is not exactly constant over the entire film surface. When the laser beam is positioned on a fringe of equal thickness,  $T$  is modulated by the imaginary part of the non linear susceptibilities only. Between two fringes, both  $X'$  and  $X''$  modulate  $T$ . By this way, the complex values of  $X_{113}$ ,  $X_{333}$ ,  $X_{133}$ ,  $X_{333}$  can be evaluated from equations (4) and (5) and from the measurement of  $\Delta T_s$  and  $\Delta T_p$  at  $\Omega$  and  $2\Omega$ .

Moreover, if  $P_1(\cos\theta)$  is the  $l^{\text{th}}$  Legendre polynomial, we have [3] :

$$X_{113} = \langle P_1(\cos\theta) \rangle - \langle P_3(\cos\theta) \rangle \quad (8)$$

$$X_{333} = 3\langle P_1(\cos\theta) \rangle + 2\langle P_3(\cos\theta) \rangle \quad (9)$$

So, the two order parameters  $\langle P_1 \rangle$  and  $\langle P_3 \rangle$  of the chromophores inside the film can be measured by PFOI. Notice that  $\langle P_2 \rangle$  and  $\langle P_4 \rangle$  can only be extracted from the  $X^3$  components if their microscopic origins are well identified [13].

The rigorous analysis of the E/O polarimetric experiment (Fig. 2) [7,10] can be obtained from equations (4), (8), (9), in which the intensity transmission coefficient  $T=tt'$  ( $t$  : amplitude transmission coefficient) is replaced by the output signal :

$$S = \frac{tstp' - ts'tp}{tsts' + tptp'} \quad (10)$$

$S$  is a linear combination of  $\langle P_1 \rangle$  and  $\langle P_3 \rangle$  with coefficients calculated by the above described method.

### Experimental

The three host polymers were : PMMA (ORKEM,  $M_w = 124000$ ,  $M_n = 64000$ ), PS (DOW,  $M_w = 1130000$ ,  $M_n = 17000$ ) and polystyrene acrylonitrile (SAN) (BASF,  $M_w = 120000$ ,  $M_n = 63000$ , Molar styrene content : 58 %).

Polymer plus 7,5 wt % of Disperse Red One (DRI : 4-(N ethyl-N (2 hydroxyethyl)amino 4' nitroazobenzene) was dissolved in methylisobutyl-cetone and casted onto  $\text{SnO}_2$  coated slides. Films (10  $\mu\text{m}$  thick) were dried under vacuum for 16 h at  $T_g + 10^\circ\text{C}$ . The residual solvent content was less than 0,2 wt %. Further drying did not affect the dynamics of the dopant. A thin gold layer was sputtered onto the film surface. Samples were poled in situ on the optical set up ( $E_{\text{pol}} = 30 \text{ volts}/\mu\text{m}$ ,  $\theta_{\text{pol}} = 105^\circ\text{C}$ ,  $t_{\text{pol}} = 60 \text{ s}$ ). Orientation of the dopant was kept constant during the film cooling by setting  $V_{\text{pol}}/T = \text{Cte}$  as the temperature was decreased.

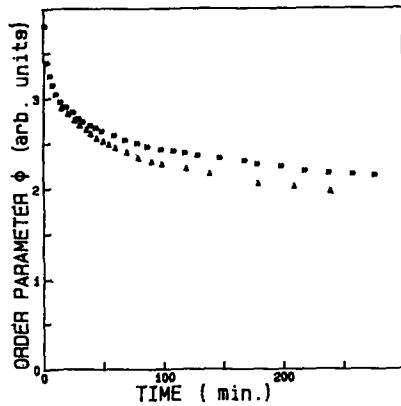


Fig.3 Decay of the order parameter  $\phi(t)$  PMMA/DRI guest-host system (30°C). Aging times at 60°C. \*\* : 64h.  $\Delta\Delta$  : 1 h.

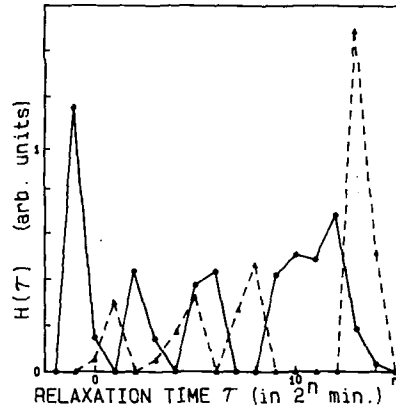


Fig.4 Relaxation time spectra corresponding to Fig.3. Dashed line : aging 64 h at 60°C.

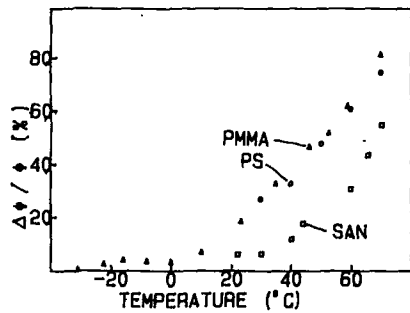


Fig.5 Relative decay of the order parameter during the 100 first minutes after the poling field removal.

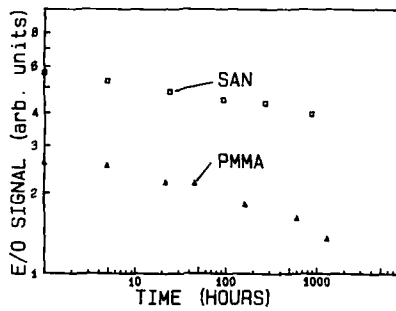


Fig.6 Long term relative decay of the order parameter in PMMA plus 7.5 wt % DRI and SAN plus 13 wt % DRI.

The chromophores orientation was measured by the E/O polarimetric version of the PFOI method. Taking into account the size of the HeNe laser beam ( $\lambda = 633 \text{ nm}$ ), the detected signal was proportional to the order parameter  $\theta = 0.025\langle P_1 \rangle + \langle P_3 \rangle$ .

#### Dynamics in the glassy state

The decrease of the order parameter  $\theta$  after the removal of the poling field is plotted Fig. 3. An instantaneous decrease of the signal is observed at  $t = 0^+$ . It reflects a  $\chi^3(-\omega; \omega, 0, 0)$  effect [12,13] which in the following will be systematically ignored.

The spectrum  $H(\tau)$  of the order parameter  $\theta(t)$  can be defined by [14] :

$$\theta(t) = \int_0^{\infty} H(\tau) \exp(-t/\tau) d(\text{Log}\tau) \quad (11)$$

In the short term regime, the spectrum  $H(\tau)$  of DRI in PMMA at 30°C is spread over more than four decades. Aging of the polymer prior to the field removal increases the relaxation times (Fig. 4). This phenomenon can be reproduced many times by refreshing the polymer at  $T > T_g$  and has been interpreted as a decrease of the polymer free volume [6]. A temperature decrease stabilizes the dopant orientation (Fig.5). In the case of PMMA, dopant motion is almost frozen below 0°C. All these results suggest that DRI behave like rigid rods dispersed in more or less constrained sites in the polymer [7]. In this model, magnitude and temperature of the secondary transition of the host polymer would be of great importance for the stabilization of the dopant orientation.

The glassy temperatures of the DRI doped PMMA, PS and SAN are similar, 96, 95 and 95°C respectively. In contrast, PMMA exhibits a well marked secondary transition near 5-15°C whereas secondary effects are weak in PS and SAN, and occur above  $T_g = 40-50^\circ\text{C}$  [16]. Surprisingly, the deorientation of DRI, measured by the relative decay of the order parameter  $\theta$  during the first 100 minutes, is comparable in PMMA and PS but much slower again in SAN (Fig. 5). The same result occurs again in the long term regime (Fig.6).

This experimental evidence supports the possibility of dopant/polymer molecular interactions [6] and/or dipolar coupling with residual internal field [8].

In the case of SAN, the oriented polymer dipoles maintain a residual directing field  $E_d(o)$  after the poling field removal.  $E_d(o)$  is the superposition of the directing field  $E_d(\text{pol})$  under  $+E_{p,01}$  in the rubbery state ( $T > T_g$ ) and of the directing field under  $-E_{p,01}$  in the glassy state. Following the Onsager calculation [19], it is easy to see that

$$\frac{E_d(o)}{E_d(\text{pol})} = \frac{2\epsilon_g + 1}{2\epsilon_r + 1} \cdot \frac{2\epsilon_r + n^2}{2\epsilon_g + n^2} \left[ 1 - \frac{\epsilon_g}{\epsilon_r} \cdot \frac{2\epsilon_r + 1}{2\epsilon_g + 1} \right] \quad (12)$$

Where  $n \approx 1.5$  is the SAN refractive index,  $\epsilon_r \approx 10$  and  $\epsilon_g \approx 3$  are the static dielectric constants in the rubbery and the glassy states. Thus,  $E_d(o)$  does not exceed 10 to 20 % of its value during the poling and cannot explain the DRI stability in SAN.

Assuming dipole moments,  $\mu_1 \approx 8\text{D}$  and  $\mu_2 \approx 3\text{D}$  for the DRI and the nitrile group in the SAN respectively, the dipole/dipole rotational energy barrier experienced by the DRI is approximatively  $\mu_1 \mu_2 / 2 \text{ ed}^3$  and remains greater than the thermal energy  $kT$  at 300 K at distances  $d$  up to  $8 \text{ \AA}$  larger than the monomers length.

Clearly a more detailed analysis is needed but this crude interpretation of the DRI/SAN interactions already suggests that the DRI deorientation is strongly dependant of the CN groups rotational diffusion. The smaller mobility of these side chain groups [18] may explain the increased stability of the orientation of DRI in SAN.



References

1. D.R.Ulrich, *Mol.Cryst.Liq.Cryst.*, 160 (1), 31 (1988).
2. G.R.Meredith, J.G.Van Duren, D.J.Williams, *Macromol.*, 15, 1385 (1982).
3. K.D.Singer, M.G.Kuryk, J.E.Sohn, *J.Opt.Soc.Am.B* 4 (6), 908 (1987).
4. L.A.Blumenfeld, F.P.Chernyakovskii, V.A.Gribanov, I.M.Kanerskii, *J.Macromol. Sci. - Chem A*, 6 (7), 1201 (1972).
5. H.L.Hampsch, J.Yang, G.K.Wong, *Macromol.*, 21, 526 (1988).
6. H.L.Hampsch, J.Yang, G.K.Wong, J.M.Torkelson, *Pol. Com.*, 30, 40 (1989).
7. R.Meyrueix, G.Mignani, *Int.Congr.Opt.Sci.Eng.of SPIE Int.Soc.Opt.Eng. Paris, April 24-28, Paper 112728, (1989).*
8. M.A.Mortazavi, A.Knoesen, S.T.Kowel, B.G.Higgins et al., *J.Opt.Soc.Am. B*, 6 (4), 733 (1989).
9. M.Sigelle, R.Hierle, *J.Appl.Phys.*, 52, 4199 (1981).
10. G.Khanarian, T.Che, R.N. De Martino et al. *SPIE*, Vol. 824, p.72 (1987).
11. G.H.Cross, I.R.Girling, I.R.Peterson, N.A.Cade, *Elect.Lett.*, 21
12. H.Uchiki, T.Kobayashi, *J.Appl.Phys.*, 64 (5), 2625 (1988).
13. M.G. Kuzyk, C.W.Dirk, *Appl.Phys.Lett.*, 54 (17), 1628, (1989).
14. J.D.Ferry, *Viscoelastic properties of polymers*, Wiley, (1980).
15. G.T.Boyd, *Thin Solid Films*, 152, 295 (1987).
16. L.C.E.Struik, *Polymer*, 28, 57 (1987).
17. P.Yeh, *J.Opt.Soc.Am.*, 69, 742 (1979).
18. C.Ye, N.Minami, T.J.Marks, J.Yong, G.K.Wong, *Macromol.*, 21 2999, (1988).
19. C.J.F.Böttcher, *Theory of electrical polarization*, Elsevier, (1973).

SECOND ORDER NONLINEAR OPTICS AND POLYMER PHYSICS OF CORONA POLED,  
DOPED POLYMER MATERIALS

HILARY L. HAMPSCH\*, JIAN YANG\*\*, GEORGE K. WONG\*\*, JOHN M.  
TORKELSON\*\*\*

\*Department of Materials Science and Engineering; \*\*Department of Physics and Astronomy;  
\*\*\*Department of Chemical Engineering; Northwestern University, Evanston, Illinois 60208.

INTRODUCTION

Doped glassy polymers have been examined as potential materials for nonlinear optical (NLO) device applications[1-11]. In these systems, dopants with excellent nonlinear optical capabilities are dispersed in glassy polymer matrices with good physical properties to make versatile and efficient NLO materials[1-4]. The optical technique of second harmonic generation (SHG), conversion of light of frequency  $\omega$  to light of frequency  $2\omega$ , is performed as a function of time to examine the temporal stability of NLO dopant orientation in the polymer matrix[1-4]. Through the use of poling, the NLO dopants are aligned into the noncentrosymmetric orientation required for SHG to occur[1-4,7]. Polymeric NLO materials have a number of advantages over the current commercial inorganic crystals, including ease of fabrication and processability, low laser damage, low cost, and excellent chemical and physical resistance[8-10]. Due to the relaxation behavior characterizing glassy polymers even at temperatures well below the glass transition temperature  $T_g$ , the dopants can disorient as a function of time following poling[1-4,12,13]. This results in a loss of optical performance with time. The purpose of this work is to examine the basic polymer physics that govern the temporal stability of the dopant orientation and disorientation and related optical behavior as a function of the local microenvironment surrounding the NLO dopants. Systems studied include bisphenol-A-polycarbonate (PC), polystyrene (PS) and poly(methyl methacrylate) (PMMA) doped with well characterized NLO dyes such as 4-dimethylamino-4'-nitrostilbene (DANS) and 4-amino-4'-nitroazobenzene (or disperse orange 3, DO3).

Second order NLO effects are only observed in systems when the dopants are oriented noncentrosymmetrically in the polymer matrix[8]. Contact[1] and corona [2-7] poling, both involving large electric fields imposed across the polymer film, are used to orient the NLO chromophores. Corona poling creates the electric field via discharge-generated ions that are accelerated towards the film surface. The bottom of the sample is grounded, so a large field is produced across the film normal to the surface and the highly polar dopants with large dipole moments align in the field direction. Poling can be performed at any temperature as long as the polymer segments have enough mobility (or the polymer has enough local free volume) to allow the dopants freedom to rotate along the electric field vector[1]. When the orienting field is generated by a corona discharge, significant SHG signal can be observed even when poling doped PMMA films at room temperature. This is not observed when using contact poling. When the applied field is removed, the relaxation and mobility processes in the polymer release the dopant from its field-imposed orientation. Dopants in a local microenvironment where there is sufficient mobility are free to rotate out of alignment and thus no longer contribute to the SHG intensity (experimentally seen as a decay of the SHG intensity with time). In-situ studies allow measurement of the SHG intensity during and after poling while the sample is in the beam path; both the rotation of the dopant into alignment during poling and the intensity decay after the applied field is removed can be examined without moving the sample and introducing error[1].

The angle of dopant orientation is related to the observed SHG intensity. By observing changes in the SHG intensity with time, information can be obtained about the dopant orientation and its relationship with the segmental mobility and free volume of the local microenvironment surrounding the NLO dopant. Assuming a free gas approximation, the poled second order nonlinear susceptibility is given by[8-10]

$$\chi^{(2)}_{333} = NF\beta_{zzz} \langle \cos^3\theta \rangle \quad (1)$$

where  $\chi^{(2)}_{333}$  is the second order nonlinear optical susceptibility and is the tensor component responsible for SHG.  $N$  represents the number of dopants,  $F$  is a local field factor, and  $\beta$  is the second order hyperpolarizability.  $\beta$  is a molecular parameter describing the delocalization in the dopant causing the NLO response, and relates the microscopic second order NLO behavior to the

macroscopic NLO behavior. The subscript "3" refers to the direction of the orienting (poling) field and "z" represents the axis of the molecule parallel to the molecular dipole moment (assuming one predominant component of the molecular tensor).  $\theta$  represents the angle between the z and 3 directions[9]. In addition, a relationship for the observed SHG intensity and the  $\chi^{(2)}$  parameter has been approximated for the system used in this experiment such that[1]

$$\chi^{(2)}_{\text{film}} = (I_{\text{film}}/I_Q)^{1/2} (2/\pi) (n^3/l^2)^{1/2}_{\text{film}} (l_c^2/n^3)^{1/2}_Q \chi^{(2)}_Q \quad (2)$$

where the subscript Q represents a quartz reference used to normalize continuously the data, I is the SHG intensity,  $I_{\text{film}}/I_Q$  is the experimentally measured intensity ratio, n is the index of refraction, l is the film thickness, and  $l_c$  is the coherence length of the quartz ( $\sim 20\mu\text{m}$ ) [8-10]. This development involves many assumptions[3,9], but it can be shown[3,8-10] that in all cases the observed SHG intensity can be related directly to the dopant orientation, and thus to the relaxation behavior of the surrounding local microenvironment.

Physical aging[1,3,12,13], or sub-T<sub>g</sub> annealing, causes changes in the relaxation times of the chain segments by changing the local density and mobility. The aging process can be described as follows: as an amorphous polymer is cooled from the melt or rubbery state, it passes through a glass transition (T<sub>g</sub>) to an initial glassy state at a given temperature T<sub>a</sub> known as the aging temperature. Since the polymer glass is a nonequilibrium supercooled liquid, the thermodynamic variables including entropy and enthalpy will change with time. The specific volume of the material will spontaneously decrease, tending towards its equilibrium value. The rate of this change and its magnitude are dependent on the aging temperature T<sub>a</sub>, but can be significant in some materials even at room temperature. The decrease in specific volume causes a densification of the material, and a decrease of the amount of local free volume in the polymer matrix. In addition, photochromic studies[12] have shown that the amount and distribution of local free volume both change during aging, with larger pockets of free volume decreasing in size more rapidly than smaller pockets. Thus, as the amount of local free volume decreases, chain packing increases, and the segmental mobility of the polymer chains decreases. This will decrease the amount of rotational freedom available to the NLO dopant. If aging is performed during the poling process, the polymer segments will be allowed to densify around oriented dopants, making it more difficult for them to rotate out of their imposed orientation following the removal of the applied field. This will improve the temporal stability of the NLO material. If aging is performed before poling, the polymer will be densified around randomly oriented dopants. This will decrease the number of dopants in regions of sufficient mobility to have the freedom to orient in response to the applied corona field. In the studies of aging before poling described here, poling is performed at 25°C or 60°C, temperatures well below the glass transition ( $\sim 85-95^\circ\text{C}$  for the doped samples), so that the thermal history created by the aging will not be erased during poling. It would thus be expected that aging before poling will decrease the magnitude of the SHG intensity that can be achieved during poling. By examining physical aging before and during poling using NLO techniques, a sensitive measure of polymer mobility is obtained.

## EXPERIMENTAL

Details of film preparation and the optical apparatus are described elsewhere [1,2]. High molecular weight PC, PMMA and PS films doped with 4 wt.% optical chromophores are spun to a final film thickness of 1.5-2.5  $\mu\text{m}$ . A week long drying procedure (involving temperatures ranging from 25°C to 100°C under ambient and vacuum conditions) ensures that the maximum amount of solvent is removed before the experiments begin. Solvent removal is followed using absorbance spectroscopy. The glass transition temperature was measured using differential scanning calorimetry (Perkin Elmer DSC-2, 10°C/min) to be about 85°C for the doped PMMA films, 95°C for the doped PC films, and about 88°C for the doped PS films. Thermal history is erased by heating the films 25°C above T<sub>g</sub> for at least 3 hours before each experiment. The erasure is important in ensuring the minimum sample-to-sample variation due to changes in thermal history[3]. SHG intensities are measured on a QuantaRay q-switched Nd:YAG laser with a 1.064 $\mu\text{m}$  fundamental (SHG intensity observed at  $\lambda=532\text{nm}$ ). The corona discharge is generated by a tungsten needle biased with -3000V across an air gap (relative humidity 50%) of 0.6 cm normal to the polymer film.

## RESULTS AND DISCUSSION

Physical aging is performed before and during poling in order to decrease and redistribute the local free volume and decrease segmental mobility around the NLO dopants. Aging before poling decreases the fraction of dopants able to orient (indicated by decreased SHG intensity) but does not affect the shape of the SHG intensity curve. This is due to decreased local free volume and segmental mobility reducing the rotational mobility of the dopant in the matrix. Figure 1 examines the

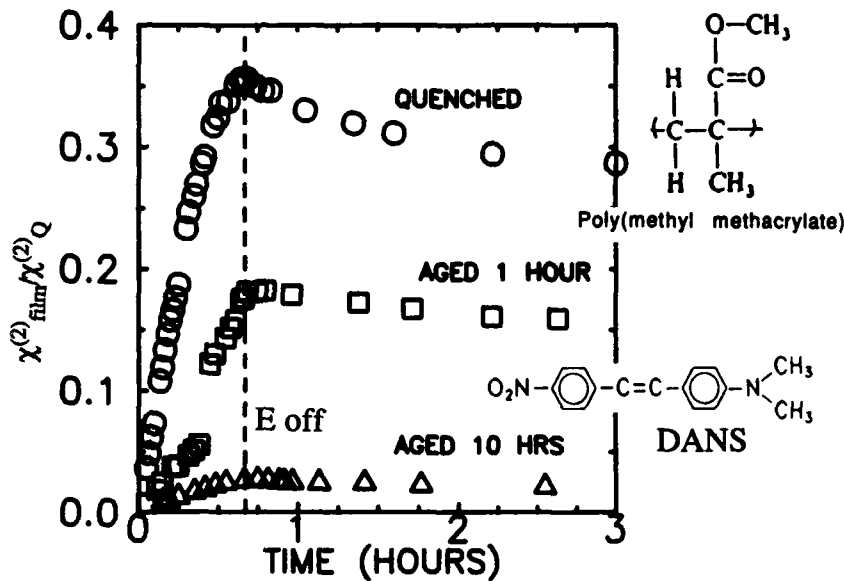


Fig 1. The effect of physical aging at 25°C before corona poling in PMMA+4% DANS (4-dimethylamino-4'-nitrostilbene) (poled @ 25°C, 40 minutes). Films are quenched (O), or aged for 1 hour (□) or 10 hours (△) before poling. Dashed line indicates time when the electric field is removed.  $\chi^{(2)}_{\text{film}}$  is the second order nonlinear optical susceptibility of the doped film and is proportional to  $\langle \cos^3\theta \rangle$ , where  $\theta$  is the angle between the electric field lines and the dopant molecular axis.  $\chi^{(2)}_{\text{film}}/\chi^{(2)}_Q$  (where  $\chi^{(2)}_Q$  is the second order susceptibility of a quartz reference) is proportional to  $[I_{\text{film}}/I_Q]^{1/2}$ , where  $I_{\text{film}}$  and  $I_Q$  are the SHG intensities of the sample and the quartz reference, respectively. Error limits are the size of the symbols in the figure.

SHG intensity and related dopant orientation in PMMA +4 wt.%DANS films as a function of aging time before poling. The ratio of  $\chi^{(2)}_{\text{film}}/\chi^{(2)}_Q$  (related to  $(I_{\text{film}}/I_Q)^{1/2}$  and  $\langle \cos^3\theta \rangle$ ) is plotted versus time in hours for samples aged for 0, 1, or 10 hours at 25°C before corona poling (poled @ 25°C for 40 minutes). At time equal to zero, the field is applied, and the dopants are free to rotate in response to the gradient across the material. The dashed line indicates the time the corona field is shut off. As the amount of time before aging increases, the magnitude of the achievable SHG intensity decreases. The sample aged 1 hour before poling has a magnitude of only 40% of the magnitude of the quenched sample at the time the field is removed. After the applied field is removed, the dopants in regions of sufficient local free volume or segmental mobility are free to rotate out of their poling-imposed orientation and thus decrease the net SHG

intensity. The shapes of the normalized intensity curves are independent of aging time before poling. This indicates that the number of dopants able to orient does not affect the mechanism of dopant orientation and disorientation.

Figure 2 summarizes aging data for PS and PMMA films aged for 0, 1, or 10 hrs at 25°C before poling at 60°C or 25°C. The value of  $\chi_{\text{film}}^{(2)}/\chi_Q^{(2)}$  at the time the applied field is removed as a function of aging time before poling is plotted in Figure 2. It can be seen in all cases that as aging time before poling increases, the amount of dopants that can orient into the field direction in response to the same applied field decreases. Films poled at 60°C show greater magnitudes of signal intensity, particularly at shorter aging times before poling than those films poled at 25°C. It is interesting to note that the doped PMMA films show a greater effect of aging than the doped PS films poled under the same conditions, as seen by a greater decrease in achievable orientation as a function of aging time. The magnitudes of  $\chi_{\text{film}}^{(2)}/\chi_Q^{(2)}$  at the time the field is removed for the doped PS films decrease almost linearly with aging time before poling for the first 10 hours, but in the doped PMMA films the magnitude decreases more rapidly at shorter times. These results

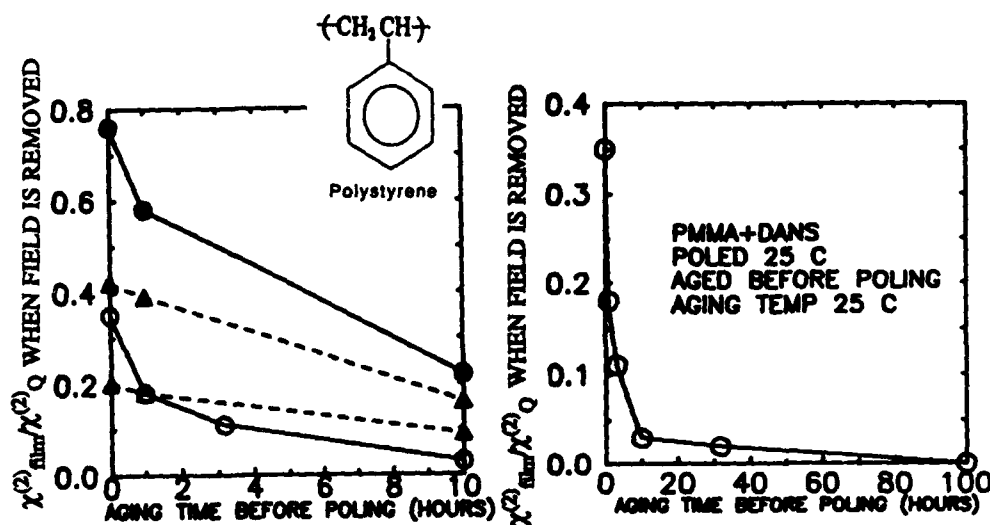


Fig 2. The effect of aging time before poling on the value of  $\chi_{\text{film}}^{(2)}/\chi_Q^{(2)}$  when the applied field is removed. PMMA+4%DANS films poled at 25°C(O) or 60°C(●) and PS+4% DANS films poled at 25°C(Δ) or 60°C(▲).

Fig 3. The effect of aging time before poling on the value of  $\chi_{\text{film}}^{(2)}/\chi_Q^{(2)}$  when the applied field is removed over a longer time scale. PMMA+4%DANS films poled at 25°C(O). Note that no signal is obtained for the films aged 100 hrs before poling.

indicate that PMMA shows more efficient aging on the size scale related to the dopant than PS at aging temperatures of 25°C for the time frames indicated in the figure. Figure 3 shows a plot of a PMMA+4%DANS films aged at 25°C before poling at 25°C over longer time periods. This indicates that the greatest effect of aging occurs under these conditions over the first 10 hours, but that a measurable decrease in SHG magnitude still occurs over the next several days. After aging for 100 hours at 25°C before poling, no SHG intensity was observed. This implies that no dopants were able to orient in response to the applied field and that the aging before poling process

annealed out regions of sufficient local free volume and mobility to allow the dopants to rotate in response to the applied field. This agrees with results obtained using photochromic techniques[12].

Samples aged during poling show improved temporal stability of the SHG intensity, indicating a decrease in free volume and segmental mobility. This is indicated in Figure 4, where the ratio of  $\chi^{(2)}_{\text{film}(t)}/\chi^{(2)}_{\text{film}(t=0)}$  after the applied field is removed is plotted versus time for contact poled

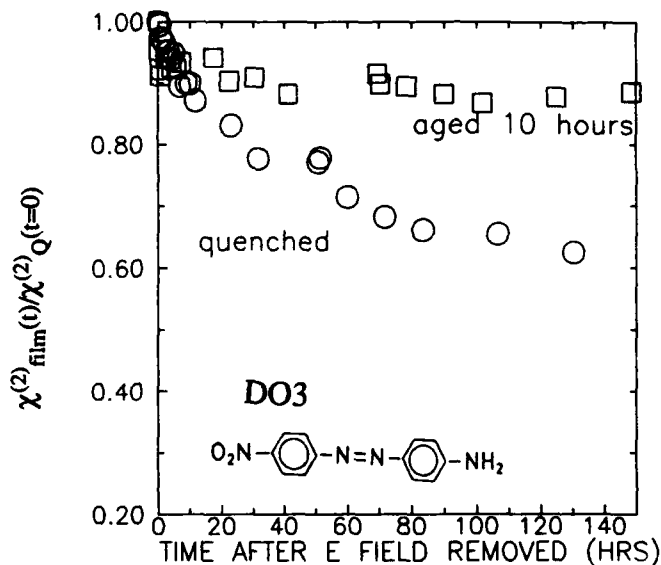


Fig 4. Effect of physical aging during contact poling on the dependence of  $\chi^{(2)}_{\text{film}(t)}/\chi^{(2)}_{\text{film}(t=0)}$  versus time over long time scales. Measurement at time equals zero represents film about 5 mins after removal of the electric field. Contact poled PC+4%DO3 quenched (O) and aged 10 hours at 25°C (□).

PC films doped with 4% DO3. The films were either quenched following poling (poled @ 100°C for 60 min), or aged for 10 hours at 25°C with the electric field still applied so that the dopants could not rotate out of alignment during aging. After about 150 hours following removal of the field, the quenched films lose about 40% of their original intensity, whereas samples aged during contact poling lose only 10% of their original intensity over the same time frame. There is obviously significant improvement of the temporal stability of dopant orientation in these materials upon aging during poling. This type of experiment has been performed on a variety of dopants in PS and PMMA as well, and similar results are seen[1]. This should be a general phenomenon for all glassy polymer matrices under conditions of physical aging.

## CONCLUSIONS

SHG is a sensitive technique for probing glassy polymer physics at temperatures well below  $T_g$ . Significant physical aging effects in PMMA and PS can be observed for aging before poling in as little as 1 hour at 25°C. Aging during poling greatly increases the temporal stability of dopant orientation after the applied field is removed over the time scale of these experiments. The SHG

intensity can be related to the dopant orientation, and to the characteristics of the local microenvironment surrounding the dopant in the glassy matrix.

#### ACKNOWLEDGEMENTS:

We gratefully acknowledge the financial support of the Materials Research Center at Northwestern University (Grant DMR88-20280), the Unisys Corp., and fellowships from the American Association of University Women and IBM (HLH). We appreciate helpful discussions with Dr. L. M. Hayden from Unisys Corp., and Dr. S. G. Grubb and Ms. S. J. Bethke from Amoco Technology Company.

#### REFERENCES

1. H. L. Hampsch, J. Yang, G. K. Wong, J. M. Torkelson, *Polym. Commun.* **30**, 40 (1989); *Macromolecules* **21**, 526 (1988); *Macromolecules*, submitted.
2. H. L. Hampsch, G. K. Wong, J. M. Torkelson, S. J. Bethke, S. G. Grubb, *Proc. SPIE* **1104**, in press.
3. H. L. Hampsch, J. M. Torkelson, S. J. Bethke, S. G. Grubb, *J. Appl. Phys.*, in press.
4. S. J. Bethke, S. G. Grubb, H. L. Hampsch, J. M. Torkelson, *Proc. SPIE*, submitted.
5. M. Eich, B. Reck, D. Y. Yoon, C. G. Wilson, G. C. Bjorklund, *J. Appl. Phys.* **66**, 3241 (1989).
6. M. Eich, A. Sen, H. Looser, G. C. Bjorklund, J. D. Swalen, R. Tweig, D. Y. Yoon, *J. Appl. Phys.* **66**, 2559 (1989).
7. K. D. Singer, M. G. Kuzyk, W. R. Holland, J. E. Sohn, S. J. Lalama, R. B. Comizzoli, H. E. Katz, M. L. Schilling, *Applied Physics Letters* **53**, 1800 (1988).
8. A. J. Heeger, J. Orenstein, D. R. Ulrich, Eds., *Nonlinear Optical Properties of Polymers* (*Mater. Res. Soc. Proc.* **102**, Pittsburgh, PA 1988).
9. D. J. Williams, Ed. *Nonlinear Optical Properties of Organic Properties of Polymeric Materials*, ACS Symposium Series #233 (American Chemical Society, Washington, DC, 1983).
10. D. S. Chemla, J. Zyss, Eds. *Nonlinear Optical Properties of Organic Molecules and Crystals; Vol. 1 and 2* (Academic Press, New York, 1987).
11. G. T. Boyd, *Thin Solid Films* **152**, 295 (1987); *J. Opt. Soc. Am. B*, **6**, 685 (1989).
12. J. G. Victor, J. M. Torkelson, *Macromolecules* **21**, 3490 (1988); **20**, 2241 (1987); in preparation.
13. I. M. Hodge, *Macromolecules* **18**, 1980 (1985); **16**, 898 (1983); **15**, 762 (1982).

## ENHANCED THIRD ORDER OPTICAL NONLINEAR RESPONSE IN POLYTHIOPHENE FILMS ——— POLARON CONTRIBUTIONS

LINA YANG<sup>1</sup>, R. DORSINVILLE<sup>1</sup>, R. ZAMBONI<sup>2</sup>, C. TALIANI<sup>2</sup>, R. TUBINO<sup>3</sup>,  
and R. R. ALFANO<sup>1</sup>

<sup>1</sup>Institute for Ultrafast Spectroscopy and Lasers,  
Departments of Electrical Engineering and Physics,  
The City College of the City University of New York, New York 10031

<sup>2</sup>Istituto di Spettroscopia Molecolare Consiglio Nazionale delle  
Ricerche Via de' Castagnoli 1, 40126 Bologna, Italy

<sup>3</sup>Istituto di Fisica dell'Universita, Via Vienna 2, Sassari, Italy

### ABSTRACT

The enhancement of the third order nonlinear susceptibility  $\chi^{(3)}$  of an homologous series of polycondensed thiophene based polymers was observed about photoinduced polaronic bands by a novel "pump-probe" degenerate four wave mixing technique. Enhancement of the degenerate four wave mixing signal for more than an order of magnitude was achieved with response time of less than 25 ps. The intrachain polarons contribution is proposed as the possible mechanism responsible for the observed enhancement.

### INTRODUCTION

The fast growing field of applications using ultrashort light pulses has resulted in a greater interest in materials having large third order nonlinear effect with an ultrafast response time. Organic molecules and polymers have long been known to exhibit large and fast  $\chi^{(3)}$ . In spite of many investigations, the mechanisms governing the various nonlinear optical response of organic materials are not well understood. Considerable interest has been directed to the  $\pi$  electron systems, such as polyacetylene<sup>1,6</sup> and polythiophene<sup>7,11</sup>, both form model systems of quasi-one dimensional semiconductors. The electronic excitations of these quasi-one dimension semiconductors are different from the electron-hole pairs found in ordinary semiconductors. After doping or photoexcitation, rapid lattice relaxations due to the strong electron-phonon coupling result in the formation of self-trapped excitations such as solitons, polarons and bipolarons with their associated electronic states inside the gap. Consequently, the redistribution of oscillator strength, produced in less than a picosecond, is proposed as the possible reason for the large nonlinear optical effects in these polymers. Nonlinear excitations are expected to play an important role in the nonlinear optical properties and charge transport in polymers which will be possibly used in the future generation of ultrafast computational devices.

In the nondegenerate ground state systems of polythiophene(PT), polarons and bipolarons are predicted<sup>12,13</sup> as the dominant charge carriers after photoexcitation or doping. In our previous work on PT<sup>7,8</sup>, the third order nonlinearity in polycondensed thiophene based polymers was investigated using a degenerate four wave mixing technique. The dispersion spectra of  $\chi^{(3)}$  was obtained about the absorption region. The value of  $\chi^{(3)}$  inside the absorption region was also found to be linearly proportional to the absorption coefficient



$\alpha$ . This result strongly suggests that a population grating dominates in the absorption region. Below gap measurement at 1064 nm gave a  $\chi^{(3)}$  value of  $10^{-11}$ esu. There is an interest in the below gap  $\chi^{(3)}$  measurements since 1064 nm is inside one of the photoinduced polaronic bands which was found by steady-state photoinduced absorption measurements<sup>14</sup> (corresponding to the  $\omega_s$  transition, see the inset of Fig. 1).

In this paper, we have extended our previous work on PT and measured  $\chi^{(3)}$  at 1064 nm when the PT sample is photoexcited by above gap excitation at 532 nm. The purpose of the present work is two fold. Firstly, the experimental studies<sup>3,4,6,11</sup> to date have only studied resonant enhanced  $\chi^{(3)}$ , either inside the absorption gap or due to two and three photon resonance. The mechanisms responsible for these third order nonlinearity are found to be controversial. We have measured  $\chi^{(3)}$  directly inside the polaronic bands. In fact, this is the first experiment to provide direct information on the possible role played by polarons or bipolarons in the third order optical nonlinearities. Secondly, there is no time resolved measurements to monitor directly the dynamics of polarons and bipolarons in polythiophene. The present novel pump-probe degenerate four wave mixing (DFWM) technique provides a function to trace the picosecond dynamics of nonlinear photoexcitations for those systems in which the ground state degeneracy is weakly lifted. Direct enhancement of  $\chi_{1064nm}^{(3)}$  about photoinduced polaronic bands, in addition, the enhanced  $\chi^{(3)}$  is found to be fast (< 25 ps), are reported in this paper.

## EXPERIMENT

The polythiophene samples are thin films (1000 - 2500 Å) electrochemically polymerized on tin oxide glass substrates. The detailed information about the polythiophene polymer samples were described elsewhere<sup>17,18</sup>.

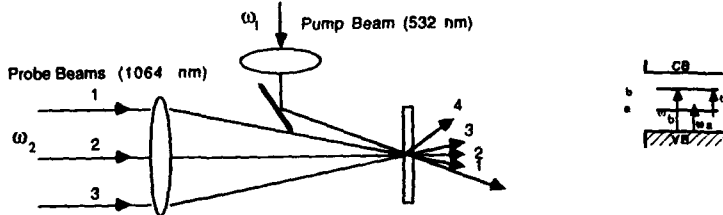


Fig.1 The geometry of "pump-probe" DFWM technique. The inset shows the schematic diagram of the two midgap states corresponding to positively charged polarons and bipolarons.

A 10-Hz mode-locked Quantel Nd:YAG laser system with a second-harmonic generator was used to generate 25 ps pulses at 1064 and 532 nm. A new pump-probe DFWM technique is introduced and schematically shown in Fig. 1. The fundamental output at 1064 nm is divided into three beams and used in a degenerate four wave mixing (DFWM) geometry. This part of the setup was described in detail in Ref. 7. A fourth beam at 532 nm is added to the DFWM setup and acts as a pump beam. The 532 nm beam has the same polarization direction as the 1064 nm beams. In this configuration, the 532 nm beam excites PT sample and the DFWM beams at 1064 nm probe the excited system at different times subsequent to the 532 nm excitation. The

experiments have been performed at room temperature.

## RESULTS

Fig. 2 illustrates the *increased* DFWM signal at 1064 nm as the function of delay between 532 and 1064 nm beams. The signal was detected in the phase matching direction  $\vec{k}_4 = \vec{k}_1 + \vec{k}_2 - \vec{k}_3$ . The data was obtained with 3 DFWM beams fixed at "0" delay (that is, they are spatially and temporally overlapping). The 532 nm beam is delayed (shown as the inset of Fig. 2). It is apparent that when 532 nm overlaps with three 1064 nm beams, a maximum enhancement is achieved. If 532 nm arrives too early, or too late relative to the 1064 nm laser pulses, there is no enhancement. The enhancement follows the 532 nm laser pulse which indicates that it is truly photoinduced by 532 nm beam. Notice that when three 1064 nm beams overlap, there is a non-resonant signal regardless of the presence of the 532 nm beam. For simplicity, this nonenhanced signal has been taken as the "0" background for Fig. 2. The Y axis represents the *increased* DFWM signal.

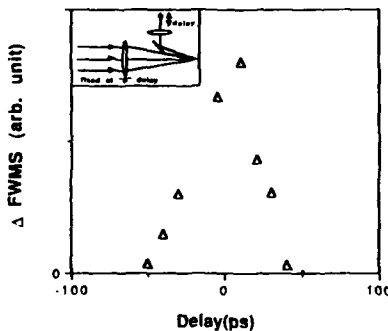


Fig.2 The increased DFWM signal ( $\Delta$  FWMS) at 1064nm of PT as a function of delay between 532 and DFWM 1064nm beams.

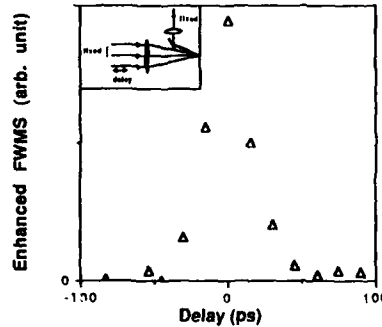


Fig.3 Time resolved enhanced DFWM signal at 1064 nm when 532 nm beam is fixed at 0 delay and one of 1064 nm beams is delayed.

The insets show the experimental arrangements.

In order to determine the response time of the enhanced DFWM signal, one of the probe beams at 1064 nm for the DFWM is delayed and the other two 1064 nm and 532 nm beams are fixed at "0" delay (see inset of Fig. 3). The time resolved enhanced DFWM signal (includes the nonresonant part) is thus obtained and displayed in Fig. 3. The results clearly show that the response time is still limited by the laser pulse resolution ( $< 25$  ps) which indicates the enhanced DFWM signal at 1064 nm is ultrafast.

## DISCUSSION

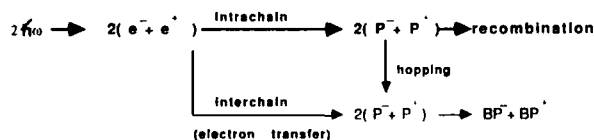
We have observed the enhancement of the DFWM signal using the novel pump-probe DFWM technique. This result is rather interesting and surprising. In the absence of  $\omega_1$  (532 nm beam), the energies of the stationary excited

states in PT are much higher than the photons at  $\omega_2$  (1064 nm) since the lowest excited state is at  $E > 2eV$ . Without the excitation beam at 532 nm, the DFWM measurements at 1064 nm give  $\chi_k^{(3)} = \chi_k^{(3)}$  which has been obtained in our previous experiments<sup>7,8</sup>. With the above new arrangement (shown in Fig. 1), when PT system is photoexcited above the energy gap by 532 nm (2.33 eV), two midgap states are formed inside the gap (shown in the inset of Fig. 1). The key point is that the probe beams at 1064 nm now could be in resonant with the transitions:  $\omega_k$  (for  $BP^+$  and  $P^+$ ) and  $\omega'$  (for  $P^+$  only). Now  $\chi^{(3)}$  obtained from DFWM measurements has a triply resonant term<sup>19</sup>:

$$\chi_k^{(3)} = \frac{NA_k^4}{(\omega_{ij} - \omega_2 - i\Gamma_{ij})^3},$$

where,  $ij = vb$  (or  $ab$ ),  $A_k$  includes the dipole matrix element for the transitions between valence band and the polaronic band  $b$  (or between polaronic bands  $a$  and  $b$ ),  $\Gamma_{ij}$  is the phenomenological damping factor, and  $N$  is the number of polarons or bipolarons per unit volume. The full expression of  $\chi^{(3)}$  is  $\chi^{(3)} = \chi_k^{(3)} + \chi_k^{(3)}$ . The enhancement of DFWM signal at 1064 nm is expected when the system is photoexcited by 532 nm. In other words, we have observed a photoinduced enhancement of DFWM signal at 1064 nm because of the resonance of  $\chi^{(3)}$  about the photoinduced polaronic bands in PT.

The fast response time of enhanced DFWM signal was deduced from Fig. 3. Much longer decay time was expected since bipolarons are the dominant excitations observed in the previous experiments<sup>14</sup> which are considered as metastable species. Considering that after electron-hole photoinjection, chain distortions will quickly form around these single charges, leading to the formation of polarons (results from a bound neutral and charged soliton pair). Generally, there are two main proposed pathways for photogenerated polarons to decay shown in the following diagram.



Polaron pairs formed in the same chain will quickly recombine through the geminate recombination (intrachain process). Thus, the intrachain polarons should have a very short lifetime. In general, this pathway dominates, only those rare polarons escape the geminate recombination by hopping to the neighbouring chains or, are directly photogenerated by electrons and holes formed on different chains (because of the finite transverse bandwidth due to interchain coupling; interchain electron transfer processes) can yield the bipolarons observed in steady-state photoinduced absorption spectra<sup>14</sup>. The long lifetime of those photoexcitations can be rationalize, for a single charged bipolaron would be metastable; recombination could occur only when two electrons (or two holes) hop together from one chain to another. The fast intrachain process has been probably observed in our measurements. The rise slope is limited by our laser resolution which indicates that the formation time of intrachain polaron pairs are very fast which is in consistent with the

theoretical predictions<sup>12,13</sup>. The lifetime of intrachain polarons is  $< 25$  ps as deduced from the fast decay slope. The long decay component correspondent to bipolarons is missing from our measurements. We believe this component is small in the picosecond time region. Our measurements is consistent with the recent photoinduced absorption studies of polythiophene<sup>16</sup>, where it was estimated that only 0.02 of the initial excitations survive and are mobile beyond 25ps.

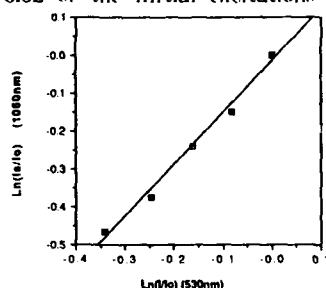


Fig.4 The enhanced DFWM signal at 1064 nm as a function of 532 nm pump fluence.

The hypothesis of intrachain polarons recombination can be tested by investigating the pumping fluence( $F$ ) dependence of the photoinduced enhancement of the DFWM signal. The resonant part of  $\chi^{(3)}$  is linearly dependent on the number of the photogenerated polarons per unit volume  $N_p$ . The number of polarons per unit volume  $N_p$  would yield a steady-state density that grows as  $F$  without saturation when bimolecular recombination term is omitted from the rate equation of the photogeneration of polarons. The curve in Fig. 4 is a plot of the photoenhanced DFWM signal as a function of pump fluence at 532nm within a limited fluence range  $\sim 10^{15}$  photons/cm<sup>2</sup>. It is apparent that the enhanced signal is increasing as the fluence of 532nm beam increases. The slope is found to be about 1.38 giving sublinear dependence of  $\chi^{(3)}$  on  $F$ . Due to the sensitivity of our detection system at lower fluence and the damage to the sample with larger fluence (532 nm is strongly absorbed in PT), the dynamic range of the fluence is limited to the order of  $10^{15}$  photons/cm<sup>2</sup>. At this fluence level, we believe that we are operating near the saturation region which normally has a reduced slope. Similar saturation of a simple volume(or phase-space) filling of the lattice by photogenerated solitons has been observed in Trans-(CH),<sup>2</sup>. The enhanced signal shown in Fig. 4 includes the nonresonant part which could also reduce the observed slope to less than 2. Typically, one order of magnitude enhancement of the signal is observed within our fluence range.

## CONCLUSION

Photoinduced enhancement of  $\chi^{(3)}$  about polaronic bands in polythiophene on picosecond time scale was observed for the first time by a novel "pump-probe" DFWM technique. Intrachain polarons are most likely to be responsible for this enhancement at times less than 25 ps.

## ACKNOWLEDGEMENTS

This work was supported at City College of New York in part by National Science Foundation (contract NSF - R II 88 02964), by Hamamatsu Photonics K. K., and by the City College Faculty Award Program.

## REFERENCE

- (1) C. V. Shank, R. Yen, R. L. Fork, J. Orenstein and G. L. Baker, Phys. Rev. Lett. **49**, 1566(1882), Phys. Rev. B **28**, 6095(1883).
- (2) L. Rothberg, T. M. Jedju, S. Etemad and G. L. Baker, Phys. Rev. Lett. **57**, 3229(1886), Phys. Rev. B **36**, 7524(1887).
- (3) F. Kajzar, S. Etemad, G. L. Baker and J. Messier, Solid State Comm. **63**, 1113(1887).
- (4) M. Sinclair, D. Moses, K. Akagi, and A. J. Heeger, Phys. Rev. B **38**, 10724(1888).
- (5) D. M. Mackic, R. J. Cohen and A. J. Glick, Phys. Rev. B **39**, 3442(1889).
- (6) W. S. Fann, S. Benson, J. M. J. Madey, S. Etemad, G. L. Baker and F. Kajzar, Phys. Rev. Lett. **62**, 1492(1889).
- (7) L. Yang, R. Dorsinville, Q. Z. Wang, W. K. Zou, P. P. Ho, N. L. Yang, R. R. Alfano, R. Zamboni, R. Danieli, G. Ruani and C. Taliani, J. Opt. Soc. Am. B **6**, 753(1889).
- (8) R. Dorsinville, L. Yang, R. R. Alfano, R. Zamboni and C. Taliani, Opt. Lett. **14**, 1321(1889).
- (9) R. Worland, S. D. Phillips, W. C. Walker and A. J. Heeger, Synth. Metals **28**, D663(1889).
- (10) B. P. Singh, M. Samoc, H. S. Nalwa and P. N. Prasad, submitted for publication.
- (11) R. Zamboni, C. Taliani, G. Ruani, A. J. Pal and F. Kajzar, submitted for publication.
- (12) W. P. Su and J. R. Shrieffer, Proc. Natl. Acad. USA **77**, 5626(1880).
- (13) R. Ball, W. P. Su and J. R. Shrieffer, J. Phys.(Paris) Colloq **44**, c3(1883).
- (14) Z. Vardeny, E. Ehrenfreund, O. Braflman, M. Nowak, H. Schaffer, A. J. Heeger and F. Wudl, Phys. Rev. Lett. **56**, 671(1886).
- (15) Z. Vardeny, H. T. Grahn, A. J. Heeger and F. Wudl, Synth. Metals **28**, C299(1889).
- (16) S. D. Phillips, G. Yu and A. J. Heeger, Synth. Metals, **28**, D669(1889).
- (17) R. Danieli, C. Taliani, R. Zamboni, G. Giro, M. Biserni, M. Mastragostino, and A. Testoni, Synth. Met. **14**, 325(1886).
- (18) P. Di Marco, M. Mastragostino and C. Taliani, Mol. Cryst. Liq. Cryst. **117**, 241(1885).
- (19) Y. R. Shen, *The Principles of Nonlinear Optics* (Join Wiley & Sons, Inc. 1884) Chap. 14.

## PHOTOEXCITATIONS IN POLY(2,5-THIENYLENE VINYLENE)

I. D. W. SAMUEL\*, A. J. BRASSETT\*, N. F. COLANERI\*, R. A. LAWRENCE\*, D. D. C. BRADLEY\*, K. E. MEYER\*, R. H. FRIEND\*, H. MURATA\*\*, S. TOKITO\*\*, T. TSUTSUI\*\* and S. SATO\*\*

\*Cavendish Laboratory, Madingley Road, Cambridge CB3 0HE, UK.

\*\*Department of Materials Science and Technology, Graduate School of Engineering Sciences, Kyushu University, Kasuga, Fukuoka, 816 Japan

## ABSTRACT

Poly(2,5-thienylene vinylene), PTV, can be conveniently prepared via a precursor route to give coherent films suitable for optical measurements. Photoexcitation above the band gap at 1.8 eV gives rise to two transient absorption peaks at 0.44 eV and 1.0 eV that are associated with bipolarons that live for times of order a few ms at 80 K. Photoluminescence, comparable in intensity to the Raman scattering, is found at energies above the band edge, and we assign this to a hot recombination process. Pump and probe measurements of the induced bleaching at 2 eV show a very fast rise and initial fall time, which are within the 100 fsec resolution of the measurement.

## INTRODUCTION

Photoexcitation of conjugated polymers provides fundamental information about the electronic structure of these materials and of their excited states. The electronic excitations of the  $\pi$  electrons coupled to the  $\sigma$ -bonded polymer chain take the form of self-localised polarons [1,2], or solitons for the special symmetry of *trans*-polyacetylene [3]. The relaxation of the structure has the effect of pulling energy levels away from the band edge into the semiconductor gap. Anisotropy in the electronic structure determines the dynamics for relaxation and recombination of photoexcitations, and it is appropriate to make a distinction between intra- and inter-chain excitations. We consider that intrachain photoexcitation across the  $\pi$ - $\pi^*$  gap creates predominantly intra-chain polaron excitons, which may then decay radiatively, and that separation of charge to form polarons or bipolarons requires interchain motion of charge [4]. The polaron-exciton can be studied by its radiative decay through measurement of photoluminescence, PL. Charged photoexcitations can be studied by measurement of photoinduced optical absorption, PA, due to transitions between the gap states and the band edges. Most measurements are sensitive only to the long-lived excitations, and the experimental evidence is that these are doubly-charged bipolarons, formed by coalescence of two like-charged polarons, as observed in poly(phenylene vinylene), PPV [4], in polythiophene [5] and its alkyl side chain derivatives [6,7].

Poly(arylene vinylene)s can be conveniently prepared via a solution-processible precursor polymer which is either a sulphonium polyelectrolyte or is derived from this. Polymers prepared by these routes can be obtained as coherent, dense films, and in a state of high purity. It is also possible to control bandgap over a range of energies, by selection of the arylene group, and these polymers provide therefore an excellent series for experimental study. To date, the most extensively studied of the poly(arylene vinylene)s has been poly(*p*-phenylene vinylene), PPV [4, 8] which shows the onset of the optical absorption due to  $\pi$ - $\pi^*$  transitions at 2.5 eV. In this paper we study the effect of the replacement of the phenylene by a thienylene moiety upon the excited states of the polymer. This polymer, poly(2,5-thienylene vinylene) [PTV] has been found to have a band gap 25% lower than that of PPV [9,10]. We find that the long-lived charged photoexcitations have the spectroscopic signature of bipolarons, and that the degree of confinement deduced from the splitting of the two gap states, of 0.56 eV, is extremely low. In contrast to the case of PPV we find that the quantum yield for PL due to intrachain polaron-excitons is very low, being no stronger than the Raman scattering. This indicates that there is an extremely efficient non-radiative decay channel for these excitations, and consistent with this we find that the transient optical response at the band edge is very fast.

## EXPERIMENTAL

The samples of PTV used in this study were synthesised via a modified sulphonium polyelectrolyte precursor-route in which the sulphonium polyelectrolyte is first synthesised by

base-induced polymerisation of the 2,5-thienylene-bis(methylene dimethylsulphonium chloride) monomer, and the sulphonium group replaced with a methoxy group. This polymer is used as the processible precursor, and full conversion to PTV is achieved by heating at temperatures between 100 °C and 200 °C under flowing N<sub>2</sub> containing dry gaseous HCl. Conversion was confirmed by checking for the absence of the characteristic vibrations of the saturated precursor groups in the infrared spectrum, and the absence of a signal from sp<sup>3</sup>-hybridized carbons in the high resolution solid-state <sup>13</sup>C-NMR [9,10].

For optical measurements thin films of the PTV precursor were spin-coated onto sapphire substrates from THF solution. After thermal conversion to PTV, the samples had a typical optical density of order 1.5 - 2.5 at the peak in their absorption spectra. Film thicknesses, determined from their reflectivity by a multiple beam interference technique, were between 80 nm and 140 nm. CW optical measurements were performed in an Oxford Instruments CF 204 optical-access helium cryostat, allowing temperature control between 10 K and room temperature. Thermal contact to the samples was provided by a helium exchange gas within the sample space. Absorption and induced absorption measurements were performed in the visible and near infrared spectral regions (0.4 eV - 4 eV) using a tungsten halogen source, dispersed with a grating monochromator and measured with a photomultiplier tube, silicon photodiode, or cooled indium antimonide detector.

Photoinduced absorption was measured by probing the absorption of light from the tungsten halogen lamp during laser photoexcitation with a CW argon ion laser, mechanically chopped in the frequency range 10 - 4000 Hz. Luminescence spectra were recorded at room temperature in a 90° scattering geometry, using a modified Coderg PH1 double monochromator and a Hamamatsu R943-02 photomultiplier tube.

Transient measurements of photoinduced bleaching were performed using pump and variable-delay probe techniques, with 100 fsec light pulses of wavelength centred at 630 nm, produced by a dye laser, with saturable absorber and dispersion compensation, synchronously pumped by the doubled output from a mode-locked Nd:YAG laser. Measurements were performed at room temperature, with a pulse repetition rate of 76 MHz, and the pump beam mechanically chopped at 2 kHz, and signal detection was performed with a lock-in amplifier referenced to the chop frequency of the pump beam.

## RESULTS

### Optical Absorption

The low temperature optical absorption spectrum is shown in figure 1. At room temperature, the onset of the  $\pi$ - $\pi^*$  transition in PTV occurs just below 1.8 eV, and the absorption edge shifts to lower energies at lower temperatures, by about 0.03 eV lower at 15 K. In addition, the phonon features in the absorption edge become more pronounced as the temperature is decreased. These features are more clearly visible in a measurement of the thermal modulation of the absorption edge, which is shown also in figure 1 as the fractional change in transmission upon heating the sample from 80 K to 100 K. This difference spectrum shows three sharp derivative features with local maxima at 1.82 eV, 2.03 eV, and 2.21 eV, corresponding to the phonon peaks in the absorption spectrum.

### Photoluminescence

In contrast to the PL in PPV which is strong, with a quantum yield of several % [4,11], we find in PTV that it is very weak. For the samples used in the present work we can see this as a broad background to the Raman signal, but there is some variation between samples prepared from different batches, and other samples show no detectable PL. Figure 2 shows PL for excitation at 457.9 nm. Note the presence of sharp Raman lines on the spectrum. These are discussed elsewhere [12]. The figure also shows that the slight oxidative doping of the sample due to handling in air leads to a quenching of the luminescence, a process which can be reversed by heating to 150°C under high vacuum for several hours. The spectral profile of the photoluminescence band depends in detail on the wavelength of excitation, but all of the emission always appears above the band edge at 1.8 eV. Because the photoluminescence intensity is of the same order as that of the Raman signal, we estimate the quantum yield to be as low as 10<sup>-5</sup>.

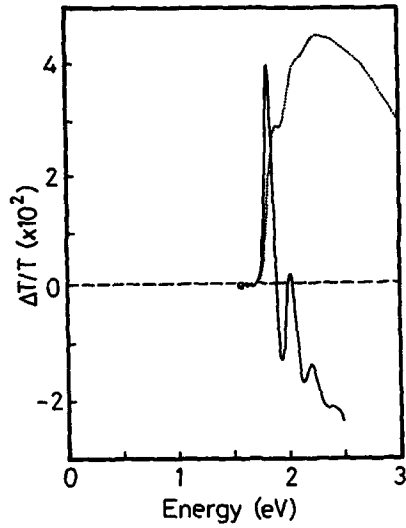


Figure 1 Optical absorption spectrum for a PTV thin film at 80K, shown as the broken line, and the thermal modulation spectrum obtained as the fractional difference in optical transmission at 80 and 100 K,  $[T(80) - T(100)]/T(80)$ .

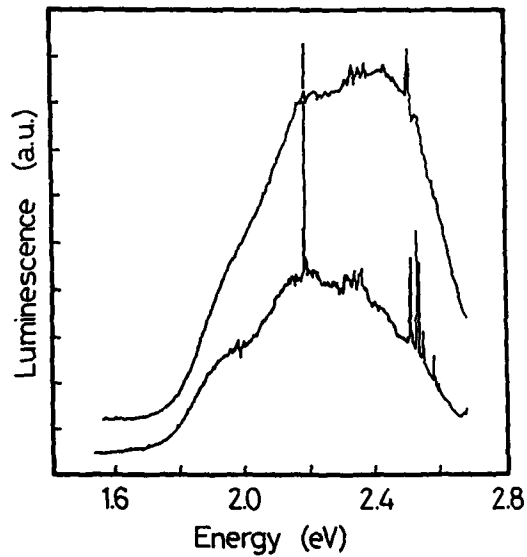


Figure 2 Photoluminescence from PTV following excitation at 457.9 nm. The upper spectrum (displaced for clarity) was recorded after heating the film at 150 °C under a vacuum of  $10^{-4}$  mbar for 12 hrs.



### CW Photoinduced Absorption

The PA spectrum of PTV at 80 K is shown in figure 3. To obtain the data below 2.3 eV the sample was photoexcited with about 200 mW/cm<sup>2</sup> of the 488 nm (2.54 eV) line and for the data above 2.3 eV excitation was with the multiline UV output of the argon ion laser, though data below 2.3 eV were similar for both excitation energies. Two absorption features (~0.7 eV FWHM) appear below the band edge, peaking near 1 eV and 0.44 eV. On the basis of the number of peaks and their position relative to the band edges, we assign them to subgap transitions associated with bipolarons, the long-lived charged species which typically result from photoexcitation of a non-degenerate ground state polymer [1-3]. Their identification as resulting from charged excitations is consistent with the previously reported observation of photoinduced infrared active vibrational modes in PTV [13]. The energy separation of the two subgap features, only 0.56 eV, is much smaller than that which has been measured in other non-degenerate ground state conjugated polymers such as PPV [4,11], poly(thiophene) [5] and poly(3-hexyl thienylene) [6,7] and as discussed below suggests that the degree of confinement in this material is small.

Associated with the induced absorption below the band edge, we expect to find photoinduced bleaching (PB) at and above the band edge, to satisfy the sum rule

$$\int_0^{\infty} \delta\alpha(\omega) d\omega = 0 \quad (1)$$

where  $\delta\alpha$  is the change in absorption coefficient at frequency  $\omega$ . The photoinduced absorption spectrum of PTV shows a general shift to induced bleaching above the band edge, but it is clear that the bleaching must extend far into the UV to satisfy the sum rule. Superimposed on this we observe three regularly-spaced derivative features with maxima at energies 1.78 eV, 1.97 eV, and 2.15 eV. These features can be attributed to electromodulation of the band edge due to local fields associated with the presence of charged photoexcitations. This is well established in the case of polyacetylene prepared by the Shirakawa route [14,15] for which the electroabsorption signal was found to reproduce the photoinduced band edge features, with both spectra varying with probe photon frequency as  $\partial^2\alpha/\partial\omega^2$ . The thermal modulation (TM) spectrum, however, varies as  $\partial\alpha/\partial\omega$

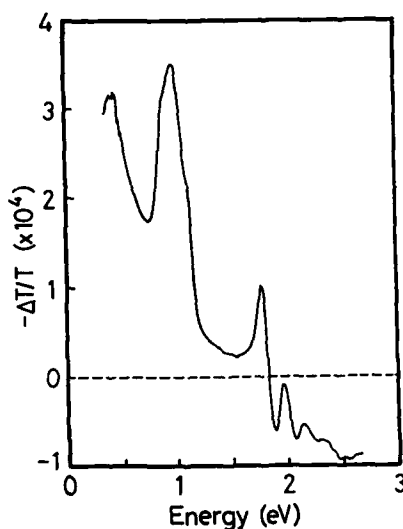


Figure 3 The photoinduced absorption spectrum of PTV recorded at 80 K following chopped CW excitation at 488 nm. The data above 2.3 eV were recorded with excitation by the multiline UV output of the Ar<sup>+</sup> laser.

[15], and we note that, as expected, the TM signal shown in figure 1 is of opposite sign to the PA at the band edge and red-shifted (by 0.05 eV). As discussed in detail elsewhere [12], measurements of the temperature, laser intensity and chop frequency dependence of the photoinduced subgap transitions and band edge features of figure 3 confirm that they have a common origin.

#### Transient Photoinduced Bleaching

Figure 4 shows the induced bleaching at 2 eV due to excitation at 2 eV, as a function of time delay between pump and probe. As previously found for polyacetylene [16,17], polythiophene [18] and polydiacetylene [19], the initial response is fast, and within the system resolution. The initial decay for the PTV sample shown here is extremely fast, falling to 50% of its peak value within system resolution of about 100 fsec. At longer times the decay of the bleaching slows down. The ratio of the intensity of the fast and slow components does show some variation between samples, and the data shown in figure 4 are within the middle of the range of the observed behaviour. We consider that the long-lived signal is due, at least in part, to thermal modulation of the sample by the pump beam. As seen in figure 1, however, the thermal modulation signal is changing rapidly at 2 eV, and it is not straightforward to make comparison with the TM spectrum. The very rapid decay of induced bleaching in PTV at short times is of considerable interest, since for most other polymers of this type the initial decay, though fast, has been resolved, with typical decay times of order 1 psec.

#### DISCUSSION

The most striking observation we have made is the widely differing behaviour of PPV and PTV. PPV shows a high quantum yield for PL, and this is due to the radiative decay of intrachain polaron excitons. We consider that most of the oscillator strength in the  $\pi$ - $\pi^*$  absorption band is due to intrachain excitations which create these excitons, and that the quantum yield for PL from radiative decay of these excitons is determined by the competing non-radiative decay channels. In the case of PPV, we can track from model oligomers, for which the PL quantum yield is very high, to the 8% value for PPV through control of conjugation length by partial thermal conversion of the sulphonium precursor [4]. We consider that the result of introducing conjugation along the polymer chain is to allow non-radiative decay channels to become effective, probably through rapid diffusion to defect sites which allow non-radiative decay.

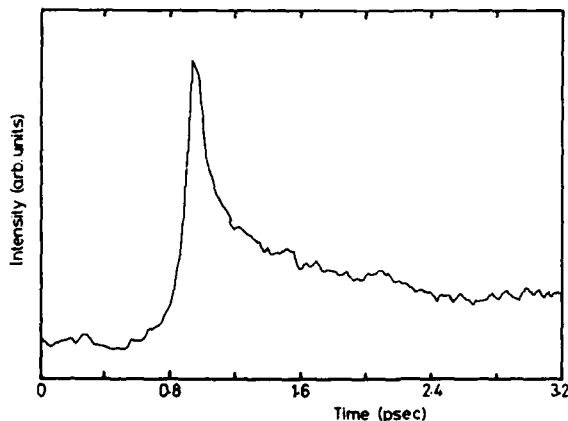


Figure 4 Time variation of photoinduced bleaching at 2 eV, measured at room temperature. Pump and probe polarisations are parallel to one another.

PTV, in contrast, shows a very low quantum yield for PL. In addition, whereas the emission from PPV consists of a well-defined band with resolved vibrational structure and appears below the absorption edge, the weak emission in PTV is above the edge and has a spectral profile dependent upon excitation energy. This suggests that the emission from PTV is due to hot geminate recombination rather than the decay of thermally equilibrated singlet excitons as in PPV. We do not consider that the initial optical excitation of the polymer chain should be greatly different for these two polymers, and we consider that intrachain excitation of a neutral excited state is still dominant. The very weak PL is then due to non-radiative decay channels which are extremely efficient for PTV; if we use the upper bound of the quantum yield for the PL of  $10^{-5}$  and a radiative lifetime of order  $10^{-9}$  sec, we expect to see a lifetime for the excited state of  $10^{-13}$  sec. Turning to the measurement of the photoinduced bleaching at 2 eV, we can expect that the  $\pi$ - $\pi^*$  transition strength will be bleached by the photoexcitation of both charged and neutral photoexcitations, but that bleaching due to neutral intra-chain excitations should be dominant, at least at short times. Thus, we consider that the very rapid initial decay of the induced bleaching is associated with the very rapid non-radiative recombination of the intra-chain excitons. The mechanism for this, perhaps similar to that in polydiacetylenes [19], remains poorly understood; it may perhaps be possible to consider this through a description in terms of a level crossing between ground and excited electronic states at a value of configuration coordinate that is much more readily accessible for PTV than for PPV.

We have discussed elsewhere [12] the nature of charged bipolarons which are seen in the CW PA experiments. Of note is the very small separation between the two gap states, which within the model of Fesser et al [1] gives a very low value for the confinement parameter which characterises the asymmetry between the aromatic and quinoid chain conformations.

#### REFERENCES

1. K. Fesser, A.R. Bishop, D.K. Campbell, *Phys.Rev.B* **27**, 4804 (1983).
2. S. Brazovskii and K. Kirova, *JETP Lett.* **33**, 4 (1981).
3. A. J. Heeger, S. Kivelson, J. R. Schrieffer, W-P. Su, *Rev. Mod. Phys.* **60**, 781 (1988).
4. R. H. Friend, D. D. C. Bradley, P. D. Townsend, *J. Phys. D: Appl.Phys.* **20**, 1367 (1987).
5. Z. Vardeny, E. Ehrenfreund, O. Brafman, M. Nowak, H. Schaffer, A. J. Heeger and F. Wudl, *Phys. Rev. Lett.* **56**, 671 (1986).
6. Y. H. Kim, D. Spiegel, S. Hotta and A. J. Heeger, *Phys. Rev. B* **38**, 5490 (1988).
7. J. Rühe, N. F. Colaneri, D. D. C. Bradley, R. H. Friend and G. Wegner (to be published).
8. D. D. C. Bradley, *J. Phys. D: Appl. Phys.* **20**, 1389 (1987).
9. S. Yamada, S. Tokito, T. Tsutsui, S. Saito, *J. Chem. Soc., Chem. Commun.* 1448 (1987).
10. S. Tokito, T. Momii, H. Murata, T. Tsutsui, S. Saito, *Polymer* (in press).
11. D. D. C. Bradley, N. F. Colaneri, R. H. Friend, *Synthetic Metals* **29**, E121 (1989).
12. A. J. Brassett, N. F. Colaneri, D. D. C. Bradley, R. A. Lawrence, R. H. Friend, H. Murata, S. Tokito, T. Tsutsui and S. Saito (preprint).
13. C. M. Foster, Y. H. Kim, N. Uotani and A. J. Heeger, *Synthetic Metals* **29**, E135 (1989).
14. J. Orenstein, G. L. Baker and Z. Vardeny, *J. Physique Colloq.* **44**, C3-407 (1983).
15. N. F. Colaneri, R. H. Friend, H. E. Schaffer and A. J. Heeger, *Phys. Rev. B* **38**, 3960 (1988).
16. C. V. Shank, R. Yen, J. Orenstein and G. L. Baker, *Phys. Rev. B* **28**, 6095 (1983).
17. Z. Vardeny, J. Strait, D. Moses, T-C. Chung and A. J. Heeger, *Phys. Rev. Lett.* **49**, 1657 (1982).
18. Z. Vardeny, H. T. Grahn, A. J. Heeger and F. Wudl, *Synthetic Metals* **28**, C299 (1989).
19. B. I. Greene, J. Orenstein, R. R. Millard and L. R. Williams, *Phys. Rev. Lett.* **58**, 2750 (1987).

OPTICAL CHARACTERIZATION OF POLYDIACETYLENE LANGMUIR-BLODGETT  
FILM ON SILICON SUBSTRATES.

P. MILLER, A.K.M. RAHMAN, S.V. BROUDE and S. TRIPATHY\*  
University of Lowell, Departments of Physics and Chemistry\*,  
Lowell, MA, 01854.

ABSTRACT

A bilayer of a surfactive polydiacetylene (15-8 PDA) has been deposited by Langmuir-Blodgett technique on a smooth Silicon substrate using a commercial Lauda film balance [1]. The morphology of the deposited film has been studied by cross-polarized optical microscopy, and laser light scattering microscopy. Usual crystalline domains with size ranging from 5 to 50  $\mu\text{m}$  can be seen between cross polarizers. Nonuniformities and voids in the film are observed by imaging the scattered light from a visible laser beam incident at grazing angle onto the film.

Raman scattering study on these bilayers have been carried out to investigate their vibronic structure. Information about vibronic levels from PDA has been used to define the extent of disorder and crystalline phase of the bilayer.

INTRODUCTION

Polydiacetylene is a promising material for nonlinear optical applications because of its large third order susceptibility. In addition, the molecule can be engineered to improve its nonlinear properties by attaching appropriate side groups onto the monomer [2]. To be suitable for optical applications, the material has to have also good linear optical properties. Any micron-range defects produced during the processing of the polymer will give rise to scattering centers. There is a strong interest in studying the morphology of these materials and in developing fast, reliable and nondestructive techniques to control and monitor their optical quality and uniformity.

Using Langmuir-Blodgett (LB) technique, polydiacetylene may be produced as ultra thin multilayers with polycrystalline structure [1]. This versatile technique produces films with thickness and chemical nature controllable down to a single molecular layer. However, unavoidable structural defects remain obstacles for technological applications of these LB films [3].

Cross-polarized optical microscopy, laser light scattering microscopy and Raman scattering were used to investigate ultrathin LB films of the 15-8 polydiacetylene. Each of these characterization technique is discussed as a potential inspection tool for this particular material.

PREPARATION OF THE FILMS

Monolayer films of 15-8 diacetylene monomer were prepared at the air-water interface using LB technique. The subphase contained a solution of  $\text{CoCl}_2$  of concentration  $2.5 \times 10^{-4} \text{ M}$  in water. The water used was double distilled and purified by Millipore Milli-Q purification system. A constant temperature

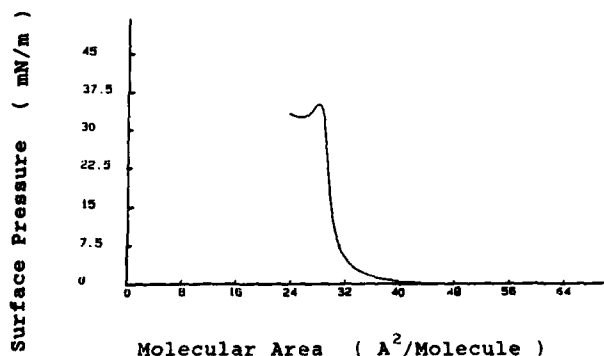


Fig. 1: Pressure-area isotherm of Co-Diacetylene

bath was used to control the subphase temperature. The diacetylene monomer was dissolved in HPLC grade chloroform to a 1-2mM concentration. The monomer solution was spread onto  $\text{CoCl}_2$  subphase and the pressure-area isotherm was obtained to determine if the cobalt salt of this diacetylene monomer forms a stable monolayer film at the air-water interface. The pressure-area isotherm shown in Fig. 1 indicates that this system does in fact form a good monolayer. After obtaining reproducible pressure-area isotherms, the monomer solution was spread once again onto  $\text{CoCl}_2$  subphase and slowly compressed at speeds of about  $5 \text{ \AA}^2 \text{ mol}^{-1} \text{ min}^{-1}$  to surface pressure of  $15 \text{ mN/m}$ . Monolayer films were annealed for 30 minutes prior to film deposition. The constant film pressure indicates that the film is optimally packed. Monolayer also proved to be very stable as a constant pressure of  $15 \text{ mN/m}$  could be maintained for prolonged periods of time without film collapse. An automatic dipper was used to deposit the monolayer film onto the substrate by slowly lowering and raising the substrate into and out of the subphase. For multilayer deposition, the monolayer- or bilayer-coated substrate (depending on whether the substrate is hydrophilic or hydrophobic) was left to dry for at least one hour to assure good adhesion of the film to the substrate before subsequent dipping. The films were polymerized on the substrate by exposure to UV radiation ( $400 \text{ \mu W/cm}^2$ ,  $\lambda = 254 \text{ nm}$ ) for 10 minutes for blue phase and 30 minutes for red phase.

#### LASER LIGHT SCATTERING MICROSCOPY

Laser light scattering microscopy has been reported for investigation of dislocation and point defects in inorganic single crystals [4,5]. We use a similar technique to characterize mono- and multilayers of LB films. A visible laser beam (HeNe, for instance) is focused on a small spot at grazing angle (Fig. 2) ( $4-6^\circ$  with respect to the surface plane) on the microscope sample stage. The light scattered out of the specular reflected beam from the sample is collected by the microscope objective and imaged through the eyepiece. This is similar to a dark field microscope but here the source is a

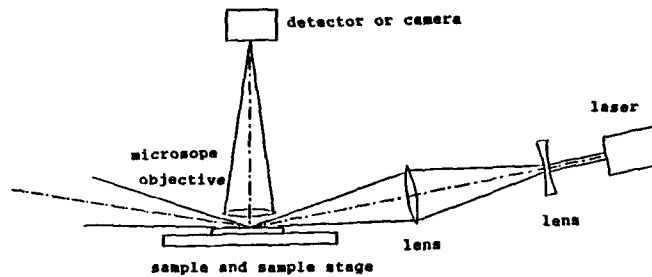


Fig. 2: Laser optical microscope diagram.

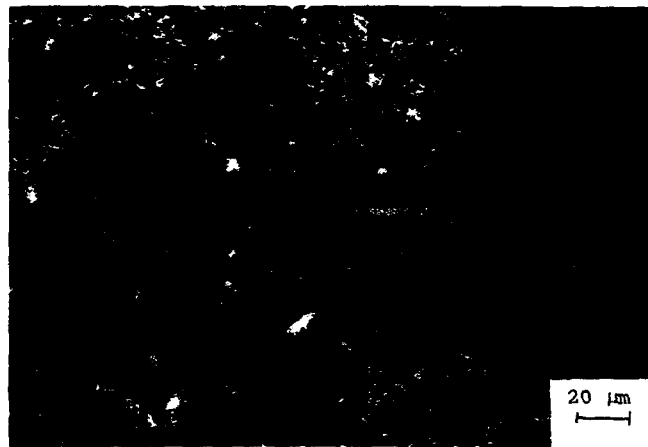


Fig. 3: Laser light scattering micrograph of a bilayer of PDA 15-8

coherent laser beam. Fig. 3 shows a two layer film of PDA 15-8 on Si substrate observed by this technique. The scattering is maximal for p-polarization of the incident beam because the total electric field on the surface (incident + reflected) is at a maximum. This ultramicroscopy is only possible with optically polished substrate since surface roughness would mask the weak scattering from the film. The laser scattering micrographs exhibit submicron scatterers distribution with a lateral resolution of about 2 microns.

It is not clear now whether the scattering is a result of a high density of pinholes, dislocations and grain boundaries in the polymeric crystal lattice, or is a coherent process involving individual molecular electric dipole moments in our almost two-dimensional arrangement. Investigations are

continuing to determine the evolution of these lattice defects in the monomer phase and during the polymerization process.

Using the relative scattering intensity ( $I_s/I_0$ ), a rough estimate of the scattering losses for a beam propagating in the LB material can be found. First the total scattering cross-section ( $\sigma$ ) can be derived using :

$$I_s/I_0 = (1 + R^2 + 2 R \cos(2 \vartheta_i)) \eta \sigma S^{-1} \quad (1)$$

where  $\eta$  is the collection efficiency and  $S$  is the beam cross section.  $R^2$  ( $=.32$ ) is the coefficient of reflection of the substrate for a given angle of incidence ( $\vartheta_i=85.6^\circ$ ) and for p-polarised incident light. The scattering cross section enables us to express the linear scattering losses per unit length as :

$$\alpha_s = \sigma V^{-1} = I_0^{-1} [ I_0 \eta (d/\cos(\vartheta_i)) (1 + R^2 + 2 R \cos(2 \vartheta_i)) ]^{-1} \quad (2)$$

where  $V$  is the volume of interaction with the beam and  $d$  the thickness of the film ( $d = 70\text{\AA}$  [11]).

We measure with a HeNe ( $\lambda=632.8\text{nm}$ ) a relative scattering intensity of  $3 \times 10^{-6}$ . Assuming a collection efficiency of .24 for our microscope objective of N.A.=0.65, we calculated a linear scattering loss coefficient of  $700\text{m}^{-1}$  or  $3 \times 10^4 \text{dB/m}$ . These extremely high scattering losses prejudice any technological optical applications of these LB PDA films unless drastic improvement are made in the processing of those films. Some improvements have already been reported. Okado et al. [6] have proposed a superlattice structure to avoid crystallisation to occur. Others [7] have suggested the use of appropriate substrate in order to realize lattice constant matching conditions between the substrate and the first deposited monolayer.



Fig. 4: (left) 2 layers and (right) 4 layers of PDA 15-8 L.B. film as seen under cross-polarized microscope.

### CROSS-POLARIZED OPTICAL MICROSCOPY

As seen under cross-polarized microscope, the cobalt salt polydiacetylene bilayer exhibits birefringence. Two-dimensional domains with sizes ranging from 1 to 50 microns were observed (Fig. 4). Spherulitic type morphology as reported by Day et al. [1] in their work using a lithium salt acetylene monolayer polymerized at the air-water interface was not observed in this experiment.

When more than two layers are deposited, cross-polarized micrographs show better contrast which reflects a stronger birefringence of the film. Therefore, domains in additional layers must align themselves with the original layers and some form of L.B. epitaxial crystal growth [6] occurs right after the first dipping.

### RAMAN SCATTERING

Vibronic structure of the PDA 15-8 film can be studied using Raman scattering. However, because of the weak spontaneous Raman signal, some form of enhancement is necessary to study monolayers, in order to avoid rather long scanning time. Chen et al. [8,9] have used thin silver coating, while Burzynski et al. [10] have used an optical wave guide arrangement to record Raman spectra of polydiacetylene L.B. films.

The spectrum shows two strong peaks, one due to the stretching vibration of C=C, the second due to the stretching of C≡C. Those peaks are located for the blue phase PDA 15-8 (less than 5 min UV exposure) at  $1461\text{ cm}^{-1}$  and  $2081\text{ cm}^{-1}$  while for the red phase (30 min UV exposure or more), they are at  $1521\text{ cm}^{-1}$  and  $2121\text{ cm}^{-1}$ . For a UV exposure time between 5 and 30 min, both phases are present in the film and the spectrum exhibits all 4 peaks as shown on fig. 5b. We must point out that since we use 488nm as excitation wavelength, the red phase is in resonance with the incident beam and their associated vibrational peaks are enhanced over those of the blue phase.

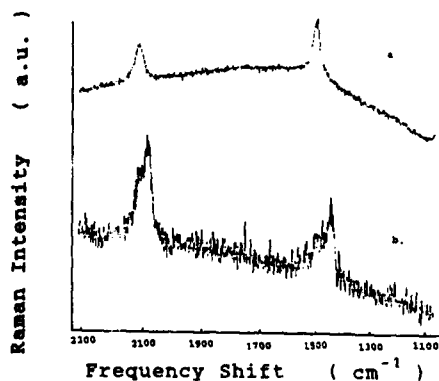


Fig. 5: Raman Scattering of 4 layers L.B. film of PDA 15-8 (a) in the red phase and (b) in a mixture of red and blue phase. (a) is enhanced by a thin layer (100Å) of silver.



## CONCLUSIONS

Polydiacetylene LB films have been investigated by three complementary optical techniques. Laser light scattering is a simple tool to study submicron defect distribution and nonuniformity in the films. Moreover, it gives some quantitative informations on the scattering losses when a light beam propagates through the particular material. This technique is however limited to the study of films on optically smooth substrates for which the scattering from surface roughness is negligible. The lateral resolution is limited to a couple of microns. Reflection microscopy between crossed polarizers offers better resolution but is less sensitive to submicron defects since as opposed to light scattering microscopy it uses a bright field. It is a sensitive tool to view crystalline domains in the PDA LB films and to study their size, shape and arrangement layer by layer. In particular, we have confirmed that improvement in the degree of crystallinity occurs after the first two layers have been deposited on the substrate. Finally, the degree of polymerization can be studied using Raman scattering since the blue phase and the red phase of polydiacetylene shows distinct Raman signatures.

## REFERENCES

1. D. Day and J.B. Lando, *Macromolecules* **13**, 1478 (1980).
2. H. Nakanishi, H. Matsuda, S. Okado and M. Kato, in *Nonlinear Optics of Organics and Semiconductors* edited by T. Kobayashi, Springer-Verlag (1989), pp155-162.
3. P. Lessieur, A. Barraud and M. Vandevyver, *Thin Solid Films*, **152**, 165 (1987).
4. K. Moriya and T. Ogawa, *Japn. J. of Appl. Phys.* **22** (4), 1207 (1983).
5. T. Ogawa and N. Nango, *Rev. Sci. Instrum.* **57** (6), 1135 (1986).
6. S. Okado, H. Nakanishi, H. Matsuda, M. Kato, T. Abe and H. Ito, *Thin Solid Films*, **179** (1989).
7. I.R. Peterson, in *Polydiacetylenes*, edited by D. Bloor and P.R. Chance, Martinus Nijhoff Publishers, (1985), pp377-388.
8. Y.J. Chen, G.M. Carter and S.K. Tripathy, *Solid State Comm.* **54** (1), 19 (1985).
9. Y.J. Chen, S.K. Tripathy, G.M. Carter, B.S. Elman, E.S. Koteles and J. George, Jr, *Solid State Comm.* **58** (2), 97 (1986).
10. R. Burzynski, P.N. Prasad, J. Biegajski and D.A. Cadenhead, *Macromolecules* **19**, 1059 (1986).
11. J.B. Lando, in *Polydiacetylenes*, edited by D. Bloor and P.R. Chance, Martinus Nijhoff Publishers, (1985), pp363-370.

ELECTRONIC STRUCTURE OF LONG POLYENES:  
STATES AND TRANSITION DIPOLES

BRYAN E. KOHLER

Chemistry Department, University of California, Riverside, CA 92521, U.S.A.

ABSTRACT

Electronic excitation energies and transition dipoles measured for symmetrically substituted linear polyenes ( $R-(CH=CH)_N-R$ ) with chain lengths  $n$  ranging from 2 to 8 are well fit by the functional form  $A+B/N$ . Extrapolation to the long chain limit correlates the band gap transition of polyacetylene with the polyene  $1^1A_g$  to  $1^1B_u$  transition. The amount by which the highly correlated polyene  $2^1A_g$  state is lower than the  $1^1B_u$  state increases with increasing chain length, extrapolating to roughly half of the  $1^1B_u$  excitation energy. The  $1^1A_g$  to  $1^1B_u$  transition dipole magnitude per chain repeat unit attains a maximum value of 3.0 Debye at an effective conjugation length 5 double bonds.

Careful studies on linear polyenes provides insight into the electronic structure of polyacetylene.

1. INTRODUCTION

Our understanding of polyene electronic structure has advanced significantly during the last decade [1]. The discovery that the lowest energy excited singlet state for linear polyenes is not the  $1^1B_u$  state derived by promoting a single electron from the highest energy occupied molecular orbital (HOMO to the chemist, top of the valence band to the physicist) to the lowest energy unoccupied molecular orbital (LUMO to the chemist, bottom of the conduction band to the physicist) but, rather, the  $2^1A_g$  state that can roughly be described as a double excitation from the HOMO to the LUMO is especially important. This unexpected ordering of excited states calls attention to the unusual importance of electron correlation in these molecules and raises questions about theoretical models for linear polyenes, including polyacetylene, that neglect explicit consideration of electron-electron interactions [1-3].

This contribution reviews two aspects of linear polyene electronic structure that are of special interest with respect to conjugated polymers. These are the chain length dependence of  $1^1A_g$  to  $2^1A_g$  and  $1^1B_u$  excitation energies and transition dipole magnitudes. A detailed discussion of how the polyene  $2^1A_g$  state isomerization behavior and excitation energy extrapolated to longer chain length is consistent with the transient absorption spectra and thermal isomerization of polyacetylene has been published elsewhere [4].

## 2. $2^1A_g$ and $1^1B_u$ EXCITATION ENERGIES

Excitation energies of finite polyenes with the general structure  $R-(CH=CH)_N-R'$  depend on the substituents R and R' and on the microscopic local environment (solvent). However, for  $N > 3$  the  $2^1A_g$  state lies below the  $1^1B_u$  state for all substituents and all solvent environments that have so far been investigated [1,5]. The fact that the  $2^1A_g$  state is electronically distinct from the  $1^1B_u$  state, that is, that it is not the  $1^1B_u$  state in a geometry distorted with respect to the ground state equilibrium geometry, deserves special emphasis. In linear polyenes the electronic configuration of the  $2^1A_g$  state differs fundamentally from that of the  $1^1B_u$  state (double versus single excitation in a molecular orbital picture) and lies lower in energy for all reasonable nuclear configurations (Figure 1).

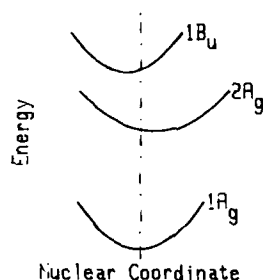


Figure 1. The ordering of electronic states in linear polyenes. The dashed line marks the geometry that minimizes the electronic energy of the ground state. The displacement of the excited state minima from the dashed line indicates that the electronic energies of excited states can often be reduced by distorting from the ground state geometry. In linear polyenes the "doubly excited"  $2^1A_g$  state lies below the "band gap"  $1^1B_u$  state for all reasonable conformations.

For the chain length dependence of  $2^1A_g$  and  $1^1B_u$  excitation energies we have selected a data set restricted to symmetrically substituted molecules ( $R=R' = -H, CH_3, \text{ or } -\text{phenyl}$ ) in low temperature *n*-alkane matrixes [6-15]. For this data set spectra have resolved vibrational fine structure and vibrationally relaxed electronic excitation energies can be unambiguously determined. The data are summarized in Table 1.

Lacking an analytical model for the functional form that excitation energy versus chain length (the  $N$  in  $R-(CH=CH)_N-R'$ ) should have, we follow the tradition of taking a power series in  $1/N$ , truncated to first order and use the idea of an effective conjugation length for substituents [16]. That is, in our analysis of the data in Table 1  $N$  is replaced by

$$N_{\text{eff}} = N + N(R) + N(R') \quad (1)$$

Table 1

Dependence of  $1^1B_u$  0-0 Excitation Energies on Chain Length for Molecules in the Series  $R-(CH=CH)_N-R$

N	R	$2^1A_g$ $\nu_{0-0}$ ( $cm^{-1}$ )	$1^1B_u$ $\nu_{0-0}$ ( $cm^{-1}$ )	Conditions
3	H	-----	36850	3-methylpentane at 77K, Ref. 6
4	H	28560	32100	n-octane at 4.2K, Ref. 7
6	H	21640	26430	EPA glass at 77K <sup>a</sup> , Ref. 8
7	H	19630	24100	EPA glass at 77K <sup>b</sup> , Ref. 8
3	CH <sub>3</sub>	-----	35130	n-undecane at 12K
4	CH <sub>3</sub>	28740	32180	n-undecane at 4.2K, Ref. 9
5	CH <sub>3</sub>	24560	27680	n-nonane at 4.2K, Ref. 10
7	CH <sub>3</sub>	19520	24180	n-pentadecane at 4.2K, Ref. 11
8	CH <sub>3</sub>	17870	22770	n-hexadecane at 4.2K, Ref. 12
2	phenyl	-----	27755	average of two sites, n-decane at 4.2K, Ref. 13
3	phenyl	25350	25900	n-dodecane at 4.2K, Ref. 13
3	phenyl	25610	26050	n-tridecane at 4.2K, Ref. 13
4	phenyl	22270	24380	n-dodecane at 4.2K, Ref. 14
5	phenyl	20130	23070	n-decane at 4.2K, Ref. 15
6	phenyl	18260	21930	n-dodecane at 4.2K, Ref. 15

<sup>a</sup>) taken from Figure 2 by digitizing a xerox copy of the original figure and then least squares fitting a Gaussian to the 0-0 band.

<sup>b</sup>) taken from Figure 3 by digitizing a xerox copy of the original figure and then least squares fitting a Gaussian to the 0-0 band.

where  $N(-H)=0$  and  $N(-CH_3)$  and  $N(-phenyl)$  are the two constants for the effective conjugation lengths of these substituents that best fit the data. This simple, empirical model gives a convenient and quantitative summary of the measured excitation energies as can be seen in Figure 2.

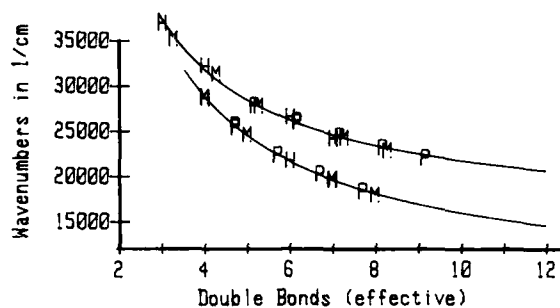


Figure 2. Excitation energies for symmetrically substituted linear polyenes  $R-(CH=CH)_n-R$ . Experimental energies are plotted as letters: H for  $R=-H$ , M for  $R=-CH_3$ , and P for  $R=-phenyl$ . The upper curve shows  $1^1B_u$  excitation energies versus the effective number of double bonds ( $N$  for  $R=-H$ ,  $N+2(0.13)$  for  $R=-CH_3$ , and  $N+2(1.58)$  for  $R=-phenyl$ ). The lower curves gives  $2^1A_g$  excitation energies versus the effective number of double bonds ( $N$  for  $R=-H$  and  $R=-CH_3$ ,  $N+2(0.85)$  for  $R=-phenyl$ ). The best fit by  $E=A+B/N_{eff}$  (solid lines) has a long chain limit of  $7300\text{ cm}^{-1}$  for the  $2^1A_g$  state and  $14900\text{ cm}^{-1}$  for the  $1^1B_u$  state.

For the  $2^1A_g$  excitation energy  $N(-CH_3)=0.13$  and  $N(-phenyl)=1.58$ ; for the  $1^1B_u$  excitation energy  $N(-CH_3)=0.01$  and  $N(-phenyl)=0.85$ . Although it is not surprising that the effective conjugation length of a substituent is different for the transitions to the  $2^1A_g$  and  $1^1B_u$  states, we haven't yet settled on the simple picture that best rationalizes this.

The infinite chain limits of the  $2^1A_g$  and  $1^1B_u$  excitation energies are  $7300\text{ cm}^{-1}$  (0.91 eV) and  $14900\text{ cm}^{-1}$  (1.85 eV), respectively. Of course, these energies are 0-0 excitation energies for molecules isolated in an n-alkane crystal so they are only approximate guides to the excitation energies expected for a pure polyene crystal.

There have been a number of studies of the dependence of polyene excitation energies on molecular environment. In fact, the observation that the origin of the strongly allowed absorption ( $1^1A_g$  to  $1^1B_u$ ) exhibited different solvent shift behavior than did the fluorescence origin ( $2^1A_g$  to  $1^1A_g$ ) was strong evidence that these two transitions involved different

electronic states [17]. Systematic solvent shift studies on diphenylpolyenes [18,19] and unsubstituted polyenes [8] are reasonably summarized by the expression

$$\bar{\nu} = \bar{\nu}_0 + K((n^2-1)/(n^2+2)) \quad (2)$$

where  $\nu_0$  is the transition energy for the isolated molecules,  $K$  is a constant independent of the polyene chain length, and  $n$  is the refractive index of the solvent. For the  $1^1A_g$  to  $1^1B_u$  transition  $K=10^4 \text{ cm}^{-1}$ ; for the  $1^1A_g$  to  $2^1A_g$  transition  $K$  is at least an order of magnitude smaller.

Because the  $1^1A_g$  to  $2^1A_g$  transition is almost insensitive to microscopic molecular environment, the  $7300 \text{ cm}^{-1}$  (0.91 eV) value extrapolated from the data in Table 1 is a reasonable estimate for the energy difference between fully relaxed  $2^1A_g$  and  $1^1A_g$  states for a pure polyacetylene crystal. The vertical transition energy (ground state equilibrium geometry for both states) is typically  $2000 \text{ cm}^{-1}$  (.25 eV) higher.

The much greater solvent sensitivity of the  $1^1B_u$  excitation energy suggests that it may significantly decrease in going from an n-alkane to a polyacetylene environment. Unfortunately, the approximate solvent shift theory given in equation 2 is not useful for describing the kinds of resonant interactions that characterize a pure polyene crystal. The best we can do is take the maximum magnitude of the  $1^1A_g$  to  $1^1B_u$  transition dipole of 3 Debye per polyene repeat unit (see section 3 below) and the interchain separation of 4.12 Angstroms [20] and estimate the magnitude of the shift from the resonant interactions by

$$\delta\bar{\nu} = -\mu^2 / (hCr^3) \quad (3)$$

where  $\mu$  is the transition dipole,  $r$  is the interchain separation,  $h$  is Planck's constant and  $C$  is the speed of light. This gives a correction of  $-650 \text{ cm}^{-1}$  to  $14270 \text{ cm}^{-1}$  (1.77 eV) for the energy difference between fully relaxed  $1^1B_u$  and  $1^1A_g$  states. Adding the  $2000 \text{ cm}^{-1}$  for the transition at the ground state geometry (band maximum) gives an excitation energy of  $16270 \text{ cm}^{-1}$  (2.0 eV) which is in reasonable agreement with the polyacetylene absorption spectrum.

Finally, we note that, in a zero order description the  $1^1B_u$  state involves a single excitation and the  $2^1A_g$  state involves a double excitation from the HOMO to the LUMO. That the  $1^1A_g$  to  $1^1B_u$  transition dipole is large has been established by experiment. In a zero order description the  $2^1A_g$  to  $1^1B_u$  transition dipole is equally large. Thus, long polyenes should exhibit classical excited state absorption: that is, excitation into the dipole allowed  $1^1B_u$  state should be followed by rapid decay to the lower lying, relatively long lived,  $2^1A_g$  state from which transient absorption from  $2^1A_g$  to  $1^1B_u$  will be seen (Figure 3). The direct

observation of this transient absorption in simple polyenes [21] suggests alternative interpretations for the transient spectra measured for polyacetylene films.

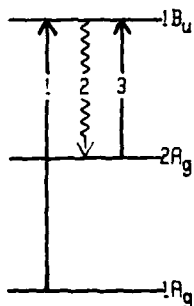


Figure 3. Excited State absorption in linear polyenes. Excitation to the dipole allowed  $1^1B_u$  state (1) depletes the ground state bleaching the normal absorption spectrum. Picosecond relaxation to the  $2^1A_g$  state (2) makes possible a new dipole allowed transient absorption (3) from  $2^1A_g$  to  $1^1B_u$ .

### 3. $1^1A_g$ to $1^1B_u$ TRANSITION DIPOLES

Nonlinear optical susceptibilities are often calculated as perturbation sums of products of transition dipoles over energy denominators. Thus, an understanding of the linear susceptibility (transition dipole) is a necessary condition for understanding the more complex nonlinear responses. It is somewhat ironic that, for the linear polyenes, there are a number of measurements of nonlinear susceptibilities but little data on the transition dipoles that are key to these higher order responses. It is for this reason that we have measured absolute absorption spectra (molar extinction coefficient  $\epsilon$  versus wavelength) for the  $1^1A_g$  to  $1^1B_u$  transition for the  $\alpha,\omega$ -diphenylpolyenes with 2 through 8 double bonds in the polyene chain and, using the relation

$$|\mu|^2 = 9.186 \times 10^{-3} \text{ Debye}^2 \text{ mol}^{-1} \text{ cm} [(2n^2+1)/3n^2]^2 \int \epsilon d \ln \bar{\nu}, \quad (4)$$

have extracted the *in vacuo* transition dipoles. A detailed discussion of the large number of experiments that resulted in the data reproduced in (Table 2 and graphically displayed in Figure 4 has been given elsewhere [22]. The most striking feature of the  $1^1A_g$  to  $1^1B_u$  transition dipole magnitudes is their relatively weak dependence on polyene chain length (Figure 4). It is clear that an asymptotic value is rapidly attained and that, for the longer chains, the transition dipole per polyene repeat unit actually decreases with increasing chain length.

Table 2

n for $\phi-(CH=CH)_n-\phi$	solvent(a)	$\epsilon_{\max}$ in $\text{mol}^{-1} \text{ l cm}^{-1}$	$\int \epsilon d \ln \nu$ in $\text{mol}^{-1} \text{ l cm}^{-1}$	$ \mu $ in Debye (b)
2	T	38630±59	5010±30	5.99±.70
	M	50110±2190	7280±300	
	D	37030±2650	5050±440	
3	T	64550±3520	8810±510	7.50±.26
	M	68170±2820	9590±410	
	D	58480±4000	8590±500	
4	T	93830±14640	12670±2020	8.76±.07
	M	86990±5760	11880±770	
	D	93100±10410	12280±1350	
5	T	93300±1025	12770±430	8.99±.24
	M	10130±14760	13540±1850	
	D	93400±8470	12480±1100	
6	T	99620±2670	13250±390	8.89±.21
	M	87246±6050	11780±880	
	D	97540±7690	12880±1040	
7	T	110590±15130	14710±2050	10.13±.58
	M	122790±12130	16770±1780	
	D	126730±19220	17740±2530	
8	T	-	-	8.18±.18
	M	75177±16480	10870±2400	
	D	80690±15210	10260±2800	

a) T = toluene, M = methylene chloride, D = N,N-dimethylformamide

b)  $|\mu|^2 = 9.184 \times 10^{-3} \text{ mol l}^{-1} \text{ cm debye}^2 [(2n^2+1)/3n^2]^2 \int \epsilon d \ln \nu$ ;  
n values used were 1.4961 for toluene, 1.4242 for methylene chloride and 1.4305 for  
N,N-dimethylformamide.



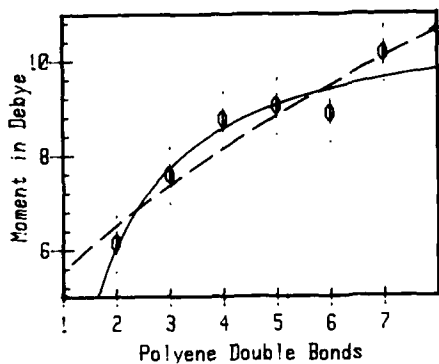


Figure 4. Transition dipole magnitudes versus polyene double bonds for the diphenylpolyene series. The points are the best values of the vacuum  $1^1A_g$  to  $1^1B_u$  transition dipole magnitudes. The solid line is the best fit to these data by  $|\mu|=A+B/N$ ; the dashed line is the best fit to these data by  $|\mu|=(A+BN)^{1/2}$ .

Given that even rather sophisticated molecular orbital theories cannot even properly order the low lying excited singlet states of linear polyenes [1], it is not surprising that the proper functional form for a plot of transition dipole versus polyene chain length is an open question. An empirical fit of the transition dipole magnitude for the diphenylpolyene series by

$$|\mu| = A+B/N \quad (5)$$

gives  $A \approx B=11$  Debye. For these parameters, the maximum transition dipole magnitude per polyene repeat unit is 3.0 Debye which is reached at  $N=2$ .

The degree to which the phenyl rings extend the effective conjugation length of the substituted polyene chain was empirically determined in section 2. by simultaneously fitting  $1^1A_g$  to  $1^1B_u$  excitation energies of both series by  $A+B/N$  for the unsubstituted polyenes and  $A+B/(N+2C)$  for the diphenylpolyenes. Fitting the transition dipole magnitudes by

$$|\mu|=A+B/(N+2C) \quad (6)$$

where  $C=1.6$  (the value determined by the fit to the excitation energies) gives  $A=13.6$  Debye and  $B=-37.6$  Debye per effective double bond. With these parameters the maximum transition dipole magnitude per polyene repeat unit is 1.2 Debye which is reached at an effective conjugation length of 5.5 double bonds. This very early saturation of the transition dipole magnitude is at variance with some of the more optimistic predictions of approximate molecular orbital methods [23].

Finally, we note that the values for the transition dipole magnitudes that we have determined are fully consistent with the observed dependence of  $1^1A_g$  to  $1^1B_u$  excitation

energy on solvent polarizability. Diamond and Hudson [17,18] determined that the solvent shift behavior for all the diphenylpolyenes in the series  $\phi-(\text{CH}=\text{CN})_N-\phi$  with  $N=1-6,8$  was well described by equation 2 and that, within experimental error, the value of  $K$  was the same for all of the molecules ( $9870 \pm 740 \text{ cm}^{-1}$ ).  $K$  has the form [24]

$$K = |\mu|^2 P / V_s \quad (7)$$

where  $\mu$  is the  ${}^1A_g$  to  ${}^1B_u$  transition dipole,  $V_s$  is the volume of the solute and  $P$  is a constant. For the diphenylpolyenes

$$V_s = V_{\text{phenyls}} + V_{\text{chain}} = V_{\text{phenyls}} + NV_{\text{chain unit}} \quad (8)$$

so the constancy of  $K$  implies that the transition dipole magnitude should be fit by

$$|\mu| = (A + BN)^{1/2} \quad (9)$$

Figure 4 shows that the transition dipoles reported here are consistent with this expectation, although the standard deviation of fit for this form is approximately 20% higher than that obtained when the data are fit by equation 5. When equation 9 is used the maximum transition dipole magnitude is 4.4 Debye at a chain length of 3 double bonds for both  $N$  and  $N_{\text{eff}}$ . The important point is that, when either form is fit to the data, the transition dipole magnitude per polyene repeat unit for chains with more than 5 effective double bonds decreases with increasing chain length.

#### 4. ACKNOWLEDGEMENTS

This work has benefitted from support by the NSF (CHE8803916) and NIH (Ey06466) and the interest and comments of R.R. Chance.

#### 5. REFERENCES

1. B.S. Hudson, Bryan E. Kohler and K. Schulten, *Excited States* **6**, 1 (1982).
2. K. Schulten, I. Ohmine and M. Karplus, *J. Chem. Phys.* **64**, 4422 (1976).
3. I. Ohmine, M. Karplus and K. Schulten, *J. Chem. Phys.* **68**, 2348 (1978).
4. B.E. Kohler, *J. Chem. Phys.* **88**, 2788 (1988).
5. B.E. Kohler, C. Spangler and C. Westerfield, *J. Chem. Phys.* **89**, 5422 (1988). Table IV in this paper summarizes information for unsubstituted and alkyl substituted polyenes with 4 through 8 double bonds in conjugation.

6. M.F. Granville, B.E. Kohler and J.B. Snow, *J. Chem. Phys.* **75**, 3765 (1981).
7. M.F. Granville, G.R. Holtom and B.E. Kohler, *J. Chem. Phys.* **72**, 4671 (1980).
8. R. Snyder, E. Arridson, C. Foote, L. Harrigan and R.L. Christensen, *J. Am. Chem. Soc.* **107**, 4117 (1985).
9. J.R. Anders and B.S. Hudson, *J. Chem. Phys.* **72**, 4671 (1980).
10. R.L. Christensen and B.E. Kohler, *J. Chem. Phys.* **63**, 1837 (1975).
11. J.H. Simpson, L. McLaughlin, D.S. Smith and R.L. Christensen, *J. Chem. Phys.* **87**, 3360 (1987).
12. B.E. Kohler, C. Spangler and C. Westerfield, *J. Chem. Phys.* **89**, 5422 (1988).
13. W.M. Heatherington, III, Thesis, Stanford University, Stanford, CA (1977).
14. As measured in this laboratory by C. Westerfield.
15. J.S. Horwitz, T. Itoh, B.E. Kohler and C.W. Spangler, *J. Chem. Phys.* **87**, 2433 (1987).
  
16. J.L. Bredas, R. Silbey, D.S. Doudreaux and R.R. Chance, *J. Am. Chem. Soc.* **105**, 6555 (1983).
17. B.S. Hudson and B.E. Kohler, *J. Chem. Phys.* **59**, 4984 (1973).
18. J. Diamond, Thesis, Stanford University, Stanford, CA (1978).
19. L.A. Sklar, B.S. Hudson, M. Petersen and J. Diamond, *Biochem.* **16**, 813 (1977).
20. R.H. Baughman, B.E. Kohler, I.J. Levy and C. Spangler, *Synthetic Metals* **11**, 37 (1985).
21. S.M. Bachilo and S.L. Bondarev, *Opt. Spectrosc. (USSR)* **65**, 177 (1988).
22. B.E. Kohler and J.A. Pescatore, Jr., Proc. Mons NATO Advanced Research Workshop, in press.
23. B.M. Pierce, *J. Chem. Phys.* **91**, 791 (1989).
24. A.J. Amos and B.L. Burrows, *Advan. Quantum. Chem.* **7**, 303 (1973).

THEORETICAL CALCULATIONS ON NONLINEAR SUSCEPTIBILITIES  
OF ORGANIC CRYSTALS

YUZO ITOH, TOMOYUKI HAMADA, ATSUSHI KAKUTA, AND AKIO MUKOH  
Hitachi Research Laboratory, Hitachi Ltd., 4026 Kuji-cho, Hitachi, Ibaraki,  
319-12 Japan

## ABSTRACT

Theoretical calculations on nonlinear susceptibilities of organic crystals are made. Under the oriented gas model approximation, nonlinear susceptibility of a crystal can be calculated both from the molecular hyperpolarizability and crystal structure data. Molecular hyperpolarizabilities are calculated by an *ab initio* molecular orbital (MO) method and the energy minimum crystal structures are obtained by an empirical atom-atom pairwise potential method. Finally the effect of intermolecular interactions on molecular hyperpolarizabilities, which is neglected in the above approximation, is investigated quantitatively by using a "super molecule" method of *ab initio* MO calculations.

## INTRODUCTION

Most organic crystals are molecular with the molecules being bound by weak van der Waals forces. Accordingly, the oriented gas model approximation, in which intermolecular interactions caused by molecular packing in the crystal are neglected, is usually good. Under this approximation we can calculate nonlinear susceptibility of a crystal from molecular hyperpolarizabilities and the crystal structure information.

There have been many theoretical investigations on hyperpolarizabilities of molecules [1-20]. However, most of them used empirical or semi-empirical methods. Theoretical calculations by *ab initio* MO methods on hyperpolarizabilities of relatively large molecules [7,17,19], which are interesting for nonlinear optical applications, are very few. Semi-empirical methods are very convenient to evaluate relatively accurate hyperpolarizabilities with a relatively small cpu time, but the *ab initio* method is necessary to analyse them more deeply and comprehensively. First, some calculation methods of hyperpolarizabilities by the *ab initio* MO method were investigated and compared to each other.

Secondly, since very few theoretical studies on crystallization properties of organic nonlinear materials have been done, these properties were investigated by crystal energy calculations using empirical atom-atom pairwise potentials.

Finally, the effect of intermolecular interactions by molecular packing in the crystal on hyperpolarizabilities was quantitatively investigated by a "super molecule" method of *ab initio* MO calculations. So far only one paper from this viewpoint [7] has been presented, in which the effect of hydrogen-bonding in the crystal on hyperpolarizabilities was investigated. However, only the electrostatic interaction was treated for intermolecular interactions. Then, in the present treatment all short range intermolecular interactions were included.

THEORETICAL CALCULATIONS ON HYPERPOLARIZABILITIES BY THE *AB INITIO* METHOD

There were several approaches to the calculation of molecular hyperpolarizabilities of organic nonlinear optical materials. (1) The hyperpolarizability is obtained from the differential of the ground state energy with respect to the electric field. The ground state energy is calculated by the self-consistent procedure in the presence of an external

electric field. The differential of the energy value can be performed numerically (coupled Hartree-Fock, CHF)[21] or analytically (coupled-perturbed Hartree-Fock, CPHF)[22]. The former, which is sometimes called the finite field method, is a more practical and popular method[6,17], however, the latter gives more accurate values. (2) In the time independent perturbation theory, the hyperpolarizability is obtained by the electric dipole perturbation in the expansion of the one-electron orbitals, which is equivalent to an expansion of many electron states. The molecular orbitals are obtained by a single SCF calculation without external electric field. (3) In the time dependent perturbation theory, the hyperpolarizability is evaluated by the same method as (2) but the perturbed states are expanded by the molecular eigenstates. To calculate reliable molecular eigenstates, in particular excited ones, the electron correlations should be considered, for example, by the configuration interactions. This kind of treatment needs a large scale of calculation, so that method (3) is usually used with a semi-empirical MO method. This last method is not considered here.

At first, the basis set dependence of hyperpolarizabilities was investigated and the difference between the hyperpolarizability values was calculated by the CPHF method (method(1)) and the time independent perturbation method (method (2)). The *ab initio* MO calculations were done using HONDO 7[23] for method (1), and GAUSSIAN 80[24] for method (2). These programs were modified for the Hitachi M682H and super computer S820 systems. Both calculations were done at the Hartree-Fock level.

The calculated results of the hyperpolarizability  $\beta$  of urea and p-nitroaniline (p-NA) by the two methods and their basis set dependences are shown in Table I. On the basis set dependence, at least a split valence type basis set is necessary to evaluate reliable hyperpolarizability values. Comparing these values of p-NA obtained by methods (1) and (2), the former are closer to the experimental ones than the latter method, which is similar to the case for the linear polarizabilities of polyene oligomers[17]. Urea has nearly the same values in both methods. This is considered to reflect the fact that the CPHF method included the average electron-electron interaction self-consistently under the electric field perturbation in contrast with the time independent perturbation method, as indicated by Andre et al.[17] for the linear polarizabilities, and a large  $\pi$  conjugated system such as p-NA, is significantly influenced by the interactions.

#### CRYSTAL ENERGY CALCULATIONS

In our previous paper[28], as a first step for estimation of crystal structures, the intermolecular interaction energies between two molecules in

TABLE I  $\beta$  values in units of  $10^{-30}$  esu calculated by *ab initio* method

Basis Set	STO-3G	3-21G	4-31G	6-31G	6-31G*	LP-31G (ECP)	Experimental	
Urea	CPHF <sup>b</sup>	0.177	0.501	0.555	0.559	0.485	0.522	0.45 <sup>25</sup>
	time indep.PT <sup>c</sup>	0.163	0.451	0.460	0.530	0.473	0.495	(at 1.06 $\mu$ m)
p-NA	CPHF <sup>b</sup>	4.210	8.038	9.994	10.194		9.202	9.6 <sup>26</sup>
	time indep.PT <sup>c</sup>	2.503	3.641	4.013	4.200		3.930	(at 1.907 $\mu$ m)

a ECP : effective core potential method.<sup>27</sup>

b CPHF : coupled perturbative Hartree Fock method.

c time indep.PT : time independent Perturbation Theory.

various intermolecular configurations were calculated by using the empirical potential functions and the relationship between the calculated results and the existence of inversion centers in the crystals was investigated for typical nonlinear optical materials.

The extension of the method to a crystal energy calculation including a large number of molecules was considered. To obtain the minimum energy crystal structure, a specific approach, where a space group was assumed, was used. This procedure drastically reduced the degrees of freedom to be considered in the calculation. Under this condition, the crystal energy was minimized on various degrees of freedom generated by combining six parameters of the crystal (lattice constants) to six parameters of the molecule (translation and rotation). The same calculations were repeated in order for the other space groups. Finally the required crystal structure was obtained by selecting the one which had the minimum energy from the minimum energy structure of each space group.

A number of crystal energy calculation methods have been investigated so far[29-31], and a calculation method from among the empirical calculation methods using atom-atom pairwise potentials was chosen. In this method intermolecular interaction energy is expressed as,

$$V_T = U_V + U_E \quad (1)$$

$$U_V = \frac{1}{2} \sum_i \sum_j (-A_{ij} / r_{ij}^6 + B_{ij} / r_{ij}^{12}) \quad (2)$$

$$U_E = \frac{1}{2} \sum_i \sum_j Q_i Q_j / r_{ij} \quad (3)$$

where  $U_V$  is the van der Waals potential including the repulsion by the electron orbital overlap, which is known as the Lennard-Jones potential function,  $U_E$  is the electrostatic Coulomb potential,  $r_{ij}$  is the interatomic distance,  $A_{ij}$  and  $B_{ij}$  are Lennard-Jones parameters,  $Q_i$  is the partial charge of the  $i$ -th atom, which is obtained by MO calculations and discussed in detail later. The summations with respect to  $i$  and  $j$  are taken for atoms included in the unit cell and in the crystal, respectively. In principle, the latter should be taken for atoms at infinite distance. In practice, the range of the summation is limited to a certain finite distance, at which the crystal energy is considered to be convergent.

A difficult problem arises from the convergence of the calculated crystal energy since the electrostatic potential energy is not convergent in the long distance region due to its long range interaction property. Thus the accelerated convergence method developed by Ewald[30,32] was used. The electrostatic energy is expressed as,

$$U_E = \frac{1}{2} \sum_{i,j} Q_i Q_j / r_{ij} + \frac{1}{2\pi V} \sum_{\mathbf{h}_\lambda \neq 0} |F(\mathbf{h}_\lambda)|^2 h_\lambda^{-2} \exp(-b^2) \quad (4)$$

$$-K \sum_{\text{CELL}} Q_i^2 \quad (5)$$

$$F(\mathbf{h}_\lambda) = \sum_{\text{CELL}} Q_i \exp(-2\pi i \mathbf{h}_\lambda \cdot \mathbf{r}_{ij}) \quad (5)$$

$$b^2 = \pi h_\lambda^2 / K^2 \quad (6)$$

where ERFC is the error function,  $V$  is the volume of the unit cell,  $\mathbf{h}_\lambda$  is the reciprocal space vector, and  $K$  is the convergence parameter. In this particular method, the summation is done for both real and reciprocal spaces.

Table II shows the minimum energy structures of typical organic nonlinear optical materials, calculated by optimizing all degrees of freedom under the restriction of the space group symmetry experimentally obtained[33-35]. Good agreement is achieved between the experimental[33-35] and calculated structures. It should be noted that the empirical parameters, which were not developed for the purpose of the crystal optimization of our target materials, reproduce observed crystal structures very well. There is still some slight difference, which might be improved by raising the accuracy

TABLE II Cell dimensions of observed and minimum energy crystal structures

Molecules		Cell Dimensions			Crystal Energies	
		a /Å	b /Å	c /Å	$\beta$ /deg.	/kJ mol <sup>-1</sup>
MNA	Exp. <sup>37</sup>	8.2525	11.62	7.585	94.08	-431.32 <sup>a</sup>
	Calc.	8.2	11.6	7.6	94.1	-444.42
p-NA	Exp. <sup>38</sup>	12.336	6.07	8.592	91.45	-445.99 <sup>a</sup>
	Calc.	12.5	6.1	8.8	91.5	-451.22
xanthone	Exp. <sup>39</sup>	13.63	14.11	4.86	90.0	-428.45 <sup>a</sup>
	Calc.	13.8	14.3	4.9	90.0	-435.74
2-7-dinitro -xanthone	Exp. <sup>b</sup>	6.136	36.892	5.089	90.0	-682.03 <sup>a</sup>
	Calc.	6.5	36.1	5.3	90.0	-703.38

<sup>a</sup> Calculated using observed crystal structures.

<sup>b</sup> Details of these crystallographic data will be described elsewhere.

of the calculation of partial charges.

The method which is ordinarily used to obtain atomic partial charges of the molecule is the Mulliken's population analysis (PA). However, it is not accurate enough to reproduce physical properties, such as the dipole moment. A more accurate method, called the potential derived (PD) method, has been developed [36]. In this method atomic partial charges of the molecule were determined by the least square method so as to reproduce electrostatic potential accurately around the molecules. The electrostatic potential can be directly obtained by MO calculations. In Table III, dipole moments of 2-methyl-4-nitroaniline (MNA) calculated from the atomic partial charges obtained by the PA and PD methods are shown compared with those directly calculated by the MO method using the dipole moment operator, and one obtained experimentally. Apparently the PD method is more accurate than the PA one and the former should be used in more reliable crystal energy calculations.

TABLE III Dipole moment of MNA calculated from atomic partial charges /Debye

	$\mu_x$	$\mu_y$	$\mu_z$	$ \mu $
PA(CNDO)	-0.138	0.0029	-7.0984	7.0994
PA(MNDO)	-0.0614	0.0016	-7.0186	7.0189
PA(ab initio)	-0.3044	0.0	-5.6683	5.6764
PD(ab initio)	-0.2918	0.0	-5.8450	5.8523
Direct	-0.2565	0.0	-5.9558	5.9614
Experimental <sup>39</sup>	-	-	-	6.3

## THE EFFECT OF INTERMOLECULAR INTERACTIONS ON HYPERPOLARIZABILITIES

In theoretical calculations of crystal nonlinear susceptibilities under the oriented gas model approximation, the effect of intermolecular interactions in the crystal on molecular hyperpolarizabilities is neglected. This effect is generally thought to be small since most organic crystals are molecular, and hence held by weak van der Waals interactions. However, in fact, there are many organic crystals in which strong intermolecular interactions such as charge transfer or hydrogen bonding exist. Some of these kinds of crystals have large optical nonlinearity and are interesting for industrial applications. So far this effect in organic nonlinear optical materials has not been investigated quantitatively, except for the case of urea[7], in which the effect of electrostatic interactions of hydrogen bonding on hyperpolarizabilities was evaluated by the CHF method with *ab initio* MO calculations.

In order to include all short range intermolecular interactions, a "super molecule" method was taken. In this method two or more molecules were treated as one super molecule in the MO calculations. Then the difference between a physical property of one molecule obtained by the super molecule method and that by an ordinary MO calculation of one molecule is thought to be the effect of intermolecular interactions on the property. In this treatment, the basis set superposition error (BSSE)[38] should be compensated for.

The hyperpolarizability of the super molecule was calculated by the *ab initio* CPHF method. The super molecule was constructed from two nearest neighbor molecules in the MNA crystal[33], shown in Figure 1. In Table IV, the hyperpolarizability of one molecule obtained by the ordinary MO calculations, those of two molecules in the MNA crystal by the oriented gas model approximation, and those by the super molecule method are listed. Those values are after BSSE correction by the method of Boys and Bernadi[38]. In the table,  $z$  and  $z'$  are polar axes of the single molecule and the crystal, respectively. Comparing the hyperpolarizability values of two molecules by the oriented gas model and the super molecule methods, it is concluded that the short range (nearest neighbor) intermolecular interactions in the crystal reduce the hyperpolarizability values of the MNA molecule about 25 %.

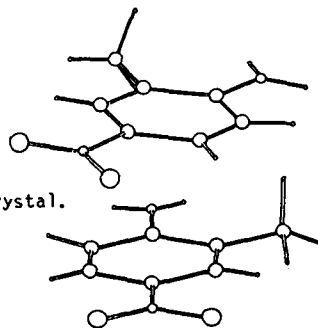


FIGURE 1.  
Two nearest neighbor molecules in the MNA crystal.

TABLE IV The effect of intermolecular interactions on hyperpolarizabilities  
/ $10^{-30}$  esu

	$\beta_{zzz}$	$\beta_{z'z'z'} (2 \times \text{Monomer})$	$\beta_{z'z'z'} (\text{Dimer})$
STO-3G	4.219	5.942	5.215
4-31 G	9.991	13.814	11.032



## REFERENCES

1. G. P. Agrawal and C. Flytzanis, *Chem. Phys. Lett.* **44**, 366 (1976).
2. C. C. Cojan, G. P. Agrawal, and C. Flytzanis, *Phys. Rev.* **B15**, 909 (1977).
3. G. P. Agrawal, C. Cojan, and C. Flytzanis, *Phys. Rev.* **B17**, 776 (1978).
4. E. F. McIntyre and H. F. Hameka, *J. Chem. Phys.* **68**, 3481 (1978).
5. O. Zamani-Khamiri, E. F. McIntyre, and H. F. Hameka, *J. Chem. Phys.* **72**, 5906 (1980).
6. J. Zyss, *J. Chem. Phys.* **70**, 3333 (1979).
7. J. Zyss and G. Berthier, *J. Chem. Phys.* **77**, 3635 (1982).
8. S. J. Lalama and A. F. Garito, *Phys. Rev.* **A20**, 1179 (1979).
9. A. F. Garito, J. R. Heflin, K. Y. Wong, and O. Zamani-Khamiri, in *Nonlinear Optical Properties of Polymers*, edited by A. J. Heeger, J. Orenstein, and D. R. Ulrich (*Mater. Res. Soc. Proc.* **109**, Pittsburgh, PA 1988).
10. M. G. Papadopoulos, J. Waite, and C. A. Nicolaides, *J. Chem. Phys.* **77**, 2527 (1982).
11. J. Waite and M. G. Papadopoulos, *J. Chem. Phys.* **82**, 1427 (1985).
12. V. J. Docherty, D. Pugh, and J. O. Morley, *J. Chem. Soc., Faraday Trans. II* **81**, 1179 (1985).
13. J. O. Morley, *J. Chem. Soc., Perkin Trans. II* 1351 (1987); *ibid.*, 103 (1989).
14. E. M. Svendsen, C. S. Willand, and A. C. Albrecht, *J. Chem. Phys.* **83**, 5760 (1985).
15. D. Li, T. J. Marks, and M. A. Ratner, *Chem. Phys. Lett.* **131**, 370 (1986).
16. C. P. DeMelo and R. Silbey, *Chem. Phys. Lett.* **140**, 537 (1987).
17. J.-M. Andre, C. Barbier, V. Bodart, and J. Delhalle, in *Nonlinear Optical Properties of Organic Molecules and Crystals*, Vol. 2 edited by D. S. Chemla and J. Zyss (Academic Press, New York, 1987) p. 137
18. B. Kirtman, *Chem. Phys. Lett.*, **143**, 81 (1988).
19. G. J. B. Hurst, M. Dupuis, and E. Clementi, *J. Chem. Phys.* **89**, 385 (1988).
20. C. W. Dirk and M. G. Kuzyk, *Phys. Rev.* **A39**, 1219 (1989).
21. H. D. Cohen and C. C. J. Roothaan, *J. Chem. Phys.* **43**, 534 (1965).
22. P. Pulay, *J. Chem. Phys.* **78**, 5043 (1983).
23. M. Dupuis, J. D. Watts, H. O. Villar, and G. J. B. Hurst, QCPE No. 544, modified for Hitachi M682H and S820 systems by the present authors.
24. J. S. Binkley, R. A. Whiteside, R. Krishnan, R. Seeger, D. J. DeFrees, H. B. Schlegel, S. Topiol, L. R. Kahn, and J. A. Pople, GAUSSIAN 80, QCPE No. 500 modified for M680H and S820 systems by the present authors.
25. I. Ledoux and J. Zyss, *Chem. Phys.* **73**, 203 (1982).
26. C. C. Teng and A. F. Garito, *Phys. Rev.* **B28**, 6766 (1983).
27. S. Topiol and J. W. Moskowitz, *J. Chem. Phys.* **70** 3008 (1979).
28. Y. Itoh, K. Ohno, M. Isogai, and A. Kakuta, *Mol. Cryst. Liq. Cryst.* **170**, 259 (1989).
29. U. Berkert, N.L. Allinger, *Molecular Mechanics*, (Am. Chem. Soc., Washington, D.C., 1982).
30. D. E. Williams, *Acta Cryst.* **27**, 133 (1978).
31. A. I. Kitaigorodsky, *Chem. Soc. Rev.* **7**, 253 (1952).
32. P. P. Ewald, *Ann. Physik.* **64**, 253 (1952).
33. G. F. Libscomb, A. F. Garito, and R. S. Narang, *J. Chem. Phys.* **75**, 1509 (1981).
34. K. N. Trueblood, E. Goldish, and J. Donohue, *Acta Cryst.* **14**, 1009 (1961).
35. S. C. Biswas and R. K. Sen, *Ind. Pure & Appl. Phys.* **20**, 414 (1982).
36. S. R. Cox and D. E. Williams, *J. Comput. Chem.* **2**, 304 (1981).
37. J. A. Sardo, T. L. Sardo, G. M. Fernandez, R. Gomperts, S. Chin, and E. Clementi, *J. Chem Phys.* **Pb90Pb**, 6361 (1989).
38. S. F. Boys and F. Bernardi, *Mol. Phys.* **19**, 553 (1970).
39. J. Czekalla and G. Wick, *Z. Electrochem., Ber. Bunsenges. Physik. Chem.* **65**, 727 (1961).

## ELECTRONIC STRUCTURES AND NONLINEAR OPTICAL PROPERTIES FOR CROSS-CONJUGATED POLYENE

YUHEI MORI AND YOSHIMICHI OKANO

ATR Optical and Radio Communications Research Laboratories,  
Sanpeidani, Inuidani, Seika-cho, Soraku-gun, Kyoto, 619-02, Japan

### ABSTRACT

For several cross-conjugated molecules, molecular excited states and third-order nonlinear susceptibilities  $\gamma$  are calculated by semi-empirical molecular orbital method. The calculated  $\gamma$  are compared with each other and the reason for the differences are discussed in terms of the orbital shapes which contribute mainly to  $\gamma$ . The reason that long polyene chains have large  $\gamma$ , is ascribed to the large transition moment which is explained by the signs of the LCAO coefficients. On the other hand, it is found that the cross-conjugated molecules in which two similar-length chain cross at the center is not good for large third-order susceptibility.

### INTRODUCTION

Over the past 10 years or so, nonlinear optical properties for conjugated molecules have attracted much interest, in particular the third-order susceptibility  $\gamma$  of polyenes. In the early stages, Rustagi *et.al.* [1] and Agrawal *et.al.* [2] lead the analytic investigation of the dependence of  $\gamma$  on the chain length. In recent years, some works were done using the molecular orbital method to calculate the third-order susceptibilities for finite polyenes [3-6]. Garito *et.al.* [5] and Yamaguchi *et.al.* [6] calculated  $\gamma$  by CNDO/S-CI and indicated the significance of upper excited  $A_g$  state for third-order susceptibility in addition to the ground and  $B_u$  excited state which is observed in an absorption spectrum. Pierce [7] also did calculations for short polyenes and pointed out that CI calculation including doubly excited states is necessary, especially to obtain a correct sign of  $\gamma$  for ethylene and butadiene. These works concern unsubstituted polyenes. Flom *et.al.* [8] measured third-order susceptibilities for three derivatives of polyacene quinone and suggested that the third-order coefficients are not simply correlated with the conjugation length. But there are few works which treat substituted polyene systems. In this work, we calculate the molecular orbitals and third-order susceptibilities for some cross-conjugated polyenes. For the calculation of various molecules, it is important to know which part of the molecule contributes mainly to the  $\gamma$  value. This will be clarified if we investigate the shapes and distributions of the molecular orbitals.

## CALCULATION

Molecular structures, orbitals and third-order susceptibilities are calculated for molecules listed in Fig. 1. The structures *i.e.* bond lengths and angles for these molecules are calculated using a MNDO program, assuming planar configuration. With these optimized structures, excitation energies and transition moments are obtained by the CNDO/S-CI method. 60 configurations are taken into account for CI only for singly excited states. Third-order susceptibilities are calculated by the following equation [9-10].

$$r_{ijkl} = \frac{1}{4} \sum_{l,m,n} \left\{ \frac{1}{6} P^{ijkl} \frac{r_{gt}^i r_{lm}^j r_{mn}^k r_{ng}^l}{(E_{lg} + 3\hbar\omega)(E_{mg} - 2\hbar\omega)(E_{ng} - \hbar\omega)} + \frac{1}{6} P^{ijkl} \frac{r_{gt}^j r_{lm}^i r_{mn}^k r_{ng}^l}{(E_{lg} + \hbar\omega)(E_{mg} - 2\hbar\omega)(E_{ng} - \hbar\omega)} \right. \\ \left. + \frac{1}{6} P^{ijkl} \frac{r_{gt}^j r_{lm}^k r_{mn}^i r_{ng}^l}{(E_{lg} + \hbar\omega)(E_{mg} + 2\hbar\omega)(E_{ng} - \hbar\omega)} + \frac{1}{6} P^{ijkl} \frac{r_{gt}^j r_{lm}^k r_{mn}^l r_{ng}^i}{(E_{lg} + \hbar\omega)(E_{mg} + 2\hbar\omega)(E_{ng} + 3\hbar\omega)} \right\} \quad (1)$$

where  $i, j, k$  and  $l$  are  $x, y$  or  $z$ .  $l, m, n$  are excited or ground states.  $r$  is a transition dipole moment, and  $P$  means the sum of the permutations. The excitation energy is assumed to be  $\hbar\omega = 0.656eV$ . The isotropic averaging is obtained by.

$$r = \frac{1}{5} \left[ \sum_i r_{iiii} + \frac{1}{3} \sum_{i \neq j} (r_{ijij} + r_{ijji} + r_{jiji}) \right] \quad (2)$$

The obtained  $\gamma$  values are compared for some conjugated molecules. According to eq.(1), one sequence of four transition moments, which have non-zero value starting and ending at the ground state, contribute to the third-order susceptibility. As the molecules in Fig. 1 have  $C_{2h}$  symmetry, the process is  $g \rightarrow B_u \rightarrow A_g \rightarrow B_u \rightarrow g$ . Working in the two state approximation, the central  $A_g$  can be the ground state, but it is said that the  $A_g$  excited state is also important. In the present study, we used the approximation that there are various possible  $A_g$  excited states and that the first and third  $B_u$  are the same. After we calculated the third-order susceptibilities, the CI states, and the orbitals which contribute to the susceptibilities, are extracted.

## RESULTS AND DISCUSSION

The molecules and corresponding calculated  $\gamma$  are shown in Fig. 1. First, let us consider the unsubstituted polyene (a). Looking into the orbitals for this molecule is necessary to compare the results with some other molecules later. For the third-order nonlinearities, the main contribution is from

$$g \rightarrow B_u \rightarrow g \rightarrow B_u \rightarrow g \quad (\text{term 1})$$

and

$$g \rightarrow B_u \rightarrow A_g \rightarrow B_u \rightarrow g \quad (\text{term 2})$$

where  $B_u$  and  $A_g$  are excited states. The contribution of the term 2 has positive sign, while the term 1 negative. The contribution of term 2 is more significant, as the measured  $\gamma$  is

positive for finite polyene [11]. The energy levels which are used in the transition of term 2, are shown in Fig 2, and the orbitals which constitute each excited state are also shown. The contribution from term 1 is  $\gamma_{\text{part}} = -520 \times 10^{-36} \text{ esu}$ , and from term 2,  $\gamma_{\text{part}} = 600 \times 10^{-36} \text{ esu}$ . The orbital distributions are shown in Fig. 3, where the size of the symbol for each atom represents the magnitude of the LCAO coefficient and the color represents the sign. The first transition  $g \rightarrow A(B_u)$  is a well known HOMO-LUMO transition where a  $\pi$ -electron which has distribution on double bonds move to another orbital which has distribution mainly on single bonds as is seen from  $u$  to  $x$  in Fig 3. As for the next transition  $A(B_u) \rightarrow B(A_g)$ , the transitions from orbital  $x$  to  $y$  and from  $v$  to  $u$  are used. The shapes of these orbitals are shown in Fig. 3. On comparing the orbitals  $x$  and  $y$ , most of the respective coefficients of the atoms on the left side of the chain have the same sign for  $x$  and  $y$ , while most of those on the right side have opposite signs. This applies also to  $u$  and  $v$ . This phenomenon makes the transition dipole very large. If the chain length is longer, the width of an orbital becomes wider. Then the transition dipole becomes greater. This makes the effect of term 2 greater. This is one of the main reasons that the third-order susceptibility is large for long polyenes.

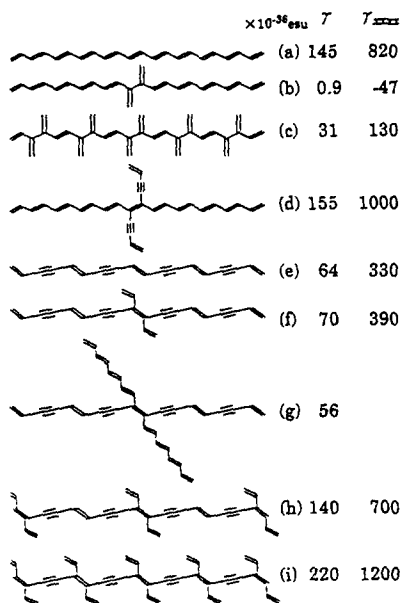


Fig. 1 Calculated molecules and third-order susceptibilities.

In the case of molecule (b) in Fig. 1, where the molecule is conjugated but alternating double and single bonds are broken, the calculated  $\gamma$  value is small. For this molecule, there is a contribution of the  $A_g$  excited states, but it is not so large as that of molecule (a). This is because the phenomenon described above i.e. the increase of the transition moments for the  $B_u \rightarrow A_g$ , does not occur. The  $\gamma$  value for the molecule (c) is a little better than (b), but not as good as for (a). It is presumed that alternating double and single bonds make the  $A_g$  excited state significant.

In the case that a few substituents are added such as (d) and (f), the calculated  $\gamma$  values are a little greater than for the corresponding unsubstituted chain (a) or (e). In these cases, another process,  $g \rightarrow B_u \rightarrow A_g \rightarrow B_u \rightarrow g$  where side chains play a role, helps the third-order susceptibility a little in addition to the terms 1 and 2 described above for molecule (a).

Next let us go to the case in which the length of the conjugated side chain becomes longer and two conjugated chains cross each other at the center, as shown in Fig. 1 (g). The calculated  $\gamma$  value is a little smaller than that of (e) or (f), though this molecule (g) has more conjugated bonds. The excited states and orbital transitions which contribute to  $\gamma$  are shown in Fig. 4. The contribution from the term  $g \rightarrow A \rightarrow B \rightarrow A \rightarrow g$  is  $\gamma_{part} = 210 \times 10^{-36} esu$ , from  $g \rightarrow A \rightarrow C \rightarrow A \rightarrow g$ ,  $\gamma_{part} = 230 \times 10^{-36} esu$ , and from  $g \rightarrow A \rightarrow g \rightarrow A \rightarrow g$ ,  $\gamma_{part} = -500 \times 10^{-36} esu$ . For transition  $A \rightarrow B$ , the significant orbital transitions are  $x \rightarrow y$  and  $v \rightarrow u$ .

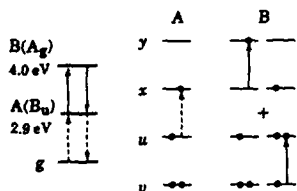


Fig. 2 Excited states (A, B) which contribute to  $\gamma$  and orbital transitions which are involved in the excited states for molecule (a).

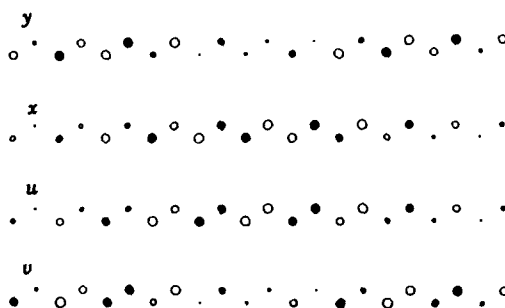


Fig. 3 Molecular orbitals. Symbol size indicates the magnitude of the LCAO coefficient. A black dot means negative and a circle means positive.

For transitions  $A \rightarrow C$ , the orbital transition  $x \rightarrow z$  is most effective. If we concentrate on the polyene side chain in (g), the  $x \rightarrow y$  transition is similar to that of the  $x \rightarrow y$  transition of molecule (a). On comparing  $x$  and  $y$ , only for the polyene side chain in Fig. 5, most of the LCAO coefficients for  $x$  and  $y$  have the same signs on the left side of the molecule, and opposite signs on the right. In Fig. 5x, the orbital extends along both sides of the chain. For the polydiacetylene side chain, the signs of the respective coefficients are different on the left, and are the same on the right. This means that the two types of chain weaken each other's transition moments. As for the  $x \rightarrow z$  transition, it is seen that the direction of the transition moment is along the polydiacetylene chain, but the orbital distributions of upper and lower levels do not overlap much. This type molecule, i.e. two conjugated chains crossing each other at the center has disadvantages in regard to obtaining large third-order susceptibility.

On the other hand, if the molecule has side conjugated chains located periodically, such as (h) and (i) in Fig. 1, the more the number of the side chains, the greater becomes the  $\gamma$  as is seen in Fig. 1. In these cases, the transitions from  $B_u$  excited state to  $A_g$  excited state is significant and most of the LCAO coefficients for the upper and lower orbitals of the effective transition have the same signs on one side and opposite signs on the other side. In these respects, these cases are similar to the case of molecule (a).

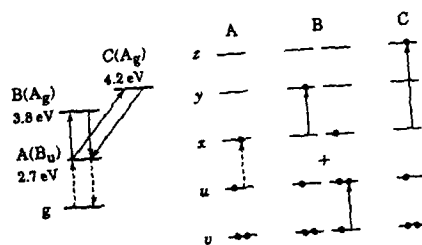


Fig. 4 Excited states (A, B, C) which contribute to  $\gamma$  and orbital transitions which are involved in the excited states for molecule (g).



Fig. 5 LCAO coefficients of molecular orbitals for molecule (g).

## CONCLUSIONS

The third-order nonlinear susceptibilities are calculated for several cross-conjugated finite chains. In general, the more conjugated bonds the molecule has, the greater is the  $\gamma$ . This is seen by the calculation where only a few conjugation carbon substituents are added or where substituents are added periodically. But the cross-conjugated system where two similar-length chain cross at the center does not have good third-order susceptibility. The approximation here, is within singly excited states and the motions of atoms are not taken into account. The calculation considering doubly excited states, and considering soliton or polaron for longer chain, are left for further study.

## REFERENCES

1. K. C. Rustagi, and Ducuing, *Opt. Comm.* **10**, 258 (1974).
2. G. P. Agrawal, and C. Flytzanis, *Chem. Phys. Lett.* **44**, 366 (1976); G. P. Agrawal, C. Cojan, and C. Flytzanis, *Phys. Rev. B* **17**, 776 (1978).
3. C. P. DeMelo, and R. Silbey, *Chem. Phys. Lett.* **140**, 537 (1987).
4. G. J. B. Hurst, M. Dupuis, E. Clementi, and E. Clementi, *J. Chem. Phys.* **89**, 385 (1988).
5. A. F. Garito, J. R. Heflin, K. Y. Wong, and O. Zamani-Khamiri, *Mat. Res. Soc. Simp. Proc.* **109**, 91 (1988).
6. Yamaguchi, Nakano, Okumura, and Fueno, *Abstracts of Third Polymer Electronics Symposium Japan*.
7. B. A. Pierce, *Mat. Res. Soc. Simp. Proc.* **109**, 109 (1988).
8. S. R. Flom, G. C. Walker, L. E. Lynch, L. L. Miller, and P. F. Barbara, *Chem. Phys. Lett.* **154**, 193 (1989).
9. R. Loudon, in *The Quantum Theory of Light*, edited by Clarendon (Oxford, 1983), p. 318.
10. J. A. Armstrong, N. Bloembergen, J. Ducuing, and P. S. Pershan, *Phys. Rev.* **127**, 1918 (1962).
11. J. F. Ward, and D. S. Elliot, *J. Chem. Phys.* **69**, 5438 (1978).

## QUANTUM LATTICE FLUCTUATIONS AND NONLINEAR OPTICS OF CONDUCTING POLYMERS

J. YU, B. FRIEDMAN AND W.P. SU

Department of Physics, University of Houston, Houston, Texas 77204-5504

### ABSTRACT

Quantum lattice fluctuations of conjugated polymers in the form of virtual soliton-antisoliton pairs have important effects on the nonlinear optical properties. Quantitative calculations of nonlinear susceptibilities based on the solitonic molecular model are presented.

### INTRODUCTION

Recent experimental interest on the nonlinear optical properties of conducting polymers calls for a detailed theoretical understanding of the underlying microscopic mechanism[1].

For frozen lattices, the  $\chi^{(3)}$  due to noninteracting electrons has been calculated[2,3] and shows good agreement with experiment[4]. There are, however, important discrepancies. The existence of a pronounced two-photon resonance peak in the  $\chi^{(3)}$  spectrum is especially acute. We address this problem by taking into account the quantum motion of the lattice.

Among all possible fluctuations of the lattice in the ground state, we single out those anharmonic components which can be regarded as virtual soliton-antisoliton pairs. A single virtual soliton-antisoliton pair behaves very much like a diatomic molecule (hence solitonic molecule) as far as photophysics is concerned.

In this article we give a brief description of a solitonic molecule. Some linear optical properties of such a molecule are described. The nonlinear optical properties of this molecule are then discussed.

### CONFIGURATIONAL COORDINATE AND VIRTUAL $S\bar{S}$ PAIRS

For quantitative discussions on trans-polyacetylene we take the *SSH* model[5]. In the adiabatic approximation the electronic spectrum is completely determined by any given lattice configuration  $\{u_n\}$ . The total energy is the sum of nuclear kinetic energies plus an effective potential energy  $V(\{u_n\})$ , which in turn comprises the elastic energies of the  $\sigma$ -bonds and the energies of the occupied electronic states

$$H = \frac{M}{2} \sum_n \dot{u}_n^2 + V(\{u_n\}) \quad (1)$$

$$V(\{u_n\}) = \frac{K}{2} \sum_n (u_n - u_{n-1})^2 + \sum_{i,\sigma} n_{i,\sigma} \epsilon_{i,\sigma} \quad (2)$$

The effective Hamiltonian in (1) describes a group of atoms interacting through a complicated interatomic potential. Static classical solutions are obtained by minimizing  $V$  with respect to  $\{u_n\}$ . Thus a uniform dimerization  $u_n = (-1)^n u_0$  is found to exist in the ground state of an undoped chain. Correspondingly there is a gap at the center of the electronic energy band separating the conduction band from the valence band. Experimentally a strong smearing in the absorption curve is seen near the edge of the gap. This seems to be an intrinsic property. To explain such a subgap absorption tail we imagine the presence of virtual  $S\bar{S}$  pairs in the ground state due to quantum fluctua-



tion of nuclear motion. An  $S\bar{S}$  pair represents a local depression of the bond alternation order and thus is accompanied by some localized electronic gap states. These states can induce subgap optical absorption. Here we are assuming a dilute gas of virtual  $S\bar{S}$  pairs. Therefore we can focus on an  $S\bar{S}$  pair.

There are several ways to describe an  $S\bar{S}$  pair. One possible way adopted by Sethna and Kivelson[6] is

$$\Phi_n = (-1)^n u_n = \Phi_0 \left\{ 1 + \tanh\left(\frac{2x_0}{\xi}\right) \left[ \tanh\left(\frac{x-x_0}{\xi}\right) - \tanh\left(\frac{x+x_0}{\xi}\right) \right] \right\}, \quad (3)$$

the configurational coordinate  $x_0$  here measures the separation between  $S$  and  $\bar{S}$ . Note that  $x_0$  and  $-x_0$  correspond to the same lattice configuration. In letting  $x_0$  run through all positive numbers we are considering quantum fluctuations of the form of an  $S\bar{S}$  pair with various separations. We have used the above configurations to treat the optical properties of polyacetylene in previous publications[7-9]. In this article we adopt a somewhat different parameterization

$$\Phi_n = \Phi_0 \left\{ 1 + \tanh\left(\frac{2|x_0|}{\xi}\right) \left[ \tanh\left(\frac{x-x_0}{\xi}\right) - \tanh\left(\frac{x+x_0}{\xi}\right) \right] \right\} \quad (4)$$

so that the configurational coordinate runs through all real numbers. For negative  $x_0$  (4) represents lattice configurations which increase dimerization. Therefore (4) includes both breather[10] and  $S\bar{S}$  types of fluctuations. Within the family of lattice configurations that we have singled out in (4) the total energy in (1) can be expressed in terms of the collective coordinate  $x_0$

$$E_p(x_0) + \frac{M(x_0)}{2} \dot{x}_0^2. \quad (5)$$

By making a coordinate transformation from  $x_0$  to  $s$  the energy can be brought into the

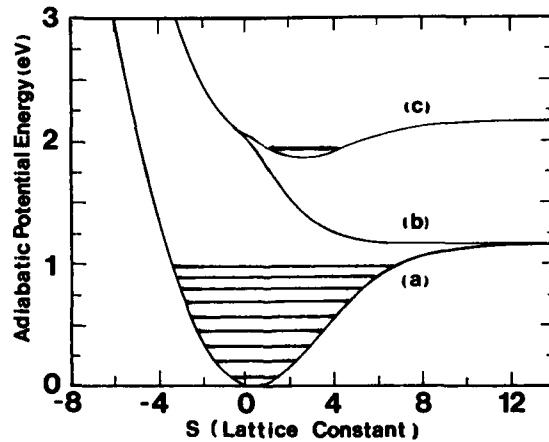


Figure 1. Adiabatic potential energy curves for the electronic ground state (a), the first excited state (b) and the second excited state (c) of trans-polyacetylene. The energy of some of the bound vibrational states are shown as horizontal lines. The classical energy gap is at about 2.0eV.

canonical form [see Appendix]

$$E_p(s) + \frac{M}{2} \dot{s}^2. \quad (6)$$

By solving the *Schrödinger* equation one obtains vibrational bound states  $\Psi_n(s)$ ,  $n=0, 1, 2, 3, 4, \dots$  as shown in Fig. 1 (curve a) for the electronic ground state. The same thing can be done for the second electronic excited state (curve c). Curve b is the potential energy curve for the first electronic excited state. Since this potential is repulsive there are no bound states. We can assume that the motion of the collective coordinates  $s$  in this potential is classical, i.e. any vibrational eigenfunction can be taken to be a delta function  $\delta(s - s_0)$ .

Fig. 1 resembles the potential energy diagram of a typical diatomic molecule. By photoexcitation the system can be brought to its first excited electronic state. It will then go downhill along curve (b) leading eventually to the dissociation of the solitonic molecule into real solitons. The real time dynamics of the photogeneration of solitons has been extensively studied in the past[11,12].

The ground state vibrational wave function determines the Franck-Condon factor of optical transitions and therefore the optical absorption spectrum. The broad subgap absorption tails in various conducting polymers are well accounted for in this approach[7,8]. Of course, Fig. 1 also contains other interesting features. Some of them remain to be explored. We will focus on the nonlinear optics hereafter.

Before we do that it is useful to display the potential energy diagram of cis-polyacetylene. By adding a symmetry-breaking term[13] to the *SSH* Hamiltonian, at large  $s$  all the potential energy curves are lifted (Fig. 2) because of the linear confining potential between a soliton and an antisoliton.

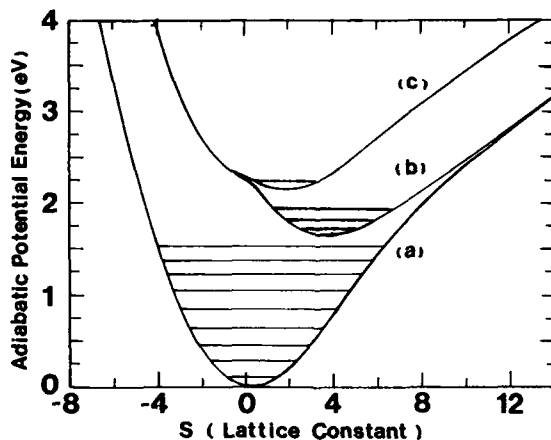


Figure 2. Adiabatic potential energy curves for cis-polyacetylene. The notations are the same as in Fig. 1. The classical energy is at about 2.25eV.

#### NONLINEAR OPTICS OF A SOLITONIC MOLECULE

Knowing the vibrational states and the corresponding electronic wave functions in Figs. 1-2 one can in principle calculate the nonlinear susceptibilities by employing the standard formulas such as

$$\chi^{(3)}(3\omega; \omega, \omega, \omega) = e^4 \sum_{nml} f_{gn} f_{nm} f_{ml} f_{lg} \left[ \frac{1}{(E_{ng} - 3\omega)(E_{mg} - 2\omega)(E_{lg} - \omega)} + \frac{1}{(E_{ng} + \omega)(E_{mg} - 2\omega)(E_{lg} - \omega)} + \frac{1}{(E_{ng} + \omega)(E_{mg} + 2\omega)(E_{lg} - \omega)} + \frac{1}{(E_{ng} + \omega)(E_{mg} + 2\omega)(E_{lg} + 3\omega)} \right], \quad (7)$$

where  $E_{ng} = E_n - E_0$ ,  $\hbar = 1$ , and  $f_{\alpha\beta}$  is the dipole matrix element. The summation over all intermediate states requires considerable amount of computation. Also, there is a question of how many states one needs to sum over. This is because the higher

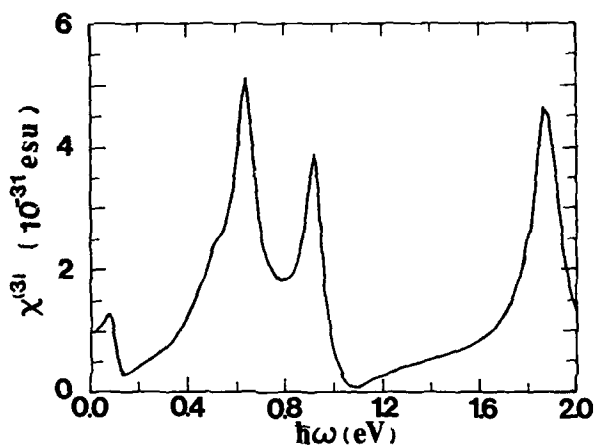


Figure 3.  $\chi^{(3)}(3\omega)$  spectrum of a single virtual  $S\bar{S}$  pair in trans-polyacetylene.

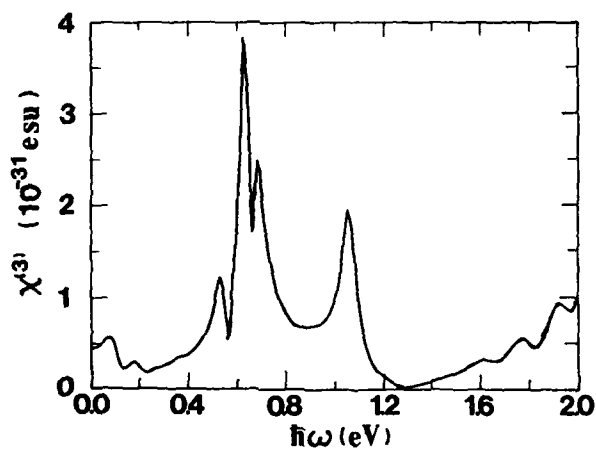


Figure 4.  $\chi^{(3)}(3\omega)$  spectrum of a single virtual  $S\bar{S}$  pair in cis-polyacetylene.

electronic excited states are extended. They are associated with more than one  $S\bar{S}$  pair. We have so far included only those intermediate states with energy less than the classical energy gap. The calculated  $\chi^{(3)}$  for a single virtual  $S\bar{S}$  pair is shown in Fig. 3 and 4 for trans-polyacetylene and cis-polyacetylene respectively. A half width  $\Gamma = 0.05\text{eV}$  has been given to all the excited states to smear out the divergent peaks. A few comments about the results are in order.

1. A two photon resonance peak appears very naturally in this type of calculation, simply because of the existence of the vibrational bound states associated with the even parity second electronic excited state (potential energy curve c).

2. To get some idea about the magnitude of the susceptibility we have reproduced in Fig. 5 the  $\chi^{(3)}$  of a frozen uniformly dimerized lattice with 160 sites[3]. By assuming several virtual  $S\bar{S}$  pairs in a 160 site chain the two photon resonance peak comes out to be a few times above the background in Fig. 5 in the same energy range. The three photon resonance peak is still substantially below that of the noninteracting electron model. This difference might be reduced by including more intermediate states in our calculation.

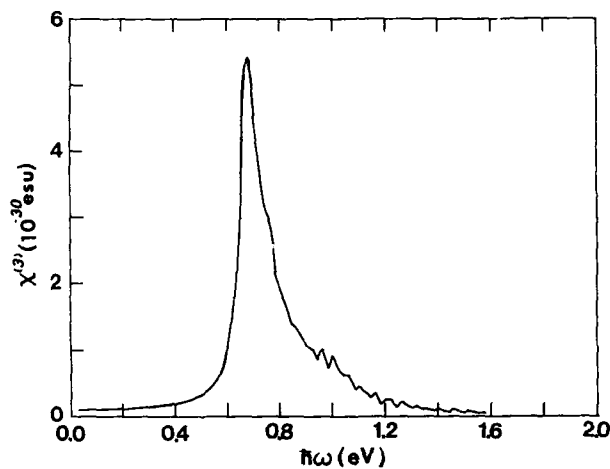


Figure 5.  $\chi^{(3)}(3\omega)$  spectrum of a frozen uniformly dimerized chain with 160 sites.  $\Gamma = 0.05\text{eV}$ .

3. A comparison of Fig. 3 and Fig. 4 shows that cis-polyacetylene has a smaller  $S\bar{S}$  induced nonlinear susceptibility than trans-polyacetylene. They differ, however, only by a factor of two, instead of the huge disparity previously discussed in Ref. 9. It is not clear at present whether an  $SSH$  type model adequately describes cis-polyacetylene.

We thank A.J. Heeger for an earlier collaboration on this subject. This work was partially supported by the Robert A. Welch Foundation and by the Texas Advanced Research Program under Grant No. 1053.

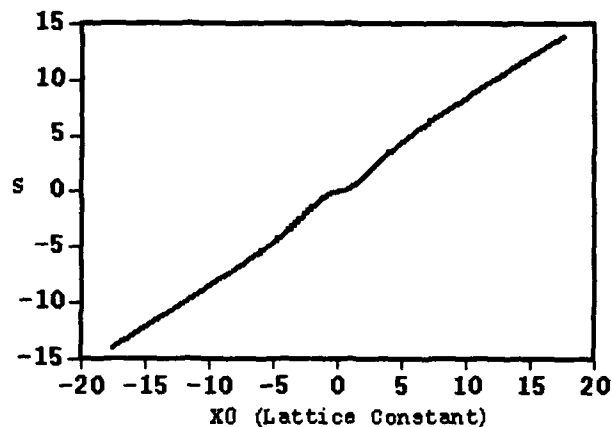


Figure 6. Relation between the two configurational coordinates.

#### REFERENCES

1. See for example, *Nonlinear Optical Properties of Polymers*, edited by A.J. Heeger, J. Orenstein, and D.R. Ulrich (Materials Research Society, 1988).
2. Weikang Wu, *Phys. Rev. Lett.* **61**, 1119 (1988).
3. J. Yu, B. Friedman, P.B. Baldwin, and W.P. Su, *Phys. Rev. B* **39**, 12814(1989).
4. W.S. Fann et al., *Phys. Rev. Lett.* **62**, 1492(1989).
5. W.P. Su, J.R. Schrieffer, and A.J. Heeger, *Phys. Rev. Lett* **42**, 1698(1979); *Phys. Rev. B* **22**, 2099(1980).
6. J.P. Sethna and S. Kivelson, *Phys. Rev. B* **26**, 3513(1984).
7. J. Yu, H. Matsuoka, and W.P. Su, *Phys. Rev. B* **37**, 10367(1988).
8. B. Friedman and W.P. Su, *Phys. Rev. B* **39**, 5152(1989).
9. M. Sinclair et al., *Synth. Met.* **28**, D655(1989).
10. A.R. Bishop, D.K. Campbell, P.S. Lomdahl, B. Horovitz, and S.R. Phillpot, *Phys. Rev. Lett.* **52**, 671(1984).
11. W.P. Su and J.R. Schrieffer, *Proc. Natl. Acad. Sci. USA* **77**, 5626(1980).
12. See the article by S. Etemad, G.L. Baker, L. Rothberg, and F. Kajzar in Ref. 1.
13. S.A. Brazovskii and N. Kirova, *Pis'ma Zh. Eksp. Teor. Fiz.* **33**, 6(1981) [*JETP Lett.* **33**, 4(1981)].

#### APPENDIX

The relation between the two configurational coordinates  $s$  and  $x_0$  is defined by the following differential equation:

$$\frac{ds}{dx_0} = c\sqrt{M(x_0)} \quad (8)$$

where  $c$  is a constant[7]. Equation (8) can be integrated numerically. The result is plotted in Fig.6.

THEORETICAL STUDIES of the NONLINEAR OPTICAL  
PROPERTIES of L-ARGININE PHOSPHATE

C. A. Langhoff, Dow Chemical, 1776 Building, Midland, MI 48674

This paper will present quantum calculations on the L-arginine part of the nonlinear crystal L-arginine phosphate. The emphasis here will be on understanding the NLO properties in terms of the excited states of the system and accompanying charge movements in these excited states. Both the carboxylate and the guanidyl ends of the molecule contribute to the values of  $\beta$ . The guanidyl seems to be the bigger contributor, but the contribution varies with the particular tensor component. The properties of the crystal will not be discussed here.

#### Introduction

The number of nonlinear optical crystals has been growing in recent years. Several organic crystals have appeared and have generated considerable interest and promise. The Nonlinear Optical Materials group at Livermore Labs has shown that the deuterated version of L-arginine phosphate is a good candidate for use in doubling and mixing Nd laser harmonics[1-2]. Japanese workers have also studied the growth and optical properties of the crystal[3]. This organic material can be grown in large crystals and has many acceptable properties with regard to nonlinearity, absorption, and damage threshold.

The group at Livermore [1-2] has shown that the bulk of the nonlinear susceptibility of these crystals is due to the L-arginine part of the crystal and not the phosphate ion. This is evidenced by the fact that several other crystals involving L-arginine without any phosphate show significant NLO activity. For the purposes of this study, we will concentrate solely on the L-arginine molecule. The system will be treated as an oriented gas as no consideration is taken of the local field factors.

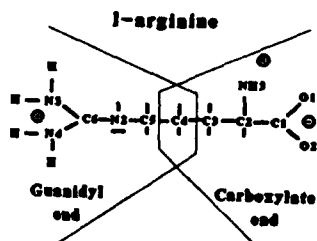
This paper specifically will deal with a theoretical study of the excited state electronic properties of L-arginine. The intent is to understand the origins of the nonlinearity in terms of excited state structure and charge transfer effects. The contribution of intramolecular charge transfer transitions is the accepted model of the origin of the second order nonlinearity in organic molecules. Since L-arginine chemically can be understood as having two possible contributing groups, the amino-carboxylate end and the guanidyl end, we have done calculations on two molecular pieces which mimic both ends of the arginine molecule. It is the intent of this paper to show how these molecular "pieces" contribute to the NLO properties of the entire molecule. Do they contribute independently or cooperatively? No attempt will be made here to calculate

and compare these theoretical properties to those measured in the crystal. This will be the subject of a future paper.

#### Calculational Details

The calculations were done at the CNDO/S level. The basic program was a modified version of one available from the Quantum Chemical Program Exchange (No. 333). Modifications were necessary to adjust for precision problems in the diagonalization routine as they were run on a VAX 8650. The excited state spectrum was computed on a single CI basis using up to 200 configurations. Several subsidiary programs were written to compute both the linear susceptibility,  $\alpha$ , and the second order nonlinear susceptibility,  $\beta$ , tensors. The complete tensors were computed, but only results concerning the  $\beta$  values will be discussed here. Charge densities for both the ground state and the changes in density upon excitation from the ground state or between excited states are calculated and plotted in a bargraph format. These charge densities changes were used together with an excited state analysis of a given  $\beta$  tensor element to select and understand the contribution of certain transitions to the nonlinearity.

The coordinates were taken from the crystal structure of Aoki, et. al. [4]. Because several of the hydrogen atoms were not found in the structure, we inserted them by the following procedure. The coordinates as given by [4] were converted into the format appropriate to be read by the geometry optimization program MOPAC available through the QCPE. Using a MNDO Hamiltonian, the position of all the hydrogens in the molecule were optimized. These coordinates were then used in the quantum calculations. Three molecules were used in the calculations. The first was the entire arginine molecule. Two molecules were generated from the coordinates of the arginine system each of which used one end of the arginine molecule, either the carboxylate (denoted henceforth CBX) or the guanidyl (denoted henceforth GUAN) ends. They were terminated by symmetric methyl groups. The hydrogens were optimized with MOPAC as with arginine. The coordinate systems of these latter two molecules were arranged so that either the carboxylate or the guanidyl groups were in the xy plane. This facilitated the identification of pi orbitals in these systems. A stick diagram of these molecules is shown in Figure 1.



**Figure 1**  
Schematic of the L-arginine molecule as it exists in the LAP crystal

## Results

Before presenting the results of the calculations, a brief review of the geometry of these molecules will be given. In arginine, the carboxyl group, C1, O1, and O2, is approximately planar with carbon C4, but not with the quaternary nitrogen, N1. Hence, one would not expect strong  $\pi$  conjugation between these groups. The entire guanidyl group, N2, N3, N4, and C6 is quite planar. One might expect some charge donation upon excitation from the lone pair of electrons on N2 into the local  $\pi$  system. This is indeed observed and will be pointed out later. In the crystal the connecting chain of carbon atoms between carboxylate and guanidyl groups indicates that there would be little  $\pi$  conjugation between the groups and, hence, little chance of charge movement between them.

A few selected excited states of the system as calculated are listed in Table I. One can make some reasonable assignments of the arginine state in terms of the component groups. The lower energy states at 274nm and 260nm are carboxylate transitions. The state at 200nm is the guanidyl transition. The correlation is quite reasonable for this level of calculation.

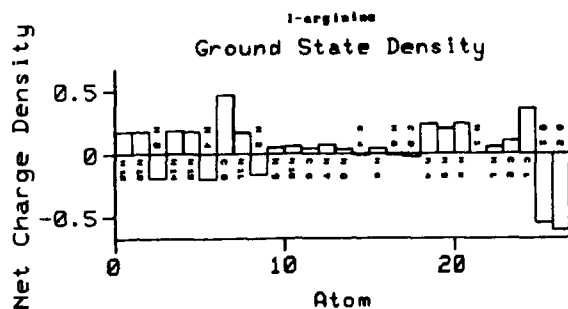
Table I

Calculated Excited States

State	L-arginine		Carboxylate End		Guanidyl End	
	$\lambda$ (nm)	Osc. Str.	$\lambda$ (nm)	Osc. Str.	$\lambda$ (nm)	Osc. Str.
1	321.88	0.0011				
2	316.67	0.0004				
3	274.81	0.0011	277.4	0.0027		
4	260.28	0.0003	251.37	0.0009		
5	252.79	0.0006				
6	200.35	0.2965			199.39	0.4220
7	176.16	0.1393	174.51	0.1548		
8	167.7	0.3607			170.38	0.4668
9	167.23	0.0227				
10	163.73	0.0324	164.84	0.1279		
11	162.8	0.3448	162.70	0.2285		
12	159.35	0.0419			158.71	0.0182
13	157.03	0.0213				
14	153.66	0.0210	152.50	0.0539		
19	143.71	0.1419	143.16	0.2911		
37	123.02	1.4878	126.94	0.2264	129.36	3.4136
39	122.66	1.7122				

The ground state charge densities are shown in Figure 2. There is a strong dipole at the carboxylate end between C1(positive) and the two oxygens(negative). The protonated amine group at N1 shows a net positive charge as expected from the simply drawing in Fig. 1. The positive charge on the guanidyl is located on the two  $\text{NH}_2$  groups as well as C6. Nitrogen N2 and its hydrogen H11 are approximately neutral. This would indicate that there is little net charge transfer from N2 to N3, N4, and C6 in the ground state.





**Figure 2**  
**Ground state charge density as calculated**

Each element of the  $\beta$  tensor was subjected to an analysis of its magnitude with respect to the excited states of the system. This included a convergence plot to check whether one has included all the contributions to its magnitude. All of the major components for arginine, CBX, and GUAN appeared to converge. Since the total value of  $\beta$  is a linear sum of contributions from the sum over states, each state contribution to a tensor element is listed. Thus one can analyze each tensor element in terms of its excited state contributors. This is similar to the analysis scheme of Dirk and Kuzyk[5].

The  $\beta$  tensor in the crystal coordinate system for arginine is shown in Table II. The xyz coordinates of this tensor correspond to a, b, and c\* of the crystal. Note that this is not the  $\beta$  tensor of the crystal itself as no account has been taken of the second molecule in the unit cell.

**Table II**

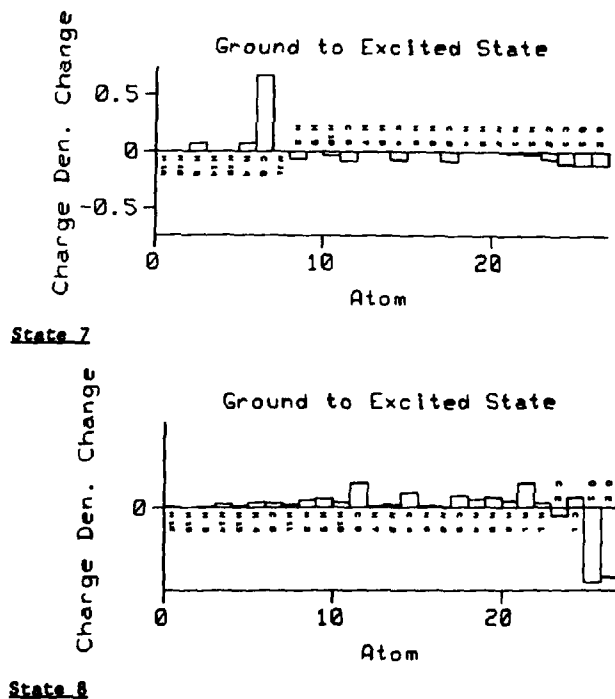
		$\beta(i,j,k)$ [esu units, $10^{-30}$ cm <sup>5</sup> /SV]			
		j\k	X	Y	Z
i - X	X		-0.4818	-0.0559	-0.7248
	Y		-0.0559	0.2737	-0.3160
	Z		-0.7248	-0.3160	-1.2101
i - Y	X		-0.0445	0.2705	-0.2901
	Y		0.2705	-2.0774	-0.2094
	Z		-0.2901	-0.2094	-2.1380
i - Z	X		-0.7228	-0.2967	-1.2217
	Y		-0.2967	-0.1804	-2.1965
	Z		-1.2217	-2.1965	-3.1538

There are four major components in the tensor,  $\forall\forall\forall$ ,  $\forall\forall Z$ ,  $Z\forall Z$ , and  $ZZZ$ . Table III compares the major tensor components of L-arginine, CBX, and GUAN.

**Table III**  
**Comparison of  $\beta$  for L-arginine, CBX, and GUAN**

Tensor Element	$\beta(i,j,k)$ [esu units, $10^{-30}$ cm <sup>5</sup> /SV]		
	L-ARGININE	CBX	GUAN
XZZ	-1.21	-0.08	-0.97
YYY	-2.09	-2.07	0.24
YZZ	-2.14	-0.71	-1.05
ZXZ	-1.22	-0.09	-0.98
ZYZ	-2.20	-0.73	-1.06
ZZZ	-3.15	-0.38	-1.13

Upon transforming the tensors of the CBX and GUAN fragments, one can see that the YYY component is due principally to the carboxylate group through excited states 8 and 58. The remaining tensor elements have major contributions from the guanidyl group through states 7, 12, and 19. The carboxylate group also contributes to these states and to  $\beta$ , but to a lesser degree. State 7 is the most important of these contributors. The changes in electron densities upon excitation to states 7 and 8 are illustrated in Fig. 3.



**Figure 3**  
**Charge density changes upon excitation for L-arginine**

State 7 is primarily an excitation from N1, C5, C4, and C3 to C6, N2 and N3. State 8 involves the donation of charge from several sources at the carboxylate end of the molecule to the oxygens. Several other excited states also show similar charge transfers.

#### Conclusions

A quantum mechanical description at the CNDO/S level can be used to understand the origins of the optical nonlinearity of a complex molecule such as L-arginine. The method seems to do a reasonable job of predicting the movement of charge upon excitation which is the major contributor to the nonlinear effect. The intramolecular charge transfer transitions which give rise to large  $\beta$  values in molecules such as p-nitroaniline, also seem to be the active excited states for L-arginine. Furthermore, the carboxylate and guanidyl ends of the molecule contribute reasonably independently as would be expected from simple chemical considerations. For most tensor components of  $\beta$ , the guanidyl group is the major contributor, although this is not always true.

#### References

1. D. Eimerl, S. Velso, L. Davis, F. Wang, G. Loiacono, and G. Kennedy, IEEE J. Quantum Electronics, 25(2),179(1989).
2. S. Velso, L. Davis, F. Wong, S. Monaco, and D. Eimerl, SPIE Symposium, 824, 178(1987).
3. T. Sasaki, A. Yokotani, K. Fujimoto, T. Yamanaka, and S. Nakai, Tech. Rep. of Osaka U., 39, 25(1989).
4. K. Aoki, K. Nagano, and Y. Iitaka, Acta. Cryst., B27,11(1971).
5. C. Dirk and M. Kuzyk, Phys. Rev. A, 39(3),1219(1989).

## EFFECTS OF IN-PLANE $\pi'$ BONDING ON ELECTRONIC TRANSITION ENERGIES FOR INORGANIC POLYMERS

KIM F. FERRIS, STEVEN M. RISSER AND ANGELA K. HANSON  
Pacific Northwest Laboratory, Materials and Chemical Sciences Center, Richland, WA.

### ABSTRACT

The electronic structure of organic and inorganic polymeric systems are well described in terms of their molecular symmetry, even with the large bond polarity shown by such systems as polyphosphazenes. We have performed calculations using the semi-empirical CNDO/1 method to determine the valence electronic structure for a series of model phosphonitrilic and organic compounds. The optical transition energies for phosphonitrilic compounds are greater than their organic counterparts as a result of in-plane  $\pi'$  bonding interactions. The extent of these interactions is modulated by the electronegativity of the substituent groups on the phosphorus atoms. We report values for the vertical ionization energy and electronic absorption wavelengths, and use molecular orbital contour analysis to show the effects of ligand electronegativity on the  $\pi'$  network.

### INTRODUCTION

Phosphonitrilic compounds have emerged from the general class of inorganic polymers because of a set of unique properties which makes them potentially useful candidates for optical applications. Many of these properties are simply the result of the unusual chemical bonding characteristics between first and second row elements constituting the P-N backbone in these species. Other important properties stem from the ease with which substituent groups on the phosphorus may be altered, resulting in markedly different physical characteristics [1].

The nature of the P-N bonding gives rise to two independent  $\pi$  networks; the normal out-of-plane  $\pi$  network as is seen in organic polymers, and an in-plane  $\pi'$  network. The presence of the second network is largely responsible for the large increase in optical transition energies, keeping the polymer transparent in the visible region. The conjugation of these  $\pi$  networks is also responsible for the large non-linear optical properties recently observed and calculated for these polymers [2]. The generally better materials properties of these inorganic polymers, however, means these materials may be more useful than organic polymers for fabricating practical devices such as optical switches and power limiters.

Our approach to understanding and predicting the physical properties of these systems is to develop a fundamental picture of these materials based upon their molecular and electronic structure. In this paper, we report the results of electronic structure calculations on a series of phosphonitrilic systems  $(F_2PN)_3$ ,  $(F_2PN)_4$  and  $(F_2PN)_5$  and organic systems  $(C_5H_5N)$  and  $(C_3H_3N_3)$  using the CNDO/1 formalism with configuration interaction, in order to compare orbital interactions and electronic transitions in these materials. The two principal electronic features examined are the vertical ionization potentials and ultraviolet absorption spectra, while orbital contour diagrams will be presented to show some of the unique bonding interactions of the  $\pi'$  network.

### METHODS

Semiempirical valence electron molecular orbital methods were used to evaluate the electronic structure of  $(F_2PN)_3$ ,  $(F_2PN)_4$ ,  $C_5H_5N$  and  $C_3H_3N_3$  and were compared to *ab initio* results [3] where applicable. Vertical ionization potentials for the molecules were estimated from the one-electron orbital eigenvalues using Koopman's theorem. Molecular orbital contour plots were generated using QCPE program #340 [4] that was modified to allow the user to delete the contribution of individual atomic centers from the molecular orbital plot.

UPS spectra were simulated using the superpositions of gaussian absorption profiles with a FWHM=0.35 eV and the dielectric relaxation model in ref.[5]. Coulomb integrals were evaluated using the Mataga-Nishimoto interpolation formula[6], and the Pople-Segal formalism[7] was used for core Hamiltonian matrix terms. One center gamma integrals and vertical ionization potentials were taken from the MINDO/3 parameterization in MOPAC 4.0 (QCPE #455). For the phosphonitrilic species, the ratio of s and p orbital exponents was kept constant while they were being re-optimized to reproduce the electronic structure determined by ab initio computations and experimental vertical ionization potential data. Ultraviolet absorption transitions were evaluated using a 4x4 configuration interaction scheme for organic species, and an 8x8 for inorganics. Further details on the electronic structure method are available in ref [8].

## RESULTS AND DISCUSSION

Typical organic polymers are constituted of first row elements in the polymer backbone, with classical chemical bonding interactions characterized by the small electronegativity differences between adjacent bonding pairs. On the other hand, common inorganic species, such as carbides, nitrides and oxides, invoke chemical bonding situations in which there are large size and electronegativity differences along the polymer backbone. The involvement of lone pair orbitals on bridging atoms in the backbone can perturb classical  $\pi$  type interactions, and create in-plane p orbital interactions which have been described as  $\pi'$  bonding.

In order to clarify the organic vs. inorganic backbone and  $\pi$  vs.  $\pi'$  bonding interaction issues, molecular orbital calculations were performed on the small cyclic molecules,  $((F_2PN)_3, (F_2PN)_4, C_5H_5N$  and  $C_3H_3N_3$ ), as models for organic and inorganic systems. For pyridine, the calculated vertical ionization potentials (Table 1) and orbital ordering ( $1a_2(\pi), 11a_1(\sigma,n), 2b_1(\pi) \dots$ ) were in good agreement with the experimental values reported by Batich et.al.[9]. The electronic transition energy was calculated to be ~267 nm compared against 286 nm measured experimentally[10]. Previous estimates for pyridine by Duke et.al. [5] had used a  $1a_2(\pi), 2b_1(\pi), 11a_1(\sigma,n) \dots$  orbital ordering in order to compare against the measured ionization potentials for pyridine and its alkyl substituted derivatives. The presence of high lying  $\pi$  molecular orbitals results in the  $\pi-\pi^*$  optical transition observation in a manner similar to benzene. Analysis of our optical transition eigenfunctions shows that the orbital transitions are essentially 100%  $n-\pi^*$  for pyridine and 87%  $n-\pi^*$  for triazine, consistent with the experimental measurements of Innes[11], and later calculations by Ridley and Zerner[12].

The vertical ionization potentials for triazine are given in Table 1, and also show good agreement with the experimental values reported by Gleiter et.al.[13]. The orbital interactions of the nitrogen lone pairs is defined by the molecular symmetry, which results in the  $e'(\sigma,n)$  linear combination being the uppermost orbital in the occupied orbital manifold. Such

Table 1 - Vertical ionization potentials(eV) for  $C_5H_5N$  and  $C_3H_3N_3$

$C_5H_5N$		$C_3H_3N_3$	
Calculated	Experimental[9]	Calculated	Experimental[13]
9.7 ( $\pi$ )	9.7 ( $\pi$ )	10.37 $e'(\sigma,n)$	10.37 $e'(\sigma,n)$
9.82 ( $\sigma,n$ )	9.8 ( $\sigma,n$ )		
10.8 ( $\pi$ )	10.5 ( $\pi$ )	11.82 $e''(\pi)$	11.67 $e''(\pi)$
11.5 ( $\sigma$ )	12.5 ( $\sigma$ )		
14.6 ( $\pi$ )	12.6 ( $\pi$ )	13.97 ( $\sigma,n$ )	13.2 ( $\sigma,n$ )

patterns recur in the phosphonitrilic systems as described below. For triazine, the first electronic transition energy was 259 nm compared to an experimental value of 274 nm [10].

The electronic structure of organic polymers is characterized by  $\sigma$  and out-of-plane  $\pi$  bonding networks, while inorganic polymers may also exhibit in-plane  $\pi'$  bonding interactions. Electronegativity differences along the backbone have been shown to play an important part in determining the interaction of the in-plane nitrogen orbitals. However, the molecular

symmetry of the phosphonitrilic systems also offer the interesting contrasts for the electronic transitions with organic compounds. As opposed to benzene, pyridine, and the triazines where the ligand attached to the ring backbone remains coplanar with the ring, the phosphonitrilic ligands are oriented above and below the ring. These orientations present a possible  $\pi$ -like path for electronic transitions which would formally be called a charge transfer (CT) transition, nitrogen  $\pi$  to ligand.

Table 2 - Vertical ionization potentials (eV) for  $(NPF_2)_n$ ,  $n=3,4,5$  [14].

n=3		n=4		n=5	
Calculated	Expt'l	Calculated	Expt'l	Calculated	Expt'l
--	--	10.7	10.7	--	--
11.4	11.4	11.6	11.5	11.4	11.4
--	--	12.6	12.5	12.7	12.5
13.0	13.1	13.5	13.6	14.6	13.3
--	--	14.9	14.9	--	--
14.8	15.4	--	--		

The vertical ionization potentials for the cyclic phosphonitrilic series are given in Table 2. Given the orthogonality of the  $\pi$  and  $\pi'$  networks, simple molecular symmetry arguments determine the orbital pattern of the uppermost occupied molecular orbitals. For example, the first ionization potential for the cyclic trimer corresponds to the pair of doubly degenerate orbitals ( $e'$  and  $e''$ ), one of which contains the in plane  $\pi'$  interactions, the other, the out-of-plane  $\pi$  orbital. Higher ionization potentials arise from singly degenerate  $\pi$  and  $\pi'$  interactions, and the P-N  $\sigma$  network respectively. In comparison with the organic species, the UPS simulation plays a critical role in determining the quality of the calculated vertical ionization data. The differences in electronegativity and size between the first and second rows of the period table result in  $\pi$  interactions weaker than for their organic counterparts. Thus, the orbital manifold described by the possible nitrogen p orbital interactions contains both degenerate and nearly degenerate linear combinations. Degenerate and nearly degenerate orbital eigenvalues become unresolvable with the finite linewidths seen with normal experimental measurements.

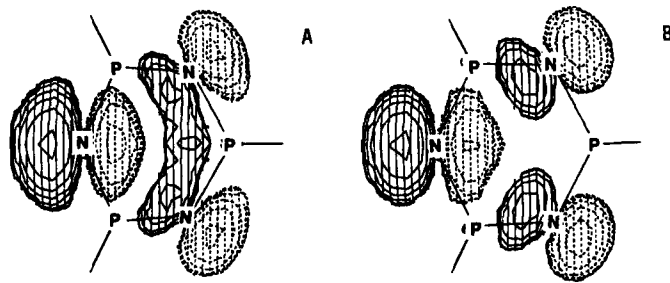


Figure 1 - Orbital contour for  $\pi'$  interactions in (a)  $(F_2PN)_3$  and (b)  $(H_2PN)_3$ . Ligand orbital contributions omitted for clarity.

Ligand electronegativity has significant effects on the electronic transitions of these species. Previous work [3] has shown that the location of the  $\pi$  orbitals in the occupied orbital manifold is particularly sensitive to these effects, becoming higher in energy with decreased ligand electronegativity. The interactions of the  $\pi'$  orbitals become less pronounced under these conditions (Figure 1). The net effect is to decrease the  $\pi$ -LUMO energy difference, and subsequently the electronic transition energy becomes smaller. The experimental values for

electronic absorption for the series  $(X_2P-N)_3$ ,  $X=F, Cl, Br$  changes from ~149 nm to 195 nm respectively[1].

In Table 3, we report the lowest electronic transition for the phosphonitrilic systems. In more descriptive terms, this transition has been defined as a charge transfer band between the  $\pi$  system and ligands. The one-electron eigenfunction analysis shows that the  $\pi$  orbital is a classical out-of-plane bonding orbital involving nitrogen p-orbitals polarized in a manner consistent with the electronegativity difference between the P and N atoms. Participation of the phosphorus orbitals is affected by similar energetic and symmetry concerns.

Table 3 - Electronic absorption wavelengths (nm) for  $(NPF_2)_n$

	Calculated	Experimental [15]
$(NPF_2)_3$	149	149
$(NPF_2)_4$	162	148
$(NPF_2)_5$	155	---

#### SUMMARY

The electronic structure of both organic and inorganic materials can be well described using semiempirical molecular orbital methods. There are many similarities between conventional organic species and phosphonitrilic systems, with the electronic structure of both systems characterized by their molecular symmetry, even with the large bond polarity shown by the phosphonitrilic systems. A major difference is the extent of interaction of the  $\pi$  bonding networks and its effect on electronic transition energies. These effects are strongly dependent on the electronegativity of the ligand attached to the phosphorus. Thus, phosphonitrilic materials offer comparable electronic and tunable optical properties to organic materials.

#### REFERENCES

- [1] H.R. Allcock in "Phosphorus-Nitrogen Compounds" New York: Academic Press (1972).
- [2] S.M. Risser and K.F. Ferris, Laser Induced Damage in Optical Materials: 1989, NBS Spec. Publ., (submitted).
- [3] K.F. Ferris, P. Friedman, and D.M. Friedrich, Int. J. Quant. Chem. S22, 207, (1988); K.F. Ferris and C.B. Duke, Int. J. Quant. Chem. S23, (1989) in press.
- [4] W.L. Jorgensen, QCPE Program No. 340, (1970).
- [5] C.B. Duke, W.R. Salaneck, T.J. Fabish, J.J. Ritsko, H.R. Thomas, and A. Paton, Phys. Rev. B 18, 5717, (1978).
- [6] N. Mataga and K. Nishimoto, Z. Phys. Chem. 13, 140, (1957).
- [7] J.A. Pople and G.A. Segal, J. Chem. Phys. 43, 5136, (1965).
- [8] N.O. Lipari and C.B. Duke, J. Chem. Phys. 63, 1748, (1975); C.B. Duke, K.L. Yip, G.P. Ceasar, A.W. Potts, and D.G. Streets, J. Chem. Phys. 66, 256, (1977).
- [9] C. Batich, E. Heilbronner, V. Hornung, A.J. Ashe, D.T. Clark, U.T. Coble, D. Kilcast, and I. Scanlan, J. Amer. Chem. Soc. 95, 928, (1973).
- [10] Physical Constants of Organic Compounds in "CRC Handbook of Chemistry and Physics", 52nd Edition, Cleveland, OH: Chemical Rubber Co., (1970).
- [11] K.K. Innes, J.P. Bryne, and I.G. Ross, J. Mol. Spectr. 22, 125, (1967).
- [12] J. Ridley and M. Zerner, Theoret. Chim. Acta 32, 119, (1973).
- [13] R. Gleiter, E. Heilbronner, and V. Hornung, Helv. Chim. Acta 55, 255, (1972).
- [14] G.R. Branton, C.E. Brion, D.C. Frost, K.A.R. Mitchell, and N.L. Paddock, J. Chem. Soc. A, 151, (1970).
- [15] B. Lakatos, A. Hesz, Z. Vetessy, and G. Horvath, Acta Chim. Acad. Sci. Hung. 60, 309, (1969).

THEORETICAL CALCULATIONS OF THE NONLINEAR DIELECTRIC  
FUNCTION OF INHOMOGENEOUS THIN FILMS

STEVEN M. RISSER AND KIM F. FERRIS  
Pacific Northwest Laboratories, Materials and Chemical Sciences Center, Richland, WA

ABSTRACT

The dielectric function of inhomogeneous materials is composed of linear and nonlinear responses which are sensitive to the film microstructure as well as the intrinsic properties of the materials. We have developed a method to self-consistently determine the linear and non-linear contributions to the dielectric function of films with random microstructure. This method is based upon a numerical solution of the general electrostatic equations and is applicable to arbitrary shapes and orientations of model defects. This method provides near exact solutions to the linear response of the dielectric function. We have shown that the nonlinear part of the dielectric function is extremely sensitive to the void shape and void fraction.

INTRODUCTION

Dielectric films having identical chemical composition can exhibit substantial variation in their optical properties, which may be significantly different from those intrinsic to the bulk crystalline materials. The film deposition technique plays a large role in determining these variations, due to the large differences in the microstructure observed for the different preparation methods. The dielectric properties of the films are sensitive to the parameters of the microstructure, such as void and particle shape and size.

Quasi-static and effective medium methods [1,2] have been developed to model the real part of the dielectric function in the long wavelength limit. These methods include varying degrees of information about the microstructure of the film. Dynamic corrections to these models can include a rough degree of microstructural information for conditions where the wavelength of light approaches the particle size. However, all these methods contain implicit assumptions about the extent and randomness of the microstructure and do not treat the nonlinear optical properties of the media. Because of the complex nature of the boundary conditions imposed on solutions of Maxwell's equations for a film composed of many particles of varying shapes, analytic solutions to determine the optical properties are not feasible.

Such restrictions can be eliminated by computational approaches to the governing electrostatic equations. By modelling material microstructure by a series of finite elements, self-consistent methods can provide effective solutions to the polarizability. In this paper, we present numerical solutions of Maxwell's equations to determine the effects of microstructure on the nonlinear part of the dielectric function of inhomogeneous media.

METHODS

The macroscopic dielectric response of a body in the long wavelength limit is given by:

$$\vec{D} = \epsilon_0 \vec{E} + \vec{P} \quad (1)$$

where  $E$  is the macroscopic electric field,  $P$  is the macroscopic polarization,  $D$  is the electric displacement and  $\epsilon$  is the dielectric function. Microscopically, the local polarization is given by:



$$\vec{p}(\vec{r}) = \chi^{(1)}(\vec{r}) \vec{E}(\vec{r}) + \chi^{(2)}(\vec{r}) \vec{E}(\vec{r}) + \dots \quad (2)$$

where  $p$  is the local polarization,  $\chi$  is the local electric susceptibility and  $E$  is the local electric field. The local electric field is equal to the sum of the applied external field and the field due to all the induced dipoles.

$$\vec{E}_{\text{ind}}(\vec{r}_i) = \vec{E}_0 + \sum_{i \neq j} \frac{[\vec{p}(\vec{r}_j) (\vec{r}_i - \vec{r}_j)](\vec{r}_i - \vec{r}_j) - \vec{p}(\vec{r}_j) [\vec{r}_i - \vec{r}_j]^2}{4\pi\epsilon_0 [\vec{r}_i - \vec{r}_j]^5} \quad (3)$$

These equations determine the relationship between the electric field at a given point and the local polarization of the whole volume. The nature of this relationship prevents analytic solutions for any but the most simple forms for  $\chi(r)$ .

The volume of interest is divided into cubes of side  $a$ , with the susceptibility for each cube set equal to the value at the center of the cube. The local polarization for each cube is then determined from the susceptibility and the applied external field (eq. 2) for initial values of the polarizations in the self-consistent determination. These values are then used to determine the local electric field at each cube (eq. 3), with the process iterated in a self-consistent fashion until corrections are on the order of  $10^{-15}$ . The dielectric function is calculated by averaging the local field and polarization within the volume and using these as the macroscopic values (eq. 1).

## RESULTS AND DISCUSSION

The microstructure of thin films leads to large spatial variations in the electric susceptibility. Calculations were performed for a variety of microstructures and a range of magnitudes for the linear and nonlinear susceptibilities. The effects of microstructure were modelled by replacing random cubes with either vacuum or a cube containing a void of given shape. The nonlinear part of the dielectric function was determined in two ways. One was to perform calculations for a given microstructure both with and without a nonlinear term in the susceptibility, and compare the results. The second was to calculate the dielectric function for a range of applied field strengths and determine the linear contribution by extrapolation to zero applied field.

The random nature of the microstructural variations prevents a general analytic solution for the dielectric function. There are a few simple geometries for which the dielectric function for a spatially varying susceptibility can be calculated. One of these geometries is a spherical volume with the electric susceptibility held fixed in magnitude, but oriented in the radial direction within the sphere. The local polarization is found to be a separable function of  $r$ ,  $\theta$ , and  $\phi$ . In Figure 1, the radial part of the polarizability function is plotted against the radius for both the analytic and numerical solutions. The numerical calculations were performed by mapping the sphere into a  $15 \times 15 \times 15$  array of cubes. The figure shows that except near both the inner and outer boundaries, the agreement is very good, with the differences being caused by the incomplete mapping of a sphere into a lattice of cubes.

The optical properties of dielectric materials are usually described in terms of the linear portion of the dielectric function. With the advent of higher power laser systems, it will become increasingly important to be able to evaluate the non-linear response of this property. The effective medium approximations developed to date are not capable of calculating the nonlinear part of the dielectric function. Our numerical method was extended to include a field dependent term in the polarizability, with the general solution method and convergence criteria remaining unchanged. The dielectric function of the array of cubes was calculated at a series of field strengths, and also for a range of void fractions

within the film.

In Figure 2, the nonlinear component of the dielectric function is plotted against the void fraction for two types of void shapes, oblate spheroidal void shapes, and cubic void shapes. Void effects were modelled by setting the susceptibility and the self-induced field term for the cubes containing voids equal to the values determined for a cube containing those shape defects. The results in Figure 2 demonstrate that the nonlinear part of the dielectric function is extremely sensitive to the void shape, even at low void fractions. Similar discrepancies are shown to exist for column defect type voids.

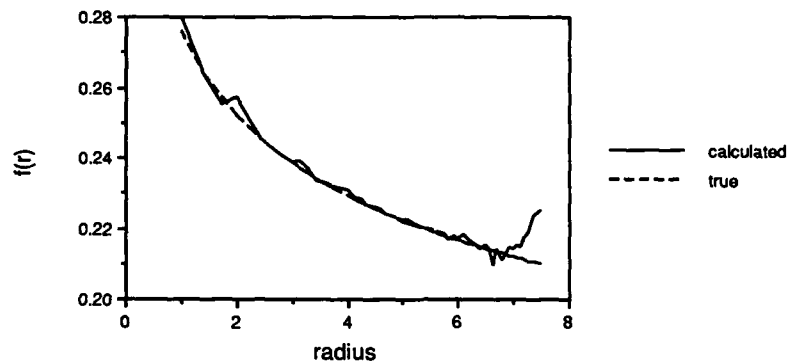


Figure 1. Radial part of the polarization for a sphere with a radially oriented electric susceptibility. Both the analytic and numeric results are shown. The numeric results were calculated by mapping a sphere into a  $15 \times 15 \times 15$  array of cubes.

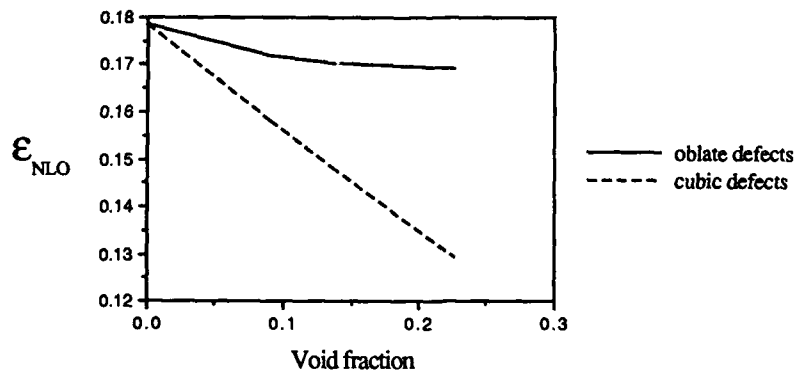


Figure 2. Nonlinear dielectric function vs. void fraction. Shown are the results for oblate spheroidal shaped voids, and cubic voids. The applied external field is held constant for these calculations.

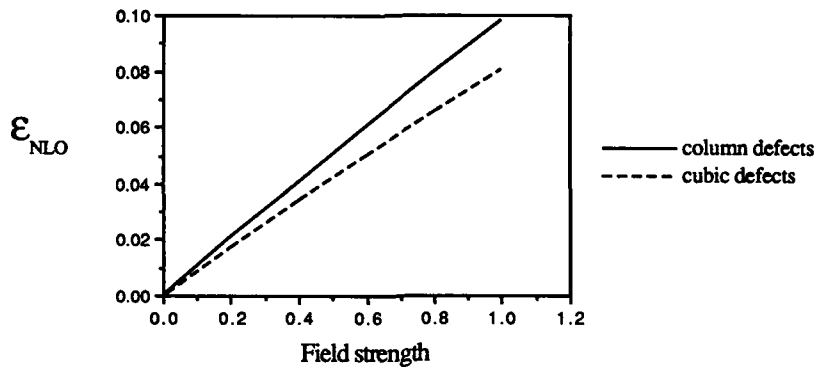


Figure 3. Nonlinear part of the dielectric function vs. applied field strength. Plotted are the results for cubic defects, and column defects. The void fraction is 0.469 for both calculations.

As expected, the nonlinear contribution was also shown to be sensitive to the strength of the applied field at constant void fraction. Figure 3 plots the magnitude of the nonlinear dielectric function against the applied field strength for random cubic and random column shaped voids. Column defects were formed by placing cubic defects in our lattice model adjacent to each other in a straight line fashion as to span the width of the lattice in the direction of the applied field. Although the void fraction is the same for both calculations, the column defects show a distinctly larger nonlinearity than do the random cubic defects.

Previous work by Aspnes and others have shown that the linear portion of the dielectric function is sensitive to microstructural information. Non-linear contributions demonstrate similar characteristics and will play an important part for the high field applications of materials. The non-linear portion of the dielectric function may be determined from the deviation from linearity as a function of applied field. This information, combined with knowledge of the void fraction, will permit the incorporations of microstructural information into our models of dielectric films. For films where the void shapes are well characterized, the results from Figure 2 show the ability to determine the void fraction in the sample by simple optical measurements.

## CONCLUSIONS

A numeric solution method has been used to model the linear and nonlinear part of the dielectric function for inhomogeneous media. Comparison to analytic solutions show very good agreement for linear susceptibilities. The nonlinear part of the dielectric function has been shown to be extremely sensitive to the shape of voids present, even at low void fractions.

## REFERENCES

1. D.E. Aspnes, *Thin Film Solids*, **89**, 249 (1982).
2. D. Stroud and F.P. Pan, *Phys Rev B*, **17**, 1602 (1978).

NONLINEAR OPTICAL STUDIES OF MIXED  $\pi$ -CONJUGATED POLYMER  
MULTILAYERS BY SECOND HARMONIC GENERATION

H. KOEZUKA, T. KURATA, A. TSUMURA AND H. FUCHIGAMI  
Mitsubishi Electric Corporation, Materials & Electronic Devices  
Laboratory, 1-1 Tsukaguchi Honmachi 8-Chome, Amagasaki, Hyogo 661  
Japan

ABSTRACT

The structures of the mixed LB monolayers, composed of two different kinds of  $\pi$ -conjugated system, poly(3-hexylthiophene) (PHT) and pentacosanoic acid (DA), have been investigated mainly by a second harmonic generation (SHG) Maker fringe method. The mixed LB films partly contain a double-layered structure consisting of PHT and DA. The second harmonic radiation has been produced from slightly twisted PHT in the double layer. Both UV-polymerization of DA and successive heat-treatments enhanced the SHG intensities. The enhancement of the SHG intensities has been elucidated by the enlargement of the PHT twisting and the interaction between PHT and a newly formed  $\pi$ -conjugated system.

1. INTRODUCTION

$\pi$ -Conjugated polymers have been intensively investigated as candidates of nonlinear optical materials[1]. Since the nonlinear susceptibilities greatly depend on the orientational order of chromophores, a Langmuir-Blodgett(LB) technique has been widely utilized to orient the chromophores. Second harmonic generation (SHG) can be applicable to study the chromophore orientation in ultra-thin films because of its high sensitivity [2].

We have prepared mixed monolayers consisting of two different kinds of  $\pi$ -conjugated system, that is, poly(3-hexylthiophene) (PHT) and amphiphilic pentacosanoic acid (DA) (Fig. 1). The structures of the obtained monolayers with various mixing ratios of PHT to DA have been investigated primarily by means of a SHG Maker fringe method. The SHG intensity dependence on the mixing ratio of two compounds and the effect of the polymerization of DA and the successive heat-treatment on the SHG intensity will be also reported.

2. EXPERIMENTAL

PHT was synthesized according to Yoshino et al [3]. DA was purchased from Wako Chemical Ltd. and was used without further purification. The chloroform solution containing both PHT and DA was spread on a subphase with cadmium chloride ( $3 \times 10^{-4}$  M) and sodium bicarbonate ( $1 \times 10^{-4}$  M). The temperature of the subphase was kept at 20 °C. Monolayer was transferred to a glass substrate at the speed of 50 mm/min by an usual vertical dipping method. The surface pressure was maintained at 15 mN/m during the deposition. All the obtained LB films were Y-type and the transfer ratio was almost unity for all the cases. After the deposition, the samples were irradiated for 8 min by a high-pressure mercury lamp through a filter (254 nm,  $1 \text{ mW/cm}^2$ ) and were

successively heat-treated at 90 °C for 15 min in air. The UV-irradiation polymerized DA molecules inside the LB films to give the so-called blue-form poly-DA. The heat-treatment transformed the blue-form into red-form.

SHG Maker fringes were measured with a Q-switched Nd:YAG laser (Quantel YG-571, 1.06  $\mu\text{m}$ , 10 Hz repetition). The pulse energy and the polarization of the fundamental wave were controlled to be 5 mJ and to be horizontally polarized, by using an attenuator and a Glan laser prism, respectively. The polarization was changed by rotating a half wavelength plate. The laser beam was focused on a sample placed onto the rotating stage with a 50-cm focal length lens. Second harmonic radiation generated from the samples was detected by a photomultiplier (Hamamatsu, model R928) after passing it through an IR-cut filter and KL-53 bandpass filter (Toshiba). The signals from the photomultiplier were processed with a Boxcar averager (Stanford Research Systems, model SRS-250). All the measuring systems were controlled with a personal computer (Yokogawa-Hewlett-Packard, model 236).

### 3. RESULTS AND DISCUSSION

Surface pressure ( $\pi$ )- area per DA molecule (A) isotherms at each mixing ratio were measured in order to obtain the information on the monolayer film structures. Fig. 1 shows the relationship between molecular area (A) and the mixing ratio. The A was calculated only on the basis of the number of DA molecules spread on the subphase. The A linearly increased with the addition of PHT until the ratio of the PHT repeating unit to DA reached unity. However, it did not increase in such a way when PHT was further added. These results suggest that the addition of the PHT beyond the mixing ratio of unity has caused the structural change of the monolayer.

Fig. 2 shows typical SHG Maker fringe patterns of as-grown PHT-DA (1:1) monolayer deposited on both sides of a glass substrate. Other systems exhibited the similar patterns. The appearance of the fringe pattern is attributed to the interference of the second harmonic radiation from the monolayer on both sides of the substrate. For all the SHG measurements, only the p-polarized harmonic radiation was observed for p- (p-p) and s- (s-p) polarization of the fundamental wave. In addition, the SHG signals were independent of the rotation in the vertical plane. These observations indicate that the nonlinear polarization has no components inside the film plane and is in-plane isotropic. The LB films, therefore, have only two independent tensor components of nonlinear optical coefficient, that is,  $d_{33}$  and  $d_{31}$  ( $=d_{32}=d_{24}=d_{15}$ ) [4]. The SHG intensity increased with the mixing ratio of PHT to DA. On the contrary, no SHG has been detected for the LB films with only DA molecules. It is, therefore, concluded that the SHG signals originate from PHT.

The SHG intensities at the incident angle of 60° were plotted against the deposited number (Fig. 3). The SHG intensities for odd number of monolayers were larger than those for even ones (odd-even effect). This result is consistent with that the LB films are Y-type. Though the first layer has sometimes shown peculiar behavior for SHG measurements [5], such behavior has not been observed for our case.

The SHG intensities should increase with the square of

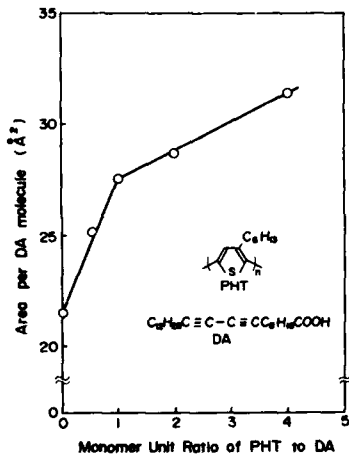


Fig. 1 Relationship between the area per DA molecule and the ratio of PHT repeating unit to DA. The inset represents the chemical structures of PHT and DA.

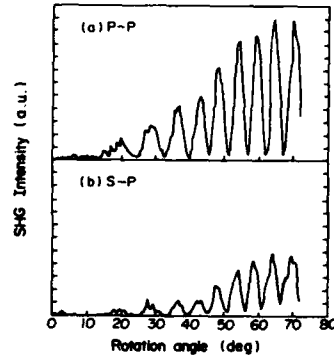


Fig. 2 Typical SHG Maker fringe pattern of as-grown PHT-DA(1:1) LB monolayer deposited on both sides of a glass substrate.

effective nonlinear optical coefficient. The square roots of the observed SHG intensities,  $(I_{SHG})^{1/2}$  for the mixed monolayers were plotted against the surface density of the PHT repeating unit on

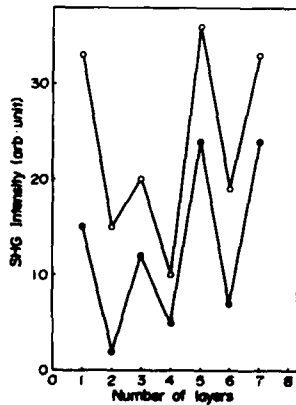


Fig. 3 Dependence of the SHG peak intensity on the number of layers. Samples are as-grown PHT-DA(1:1) LB films. (O) and (●) correspond to P-P and S-P polarizations, respectively.

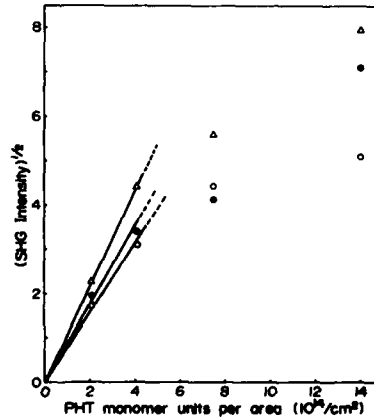


Fig. 4  $(SHG \text{ intensity})^{1/2}$  vs. PHT repeating unit per area plots for PHT-DA LB films. (O), (●) and (Δ) correspond to the as-grown, UV-treated and heat-treated samples, respectively.

the water surface for the s-p polarization (Fig. 4). The  $(I_{\text{SHG}})^{1/2}$  linearly increased until the surface density reaches  $4 \times 10^{14} \text{ cm}^{-2}$  corresponding to the mixing ratio of unity. The same behavior has been also observed for the p-p polarization. The increasing amount diminished beyond that point, that is, all the added PHT did not contribute to the SHG. The structural change of LB films has been again suggested beyond the mixing ratio of unity.

The same behavior was also observed for the samples after UV- and successive heat-treatment. However, the samples after such treatments gave stronger SHG intensities than as-grown ones for the p-p and the s-p polarization. When the LB films with only DA was polymerized by UV-irradiation the enhancement of the SHG intensity has not been observed. It is implied from above observations that the polymerization of DA has made PHT more SHG-active.

All the LB films gave X-ray diffraction patterns having seven peaks although UV-irradiation and successive heat-treatment a little made the patterns vague. The X-ray diffraction measurements clearly indicate the formation of well-ordered layered structure for all the samples. The PHT chain is, therefore, considered to extend in the lateral direction. Thus, the dominant  $\beta$  seems to exist not along the polymer chain, but along the symmetrical axis of the PHT repeating unit (thiophene ring). Fig. 5 depicts the possible configurations for the PHT on the subphase, where a rectangle stands for the side view of a thiophene ring and a line represents a hexyl chain. The configuration (a) having parallel  $\beta$ 's is the most SHG-active, but it is unfeasible because of highly steric hindrance between hexyl chains. The most stable configurations for PHT is the (b) where the  $\beta$  of each thiophene ring is opposite to those of the neighboring ones, becoming SHG-inactive. More believable configurations for PHT on the water surface seem to be (c) or (d). In both configurations, hexyl chains have a tendency to go away from the water surface on account of their hydrophobic properties. The configuration (c) is SHG-inactive since the each  $\beta$  again cancels out with each other. In order to become SHG-active for PHT, the thiophene ring has to slightly twist on the water surface like the configuration (d). The twisting has been caused by a suitable packing of DA and PHT because the mixed monolayers consisting of PHT and stearic acid have not produced any second harmonic radiation. The twisting of the

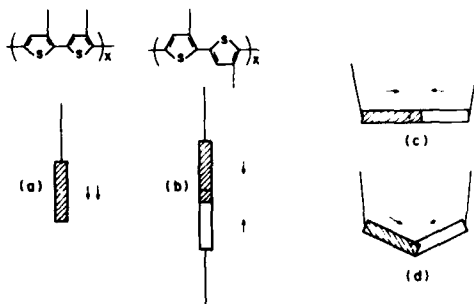


Fig.5 Possible configurations of PHT on the subphase.

thiophene rings in poly(alkylthiophene)s themselves has been also observed by NMR [6].

Fig. 6 illustrates the structures of the mixed monolayers having PHT and DA. When the mixing ratio of PHT to DA is below unity, the LB films has a double-layered structure like Fig. 6(a). Fig. 6(a) indicates that all the amount of the mixed PHT contributes to the production of the second harmonic radiation, which is supported by the results in Fig. 4. The structure (a) should lead to the expansion of the bilayer distance compared with the LB films having only DA molecules. Indeed, the addition of PHT enlarged the bilayer distance by ca. 1-2 Å. The structure (a) may be expected to prevent the UV polymerization of DA because of the larger distance between DA molecules. Ogawa *et al* has recently reported that the polymerizable distance between DA molecules are relatively large [7]. Even in the structure as illustrated in Fig. 6(a), DA molecules are considered polymerizable. The polymerization of the DA molecules slightly increased the bilayer distance, leading to the shrinkage of the lateral distances between each DA. The shrinkage has compressed the PHT chains resulting in the enlargement of the PHT deformation. That is one reason why the polymerization of the DA molecules increases the SHG intensity. The PHT deformation by itself can not explain that the SHG intensities for both the p-p and the s-p polarizations have increased after the polymerization of DA, leading to the increase of the  $\beta$  itself. Another reason for the enlargement of the SHG intensity might be, therefore, due to the interaction between PHT and a newly formed  $\pi$ -conjugated system.

The heat-treatment has transformed the blue-form poly-DA into the red-one, which is confirmed by absorption spectroscopy. The heat-treatment expanded the bilayer distance further by more than 1 Å, resulting in the additional compression of PHT. It is considered reasonable that the SHG intensity has increased compared with the case before the heat-treatment. The enhancement of the SHG intensity is not due to the resonance effect since the red-form has smaller absorbance at 552 nm than

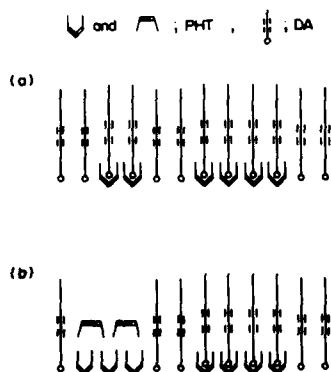


Fig. 6 Schematic structures of the mixed Langmuir monolayers containing PHT and DA. (a) and (b) correspond to the cases in which the ratio of the PHT repeating unit to DA is 1:1 and 2:1, respectively.



the blue-one. The results of the SHG measurements for the heat-treated LB films have been analyzed by a simple distribution model [8]. The model has the following assumptions: (1) the molecular axis is consistent with the direction of the main component of  $\beta$ , (2) the axis is inclined at an average angle  $\phi$  to the surface normal with a random azimuthal angle. These assumptions are rational that our systems have only two independent tensor components of nonlinear optical coefficient. The angle  $\phi$  has been roughly estimated to be  $77^\circ$  from the comparison of the SHG intensities for the p-p and s-p polarizations according to reference [8]. This estimation also supports the twisting of the thiophene rings. The  $\beta$  of the thiophene ring has been also calculated to be ca.  $5 \times 10^{-30}$  esu, neglecting the local field factor.

The addition of PHT beyond the mixing ratio of unity did not enlarge the SHG intensity so much. It is, therefore, considered that some parts of the further added PHT should be SHG-inactive. The possible structure of the LB films with the mixing ratio beyond unity is shown in Fig. 6(b) where some of the mixed PHT are squeezed out from the monolayer to aggregate. This model elucidates the small increase in both the area per DA molecule (Fig. 1) and the  $(I_{\text{SHG}})^{1/2}$  (Fig. 2) when further PHT is added to the system with  $\text{PHT/DA}=1$ .

In conclusion, the mixed monolayers consisting of PHT and DA have been prepared and their structures have been investigated primarily by a SHG Maker fringe technique. It has been confirmed that a part of DA molecules superimposes onto PHT and the observed SHG originates from the slightly twisted PHT inside the monolayers. The polymerization of DA and successive heat-treatment have enlarged the SHG intensity. The enlargement has been elucidated by the increase of the PHT deformation with the polymerization of DA and the interaction between PHT and a newly formed  $\pi$ -conjugated system (poly-DA).

#### 4. REFERENCES

- [1] See, for example, *Nonlinear Optical Properties of Polymers*, edited by A. J. Heeger, J. Orenstein and D. R. Ulrich (MRS, Pittsburgh, 1988).
- [2] G. Khanarian, *Thin Solid Films*, 152, 265 (1987).
- [3] R. Sugimoto, S. Takeda, H. B. Gu and K. Yoshino, *Chem. Express*, 1, 635 (1986).
- [4] I. R. Girling, N. A. Cade, P. V. Kolinsky, J. D. Eaels, G. H. Cross and I. R. Peterson, *Thin Solid Films*, 132, 101 (1985).
- [5] I. Ledoux, D. Josse, P. Fremaux, J. -P. Piel, G. Post, J. Zyss, T. McLean, R. A. Hann, P. F. Gordon and S. Allen, *Thin Solid Films*, 160, 217 (1988).
- [6] P. Love, R. Sugimoto, K. Yoshino, *Japan J. Appl. Phys.* 27, L1562 (1988).
- [7] K. Ogawa, H. Tamura, M. Hatada and T. Ishihara, *Langmuir*, 4, 903 (1988).
- [8] P. F. Heinz, H. W. K. Tom and Y. R. Shen, *Phys. Rev. A* 28, 1883 (1983).

EFFICIENT SECOND HARMONIC GENERATION IN HYDRAZONE,  
DERIVATIVES OF SUBSTITUTED AROMATIC ALDEHYDES

RICHARD S. POTEEMBER, ROBERT C. HOFFMAN, AND KAREN A. STETYICK  
The Johns Hopkins University, Applied Physics, Johns Hopkins Road, Laurel, MD  
20723-6099

ABSTRACT

Hydrazone, 1,1-dimethylhydrazone, methylhydrazone, phenylhydrazone and p-nitrophenyl hydrazone derivatives of substituted aromatic aldehydes were prepared and screened for second harmonic generation using the Kurtz powder technique. One compound, 4-nitro-3-methoxybenzaldehyde hydrazone exhibited a second harmonic signal up to 32 times that of ammonium dihydrogen phosphate (ADP) and 4-nitrobenzaldehyde hydrazone exhibited a second harmonic signal five times higher than previously reported, up to 40 times that of ADP. 3-methyl-4-nitrobenzaldehyde hydrazone, 4-nitrobenzaldehyde phenylhydrazone, 1-naphthaldehyde phenylhydrazone, 1-pyrenecarboxaldehyde phenylhydrazone exhibited second harmonic signals 25, 2.5, 5 and 20 times that of an ADP standard.

INTRODUCTION

Second harmonic generation in organic materials, such as MNA (2-methyl-4-nitroaniline), has been studied for many years [1]. Second harmonic generation in those materials arises from the large nonlinear polarizability of the  $\pi$ -bond structure and the asymmetrical charge distribution associated with donors and acceptors on the molecule. The polarizability for any substance is

$$P = \epsilon_0 \chi_1 E + \epsilon_0 \chi_2 E^2 + \epsilon_0 \chi_3 E^3 + \dots \quad (1)$$

where  $\epsilon_0 \chi_1 E$  is the linear polarizability term associated with linear refraction. The second term is the second-order nonlinear polarizability responsible for second harmonic generation in anisotropic crystals, a term which vanishes in isotropic materials. The third-order nonlinear polarizability is responsible for four-wave mixing effects, photorefraction, and optical bistability.  $P$  is the macroscopic polarization,  $\epsilon_0$  is the permittivity of free space,  $E$  is the electric field, and  $\chi$  is the dielectric susceptibility. For second harmonic generation,  $\chi$  is a third rank tensor of the form  $\chi_{ijk}^{(2\omega)}$ . The second-order nonlinear term then takes the form

$$P_i^{(2\omega)} = \epsilon_0 \chi_{ijk}^{(2\omega)} E_j^{(\omega)} E_k^{(\omega)} \quad (2)$$

$$i, j, k = 1, 2, 3.$$

The numerical values of the tensor coefficients are usually represented by the symbol  $d$  [2] and are functions of frequency and temperature. The units of  $\chi_{ijk}^{(2\omega)}$  are different from that of the first order linear susceptibility term  $\chi_{ij}(\omega)$ . The first order term is a dimensionless ratio, whereas the second order susceptibility tensor has units of inverse electric field, or m/V in the mks system [2]. Organic molecules have the advantage of being amenable to molecular engineering. For example, 2-methyl-4-nitroaniline (MNA) consists of a nitro acceptor group and an amino donor group separated by a conjugated ring system. This molecule is very polarizable, has a high degree of charge transfer and thus is an excellent material for second order harmonic generation [1].

It has been shown that the second harmonic generation effect observed in organic molecules such as MNA is enhanced by the presence of extended conjugation and by the presence of a charge-transfer excitation near the harmonic wavelength in an organic molecule. This spectroscopic charge-transfer excitation arises from the presence of donor and acceptor groups on the conjugated system [3].

Potential second harmonic generation materials are often tested using the well-known powder susceptibility measurement technique initially used by Kurtz and Perry [4]. In this technique a powdered sample is placed in a cuvette and irradiated with pulses from a Nd:YAG laser operating at a wavelength of 1064 nm ( $\omega$ ). There are no restrictions on the frequency of the fundamental, provided that the sample is transparent to the harmonic frequency. If the powdered sample is a material that is suitable for second harmonic generation, light at twice the fundamental ( $2\omega$ ) will be emitted by the sample (532 nm). Because the powdered sample contains crystalline grains that are randomly oriented crystallographically, the emitted second harmonic is weak but is easily detectable with electron multiplier phototubes. The powder method can also be used to test whether the material can be phase matched. This is accomplished by measuring the total second harmonic output; (532 nm) is measured while the crystallite size of the powdered sample is varied. Phase matchable materials show an increase in the second harmonic output with increasing crystallite size that saturates once the coherence length of the fundamental and harmonic is exceeded. Non-phase matchable materials show an increase in second harmonic output with increasing crystallite size up to the coherence length, and then exhibit a sharp decrease in second harmonic output with increasing crystallite size above the coherence length. The crystallite size at which the decrease occurs is typically on the order of a few micrometers [4]. Some materials, even though they have acentric electron distributions and net dipole moments, often crystallize in a centrosymmetric crystal system, and therefore exhibit a weak or nonexistent second harmonic signal.

It is possible to shift the cutoff wavelength ( $\lambda_c$ ) in a predictable manner by using Dewar's rules [5], by which adjustment of the absorption edge is achieved by selective placement of substituent groups on an aromatic ring. For example, in the disubstituted benzene a donor group is arbitrarily defined as a "D" position. All other positions relative to the donor group are defined as "D" or "A" for donating ability or accepting ability, respectively. Placement of an electron withdrawing substituent at a "D" position or placement of a donor at an "A" position will result in a hypsochromic (blue) shift. Placement of a donor at a "D" position or placement of an acceptor at an "A" position will produce a bathochromic shift (red) shift. In this way ( $\lambda_c$ ) can be shifted, within limits, to allow optimization for a particular harmonic frequency.

## RESULTS AND DISCUSSION

We have investigated a class of compounds that has received little attention since the initial investigation by Davydov et al. in 1977 [6]. The prototype compound of the series is 4-nitrobenzaldehyde hydrazone (NBAH). Second order harmonic generation has also been observed in Langmuir-Blodgett monolayers of phenylhydrazone dyes [6a]. These compounds are synthesized (Figure 1) by reacting an aromatic aldehyde (4-nitrobenzaldehyde) with the appropriate hydrazine (hydrazine hydrate) [7]. This compound was reported initially to have a powder efficiency 2.5 times that of urea (12.5 times ammonium dihydrogen phosphate) by Davydov et al. However, we have observed powder efficiencies that are much higher (on the order of 40 times that of ammonium dihydrogen phosphate). As a result, we have synthesized various analogues of the compound both to determine if the SHG efficiency could be enhanced and if there are similar molecules with high SHG efficiencies. Ammonium dihydrogen phosphate (ADP)

was chosen for a standard because of its availability in high purity form, and for its prevalence in the literature as an accepted standard.

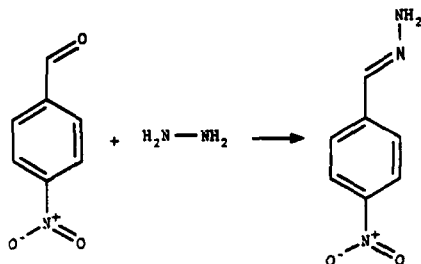


Figure 1 4-Nitrobenzaldehyde Hydrazone Synthesis

The hydrazine, methylhydrazine, dimethylhydrazine and phenylhydrazine derivatives of 3-methoxy-4-nitro benzaldehyde were synthesized. Two derivatives, 3-methoxy-4-nitrobenzaldehyde hydrazone and 3-methoxy-4-nitrobenzaldehyde methylhydrazone were found to have high SHG efficiencies. The hydrazone derivative (3-methoxy-4-nitrobenzaldehyde hydrazone) had the highest SHG powder efficiency, about 32 times that of ADP. This compound has an important advantage over 4-nitrobenzaldehyde hydrazone in that the transmission window extends farther towards the ultraviolet, allowing for the possibility of SHG of semiconductor laser sources. The methylhydrazone derivative exhibited an SHG efficiency about 16 times ADP (Table I).

The hydrazine, methylhydrazine, dimethylhydrazine and phenylhydrazine derivatives of 3-methyl-4-nitro-benzaldehyde were also synthesized and all but one were found to have small SHG efficiencies. The hydrazone derivative of 4-nitro-3-methyl-benzaldehyde had an SHG efficiency 25 times ADP.

There is no pattern that emerges from the data that allows a reliable prediction whether or not a particular derivative or family of derivatives will exhibit a high SHG efficiency. The data shows that minor chemical changes can result in significant changes in the packing of molecules in the crystal, often in turn resulting in large variations in SHG efficiency, as in the case of 4-nitrobenzaldehyde hydrazone versus 4-nitrobenzaldehyde methylhydrazone (40 times ADP vs. 0.005 times ADP, respectively). The efficiencies and UV cutoff wavelengths for the most efficient compounds are also shown in Table I.

## EXPERIMENTAL

The materials for second harmonic generation synthesized and studied in this research are a class of compounds based on 4-nitrobenzaldehyde hydrazone, which is a known material for second harmonic generation [6]. This molecule served as the model for an entire series of hydrazone derivatives of aromatic aldehyde.

The potential second harmonic generation materials are screened using well-known powder susceptibility measurements initially used by Kurtz and Perry [4]. In this technique a powdered sample is placed in a cuvette and irradiated with 10 ns pulses from a Nd:YAG laser operating at a wavelength of 1064 nm ( $\omega$ ). If the powdered sample is a material that is suitable for second harmonic generation,

Table I: Efficiency and Cutoff Wavelength of SHG Materials

SHG COMPOUND	EFFICIENCY x ADP	UV CUTOFF
4-nitrobenzaldehyde hydrazone	40	490 nm
4-nitrobenzaldehyde phenylhydrazone	2.5	525 nm
4-nitro-3-methoxybenzaldehyde hydrazone	32	442 nm
4-nitro-3-methoxybenzaldehyde methylhydrazone	10	452 nm
4-nitro-3-methylbenzaldehyde hydrazone	25	444 nm
1-naphthaldehyde phenylhydrazone	5	474 nm
1-pyrenecarboxaldehyde phenylhydrazone	20	510 nm

light at twice the fundamental ( $2\omega$ ) will be emitted by the sample (532 nm). The powdered samples contain crystalline grains that are randomly oriented, therefore, the emitted second harmonic is expected to be very weak. However, it can be easily detectable with electron multiplier phototubes. In this way large numbers of compounds were initially screened for suitability as materials for second harmonic generation.

#### OPTICAL MEASUREMENTS.

The compounds were screened for second harmonic generation using the optical apparatus described below. A Quantel YG580 Q-switched Nd:YAG laser operating at 1064 nm was used as the laser source. The incident intensity of the laser was reduced by a neutral density filter both to prevent damage of the harmonic material and to prevent saturation of the electron multiplier phototubes. The beam is split into two components of equal intensity; one is directed into a reference cell containing ammonium dihydrogen phosphate (ADP). The ADP standard contains particles between 0.25 and 0.35 mm in size. The residual 1064 nm radiation is filtered by a Schott BG-38 infrared blocking filter and an Ealing 532 nm band pass interference filter before being detected by a RCA 1P21 photomultiplier tube. The remaining beam is directed into a 10 cm diameter Labsphere integrating sphere containing the powdered sample in a 0.1 cm glass cell. The powdered sample was sized with sieves whenever possible to the same size range as the ADP standard. The integrating sphere collects all of the emitted harmonic light so that scattering does not affect the observed SHG efficiency. The cell is positioned so the incident laser energy falls at normal incidence to the cell. At a right angle to the incident beam a photomultiplier tube detects the emitted second harmonic generation at 532 nm. The residual 1064 nm radiation is removed first with a Schott BG-38 glass filter and then with an Ealing 532 nm bandpass filter. The waveforms were recorded on a storage oscilloscope and

compared with the waveform from the ADP standard. Although an integrating sphere was not used on the reference cell, the ratio of the amplitude of the ADP reference signal and the same ADP cell in the integrating sphere is a constant. The reference cell was not used for every measurement, but to establish at the beginning of a sample testing run, in which five to ten samples were tested, the constancy of the laser energy with time.

## CONCLUSIONS

We have shown that it is possible to shift the absorption edge of second harmonic generation materials by the selective placement of a methoxy donor group on the 4-nitrobenzaldehyde hydrazone molecule according to the empirical Dewar system. A spectral shift from 490 nm to 442 nm was achieved in 4-nitro-3-methoxybenzaldehyde hydrazone and a shift to 444 nm was achieved in 2-nitro-3-methylbenzaldehyde hydrazone. A modest loss in second harmonic generation efficiency was sacrificed to achieve this end. The efficiency of 4-nitrobenzaldehyde hydrazone, 4-nitro-3-methoxybenzaldehyde hydrazone and 4-nitro-3-methylbenzaldehyde hydrazone were found to be 40, 32 and 25 times ADP, respectively. We are continuing to explore this class of nonlinear optical materials.

## REFERENCES

- [1] B. F. Levine, C. G. Bethea, C. D. Thurmond, R. T. Lynch, and J. L. Bernstein, "An Organic Crystal with an Exceptionally Large Optical Second Harmonic Coefficient: 2-Methyl-4-Nitro Aniline", *J. Appl. Phys.* 50, 2523 (1979).
- [1a] J. Halbout, S. Blit, W. Donaldson, and C. L. Tang, *IEEE Journal of Quantum Electronics*, Vol. QE-15, No. 10 (1979) 1176.
- [2] G.C. Baldwin, *An Introduction to Nonlinear Optics*, Plenum Press: New York, 81 (1969).
- [3] J. L. Oudar, *J. Chem Phys.* 67, 446 (1977).
- [4] S. Kurtz and T. T. Perry, "A Powder Technique for the Evaluation of Nonlinear Optical Materials," *J. Appl. Phys.* 39, 3798 (1968).
- [5] M. J. S. Dewar, *J. Chem. Soc.*, 2329 (1950).
- [6] B. L. Davydov, S. G. Kotocshchikov, V. A. Nefedov, "New Nonlinear Organic Materials for Generation of Second Harmonics of Neodymium Laser Radiation," *Sov. J. Quantum Electronics (Eng. Trans.)* 7, 129 (1977).
- [6a] D. Lupo, W. Prass, U. Sceunemann, and I. Ledoux, *J. Opt. Soc. Am. B*, (5) 2, (1988) 300.
- [7] Beilstein, "Beilstein's Handbuch der Organischen Chemie," 7, 256.

## Author Index

- Aldissi, Mahmoud, 311  
 Alfano, R.R., 437, 631  
 Alleaume, M., 27  
 Amiell, J., 27  
 Andreatta, Alejandro, 269  
 Anzai, H., 107  
 Armes, Steven P., 311  
 Aron, Kenneth P., 499  
 Ashwell, G.J., 507  
 Assadi, Azar, 403  
 Attanasio, D., 143  
 Awaga, Kunio, 33  
  
 Babu, K.N., 583  
 Bader, Mamoun M., 551, 563  
 Bain, Art N., 443  
 Bando, H., 107  
 Bao, J.S., 347  
 Bard, Allen J., 199  
 Barraud, A., 537  
 Baum, Chris, 155  
 Bellitto, C., 143  
 Beno, M.A., 177  
 Beranger, Marc, 171  
 Bi, Xian-Tong, 347  
 Biradar, Ashók M., 525  
 Bitler, Steven P., 499  
 Blohm, Margaret L., 199  
 Bolognesi, A., 397  
 Bonamico, M., 143  
 Botta, C., 397  
 Bouyssoux, G., 359  
 Bradley, D.D.C., 637  
 Brassett, A.J., 637  
 Bravic, G., 27  
 Brooks, J.S., 217, 251, 257  
 Broude, S.V., 643  
 Brown, S.E., 245  
 Bryson, Paul, 443  
 Budz, S., 177  
 Burdge, G.L., 557  
 Burroughes, J.H., 425  
  
 Campbell, D.K., 419  
 Cao, X.F., 607  
 Catelliani, M., 397  
 Chaikin, P.M., 217, 227, 239,  
 251  
 Chamberlin, R.V., 227  
 Chang, T.Y., 557  
 Chasseau, D., 27, 131  
 Chen, M., 607  
 Chen, Wen-Chang, 589, 595  
 Cheng, L.-T., 487  
  
 Chiang, Long Y., 15, 77, 217,  
 227, 239, 251, 257  
 Child, Andrew D., 369  
 Chung, O.H., 257  
 Colaneri, N.F., 637  
 Conwell, Esther M., 409  
 Cooper, D.E., 557  
 Coronel, P., 537  
 Cowan, Dwaine O., 165  
 Cui, Changxing, 391  
 Cuniberti, C., 459  
 Cunningham, P., 557  
  
 Dalton, Larry R., 443, 551,  
 563, 607  
 Dawnay, E.J.C., 507  
 Day, P., 131  
 DeGroot, Donald C., 317  
 Delhaes, P., 27  
 Dellepiane, G., 459  
 Desiraju, G., 487  
 Destri, S., 397  
 Devine, Robert L.S., 563  
 Dirk, C.W., 543  
 Dixit, S.N., 419  
 Donald, D.S., 487  
 Dorsinville, R., 437, 631  
 Duan, Hailing, 165  
 Ducasse, L., 131  
 Duret, Denis, 171  
 Dykins, J., 341  
  
 Endoh, Makoto, 63  
 Epstein, Arthur J., 283, 293,  
 341, 353  
 Ermer, Susan P., 499  
 Euler, William B., 375  
  
 Fang, T., 543  
 Fann, Yang-Cheng, 161  
 Fares, V., 143  
 Ferris, Kim F., 683, 687  
 Fichou, Denis, 379  
 Flom, Steven R., 595  
 Fortune, N.A., 217  
 Fox, Marye Anne, 199  
 Friedman, B., 671  
 Friend, R.H., 425, 637  
 Fuchigami, H., 691  
  
 Gaillard, F., 359  
 Gammel, J. Tinka, 419  
 Garin, J., 89  
 Garito, A.F., 467, 519  
 Garoche, P., 205

- Gaultier, J., 131  
 Gill, Benjamin C., 375  
 Ginder, John M., 353  
 Giribone, D., 459  
 Goodrich, R.G., 125  
 Goshorn, D.P., 15, 77  
 Gregg, Brian A., 199  
 Grossman, C.H., 519
- Haase, Wolfgang, 525  
 Hamada, Tomoyuki, 659  
 Hamill, Gregory P., 567  
 Hampsch, Hilary L., 625  
 Hanack, Michael, 189  
 Hannahs, S.T., 251, 257  
 Hansen, Glenn A., 499  
 Hanson, Angela K., 683  
 Heeger, A.J., 269  
 Hellwarth, R.W., 607  
 Henry, R.A., 601  
 Heritier, M., 205  
 Hironaga, K., 137  
 Hirsch, A., 189  
 Hoener, Carolyn F., 431  
 Hoffman, Robert C., 697  
 Holland, W.R., 543  
 Hollins, R.A., 155  
 Hoover, J.M., 601  
 Horn, Keith A., 513  
 Horowitz, Gilles, 379  
 Houbib, H., 131  
 Hsueh, K.F., 341  
 Huang, X.Z., 263  
 Hwang, Jyun-Huei, 305, 329
- Imperatori, P., 143  
 Inabe, Tamotsu, 33  
 Inoue, Katsuya, 39  
 Itoh, Koichi, 51, 63  
 Itoh, Yuzo, 659  
 Iwamura, Hiizu, 39
- Jansen, Susan Ann, 161  
 Javadi, H.H.S., 245  
 Jenekhe, Samson A., 589, 595  
 Jeyadev, Surendar, 409  
 Jiang, J.P., 607  
 Jones, M. Thomas, 149
- Kahn, O., 537  
 Kakuta, Atsushi, 659  
 Kamath, Manjunath B., 583  
 Kanatzidis, Mercuri G., 317  
 Kang, W., 251  
 Kannewurf, Carl R., 317  
 Katz, H.E., 543  
 Kajzar, F., 613  
 Kepler, R.G., 453  
 Kernevez, Nelly, 171  
 Kertesz, Miklos, 391
- Kini, A.M., 177  
 Kinoshita, N., 107  
 Kinoshita, Takamasa, 51, 63  
 Knoesen, A., 601  
 Koezuka, H., 691  
 Koga, Noboru, 39  
 Kohler, Bryan E., 649  
 Kowel, S.T., 601  
 Kruger, Jerome, 165  
 Kuczynski, A.P., 507  
 Kumar, S.N., 359  
 Kurata, T., 691  
 Kurmoo, M., 131
- Lahti, Paul M., 83  
 Lange, A., 189  
 Langhoff, C.A., 677  
 Lapouyade, R., 27  
 Laversanne, R., 245, 323  
 Lawrence, R.A., 637  
 Lazaro, F.J., 89  
 LeBlanc, Jr., Oliver H., 119  
 Leung, Doris S., 499  
 Levinson, Mark, 567  
 Lichty, L.R., 385  
 Lindsay, G.A., 601  
 Lipscomb, G.F., 467  
 Lo, Saukwan, 595  
 Loh, Jr., E.Y., 419  
 Lovejoy, Steven M., 499  
 Lowe-Ma, C.K., 557  
 Luzzati, S., 397  
 Lytel, R., 467
- MacDiarmid, Alan G., 283, 293,  
 335, 341, 353  
 Maki, Kazumi, 233, 263  
 Manohar, S.K., 335  
 Marcy, Henry O., 317  
 Maruo, Toshio, 149  
 Maruyama, Yusei, 33  
 Marynick, Dennis S., 369  
 Marzocco, Charles, 329  
 Mazumdar, S., 419  
 McLean, Malcolm R., 563  
 Menardo, C., 335  
 Meredith, G.R., 487  
 Messmer, Richard P., 119  
 Metzger, Robert M., 531  
 Meyer, K.E., 637  
 Meyrueix, R., 619  
 Mignani, G., 619  
 Miller, P., 643  
 Miller, R.D., 447  
 Min, Dong, 149  
 Minato, Masaki, 83  
 Misaki, Y., 3  
 Mizes, Howard A., 409  
 Modarelli, David A., 83  
 Montambaux, G., 217



- Morand, J.P., 27  
 Mori, Yuhei, 665  
 Moron, M.C., 89  
 Mortazavi, M.A., 601  
 Moussavi, Mehdi, 171  
 Mukoh, Akio, 659  
 Murata, H., 637  
 Murata, K., 107
- Nagy, S., 341  
 Nahata, Ajay, 513  
 Nakanishi, K., 137  
 Nallicheri, R.A., 577  
 Naughton, M.J., 227, 257  
 Nayak, Kasinath, 369  
 Nechtschein, M., 335  
 Newman, P.R., 557  
 Nielsen, A.T., 155
- Okamoto, Masayuki, 63  
 Okano, Yoshimichi, 665  
 Ota, Michiya, 71  
 Otani, Sugio, 71
- Pal, A.J., 613  
 Palacio, F., 89  
 Panetta, Charles A., 531  
 Papaefthymiou, Georgia C., 567  
 Patrizio, S., 143  
 Perenboom, Jos. A.A.J., 217  
 Pesty, F., 205  
 Pfeiffer, Matthias, 525  
 Piaggio, P., 459  
 Polak-Dingels, P., 557  
 Polis, David W., 443, 551  
 Potember, Richard S., 697
- Rahal, M., 131  
 Rahman, A.K.M., 643  
 Rath, Nigam P., 149  
 Ray, Anjan, 341, 353  
 Rein, M., 189  
 Renz, G., 189  
 Reyes, J., 89  
 Reynolds, John R., 369  
 Risser, Steven M., 683, 687  
 Rosner, R.B., 363  
 Rossitto, Frank C., 83  
 Rossoni, Philip G., 567  
 Ruani, G., 613  
 Ruaudel-Teixier, A., 537  
 Rubner, M.F., 363, 577  
 Ruiz, Jose P., 369
- Saito, G., 137  
 Saito, Gunzi, 95  
 Saito, S., 637  
 Samuel, I.D.W., 637  
 Samuel, L., 447
- Sanda, P.N., 447  
 Sandman, Daniel J., 567  
 Sapochak, Linda S., 443  
 Sasabe, H., 519  
 Sasagawa, Noriko, 39  
 Satoh, Kazunobu, 63  
 Schilling, M.L., 543  
 Secourgeon, Lilliane, 171  
 Shi, X.D., 239  
 Shichiri, Toyohiro, 63  
 Shieh, Woan-Ru, 329  
 Shinar, J., 385  
 Singer, K.D., 543  
 Singh, Megh, 149  
 Smith, P., 269  
 Spangler, C.W., 443  
 Steier, William H., 563  
 Stetyick, Karen A., 697  
 Su, W.P., 671  
 Sugimoto, T., 3  
 Svensson, Christer, 403  
 Swanson, L.S., 385  
 Szablewski, M., 507
- Takui, Takeji, 51, 63  
 Taliani, C., 613, 631  
 Talwar, Satya S., 583  
 Teki, Yoshio, 51, 63  
 Thompson, D., 447  
 Tindall, P., 15  
 Tokito, S., 269, 637  
 Tokumoto, M., 107  
 Torkelson, John M., 625  
 Travers, J.P., 335  
 Tripathy, S., 643  
 Tsumura, A., 691  
 Tsutsui, T., 637  
 Tubino, R., 397, 437, 631
- Upasani, Ravindra B., 15, 77, 239, 251
- Vaca, P., 323  
 Vanderah, David J., 155  
 Vermehren, P., 189  
 Virosztek, Attila, 233
- Wada, T., 519  
 Walser, A.D., 437  
 Wang, C., 347  
 Wang, H.H., 177  
 Warren, L.F., 557  
 Washington, G., 543  
 Wei, Y., 341  
 Willander, Magnus, 403  
 Williams, J.M., 177  
 Wnek, G.E., 341  
 Wolfe, James F., 499  
 Wong, George K., 625  
 Wróbel, Stanislaw, 525

Wu, Chun-Guey, 317  
Wu, J.W., 467

Xu, Jing-Chun, 125

Yamada, A., 519  
Yamada, S., 519  
Yamochi, H., 137  
Yan, X., 227  
Yang, Jian, 625  
Yang, Lina, 631  
Yang, Sze C., 305, 329  
Yardley, James T., 513  
Yoshida, Z., 3  
Yoshino, K., 385  
Yost, Elizabeth A., 567  
Yu, J., 671  
Yu, L.P., 607  
Yudasaka, M., 137

Zamboni, R., 613, 631  
Zeigler, J.M., 453  
Zhang, D., 305  
Zumsteg, F.C., 487

## Subject Index

- ab initio molecular orbital method, 659  
 angular dependence, 257  
 anion ordering transition, 239, 245  
 anisotropy of coherence length, 107  
  
 band structures in  $(ET)_2X$  salts, 119  
 $\kappa$ -(BEDT-TTF) $_2$ Cu(NCS) $_2$ , 95, 125  
 $\beta$ -(BEDT-TTF) $_2$ X, 107  
 below gap excitation, 437  
 bipolaron, 379  
 bipolaronic charge carrier, 375 intermediate, 443  
 block conjugated copolymer, 589  
 4,4'-(butadiyne-1,4-diyl)-bis(2,2,6,6-tetramethyl-4-hydroxypiperidin-1-oxyl), 567  
  
 charge density wave (CDW), 233, 263  
   hopping transport, 447  
   transfer complex, 15, 27, 161, 165, 217, 245  
 chromophore dipole-dipole interaction, 619  
 colloidal dispersion, 311  
 compressibility, 131  
 conducting polymer, 283, 317, 335, 369  
   composite, 347  
   fiber, 269  
   intrinsic feature, 269  
    $\pi$ -conjugated polymer, 447  
 corona onset poling, 601  
 coumaromethacrylate methylmethacrylate copolymer, 601  
  
 1D fluctuation, 205  
 2-(3,5-di-*t*-butyl-4-hydroxyphenyl)isobutyl methacrylate, 77  
 2,6-dibromo-*N*-methyl-4-nitroaniline, 513  
 Debye temperature, 125  
  
 degenerate four wave mixing (DFWM), 607, 631 picosecond, 595  
 dichroism, 137  
 dimethyltetrathiotetracene, 149  
 diphenylpolyene, 443  
 doped glassy polymer, 625  
  
 earth field magnetometry, 171  
 electric field poling, 543 permittivity, 525  
 electrical conductivity, 323  
 electrically conducting solid, 177  
 electroabsorption spectrum, 453  
 electrochemical oxidative polymerization, 369  
 electrochromic material, 329  
 electron donating radicalenes, 3  
 electronic driving force, 391 excitation energy, 649  
 electro-optic material, 543  
 electrooptic waveguide operation, 467  
 electropolymerization of aniline, 359  
 emeraldine, 283, 293  
 ENDOR technique, 51  
 EPR spectroscopy, low field, 171 within the polymer matrix, 161  
 exciton band, 453  
  
 ferroelectric liquid crystal, 525  
 ferromagnetic behavior, 71 intermolecular interaction, 33, 89  
  
 field desorption mass spectrometry (FD-MS), 341  
 effect transistor, 403  
 induced spin density wave transition (FISDW), 217, 227, 233, 239, 257  
 formation of switching and memory storage, 165

- Fourier transform infrared spectrometry (FTIR), 359
- ground state ferrimagnets, 15
- Hall effect measurement, 403
- helical conformation, 391
- hepta(tetrathiafulvalene) pentaiodide, 137
- hexakis(alkylthio)benzene, 27
- $\alpha, \alpha, \alpha, \alpha', \alpha', \alpha'$ -hexanitro-*p*-xylene, 155
- high magnetic field, 217
- spin density organic solid, 15
- organic molecules, 39, 51, 63
- highly ordered smectic phase, 525
- insulator-metal transition, 409
- intercalative polymerization, 317
- inter-molecular charge transfer, 305
- L-arginine phosphate, 677
- Langmuir Blodgett film, polydiacetylene, 643
- polypyrrole, 363
- technique, 531, 537
- leucoemeraldine, 283, 293
- ligand electronegativity, 683
- liquid crystal, 199
- magnetic memory, 537
- polymers, 51
- susceptibility, 323
- magnetoresistance, 403
- metal diselenolene complex, 177
- dithiolene complex, 177
- insulator-semiconductor (MIS), 425
- MISFET structure, 425
- moisture effect, 335
- molecular electronics, 531, 537
- spin separation, 15
- multifrequency memory device, 507
- $\alpha$ -nitronyl nitroxide, 33
- 1,2- and 2,3-naphthalocyanine, 189
- 4-nitro-3-methoxybenzaldehyde hydrazone, 697
- 4-nitrobenzaldehyde hydrazone, 697
- nickel (II) bis(1,3-dithiole-2-thione-4,5-diselenolate), 177
- nonlinear dielectric function, 687
- optical device, 625
- second order, 499
- organic crystal, second order, 487
- properties, 507, 513, 613, 677
- conducting polymer, 671
- cross conjugated polyene, 665
- polymer, 467
- polythiophene, 631
- quadratic, 519
- second order, 557, 563, 601
- third order, 551, 557, 595, 607, 631
- response, 467
- second order, 543
- susceptibility, 659, 671
- second order, 499
- oligomeric bridged mixed valence compound, 189
- optical absorption spectra, 305
- quality crystal, 557
- optically detected magnetic resonance spectra (ODMR), 385
- organic ferromagnetic materials, 27, 39, 77
- magnetic materials, 83
- polyradicals, 83
- rectifier, 531
- superconductor, 95, 131
- organo-magnetic material, 63
- o*-tolidine, 161
- para-stilbeneoxyl radicals, 83
- Peierls-Hubbard Hamiltonian, 419
- pentacosanoic acid, 691
- pernigraniline, 283, 293
- Perot Fabry interferometry, 619
- phase transition reentrance, 205, 217, 227

- photochromic switching, 507  
 photochromism, 507  
 photoinduced absorption spectroscopy, 613  
 photoluminescence, 385, 637  
 photovoltaic cell, 199  
 phthalocyanine, 189  
 picosecond photocurrent, 437  
 polarons, 293, 443  
 poly(1,4-bis(3-quinolyl)-1,3-butadiene), 583  
 poly(2,5-dimethoxy-p-phenylene vinylene), 269  
 poly(2,5-thienylene vinylene), 269  
   photoexcitation, 637  
 poly(3-alkylthiophene), 397  
 poly(3-hexylthiophene), 385, 403, 691  
 poly(p-phenylene sulfide), 459  
 poly(p-phenylene terephthalamide), 269, 347  
 poly(phenyl methyl silane), 453  
 poly(phenyldiacetylenes), 39  
 polyacetylene, 419, 425  
   trans-, 409, 431  
   stretched, 437  
 polyaniline, 283, 293, 305, 311, 317, 323, 329, 335, 347, 353, 359  
 polyazine, 375  
 polydiacetylene, 567, 577, 583  
 polyene, 649  
 polyheterocycles, 363, 369  
 polymeric surfactant, 311  
 polynuclear aromatic (COPNA) resin, 71  
 polyoxoanion, 143  
 polyphenoxy radicals, 77  
 polyphosphazene, 683  
 polypyrrole, 317, 363  
 polysilane, 447  
 polythiophene, 391  
 polytoluidine, 341  
 polyurethane segmented, 577  
 porphyrins, 199  
 pressure dependence, 131  
 quantum  
   calculation, 677  
   confinement size effect, 589  
   efficiency, 453  
   Hall effect, 251  
   lattice fluctuation, 671  
 quasi one-dimensional  
   organic conductor, 227  
   spin structure, 63  
 quinolinium bis(tetra-cyanoquinodimethane), 171  
 rapid oscillation, 217, 251  
 residual resistivity, 107  
 resonant Raman scattering, 397, 643  
 reversible photoproduction, 431  
 Schiff base metal organic polymers, 89  
 second  
   harmonic generation, 563, 625, 691, 697  
   d.c. electric field induced (EFISH), 499  
   phase matched (PMSG), 519  
   hyperpolarizability, 595  
   order phase transition, 205  
 semiconductor superlattice  
   organic polymer, 589  
   semi-empirical molecular orbital method, 665  
 shish kebab complex, 189  
 single crystal  
   ESR spectroscopy, 63  
   x-ray diffraction, 149  
 solvatochromism, 353  
 sound propagation, 233  
 specific heat measurement, 125  
 spin  
   density wave (SDW), 239, 263  
   transition, 537  
 strained induced transition, 577  
 structureless transition, 245  
 sum frequency mixing, 519  
 superconducting transition, 125  
 superexchange interaction, 63  
 supermolecule, 659  
 superparamagnetic behavior, 89  
 synthetic metal, 149  
   low dimensional, 143  
 1,2,4-trichloro-8-nitrophenoxazin-3-one, 563  
 tetrahydroxypiperazine, 375  
 tetranitroquinodimethane (TNQ), 155  
 tetrathiafulvalene radical cation salt, 143  
 thermochromic transition, 577

thin film  
  capacitor, 363  
  formation, 137  
  superlattice, 363  
thiophene oligomer, 379  
third harmonic generation,  
  613  
(TMTSF)<sub>2</sub>ClO<sub>4</sub>, 257  
(TMTSF)<sub>2</sub>PF<sub>6</sub>, 251  
topology, 51  
transfer integrals, 119  
transition dipoles, 649  
triarylmethane resins,  
  dehydrogenated, 63  
tunneling density of  
  state, 263  
  
x-ray induced transformation,  
  567  
  
Young's modulus, 245

---

MATERIALS RESEARCH SOCIETY SYMPOSIUM PROCEEDINGS

---

ISSN 0272 - 9172

- Volume 1—Laser and Electron-Beam Solid Interactions and Materials Processing, J. F. Gibbons, L. D. Hess, T. W. Sigmon, 1981, ISBN 0-444-00595-1
- Volume 2—Defects in Semiconductors, J. Narayan, T. Y. Tan, 1981, ISBN 0-444-00596-X
- Volume 3—Nuclear and Electron Resonance Spectroscopies Applied to Materials Science, E. N. Kaufmann, G. K. Shenoy, 1981, ISBN 0-444-00597-8
- Volume 4—Laser and Electron-Beam Interactions with Solids, B. R. Appleton, G. K. Celler, 1982, ISBN 0-444-00693-1
- Volume 5—Grain Boundaries in Semiconductors, H. J. Leamy, G. E. Pike, C. H. Seager, 1982, ISBN 0-444-00697-4
- Volume 6—Scientific Basis for Nuclear Waste Management IV, S. V. Topp, 1982, ISBN 0-444-00699-0
- Volume 7—Metastable Materials Formation by Ion Implantation, S. T. Picraux, W. J. Choyke, 1982, ISBN 0-444-00692-3
- Volume 8—Rapidly Solidified Amorphous and Crystalline Alloys, B. H. Kear, B. C. Giessen, M. Cohen, 1982, ISBN 0-444-00698-2
- Volume 9—Materials Processing in the Reduced Gravity Environment of Space, G. E. Rindone, 1982, ISBN 0-444-00691-5
- Volume 10—Thin Films and Interfaces, P. S. Ho, K.-N. Tu, 1982, ISBN 0-444-00774-1
- Volume 11—Scientific Basis for Nuclear Waste Management V, W. Lutze, 1982, ISBN 0-444-00725-3
- Volume 12—In Situ Composites IV, F. D. Lemkey, H. E. Cline, M. McLean, 1982, ISBN 0-444-00726-1
- Volume 13—Laser-Solid Interactions and Transient Thermal Processing of Materials, J. Narayan, W. L. Brown, R. A. Lemons, 1983, ISBN 0-444-00788-1
- Volume 14—Defects in Semiconductors II, S. Mahajan, J. W. Corbett, 1983, ISBN 0-444-00812-8
- Volume 15—Scientific Basis for Nuclear Waste Management VI, D. G. Brookins, 1983, ISBN 0-444-00780-6
- Volume 16—Nuclear Radiation Detector Materials, E. E. Haller, H. W. Kraner, W. A. Higinbotham, 1983, ISBN 0-444-00787-3
- Volume 17—Laser Diagnostics and Photochemical Processing for Semiconductor Devices, R. M. Osgood, S. R. J. Brueck, H. R. Schlossberg, 1983, ISBN 0-444-00782-2
- Volume 18—Interfaces and Contacts, R. Ludeke, K. Rose, 1983, ISBN 0-444-00820-9
- Volume 19—Alloy Phase Diagrams, L. H. Bennett, T. B. Massalski, B. C. Giessen, 1983, ISBN 0-444-00809-8
- Volume 20—Intercalated Graphite, M. S. Dresselhaus, G. Dresselhaus, J. E. Fischer, M. J. Moran, 1983, ISBN 0-444-00781-4
- Volume 21—Phase Transformations in Solids, T. Tsakalakos, 1984, ISBN 0-444-00901-9
- Volume 22—High Pressure in Science and Technology, C. Homan, R. K. MacCrone, E. Whalley, 1984, ISBN 0-444-00932-9 (3 part set)
- Volume 23—Energy Beam-Solid Interactions and Transient Thermal Processing, J. C. C. Fan, N. M. Johnson, 1984, ISBN 0-444-00903-5
- Volume 24—Defect Properties and Processing of High-Technology Nonmetallic Materials, J. H. Crawford, Jr., Y. Chen, W. A. Sibley, 1984, ISBN 0-444-00904-3
- Volume 25—Thin Films and Interfaces II, J. E. E. Baglin, D. R. Campbell, W. K. Chu, 1984, ISBN 0-444-00905-1

---

**MATERIALS RESEARCH SOCIETY SYMPOSIUM PROCEEDINGS**

---

- Volume 26—Scientific Basis for Nuclear Waste Management VII, G. L. McVay, 1984, ISBN 0-444-00906-X
- Volume 27—Ion Implantation and Ion Beam Processing of Materials, G. K. Hubler, O. W. Holland, C. R. Clayton, C. W. White, 1984, ISBN 0-444-00869-1
- Volume 28—Rapidly Solidified Metastable Materials, B. H. Kear, B. C. Giessen, 1984, ISBN 0-444-00935-3
- Volume 29—Laser-Controlled Chemical Processing of Surfaces, A. W. Johnson, D. J. Ehrlich, H. R. Schlossberg, 1984, ISBN 0-444-00894-2
- Volume 30—Plasma Processing and Synthesis of Materials, J. Szekely, D. Apelian, 1984, ISBN 0-444-00895-0
- Volume 31—Electron Microscopy of Materials, W. Krakow, D. A. Smith, L. W. Hobbs, 1984, ISBN 0-444-00898-7
- Volume 32—Better Ceramics Through Chemistry, C. J. Brinker, D. E. Clark, D. R. Ulrich, 1984, ISBN 0-444-00898-5
- Volume 33—Comparison of Thin Film Transistor and SOI Technologies, H. W. Lam, M. J. Thompson, 1984, ISBN 0-444-00899-3
- Volume 34—Physical Metallurgy of Cast Iron, H. Fredriksson, M. Hillerts, 1985, ISBN 0-444-00938-8
- Volume 35—Energy Beam-Solid Interactions and Transient Thermal Processing/1984, D. K. Biegelsen, G. A. Rozgonyi, C. V. Shank, 1985, ISBN 0-931837-00-6
- Volume 36—Impurity Diffusion and Gettering in Silicon, R. B. Fair, C. W. Pearce, J. Washburn, 1985, ISBN 0-931837-01-4
- Volume 37—Layered Structures, Epitaxy, and Interfaces, J. M. Gibson, L. R. Dawson, 1985, ISBN 0-931837-02-2
- Volume 38—Plasma Synthesis and Etching of Electronic Materials, R. P. H. Chang, B. Abeles, 1985, ISBN 0-931837-03-0
- Volume 39—High-Temperature Ordered Intermetallic Alloys, C. C. Koch, C. T. Liu, N. S. Stoloff, 1985, ISBN 0-931837-04-9
- Volume 40—Electronic Packaging Materials Science, E. A. Giess, K.-N. Tu, D. R. Uhlmann, 1985, ISBN 0-931837-05-7
- Volume 41—Advanced Photon and Particle Techniques for the Characterization of Defects in Solids, J. B. Roberto, R. W. Carpenter, M. C. Wittels, 1985, ISBN 0-931837-06-5
- Volume 42—Very High Strength Cement-Based Materials, J. F. Young, 1985, ISBN 0-931837-07-3
- Volume 43—Fly Ash and Coal Conversion By-Products: Characterization, Utilization, and Disposal I, G. J. McCarthy, R. J. Lauf, 1985, ISBN 0-931837-08-1
- Volume 44—Scientific Basis for Nuclear Waste Management VIII, C. M. Jantzen, J. A. Stone, R. C. Ewing, 1985, ISBN 0-931837-09-X
- Volume 45—Ion Beam Processes in Advanced Electronic Materials and Device Technology, B. R. Appleton, F. H. Eisen, T. W. Sigmon, 1985, ISBN 0-931837-10-3
- Volume 46—Microscopic Identification of Electronic Defects in Semiconductors, N. M. Johnson, S. G. Bishop, G. D. Watkins, 1985, ISBN 0-931837-11-1
- Volume 47—Thin Films: The Relationship of Structure to Properties, C. R. Aita, K. S. SreeHarsha, 1985, ISBN 0-931837-12-X
- Volume 48—Applied Materials Characterization, W. Katz, P. Williams, 1985, ISBN 0-931837-13-8
- Volume 49—Materials Issues in Applications of Amorphous Silicon Technology, D. Adler, A. Madan, M. J. Thompson, 1985, ISBN 0-931837-14-6



---

MATERIALS RESEARCH SOCIETY SYMPOSIUM PROCEEDINGS

---

- Volume 50—Scientific Basis for Nuclear Waste Management IX, L. O. Werme, 1986, ISBN 0-931837-15-4
- Volume 51—Beam-Solid Interactions and Phase Transformations, H. Kurz, G. L. Olson, J. M. Poate, 1986, ISBN 0-931837-16-2
- Volume 52—Rapid Thermal Processing, T. O. Sedgwick, T. E. Seidel, B.-Y. Tsaur, 1986, ISBN 0-931837-17-0
- Volume 53—Semiconductor-on-Insulator and Thin Film Transistor Technology, A. Chiang, M. W. Geis, L. Pfeiffer, 1986, ISBN 0-931837-18-9
- Volume 54—Thin Films—Interfaces and Phenomena, R. J. Nemanich, P. S. Ho, S. S. Lau, 1986, ISBN 0-931837-19-7
- Volume 55—Biomedical Materials, J. M. Williams, M. F. Nichols, W. Zingg, 1986, ISBN 0-931837-20-0
- Volume 56—Layered Structures and Epitaxy, J. M. Gibson, G. C. Osbourn, R. M. Tromp, 1986, ISBN 0-931837-21-9
- Volume 57—Phase Transitions in Condensed Systems—Experiments and Theory, G. S. Cargill III, F. Spaepen, K.-N. Tu, 1987, ISBN 0-931837-22-7
- Volume 58—Rapidly Solidified Alloys and Their Mechanical and Magnetic Properties, B. C. Giessen, D. E. Polk, A. I. Taub, 1986, ISBN 0-931837-23-5
- Volume 59—Oxygen, Carbon, Hydrogen, and Nitrogen in Crystalline Silicon, J. C. Mikkelsen, Jr., S. J. Pearton, J. W. Corbett, S. J. Pennycook, 1986, ISBN 0-931837-24-3
- Volume 60—Defect Properties and Processing of High-Technology Nonmetallic Materials, Y. Chen, W. D. Kingery, R. J. Stokes, 1986, ISBN 0-931837-25-1
- Volume 61—Defects in Glasses, F. L. Galeener, D. L. Griscom, M. J. Weber, 1986, ISBN 0-931837-26-X
- Volume 62—Materials Problem Solving with the Transmission Electron Microscope, L. W. Hobbs, K. H. Westmacott, D. B. Williams, 1986, ISBN 0-931837-27-8
- Volume 63—Computer-Based Microscopic Description of the Structure and Properties of Materials, J. Broughton, W. Krakow, S. T. Pantelides, 1986, ISBN 0-931837-28-6
- Volume 64—Cement-Based Composites: Strain Rate Effects on Fracture, S. Mindess, S. P. Shah, 1986, ISBN 0-931837-29-4
- Volume 65—Fly Ash and Coal Conversion By-Products: Characterization, Utilization and Disposal II, G. J. McCarthy, F. P. Glasser, D. M. Roy, 1986, ISBN 0-931837-30-8
- Volume 66—Frontiers in Materials Education, L. W. Hobbs, G. L. Liedl, 1986, ISBN 0-931837-31-6
- Volume 67—Heteroepitaxy on Silicon, J. C. C. Fan, J. M. Poate, 1986, ISBN 0-931837-33-2
- Volume 68—Plasma Processing, J. W. Coburn, R. A. Gottscho, D. W. Hess, 1986, ISBN 0-931837-34-0
- Volume 69—Materials Characterization, N. W. Cheung, M.-A. Nicolet, 1986, ISBN 0-931837-35-9
- Volume 70—Materials Issues in Amorphous-Semiconductor Technology, D. Adler, Y. Hamakawa, A. Madan, 1986, ISBN 0-931837-36-7
- Volume 71—Materials Issues in Silicon Integrated Circuit Processing, M. Wittmer, J. Stimmell, M. Strathman, 1986, ISBN 0-931837-37-5
- Volume 72—Electronic Packaging Materials Science II, K. A. Jackson, R. C. Pohanka, D. R. Uhlmann, D. R. Ulrich, 1986, ISBN 0-931837-38-3
- Volume 73—Better Ceramics Through Chemistry II, C. J. Brinker, D. E. Clark, D. R. Ulrich, 1986, ISBN 0-931837-39-1
- Volume 74—Beam-Solid Interactions and Transient Processes, M. O. Thompson, S. T. Picraux, J. S. Williams, 1987, ISBN 0-931837-40-5

---

MATERIALS RESEARCH SOCIETY SYMPOSIUM PROCEEDINGS

---

- Volume 75—Photon, Beam and Plasma Stimulated Chemical Processes at Surfaces, V. M. Donnelly, I. P. Herman, M. Hirose, 1987, ISBN 0-931837-41-3
- Volume 76—Science and Technology of Microfabrication, R. E. Howard, E. L. Hu, S. Namba, S. Pang, 1987, ISBN 0-931837-42-1
- Volume 77—Interfaces, Superlattices, and Thin Films, J. D. Dow, I. K. Schuller, 1987, ISBN 0-931837-56-1
- Volume 78—Advances in Structural Ceramics, P. F. Becher, M. V. Swain, S. Sōmiya, 1987, ISBN 0-931837-43-X
- Volume 79—Scattering, Deformation and Fracture in Polymers, G. D. Wignall, B. Crist, T. P. Russell, E. L. Thomas, 1987, ISBN 0-931837-44-8
- Volume 80—Science and Technology of Rapidly Quenched Alloys, M. Tenhover, W. L. Johnson, L. E. Tanner, 1987, ISBN 0-931837-45-6
- Volume 81—High-Temperature Ordered Intermetallic Alloys, II, N. S. Stoloff, C. C. Koch, C. T. Liu, O. Izumi, 1987, ISBN 0-931837-46-4
- Volume 82—Characterization of Defects in Materials, R. W. Siegel, J. R. Weertman, R. Sinclair, 1987, ISBN 0-931837-47-2
- Volume 83—Physical and Chemical Properties of Thin Metal Overlayers and Alloy Surfaces, D. M. Zehner, D. W. Goodman, 1987, ISBN 0-931837-48-0
- Volume 84—Scientific Basis for Nuclear Waste Management X, J. K. Bates, W. B. Seefeldt, 1987, ISBN 0-931837-49-9
- Volume 85—Microstructural Development During the Hydration of Cement, L. Struble, P. Brown, 1987, ISBN 0-931837-50-2
- Volume 86—Fly Ash and Coal Conversion By-Products Characterization, Utilization and Disposal III, G. J. McCarthy, F. P. Glasser, D. M. Roy, S. Diamond, 1987, ISBN 0-931837-51-0
- Volume 87—Materials Processing in the Reduced Gravity Environment of Space, R. H. Doremus, P. C. Nordine, 1987, ISBN 0-931837-52-9
- Volume 88—Optical Fiber Materials and Properties, S. R. Nagel, J. W. Fleming, G. Sigel, D. A. Thompson, 1987, ISBN 0-931837-53-7
- Volume 89—Diluted Magnetic (Semimagnetic) Semiconductors, R. L. Aggarwal, J. K. Furdyna, S. von Molnar, 1987, ISBN 0-931837-54-5
- Volume 90—Materials for Infrared Detectors and Sources, R. F. C. Farrow, J. F. Schetzina, J. T. Cheung, 1987, ISBN 0-931837-55-3
- Volume 91—Heteroepitaxy on Silicon II, J. C. C. Fan, J. M. Phillips, B.-Y. Tsaur, 1987, ISBN 0-931837-58-8
- Volume 92—Rapid Thermal Processing of Electronic Materials, S. R. Wilson, R. A. Powell, D. E. Davies, 1987, ISBN 0-931837-59-6
- Volume 93—Materials Modification and Growth Using Ion Beams, U. Gibson, A. E. White, P. P. Pronko, 1987, ISBN 0-931837-60-X
- Volume 94—Initial Stages of Epitaxial Growth, R. Hull, J. M. Gibson, David A. Smith, 1987, ISBN 0-931837-61-8
- Volume 95—Amorphous Silicon Semiconductors—Pure and Hydrogenated, A. Madan, M. Thompson, D. Adler, Y. Hamakawa, 1987, ISBN 0-931837-62-6
- Volume 96—Permanent Magnet Materials, S. G. Sankar, J. F. Herbst, N. C. Koon, 1987, ISBN 0-931837-63-4
- Volume 97—Novel Refractory Semiconductors, D. Emin, T. Aselage, C. Wood, 1987, ISBN 0-931837-64-2
- Volume 98—Plasma Processing and Synthesis of Materials, D. Apelian, J. Szekely, 1987, ISBN 0-931837-65-0

---

MATERIALS RESEARCH SOCIETY SYMPOSIUM PROCEEDINGS

---

- Volume 99—High-Temperature Superconductors, M. B. Brodsky, R. C. Dynes, K. Kitazawa, H. L. Tuller, 1988, ISBN 0-931837-67-7
- Volume 100—Fundamentals of Beam-Solid Interactions and Transient Thermal Processing, M. J. Aziz, L. E. Rehn, B. Stritzker, 1988, ISBN 0-931837-68-5
- Volume 101—Laser and Particle-Beam Chemical Processing for Microelectronics, D.J. Ehrlich, G.S. Higashi, M.M. Oprysko, 1988, ISBN 0-931837-69-3
- Volume 102—Epitaxy of Semiconductor Layered Structures, R. T. Tung, L. R. Dawson, R. L. Gunshor, 1988, ISBN 0-931837-70-7
- Volume 103—Multilayers: Synthesis, Properties, and Nonelectronic Applications, T. W. Barbee Jr., F. Spaepen, L. Greer, 1988, ISBN 0-931837-71-5
- Volume 104—Defects in Electronic Materials, M. Stavola, S. J. Pearton, G. Davies, 1988, ISBN 0-931837-72-3
- Volume 105—SiO<sub>2</sub> and Its Interfaces, G. Lucovsky, S. T. Pantelides, 1988, ISBN 0-931837-73-1
- Volume 106—Polysilicon Films and Interfaces, C.Y. Wong, C.V. Thompson, K-N. Tu, 1988, ISBN 0-931837-74-X
- Volume 107—Silicon-on-Insulator and Buried Metals in Semiconductors, J. C. Sturm, C. K. Chen, L. Pfeiffer, P. L. F. Hemment, 1988, ISBN 0-931837-75-8
- Volume 108—Electronic Packaging Materials Science II, R. C. Sundahl, R. Jaccodine, K. A. Jackson, 1988, ISBN 0-931837-76-6
- Volume 109—Nonlinear Optical Properties of Polymers, A. J. Heeger, J. Orenstein, D. R. Ulrich, 1988, ISBN 0-931837-77-4
- Volume 110—Biomedical Materials and Devices, J. S. Hanker, B. L. Giammara, 1988, ISBN 0-931837-78-2
- Volume 111—Microstructure and Properties of Catalysts, M. M. J. Treacy, J. M. Thomas, J. M. White, 1988, ISBN 0-931837-79-0
- Volume 112—Scientific Basis for Nuclear Waste Management XI, M. J. Apted, R. E. Westerman, 1988, ISBN 0-931837-80-4
- Volume 113—Fly Ash and Coal Conversion By-Products: Characterization, Utilization, and Disposal IV, G. J. McCarthy, D. M. Roy, F. P. Glasser, R. T. Hemmings, 1988, ISBN 0-931837-81-2
- Volume 114—Bonding in Cementitious Composites, S. Mindess, S. P. Shah, 1988, ISBN 0-931837-82-0
- Volume 115—Specimen Preparation for Transmission Electron Microscopy of Materials, J. C. Bravman, R. Anderson, M. L. McDonald, 1988, ISBN 0-931837-83-9
- Volume 116—Heteroepitaxy on Silicon: Fundamentals, Structures, and Devices, H.K. Choi, H. Ishiwara, R. Hull, R.J. Nemanich, 1988, ISBN: 0-931837-86-3
- Volume 117—Process Diagnostics: Materials, Combustion, Fusion, K. Hays, A.C. Eckbreth, G.A. Campbell, 1988, ISBN: 0-931837-87-1
- Volume 118—Amorphous Silicon Technology, A. Madan, M.J. Thompson, P.C. Taylor, P.G. LeComber, Y. Hamakawa, 1988, ISBN: 0-931837-88-X
- Volume 119—Adhesion in Solids, D.M. Mattox, C. Batich, J.E.E. Baglin, R.J. Gottschall, 1988, ISBN: 0-931837-89-8
- Volume 120—High-Temperature/High-Performance Composites, F.D. Lemkey, A.G. Evans, S.G. Fishman, J.R. Strife, 1988, ISBN: 0-931837-90-1
- Volume 121—Better Ceramics Through Chemistry III, C.J. Brinker, D.E. Clark, D.R. Ulrich, 1988, ISBN: 0-931837-91-X

---

MATERIALS RESEARCH SOCIETY SYMPOSIUM PROCEEDINGS

---

- Volume 122—Interfacial Structure, Properties, and Design, M.H. Yoo, W.A.T. Clark, C.L. Briant, 1988, ISBN: 0-931837-92-8
- Volume 123—Materials Issues in Art and Archaeology, E.V. Sayre, P. Vandiver, J. Druzik, C. Stevenson, 1988, ISBN: 0-931837-93-6
- Volume 124—Microwave-Processing of Materials, M.H. Brooks, I.J. Chabinsky, W.H. Sutton, 1988, ISBN: 0-931837-94-4
- Volume 125—Materials Stability and Environmental Degradation, A. Barkatt, L.R. Smith, E. Verink, 1988, ISBN: 0-931837-95-2
- Volume 126—Advanced Surface Processes for Optoelectronics, S. Bernasek, T. Venkatesan, H. Temkin, 1988, ISBN: 0-931837-96-0
- Volume 127—Scientific Basis for Nuclear Waste Management XII, W. Lutze, R.C. Ewing, 1989, ISBN: 0-931837-97-9
- Volume 128—Processing and Characterization of Materials Using Ion Beams, L.E. Rehn, J. Greene, F.A. Smidt, 1989, ISBN: 1-55899-001-1
- Volume 129—Laser and Particle-Beam Modification of Chemical Processes on Surfaces, A.W. Johnson, G.L. Loper, T.W. Sigmon, 1989, ISBN: 1-55899-002-X
- Volume 130—Thin Films: Stresses and Mechanical Properties, J.C. Bravman, W.D. Nix, D.M. Barnett, D.A. Smith, 1989, ISBN: 1-55899-003-8
- Volume 131—Chemical Perspectives of Microelectronic Materials, M.E. Gross, J. Jasinski, J.T. Yates, Jr., 1989, ISBN: 1-55899-004-6
- Volume 132—Multicomponent Ultrafine Microstructures, L.E. McCandlish, B.H. Kear, D.E. Polk, and R.W. Siegel, 1989, ISBN: 1-55899-005-4
- Volume 133—High Temperature Ordered Intermetallic Alloys III, C.T. Liu, A.I. Taub, N.S. Stoloff, C.C. Koch, 1989, ISBN: 1-55899-006-2
- Volume 134—The Materials Science and Engineering of Rigid-Rod Polymers, W.W. Adams, R.K. Eby, D.E. McLemore, 1989, ISBN: 1-55899-007-0
- Volume 135—Solid State Ionics, G. Nazri, R.A. Huggins, D.F. Shriver, 1989, ISBN: 1-55899-008-9
- Volume 136—Fly Ash and Coal Conversion By-Products: Characterization, Utilization and Disposal V, R.T. Hemmings, E.E. Berry, G.J. McCarthy, F.P. Glasser, 1989, ISBN: 1-55899-009-7
- Volume 137—Pore Structure and Permeability of Cementitious Materials, L.R. Roberts, J.P. Skalny, 1989, ISBN: 1-55899-010-0
- Volume 138—Characterization of the Structure and Chemistry of Defects in Materials, B.C. Larson, M. Ruhle, D.N. Seidman, 1989, ISBN: 1-55899-011-9
- Volume 139—High Resolution Microscopy of Materials, W. Krakow, F.A. Ponce, D.J. Smith, 1989, ISBN: 1-55899-012-7
- Volume 140—New Materials Approaches to Tribology: Theory and Applications, L.E. Pope, L. Fehrenbacher, W.O. Winer, 1989, ISBN: 1-55899-013-5
- Volume 141—Atomic Scale Calculations in Materials Science, J. Tersoff, D. Vanderbilt, V. Vitek, 1989, ISBN: 1-55899-014-3
- Volume 142—Nondestructive Monitoring of Materials Properties, J. Holbrook, J. Bussiere, 1989, ISBN: 1-55899-015-1
- Volume 143—Synchrotron Radiation in Materials Research, R. Clarke, J. Gland, J.H. Weaver, 1989, ISBN: 1-55899-016-X
- Volume 144—Advances in Materials, Processing and Devices in III-V Compound Semiconductors, D.K. Sadana, L. Eastman, R. Dupuis, 1989, ISBN: 1-55899-017-8

*Recent Materials Research Society Proceedings listed in the front.*

---

MATERIALS RESEARCH SOCIETY CONFERENCE PROCEEDINGS

---

Tungsten and Other Refractory Metals for VLSI Applications, Robert S. Blewer, 1986; ISSN 0886-7860; ISBN 0-931837-32-4

Tungsten and Other Refractory Metals for VLSI Applications II, Eliot K. Broadbent, 1987; ISSN 0886-7860; ISBN 0-931837-66-9

Ternary and Multinary Compounds, Satyen K. Deb, Alex Zunger, 1987; ISBN 0-931837-57-X

Tungsten and Other Refractory Metals for VLSI Applications III, Victor A. Wells, 1988; ISSN 0886-7860; ISBN 0-931837-84-7

Atomic and Molecular Processing of Electronic and Ceramic Materials: Preparation, Characterization and Properties, Ilhan A. Aksay, Gary L. McVay, Thomas G. Stoebe, J.F. Wager, 1988; ISBN 0-931837-85-5

Materials Futures: Strategies and Opportunities, R. Byron Pipes, U.S. Organizing Committee, Rune Lagneborg, Swedish Organizing Committee, 1988; ISBN 1-55899-000-3

Tungsten and Other Refractory Metals for VLSI Applications IV, Robert S. Blewer, Carol M. McConica, 1989; ISSN 0886-7860; ISBN 0-931837-98-7

Tungsten and Other Advanced Metals for VLSI/ULSI Applications V, S. Simon Wong, Seiji Furukawa, 1990; ISSN 1048-0854; ISBN 1-55899-086-2

High Energy and Heavy Ion Beams in Materials Analysis, Joseph R. Tesmer, Carl J. Maggiore, Michael Nastasi, J. Charles Barbour, James W. Mayer, 1990; ISBN 1-55899-091-7

Physical Metallurgy of Cast Iron IV, Goro Ohira, Takaji Kusakawa, Eisuke Niyama, 1990; ISBN 1-55899-090-9